PROCEEDINGS
ACRS 2018

THE 39TH
ASIAN CONFERENCE
ON REMOTE SENSING

KUALA LUMPUR

"REMOTE SENSING
ENABLING PROSPERITY"

15 - 19 Oktober 2018
Renaissance Kuala Lumpur Hotel

VOL. 5/5

ACRS2018
THE 39TH ASIAN CONFERENCE ON REMOTE SENSING
KUALA LUMPUR
"REMOTE SENSING ENABLING PROSPERITY"

POSTER SESSION
SESSION 01 & 02

Transition in NDVI of forcibly withering potted trees

Kousuke Hida(1), Mitsuharu Tokunaga(2)

Kanazawa Institute of Technology
7-1 Ohgigaoka, Nonoichi, Ishikawa 921-8501, Japan
[1]Email: b1444953@planet.kanazawa-it.ac.jp
[2]Email: mtoku@neptune.kanazawa-it.ac.jp

KEY WORDS: NIR, NDVI, withering evaluation of tree

ABSTRACT: In order to judge trees with risk of collapse, we observed and compared healthy potted trees and unhealthy potted trees with near infrared camera. In Japan, the health conditions of trees have been judged by visual diagnosis by experts but it is inefficient. Hence, a system of efficient and make quantitative judgement is urged. Therefore, in this study, even if the phenomenon of potted trees deterioration can't be confirmed by visual we verified whether it can be confirmed by decrease in NDVI. In addition, we verified whether health condition such as withering leaves and discoloration of leaves can be confirmed by comparing visible image and NDVI transition. Two similar potted Conifers were observed with near infrared camera a day. In order to clarify healthy and unhealthy subjects, one subject was forced to deteriorate with two patterns. The first pattern was sprinkling herbicide on the soil. Second, the trunk was scratched and it was applied herbicide. As results, NDVI transition of the first pattern showed a similar trend to healthy subject for several days. After that, leaves of unhealthy subjects withered, discoloration of leaves, NDVI transition tended to gradually decrease. This result showed phenomenon that the object deteriorated by sprinkled herbicide. The NDVI transition of the second pattern tended to decrease, the phenomenon of deterioration can be confirmed. In this study, the phenomenon of deterioration of potted trees could be confirmed by comparing NDVI transition of healthy potted trees and unhealthy trees which was forced to deteriorate. Also, difference in NDVI between healthy and unhealthy subjects could be shown as difference in health condition by comparing NDVI and visually images.

1. INTRODUCTION

In order to judge trees with risk of collapse, we observed and compared healthy potted trees and unhealthy potted trees with near infrared camera. In Japan, the health conditions of trees have been judged by visual diagnosis by experts but it is inefficient. Hence, a system of efficient and make quantitative judgement is urged. Therefore, in this study, even if the phenomenon of potted trees deterioration can't be confirmed by visual we verified whether it can be confirmed by decrease in NDVI. In addition, we verified whether health condition such as withering leaves and discoloration of leaves can be confirmed by comparing visible image and NDVI transition.

2. EXPERIMENT METHODS

Two similar potted Conifers were observed with near infrared camera a day. In order to clarify healthy and unhealthy subjects, one subject was forced to deteriorate with two patterns. The first pattern was sprinkling herbicide on the soil and observed at a sunny place. After a few days, the trunk was scratched and it was applied herbicide. Second, the trunk was scratched, it was applied herbicide and observed at a shade. The average of the NDVI of each object was calculated from the near infrared images moreover, the NDVI transition was compared. In addition, the NDVI transition and health condition such as withering leaves and discoloration of leaves were compared.

3. RESULTS

Fig.1 shows the NDVI transition of the first pattern. From May 28 when herbicide was sprinkled on the soil to July 11 when the trunk was scratched and it was applied herbicide, NDVI transition of withering subject showed a tendency similar to healthy subject. NDVI which observed on a sunny day tended to high and NDVI which observed on a cloudy day tended to low. It was confirmed that NDVI increase and decrease by sunlight condition. Difference such as withering leaves of both objects couldn't confirm by comparing Fig.2 which show visible image observed on May 28 with Fig.3 which show visible image observed on July 11. Sprinkling herbicide on the soil was very ineffective at deteriorating Conifers and both subjects were healthy. Therefore, NDVI transition of healthy and similar potted trees shows the same trend.
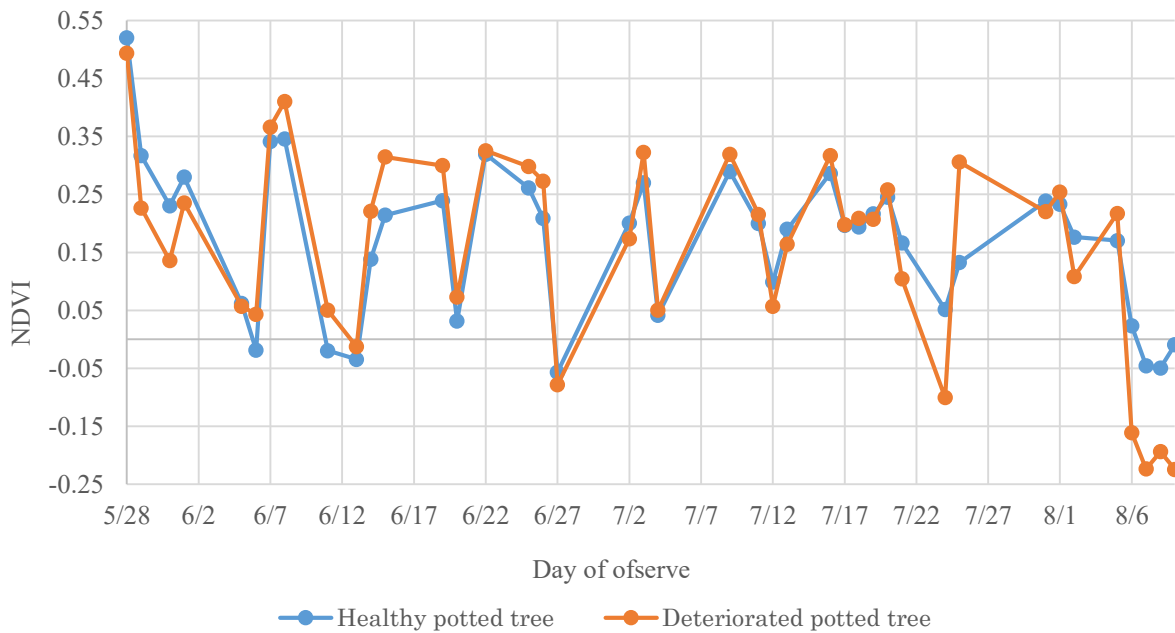
Fig.1 NDVI transition observed at a sunny place.

Fig.2 May 28, Healthy Conifer (left) and
deteriorated Conifer (right)

Fig.3 July 11, Healthy Conifer (left) and
deteriorated Conifer (right)

From July 11 the trunk was scratched, it was applied herbicide and urged deterioration. As shown in Fig.4, progress of deterioration was confirmed from withering leaves could be confirmed on the top of deteriorated subject on July 18. However, in Fig.1, July 18, difference in NDVI transition of both subjects couldn't be confirmed. In Fig.1, from July 20 to July 24, the NDVI of deteriorated subject tended to decrease. At this time, as shown in Fig.5, the deteriorated subject was withering leaves in various places. This result shows phenomenon that the leaves withered and potted trees deteriorated. In Fig.1 the NDVI of deteriorated subject exceeded the NDVI of healthy subject on July 25, August 1, and 5. Each data was observed on a sunny day, NDVI of withering leaves tended to be high and NDVI of green leaves tended to low. This result shows that NDVI of withering leaves became high by strong sunlight reflection.

Fig.4 July 18, Healthy Conifer (left) and deteriorated Conifer (right)

Fig.5 July 24, Healthy Conifer (left) and deteriorated Conifer (right)

Fig.6 shows the NDVI transition of the second pattern. Increase and decrease of NDVI transition of second pattern was smaller than first pattern. Increase and decrease of NDVI transition according to sunlight conditions was able to small by being observed at a shade. In Fig.6, from August 20 to 23, the NDVI of deteriorated subject decreased. Withering leaves couldn't confirm by comparing Fig.7 which show visible image observed on August 13 with Fig.8 which show visible image observed on August 23. However, as shown in Fig.9, Withering leaves could confirm on August 27. Thus, the decrease in NDVI between August 20 and 23 is shows sign of potted trees deterioration which can't be confirmed by visual. The NDVI of deteriorated subject decreased on August 27 and it was withering leaves in various places. In addition, September 4, as shown in Fig.10, deterioration further progressed and NDVI further decreased. This result shows degree of deterioration was the difference between NDVI of healthy potted trees and NDVI of unhealthy potted trees.
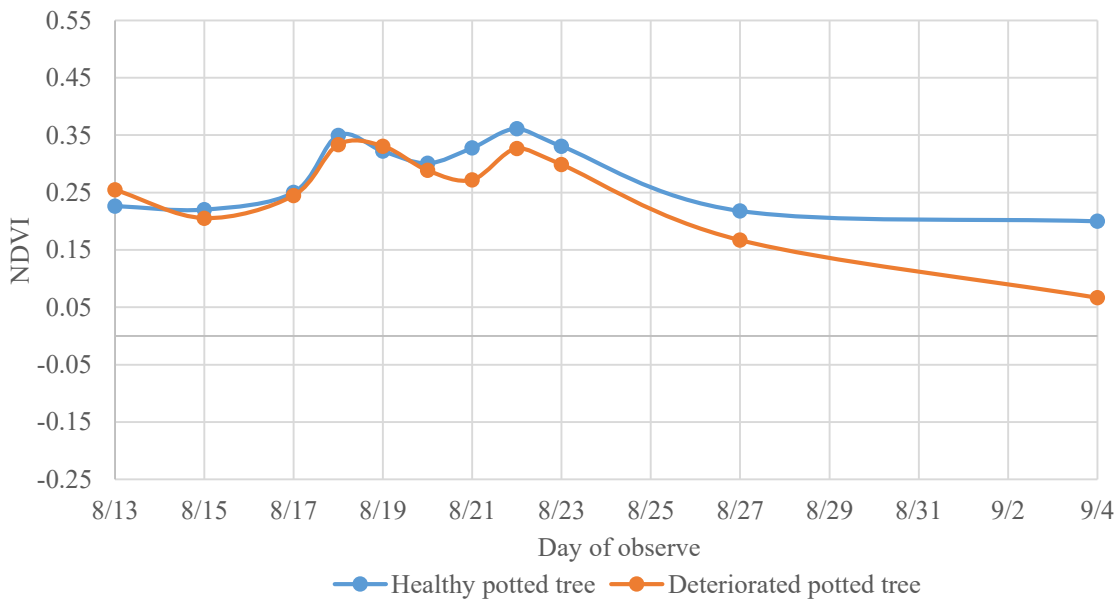

Fig.6 NDVI transition observed at a shade

Fig.7   August 13, Healthy Conifer (left) and deteriorated Conifer (right)

Fig.8   August 23, Healthy Conifer (left) and deteriorated Conifer (right)

Fig.9   August 27, Healthy Conifer (left) and deteriorated Conifer (right)

Fig.10   September 4, Healthy Conifer (left) and deteriorated Conifer (right)

4.   CONCLUSIONS

In this study, the phenomenon of unhealthy potted trees deterioration which can't be confirmed by visual was confirmed by NDVI decreased. Also, health condition such as withering leaves and discoloration of leaves was confirmed, it was the difference between NDVI of healthy potted trees and NDVI of unhealthy potted trees. However, it was the case when potted trees were observed at a shade. NDVI of withering leaves tended to be high and NDVI of green leaves tended to low when observed at a sunny place by strong sunlight reflection. In future, even if observation at a sunny place, observation method that can confirm phenomenon of potted trees deterioration by decrease in NDVI should be discovered.

The Rice Fields Analysis by the Seasonal Variation Tendency

Seiji Ito (1), Yoshinari Oguro (1), Tomohisa Konishi (1) and Jukkrit Mahujchariyawong (2)

[1] Department of Global Environment Studies, Faculty of Environmental Studies, Hiroshima Institute of Technology, 2-1-1 Miyake, Saeki-ku, Hiroshima, Hiroshima, 731-5193, Japan

[2] Department of Environmental Technology and Management, Faculty of Environment, Kasetsart University, P.O. 1072 Kasetsart, Chatuchak, Bangkok 10903, Thailand

Email: seiji@cc.it-hiroshima.ac.jp; y.oguro.yx@it-hiroshima.ac.jp; t.konishi.vd@it-hiroshima.ac.jp; mjukkrit@hotmail.com

KEY WORDS: Rice field, Thailand, NDVI, Sentinel-2/MSI

ABSTRACT   The aim of this paper is to analyze the number of rice crop times per a year from the Sentinel-2/MSI data. The study area is around the Chao Phraya River in the north area of Bangkok, Thailand. At first, we have obtained the Sentinel-2/MSI data set for a year and divided the data set into the several seasons. In the next, Normalized Difference Vegetation Index (NDVI) have been obtained by the MSI images, NDVI data without cloud has been obtained by the seasonal data set. We have estimated the number of crop times by counting where the NDVI suddenly increase and decrease from the seasonal data set of one year. The mask data of river and buildings has been create by the ISODATA classification method, a good result can be obtain. We found that many rice fields had once harvest, a part of the field had more than twice harvests.

1.   INTRODUCTION

Thailand is warm throughout the year and there are three seasons: the dry season (from November to March), the hot season (April), and the rainy season (from May to October), with low temperature and low rain in the dry season, high temperature in the hot season and heavy rain in the rainy season. Therefore, in the Chao Phraya River basin of Thailand, rice requiring a lot of water have been cultivated mainly, and harvested more than once a year. Since the number of rice crops is different with each rice field, the water supply is disorderly. It is necessary to monitor rice fields, to grasp the number of cropping times. Therefore, The aim of this paper is to recognize the number of rice crop times per a year using the Earth observation satellite image data which can observe the earth surface widely and periodically.

In this study, we use the Sentinel-2 / MSI data set of the optical satellite image of 2016 for the Chai Nat prefecture which locate in northern part of Bangkok, and obtain the number of crops in paddy field. First, the data set is divided into four seasons, and NDVI for each season is calculated. From this NDVI data set, we regard it as the number of cropping the number of times the NDVI increases significantly during a year. In this method, seasonal changes of deciduous trees and fields will also be extracted at the same time, however this study does not consider this problem.

2.   ANALYSIS METHOD

The flow chart of this study is shown in Fig.1. We have obtained the MSI data set from the web site of United States Geological Survey (USGS). This flow chart is divided into the two phases in this paper: one is the vegetation analysis by the seasonal changes, the other is production of the mask data.

2.1 The Vegetation Analysis by the Seasonal Changes

First, we calculate the NDVI from all data set, divide the data set of one year into each season. The seasonal data without clouds is generated from the seasonal NDVI data by using Maximum Value Composite (MVC) (B.N Holben, 1986). Then, the difference of NDVI for each season is calculated and we investigate them as the growth and decline degree of vegetation. When the amount of increase and decrease exceeds a threshold value, it is determined that vegetation has grown and the number of growth times during the year is counted.

2.2 Production of the Mask data

It is possible that rivers and building area are also processed in calculation of the number of crop times. Therefore, the mask data are created for the exclusion area in this phase (S. Ogawa, 2006). MSI data of two different times are classified using Iterative Self-Organizing Data Analysis Technique Algorithm (ISODATA) method which is one of the unsupervised learning. From the obtained two classification diagrams visually extract the area of the river and the building. The area discriminated as a river or a building in both classification diagrams is extracted as a mask area.
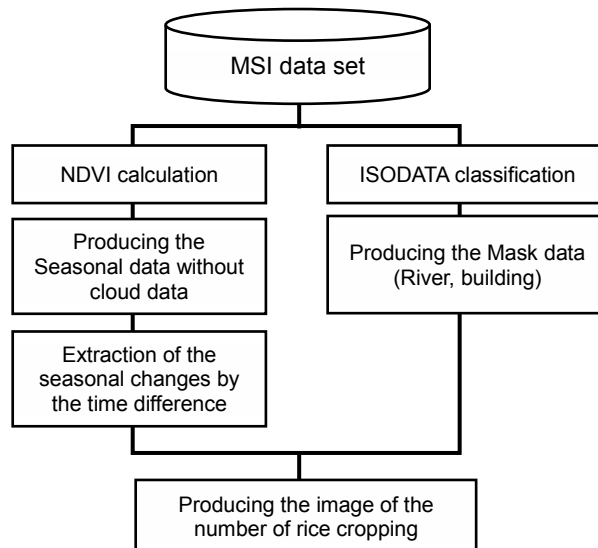
Fig. 1 the flow chart of this study

3.   EXPERIMENT AND RESULTS

We had obtained the MSI data from Mar. 2016 to Feb. 2017. Fig.2 shows one of the MSI data. MSI data have from 10m to 60m special resolution, we use the 10m resolution data. We show a part of image, since an original data size is too big (10980 x 10980 pixels). Many rice fields and Chao Phraya River can be confirm from the figure. The NDVI data had been calculated, and the seasonal data without cloud have been created as following.

- March to May
- June to July
- September to November
- December to February

The seasonal data without cloud had been created by the MVC, and the seasonal changes had been extracted from those data. The threshold for the change extraction had been set 0.2 that had been calculated it difference of NDVI between soil and vegetation pixels from the image in advance. The result of the change extraction is shown in Fig.3. This figure expresses that dark gray, light gray, white pixels are once, twice, three times of crop respectively, the black pixel is unchanged area on the year. From the figure, we found that river and building area had been extracted as the vegetation growing. Fig.4 is shown in the mask data using ISODATA method. In the ISODATA method, we had set the initial cluster numbers is 50, iteration is 100. From the ISODATA result, we divided into four cluster (river, building, soil and vegetation) by hand work. The mask data of river and building had been generated by the cluster data. From Fig.4, good mask data could be obtained relatively.

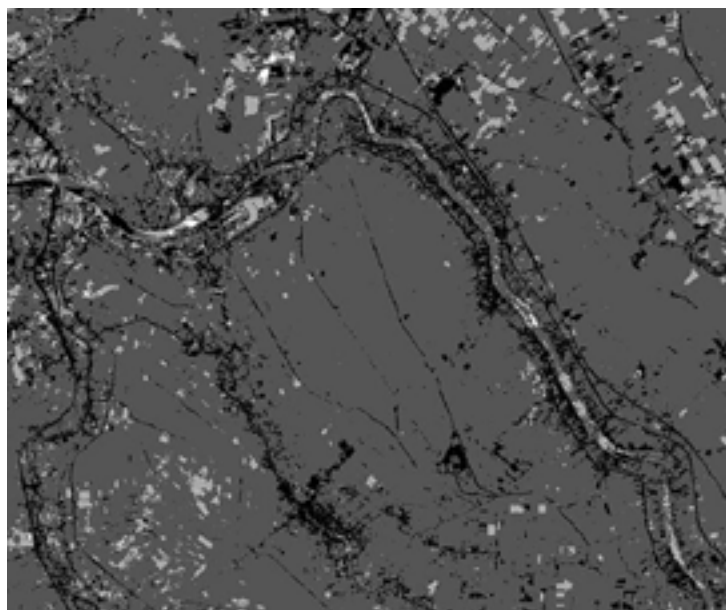Fig.2. One of the MSI data (18 Nov. 2016, Chai Nat prefecture)

Fig.3. Analysis of cropping times numbers
Black: Unchanged, Dark gray: Once, Light gray: Twice, White pixels: Three times
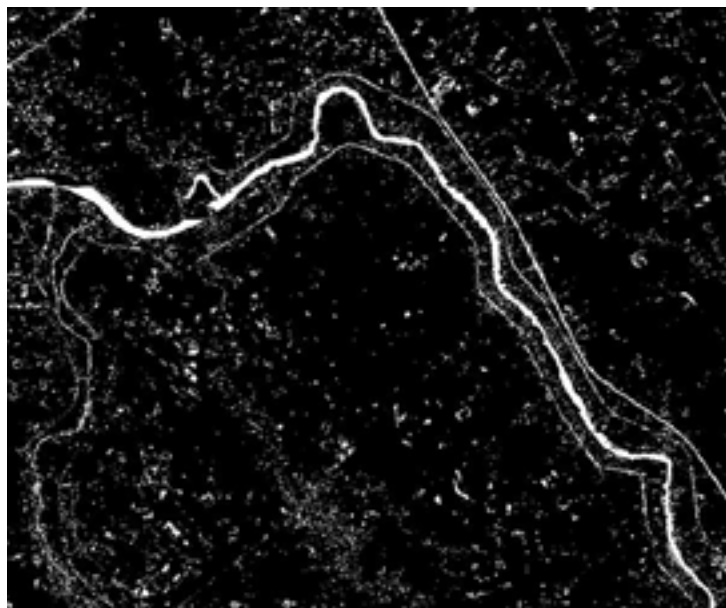

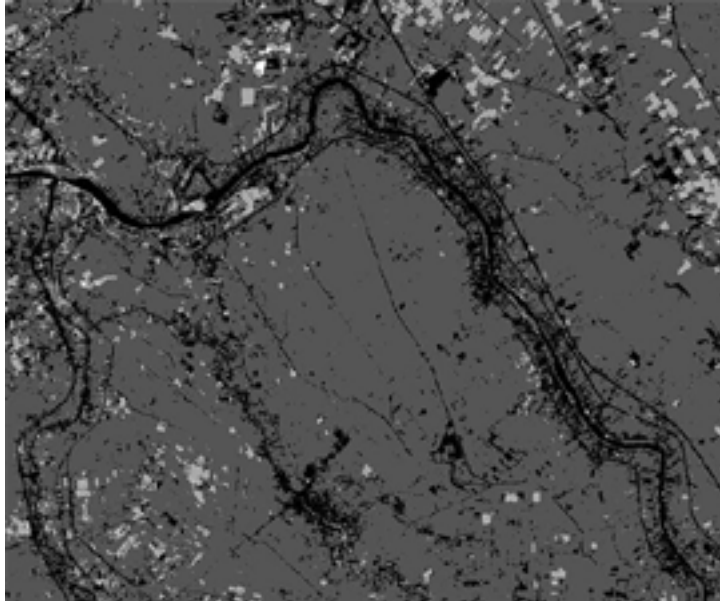Fig.4. Mask data of River and Building

Fig. 5. The number of harvest times after mask processing
Dark gray: Once, Light gray: Twice, White pixels: Three times

The number of crop times in the year is shown in the Fig.5. This figure expresses the same of Fig.3, the black pixel is not only the unchanged pixels but also excluded pixels from objects area of the research by mask data. Comparison of Fig.3 and Fig.5, it was possible to exclude areas that are unagricultural land, and we were able to obtain relatively easy to use results. Then we found that many rice fields had once harvest, a part of the field had more than twice harvests.

4.   CONCLUSIONS

In this paper, we had calculated the number of rice crop times per a year using the MSI image data. We found that a part of rice field had cropped more than twice harvest. As the future work, we will verify the accuracy of the result using ground truth data. It is necessary to propose further improvement method to increase accuracy, for example using ground truth data, mask data improvement and so on.

REFERENCES

B.N Holben, 1986. Characterization of maximum value composites from temporal AVHRR data, International Journal of Remote Sensing, 7, pp. 1417-1434.

S. Ogawa, 2006. Land Cover Analysis in Mecong River Basin and Chao Phraya Delta Using Remote Sensing Methods, Vo.27, No. 2, pp. 221-233

Retrieving Nitrogen Concentration with Hyperspectral Data and Long Short-Term Memory Model

Senlin Tang (1, 2), Xia Zhang (1), Mao Zhang (1, 2), Wenchao Qi (1, 2)

[1] Institute of Remote Sensing and Digital Earth, Chinese Academy of Sciences, Beijing, 100101, China
[2] University of Chinese Academy of Sciences, Beijing,100049, China
Email: tangsl2016@radi.ac.cn, zhangxia@radi.ac.cn, zhangmao@radi.ac.cn, qiwc@radi.ac.cn

Key words: nitrogen retrieval; winter wheat; feature selection; hyperspectral remote sensing; long-short term memory model

Abstract: Nitrogen is one of the key nutrient elements in growth of crops. Quantitative retrieval of nitrogen by hyperspectral remote sensing data provides technical guidance for irrigation and fertilizer management of crops, and is of great significance to China's digital agriculture strategy. In this paper, nitrogen retrieval experiments were carried out by a deep learning model of long short-term memory (LSTM). The partial least squares regression (PLSR) and support vector machine (SVM) algorithms were also conducted to make comparative analysis. The 248 samples of canopy spectra and corresponding leaf nitrogen contents, covering the whole growth period of winter wheat and under different coverage levels, were collected and used to validate the algorithms. The samples were allocated to calibration and validation data sets according to Nitrogen concentration values. Three groups of spectral features were extracted by successive projections algorithm from the original and the transformed spectra, and by spectral position selection and vegetation indices. The principal component analysis was used to select the optimal features. Then the optimized and unoptimized spectral features were fed respectively into LSTM model to retrieve nitrogen concentration. Compared with the retrieval using unoptimized features, the R^2 and RPD were improved from 0.7077 and 1.6776 to 0.8927 and 3.2598 by the optimized features and LSTM model. The R^2 and RPD were 0.8475 and 2.7887 for PLSR, and 0.7903 and 2.6253 for SVM respectively by the optimized features. The retrieval accuracy of Nitrogen concentration using feature optimized LSTM algorithm was superior to those of PLSR and SVM algorithms. The results demonstrate that LSTM model is able to retrieve nitrogen concentration of winter wheat effectively and has the potential to predict biophysical and biochemical parameters of other crops.

1. Introduction

Nitrogen is an important indicator of photosynthesis efficiency and overall nutritional status of vegetation (Wang, et al. 2018; Ali, et al. 2016; Akram, et al. 2014). The rapid development of hyperspectral remote sensing technology based on the spectral characteristics of ground objects has been able to monitor the growth status of crops more accurately. Hyperspectral remote sensing can obtain more realistic continuous spectrum of vegetation, and its fine spectral resolution can reflect the subtle characteristics of vegetation spectra and reflect the nuances of spectrum. High-spectral sensors mounted on aviation or space platforms can realize large area and nondestructive monitoring of crop growth, which is of great strategic significance for China's digital agriculture. (Atzberger, et al; 2013; Deshmukh, et al. 2018)

Most of the existing predictions of Nitrogen content in canopy were performed using the spectral absorption characteristic band sensitive to nitrogen concentration, the conversion form of the original spectrum and spectral indices constructed from feature bands. Mroczyk (1995) predicted the nitrogen content of sugar beet leaves under

different fertility levels based on near-infrared band and principal component regression method. Moron (2010) used the near-infrared band and PLS to estimate the total nitrogen content of cotton leaves and fresh wheat plants, respectively. Principal components and nitrogen sensitive bands were extracted on hyperspectral data from all-growing stages of rice, and the experimental results of Yi show that the modeling of artificial neural network was optimal (Yi, et al, 2007).

Retrieval of nitrogen from remote sensing is mainly based on a certain type of index, such as the original reflectance spectrum or the vegetation index.The different types of spectral features are not fully considered. In addition, extracting the representative spectral features from hyperspectral data is essential for the retrieval of nitrogen. In this study, three groups of spectral features were extracted by successive projections algorithm from the original and the transformed spectra, and by spectral position selection and vegetation indices to construct comprehensive feature space. Deep learning model referred to long short-term memory (LSTM) neural network was introduced to the retrieval of nitrogen using the comprehensive features. LSTM Neural Network has the ability to automatically autonomic learning inherent features from long time series hyperspectral data, and is not affected by gradient vanishing problem.

2. Study Area and Data

2.1 Study area and experimental sample

The study area is located in the national precision agriculture research demonstration base of Xiaotangshan, Beijing. The agricultural base belongs to temperate continental monsoon climate, with an average annual temperature of about 14 °C and an average annual precipitation of about 480 mm. The winter wheat planting area is about 100hm2, and it has a good growth state after fine irrigation and fertilization management. A total of 252samples were collected in the area of 116º26′ E to 116º27′ E and 40º10′ N to 40º11′ N.

2.2 Chemical analysis and spectral measurement

Fieldwork was carried out from April 2001 to June 2001, and from April 2001 to May 2001, using a homogenous random sampling strategy. It basically covers the whole growth period of winter wheat, including greening, jointing, grouting, and milk ripening. Experimental data including winter wheat canopy spectra and canopy nitrogen content.

The ASD FieldsSpec FR 2500 spectrometer covering the VNIR region from 350 to 2500 nm was used to measure canopy spectra in cornfield. The spectral resolution is 3 nm for the region 350-1000nm and 10 nm for the region 1000-2500nm, respectively, and the actual sampling interval is 1nm. A white BaSO4 panel was used to calibrate the collected canopy spectra with a reflectance factor. Canopy spectrum was measured with 120cm distance from the optical fiber and the field of view is 25 degree, the experimental time was from 10:00am to 14:00pm in a sunny and windless day. Each canopy sample was measured twenty times and the average spectrum was used. The content of nitrogen in leaves was determined by semi-micro kjeldahl method, each sample was repeated for 3 times and the average nitrogen content was used.

Considering severe noise associated with water absorption, the spectral regions of 1350-1480 nm, 1781-1990 nm and 2400-2500 nm were removed with reference to previous studies (Li, et al. 2014). The entire nitrogen sensitive VNIR spectral region in this study refers to the spectral region of 350-1350 nm with 1001 bands.

3. Method

The methods to extract hyperspectral data features include 1) The waveband features of the original and converted spectra was extracted by successive projection algorithm. The converted spectra include continuum

removal spectra, first derivative spectra, etc. 2) Spectral position features such as red edge position, red edge area were exacted by specific spectral position of vegetation. 3) Vegetation indices were calculated bythe mathematical combination of nitrogen sensitive bands which are mainly within the visible- near infrared region. The extracted hyperspectral data features were then used to construct comprehensive index by principal component analysis , and canopy nitrogen content of winter wheat was retrieved by LSTM model. Figure 1 shows the flowchart of nitrogen retrieval.
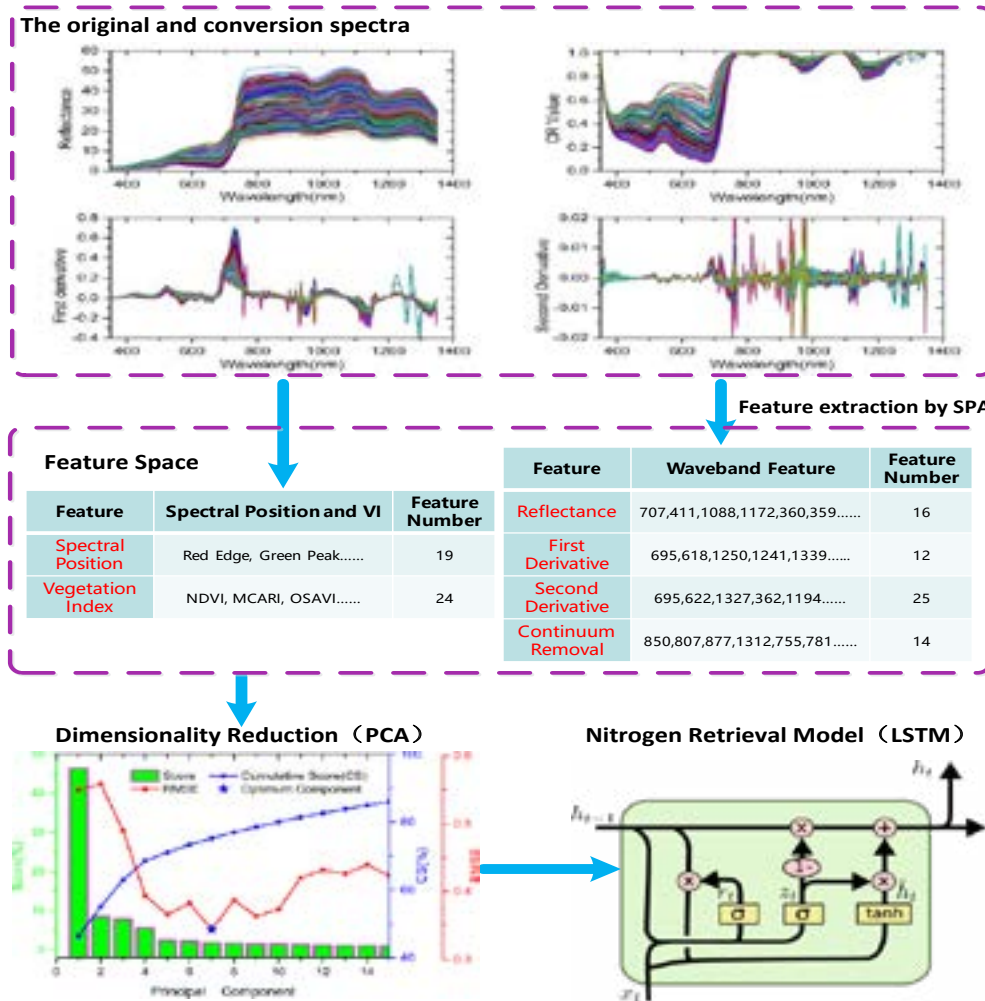

Figure 1. Flow chart of nitrogen prediction of winter wheat by LSTM

3.1 Feature extraction by successive projection algorithm

Successive projection algorithm (SPA) was proposed by Bregman in 1965, which was a forward variable selection algorithm (Duan, et al. 2018). It can effectively eliminate the collinearity effect between many wavelength variables and reduce the complexity of the modules. The main process of SPA can be summarized as follow: start by selecting an initial variable, and then adding a new variable at each iteration until the specified number of variables is reached, and finally selecting the variables that contain the minimum amount of redundancy to resolve the collinearity problem. The function of the projection is defined as:

$$P_{X_K} = X_K - (X_K^T X_{Var(m-1)}) X_{Var(m-1)} (X_K^T X_{Var(m-1)})^{-1} \tag{1}$$

where P is the projection operator, x_k is the kth column of calibration matrix X, $x_{var(m-1)}$ refers to the column selected at the (m-1)th iteration of SPA. X refer to remaining data set which the K-band was removed. The minimum root mean square error of validation set was obtained by multiple linear regression, and the optimal

selected variables could be determined.

Effective information of the original and conversion spectra could be extracted by the SPA algorithm. This algorithm can reduce the dimensionality of the hyperspectral data, maximize the interpretation information, overcome the data linear correlation and instability so as to improve the predictive reliability and detection speeds.

3.2 Dimensionality reduction by principal component analysis

Dimensionality reduction is the core idea of principal component analysis (PCA), which transforms several interrelated numerical variables into a statistical method of a few unrelated comprehensive indexes. These comprehensive indicators are the main components of the original multiple variables, each principal component is a linear combination of the original variables, and the main components are not related to each other (Roweis, et al. 1997).

The main process of PCA can be summarized as follow: firstly, the original variables were normalized, and then the correlation matrix between each variable and eigenvector of the matrix were calculated, and finally the feature roots were sorted in descending order and the corresponding principal components were calculated separately.

$$F_p = a_{1i} * Z_{X1} + a_{2i} * Z_{X2} + \cdots + a_{pi} * Z_{Xp} \tag{2}$$

Where the eigenvector a corresponds to the eigenvalues of the Z covariance matrix of one by one, Z was the normalized value of the original variable, F_p refer to pth principal component.

3.3 LSTM Modeling

In this study, features were extracted by LSTM model, which was applied to predict nitrogen content in the canopy. The input layer, the output layer, and a series of repeatedly connected hidden layers called memory blocks were composed LSTM model, which is a gated recursive neural network (Li, et al. 2017). Self-circulating memory cells can prevent any external disturbances, from one time step to another, the state can remain unchanged and further solve the vanishing gradient problem. Each block is composed of one or more self-circulating memory units and three multiplication units (input, output, and forgotten gates) that can be used to learn the long-term dependency information.

Three parameters including the squared mean square error (RMSE), the coefficient of measurement (R^2), and the predictive deviation rate (RPD , the ratio of standard deviation to RMSE) were used to evaluate the results. Generally speaking, the higher the R^2 and the RPD , the lower the RMSE, the better the model effectively. Excellent prediction with RPD and R^2 values greater than 3.0 or 0.90, whereas values from 2.5 to 3.0 (RPD) and 0.82 to 0.90 (R^2) denote "good"; Approximate quantitative predictions with RPD values between 2.0 and 2.5 and R^2 values in the range from 0.66 to 0.81; The possibility to distinguish between high and low values is revealed by RPD and R^2 values at intervals of 1.5 and 2.0 and 0.50 to 0.65; Unsuccessful" predictions with RPD and R^2 values lower than 1.5 or 0.50, respectively (Saeys, et al. 2005; Vohland, et al. 2011).

4. Results and Discussion

4.1 Distribution of calibration and validation set

The canopy sample covered the whole growth period of winter wheat, with the nitrogen concentration in the range from 1.749 to 6.396, and the average content was 4.177. The entire 248 groups of hyperspectral data were divided into 168 groups of calibration set and 80 groups of validation set by proportional 2:1. The canopy samples of winter wheat were reallocated to calibration and validation sets according to Nitrogen concentration. The

quantitative statistics for calibration, validation, and the entire dataset in table 1 were basically maintained, and figure 2 shows that statistical histogram of nitrogen was basically consistent.

Table 1. Statistics of Nitrogen contents for winter wheat samples

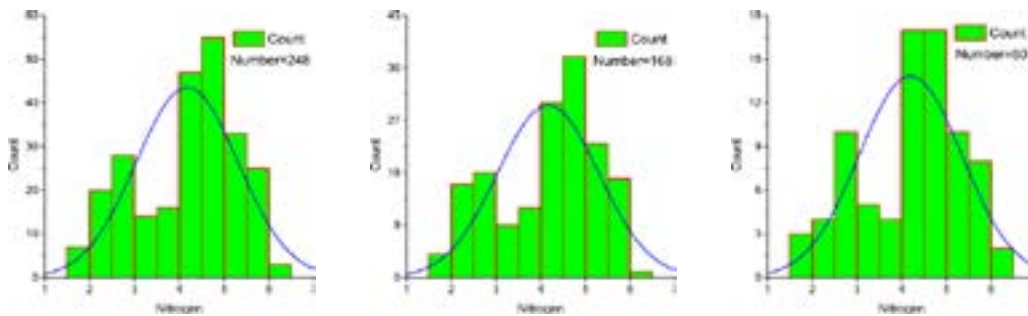| Group	Min	Max	Mean	Median	SD	CV
Calibration set (168)	1.808	6.396	4.167	4.452	1.132	0.272
Validation set (n=80)	1.794	6.129	4.197	4.446	1.152	0.274
Entire dataset (n=248)	1.794	6.396	4.177	4.448	1.136	0.272

Figure 2. (a) Entire dataset; (b) Calibration set; (c) Validation set

4.2 Prediction of Nitrogen content in canopy

The prediction model of canopy nitrogen in this experiment was based on LSTM algorithm. Hyperspectral feature extraction methods in section 3.3 can be included as follow: The original reflectance spectrum and its conversion form, spectral location characteristics, vegetation index, which build the feature space as the input of the LSTM model. As a contrast, the feature space was improved, and PCA algorithm was used to extract the principal component of the feature space. The number of principal components of the feature was determined by cross-validation, and the comprehensive index of feature space was used as input of LSTM model to predict the canopy nitrogen of winter wheat.

Table 2. Prediction accuracies of nitrogen for winter wheat samples

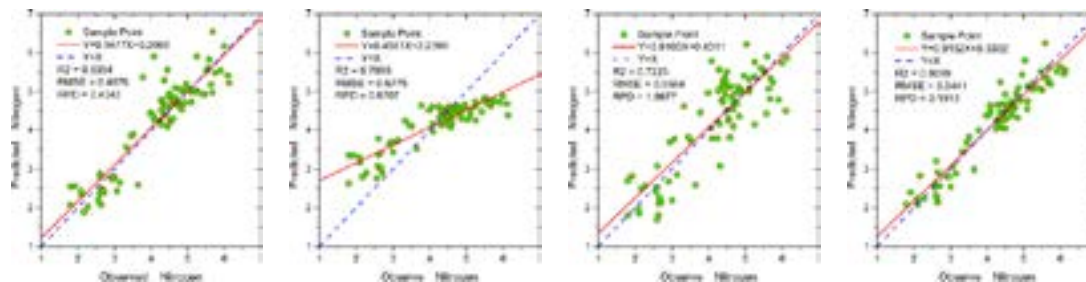| Model	Input Parameter	RPD	RMSE	R2
PLSR	PC by Feature Space	2.4342	0.4876	0.8354
SVM	PC by Feature Space	0.8707	0.6775	0.7899
LSTM	Feature Space	1.8677	0.6564	0.7223
LSTM	PC by Feature Space	3.1913	0.3441	0.9099

Figure 3. (a) PLSR; (b) SVM; (c) LSTM by Feature space; (d) LSTM by Principal component

Table 2 shows the prediction accuracy of canopy nitrogen with the feature space constructed by three feature extraction methods and the comprehensive principal component extracted by PCA, respectively. The overall nitrogen prediction accuracies derived from the feature space was unsuccessful, compared with the prediction accuracies derive from synthetic principal component extracted by PCA. PCA algorithm can improve the accuracy

of LSTM model prediction. As a comparison, the accuracies of nitrogen prediction of PLSR and SVM models were given.

The results of quantitative analysis show that LSTM model was superior to PLSR and SVM model. In the LSTM model, the RMSE and RPD values were 0.3441 and 3.1913 for the prediction using the synthetic principal component extracted by PCA, whereas the RMSE and RPD values were 0.6564 and 1.8677 for the prediction using the unoptimized feature space. According to the evaluation criteria in section 3.2, the unoptimized feature space was unsuccessful prediction, whereas the optimized feature space by PCA regard as excellent prediction. The nitrogen prediction results of optimized and unoptimized feature space is illustrated in Figure 2.

5. Conclusion

The feature space of hyperspectral data was constructed by three types of spectral features and corresponding extraction methods, which provided abundant features for predicting the nitrogen of winter wheat. Due to the high dimension of the feature space, there is serious collinearity problem. To conquer the problem, the comprehensive principal components was extracted by PCA to replace the original multidimensional variables while reducing the data dimension. Using synthetic principal components as input parameter of LSTM model, the canopy nitrogen content of winter wheat in Xiaotangshan area of Beijing was retrieved. The predictive model and accuracy were obtained. Compared with the unoptimized feature space, the RPD and R^2 values were improved from 1.8677 and 0.7223 to 3.1913 and 0.9099 respectively, and the RMSE decreased from 0.6564 to 0.3441 by the proposed method and the optimized features.

PCA can provide a new idea for the prediction of canopy nitrogen by using several finite principal component features to describe and express all the feature spaces. Although the retrieval results of this study are encouraging, there is still much work to be done in the future. On the one hand, different hyperspectral data reduction methods can be used in nitrogen retrieval, such as factor analysis, genetic algorithm and so on. On the other hand, the spectral subset which referred to the key spectral region (such as chlorophyll and protein sensitive bands) can be applied to predict nitrogen content in canopy.

6. Acknowledgment

7. References

Ali A M, Darvishzadeh R, Skidmore A K, et al. Effects of Canopy Structural Variables on Retrieval of Leaf Dry Matter Content and Specific Leaf Area from Remotely Sensed Data[J]. IEEE Journal of Selected Topics in Applied Earth Observations & Remote Sensing, 2016, 9(2):898-909.

Akram M. Effects of Nitrogen Application on Chlorophyll Content, Water Relations, and Yield of Maize Hybrids under Saline Conditions[J]. Communications in Soil Science & Plant Analysis, 2014, 45(10):1336-1356.

Atzberger C. Advances in Remote Sensing of Agriculture: Context Description, Existing Operational Monitoring Systems and Major Information Needs[J]. Remote Sensing, 2013, 5(2):949-981.

Deshmukh R, Janse P V, Karungaru S G, et al. Hyperspectral Remote Sensing for Agriculture: A Review[C]// International Conference on Cognitive Knowledge Engineering. 2018.

Duan F, Fu X, Jiang J, et al. Automatic variable selection method and a comparison for quantitative analysis in laser-induced breakdown spectroscopy[J]. Spectrochimica Acta Part B Atomic Spectroscopy, 2018, 143.

Li X, Zhang Y, Bao Y, et al. Exploring the Best Hyperspectral Features for LAI Estimation Using Partial Least Squares Regression[J]. Remote Sensing, 2014, 6(7):6221-6241.

Mroczyk W B, Michalski K M. Quantitative and qualitative analyses in near infrared analysis of basic compounds in sugar beet leaf [J]. Computers & Chemistry, 1995, 19(3):299-301.

MoróN A, GarcíA A, Sawchik J, et al. Preliminary study on the use of near-infrared reflectance spectroscopy to assess nitrogen content of undried wheat plants[J]. Journal of the Science of Food & Agriculture, 2010, 87(1):147-152.

Qiuxiang Yi, Jingfeng Huang, Fumin Wang, et al. Monitoring Rice Nitrogen Status Using Hyperspectral Reflectance and Artificial Neural Network[J]. Environmental Science & Technology, 2007, 41(19):6770-5.

Roweis S. EM algorithms for PCA and SPCA[J]. Advances in Neural Information Processing Systems, 1997, 10:626--632.

Saeys W, Mouazen A M, Ramon H. Potential for onsite and online analysis of pig manure using visible and near infrared reflectance spectroscopy. [J]. Biosystems Engineering, 2005, 91(4):393-402.

Vohland M, Besold J, Hill J, et al. Comparing different multivariate calibration methods for the determination of soil organic carbon pools with visible to near infrared spectroscopy[J]. Geoderma, 2011, 166(1):198-205.

Wang Z, Skidmore A K, Darvishzadeh R, et al. Mapping forest canopy nitrogen content by inversion of coupled leaf-canopy radiative transfer models from airborne hyperspectral imagery[J]. Agricultural & Forest Meteorology, 2018, s 253–254:247-260.

Xiang Li, Ling Peng, Xiaojing Yao, et al. Long short-term memory neural network for air pollutant concentration predictions: Method development and evaluation[J]. Environmental Pollution,2017, 231.

Treetop detection from LiDAR data using local maxima algorithm

Lindah Roziani Jamru (1), Mazlan Hashim (1), Mui How Phua (2)

[1]Geosciences & Digital Earth Centre (INSTeG),
Research Institute of Sustainable Environment
Universiti Teknologi Malaysia, 81310 UTM Johor Bahru, Malaysia
[2]Faculty of Science and Natural Resources, Universiti Malaysia Sabah, Jalan UMS 88400 Kota
Kinabalu, Sabah, Malaysia

Email: lroziani2@liveutm.my

Abstract: Light Detection and Ranging (LiDAR) sensing produces three dimensional (3D) point cloud information that are useful generating Canopy Height Model (CHM) precisely. The sensor has capability to extract the vertical biophysical information's of forest structure at different levels of spatial resolution. Although, the CHM has been successfully applied to tree top detection, not much of it has been put to use in complex tropical environment to undertake structural analysis. This study therefore, applies the local maxima algorithm with 16 combination of CHM filters (Mean, Median and Gaussian) at window sizes (3x3, 5x5, 7x7 and 9x9) for treetop detection. The results reveal that the best combination in the filters and window sizes is; (a) -9.79 (7x7; Mean and 258 trees), (b) 57.69% (9x9; Gaussian and 451 trees) and (c) 63.98% (9x9; Mean and 469 trees) respectively.

Keywords: Forest structure, LiDAR, Tropical forest, Treetop detection

Introduction

Borneo island is covered by lowland dipterocarp forest species that contains high quality timber. This category of timber generates high prices with good attraction at the markets that contributes immensely to the economic sector. The value has prompted commercialization of logging in Sabah often referred to as 'Selective logging' that allowed the timber with DBH more than 60 cm are harvested. So much of the timber between 1970s and 90s have been harvested and the consequence is degradation of the forest (Marsh & Greer, 1992). It has been estimated that 1.7% of the forest was lost per annum between 2002 and 2005 (Lagner et al., 2007); over 1.8 million ha of the forest between 1990 and 2008 (Osman et al., 2012).

Even though it benefits the economic sector, logging activities also has negative impact on the natural ecosystems leading to soil erosion, excessive runoff, changed forest structure and the degradation of biomass. Monitoring and taking forest inventory is necessary to maintain and sustain the forest ecosystem. Unfortunately, the information that should serve as prerequisite for the efficient management is outdated and not enough. Obtaining this data over a large area is expensive and time consuming if traditional methods are applied. Therefore, remote sensing is the best option where synoptic coverage and maps will be necessary to undertake adequate assessment of the forest and determining the way forward.

The application of LiDAR remote sensing for forest inventory is widely explored in literature for over twenty years (Jean et al, 2010), through its advantages of giving out 3D point clouds information enabling the treetop and their heights determined. Several algorithms have been introduced for counting and obtaining tree census and forest inventory, amongst many are the local maxima algorithm, TreeVAW, "Canopy Maxima", tree climbing algorithm, and morphology. The accuracy of each depends on the computation and the filtering process. Most of the methods were tested at particular forest context, but non applied the local maxima in the tropical lowland dipterocarp species. This may be due to the complexity of the forest itself and with issues of difficulty in some inaccessible areas. A study by Jamru, (2018) reported the accuracy index of treetop detection for broadleaf tropical forest as 69% with LiDAR data. But, better results can be achieved when higher processing takes place such as using calibration of plots and control the algorithm parameters.

This study applied the local maxima algorithm that operated with varying filters at different window sizes over the CHM at the lowland dipterocarp tropical forest with the purpose of evaluating the influence of different window sizes and CHM filters on the forest to detect the performance. The contribution here is the addition of the different window sizes of the filters.

Material and Methods

Study area

Danum valley located at Borneo island (Figure 1) that is dominated by 88% of the lowland dipterocarp forests. Four variants in the lowland vegetation can be distinguished in the study area, which are *Parashorea malaanonan* type, *Saraca, Eugenia*, *Pterospermum, Leea* and *Dillenia* (March & Greer 1992). The study area is generally undulating and hilly whose logging began since 1988 (Innoprise Corporation 1992, unpublished data).
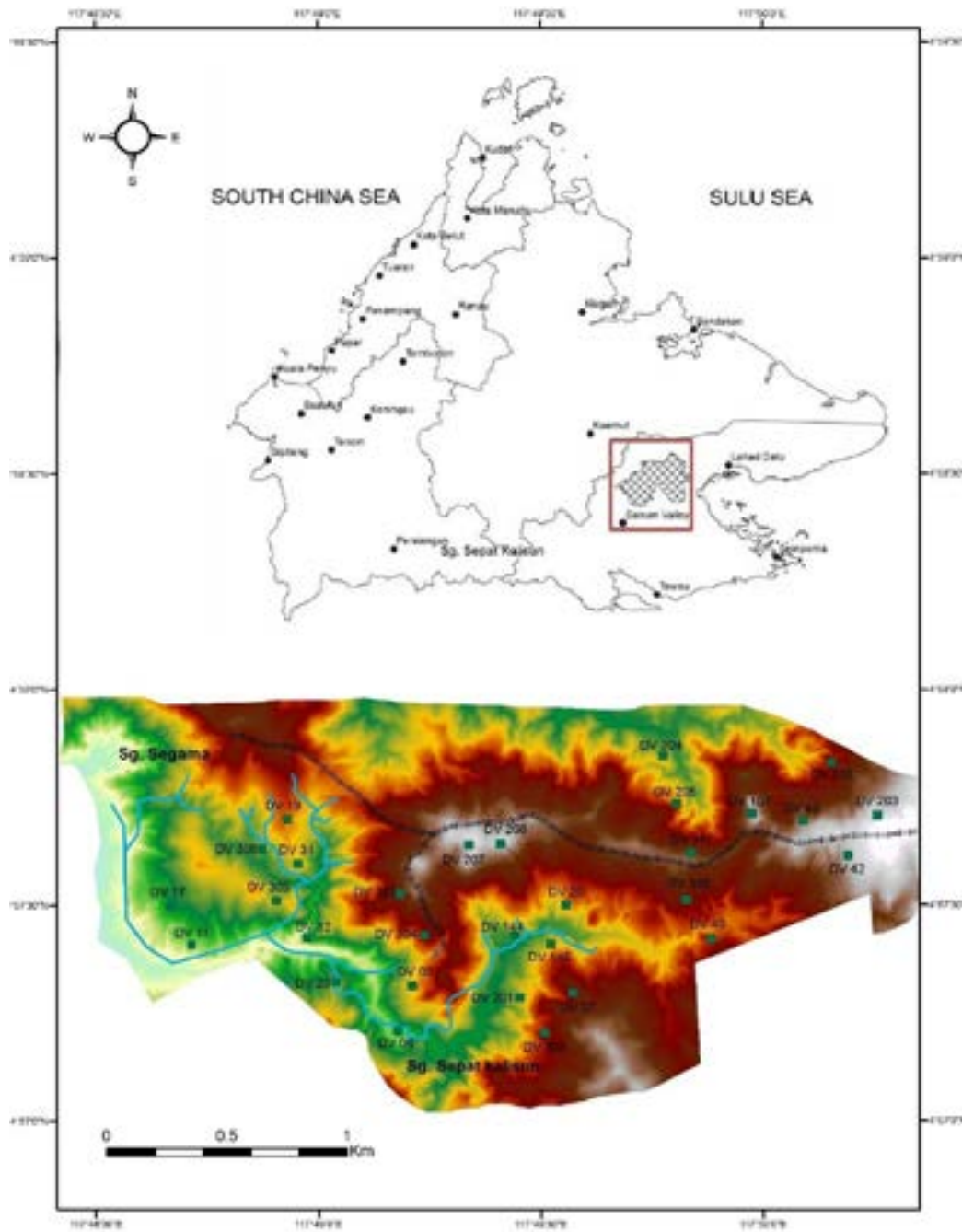

Figure 1: Map of study area

LiDAR data and In-situ measurement

LiDAR data were acquired using laser Optech C200 HD ILRIS system with total area has been scanning was 20.59 km². Table 1 showed the parameter of LiDAR systems. In this study, a sample plot selected among 30 plots has been measured within the study area. Trees with DBH 10 cm and above were measured. The parameters was recorded are tree height, DBH, tree position and crown area.

Table 1. Parameter of LiDAR systems

Parameter	Specification
Data acquisition	11/10/2013
Laser frequency	75 Hz
Flying speed	90 KPH
Flying height	500m
Laser swath width	693m
Scan angle	14.2 degrees
Swath overlap	35%

Treetop detection

Figure 2 shows the flowchart of treetop detection used in this study where the CHM produces normalized point clouds as input data. The point clouds that hit the surface of tree crowns were extracted and isolating those that penetrated through the canopy. Then, the tree detection algorithm were applied to detect the treetop of individual tree. There are three filters used in the local maxima algorithm, which are Mean, Median and Gaussian, that were tested with different sizes of the windows (Figure 3) to evaluate the treetop detection. The tree boundaries were also extracted based on the value of the cell within the window size and the highest point identified as the treetop mark. A subset was created using the tree height threshold, which is 1.37 m. The tree crowns and the treetop were both detected.
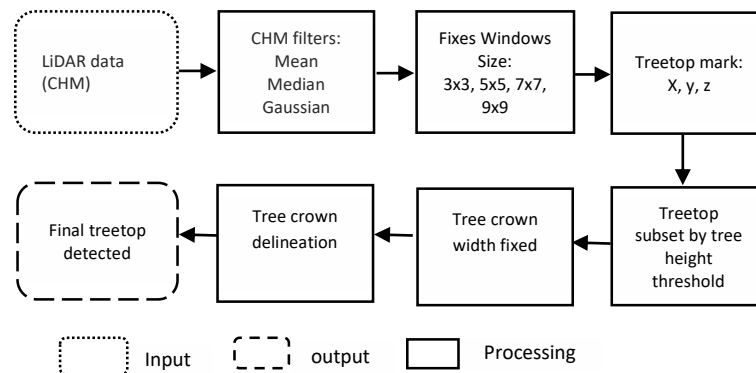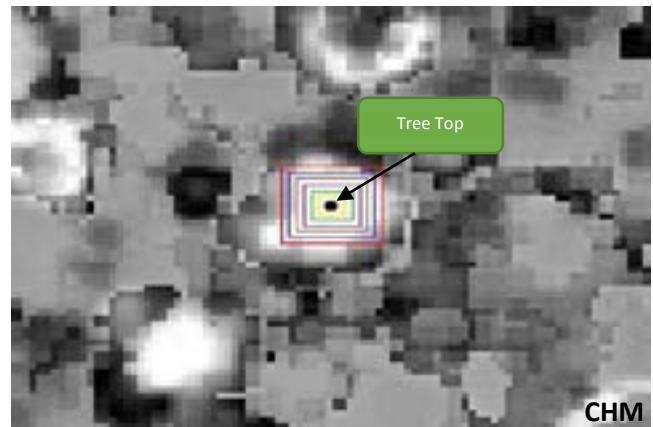
Figure 2: Flow chart of treetop detection

FWS: ☐ 3x3 ☐ 5x5 ☐ 7x7 ☐ 9x9 ☐ 11x11 ☐ 13x13

Figure 3: Illustration of FWS in the CHM

Accuracy assessment

The accuracy of detected treetops calculated based on equation below:

Absolute error = Number of tree detected – Number of tree observed   equation (1)

Relative Error (%) = (Number of tree detected – Number of tree observed) x100 equation (2)
                          Number of tree observed

Results and Discussions

The objective of this study was to evaluate the influence different types of filtering in different window sizes to improve the accuracy of inventory from LiDAR data. The algorithm based on local maxima could detect treetop based on the highest point of each tree. Figure 4 shows the maps of detected treetops using varying combinations of filters and window sizes. It can be seen that the local maxima algorithm applied to the canopy size is an important parameter however, with window size 9x9 the largest window gave low correlations when it was dedicated to tree top only, while the small windows size 3 x3 with less "noise" produced better results of canopy morphology close to tree top and noise overestimated the number of tree tops.

	LiDAR –Detected Trees			
WS	No Filter	Mean	Median	Gaussian
x3				
x5				
x7				
x9				
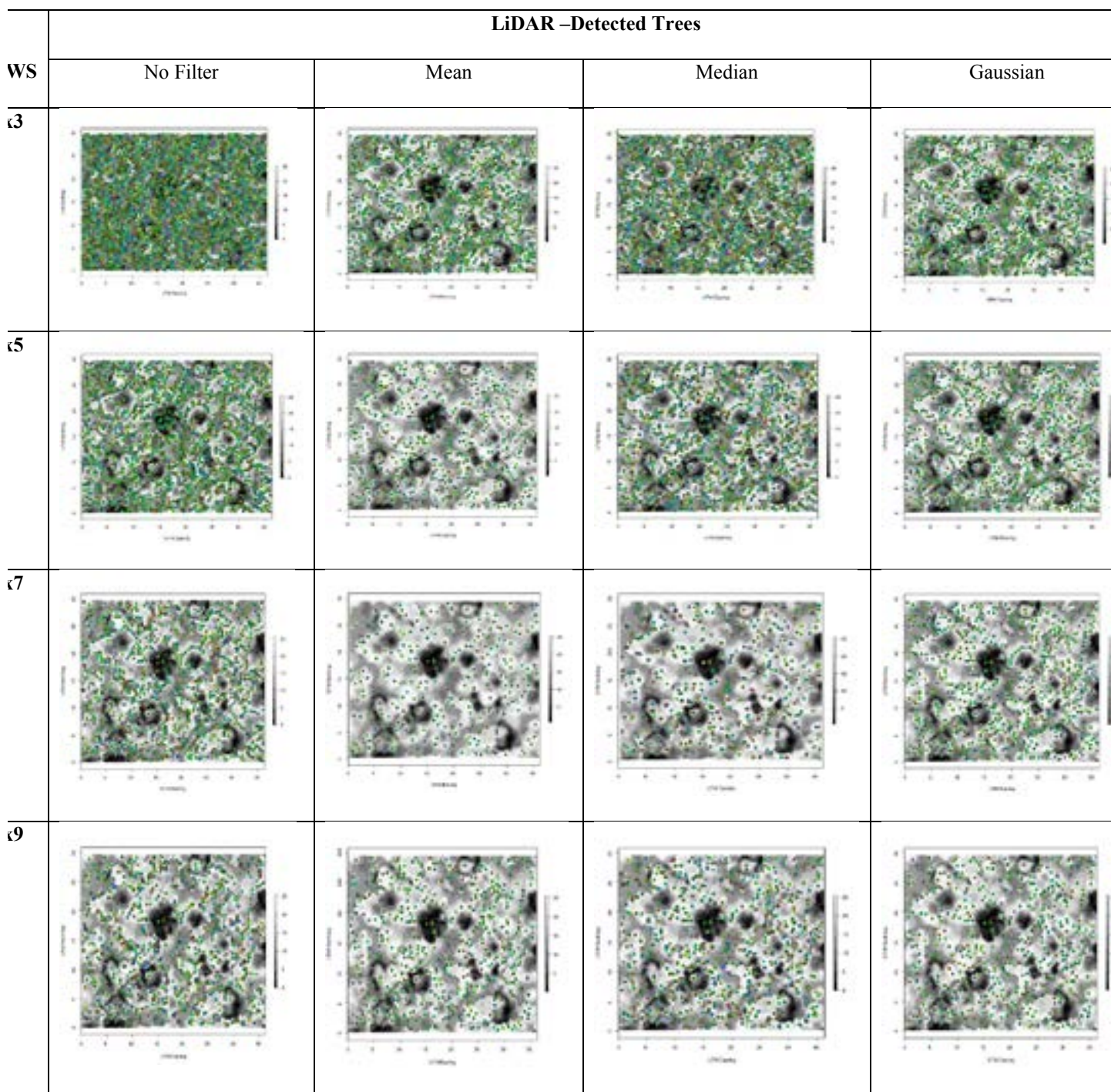
Figure 4: maps of treetop detected using varying combinations of filter and window size

Figure 5 shows the total number treetop detected for 16 combination of filters and window sizes. The raw data that had no filter recorded the highest error and the number of tree detected were 8131 trees. Even though, there is no filter applied, but the window size still influenced the detected treetop for the raw data, where the lowest trees detected by window size 9x9 totaled 1809 trees. With noise tree estimate becomes over but with the use of filters better result are achieved. For the most accurate results, the filters of Mean, Median and Gaussian were

applied with the combination four different size window is 3x3,5x5,7x7 and 9x9. The detected treetops ranged from 258 to 5815. The accurate combination for both filters and window size for treetops detection were (a) window size of 7x7 and Mean filter with 258 treetops detected, (b) window size 9x9 and the Gaussian filter, with 451 treetops detected and (c) window size of 9x9 and the Mean filter, with 469 treetops detected. Between three of the filters, Median filter tend to overestimate the treetops with detected treetops ranged between 1334 to 5815 trees.
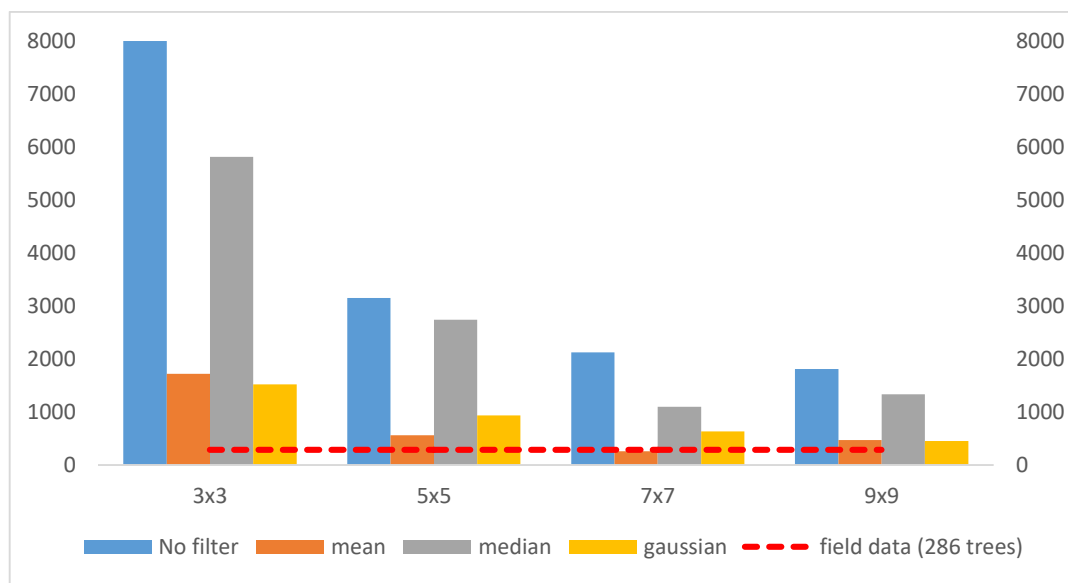

Figure 5 : Graf of detected treetops

The relative error recorded for detection treetops ranged from -9.79 to 2743 %. As expected, the raw data has the highest relative error with 2743 %. Figure 6 showed the relative error for 16 combination of filtering and window size. The relative error for the best combination was (a) -9.79 (7x7 and mean); (b) 57.69% (9x9 and Gaussian) and (c) 63.98% (9x9 and mean).The window size influences for search in local maximum to get highest point for treetops detection while small or large window size lead to the error. The results show that window size 7x7 is the best size to get the accurate number of trees closed to ground data. The size is medium window size that can remove the false treetops by applying the horizontal threshold (H). Even though, the task of detection treetops was the tough process, but the results of the study are important for tree census and forest inventory. There could some error during the process treetops detection due to the complexity of the forest itself. But, the estimation results are accepted has correlation with the ground data. The results underestimated due to small trees were overlapping with the big ones, considered as the branches of the big tree. Meanwhile, overestimations could also happen, when the tree crown so big that some branches extend far from the crown. The algorithm fails to identify extending branches as a false treetops that leads to overestimation.
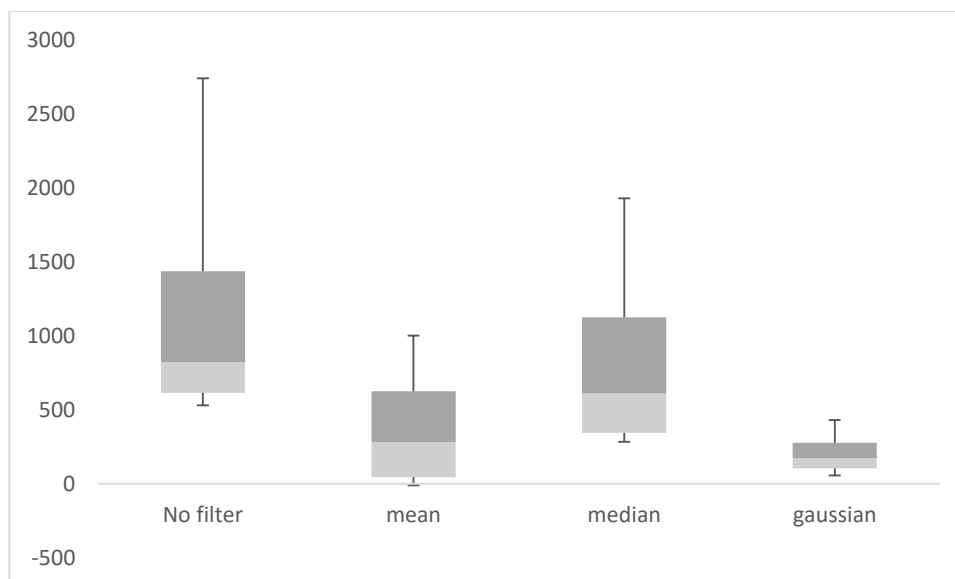
Figure 6: Relative error %

Conclusions

LiDAR data provides three dimensional data that could estimate the number of the trees and the their location in the forest by the potentials of filters to generate accurate results. This study, reveals that the influence both of CHM filtering and window sizes together was a good approach for treetops detection. From the results, the best CHM filtering is Mean filter and 7x7 window size is the best size to detect treetops of the lowland dipterocarp forest. The species of trees consist of broadleaf suitable to the medium window size, not too small and not too large. The capability of algorithms to detect treetops provided valuable information on tree census for forest inventory and management. This study also proved that LiDAR is a suitable technology for treetops detection. The capability to obtain tree counting and the spatial distribution over large areas using this method can be the best method can provide input data to inventories. Also less field survey were needed just for validation purposes.

References

Jamru, L. R. 2018. Correction pit free canopy height model derived from LiDAR data for the broad leaf tropical forest IOP Conf. Series: Earth and Environmental Science 169, 012113 doi :10.1088/1755-1315/169/1/012113

Jean-Matthieu Monnet, Eric Mermin, Jocelyn Chanussot, Frédéric Berger. Tree top detection using local maxima filtering: a parameter sensitivity analysis. 10th International Conference on LiDAR Applications for Assessing Forest Ecosystems (Silvilaser 2010), Sep 2010, Freiburg, Germany. 9 p., 2010. <hal-00523245>.

Langner, A., Miettinen, J., Siegert, F., 2007. Land cover change 2002-2005 in Borneo and the role of fire derived from MODIS imagery. *Global Change Biology*, 13, pp. 2329-2340.

Marsh, C. & Greer, A. G. 1992. Forest land-use in Sabah,Malaysia: an introduction to Danum Valley. Phil. Trans. R. Soc. Lond. B 335, 331-340. (doi:10.1098/rstb.1992.0025).

Osman, R., Phua, M-H., Ling, Z.Y., and Kamlun, K.U. 2012. Monitoring of deforestation rate and trend in Sabah between 1990 and 2008 using multitemporal Landsat data. *Journal of Forest Science*, 28. No.3, 144-151.

Popescu, S.C.; Wynne, R.H. Seeing the trees in the forest: using lidar and multispectral data fusion with local filtering and variable window size for estimating tree height. Photogram. Eng. Remote Sens. 2004, 70, 589-604.

MAPPING LAND DEGRADATION IN NUWARA ELIYA DISTRICT USING MULTI-TEMPORAL SATELLITE IMAGES AND SPECTRAL MIXTURE ANALYSIS METHOD

Chathumal M.Weththasinghe Arachchige (1), Gamage S.N. Perera (1)

[1] Faculty of Geomatics, Sabaragamuwa University of Sri Lanka, P.O. Box 02, Belihuloya, 70140, Sri Lanka.
Email: chathumal93@gmail.com; sanka@geo.sab.ac.lk;

KEY WORDS: Remote Sensing, Land Degradation.

ABSTRACT

One of the major problem facing Asia as well as Sri Lanka is the threat of land degradation due to climatic factors and human influences. The process of land degradation in Sri Lanka has increased rapidly specially in districts like Nuwara Eliya. Taking advantages of the hyperspectral imagery and developing methods such as spectral mixture analysis (SMA) are recently much recommended methods for vegetation studies in arid, semiarid as well as tropical lands.Three cloud free Landsat TM, ETM+ and OLI-TIRS scenes covering Nuwara Eliya district were selected for the study. Imageries were acquired in dry season in the study area (January and February) in years 2001, 2007 and 2016, respectively. A linear mixture model (LMM) was adopted using the endmembers derived from the image. Principle component analysis (PCA) was applied to identify the dimensionality of the data and to derive three pure endmembers. Fraction images of endmembers were used to identify regrowing and degraded areas. It was done by the visual interpretation and secondly change vector analysis (CVA) was applied to determine and analyse land cover change map and evaluate the degradation process in the study area. The CVA result shows that there is 500.98 km2 area under regrowing class and 110.27 km2 area under degraded class in the period of 2001 to 2007. In the period of 2007 to 2016 there is 153.82 km2 area under regrowing class and 343.80 km2 area under degraded class and clearly shows the degradation process undergoing in the study area.

1   INTRODUCTION

Land degradation is the reduction in the capacity of the land to provide ecosystem goods and services. It involves physical, chemical and biological processes. Physical processes include alterations in soil structure, environmental pollution and unsustainable use of natural resources. Chemical processes include acidification, leaching, salinization and biological processes include reduction of biomass and biodiversity ("Land degradation neutrality resilience", 2007). In general, land degradation is a slow process that is often neglected or goes unnoticed by the local population. Most previous research on land degradation was conducted in semiarid or arid environments for monitor the risks. There are also wet lands that can be affected by land degradation conditions.In Sri Lanka there is a considerable land degradation risk in Nuwara Eliya district, leading to changes in soil structure, loss of soil fertility and soil erosion. Land degradation in the Nuwara Eliya district is mainly caused by improper agricultural practices, deforestation, and associated soil erosion. In this case Identifying and mapping the degradation risks using the conventional mapping with the field investigations are very difficult. therefore with the development of the remote sensing technology these issues can be addressed more efficiently.

2   METIRIAL AND METHODS

2.1   Study Area

Nuwara Eliya district is located in the hill country of Central Province. The terrain is generally consists mountainous, deep valleys. Altitudes of the district vary from 300 to 2,000 m due to mountainous landscape. Out of the total lands, 78% is located on slopes more than 30% gradient and 15% of the lands on more than 60% slopes. Total population of the district is 761,000. 49.7 % are male and 61.3% are above 20 years. Total extent of the District is 174,100 ha indicating a per capita land use of 0.23 ha. ("Land degradation in up and mid country", 2010) There are 5 divisional Secretariats in Nuwara Eliya, (Ambagamuwa, Kotmale, Walapane, Hanguranketa and Nuwara Eliya), and further divided into 491 GramaNiladhari Divisions (GNDs). There are 1,134 villages found under the administration of these GNDs. The land extent is distributed among the 5 DSDs. The local administration structure is represented by 5 PradesiyaSabhas, 2 Urban Councils and 1 Municipal Council. Further, there are 180 tea estates within the district.

Figure 1 Nuwara Eliya District in Sri Lanka

2.2   Methodology

The multi-spectral data from LANDSAT-5, LANDSAT-7 and LANDSAT-8 Satellite images are obtained for this study.
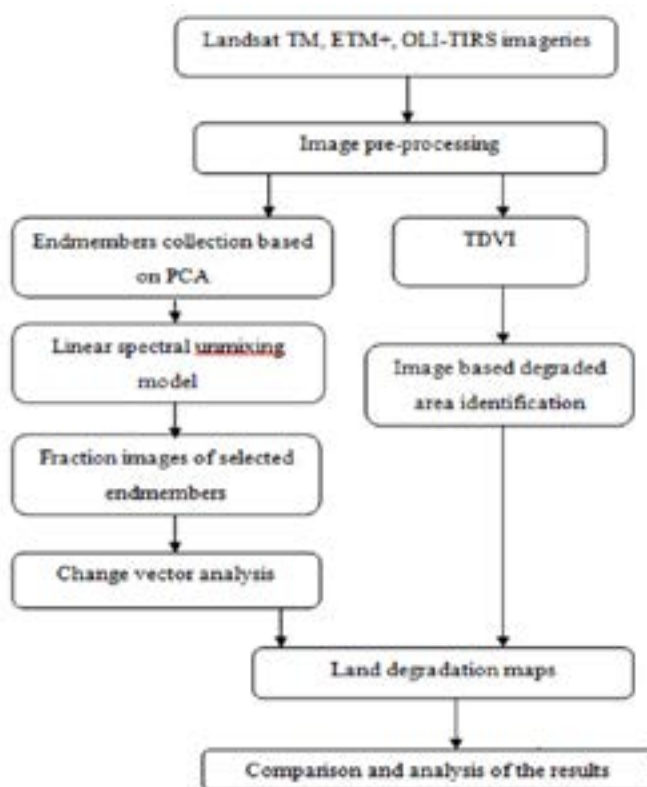

Figure 2 Method Adopted

2.2.1   Spectral Mixture Analysis

In order to assess the land cover types in the study area the application of multitemporal spectral mixture analysis was adopted. This method involves image endmembers selection, image fraction production, classification of SMA fractions and finally interpretation of the fraction images. The aim of SMA is to estimate how each ground pixel is divided up among different cover types known as endmembers. The image endmembers were derived from the image feature space, assumed to present the purest pixels in the image. This was done using the early mentioned principle component analysis. The four endmembers soil, green vegetation and shade were defined. The second step in SMA is to estimate for each pixel the abundance of each general endmembers by applying a linear mixing equation. The general mathematic model of the Linear Mixing Model (LMM) can be expressed as:

$$DN = \sum F_i \times DN_i + E_i \qquad\qquad\qquad (2.1)$$

$$\sum F_i = 1 \qquad\qquad\qquad (2.2)$$

Where:

DN - relative radiance in band i for each pixel

DN_i - relative radiance in band i for each endmembers k

Fi - fraction of each image endmembers k calculated band by band k each of n endmembers

E_i -reminder between measured and modeled DN (band residuals)

These calculations were done using the ENVI 5.1 software. Three endmembers selected from the PCA analysis were input to the linear unmixing tool in the ENVI 5.1 software. Soil fraction, green vegetation fraction and shade fractions were obtained using the derived endmembers for the three Landsat images.

$$RMSE = \sqrt{\sum E_i^2} \tag{2.3}$$

For each unmixing there is a Root Mean Square Error image to validate the process. Values of the fraction should be in the range of 0 and 1. Pixels having high RMS values and/or fractions lower 0 or larger than 1 indicated an unmodelled compositional variability in the scene (Schweik and Green, 1999).

2.2.2 Change Vector Analysis

In this study Change Vector Analysis (CVA) is used for detecting and characterizing land cover change. Soil fraction images and vegetation fraction images were considered for this analysis (Khiry, 2007). The length of the change vector indicates the magnitude of change, while its direction indicates the type of the change. In this study the magnitude of vectors was calculated among spectral changes between the endmember fractions images (soil and green vegetation) of dates 2001/2007 and 2007/2016 respectively. Fraction of vegetation was placed along the X-axis and the fraction of sand soil placed along the Y-axis. The magnitude of the vector was calculated from the Euclidean Distance and represented the difference between the pixel values of the fraction images for sand soil and vegetation cover respectively between the dates 2001/2007 and 2007/2016 as shown in equation (2.4).

Where:

$$R = \sqrt{(y_b - y_a)^2 + (x_b - x_a)^2} \tag{2.4}$$

R - Euclidean Distance

y_a - fraction value of sand soil from date 2

y_b - fraction value of sand soil from date 1

x_a - fraction value of vegetation cover from date 2

x_b - fraction value of vegetation cover from date 1

Change direction is measured as the angle of the change vector from pixel measurement at time 1 to the corresponding pixel measurement at time 2

Table 2.1 Direction image classified classes

Classes	Brightness	Greenness
Regrowth	-	+
Persistence	-	-
Degradation	+	-
Persistence	+	+

Angels measured between 90° and 180° indicated an increase in soil and decrease in vegetation cover, this representing an increase of degraded areas. Angels measured between 270° and 360° indicate a decrease of soil and increase of vegetation cover, this representing re-growth of vegetation cover. Angels measured between 0 to 90° and 180° to 270° indicate either increase or decrease in both of sand soil and vegetation cover. This change is represented as persistence, which represents either an increase or decrease in sand soil and vegetation in the study area.

By observing the soil fraction difference image and the vegetation fraction difference image, highly soil and vegetation changed areas can be identified. Then the identified area can be used to define the threshold values and to classified magnitude of the land cover change of two time periods. Two classified direction images were obtained for 2001/2007 and 2007/2016 time period. The magnitude of the classified directions can be taken from the early mentioned magnitude images. These classifications were done using the decision tree classification tool in ENVI 5.1 software.

2.2.3   Index Differencing

In this research for the comparison of the CVA analysis results, TDVI (Transformed difference vegetation index) differenced map were used. TDVI is a promising way of identifying the land degradation.

$$TDVI = 1.5 * \frac{(NIR-R)}{(\sqrt{NIR^2 +R+0.5}\;)}$$
(2.5)

Near infrared band (NIR) and red band(R) of a satellite image is used to calculate the TDVI. TDVI calculation was applied for the all three images of 2001, 2007 and 2016. Then the image differencing was done between 2001-2007 and 2007-2016. Image based threshold values were identified and TDVI difference map was classified according to the land cover change. (Regrowth, persistence and degraded)

3   RESULT AND DISSCUSION

3.1   Analization of fraction images

The most critical step in SMA is the selection of endmembers to produce of fractions image. Endmembers must be representative of the main materials in the image scene. All of the spectral variance of the scenes is included by the mixture model, while reducing the total RMS error. The number of endmembers is restricted to the number of Landsat bands used in this analysis. Based on the literature three endmembers were selected, soil, green vegetation and shade. The fraction images and RMS error of each reference endmember were computed for each pixel of the different Landsat imagery. High fraction will be brighter than areas of low fraction in the displayed fraction images.

These images also displayed in the grey scale ranging 0 to 1. Higher fractions of vegetation are indicated by the white area while lower fractions of vegetation represented by the dark areas. From the statistics of these vegetation fraction images it can be seen that there is a decrement of vegetation over the region throughout the period of 2001 to 2016. The mean soil fraction over the study area was 0.136, 0.156, and 0.177 in 2001, 2007 and 2016 respectively. The mean vegetation fraction over the study area was 0.136, 0.156, and 0.177 in 2001, 2007 and 2016 respectively.
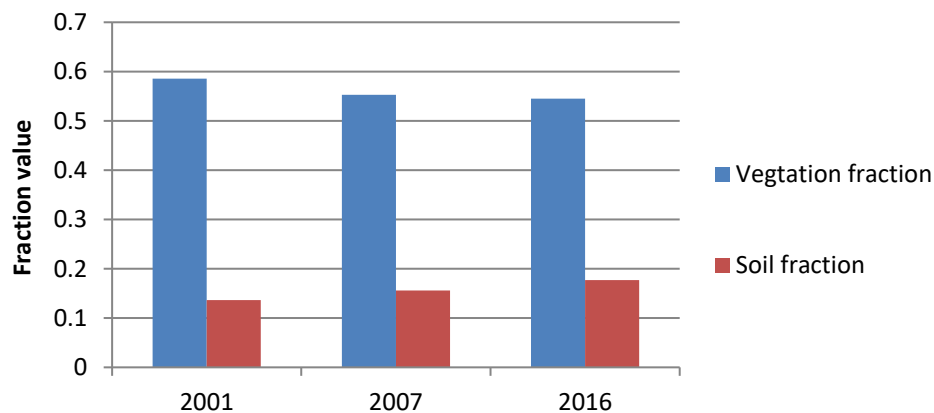
Graph 3-1 Vegetation and soil mean fraction over the time period

This graph indicates the increment of soil and the decrement of the vegetation over the time period in the study area. Therefore the land degradation can be roughly identified from the observation of the soil and vegetation fractions.vegetation fractions are shown in the below figure.
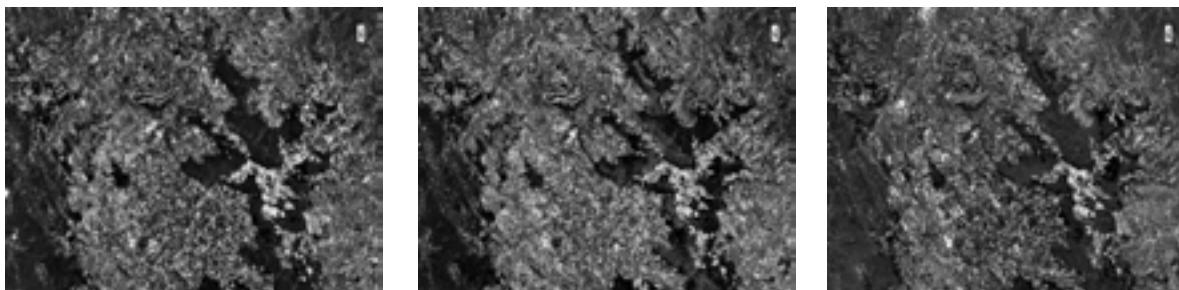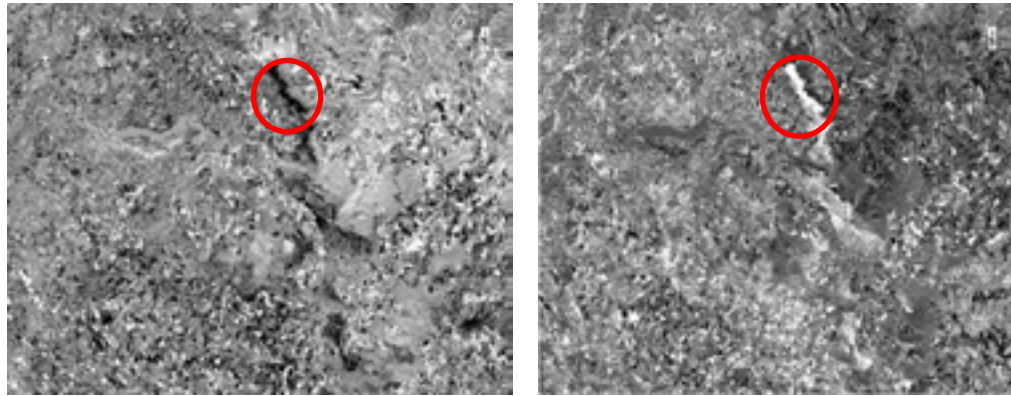

Figure 3 Soil fraction images in 2001, 2007, 2016 (left to right)

3.1.1 Vegetation Fraction Differences

Figure 4 Vegetation fraction images 2001/2007 (left), 2007/2016 (right),

Changes can be observed from both vegetation and soil difference images. Positive difference between two time periods, indicate by the bright color areas where dark color areas represent the negative differences. When considering the soil fraction difference images, it shows that the areas in bright color have high final stage soil fraction value than the initial soil fraction value. Then it can be identified as an area where the soil has increased. Then it helps to map the degraded area. This applies the same way to the vegetation fraction differences. That gives the areas where the vegetation cover increase or decrease. Regrowth areas can be clearly identified from this difference images. The selected area in figure(4) shows an increase of vegetation in 2001 to 2007 time period while the same area in 2007 to 2016 time period shows an increase of vegetation. These identified areas from the difference images can be used for the threshold selection for the CVA analysis.

3.2 CVA analysis

The soil and vegetation fractions from SMA were used as an input for Change Vector Analysis (CVA) to analyze land degradation in the period of 2001 to 2007 and of 2007 to 2016. The resulting images of CVA display magnitudes and directions of the changes. Since only soil and vegetation fractions were applied in this analysis, only three possible classes of change were being recognized (Table 3:1)

Table 3.1 Possible change classes from both input and related types of change

Class	Soil Fraction	Vegetation Fraction
Regrowth	-	+
Degraded	+	-
Persistence	+ -	+ -

The degraded areas in CVA are characterized by an increase of sand fraction and decrease in vegetation fraction. This is measured by a positive angle of sand fraction and a negative angle of vegetation fraction. The re-growth class was characterized by an increase of vegetation cover and a decrease of soil. The persistence class was indicated by simultaneous increase or decrease in both sand and vegetation fractions. Land cover change map including land degradation are presented between 2001 to 2007 and 2007 to 2016 respectively. The threshold of final magnitude was defined for each change class by observing the magnitude image and the fraction difference images.

From this threshold selection the land degradation maps were obtained. Two maps were displayed and the statistics were given below in table (3.2) for the two time periods.
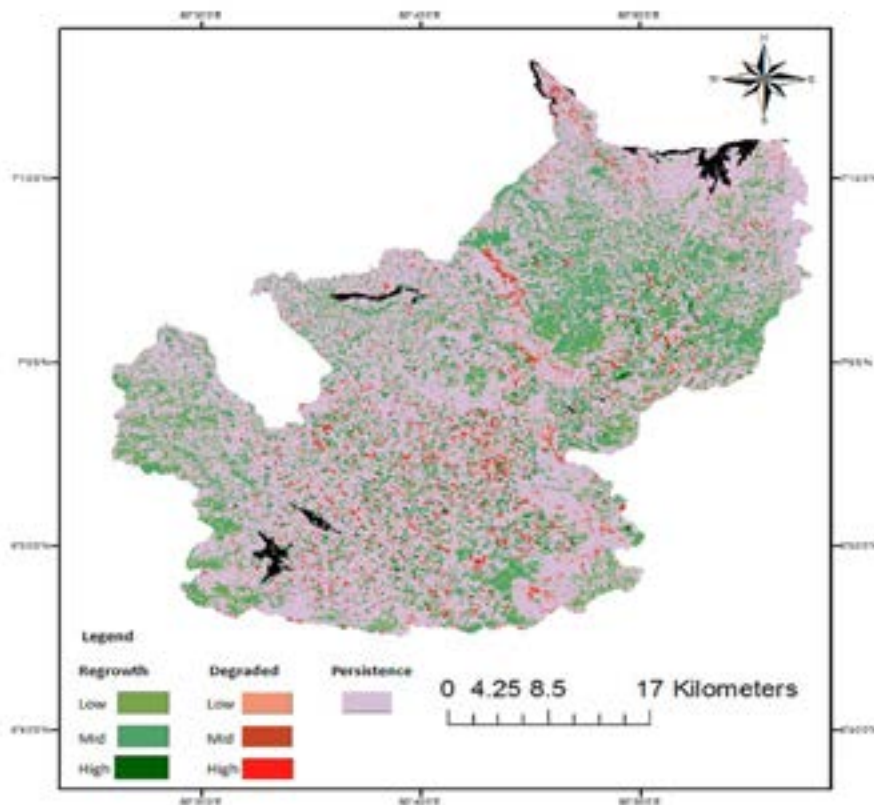
3.2.1   Land Degradation Maps of Change Vector Analyse

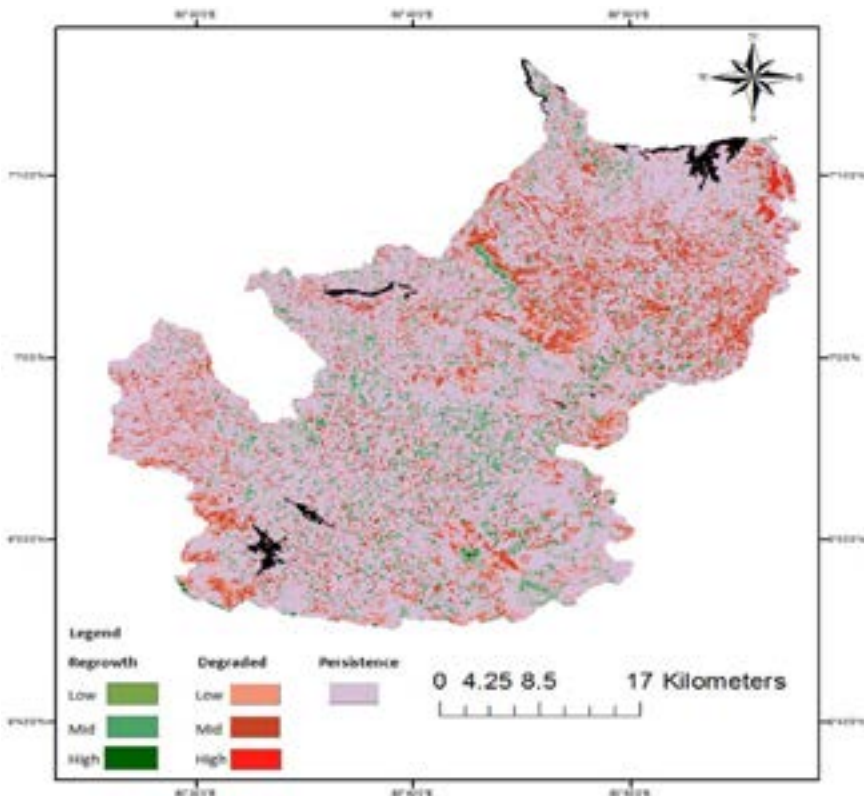Figure 5 **Land degradation map of change vector analyze (2001 – 2007)**

Figure 6 **Land degradation map of change vector analyze (2007 – 2016)**

Table 3.2 Statistical table of degradation and regrowth process of 2001 – 2016 time period

Degradation			2001-2007				
Low		Medium		High		Sum	
30.25 km²	27.44%	76.74 km²	69.6%	3.27 km²	3 %	110.27 km²	100%
Regrowing			2001-2007				
Low		Medium		High		Sum	
181.48 km²	60.67%	303.89 km²	60.67%	15.61 km²	3.12%	500.98 km²	100%
Degradation			2007-2016				
Low		Medium		High		Sum	
122.66 km²	35.68%	217.09 km²	63.14%	4.06 km²	1.18 %	343.80 km²	100%
Regrowing			2007-2016				
Low		Medium		High		Sum	
48.06 km²	31.24%	101.29 km²	65.80%	4.5 km²	2.9%	153.82 km²	100%

3.2.2   Comparison of The CVA Results

This comparison was done with the land degradation maps based on the TDVI index differences for the two time periods. The TDVI index was used because it does not contain the saturation concerns that NDVI has and also minimizes the influence of the soil background. When compare the results it can be seen that both shows similar land cover changes. In the CVA analysis, the results include more information than the TDVI based maps because of the additional analysis in soil and vegetation fractions by CVA allow for more detailed classification of land cover. The following figures show the visual similarity between the maps.
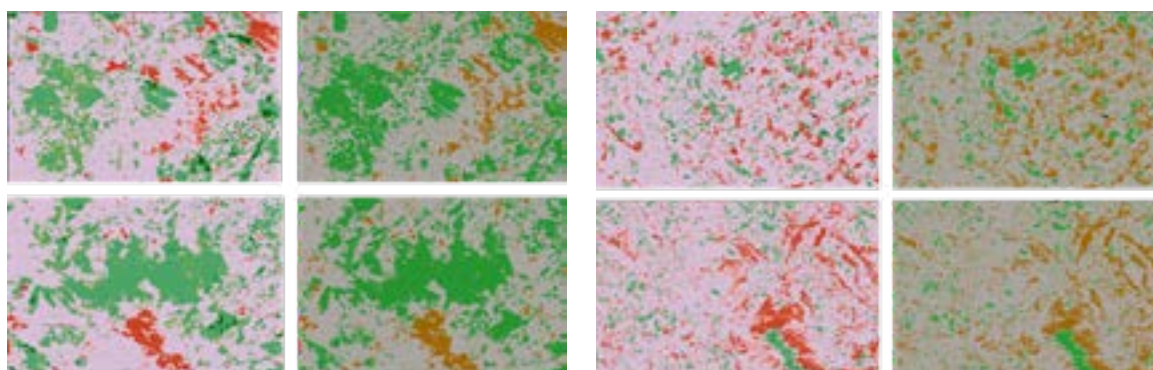
Figure 7 CVA change maps with the corresponding TDVI based maps (left - 2001/2007, right - 2001/2007)

4   CONCLUSION

Spatial and temporal data of remote sensing were used to understand the phenomena of degradation processes in Nuwara Eliya district. SMA technique was adopted to map and analyze the degradation processes using the above mention data. Combinations of multispectral mixture analysis of Landsat imagery used to examine the nature of the land degradation processes in the study area in the years 2001, 2007 and 2016. When analyzing the fraction images it shows an increment of soil and a decrement of the vegetation proving the undergoing land degradation. This concludes that SMA applied to Landsat imagery such as TM and ETM+ is an efficient technique in mapping and monitoring desertification processes in the study area.

CVA maps the degraded areas and proves the increase of such areas from 2007 to 2016 than from 2001 to 2007. Meanwhile, the results of CVA analysis show a pattern of decrement in re-growth areas from the time period 2001 to 2016. On the other hand CVA results show an increase in persistence areas during the addressed periods. For this study, if there any filed data about the degradation condition in the study area; it would be great for the evaluation. Hence According to the result of this research, it was found that Nuwara Eliya district is under the threat of the land degradation as it is one of the major district affected by land degradation in Sri Lanka.

References

References from other literature:

Khiry, M.A.,2007. Spectral Mixture Analysis for Monitoring and Mapping Desertification Processes in Semi-Arid Areas. (first ed.), Rhombos-Verlag, Berlin.

Schweik, M.C. and Green, M.G. (1999). The Use of Spectral Mixture Analysis to Study Human Incentives, Actions, and Environmental Outcomes. Social Science Computer Review, Vol. 17 No. 1, 40-63.

Wijeratne, M.A., 2010. Land degradation in up and mid country and control measures, Ministry of Environment & Renewable Energy, Battaramulla, Sri Lanka.

References from websites:

Land degradation neutrality resilience at local, national and regional levels.(2017). Retrived August 28,2017 from http://www.unccd.int/Lists/SiteDocumentLibrary/Publications/Land_Degrad_Neutrality_E_Web.pdf.

HIGH TEMPORAL RESOLUTION OF SENTINEL-1A DATA FOR PADDY FIELD IDENTIFICATION BASED ON CHANGE DETECTION METHOD

Agustan (1), Swasetyo Yulianto (1), Anisah (1), Lena Sumargana (1), Budi Heru Santosa (1)

[1] Center for Regional Resources Development (PTPSW), Agency for the Assessment and Application of Technology (BPPT), Jalan M.H. Thamrin No. 8, Jakarta, Indonesia

Email: agustan@bppt.go.id

KEY WORDS: change detection, sentinel-1A, image classification, paddy growth stage

ABSTRACT: Sentinel satellite imagery with radar sensors for one particular area with the same orbit can be compared every 6 days and freely available to be downloaded. This advantage can be exploited to identify land cover changes in a region regularly. Paddy is fast-growing crop with approximately 120 days life cycles. Hence, paddy growth stage can be monitored with this radar sentinel satellite. In addition, radar satellite is also cloud free and therefore it is suitable for tropical region such as Indonesia. This paper describes a study of paddy field identification based on the change detection method of paddy growth stage. Sentinel-1A images for Indramayu region in West Java from January 2018 to June 2018 are downloaded and processed using SNAP software. It is found that there are certain regions that show rapid changes over this time period including inundated, growing and harvested stages. That rapid changes area can be indicated as paddy fields. In addition, by validating the images with regular field observations every month from Area Frame Sampling campaign, it is found that the accuracy of paddy field identification is around 95%. By examining the relationship of backscatter value of the images to a complete paddy growth stage, it is found that the VH polarization gives a narrower range compare to VV polarization. The backscatter range for land preparation is approximately 0.073 to 0.0389, for early vegetative is approximately 0.0030 to 0.0114, for late vegetative is approximately 0.0113 to 0.0245, generative is approximately 0.0160 to 0.0337; and for harvesting is approximately 0.0096 to 0.0377 respectively.

1. INTRODUCTION

Thematic map that presents paddy field location should be available in detail scale. Usually, paddy field map is derived from remote sensing method by utilizing optical image such as MODIS (i.e. Xiao et al., 2006 and Gumma et. al., 2011); Ikonos (i.e. Kim et al., 2005 and Bannari et al., 2006), and Quickbird (i.e. Wu et al., 2004 and Gnyp et al., 2010). These optical data sets have advantages in spectral resolution and therefore it is easy to discriminate paddy field distribution on the ground. However, cloud constraint especially for tropical region, sometimes makes difficulties to extract the information at the ground. Therefore, radar-based satellite system could be a compliment to address this problem.

The utilization of radar-based satellite system for agricultural sector or crop monitoring had been studied for many years such as by Le Toan et al., (1997), Lopez-Sanches et al., (2011) and Inoue et al., (2014). These studies

show the ability of radar sensor for crop monitoring based on backscatter and polarimetric analysis. One advantage of radar system is the polarimetric feature that sensitive to height variation. Variation or changes on object's height can be used as important signature for crop monitoring.

The launching of Sentinel-1A satellite on 2014 and Sentinel-1B on 2016 that carries C-band synthetic aperture radar (SAR) sensor that constellates each other, enable user to obtain image for the same location every 6 days (Torres et al., 2012). The temporal resolution for each satellite actually is 12 days with 10 meter spatial resolution. This program are developed and operated under the Global Monitoring for Environment and Security (GMES) framework. The high temporal resolution is useful for continuous monitoring system such as crop monitoring.

Paddy field can be identified by rice plant life cycle that generally between 100 to 210 days with clear changes in physical or growth stage (Vergara, 1991). Based on this feature, paddy field will be identified as an area that covered by vegetation and changes periodically and should be flooded in one cycle. This paper discusses the ability of high temporal resolution of Sentinel-1A image to identify paddy field for thematic mapping.

2. DATA AND METHOD

To assess the ability of Sentinel-1A in identifying paddy field, data that covers at least one life cycle for rice plantation should be gathered. The study area for this research is Indramayu regency, one of the main rice producers in West Java, Indonesia. Usually, the rice that planted in Indramayu has 120 days life cycle or approximately 4 months for one planting season. For that reason, data from January 2018 to June 2018 are downloaded from Copernicus Open Access Hub (https://scihub.copernicus.eu/dhus/#/home). Based on previous literatures, this research utilizes interferometric wide swath mode (IW mode), dual polarization (Vertical-Vertical and Vertical-Horizontal) level 1 in ground range, multi-look, detected products (GRD). These data sets are processed by a free and open source Sentinel Application Platform (SNAP) toolbox.
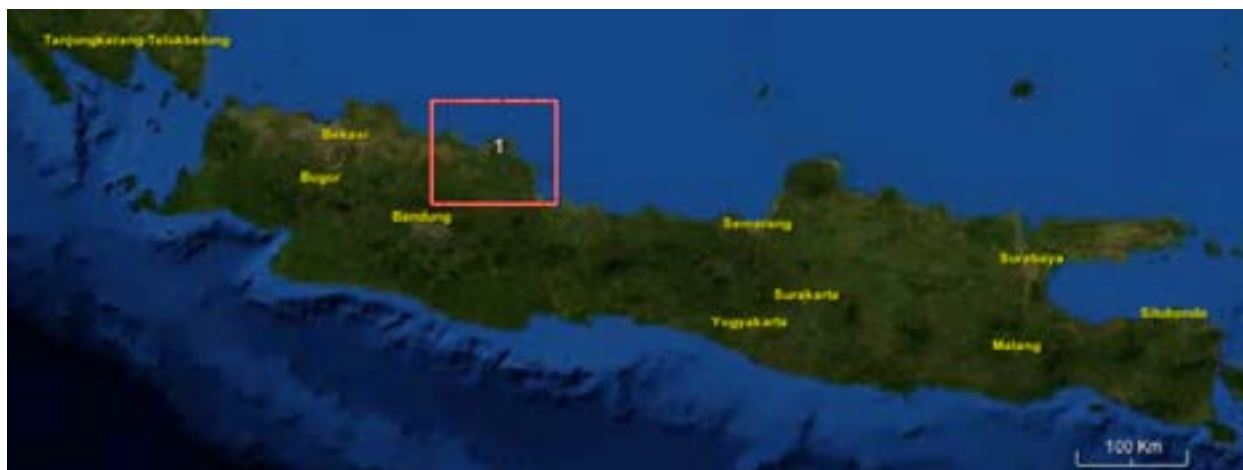

Figure 1. Location of Indramayu and Sentinel-1A data (red box) in Java Island as study area

To address the hardware limitation especially the memory shortage, all the data are clipped to specific region and then are processed. Data processing chain for GRD data type is set to graph builder for batch data processing.

The main steps are applying orbit file, calibration, speckle filter, and then terrain correction. The final image gives a sigma naught (σ^0) that represents original backscatter value for both VV and VH polarization.
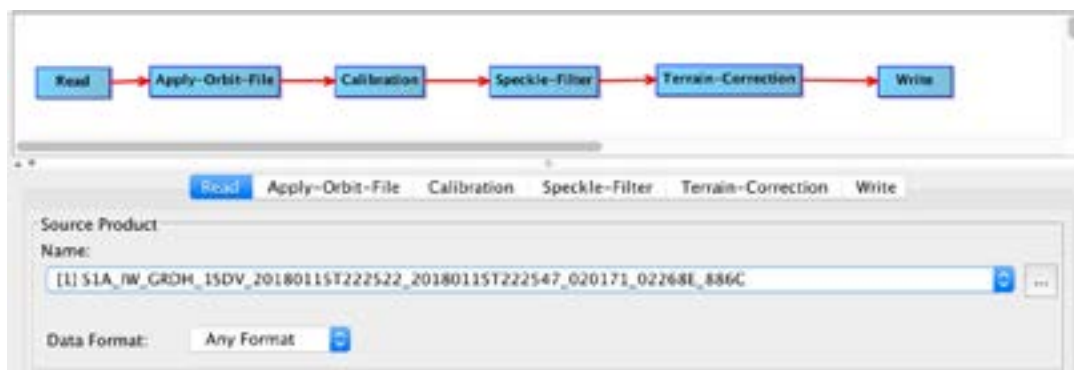

Figure 2. Graph builder for batch processing

Fortunately, there is a campaign under Area Frame Sampling framework for paddy growth stage observation in this region that carried out every fourth week of the month. This information is used for validation by set the location as control point. Therefore, only 6 Sentinel-1A data are processed which are observed on January 27th, February 20th, March 28th, April 21st, May 27th and June 20th.

3. RESULT AND DISCUSSION

The final results of dual polarization Sentinel-1A data processing are visualized in primary color composite as σ^0VV for red, σ^0VH for green and σ^0VV$/\sigma^0$VH for blue and illustrated in Figure 3.
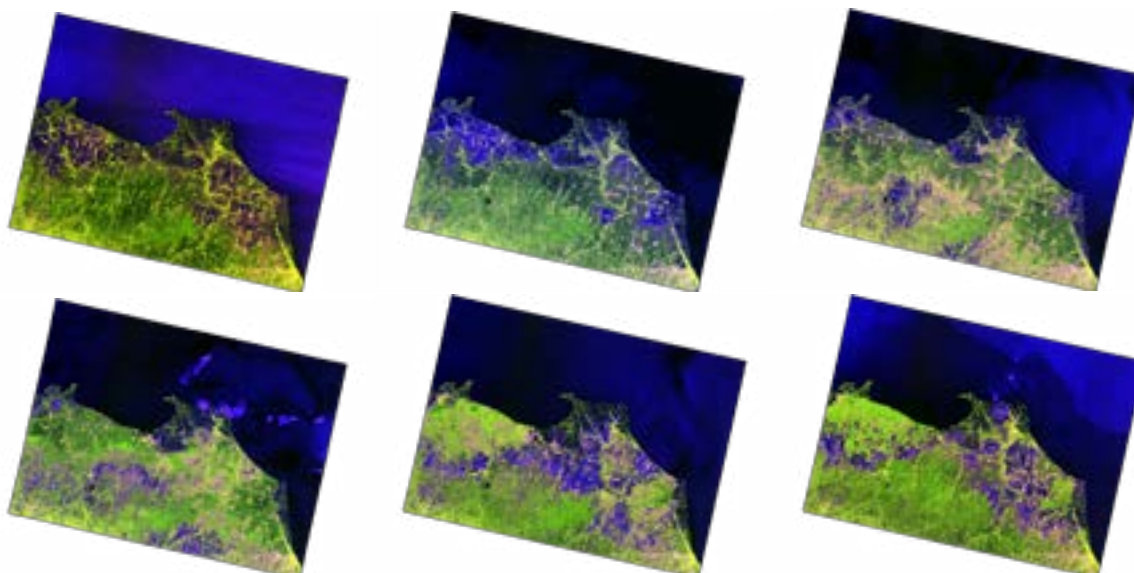

Figure 3. Final result in RGB composite. From left in upper part: January 27th, February 20th, March 28th, and from left in lower part: April 21st, May 27th and June 20th.
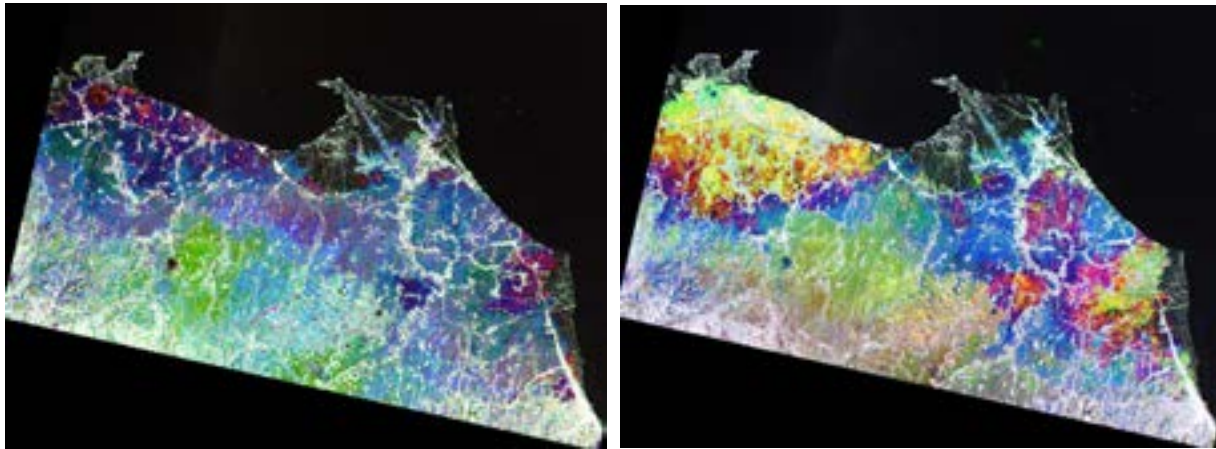
Figure 4. Illustration of land cover changes detected by Sentinel-1A in primary color composite: January 27th (red), February 20th (green), and March 20th (blue) in the left image; whereas April 21st (red), May 27th (green) and June 20th (blue) in the right image.

Land cover change is clearly shown by applying stacking data and visualizing in primary color composite as illustrated in Figure 4. Colored areas indicate rapid changes in 52 days (left image) and 60 days (right image). These rapid changes are associated with short-time crop life cycle, and in this case are rice plantation.

In addition, to assess the backscatter value of the image, ground truths from Area Frame Sampling campaign are overlaid and analyzed by using tools that are provided in SNAP. The location of Area Frame Sampling campaign is illustrated in Figure 5.
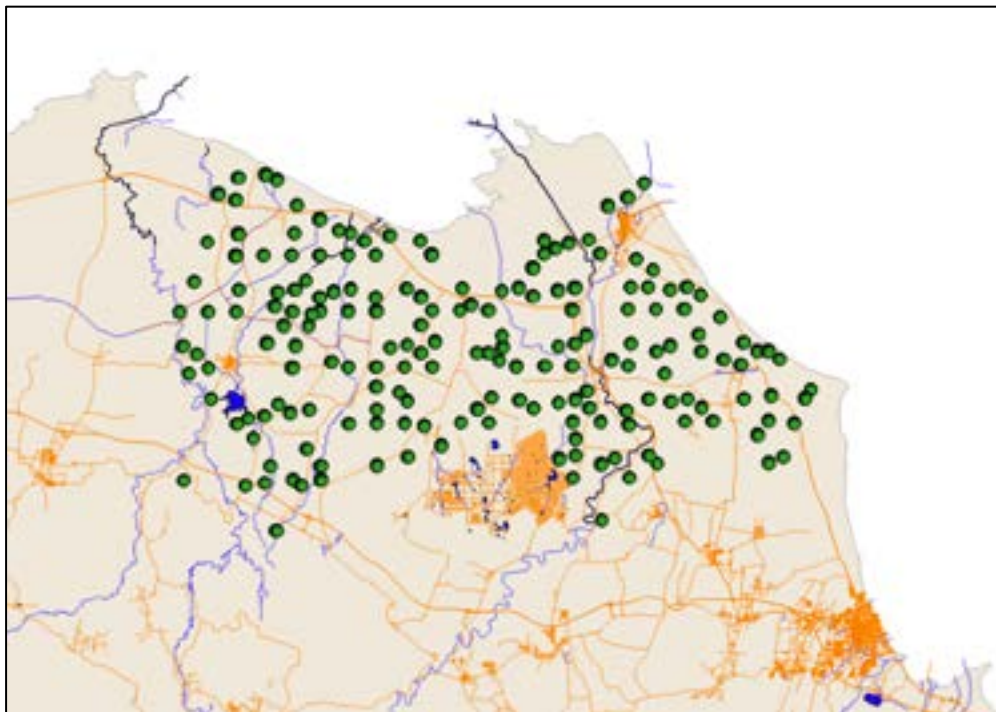

Figure 5. Distribution of 3387 observation points from Area Frame Sampling (green circle) as ground truth for Indramayu Region, West Java.

Table 1. Example of pixel value extraction and validation from field campaign

Latitude	Longitude	Image Date	Sigma_0 VH	Sigma_0 VV	Ground Truth Date	Ground Truth Value
-6.559311	108.029385	1/27/18	0.015246253	0.060355175	2018-01-27	6
-6.52257	108.130265	1/27/18	0.009351091	0.042256512	2018-01-27	6
-6.509824	108.001054	2/20/18	0.028982354	0.092287131	2018-02-20	6
-6.521682	108.130232	2/20/18	0.033525202	0.101875447	2018-02-20	6
-6.52258	108.130232	2/20/18	0.023431322	0.143588141	2018-02-20	6
-6.368429	108.234077	2/20/18	0.002892515	0.005166989	2018-02-20	6
-6.368429	108.234975	2/20/18	0.002134267	0.004360302	2018-02-20	6
-6.369328	108.234077	2/20/18	0.00756973	0.013779291	2018-02-20	6
-6.521719	108.130277	3/16/18	0.048140034	0.089379467	2018-03-16	6
-6.522618	108.130277	3/16/18	0.054879494	0.186148807	2018-03-16	6
-6.55936	108.029339	4/21/18	0.033864543	0.10031914	2018-04-21	6
-6.521721	108.13022	4/21/18	0.027976893	0.122658789	2018-04-21	6
-6.522619	108.13022	4/21/18	0.029774463	0.115523502	2018-04-21	6
-6.559323	108.02938	5/27/18	0.03126451	0.105629347	2018-05-27	6
-6.521683	108.130261	5/27/18	0.025587317	0.105892561	2018-05-27	6
-6.522581	108.130261	5/27/18	0.044676565	0.131874517	2018-05-27	6

Characteristic of paddy growth stage based on backscatter value can be determined by applying statistical data analysis method (i.e. removing outliers and filtering) for backscatter and its field observation value.

Table 2. Summary of Backscatter Value and Paddy Growth Stage

	VH min	VH max	VV min	VV max
Early Vegetative	0.003022372	0.011471651	0.01838165	0.11572706
Late Vegetative	0.011379626	0.024561392	0.036744998	0.123923079
Generative	0.016035783	0.033785921	0.046897581	0.108483001
Harvesting	0.009658071	0.037758555	0.044809434	0.133785455
Land Preparation	0.007397891	0.038979637	0.044757748	0.145751362

4. CONCLUSION

This paper shows the possibility of high-temporal resolution of Sentinel-1A data for paddy field identification. By applying stacking method and color composite visualizing technique, areas with rapid changes due to short-life crop type such as paddy plantation can be identified. By examining the relationship of backscatter value of the images to a complete paddy growth stage, it is found that the VH polarization gives a narrower range compare to VV polarization. The backscatter range for land preparation is approximately 0.073 to 0.0389, for early vegetative

is approximately 0.0030 to 0.0114, for late vegetative is approximately 0.0113 to 0.0245, generative is approximately 0.0160 to 0.0337; and for harvesting is approximately 0.0096 to 0.0377 respectively.

5. REFERENCES

Bannari, A., Pacheco, A., Staenz, K., McNairn, H. and Omari, K., 2006. Estimating and mapping crop residues cover on agricultural lands using hyperspectral and IKONOS data. Remote sensing of environment, 104(4), pp.447-459.

Gnyp, M.L., Yao, Y., Miao, Y., Yu, K., Huang, S., Dornauf, E., Hütt, C., Lenz-Wiedemann, V.I.S., Laudien, R., Jiang, R. and Chen, X., 2010. Evaluating within-field rice growth variability using Quickbird and Ikonos images in Northeast China. Proceedings of the 3rd ISDE Digital Earth Summit.

Gumma, M.K., Nelson, A., Thenkabail, P.S. and Singh, A.N., 2011. Mapping rice areas of South Asia using MODIS multitemporal data. Journal of applied remote sensing, 5(1), p.053547.

Inoue, Y., Sakaiya, E. and Wang, C., 2014. Capability of C-band backscattering coefficients from high-resolution satellite SAR sensors to assess biophysical variables in paddy rice. Remote Sensing of Environment, 140, pp.257-266.

Kim, S.J., Lim, H.J., Hong, S.M., Lee, M.S., Park, G. and Kwon, H.J., 2005. Development of agriculture-related data inventories using IKONOS images. *Korean Journal of Remote Sensing*, *21*(5), pp.425-431.

Lopez-Sanchez, J.M., Ballester-Berman, J.D. and Hajnsek, I., 2011. First results of rice monitoring practices in Spain by means of time series of TerraSAR-X dual-pol images. IEEE Journal of selected topics in applied earth observations and remote sensing, 4(2), pp.412-422.

Torres, R., Snoeij, P., Geudtner, D., Bibby, D., Davidson, M., Attema, E., Potin, P., Rommen, B., Floury, N., Brown, M. and Traver, I.N., 2012. GMES Sentinel-1 mission. Remote Sensing of Environment, 120, pp.9-24.

Vergara, B.S., 1991. Rice plant growth and development. In *Rice* (pp. 13-22). Springer, Boston, MA.

Xiao, X., Boles, S., Frolking, S., Li, C., Babu, J.Y., Salas, W. and Moore III, B., 2006. Mapping paddy rice agriculture in South and Southeast Asia using multi-temporal MODIS images. Remote Sensing of Environment, 100(1), pp.95-113.

---o0o---

INVESTIGATING THE POSIBILITY OF MONITORING THE RECOVERY OF TSUNAMI DAMAGES PADDY FIELDS USING MODIS 16 DAYS COMPOSITE NDVI

Ryota Uemachi[1], Kazuhiro Naoki[1], Kohei Cho[1]

[1]Tokai University

4-1-1 Kitakaname Hiratsuka, Kanagawa 259-1292, Japan,

kohei.cho@tokai-u.jp

**KEY WORDS:** Disaster, Great East Japan Earthquake, Tohoku, Aqua, Terra

ABSTRACT: On March 11, 2011, the magnitude 9.0 earthquake struck Tohoku Area of Japan. At that time, a large-scale tsunami associated with the earthquake hit the large area along the coast of Tohoku Area including many paddy fields. In the previous study, the authors have investigated the possibility of using MODIS 16 days composite NDVI for monitoring the recovery condition of the tsunami damaged paddy fields. The authors have selected a number of test sites for normal paddy fields, inundated inshore paddy fields, and inundated inland paddy fields. Usually, the NDVI of typical paddy field gradually increase from May to August and suddenly decreases in September to October due to harvesting. However, in the damaged paddy fields, the NDVI did not increase much. However, once the paddy fields are recovered, the seasonal NDVI pattern became almost the same as that of normal paddy field. The results well matched with the paddy recovery report provided from the local government. However, the 16 days composite NDVI often showed abnormally low values mainly due to snow and clouds. These abnormal data make it difficult to identify the recovery condition of the paddy fields. The authors have examined the ways to identify the abnormal NDVI values and interpolated them with the NDVI of before and after the event. The result suggested that the abnormal values are well removed without removing the reduction pattern affected by the tsunami.

1. INTRODUCTION

Remote Sensing is a necessary technology for monitoring the damages of disasters. On March 11, 2011, Great East Japan Earthquake with a magnitude of 9.0 struck the northeast part of Japan. Especially, the huge area along the coast of Tohoku Region was seriously damages by the tsunami associated with the earthquake. The maximum height of tsunami was 9.3m recorded in Soma, Fukushima (JMA, 2011), and the total of 561 sq. km was inundated by the tsunami (Nagayama et al., 2011). 19,667 people were lost and 2,566 people are still missing (FDMA, 2018). At that time, more than 5000 satellite images were taken within two weeks after the disaster under the international cooperation (Takahashi et al., 2012). The comparison of the satellite images taken before and after the disaster enhanced the serious damages of the area. Since 2011, the authors are monitoring the recovery of the tsunami damaged areas of the Miyagi Prefecture by ground survey and satellite image data analysis (Cho et al., 2013,2014,2015). In the previous study (Uemachi, 2017), the authors have applied multi temporal analysis of MODIS 16 days composite NDVI (NASA, 2018) to evaluate the recovery status of paddy fields. The result suggested the usefulness of using NDVI for paddy field recovery monitoring. However, in some areas, the 16 days composite NDVI showed abnormally low values mainly due to clouds. These abnormal data make it difficult to identify the recovery condition of the paddy fields. In this study, the authors have examined the ways to identify the abnormal values of NDVI f and interpolate the value with the NDVI of before and after the event.

2. TEST SITE

The Authors have selected Wakabayashi-ku, of Sendai, Miyagi Prefecture as the test site. Figure 1 shows the location of the test site of this study. The dotted line box shows the test site for evaluating how the 16 days MODIS images are composed to single image. The solid line box shows the test site for evaluation the multi-temporal change of NDVI. The map on the right shows the enlargement of the area using the inundated map of Miyagi Prefecture produced by Geological Survey Institute (GSI) of Japan (GSI, 2011). The red colored area is the area inundated by the Tsunami, and most of the area are paddy fields. The authors have selected two types of paddy field which are normal paddy field and inundated paddy field. The normal paddy field is the paddy field which were not suffered by the Tsunami. Inundated paddy field is the paddy field which was inundated by the Tsunami.
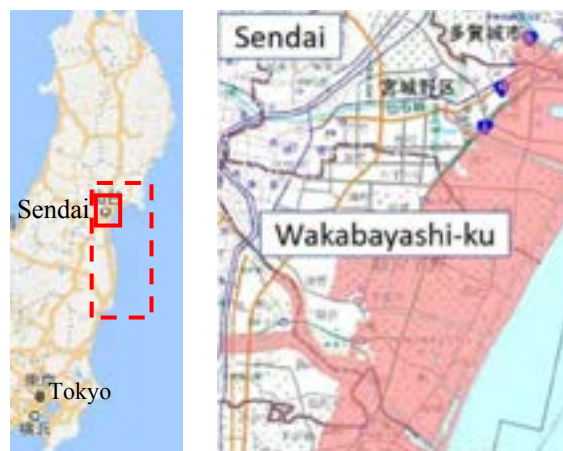
Figure 1. Location of the test site
(■ inundated area, from GSI)

3. ANALYZED DATA

NDVI (Normalized Difference Vegetation Index) defined by the following formula is a typical index for estimating the condition of vegetation (Weier et al., 2000).

$$NDVI = (NIR – VIS)/(NIR + VIS) \qquad (1)$$
Where NIR: Near infrared band
VIS: Visible red band

In this study, the 16 days composite of MODIS NDVI dataset (MOD13Q1) provided by NASA was analyzed(NASA, 2018). Table 1 show the specifications of MODIS(NASA, 2015). In MODIS NDVI dataset, Band 1 is used for VIS and Band 2 is used for NIR in calculating NDVI with formula (1) . Table 2 show the pixel reliability data of MODIS provided by NASA. This pixel reliability data is used in MOD13Q1 when calculating 16 days composite MODIS NDVI. In addition, band 3 was used for used for detect the bright area such as cloud or snow. For an example, if only the data of three days among 16 days were Good Data (0) and the others were No Data (-1), the three data are averaged for calculating the 16 days composite. In case of cloudy for 16 days, the highest NDVI value within the 16 days will be used. Figure 2 show 16 days MODIS images from July 28 to August 12, 2014. Certain areas of each images are covered with clouds. Figure 3(a) shows the result of 16 days composite. Most of the clouds are well rejected. Figure 3(b) shows which day is used for each location.

Table 1. Specifications of MODIS (NASA, 2015)

Band	Wavelength	IFOV	Swath
1	0.620 -　0.670 μ m	250m	2330km
2	0.841 -　0.876 μ m		
3	0.459 -　0.479 μ m	500m	
4 - 7	0.545-　2.155 μ m		
8 - 36	0.405 - 14.385 μ m	1000m	

Table 2. MODIS pixel reliability (NASA, 2018)

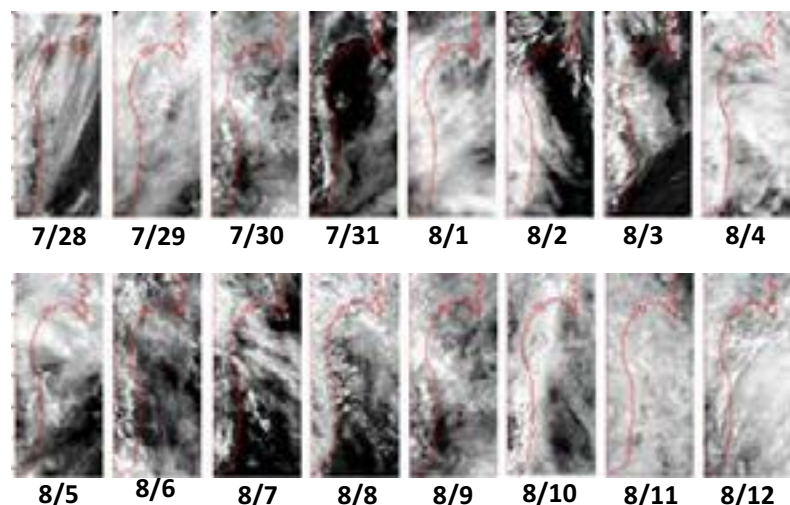| Rank Key	Summary QA	Description
-1	Fill/No Data	Not Processed
0	Good Data	use with confidence
1	Marginal Data	Useful, but look at other QA information
2	Snow/Ice	Target covered with snow/ice
3	Cloudy	Target not visible, covered with cloud

7/28　7/29　7/30　7/31　8/1　8/2　8/3　8/4

8/5　8/6　8/7　8/8　8/9　8/10　8/11　8/12

Figure 2. MODIS image of 可視光赤 2017
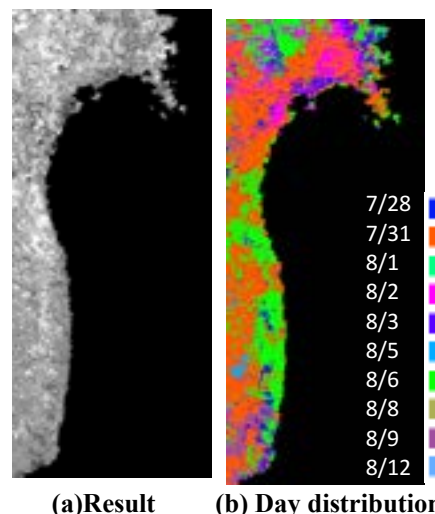

(a)Result　　(b) Day distribution

Figure 3. MODIS 16 days composite.

4. METHODOLOGY
4.1 Test Area Selection

Figure 4 shows a part of the agricultural recovery map of the Sendai Area prepared by the Miyagi prefectural Government (2015). The area framed in red is the area suffered by the Tsunami. The area colored in white corresponds to the area where the Tsunami did not come or not much affected by the Tsunami. The area colored in yellow corresponds to the area where the recovery project started in 2011, green area started in 2012, and purple area started in 2013. It is clear that the agricultural recovery project started from the inland area where the damages of the Tsunami was lighter than inshore area. Then the recovery project was expanded toward to the inshore area. The authors have selected two test areas from the four colored areas as shown on Figure 4. ● show the test areas selected from normal inland paddy field which were not affected by the Tsunami. ● show test areas selected in the recovery project area started in 2011(hereafter referred to as Area2011). ● show test areas selected in the recovery project area started in 2012(hereafter referred to as Area2012), and ● show test areas selected in the recovery project area started in 2013(hereafter referred to as Area2013).

Figure 4. Paddy Field Recovery Project Map

4.2 Evaluation of Irregular value of NDVI in 16 days composite

Figure 5 shows the MODIS NDVI seasonal variation of a normal paddy field of this region. This graph was derived by averaging NDVI of normal paddy field which were not suffered by the Tsunami for 2010 to 2017. (see ● in Figure 4).

In Tohoku Region, the NDVI of a paddy field gradually increase from May after the rice planting, and reaches to the peak in August. From September to October, NDVI suddenly goes down after the harvesting.

However, when we checked the NDVI seasonal variation of various paddy fields, some irregular change of NDVI is often observed. Figure 6 show such examples. The numbers in the graph correspond to the pixel reliability key described in Table 2. 2 corresponds to snow/ice and 3 corresponds to clouds. So, we can understand that big reduction of NDVI are caused by the snow or clouds cover during the 16 days. This will make it difficult to understand the condition of the paddy field. Moreover, even though the pixel reliability key is 3(cloudy), many of the NDVI value looked normal. So, simply using the pixel reliability key for extracting irregular value is not appropriate. Also, it has become clear that most of the points where the NDVI were 0, were the areas which were covered with snow. This also need to be solved.
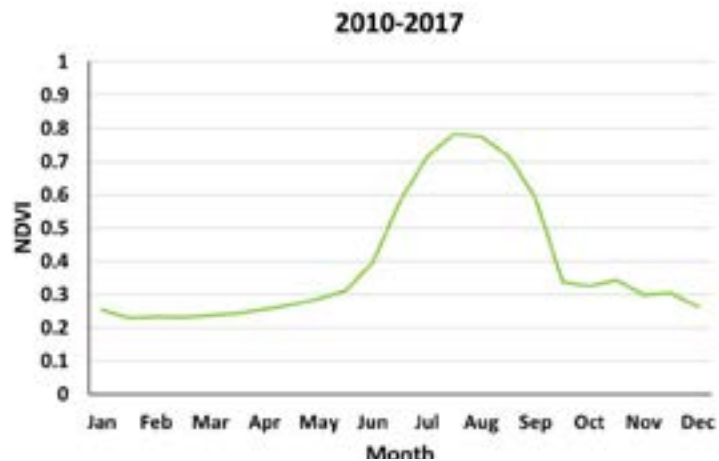

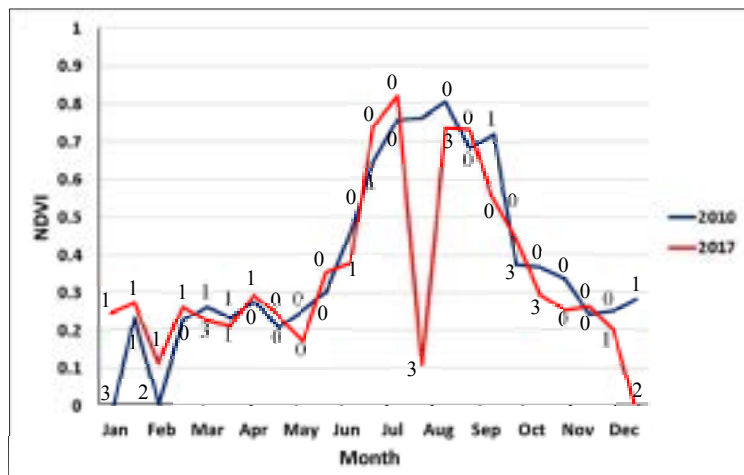**Figure 5. NDVI seasonal variability of normal paddy field.**

Figure 6. Irregular value of NDVI in the seasonal variability of normal paddy field.

4.3 Interpolation of Irregular value of NDVI in 16 days composite

The authors have examined ways to extract the irregular value of NDVI by comparing the NDVI value of before and after the period. In this study we defined the following two equations to interpolate the irregular value of NDVI.

(1) First Condition
If NDVI(t-1)-NDVI(t)>0.1 and
If NDVI(t+1)-NDVI(t)>0.1
or NDVI(t)=0
then
NDVI(t) = {NDVI(t-1)+NDVI(t+1)}/2   (1)

(2) Second Condition
If NDVI(t)＜0.1 and If NDVI(t+1)＜0.1
then
NDVI(t) = {NDVI(t-1)+NDVI(t+2)}/2   (2)
   t: target period (1 ~23)

The result of applying this method to the data of Figure 6 is shown on Figure 7. The seasonal variability became similar to the normal paddy field as shown on Figure 5.


Figure 7. Irregular value of NDVI in The seasonal variability of normal paddy field.

5. RESULT

The interpolation method was applied to the 16 days composite MODIS NDVI for the paddy fields selected in Figure 4. The result of before and after applying the method are shown on Figure 8 to 11. In all four cases, by applying the proposed method, irregular reduction of NDVI during the winter due to the snow cover (see (a) of each figure) were well interpolated by the data of before and after the period and normal paddy filed pattern became clear as seen in (b) of each figure. As a result, the normal paddy field patterns are clearly observed in figure 8(b). At the same time, the NDVI reduction pattern in year 2011 and 2012, due to the effect of Tsunami, is preserved after applying the method.
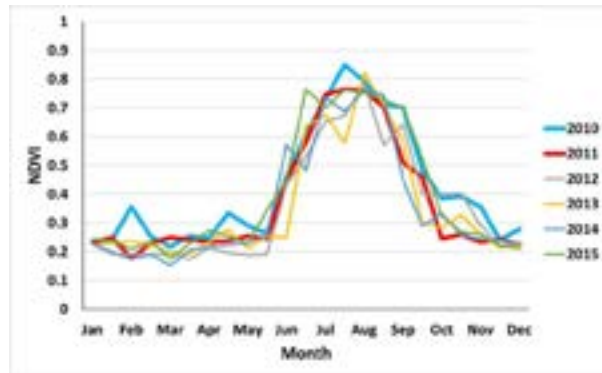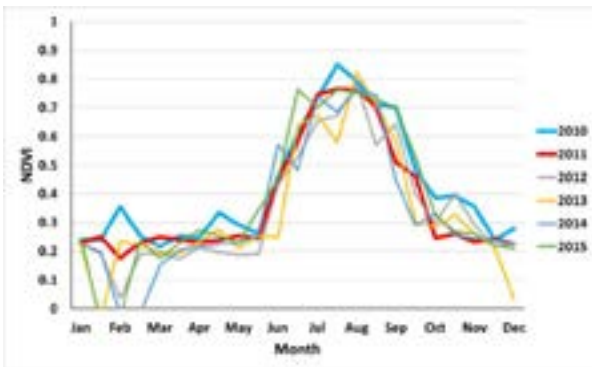
(a) Before

(b) After

Figure 8.● MODIS NDVI seasonal variability of normal inland paddy fields
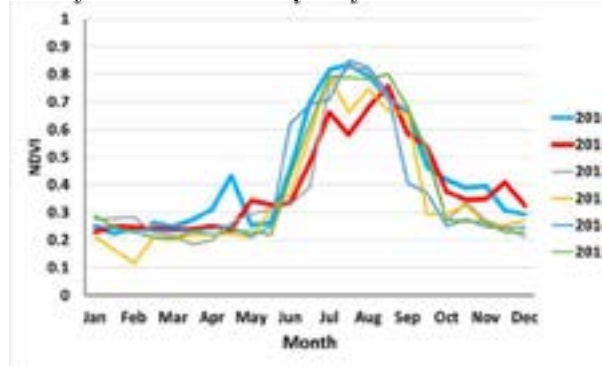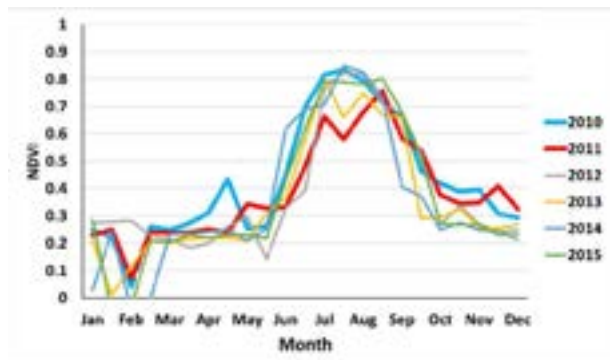
(a) Before

(b) After

Figure 9. ●MODIS NDVI seasonal variability of inland paddy fields which were invaded by Tsunami.

(a)Before   (b) After

Figure 10. ●MODIS NDVI seasonal variation inshore paddy fields which were damaged by the Tsunami.

(a) Before   (b) After

Figure 11. ●MODIS NDVI seasonal variation inshore paddy fields which were seriously affected by Tsunami,
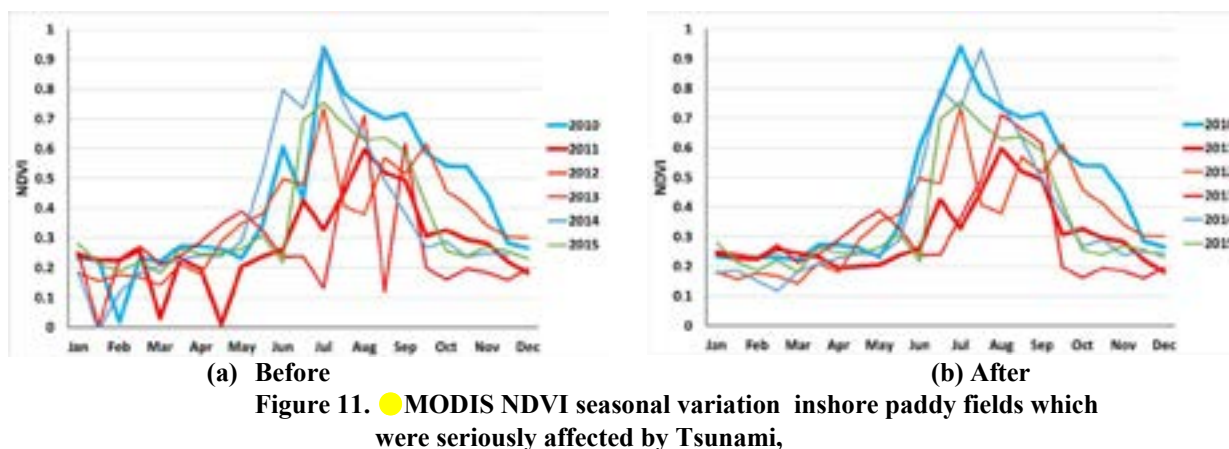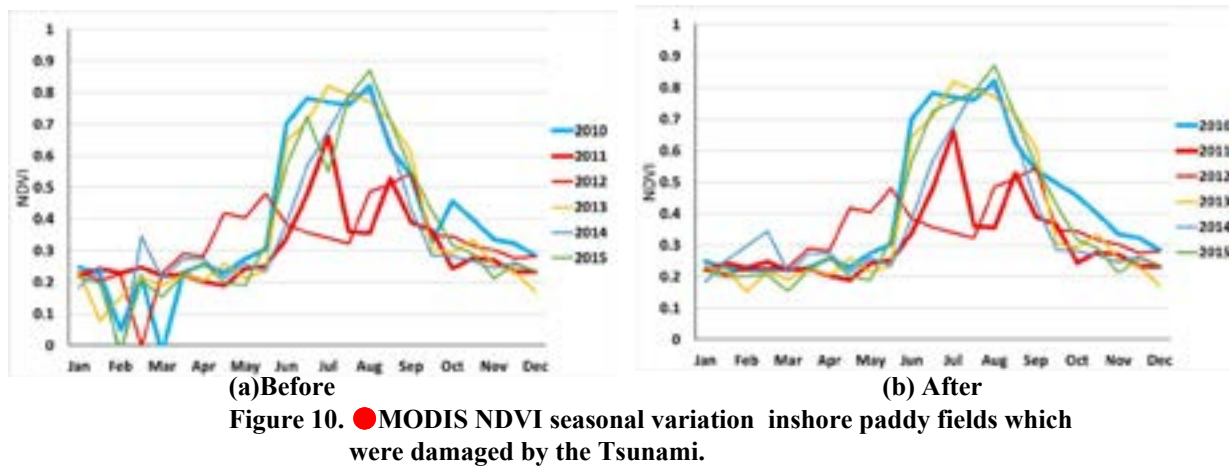
Figure 10 show the MODIS NDVI seasonal variation of the red area (●) in Figure 2. Even after the interpolation, the reduction in the summer season of 2011due to the Tsunami is preserved. As for Figure 11(a), the irregular reduction of NDVI during the summer season are making it difficult to understand the recovery situation of the paddy field. However, by applying the interpolation method, the recovery situation of the paddy field from 2011 to 2014 became much clear in Figure 10(b) or Figure 11(b).

6. CONCLUSION

The authors have been analyzing the time series of the MODIS 16 days composite NDVI data for evaluating the recovery condition of paddy fields in Wakabayashi Area of Miyagi prefecture damaged by the huge tsunami caused by the Japan earthquake occurred on March 11, 2011. The previous study suggested the usefulness of using NDVI for paddy field recovery monitoring. However, in some areas, the 16 days composite NDVI showed abnormally low values mainly due to clouds. In this study, the authors have examined the ways to identify the abnormal values of NDVI f and interpolate the value with the NDVI of before and after the event. By introducing two equations, most of the abnormal NDVI values were well extracted and interpolated by averaging the data before and after the event. As a result, the possibility of identifying the paddy field recovery conditions from the seasonal change of MODIS 16days composite NDVI has increased.

REFERENCES

JMA, 2011, The 2011 off the Pacific coast of Tohoku Earthquake Observed Tsunami, Available online: http://www.jma.go.jp/jma/en/2011_Earthquake/chart/2011_Earthquake_Tsunami.pdf

Nagayama, T., K. Inaba, T. Hayashi and H. Nakai, 2012, How the National Mapping Organization of Japan responded to the Great East Japan Earthquake?, Proceedings of FIG Working Week 2012, (TS03K-5791)1-15, Available online: Fire and Disaster Management Agency(FDMA), 2018, http://www.fdma.go.jp/bn/higaihou/pdf/jishin/158.pdf

Takahashi , M., M. Shimada, 2012, Disaster monitoring by JAXA for Japan Earthquake using satellites, Paper of the 10th International Workshop on Remote Sensing for Disaster Management, Available online:

Cho K., K. Fukue, O. Uchida, K. Terada, C.F. CHEN, 2013, Monitoring Environmental Recovery of Damaged Area in Tohoku, Japan from Space & Ground for Environmental Education, Proceedings of the 34th Asian Conference on Remote Sensing, SC03, pp.709-716.

Cho K., E. Baltsavias, F. Remondino, U. Soergel, H. Wakabayashi, 2014, RAPIDMAP Project for Disaster Monitoring, Proceedings of the 35th Asian Conference on Remote Sensing, OS-145, pp.1-6.

Cho K., K. Fukue, O. Uchida, K. Terada, H. Wakabayashi, T. Sato, C.F. Chen, 2015, A Study on Detecting Disaster Damaged Areas, Proceedings of the 36th Asian Conferenceon Remote Sensing, SP.FR2, pp.1-4.

Uemachi R., K. Naoki, K. Cho, Monitoring The Recovery of Tsunami Damaged Paddy Fields Using MODIS NDVI, Proceedings of the 38th Asian Conference on Remote Sensing, PS-04-ID-844, pp.1-4. October 2017.

NASA, 2018, https://ladsweb.modaps.eosdis.nasa.gov/missions-and-measurements/products/vegetation-indices/MYD13Q1/

NASA, 2015, http://modis.gsfc.nasa.gov/about/specifications.php

GSI, 2011, http://www.gsi.go.jp/kikaku/kikaku60003.html

Weier J., D. Herring, 2000, http://earthobservatory.nasa.gov/Features/MeasuringVegetation/ .

How the strongest La-Nina affected the equatorial tropics? Global analysis in 2010 with TRMM satellite

Muhamad Afifi Md Yatim (1), Fathiera Mansor (1), Aina Afifah bt. Mohd Yusof (1), Mohd. Nadzri Mohd. Reba (1,2), Mohd. Rizaludin Mahmud (1,2)

[1] Faculty of Built Environment & Surveying, Universiti Teknologi Malaysia, 81310, Johor Bharu, Malaysia
[2] Geoscience & Digital Earth Centre (InsTeG), Faculty of Built Environment & Surveying, Research Institute for Sustainable Environment, Universiti Teknologi Malaysia, 81310, Johor Bharu, Malaysia

Email: afie0913@gmail.com; firamansor888@gmail.com; ainayusof@gmail.com; rizaludin@utm.my; nadzri@utm.my

Abstract: This study analyzed the rainfall pattern changes in humid tropics at monthly scale during the strongest La-Nina event ever using Tropical Rainfall Measuring Mission (TRMM) satellite. At present the evidences had showed that the rainfall are changing and increasing in general in the tropics. However, specific characteristics of change including rate, quantity, and pattern was less elaborated. This parameters are critical to us in understand the changes, the cause, and most importantly figure out an appropriate method to adapt for the future scenarios. To anticipate the aforementioned issue, we had initiated the analysis to determine; 1) the trend of rainfall changes (events, quantity and spatial size) and 2) the rate of rainfall changes. The number of different rainfall events are determined to inform us the trend of impact of the La-Nina. On the other hand, the changes of rainfall quantity and spatial size primarily the increment cases would provide us with quantitative information how much the changes had occurred in specific areas and how large is the extent; whether it is a synoptic scale event or it was the aftermath effect at microscale. Finally, the rate of rainfall changes informed us how quick is the changes happen. The output from all the analyses will be used to classify types of impact that experienced by different parts of humid tropics; the most affected region by this La-Nina event.

Keywords: Climate Change, Big Geodata, Space Precipitation, GIS based analysis, Anomalies

1.0 INTRODUCTION

La Nina is a global phenomenon that caused extra rainfall occurrences; a result of the sea surface temperature decrement under the normal levels. This heavy rainfall is likely to cause catastrophes such as flood, sea level rises, and environmental safety due to heavy torrential rainfall. Adaptation to the hydro-meteorological changes is a major concern for many tropical region especially in the tropics (Wang et al. 2010; Wang et al. 2012; van der Voorn et al. 2012). However, specific characteristics of change including rate, quantity, and pattern was less elaborated. This parameters are critical to us in understand the changes, the cause, and most importantly figure out an appropriate method to adapt for the future scenarios (Beniston et al. 2012).

At present, the evidences had showed that the tropics has been claimed to be highly sensitive to environmental changes (Trenbeth, 2011). Rainfall are changing and increasing in general in the tropics (Chadwick et al. 2013). In the past decade, rainfall seasonality has been highly varied among different part of tropical region (Feng et al. 2013, Allan et al. 2010). The occurrences of extreme events such as La-Nina might exacerbates the significant changes of rainfall in this region due to high presence of vapor and cloud formation process. A thorough study on this is still inadequate and need quick attention. The availability of global satellite precipitation would be useful to address this concern.

Therefore this study investigates the impact of one of the strongest La-Nina in 2010 at global scale. Three objectives has been established, 1) measuring the rainfall changes, 2) analyzing the changes between different regions in the world, and 3) studying the trend of the rainfall changes. To materialize the objective we used the global dataset of widely used Tropical Rainfall Measuring Mission (TRMM). The output from all the analyses will be used to classify types of impact that experienced by different parts of world region particularly the humid tropics; the most likely affected region by the La-Nina event.

2.0 MATERIALS & METHOD

2.1 Global analysis on the impact of 2010 La-Nina

The impact of the 2010 La-Nina were measured by two means, first is the rainfall changes and secondly is the spatial occurrence of the events. Both analysis were relatively against the control environment of 2003. We select 2003 due to the absence of any major El-Nino or La-Nina during the year based on the global Oceanix Nino Index (ONI) Therefore, the data provides suitable control environment to measure the La-Nina effect. The rainfall changes were measured by summing up the total rainfall amount from June to December, the period in

2010 where La-Nina intensely occurred. Subsequently, the rainfall changes over specific region was identified. To evaluate the trend of the rainfall changes, the monthly rainfall average time series were developed.

2.2   Global precipitation data

Monthly rainfall data namely TRMM 3B43 from the Tropical Rainfall Measuring Mission (TRMM) were used as the primary data. The data was obtained from the Goddard Earth Sciences Data and Information Center through the official website of http://mirador. gsfc. nasa. gov. The TRMM data were chosen because of its high resolution (0.25 deg.), intensive global coverage and precise measurement. The data also has been widely used and recommended by many experts due to the mentioned factors.

2.3   World region of vector GIS data

We create the vector data of the border of major regions in the world. There were ten respective region, 1) North America, 2) South America, 3) Europe, 4) Russia, 5) Africa, 6) North Africa-Southwest Asia, 7) East Asia, 8) South Asia, 9) Southeast Asia, and 10) Africa. This vector is purposely used to extract individual rainfall data for each region in the data processing.

3.0   RESULTS AND DISCUSSION

On average, rainfall increment was dominant in most region in the world except North America and Africa (Table 1). Major increment of rainfall was occurred in Southeast Asia (47%) and South Asia in (24%). Minor increment (<10%) were indicated in Europe, South America, Australia-Oceania and the rest part of Asia. Figure 1 had clearly showed that La-Nina exacerbates heavier rainfall throughout Southeast Asia region and South Asia.

Table 1. Summary of the rainfall increment during 2010 La-Nina

Region	Region no.	Rainfall (mm/month)		Percent of increment (%)
		2010	2003	
Southeast Asia	9	254	207	46.8
South Asia	8	170	145	24.8
Europe	3	89	79	10.8

East Asia	7	95	86	9.0
Australia and Oceania	10	64	55	9.0
South America	2	88	85	3.3
Russia	4	65	62	2.8
Africa	5	63	66	-2.7
North Africa & South-West Asia	6	15	19	-3.8
North America	1	81	86	-4.8

The differences between the 2010 and 2003 rainfall also confirmed that assumption (Figure 2). Based on that figure too, we could made conclusive remarks that Southeast Asia suffered the impact the most and significant increment was taken place in the equatorial region. The monthly time series indicated that the increment occurred gradually since June until December (Fig. 3). Nonetheless, the figure also revealed that the rainfall increment occurred substantially in major part of west Africa and North America but with minimal amount.

(a) Jun – Dec 2003
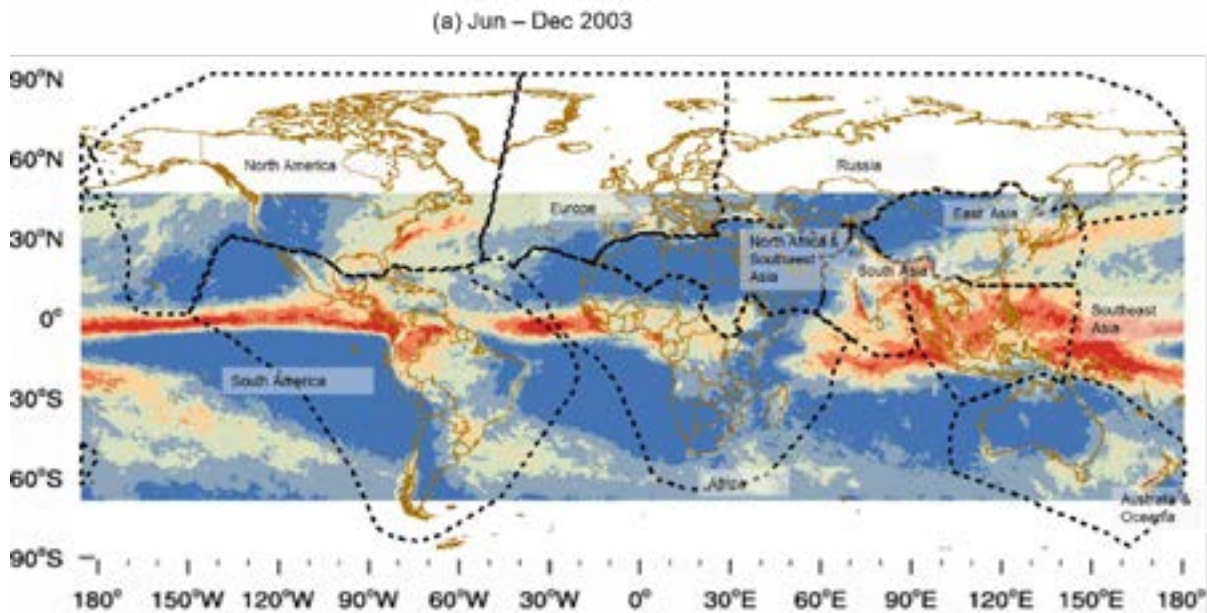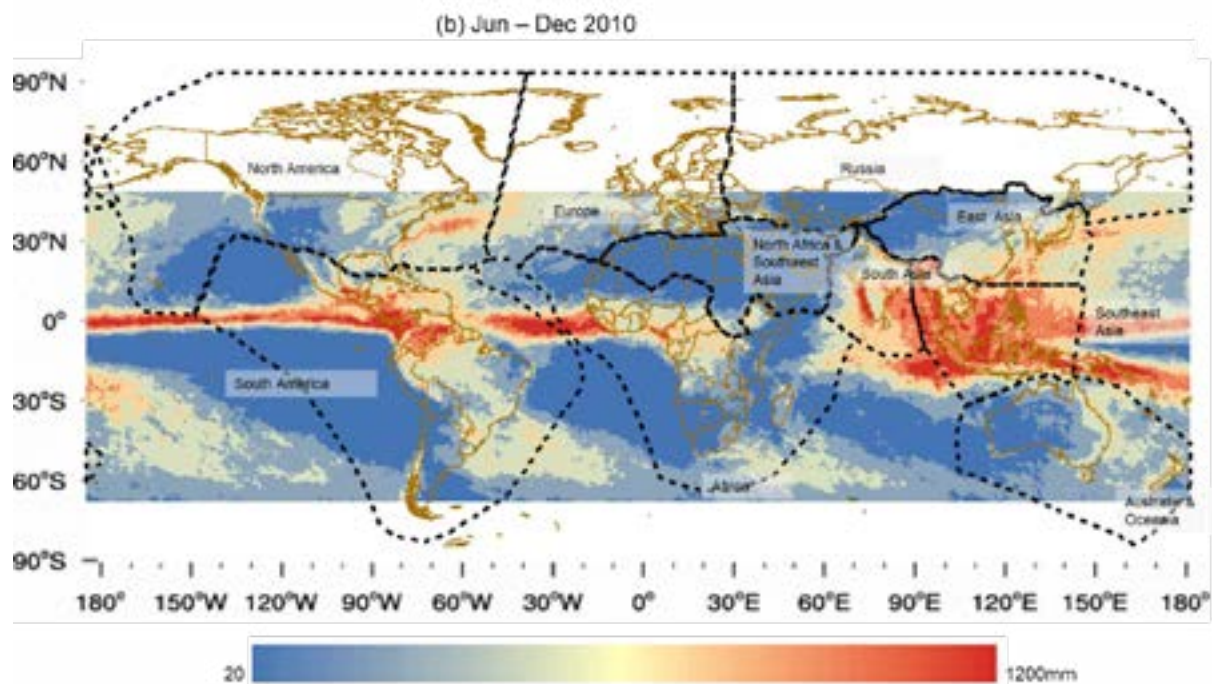
Figure 1. Six month accumulated rainfall (June-Dec) from TRMM satellite. (a) 2003, (b) 2010.
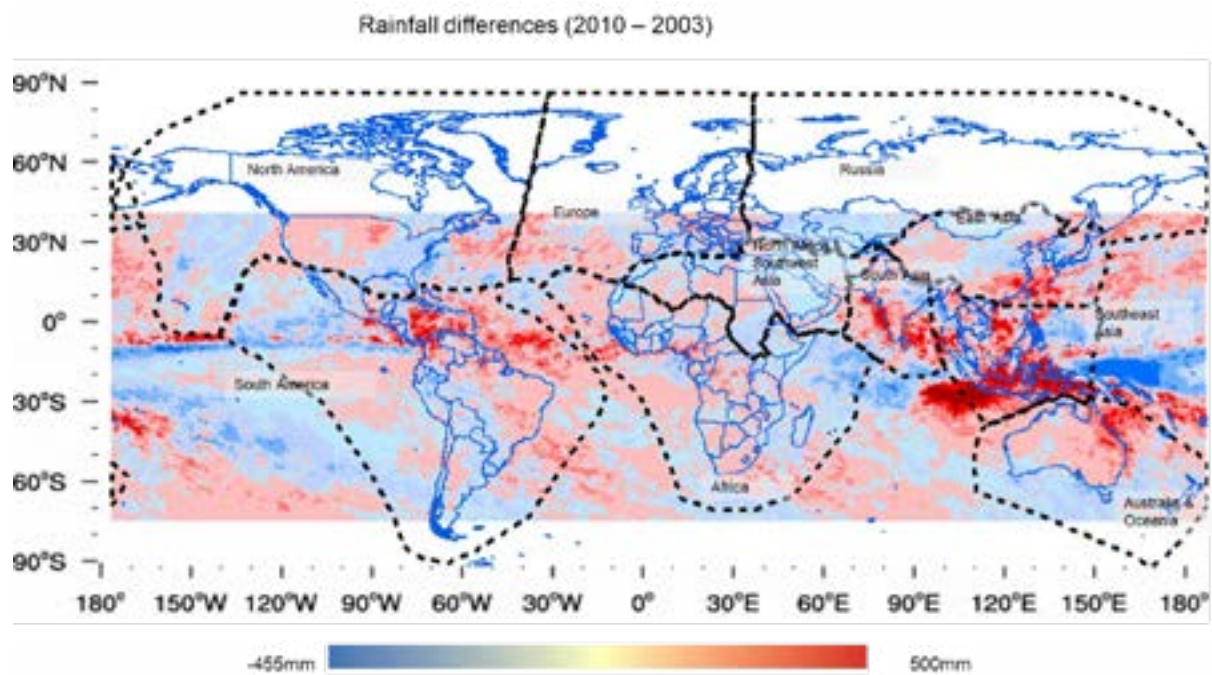
Figure 2. Rainfall differences (2010-2003)
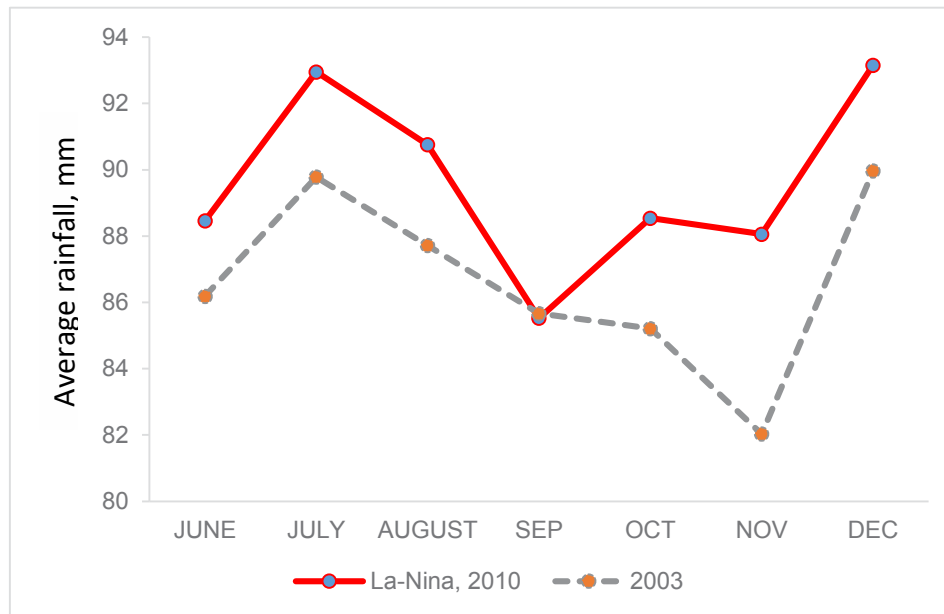
Figure 3. Monthly rainfall increment during La-Nina

4.0   CONCLUSION

This study has found out that the La Nina event in 2010 had impacted the Southeast Asia region the most compared to other region. In general, the dominant effect for most equatorial humid tropics was experiencing rainfall increment with varied intensity. The rainfall had increased significantly and it had been occurred gradually since June until December. The output of this study is useful to initiate appropriate adaptation, mitigation and prevention framework at local scale.

ACKNOWLEDGEMENT

REFERENCES

Allan, R. P., B. J. Soden, V. O. John, W. Ingram, and P. Good, (2010). Current changes in tropical precipitation. Environ. Res. Lett., 5 (2), 025 205, doi:10.1088/1748-9326/5/2/ 025205

Beniston, M., Stofel, M., Harding, R., Kernan, M., Ludwig, R., Moors, E., Samuels, P.,Tockner, K., (2012). Obstacles to data access for research related to climate and water: implications for science and EU policy-making. Environ. Sci. Policy 17,41–48.

Chadwick, R., Boutle, I., Martin, G. (2013). Spatial patterns of precipitation change in CMIP5: Why the rich do not get richer in the tropics. J. Climate, 26, 3803-3822.

Feng, X., Porporato, A., Iganacio Rodriguez, I. (2013). Changes in rainfall seasonality in the tropics. Nature Climate Change, 3, 811-815.

Trenbeth, E. K. (2011). Changes in precipitation with climate change. Climate Research, 47, 123-138.

van der Voorn T, Pahl-Wostl C, Quist J (2012) Combining backcasting and adaptive management for climate adaptation in coastal regions: a methodology and a South African case study. Futures 44:346–364

Wang X-J, Zhang J-Y, Wang G (2010) Climate change and water management adaptation for China. Xth Kovacs Colloquium, Paris, France. IAHS-AISH, pp 258–259

Wang X-J, Zhang J-Y, Shahid S et al (2012a) Catastrophe theory to assess water security and adaptation strategy in the context of environmental change. Mitig. Adapt. Strateg. Glob. Chang. doi:10.1007/s11027-012-9443-x

CLIMATOLOGICAL ANALYSIS OF VARIATIONS IN THERMAL COMFORT AND UHI OVER THE PUNE METROPOLITAN REGION

Vinayak B (1), Shirishkumar Gedam (1)
[1]CSRE, Indian Institute of Technology- Bombay, Powai,
Mumbai-400076, Maharashtra, India

Email: vinayakbhanage@iitb.ac.in; shirish@iitb.ac.in

KEY WORDS: MODIS, Seasonal and Diurnal Variation, Urban Heat Island, Urban Thermal Field Variance Index

ABSTRACT: This study investigates the seasonal and diurnal variation of Urban Heat Island (UHI) over Pune Metropolitan Region (PMR) of Maharashtra, India. The measurements of Land Surface Temperature (LST) were derived from the day and nighttime datasets available from MODIS satellite for the period of 2006-2016. This eleven years of data were processed and climatological averaged LST data were obtained for the seasonal and diurnal scale. The method of fringe analysis was used to estimate the phenomenon of Urban Heat Island (UHI). The large variations in the seasonal and diurnal pattern of UHI have been observed over PMR. To assess the impact of UHI on the quality of urban life, Urban Thermal Field Variance Index (UTFVI) is calculated on a diurnal and seasonal scale. Our analysis shows that during the daytime of the summer season densely populated southern part of the region shows the strongest UHI (3.10^0c) while in the night northeastern part of the PMR experiences the maximum magnitude of UHI (5.81^0c). In a winter spell, extremely small variation is noticed on a diurnal scale, whereas in general, it shows the highest intensity of UHI over Northeastern parts of the PMR. An analysis of UTFVI emphasizes that more than 80 % of the area of PMR has Normal to excellent conditions for urban living on both seasonal and diurnal scale. The combined analysis of UTFVI and UHI explains that in most of the part of PMR have suitable urban living conditions but an intensity of UHI is ranging from -3.73^0c to 5.81^0c which indicates the necessity to apply area wise proper mitigation strategies in order to reduce the intra-city effect of the UHI.

1. INTRODUCTION

Urbanization is the process where an escalating percentage of a population lives in urban and its suburban areas. This process is often associated with industrialization and modernization, as a large number of people shift from rural area to urban areas (Tumbe et al., 2016). These urban areas generate their own climatic domain that is dissimilar from their surrounding rural area. In India, about 34% of the population lives in the urban area and it has been projected that India will add 300 million new urban residents by 2050. (United Nations, 2018). This increasing trend of urbanization in India is one of the important factors which will affect the quality of an urban life. The increasing population of an urban area indicates the higher discharge of anthropogenic energy which triggers the modification of the local climate. The phenomenon of an Urban Heat Island (UHI) is one of the most noticeable human-induced modifications of the local climate. It mainly refers to the phenomenon of elevated atmospheric and surface temperatures of an urban area as compared to the surrounding rural area (Oke et al., 1973). Some time depending upon the response of local, physical and biophysical factors to the urban microclimatic conditions leads to having negative thermal alterations with the rural area this phenomenon is known as Urban Cool Island (UCI) (Martins et al., 2016; Rasul et al., 2015). There are mainly three types of UHI i.e. Surface Urban Heat Island (SUHI), Canopy Layer Urban Heat Island (CLUHI) and Boundary Layer Urban Heat Island (BLUHI). In a current study, we are mainly analyzing the variation of SUHI over Pune Metropolitan Region (PMR) at a different spatial and temporal scale. In order to recognize and assess the phenomenon of SUHI, it is a necessity to analyze the behavior of LST which is very sensitive to various other factors such as Land Use Land Cover (LULC), vegetation, topography, geo-location, surface properties, and other climatic parameters etc. The Spatio-temporal changes in these kinds of variables affect the LST which brings spatial and seasonal variations in SUHI. For an assessment of SUHI, there are mainly two types of methods (a) Measuring the LST data by using the weather stations/handheld instruments etc. (b) Measuring the LST data by using the satellite/ Airborne datasets (Remote Sensing). The first approach is based upon point observations which cannot represent the conditions of the entire area hence during this analysis we have used an approach of remote sensing methods which have a higher spatial resolution. The current study has been carried out over Pune Metropolitan Region (PMR). It mainly consists of two municipal corporations Pune Municipal Corporation (PMC) and Pimpari-Chinchwad Municipal Corporation (PCMC) and part of the Military cantonment board. The outer part of the PMR mainly consists of an agricultural area. An area of PMC is characterized by the dense population and settlement while the area associated with PCMC is typified with less dense and mostly with an industrial area. To date, there is no UHI related study has been carried out by considering the continuous region of Pune Metropolitan Area. The specific objectives of this study are: (1) Analyze

and evaluate the spatial and temporal variation of UHI over the PMR (2) Assess the impact of UHI on the quality of the urban life.

2. METHODOLOGY

2.1 Study area and Data Used

PMR is the second largest city of the state of Maharashtra, India. An extent of PMR in mainly bounded between 18^0 23' North to 18^0 43' North and longitudinal extent is 73^0 42' East to 73^0 56' East (Figure 1). It lies on an average 560 m above the sea level. It covers an area of 566 square km. It has a hot semi-arid type of climate. In the summer season, an average temperature of the region is 37^0c while during the winter season it is near to the 30^0c. Due to the development of software and automobile industry the rate of urbanization of the region is increasing day by day. According to the census report of 2011, the total population of the area is 7.7 million.
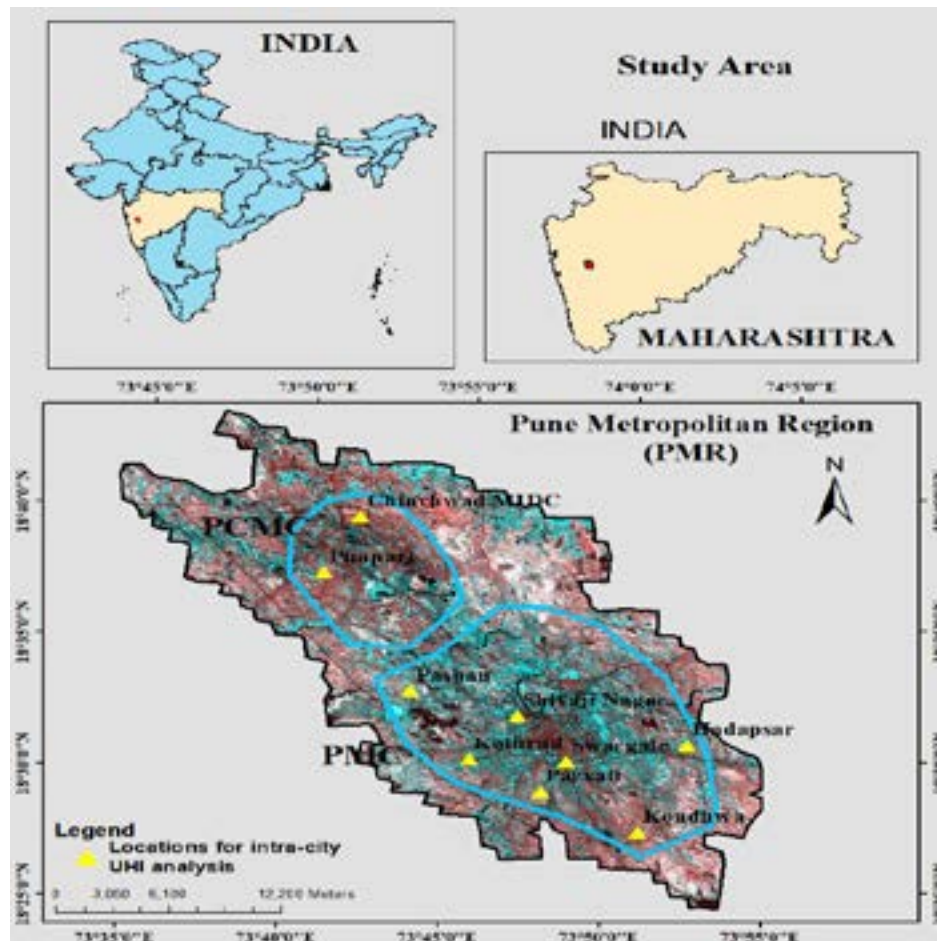
Figure 1. Study Area- Pune Metropolitan Region (PMR), Maharashtra, India

To carry out the analysis MODIS daytime and nighttime dataset for LST (MOD11A2, MYD11A2) has been obtained for the period of 2006-2016. As a part of preprocessing all the datasets were converted from Sinusoidal to Universal Transverse Mercator projection. All the LST data were converted to the monthly once. In addition, MODIS quality control flags were used to check the quality of the datasets. In further part of the processing, all the monthly (day and nighttime) datasets of LST from 2006-2016 were converted to seasonally averaged datasets of summer and winter which were used to achieve the objectives of the study.

2.2 UHI Estimation

The technique of urban-rural buffer analysis has been used to investigate the magnitude of UHI. In this technique, the difference of mean LST of the urban area and rural buffer area has been considered to compute the SUHI

magnitude (Eq.1) This method considers the averaged LST of rural buffer areas along each direction of the urban areas is the major advantage of it. In order to decide the urban boundaries, we have used MODIS Land Use Land Cover datasets.

$$\Delta T = Tu - Tr \tag{1}$$

Where,
ΔT: Surface Urban Heat Island Intensity (SUHII).
Tu: Mean Land Surface Temperature of the Urban Area.
Tr: Mean Land Surface Temperature of the Rural Buffer Area.

We have estimated the SUHII for the PMR for the two seasons i.e. summer and winter on the diurnal scale by using the averaged LST data obtained for the 2006-2011.

2.3 Ecological evaluation of Pune Metropolitan Region using UTFVI

An impact of UHI on quality of urban life has been quantified and analyzed on a seasonal and diurnal scale by computing the UTFVI. UTFVI has been calculated by using the equation (3). The values of UTFVI were classified into six classes with respect to six various indices of ecological evaluation.

$$UTFVI = \frac{Ts - Tmean}{Tmean} \tag{3}$$

Table 1 gives the detail information of six different classes that represent an ecological impact of the UHI on PMR.

Table 1. The scale of Ecological evaluation of Urban Heat Island

UTFVI	UHI Phenomenon	Ecological Evaluation
Less than 0	None	Excellent
From 0 to 0.005	Weak	Good
From 0.005 to 0.01	Middle	Normal
From 0.01 to 0.015	Strong	Bad
From 0.015 to 0.02	Stronger	Worse
More than 0.02	Strongest	Worst

3. RESULTS AND DISCUSSION

3.1 Seasonal and Diurnal variation of UHI

The spatial distribution of UHI over PMR is shown in figure 2. The results of seasonal and diurnal variation in UHI shows that during the summer season, in daytime an area covered by the Pune Municipal Corporation and Cantonment Board shows the higher intensity of UHI while the region of PCMC experiences the phenomenon of UCI. During the nighttime of the summer season, North Eastern part of the PMR shows the highest intensity of UHI whereas an UCI occurs over the region of PMC. In a winter spell, there is a very minute variation of an UHI has been observed over PMR, North Eastern part of the PMR shows the maximal intensity of an UHI during the day and night time of the winter season. The presence of barren land and mining area makes it the hotspot for the UHI.

3.2 Intra-city variation of UHI

At an intra-city level, UHI has been analyzed at a various spatio-temporal scale. During this part of the study, nine different locations of the PMR has been chosen to analyze the behavior of UHI on a various seasonal and diurnal scale. Table 2 represents the detail information of these locations. From the Figure 3, the behavior of UHI has been shown over nine different parts of the PMR on a different seasonal and diurnal scale. During this analysis, an area of Pimpri is found to be coolest (UHI = -2.69^{0}c) place while the Kondhwa spotted as a hot spot (UHI = 2.21^{0}c) for the UHI during the daytime of the summer season. The region of Chinchwad MIDC is found as a hottest part of the PMR during the period of summer nighttime (UHI = 4.04^{0}c), winter nighttime (UHI = 3.97^{0}c) and winter daytime (UHI = 2.58^{0}c) while all other locations except Kondhwa have negligible or negative magnitude of UHI during the same periods i.e. summer nighttime, winter nighttime and winter daytime.

Table 2. Locations selected for the analysis of intra-city variation of UHI

| Sr.No.	Location	Elevation (m)	Description
1	Swargate	577	The core part of the city with the high density of population and vehicle
2	Parvati	632	Hilltop located at the center of the city
3	Pashan	582	Situated along the lakeside
4	Kondhwa	617	Compilation of barren and Newly developed residential area
5	Hadapsar	582	Densely populated area
6	Shivaji Nagar	559	The core part of the city compiled with residential and commercial area
7	Pimpri	571	Less dense and compiled with residential and small-scale industrial area
8	Chinchwad MIDC	580	Less dense and compiled with residential and small-scale industrial area
9	Kothrud	588	Mid rise planned residential area
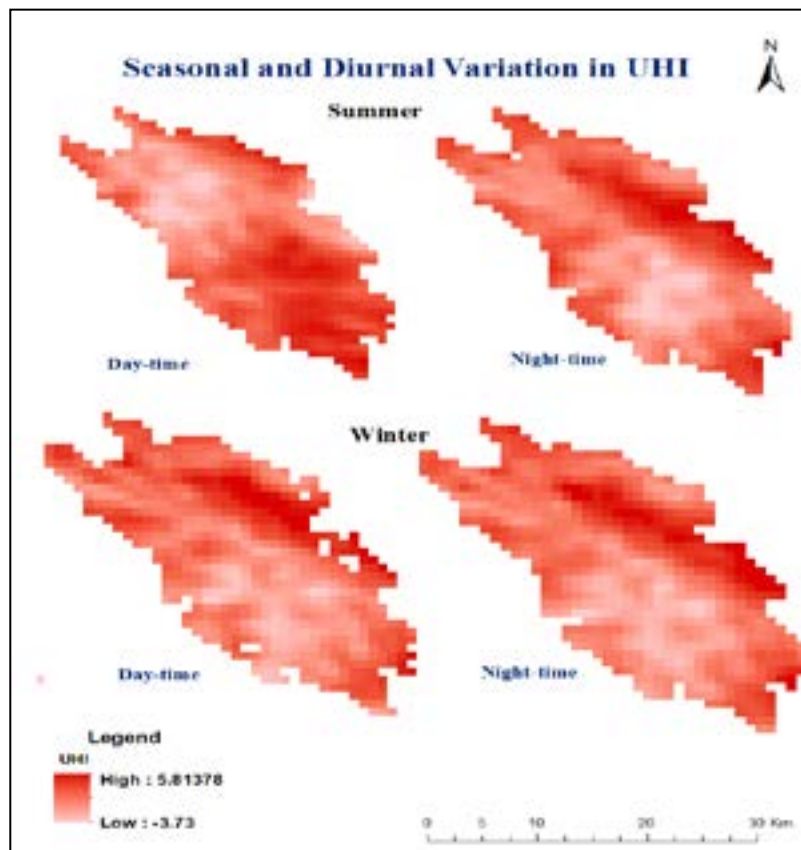
Figure 2. Intra-City variation of UHI over PMR

3.2 Seasonal and Diurnal variation of UTFVI

In order to evaluate an impact of UHI on the quality of the thermal comfort of the urban life, we have calculated Urban Thermal Field Variance Index (UTFVI) (Ahemed, 2018; Guha et. al., 2018; Kojima and Yoko., 2010). The following figure 4 represents the spatial distribution of the living quality of an urban life on a seasonal diurnal scale. The values of UTFVI that are less than 0 shows the excellent conditions while the values closer to 0.02 represent the higher impact of UHI on the quality of the urban living.
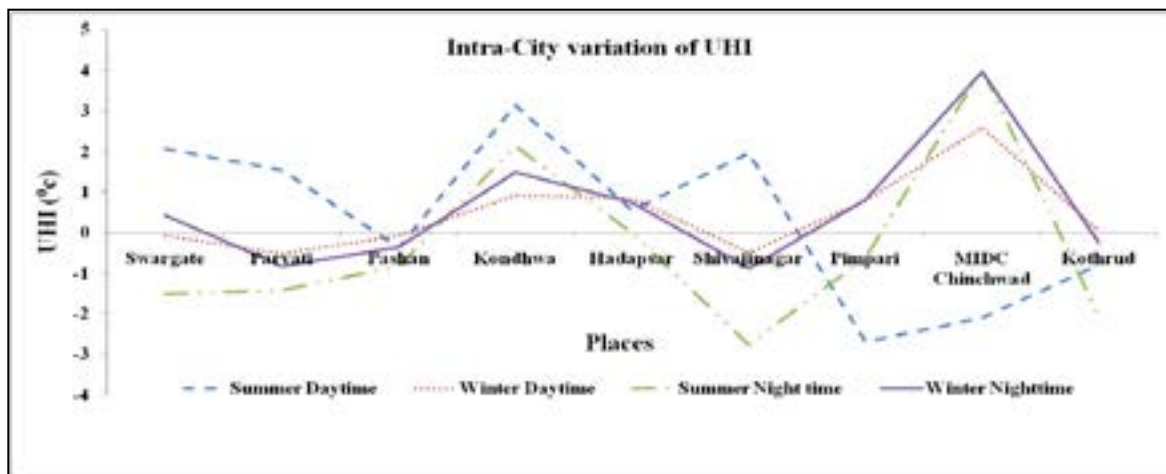
Figure 3. Seasonal and Diurnal Variation of UHI

During the daytime of the summer season, it shows no negative impact of UHI on living comfort in PMR whereas in nighttime of the summer season it shows the bad conditions over the northeastern part of the PMR. Likewise in the daytime summer conditions, nighttime and daytime of the winter season also show the good living condition in PMR except for some northeastern part of the PMR. Table 3 represents the spatial coverage of UTFVI over the PMR. This examination of UTFVI emphasizes that more than 80 % of the total area of PMR has Normal to excellent conditions for urban living on both seasonal and diurnal scale. However, the night times of the summer and winter season shows the bad ecological conditions in some part of the area.

Table 3. Spatial coverage of UTFVI

UTFVI	UHI	Ecological Evaluation	Spatial Coverage of UTFVI in %			
			Daytime Summer	Nigh time Summer	Daytime Winter	Night time Winter
Less than 0	None	Excellent	46.8	51.19	51.5	53.8
From 0 to 0.005	Weak	Good	30.9	26.9	39.7	31.2
From 0.005 to 0.01	Middle	Normal	22.3	14.4	8.76	13.8
From 0.01 to 0.015	Strong	Bad	-	7.44	-	1.04
From 0.015 to 0.02	Stronger	Worse	-	-	-	-
More than 0.02	Strongest	Worst	-	-	-	-

Figure 4. Seasonal and Diurnal Variation in UTFVI

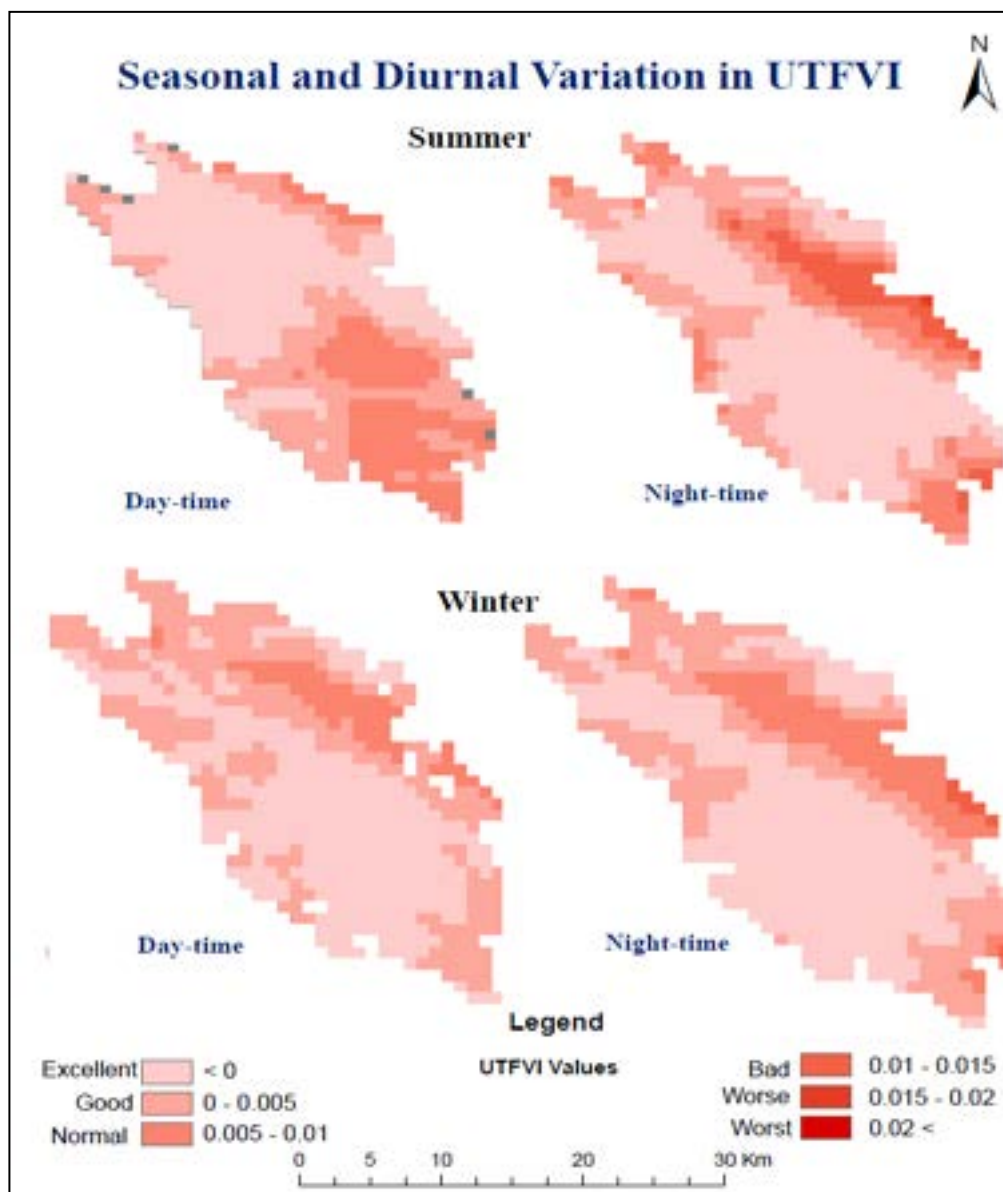## 4. CONCLUSIONS AND DISCUSSION

The LST datasets were extracted from the MODIS day and nighttime satellites for the period of 2006-2016. These 8 datasets were converted into the monthly dataset in order to retrieve the seasonal diurnal datasets. In further part of the work UHI and UTFVI has been calculated on a seasonal diurnal scale. Our analysis shows that during the daytime summer season an area PCMC shows the UCI while a densely built-up area of the central PMC represents a high intensity of UHI. During the nighttime of the summer season exactly opposite trend has been observed i.e. UCI has been observed over the central part of the PMC while high intense UHI has been observed over northeastern part of PMR. During the winter season very less amount diurnal variation has been observed over the PMR. North Eastern part of the PMR is the only area where UHI is significant. UTFVI has been calculated to analyze the quality of the urban living. On each seasonal and diurnal scale, approximately 90% of the PMR region shows the normal to excellent conditions for the quality of an urban living. North Eastern part of the city is the only area which shows bad to worse living conditions. Therefore by considering the UHI and UTFVI conditions over PMR, it is important to adopt proper mitigation strategies to improve the quality of living and reduce an effect of UHI of the city.

REFERENCES

Ahmed, S., 2018. Assessment of urban heat islands and impact of climate change on socioeconomic over Suez Governorate using remote sensing and GIS techniques. The Egyptian Journal of Remote Sensing and Space Science, 21(1), pp.15-25.S.

Guha, S., Govil, H., Dey, A. and Gill, N., 2018. Analytical study of land surface temperature with NDVI and NDBI using Landsat 8 OLI and TIRS data in Florence and Naples city, Italy. European Journal of Remote Sensing, 51(1), pp.667-678.

Martins, T.A., Adolphe, L., Bonhomme, M., Bonneaud, F., Faraut, S., Ginestet, S., Michel, C. and Guyard, W., 2016. Impact of Urban Cool Island measures on outdoor climate and pedestrian comfort: simulations for a new district of Toulouse, France. Sustainable Cities and Society, 26, pp.9-26.T. R. Oke, "City size and the urban heat island," Atmos. Environ. Pergamon Pres, vol. 7, pp. 769–779, 1973.

Rasul, A., Balzter, H. and Smith, C., 2015. Spatial variation of the daytime surface urban cool island during the dry season in Erbil, Iraqi Kurdistan, from Landsat 8. Urban climate, 14, pp.176-186..

Tumbe, C., 2016. Urbanization, Demographic Transition and the Growth of Cities in India, 1870-2020. International Growth Centre Working Paper C-35205-INC-1.

United Nations., 2018. World Urbanization Prospects: The 2018 Revision, Key Facts.

Census Data., 2011. from http://www.censusindia.gov.in/DigitalLibrary/Archive_home.aspx

FIRE ACTIVITY AND SMOKE POLLUTION IN INDONESIA
UNDER THE INFLUENCE OF DROUGHT INDUCED BY 2015 EL-NIÑO EPISODE

Radyan Putra Pradana (1), Tomonori Sato (2)

1 Indonesian Agency for Meteorology, Climatology and Geophysics (BMKG).
Jl. Angkasa I No. 2, Kemayoran, Jakarta 10720, Indonesia.
2 Faculty of Environmental Earth Science, Hokkaido University.
Kita 10 Nishi 5, Sapporo 060-0810, Japan
Email: radyan.putrapradana@bmkg.go.id; t_sato@ees.hokudai.ac.jp

ABSTRACT: During the 2015 dry season, there were massive forest fire events in Indonesia associated with the extremely dry condition due to the El-Niño event. Therefore, the synthetic study of fire events have collected global attention in recent years, especially after 1997/1998 El-Niño event brought considerable environmental and economic damages. This study aims to evaluate the impact of the latest strong El-Niño episode in 2015 in comparison to past events to understand the drought and fire conditions under which they occurred. For this purpose, a long-term reanalysis dataset, MERRA2, provided by NASA was utilized to examine the relationship between aerosol optical depth (AOD) and meteorological parameters during 1980-2015. This study also used the Global Fire Emission Dataset version 4.1 (GFED4s) to examine the biomass burning carbon emissions during 1997-2015. The fire and smoke pollution in 2015 had occurred repeatedly in southern Sumatra and south-central Kalimantan and the most severe drought and forest fires during 2015 occurred in September and October. The results indicate that fire activity in Sumatra and Kalimantan can be realistically predicted by ENSO indices. The difference in fire environments between Sumatra and Kalimantan may be partly attributed to different patterns of human activity and government policy. This study analyzed the drought as the preconditioning of the fire occurrence. Further studies will be needed to clarify the contribution of local human activity as a trigger of fires.

1. Background

1.1 Drought and fire activity in Indonesia

The Equatorial Asia in terms of atmospheric dynamics are influenced by both the Hadley and Walker Cells (Aldrian et al., 2007). The seasonal to interannual variabilities of Indonesian rainfall are characterized mainly by the monsoon (Ramage, 1971) and the El-Niño Southern Oscillation (ENSO; Philander, 1989; Ropelewski and Halpert, 1987, 1989; Halpert and Ropelewski, 1992; Hendon, 2003). Indonesia experiences two phases of monsoon every year, the wet phase from November to March, which coincides with the presence of the Inter-Tropical Convergence Zone (ITCZ) in this region (Asnani, 1993), and the dry phase from May to September, when the dry southeasterly wind blows from Australia. Ramage (1971) and Cheang (1987) identified April and October as the transitional months. During strong El-Niño (La-Niña) events or warm (cold) phases, this region experiences lower (higher) rainfall than in other years (Gutman et al., 2000) and both the intensity and spatial extent of regional drought increases (Lyon, 2004).
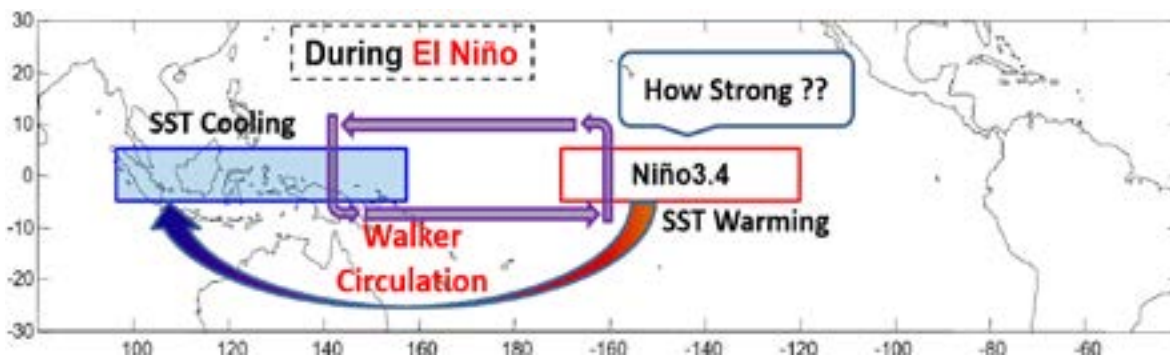
Figure 1. SST in the tropical Pacific (Niño3.4 region) and its remote impact to Indonesia

Equatorial Asia is also one of the most extremely vulnerable tropical rainforest in the world that is directly affected by ENSO cycle (Fig.1). As a consequence, it will experiences the reduction in precipitation due to the existing of

anomalous surface easterlies that reduce the local rainfall (Supari et al., 2016), followed by severe droughts during the dry season. Drought conditions are favorable for fire and haze occurrence, especially when normally moist fuels are drying out, leading to potentially flammable and thereby susceptible to fires (Takahashi et al., 2001; Cochrane, 2003; Tosca et al., 2010). Fires mainly caused by human factor and natural fires (or 'wildfires', mainly from lightening) are estimated to account for 10% of global biomass burning (Crutzen and Andreae, 1990; Heil, 2007). The human-induced fires are generally linked to land conversion activities, as fire is a cheap and fast tool to remove the original vegetation and to prepare the land for different land use systems such as cropland, plantations, grazing areas or settlements.

In Indonesia fires are typically lit during the July to October dry season mainly in Sumatra and Kalimantan islands. Forest fires have occurred periodically in Kalimantan since the 1980s (Field et al., 2015) and in Sumatra since at least the 1960s (Field et al., 2015). Field et al. (2009) attributed these differences to changing patterns of migration and land use within the region. Sumatra had relatively high rates of deforestation during the second half of the 20th century, driven in part by surges in population during the 1960s and 1970s (Field et al., 2009; Tosca et al., 2010). In contrast, Kalimantan became the target for settlement and development projects by the Indonesian government during the 1980s and 1990s after the Sumatra. Forest clearing and peatland drainage associated with one of these projects, the Mega Rice Project, contributed substantially to the emissions observed during the 1997 El-Niño (Page et al., 2002; Field et al., 2009; Tosca et al., 2010). This environmental problem due to land-use change and forest fires would cause much of the Equatorial Asia forest to transform to less dense, drought-and fire-adapted ecosystems .

1.2 Linkage between El-Niño Southern Oscillation (ENSO) and Indonesian Fires

From the global impact of El-Niño and fire activity over Indonesia region, there is strong evidence that the inter-annual variability of fire activity in Indonesia is influenced by year-to-year variations in the ocean-atmosphere circulation associated with the ENSO phenomenon. Heil (2007) attributed these relationship by analyzing the monthly horizontal visibility (25th percentile of daily values) at two locations on Sumatra and two locations on Kalimantan. To indicate periods when El-Niño related droughts have occurred in Indonesia since 1960, the Ocean Niño Index (ONI) is displayed as well (Fig. 2).
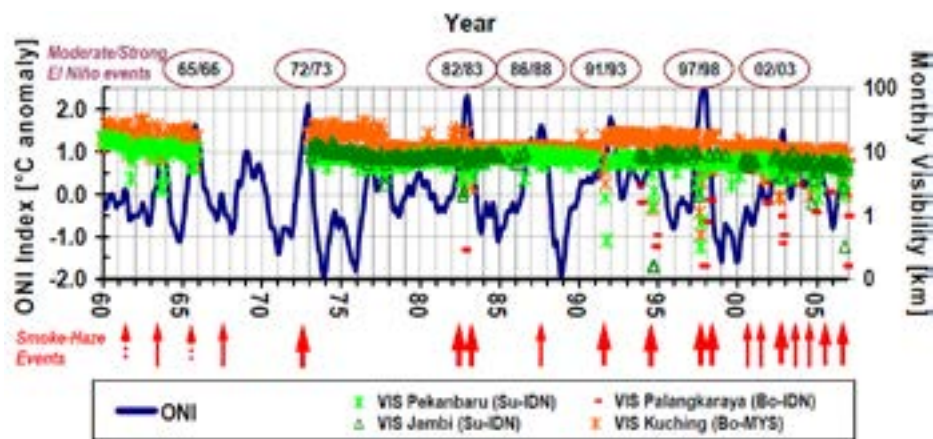
Figure 2. Development of the El-Niño Southern Oscillation (represented by the monthly Ocean Niño Index (ONI)) as well as monthly visibility (VIS) at 2 locations on Borneo (Bo) and Sumatra (Su), respectively, from 1960 to 2006 (IDN=Indonesia, MYS=Malaysia). Visibility data are missing for 1967 to 1973. Reported smoke haze events are marked with a red arrow. Dotted arrows indicate likely smoke-haze events for which written reports are missing (Heil, 2007).

From Heil (2007), since 1960 at least 19 events can be considered as severe fires years over Sumatra and Kalimantan because these years were abnormally dry during the dry season for sustained burning. Figure 2 clearly shows a unique aspect of the visibility decreasing in this region when the positive anomaly of Ocean Niño Index (ONI) occurs. It indicated a strong relationship between ENSO phase and the sensitivity of fire emissions to drought over Sumatra and Kalimantan.

Given the overwhelming occurrence of El-Niño associated with drought that have caused fire and haze, it is reasonable to hypothesize that biomass burning exerts a significant impact on the hydrological cycle across different spatial and temporal scales.

1.3 Objectives

The extreme drought conditions and inter-annual variability of fire activity in Indonesia is strongly related to the details of sea surface temperature (SST) patterns associated with the El-Niño and La-Niña events which have been documented by several earlier studies.

Fires have risen to global attention in recent years as an environmental and economic issue, especially since the 1997/1998 El-Niño Southern Oscillation event. From the prospect of pre-warning and effective fire management in Indonesia region that potentially has a global impact, it is crucial to be able to identify the key features of the El-Niño SST pattern that matters to the magnitude of fire activity and to understand the physical linkages between them.

While previous studies on ENSO events have discussed an increasing frequency of El-Niño and La-Niña events in recent decades, changes in the influence of El-Niño and La-Niña events on the magnitudes of precipitation anomaly and fire activity have been poorly discussed. Therefore, there is a need to extend researches on the impact of the intensity of both phases of ENSO, i.e., El-Niño and La-Niña, to the seasonal and inter-annual variability of Indonesian rainfall.

In September and October 2015, southern Sumatra and southern-central Kalimantan experienced fire and haze due to increasingly dry conditions that began in July to October (Fig. 7 and Fig. 8). The suppression of precipitation over large parts of Equatorial Asia has been found characteristic of strong El-Niño event. The purposes of this study are to investigate the evolution of ENSO (El-Niño and La-Niña) magnitude on precipitation distribution at regional scales focusing on 2015 episodes over the Sumatra and Kalimantan (Indonesia) regions, and to evaluate the impact of the latest strong El-Niño episode in 2015 in comparison to past events to understand the drought as the preconditioning of the fire and haze occurrence under which they occurred.
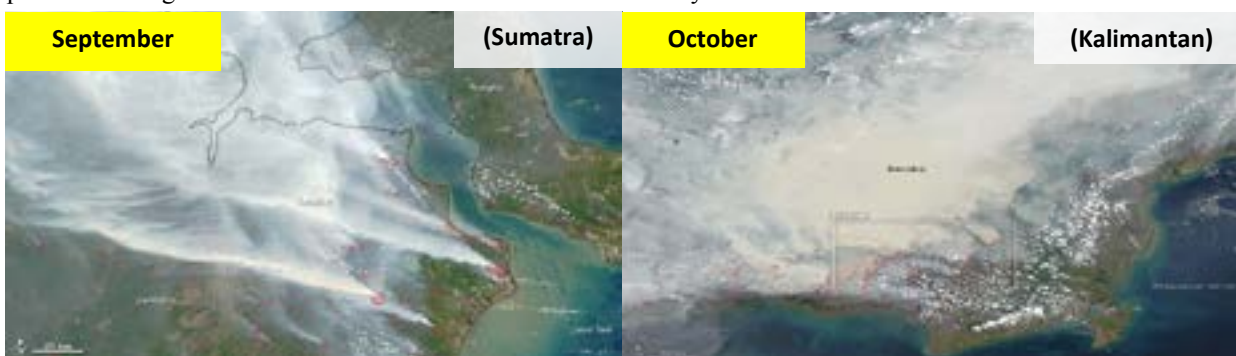

Figure 7. Fire and haze over Sumatra island on September 2015.
(https://earthobservatory.nasa.gov/IOTD//view.php?id=86681)

Figure 8. Fire and haze over Kalimantan island on October 2015.
(https://earthobservatory.nasa.gov/IOTD/view.php?id=86847&eocn=image&eoci=related_image).

2.1 Data and Methods

2.2 Global Reanalysis Data (Atmospheric Fields)

This study used the MERRA2 reanalysis dataset from 1980 to 2015 (0.5^o x 0.625^o) for some parameters such as, monthly mean precipitation, surface wind and monthly mean aerosol optical depth. Each parameter (i.e., precipitation, surface wind and aerosol optical depth) was used to calculate basic climatology to examine how large deviations during the extreme events.

The second Modern-Era Retrospective analysis for Research and Applications (MERRA-2) is an atmospheric reanalysis product provided by NASA. It replaces the original MERRA reanalysis using an upgraded version of the Goddard Earth Observing System Model, Version 5 (GEOS-5) data assimilation system. MERRA-2 includes updates to the model and to the Global Statistical Interpolation (GSI) analysis scheme of Wu et al. (2002). The major motivation for replacing MERRA with MERRA-2 is the fact that the MERRA data assimilation system was frozen in 2008 and is not capable of ingesting several important new data type because the number of observations available for assimilation in MERRA is decreasing rapidly as the older satellite instruments fail. MERRA-2 uses GEOS-5, Version 5.12.4, which is able to use the newer microwave sounders and hyper spectral infrared radiance instruments as well as other data types.

Along with the enhanced use of satellite observations in MERRA-2, a secondary motivation was to include more aspects of the Earth System. An important aspect of this is the assimilation of aerosol information, based on the off-line "MERRAero" dataset that was integrated using meteorological fields from MERRA. This aerosol product is beneficial for this study, because of the availability of the spatial distribution of smoke pollution caused by fire activity and atmospheric transport driven by meteorological factors such as surface wind. The aerosol lifetimes are driven by prescribed sea surface temperature and sea ice, daily volcanic and biomass burning emission, and high resolution inventories of anthropogenic emission sources. The analyzed aerosols affect the meteorology of MERRA-2 through direct radiative coupling with the GEOS-5 model dynamics. The MERRA-2 data was downloaded at the Goddard Earth Sciences (GES) Data and Information Services Center (DISC) (http://disc.sci.gsfc.nasa.gov/mdisc/).

2.3 Sea Surface Temperature

The sea surface temperature (SST) anomalies in the tropical Pacific are used to calculate ENSO indices which characterize the phase and strength of the ENSO cycle (Fig.9).Area averaged SST over the Niño3.4 region (5°N-5°S and 120°W-170°W) was used to define El-Niño events. Here, the deviation of 5-month running mean of Niño3.4 SST in each year relative to that of 36-year average from 1980 to 2015. The procedure of 5-month running mean is done in order to remove the intra-seasonal variation due to the Madden-Julian Oscillation in the tropical Pacific. A warm event (El-Niño) prevails if the 5-month mean SST anomaly exceeds 0.5°C threshold. The warm event is categorized as weak if the SST anomaly ranges between 0.5 - 1.0° C, moderate for the range 1.0 - 1.5°C, strong for SST anomalies 1.5 - 2°C and very strong for SST anomalies ≥ 2.0°C.In order to conduct this analysis, the COBE2-SST data are used. This monthly dataset covers the period during January 1850 to December 2015, with global coverage (89.5°N - 89.5°S, 0.5°E - 359.5°E) at 1.0^o x 1.0^o degree mesh grids.

2.3 Global Fire Emission Dataset version 4.1 (GFED4s)

In this study, the fire emissions from the Global Fire Emissions Database version 4 (GFED4s) since 1997 to 2015 was used (van der Werf et al., 2010; Randerson et al., 2012; Giglio et al., 2013). The detailed description of GFED4s is available at http://www.geo.vu.nl/~gwerf/GFED/GFED4/Readme.pdf. Below is some specifications of GFED4s in relation with the current study. The GFED4s provides monthly burned area, fire carbon (C) and dry matter (DM) emissions, and the contribution of different fire types to these emissions in order to calculate trace gases and aerosol emissions using emission factors. All these datasets are based on burned area boosted by small fire burned area, hence the "s" in the GFED4.1s name. The spatial resolution of the global files is 0.25 degrees. Thus, the different fields have 720 rows and 1440 columns. In general, ATSR and VIRS data was used before 2001 while MODIS was used after 2001. The biosphere fluxes contain monthly fire emission (BB) in g C m^{-2} month^{-1}.

3. Results

3.1 Identification of El-Niño Southern Oscillation phase

The monthly seasonal variation of SST over Niño3.4 region (for area average 5°S-5°N, 120°W-170°E) during 1980-2015 period is one of the best indicator for the ENSO phase monitoring. Figure 3 shows the increasing of SST over Niño3.4 region, and at least for three events are standing in above 28 ^{o}C for 1997 (green line) and 2015 (blue line) during June to December, but October to December for 1982 (red line) events. It was noted that, since 1980 the 2015 event is the second warmest sea surface temperature during June to December after 1997 in comparison with past events.

In order to investigate how large the anomaly SST relative to the climatology (during 1980-2015) over Niño3.4 region, the 5-month running mean statistical analysis was conducted. Figure 4 shows the ENSO phase during 1982-2015 period. The blue lines represent the La-Niña phase and the red lines represent the El-Niño phase. From this result, 1982,1986/1987,1991/1992, 1994,1997, 2002, 2004, 2006, 2009 and 2015 can be considered as El-Niño period and 1984/1985, 1988/1989, 1995/1996, 1998/2000, 2005, 2007/2008 and 2010/2011 as La-Niña period. In addition, 2015 is one of the latest extreme El-Niño events after 1982 and 1997 (Fig. 4).
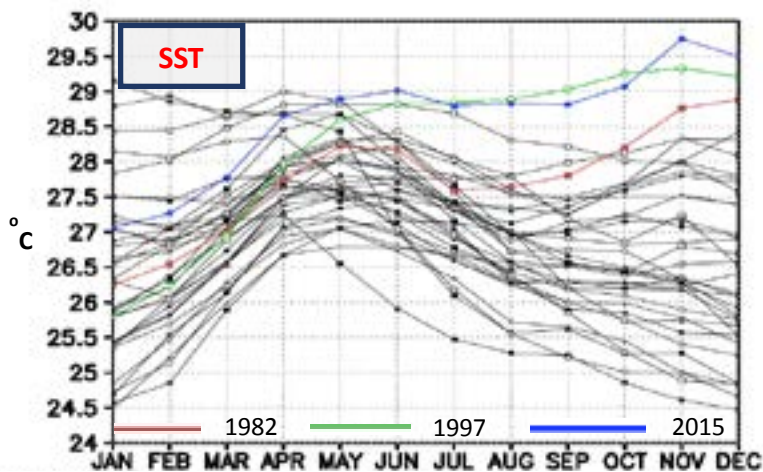
Figure 3. Monthly seasonal variation of SST over Niño3.4 (1980-2015). Multiple line represents for each year
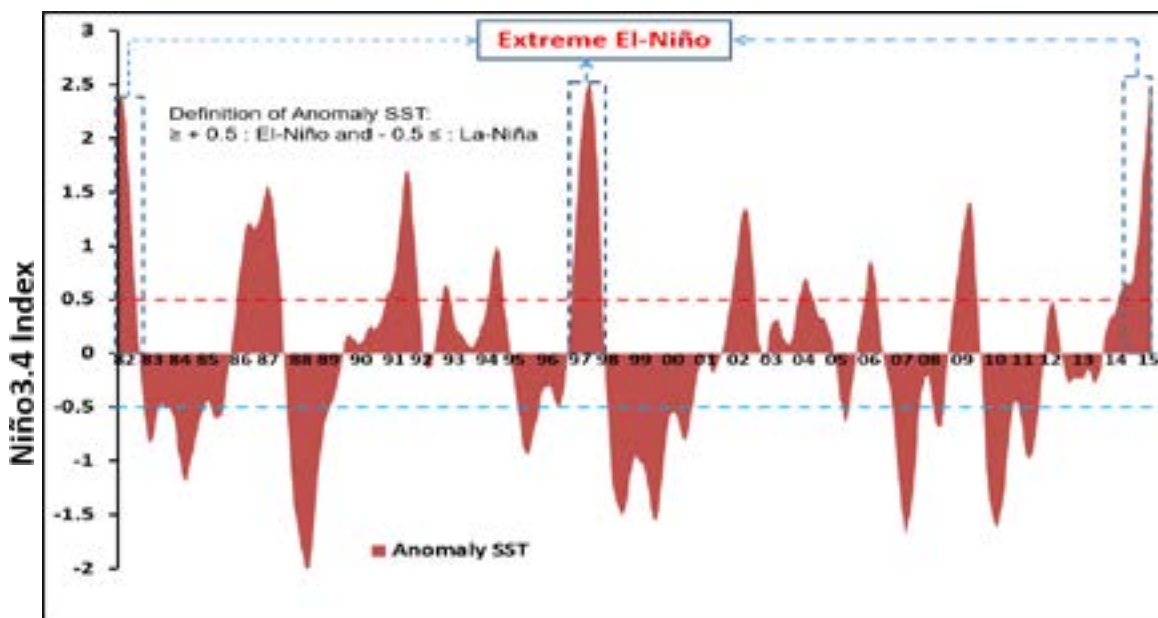
Figure 4. Identification of ENSO phase. X-axis represents monthly time series (1982-2015) and Y-axis represent amplitude of SST anomaly.

3.1 Seasonal Variation of Precipitation, Emission and Aerosol Optical Depth

The strong El-Niño event induced drought condition during the dry season, and there was a significant decrease in rainfall in El-Niño years (Fig. 5). Simultaneously, high aerosol emission (Fig. 6) and high AOD (Fig. 7) in El-Niño years are evident, resulting in predominantly air pollution from July to October.
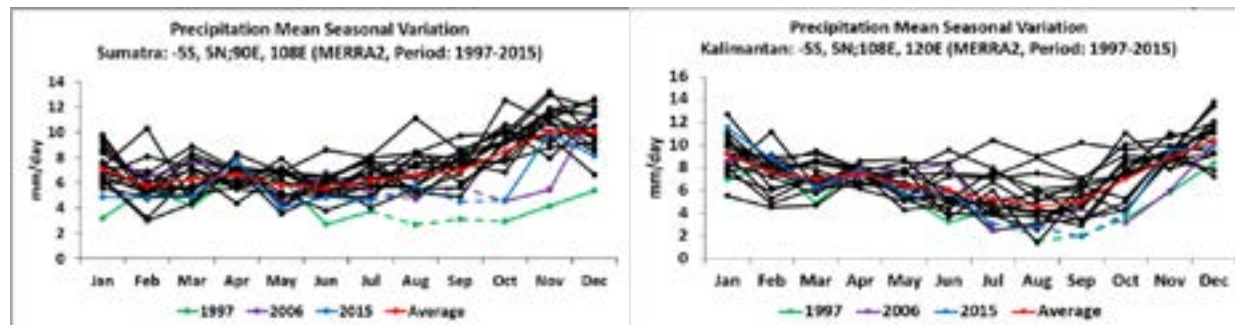
Figure 5. Mean seasonal variation (1997-2015) of precipitation for Sumatra (left) and Kalimantan (right). Dash line represents low precipitation during El-Niño years.
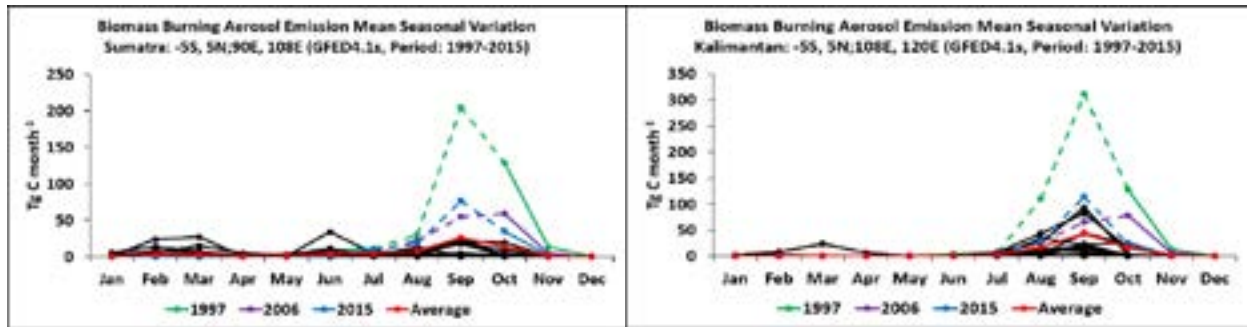
Figure 6. Mean seasonal variation (1997-2015) of biomass burning aerosol emission for Sumatra (left) and Kalimantan (right). Dash line represents high fire emission in El-Niño years.
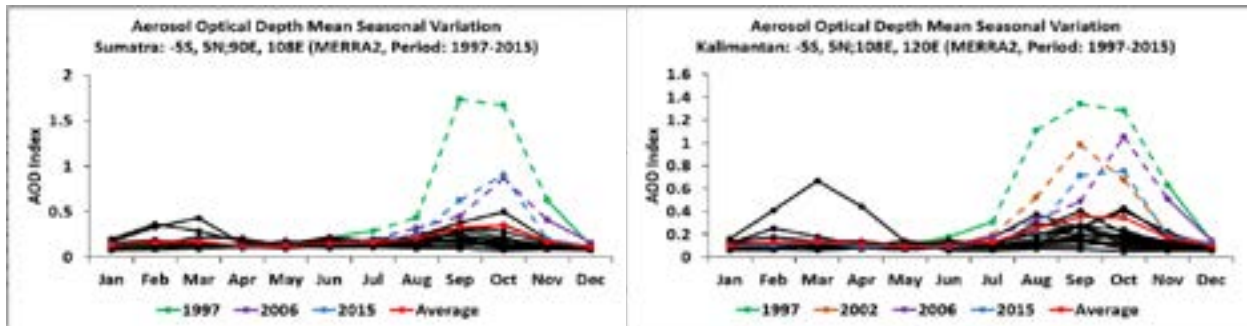
Figure 7. Mean seasonal variation (1997-2015) of aerosol optical depth for Sumatra (left) and Kalimantan (right). Dash line represents high AOD occurs in El-Niño years.

3.2 Drought condition in Indonesia during El-Niño 2015

Drought condition over Indonesia was also investigated by calculating correlation coefficients for inter-annual variation during 1980-2015 between precipitation anomaly at each grid point and Niño3.4 SST anomaly.
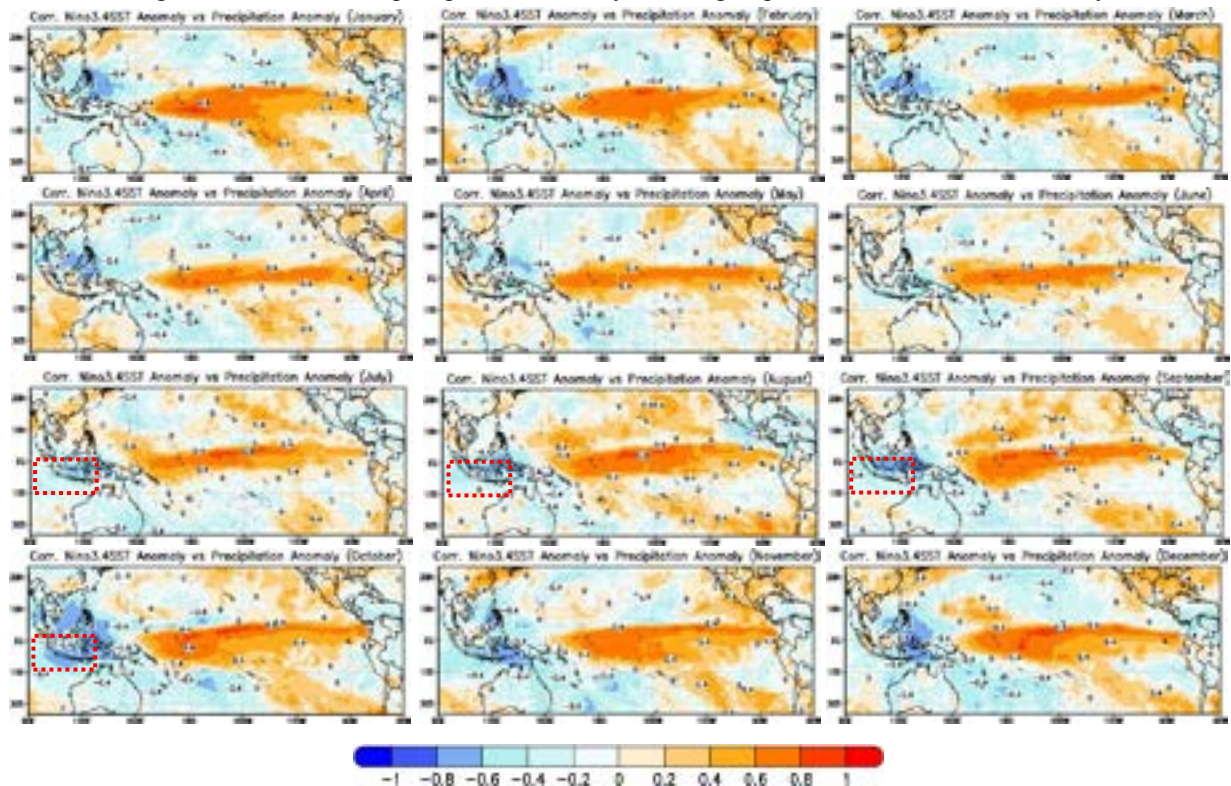
Figure 8. Correlation coefficient for inter-annual variations between monthly precipitation anomaly and SST anomaly in Niño3.4 for October to December. Red box indicates negative correlation over Sumatra and Kalimantan region.

It shows strong negative correlation between precipitation over Indonesia region and Niño3.4 SST during July to October (Fig. 8). Less precipitation due to the colder sea surface temperature than normal condition over Indonesia was supposed to weaken the convective activity. During 2015 episodes, negative precipitation anomaly in Indonesia (especially in Sumatra and Kalimantan island) began in July.

3.3 The relationship and scatter plot analysis between precipitation, emission, AOD and Niño3.4 SST index over Sumatra and Kalimantan
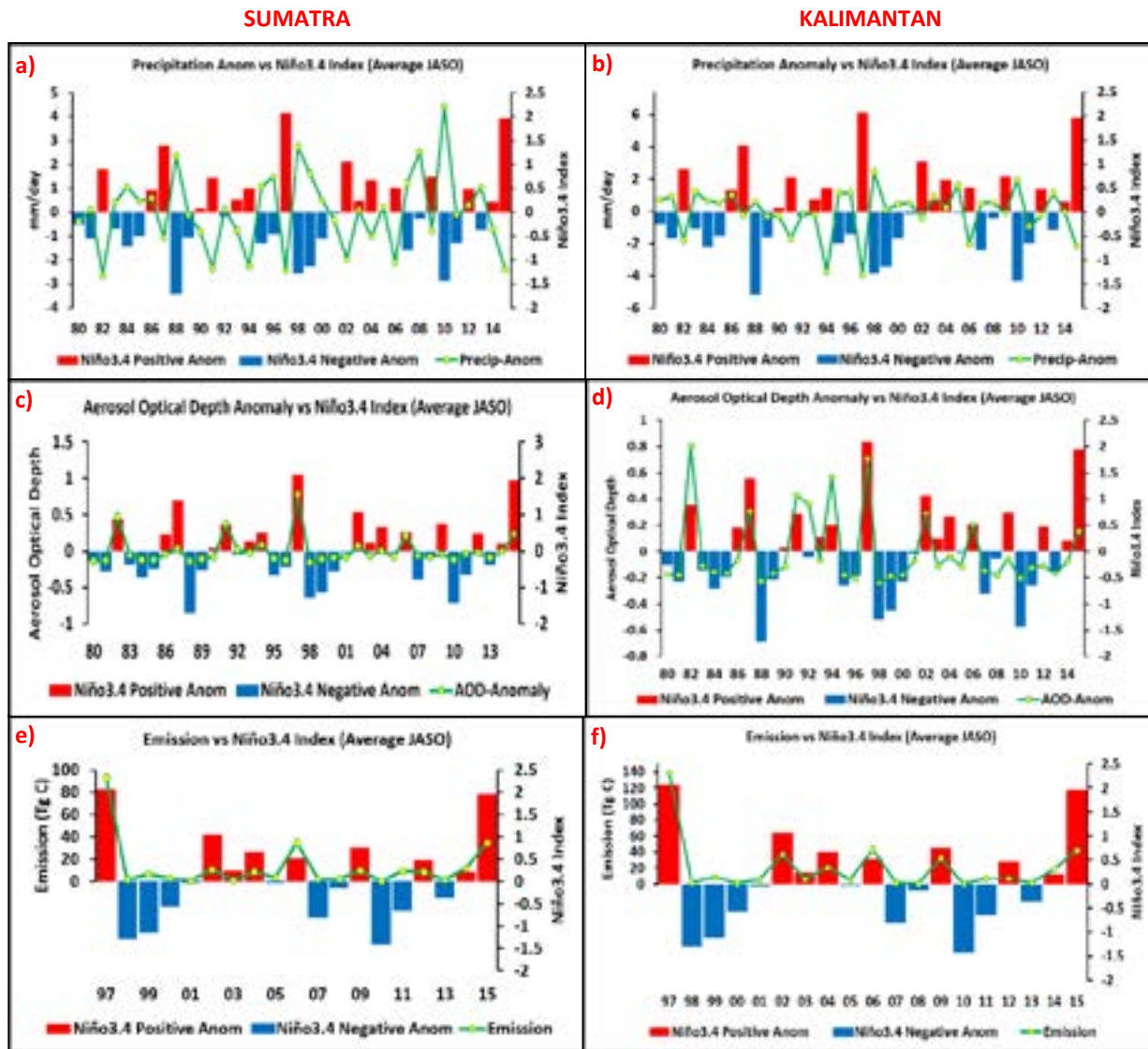
Figure 9(a-f). The relationship between precipitation, AOD, emission and Niño3.4 SST index over Sumatra (left) and Kalimantan (right) for average of JASO 1980-2015

SUMATRA   **KALIMANTAN**
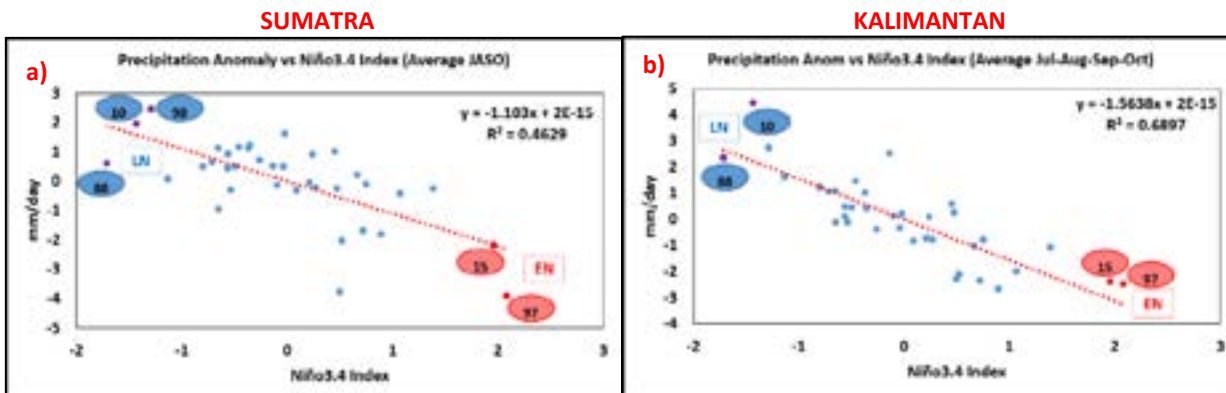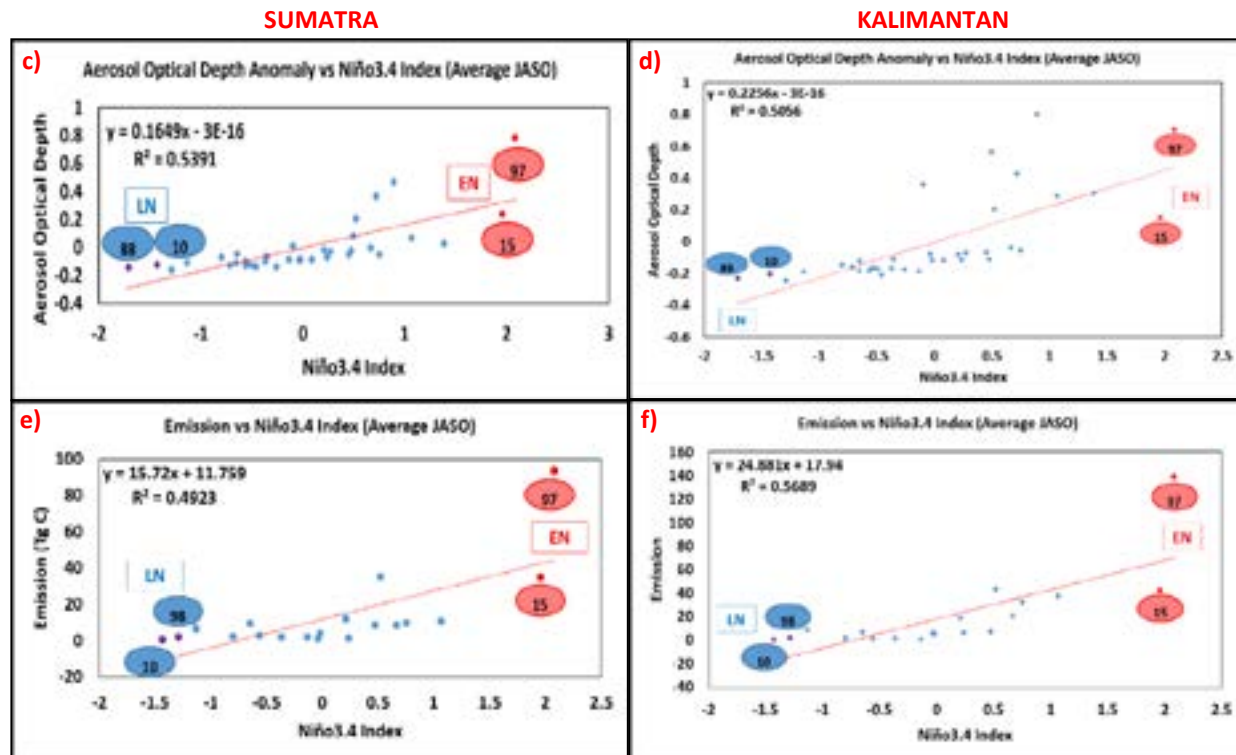
Figure 10(a-f). Scatter plot between precipitation, emission, AOD and Niño3.4 SST index over Sumatra (left) and Kalimantan (right) for average of JASO 1980-2015. Red mark for El-Niño and blue mark for La-Niña.

The strong El-Niño event induced drought condition during the dry season, and there was a significant decrease in rainfall in El-Niño years (Fig. 9a-b). Simultaneously, high aerosol emission (Fig. 9e-f) and high AOD (Fig. 9c-d) in El-Niño years are evident, resulting in predominantly air pollution from July to October. During July to October it shows strong negative correlation between precipitation and SST in Niño3.4 over Indonesia region (Fig. 10a-b). Since 1980, 2015 event was the third driest condition both in the area of Sumatra (1997, 1994, and 2015) in Fig. 9a and Kalimantan (1982, 1997 and 2015) in Fig. 9b. In Kalimantan, since 1997 it was noted that for 2015 event is the third highest of fire emission after 1997 and 2006 event (Fig. 9f), but fourth highest of AOD after 1997, 2002 and 2006 event (Fig. 9d). The strongest linear correlation between precipitation anomaly and Nino3.4 index was found for Kalimantan (R^2 of 0.69), while the connection is weaker for Sumatra (R^2 of 0.46). Meanwhile, the strongest linear correlation between AOD anomaly and Nino3.4 index was found for Kalimantan (R^2 of 0.51), while the connection is stronger for Sumatra (R^2 of 0.54). For the strongest linear correlation between fire emission and Nino3.4 index was found for Kalimantan (R^2 of 0.57), while the connection is weaker for Sumatra (R^2 of 0.50).

3.4 The spatial distribution of AOD anomaly and surface wind anomaly

In September 2015, it was seen that emissions and AOD levels in Sumatra and Kalimantan were higher than in September 2006 (Fig.9). September was the peak in 2015 of fire activity and smoke pollution over Sumatra (76.6 TgC) and Kalimantan region (114.1 TgC) while October was the peak in 2006 (58.6 TgC for Sumatra and 77.7 TgC for Kalimantan) (Fig. 9e and f). In October 2006 (Fig.10e and f), it was shown the emission and AOD in Sumatra and Kalimantan were higher than in October 2015 (Fig.10g and h). Although the emissions and AOD concentrations in September and October 2015 are smaller than in September and October 2006, the smoke pollution of polluted coverage in September and October 2015 are broader than in September and October 2006 (Fig.9d and h and 9b and f).

2742
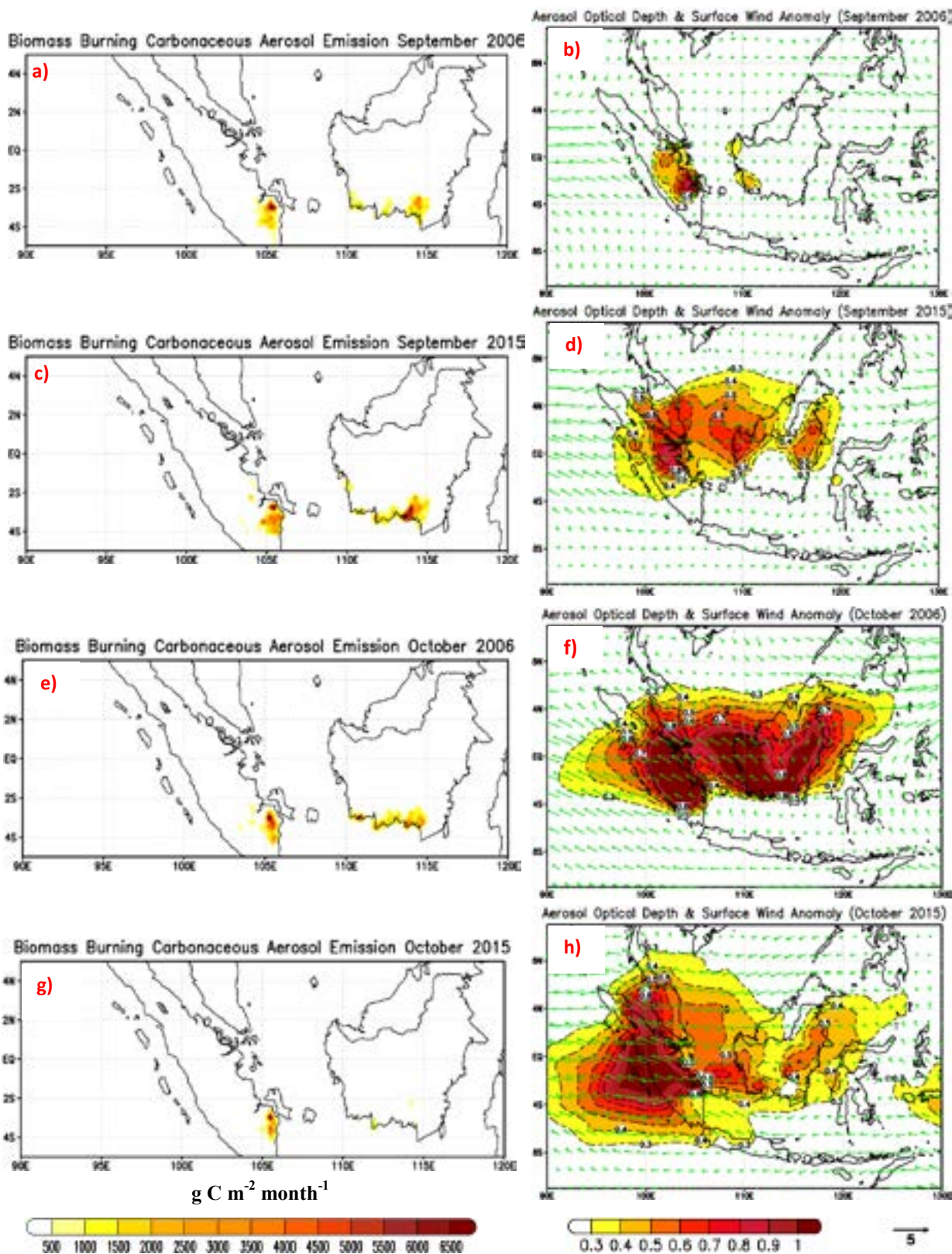
Figure 9. Fire activity (a, c, e and g) and spatial distribution of AOD (b, d, f and h) for September and October (in comparison between 2006 and 2015).

4. Conclusion

The overall objective of this study was to assess the impact of drought and to investigate the influence of the ENSO on precipitation, fire emission production and smoke plume dispersion. The relationship between ENSO condition,

precipitation anomalies and temporal and spatial relationships, Sumatra and Kalimantan has been investigated separately to examine the precondition of the fire occurrence. Inter-annual variation in precipitation anomalies during July to October (JASO) was clearly connected with ENSO phase, with abnormally dry (wet) conditions during El-Niño (La-Niña).

The 2015 drought in Indonesia began from July to October, and this situation was accompanied by strong El-Niño events after 1982 and 1997 events. From average-JASO since 1980, El-Niño 2015 was the second strongest after 1997. Since 1980, 2015 event was the third driest condition both in the area of Sumatra (1997, 1994 and 2015) and Kalimantan (1982, 1997 and 2015). High emission was not always leading to high AOD, which is dominated by moderate and strong El-Niño period.

In summary, the results indicate that fire activity in Sumatra and Kalimantan can be realistically predicted by ENSO indices.This study provided a first step towards a comprehensive understanding of the complex linkages between fire emission, climate variability atmospheric transport of fire aerosols. Several aspects, however still need to be analyzed in more detail, such as sensitivity experiment due to the local human activity as a trigger of fires**.**

5. References

Aldrian, E., Dümenil-Gates, L.,and Widodo., F. H. (2007). Seasonal variability of Indonesian rainfall in ECHAM4 simulations and in the reanalyzes: The role of ENSO. *Theor. Appl. Climatol*., **87**, 41-59.DOI: 10.1007/s00704-006-0218-8.

Ramage, C. (1971).*Monsoon Meteorology*. International geophysics series, vol. 15. Academic Press, 296 pp.

Philander, S. G. H. (1989). *El-Niño, La-Niña, and the Southern Oscillation*. International geophysical series, vol. 46. Academic Press, 289 pp.

Ropelewski, C. F.,and Halpert, M. S. (1987). Global and regional scale precipitation patterns associated with the El-Niño Southern Oscillation (ENSO). *Monthly Weather Review*, **115**, 1606-1626.

Ropelewski, C. F., and Halpert, M. S. (1989).Precipitation patterns associated with the high index phase of the Southern Oscillation. *J. Climate*,**2**, 268-284.

Halpert, M. S., and Ropelewski, C. F. (1992).Surface temperature patterns associated with the Southern Oscillation. *J. Climate*, **5**, 577-593.

Hendon, H. H. (2003). Indonesian Rainfall Variability: Impacts of ENSO and local air-sea interaction. *J. Climate*, **16**, 1775-1790.

Asnani, G. C. (1993). *Tropical Meteorology*, vol. 1. Asnani, 603 pp.

Cheang, B. K. (1987). Short and long-range monsoon prediction in Southeast Asia. In Monsoons, edited by J.S. Fein andP.L. Stephens, 579-606, John Wiley and Sons, Wiley Inter-science Publication.

Gutman, G., Csiszar,I., and Romanov, P. (2000). Using NOAA/AVHRR products to monitor El-Niño impacts: Focus on Indonesia in 1997-98.*Bull. Am. Meteorol. Soc*.,**81,** 1189-1205.

Lyon, B. (2004). The strength of El-Niño and the spatial extent of tropical drought, *Geophys. Res. Lett*, **31**, L21204.DOI:10.1029/ 2004GL020901.

Supari., Muharsyah, R., and Wahyuni, N. (2016). Impact of the 2015 Godzilla El-Niño event on the Indonesian rainfall. Science and Engineering. *Scientific Journal of PPI-UKM*, **3**. No. 1. ISSN No. 2356-2536.

Takahashi, H., Shimada, S., Ibie, B. F., Usup, A., Yudha, and Limin, S. H. (2001) Annual change of water balance and droughtindex in a tropical peat swamp forest of central Kalimantan, Indonesia. In: Rieley, J. O., and Page, S. E with Setiadi, B(eds) Peatlands for people: Natural Resource and Functions and Sustainable Management. Proceeding of theInternational Symposium on Tropical Peatland, 22-23 August 2001. Jakarta Indonesia. BPPT and Indonesia PeatAssociation (pp 63-67).

Cochrane, M. A. (2003). Fire science for rainforests. *Nature*,**421**, 913-919.

Tosca, M. G., Randerson. J. T., Zender, C. S., Flanner, M. G., and Rasch, P. J. (2010). Do biomass burning aerosols intensify drought in equatorial Asia during El-Niño? *Atmos. Chem. Phys*, **10**, 3515-3528.

Crutzen, P. J., and Andreae, M. O. (1990). Biomass burning in the tropics: Impact on atmospheric chemistry and biogeochemical cycles. *Science*, **250**, No. 4988, 1669-1678.

Heil, A. (2007). Indonesian forest and peat fires: Emission, air quality and human health. *PhD Dissertation*, Earth System Science, Max Planck Institute for Meteorology, Germany.

Field, R. D.,van der Werf, G. R., and Shen, S. S. P. (2009). Human amplification of drought-induced biomass burning in Indonesia since 1960. *Nature Geoscience*, **2**. DOI:10.1038/NGEO443.

Field, R. D., van der Werf, G. R., Fanin, T., Fetzer, E. J., Fuller, R., Jethva, H., Levy, R., Livesey, N. J., Luo, M., Torres, O., and Worden, H. M. (2016). Indonesian fire activity and smoke pollution in 2015 show persistent nonlinear sensitivity to El-Niño induced drought.*PNAS,* **113**, no. 33. 9204-9209. DOI: 10.1073/pnas.1524888113.

Wu, W. S., Purser,R.J., and Parrish,D.F. (2002). Three-dimensional variational analysis with spatially inhomogeneous covariances. *Mon. Wea. Rev*, **130**, 2905-2916.

Time-Series Analysis of Asian Elephant Habitat Change and Impact on Its Population Dynamic at Regional Scale

Nuntikorn Kitratporn (1) and Wateru Takeuchi (1)

1 Institute of Industrial Science, The University of Tokyo, 4-6-1 Komaba, Meguro-ku,
Tokyo, 153-8505, Japan
Email: tita@iis.u-tokyo.ac.jp

KEY WORDS: Asian Elephant, Conservation, Landscape Metrices, Land Cover Change

ABSTRACT: Asian elephant (Elephas Maximus) is not only ingrained in South and Southeast Asia culture, but also environmentally important as a keystone and umbrella species. Nevertheless, its overall population has continued to decline and spatially restrained which resulted in the species being designated as endangered since 1980s. Despite the overall population reduction, the census at country-level showed an increasing trend in some countries, such as in Sri Lanka and India. However, temporal and cross-countries research on elements impacting population dynamic remain limited. This study is aimed at identifying land cover and landscape changes and their relationship to Asian elephant population dynamic across all 13 range states over 1990, 2003, and 2015. The study area is based on confirmed home range of wild Asian elephants from International Union for Conservation of Nature (IUCN). We identified candidate factors potentially impact Asian elephant population which included food and refuge (forest, shrub, grassland, agriculture), physical landscape fragmentation (Patch Density and Largest Patch Index), landscape heterogeneity (Shannon Diversity Index) and human settlement. Integrating of satellite remote sensing and GIS data, we investigated the change of candidate drivers and applied logistic regression to the country-level population data available at each epoch. We identified that forest and largest patch of forest is crucial for large elephant population but should not be singlehandedly used to predict population change. Additionally, we also observed that large elephant population is likely occurs where there are high human presence and activities. This reflects the potential conflict between elephants and human. Through mapping the spatial changes and identifying drivers of Asian elephant population, our study is expected to help regional conservation to understand and incorporate the situation and needs of endangered elephants.

1. INTRODUCTION

1.1 Asian Elephant Status

The Asian elephants (Elephas maximus) is listed as endangered species in the IUCN Red List of Threatened Species (Choudhury et al., 2008). Its range has significantly reduced from approximately 2.87 million km2 in early 1900s to roughly 600,000 km2 in 2000s (Fernando & Leimgruber, 2011). At present, the Asian elephants occurs in 13 countries or range states which includes Bangladesh, Bhutan, Cambodia, China, India, Indonesia, Laos, Malaysia, Myanmar, Nepal, Sir Lanka, Thailand, and Vietnam. Their home ranges as published by IUCN are sparse and at time isolated. The main reason effecting the Asian elephant population is habitat loss and fragmentation due to growing human population and competition for resources (Peter Leimgruber et al., 2003; Madhusudan et al., 2015). Other factors that contributed to population reduction are poaching (Diana Vollmerhausen, 2014), capture of live elephants (Doyle et al., 2010), and consequence from human-elephant conflicts (Fernando & Leimgruber, 2011).

The Asian elephant census is not regularly reported. Population census data from 1990 (Santiapillai & Jackson, 1990), 2003 (Choudhury et al., 2008), and 2015 (IUCN/SSC Asian Elephant Special ist Group, 2017). The overall populations have shown a slight decline and been estimated at 50,000 elephants since 1990. However, the population data available at each range state illustrates apparent differences. Some states have a drastic reduction, while others show continuous increase (Figure 1). With variation in population exhibited among range states, possible drivers influencing such differences in elephant population are of conservation interest.
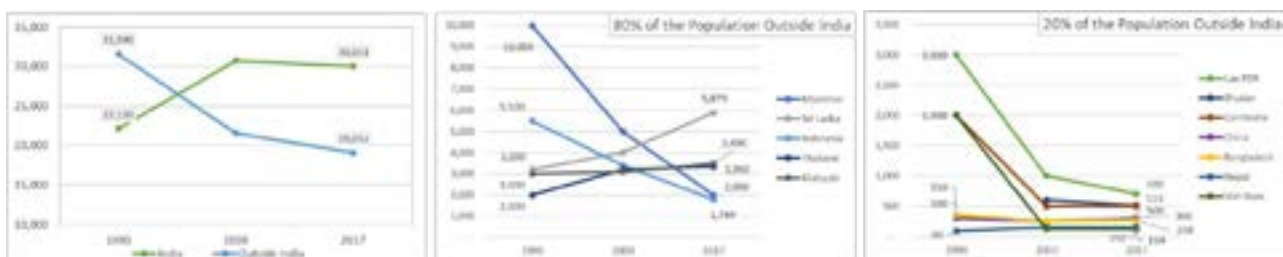

Figure 1: Wild population of Asian elephants among 13 range stages

1.2 Previous Researches Utilizing Remote Sensing

Elephants are the largest terrestrial mammal and can weight over 1,000 kilograms. With such large body size, the wild Asian elephants require large area for foraging and grazing. Satellite remote sensing has been vital in collecting characteristics of their large-scale home range. Many studies that utilized satellite-derived land surface information (e.g. land cover, NDVI, digital surface model, etc.) together with elephant presence data collected either from field observation or GPS telemetry to model habitat preference and suitability. These studies are common in almost all range states (Aini, Husin, Sood, & Saaban, 2017; Duffy & Pettorelli, 2012; Liu, Wen, Lin, Liu, & Zhang, 2016; Rood, Ganie, & Nijman, 2010; Zhang et al., 2015). Both biotic and abiotic condition commonly preferred by wild Asian elephants can be gather from such studies. Nevertheless, such researches are performed at the local scale, such as at a single park level or province level. While research across regional scale are available, they are much less in number and usually performed on a single temporal scale. Leimgruber et al., (2003) used land cover dataset to identify unfragmented wildland and its implication for Asian elephant population.

1.3 Objectives

Based on existing publications, long-term and cross-countries research on elements impacting population dynamic remain limited. We, hence, attempted to reduce this gap. Since habitat alteration is believed to be a prominent factor effecting the Asian elephant population, this study focuses at the long-term land cover and landscape change and how these may impact population dynamic. We attempted to answer two questions: (1) How does land cover and landscape within Asian elephant home ranges change over time (2) What may be the relationship between land cover and landscape changes to the Asian elephant populations.

2. MATERIALS AND METHODS

2.1 Study Area

The home ranges where wild Asian elephants occur with certainty are provided in digital format from IUCN (WWF, 2015). A 15-km buffer was generated, and any overlapping home ranges were joined. This buffer rule was based on the observation that Asian elephants moves 9.05 ±0.6 km/day in zoos (Rowell, 2014), and average large daily travel distance observed in the wild (Fernando, Leimgruber, Prasad, & Pastorini, 2012). Moreover, since the home range data was generated in early 2000s, the buffer assisted to cover uncertainty of past home range in the 1990. In addition, because population data is at country-level, any cross-border home ranges are intersected using country boundary and assigned to relevant countries. All land cover and landscape metrices for this study are generated only within this specified home range as shown in Figure 2.
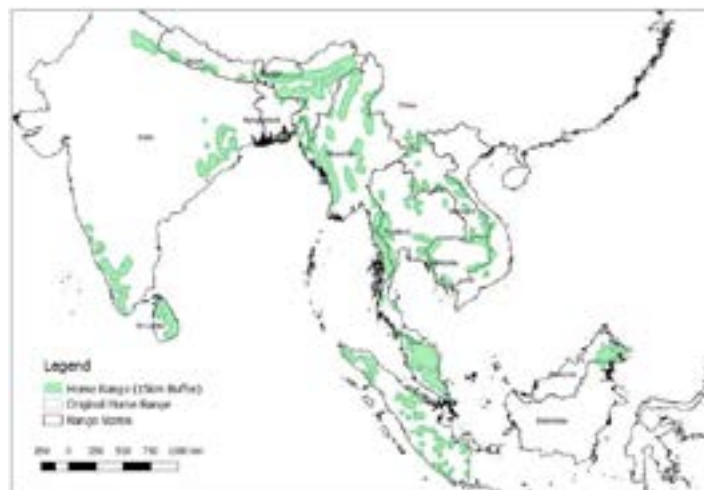
Figure 2: Study Area - Home range of wild Asian elephants with 15km buffer

2.2 Data and Methods

Figure 3 provides the overview of the dataset and the methodology used in this study. To capture the change of land cover and landscape in relation to the Asian elephant population throughout the selected period, consistent land cover maps with classification that reflect elephant's preference are necessary. Due to the lack of ground truth data and the large extent of the study area, existing land cover products was used instead of performing classification ourselves.

The ESA CCI land cover maps (CCI-Land) provide moderate spatial resolution at 300 m and an annual temporal resolution from 1992 to 2015. CCI-Land applied United Nation Land Cover Classification System (UN-LCCS) with total of 22 classes. Its predecessor version was evaluated to be suitable for climate modeling, global forest change, as well as global agriculture monitoring (Tsendbazar, de Bruin, & Herold, 2015). CCI-Land from 1992, 2003, and 2015 were used as it closely covered the study period. Elephants are generalists and live in variety of habitats including forest, shrubland and grasslands (Seidensticker, 1984). Based on use of various land cover type by elephants, we reclassified 22 classes from CCI-Land product to 6 classes including crop, forest, shrub, grass, urban, and others.
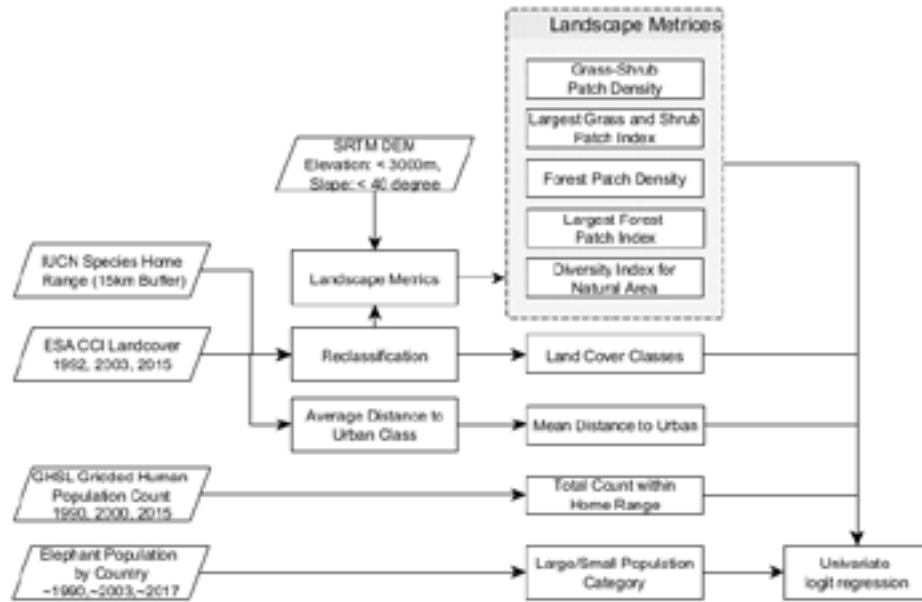
Figure 3: Overview of dataset and methodology

Human presence and activities shown significant impact to landscape and wild elephant distribution and movement (Peter Leimgruber et al., 2003). To incorporate human influence, we computed distance to urban land cover type for each pixel and calculated the average for all home range within the same country. Since the resolution of CCI-Land product may not be able to capture the level of human presence, the Global Human Settlement Layers (GHSL) population grid for 1990, 2000, and 2015 were also used. This data utilized the estimates by CIESIN GPW v.4 in aggregation with density of built-up map for more accurate distribution of human population and provide number of people at 100 m grid cell. The sum of human population count within home ranges of individual countries were computed.

Table 1: Landscape metrics used in this study

| Metrics	Unit	Description
$PD = \dfrac{n_i}{A}$	Number per km^2	the number of patches of class i divided by total landscape area
$LPI = \dfrac{\max\limits_{j=1} a_{ji}}{A}$	%	the area of the largest patch in class i divided by total landscape area
$SHDI = \sum\limits_{i=1} (P_i \ln P_i)$	-	The minus of sum of the proportional abundance of each patch type multiplied by that proportion. Increases as proportional distribution of area among patch types more equitable

Landscape metrices were considered because amount of land cover type, such as forest, alone do not provide insight into landscape structure. Herbivores, including elephants, response to patchiness of foraging resources (Murwira & Skidmore, 2005) with assumption that fragmentation negatively influence elephant habitat utilization (Leimgruber et al., 2003). Goossens et al., (2016) showed that fragmentation restrict population size due to available of resources and can lead to isolation between herds which negatively impact gene pool and genetic diversity. The landscape metrices in this study include Patch Density (PD), Largest Patch Index (LPI), and Shannon diversity Index (SHDI). PD and LPI were used in habitat fragmentation studies for various species including elephants (Peter Leimgruber et al., 2003), while SHDI was used to quantify heterogeneity of the landscape for elephants (Risch et al., 2017). The formula for each metrices are shown in Table 1. For this study, we expected fragmentation of forest (refuge and food) and grass+shrub (food) land cover class to influence elephant population.

Elevation and slope can act as natural barriers and fragmented habitat utilization. Previous habitat suitability studies in various locations identified unlikely presence of Asian elephants at elevation above 3,000 m and slope over 40 degree. We extracted elevation and slope using downscaled DEM from Shuttle Radar Topography Mission (SRTM)

to mask out land cover pixels with unsuitable elevation and slope. The resulting land cover maps were used. Calculation was done in R program. PD and LSI were computed based on 4-adjacent connected component, while 'vegan' package was used for SHDI.

2.3 Statistical Analysis

To assess the relationship between various land cover and landscape characteristic, univariate logistic regression was applied with elephant population at country level as a dependent variable (n=39, 13 countries in 3 epochs). Because the population data is based on educated guess and previous studies have highlighted concern on the accuracy of such rough estimation (Blake & Hedges, 2004; Calabrese et al., 2017), the direct use of census data can mislead the results. Hence, we simplified the population of elephants and classified into large or small population. We assigned each country to a population category: category 0: small population of <2,000 individual, and category 1: large population of ≥2,000 elephants. This threshold was adapted from previous research (Santiapillai, 1997). The relation was assessed for natural land cover type which are potentially used by wild elephants including forest, shrubland and grassland. In addition, crop and urban land cover type are of interest because they imply human activities. For human influence, mean distance to urban and total population count with in home ranges were also exploited. Lastly, all landscape metrices discussed above were assessed. All explanatory variables were checked for skewness and was transform with log10 when identified. For each univariate model, odd ratio of interest and p-value were calculated. Statistical analysis was done in R using binomial General Linear Model.

3. RESULTS

3.1 Land Cover and Landscape Change

Table 2: Changes Occurred between 1990 to 2003 and 2003 to 2015 for Nation-wide and Range-wide

Country	Nation-Wide Change		Home Range		Change in km2 (% of Total Change)			
	1990-2003	2003-2015	Area	% of Country	1990 - 2003		2003 - 2015	
Bangladesh	3,799.9	2,724.1	21,478.4	15.7	943.7	(25%)	410.9	(16%)
Bhutan	1,981.1	376.4	11,297.0	29.3	1,620.6	(82%)	181.4	(49%)
Cambodia	17,005.1	9,470.5	49,199.3	27.2	7,692.5	(46%)	3,531.4	(38%)
China	205,846.7	157,818.9	16,909.7	0.2	1,771.0	(1%)	550.8	(1%)
India	63,684.8	36,547.0	331,504.4	10.6	17,235.5	(28%)	6,273.8	(18%)
Indonesia	78,491.2	94,974.9	171,436.8	9.2	8,888.1	(12%)	17,703.2	(19%)
Laos	17,936.3	7,939.9	72,374.6	31.5	6,117.2	(35%)	3,379.8	(43%)
Malaysia	21,500.7	26,510.0	140,513.5	21.2	9,824.3	(46%)	8,587.2	(33%)
Myanmar	46,375.3	16,048.3	221,845.3	67.9	20,175.8	(44%)	6,352.5	(40%)
Nepal	5,897.2	1,548.4	20,708.5	14.0	898.6	(16%)	280.4	(19%)
Sri Lanka	5,477.9	1,859.7	44,693.4	68.3	4,833.7	(89%)	1,065.2	(58%)
Thailand	15,654.2	7,772.5	114,000.9	22.2	7,256.8	(47%)	2,218.8	(29%)
Vietnam	22,680.0	10,710.9	32,475.1	10.0	4,228.4	(19%)	1,810.8	(17%)

Table 3: Total conversion and changes occurred to forest, shrub and grass in 1990-2003 and 2003-2015, the class with the largest percent loss of total land conversion within home ranges highlighted in bold

	1992 to 2003						2003 to 2015					
	Total Conversion (km2)	Total Conversion (% of Home Range)	% of Total Conversion			Elephant Population Trend	Total Conversion (km2)	Total Conversion (% of Home Range)	% of Total Conversion			Elephant Population Trend
			Forest	Shrub	Grass				Forest	Shrub	Grass	
Bangladesh	943.65	4.39	7.7	**46.1**	17.8	−	410.85	1.91	31.4	**26.2**	1.8	+
Bhutan	1,620.63	14.35	5.1	**91.4**	0.6	+	181.44	1.61	17.8	**78.7**	0.1	−
Cambodia	7,692.48	15.64	**88.8**	10.8	0.2	−	3,531.42	7.18	**61.1**	37.3	0.1	−
China	1,771.02	10.47	10.5	**88.1**	0.0	−	550.80	3.26	22.4	**58.5**	0.2	+
India	17,235.45	5.20	38.8	**49.9**	2.4	+	6,273.81	1.89	36.4	**33.8**	2.2	−
Indonesia	8,888.13	5.18	**65.6**	0.0	0.0	−	17,703.18	10.33	**68.6**	0.0	0.0	−
Laos	6,117.21	8.45	39.3	**59.4**	0.4	−	3,379.77	4.67	56.6	**38.4**	0.2	−
Malaysia	9,824.31	6.99	40.9	0.0	0.0	+	8,587.17	6.11	**57.6**	0.0	0.0	+
Myanmar	20,175.75	9.09	35.7	**56.3**	0.1	−	6,352.47	2.86	50.1	**39.6**	0.3	−
Nepal	898.56	4.34	**76.0**	4.3	0.6	+	280.35	1.35	**40.8**	23.9	2.2	−
Sri Lanka	4,833.72	10.82	**97.0**	1.6	0.1	+	1,065.15	2.38	**54.2**	23.2	0.2	+
Thailand	7,256.79	6.37	**71.9**	18.0	0.3	+	2,218.77	1.95	**38.4**	31.8	0.1	+
Vietnam	4,228.38	13.02	**87.8**	10.8	0.0	−	1,810.80	5.58	**74.3**	21.4	0.2	−

Information on the type of land conversion provide a broad picture of land cover change dynamics. From Table 2, larger changes occurred during 1990 and 2003 in all countries except Indonesia where larger change happened during 2003 and 2015. In addition, conversion within elephant home ranges were accounted for a large portion of total change nation-wide ranging from just over 10% in Laos up to 89% in Sri Lanka. For all countries, largest conversion occurred in forest land cover type. In all range countries, the rate of change to urban increased distinctively between 2003 to 2015 in comparison of earlier period.

Table 3 showed the total conversion within each country, as well as the change from forest, shrub, and grass cover class for each country in 1992 to 2003 and 2003 to 2015. Bhutan, Cambodia, India, Sri Lanka and Vietnam experienced over 10% of land cover change within between 1990 to 2003. Countries with dominant conversion from forest cover type, as high as over 65% of total land change, during 1990 to 2003 are Cambodia, Indonesia, Nepal, Sri Lanka, Thailand and Vietnam. These countries continued to convert large forest portion in consideration of overall change during 2003 to 2015. In addition, only Indonesia illustrated over 10% change of total landscape between 2003 to 2015 with increasing forest loss in comparison to earlier period. Net loss and gain of all land cover type from both periods is shown in Table 4.

3.2 Statistical Analysis

Table 5 listed the result of univariate logistic regression model of selected variables and graph of each model are shown in Figure 4. Cropland area, forest area, urban area, human population within home range, and forest LSI yield statistically significant relationship with elephant population. As expected, forest land cover is crucial where the area of forest land cover increases, the likelihood of having large population also increases. However, the direct relationship of cropland and urban to elephant population was unexpected where increase in either variable raises the likelihood of having large elephant population. Interestingly, human population count is more influential than distance to urban. For all landscape metrics, only forest LSI is statistically significant. A large continuous forest patch has higher influence to sustain large population more than patchiness within the landscape. The larger area of the largest forest patch implies larger population group. Fragmentation of grass and shrub does not show statistically significant influence on population. Shannon diversity also does not yield significant relationship. It should be noted that some countries exhibit unique characteristics and can skew the model as highlighted in red in Figure 4. For example, high population count for India, or small cropland in Bhutan.

Table 4: Net loss and gain in percentage of total home range area from 1990 to 2015

	Crop	Forest	Shrub	Grass	Urban	Others		Crop	Forest	Shrub	Grass	Urban	Others
Bangladesh	3.271	(0.214)	(1.732)	(0.543)	0.203	(0.985)	Laos	3.386	(1.751)	(1.785)	(0.027)	0.016	0.162
Bhutan	0.072	13.725	(13.732)	(0.084)	0.014	0.006	Malaysia	0.031	(0.673)	0.041	-	0.355	0.245
Cambodia	15.426	(18.152)	2.596	0.058	0.071	0.001	Myanmar	1.314	1.329	(2.817)	0.029	0.060	0.085
China	0.779	8.487	(9.590)	(0.004)	0.323	0.006	Nepal	2.885	(2.616)	(0.310)	0.010	0.176	(0.144)
India	1.668	(0.260)	(1.884)	(0.033)	0.397	0.113	Sri Lanka	4.059	(11.171)	6.945	(0.007)	0.120	0.053
Indonesia	6.799	(7.009)	0.288	0.000	0.078	(0.157)	Thailand	1.629	(3.702)	1.826	(0.011)	0.081	0.178
							Vietnam	8.414	(14.979)	6.322	0.004	0.054	0.185

Table 5: Odd ratios and P-values of each variable in univariate logistic regression models

Variables	Odd Ratio	Univariate P-value	
Log Crop Cover	87.46	0.0014	**
Log Forest Cover	43.91	0.0009	***
Log Shrub Cover	1.42	0.3160	
Log Grass Cover	1.19	0.6260	
Log Urban Cover	8.84	0.0032	**
Log Human Population Count	7.55	0.0136	*
Log Distance to Urban	6.44	0.4210	
Log Forest PD	0.00	0.0667	
Log Shrub+Grass PD	2.38E+12	0.0855	
Log Forest LPI	12.98	0.0034	**
Log Grass LPI	0.00	0.7740	
Shannon Diversity	2.44	0.5200	

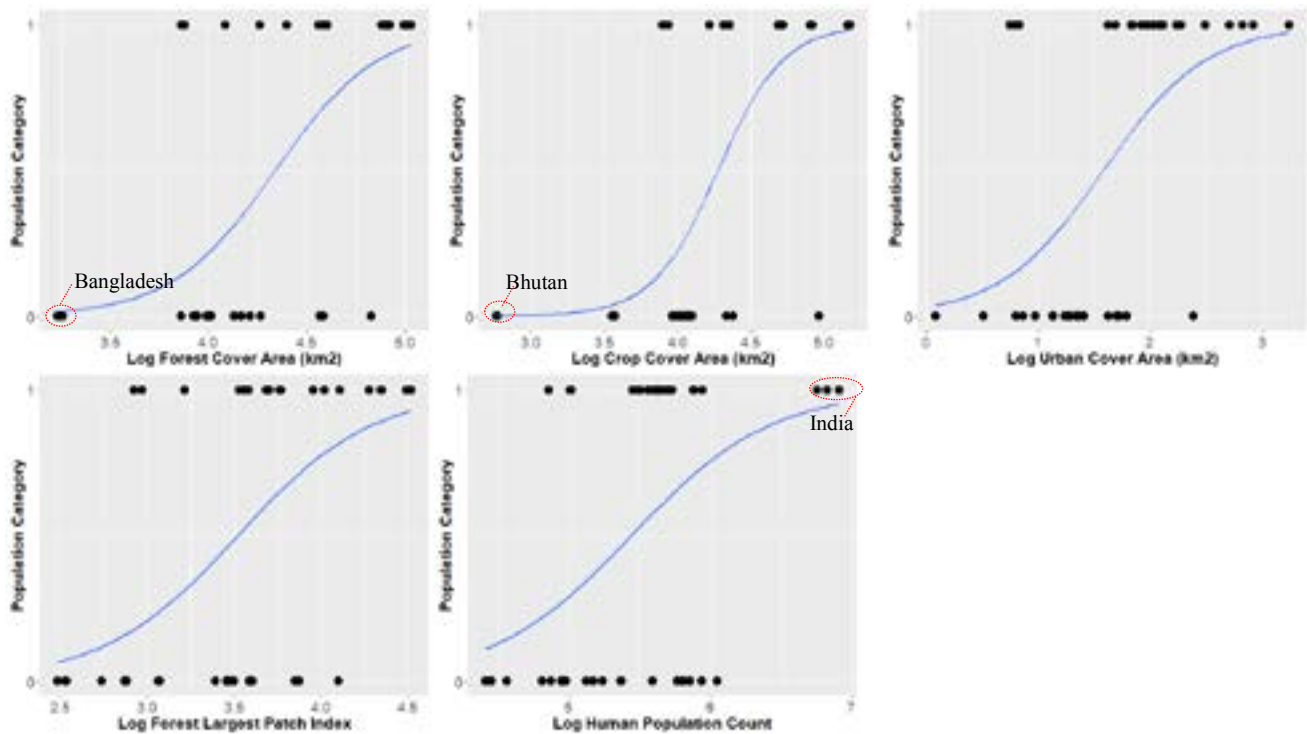Figure 4: Graphs of logistic regression for each variable showing the likelihood of having a large elephant population (Category 1) with the logistic curved represents the model-averaged response function
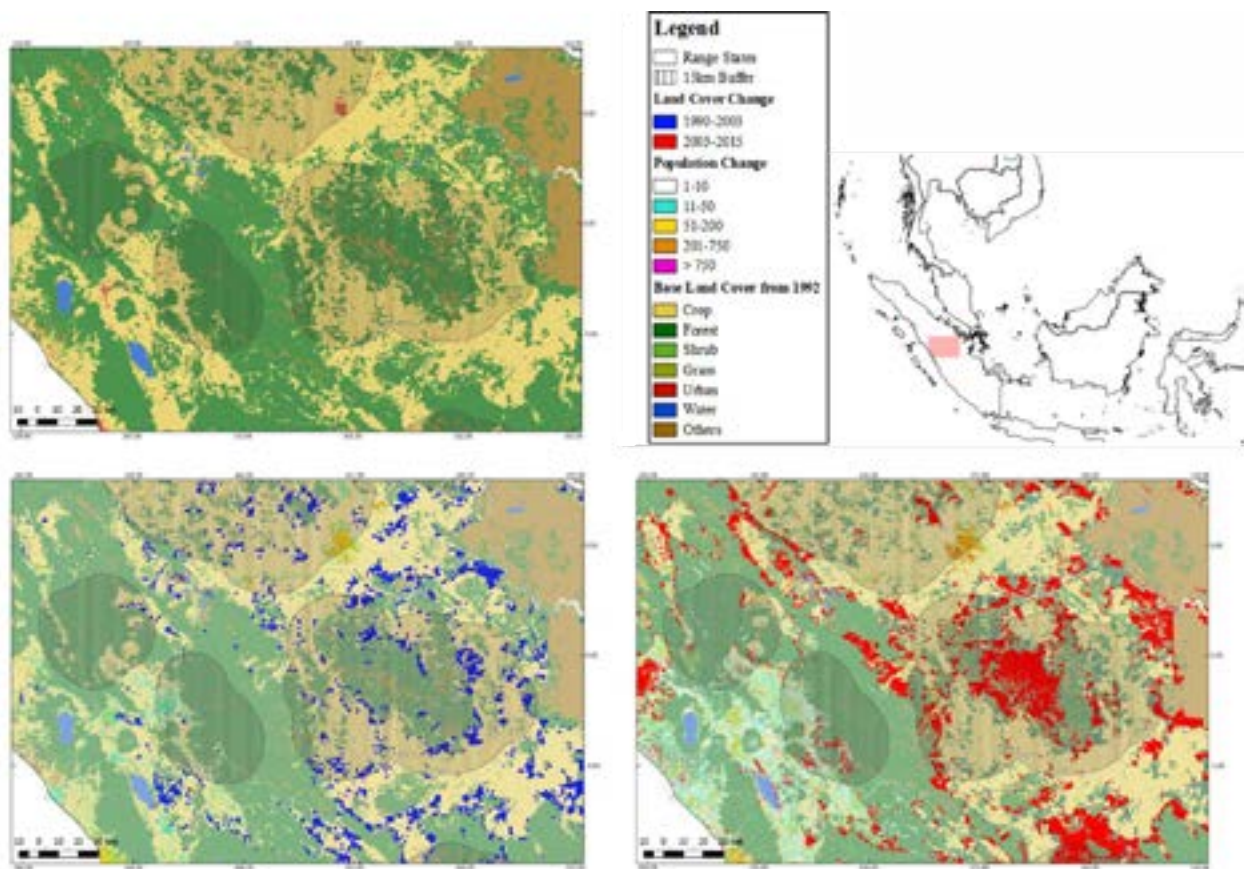

Figure 5: Example of land cover and human population change from Indonesia showing base land cover from 1992 (top-left), changes occurred from 1992-2003 (bottom-right), and changes occurred from 2003-2015 (bottom-right)

4. DISCUSSION

For the first research question on how land cover and landscape changes over time, we found that during the study period, all countries shows overall net gain of cropland and urban area with highest growth of urban especially during 2003 to 2015. On the other hand, other classes change differently among different countries, but majority of conversion occurred under forest or shrub for all countries. Nevertheless, the results showed that land cover and landscape change alone is limited to directly impact the change of elephant population. From land cover change results, forest loss and gain do not simply translate into the decrease or increase of elephant population. Sri Lanka, for example, reported a continuous increase in Asian elephant population, but its land cover change illustrated a dominant conversion of forest area. On the contrary, Myanmar, where a drastic drop of elephant population was reported, shows a net gain of forest from 1990 to 2015. Since elephant utilized various land cover type, changes of a single land cover type may not directly impact population and a combination of land cover maybe more informative. For Sri Lanka in particular, a study suggested that grasslands are essential habitat for Asian elephants and vital for future conservation of their population in Sri Lanka (Sampson, 2013). Nevertheless, grassland was not presence at all for Malaysia home range. Hence, population from different countries can exhibit unique preference depending on resource availability. Additionally, many factors may beyond land cover and landscape can impact the change in population. Myanmar reported the largest capture of live wild elephants (P. Leimgruber et al., 2011) and increasing report on poaching (Sampson et al., 2018).

For the second research question, we identify that forest area remains important in maintaining large Asian elephant population as shown in

Table 5 where statistically significant relation was identified for forest cover and forest LSI. Additionally, forest LSI illustrated the importance of conserving unfragmented forest area in order to support elephant population with healthy number. The counter-intuitive results of a direct relationship between human activities (urban, crop, and human population) to the likelihood of large elephant population reflects the situation of Asian elephants. It can be interpreted that Asian elephants are adapting to the increasing human population, but on the other hand it can also implies higher possibility of competition and confrontation between human and elephants in various range states. Such situation can intensify human-elephant conflict (HEC). From human population count logistic regression result in Figure 4, India, as highlighted in red, has the largest reported population. The country has been dealing with large incidents of HEC (Doyle et al., 2010). As human population count was found to be more influential than distance to urban. This implies that elephants may be able to adapt to live close to human settlement as long as the number of people does not increase pass certain level. Additionally, higher human population can also signify possibility of land conversion which can negatively impact elephant population. Figure 5 illustrates the higher changes of landscape along with the increase of human population.

Current studies rely on publicly available elephant census data which is at country level scale. With such coarse resolution, spatially explicit analysis is not possible. Using finer resolution dataset, such as that at individual home range scale, should be tested whether improvement can be achieved for the accuracy and explanatory power of the model. Moreover, with the limited number of dependent observations, population data from each epoch were combined for logistic regression analysis. In addition, the use of threshold to categorize elephant population was adapted from previous publication. However, a more systematic approach to identify appropriate threshold can be applied. More detailed land cover classification scheme can also be employed to better reflect elephant habitat. For example, elephants prefer open canopy and secondary regrowth forest where food is more accessible compared to that in undisturbed forest (Aini et al., 2017). Such detailed classification should be performed using higher resolution images, such as Landsat, when ground data or confidence in visual validation is available. Lastly, various variable that affects landscape fragmentation, such as road network, were not included in the current study either which mainly due to lack of updated information. Hence, more comprehensive research can be further conducted.

5. CONCLUSION

Regional landscape analysis within Asian elephant home range can provide holistic perspective for conservation. We identified similarities and differences of land cover and landscape changes among range countries. Moreover, we illustrated that forest alone cannot explain the change in elephant population. Nevertheless, it remains the most important factor in maintaining large population. Further research exploring combination of various landscape type and incorporate other social variables can provide more informative understanding. Additionally, we also found that large elephant populations are in area with intense human presence and activities which can lead to conflict. Hence, future research exploring interact between human and elephant within such competitive landscape is needed.

6. REFERENCES

Aini, S., Husin, M. Z., Sood, A. M., & Saaban, S. (2017). A GIS Based Multi-Criteria Evaluation Approach to Develop an Asian Elephant Habitat Suitability Model in Peninsular Malaysia, *47*, 10–17.

Calabrese, A., Calabrese, J. M., Songer, M., Wegmann, M., Hedges, S., Rose, R., & Leimgruber, P. (2017). Conservation status of Asian elephants: the influence of habitat and governance. *Biodiversity and Conservation*, *26*(9), 2067–2081. https://doi.org/10.1007/s10531-017-1345-5

Choudhury, A., Lahiri Choudhury, D. K., Desai, A., Duckworth, J. ., Easa, P. S., Johnsingh, A. J. ., … (IUCN SSC Asian Elephant Specialist Group). (2008). Elephas maximus. The IUCN Red List of Threatened Species 2008. *The IUCN Red List of Threatened Species 2008*, *8235*, 16. https://doi.org/http://dx.doi.org/10.2305/IUCN.UK.2008.RLTS.T7140A12828813.en

Diana Vollmerhausen. (2014). *Elephants in the Dust | The Independent*. The Independent. Retrieved from http://www.independent.co.uk/voices/comment/elephants-in-the-dust-9114448.html

Doyle, S., Groo, M., Sampson, C., Songer, M., Jones, M., & Leimgruber, P. (2010). Human-elephant conflict- what can we learn from the news? *Gajah*, *32*, 14–20.

Duffy, J. P., & Pettorelli, N. (2012). Exploring the relationship between NDVI and African elephant population density in protected areas. *African Journal of Ecology*, *50*(4), 455–463. https://doi.org/10.1111/j.1365-2028.2012.01340.x

Fernando, P., & Leimgruber, P. (2011). Asian elephants and seasonally dry forests. *The Ecology and Conservation of Seasonally Dry Forests in Asia*, 151–163.

Fernando, P., Leimgruber, P., Prasad, T., & Pastorini, J. (2012). Problem-Elephant Translocation: Translocating the Problem and the Elephant? *PLoS ONE*, *7*(12). https://doi.org/10.1371/journal.pone.0050917

IUCN/SSC Asian Elephant Special ist Group. (2017). *Asian Elephant Range States Meeting: Final Report*. Jakarta, Indonesia.

Leimgruber, P., Gagnon, J. B., Wemmer, C., Kelly, D. S., Songer, M. A., & Selig, E. R. (2003). Fragmentation of Asia's remaining wildlands: Implications for Asian elephant conservation. *Animal Conservation*, *6*(4), 347–359. https://doi.org/10.1017/S1367943003003421

Leimgruber, P., Min Oo, Z., Aung, M., Kelly, D., Wemmer, C., Senior, B., & Songer, M. (2011). Current Status of Asian Elephants in Myanmar. *Gajah*, *35*, 76–86. https://doi.org/10.5167/uzh-59037

Liu, P., Wen, H., Lin, L., Liu, J., & Zhang, L. (2016). Habitat evaluation for Asian elephants (Elephas maximus) in Lincang: Conservation planning for an extremely small population of elephants in China. *Biological Conservation*, *198*, 113–121. https://doi.org/10.1016/j.biocon.2016.04.005

Madhusudan, M. D., Sharma, N., Raghunath, R., Baskaran, N., Bipin, C. M., Gubbi, S., … Sukumar, R. (2015). Distribution, relative abundance, and conservation status of Asian elephants in Karnataka, southern India. *Biological Conservation*, *187*, 34–40. https://doi.org/10.1016/j.biocon.2015.04.003

Risch, T. S., Advisor, D., Ingram, D., Member, C., Morris, D. K., Member, C., … Member, C. (2017). STATUS , PATTERNS , AND POTENTIAL MITIGATION OF HUMAN- ELEPHANT CONFLICT IN NEPAL AND ELEPHANT HABITAT USE IN BARDIA NATIONAL PARK , NEPAL DINESH NEUPANE A dissertation presented to the faculty of Arkansas State University in partial fulfillment of the re, (May).

Rood, E., Ganie, A. A., & Nijman, V. (2010). Using presence-only modelling to predict Asian elephant habitat use in a tropical forest landscape: Implications for conservation. *Diversity and Distributions*, *16*(6), 975–984. https://doi.org/10.1111/j.1472-4642.2010.00704.x

Rowell, Z. (2014). Locomotion in captive Asian elephants (*Elephas maximus*). *Journal of Zoo and Aquarium Research*, *2*(4), 130–135. https://doi.org/https://doi.org/10.19227/jzar.v2i4.50

Sampson, C. (2013). Conserving The Land of The Giants : Critical Threats To Asian Elephant Habitat in Sri Lankan Protected Areas, 84.

Sampson, C., McEvoy, J., Oo, Z. M., Chit, A. M., Chan, A. N., Tonkyn, D., … Leimgruber, P. (2018). New elephant crisis in Asia - Early warning signs from Myanmar. *PLoS ONE*, *13*(3), 1–13. https://doi.org/10.1371/journal.pone.0194113

Santiapillai, C., & Jackson, P. (1990). *The Asian Elephant - An Action Plan for its Conservation*. Retrieved from https://portals.iucn.org/library/node/6042

Tsendbazar, N. E., de Bruin, S., & Herold, M. (2015). Assessing global land cover reference datasets for different user communities. *ISPRS Journal of Photogrammetry and Remote Sensing*, *103*, 93–114. https://doi.org/10.1016/j.isprsjprs.2014.02.008

WWF. (2015). Asian Elephant, *1973*(November), 1–4.

Zhang, L., Dong, L., Lin, L., Feng, L., Yan, F., Wang, L., … Luo, A. (2015). Asian elephants in China: Estimating population size and evaluating habitat suitability. *PLoS ONE*, *10*(5), 1–13.

RENEWABLE ENERGY CROP RECOGNITION BASED ON OBJECTED-BASED CLASSIFICATION USING MEMBERSHIP FUNCTION

Maytavee Tuathong (1), Kamolratn Chureesampant (1), Sasikan Yaemyim (1)

[1]Electricity Generating Authority of Thailand, Survey Division, Map and Geographic Information System Department, Photogrammetry and Remote Sensing Section, No. 53 Moo 2, Charunsanitwong Road, Bang Kruai, 11130, Nonthaburi, Thailand
Email: maytaavee.t@egat.co.th; kamolratn.c@ egat.co.th; sasikan.y@egat.co.th

KEY WORDS: Renewable Energy Crops; Object Based Classification; Membership Function (MF); Nearest Neighbor (NN)

ABSTRACT: Recently, the renewable energy trend continues to remarkable progress. The analysis of its potential energy crops is challenge. The remote sensing also provides the opportunity to monitoring such kind of energy crops by classification. However, the pixel-based classification, is based on quantitative pixel intensities on histogram. It cannot fully utilized the spatial information. As object-based classification is attractive approach because it considers more others attributes e.g., shape, size, color, texture and etc. Therefore, this paper addresses recognition capabilities of Landsat-8 Earth-observation satellite in comparison with fuzzy logic membership function (MF) and Nearest Neighbor (NN) algorithms and combination of MF and NN based on object-based classification. Landsat-8 satellite is used as input data as it has many effective bands that can distinguish the difference of any land use with support the object-based classification. The recognition results were generated by taking Tham Charoen subdistrict, So Phisai district, Bueng Kan province in northeastern Thailand, as the study area. The selected seven classes of renewable energy crops were pará rubber trees, oil palm trees, eucalyptus trees, mixed forests, small crops, build-up area, and water body area. Experiment results reveal that the most suitable recognition is the MF and NN combination because the supplement of an excellent mapping of linear segment for hypersurface model with small amount of data to define in the MF and the robust to noisy training data for the NN. Moreover, the assigned membership function can be applied to other region of interest areas.

1. INTRODUCTION

At the present time, trend of renewable energy crops is a prominent advancement in Thailand due to depleting of fossil fuels and negative impact on global climate when they are consumed for electricity generating. The exploration of energy crops is a significant prior task in estimating their potential energy to generate electric power. However, this investigation is still a tough, labored and time consuming work by using traditional surveying, therefore the technology of remote sensing is essential to encourage this research.

To classify energy crops on remotely sensed imagery, some of acquainted techniques are object-based classification and pixel-based classification. The pixel-based procedure analyses the spectral reflectance of every single pixel only [1], while the object-based procedure merges homogeneous parts on the imagery by considering their characteristics; color, smoothness and compactness, which more various than the pixel-based procedure. Thus, the object-based classification is inferred to be appropriate for this research. In addition, the most common algorithm for predicting classes of an object on raster image is nearest neighbor (NN) [2]. However, to distinguish the energy crops into classes, which have quite similar indicator, such as pará rubber trees, oil palm trees and eucalyptus trees with the NN is still difficult to solve this uncertainty classification. Membership function (MF) is therefore an alternative to be the solution of this classification since it can enhance the NN algorithm to be able to deal with uncertainty classification or fuzzy logic problems [3].

This research aims to study objected-based classification using combination of nearest neighbor and membership function to recognize renewable energy crops in Tham Charoen subdistrict, So Phisai district, Bueng Kan province in northeastern Thailand, including the investigation of the appropriate customized features supporting in feature considering technique. The research details are described below.

2. STUDY AREA AND DATA DESCRIPTION

The study area is Tham Charoen subdistrict, So Phisai district, Bueng Kan province in northeastern Thailand (Approximate area 8,267 hectare), as shown in Figure 1. Tham Charoen district is an agricultural area in Bueng Kan province where pará rubber trees are mostly planted. Others are small crops, oil palm trees, and eucalyptus trees which are found widespread in the district. This research focuses on seven classes namely, pará rubber trees, oil palm trees, eucalyptus trees, mixed forests, small crops, build-up area, and water body area. However, energy crops classes are rather similar characteristics and difficult to distinguish between them. Thus, four main classes separation is considered i.e., perennial plant (pará rubber trees, oil palm trees, eucalyptus trees, and mixed forests); small crops (paddy fields and planting area); build-up area and water bodies. Landsat-8 operational land imager (OLI) is the data source which consists nine multispectral bands with spatial resolution of 30 meters for bands 1 to 7 and 9. The resolution for band 8 (panchromatic) is 15 meters. The properties of Landsat-8 operational land imager (OLI) data is shown in Table 1. However, only one duration of data is not enough because many pará rubber, which shed leaves on first quarter, have been planting in Bueng Kan province, therefore multiple duration of the images are necessary, in this case the data of Landsat-8 images on 18th November 2017 (End of the year phase) and 21st January 2018 (Early year phase) are applied. Another important data sources are Google images on 31st January 2018 providing medium resolution images which are appropriate to create image object using multiresolution segmentation method.

Figure 1. Tham Charoen subdistrict boundary.

Table 1. The properties of Landsat-8 operational land imager (OLI) data.

Bands	Wavelength (micrometers)	Resolution (meters)
Band 1 : Ultra Blue (coastal/aerosol)	0.435 – 0.451	30
Band 2 : Blue	0.452 - 0.512	30
Band 3 : Green	0.533 - 0.590	30
Band 4 - Red	0.636 - 0.673	30
Band 5 - Near Infrared (NIR)	0.851 - 0.879	30
Band 6 - Shortwave Infrared (SWIR) 1	1.566 - 1.651	30
Band 7 - Shortwave Infrared (SWIR) 2	2.107 - 2.294	30
Band 8 - Panchromatic	0.503 - 0.676	15
Band 9 - Cirrus	1.363 - 1.384	30

3. METHODOLOGY

The framework is shown in Figure 2. There are six steps which consists of data preparation, pre-processing, segmentation, main-class classification, perennial plant classification, and accuracy assessment. The Landsat-8 (End of the year phase), Landsat-8 (Early year phase), and Google images are used in data preparation.
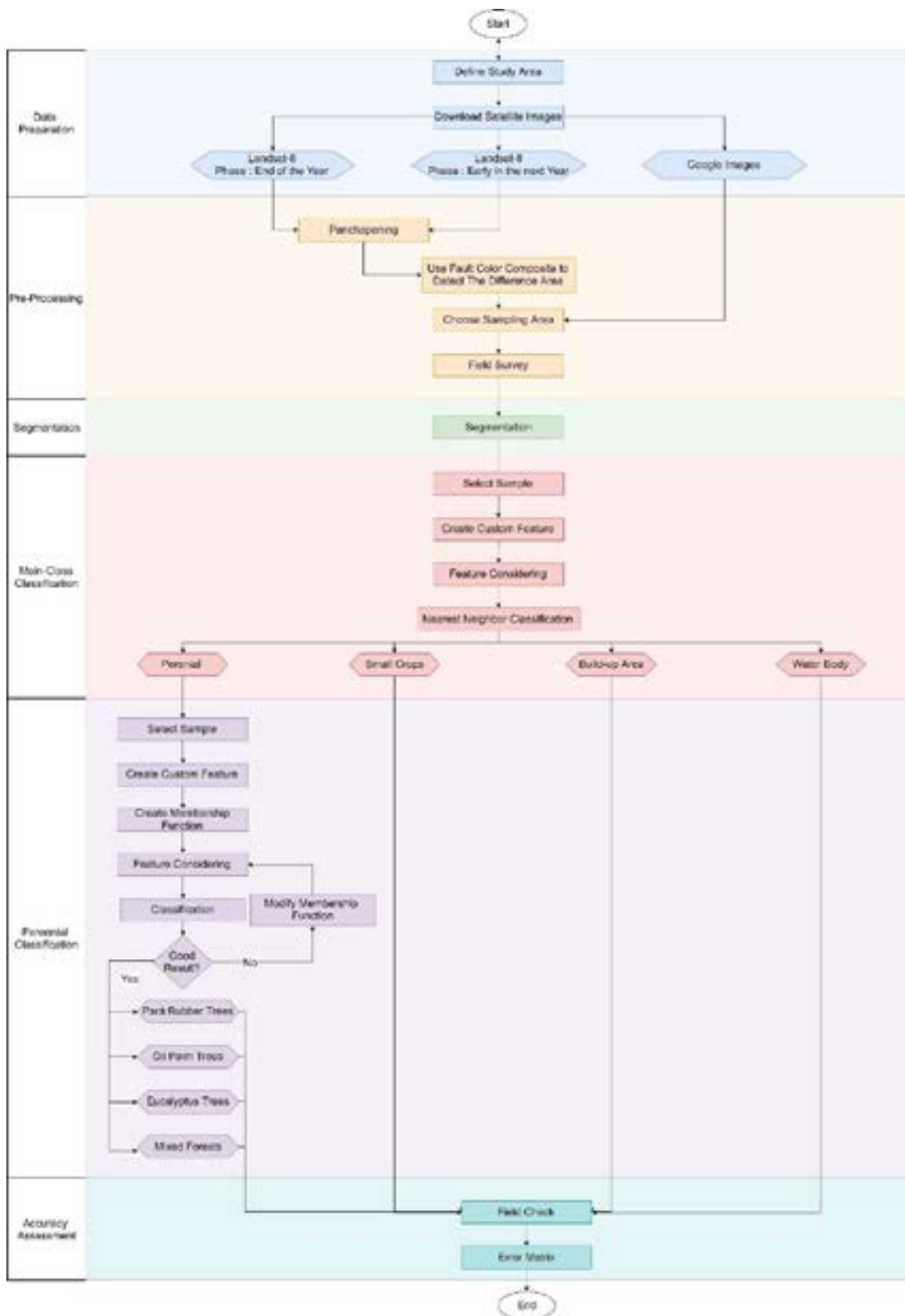
Figure 2. Framework overview.

3.1 Pre-processing

In pre-processing step, two Landsat-8 are initialized by pansharpening. Pansharpening is the process of synthesizing a high spatial resolution multispectral image from a low spatial resolution multispectral image and a high-resolution panchromatic (PAN) image [4]. The pansharpened images are applied the false color composition. Although Landsat-8 consists many effective bands such as NIR, SWIR1, SWIR2 which can display on false color composite to distinguish the difference of any land use, it cannot be defined class exactly. Therefore, Google images can be used for considering location of the sample areas because they provide real image with medium resolution. Then, sample areas are selected in order to be used as training sample areas in classification step. After the sample areas are selected, field survey is proceeded.

3.2 Segmentation

The following important step is segmentation, which creates image objects. The segmentation technique is a region-growing procedure starting at each point in the image with one-pixel objects and merging these image objects into bigger ones throughout a pair-wise clustering process. The merging procedure is based on three concepts namely, color, smoothness and compactness [5]. In this framework, multiresolution segmentation is applied, which image layer weights is significant factor. Therefore, the weights of Google images should define higher than Landsat-8. Classification is performed in the next step. According to the similarity of energy crops' characteristics, main-class classification in Section 3.3 and perennial plant classification in Section 3.4 are demanded as the following.

3.3 Main-class Classification

The step initiates with four main classes with prior training sample area i.e., perennial, small crops, build-up area, and water body area. Afterwards image objects are created in segmentation step, the four customized features and eleven basic features are generated. The Normalized Difference Vegetation Index (NDVI), and Ratio Vegetation Index (RVI) of both two Landsat-8 images data are customized features. The basic features include four bands of red (R), NIR, SWIR-1, and SWIR-2 for two phases Landsat-8 images; and three bands of red (R), green (G), blue (B) for Google images. The feature considering step is processed by the training sample area of four main classes with 15 features based on the feature optimization to obtain the optimized dimension. The 13th dimension is the best optimization dimension with 1.011 best separation distance, which comprises mean of red band for Landsat-8 (End of the year phase), Landsat-8 (Early year phase), and Google images; mean of green band for Google image; mean of blue band for Google image; mean of NIR band for Landsat-8 (End of the year phase), Landsat-8 (Early year phase); mean of SWIR-1 for Landsat-8 (End of the year phase), Landsat-8 (Early year phase); mean of SWIR-2 for Landsat-8 (End of the year phase), Landsat-8 (Early year phase); NDVI of Landsat-8 (End of the year phase), Landsat-8 (Early year phase). Therefore, the optimized 13 features are considered to classify four main classes based on nearest neighbor method. The classification results can be demonstrated into four main classes i.e., perennial, small crops, build-up area, and water body area.

3.4 Perennial Plant Classification

According to the similarity of perennial plant characteristics, it challenge to discriminate sub-classes of perennial plant i.e., pará rubber trees, oil palm trees, eucalyptus trees, and mixed forests. The differential of the NDVI and the RVI for two Landsat-8 images are computed and represented as two more customized features. There are 17 features involving in this stage. The training sample area of four sub-classes are selected to generate the membership function. The membership function (MF) is the general spectral signatures of classified class and the corresponding normalized digital numbers on each multispectral band. The empirical membership functions are studied to acquire the suitable membership functions. In feature considering step, the excellent optimization dimension is 14th dimension with 0.320 best separation distance, which comprises mean of red band for Google image; mean of green band for Google image; mean of blue band for Google image; mean of NIR band for Landsat-8 (End of the year phase), Landsat-8 (Early year phase); mean of SWIR-1 for Landsat-8 (End of the year phase), Landsat-8 (Early year phase); mean of SWIR-2 for Landsat-8 (Early year phase); NDVI of Landsat-8 (End of the year phase), Landsat-8 (Early year phase); RVI of Landsat-8 (End of the year phase), Landsat-8 (Early year phase); the differential of the NDVI; and the differential of the RVI. At last, pará rubber trees, oil palm trees, eucalyptus trees, and mixed forests class are the outcome.

3.5 Accuracy Assessment

The classification result is examined and validated by using the error matrix. The testing samples are taken into account to estimate the classification accuracy, which collected by field surveying. Nevertheless, the proper quantities of testing sample are necessary, hence the binomial probability theory [6] is applied to calculate the minimum number of testing samples.

$$N = \frac{z^2(p)(100-p)}{E^2}$$

(1)

Where N is the minimum number of testing samples, p is the expected percent accuracy, E is allowable error, and z is found in statistical tables which contain the area under the normal distribution curve.

In this calculation, the confidence level is set at 95%. It causes the z value equal to 1.96. The expected percent of accuracy and allowable error are assumed as 85% and 5%, respectively. With above formula, 196 is derived as the minimum number of testing samples. The ground truth is collected by field surveying in total 198 objects regarding to testing samples. The error matrix based on sample is calculated to determine the accuracy assessment.

4. EXPERIMENT RESULTS & DISCUSSION

Figure 3 illustrates the renewable energy crop classification result. Pará rubber trees, oil palm trees, eucalyptus trees, mixed forests, small crops, build-up area, and water body area were recognized as represented in different colors regarding the legend.
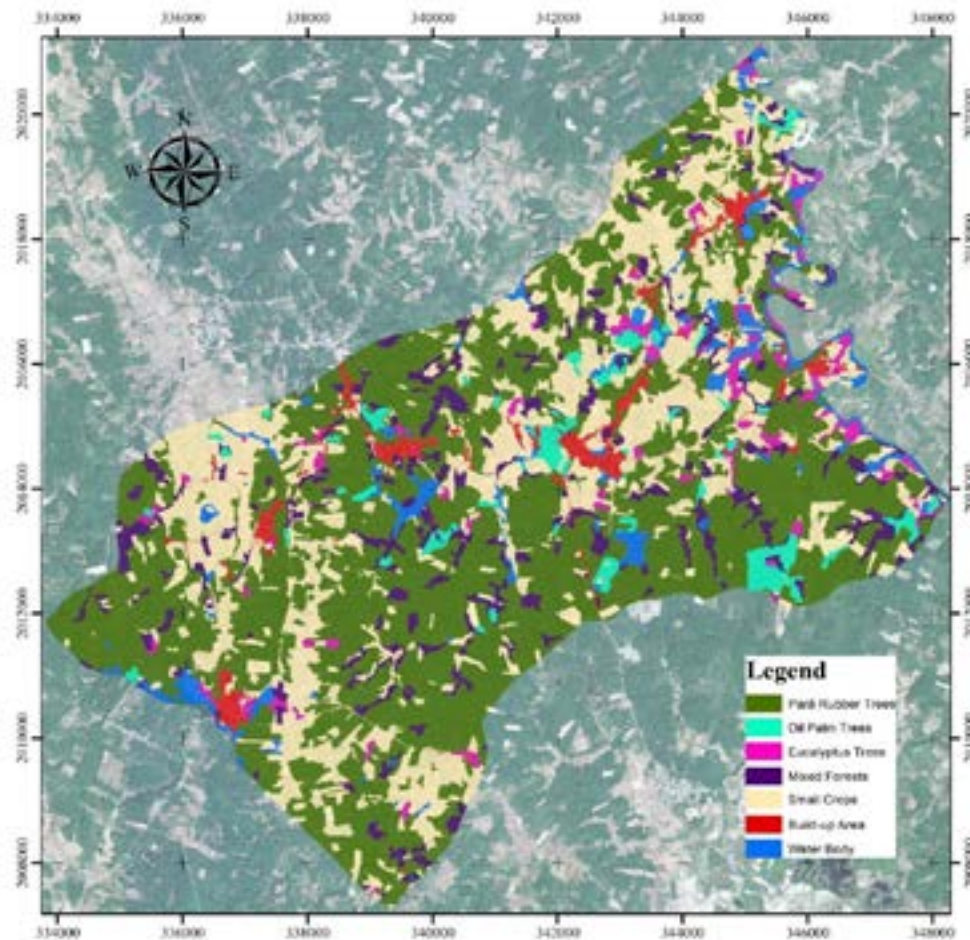

Figure 3. Renewable energy crop classification result.

Samples of pará rubber tree and small crop area classifications are displayed in Figs 4 – 5, respectively. Figure 4(a) shows the Google image acquired on 31st January 2018. Figure 4(b) shows the classification result of pará rubber tree area, which represented in green color. And Figure 4(c) shows the real location of testing sample area at 18°10'54"N, 103°28'18"E. Figs 5(a) – (c) demonstrate Google image acquired on 31st January 2018, an example of classified small crop area, and the testing sample area location at 18°10'58"N, 103°28'20"E, respectively.
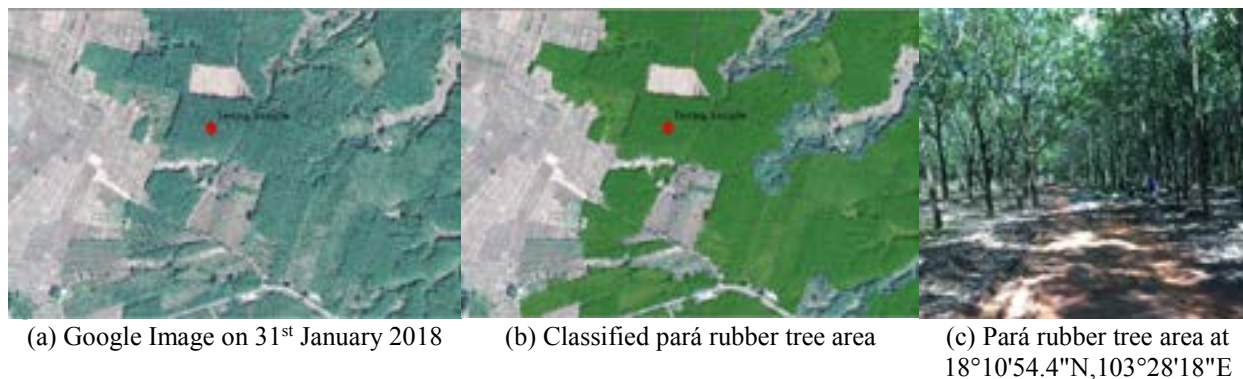

| (a) Google Image on 31st January 2018 | (b) Classified pará rubber tree area | (c) Pará rubber tree area at 18°10'54.4"N,103°28'18"E |

Figure 4. An example of pará rubber tree classification result.

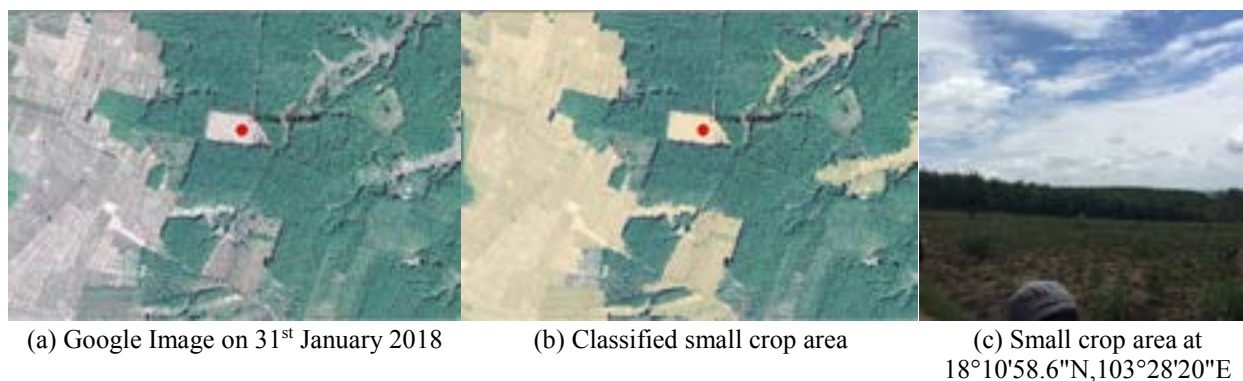| (a) Google Image on 31st January 2018 | (b) Classified small crop area | (c) Small crop area at 18°10'58.6"N,103°28'20"E |

Figure 5. An example of small crop area classification result.

Table 2 also presents the accuracy of classification's results in error matrix based on samples which compares ground truth data with results of classification. It was found that the overall accuracy is 86.36% and 0.8403 Kappa Index Agreement (KIA). The overall accuracy means the proportion of the total correctly classified image objects on the total number of testing samples. The KIA is a parameter which determine the quality of observed classification accuracy. In addition, the producer's accuracy and user's accuracy are taken into account. The producer's accuracy informs the quality of classified data, while user's accuracy informs the reliability or the probability which an image object represents the class on the ground.

As shown in the Table 2, the top row of the table shows the classes of samples randomly collecting from ground surveying and the left column shows the classes from classification procedure. In this experiment, 198 testing samples were collected and compared to the classified data. The outstanding classification's results were pará rubber tree, build-up area and water body area with 100% producer's accuracy because all the testing samples matched the truth data. Next, 96.67% producer's accuracy was found in small crops classification, which demonstrated high accuracy as well. While pará rubber tree showed the highest accuracy, the producer's accuracies for three sub-classes of perennial plant i.e., oil palm tree, eucalyptus tree, mixed forest gave lower accuracies with 75.86%, 63.16%, and 61.29%, respectively. Due to the similarity of characteristics for three sub-classes, it tough to explore customized features for discriminating among them. Furthermore, the advantages of pará rubber tree classification are seasonally shed leaves obtaining easily analysis and data availability. Consequently, classified pará rubber tree result is better than the rest of perennial plants.

Table 2. The renewable energy crop classification accuracy computed by error matrix.

User Class / Sample	Pará Rubber Tree	Oil Palm Tree	Eucalyptus Tree	Mixed Forest	Small Crops	Build-up Area	Water Body Area	Sum
Confusion Matrix								
Para Rubber Tree	31	0	1	0	0	0	0	32
Oil Palm Tree	0	22	1	6	0	0	0	29
Eucalyptus	0	0	12	5	0	0	0	17
Mixed Forest	0	7	4	19	0	0	0	30
Small Crops	0	0	0	0	29	0	0	29
Build-up Area	0	0	0	0	1	29	0	30
Water Body Area	0	0	1	1	0	0	29	31
Unclassified	0	0	0	0	0	0	0	0
Sum	31	29	19	31	30	29	29	198
Accuracy								
Producer	1.000	0.7586	0.6316	0.6129	0.9667	1.000	1.000	
User	0.9688	0.7586	0.7059	0.6333	1.000	0.9667	0.9355	
Totals								
Overall Accuracy	0.8636							
KIA	0.8403							

To summarize, these failures of classification were probably caused by segmentation step i.e., an object is heterogeneous segmentation and the variation resolution between Landsat-8 and Google images. Let us discuss about heterogeneous segmentation in accordance with three concepts of color, smoothness, and compactness. In particular color-image layer weight, the inappropriate weights were derived due to numerous image layers i.e., seven bands of Landsat-8 (End of the year phase), seven bands of Landsat-8 (Early year phase), and three bands of Google images. Consequently, the variation resolution is discussed, the extremely different resolutions affected discrepancy of image interpretation in segmentation step, in example, a tiny object in Google image is not able to be seen in Landsat-8 image.

In addition, the essential technique is the investigation all features of each perennial plant classes for obtaining the optimal membership function. Membership function is an alternative tool to analyze and identify the individual of class from uncertainty classification. Eventually, let us compare the difference of optimization dimension results in feature considering step. It reveals that the 13th and 14th are the best optimization dimension of main-class classification and perennial plant classification procedures, respectively. The amount of features in each procedure are not identical. Due to the physical variations of objects, it influences features to classification.

5. CONCLUSION

This research proposes the objected-based classification of renewable energy crops into seven classes namely, pará rubber trees, oil palm trees, eucalyptus trees, mixed forests, small crops, build-up area, and water body area by using combination of membership function and nearest neighbor in Tham Charoen subdistrict, So Phisai district, Bueng Kan province in northeastern Thailand. Membership function is used to enhance the nearest neighbor to be able to discriminate the renewable energy crops. However, the fine segmentation is also essential to derive the higher quality of classification results. To proceed the good segmentation, it is necessary to define the numerous suitable parameters, especially image layer weight, which is difficult to assign and would rather study further. The outstanding result of this classification among renewable energy crops was pará rubber tree due to the advantage of its seasonally shed leaves which brought to the usage both duration of images to clearly identify its characteristics.

REFERENCES

[1] Robert C., Weih., and Norman D., Riggan., 2010. Object-based classification vs. pixel-based classification: comparative importance of multi-resolution imagery. The International Archives of the Photogrammetry, Remote Sensing and Spatial Information Sciences., XXXVIII-4/C7

[2] Charles, Elkan., 2011. Nearest neighbor classification. University of California San Diego.

[3] Nozer D., Singpurwalla., and Jane M. Booker., 2012. Membership functions and probability measures of fuzzy sets. Journal of the American Statistical Association., 99(467), pp. 867-877.

[4] Frosti P., Johannes R. Sveinsson., and Magnus O. Ulfarsson., 2014. A New Pansharpening Algorithm Based on Total Variation. IEEE Geoscience and Remote Sensing Letters Vol.11, Issue 1, pp. 318 – 322.

[5] A.P. Carleer., O. Debeir., and E. Wolff., 2005. Assessment of Very High Spatial Resolution Satellite Image Segmentations. Photogrammetric Engineering & Remote Sensing Vol. 71, No. 11, pp. 1285–1294.

[6] Giles M. Foody., 2008. Sample Size Determination for Image Classification Accuracy Assessment and Comparison. Spatial Accuracy Assessment in Natural Resources and Environmental Sciences Shanghai, P. R. China, pp. 154-162.

Spectral analysis of main mineral pigments in Thangka

Yi Cen[1], Linshan Zhang [1,2], Xuejian Sun[1]*

[1]The State Key Laboratory of Remote Sensing Science, Institute of Remote Sensing and Digital Earth, Chinese

Academy of Sciences, Beijing 100101, China

[2]College of Earth Sciences, Chengdu University of Technology, Chengdu 610059, China

Email: cenyi@radi.ac.cn; zhanglinshan_gis@163.com; sunxj@radi.ac.cn

ABSTRACT: The identification and analysis of the mineral pigments of the Thangka are of great significance to the identification, repair, digital archiving and reproduction of the Thangka. Hyperspectral imaging technology has the characteristics of non-contact, non-destructive, fast and efficient, which can obtain images and spectrum simultaneously and quickly in large scale. In this paper, the spectral features of Thangka's main mineral pigments were analyzed, and SVM method was used to classify the Thangka. The classification accuracy is 92.7%.

KEYWORDS：Thangka, mineral pigment, spectral analysis, hyper-spectrum

1. Introduction

As a work of art, Thangka has both high historical value and artistic value [1]. The identification and analysis of the mineral pigments of the Thangka are of great significance to the identification, repair, digital archiving and reproduction of the Thangka. Traditional identification of mineral pigments is time-consuming and often based on destructive sampling methods, which can cause irreversible damage to cultural relics and works of art. Spectral analysis method has become a research hotspot because of its non-contact and quantifiable characteristics[2]. Hyperspectral imaging technology has the characteristics of non-contact, non-destructive, fast and efficient, which can obtain images and spectrum simultaneously and quickly in large scale. It is one of the most efficient, safe and non-destructive testing technologies for cultural relics detection [3-6]. In this paper, the spectral features of Thangka's main mineral pigments will be analysis, and SVM method is used to classify the Thangka.

2. Experiment

The reflectance spectrum of mineral pigments is obtained by PSR-3500 spectrometer, whose spectrum range is 350-2500 nm, spectral resolution is 2-4 nm, FOV is 25 degree, which can be used to measure the ultraviolet, visible and near infrared spectrum quickly.

When collecting, the ground powder mineral pigment is spread on the black paper, keeping the surface of the powder pigments as smooth as possible. The paper is labeled with the type of pigments as a sample of mineral

pigments powder. The bovine bone glue is blended with mineral pigment on black paper according to the Tangka painting, as a sample of mineral pigment bone glue. The blended mineral pigment bone is drawn on the Tangka canvas as a sample of the Tangka canvas.

To reduce the effect of stray light on spectrum acquisition, the process is carried out in a darkroom, The light source is halogen light source. The angle position of the optical fiber probe and the light source is fixed during the acquisition process (30 degrees). The measurement position of mineral pigment powder, bone colloid and color card sample are changed within the range of the probe. Every sample is collected with 10 spectral average to reduce the random errors in the measurement process.

3.   Results and discussion

By comparing the spectral characteristics of the same mineral pigment powder, blend bone glue and pigment on the pigment, we found that the reflectance of the powder pigment decreases after the blending of bone glue, and there are two strong absorption peaks near 1447nm and 1928nm. When the glue soluble paint on the cloth, with the reduction of water paste in the paint, the two peaks become weaker, and the absorption peak at 1447nm or even disappears. Therefore, the spectra of mineral pigment powder and pigment on the cloth are very close. Mineral pigment powder can be directly used in the analysis of the Thangka pigment spectra match and analyze in the later period.
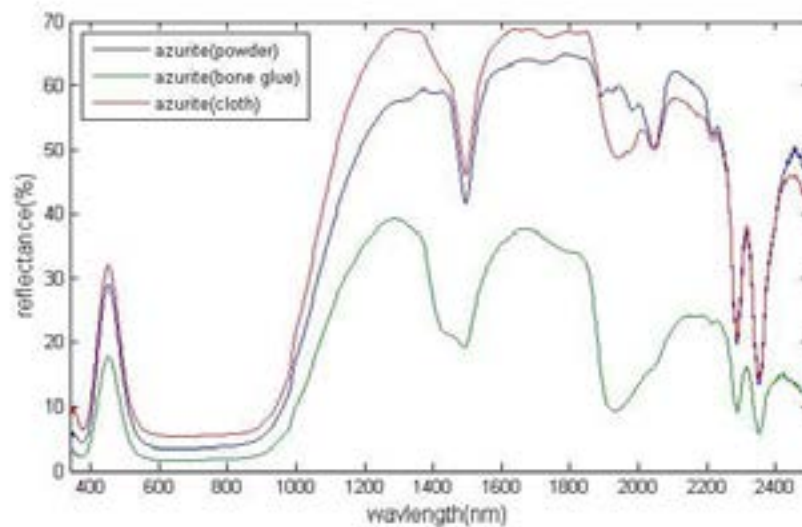

（a）
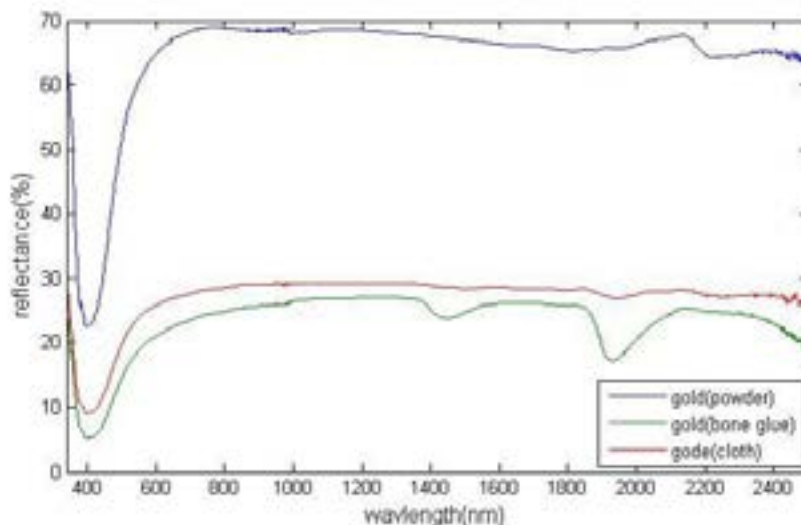
（b）

Fig.1 Azurite (a) and Gold (b) pigment powder, bone glue, cloth color spectrum after the continuum-removal

There are more than 20 kinds of mineral pigments in traditional Tangka. In this paper, we analyze five main colors, including cinnabar (3 kinds), stone green (5 kinds), stone green (5 kinds), realgar, estrogen, Turquoise yellow, ochre, gold powder, clay and inkstone.

Red mineral pigments on Thangka is cinnabar, whose mineral composition is HgS. The reflectance in the visible band rise after the first drop, and there is a deep absorption valley near 500nm (430nm-530nm). After the rapid rise of red, the reflectance curve near infrared changes slowly, and there are weak absorption valleys in the vicinity of 1940nm and 2250nm.
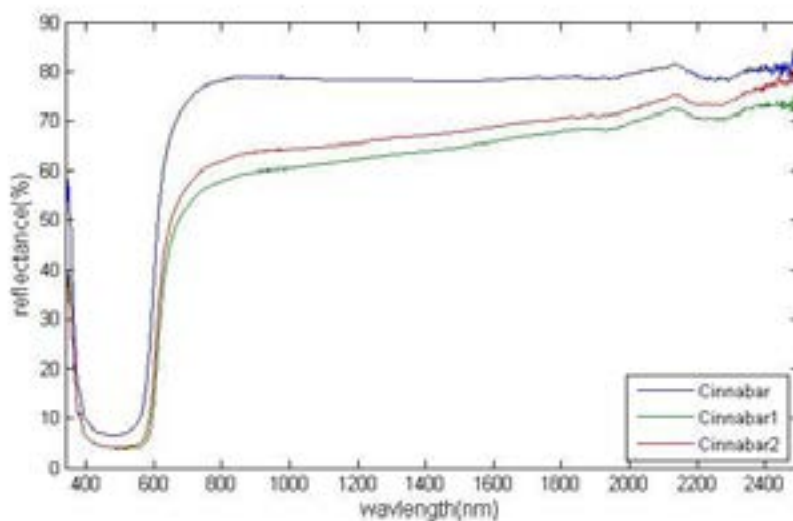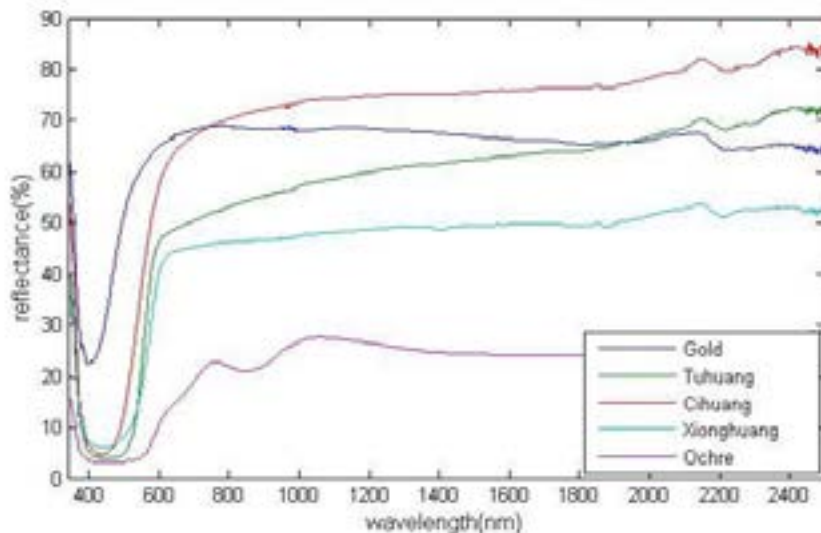

Fig.2 Spectrum of red mineral pigment powder

There are three main types of Thangka yellow mineral pigments: desert tan (realgar, orpiment), ochre, and gold, whose main components are arsenic sulfide, iron oxide and gold. Their spectral characteristics are

concentrated in the visible spectrum between 400-500nm, and the absorption valley position and absorption depth of different pigments are different. Near infrared reflectance Ochre is low, and the 860nm have appeared near the absorption peak; while desert tan, realgar, and orpiment in near infrared and shortwave infrared spectrum show high values and flat curves, with two weak absorptions in the valley near 1890nm and 2230nm. The absorption valley of gold in visible band is narrow and shallow, which can be used as the basis to distinguish it.

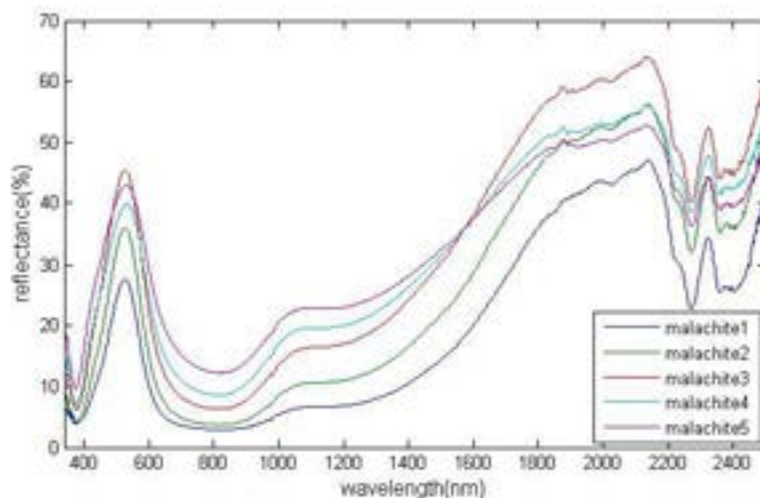**Fig.3 Spectrum of yellow mineral pigment powder**

Thangka's blue mineral pigment is azurite, which has strong absorption characteristics in 500-1000nm, 1500nm, 2040nm, 2285nm and near 2350nm, and weak absorption characteristics in 1885nm and 1980nm.
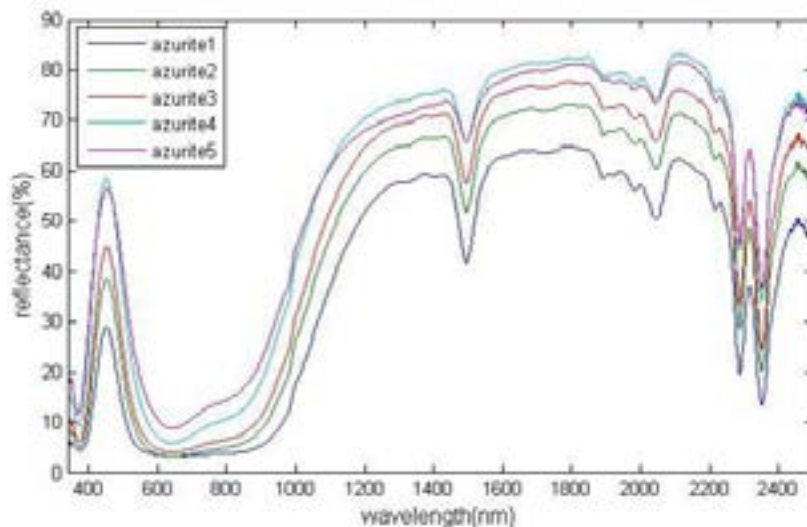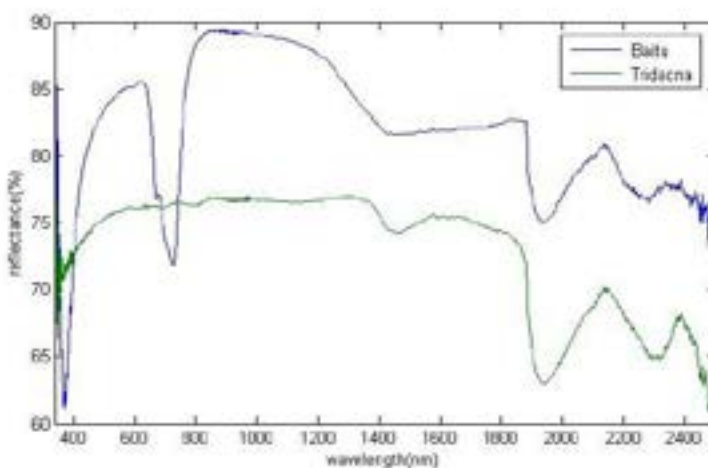

Fig.4 Spectrum of blue mineral pigment powder

Thangka's green mineral pigment is malachite, and the spectrum has a strong broad absorption feature in 550-1000nm, 2270nm and 2350nm. Although the main mineral composition of malachite and azurite are both copper carbonate, but the reflectance value of malachite in 900-1900nm increases slowly, and there is no absorption

characteristic at 1500nm, which can be used to distinguish them.

**Fig.5 Spectrum of green mineral pigment powder**

Thangka's white mineral pigments are mainly clay and clam, respectively, calcium carbonate and kaolin-clay. In the visible spectral range, clam has a weak absorption characteristic in 370nm, and the clay has two obvious absorption characteristics in the 370nm and 730nm, which can be used to distinguish them. In the short wave infrared and near-infrared spectrum, clay has obvious absorption characteristics in 1425nm, 1930nm and 2230nm, while clam has obvious absorption characteristics in 1930nm and 2320nm, plus a weak absorption characteristics in 1440nm. As for the same mineral pigment powder, the larger the mineral powder particle is, the darker the color of the pigment is, and the lower the reflectance of the spectral characteristics are.

Fig.6 Spectrum of white mineral pigment powder

Compared with traditional methods, hyperspectral technique can identify cultural relics without damage. In this paper, the Hyperspectral imager is used to obtain the hyperspectral image of Thangka, whose spectral range is 379 to 870nm, spectral resolution is 4~7nm, 344 bands totally. We select a small area of Thangka to study, which contains five main kinds of pigments of Tangka. Train SVM classifier without dimensionality reduction after

removing the noisy bands. The figure7 shows the classification result, the azurite, malachite, cinnabar and tridacna can be classified well, and the classification accuracy is 92.7%. the light-color area above the head is classified into tridacna, which need to introduce spectral information to insure pigment composition, which is also the focus and direction of future research.

(a)   (b)
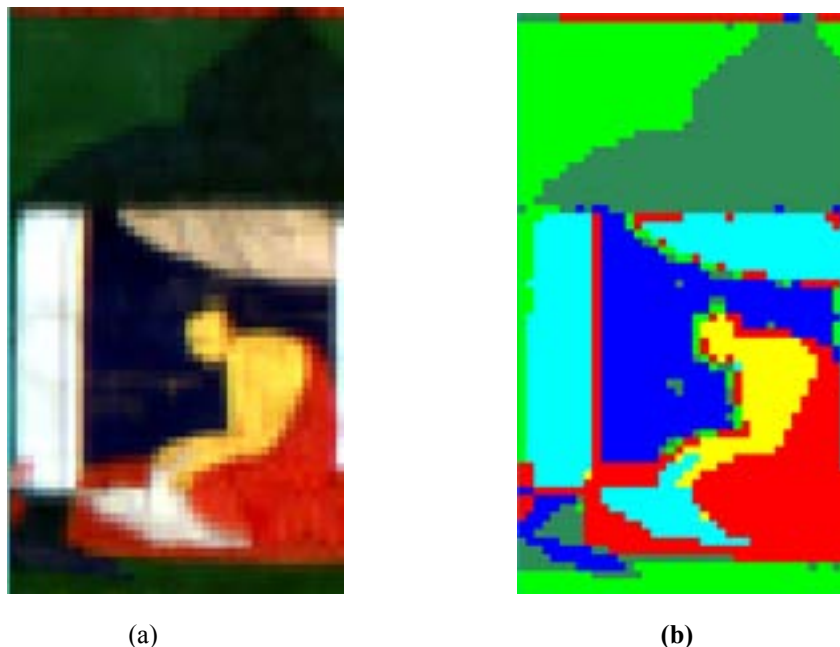
Fig.7 Thangka hyperspectral imaging (a) and SVM class result (b)

4.   Conclusion

In this paper, the spectrum of five main colors of Tangka mineral pigment were analyzed, and the spectral characteristics of visible, near infrared and short-wave infrared spectra of different colors of mineral pigments were summarized. It is shown that the larger the mineral pigment powder particle, the darker the color of the pigment, the lower its characteristic reflectance. And SVM method was also used to classify the Thangka hyperspectral image, the final classification accuracy is 92.7%.

Reference

[1]   WANG Rui.The collection and appreciation of Thangka [B]. The China Books Publishing Company, 2013.

[2]   LIANG Jin-xing, WAN Xiao-xia. Spectroscopy and Spectral Analysis, 2017, 37(8): 2519-2526.

[3]   SHI Ning-chang, LI Guang-hua, LEI Yong, et al. Sciences of Conservation and Archaeology, 2017, 29(3): 23-28.

[4]   ZHONG Yan-fei, MA Ai-long, ONG Yew-soon, et al. Applied Soft Computing, 2018, 64(3): 75-93.

[5]   WU Feng-qiang, YANG Wu-nian, LI Dan. Acta Mineralogica Sinica, 2014, 34(2): 166-170.

[6]   GONG Meng-ting, FENG Ping-li. Sciences of Conservation and Archaeology, 2014, 26(4): 76-83.

ASSESSMENT OF DROUGHT IMPACTS IN DIFFERENT LAND COVERS USING A REMOTE SENSING INDEX: A CASE STUDY IN ANDONG, S. KOREA

Yun-Jae Choung (1), Seung-Hyeon Lee (1), Hyun-Ji Cho (1), Hyeon-Cheol Park(1)

[1] Institute of Spatial Information Technology Research, GEO C&I Co., Ltd., 435 Hwarang-ro, donggu, Daegu, Republic of Korea
Email: chyj@geocni.com, shlee@geocni.com, hjcho@geocni.com, hcpark@geocni.com

KEY WORDS: Drought, NDMI, Landsat images

ABSTRACT: Drought monitoring using the remote sensing instruments is efficient for assessing the drought impact in the different land covers. This research employed the normalized different moisture index (NDMI) generated using the Landsat image acquired in Andong, South Korea in the drought period for assessing the drought impact in the different land covers. The statistical results show that, in the Landsat image acquired in the drought period, the NDMI value measured in the vegetation area is higher than the NDMI values measured in the other land covers.

1. INTRODUCTION

Drought monitoring is necessary for evaluating the drought impacts on human societies (Su et al., 2016). The satellite images acquired by the earth observation satellite sensors are useful for assessing the drought impacts in the huge areas because they can provide the drought information in huge areas without human access (Senay et al., 2015). This research employed the normalized difference moisture index (NDMI) generated using the Landsat image acquired in Andong, South Korea in the drought period for assessing the drought impacts in the different land covers.

2. METHODOLOGY

In the first step of the proposed methodology, the ndmi image is generated using the near infrared band and the middle infrared band of the given Landsat image that was acquired in Andong, South Korea during the drought period (February 12, 2015). The below equation shows the formula for generating the ndmi image (Rokni et al., 2014).

$$\text{NDMI} = \frac{NIR - MIR}{NIR + MIR} \qquad (1)$$

In the above equation, the NIR represents the near infrared band, while the MIR represents the middle infrared band of the given Landsat image. In the NDMI image, the pixels representing the features with the huge moistures have the values close to 1, while the pixels representing the features with few moistures have the values close to -1.

The next step in the proposed methodology is to measure the ndmi values in the different land covers (vegetation, water, urban and soil). Figure 1 shows the comparison of the NDMI image (see the Figure 1(a)) measured in the different land covers (see the right image of Figure 1(b)).
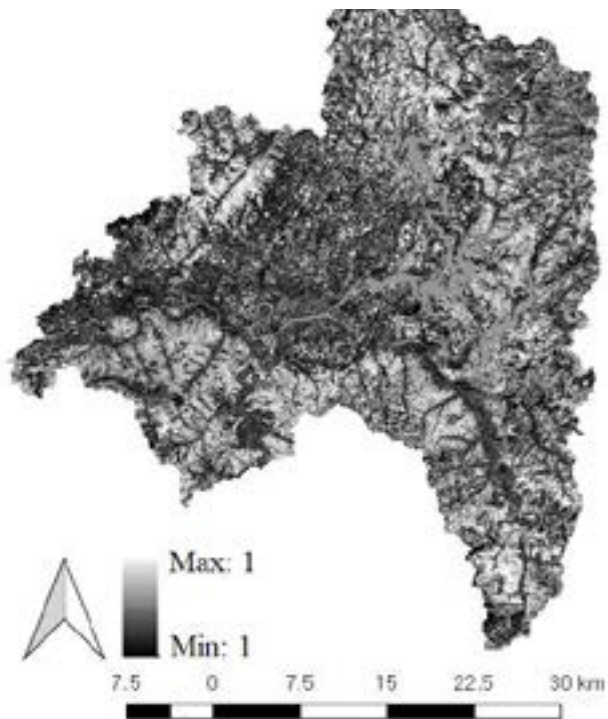
(a)

(b)

Figure 1. Comparison of the NDMI image measured in the different land covers: (a) NDMI image, (b) Different land covers in the Landsat image

3. RESULTS

water and soil). Table 1 show the results of the measured NDMI values in the different land covers.

Table 1. Example of the measured NDMI values in the different land covers

Land cover	NDMI value
Vegetation	0.086
Urban	-0.031
Water	0.037
Soil	-0.12

4. CONCLUSIONS

As seen in Figure 1 and Table 1, in the Landsat image acquired in the drought period, the NDMI value is measured in the vegetation area is higher than the NDMI values measured in the other land covers. This research contributes to assess the drought impact in the different land covers by measuring the NDMI values in the different land covers. In future research, the changes of the NDMI values in the different seasons would be tested in each land cover.

References

Rokni, K., Ahmad, A., Selamat, A., Hazini, S. 2014. Water Feature Extraction and Changing Detection Using Multitemporal Landsat Imagery. Remote Sensing, vol. 6, pp. 4173-4189.

Su, Z., He, Y., Dong, Z., Wang, L. 2016. Drought Monitoring and Assessment Using Remote Sensing. In: Remote Sensing of Hydrological Extremes, edited by Lakshmi V., Springer Remote Sensing/Photogrammetry. Springer, Cham, pp. 151-172.

Senay, G.B., Velpuri, N.M., Bohms, S., Budde, M., Young, C., Rowland, J., Verdin, J.P. 2015. Drought Monitoring and Assessment: Remote Sensing and Modeling Approaches for the Famine Early Warning Systems Network. USGS Staff - - Published Research, Elsevier, 30 p.

Application of Geo-Informatics for Environmental Health Assessment (EHA) on Iron-Ore Mines area, Noamundi Block, Jharkhand, India

Kunal Kanti Maiti (1), Jatisankar Bandyopadhyay (1), Debashish Chakravarty (2), Sonjay Mondal (1)

[1]Department of Remote Sensing and GIS, Vidyasagar University, Midnapore-721102, West Bengal, India
[2] Department of Mining Engineering, Indian Institute of Technology Kharagpur, 721302, West Bengal, India

Email: kunal.rs.gis@gmail.com ; jatib@mail.vidyasagar.ac.in ; dc@mining.iitkgp.ernet.in ; sonjaymondal@gmail.com

Abstract:

The impact of mining and mineral extraction activities have very significant role for land, air and water bodies in any operational mines and its surrounding areas. Multispectral satellite data have demonstrated its ability to detect, monitoring of geo-environmental change based on remote sensing applications. The Noamundi iron-mine in the Paschim Singhbhum district of Jharkhand is one of the important mining areas since the eighteenth century. The main iron-ore in this area is hematite. The use of normalized difference vegetation index (NDVI), measures the amount of greenery/ vegetation in the area. At the present time, it has become obligatory to study and analyze the impacts of mining on its surrounding area with the use of remote sensing (RS) and geo-spatial information system (GIS) to generate thematic maps for environmental impact assessment (EIA) over the mining affected area. Therefore, it can be concluded that increase in mining activities is damaging the vegetation, land, and environment. The present study can be useful to identify the degraded area due to mining activity and necessary environmental management plan (EMP) with their societal aspects can be taken up to mitigate the problem.

Keywords: Iron-Ore, NDVI, GIS, EIA, EMP.

Introduction

Environmental health represents the aspects of human health (as well as quality of life) that are determined by bio physicochemical, social and psychosocial factors in the environment. Mining refers to the process of extracting metals and minerals. It plays a major role in improving the economy of the country in the world, but it has a lot of harmful effects on the Geo-environment. It is necessary for us to know first what the problem is, so that we can take necessary step to find the solution. Mining requires large forest areas to be clear, this leads to deforestation and disturbing the balance of nature. Chemicals from the mines and poisonous gases get deposited on land, making the soil unfit for plant's growth. The forest that is cleared for mining purposes are home to a large number of organisms in the land and its indiscriminate clearing puts the survival of a large number of animal species at stake. The cutting down of and release of the harmful substance is the threat to a number of plants, trees, birds and animals that dwells in the forests. The Environmental vulnerability assessment was carried out by using analytical hierarchy process (AHP) and GIS for solving spatial planning problems (Anh et al. 2014).

The Jharkhand state is a full of mining prosperity. The major economic development of this state based on the mining and Noamundi is a major mining area in the state. The area has been site of a good industrial region for its cheap labour and surrounding mining area. Though it effect the environment but trade of between environment and industrial development can be made to minimize the pollution of the surrounding environment.

Materials and methods

Study area

Noamundi block is the southern part of the West Singhbhum district in Jharkhand. It Covers the study boundary from Latitude 22° 01' 30"N to 22° 21' 15" N and Longitude 85° 12' 30" to 85° 39' 30"E. It is surrounded by Tonto block in the north side, Manoharpur block in the west side, Jagannathpur and Hatgamhariya block in the east side and south side has Odisha. The total area of Noamundi block is 625.25 sq. km.

Figure 1: Location map - a) India ; b) Jharkhand; c) West Singhbhum district highlight in Noamundi block ; d) Google imagery in Noamundy block.

Data used

Table 1 shows the data used for study of environmental health.

Table 1: Data used

Sl No	Data	Source
1	Landsat 8 OLI	USGS
2	Topographical map	Survey of India
3	MODIS	USGS
4	Geomorphology	GSI
5	Water Quality	Sample collected from field and tested in laboratory

Methodology

Analytical Hierarchy Process (AHP) based GIS has been used to solve spatial planning problems for environmental health assessment. The ranking and assessment of the environmental health is possible by analyzing the variety of GIS thematic layers i.e. LU/LC, AOD, geomorphology, water quality, NDVI, LST, transport density, which are much suitable for GIS analysis. These seven factors are used to analyze in a GIS environment using the

weighted analytical hierarchical process model. Methodology flow chart of the environmental health assessment is shown in Figure 2.
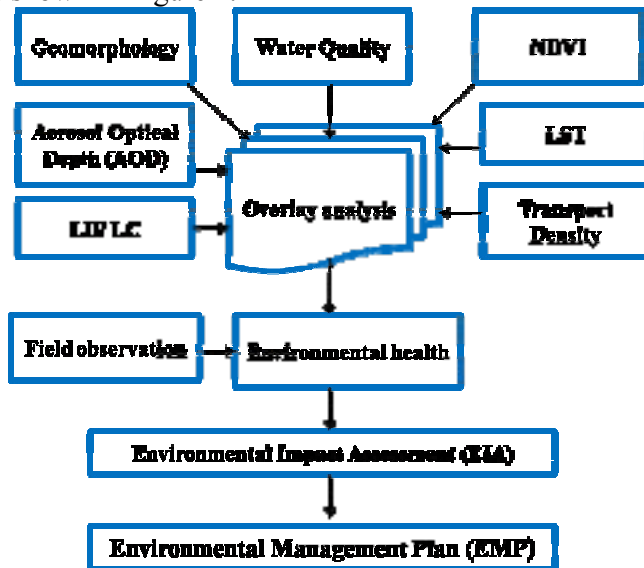

Figure 2: Methodology flow chart shows the variety of GIS parameter to analyze the environmental health and impact of environment for management of environment.

Results and discussion

Land use/ Land cover (LU/ LC)

The Land use/ Land cover (LU/ LC) is one of the important thematic factor of environmental health assessment. The LU/ LC map is prepared from Landsat 8 (2017) satellite imagery by using spectral signature based supervised classification techniques. There are eight classes in the figure 3, namely dense forest, agricultural land, agriculture fallow, open forest, built-up land, mining area, water bodies and river/stream. It shows that the region contains dense forest area 40%, agricultural land area 25%, agriculture fallow area 12%, open forest area 9%, built-up land area 8%, mining area 3%, water bodies 1% and river/stream 1%.
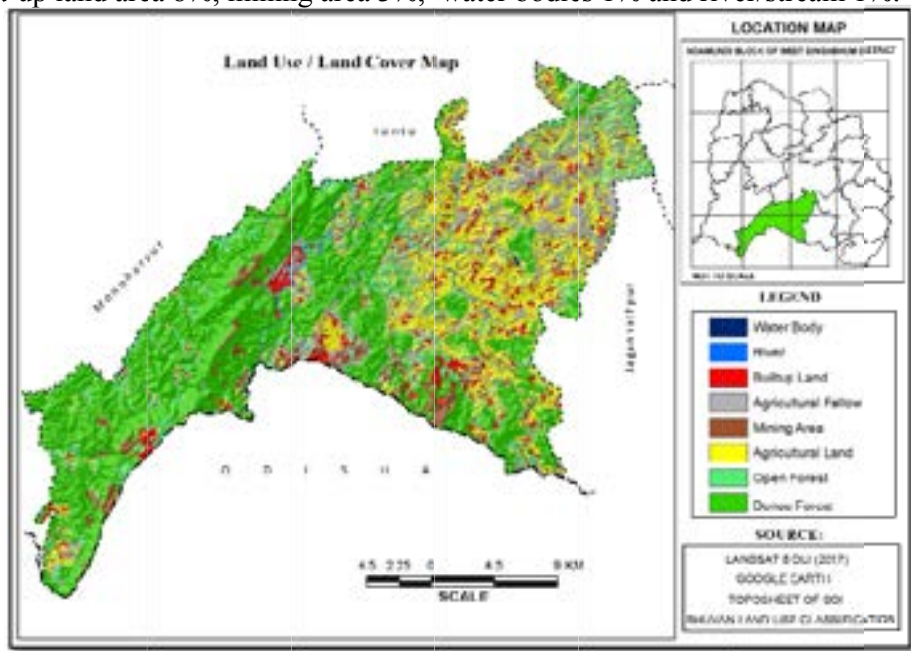

Figure 3: Land use/ Land cover map of the present study area.

2773

Aerosol Optical Depth (AOD)

Microscopic organic and inorganic suspended particles present in the atmosphere are called Aerosol. Aerosol Optical Depth (AOD) is the measure of aerosol concentration with a Column of air from earth's surface to the top of atmosphere (Al-Timimi et al. 2017). Generally, AOD represents the ambient air quality. The environmental health condition is defined by aerosol concentration. Higher the AOD value means the air quality is poor. The average AOD (figure 4) over the Noamundi block varies from 0.32 to 0.41. In the eastern part of the block is covered by relatively low AOD, and from the eastern part the AOD increases gradually towards western part of the block. The western part of this block is covered by mining areas, built-up land and high road density. Though in the western part is covered by dense forest, due to the mining activities, the aerosol expand to the entire region with wind blow. In the middle part of this block convey medium AOD (about 0.35 to 0.38). This area is covered by mining and different industries. And in the Eastern part, the AOD is less (0.32) than the others parts of the block.
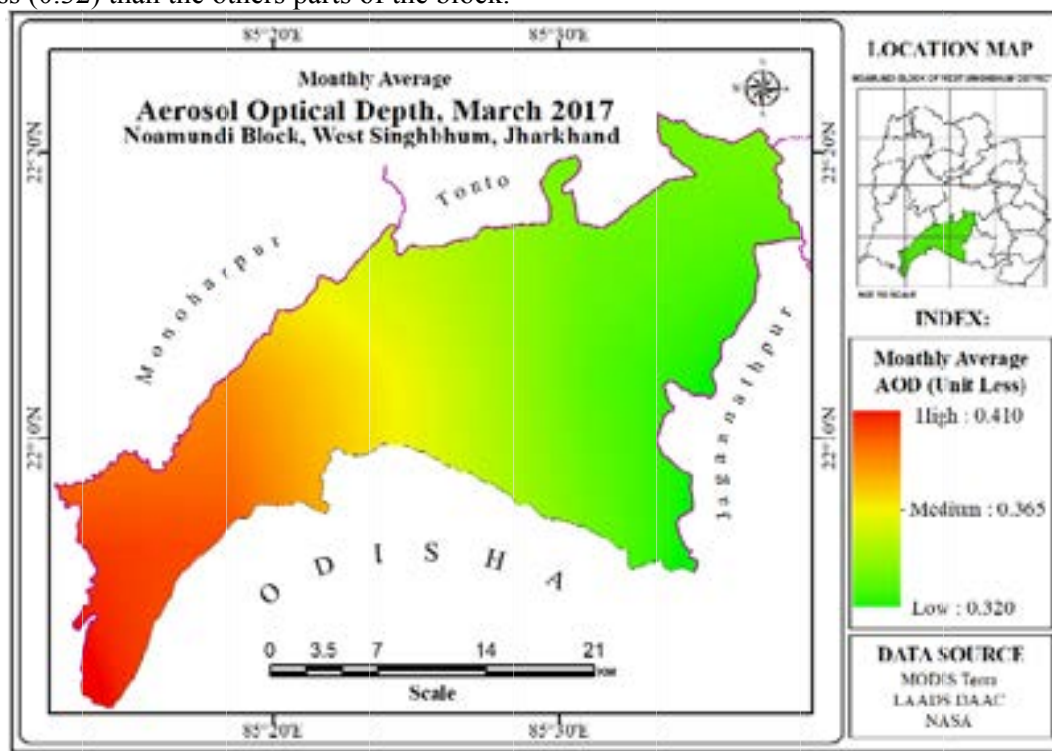

Figure 4: AOD map

Geomorphology

Geomorphological study, the evolution and changes of earth surface features, is a process which contains the progressive steps of biophysicochemical changes over and near the earth surface. Due to urbanization and heavy iron ore mining activity the morphological features of Noamundi area was destroyed day by day. There are eight geomorphological unit in the figure 5. Structural hills and valleys features are occupied most of the area about 48.69% of area. Pediment and Pediplain are the 2nd largest geomorphic unit of this area. The River Karo was found in the middle portion of this block. This river flow from the south to north direction in this block and after few kilometers later it falls in North Koel River. Mostly the water bodies are found in the pediment and pediplain complex. Geographically this region contains about 0.54% and they are very much important for irrigational purpose.
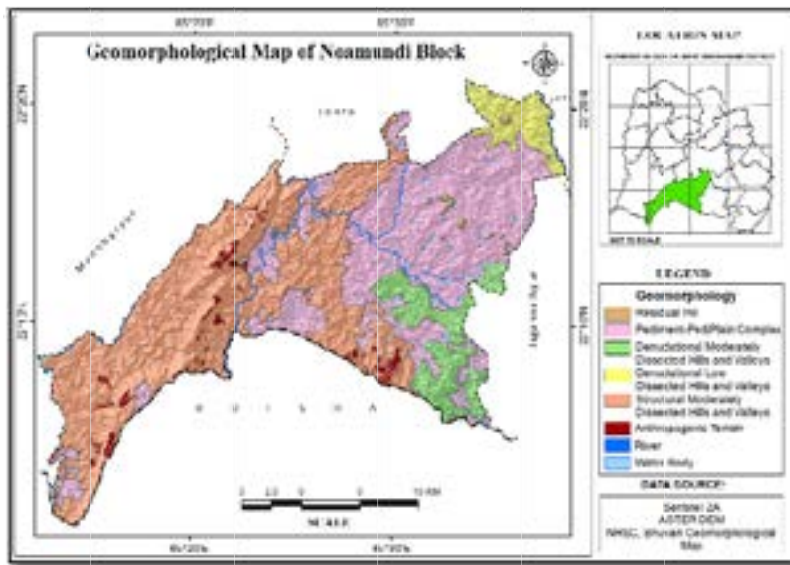
Figure 5: Geo-morphological map

Water Quality

Water quality is also a prime natural measure of environmental health. The availability and quality of surface or ground water have been deteriorated due to some important factors like increasing population, industrialization, urbanization etc. (Tyagi et al., 2013). The amount of water needed varies depending on mine size, mineral being extracted and the process used for extraction. (Naik and Sahu, 2015) Water Quality Index is a criterion to determine the quality of water and check the usability of water for various purposes. Total 18 samples was collected from different parts of this block and tested different parameter to measure water quality index (WQI) according to Brown et al (1972). For showing the spatial variation of Water Quality Index in Noamundi block and surrounding area Kriging Interpolation method was applied. In the figure 6, it would be seen that most of the area has poor to very poor water quality except like Dumarjoa, Bambaisai, karampada, Bhangaon village areas. It also seen that near Gua areas has very bad water quality.
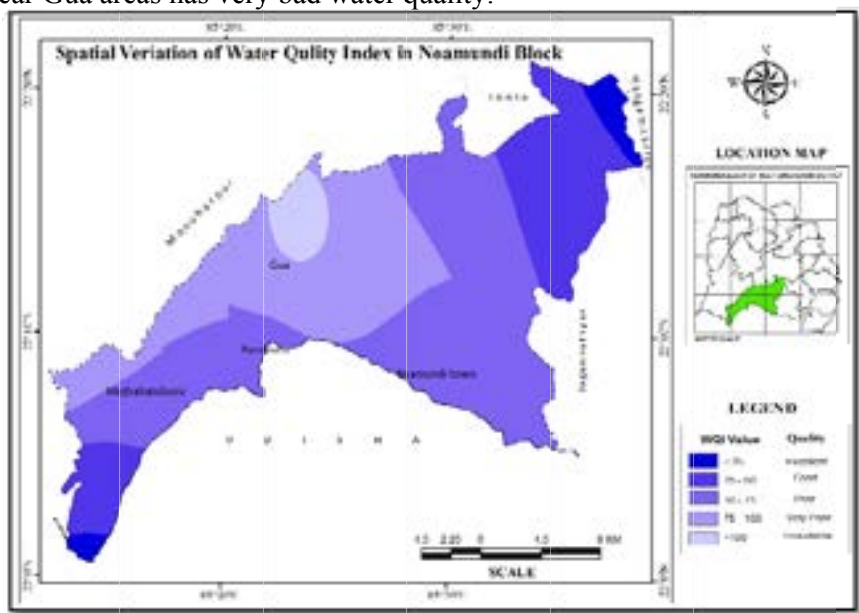

Figure 6: Spatial variation of WQI in Noamundi

NDVI

The NDVI maps for the year 2017 were generated for assessing the vegetation condition (figure 7). The block Noamundi was also forest prone area. About 50% area of Noamundi has under reserve or protected forest. The forests are located at West, South-West, South, North-East and Mid-Western part of Noamundi. The whole forested area falls under two division Saranda division and Chaibasa division. The western parts fall under Saranda division and the eastern parts fall under Chaibasa division. The natural vegetation of Noamundi block is corrected and as follows: Sal, Neem, Mahua, Gamhar Bamboo Sissoo, Simul Mango etc (Sahoo et al., 2014).
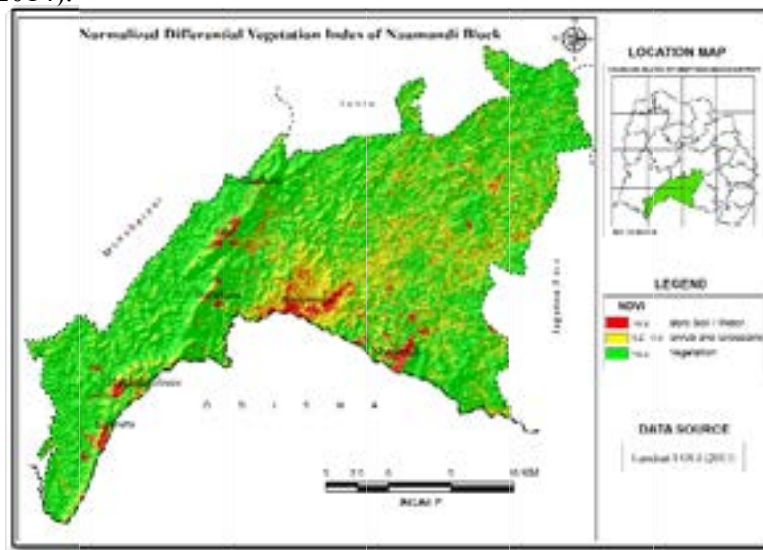
Figure 7: NDVI map

Land surface temperature (LST)

The Land surface temperature (LST) is an important parameter in expressing surface-atmospheric relations (Liu, et al. 2010). Surface temperature is one of the major factors constraining vegetation productivity, therefore the considering the influence of surface temperature. LST of earth surface depends upon exposed rock types, soil texture, soil moisture, vegetation cover, surface water bodies and land use pattern. The LST map (figure 8) generated from Landsat 8 of 2017 reveals that the maximum temperature are 32^0C, mean temperatures are 26^0C and minimum temperature are 20^0C.

Figure 8: LST map

Transportation density

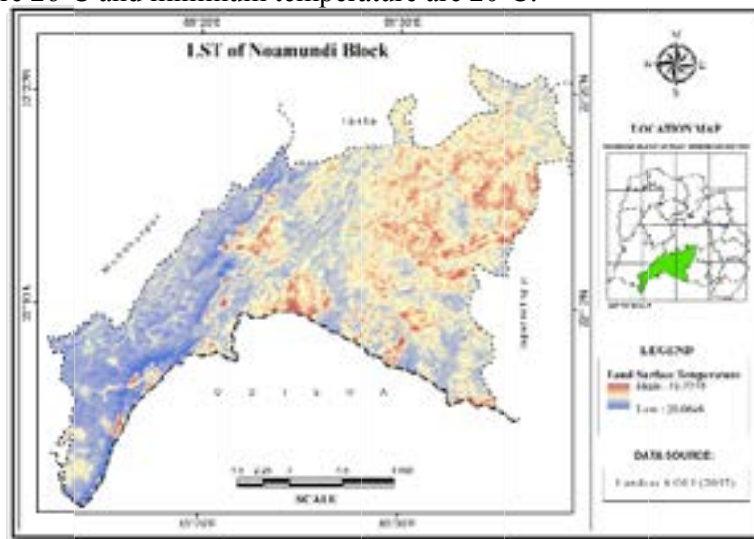In the mining, area transportation is very effective on the environment. In this study area mines, dust abolishes the vegetation and make degradation. Most of the conditions of the roads are very bad. But where the condition of the road is bad and density of transportation is very high there degradation of forest is very sensitive. In this block highest transportation density (figure 9) in Noamundi town area.
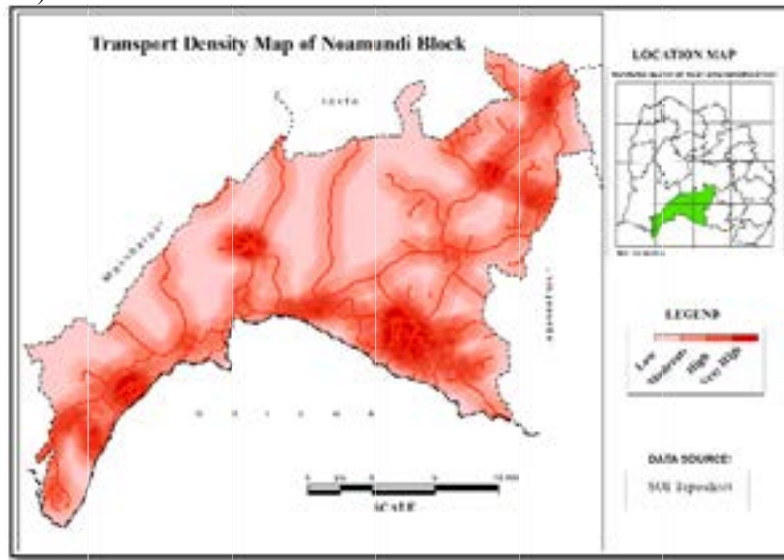
Figure 9: Transport density map

Environmental Health Assessment (EHA)

Spatial data of the seven criterions (Land use/ land cover, air quality, transport density, water quality, NDVI, LST and geomorphology) were prepared as a thematic layer and overlaid together for environmental health assessment. The each condition and parameter with weighted overlay is used for analysis to derive associative and sensitivity with the environmental health. In this area environmental health condition are showing figure 10. this analysis, the impact of environmental health badly effects i.e. soil erosion, surface and ground water, air pollution, land degradation, flora and fauna, also affect the human beings.

Figure 10: EHA map of Noamundi block

Environmental Impact Assessment (EIA)

It is noted that mining associated areas are affected on geo-environment by mining activity. It mainly contains atmospheric pollution, deforestation, land degradation, surface and ground water. The environmental Impact as follows:

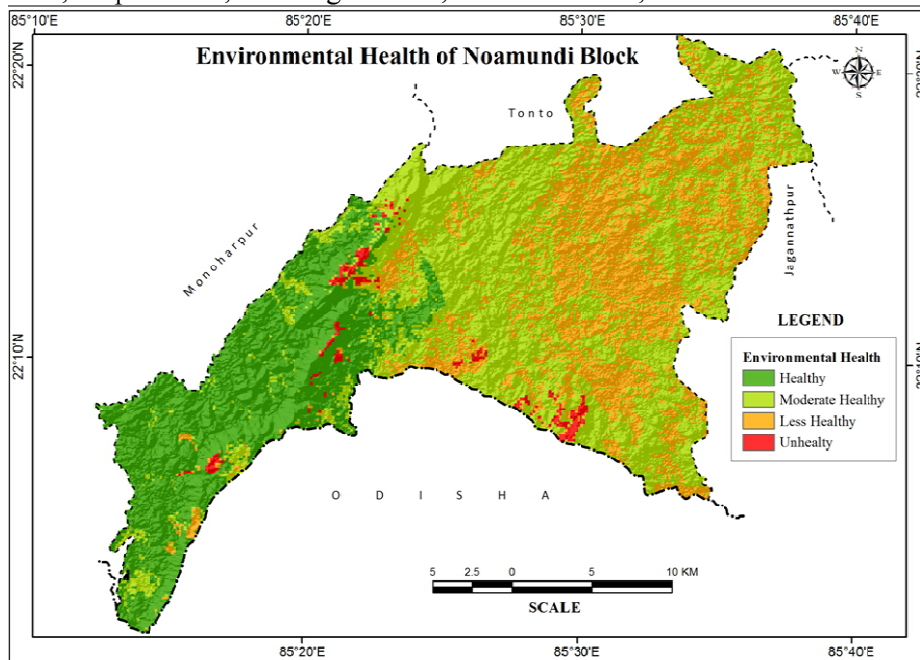**Effect of Water:** Due to low underground water column and improper drainage system associated with mining area, local people belongs to mining area are dependent on the water supply of the government bodies. The accumulated rain water and sometimes pond related water fulfill the more requirement of those peoples. This kind of leached water is not good to maintain the drinking water quality. The pH content of the drinking water is disturbed due to leaching process specially in the metal mining areas. The usability of such water sulfide contaminated water gives the direct impact on health and oxidation of the equipments (Mondal et al. 2016).

Impact on Air Quality: The whole process of vegetation clearing, road construction, machines working, drilling, blasting, crushers and transportation result in poor air quality in the surrounding area and may deteriorate due to particulate emissions. The impact zone could include even villages in the surroundings depending on the wind speed and direction. So, it is the major causes of health disease of workers. Mask should be made mandatory to all the workers including the supervisors and visitors while in mining areas.

Impact of mines on vegetation and temperature: In the above mentioned analysis, it's clear that if vegetation gets destroyed due to industrial and developmental purposes, pollution will be spreading in surrounding areas also, if it is going to continue, ultimately the land conditions will be polluted and temperature rise will be high. So lots of vegetated areas were deforested for open cast mining and lot of dust particles upraised due to mining activity get suspended in the air and potentially effects on the surrounding vegetation.

Effects on Biodiversity: The mining was impact on habitat due to deforestation, transport infrastructure, mine infrastructure, drilling, blasting in mines, etc. Most of the tracks carried ores passing in these roads were not covered and the roads not made wet through sprinkling, that's generate dust. Thus, the vegetation along the entire length of the road is covered with dust thereby affecting the growth and reducing palatability to whatever wildlife using the area. This could be the case of elephants in West Singhbhum areas, where elephants are often confined to several fragments of natural areas and finding difficulties to roam freely in the range. It can also see that the blasting and vibration can also effects on animals especially elephants in the surroundings.

Figure 11: Environmental impact: a) Land degradation; b) water pollution; c) air pollution.

Environmental Management Plan (EMP)

The iron ores are carried by trucks to take the dumping places/trade and transporting, then in this areas are air, land, and water are polluted. The environmental management plan as follows:

- Water sprinkling system to be carried out in dusty areas, roads /transportation, for controlling the air pollution.

- Encasement of noise generating equipment maintenance and vibration measurement of all rotating equipment and transport system will help in the improvement of noise reduction.
- A good environment management policy to takes its commitment to quality of health, safety for environmental sustainability save our future.
- To ensure systemic and sustainable mining, all the leaseholders shall implement the progressive mine closure plan and reclaimed or rehabilitate the mined out areas in the systematic manner before opening new mining start
- The top soil contains decomposed organic materials (humus) and maximum biological activity. So the top soil management is the important in mining areas.
- The mined out areas will be backfilled and planted with native plant species, preferably those recorded in the surrounding natural habitats.
- The erosion prone areas will be treated appropriately through geo-textile/ planting/check dams for controlling erosion.
- For conservation of the water sources, it is recommended to promote rain water harvesting mechanisms in mining sites to reduce dependence on water from the rivers for use in mines.
- Re-vegetation in reclaimed area (Planting grasses and broad leaf tree) controlling Soil/ sediment erosion.
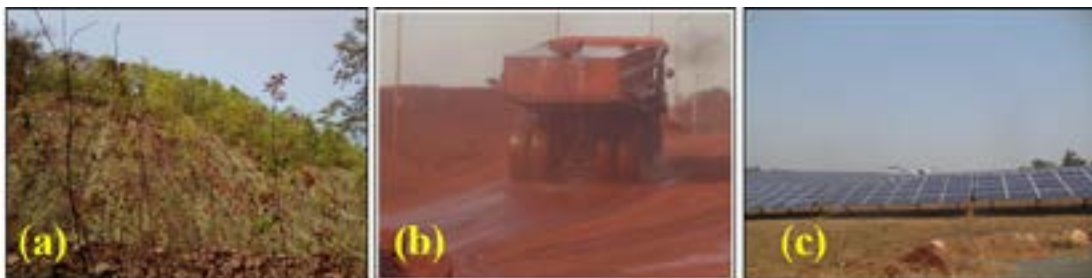

Figure 12: Some environmental management plan: a) Geo-textile for slope stability management; b) Water sprinkling for controlling the air pollution; c) Solar power plant in Noamundi mines area.

Conclusion

This study indicates that Land use/ Land cover, Air Quality, geomorphology, Water quality, Vegetation cover, land surface temperature, and transport density influence the effect on environmental health quality and life cycle of organism. The environmental health assessment mapping using weighted based geospatial analysis defines that mitigation of vegetation due to industrial developmental purpose and increasing of mining area spread the pollution effect in the area. This also affect the rise of atmospheric temperature and thereby hamper the ecosystem. Similarly, the small mining companies do not have proper railway yards; it uses road for transportation. As a result, the overburden particle and dust particles are mixed with air and reduces good ambient air quality. The assessment of the layer parameters, applicability with real world and different mitigation method will improve and maintain the required environmental health of the area.

References

Anh, N. K., Phonekeo, V., My, V. C., Duong, N. D., & Dat, P. T. (2014). Environmental hazard mapping using GIS and AHP–A case study of Dong Trieu District in Quang

Ninh Province, Vietnam. In IOP Conference Series: Earth and Environmental Science (Vol. 18, No. 1, p. 012045). IOP Publishing.

Al-Timimi, Y. K. A., & Khraibet, A. C. (2017). Impact of aerosol on air temperature in Baghdad. Journal of Applied and Advanced Research, 2(6), 317-323.

Brown, R. M., McClelland, N. I., Deininger, R. A., and O'Connor, M. F. (1972). A water quality index-crashing the psychological barrier. In Indicators of environmental quality (pp. 173-182). Springer, Boston, MA. http://dx.doi.org/10.1016/b978-0-08-017005-3.50067-0

Liu, W., Wang, S., Zhou, Y., Wang, L., & Zhang, S. (2010, June). Analysis of forest potential fire environment based on GIS and RS. In Geoinformatics, 2010 18th International Conference on (pp. 1-6). Ieee.

Mondal, S., Maiti, K. K., Chakravarty, D., and Bandyopadhyay, J. (2016). Detecting risk buffer zone in open-cast mining areas: a case study of Sonepur–Bajari, West Bengal, India. Spatial Information Research, 24(6), 649-658.

Sahoo, A.K.; Sarkar, D.; Singh, S.K.; Obi Reddy G.P.;Dhyani, B.L.; Mishra, P.K. and Sharda, V.N. (2014), Soil Erosion Jharkhand, NBSS Publ. No. 159, BBSS & LUP (ICAR), Nagpur, 39 p.

Naik, A. and Sahu, H. B.,(2014-2015) Impact of iron ore mining on water quality,Department of Mining Engineering, NIT Rourkela

Tyagi, S., Sharma, B., Singh, P., Dobhal, R., (2013), Water Quality Assessment in Terms of Water Quality Index, American Journal of Water Resources, 2013, Vol. 1, No. 3, 34-3, DOI:10.12691/ajwr-1-3-3

Visualization of Deforestation in the Paraguayan Chaco using Google Earth Engine

Maria Leticia Cardozo (1), Shou-Hao Chiang (2)

[1] International Environmental Sustainable Development Program, National Central University,
No. 300, Zhongda Rd., Zhongli District, Taoyuan City 32001, Taiwan
[2] Center for Space and Remote Sensing Research, National Central University,
No. 300, Zhongda Rd., Zhongli District, Taoyuan City 32001, Taiwan
Email: lesocardozo@gmail.com; gilbert@csrsr.ncu.edu.tw

KEY WORDS: Forest clearance, Landsat, Paraguay.

ABSTRACT: Forests act as a reservoir of biodiversity, shelter to wildlife and carbon sinks, and mitigates climate change. Despite their importance, they have been threatened by human activities such as unsustainable logging, agricultural expansion, cattle ranching, fuel wood collection and others, which are the main drivers of deforestation. The objective of this study is to visualize and describe the deforestation process of the Chaco, in Paraguay, South America, by means of remote sensing analysis through the cloud-based Google Earth Engine (GEE) platform. The study area is part of the second largest forest area in South America, it has a great biodiversity, with two marked Eco-region in it, the Dry Chaco and the Wet Chaco. According to the United States Agency for International Development (USAID) in 2017, the Paraguayan Chaco has experienced a lot of land use changes and deforestation. Landsat images from the whole year of 2013 and 2017 were collected, and since the study area is covered by multiple Landsat's scenes and the process of image collecting and preprocessing would take a lot of time and storage, the usefulness of GEE to reduce the task is remarkable and will be introduced. In GEE, the integrated development environment (IDE) for the rapid creation of prototypes using JavaScript API is able to define the study area, preprocess the images, including the elimination of cloud pixels of the scenes, composite and evaluate the changes of study area. Following the above functionalities embedded in GEE, the visualization and interpretation of the deforestation in the Paraguayan Chaco were performed. The results show that deforestation in the study area increase from the year of 2013 to 2017, and is clearly visualized and interpreted with rectangular geometric features of forest clearance. This study suggests that GEE is an effective tool for rapid image processing and land monitoring.

1. INTRODUCTION

The Paraguayan Chaco is one of the major wooded grassland areas in central South America, is known as the western or occidental region of Paraguay (Caldas et al., 2013). The Great American Chaco is the second largest forest area in South America and 25% of its total area covers the Paraguayan Chaco, is a unique natural area as it contains a huge diversity of environments, such as riparian forests, dry forests, savannahs and pastures and desert scrub (PNUMA, 2013).

The climate of the region is mainly predominant by two seasons: dry from May to October and rainy from November to April. Drought and flooding characterize the climate of the Paraguayan Chaco, the summer is long, hot and wet, while the winters are short, mild and dry (Grassi et al. 2005).

The Chaco has been converted from forest to cattle ranching, pasture and agriculture over long periods, but the rate of land use conversion has accelerated in recent years and this has positioned Paraguay among the countries with the highest rates of deforestation, mainly located in the Chaco (Bauman, et al., 2017).

The expansion of the Chaco is approximately 246,925 km², due to his large area, working with high resolution satellite images is a challenge, this study used GEE to overcome this.

1.1 Google Earth Engine

GEE is a cloud-based platform for planetary-scale geospatial analysis that consists of a multi-petabyte analysis-ready data catalog. It is accessed and controlled through an Internet accessible Application Programming Interface (API) and an associated web-based Interactive Development Environment (IDE) that enables rapid prototyping and visualization of complex spatial analyses using the Javascript API (Gorelick et al., 2017).

The Data Catalog is continuously updated with new satellite images; the interface allows exploring, visualizing and analyzing data. It includes a code editor, where users can perform analysis with already integrated algorithms or can create its own algorithm. The Earth Engine code editor (Fig. 1) is a web-based IDE for the Earth Engine JavaScript API. Code Editor features are designed to make developing complex geospatial workflows fast and easy (Kalogirou et al., 2013).
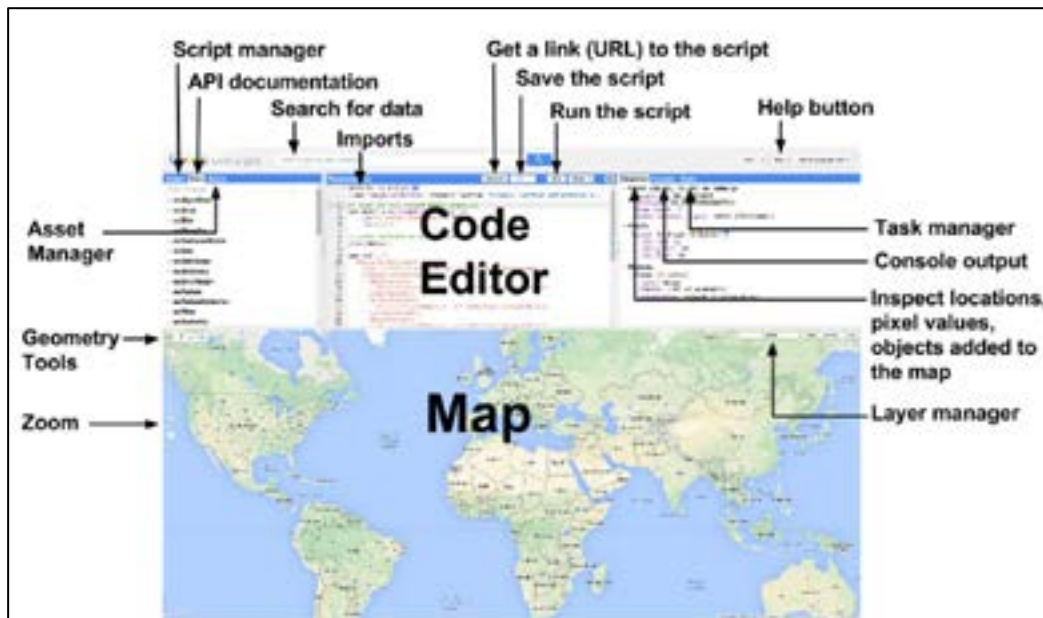
Figure 1. Elements of Earth Engine Code editor (Google Earth Engine, 2018).

Besides from visualizing and performing analysis, the results can be download or keep them saved in the personal account of GEE, furthermore, these can be shared with the creation of a simple link of the work done. Shape files, feature and charts can be import in the interface as well, to work with them in the interface.

2. STUDY AREA

The study area is the Paraguayan Chaco, located in the Western or Occidental Region of Paraguay, South America; with an extension of 246,925 km² which includes the departments of Boquerón, Alto Paraguay, and Presidente Hayes.

Figure 2. Location of the Paraguayan Chaco.

3. METHODS

This study uses images from Landsat 8 OLI TIRS, having 30m resolution, and covering the Paraguayan Chaco area with 16 scenes (paths and rows) in total.

The collection criteria of images were no data missing, cloud score less than 10% and corresponded to the study area, over the whole year of 2013 and 2017.

The collection and processing of images including the elimination of cloud pixels of the scenes, composite and visualization of the study area were performed in GEE, using JavaScript API, that includes specific algorithm to work with Landsat images.

The Landsat algorithm applies standard Top Of Atmosphere (TOA) reflectance calibration for the conversion of row data (digital number, DN) to TOA reflectance. It includes the ee.Algorithms.Landsat.simpleComposite to perform the image composite, with this algorithm were possible to filter the images cloudiness and the conversion from DN to TOA. The detailed procedure performed was as follows:
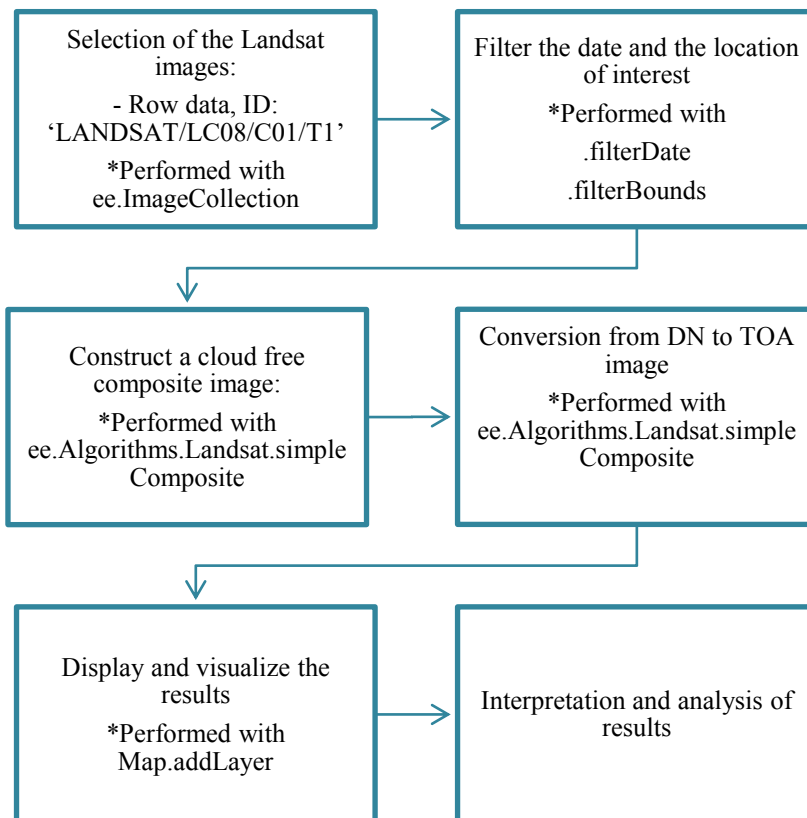
Figure 3. Workflow of the study.

For visualization of results, the RGB bands filter selected was in natural color, with the red (4), green(3) and blue(2) bands. For the visual interpretation of the Landsat images, the following parameters were taken into account:

Coverage		Images	Elements of visual interpretation
Landsat image	Forest		Color: Dark green Texture: rugged Shape: irregular
	Other vegetation (pasture, cropland.)		Color: light green Texture: rugged Shape: irregular
	Bare soil		Color: light brown Texture: smooth Shape: regular

Figure 4. Visual interpretation elements for types of coverage.

Taking into account the established interpretation parameters, the coverage of bare soil corresponds to Deforestation. Therefore, for purposes of visual interpretation and analysis, forest and deforestation can be observed from Landsat images in the study area within the study period.

2784

4. RESULTS

The results show that deforestation in the study area increase from the year of 2013 to 2017, the forest coverage from the year of 2013 have changed to the year of 2017, marked as red squares in Figure 7.

Figure 5. Landsat 8 OLI TIRS natural color image from 2013 in the study area.

Figure 6. Landsat 8 OLI TIRS natural color image from 2017 in the study area.

2013

2017

Figure 7. Visualize deforestation spreads between the year of 2013 and 2017.

Forest cover decreased in the year of 2017, most of these can be observed as changes from forest (2013) to bare soil cover (2017). Other vegetation, like pasture, cropland increased in the study period as well.

Thus, the deforestation is clearly visualized and interpreted with rectangular geometric features of forest clearance which were more widespread in the northwest and northeast part (Figure 7) of the Paraguayan Chaco.

Moreover, the Landsat images used in the study area covers a total of 16 scenes, having worked with that huge amount of images, including acquisition and processing, it would have taken a lot of time and storage space, which was countered using GEE, as all this process were done in a few minutes and all this saved in the GEE cloud.

5. Conclusion

GEE demonstrated to be a convenient tool to quickly process a large amount of satellite images, since if the usual procedure of downloading satellite images and processing them, it will take a lot of time. The advantages to work with GEE are that users only need a Google account to have access to the platform and internet connection as well, it saves a lot of time and data storage for image visualization and analysis, it already provide a considerable amount of specialized build-in algorithm and functions to work with, and the possibility of creating your own; share the work done only through a web link, all results can be downloaded and the main advantage is that it is a free platform.

The disadvantages may be that continuous Internet connection is needed and in developing countries this can be a problem and users need prior knowledge of basic programming.

Therefore, GEE has more advantages than disadvantages, as working with a lot of images can be easier in GEE platform than in traditional GIS software.

For future work can be mentioned that this research is currently on the stage of data acquisition, visualization and interpretation. The next stages is to perform the classification of land use. Based on it, this study will analyze the land use change, deforestation rate and determine driving forces of those changes.

6. REFERENCES

Baumann, M., Israel, C., Piquer-Rodriguez, M., Pizarro, G., Volante, J., Kuemmerle T.,   2017. Deforestation and cattle expansion in the Paraguayan Chaco 1987–2012. Springer. 17 (4), pp. 1179–1191.

Caldas, M., Goodin, D., Sherwood, D., Campos Krauer, J., Wisely, S., 2013. Land-cover change in the Paraguayan Chaco: 2000–2011. Journal of Land Use Science. 10 (1), pp. 1-18.

Gorelick, N., Hancher, M., Dixon, M., Ilyushchenkb, S., Thau, D., Moore, R., 2017. Google Earth Engine: Planetary-scale geospatial analysis for everyone. ELSEVIER, 202, pp. 18-27.

Grassi, B., Pastén, A., Armoa, J., 2005. Un análisis del comportamiento de la   precipitación en el Paraguay. Final report: Polytechnic Faculty, National University of Asuncion.

Kalogirou, V., Solimini, Ch., Paganini, M., Arino, O., 2013. Deforestation Mapping   Using The Google Earth Engine: first Experiments In Boqueron, Paraguay. Living Planet Symposium ESA 722, pp. 267-270

PNUMA-Programa de la ONU para el Medio Ambiente., 2013. Evaluación de Vulnerabilidad e Impacto del Cambio Climático en el Gran Chaco Americano. Centro de conocimiento para el Gran Chaco Americano y cono sur. Retrieved June 12, 2018, from http://www.desarrollo.org.py/admin/app/webroot/pdf/publications/22-06-2017-08-36-20-1281362229.pdf

Construction of Correlation Model of Regional *Phyllostachys Edulis*'s age and TLS Intensity

Xu Wenbing (1, 2), Cheng Xiaojun (1)，Li Quan(1)

[1] College of Surveying and Geo-informatics, Tongji University, Shanghai 200092，China

[2] School of Environment & Resource, Zhejiang A&F University, Hangzhou, Zhejiang 311300,China

Email: xuwb97@163.com; cxj@tongji.edu.cn; 815644889@qq.com

Abstract: In this paper, a correlation model of regional *Phyllostachys Edulis*'s age and Terrestrial Laser Scanning (TLS) intensity is proposed. A 10m*10m sample plot of *Phyllostachys edulis* is scanned by a Leica ScanStation C05 Terrestrial Laser Scanner. Then the point cloud of the *Phyllostachys edulis* is extracted. Moreover, the intensity data of the extracted point cloud is analyzed and the original intensity is corrected through a polynomial model. The relationship between the ages of *Phyllostachys edulis* and corrected intensity data is then investigated and a correlation model is constructed. The experiment results show that the correlation coefficient between the actual surveyed age data and the age data estimated by the proposed model are relatively high, which demonstrates the accuracy of the proposed model.

Keywords: *Phyllostachys edulis*; terrestrial laser scanning technology; laser intensity; polynomial model

With the development of precision forestry, traditional survey methods of forest resource face challenges and innovations. Terrestrial laser scanning technology can quickly acquire 3D spatial information without damaging trees, which is conducive to protecting the ecological environment (Zhao Yang et al., 2010). Terrestrial laser scanning technology has been applied to the construction of single-wood 3D models and biomass estimation in forestry. Pfeifer et al. (2004) and Teobaldelli et al. (2008) used terrestrial laser scanning technology to acquire point cloud data, and extracted relevant data from point cloud data into tree modeling software for manual or semi-automated forest 3D modeling. Wang Jian et al (2009), Gorte et al (2004) and Cote et al (2009) directly used the ground 3D laser scanner to obtain point cloud data, processed the data through the algorithm, extracted the feature information of the forest form, and realized the 3D model construction. In terms of forest biomass research, Cao Lin et al. (2013), Li Wang et al. (2015), Popescu et al. (2003) used small airborne LiDAR to obtain canopy structure and attribute information of forest trees, combined with multi-spectral imagery to construct model estimation samples.

Phyllostachys edulis is a common plant in southern China and belongs to the family Hemu. It cannot be as long as the annual rings of trees (Wu Ganning et al., 2013), while the age of bamboo is used for cultivation management, harvesting and utilization, scientific research, etc. It is of great significance (Yang Fufu, 1965) and is also essential for measuring bamboo biomass (Zhou Guomo et al., 2011). At present, judging the age of bamboo is based on human experience, age-age method and bamboo stalk skin color method, which requires a lot of manpower and time, and the accuracy is difficult to evaluate. In this paper, the terrestrial laser scanning

is used to obtain the laser intensity information of bamboo and bamboo stalks, and the mathematical model of the age of the bamboo and its laser intensity is constructed.

1 Test area and test data collection

The test area is located in Lin'an District, Hangzhou City, Zhejiang Province (119°40'E, 30°15'N). In the bamboo forest, four plots of 10 m × 10 m were measured, and the four corners were made of stainless steel tubes as piles to make a fixed plot. The test data was collected with a Leica ScanStation C05 terrestrail laser scanner, which uses a compact pulsed green laser with a wavelength of 532 nm. Mark and number all the bamboos in the plot, and investigate the bamboo age of each bamboo by the experienced person; use the scanner high-resolution mode to perform panoramic scan on 5 stations to obtain point cloud data, including the spatial three-dimensional coordinate information of the target and laser intensity information.

2 Data processing methods

2.1 Extraction of bamboo stalk point cloud data.

(1) According to the artificially determined age of bamboo, use the Fence function to select 5 bamboos of 1~4 years old respectively, remove the interference points, and only retain the point cloud data of the bamboo stalk parts; (2) use the 0.05m×0.05m Fence box to intercept each. In order to avoid the uncertainty of the point cloud of the edge of the bamboo raft, the Fence box intercepts the point cloud in the horizontal middle part of each section; (3) Using the Export function, the box is 0.05m*0.05m The point cloud data is exported in the standard format .PTX format, and the number of point clouds and laser intensity information in each box are obtained.

2.2 Data processing of laser intensity.

Scanning distance, angle of incidence, surface characteristics of the target, internal mechanism of the scanner, external environment (Kukko et al., 2008; Pesci et al., 2008; Fang Wei et al, 2015; Anttila et al., 2016) would influence the laser intensity. The intensity information need to be normalized to eliminate the influence of these factors before being effectively utilized. This test completed the data acquisition for the same test sample, the same 3D laser scanner and the same time period, so the influence of the internal mechanism of the scanner and the scanning environment on the laser intensity was not considered.

In this paper, the laser intensity correction model based on polynomial is used to correct the scanning distance and incident angle effect. The fitting relationship is as shown in equation (1) (Tan Kai et al., 2015).

$$I + v = \sum_{i=0}^{n} K_i P^i \tag{1}$$

Where: I is the original value of the laser intensity recorded by the instrument; v is the residual value of the laser intensity value; $K_i (i = 0,1,2, \cdots, n)$ is a polynomial coefficient; n is a polynomial order, different scanners,

The value of n is different; P is a variable, $P = \frac{\cos\theta}{R^2}$, which is a function of the incident angle and the range value of the scanning geometry, where: θ is the angle between the incident laser beam and the scan point normal vector. R is the distance from the center of the scanner to the scanning point.

Therefore, an error equation is established for each point, as in equation (2). The model coefficient can be obtained by adjusting the least squares principle $[K_0, K_1, K_2, \cdots, K_n]^T$.

$$v = [1, P, P^2, \cdots, P^n] \cdot [K_0, K_1, K_2, \cdots, K_n]^T - I \tag{2}$$

It can be known from the relationship of P that the laser intensity of the same target differs with the distance and the angle of incidence. It is necessary to eliminate the influence of the distance value and the incident angle to avoid the isomerism of the laser intensity and the phenomenon of the foreign matter in the same spectrum. Assuming that the standard ranging value R_s, the standard incident angle θ_s, is defined, the standard variable can be obtained as in equation (3).

$$P_s = \frac{\cos\theta_s}{R_s^2} \tag{3}$$

Where: R_s can take any value within the range of scanning distance, usually taking the mean of the scanning distance; θ_s is any value within $0°\sim90°$, usually taking the mean of the incident angle. Bringing the standard variable into equation (1) and yields equation (4).

$$I_s + v_s = \sum_{i=0}^{n} K_i P_s^{\,i} \tag{4}$$

Where: I_s is the intensity observation at the standard range value and the standard incident angle; v_s is the residual.

Scanning the same geometry, the laser intensity value is only affected by the target reflectivity if the incident angle and the ranging value are the same for each point. This test considers that in the virtual and real scanning environment, the environmental noise and system noise are equal, that is, $v_s = v$. Therefore, the equation (5) can be obtained from the equation (1) and (4).

$$I_s = I + \sum_{i=1}^{n} K_i \left(P_s^{\,i} - P^i \right) \tag{5}$$

It can be known from equation (5) that I_s is independent of the ranging value and the incidence angle. Therefore, after correction by the polynomial model, I_s is the corrected intensity value, which is only related to the scan target, that is, the surface property of the bamboo.

2.3 Statistical analysis of data. Matlab2010 is used to calculate the fitting error and model coefficient K of the polynomial correction model, and correct the distance and incident angle of the original laser intensity according to the correction model. Finally, the mathematical model of the bamboo age and its laser intensity is fitted by regression analysis and verified. The feasibility of the model.

3 Data processing and analysis

3.1 Bamboo stalk laser strength correction

(1) Determine the polynomial order n value. Correcting the laser intensity value requires determining a parameter, the polynomial order n value of the different scanners. From equation (1), the polynomial model with different n values is selected to process all the scan data in the experiment, and the error in the fitting and the running time of the program are calculated, as shown in Fig. 1. It can be seen from Fig. 1 that the error in the fitting is negatively correlated with the n-value of the polynomial order, and the running time is positively correlated with it. When n=4, the two curves intersect, so the polynomial order n of the test takes a value of 4.
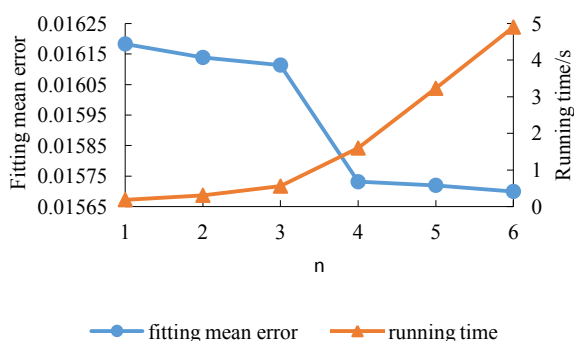
Fig.1 Fitting error and running time change with the degree of polynomial

(2) Determine the model coefficient K and the standard variable P_s. From equation (2), the model coefficient K value is calculated to obtain K_1=-0.17763452, K_2=0.648256124, K_3=-0.887632814, and K_4=0.38538642. Calculate the mean of all scanning distances and incident angles, and obtain the standard distance value R_s=2.905 m and the standard incident angle θ_s=0°. From the equation (3), the standard variable P_s=0.118 is obtained.

(3) Correct the laser intensity. The average laser intensity and the standard and the distribution of R, $\cos\theta$ and P_s between the 1st and 10th sections of the 1st to 4th year old bamboo stalks were calculated from the formula (5). Table 1 lists the calculated values of the indicators between the first and second quarters of bamboo stalks from 1 to 4 years old. It can be seen from Table 1 that the standard deviation of bamboo stalks of different ages is reduced after correction, and the laser intensity of bamboo stalks of different ages is very good. The distinction is basically non-overlapping, and the formula (5) can effectively remove the laser intensity deviation caused by the ranging value and the incident angle.

Table 1 Before and after correction of bamboo stalk laser intensity

Table 1

Index	Age	1year		2year		3year		4year	
	Trunk	1	2	1	2	1	2	1	2
mean	original	0.19550	0.20057	0.19160	0.19469	0.20477	0.20802	0.21708	0.21730
	corrected	0.20029	0.20051	0.19284	0.19577	0.20474	0.20766	0.21520	0.21539
STD	original	0.00751	0.01009	0.00495	0.00789	0.01086	0.00647	0.01229	0.01062

|	corrected	0.00409	0.00600	0.00151	0.00651	0.00829	0.00360	0.01218	0.00941
R/m	MIN	0.98312	0.91759	1.54333	1.48274	1.22692	1.11973	1.38732	1.42932
	MAX	3.84223	3.83117	3.87877	3.84581	5.04894	5.03430	4.18762	4.22301
$cos\theta$	MIN	0.93120	0.95788	0.78819	0.82755	0.93099	0.94349	0.98490	0.93471
	MAX	0.99349	0.99695	0.99280	0.99816	0.98820	1.00000	0.99387	0.98276
Ps/(m^{-2})	MIN	0.06730	0.06792	0.06599	0.06749	0.03877	0.03946	0.05668	0.05511
	MAX	0.96345	1.13766	0.33091	0.37641	0.61846	0.75251	0.51173	0.45753

3.2 Phyllostachys puberty and laser intensity fitting

The relationship between the bamboo age and the laser intensity corrected by the polynomial model is shown in Fig. 2. The laser intensity of the 1-year-old and 2-year-old bamboo stalks overlaps in the third section, and the laser intensity between the other bamboo sections does not overlap, and the laser intensity of the 4-year-old bamboo stalk (0.210~0.215)>3 years old (0.208~0.198)>2 years old (0.192~0.204)>1 year old (0.185~0.202). Therefore, the laser intensity can well distinguish bamboo stalks of different bamboo ages.
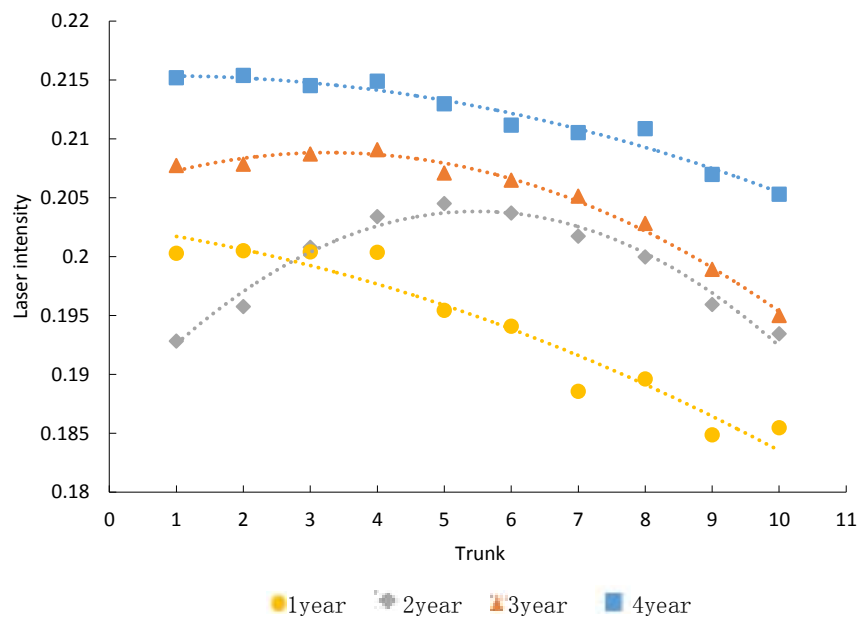
Fig.2 The relationship between different age trunk in laser intensity

3.3 Correlation between bamboo age and laser intensity

In the experiment, 5 trees of 1 year old, 2 years old, 3 years old, and 4 years old bamboo were selected. The laser intensity of bamboo stalk was taken as the measured data, and the relationship was compared with the function fitting laser intensity. The relationship is shown in Fig. 3. It can be seen from Fig. 3 that the simulated laser intensity and the measured laser intensity of different bamboo ages are close, and R^2 is above 0.95, and the RMSE is only 0.020. Explain that the function model can simulate the actual situation of laser intensity of different bamboo ages.
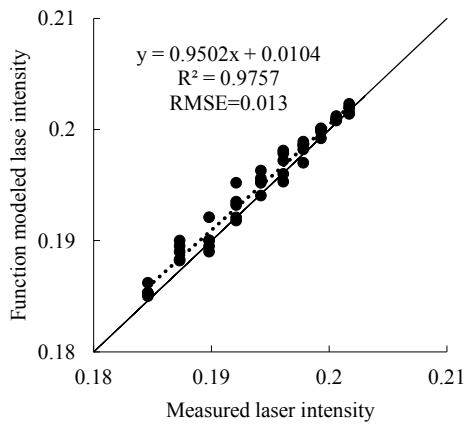
(a) Laser intensity of 1 year's trunk
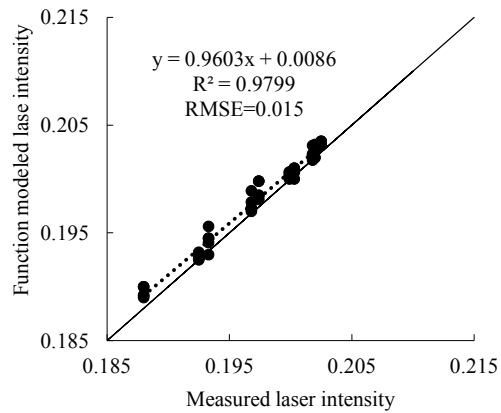
(b) Laser intensity of 2 years' trunk

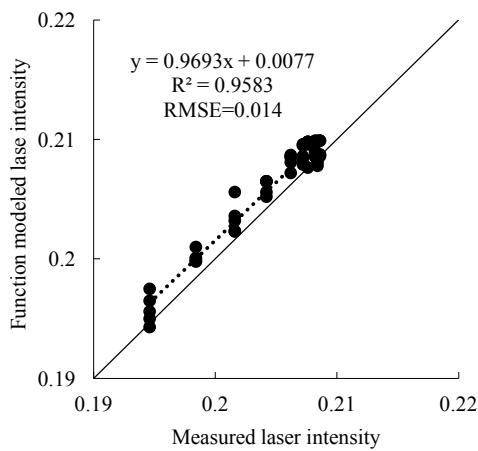(c) Laser intensity of 3 years' trunk
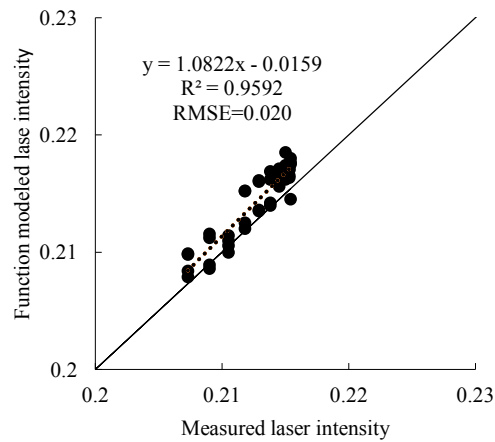
(d) Laser intensity of 4 years' trunk

Fig.7 The relationship between different age trunk's function modeled laser intensity and measured laser intensity

3.4 Mathematical model of bamboo age and laser intensity

The polynomial model was used to fit the laser intensities of different bamboo ages respectively, and the fitting model parameters and correlation coefficient R^2 were obtained. As shown in Table 2, R^2 was above 0.9. It shows that the fitting results are excellent, and the bamboo stalks of different bamboo ages can be classified and distinguished.

Table 2 The fitting parameters and R^2 of different age trunk in laser intensity

Parameters and R^2	1 year	2 years	3 years	4 years
K_0	-0.0001	-0.0006	-0.0003	-0.0001
K_1	-0.008	0.0061	0.0019	0.0002
K_2	0.2026	0.187	0.2056	0.2153
R^2	0.928	0.9655	0.9892	0.9577

By constructing the relationship model between bamboo age and laser intensity, the bamboo age can be accurately determined. The model and correlation coefficient are: $y_1 = -0.0001x^2 - 0.0008x + 0.2026$，$R^2$=0.928; $y_2 = -0.0006x^2 + 0.0061x + 0.187$, R^2=0.9655; $y_3 = -0.0003x^2 + 0.0019x + 0.2056$, R^2=0.9892; $y_4 = -0.0001 + 0.0002x + 0.2153$，$R^2$=0.9577, the lower foot is marked as bamboo age.

4 Conclusion

In this study, by analyzing the relationship between the bamboo age and the laser intensity in a specific area, the research shows that: (1) Only the laser intensity of the 2-year-old bamboo increased first and then decreased, and the other laser intensity changes gradually decreased. (2) The laser intensity of 1 year old and 2 years old is partially overlapped; (3) Mathematical model of bamboo age and its laser intensity can be constructed. The correlation coefficient of the model is high, and the bamboo age of bamboo can be accurately determined. (4) There may be differences in different areas of bamboo, and it is necessary to further study the universality and reference value of the mathematical model.

References

Anttila K, Hakala T, Kaasalainen S, et al. 2016. Calibrating laser scanner data from snow surfaces: Correction of intensity effects. Cold Regions Science and Technology, 121: 52-59.

Cao L, She G H, Dai J S, *et al*. 2013. Status and prospects of the LiDAR-based forest biomass estimation. Journal of Nanjing Forestry University (NTURAL Sciences Edition), 37(3):163-169. [in Chinese]

Cote J F, Widlowski J L, Fournier R A, *et al*. 2009. The structural and radiative consistency of three-dimensional tree reconstructions from terrestrial LiDAR. Remote Sensing of Environment, 113(5):1067-1078.

Fang W, Huang X F, Zhang F, *et al*. 2015. Mural image rectification based on correction of laser point cloud intensity. Acta Geodaetica et Cartographica Sinica, 44(5):541-547. [in Chinese]

Gorte B, Pfeifer N. 2004. Structuring laser-scanned trees using 3D mathematical morphology. International Archives of Photogrammetry and Remote Sensing, 35(B5):929-933.

Kukko A, Kaasalainen S, Litkey P. 2008. Effect of incidence angle on laser scanner intensity and surface data. Applied Optics, 47(7): 986-992.

Li W, Niu Z, Wang C, *et al.* 2015. Forest above-ground biomass estimation at plot and tree levels using airborne LiDAR data. Journal of Remote Sensing, 19(4):669-679. [in Chinese]

Pesci A, Teza G. 2008. Effects of surface irregularities on intensity data from laser scanning: an experimental approach. Annals of Geophysics, 51(5-6): 839-848.

Pfeifer N, Gorte B, Winterhalder D. 2004. Automatic reconstruction of single trees from terrestrial laser scanner data. The International Archives of the Photogrammetry, Remote Sensing and Spatial Information Sciences, Istanbul, Turkey,35:114-119.

Popescu S C, Wynne R H, Nelson R F. 2003. Measuring individual tree crown diameter with lidar and assessing its influence on estimating forest volume and biomass. Canadian Journal of Remote Sensing, 29(5):564-577.

Tan Kai, Cheng Xiaojun. 2015. TLS laser intensity correction based on polynomial model. Chinese journal of lasers, 42(3):0314002. [in Chinese]

Teobaldelli M, Puig A D, Zenone T, *et al*. 2008. Building a topological and geometrical model of poplar tree using portableon-ground scanning LIDAR. Functional Plant Biology, 35(10):1080-1090.

Wang J, Zhou G M. 2009. 3D reconstruction of tree stems based on laser scanning of standing. Microcomputer Information, 25(8-3):228-230. [in Chinese]

Wu W N, Wan T. 2003. Progress of dating methods of tree age. Journal of Green Science and Technology, 7:152-155. [in Chinese]

Yang C F. 1965. Research of identifying of bamboo's age. Scientia Silvae Siniace, 10(2):193-196. [in Chinese]

Zhao Y, Yu X X, Xin Z B, *et al*. 2010 Application and outlook of terrestrial terrestrial laser scanning technology in forestry. World Forestry Research, 23(4):42-45. [in Chinese]

Zhou G M, Liu E B, Shi Y J, *et al*. 2011. Accurate estimation for moso bamboo (*Phyllostacchys edulis*) biomass in Zhejiang province based on the lowest scale technique. Scientia Silvae Sinicae, 47(1):1-5. [in Chinese]

Computing the hourly co-efficient for downscaling the satellite precipitation data in mountainous tropical catchment

Aina Afifah bt. Mohd Yusof (1), Muhamad Afifi Md Yatim (1), Nur Fathiera Mansor (1), Mohd. Rizaludin Mahmud (1,2), Mohd. Nadzri Mohd. Reba (1,2)

[1] Faculty of Built Environment and Survey, Universiti Teknologi Malaysia, 81310, Johor Bharu, Malaysia
[2] Geoscience & Digital Earth Centre (INSteG), Faculty of Built Environment and Survey, Research Institute for Sustainable Environment, Universiti Teknologi Malaysia, 81310, Johor Bharu, Malaysia

Email: ainayusof208@gmail.com; firamansor888@gmail.com; afie0913@gmail.com; rizaludin@utm.my; nadzri@utm.my

Abstract: This study compute the co-efficient to downscale the satellite precipitation data at hourly scale in the mountainous tropical catchment. Mountainous tropical catchments which played a vital role in securing primary resources for the reservoirs and sustaining agriculture on the downstream require consistent and effective monitoring. Using satellite precipitation data as an alternative was novel however, it was constraint by the conflict of spatial resolution and size of the sub-catchments. At present, even the satellite precipitation data at the most advanced of 0.1° was having limitation to represent the local rainfall variation especially in humid tropics in Southeast Asia. By far, most of the downscaling approach were limited to monthly rainfall downscaling at larger temporal scale. As the rainfall was temporally very dynamics which varied at hourly scale, it is crucial to made the high resolution of satellite precipitation available at this scale. In order to solve that gap, we initiate the downscaling procedures by incorporating the orographic factors and wind intensity and direction with hourly scale at 200 meter resolution. The satellite precipitation data from Global Precipitation Mission (GPM) is used as sample. The output of this study would be useful to produce high resolution satellite precipitation in the mountainous humid tropics; critical inputs for high spatial and temporal hydrologic applications on the sub-catchments of the mountainous watershed.

Keywords: Rainfall, Orographic, Digital Elevation Model, Sub-Catchments

1.0   INTRODUCTION

Mountainous tropical catchments which played a vital role in securing primary resources for the reservoirs and sustaining agriculture on the downstream require consistent and effective monitoring. Using satellite precipitation data as an alternative was novel however, it was constraint by the conflict of spatial resolution and size of the sub-catchments. The spatio-temporal rainfall variation in humid tropical environment is high within small areas (Bidin & Chappell, 2003). This is implied for most humid tropical catchments in Southeast Asia where the region comprises of small land-sea ration area, small peninsular and islands. Moreover, the variation is expected to increase (Chadwick et al. 2013).

Using satellite precipitation data as an alternative was novel however, it was constraint by the conflict of spatial resolution and size of the sub-catchments. At present, even the satellite precipitation data at the most advanced of 0.1° was having limitation to represent the local rainfall variation especially in humid tropics in Southeast Asia.   Operational hydrologic analysis require continuous data especially the historical one and therefore it is important to improve those datasets. Because of that issues, effort to improve the spatial resolution was needed. It is recommended that the size to be within less than 4km due to the effective catchment size in humid tropics that is relatively small.

Most of the recent spatial downscaling algorithm could not comply with this characteristics, (i) high spatial resolution grid and (ii) high temporal resolution. Method proposed by Chen et al. (2014), Shi et al. (2015), and Cho and Choi (2015) produced satellite precipitation with 1km resolution, however, at monthly and longer rainfall scale (i.e., annual). Meanwhile, the high temporal scale of downscale rainfall algorithm by Tao & Barros (2010) required complex computation and parameters, which could not been afford by many mountainous watershed. In addition, the daily scale downscaling by Mahmud et al. (2015) was retaining the original satellite precipitation data grid (0.25 deg.). Therefore, the development reliable and operational downscale algorithm which produced both high spatial and temporal downscale data is yet to be completed.

In order to solve that gap, we initiate the downscaling procedures by incorporating the orographic factors and wind intensity and direction with hourly scale at 200 meter resolution. The satellite precipitation data from Global Precipitation Mission (GPM) is used as sample. The output of this study would be useful to produce high resolution satellite precipitation in the mountainous humid tropics; critical inputs for high spatial and temporal hydrologic applications on the sub-catchments of the mountainous watershed.

2.0 MATERIALS & METHOD

2.1 Deriving the high resolution of hourly downscaling co-efficient

There are three major process in computing the high resolution of hourly scale of downscaling co-efficient which consists of;

  i) Generating the hourly wind map
  ii) Re-gridding of the digital elevation model
  iii) Compute the slope induced surface (downscaling co-efficient)

The elaboration is given as below.

i) Generating the hourly wind map

The purpose of creating this hourly wind map is to obtain the wind vectors information which is one of the input in computing the orographic effect (downscaling co-efficient). Because most of the mountainous area do not have in-situ measurement on wind, we proposed to obtain through inter and extrapolation from the available meteorological stations network. We had identified 12 stations which distributed all over the Peninsular Malaysia. The hourly weather data consisting of direction and intensity of the wind were obtained from Malaysian Meteorological Department (MET Malaysia). The inverse distance weight (IDW) interpolation scheme was used to perform this task. Figure 1a showed the distribution of the meteorological stations.

ii) Re-gridding of the digital elevation model

The initial grid size of the digital elevation model from the Shuttle Radar Topographic Mission (SRTM)(30m) is transformed to our desired spatial downscaling grid. DEM data in height (.hgt) format obtained during the Shuttle Radar Topography Mission (SRTM) by National Aeronautics and Space Administration (NASA) and National Geospatial-Intelligence Agency (NGA). In this study, we chose 200 meter due to the high dynamics of rainfall in humid tropical regions. Prior to that, the subsequent hourly computation was conducted at this resolution. Figure 1b showed our selected study area which located at the Cameron Highland catchment and its corresponding digital elevation model.
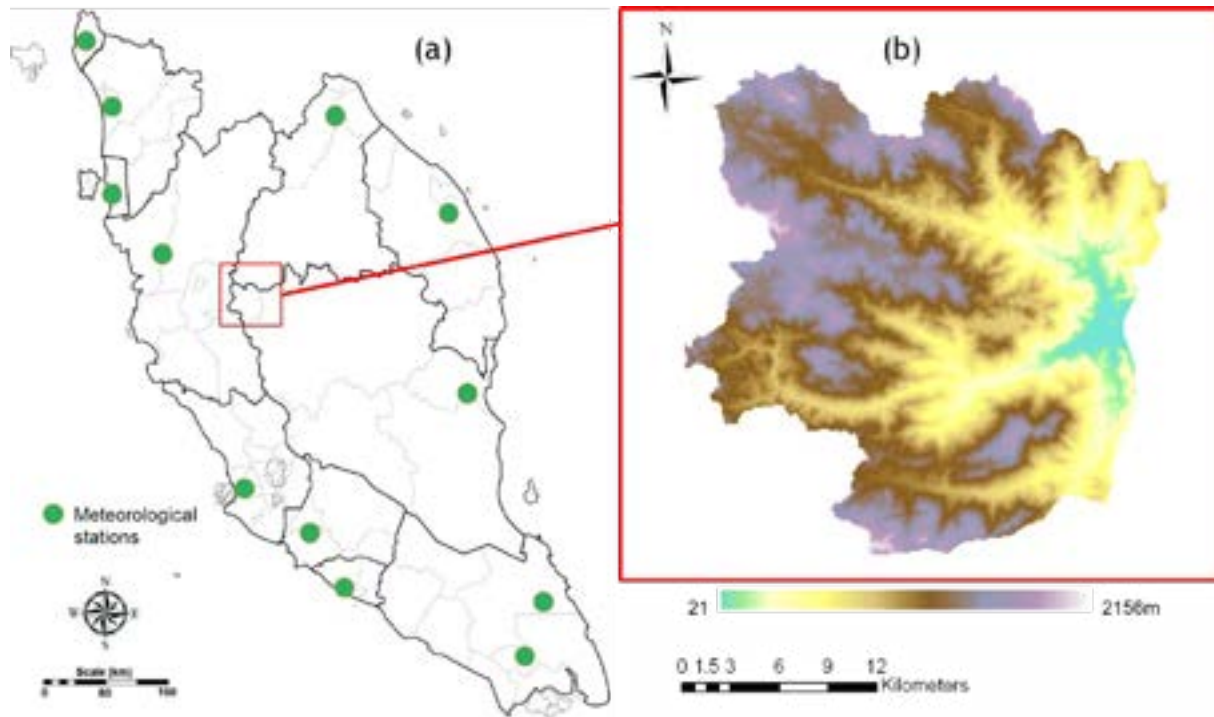
Figure 1. Meteorological stations and selected mountainous catchment area

iii) Computation of the hourly downscaling co-efficient (slope induced surfaces)

The concept of the hourly downscaling is to compute the hourly effect of orographic or in this paper referred as slope induced surfaces and use it as co-efficient in determining the proportion of rainfall in that each grid. Because the terrain variation is varied as well as the wind vectors, therefore, the slope induced surface would be unique and represent the actual condition on the ground. The slope induced surfaces is computed by modifying the procedures from the Mass & Dempsey approach (1985) to suit the nature of gridded data. The computation is expressed below and figure 2 illustrated the concept;

$$\frac{\delta h}{\delta x} = \frac{h_3 + h_6 + h_9}{3} - \frac{h_1 + h_4 + h_7}{3} \qquad \text{Eqn. 1}$$

$$\frac{\delta h}{\delta y} = \frac{h_1 + h_2 + h_3}{3} - \frac{h_7 + h_8 + h_9}{3} \qquad \text{Eqn. 2}$$

$$wsx = u . \frac{\delta h}{\delta x} \div \sqrt{\left(\frac{\delta h}{\delta x}\right)^2 + (dx)^2} \qquad \text{Eqn. 3}$$

$$wsy = u . \frac{\delta h}{\delta y} \div \sqrt{\left(\frac{\delta h}{\delta y}\right)^2 + (dy)^2} \qquad \text{Eqn. 4}$$

$$ws = |wsx| + |wsy| \qquad \text{Eqn. 5}$$

where U and V is wind vectors, dx, dy is the distances between adjacent grid points in x and y direction, dh/dx, dh/dy is slopes, h1, h2, h3 and h4 is the height of the surrounding pixels, and ws is the slope induce surfaces.
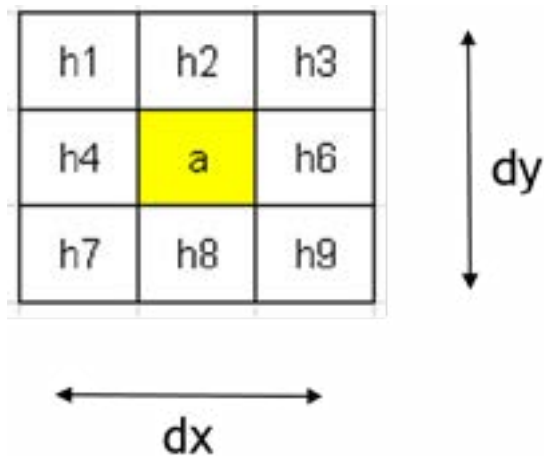
Figure 2. Illustration of the kernel of downscaling

In selecting the date and the corresponding hour for the data selection, we chose it based on two data preferences, the rain gauge and the satellite hourly measurement. First we identified the heavy rainy days (>15mm day) and later we examined at which hour the rain is occurred through the half hourly data of Global Precipitation Mission (GPM). For this study, we chose three rainy days as samples.

2.2   Downscaling technique

The computed downscaling co-efficient is then being used to produce finer resolution of hourly satellite precipitation. The concept of the downscaling is that the proportion of the rainfall is high when the slope induced surface is similar to the incoming wind vector (low value) and vice versa. Table 1 showed the weightage. The weightage then be multiplied with the hourly GPM satellite rainfall estimates. Equation 6 showed the computation. In this preliminary study, we chose a rainfall that occurred during November 10, 2015 which occurred approximately at 5pm.

$$\text{Downscale rainfall, } D = R * (\text{Co-efficient, Ws}) \qquad \text{Eqn. 6}$$

Table 1. Weightage for downscaling purpose

Direction	Weight
±1-30°, ±330-360°	1.0
±30-60°, ±300-330°	0.8
±60-90°, ±270-300°	0.6
±90-120°, ±240-270°	0.4
±120-150°, ±210-240°	0.2
±150-180°,±180-210°	0.1

3.0   RESULTS & DISCUSSION

The proposed algorithm enabled the production of satellite precipitation data with high spatial (200m) and temporal (hourly) resolution (Fig.2) from the initial grid of 0.1 degrees (10-12km) obtained from the Global Precipitation Mission (GPM). The usage of minimum inputs and less complex computation procedures are potentially to make this approach suitable for many mountainous tropical region that strongly influenced by the orographic and wind effects. In addition, it would be very useful for one that experiencing rainfall data conflict situation (DCS)(Mahmud et al. 2018).

Nevertheless, the small sample area however had limit the comprehensive visualization of the result, thus unable appreciation of the technique. In addition, the absence of the field verification made the results remained speculative. Quantitative and qualitative validation against the rain gauge measurement is recommended. All the mentioned drawbacks were expected to be included in the future works.
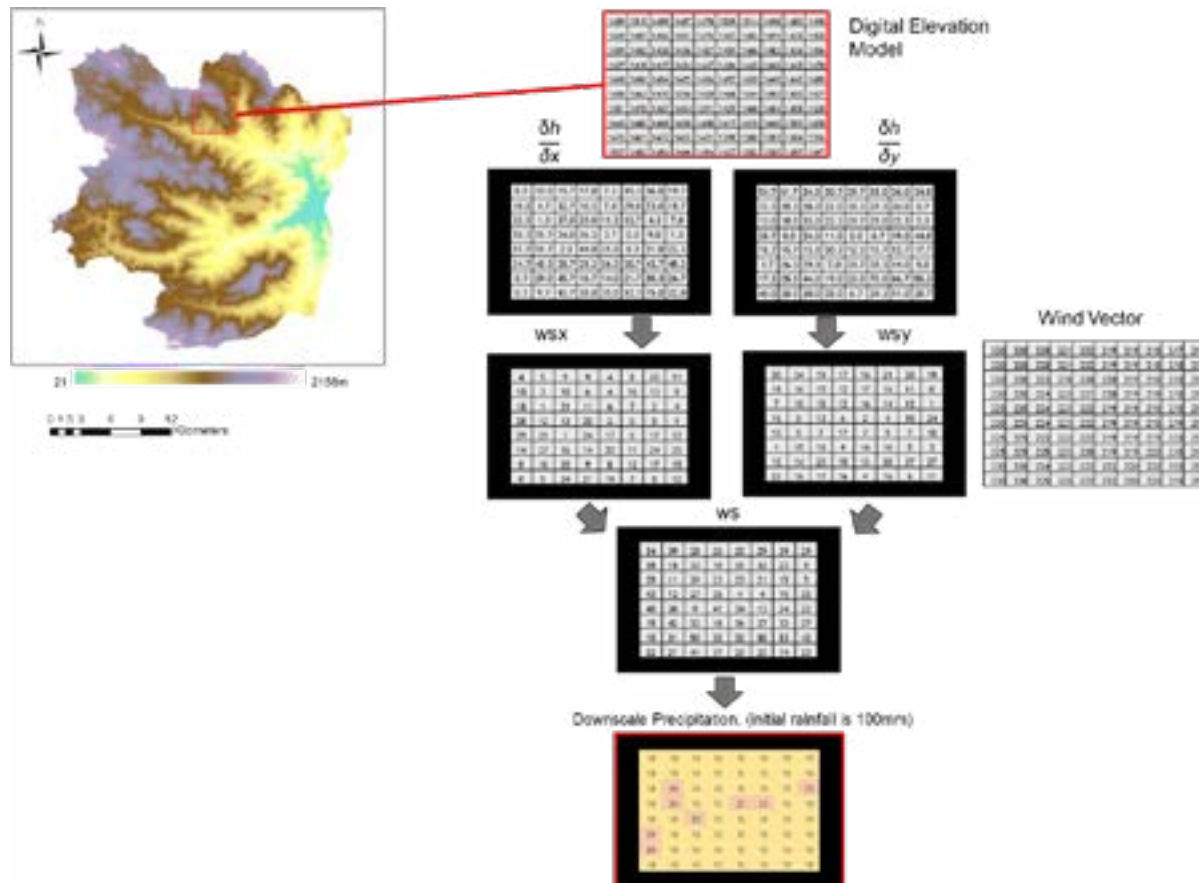
Figure 2. Co-efficient and downscaling schematic diagram (Sample).

4.0 CONCLUSION

This study demonstrated the hourly scale spatial downscaling of satellite precipitation at mountainous tropical watershed. The proposed algorithm is able to produced high spatio-temporal hourly precipitation by downscaling the 0.1° deg. resolution of GPM satellite precipitation using the co-efficient based on elevation and orographic effects. Although the reliability of the result is speculative because it was not being validated yet by the actual rainfall on the ground, the algorithm potentially gave hindsight of improvement of satellite hydrology for the critical mountainous tropical watershed.

REFERENCES

Bidin, K., Chappell, N. A. (2003). First evidence of a structured and dynamic spatial pattern of rainfall within a small humid tropical catchment. Hydrol. Earth Syst. Sci., 7, 245-253, doi:10.5194/hess-7-245-2003.

Chadwick, R., Boutle, I., Martin, G. (2013). Spatial patterns of precipitation change in CMIP5: Why the rich do not get richer in the tropics. J. Climate, 26, 3803-3822.

Chen, F., Liu, Y., Liu, Q., Li, X. (2014). Spatial downscaling of TRMM 3B43 precipitation considering spatial heterogeneity. Int. J. Remote Sens., 35, 3074-3093.

Cho H., Choi, M. (2013). Spatial downscaling of TRMM precipitation using MODIS product in the Korean peninsula. AGU, Fall Meeting, Abstract, H43G-1537.

Mahmud, M.R.; Hashim, M.; Matsuyama, H.; Numata, S.; Hosaka, T (2018). Spatial Downscaling of Satellite Precipitation Data in Humid Tropics Using a Site-Specific Seasonal Coefficient. Water, 10, 409. https://doi.org/10.3390/w10040409.

Mahmud, M.R.; Hashim, M.; Matsuyama, H.; Numata, S.; Hosaka, T. (2015). Temporal Downscaling of TRMM Rain-Rate Images Using Principal Component Analysis during Heavy Tropical Thunderstorm Seasons. Vol. 16, 5, 2264-2275. doi/10.1175/JHM-D-14-0233.1

Mass, C.F., and D.P. Dempsey, (1985). A one-level, mesoscale model for diagnosing surface winds in mountainous and coastal regions. Mon. Wea. Rev., 113, 1211-1227.

Shi, Y., Song, L., Xia, Z., Lin, Y., Myeni, R. B., Choi, S., Was, L., Ni, X., Lao, C., Yang, F. (2015). Mapping annual precipitation across mainland China in the period of 2001-2010 from TRMM 3B43 product using spatial downscaling approach. Remote Sens., 7, 5849-5878.

Tao, K., Barros, P. (2010). Using fractal downscaling of satellite precipitation products for hydrometeorological applications. J. Atmos. Ocean. Tech., 27, 409–427.

IDENTIFYING THE RELATIONSHIPS BETWEEN WATER QUALITY AND LAND COVER CHANGES IN ANGKE RIVER, INDONESIA

Prita Ayu Permatasari (1), Hefni Effendi (1), Luisa Febrina Amalo (1), Sri Muslimah (2)

¹Center for Environmental Research, Bogor Agricultural University, PPLH Building, Jl Lingkar Akademik, Kampus IPB Dramaga, Bogor, West Java, Indonesia
² Center for International Forestry Research, Jl CIFOR Situ Gede, Sindang Barang, Bogor, West Java, Indonesia
Email: pritapermatasari@gmail.com; hefni_effendi@yahoo.com; luisafebrina@gmail.com;
ms.srimuslimah@gmail.com;

KEY WORDS: Angke River, NDVI, water quality, land use, land cover

ABSTRACT: River is an important element in human life that can be used to meet daily needs. The high level of urbanization in big cities causes the quality of the river to decline due to industrialization and pollution. Angke River is one of the rivers that flows in Jakarta Megacity and is often used by local people for household purposes and irrigation. It has been widely accepted that there is a close relationship between the land cover change and water quality. This study aims to analyze the relationship between water quality and land cover changes within Angke Watershed based on the water quality monitoring data and remote sensing data in 2014 and 2016. Fine resolution satellite imagery provides opportunities for land cover monitoring and assessment. By using NDVI data, land cover changes can be identified and correlated with some water quality parameters. The result showed that percentage of dense vegetation in Angke Watershed has been decreased over the two years but water quality has been better in the same time.

1. BACKGROUND

Jakarta is one of the largest metropolitan in Southeast Asia with tremendous rate of population growth and wide range of urban problems. Total population of the Jakarta Metropolitan Area consisting of Jakarta and the neighboring districts of Bogor, Tangerang, Depok and Bekasi –abbreviated as Botadebek- in 2000 reached more than 21 million. This population consisted of about 80 percent urban population and 20 percent rural population and inhabited an area of approximately 6400 square kilometers. This population was about 10 percent of total population of Indonesia and only about 0.3 percent of total area of Indonesia. McGee (1994) estimated that the total population of the Jakarta Metropolitan Area will reach 40 million by 2020.

Morphology of Jakarta is dominated by lowland area, where its northern part related to Java Sea. More than 50% of Jakarta area is located at an altitude of less than 25 meters above sea level. Jakarta is traversed by 13 rivers flowing from upland located in the south of Jakarta to the lowland area in the north. Those 13 rivers are Mookervart River, Angke River, Pesanggrahan River, Grogol River, Krukut River, Baru Barat River, Ciliwung River, Baru Timur River, Cipinang River, Sunter River, Buaran River, Jati Kramat River, and Cakung River. Final terminal of this drainage system is commonly either natural river or artificial channel conveying water to the Jakarta Bay.

Angke River is one of the rivers that flow in Jakarta. Unfortunately, river's function as catchment areas and seawater intrusion barrier cannot be optimal due to many settlements grow not only along the river but also in water bodies. When heavy rains, Angke River always overflows to the vicinity due to its inability to accommodate the overflow discharge of water from the upper reaches in Bogor. In rainy seasons, the river annually causes local flood, usually in the districts of Pinang, Cipondoh, Ciledug (Tangerang City), Joglo, Kembangan, Rawa Buaya, Duri Kosambi, and Cengkareng (West Jakarta).

Based on utilization, the river in Jakarta is used for household purposes, fisheries, agriculture, livestock, industrial, recreational shipping, power generation, water containers, and in some places used as a household and industrial garbage dump. Directly or indirectly, the river has dual functions for both live and as a dumping ground residual materials (Hendrawan, 2005). The thirteen rivers in Jakarta have several small streams with huge potential as surface water to support human life in five areas of the city. With rapid population growth and development in Jakarta, there is the tendency of a change in condition and quality of river water in Jakarta.

Land cover and land use are very important elements in relation to water quality. Different types of land use and land cover affect the quality of water. Agricultural and household fertilizers have different chemicals within them, such as nitrogen and phosphorus. These chemicals can potentially run off into nearby water sources such as groundwater, streams and larger bodies of water. In turn, this could damage the nutrient content within that water supply, affecting the overall water quality itself (Bowden *et al*., 2015)

The high level of urbanization in Jakarta resulted in changes of land use and land cover in Jakarta and surrounding areas. Changes in land use and land cover indirectly affect water quality in Angke River. This study aim is to look at the relationship between water quality and land cover changes in Angke River in 2014 and 2016.

2. MATERIAL AND METHODS

2.1. Study Area

Angke River flows through 4 administrative areas, Bogor (upstream), Tangerang and South Tangerang (middle stream), and West Jakarta as downstream. The highest water discharge of Angke River with a length of 91.25 km and covering an area of 186 km^2 is 4.3 m^3/s. Sampling location was divided into 21 sites (Figure 1). Angke River is one of 13 river that traversed in Jakarta.

Angke River has a hydrological cycle that does not undergoes dryness throughout the year. There is significant rainfall throughout the year in Bogor. Even the driest month still has a lot of rainfall. This climate is considered to be an Af according to the Köppen-Geiger climate classification. The average temperature in Bogor is 25.2°C. The driest month is July, with 216 mm rainfall. Almost all precipitation fell in January, with an average of 442 mm. Meanwhile, the driest month in Jakarta is July, with 58 mm rainfall.
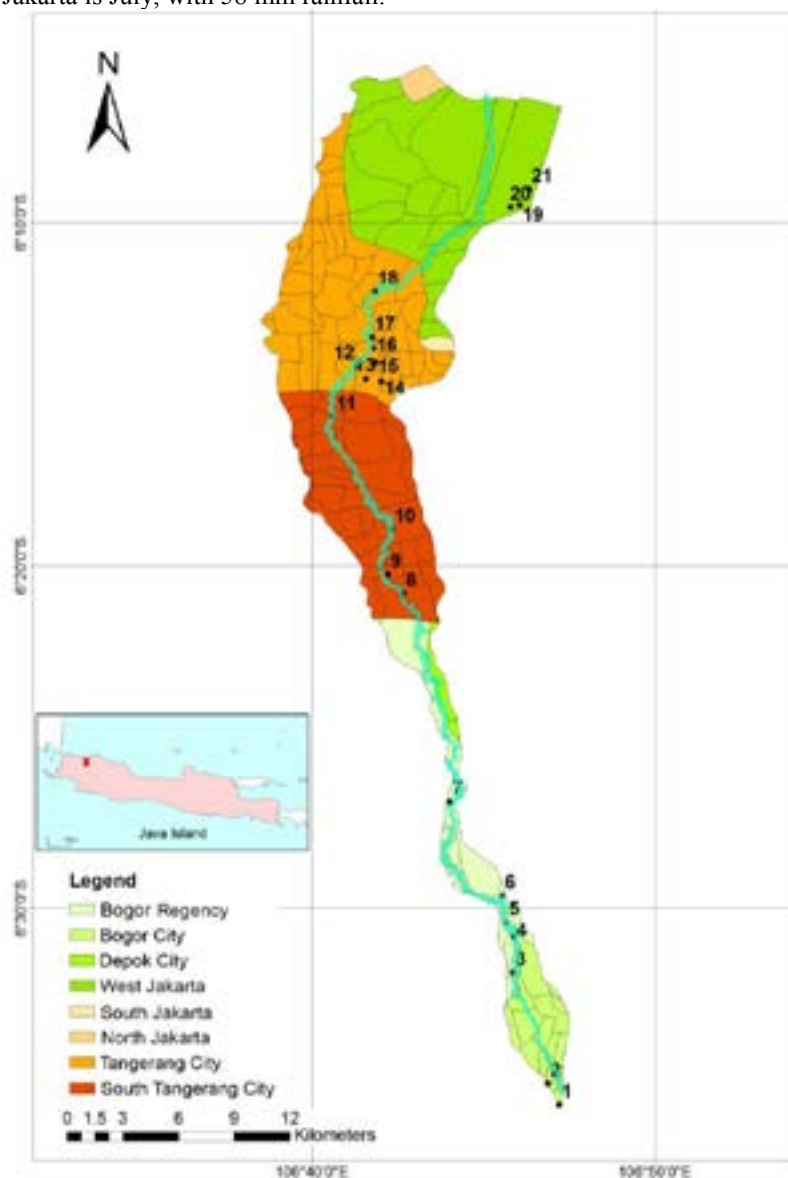
Figure 1. Study location

2.2. Sample collection and parameter measurement

A total of 21 points were sampled along the main stem of Angke River. Water sampling was carried out in rainy season and dry season in 2014 and 2016. Sampling data in those two years will be used to compare the water quality from time to time and to see land cover change effect in 2 years to water quality. A combination of spatial and temporal analyses was applied to provide more robust results for the relationship between land use and water quality. Water samples were collected 0.5 m below the water surface and at least 5 m from the riverbank using a 1000 mL

organic glass hydrophore. Duplicate samples were taken out at each sampling site. Sampling points along Angke River can be seen in Table 1.

Table 1. Water sampling location

No	Sampling Points	Administrative Area	Longitude	Latitude
1	Devris Market	Bogor City	106,7868831	-6,5955926
2	Semeru Golf Court	Bogor City	106,7811177	-6,5851482
3	Pulp and Paper Company	Bogor City	106,76425	-6,531273
4	Kemang Main Road	Bogor Regency	106,764734	-6,513605
5	Billabong Estate Bridge	Bogor Regency	106,760954	-6,506992
6	Kemang Baru Road	Bogor Regency	106,759063	-6,493939
7	Arko Main Road	Bogor Regency	106,733456	-6,448088
8	Angke Bridge	South Tangerang City	106,711	-6,346916667
9	Arjuna Road	South Tangerang City	106,7035	-6,33775
10	Ciater Main Road	South Tangerang City	106,7054444	-6,315666667
11	AMD Main Road	South Tangerang City	106,6771944	-6,261055556
12	Tajur Village	Tangerang City	106,6881389	-6,236527778
13	Pondok Marta Monitoring Station	Tangerang City	106,6928889	-6,242555556
14	Wetan Mnitoring Station	Tangerang City	106,7005778	-6,243944444
15	Puri Kartika Estate Bridge	Tangerang City	106,6973889	-6,234388889
16	Duren Village Estate Bridge	Tangerang City	106,6965556	-6,227527778
17	Ciledug Bridge	Tangerang City	106,6957778	-6,222333333
18	Ciledug Bridge	West Jakarta	106,7279722	-6,176277778
19	Pesing Kali Angke	West Jakarta	106,7676389	-6,158055556
20	Daan Mogot Road	West Jakarta	106,7632222	-6,159111111
21	Tubagus Angke Road	West Jakarta	106,772142	-6,150373

During and after sampling, four water parameters were chosen to be measured, which are important indicators of water pollution influenced by anthropogenic activities. Parameters that sampled consist of chemical oxygen demand (COD, mg/L), biochemical oxygen demand (BOD, mg/L), total suspended solids (TSS, mg/L), and dissolved oxygen (DO, mg/L).

Biochemical oxygen demand (BOD) is a measure of the amount of oxygen that bacteria will consume while decomposing organic matter under aerobic conditions. Chemical oxygen demand (COD) does not differentiate between biologically available and inert organic matter, and it is a measure of the total quantity of oxygen required to oxidize all organic material into carbon dioxide and water. COD values are always greater than BOD values, but COD measurements can be made in a few hours while BOD measurements take five days.

Total Suspended Solids (TSS) are solids in water that can be trapped by a filter. TSS can consist of various materials such as silt, decaying plant and animal matter, industrial wastes, and sewage. It represent a crucial parameter for pollution in urban areas. TSS potentially harmful for fish and aqualtic life (Rossi *et al.,* 2006). Dissolved oxygen plays a vital role for biological processes both directly through its effect on organism physiology and indirectly through its effect on the nitrogen and carbon cycles. Low oxygen conditions (hypoxia) can lead to significant die-offs in animal species (Chan *et al*., 2008)

2.3. Spatial analysis

Multi-temporal medium resolution Landsat imagery was used to obtain comprehensive coverage and analysis of the current and historical Angke Watershed. The used imagery was acquired by the same satellite sensors in different acquisition times of Landsat-8 (April 22, 2014 and February 23, 2016). The Landsat satellite data was georeferenced to UTM WGS 84 Zone 48 south. Spatial data were processed using ArcMap 10.3 software. Data processing using geographic information systems (GIS) consists of some steps such as data entry, data analysis, and data display.

The obtained imageries will be used to see changes in land cover in the last two years. Normalized difference vegetation index (NDVI) would be considered in order to maximize the contrast between built and unbuilt area along the Angke Watershed. Normalized Difference Vegetation Index (NDVI) was used widely to monitor the quality and distribution of vegetation. NDVI was, in fact, often referred to as a greenness index. This index can be computed with a simple formula (1).

$$NDVI = \frac{(NIR - Red)}{(NIR + Red)}$$

(1)

where Red is the reflectance or radiance in a visible wavelength channel (0.636 - 0.673 μm) and corresponds to band 4 for Landsat-8 and NIR is Near InfraRed (0.851-0.879 μm) corresponds to band 5 for Landsat-8. NDVI values range from +1.0 to -1.0. Areas of barren rock, sand, or snow usually show very low NDVI values (for example, 0.1 or less). Sparse vegetation such as shrubs and grasslands or senescing crops may result in moderate NDVI values (approximately 0.2 to 0.5). High NDVI values (approximately 0.6 to 0.9) correspond to dense vegetation such as that found in temperate and tropical forests or crops at their peak growth stage.

The land use and land cover change from open space to developed area usually give some negative impacts to river water quality. The contents of untreated disposal or spatial disposal items such as organic materials, salinization, nutrients, suspended sediment, enteric virus, and oil and grease are directly affecting the water quality in river basins (Peters 2016 and Athokorala 2013).

3. RESULTS

3.1. Land cover change

From 2014 until 2016 urban land made up the vast majority of total area. By 2014, land cover in the Angke River Basin is almost 90% housing. About 8% of land cover in the Angke River Basin is dryland farming. Less than 3% is a rice field located in the northern part of Jakarta. There is a nearly 1% fish farm in northern Jakarta. Land cover from 2014-2016 in the Angke River Basin did not experience any significant change (Figure 2).
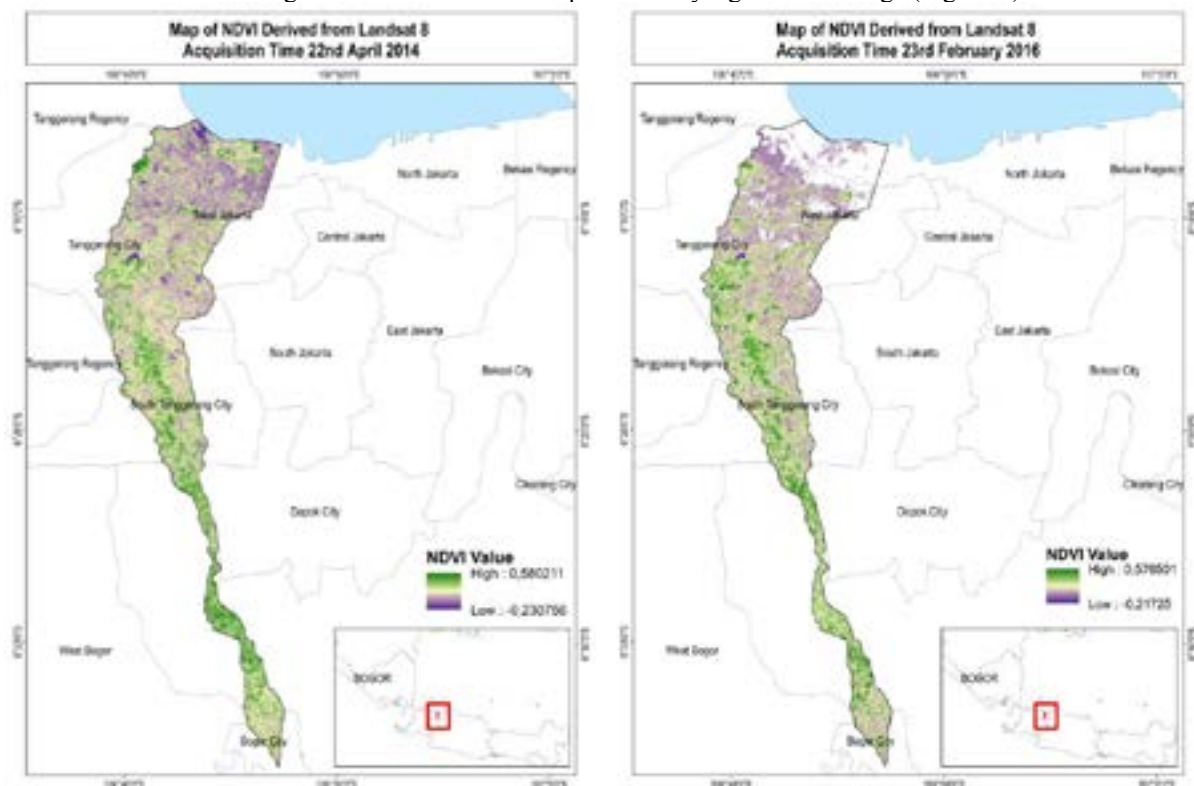

Figure 2. Map of NDVI in Angke Watershed in (a) 2014 and (b) 2016

Figure 2 shows the NDVI map of Angke Watershed. Within the vegetation cover, a portion of dark green indicates higher NDVI (0.3–0.8) that showed dense vegetation, bright green indicates shrubs and grassland, light yellow indicates built area, and purple showed water bodies and wetland. The mean NDVI values at the 21 points sampled ranged between -0.2 and 0.5. From NDVI analysis, dense vegetation has decreased from 59.56 km^2 in 2014 to 53.69 km^2 in 2016.

3.2. Temporal and spatial variations of water quality

Some provincial government in Indonesia has categorized each rivers in their administrative area into certain water quality classification. Some rivers those still have not been assigned, has been classified as water quality class II. According to Government Regulation No. 82/2001, water quality class II is allocated for water recreation infrastructure / facilities, freshwater fish cultivation, livestock, agricultural irrigation, and or other uses that require

the same water quality as those uses. The standard of water quality class II for BOD is ≤3 mg/L, COD ≤25 mg/L, TSS ≤50 mg/L, and DO ≥4 mg/L. Diagram of water quality in 21 sampling points on Angke River in 2014 and 2016 can be seen in Figures 3, 4, 5, and 6 for the parameters BOD, COD, TSS, and DO respectively.
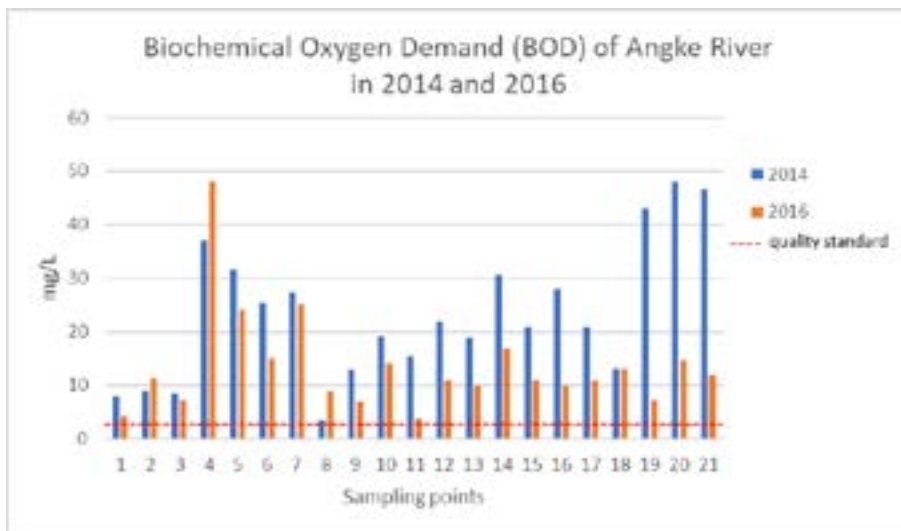

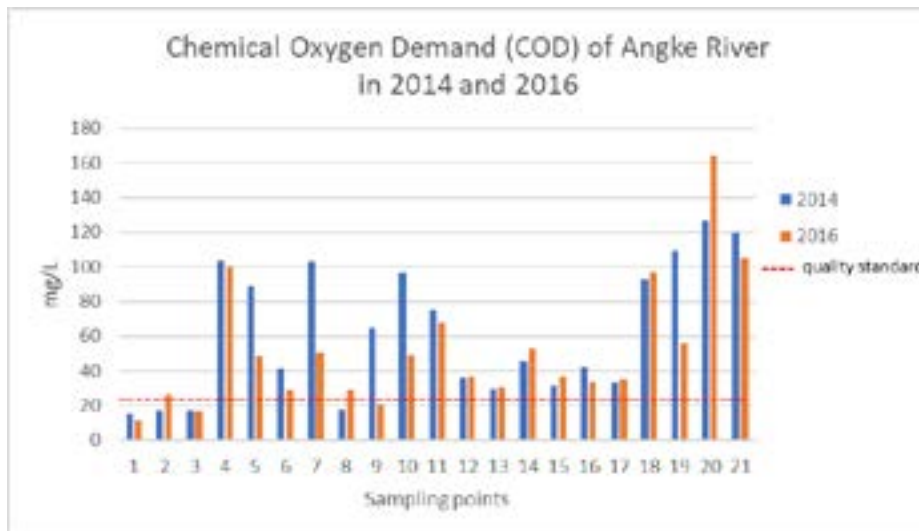Figure 3. BOD of Angke River in 2014 and 2016
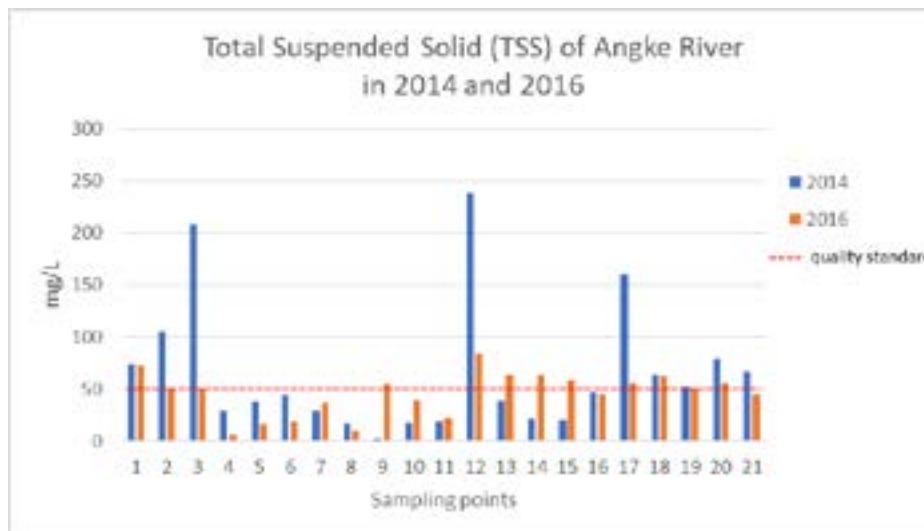

Figure 4. COD of Angke River in 2014 and 2016

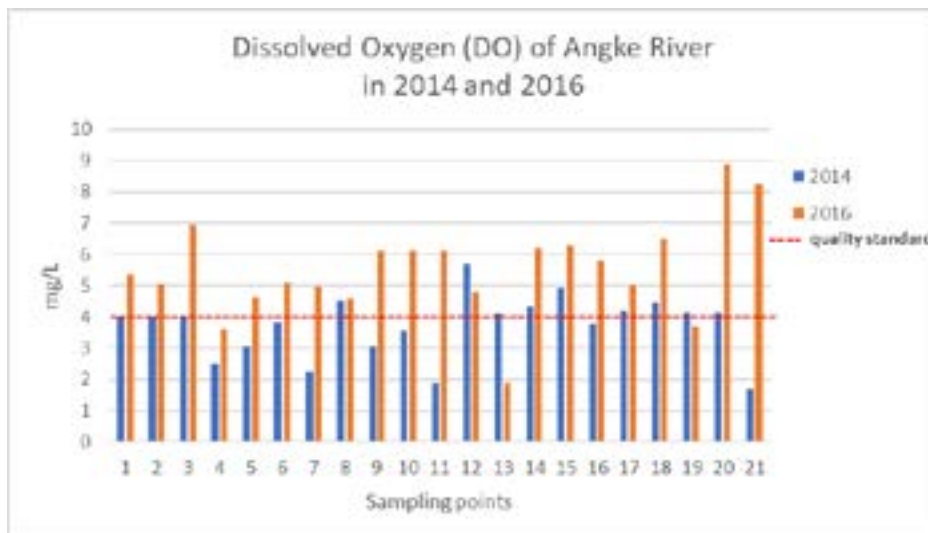Figure 5. TSS of Angke River in 2014 and 2016

Figure 6. DO of Angke River in 2014 and 2016

Based on Figure 4, it can be seen that the BOD value in 2014 was almost entirely above the BOD quality standard for water class II or exceeded 3 mg/L. In 2014, the BOD value from sampling points 1 to 21 was very fluctuative. At Bogor Regency sampling point, the BOD value has increased. Around the city of Tangerang and South Tangerang the BOD value has decreased and increased again in West Jakarta. In 2016, the BOD value decreased compared to the previous 2 years. This shows that the quality of BOD has improved over the past 2 years.

As with BOD, the COD values in 2014 and 2016 were quite high at the sampling points of Bogor Regency and West Jakarta. In contrast to the BOD which showed a decline in 2016, in the COD parameter, some sampling points showed an increase such as in the Tangerang City and West Jakarta, and some showed a decrease as in Bogor Regency and South Tangerang City.

Most of TSS values in 2014 and 2016 are below 50 mg/L. This shows TSS concentration in water is still in good condition. Compared to 2014, most of TSS values in 2016 has decreased. In 2014 and 2016, TSS value showed relatively low around Bogor Regency and South Tangerang City.

Most of dissolved oxygen value in 2014 was below 4 mg/L but in 2016, most dissolved oxygen value has increased and been at level above 4 mg/L. This showed that the oxygen level in Angke River has improved so well within 2 years although DO values was under quality standard in some locations. Almost all DO values on sampling points experienced an increase in 2016, especially in West Jakarta. This indicated that oxygen levels in the Angke River in 2016 are better than in 2014.

4. DISCUSSION

4.1. Impacts of different land uses on water quality

Generally land use types related to economic activity and development negative impacts on water quality, so positive correlations exist between percentages of these land use types and concentrations of water pollutants, while undeveloped areas such as natural forest area are related to good water quality. Different land use types are associated with different water pollution problems. For example, Tong and Chen (2002) examined the relationships of land use and water quality on regional scale in the watershed of the Ohio State, USA. They found that BOD had a significant positive correlation with residential and commercial lands, a significant negative correlation with forest, but non-significant correlation with agricultural land (Tu, 2008).

Based on sampling result, BOD values tend to be high in Bogor Regency, Tangerang City, and West Jakarta. This is related to the high built area for settlements and commercial activities in these areas. In contrast to BOD, COD is the amount of oxygen needed to decompose all organic matter contained in water (Boyd, 1990), so that all kinds of organic material, both easily dissolved and complex and difficult to decompose, will oxidize. Thus, the difference in value between COD and BOD illustrates the amount of organic material that is difficult to decompose in the waters. BOD value could be the same as COD, but the BOD cannot be greater than COD. So COD describes the total amount of organic material available. High COD is usually associated with chemical products such as oil compounds and other chemical wastes. The high COD value in Bogor and West Jakarta Districts to exceed quality standards is estimated due to high industrial activity in these two areas.

The high value of TSS in water can show high concentrations of bacteria, nutrients, pesticides and metals. The high value of TSS in water is also negatively correlated with dissolved oxygen. In general, the higher the TSS the lower the dissolved oxygen. According to Effendi (2003), TSS 81-400 mg/L shows that the suspended solids content is not good for fisheries or aquaculture. Figure 5 shows a fairly good condition in 2014 and 2016. The proportion of forested land is positively related to dissolved oxygen concentration. DO values in 2014 showed stable results at all sampling points. In 2016, the value of DO increased in West Jakarta.

4.2. Change in water quality from 2014 to 2016

In general, the results of the water quality analysis in 2016 showed better results compared to 2014. These results were different from hypothesis that estimated the reduction in dense vegetation give negative impact on water quality. However, there are several factors that can make water quality increase regardless of the decrease in dense vegetation. The less significant decrease in dense vegetation in Angke Watershed over the past two years can be one of some factors. The efforts of the local government to improve water quality along the Angke River are also one of the causes of improved water quality. In addition, differences in weather conditions in sampling period in two different years is estimated to be a factor in improving water quality. Based on the research of Ling *et al.* (2017), several water parameters such as BOD, COD, and TSS show lower results during the wet season than the dry season. In 2016, some regions in Indonesia had been affected by the unusual precipitation such as the western part of North Sumatera, the western part of West Sumatera, South Sumatera, Lampung, West part of Java, Kalimantan, Sulawesi, and Papua. The unusual precipitation is a part of the La Niña phenomenon, which had occurred starting from June to September 2016. The high rainfall in Indonesia in 2016 could be a factor in the decline of water quality parameters value such as BOD, COD, and TSS.

5. CONCLUSION

Based on water quality sampling results, different land covers along Angke Watershed indicates different impact on water quality. Residential and commercial lands have positive correlation with some water quality parameters such as BOD, COD, and TSS. From spatial analysis using NDVI, dense vegetation in Angke Watershed has been decreased from 59.56 km^2 to 53.69 in 2014 and 2016 respectively. On the other hands, the results of the water quality analysis in 2016 showed better results compared to 2014. Some factors could bet he reasons of this occurrence such as the less significant decrease in dense vegetation, the efforts of the local government to improve water quality, and the unusual precipitation that occurred in Indonesia in 2016.

6. REFERENCES

Athukorala, S.W., Weerasinghe, L.S., Jayasooria, M., Rajapakshe, D., Fernando, L., Raffeeze, M., Miguntanna, N.P., 2013. Analysis of water quality variation in Kelani River, Sri Lanka using principal componet analysis. In Proceedings of the SAITM Research Symposium on Engineering Advancements, Malabe, Sri Lanka, 27 April 2013, pp. 129–135.

Bowden, C., Konovalske, M., Allen, J., Curran, K., Touslee, S., 2015. Water Quality Assessment: The Effects ff Land Use and Land Cover in Urban and Agricultural Land. Kansas, Natural Resources and Environmental Sciences (NRES) Kansas State University.

Boyd, C.E., 1990. Water Quality in Ponds for Aquaculture. Alabama, Agriculture Experiment Station, Auburn University.

Chan, F., J. A. Barth, J. Lubchenco, A. Kirincich, H. Weeks, W. T. Peterson, and B. A. Menge., 2008. Emergence of anoxia in the California Current large marine ecosystem. Science, 319, 920.

Effendi, H., 2003. Study of Water Quality. Yogyakarta, Kanisius, 258 p (In Indonesian).

Hendrawan, D., 2005. Water quality of river and lake in Jakarta. Makara 9(1), pp. 13-19

Ling, T.Y., Gerunsin, N., Soo, C.L., Nyanti, L., Sim, S.F., Grinang, J., 2017. Seasonal changes and spatial variation in water quality of a Large Young Tropical Reservoir and its downstream river. Journal of Chemistry Volume 2017, Article ID 8153246.

McGee, T., 1994. The future of urbanization in developing countries: the case of Indonesia. Third World Planning Review 16: iii-xii.

Peters, N.E., Meybeck, M., Deborah, V.C., 2016. Effects of human activities on water quality. In Encyclopedia of Hydrological Sciences. New York, Wiley & Sons, Ltd.

Rossi, L., Fankhauser, R., Chèvre, N., 2006. Water quality criteria for total suspended solids (TSS) in urban wet-weather discharges. Water Sci Technol. 54(6-7), pp 355-62.

Tong, S.T.Y., Chen, W., 2002. Modeling the relationship between land use and surface water quality. J. Environ. Manag. (66), pp 377–393.

Tu, Q., 1990. The Researches on the Eutrophication in Chaohu Lake Heifei. Anhui, University of Science and Technology of China Press.

Response Relationship Research Between Land Use and Water Quality inBaiyangdian Lake Based on GF-2

Liu Ke(1,2),Guo Chang(1),An Zhiyuan(1,2)

[1] North China Institute of AerospaceEngineering, 065000Lang Fang, China
[2] Collaborative Innovation Center of Aerospace Remote Sensing Information Processing and Application of Hebei Province, 065000 Lang Fang , China

Email:liuke1176@163.com

KEY WORDS: GF-2; Land Use; Water Quality Parameters; Correlation Analysis

ABSTRACT: As the largest freshwater lake in northern China, Baiyangdian is one of the typical water bodies with inevitable water pollution caused by human activities. Based on the source data of GF-2 multispectral satellite imagery and sampling points of the study area, land uses of Baiyangdian have been classified into eight categories by the maximum likelihood method. Spatial analysis of GIS(Geographical Information Science) have been used to obtain 100m, 300m and 500m buffers in order to calculate the area proportion of land uses in each buffer. Pearson correlation analysis was applied to explore the relevance of area proportion, types of land use, as well as water quality parameters. The results indicated that surface water and reed land were the dominate land use types in the Baiyangdian district. Bare land and cultivated land took the second place on it. However, commercial and tourism land, living land and bare land were the main sources of pollution, which were also positively correlated with TP and TN in 500m buffer area. While these three land-use types hadlittle relationship with COD and NH_3-N. Reed land was positively correlated with TP and TN. At the buffer of 300m, the correlation could reach the maximum value, indicating that reed land would able to purify water qualities.The water with more aquatic plants were negatively correlated with COD and NH_3-N, indicating that aquatic plants have the ability to absorb COD and NH_3-N. Besides, water with less aquatic plants were positively correlated with COD and NH_3-N. There is a possibility that COD and NH_3-N were contaminated by external sources.

1. Introduction

Land-use changes, a critical factor of water quality variations in inland waters, could be easily influenced by human activities. However, the contraction between nature and humans has been aggravated under the influence of intense human activities over the past few years (Seeboonruang,2012). Therefore,a large number of domestic and international scholars have been concentrating on studies of the impacts of land use on water quality. The correlations of land use and water quality could be devided into three categories by the ratios of different land use systems, according to a water quality study in Korea with nonlinear models made by Hwang Sun-Ah et al (Hwang Sun-Ah,2016). Susanna T.Y.Tong et al used BASINS Modeling techniques to simulate the effect of land use on water quality in the little Miami river basin, and the conclusion could be drawn that there was a significant relationship between land uses and water pollutants, such as nitrogen and phosphorus (Susanna T.Y.Tong,2002). Generally speaking, building land have a negative impact on the quality of water bodies, while forest land have a positive effect on it. The conclusion was reached by HaoJingfeng et al on the calculation of water quality index WQI (Hao Jingfeng,2010). Liang Ping et al conducted a study testing the relationship of land uses and water qualities in Hanjiang with Geographically Weighted Regression and found that the contents of COD, NH_3-N, TN in water were positively correlated with the acreages of woodland (Liang Ping,2017). Similarly, Jiang Chang et al utilized the Spearman's rank correlation correlation to analyze the land use and water quality data of Hongfeng Lake in Guiyang, and the results showed that the construction land area was positively correlated with COD, NH_3-N, TP (Jiang Chang,2018). Moreover, the poor water quality may probably owing to the serious industrial and domestic polution. Correlation analysis and redundancy analysis have been applied in the study of Chongqing. The study area including six rivers was chosen. The results showed that construction land and agricultural land had obvious effects on water quality deterioration, and wood land could improve water quality significantly (Lü Zhiqiang,2016).There were many published papers studied on the relationship between land use and water quality of Taihu Lake, the third largest fresh water lake in China. For example, by means of redundancy analysis method, Zhou Wen et al have revealed that water quality could beeasily affected by landscape factors, and the water quality would be scale-dependent and location-specific. It was shown that the upstream settlement land is positively correlated with NH_3-N, TP, DO, while the

downstream cultivated land is positively correlated with NH_3-N, TP, DO (Zhou Wen,2012). Liu Qian et al used pearson correlation analysis method to find that the wood land and grassn land were negatively correlated with COD_{Mn}, which indicated that both of them had an interception and absorption effect on pollutants (Liu Qian,2016); Using the grey correlation method, Gao Bin et al found that the grey correlation degree between water quality and urban land was the highest, followed by paddy field and dry land, and the lowest in water and woodland (Gao Bin,2017). Related studies show that water quality is easily affected by the surrounding land use type.

2. Summary of Research Area

Baiyangdian lake, also known as Lake Baiyangdian, is located in the Xiong'an New Area of Baoding, a city in Hebei province, China. It is the largest freshwater lake in northern China (Ma Muyuan,2018).Famed as the "Bright Pearl", it covers a large area of 366 square kilometers, with an average water capacity of 1.32 billion vubic metres. The area of Baiyangdian lake once had reached its maximum value in history, which is a thousand square kilometers. There was a time when rivers including Jiulong River, Xiaoyi River, Tang River, Fuhe River, Caohe River, Baohe River, Qingshui River, Pinghe River and Baigouyin River was flowing into the lake, as "nine rivers into the top". Nevertheless, in recent years, the Zhulong River, Tang River, Qingshui River and Pinghe River have been dried up for a long time. While Caohe River, Xiaoyi River and Baohe River have either shrunk or become seasonal. The Fuhe River, the only perennial river nowadays, is also the main drainage channel for domestic sewage and industrial waste water in Baoding (Liang Huiya,2017).

Baiyangdian is one of the shallow closed-basin lakes. Thus the self-regulation ability of the lake is considerably low. Faced with the double predicament of water pollution and water shortage, the watershed area of Baiyangdian is shrinking and splitting. Because of the serious eutrophication in Baiyangdian, the ecological function in this area have been sharply declined and the ecosystem balance have become more fragile (Ma Jing,2008).

"Hebei Xiongan New Area Planning Outline" have been implementedin April 2018, by the Chinese Communist Party Central Committee, puting forward the concept of "Implement ecological restoration of Baiyangdian, strengthen ecological construction, and carry out comprehensive environmental management." Therefore, it is necessary to take Baiyangdian lake as the study area to explore the impact of land use types on water quality and find out the key factors ofecological environment management in Baiyangdian lake.

3. Land Use Classification in Each Buffer Zone

At 3th November, 2017,16 field sampling points had been completed and the water quality monitoring indicators,including chemical oxygen demand (COD), ammonia nitrogen (NH_3-N), total phosphorus (TP) and total nitrogen (TN) (Table 1) had been received. Four multispectral images of 22th March 2018 of GF-2 high-resolution imaging satellitein have been downloaded. The images, which had the closest sampling time and the most similar climatic characteristics, were processed for radiometric correction, geometric correction, mosaic and clipping. Referring to "Classification of land use status" (GBT 21010-2017) and the actual situation of Baiyangdian lake in 2017,the land use types of Baiyangdian lake could be divided into eight categories by using maximum likelihood method (Xia Rui,2010).

The land use types, including reed land, cultivated land, bare land, commercial and tourism land, living land and the water with a large number of hydrophyles (lotus root and other aquatic plants with high coverage), abandoned aquaculture ponds, ordinary water (the water without or with a little vegetation coverage on surface) (Zhang Min,2016). Combined with field sampling for supervised classification, the classification results were corrected peripheral photographing and attribute information entry to ensure the classification accuracy.

The sampling points were selected in the center of each buffer area, and the results of the buffer zone and land use type classification were superimposed after samples with a radiu of 100m,300m and 500m buffer zone were respectively selected. The land use types of different buffer zones of each sampling point were obtained (Figure 1). The area proportion of land use types in different buffer zones of each sampling point was calculated.(Figure 2-4).

Table 1 Field sampling point water quality parameters

| Number	Sampling location	COD（mg·L^{-1}）	NH$_3$-N（mg·L^{-1}）	TP（mg·L^{-1}）	TN（mg·L^{-1}）
1	Sediment1	41	0.338	0.124	3.039
2	Sediment2	24	0.347	0.036	2.979
3	Wangjiazhai Resort	39	0.318	0.094	3.589
4	Wangjiazhai Village	47	0.880	0.151	4.219
5	Xing cao Hillock	41	0.379	0.125	3.429
6	Lu jia Bay	45	0.367	0.139	3.989
7	Duck Ring	52	1.402	0.157	7.529
8	Yeouido	42	1.492	0.180	8.579
9	Cultural Garden	32	1.141	0.130	7.519
10	Little Zhangzhuang	38	0.996	0.128	7.169
11	Xue Jiadian	46	0.338	0.101	5.049
12	Circle duck Pit	30	0.414	0.176	8.109
13	Duck Pit	17	0.579	0.168	7.979
14	Circle head Township	22	0.399	0.166	7.909
15	Shao Zhuangzi	8	0.437	0.170	7.989
16	Guangzhuang Zhangzhuang Village	4	0.437	0.164	6.819
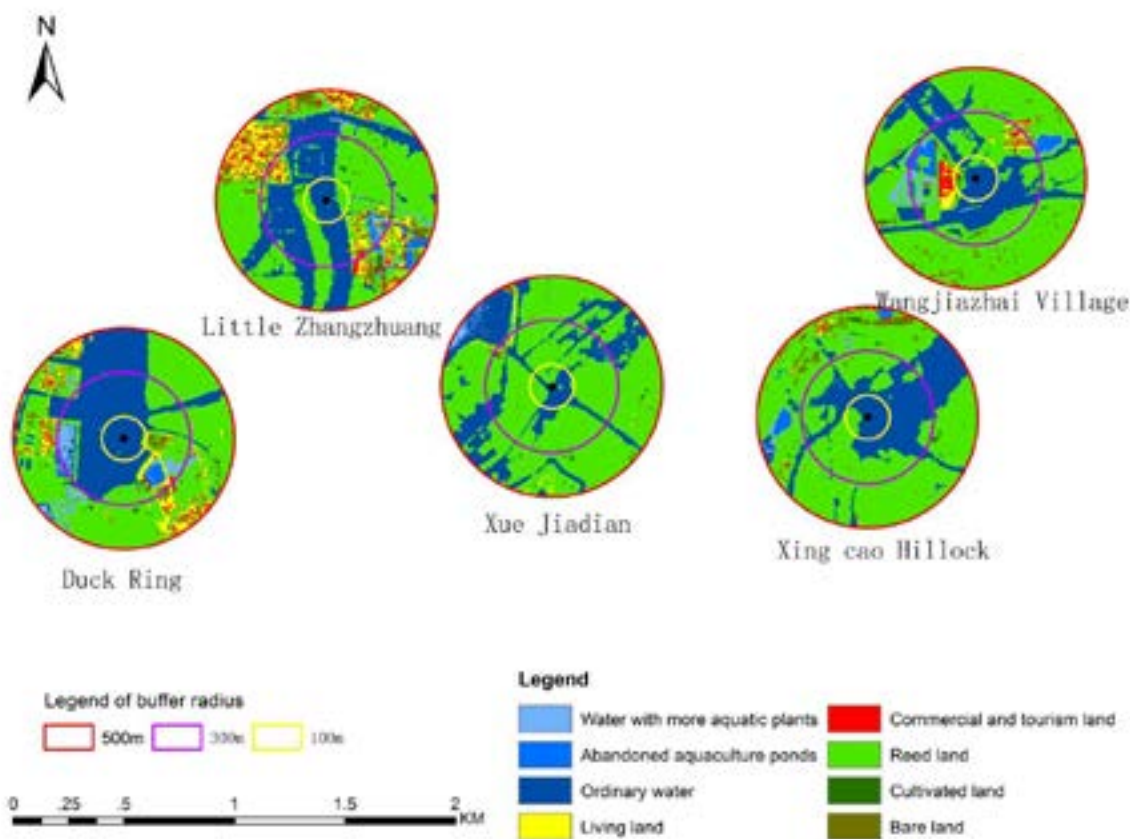
Figure 1 Partial buffer land use classification results in Baiyangdian lake

Figure 2 Proportion of land type area of 16 sampling points in 100m buffer zone
(The vertical axis is the area ratio of land use type, and the horizontal axis is the name of 16 sample points.The order of the land use type is bare land, cultivated land, reed land, commercial and tourism land, living land,ordinary water, abandoned aquaculture ponds, the water with more aquatic plants.)
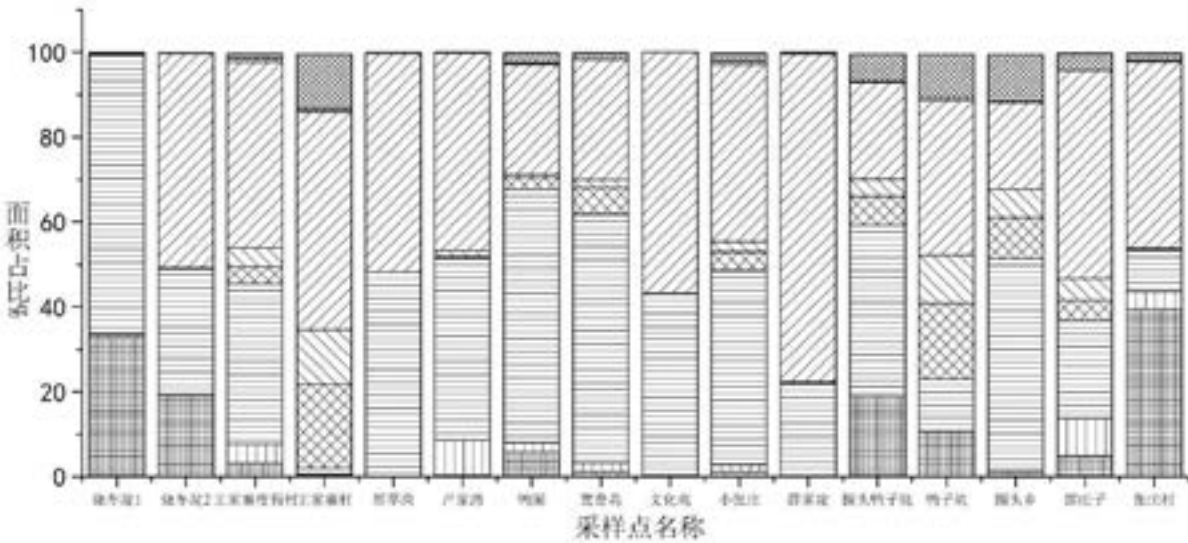
Figure 3 Proportion of land type area of 16 sampling points in 300m buffer zone
(The vertical axis is the area ratio of land use type, and the horizontal axis is the name of 16 sample points.The order of the land use type is bare land, cultivated land, reed land, commercial and tourism land, living land,ordinary water, abandoned aquaculture ponds, the water with more aquatic plants.)
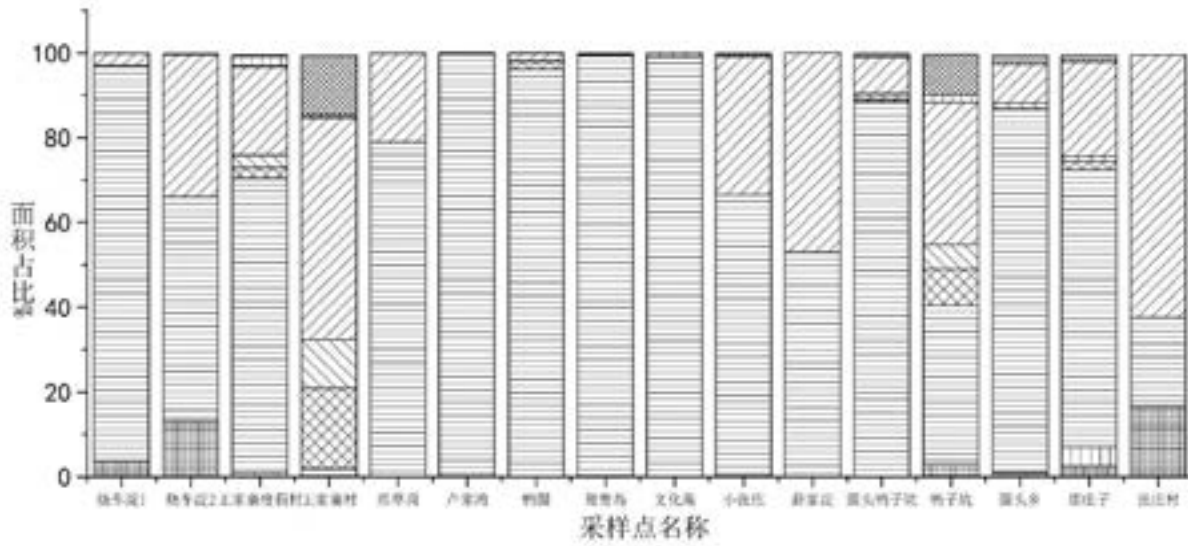
Figure 4 Proportion of land type area of 16 sampling points in 500m buffer zone
(The vertical axis is the area ratio of land use type, and the horizontal axis is the name of 16 sample points. The order of the land use type is bare land, cultivated land, reed land, commercial and tourism land, living land,ordinary water, abandoned aquaculture ponds, the water with more aquatic plants.)
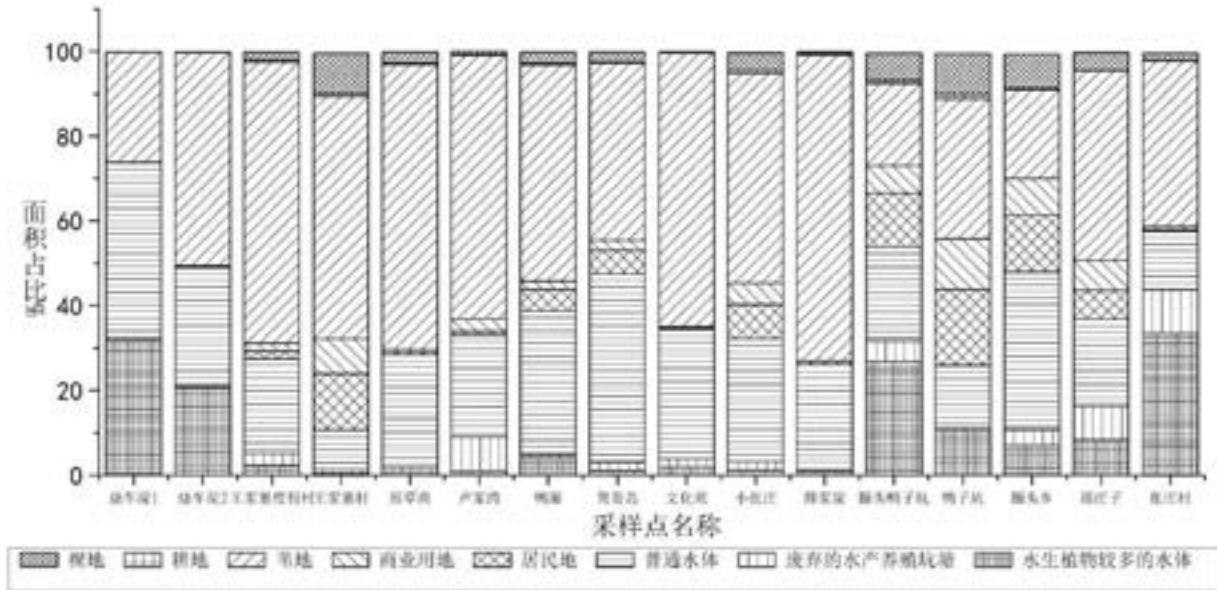
4. Response Relationship Between Land Use and Water Quality

According to the Environmental Quality Standards ofSurface Water (GB 3838-2002), it could be determined that the water quality of Baiyangdian lake sampling points mostly belongs to oxygen consumption,nitrogen and phosphorus pollution (Figure 5).

Because the Fuhe River is only river that flow into the lake, it is possible that the water pollution could be affected by the land use status of the lake area itself. The correlation between the area proportion of land use types and the water quality monitoring indicators was analyzed (Table 2-4). According to the results of statistical classification, the abandoned aquaculture ponds accounted for a small propotion of the 100m buffer zone of each sampling point. Therefore, it's not scientific to discuss the correlation between land use types and water quality parameters of abandoned aquaculture ponds in the 100m buffer zone.
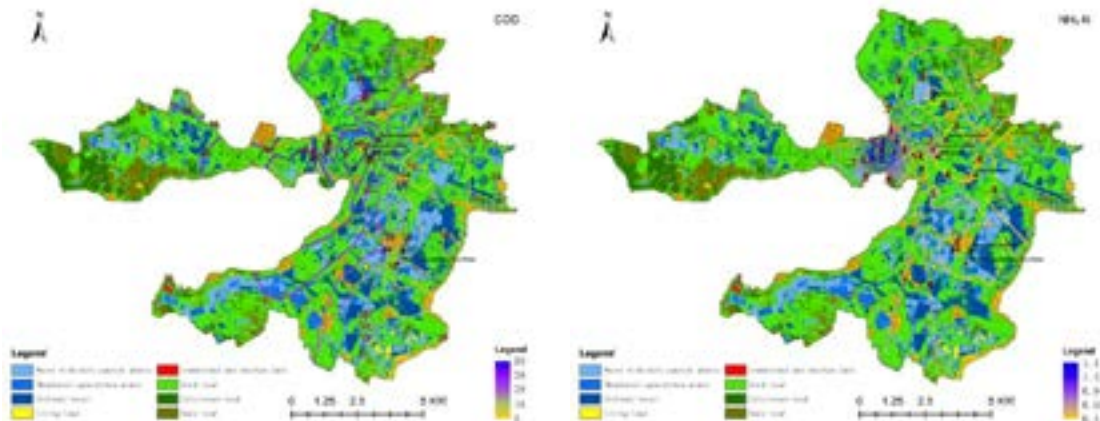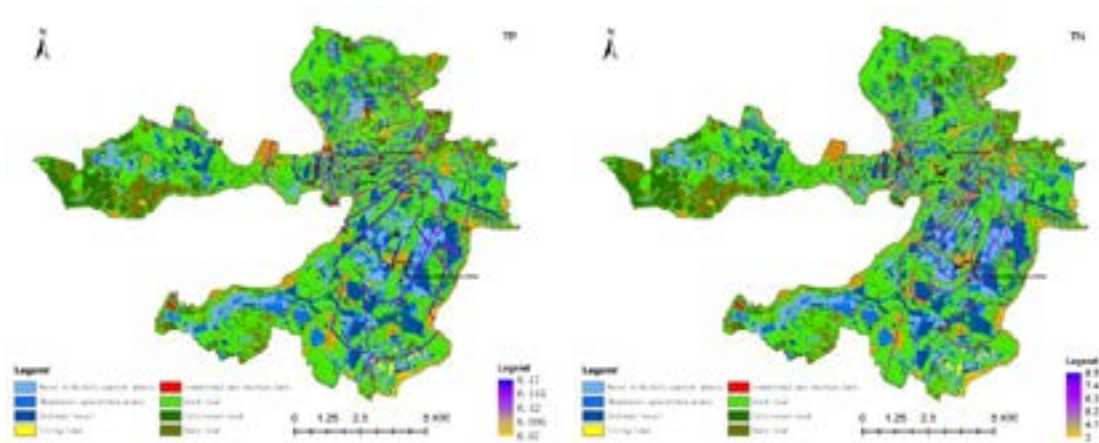
Figure 5 The picture of study area and main pollution type
（The base map is a land use classification map, and the contour is the Kriging interpolation result）

4.1 Within 100m Surrounding Area

Table 2 Correlation coefficient between land area type and water quality parameters in 100m

Land use type	Buffer distance/m	COD	NH₃-N	TP	TN
Cultivated land	100	0.37	-0.14	0.06	-0.07
Reed bed	100	-0.31	-0.16	-0.11	-0.09
Commercial and tourism land	100	0.15	-0.11	-0.19	-0.60
Living land	100	0.17	0.10	-0.03	-0.30
Bare land	100	0.04	0.06	0.21	-0.31
Water with more aquatic plants	100	-0.51	-0.31	-0.28	-0.25
Ordinary water	100	0.33	0.22	0.08	0.16

* indicates a significant correlation at the 0.05 level (both sides).

COD: The largest negative correlation is the water with more aquatic plants, the correlation coefficient is -0.51, followed by is the reed land, the correlation coefficient is -0.31, and the cultivated land and ordinary water are positively correlated with COD, and the correlation coefficients are 0.37 and 0.33. Commercial and tourism land, living land and bare land have low correlation with COD, it can be speculated that there is little relationship with COD concentration. According to the field investigation, the aquatic plants are mainly lotus roots, which are mostly distributed in the water between the land and the channel. Some areas are submerged aquatic plants, and the reeds are mainly terrestrial. The aquatic reeds are more than 2 meters on the shore. The results showed that aquatic plants have a better effect on COD, and terrestrial reeds have less COD purification ability than aquatic reeds.

NH₃-N: The same as COD, the largest negative correlation is the water with more aquatic plants with a correlation coefficient of -0.31. It can be seen that aquatic plants have an absorption effect on NH₃-N, but it is not strong. Other land types are related to NH₃-N. It also shows that the correlation between NH₃-N and the adjacent environment is not obvious, and within 100m buffer, it is mainly carried by the water itself.

TP: The largest negative correlation is the water with more aquatic plants, the correlation coefficient is -0.28. The aquatic plants have the possibility of absorbing NH₃-N, and the other land types have little relationship with TP. It shows that TP is similar to NH₃-N, which has little correlation with the adjacent environment. Within 100m buffer, it is mainly carried by the water itself.

TN: The correlation with commercial and tourism land is -0.6, followed is the living land, bare land and water with more aquatic plants. In the range of 100m, the commercial and tourism land is mainly based on scenic spots, and the surrounding villages have high vegetation coverage and good environmental planning.

In the buffer of 100m, aquatic plants have a better improvement effect on water quality, and the scenic spots are conducive to the purification of TN. Living land, bare land and cultivated land have little effect on the water quality of adjacent water.

4.2 Within 300m Surrounding Area

Table3 Correlation coefficient between land area type and water quality parameters in 300m buffer

Land use type	Buffer Distance/m	COD	NH₃-N	TP	TN
Cultivated land	300	0.11	0.04	0.04	-0.05
Reed bed	300	0.12	-0.29	-0.56*	-0.55*
Commercial and tourism land	300	-0.15	-0.01	0.39	0.21
Living land	300	-0.04	0.14	0.43	0.24
Bare land	300	-0.24	0.00	0.47	0.28
Water with more aquatic plants	300	-0.43	-0.44	-0.10	-0.22
Abandoned aquaculture ponds	300	-0.17	-0.22	0.18	0.04
Ordinary water	300	0.45	0.28	0.00	0.02

* indicates a significant correlation at the 0.05 level (both sides).

COD: The largest negative correlation is the water with more aquatic plants, the correlation coefficient is -0.46, and the ordinary water is positively correlated with COD. The correlation coefficient is 0.45, which is slightly enhanced compared with the 100m range. Reed land, commercial and tourism land, livingland and bare land have weaker relationship with COD. The biggest difference from the 100m range is that the influence of reed land is weakened.

NH₃-N: Similarly to the situation of COD in the range of 100m, the largest negative correlationis water with more aquatic plants, the correlation coefficient is -0.44, slightly enhanced compared with 100m, and other land types are weaker than NH₃-N. The same as the 100m range, it indicating that the correlation between NH₃-N and the surrounding environment is small, the local sourcesare weak, and aquatic plants have an effect of absorption.

TP: The largest negative correlation is reed land, reaching -0.56. Bare land, living land and commercial and tourism land are positively correlated, and other land types are weakly correlated with TP. It can be seen that in the range of 300m, the influence of the surrounding environment on TP is enhanced compared with 100m, and the reed land has an absorption effect on TP.

TN: Similar to the performance characteristics of TP, the correlation between reed land is -0.55, but the correlation between living land, bare land and commercial and tourism land is weak. The influence of the surrounding environment on TN is quite different from that of 100m, and the reed land has a strong absorption effect on TN.

The same range as 100m, water with more aquatic plants and reed land have better effect on water quality, aquatic plants have absorption of COD and NH₃-N, which is different from the reed land. The reed landcan reduce the content of TN and TP, which is significantly improved over the 100m range.

4.3 Within 500m Surrounding Area

Table 4 Correlation coefficient between land area type and water quality parameters in 500m buffer

Land use type	Buffer Distance/m	COD	NH₃-N	TP	TN
Cultivated land	500	0.07	-0.03	0.27	0.23
Reed bed	500	0.45	0.08	-0.49	-0.45

Commercial and tourism land	500	-0.31	0.00	0.55*	0.48
Living land	500	-0.20	0.13	0.56*	0.53*
Bare land	500	-0.20	0.05	0.55*	0.41
Water with more aquatic plants	500	-0.52*	-0.40	0.01	-0.05
Abandoned aquaculture ponds	500	-0.56*	-0.26	0.40	0.24
Ordinary water	500	0.34	0.34	-0.05	0.10

* indicates a significant correlation at the 0.05 level (both sides).

COD: The largest negative correlation are the water with more aquatic plants and abandoned aquaculture ponds, with correlation coefficients of -0.52 and -0.56, respectively. The reed land is slightly positively related to ordinary water, and the correlation of other land types is not obvious.

NH$_3$-N: The largest negative correlation is the water with more aquatic plants with a correlation coefficient of -0.40. Other land types are weakly correlated with NH$_3$-N. Same as the range of 100m and 300m, indicating that the local source of NH$_3$-N is weak and the aquatic plants can absorb it.

TP: The maximum negative correlation is reed land, which is -0.49, similar to the range of 100m and 300m. Commercial and tourism land and living land are positively correlated, the correlation coefficient are 0.55 and 0.56. Large scale land for tourism use and living land are important source of TP in Baiyangdian. From 100m to 500m, the influence of the surrounding environment on TP is gradually increased.

TN: The correlation between reed land is -0.45, and the living land is 0.53,which is one of the most important sources of TN. The impact of bare land and commercial and tourism land are higher than 300m. The influence of the surrounding environment on TN is quite different from that of 100m and 300m. With the change of distance, TN has became uncertain.

In the 500m range, living land may be the one of local sources of TP and TN. Commercial and tourism land may be the one of local sources of TP. Commercial areas and bare land may be local sources of TN, but doesn't significant. The water with more aquatic plants and reed land have better effects on the improvement of water quality. Aquatic plants have absorption effects on COD and NH$_3$-N, while reed land have better purification effects on TN and TP.

In general, aquatic plants and reed have a purify effect on water in the range of 100m~500 m. Aquatic plants mainly absorb COD and NH$_3$-N, while reed is beneficial to the reduction of TP and TN. Living land and commercial and tourism land may be local sources of TN and TP, while ordinary water is positively related to all pollutants. As the distance increases, the pollution trend is weakened, indicating that around the water exist the frequent discharges behavior.

5. Conclusion

Studies have shown that aquatic plants and reeds have a purifying effect on water. Aquatic plants have the ability to absorb COD and NH$_3$-N pollution in the range of 100m~500m. Reeds in the range of 300m~500m are beneficial to the reduction of TP and TN concentrations, but there is a possibility of positive correlation with COD at 500m. Living land, commercial and tourism land might be the local sources of TN, and living land could be one of the important local sources of TP. Living land has frequent sewage discharges mainly based on TN and TP. This conclusion was basically consistent with the results of Liu Feng et al on the study of Baiyangdian. In contrast with TP and TN, ordinary water accounts for the large propotion of the main water bodies, which has a positive correlation with the concentration of COD and NH$_3$-N (Liu Feng,2010). Living land, commercial and tourism land are related to TP and TN, and have little relationship with COD and NH$_3$-N, indicating that NH$_3$-N and COD are carried by water itself, and external pollution were existed.

References

Gao Bin, Xu Youpeng, Wang Qiang, Yang Jie, Shen Shunzhong, Xu Xing. Effects of land use changes on water quality of the plain area in Taihu Basin. Journal of Agro-Environment Science, 36(6), pp. 1186-1191.

Hao Jingfeng, Liu Hongyu, Hu Junna, Cao Xiao. Influence of Land Use on Water Quality in Urban Area—A Case Study of Zijin Mountain in Nanjing. Journal of Nanjing Normal University(Natural science edition), 33(1), pp. 125-129.

Hwang Sun-Ah, Hwang Soon-Jin, Park Se-Rin, Lee Sang-Woo, Yu Y.Jun. Examining the Relationships between Watershed Urban Land Use and Stream Water Quality Using Linear and Generalized Additive Models. Water, 8(4), pp. 155.

Jiang Chang, Liu Hongyan, Chen Zhu, Rao Cheng, Li Zhengdao, Yang Tongshuan, Wu Pan. Response relationship between land-use change and water quality in Hongfeng Lake basin based on GIS. Journal of Agro-Environment Science, 37(6), pp. 1232-1239.

Liang Huiya, Zhai Deqin, Kong Xiaole, Quan Ruiqiang, Wang Shiqin. Sources, migration and transformation of nitrate in Fuhe River and Baiyangdian Lake, China. Chinese Journal of Eco-Agriculture, 25(8), pp. 1236-1244.

Liang Ping, Guo Yiming, Liu Wenwen. Identifying the Relationship between Land Use Types and Water Quality of Han River Watershed Using Geographically Weighted Regression Model. Safety and Environmental Engineering, 24(2), pp. 67-74, 90.

Liu Feng, Liu Jingling, Zhang Ting, Chen Qiuyin. Land Use Change and Its Effects on Water Quality in Baiyangdian Lake of North China During Last 20 Years. Journal of Agro-environment Science, 29(10), pp. 1868-1875.

Liu Qian, Liu Yongjie, Yu Hui, Yang Chao, Niu Yong, Niu Yuan. The Correlation Study of Land Use And Water Quality Pollution Condition in Taihu Lake Watershed.Environmental Engineering, 2016, 8, pp. 11-17.

Lü Zhiqiang, Qing Xuyao, Ren Yufen, Wang Xiaoke, Pang Rong. Effects of land use pattern on water quality in mountainous city—a case study of Chongqing City. Journal of Lake Sciences, 28(2), pp. 319-327.

Ma Jing, Zhang Suzhen, Wang Yukun, Liang Yun. Primary Study of Ecological Carrying Capacity in Baiyangdian Lake. South-to-North Water Transfers and Water Science& Technology, 6(5), pp. 94-97.

Ma Muyuan, Cui Lijuan, Zhang Manyin, Wang Xuemei, Yu Yilei. Primary production of periphyton and their relationship to water quality in Baiyangdian Lake, China. Acta Ecologica Sinica, 38(2), pp. 443-456.

Seeboonruang, Uma. A statistical assessment of the impact of land uses on surface water quality indexes. Journal of Environmental Management, 2012, pp. 134-142.

Susanna T.Y.Tong, Wenli Chen. Modeling the relationship between land use and surface water quality.Journal of Environmental Management, 2002, 66, pp. 377-393.

Xia Rui, Li Yunmei, Wang Qiao, Xu Enhui, Jin Xin, Wang Yanfei. Research on the Relationship between Land Use and Transit Water Quality Response in Wuxi City Based on Remote Sensing. Geography, 30(1), pp. 130-133.

Zhang Min, Gong Zhaoning, Zhao Wenji, A Duo. Landscape pattern change and the driving forces in Baiyangdian wetland from 1984 to 2014. Acta Ecologica Sinica, 36(15), pp. 4780-4791.

Zhou Wen, Liu Maosong, Xu Chi, He Ge, Wang Lei, Yang Xuejiao. Response of river water quality to background characteristics of landscapes in Taihu Lake basin. Acta Ecologica Sinica, 32(16), pp. 5043-5053.

CORRELATION OF DESERTIFICATION WITH LAND AND WATER USE IN TURKEY

Gaye Onursal Denli (1), Hayri Hakan Denli (1)

[1] Istanbul Technical University, Civil Engineering Faculty, Geomatics Department,
Maslak, 34469 Istanbul, Turkiye
Email: onursal@itu.edu.tr; denli@itu.edu.tr

KEY WORDS: Climate, Desertification, Water, Land use

ABSTRACT: Drought is defined as a natural event that occurs when the amount of precipitation is significantly less than normal, causing severe hydrological imbalances that negatively affect land resources and production systems. Majority of Turkey is located in the Mediterranean Climate Zone where significant differences in seasonal rainfall can be observed. Since one of the characteristics of the Mediterranean Climate Zone is the periodic variations of rainfall amounts, drought episodes are inevitable. As a result, drought is one of the climate-related problems that Turkey experiences and likely to encounter frequently. Along with that, incorrect use of land, wrong agricultural policy and the wastage of water added to the drought will have a very serious problem. Turkey experienced the worst drought in last 44 years in 2017, due to a substantial decrease in rain levels. Non-sustainable agricultural practices cause pollution of freshwater resources and deterioration of arable land. Freshwater resources constitute only 2.5 percent of the world's water resources. However, less than 1 percent of all freshwater resources can be used by ecosystems and people. Turkey utilizes approximately 75% of its fresh water for the irrigation and cultivation of its crops. In the current drought, Turkish farmers now need to irrigate and use their supply of water more effectively. Up until now poor irrigation techniques have not caused serious difficulties but it will be after that. Analysis of satellite images reveals the drought of many important water resources and agriculture regions in Turkey. Turkey Desertification Risk Map has been created based on all analysis and is of great importance for the future of the country. In this study, the impact of desertification will be emphasized, presented with maps and satellite imagery and the measures to be taken against the sensitivity of the subject will discussed.

1. LAND USE in TURKEY

Turkey, 27.6% of its land covered with forests and 31.1% of its land covered with agricultural areas has many plant species and rich fauna resources; is among the countries rich in biodiversity among temperate generations. The distribution of Land Use Classes in Turkey is shown below.

Land Use Classes in Turkey

Forest (27,6)

Rangeland (18,6)

Agricultural Land (31,1)
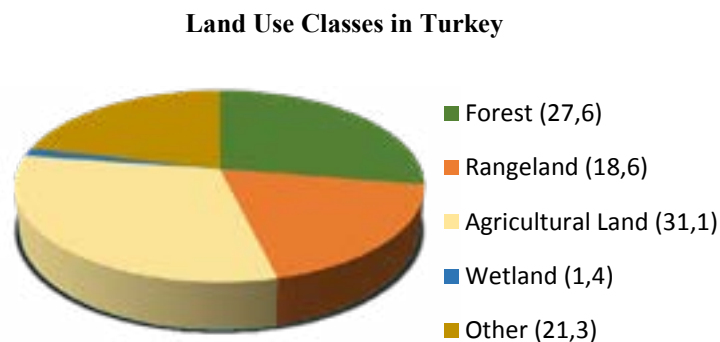
Wetland (1,4)

Other (21,3)

Figure1. Land Use Classification (URL1).

There are a large number of ecosystems in Turkey based on ecological and floristic composition of forest habitats, and the function of each ecosystem is more or less different. The Mediterranean biogeographic region covers all the coastal regions of the Mediterranean and the western part of Thrace and includes many

different ecosystems. Turkey's areas according to topographical structure, climate and soil differences are very rich in terms of plant diversity. But degradation and fragmentation of agricultural areas effected land and water use negatively. Especially fragmented agricultural areas needs land consolidation. Irrigation systems should be regulated in this operation. But this operation requires huge and complex organization and big budget.

In areas where Mediterranean climate is influential, ecosystem can range from sea level to the highest parts of the mountains depending on soil-climate-plant relationships. The continental climate and steppe plants are suppressed in Central and East Anatolia region. The Europe-Siberian biographical region stretches from North Anatolia to the Black Sea and Thrace Region to the Black Sea. It is the wettest climatic region, with a large part covered with forests. More than half of the forest ecosystems in Turkey have been destroyed. Too much deforestation activities reduced rains.

2. WATER USE in TURKEY

Water is essential for human security and sustainable socio-economic development. It is an essential element for the eradication of poverty and hunger. More than half of the world population will be living with water shortage within 50 years because of a worldwide water crisis, according to a report issued by the United Nations Environment Program. In other words, it is highly unlikely that there is going to be enough water for everybody unless the necessary steps are taken at regional and global level. While the world's population grew three fold, water use increased six fold during the same period. The demand on water resources will continue to increase during the next twenty-five years. The problem is further aggravated by the uneven water distribution on earth.

Turkey is situated in a semi-arid region, and has only about one fifth of the water available per capita in water rich regions such as North America and Western Europe. Water rich countries are those which have 10.000 cubic meters of water per capita yearly (URL2). Turkey is one of the most water rich countries of the Mediterranean, but due to an enormous population increase from 28 million in the 1960's to 68 million in 2000 the availability of water resources has already decreased from around 4000 m^3 to 1500 m^3 per capita/year today (Bayram et al.,2014).

Water demand in Turkey approximately has doubled in the second half of the last century. Another point is that Turkey's water is not always in the right place at the right time to meet present and anticipated needs. Increasing agricultural production by irrigation is one of the most important means for combating poverty and hunger in developing countries. In arid and semi-arid regions where precipitation is generally limited to four or five months a year, water resources development projects are indispensable for sustainable socio-economic development. A case in point is the Middle East (URL2).

Rivers are one of the main sources of freshwater. 70 percent of the total easily accessible water is provided by rivers. The Euphrates and the Tigris are two of the most famous rivers in the world. The combined water potential of the two rivers is almost equal to that of the Nile River. Both rise in the high mountains of north-eastern Anatolia and flow down through Turkey, Syria, and Iraq and eventually join to form the Shatt-al-Arab 200 km before they flow into the Persian Gulf. They account for about one third of Turkey's water potential. Both rivers cross the south-eastern Anatolia region which receives less precipitation compared to other regions of Turkey. Turkey contributes 31 billion cubic meters or about 89 per cent of the annual flow of 35 billion cubic meters of the Euphrates. As to the Tigris, the picture is entirely different. 52 per cent of the total average flow of 49 billion cubic meters come from Turkey.
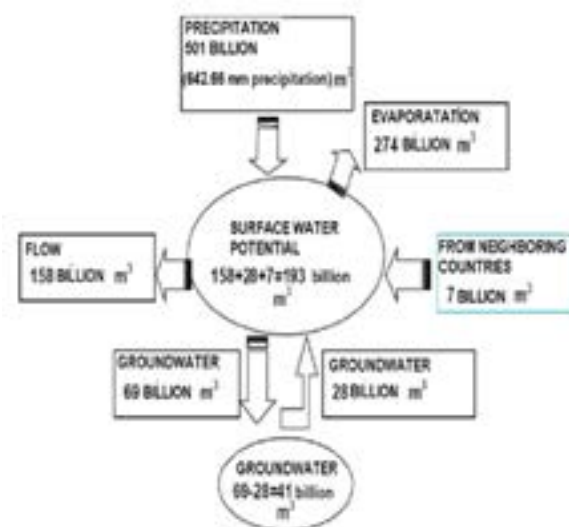
Figure 2. The Water Potential of Turkey (Altinbilek, 2004)

73.2% of the total water supply of Turkey is used for agricultural irrigation, remaining 15.5% and 11.3% are used for drinking-domestic and industrial purposes, respectively (Bayram et al., 2014).

2.1 Agricultural Irrigation

Agriculture is the largest user of water in Turkey with 75 percent of the total consumption. Turkey has developed 50 percent of total irrigable land so far. Water is a limiting factor for agriculture throughout much of Turkey. Turkey, like many countries today, faces challenges in efficiently developing and managing its agricultural water resources while trying to protect water quality and the environment. However, Turkey has some difficulties and problems on water use for agriculture Evaluation of the current situation ends in the conclusion that Turkey needs a comprehensive monitoring and evaluation system both at basin and scheme level, and rehabilitation of irrigation systems for efficient water use in agriculture (Cakmak, 2004).

The growing period for most crops in Turkey are the summer months of June, July, and August during which there is almost no rain and rivers have their lowest base flows. Therefore, water storage is essential. DSI projects are generally based on surface (gravity) irrigation methods, using either classical open channel systems or raised canalets. Sprinkler irrigation has been used in certain projects under specific conditions. Almost 90 percent of the total areas use surface irrigation methods (furrow, basin, and flooding).

Figure 3. Surface (Gravity) Irrigation.

The remaining area of an estimated 200,000 ha uses pressurized irrigation which is common among farmers throughout the country that is not enough.

Figure 4. Pressurized and Sprinkler Irrigation

The ratio of irrigation requirement of delivered water is over one. The delivered water is about two or three times of that needed. The main reason for this is that there is a large amount of water loss at both scheme and field levels. The irrigation water price is too low which leads to excessive water use in agriculture.

3. DESERTIFICATION

3.1. Current Status of Desertification in Turkey

Turkey is home to an estimated 77.7 million people and is approximately 301,382 square miles in size which is larger than some cities. The country is home to diverse topography with includes many mountain ranges, forests, coastline, and its inland tundra, which is partial desert and partial fertile land. During the months of April to August, Turkey experiences very little precipitation and its temperature averages around 24 degrees Celsius.

During the winter season each year Turkey experiences high levels of precipitation, which accounts for the majority of the precipitation that Turkey gets annually. Starting in December of 2006 and lasting until November of 2008, Turkey experienced a major drought that lowered the levels of its water reservoirs and dams by over 50 percent. In late 2012 Turkey experienced a mild drought and in the fall of 2013 the drought worsened and spread out across much of the southern and central areas of Turkey. As the article, "Drought in Turkey", "The cumulative precipitation for all of Turkey between October 1, 2013 and January 17, 2014 was 37% less than the long-term average and 47.4% less than the average for 2013" (Kurnaz, 2014).

In Turkey agriculture is one of the largest industries, and it has recently emerged as one of the world's largest exporters of food. Over the past few decades much of Turkey's economic growth is a result of its agricultural production. Presently, the agriculture industry makes up twenty percent of the employment opportunities in Turkey. While agricultural exports only accounted for 9% of Turkey's export earnings approximately, 50% of the manufactured exports also originate in the agricultural sector.

For a long time Turkey has faces relatively little trouble managing its water resources due to an abundance of annual rainfall. In fact, Turkey utilizes approximately 75% of its fresh water for the irrigation and cultivation of its crops. In the current drought, however, many of Turkey's reservoirs and dams have been drained in order to water the crops. The majority of the dams and reservoirs in Turkey have dropped below 50% capacity in 2014 and consistently seen decreases. Since there is normally an abundance of water and no need to irrigate and regulate usage among farmers, the current drought environment is one in which water is being wasted and not used correctly. For thousands of years farmers in Turkey have been able to grow crops without the need for irrigation; however, Turkey's drought, rising population, and increase in crop production will combine to prevent farmers from continuing to use the same methods that they have been using (Kurnaz, 2014). Turkish farmers have to use of surface water / underground water more effectively for irrigation. The signs of the drought in Turkey are shown with very clearly examples given below.

Figure 5. Salt Lake in Central Anatolia (URL3)

Due to global warming, drought and agricultural irrigation, Salt Lake shrank 85 percent in 90 years. Therefore, Beysehir Lake was Turkey's second largest lake. While the water surface area of Tuz Gölü is 92 thousand 600 hectares in 1987, it can be seen clearly in the satellite pictures which has decreased to 32 thousand 600 hectares in 2005.

Figure 6. Meke Lake in Konya Karapinar

Meke Lake in central Turkey has largely dried up due to faulty irrigation methods, which drained off underground water sources feeding the lake, according to experts. Wild flooding irrigation is one of the causes of desertification in Turkey.
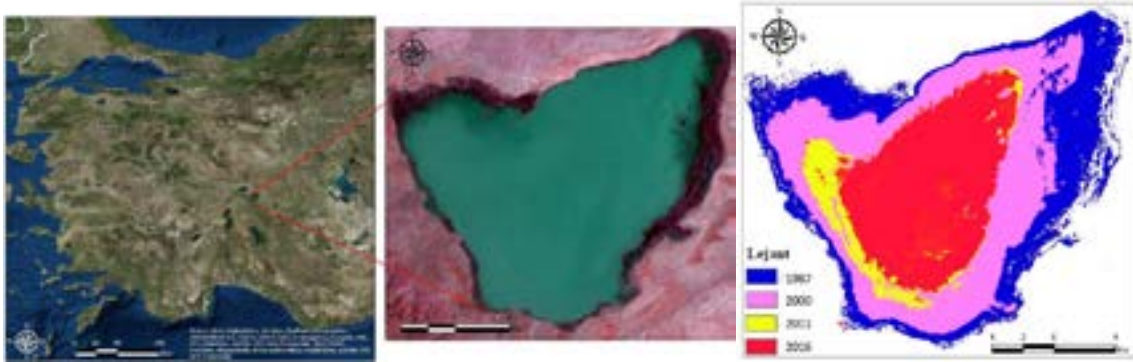
Figure 7. Aksehir Lake (1987-2016 Landsat (4, 2, 3 Band combination)) in Central Anatolia. (Kaplan, 2016)

According to the results of NDWI analysis applied to the images;
The water area of Aksehir Lake has decreased considerably from 1987 to 2016 (Figure x). While the area covered with water in the lake was approximately 324 km 2 in 1987, it decreased to 100 km 2 in 2016. The study shows that water field changes from the NDWI results decrease at the same rate every year (Kaplan, 2016).
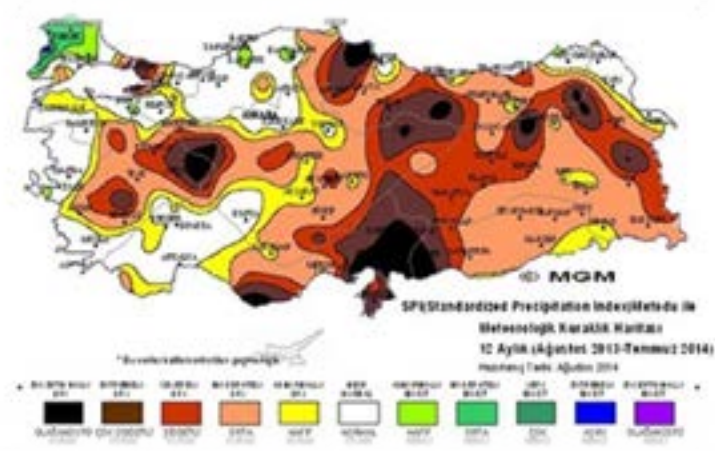

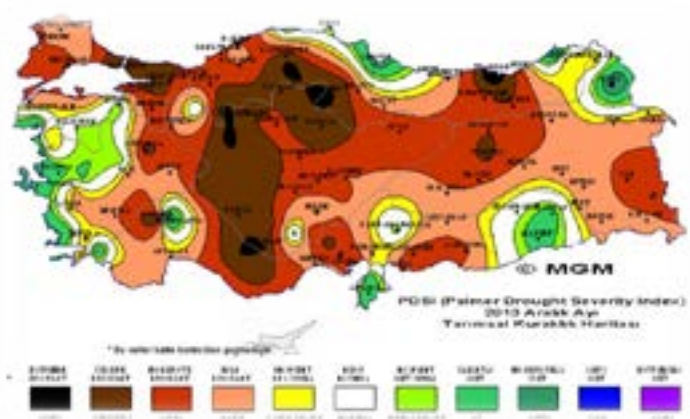Figure 8. Turkey's Average Drought Map with SPI (Standardized Precipitation Index) method (URL4).

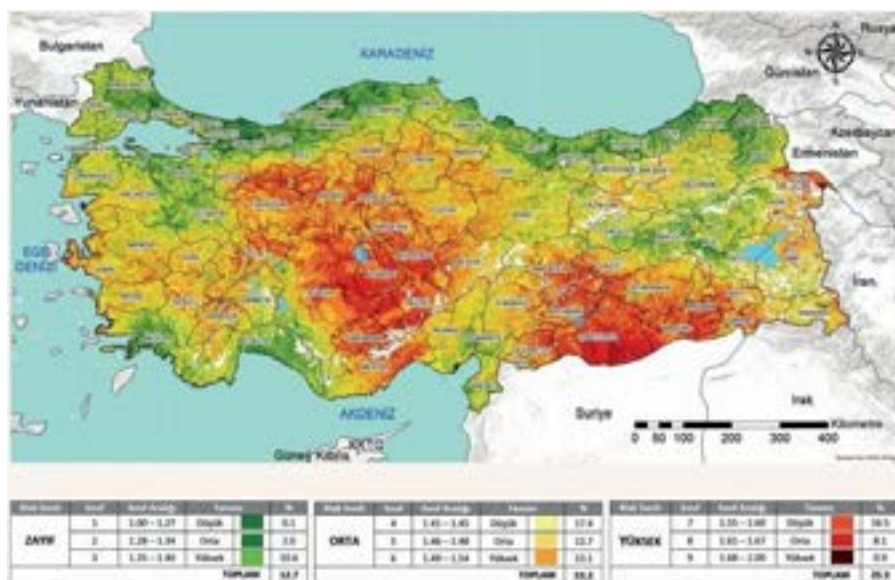Figure 9. Agricultural Drought Map of Turkey for 2013 (PDSI) (URL4).

Figure 10. Desertification Risk Map of Turkey (URL5)

4. SUGGESTIONS

In recent decades Turkey has made great strides in water resources development for domestic use, irrigation, and flood control and power generation. The dams and reservoirs built have enabled Turkey to save water from its brief seasons of rainfall to use throughout the year for various purposes, agriculture in particular. Rain-fed agriculture in Turkey is being realized almost to the maximum level. As a result, increasing agricultural productivity has become primarily dependent upon irrigation by using modern techniques.

Water pricing should be provided to consume less water and encourage water saving. Beside the price, unconscious irrigation, old irrigation systems, causes the use of excess water in agriculture. Inefficient use of irrigation water not only makes it necessary to divert and/or pump large amounts of water, but it also results in environmental degradation by such phenomena as water logging, salinization and pollution, and it causes health risks.

In agricultural-dry areas, irrigation should be consciously programmed. New and modern irrigation methods should be used. Farmers should be informed and educated about proper irrigation methods and underground hazards.

Turkey does not have a comprehensive water law, though a number of organizations exist for water management. Almost every organization has a special law for itself. In some cases there may be overlap. More than one law may lead to some problems. Furthermore the lack of coordination between authorities that must work together at local and provincial levels powered by different law for the same act causes some difficulties. With a detailed and single law, water management should be kept under control. At the same time;

• Implementation of legal arrangements should be realized,
• Improving of operation and maintenance services,
• Enhancing pressure irrigation systems such as drip and micro irrigation, instead of gravity irrigation to cut evaporation and wind-drift losses,
• Providing of water delivery planning and irrigation scheduling,
• Training water user on modern technology,
• Considering the socio-economic impacts of irrigated agriculture on targeted groups,
• Land consolidation should be done to prevent land fragmentation and deformation,
• Relevant laws should be prepared to prevent land fragmentation.

REFERENCES

Bayram, T., Erkus, A., Öztürk, D., 2014, "The Past, Present and Future of Water Resources in Turkey", Journal of the Institute of Natural & Applied Sciences 19 (1-2):70-74.

Altinbilek D., 2004, Development and management of the Euphrates–Tigris basin. Int. J. Water Resour. Dev. 20: 15–33.

Cakmak b., Unver I. H. O., Akuzum T., 2004, Agricultural Water Use in Turkey, Water International, 29:2, 257-264.

Kaplan, G., Avdan, U., Avdan, Z., Yildiz, N.D., 2016, "Landsat Uydu Görüntüleri Kullanilarak Kuraklik Izlenmesi (Aksehir Gölü Örnegi,), 6. UZAKTAN ALGILAMA-CBS SEMPOZYUMU (UZAL-CBS 2016)"; Investigating drought using Landsat satellite images (Akhisar Lake case study), 6. REMOTE SENSING-GIS SYMPOSIUM, 5-7 October 2016, Adana, Turkey

Kurnaz, L., 2014, "Drought in Turkey." Ipc.sabanciuniv.edu. Istanbul Policy Center, Apr. 2014.

URL1: http://www.ogm.gov.tr
URL2: http://www.mfa.gov.tr
URL3: http://uzay.tubitak.gov.tr
URL4: http://www.mgm.gov.tr
URL5: http://www.cem.gov.tr

UTLIZING UNMANNED AERIAL VEHICLE TO IDENTIFY THE RICE LODGING AREA

Li-Chi Wang, Re-Yang Lee, Tsai-Chih Chao, Xin-Zhan Peng,

Yu-Kun Zheng

Department of Land Management, Feng-Chia University

NO. 100, Wenhwa Rd., Seatwen, Taichung, 40724 Taiwan (R.O.C.)

E-mail: lichi92321@gmail.com; rylee@fcu.edu.tw; v45837153@gmail.com;

p9603200@gmail.com; a852456cheng@gmail.com

KEY WORDS: rice lodging, uav, random forest

ABSTRACT: Because of frequent natural disasters in Taiwan, farmers often suffer from huge losses. In order to help the farmers maintain the livelihood, the Council of Agriculture enacted "Implementation Rules of Agricultural Natural Disaster Relief" in 1990. This act first evaluates the damage to the agriculture and then provides assists reimbursements, loans with low interest or money assist. However, the government officials evaluate the damage only by their eyes, without any supporting data. This has been controversial. It not only takes a lot of time, resources and budget but also occurs doubtful accuracy of the damage. Because of executing inappropriate techniques to measure the cop damage, the Taiwanese government often has disagreements with the farmers regarding to the reimbursement.

This study selected Dapi Township in Yunlin as the study area, which suffers from heavy rain frequently. The main crop in Dapi is rice. The study area is about 120 hectares of rice field. This study uses Unmanned Aerial Vehicle (UAV) to get RGB color images of rice fields. With these images, we apply Random Forest (RF) to identify the rice lodging. The results of this study can contribute to decreasing the conflict between farmers and Taiwanese government as well as the expense on the assessment.

1. INTRODUCTION

Geographically, Taiwan is located on the edge of the Asian continent within the continental and oceanic climate, thus the climate is changeable. When the summer comes, it is vulnerable to the influence of the marine air mass and suffered from many typhoons. Natural disaster is unable to be avoided in the cultivation process of rice. With the heavy rain, the rice collapsed, for the force was out of the load-bearing capacity of the stalk. In addition, when the field became muddy and the rice plants were full of moisture, the long-term muggy environment brought on the germination of rice and the farmers faced serious loss. In response to the above-mentioned problems, the Council of Agriculture enacted "Implementation Rules of Agricultural Natural Disaster Relief" in 1990. The act evaluates the situation whether the farmland has been re-cultivated, converted and harvested as a basis for estimating losses. In order to reduce farmers' losses and maintain their basic livelihood, the government offers cash assistance, subsidies or low-interest loans. To date, the amount of relief has exceeded 12 billion US dollars.

Since the government often over-compensates the assists reimbursements, which imposes an additional financial burden on the government. This situation is due to the lack of accuracy in the survey techniques. After interviewing the staffs of the Ministry Agriculture, it is known that the current survey methods are still artificial. Not only does it require a lot of manpower for each survey, but it also takes a lot of time to evaluate the damage, which makes the investigation costly. Farmers and the government inevitably have different disputes about the damage area.

In Taiwan, it is difficult to acquire cloud-free aerial photos and satellite images. In contrast, UAV has the advantages of low environmental constraints, high maneuverability, high ground resolution, low cost and low personnel, so it would be more beneficial to agricultural monitoring. However, there are only few domestic literatures on applying UAV to agriculture. Therefore, this study would use UAV as a tool for collecting images. These UAV images were then used to identify the rice lodging by executing the supervised classification algorithm.

Because UAV have a higher spatial resolution, conventional statistical methods do not provide effective and accurate classification for complex and voluminous information (Lei, 2006). Thus, to overcome this problem, many scholars have applied machine learning algorithms to remote sensing classification (Lu, 2002; Lei, 2007; Schapire et al, 2005). Compared with support vector machines and artificial neural networks, random forests (RFs) have a relatively low computational burden and not sensitive with multiple linear variables as well as abnormal values (Rodriguez-Galiano et al., 2012). In addition, RFs have outstanding performance in linear algebra. Based on these advantages, this research used RFs to identify the rice lodging at Dapi Township in Yunlin County.

The purposes of this study are listed as follows:

1. Establish an objective rice lodging interpretation system to automatic acquire accurate damage areas and reduce conflicts between farmers and the government.
2. Evaluate whether UAV images and the RF classifier are applicable to large-scale farmland interpretations.
3. Enrich the research materials of UAV application in agriculture.

2. METHODS AND MATERIALS

This study intends to establish an automatic procedure to derive the rice lodging fields using UAV images. The appropriate training sites were first selected using ERDAS Imagines software. The RF classifier was then used to classify the rice lodging fields. Finally, the classification results were verified using the ground truth data. The procedures are described as follows:

2.1 Study area

Dapi Township is located at the southern of Yunlin County, Taiwan (Figure 1). The topography of Dapi is a broad plain and the geology is alluvial soil. The soil is fertile and suitable for farming. The rice planted area was 2,825 hectares at Dapi Township in 2017, ranking third in Yunlin County. Under the influences by the summer southwest monsoon and high temperature during May to September periods, thunderstorms and typhoons resulting in heavy rain often make rice stems lodging. For this purpose, this study selected 120 hectares of rice fields as the test area to establish an rice lodging interpretation system to automatic acquire accurate damage fields.
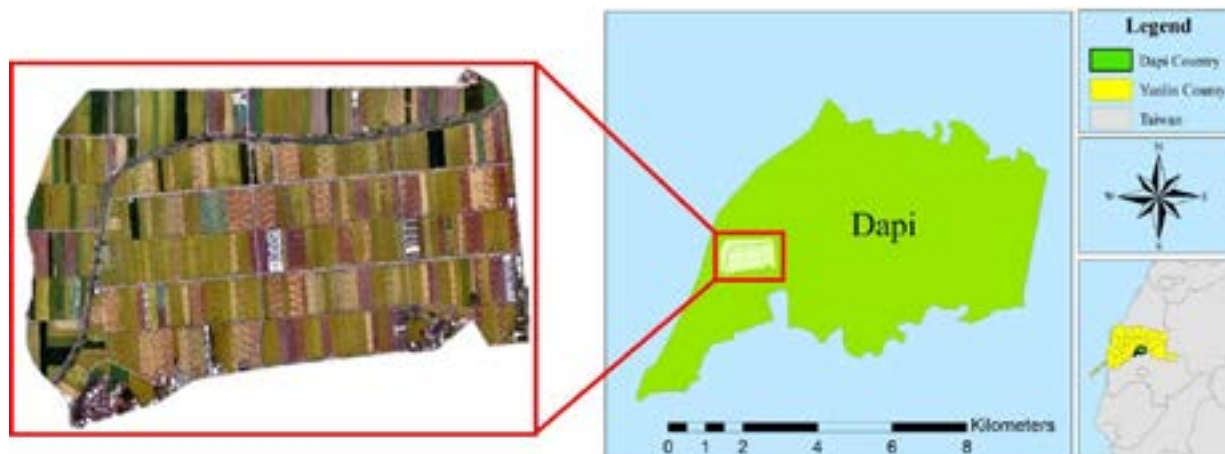

Figure 1 The location of Dapi county

2.2 UAV

Since the study area covers a wide range of 120 hectares, a long-endurance UAV is necessary. CW-10 with the characteristics of fixed-wing and quadcopter UAV, which has good endurance, fast flight speed and stable landing mode, was selected to acquire the images. In addition, CW-10 features an industrial grade flight controller with high scalability and reliability for large field areas. In this study, CW-10 is equipped with a high-resolution visible light camera, Canon Ixus 127, providing three bands of red, green and blue.

2.3 Image stitching

The image of the research area is composed of multiple UAV photos using pix4D software. The principle of stitching is the use of improved Scale Invariant Feature Transform (SIFT) algorithm. After detecting and matching the characteristic points, the error characteristic points were corrected by adjusting matrix calculation coordinates. (Figure 2)
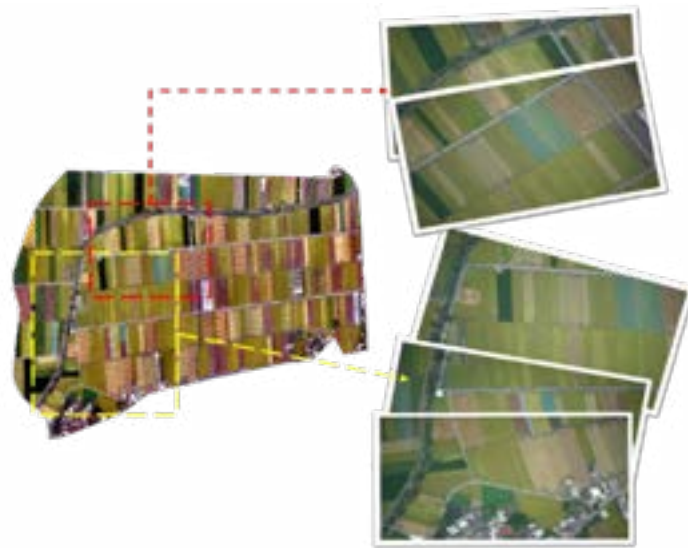

Figure 2 The diagram of image stitching

2.4 Selecting training sites

In this study, RF was used as a classification tool. Therefore, the representative training sites were selected for rice and rice lodging using ERDAS IMAGINES (Figure 3)。Examples of rice and lodging training sites are shown in Figure 4 and Figure 5, respectively. The image was classified into two categories: rice and lodging.
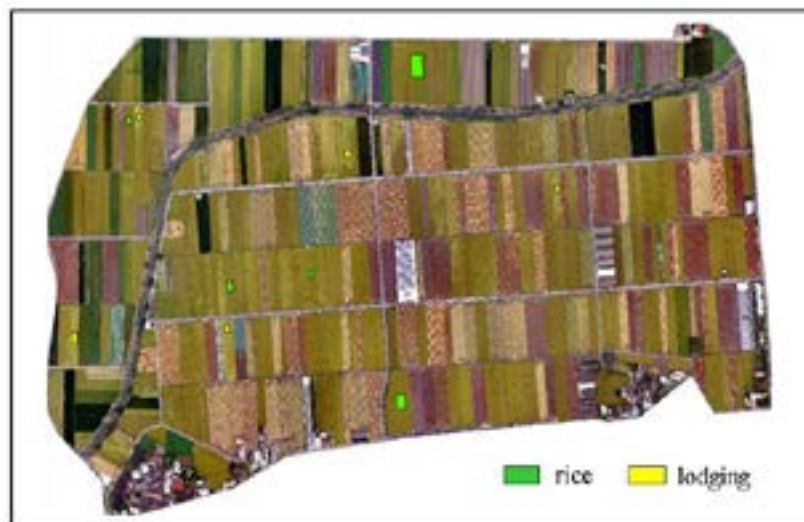

Figure 3 Training sites
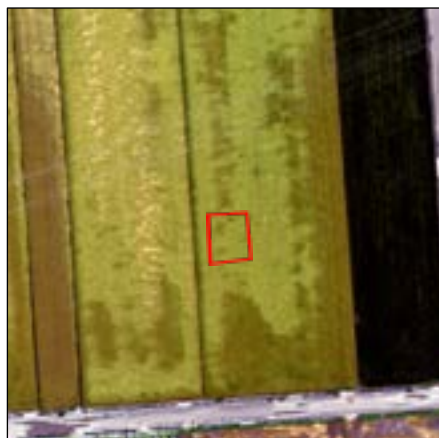
Figure 4 The rice of training sites   Figure 5 The lodging of training sites

2.5 Random Forest

Random Forest is an ensemble of Decision Trees. Decision tree is a system that processes the classification by the independent variables of each node, starting from the root to the end point, called the "leaf", performing a series of classifications. Each independent variable on the node can split more than two child nodes, and each child node represents a variable branch. Each split branch represent an output result, and all the output results represent predictions from different classifications. To build a random forest model needs large amount of memory of computer and time, and the different bands shows different results. Therefore, before processing random forest, we should establish an OOB estimation of error rate first. The detection of OOB error rate formula is as follows:

$$OOB \ \ error \leq \frac{P(1-S^2)}{S^2}$$

(P value represents the average degree of correlation between trees, and S value represents the classified ability of trees)

The number of characteristic variable in this study is three (R, G, B), and the OOB error rate analysis of the characteristic variables is performed from 100 to 300 decision trees. When the number of decision trees increased, the OOB error rate also decreased. But when it reached a certain amount (after 300), the error rate tended to be flat or even upward. Finally, the best performance was found when the characteristic variable is 2. Therefore, we selected 292 trees with the characteristic variable 2 for program to obtain the result of image (Figure 6).
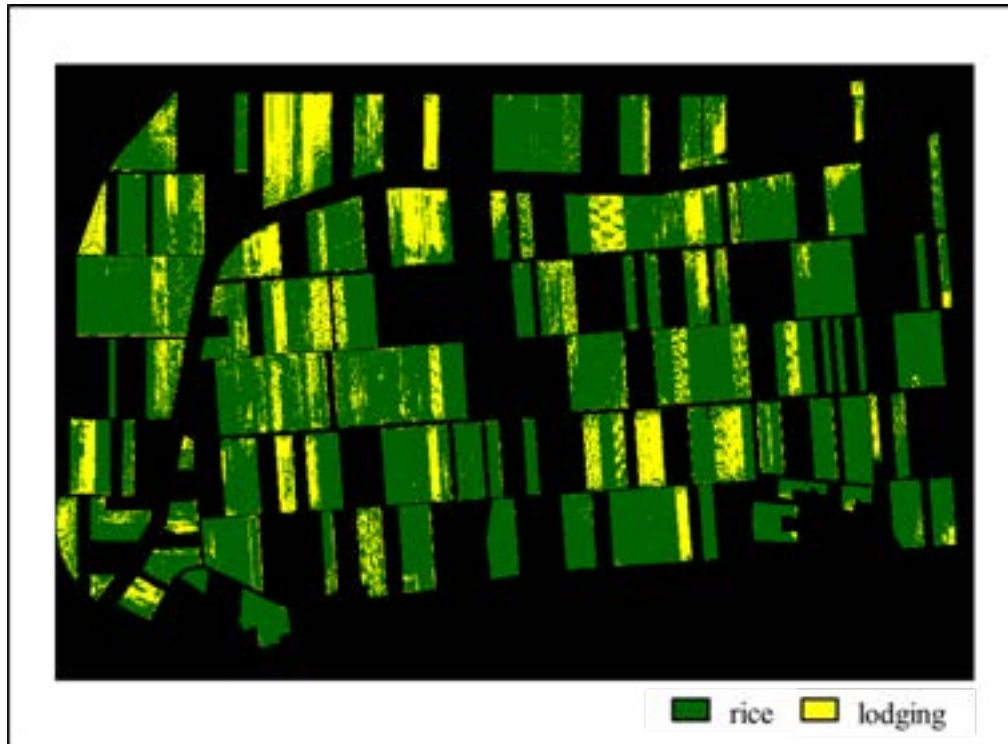
Figure 6   The classified image of RF

2.6   Accuracy analysis

After obtaining the result of image, we compared with the ground truth to carry out the accuracy analysis. The analysis results were shown in the table 1.

Table 1 *The accuracy before adjustment*

	Type	Producer's Accuracy	User's Accuracy	Overall Accuracy	Kappa
Accuracy	Rice	92.634%	96.686%	93.457%	0.875
	Lodging	94.805%	88.721%		

2.7   Error analysis

After preliminary analysis of the result of the RF classification, we found that the other land cover types were misjudged as rice or lodging. For instances, the pixel values of some poles and water channels were similar to those of lodging, which can easily lead to commission errors. Therefore, error analysis is necessary to find out the misjudgments of classification, and then to correct them.

According to the Figure 7, the dark green area is the rice field, while the yellow block is the lodging area. However, the RF classifier misinterpreted the wires to the lodging area. The bare land was also classified as the lodging fields. We should remove the misinterpreted pixels to increase the accuracy.
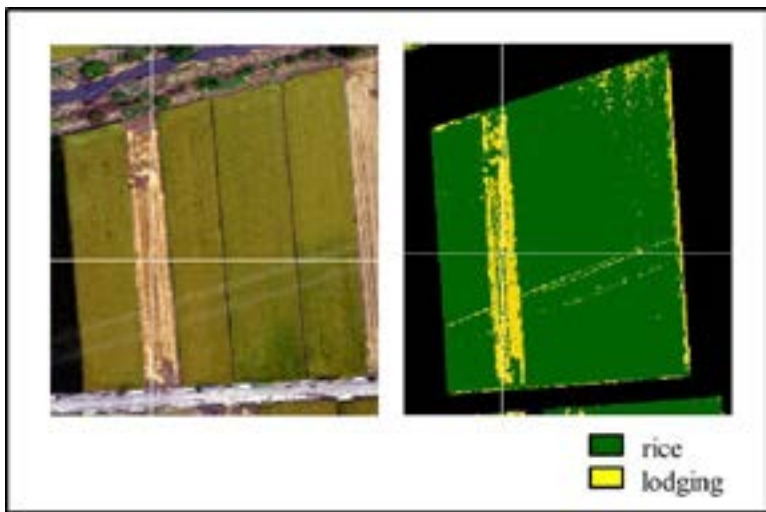

Figure 7 The misjudgment of the image

2.8 Error correction

Figure 8 shows the classification result (RF before adjustment) is messy. Therefore, we use the function of ERDAS IMAGINE, "Fill", to remove the "salt and pepper" and get a "clean" image (RF after adjustment).
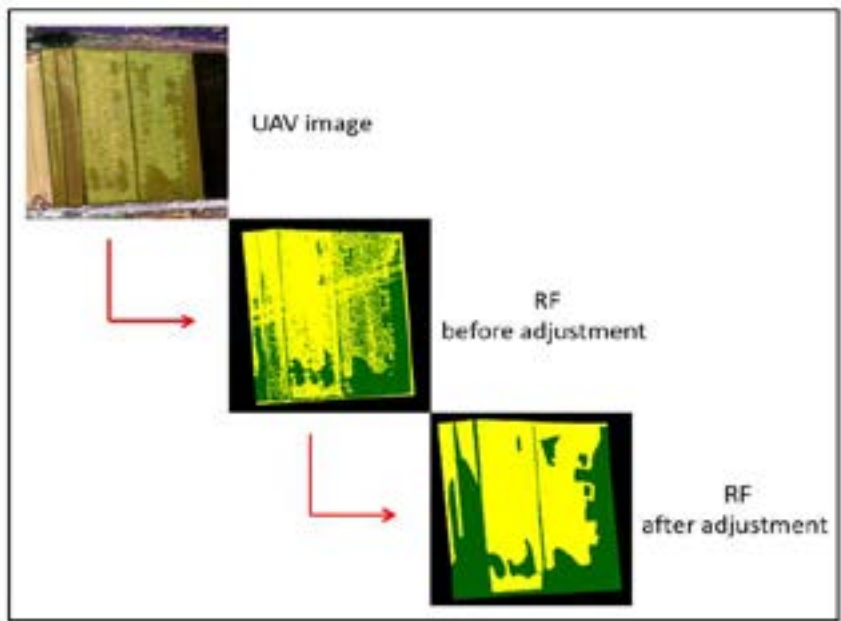

Figure 8 The process of correction

2835

2.9 Calculation of the lodging rate

To calculate the lodging rate, it needs to overlay the cadastral map and the results of the previous classification (Figure 9). After the overlay is completed, the data of rice and the lodging area in each field is shown in the Excel tables. Through calculation, we can obtain the total lodging rate of the target and the lodging rate of each field.
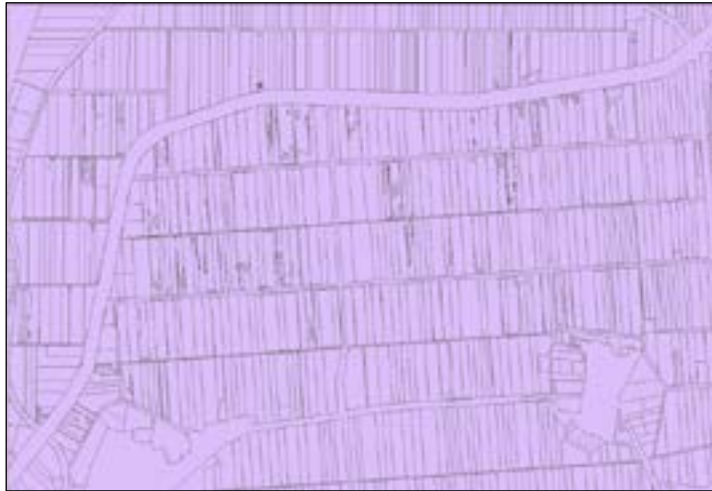

Figure 9 Overlay (after)

3. RESULTS AND DISCUSSION

3.1 RESULTS

Table 2 is the calculation result of the lodging rate. According to the current regulations, when the single township (town, city, district) meets the disaster and its affected area of agricultural products has reached more than 5% of the township, and each field reaches 20% losses of agricultural products in the area, you may apply to the government for cash assistance or low-profit loans.

Table 2 *The calculation of lodging rate*

Number	Rate	Number	Rate
PB022210100008	*0.0366%*	PB022219480000	*16.3003%*
PB022218200000	*0.1436%*	PB022219490000	*71.4223%*
PB022218210000	*7.1168%*	PB022219500000	*94.0873%*
PB022218220000	*35.0924%*	PB022219510000	*97.2452%*
PB022218310000	*0.0031%*	PB022219520000	*40.0000%*
PB022218320000	*0.0334%*	PB022219560000	*0.0029%*
PB022218350000	*0.0038%*	PB022219570000	*0.0115%*
PB022218570000	*0.0057%*	PB022219640000	*0.0261%*
PB022218580000	*0.0004%*	PB022219710000	*0.2174%*
PB022218610001	*0.0037%*	PB022219720000	*0.0197%*
Rice Area	436313.76	**Lodging Area**	36732.68
Total Area	473046.44	**Total Rate**	7.7651%

3.2 DISCUSSION

In the research, the accuracy has reached 93.457% before the correction of misjudgment. It indicates that the method is feasible for the interpretation of large-area paddy fields. The accuracy will reach 100% after correcting errors by professional judgments. In addition, the process does not take much time, so it could be a comparative material for the future academic research.

UAV has been used for several years, however, the domestic literatures on UAV are still insufficient. This study used random forest algorithm to classify the rice lodging. It is expected that the research can be further studied and compared by different image processing methods to enrich literatures on UAV and the interpretation of rice losses. In addition, the method can also be applied on other agricultures, not limited to the interpretation of rice and rice lodging to improve the efficiency of overall agricultural compensation.

REFERENCE

Kun-Che, L., 2002. Decision Trees Based Image Data Mining and its Application on Image Processing (Masters' thesis). Feng Chia University, Taichung, Taiwan.

Schapire, R. E., M. Rochery., M. Rahim., and N. Gupta., 2005. Boosting with prior knowledge for call classification. *IEEE Transactions on Speech and Audio Processing, 13(2):174-181.*

Lei, T.C., T.Y. Chou., T.Y. Cheng., 2006. A Study of Extraction Paddy Field from Quickbird Image. *Journal of Photogrammetry and Remote Sensing, 11(3):297-310*

Lei, T.C., T.Y. Chou., S. Wan., L.S. Yang., J.J. Syu., 2007. Space Characteristic Classifier of Support Vector Machine for Satellite Image Classification. *Journal of Photogrammetry and Remote Sensing, 12(2):145-163*

Rodriguez-Galiano, VF., M Chica-Olmo., F Abarca-Hernandez., Peter M Atkinson., C Jeganathan., 2012. Random Forest classification of Mediterranean land cover using multi-seasonal imagery and multi-seasonal texture. *Remote Sensing of Environment. 121: 93-107*

Xu, Y.X., Z.H. Zhu, Y.Y. Liu., 2006. Developing Technique For The Detection And Removal of Cloud and Haze in Satellite Images. *Remote Sensing for Land & Resources. 18(3): 23-28.*

A Study on the Development of a Radar Data 3D Profile Technique Using the Unity 3D Engine

Seung-Hyeon Lee[1*], Hyeoung-Wook Choi[2], Yu-Yeon Lee[3], and Yong-Cheol Seo[4]

[1]Institute of Spatial Information Technology Research, GEO C&I Co., Ltd., 435 Hwarang-ro, dong-gu, Daegu, Republic of Korea. E-mail: shlee@geocni.com
[2]Institute of Spatial Information Technology Research, GEO C&I Co., Ltd., 435 Hwarang-ro, dong-gu, Daegu, Republic of Korea. E-mail: hwchoi@geocni.com
[3]Institute of Spatial Information Technology Research, GEO C&I Co., Ltd., 435 Hwarang-ro, dong-gu, Daegu, Republic of Korea. E-mail: yylee@geocni.com
[4]Department of Civil Engineering, Pukyoung National University, 365 Sinseon-ro, Nam-Gu, Busan, Republic of Korea. E-mail: suk@pknu.ac.kr

KEYWORDS: Rainfall radar, 3D profile, Unity 3D, Open Map, user-intuitive

ABSTRACT: This study deals with the vertical profile analysis function using the Unity 3D engine based on the three-dimensional (3D) modeling of rainfall radar observation information. To develop a rainfall radar observation data 3D profile visualization technique, a 3D cumulative rainfall model enabling 3D analysis was first created. The cumulative rainfall model was converted to the grid-based rainfall distribution of real-time-created rainfall distribution data so as to superimpose the grid data, thus creating the data regarding the rainfall accumulated at points according to the time changes. In addition, to display the cumulative rainfall data in 3D, a [Z]-value data raw file, which provides 3D high values by matching the grid data according to the legend table, was separately created. The profile function designed for the visual analysis of the created 3D cumulative rainfall model was developed using the Unity 3D platform, and a visualization display tool enabling diverse analyses through the use of the 3D rendering tool was constructed. Furthermore, the 3D cumulative rainfall model, which was created to provide the proposed profile-technique-based user service, was linked with Google Open Map so as to spatially display the rainfall distribution, and by applying the profile module, a function was implemented to quantitatively analyze the sectional distribution via 3D modeling. As a result of the use of the developed 3D profile tool, it is deemed possible to conduct quantitative analysis of a 3D display.

1. Introduction

In the past, the point observation data of ground rainfall observation stations were mainly used for rainfall observation. Such point observation data are still very useful at present as data on the rains actually falling on the ground. Such data, however, are still not sufficient to be used for analyzing the spatial distribution of rainfall for the prediction of the movement path of the precipitation cluster or the amount of rainfall required for the prediction of sudden heavy rainfall in a wide area. Therefore, to supplement such ground observation data, rainfall prediction technologies using remote sensing equipment like radar and satellites have been actively applied of late. Advanced

countries have developed and actively used tools for the multidimensional visualization of remote sensing data for the prediction and monitoring of natural disasters frequently occurring in urban areas. The National Climatic Data Center (NCDC) of the National Oceanic and Atmospheric Administration (NOAA) in the U.S. developed and released the Weather and Climate Toolkit (WCT), a visualization tool that models the tornado occurrence data observed from the climate observation radar network installed in urban areas, three-dimensionally, visually monitors them by connecting them with Google Map information, and analyzes the movement path. In addition, the National Aeronautics and Space Administration (NASA) in the U.S. and the Japan Aerospace Exploration Agency (JAXA) in Japan are visualizing satellite-based climate observation data three-dimensionally on the earth surface information through the Tropical Rainfall Measuring Mission (TRMM) project so that the users can make intuitive and prompt decisions.

In South Korea, however, while it is possible to acquire climate data with high accuracy and a spatiotemporal resolution using remote sensing equipment, such as a high-precision rainfall radar, the multidimensional display services for accurate spatial adjustment and visualization analysis are not sufficient. Furthermore, when the data related to the rainfall and climate data obtained so far are visualized, the processed two-dimensional (2D) image data are simply superimposed on the low-resolution map of the country.

As such, this study did not use such simple planar display techniques and described the function development for more effective visualization monitoring and analysis. Towards this end, a three-dimensional (3D) model creation and service technique capable of displaying rainfall information more effectively using the rainfall observation data of the high-precision small rainfall radar currently under operation was devised. Moreover, for the implementation of a user analysis function that exceeds the concept of simple visual information provision, a 3D rainfall model creation and vertical profile function capable of multidimensional monitoring by integrating the rainfall observation data generated according to the time series using the commercial Unity 3D engine was additionally developed.

2. Radar Observation Data File Conversion for 3D Cumulative Rainfall Model Creation

2.1 Single rainfall information image data conversion for 3D cumulative rainfall model creation

The rainfall data are provided in a text file format. The radar provided by the text file is expressed in a 2D ASCII matrix format based on the grid unit resolution according to the observation range. The data of the text file are divided into individual data elements using ASCII values, such as "0x20" (blank) and "0x0D, 0x0A" (line feed), as delimiters. Each individual data element of the radar observation data used in this study is arranged in a 2D element unit with a ▨ × ▨ size. [Figure 1] shows the rainfall radar provided in a text file format.

FIGURE 1. Rainfall radar source data

For the radar observation information user visualization service, the initially received data must be processed into an image format. In this study, such processing was performed by converting the observed values corresponding to each pixel into grids, and designating values corresponding to the rainfall intensity standard

pseudo-color legend [Figure 2].

| (a) Image conversion algorithm | (b) Rainfall standard pseudo-color | (c) Image conversion result |

FIGURE 2. Image processing results of radar observation data

2.2 Cumulative rainfall creation through single rainfall image data composite operation

To express the time-series-based cumulative rainfall model through the cumulative operation of the single rainfall data obtained from radar observation and image processing, an algorithm for the cumulative operation of the converted single rainfall data was implemented. In the case of cumulative operation, the value was calculated by summing up the values corresponding to the same coordinate (grid) area based on the grid-type source data [Figure 3].
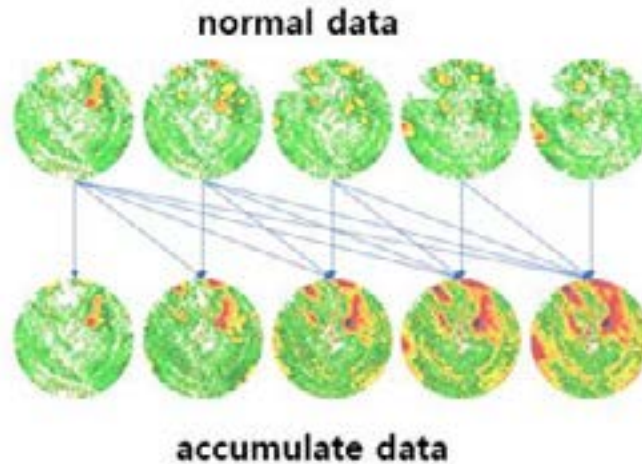

FIGURE 3. Concept of the cumulative rainfall data creation operation algorithm

2.3 Creation of the 3D cumulative rainfall model

To regenerate the cumulative rainfall image data computed in a 2D plane as a 3D model, the height value ([Z] value) data are additionally required. In this study, the [Z] value was defined as the quantitative legend value of the rainfall intensity for a visual profile. In addition, to express the amount of rainfall summed up by point (grid unit) as [Z], RAW file data were separately generated to create a 3D model connected real-time with the 2D image model. The algorithm was constructed so that the [Z] value RAW file data constructed for 3D model creation could be automatically generated when the cumulative rainfall 2D image and the single rainfall file are combined. In addition, based on this algorithm, a cumulative rainfall 3D model capable of 3D visualization rendering through the single rainfall information image creation of the radar data observed in real time, cumulative rainfall operation, 3D [Z] data creation, and integration was implemented [Figure 4].
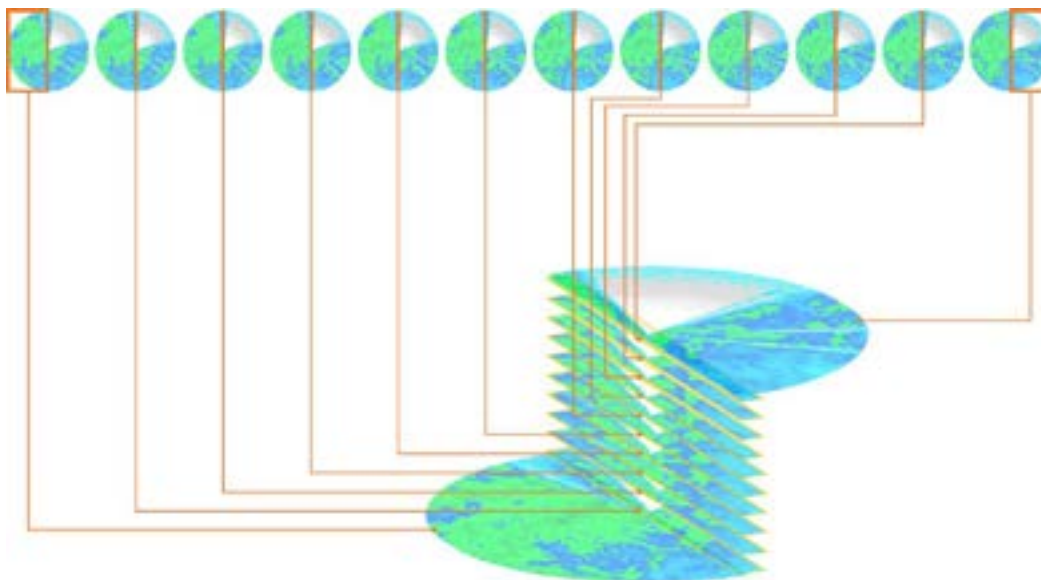
FIGURE 4. 3D cumulative rainfall modeling process

3. Rainfall Radar Observation Cumulative Rainfall Model 3D Rendering and Profile Function Implementation Using Unity 3D

To implement the profile function of the 3D cumulative rainfall data model, a module capable of performing the profile function was implemented by accessing the 3D model rendering function of Unity 3D (terrainData) and by modifying only the arbitrary part of the Resolution Terrain Width*Terrain Length implemented as the entire grid model according to the user setting. The 3D model created by this function can perform the vertical profile function at the position desired by the user, and can analyze the rainfall pattern at the same point in the time series unit based on the pseudo-color appearing on the cross-section. Furthermore, a function capable of analyzing the position-based rainfall distribution in various ways was additionally provided by mapping the 3D cumulative rainfall model implemented in this study to Google Map [Figure 5].
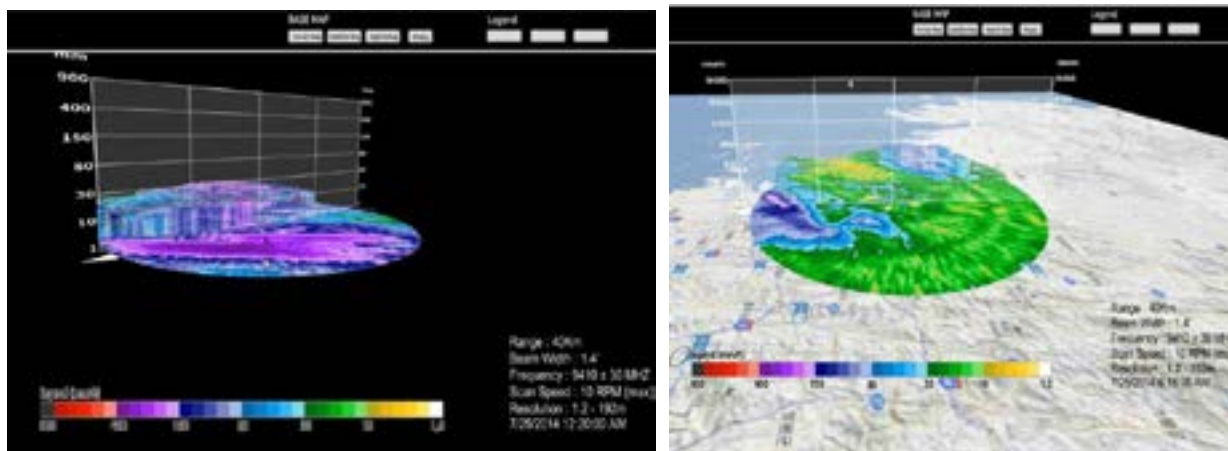
(a) Profile function implementation **(b) Google-based 3D profile model mapping**

FIGURE 5. Vertical profile function implementation results

4. Conclusion

This study described the development of the three-dimensional (3D) observation data vertical profile function based on Unity 3D and Google Open Map to expand the visualization function for rainfall radar observation information. The developed vertical profile visualization analysis function exceeds the past simple planar display service techniques and can effectively analyze the rainfall pattern, thereby enabling more intuitive services. In addition, the software developed in this study was developed based on a universal 3D graphics platform that does not require a separate license, providing benefits in terms of scalability. In the future, it is expected that rainfall

radar observation information will be intuitively monitored using the developed profile module, and that the module will be utilized for highly reliable rainfall prediction and monitoring through quantitative change trend analysis.

REFERENCES

H.Y. Choi, S.M. Kang, K.I. Kim, D.Y. Kim, Y.J, Choung, 2015. Development of the Visualization Prototype of Radar Rainfall Data Using the Unity 3D Engine. Journal of the Korean Association of Geographic Information Studies, 18(4), pp. 131-144

J.H. Park, B.S. Kang, G.S. Lee and E.R. Lee, 2007. Flood Runoff Analysis using Radar Rainfall and flood Model for Namgang Dam Watershed," Journal of Korea Association of Geographic Information Studies, 10(3), pp. 13-21

B.J. Jang, S.H. Lee, S.H. Lee, K.S. Moon, V. Chandrasekar and K.R. Kwon, 2013. A Visualization Method of High Definition Water Radar Information for Various GIS Platforms. Journal of Korea Multimedia Society, 16(11) pp. 1239-1249

B.J. Jang, K.H. Lee, D.R. Lee and S.H. Lim, 2014. High-precision and 3D GIS Matching and Projection based User-friendly Radar Display Technique. Journal of Korea Water Resource Association, 47(12), pp. 1145-1154.

3D MODELLING AND DEPTH ESTIMATION OF SHALLOW WATER ENVIRONMENTS USING A CUSTOMIZED UNMANNED SURFACE VEHICLE

Trizia Mae A. Badong (1), Reena Louise E. Manalac (1), Ayin M. Tamondong (1), Patrick Joseph M. Ostrea (2)

[1] University of the Philippines Diliman, Department of Geodetic Engineering, University of the Philippines Diliman Campus, 1101 Quezon City, Philippines
[2] Eisenpatt Industrial Engineering Services, 50 Lalaine Bennet St. BF Resort Village, Las Pinas City, Philippines
Email: tabadong1@up.edu.ph; remanalac@up.edu.ph; amtamondong@up.edu.ph; patrick.ostrea@eisenpatt.com

KEY WORDS: Echo Sounder, Global Navigation Satellite System, Bathymetric Survey, Photogrammetry

ABSTRACT: Modelling and mapping of shallow (less than 20 meters) water environments are vital in sustaining and maintaining ecosystems under water, yet it is one of the constraints of conventional hydrographic survey methods which uses large and heavy vessels, which harms both itself and the ecosystems involved. The aim of this research is to test an alternative way to address this problem through the use of a customized Unmanned Surface Vehicle (USV) that is equipped with a Global Navigation Satellite System (GNSS) receiver, echo sounder, video recording device, and motion corrector. The designed USV costs lower compared to the commercialized vehicles. A bathymetric survey was done using a GNSS receiver and a measuring rod on the chosen study area which consists of different seabed types such as corals, rocks, and sand, before the deployment of the USV for the establishment of control points under water. The depth of different seabed types was determined using an echo sounder which was normalized using tide corrections and then verified using points from the bathymetric survey. The extracted data was used to produce a bathymetric map of the area which resulted to an average residual of approximately 0.164 meters. The acquired images from the USV were used to produce a 3D model of the area which was then compared to the previously produced surface. The produced bathymetric map and 3D model evidently show that the use of the customized USV is an effective alternative to the conventional hydrographic survey methods in sustaining and maintaining shallow environments as it dealt minimal damage to the environments.

1. INTRODUCTION

1.1 Background of the Study

In order to sustain the marine resources in the Philippines, hydrographic surveying may be done in order to monitor and characterize the bodies of waters. However, conventional hydrographic surveying methods such as the use of lead lines, sounding poles, and doing wire and bar sweeps do not only yield limited data, they may also damage the shallow water environments. This is resolved by recent technology that has brought about new methods in surveying, namely, echo sounding, the use of sound waves to measure data.

Further developments in technology have allowed a solution to the harm caused by the conventional method of echo sounding on shallow water environments. These include Unmanned Surface Vehicles (USV), which are fully autonomous navigating marine vehicles, much like Unmanned Aerial Vehicles (UAV) or drones, that are equipped with an echo sounder and Global Navigation Satellite System (GNSS) and may also be equipped with a video recording device. The small size of these vehicles allows it to freely roam shallow waters, some with depth of less than a meter. Researches have tackled this subject, however, they have yet to provide an assessment of the accuracy of using this method.

1.2 Objectives

The objectives of this study is to produce a 3D model and bathymetric map of the study area using photogrammetry and Sound Navigation and Ranging (SONAR), respectively, and to determine the factors to consider when using a USV.

1.3 Significance of the Study

The biodiversity and heavy reliance on marine resources of the country calls for necessary action to protect and conserve its surrounding waters. The purpose of this study is to propose an efficient way to protect and conserve shallow water environments by monitoring and characterizing these without posing a threat to said environments. To compensate for the lack of advanced technology and financial resources, this study will design a lower cost USV compared to commercialized USVs.

1.4 Scope and Limitations

The chosen area for this study is a fish sanctuary located at Barangay Malabrigo in Lobo, Batangas, Philippines. The area is composed of different water environments such as corals, rocks, and sand. This study will focus on three dimensional (3D) modelling and bathymetric mapping of different shallow water environments such as corals, sand, rocks, seagrass using photogrammetry and SONAR, respectively. In gathering data for this, a customized USV will be used. Since videos will be taken during deployment of the vessel, the photographs to be used will be extracted from the videos. The camera to be used does not have its own GNSS or Global Position System (GPS), therefore the photographs will be done manually. Furthermore, geotagging all photographs will not be done due to the large amount needed.

2. REVIEW OF RELATED LITERATURE

2.1 Sound Navigation and Ranging (SONAR)

Gary Wilson and Joseph Richards used a survey-grade echo sounder and differential global positioning system to produce bathymetric maps of small reservoirs in Moberly, Missouri on December 2003. The echo sounder was set at 200 kHz, which was used to measure the water depths and was then processed in ArcGIS. After processing the data, the researchers determined the factors that affect accuracy include quality and calibration of the measurement system, transect intervals, data density, and vessel errors. Considering that this was done in small reservoirs, numerous more factors may affect accuracy when surveys are done in seas or oceans.

Alexander Gavrilov, Iain Parnum, Paulus Siwabessy, and company characterized the seafloor in Australia's coastal zone using multibeam (MBS) and single beam (SBS) echo sounders in December 2012. The researchers stated the importance of this as the area was poorly monitored and that these methods were able to cover large areas in a small amount of time. A comparison of the same two systems used for seafloor habitat mapping was done by 3 mentioned authors, as well as Miles Parsons in 2014. For this research, three classes of surfaces were surveyed, namely, rhodolith or hard seabeds, sand, and mixed. Overall, the MBS resulted in the highest classification accuracy with 91%, while the SBS resulted in 84% and 69% at 200 kHz and 38 kHz, respectively. Although the MBS is much more accurate than the SBS, these are rarely used in shallow water environments due to its size. Additionally, these are more expensive compared to the SBS.

2.2 Photogrammetry

In a 2015 research, Capra, Dubbini, Bertacchini, Castagnetti, and Mancini evaluated the quality of 3 low-cost cameras for underwater photogrammetry at a depth of 15 meters, namely, Canon Power Shot G12, Intova Sport HD, and GoPro HERO 2. Out of the three, the Canon Power Shot G12 resulted in the smallest error of 0.524 mm, while the GoPro Hero2 resulted in the largest error of 43.037 mm. Although the GoPro Hero2 showed the least promise, the more recent cameras released by the GoPro company have greatly improved in quality, which may result in less error in future underwater photogrammetry studies.

For the monitoring of coral colonies, a comparison of photogrammetry and using geometric formulas was done by Kikuzawa, Toh, Ng, Sam, Taira, Afiq-Rosli, and Chou. The research team used an imaging software named ImageJ and evaluated the accuracy of the measured planar area by linear measurement calculations. To be able to compare the two methods, they used linear regression with Shapiro-Wilk and Levene's test. The researchers concluded that photogrammetry is an accurate and non-evasive method in monitoring corals, however, this method is dependent on the quality of the images.

2.3 Unmanned Surface Vehicle (USV)

Marco Bibuli and company's Unmanned Surface Vehicles for Automatic Bathymetry Mapping and Shores' Maintenance (2014) cited that the use of USVs is a welcome alternative for the monitoring of coastal environments as this solves the challenges faced by the capability of conventional vessels to freely navigate areas of interest. They cited that the three main advantages of USVs are their small to medium sizes that allow a number of them to navigate through waters of with depths from 0.3 to 0.5 meters, their full autonomy during deployment, and their sensing capabilities. Thomas Pastore and Dr. Ronald Kessel (2009) also found using USVs advantageous due to their reduced life-cycle cost and the increase in personal safety. They also stated that the USV community may benefit from other classes of unmanned systems as there is an overlap in certain aspects. Furthermore, Jiucai Jin and company's Active and Passive Underwater Acoustic Applications using an Unmanned Surface Vehicle (2016) confirmed that USVs can benefit underwater acoustic researches. The research also stated several oceanic applications of USVs such as bathymetry, underwater acoustics research, environment survey, and marine rescue.

In a research of Fumagalli, Bibuli, Caccia, et. al. (2014), a USV composed of two vehicles was used. The first vehicle being the leading vehicle in charge of the navigation, while the second vehicle was the towed vehicle, which is composed of a camera and echo sounder for synchronized data acquisition. The research also enumerated several uses of USVs such as monitoring of shallow water habitats for sustainability and maintenance, detection of mineral deposits and morphological formations, identification of physical and biological connections for environmental management, and discovery of artifacts, settlements, and shipwrecks which are impossible for conventional vessels.

3. METHODOLOGY

There are two main systems that will be used to gather different datasets. GNSS will be used to gather bathymetric data while USV will be used for photogrammetry and SONAR data. Afterwards, these different datasets will be compared to each other and an analysis will be made from the results.

3.1 Instrument Availability

3.1.1 Unmanned Surface Vehicle

Figure 1. Final Design of the customized USV

A customized Unmanned Surface Vehicle (USV) which was assembled by Sir Patrick Ostrea, will be used to gather images and SONAR data (Figure 1). The USV is a monohull with reverse chine airboat with skid steer that is 2.5 meters in length and 0.95 meters in width in order to obtain a hull speed of 3.4 kilometers per hour and weighs 35 kilograms.

The USV is equipped with a Here+ RTK GNSS with 70 channels that utilizes GPS, GLONASS, BeiDou, and Galileo, Garmin echoMAP 43dv that has a transducer and GPS, with a 5 Hz receiver frequency and 455 Hz maximum frequency for downscan, and a maximum depth of 335.28 meters at 77 Hz in saltwater. It is also equipped with a GoPro HERO5 that has a 14 millimeter wide field of view, a 4.5 millimeter by 6.2 millimeter sensor size, and an RGB color filter array.

The camera and echo sounder both have an offset of 0.304 meters, 0.634 meters, and 0.3635 meters on the x, y, and z axis respectively. These offsets were considered throughout the research. The orientation of axes can be seen in figure 2.
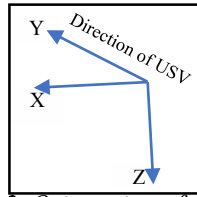
2845

Figure 2. Orientation of the Axes

3.1.2 Other Instruments

The instruments used for the acquisition of bathymetric data were Spectra Precision SP80 GNSS Receiver, steel tape, and 4 pieces of 1.13 kilograms weights which were used as control points for the photogrammetry. The GNSS receiver utilizes GPS, GLONASS, BeiDou, Galileo, QZSS, and SBAS, and has 240 channels with a frequency ranging from 800 to 2100 MHz. Its range is greater than 40 kilometers and its Real Time Kinematic (RTK) accuracy is 8 millimeters plus 1 part per million in the horizontal and 15 millimeters plus 1 part per millions, while its Post Processed Kinematic (PPK) accuracy is 3 millimeters plus 0.5 parts per million in the horizontal, and 5 millimeters plus 0.5 parts per million in the vertical. The software used for the processing of the data gathered are Video to Images Converter, Agisoft Photoscan, Geosetter, ArcMap 10.3, SonarTRX, Cloud Compare, Microsoft Excel, and WXTide.

3.2 Data Gathering

3.2.1 Bathymetric Survey

The researchers observed a specific point near the study for 1 hour which was then used as the base point for the bathymetric survey using the SP80 GNSS Receiver. For the control points, weights were scattered at the area of interest. During the lowest tide of the day, the coordinates of the control points and random points for bathymetry were measured in order to reach the deeper parts of the area. In order to compute for the depths of other points, the depth of one point was recorded.

3.2.2 Photogrammetry

The speed of the USV was set to 2 kph and the recording frequency of the Here+ RTK 5 Hz. For the video acquisition, the camera was set to wide angle mode with a frame rate of 120 frames per second, and a flat color with a white balance of 5500K.The deployment of the USV was done during the highest tide of the day to ensure a good overlap between the images. The distance between the transect lines was set to 1 meter but due to the current, the USV was not able to follow straight paths. The path of the USV can be seen in Figure 3.

Figure 3. Path of the USV

3.3 Data Processing

3.3.1 Bathymetric Survey

The measured depth of a point which is equal to 0.775 meters, was normalized using Equation 1 below. The tide correction was subtracted to the measured depth because the tide recording at that time is above the mean sea level (MSL). This tide

correction was obtained using the program WXTide. The nearest tide station, Anilao, to the study was chosen and the tide readings were extracted every 1 minute. Since the time zone used in WXTide is Central Standard Time (CST), which is 13 hours ahead of Philippine time, the local time was first adjusted to CST.

$$Normalized\ Depth_x = Measured\ Depth_x - TC \qquad (1)$$

Let   x   - point with measured depth

TC   - tide correction at the time of measurement

After getting the normalized depth of the point, the other depths of the points were estimated using Equation 2. The absolute value of the difference in elevation of point x and point i was added to the normalized depth of point x when the elevation of point x is greater than the elevation of point i to estimate the normalized depth of point i. Otherwise, the absolute value of the difference in elevation of the points was subtracted to the normalized depth of point x.

$$Normalized\ Depth\ of\ Point_i = Normalized\ Depth\ of\ Point_x +/- |z_i - z_x| \qquad (2)$$

Let   i   - points without measured depths

z   - elevation of a point

3.3.2 Photogrammetry

Photographs were extracted from the videos recorded every 0.5 second (or 60 frames per second) using the video to images converter to ensure at least 70% overlap between the photographs. The coordinates to be used for the images was taken from the RTK data that was converted from WGS84 Geographic coordinates to UTM Zone 51N by using the Project tool under the Data Management toolbox in ArcMap. Afterwards, yaw and offset corrections were applied directly due having the same projection.

The adjusted coordinates were then used to geotag manually every 50 photographs using the GeoSetter program. The Agisoft Photoscan software was then used to generate the point cloud, 3D model, and orthophoto of the seabed. The point cloud was interpolated using the Inverse Distance Weighting (IDW) method under Spatial Analyst Toolbox in ArcMap in order to generate a surface.

3.3.3. SONAR

The SonarTRX software was used to open and extract necessary information from the echo sounder data, namely, coordinates and GPS time. The GPS time of the SONAR and RTK data were matched in order to extract the correct yaw value. Afterwards, the horizontal coordinates from the echo sounder were adjusted using the offset and yaw values from the RTK data. The tide corrections from WXTide were also applied to the depth recordings of the echo sounder. The Cloud Compare software was then used to display the point cloud data of the SONAR. The generated point cloud was also interpolated in ArcMap using IDW to create a surface. Afterwards, a bathymetric map was created using the interpolated surface.

3.3.4. Comparison

To be able to compare the bathymetric data and SONAR data, the bathymetric points were plotted on the interpolated surface of SONAR using ArcMap. The corresponding depth of the pixels where the bathymetric points fall were recorded. The residuals of the SONAR depths from the bathymetric points were computed using Equation 3.

$$r_i = depth(s)_i - depth(b)_i \qquad (3)$$

Let   r   - residual

s   - pixel value from the interpolated surface of SONAR

b   - bathymetric point

Similarly, to be able to compare the SONAR and Photogrammetry data, the interpolated surfaces of these two must also be plotted in ArcMap. Before recording the corresponding pixel values (depth) of the two, the pixel values from the

Photogrammetry surface must be normalized first with the surface of the SONAR data. Equation 4 was used for the normalization of the depth of the surface.

$$\text{Normalized Depth}(p)_i = Depth(p)_i + \left[\frac{\sum Depth(s)_i - Depth(p)_i}{N}\right] \qquad (4)$$

Let   p   - pixel value from interpolated surface of Photogrammetry
           N   - total number or pixels being compared

Finally, the residuals of the photogrammetry depths from the SONAR depth were computed using Equation 5.

$$r_i = depth(p)_i - depth(s)_i \qquad (5)$$

Let   r   - residual
           p   - normalized pixel value from interpolated surface of photogrammetry
           s   - pixel value from interpolated surface of SONAR

4. RESULTS AND ANALYSIS

4.1 Results for Bathymetric Survey

During the lowest tide on the 30th of April, four control points were measured. On the lowest tide of the day after, bathymetric points were measured in between the control points. However, points near the two control points placed on the deeper part of the area were not measured due to the depth of the water being higher than the length of the rod of the GNSS receiver. A total of 56 bathymetric points were measured.

In order to use the bathymetric points for validation, the coordinates were converted to UTM and the measured depth was normalized by applying tide corrections to be able to lessen the error. The convert coordinates were plotted in Google Earth for checking.

4.2 Results for Photogrammetry

The USV was first tested and deployed in Bolinao, Pangasinan in order to gather data on surfaces with seagrass. This proved difficult as the water was turbid with numerous floating objects. Due to this, the surface was not clearly seen in the extracted images. Moreover, it could be seen that the camera was covered several times throughout the video with seagrass and seaweed. The following survey dates considered these factors and chose to focus on still objects.

After matching the GPS time of every 50 image to the GPS time in the RTK data, the location of the images was determined. Afterwards, these were adjusted due to the offset given by the position of the instrument.

Figure 4 shows the generated point cloud from the stitching of images in Agisoft PhotoScan. It can be seen that there is a blank area near the right side and very few areas that consist of sand only. This is mainly because Agisoft PhotoScan was not able to generate tie points in areas with a uniform surface because of the lack of distinctive features.
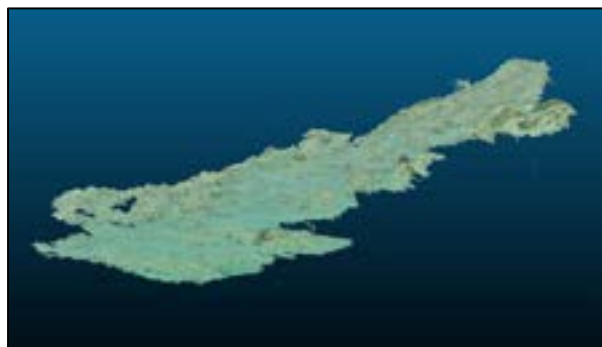

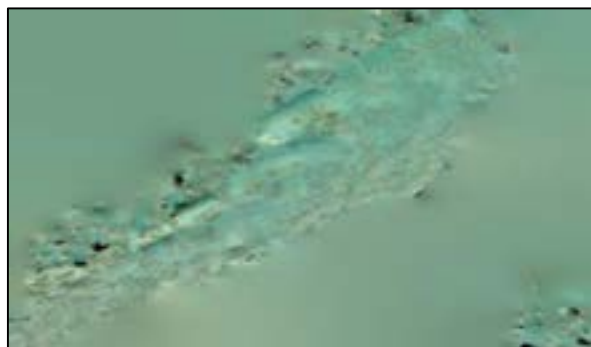Figure 4. Auxiliary View of Dense Point Cloud   Figure 5. Generated Texture of Surface

From the dense point cloud and the generated texture, a 3D model was produced. It can be seen from the generated 3D model in Figure 6 that corals, especially hard corals, and rocks were modelled more properly compared to uniform surfaces like sand and moving or floating objects such as soft corals and seaweeds. There are also spikes on the model which may have been caused by floating objects such as fishes.
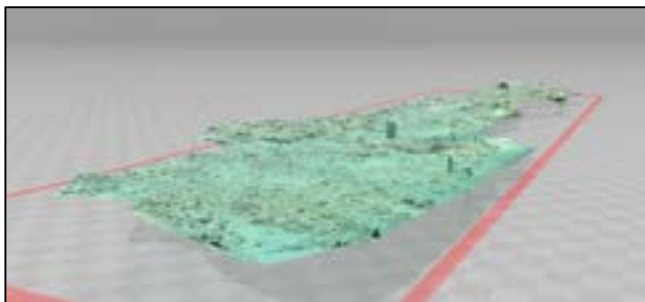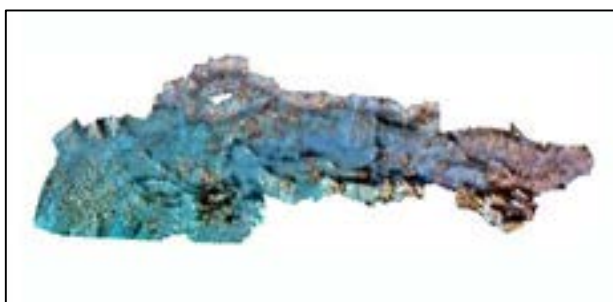

Figure 6. Auxiliary View of 3D Model
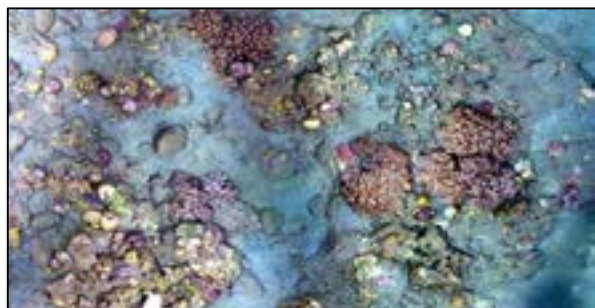

Figure 7. Orthophoto
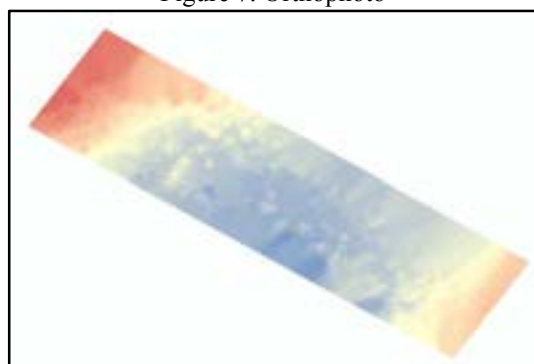

Figure 8. Enlarged View of Orthophoto

Figure 9. Interpolated Surface of Dense Point Cloud

In the orthophoto, the noise cannot be seen, however, the shadow from the USV is evident all throughout the length of the photograph. Furthermore, the scattered light from the sun can be seen clearly, especially on the right side of the orthophoto. Despite these, most of the parts of the orthophoto are clear, and the features of the corals are distinguishable as seen in Figure 8.

To be able to visualize the results of the photogrammetry process, an interpolated surface using IDW in ArcGIS was generated using the point cloud. However, since the dense point cloud consists of more than 27 million points, this was trimmed down to approximately 12,000 points using Cloud Compare. The generated interpolated surface can be seen in Figure 9. Here, you can see the shallow parts of the area in red, while the deeper parts are in blue. The rough texture that can be seen in the center of the length of the image implies the position of the corals and rocks. while the smooth texture, mostly among the sides of the surface pertains to the sand or uniform surfaces of the area.

4.3 Results for SONAR

Figure 10. Interpolated Surface Using IDW

A total of 10 thousand points was extracted from the SONAR data. Like the steps taken in photogrammetry to visualize the surface, the same will be done using the points from the adjusted SONAR data. Figure 10 shows the generated interpolated surface. For this surface, the darker blue parts correspond to the deeper parts of the area, while the lighter shades correspond to the shallow parts. The dot-like patterns along the diagonal of the figure shows the distinctive features of the area such as corals and rocks.

The created bathymetric map of the study area can be seen on the Figure 11. The minor contour interval is 0.25m while the major contour interval is 0.75m. The small closed contour lines or the peaks on the map shows the highest points of the surface which symbolizes the clumps of the corals. It shows that the depth of the area is increasing from the northeast to the southwest direction which is also consistent with the bathymetric points measured on the area and the 3D model. Other necessary information such as coordinate system, datum, scale, legend, etc. can also be found on the map.
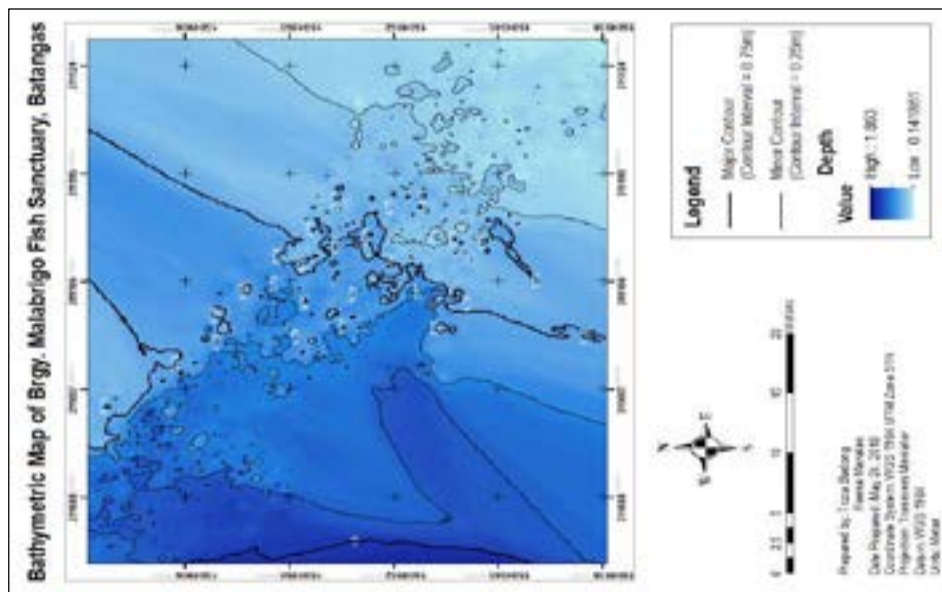
Figure 11. Produced Bathymetric Map of the Study Area

4.4 Analysis

In order to compare the SONAR data to the bathymetric points, the two data sets were overlapped. Due to 2 points in the bathymetric survey having no overlap in the SONAR point cloud, these were not included in the computation. The average residual of the depths resulted in approximately 0.164 meters.

Figure 12. Overlap of Interpolated Surfaces and bathymetric Points

Similar to the previous comparison, the generated surfaces were overlaid for analysis (shown in Figure 12). Also, the points from the photogrammetry point cloud that did not have an overlap with the SONAR point cloud were not included in the computation. It can be seen from Figure 12 that both surfaces show the same pattern in depth. Around the upper

left and lower right of both surfaces show that shallow part of the area. The center of the surfaces both show the several changes in depth that signify the area with corals and rocks.
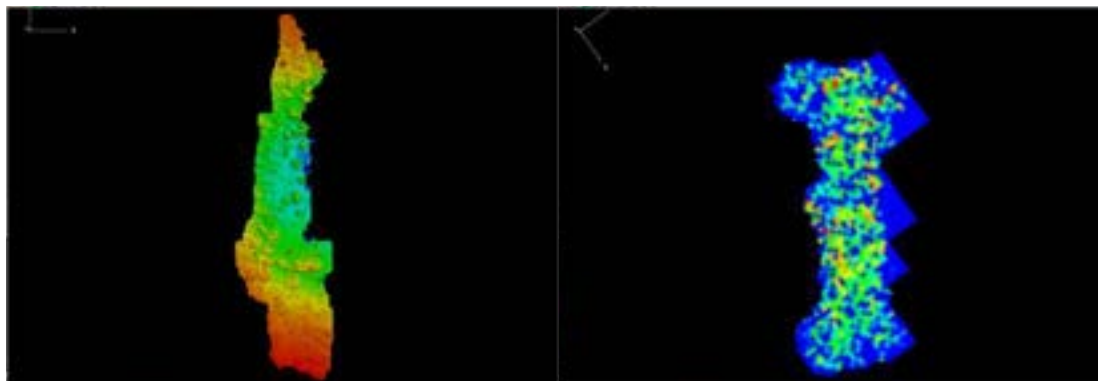

Figure 13. Generated Digital Surface Model Using Photogrammetry Point Clouds (left) and SONAR Point Clouds (right)

Figure 13 is the Digital Surface Models (DSM) of the photogrammetry point cloud and SONAR point cloud, respectively. For the first DSM, the outlines of the corals and rocks are easy to comprehend as well as the change in depth. For the second DSM, it is similar to the first DSM in a way that the area of where the corals and rocks are can be determined. However, it is not as clear as the first because the number of points to generate the DSM is significantly less with the first DSM using 27 million points and the second using only approximately 12,000. Furthermore, the trend of the depth in the SONAR DSM cannot be distinguished.

5. CONCLUSION

Using the customized USV, a 3D model and bathymetric map shown in Figures 6 and 11, was produced using low-cost equipment and dealt minimal damage to the environment. An average residual of 0.164077 was observed between the surfaces generated.

There were many factors that affected the quality of the acquired data during the data gathering of this research. These factors were illumination, surface type, depth, field of view of camera, speed of the USV, and the turbidity of water. For the illumination, it is better to have more light so that more features can be seen rather than it being dark and having to rely on an external source such as a flashlight, but the scattering of the light must also be considered. The methodology of this research is effective for still surfaces such as corals, rocks, and sand. But in the case of uniform surfaces such as sand, distinct features are needed to aid in the stitching of photographs. On the other hand, modelling seagrass is hard due to its movement. Holding all other factors constant, surveying deeper waters will give you greater overlaps between the photographs. However, the visibility of the bottom surface must be considered in surveying deeper waters. Greater field of view of the camera will also give you greater overlaps between the photographs. The speed of the USV must be based on the quality of the photographs that the camera can take, the depth of the water, and the desired overlap percentage between the photographs. Using USV on turbid water is not recommended because the bottom of the surface will not be visible. The battery of the equipment must also be considered especially when surveying large areas.

6. RECOMMENDATIONS

For the USV design, it is recommended to use a camera capable of GPS or at least place the camera directly below the GNSS receiver of the USV to avoid applying offset corrections which consumes time and may be a source for more errors (e.g. computational error). It also recommended to attach other sensors on the USV for more data.

For future similar studies, the researchers recommend taking oblique photographs of the surface to get more accurate heights of the features. Sidescan echo sounding is also recommended to be able to obtain the texture of the surface. It would also be of great help in the modeling of the surface if all photographs that will be used are geotagged. Finally, maximize the use of the orthophoto by classifying its features.

7. REFERENCES

Bibuli, M., Bruzzone, G., Caccia, M. Fumagalli, E., Saggini, E., Zereik, E., … Ivaldi, R. (2014). Unmanned surface vehicles for automatic bathymetry mapping and shores' maintenance.

Capra, A., Dubbini, M., Bertacchini, E., Castagnetti, C., & Mancini, F. (2015). 3D reconstruction of an underwater archaeological site: Comparison between low cost cameras. In: The International Archives of the Photogrammetry, Remote Sensing and Spatial Information Sciences, Vol. XL-5/W5, Piano di Sorrento, Italy.

Climate change indicators: Oceans. (2010). Retrieved from https://www.epa.gov/climate- indicators/oceans

Drap, P., Seinturier, J., Scaradozzi, D., Gambogi, P., Long, L., & Gauch, F. (2007). Photogrammetry for virtual exploration of underwater archaeological sites. Paper presented at the XXIth International CIPA Symposium, Athens, Greece.

Drap, P., Seinturier, J., Hijazi, B., Merad, D., Boi., J., Chemisky, B., … Long, L. (2015). The ROV 3D project: Deep-sea underwater survey using photogrammetry applications for underwater archaeology. Journal on Computing and Cultural Heritage. doi: 10.1145/2757283

Five effects of climate change on the ocean. (nd). Retrieved from https://www.conservation.org/publications/Documents/CI_Five-Effects-of-Climate-Change-on-the-Ocean.pdf

Fumagalli, E., Bibuli, M., Caccia, M., Zereik, E., Del Bianco, F., Gasperini, L., … Bruzzone, G. (2014). Combined acoustic and video characterization of coastal environment by means of unmanned surface vehicle.

Gavrilov, N., Duncan, A., McCauley, R., Parnum, I., Penrose, J., Siwabessy, P., … Tseng, Y. (2012). Characterization of the seafloor in Australia's coastal zone using acoustic techniques.

Guo, T., Capra, A., Troyer, M., Gruen, A., Brooks, A.J., Hench, J.L., … Dubbini, M. (2016). Accuracy assessment of underwater photogrammetric three dimensional modelling for coral reefs. In: ISPRS Archives, Vol. XLI-B5.

Jin, J., Zhang, J., Lv, Z., Shao, F., Li, M., Liu, L., & Zhang, P. (2016). Active and passive underwater acoustic application using an unmanned surface vehicle.

Kikuzawa, Y., Toh T., Ng., C., Sam, S., Taira, D., Afiq-Rosli, L., & Chou, L. (2018). Quantifying growth in maricultured corals using photogrammetry. Aquaculture Research, 1-7. doi: 10.1111/are.13683

Maas, H. (2015). On the accuracy potential in underwater/multimedia photogrammetry. Sensors, 15, 18140-18152.

Manley, J., Leonardi, A., & Beaverson, C. (2016). Research to operations: Evaluating unmanned surface vehicles.

Parnum, I., Siwabessy, J., Gavrilov, A., & Parsons, M. (2014). A comparison of single beam and multibeam SONAR systems in seafloor habitat mapping.

Pastore, T., & Kessel, R. (2009). Unmanned surface vessels for surface and subsurface threats in harbours: Background and practical lessons.

Rodriguez, D., Franklin, M., & Byrne, C. (2012). A study on the feasibility of autonomous surface vehicles.

Seinturier, J., Drap, P., Durand, A., Cibecchini, F., Vincent, N., Papini, O., & Grussenmeyer, P. (2004). Orthophoto imaging and GIS for seabed visualization and underwater archaeology. In: XXXII CAA, Prato, Italy.

Seto, M.L., & Crawford, A. (2015). Autonomous shallow water bathymetric measurements for environmental assessment and safe navigation using USVs.

Wilson, G., & Richards, J. (2006). Procedural documentation and accuracy assessment of bathymetric maps and area/capacity tables for small reservoir: U.S. Geological Survey scientific investigations report 2006-5208

Coastal And Shallow Water Sea Bed Mapping Using Imagery-Derived Bathymetric Approach

Kelvin Kang Wee, Tang (1,2) & Mohd Razali Mahmud (1)

[1] GeoCoastal Research Unit, Geospatial Imaging and Information Research Group (GI2RG),
Universiti Teknologi Malaysia, 81310 Johor Bahru, Malaysia
[2] Department of Survey and Mapping Johor, Department of Survey and Mapping Malaysia,
Wisma Persekutuan Johor Bahru, 80000 Johor Bahru, Malaysia
Email: tkwkelvin2@live.utm.my; kelvin@jupem.gov.my

KEY WORDS: Imagery-derived bathymetry, coastal, shallow water

ABSTRACT: Bathymetric mapping over coastal and shallow water region using vessel-based acoustic system is sometime hostile and inaccessible. It requires extensive amount of effort, time and money when it comes to the near shore and coastal region. Today, imagery-derived bathymetry has becoming popular and provides an alternative data gathering technique in particular the coastal and shallow water environment. The high refresh rate of imaging satellite data recorded every place on earth in high frequency rate has make it possible to distinguish the sea bed topography changes with periodic calculation of coastal bathymetries. Many initial attempts of using remotely sensed data and radiometric technique to estimate water depth over clear and shallow water had been developed since the past two decades. Throughout their remarkable efforts, a wide variety of algorithms for bathymetry retrieval have been developed and empirical models have been established to form the statistical relationship between image pixel values and water depth values. This paper highlights the ratio transform attempt proposed by Stumpf et al. to extract bathymetric information along the coastal region of Penang Island, Malaysia via Landsat-8 medium resolution (~30m) images. In the course of experiment, results have indicated that imagery-derived bathymetry technique can be valuable as a reconnaissance tool to vessel-based echo sounding survey. Conversely, multispectral imageries offer safe, time- and cost-effective solution to map the sea bed topography over broad areas.

1. INTRODUCTION

Making up more than 70 percent of the Earth's surface, the ocean is the largest component of earth's exterior. Today, more than 80 percents of international trade in the world is carried by sea (IHO, 2005) and more than 60 percent of the world's population inhabit at the valnerable coastal zone. The densely populated coastal zones are getting extremely versatile and dynamic (Syvitski et al. 2005). Human's activities have significantly affected coastline changes with the drastic expansion of coastal cities. Despite changes evolved by extreme weather events, erosion and currents, nearshore and coastal engineering activities can modify the coastal landscapes significantly. Therefore, accurate and periodic monitoring of the coastal zones also provide a better understanding of the scientific interaction and relationship between human and natural phenomena (Lu et al., 2011; Sun et al., 2012; Du et al., 2012).

At present, bathymetry depths are surveyed via acoustic gear (e.g. SBES & MBES) deployed from sea surface or submerged vessels. Hence, unmanned surface vehicle (USV) and remotely operated vehicle (ROV) are popular nowadays. Although these modern surveys have revealed invisible hazards previously unknown or imperfectly positioned, yet it is timely consuming and labour intensive when it comes to the near shore and coastal region as swath widths can be very narrow in shallow waters. Significant changes at those regions are almost not practical to be attempted using acoustic method. As a result, some of the charts that are used are out of date and may not always expose the potential hazards to users.

Monitoring the Earth's surface using satellite remote sensing approach has become more and more popular because of its vast spatial coverage and flexibility. The possibility of using remote sensing technology in bathymetric surveying has been addressed as early as the late 1960s (Polcyn and Sattinger, 1969; Brown et al., 1971; Ibrahim, 1988). Since the past two decades, numerous radiometric techniques to estimate water depth from remotely sensed data had been aggressively developed. Throughout remarkable efforts, a wide variety of bathymetry retrieval in either analytic, empirical or semi-analytic approaches have been established. At present, imagery-derived bathymetric technique has proven itself as a useful reconnaissance tool for near-shore bathymetric mapping (Pe'eri et al., 2013, Jawak et al., 2015; Jégat et al., 2016), and also being utilized in nautical charting (Mavraeidopoulos et al., 2017).

This study incorporates space-borne remote sensing and GIS techniques to map the coastal and shallow water areas. It is conducted to investigate and assess the appropriateness of extracting bathymetry information from optical multispectral satellite image. The ratio transform attempt proposed by Stumpf et al. (2003) is adopted in this study to extract bathymetric information along the coastal region of Penang Island, Malaysia via Landsat-8 medium resolution (~30m) multispectral images to generate a bathymetry map. By evolving the appropriate bands combination, these remotely-sensed data can become major supplementary sources for detecting water feature and obtaining water depth over the study area.

2. AREA OF STUDY

This study is focused on Penang Island, Malaysia, which is situated on the northwest coast of Peninsular Malaysia by the Strait of Malacca (Figure 1). Formerly, this fascinating island was named Prince of Wales Island when it was occupied by the British colonialism in the 18th century. It is geographically located between 5°5'40.5" to 5°36'8.11" at the latitude north and 100°10'12.0" to 100°33'13.22" at the longitude east. It is complemented with lavishness tropical rainfall forest and fringing beautiful sun-drenched beaches. Its marine environment is also blessed by homogeneous seabed topography and tranquil sea which supports various industrial activities such as port operation, fishery cannery as well as encourages the tourism in coastal areas. Generally, this study is limited to the coastal and shallow water areas which are distributed along the 104km coastal belts off the 293 km^2 irregularly shaped island.

Figure 1: The study area of Penang Island, Malaysia (Google Earth. 2018).

3. DATA AND METHODOLOGY

This study comprises three (3) major stages which incorporating satellite remote sensing and GIS techniques to extract bathymetric information from multispectral satellite images. The overall research methodology and processing stages such image pre-processing, image processing or bathymetric model construction as well as post data verification to assess the data accuracy is shown in Figure 2 below. The selection of data set potentially useable for satellite bathymetry mapping was based on the condition of the satellite image, significantly spectral coverage, spectrum range and ground resolution. As for this study, freely downloadable Landsat-8 satellite images dated 27th February 2014 which covers the entire Penang Island has been utilised in this case study (Figure 3). The multispectral images can be obtained from the United States Geological Survey (USGS) official website (http://glovis.usgs.gov/). Most of the satellite imagery processing tasks are conducted using ENVI 4.8 image processing software and ESRI ArcGIS 10.0 software.
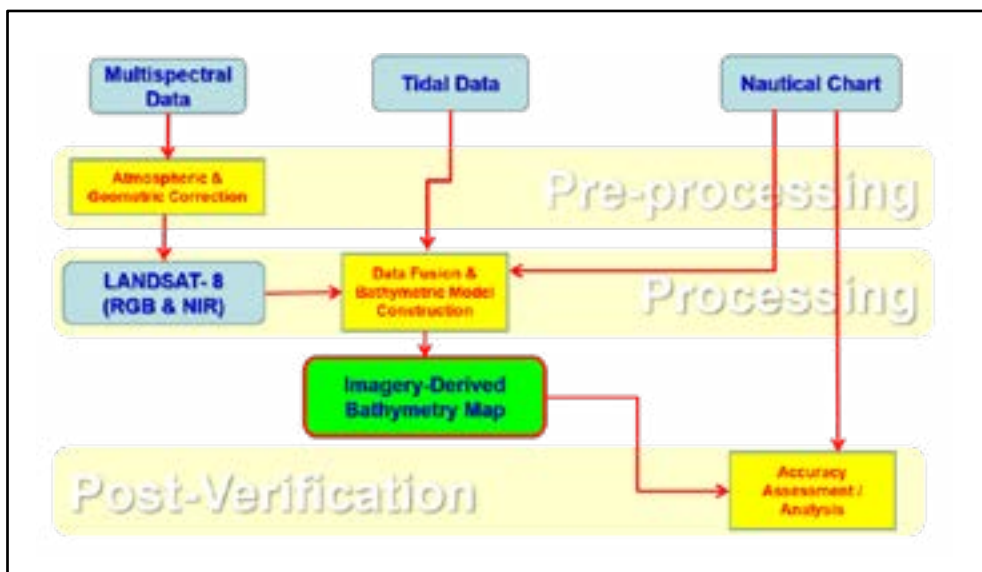
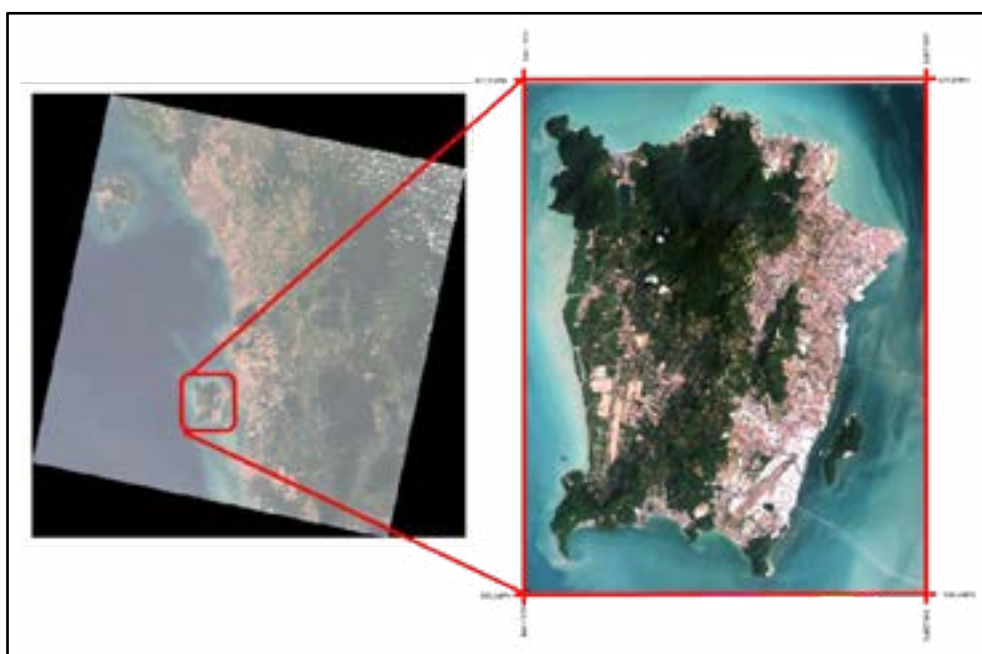Figure 2: The overall methodology and processing stages performed in this study.

Figure 3: Landsat 8 satellite image of Penang Island dated 27th February 2014.

Several ancillary data include tidal observation records obtained from nearest tide gauge station located at Kedah Pier and Nautical Chart - MAL 5529 of Pelabuhan Pulau Pinang produced by National Hydrographic Centre, Royal Malaysian Navy are utilised in this project. Hence, when multiple data are integrated together, it is vital to make sure that all the data are referenced to the same survey datum, both horizontal and vertical.

4.1 Image Pre-processing

Prior attempting to bathymetric model construction, image pre-processing tasks like radiometric, atmospheric and geometric correction have to be carried out in order to remove the undesired atmospheric effects, unnecessary path radiance, unwanted sea surface reflectance as well as correcting the geometry distortion of the imagery.

Radiometric correction allows the determination of the parameters of the radiometric calibration model, which aims to convert the electrical signal measured by the instrument, transformed in digital number (DN) into physical

spectral radiance measured at the sensor. Essentially, the radiation recorded at the satellite sensor may be influence by a range of unpredicted effects when it passes through the atmosphere properties such as the amount of water vapour, gas molecules, distribution of aerosols, suspended particles of dust which may change its transmittance. In order to eliminate the atmospheric errors, dark object subtraction (DOS) technique has been applied to derive a good estimate of the true at-ground upwelling radiance and then convert them into reflectance.

Subsequently, spatial sub-setting via normalised difference water index (NDWI) has been performed to distinguish between land features and water surface (McFeeters, 1996). The near-infrared (IR) is specifically sensitive to varying vegetation biomass, emphasizes soil-crop as well as land-water boundaries. In this case, the IR (band 5) and green (band 3) of the Landsat-8 are adopted to perform the spatial sub-setting process.

$$NDWI = \frac{L_{obs}(\lambda_R) - L_{obs}(\lambda_{IR})}{L_{obs}(\lambda_R) + L_{obs}(\lambda_{IR})} \qquad \text{(Equation 1)}$$

Where, $L_{obs}(\lambda_R)$ and $L_{obs}(\lambda_{IR})$ are the reflectance of red and NIR bands, respectively. Generally, IR absorption by water is greater than the visible spectrum. Therefore, water pixels will be typically characterised by lower IR band pixel values if compared to red band pixel values. The NDWI value usually ranges from -1 to 1 and zero is set as the threshold. Hypothetically, it is water mass if the NDWI value is positive; and it is non-water region if NDWI value is smaller than zero. As a result, water masses would have positive NDWI values.

4.2 Bathymetric Model Construction

According to the principle of Beer-Lambert Law, intensity of light decreases exponentially with depth, to relate the observed reflectance from the optical sensor to the water depth. Theoretically, the relationship between a pair of water-penetrating wavelengths can be empirically derived via the linear inversion approach. Stumpf et al. (2003) has developed this simplified linear regression algorithm to determine the bathymetric depth (Z) from two tuneable constant coefficients (m_0 and m_1) and a ratio of observed reflectance of two consecutive bands (R_i and R_j). It uses the division between observed reflectance log values to estimate water depth. Equation 2 below demonstrates the Stumpf et al.'s algorithm:

$$Z = m_0 * \frac{\ln(R_w(\lambda_i))}{\ln(R_w(\lambda_j))} - m_1 \qquad \text{(Equation 2)}$$

where   Z = depth value from derived depth
        R_w = observed reflectance value of band i and band j
        m_0 = tuneable constant to scale the ratio to depth
        m_1 = offset of a depth
        n = constant value

A set of measured bathymetric points has been chosen for the bathymetry inversion calibration process. Least square regression analysis is then being adopted to approximate the best fit value to resolve the two unknown tuneable constants (m_0 and m_1) in the above-mentioned equation. Hence, it is possible to extract the diffuse attenuation coefficients using Equation 3 and Equation 4 below. Practically, it is an important application in data fitting in solving the two unknown tuneable constants. The determined tuneable constants are then being inserted back into Equation 2 to construct the imagery-derived bathymetric model and being plotted into a bathymetric map.

$$\hat{x} = (A^T A)^{-1} A^T \hat{y} \qquad \text{(Equation 3)}$$

$$\begin{bmatrix} m \\ c \end{bmatrix} = \left(\begin{bmatrix} x_1 & 1 \\ x_2 & 1 \\ \vdots & \vdots \\ x_n & 1 \end{bmatrix}^T \begin{bmatrix} x_1 & 1 \\ x_2 & 1 \\ \vdots & \vdots \\ x_n & 1 \end{bmatrix} \right)^{-1} \begin{bmatrix} x_1 & 1 \\ x_2 & 1 \\ \vdots & \vdots \\ x_n & 1 \end{bmatrix}^T \begin{bmatrix} y_1 \\ y_2 \\ \vdots \\ y_n \end{bmatrix} \qquad \text{(Equation 4)}$$

4.3 Accuracy Assessment

The accuracy data assessment is an important step in the determining the usability of the manipulated data or commonly known as the quality assurance as well. Indeed, it involves a comparison of the water depth (Z) derived from bathymetric modal against the vertical measurement value obtained from vessel-based bathymetric survey or endorsed data extracted from the nautical charts. A further quantitative comparison and analysis was commenced to examine the accuracy between 50 imagery-derived bathymetric depths and endorsed shown in the nautical charts.

The accuracy assessment was done based on the precision uncertainty, correlation coefficient (r) and correlation of determination (r^2) between satellite-derived bathymetry data and depths extracted from endorsed nautical chart. Besides that, root mean square error (RMSE) test was also being used to evaluate the satellite-derived bathymetry accuracy.

5. RESULT AND DISCUSSION

Figure 4 below shows the water surface area extracted from the Landsat-8 multispectral images. The water masses are shown in (a) blue band, (b) green band, (c) red band and (d) infrared respectively. These bands were extracted in order to be utilized in computing the water depths within the study area.
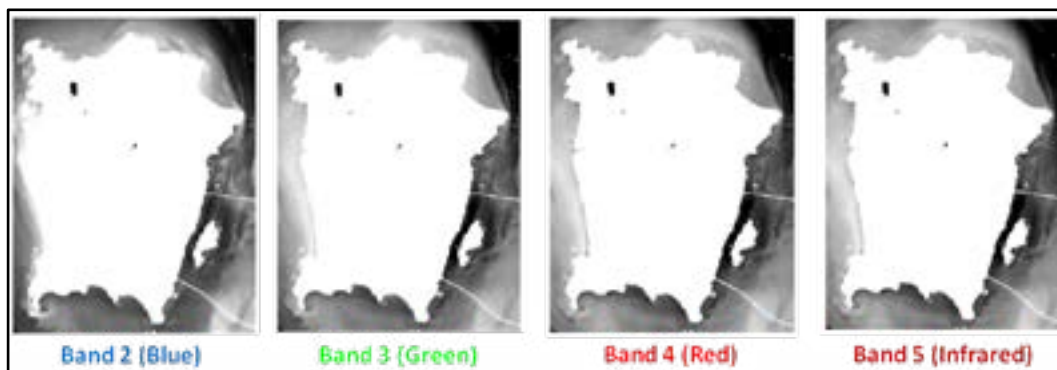

Figure 4: Water surface area extracted from Landsat-8. Image (a) blue (band 2); (b) green (band 3); (c) red (band 4); and (d) NIR (band 5).

Figrue 5 demonstrates the estimate water depths computed via the above-mentioned imagery-derived bathymetry model developed by Stumpf et al. (2003) using two respective visible bands, which are band 2 (Blue) and band 3 (Green). Base on the imagery-derived bathymetric data, the depths of the seabed vary with locations. The result depicted that the water level recorded around the study area were between datum level to more than 18.6m below the respective chart datum (CD).
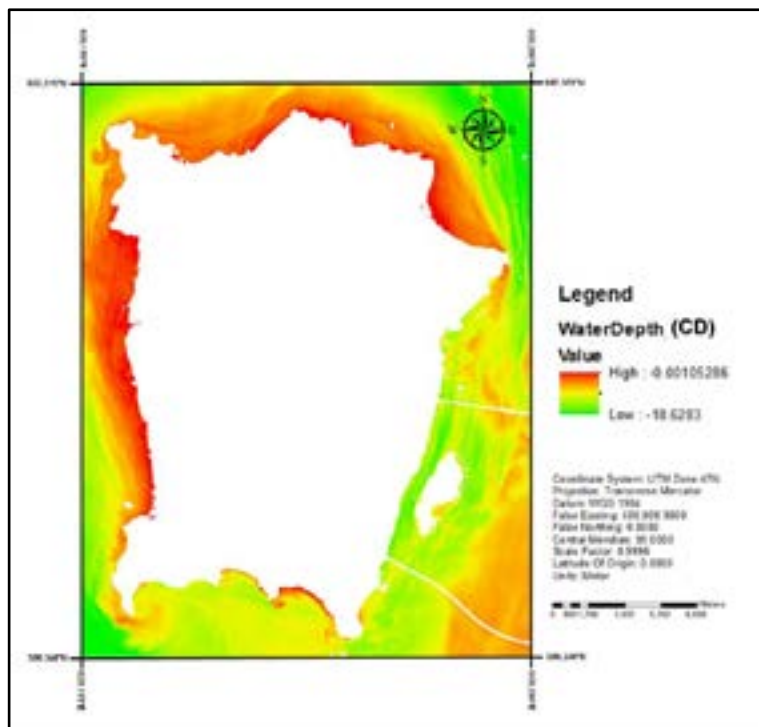

Figure 5: Bathymetry maps derived based on Stumpf et al. approach over the study area.
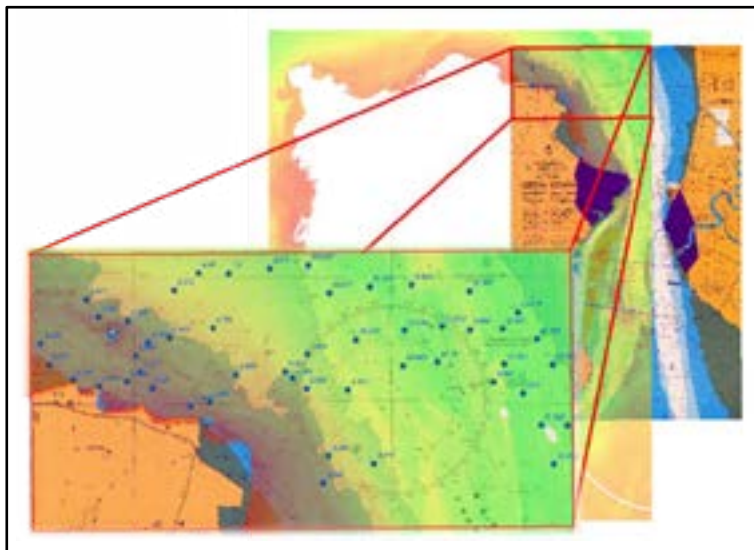Image (a) bathymetric model in CD; and (b) Bathymetric model in MSL.

Figure 6: Data Quality Assessment of Checking Area.

In order to quantitatively evaluate and assess the accuracy of the imagery-derived bathymetry, data quality assessment was done by using 50 check points taken out from the MAL5529. Figure 6 below illustrates the 50 randomly selected checking data which were located at the northeast of the Penang Island.
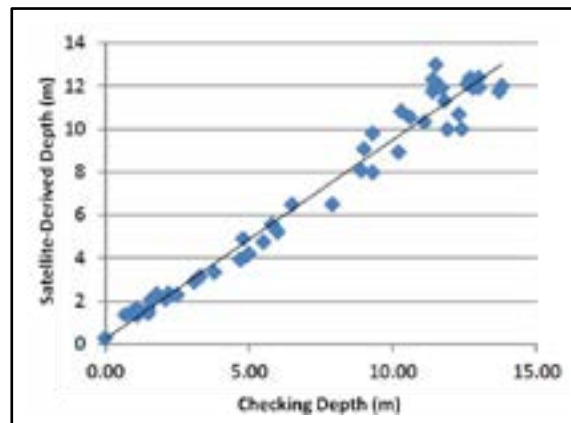

Figure 7: Correlation between the imagery-derived bathymetry depth and endorsed depth.

The elected satellite-derived bathymetry points within the checking area were ranged from datum level to 13.8m in depth with relative to the CD. Detailed results of plotting satellite-derived depth against the endorsed depth across the study area were presented in Figure 7. The correlation coefficient (r) between the derived bathymetry depth and testing data is 0.9065 and the correlation of determination (r^2) achieved is 0.82 based on the linear regression modal. Based on the data accuracy assessment, the uncertainties recorded were ranged from -2.40m to 1.49m. The highest RMSE recorded was of 2.401m, while the lowest RMSE was of 0.005m. Total RMSE calculated based on the endorsed 50 reference points was 0.655m.

6. CONCLUSION

In the completion of this study, the research goal and objectives are successfully attained. A shallow water coastal bathymetry map has been successfully mapped via the space borne bathymetric mapping technique. The proposed derivation method which gauging the relative attenuation of blue (band 2) and green (band 3) radiations. The results presented above show that this empirical model represent a promising outcome and able to provide realistic seabed terrain profiles. Feasibly, it can be used to complement data from SBES, which normally obtained at medium to course profiling resolution for the purpose of survey reconnaissance to distinguish the coastal and shallow water seabed topography or the detection of coastline change by stacking a time-series data.

REFERENCES

1. Bierwirth, P., Lee, T., & Burne, R. (1993). Shallow sea-floor reflectance and water depth derived by unmixing multispectral images. *Photogrammetric Engineering and Remote Sensing;(United States), 59*(3).

2. Dierssen, H. M., Zimmerman, R. C., Leathers, R. A., Downes, T. V., & Davis, C. O. (2003). Ocean color remote sensing of seagrass and bathymetry in the Bahamas Banks by high-resolution airborne imagery. *Limnology and Oceanography, 48*(1part2), 444-455.

3. Doxani, G., Papadopoulou, M., Lafazani, P., Pikridas, C., & Tsakiri-Strati, M. (2012). Shallow-water bathymetry over variable bottom types using multispectral Worldview-2 image. *International Archives of the Photogrammetry, Remote Sensing and Spatial Information Sciences, 39*(8), 159-164.

4. Gao, J. (2009). Bathymetric mapping by means of remote sensing: methods, accuracy and limitations. *Progress in Physical Geography, 33*(1), 103-116.

5. Hamylton, S. M., Hedley, J. D., & Beaman, R. J. (2015). Derivation of high-resolution bathymetry from multispectral satellite imagery: a comparison of empirical and optimisation methods through geographical error analysis. *Remote Sensing, 7*(12), 16257-16273. doi:10.3390/rs71215829

6. Jawak, S. D., Vadlamani, S. S., & Luis, A. J. (2015). A synoptic review on deriving bathymetry information using remote sensing technologies: models, methods and comparisons. *Advances in Remote Sensing, 4*(02), 147.

7. Ji, L., Zhang, L., & Wylie, B. (2009). Analysis of dynamic thresholds for the normalized difference water index. *Photogrammetric Engineering & Remote Sensing, 75*(11), 1307-1317.

8. Jupp, D. (1988). *Background and extensions to depth of penetration (DOP) mapping in shallow coastal waters.* Paper presented at the Symposium on Remote Sensing of the Coastal Zone, Gold Coast, Queensland.

9. Lyzenga, D. R. (1978). Passive remote sensing techniques for mapping water depth and bottom features. *Appl Opt, 17*(3), 379-383. doi:10.1364/AO.17.000379

10. Lyzenga, D. R. (1985). Shallow-water bathymetry using combined lidar and passive multispectral scanner data. *International journal of remote sensing, 6*(1), 115-125.

11. Lyzenga, D. R., Malinas, N. R., & Tanis, F. J. (2006). Multispectral bathymetry using a simple physically based algorithm. *Ieee Transactions on Geoscience and Remote Sensing, 44*(8), 2251-2259. doi:10.1109/Tgrs.2006.872909

12. Pacheco, A., Horta, J., Loureiro, C., & Ferreira, Ó. (2015). Retrieval of nearshore bathymetry from Landsat 8 images: a tool for coastal monitoring in shallow waters. *Remote sensing of environment, 159*, 102-116.

13. Pe'eri, S., Madore, B., Nyberg, J., Snyder, L., Parrish, C., & Smith, S. (2016). Identifying bathymetric differences over alaska's north slope using a satellite-derived bathymetry multi-temporal approach. *Journal of Coastal Research*, 56-63. doi:10.2112/Si76-006

14. Said, N. M., Mahmud, M. R., & Hasan, R. C. (2017). Satellite-derived bathymetry: Accuracy assessment on depths derivation algorithm for shallow water area. *International Archives of the Photogrammetry, Remote Sensing & Spatial Information Sciences, 42*.

15. Stumpf, R. P., Holderied, K., & Sinclair, M. (2003). Determination of water depth with high-resolution satellite imagery over variable bottom types. *Limnology and Oceanography, 48*(1), 547-556.

16. Tang, K.K.W., & Pradhan, B. (2015). *Converting digital number into bathymetric depth: A case study over coastal and shallow water of Langkawi Island, Malaysia.* Paper presented at the FIG Working Week 2015, Sofia, Balgeria.

17. Zheng, G., Chen, F., & Shen, Y. (2017). Detecting the water depth of the South China Sea reef area from WorldView-2 satellite imagery. *Earth Science Informatics, 10*(3), 331-337.

RETRIEVAL OF SUBMARINE GROUNDWATER DISCHARGE FLOW RATES USING AIRBORNE THERMAL INFRARED DATA ACQUIRED AT TWO DIFFERENT TIDAL HEIGHTS

Ki-mook Kang (1), Duk-jin Kim* (1), Bong-Gwan Kim (1), Eunhee Lee (2), Seung Hee Kim (1),
Yunjee Kim (1), Kyoochul Ha (2), Dong-Chan Koh (2), Yang-Ki Cho (1), and Guebuem Kim (1)

[1] School of Earth and Environmental Sciences, Seoul National University, Republic of Korea
[2] Groundwater & Ecohydrology Research Center, Geologic Environment Division, Korea Institute of Geoscience and Mineral Resources (KIGAM), Republic of Korea

Email: mook0416@snu.ac.kr; djkim@snu.ac.kr; bongan@snu.ac.kr; eunheelee@kigam.re.kr;
dalcomeboy@snu.ac.kr; yunjee0531@snu.ac.kr; hasife@kigam.re.kr; chankoh@kigam.re.kr;
gkim@snu.ac.kr; choyk@snu.ac.kr

KEY WORDS: Submarine groundwater discharge (SGD), thermal infrared (TIR) remote sensing, Jeju Island, sea surface temperature (SST), temperature anomaly

ABSTRACT: Submarine groundwater discharge (SGD) plays an important role in coastal biogeochemical processes and hydrological cycles, particularly off volcanic islands standing in oligotrophic oceans. However, limited access of SGD measurements over a large scale prevents from fully understanding the spatio-temporal variations. This study tries to quantify the temporal and spatial variations of SGD using four airborne thermal infrared (TIR) surveys over the entire coast of Jeju Island, Korea. The surveys were done twice, each during high and low tide, and the data showed a linear correlation between the temperature anomaly and squares of groundwater velocity and a negative exponential correlation between the anomaly and depth (included tide height and bathymetry). Using these relationships, a new analytic equation for estimating the SGD flow rates using temperature anomaly at any tide height was derived. The method was validated using the measured SGD flow rates with in-situ measurement using a current meter at Gongcheonpo Beach. Despite difficulty of the on-site observation of SGD flow rates, the SGD flow rates were directly retrieved using the temperature anomaly in combination with high-resolution coastal bathymetry map and tide height. This approach is expected to be applied to rapid and efficient estimation of SGD over coastal areas off oceanic islands where fresh groundwater discharge is significant and results in great impact on coastal ecosystems.

1. INTRODUCTION

Submarine groundwater discharge (SGD) has been recognized as an important coastal process in transporting materials from continental to marine environments (Burnett, Bokuniewicz, Huettel, Moore, & Taniguchi, 2003; Kim, Ryu, Yang, & Yun, 2005; Kim & Swarzenski, 2010). SGD is an important source for the introduction of nutrients, contaminants, and other significant chemical components into coastal waters (Schmidt, Santos, Burnett, Niencheski, & Knöller, 2011). In particular, the SGD in many volcanic islands occurs at high flow rates due to the typically high topographic relief, high permeability of basaltic rocks, and high tidal range (Garrison, Glenn, & McMurtry, 2003; Kim, Lee, Park, Hwang, & Yang, 2003). Such large SGD from volcanic islands has significant implications for coastal environments and their ecology. Volcanic islands such as Jeju Island, off the south coast of Korea, rely on groundwater as their main source of drinking water, so their coastal aquifers are particularly sensitive to both marine and terrestrial stressors (Kim, Kim, & Hwang, 2011; Lee & Kim, 2007). Thus, quantifying SGD on Jeju Island is essential for developing appropriate groundwater management strategies and understanding coastal geochemical processes and hydrological cycles.

Since the 1970s, thermal infrared (TIR) remote sensing techniques have been employed for detecting SGD spatially, using the difference in surface temperatures between groundwater and sea water (Deutsch. 1974; Wilson & Rocha, 2012). Airborne TIR remote sensing has been used in an attempt to show the spatial variability of SGD at higher spatial resolutions than space-borne TIR imagery is capable of demonstrating (Kelly, Glenn, & Lucey, 2013; Mejías et al., 2012; Tamborski, Rogers, Bokuniewicz, Cochran, & Young, 2015). Our research team has previously presented the possibility of detecting SGD around Jeju Island using airborne TIR imagery (Lee et al., 2016a). However, earlier studies mainly focused on the plume area for extracting SGD flow rate without considering the tide height and bathymetry. Despite the importance of knowing the SGD amount along the entire coast of Jeju Island, no studies of SGD flow rates using TIR remote sensing have yet been reported from the island, except in those using on-site measurements.

In this study, we retrieve the total SGD flow rate in Jeju Island using airborne TIR data acquired at both high and low tides. We also introduce a method that includes bathymetry and tidal range to translate spatially explicit airborne TIR data into total SGD rates for Jeju Island. Methodologically, it is based on Bernoulli's theory and the Parallelized Large-Eddy Simulation Model (PALM).

2. STUDY AREA AND DATA ACQUISTION

We conducted experiments on three sites (Fig. 1): (a) Kimnyung Bay is located on the northern coast of Jeju Island, where Cheonggulmul, near Kimnyung Bay, has long been known for its natural outdoor bathing pool due to abundant groundwater discharge; (b) Bangdu Bay, on the eastern coast, is also an active site for SGD, known to play a major role in nutrient budgeting from SGD (Hwang, Lee & Kim, 2005); and (c) Gongcheonpo Beach, on the southern coast, is characterized by fractured volcanic rocks with point-sourced groundwater discharges (Lee et al., 2016b). These are highly suitable and important sites for studying the characteristics of SGD on a regional scale. We carried out four airborne TIR surveys to detect sea surface temperature (SST) anomalies along the entire coast of Jeju Island (Fig. 1).
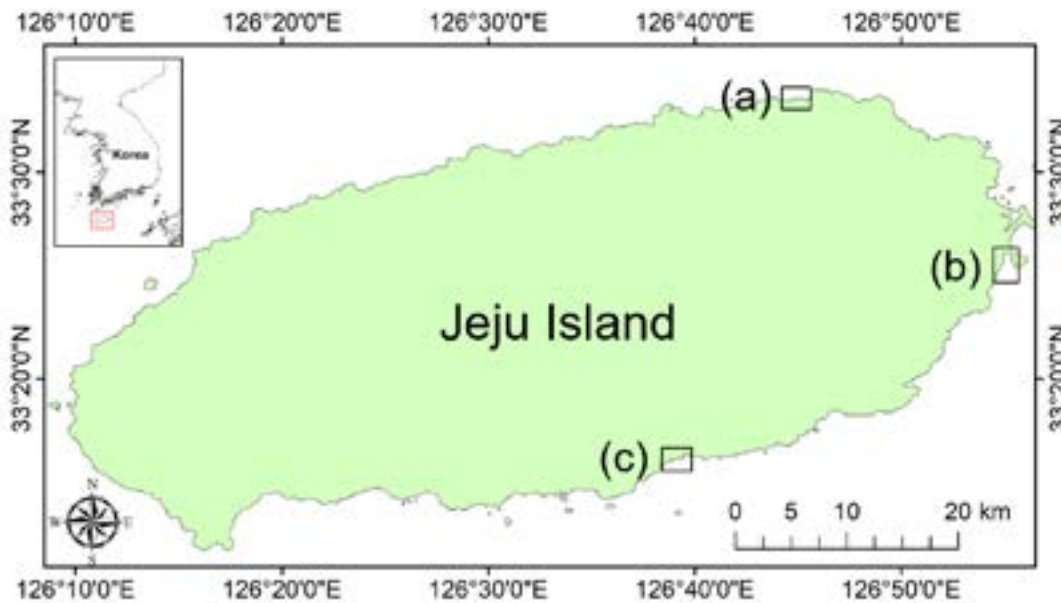
Figure 1 Study area (Jeju Island, South Korea); (a) Kimnyung Bay, (b) Bangdu Bay, and (c) Gongcheonpo Beach were chosen for further analysis.

3. AIRBORNE THERMAL INFRARED DATA

The airborne TIR data were atmospherically corrected using the atmospheric radiative transfer model SBDART (Santa Barbara DISORT Atmospheric Radiative Transfer) (Ricchiazzi, Yang, Gautier, & Sowle, 1998). The atmospheric temperature, humidity, and pressure were measured using an onboard thermometer/hygrometer. Earlier studies showed that the RMSE between in-situ measurements and the airborne TIR sensor data is about 0.40 °C (Kang, Kim, Kim, Cho, & Lee, 2014; Kim et al., 2015). Furthermore, the atmospherically corrected TIR data were also georeferenced using positions, sensor orientations, and altitude information such as yaw, pitch, and roll, taken from an onboard GPS/inertial measurement unit (Fig. 2). The georeferencing was carried out automatically using a simple collinearity equation since the acquired TIR data points numbered in the tens of thousands, and the Ground Control Points (GCPs) were hard to recognize in the coastal regions or in the open sea. All of the airborne remote sensing system's components were automatically synchronized with GPS time (Kim et al., 2015).
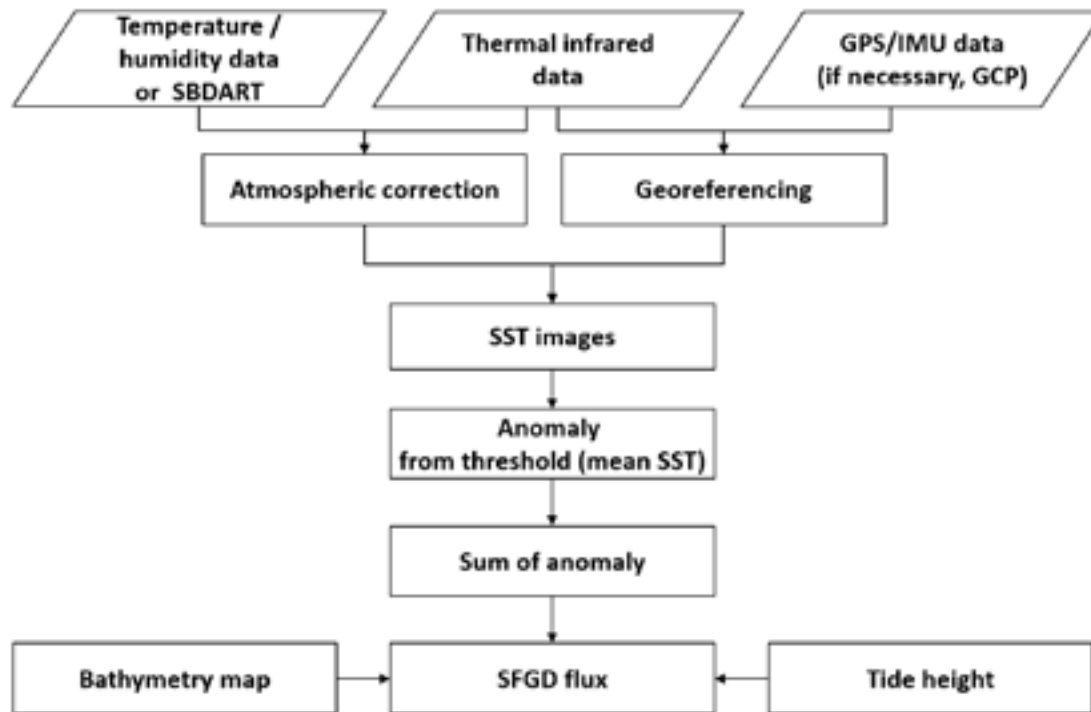
Figure 2 Flowchart for estimating the SGD flux from airborne TIR data

## 4. EQUATION OF SGD FLOW RATE USING MODEL

The equation was analytically derived from the simulated results from Bernoulli's theory and the PALM model (Raasch and Schröter, 2001). The depth and velocity of the source groundwater were varied to find their relationships with the anomaly between the SGD and the sea surface. We found the anomaly to increase by the square when the velocity of the groundwater increased. On the other hand, we found that the anomaly gradually increased when the depth decreased before converging to a constant value. Assuming constant groundwater volume and velocity, the result also represents the negative exponential function between the anomaly and constant depth. Thus, the SGD flow rate can be expressed as the product of the linear and exponential correlation terms as shown:

$$Q = kae^{0.5\alpha h}, \tag{1}$$

where h is the water column depth from the tide-corrected ocean surface to the seafloor using tide height (H) and high-resolution bathymetry data (d), respectively ($h = d + H$); α is the coefficient of depth's function; and the coefficient (k) is the constant with respect to the tide height and groundwater velocity. The coefficient of depth's function (α) can be determined using the simulated result of the PALM, of which temperature anomaly is estimated based on flow velocity.

5. RESULT

We extracted the results of a mosaicked (all flight paths) SST map along the coast generated from the airborne TIR data, collected over two full tidal cycles, overlaid on a combined bathymetry and topography map. The influence of SGD on SST was clearly observable as the SST changed dynamically depending on the tide height. Fig. 3 shows the SGD flow rates at (a) Kimnyung Bay, (b) Bangdu Bay, and (c) Gongcheonpo Beach using the anomalies between SGD and mean SST. Since airborne TIR surveys along the entire coast of Jeju Island were performed within 1–2 hours, we were able to quickly retrieve the SGD flow rate using the sum of the anomalies' responses to the tidal range.
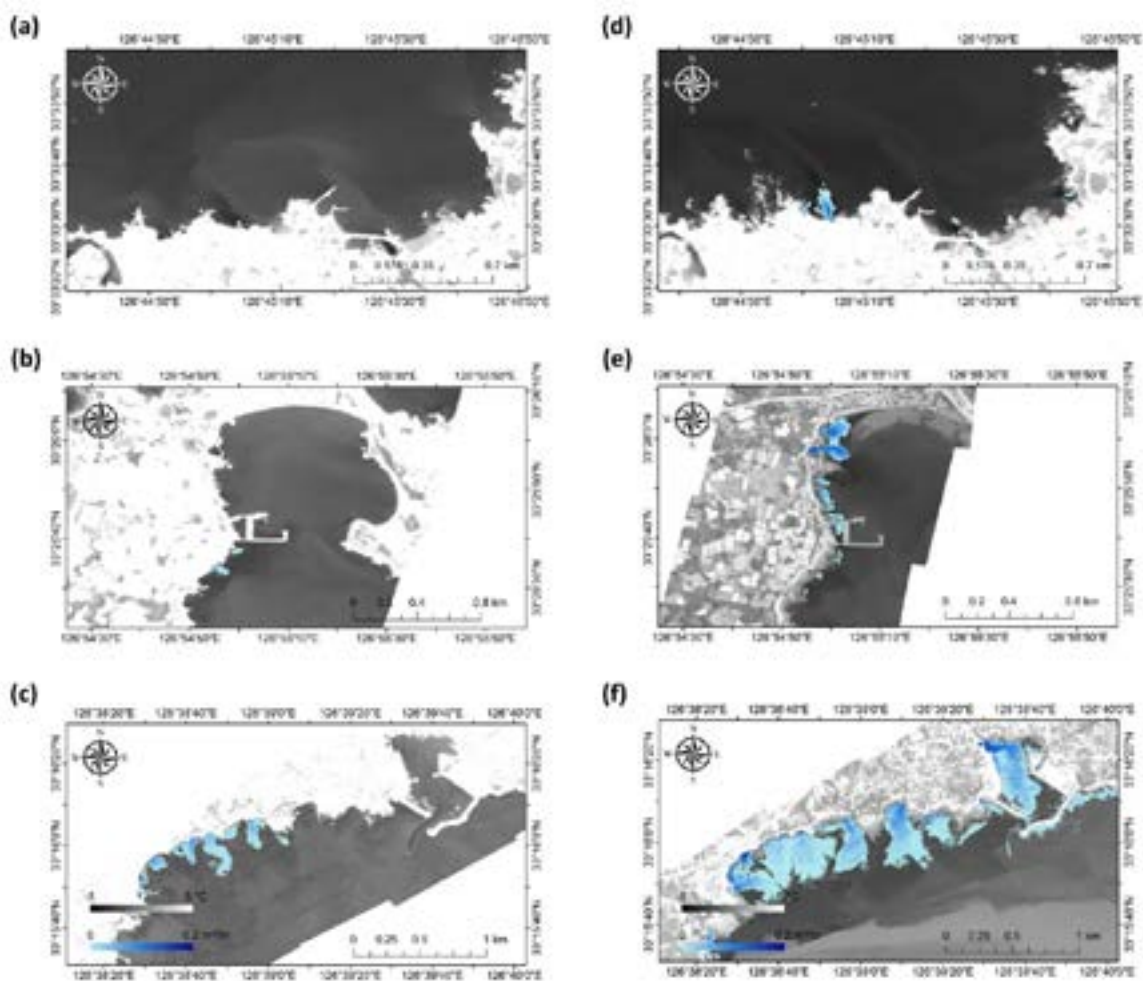
Figure 3 Geo-referenced SST anomaly and flow rate map at the three study locations: (a) Kimnyung Bay at high tide, (b) Bangdu Bay at high tide, (c) Gongcheonpo Beach at high tide, (d) Kimnyung Bay at low tide, (e) Bangdu Bay at low tide, and (f) Gongcheonpo Beach at low tide.

6. CONCLUSION

In this study, we obtained spatiotemporal airborne TIR data for the estimation of the SGD flow rate into coastal waters around Jeju Island, Korea. We collected four airborne TIR datasets to cover two complete tidal cycles and found a highly linear correlation between the SST anomalies recorded by TIR and the tide height. We derived a new equation to extract SGD flow rates with two airborne TIR datasets, each acquired at different tide heights. The equation was analytically derived from the simulated results from Bernoulli's theory and the PALM model describing a linear correlation between the anomaly and the squared groundwater velocity. A negative exponential correlation was found between the anomaly and water column depth (tide height and bathymetry included). This study shows that surface temperature anomalies between groundwater and sea water, used in conjunction with tide height and bathymetry maps, are effective tools for quantifying SGD. As it was possible to conduct airborne TIR surveys along the entire coast of Jeju Island in only 1–2 hours, we could conceivably quickly retrieve the SGD flow rate over a large area using the sum of the anomalies' response to tide height.

REFERENCE

Burnett, W. C., Bokuniewicz, H., Huettel, M., Moore, W. S., & Taniguchi, M. (2003). Groundwater and pore water inputs to the coastal zone. Biogeochemistry, 66, 3–33. DOI:10.1023/B:BIOG.0000006066.21240.53.

Deutsch M. 1974. Survey of remote sensing applications. Water Well Journal, 28(7), 35-38.

Garrison, G. H., Glenn, C. R., & McMurtry, G. M. (2003). Measurement of submarine groundwater discharge in Kahana Bay, O'ahu, Hawaii. Limnology and Oceanography, 48(2), 920–928. DOI:10.4319/lo.2003.48.2.0920.

Hwang, D.-W., Lee, Y.-W., & Kim, G. (2005). Large submarine groundwater discharge and benthic eutrophication in Bangdu Bay on volcanic Jeju Island, Korea. Limnology and Oceanography 50(5), 1393–1403. DOI: 10.4319/lo.2005.50.5.1393.

Kang, K.-M., Kim, S. H., Kim, D.-J., Cho, Y.-K., & Lee, S.-H. (2014). Comparison of coastal sea surface temperature derived from ship-, air-, and space-borne thermal infrared systems. In IEEE Geoscience and Remote Sensing Symposium, 4419–4422. DOI:10.1109/IGARSS.2014.6947471.

Kelly, J. L., Glenn, C. R., & Lucey, P. G. (2013). High-resolution aerial infrared mapping of groundwater discharge to the coastal ocean. Limnology and Oceanography: Methods, 11(5), 262–277. DOI: 10.4319/lom.2013.11.262.

Kim, D., Jung, J., Kang, K.-M., Kim, S. H., Xu, Z., Hensley, S.,…Duersch, M. (2015). Development of a cost-effective airborne remote sensing system for coastal monitoring. Sensors, 15, 25366–25384. DOI:10.3390/s151025366.

Kim, G., Kim, J. S., & Hwang, D. W. (2011). Submarine groundwater discharge from oceanic islands standing in oligotrophic oceans: Implications for global biological production and organic carbon fluxes. Limnology and Oceanography, 56(2), 673–682. DOI: 10.4319/lo.2011.56.2.0673.

Kim, G., Lee, K.-K., Park, K.-S., Hwang, D.-W., & Yang, H.-S. (2003). Large submarine groundwater discharge (SGD) from a volcanic island. Geophysical Research Letters 30, 2098. DOI: 10.1029/2003GL018378.

Kim, G., Ryu, J.-W., Yang, H.-S., & Yun, S.-T. (2005). Submarine groundwater discharge (SGD) into the Yellow Sea revealed by 228 Ra and 226 Ra isotopes: implications for global silicate fluxes. Earth and Planetary Science Letters, 237(1), 156–166. DOI:10.1016/j.epsl.2005.06.011.

Kim, G. & Swarzenski, P. W. (2010). Submarine groundwater discharge (SGD) and associated nutrient fluxes to the coastal ocean. In: Liu KK., Atkinson L., Quiñones R., Talaue-McManus L. (eds) Carbon and Nutrient Fluxes in Continental Margins. Global Change – The IGBP Series. Springer, Berlin, Heidelberg. pp. 529–538. DOI:10.1007/978-3-540-92735-8_11.

Lee, E., Kang, K.-M., Hyun, S.-P., Lee, K.-Y., Yoon, H., Kim, S. H.,…Ha, K. (2016a). Submarine groundwater discharge revealed by aerial thermal infrared imagery: a case study on Jeju Island, Korea. Hydrological Processes, 30(19), 3494–3506. DOI:10.1002/hyp.10868.

Lee, E., Yoon, H., Hyun, S. P., Burnett, W. C., Koh, D.-C., Ha, K.,…Kang, K.-m. (2016b). Unmanned aerial vehicles (UAVs)-based thermal infrared (TIR) mapping, a novel approach to assess groundwater discharge into the coastal zone. Limnology and Oceanography: Methods, 14(11). DOI:10.1002/lom3.10132.

Lee, J.-M. & Kim, G. (2007). Estimating submarine discharge of fresh groundwater from a volcanic island using a freshwater budget of the coastal water column. Geophysical Research Letters, 34, L11611. DOI: 10.1029/2007GL029818.

Mejías, M., Ballesteros, B. J., Antón-Pacheco, C., Domínguez, J. A., Garcia-Orellana, J., Garcia-Solsona, E., & Masqué, P. (2012). Methodological study of submarine groundwater discharge from a karstic aquifer in the Western Mediterranean Sea. Journal of Hydrology, (464–465), 27–40. DOI:10.1016/j.jhydrol.2012.06.020.

Raasch, S. & Schröter, M. (2001). PALM–a large-eddy simulation model performing on massively parallel computers. Meteorologische Zeitschrift, 10(5), 363–372. DOI:10.1127/0941-2948/2001/0010-0363.

Ricchiazzi, P., Yang, S., Gautier, C., & Sowle, D. (1998). SBDART: a research and teaching software tool for plane-parallel radiative transfer in the earth's atmosphere. Bulletin of the American Meteorological Society, 79, 2101–2114. DOI:10.1175/1520-0477(1998)079<2101:SARATS>2.0.CO;2.

Schmidt, A., Santos, I. R., Burnett, W. C., Niencheski, F., & Knöller, K. (2011). Groundwater sources in a permeable coastal barrier: Evidence from stable isotopes. Journal of Hydrology, 406(1–2), 66–72. DOI:10.1016/j.jhydrol.2011.06.001.

Tamborski, J. J., Rogers, A. D., Bokuniewicz, H. J., Cochran, J. K., & Young, C. R. (2015). Identification and quantification of diffuse fresh submarine groundwater discharge via airborne thermal infrared remote sensing. Remote Sensing of Environment, 171, 202−217. DOI:10.1016/j.rse.2015.10.010.

Wilson J, & Rocha C. (2012). Regional scale assessment of Submarine Groundwater Discharge in Ireland combining medium resolution satellite imagery and geochemical tracing techniques. Remote Sensing of Environment, 119, 21-34. DOI:10.1016/j.rse.2011.11.018.

Estimation of Three Dimensional Shoreline Using Terrestrial Laser Scanning Data : Case Study at Bangameori Beach

Kong-Hyun Yun[1] , Yeong Sun Song[2] and Gihong Kim[3]

[1]*Institute of Engineering Research, Yonsei University, ykh1207@yonsei.ac.kr*

[2]*Dept. of Aerial Geoinformatics, Inha Technical College, point196@inhatc.ac.kr*

[3]*Dept. of Civil Engineering, Gangneung-Wonju National University, ghkim@gwnu.ac.kr*

KEY WORDS: Shoreline, Laser Scanning data, Coastal Erosions, Bangamoeri beach.

ABSTRACT: In the coasts of western south Korea, the problem of coastal erosions is a serious social issue for the local residents in that area. Also these phenomena are regarded as potential threat to the existing buildings on the coastal zone. Global warming and human activities for the social infrastructure developments are the assumed causes for the coastal erosions. In this paper, we estimated the shoreline changes using existing two dimensional shorelines digital map which was published in the 2013 by KHOA(Korea Hydrographic and Oceanographic Agency) and recently acquired terrestrial laser canning data at Bangameori beach in the west coast of south Korea during roughly 10 years. In this research, we collected existing two dimensional shorelines published by KHOA in the year 2013. However, unfortunately we cannot obtain AHHWL(Approximately Highest High Water Level) including three dimensional position in the old years due to the data absence. So we proposed following steps for the acquisition of shorelines in the old years. First, we delineated the shoreline derived existing map in the year 2013. It contains only two dimensional position. There is no height information for AHHWL. Second, we use stereo pair of scanned images in the year 2013 After photogrammetric orientation process is accomplished using bundle adjustments We can obtain accurate height information. Last we can trace the two dimensional position on the AHHWL in the remaining year. And in the 2018, we collected and processed the laser scaning data at the same area. Finally, we compare the difference between two shoreline data sets.

1. INTRODUCTION

Understanding the complex causes on coastal transformation related to the management remains very challengeable in spite of numerous research programs for the fully recognition behavior(Zhang et al., 2004; Dickson et al., 2007; Nicholls and Cazenave, 2010; Nicholls et al., 2012, 2013). Moreover, it is very difficult to discriminate the main causes for the coastal behavior for event-driven changes and longtime cumulative changes in the inter-annual period (Fenster et al., 2001; Woodroffe and Murray-Wallace, 2012)

The practical problem of understanding the coastal behavior is the scarcity of multi decadal datasets being a major obstacle to the accurate quantitative analysis and trends in shoreline environments(Le Cozannet et al., 2014; Garcin et al., 2016). Recently the availability of higher frequency of aerial images and high spatial resolution Lidar becomes to the attractive data sources for the shoreline change analysis. Especially airborne and terrestrial laser scanning data come to be a valuable data from annual to decadal change analysis in the local area(Pye and Blott, 2016).

In this study, approximately during 10 years for the coastal study digital aerial photos and terrestrial lidar scanning data were used. In the process of it, the photogrammetric principles were applied. Finally, we recognized the coastal erosion trends in the research area.

2. RESEARCH AREA AND DATA SETS

The study area is relatively small region (latitude 37° 17' N, longitude 126° 34' E) of approximately 200,000 m^2 located in Bangamori beach, west coast of south Korea. It is about 1~9m above sea level and has relatively very flat terrain relief of 0.5 to 2.5m. Figure 1 shows the study site. Generally, to obtain a stereo model containing the shoreline from aerial images, it is enough to use one pair of images; one is seaward and the other landward images with respect to the shoreline. One inland photograph is added to build a block of photographs in an attempt to test whether this addition of photographs may resolve the problem of photogrammetry in coastal areas. GCPs were carefully selected more than 15points from 30 candidates found from photographic images, considering that (1) they must have time-invariant characteristics, meaning that they are same over photographs of different years, (2) they have enough space for the GPS-VRS surveying, and last (3) they are evenly distributed over the research area. Before the GPS-VRS

surveying, they were explored to check whether they really exist, how to access them and how suitable to use GPS-VRS.

Figure 1. Coverage of this study area marked with red ellipsoid: (Image source: map.daum.net)

3. SHORELINE EXTRACTION

For accurate mapping shorelines over 10 years including coastal changes, it needs high spatial resolution aerial images and unchanged evenly distributed GCPs. In this research, first, we collected existing two dimensional shorelines published by KHOA in the year 2013. Unfortunately we cannot obtain AHHWL(Approximately Highest High Water Level) including three dimensional position in the old years. So we used following steps for the acquisition of shorelines in each collected aerial image pair. First, we delineated the shoreline derived existing map in the year 2013. It contains only two dimensional position. There is no height information for AHHWL. Second, we use stereo pair of scanned images in the year 2013. After photogrammetric orientation process is accomplished using carefully selected GCPs. We can obtain accurate digital elevation models Last we can extraction the two dimensional position on the AHHWL in the remaining year. In the process of terrestrial laser scanning data, First, we acquired the data set in the Feb, 2018 with GPS-VRS surveying. The C10, the model of terrestrial laser scanner was used. Considering the range of laser scanner is roughly 40~100m, we acquired the scanning data at 15 points along the beach with 1km length. for sufficient coverage. Figure 1. shows the acquired data set in the research area. In the raw data sets, registration from the several scanning data sets is the first process. And then we extract the 4.4m contour line which means the shoreline in the research area.
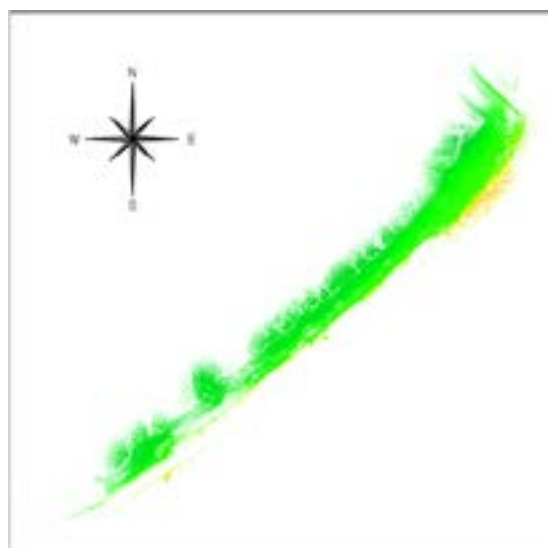
Figure 1. Coverage of Terrestrial laser scanning data

2866

Figure 2~4 shows the shoreline changes from 2009 to 2018. The elevation line with yellow mark derived from the photogrammetric process in the 2009 year. In the 2018, elevation lines were extracted from laser scanning data sets. In the northern part of beach, the examination shows that beaches gradually have been eroded especially in the lower elevations

Figure 2. Generated shoreline in the year 2009 and 2018

Figure 3. Generated sea level with 3.0m in the year 2009 and 2018

Figure 4. Generated sea level with 2.0m in the year 2009 and 2018

Figure 5. Detailed look of beaches

Figure 6. Recently constructed small embankment on the beach

4. CONCULSIONS AND FUTURE WORKS

Quantitative information on shoreline position is very important to the varied aspects of coastal management, including coastal defense, climate change adaptation, coastal hazard and economic zoning. Therefore, most research has been done with the emphasis on the shoreline change analysis with respect to the sparse documented reference data. In this study, Aerial images and terrestrial laser scanning data were used to calculate shoreline changes in three dimension over midterm period, approximately 10 years. The results show that some shoreline retreat has been done in the northern part of Bangameori beach. Future works will be done on the more detailed analysis using on-site ancillary data

REFERENCES

Dickson, M.E.,Walkden, M.A., Hall, J.W., 2007. Systemic impacts of climatic change on an eroding coastal region over the twenty-first century. Clim. Chang. 84:141−166.

Fenster, M.S., Dolam, R., Morton, R.A., 2001. Coastal storms and shoreline change: signal or noise? J. Coast. Res. 17, 714−720.

Le Cozannet, G., Garcin, G., Yates, M., Idier, M., Meyssignac, B., 2014. Approaches to evaluate the recent impacts of sea-level rise on shoreline changes. Earth Sci. Rev. 138:47−60.

Nicholls, R.J., Bradbury, A., Burningham, H., Dix, J.K., Ellis, M., French, J., Hall, J.W., Karunarathna, H.U., Lawn, J., Pan, S., Reeve, D.E., Rogers, B., Souza, A., Stansby, P.K., Sutherland, J., Tarrant, O., Walkden, M.J.A., Whitehouse, R., 2012. iCOASST – integrating coastal sediment systems. ICCE2012 International Conference on Coastal Engineering, Santander, ES, 01−06 Jul 2012 (15 pp.).

Nicholls, R.J., Cazenave, A., 2010. Sea-level rise and its impact on coastal zones. Science 328:1517−1520.

Nicholls, R.J., Townend, I., Bradbury, A.P., Ramsbottom, D., Day, S.A., 2013. Planning for long-term coastal change: experiences from England and Wales. Ocean Eng. 71:3−16.

Pye, K., Blott, S.J., 2016. Assessment of beach and dune erosion and accretion using LiDAR: impact of the stormy 2013−14 winter and longer termtrends on the Sefton Coast, UK. Geomorphology 266:146−167.

Woodroffe, C.D.,Murray-Wallace, C.V., 2012. Sea-level rise and coastal change: the past as a guide to the future. Quat. Sci. Rev. 54:4−11.

Zhang, K., Douglas, B.C., Leatherman, S.P., 2004. Global warming and coastal erosion. Clim. Chang. 64:41−58.

Investigating Coral Reef Loss and Its Causes around Panggang Island, Seribu Islands, Indonesia

Aulia Leedsyawati Zeintrinanda and Susanna Nurdjaman

Departement of Oceanography, Faculty of Earth Sciences and Technology, Institut Teknologi Bandung, 40132 Bandung, Indonesia
Email : aulialzein95@gmail.com; susanna@fitb.itb.ac.id

KEY WORDS: Coral Reef Growth, Sea Water Quality, Thermal Stress.

ABSTRACT

The growth of coral reefs is influenced by two factors that are natural and anthropogenic factors, which natural factor include salinity, temperature, light and solar radiation, nutrients, and depth. The objective of this study was to examine the changes in coral reefs area around Panggang Island and to know whether oceanographic parameters such as temperature, chlorophyll-a, salinity, pH, brightness, hotspots, thermal stress, El Niño Southern Oscillation (ENSO), and Indian Ocean Dipole (IOD) influence the change. The method used in this research is remote sensing and field data observation. The image data used comes from Landsat 7 ETM$^+$ (2001-2003) and Landsat 8 OLI / TIRS (2013-2016) for coral reefs. NOAA Coral Reef Watch Satellite Monitoring data (2013-2016) for Sea Surface Temperature (SST) and Aqua Modis data (2002-2003 and 2013-2016) for chlorophyll-a. Field data for seawater quality in April 2016 obtained from National Institute of Aeronautics and Space. Meanwhile, Ocean Nino Index and Dipole Mode Index downloaded from Jamstec and NOAA websites.

The results showed that the average rate loss of coral reefs area around Panggang Island, during 2001-2016 is 10.74 ha /year. The highest coral reef loss occurs in the 2013-2014 (42.9 ha), this is due to thermal stress in December 2013 to April 2014 which reached -2.25ºC / week. In 2014-2015 the coral reef area is increase by 37.3 ha, this is due to the coral planting activities in the study area. During 2013-2016 there is only one hotspot, so the phenomenon does not affect the change of coral width. ENSO and IOD didn't seem to affects the coral reef loss in the study area. According to field observation in April 2016, the parameters that meet the reef growth standards are chlorophyll-a and pH, while temperature, salinity, and brightness does not meet the coral reef standards.

1. INTRODUCTION

Reefs are important massive deposits of calcium carbonate which are mainly produced by corals (phylum Cnidaria, Anthozoa class, order Madreporaria or Scleractinia) with a few additions of calcareous algae and other organisms that secrete calcium carbonate (Nybakken, 1988). This ecosystem is composed of a collection of coral animals that are symbiotic with zooxanthellae algae and have varied colors (derived from algal pigments) (Suharsono, 2008).

As an ecosystem rich in marine biota and variations in coral animal color, coral reefs have their own unique and beautiful aesthetic value. Its beauty can be utilized in the field of tourism for recreation facilities and learning. Another benefit of this ecosystem is that it can be a natural breakwater. Breakwater is important to dissipate or reduce wave energy that can cause erosion (Miththapala, 2008). Coral reefs also have an important role in the cycle of biology, chemistry, and physics. The role of coral reefs in the chemical cycle is in the carbon cycle, the CO_2 in the sea will be used by coral animals to form calcite deposits.

Waters in Indonesia have the widest coral reef habitat of 51,000 km^2 (COBSEA, 2011) this is because Indonesia waters is a suitable place for coral growth. Besides having the largest coral reef habitat, Indonesia, especially in the Sulawesi region, has the largest coral species in the world. In Indonesia, up to 80 different coral genera can be found (Suharsono, 2008).

Currently 75% of the coral reefs on earth face various threats from local and global stressors (Manikandan et al., 2016). Coral reef growth can be threatened because it is limited by various factors such as salinity, temperature, light and solar radiation, nutrients, depth (Buchheim, 2013), currents, and waves (Jokiel, 2008) in the growing environment of coral reefs. According to Wooldridge (2009), coral survival against thermal stress can be reduced due to poor water quality due to increased inorganic nutrients.

Several studies on the topic of mapping and study of changes in coral reef area have been carried out by Helleyna (2008); Pasaribu (2008); Manullang, et al., (2014); and Nasution (2017) in Indonesian waters. The study uses remote sensing methods, namely satellite imagery. But it has shortcomings in comparing or monitoring coral reefs in the long term, so we intend to conduct research on changes in coral reefs in more than a decade and seen it annually.

2. METHODS

The study area was chosen in the waters around Panggang Island (Figure 1) which belonged to the southernmost region of the Thousand Islands Marine National Park or precisely at 5°44'15.43 " - 5°45'5.89" of South Latitude and 106°35'10.31" - 106°37'17.58 " of East Longitude. The time from the research data used is the data of the past 17 years, which is comparing the extensive coral data of 2001, 2002 and 2003 for Landsat 7 ETM$^+$ data. Then 2013, 2014, 2015 and 2016 for Landsat 8 OLI / TIRS data.

Figure 1 Study Field Area of Panggang Island. (Source: Google Earth, 2017)

The method used in this study is processing satellite image data using ErMapper to determine changes in living coral area, processing field data using Surfer software, and processing SST, salinity and chlorophyll-a using SeaDAS and Excel software.

2.1 Methods of Processing Coral Reef Satellite Images

The data used are Landsat 7ETM $^+$ and 8 OLI/TIRS images. This image can be used in the study area because it has a spatial resolution of 30 m. The first stage of image processing is to make radiometric correction, geometry correction, then water column correction. After making corrections, image interpretation is also done by classifying the waters bottom substrates.

2.1.1 Radiometric Correction

Radiometric correction is done to improve image quality due to interference in the atmosphere, such as haze or other scattering objects. In this study radiometric correction method with histogram shift was carried out. The histogram shift method uses an assumption that, if there is no atmospheric influence, then the digital value of the image coverage must be found with a pixel value with zero. Histogram shift can be done by reducing all pixel values in image coverage with bias values. So the corrected digital value is:

$$Coreccted\ DN_i = DN_i - DNmin_i(Bias_i) \tag{1}$$

with,
DN = Digital Number
$i = band$ number-i

2.1.2 Geometry Correction

Geometry correction is done on the image to improve the position of objects in the image in accordance with the actual position in the field. Referrals for actual positions in the field refer to Basic Geospatial Information (BGI), namely *Rupa Bumi Indonesia* map (RBI), Indonesian Coastal Environment map, Indonesian Marine Environment map, high resolution upright image or other corrected image, or field coordinate data using GPS receiver. For measuring coordinates in the field using GPS receivers are determined on objects that are clearly visible on the image and relatively unchanged, such as bridges, piers, intersections of roads, or buildings.

2.1.3 Water Columns Correction

Water column correction is carried out to improve image quality by reducing interference in the water column (Prayuda, 2014). The technique that will be carried out in this study uses a correction with an algorithm developed

by Lyzenga (1981). The basic assumption for this correction is that the light that enters the water column decreases exponentially with increasing water depth (attenuation). Lyzenga Algorithm (1978) in Asriningrum (2008):

$$Y = ln\,(TM_1) + k_i/k_j\,ln\,(TM_2) \tag{2}$$

with,

Y : the result image of extraction of the waters floor
TM_1 : digital number of first Landsat TM channel
TM_2 : digital number of second Landsat TM channel
k_i/k_j : attenuation coefficient number

The attenuation coefficient value for the original Lyzenga is obtained by detailed sampling and plotting to ensure the object is the same but the depth difference. k_i/k_j is the ratio of dimming coefficients of band i and band j, obtained from the sampling of deep sea pixels. This value can also be known by performing the following calculations:

$$\frac{k_i}{k_j} = a + \sqrt{a^2 + 1} \tag{3}$$

with,

$$a = \frac{Varian_{TM_1} - Varian_{TM_2}}{2 \times covarian\,TM_1\,dan\,TM_2} \tag{4}$$

2.1.4 Image Interpretation

Image interpretation is the process of detection, classification, identification and analysis, and delineation (Sutanto, 1994). In interpreting, there are 9 main elements of interpretation, namely: hue/color, texture, shadow/height, size, pattern, association, location, shape, and convergence of evidence. The main process in digital image interpretation is image classification. Image classification is broadly divided into two, namely pixel-based image classification (pixel based) and the other is object-based. Pixel-based image classification consists of supervised and unsupervised image classification.

Table 1 Key to Color Interpretation for Basic Substrate Classification.

No	Warna	Objek
1	Purple and Black	Land
2	Blue	Sea
3	Cyan and light green	Living Coral
4	Dark green	Dead Coral
5	Yellow	Rubble
6	Orange	Sea grass
7	Red	Sand

(Source: COREMAP, 2001)

The classification used is the unsupervised classification, which is to do classification by grouping pixel images into several classes based only on certain statistical calculations without specifying pixel samples (training) used by the computer as a reference for classifying. The reinterpretation process can be assisted visually by using a color composite image based on the interpreter's knowledge, or based on fieldwork data as a basis for classification. The key to color interpretation in conducting classification was obtained from COREMAP, 2001 (Table 1). After several classes have been classified, the area of living coral was calculated.

2.2 Data Processing of Sea Water Quality

NOAA data OI v2 SPL is a netcdf file while the chlorophyll-a data and salinity are nc files, all three are opened using the SeaDas application. The SST data downloaded from the website is from 1981 to 2017. The ONI and DMI data is processed using Ms. Excel to tidy up. Both of these data already have a value since downloaded from the site that has been mentioned, so that the process is only needed to create graphics.

2.2.1 Calculation of Hotspot

This calculation is needed to see whether there is a temperature exposure that exceeds the maximum monthly limit of water climatology in the study area as an indication of a decrease in living coral area. Hotspot calculations can be calculated using the equation by Gleeson and Strong (1995):

$$Hotspot = SST - MMM\_SST\_climatology \tag{5}$$

with,

SST = Sea Surface Temperature

$MMM\_SST\_climatology$ = Maximum value of SST monthly climatology

Climatology in the n-th month is obtained by averaging the daily SST to monthly, then the monthly average is averaged back in the n-th month.

Table 2 The Level of Stress on Coral Reefs and Their Potential for Bleaching.

Stress Level	Definition	Potential Bleaching Intensity
No stress	Hotspot < 0	No bleaching
Observe bleaching	0 < Hotspot < 1	-
Bleaching warning	1 ≤ Hotspot and 0 < DHW < 4	Potential Bleaching
Bleaching Alert level 1	1 ≤ Hotspot and 4 ≤ DHW < 8	Bleaching
Bleaching Alert level 2	1 ≤ Hotspot and 8 ≤ DHW	Deaths

(Source: https://coralreefwatch.noaa.gov/satellite/methodology/methodology.php)

Coral mass bleaching has been shown to be caused by prolonged periods of thermal stress. So it is necessary to calculate DHW (Degree Heat Week) which accumulates hotspots that are more than 1°C for 12 weeks. The DHW calculation is a cumulative measurement of the intensity and duration of thermal stress and has a ° C-week unit. DHW calculations can use the equation:

DHW = 0.5 * sum of 24 Hotspots (2 times a week) (6)

2.2.2 Water Quality Standard for Coral

Coral-forming animals have a tolerance to a certain extent to survive in their environment. Indonesia Decree of the Minister of Environment Number 51 of 2004 explained that coral has certain parameter values so that its growth remains optimum. This parameter limit is stated in the sea water quality standard for marine biota (Table 3).

Table 3 Sea Water Quality Standards for Marine Biota.

Number.	Parameters	Unit	Standards
	PHYSICS		
1	Brightness	M	*coral*: >5
2	Turbidity	NTU	<5
3	Total suspended solids	mg/l	*coral*: 20
4	Temperature	^{0}C	*coral*: 28-30
	CHEMISTRY		
1	pH	-	7-8,5
2	Salinity	$^o/_{oo}$	*coral*: 33-34
3	Dissolved Oxygen (DO)	mg/l	>5
	BIOLOGY		
1	Plankton		Not *bloom* (>75 $\mu g/l$)

(Source: modified from Indonesia Minister of Environment Decree Number 51 of 2004 and Mitchell, 1988)

3. RESULTS AND DISCUSSION

The results of the mapping can be used to calculate changes in reef area. From here the author can pay attention to whether there is damage to coral reefs that occurred during the study time in the study area. During the study period there were problems in data processing, including damage to Landsat 7 ETM[+] sensors after 2003, and also the presence of thick clouds in image data so that data were not available. As a result of this, this study has data shortages or vacancies from 2004 to 2012.

3.1 Changes in Living Coral Area

Table 4 contains the results of the extent of living coral and dead coral during 2001-2016.In 2001 to 2002, there were additional areas of Living coral at 4.9 ha. In the same year the dead coral was reduced by 9.6 ha. If we look at Figure 2, the area of living coral and dead coral has an inversely related relationship. When the area of living coral decreases, the area of dead coral increases and vice versa.

Tabel 4 Changes in Living Coral Areas in Each Year (2001-2016).

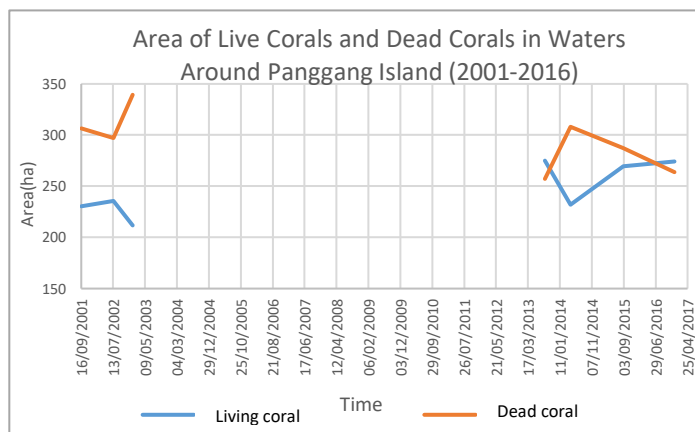| Class	Area (ha)						
	9/17/2001	8/3/2002	1/10/2003	8/25/2013	4/22/2014	8/31/2015	12/23/2016
Living Coral	230.5	235.4	211.7	275	232.1	269.4	274.2
Dead Coral	306.3	296.9	339.345	257.2	308.3	287.415	263.835

Figure 2 Graphic of Area of Living Coral and Dead Coral in Waters around Panggang Island (2001-2016).

3.2 The Rate of Change Area in Living Coral

From both data sources we can see that the rate of change is generally negative (Table 5). This means that there was a decrease in living coral area during the study in the research area. In 2001-2003 the rate of change in the area of living coral was negative in 2003, which amounted to -6.12% per year (Table 5).
In 2013-2016 the highest rate of negative change was aimed at 2014, which was 23.4 percent per year. The average rate of change during 2001-2003 was -10.46 ha / year. While for 2013-2016 the average is not much different, namely -10.93 ha / year. Overall, the average rate of change in the study area for 16 years is -10.74 ha / year or -3.69% / year.

Table 5 Change Rate in Living Coral Area in Waters around Panggang Island (2001-2016).

Satellite	Year	Change Rate	
		ha/year	%/year
Landsat 7	2001-2002	4,90	2,55
	2002-2003	-25,82	-10,97
	2001-2003	-18,80	-6,12
	Average rate	-10,46	-4,21
Landsat 8	2013-2014	-64,35	-23,4
	2014-2015	27,98	12,05
	2015-2016	3,60	1,34
	2013-2016	-0,34	-0,13
	Average rate	-10,93	-3,34
Average change rate		-10,74	-3,69

3.2 El Niño Southern Oscillation and Indian Ocean Dipole Condition

There are several events that can affect temperature anomalies in Indonesia, namely the ENSO (El Niño Southern Oscillation) and IOD (Indian Ocean Dipole) phenomenon. Water surface temperature in Indonesia will rise if La Ni-ña or negative IOD occur. Conversely, when a positive El Niño or IOD phenomenon occurs, the temperature in Indonesian waters will cool. Therefore, ONI and DMI are needed to see if there is a connection between the effects of IOD and ENSO phenomena with changes in temperature in the study area.

There was an increase in the ONI value in 2015 accompanied by a positive DMI in the same year. This phenomenon influences the increase in SST trends in almost all Indonesian waters. However, in the study area itself, there is no significant influence from this phenomenon. If we review Figure 3 throughout August 2013 to September 2014 there was a positive IOD, and in early 2014 was also strengthened by the presence of positive ENSO. This causes an SST anomaly in the study area to reach negative 1.25℃. The decline in living coral area also occurred in 2014 as much as -23.4% from the previous year. In 2015 there was a positive ENSO and also a positive IOD whose index was quite high from the previous time. This causes an SST anomaly in the study area to reach from -2.5 ℃. However, the decline in living coral area did not occur in 2015 from the previous year. The increase in coral area in 2015 due to coral planting activities. One of them was planting by the Marine Base Defense Battalion (Yonmarhanlan) III on Pramuka Island and Pulau Karya as many as 9,000 corals were planted in the area in July 2015 (Wandi, 2015). In November 2016 it was seen that there was a negative ENSO, in the study area there was an increase in temperature. In Figure 3 it is seen that the highest positive anomaly in November 2016 reaches a value of 0.25℃. In 2015-2016 there was no coral reef loss.
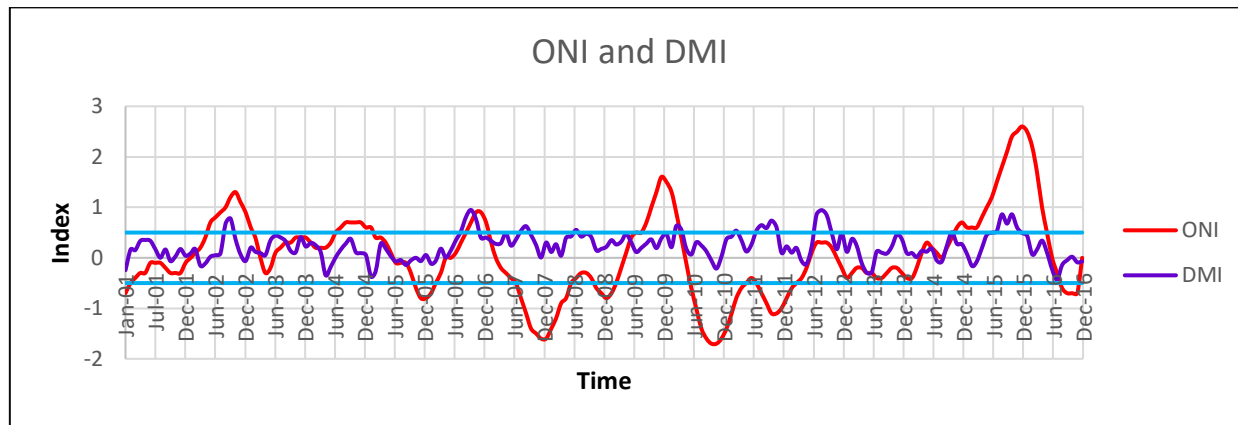

Figure 3 Graphic of ONI and DMI from 2001 to 2016.

3.3 Hotspot and Degree Heat Week (DHW)

In this study hotspot calculations were also carried out. However, in the course of the data processing results show that most temperatures in this area experience an anomaly less than -1℃. So that it is done by plotting the -1℃ anomaly using a hotspot calculation in Figure 4. Likewise with DHW, calculations are done using Equation 6, but are changed to less than -1℃ which is accumulated.
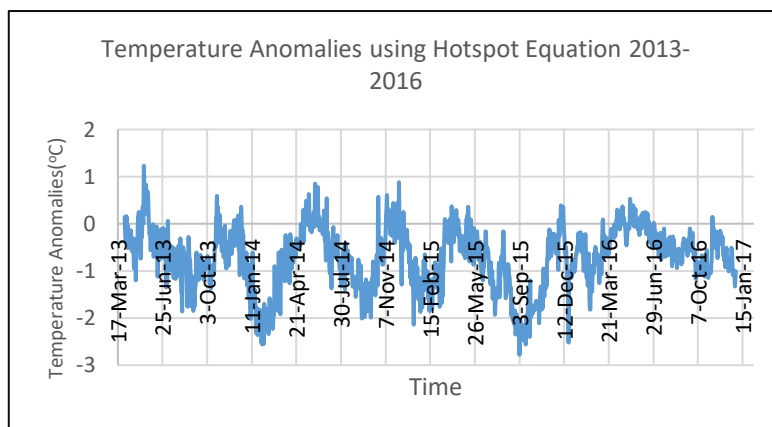

Figure 4 Temperature Anomalies in Field Study using Hotspot Equation.

During the occurrence of positive temperature anomalies there is no time to be intersected or adjacent which can affect changes in the extent of coral in the study area Figure 6 shows the period of thermal stress experienced by corals per week during 2013-2016. From Figure 3, the temperature anomaly values are more than 1℃ and less than -1℃. The sampling results are then averaged per week and obtained values as in Figure 6. Figure 6 shows a long negative thermal stress in December 2013 to April 2014. This can lead to the highest degradation of living coral, which is 42.9 ha from 2013 to 2014. In 2015 there was no degradation of living coral area, although there was

considerable and long-term thermal stress from July to November 2015. This could be due to the influence of campaigns and coral planting activities that had more impact on the study area.
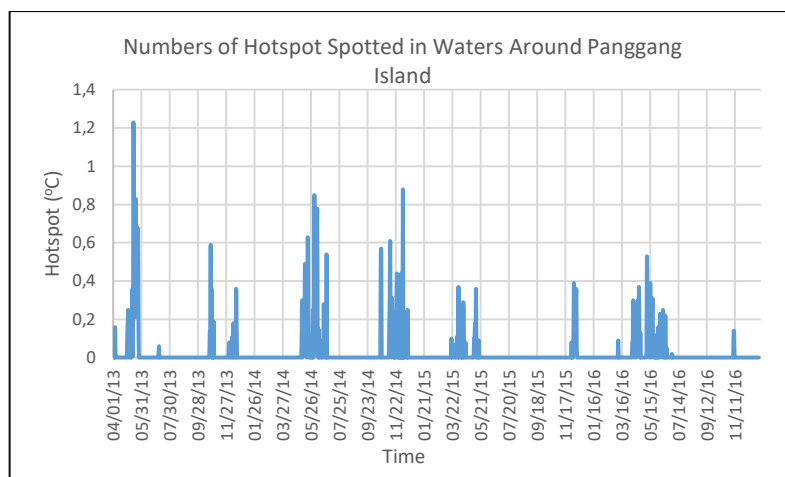

Figure 5 Numbers of Hotspot Spotted in Waters around Panggang Island.

Figure 5 shows positive temperature anomalies in the study area. The highest anomaly occurred in May 2013, which was around 1.29ºC.
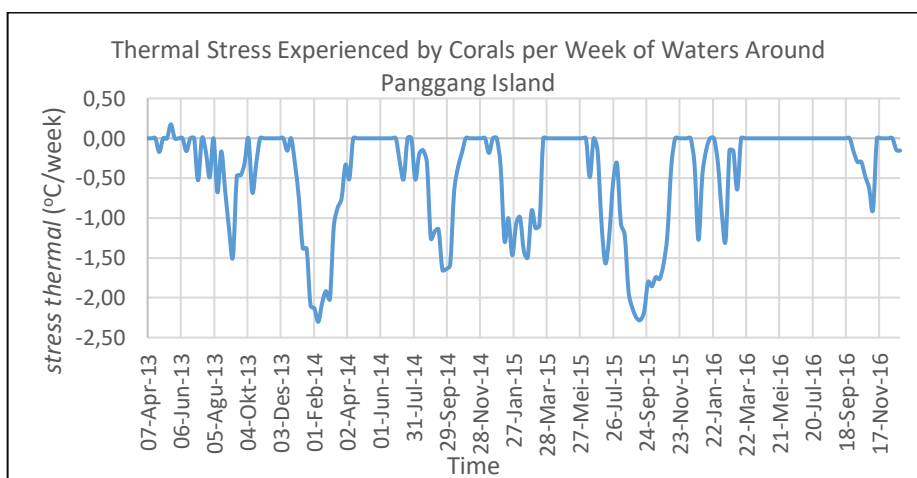

Figure 6 Thermal Stress Experienced by Corals per Week of Waters around Panggang Island.

3.4 Water Quality

In the survey results we can see that the temperature range in the study area waters is 29.66 - 31.34ºC (Figure 7). While the average temperature above is more than the existing quality standard which is around 30.11ºC. Of all data stations, there are 11 data stations that do not meet the temperature quality standard, which is more than 30ºC. This means that generally in this study area the quality standards for temperature are not met. Only around the northern part of the study area alone meets the quality standards for temperature. Also in Figure 7 you can see the spatial distribution of chlorophyll-a concentration in the study area. In the waters north of Panggang Island the chlorophyll-a concentration tends to be higher than in the southern part, which is more than 1.43 mg/m³. Whereas in the south it is only about less than 1 mg/m³.

The measurement results in the field show that the pH of the study area is around 7.51-7.83 (Figure 8), with an average of 7.67 which is still included in the quality standard for ideal coral growth. According to the quality standard, the salinity of sea water for coral reefs is around 33-34 ppt, while the measured in the field is around 31.47-32.05 ppt (Figure 8). So this salinity is less than the existing quality standard threshold for ideal coral growth. This can be due to weather or the ongoing season in the study area during measurement or measurement errors.

Brightness in the study area is quite good because only a few are below the quality standard. The quality standard for brightness is below 5 meters. Although there are some brightness that does not reach 5 meters, the depth at the station does not reach 5 meters so it can be considered quite good (Figure 9).
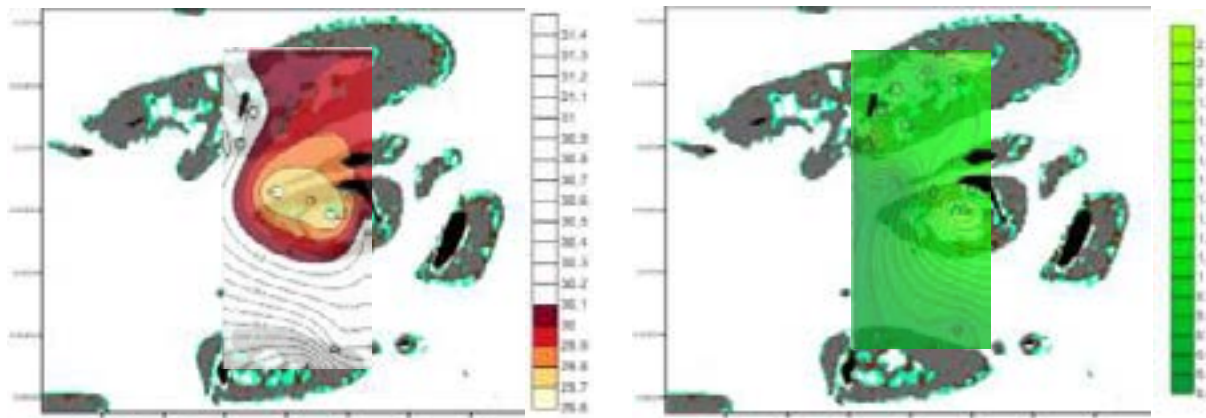
Figure 7 Spatial Distribution of Temperature (ºC) (Left) and Chlorophyll-A (mg/m^3) (Right) around Panggang Island, Thousand Islands In 2016.
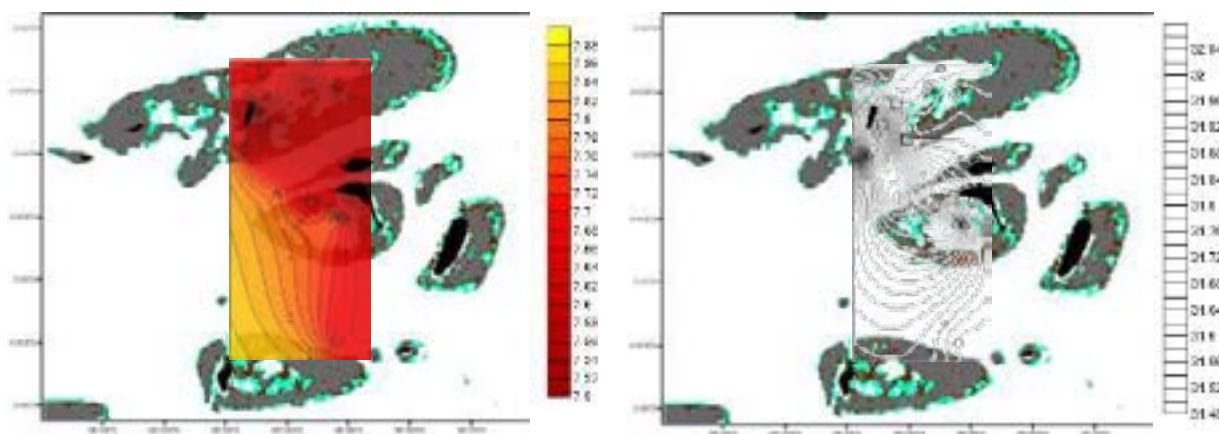

Figure 8 Spatial Distribution of pH (Left) and Salinity (ppt) (Right) around Panggang Island, Thousand Islands In 2016.
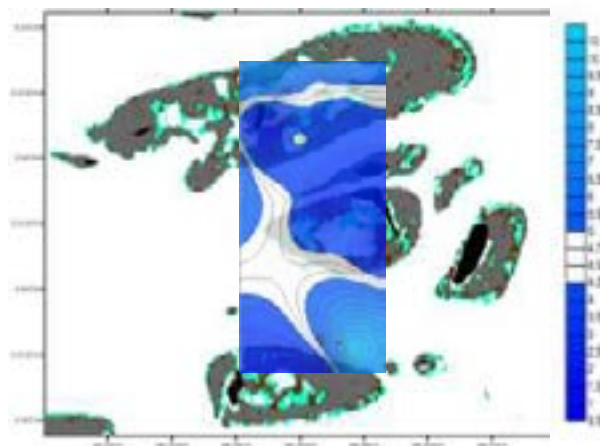

Figure 9 Spatial Distribution of Brightness (m) around Panggang Island, Thousand Islands in 2016.

In general, the water conditions in the study area when the survey was still included in the quality standard for coral ideal growth. It's just that salinity is below the quality standard, but salinity in the study area is found to be around 31-32 ppt (Manullang, et al., 2014). Besides that, temperature, chlorophyll-a, pH, and brightness support good growth for corals in accorandce with existing quality standards.

In the study area, there were more living coral in areas with chlorophyll-a concentration and higher temperatures (chlorophyll-a> 0.9 mg/m^3 and temperature> 29.9 ºC) but still in the water quality standard for corals. Then in waters with a pH lower than 7.7-7.8 and in areas with a fairly spatially pH. As for salinity, although it does not meet

quality standards, living coral are more common in areas with lower salinity. The influence of sea water quality spatially cannot be seen to affect the condition of coral reefs because the research time is different.

3.5 Chlorophyll-a and Salinity

Chlorophyll-a concentration is spatially obtained from Aqua MODIS data. Because the SST parameter cannot be concluded whether it affects coral conditions in the study area, it is seen also the chlorophyll-a parameter. According to Wooldridge (2009), chlorophyll-a can be used as a parameter to see the presence of nutrients in a waters. Nutrients themselves needed by corals to grow and develop. If nutrients have good (or high) values, corals can grow better than areas that have less nutrients. However, excess nutrients are also not good for coral growth, in this case when algae bloom (Mitchell, 1988).

The satellites that took the data just started operating in July 2002, therefore the Landsat 7 ETM + data was seen to have an effect in 2002-2003. Then Landsat 8 OLI / TIRS data from 2013 to 2016. Aqua MODIS observation data is incomplete, so there is some data that is emptied. Figure 10 is the result of an overlay of living coral area data and chlorophyll concentration in 2002-2003. From the graph, there was a decrease in chlorophyll-a concentration in August 2002 to October 2002. During the study, chlorophyll-a concentration met the quality standards set by KMLH in 2004, namely the concentration did not cause algae bloom or not more than 75 mg/m^3 .
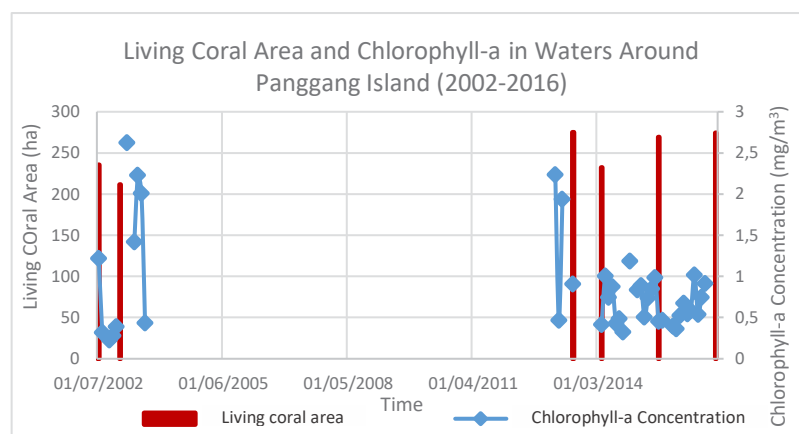

Figure 10 Living Coral Area and Chlorophyll-a around Panggang Island (2002-2016).

Temporal salinity is also processed to see if there is an influence of salinity values in the study area on the condition of coral reefs. But in the process in the study area from Aquarius data there was no salinity value. So this salinity value is taken based on the area closest to the study area which has a salinity value, which is at 108.5 BT and -5.73967 LS or in the southern Java Sea. Because it is not in the data study area, it cannot be seen whether it affects the extent of coral changes or not.

4. CONCLUSION

The area of coral living in the waters around Panggang Island in 2001-2003 (Landsat 7 ETM +) and 2013-2016 (Landsat 8 OLI / TIRS) was degraded. With an average rate of change for 16 years of -10.74 ha/year. The highest decrease in coral area occurred in 2013-2014, which was 42.9 ha. With a rate of change of -23.4%/year or -64.35 ha/year due to the presence of thermal stress in December 2013 to April 2014, the maximum value reached -2.25ºC/week. The highest addition of coral area occurred in 2014-2015, which amounted to 37.3 ha. With the rate of change of 12.05% / year or 27.98 ha/year due to coral planting activities by various institutions in the waters around Panggang Island during 2015.

Spatially, the parameters that meet the quality standards in April 2016 in the waters around Panggang Island are chlorophyll-a and pH. While those that do not meet the quality standards are brightness, salinity, and temperature. Temporally SST which increased in the period 2001-2003 caused extensive degradation of coral at 18.8 ha. In the 2013-2016 period there was only one hotspot, on May 14, 2013, but did not result in a change in the living coral area. Beside natural factor which cause coral degradation, anthropogenic factors such as tourist and other activity may cause the coral degradation too.

References

Asriningrum, W., Arief, M., and Tjahjono, B., 2008. Analisis Geomorfologi Terumbu di Kabupaten Sikka, Pusat Pengembangan Pemanfaatan Penginderaan Jauh, LAPAN, pp. 19-20.

Buchheim, J., 2013. Coral Reef Bleaching, Marine Biology Learning Center Publications, Retrieved December 11, 2016, from http://www.marinebiology.org/coralbleaching.htm.

COBSEA, 2011. A Regional Approach to the Sustainable and Ecosystem-Based Management of Coastal Erosion in the East Asian Seas Region: A Resource Document, COBSEA Secretariat, Bangkok.

COREMAP, 2011. Laporan Kegiatan Pemetaan Terumbu Karang Menggunakan Data Inderaja and SIG, Jakarta, 2001.

Gleeson, M.W. and A.E. Strong, 1995, Applying MCSST to coral reef bleaching, Adv. Space Res, 16(10);10151-10154.

Helleyna, F, 2008. Studi Kondisi Terumbu Karang di Pulau Pari - Kepulauan Seribu dengan Menggunakan Citra Landsat ETM, Tugas Akhir Sarjana, Program Studi Oseanografi. FITB-Institut Teknologi Bandung, Bandung, pp. 23.

Jokiel, P. L., 2008. Biology and Ecological Functioning of Coral Reefs in the Main Hawaiian Islands, Ed. B. R. Dodge, Coral Reefs of the USA, Springer Science, pp. 494-501.

Manikandan, B., Ravindran, J., Vidya P.J., and Murali, R. M., 2016. Bleaching and recovery patterns of corals in Palk Bay, India: An indication of bleaching resilient reef, Regional Studies in Marine Science Journal, http://dx.doi.org/10.1016/j.rsma.2016.07.005, pp. 1.

Manullang, J.C., Hartoni, and Surbakti, H., 2014. Analisis perubahan luasan terumbu karang dengan menggunakan data penginderaan jauh di perairan Pulau Pramuka Kabupaten Administratif Kepulauan Seribu, Maspari Journal, Vol. 6, No. 2, pp. 124.

Minister of Environment Decree No. 51 of 2004. Retrieved December 20, 2016, from www.ppk-kp3k.kkp.go .id/ver3/media/download/RE_keputusan-menteri-negara-lingkungan-hidup-nomor-51 -tahun-2004_20141008143942.pdf.

Mitchell, P. 1988. Atlas of Alberta Lakes. University of Alberta Press. pp: 675. http://sunsite.ualberta.ca/Projects/Alberta-LakesProyectoagua/waterproject. 2009.

Miththapala, S., 2008. Coral Reefs, Coastal Ecosystems Series (Vol 1) + iii, Colombo, Sri Lanka: Ecosystems and Livinglihoods Group Asia, IUCN, pp. 7.

Nasution, M.I., 2017. Studi Perubahan Luasan Terumbu Karang Di Perairan Utara Kecamatan Sekotong, Pulau Lombok, Nusa Tenggara Barat, Tugas Akhir Sarjana, Program Studi Oseanografi. FITB-Institut Teknologi Bandung, Bandung, pp. 12.

Nybakken, J.W., 1988. Biologi Laut: Suatu Pendekatan Ekologis, Gramedia, Jakarta, pp. 305.

Pasaribu, R.A., 2008. Studi Perubahan Luasan Terumbu Karang dengan Menggunakan Data Penginderaan Jauh di Perairan Bagian Barat Daya Pulau Moyo, Sumbawa, Tugas Akhir Sarjana, Program Studi Perikanan and Kelautan, Institut Pertanian Bogor, Bogor.

Prayuda, B., 2014. Panduan Teknis Pemetaan Habitat Dasar Perairan Laut Dangkal, Ed: Suyarso, LIPI, Jakarta.

Suharsono, 2008. Jenis-Jenis Karang di Indonesia, Jakarta: COREMAP PROGRAM.

Sutanto, 1994. Penginderaan Jauh Jilid I, Gadjah Mada University Press, Yogyakarta.

Wooldridge, S. A., 2009, Water quality and coral bleaching thresholds: Formalising the linkage for the inshore reefs of the Great Barrier Reef, Australia, Marine Pollution Bulletin, pp. 745

NOAA, 2011. NOAA Coral Reef Watch Methodology, Retrieved March 8, 2018, from https://coralreefwatch.noaa.gov/satellite/methodology/methodology.php.

Wandi, 2015. TNI Gelar Penanaman Trumbu Karang di Kepulauan Seribu, Retrieved March 8, 2018, from http://poskotanews.com/2015/07/31/tni-gelar-penanaman-trumbu-karang-di-kepulauan-seribu/.

PERFORMING VISUAL ANALYSIS USING HIGH RESOLUTION IMAGES TO IDENTIFY AND ESTIMATE MILITARY ASSET CAPABILITY

Maj. Mohamad Wasli Musa (1), Capt. Hasnul Hady Karim (1), Col. Abdul Rashid Modzni (1)
1 Malaysian Remote Sensing Agency (MRSA), Ministry of Energy, Science, Technology, Environment & Climate Change (MESTECC), No.13 JalanTun Ismail, 50480, Kuala Lumpur, Malaysia
Email: wasli@remotesensing.gov.my ; hhady@remotesensing.gov.my ; rashid@remotesensing.gov.my

Keywords: Visual analysis, High resolution, Military features, Estimation, Critical geoinfo

Abstract: Nowadays, remote sensing imagery data is an important element to provide critical information about the situation or event in earth surface. Implementation of high resolution images for visual analysis has fundamental to identify critical information needed. By utilizing high resolution images, visualization will depict features clearly to perform accurate measurement. Basic measurement will assist feature size calculation to understand the possible space for certain asset. However, understanding and knowledge about surrounding environment will guide analyst to perform information verification. By manipulating the combination of high resolution image features, high accuracy image processing and geographic information system measurement tools would be able to enhance visualisation analysis to answer critical question that needed for decision making proses consideration. In this paper, visualisation analysis is to predict amount of asset that possible to relative strength of military operation. The aim of this study is to evaluate the opportunities of high resolution imagery satellite in term to identify critical information to be manipulated into military decision process.

INTRODUCTION

The advantages of high resolution image is perfectly depict the feature elements on the ground based on location, position and orientation. These elements assist the analyst able to detect and recognise selected object accurately and identifying possible critical information should be extracting out to support geospatial information needed. Some of the features element able to answer the critical question by performed basis mensuration. Image accuracy and integrity are essential to influence the result produce by visual analysis especially involve the remote area that not be able to be access on ground verification.

The intangible information such as type and function can be extracting out indirectly through the merging of feature element and object characteristic. Knowledge and basic dimension about study subject (geospatial information) will assist the visual analysis proses and increase successful to identify significant information to answer critical question in military decision making process. Skill and knowledge to recognise possible military installation is not to be discuss on this paper. On this study, the basic knowledge is by measuring the object size and space to identified military installation and total armoured vehicle.

OBJECTIVE

The aim of this study is to estimate of military total asset (armoured vehicle) to assess possible total strength (level unit of command) by measuring garage building size and space dimension (width and long) using remote sensing high-resolution image.

METHODOLOGY

The measurement size using standard geography information system (GIS) tools to identify space that possible to store asset. On this study area, the building is possible recognise as tank garage (based on shape, pattern and surrounding). In order to estimate total of tank that possible to occupied the garage, measurement of garage space equivalent with tank size will assist to estimate the information required. By implementing the basic skills interpretation and GIS knowledge, the method in Figure 1 can be utilised.
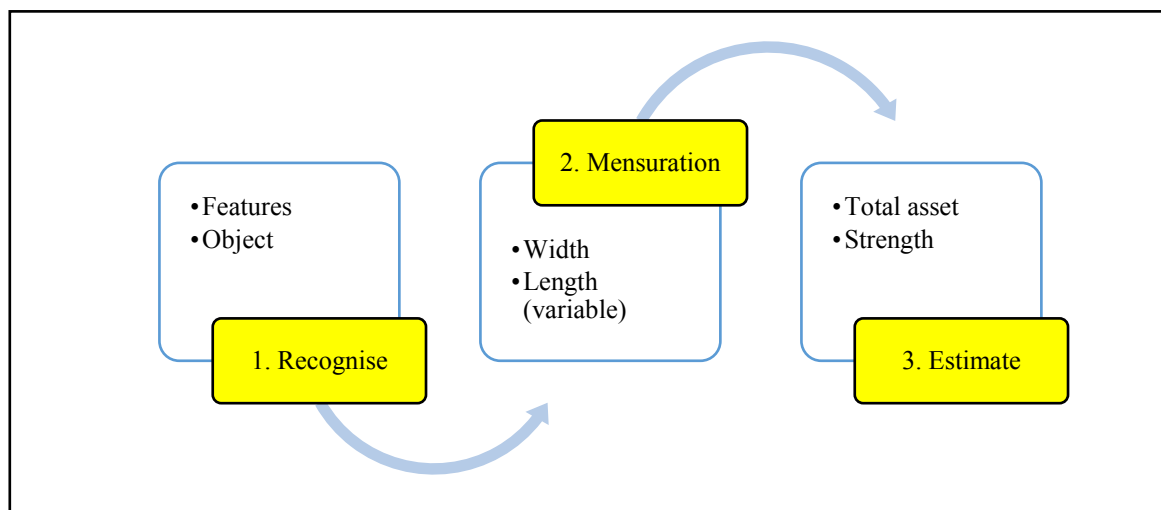
Figure 1: Basic Method Visual Analysis to Estimate Military Asset

Garage dimension (width x length) is **variable number** to estimate the calculation. On this study, the garage dimension is **10 meter** width and **15 meter** length that possible for single tank occupied.

Area and Features Detail

This visual analysis will implement the basic comparison between size and space that refers to tank and garage. Possible tank size and garage space will divided to predict possible space location could occupy by tank. To locate and recognise the tank garage, identify the pattern and shapes are potential to produce an accurate result. Familiarise the ground operation will support the accuracy of detection area as shown in Figure 2.

Figure 2: Possible Tank Garage
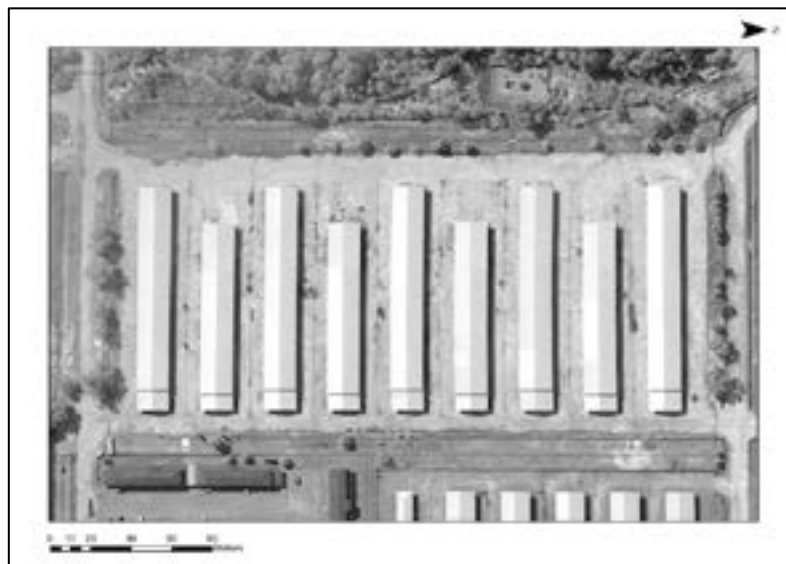(Satellite image © 2016 DigitalGlobe.)

This study refer the basic information as below:

    a.   Sensor: World View Satellite 01 (WV01)
    b.   Date of Image: 12 Dis 2016
    c.   Resolution: PAN 0.5 meter
    d.   Type: Military Base (Army)
    e.   Status: Area occupied, serviceable, operational and partly camouflage.
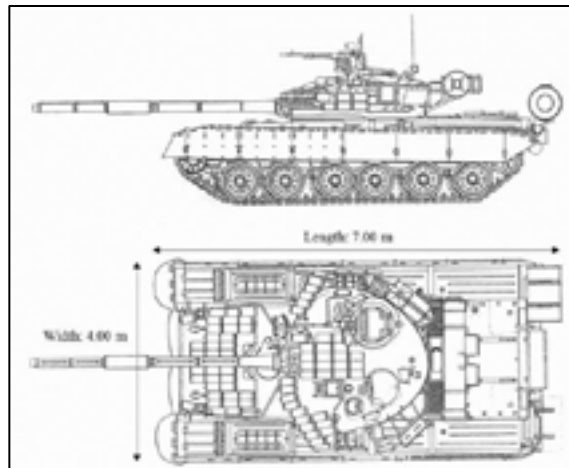   f.   Standard tank asset size as shown in Figure 3.

Figure 3: Tank Basic Size

ESTIMATION RESULTS

In Figure 3, garage has been categories by type base on size. Image visual recognise there are five (5) Garage Type A and four (4) Garage Type B (refer Figure 2).

a.   **Type A**: Garage dimension with 110 meter length and 16 meter width is possible for medium Main Battle Tank (MBT).

b.   **Type B**: Garage dimension with 70 meter length and 16 meter width is possible for Support Armour and Recovery Vehicle (ARV).
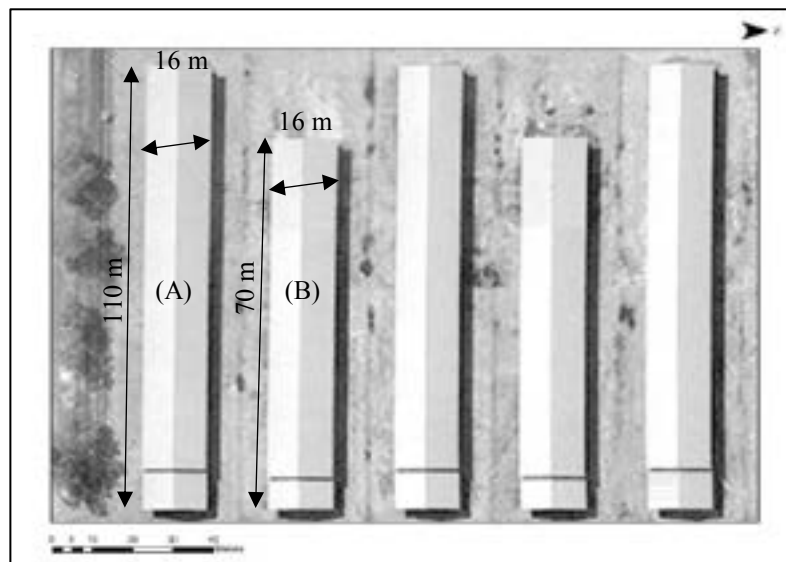
Figure 3: Garage Type Categories
(Satellite image © 2016 DigitalGlobe.)

By understanding the garage specification as in Figure 3, each armoured vehicle should have enough space for load and unload activities. That means possible space (variable) for one tank is 150 square meter each (L10 x W15 meter) or more. On this calculation, **length dimension** is essential to estimate the possible total of armoured vehicle for MBT and ARV. The calculation possible total tanks occupied the garage are as follows:

a.   Total Garage Type A = 5
        Garage Length/ Possible width space for single MBT: 110m / 10m = 11
        Total MBT in Single Garage x total Garage Type A: 11 MBT x 5 = 55
        Overall MBT in Garage Type A: Possible 55 MBT

    a.   Total Garage Type B = 4
                   Garage Length/ Possible width space for single ARV: 70m / 10m = 7
                   Total ARV in Single Garage x total Garage Type B: 7 x 4 = 28
                   Overall ARV in Garage Type B: Possible 28 ARV

CONCLUSION

Based on this calculation, total 55 MBT and 28 ARV are possible strength for regiment[1] consists with Four (4) Squadron, including Regimental Headquarters. Although, the exactly strength might be different but the calculation can estimate the possible strength based on garage visualise. Using the different date of images can provide good visualisation and comparison in term to identify possible type of MBT around the garage. In this case, there are no MBT or ARV appear on the ground, and make analysis totally depend on concept space and size. Confirmation on the ground is a good approach to understanding the possible layout and deployment to support the imagery visual analysis. However, system knowledge database and image signature database are required to be develop or integrate to facilitate and increase the result accuracy in future study.

REFERENCES

Maj Mohamad Wasli (2014), Google Earth Online Mapping Application: The Opportunities and Challenges to Malaysian Defence Security, Executive Diploma in Strategic And Defence Studies, UPNM.

ARSM RSDIAS Portal. Retrieved from https://joint.remotesensing.gov.my

Image Source: Satellite image 2016 © DigitalGlobe. from https://services.digitalglobe.com/myDigitalGlobe

Tank Blueprints from https://www.the-blueprints.com

---

[1] *One Tank Regiment consists with Four Tank Squadron and each squadron equivalent fourteen tanks (basic doctrine)*

Vegetation and built –up area transformation on coastal area as capital city: case study of Makassar city, Sulawesi Island, Indonesia

Syazwi Quthbi Al Azizi (1), Nurjannah Nurdin (2) (3)

[1] Urban and Regional Planning Department, Hasanuddin University, Jl. Malino, Borongloe, Bontomarannu, Kabupaten Gowa, 92119. Indonesia.
[2] Marine Science Department, Hasanuddin University, Jl.Perintis Kemerdekaan km.10, Makassar, 90245. Indonesia.
[3] Center for Regional Development & Spatial Information (WITARIS), Hasanuddin University, Jl.Perintis Kemerdekaan km.10, Makassar, 90245. Indonesia.
Email: cicisawi@gmail.com; nurj_din@yahoo.com; akbarmuhammad.1818@yahoo.com

Abstract: Makassar City's population has been reaching 2.03% annually. Based on that data, it can be assumed that the extend of buildings also increasing along with the growth of population. The objective of this study are to distinguish difference of NDVI and NDBI in Makassar City in year 1998 and 2018, using Landsat-5 and Landsat-8 OLI imageries, and also to compare 2018 processed imagery, both NDVI and NDBI actual condition. This Study was used moderated spatial resolution Landsat in 1998 to 2018. Field study was conducted on Makassar city, Sulawesi island. The normalized difference built-up index and normalized difference Vegetation Index were used for mapping urban built-up areas and vegetation area. The methods for extraction of built-up and vegetation areas using Landsat imagery comprised four major steps: preprocessing and examination of satellite data, image enhancement through resolution merging, development of vegetation and built-up area extraction method, and accuracy assessment. The analysis of NDVI and NDBI in Makassar city showed the qualitative information about the vegetation and built-up area for 20 years (1998 to 2018). The time series of the annual averages of NDVI and NDBI values showed a decrease in vegetation rates and an increase in built-up areas.

Keywords: built up area, vegetation, Landsat, Makassar city

1. INTRODUCTION

Makassar City's population has been reaching 2.03% annually. Based on that data, it can be assumed that the extend of buildings also increasing along with the growth of population. This phenomena not only happened in Makassar City, but also in other metropolitan cities around the world. Acording to The prospect of World Urbanization, revision 2014, cities expansion has been reaching the stage where more than 54% of global population living in urban areas. This number will be growing over time and it is predicted that the world's population will be increased by 66 % or 5 billion people by the year 2050 (Gago et al. 2013). Most of this population growth will take place in developing countries, including Indonesia. Some study of build-up area were conducted that use Landsat imagery data (Wang et al. 2018, Nong et al. 2014).

The development and growth of Makassar City as the main town of the metropolitan area of Mamminasata, recognized by intensively occurring urbanization and village-city migration. Remote sensing technology can be applied as a method to efficiently identify built-up areas and vegetation in

Makassar City, within short period of time and with accountable result. Vegetation and built-up areas identification were done digitally using Normalized Difference Vegetation Index (NDVI) and Normalized Difference Built-up Index (NDBI) variables respectively (Wang et al. The objective of this study are to distinguish difference of NDVI and NDBI in Makassar City in year 1998 and 2018, using Landsat-5 and Landsat-8 OLI imageries, and also to compare 2018 processed imagery, both NDVI and NDBI actual condition.

2. MATERIAL AND METHODS

2.1 Study area

This research was conducted among the vegetation and build up area in Makassar city, South Sulawesi, Indonesia which The geographical boundary between 119º18'27,97" – 119º32' 31,03"E longitude and 5º14'49" – 5º30'30,18"S latitude. Makassar is one of thirty-four capital provinces in Indonesia.
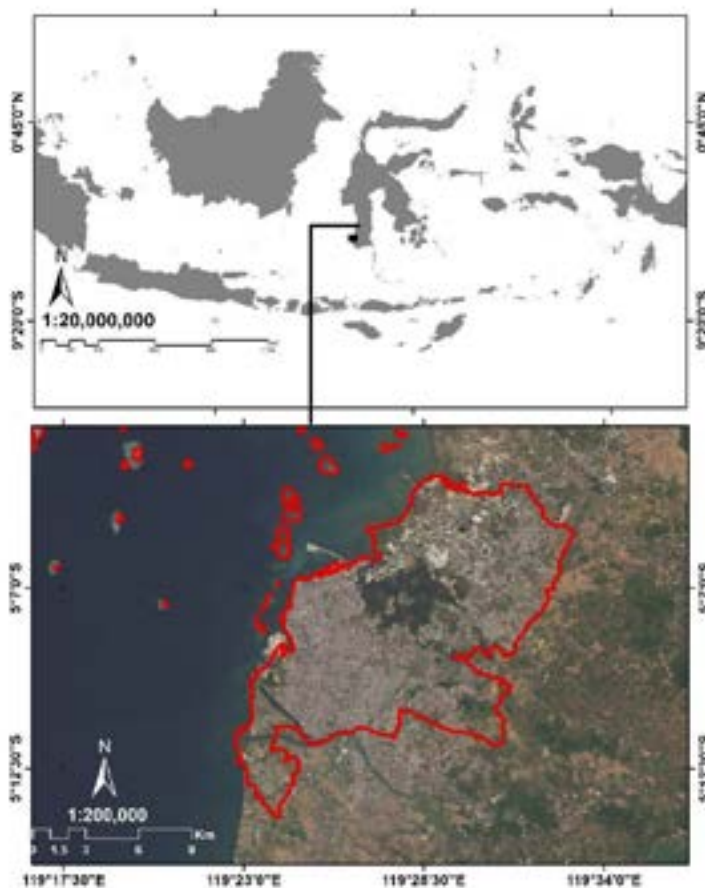

Figure 1. Map of the study area, Makassar city in Sulawesi island, Indonesia

2.2 Data Collection

The study was carried out using multi-temporal satellite images of Landsat. The Landsat images data was downloaded from USGS data archive (http://www.eros.usgs.gov) including A Landsat Thematic

Mapper (TM) images (08 August 1998) and a Landsat 8 (Operational Land Imager, OLI) image (15 August, 2018)), were used in this study. Landsat image was processed using software ArcGIS 10.5 from ESRI.

2.3 Pre-Processing Imagery

Time series data Landsat imagery were used in this research to obtain information about actual vegetation and build-up area from two time series. We preferred to use Landsat TM and OLI after geometrically, radiometrically corrected, and cropping images.

2.4 NDVI and NDBI Measures

In this study, two spectral indices were discussed, including Normalized Difference Vegetation Index and Normalized Difference Built-up Index. NDVI can be calculated as a ratio of red and the NIR bands of a sensor system, NDVI = (Infrared - Red)/(Infrared + Red). NDVI process produces new image with the value of pixel ranges from -1 to +1. NDBI is one of the widely applied indices for reinforeing building information and extracting built-up land from urban areas. Za et al. (2003). Develop NDBI values using data from Landsat TM imagery and can be used on Landsat OLI images with the equation, NDBI = (MIR-NIR)/(MIR + NIR).

2.5 Field survey

The field survey used in this study is to determine the vegetation and the built-up area in Makassar City. Field survey, carried out by taking vegetation and built-up coordinate points using Global Positioning System (GPS). The results of the field survey data are used to supporting data in identifying vegetation and built-up area in Makassar City with Geography Information System (GIS) based applications using ArcGIS software.

2.6 Accuracy assessment

Accuracy assessment was being conducted by Kappa Coefficient (k) for accuracy assessment which relies on image training area. Training area was delineation based on ground observation with 50 samples of training area with random sampling method.
Kappa ' mathematical accuracy is :

$$K = \frac{N \sum_{i=1}^{r} X_{II} - \sum_{i=1}^{r}(X_{i+} * X_{+i})}{N^2 - \sum_{i=1}^{r}(X_{i+} * X_{+i})} \text{(Congalton, et al. 1999)}$$

Where :
N : the total Number of cell in the matrix,
r : the number of rows in the matrix,
X_{ii} : the number in row i and column i
x_{+1} : the total observations for column i, and
x_{1+} : the total observations in row i

3. RESULT AND DISCUSSION

3.1 Result

NDVI and NDBI

The analysis of NDVI and NDBI in Makassar city showed the qualitative information about the vegetation and built-up area for 20 years (1998 to 2018). The time series of the annual averages of NDVI and NDBI values showed a decrease in vegetation rates and an increase in built-up areas (Table 1 and 2). Image analyze results using parameters Normalized Difference Vegetation Index (NDVI)in 1998 to 2018 showed the high density category was decreased by 2.392 ha and increased by 1.990 ha for medium density category (Table 1).

Table 1. Result of NDVI on 1998 and 2018 in Capital Of The Province Of South Sulawesi

Years	NDVI						Total (Ha)
	Low		Medium		High		
	Ha	%	Ha	%	Ha	%	
1998	4153	22.5	8353	45.23	5961	32.28	18467
2018	4555	24.7	10343	56.01	3569	19.3	

From three samples within same location, which each of them has been zoomed in, vegetation index value can be observed (Figure 2).

Figure 2. Results of NDVI classification in 1998 using Landsat-5 imagery with acquisition on August 8, 1998 and OLI Landsat-8 imagery for 2018 with acquisition on August 15, 2018. (A) arrow describes that the location since 1998 until 2018 already has low vegetation index. To the direction of (B) arrow, it can be seen that the vegetation index has been decreasing, At the beginning in 1998 the value was high (Thick Green), but then changes into Medium (Yellow) in 2018, even so, not 100% of the area experiencing changes. Meanwhile, for the (C) arrow it decreasing in 2018 into medium level, wich marked with Yellow colour.

Detection of the built-up area in Makassar city is carried out digitally using the NDBI variable introduced by Zha et al. 2003. Image analyze results using parameters Normalized Difference Built-Up Index (NDBI)in 1998 to 2018 showed the high density category was increased by 187 ha and decreased by 497 for medium density category (Table 2).

Table 2. Result of NDBI on 1998 and 2018 in capital province of Sulawesi island

Years	NDBI						Total (Ha)
	LOW		Medium		HIGH		
	Ha	%	Ha	%	Ha	%	
1998	3296	17.85	8331	45.11	6840	37.04	18467
2018	3606	19.53	7834	42.42	7027	38.05	

Same as NDVI, from three samples which each of them has been zoomed in within same location but different years, changes of built-up area index value can be observed (Figure 3).
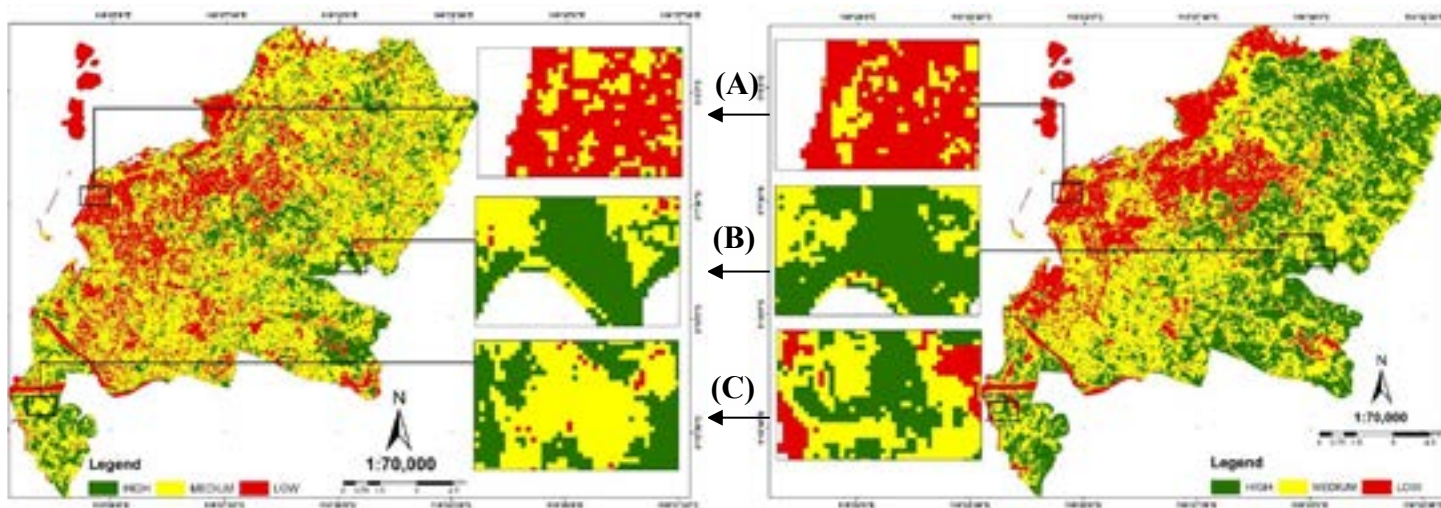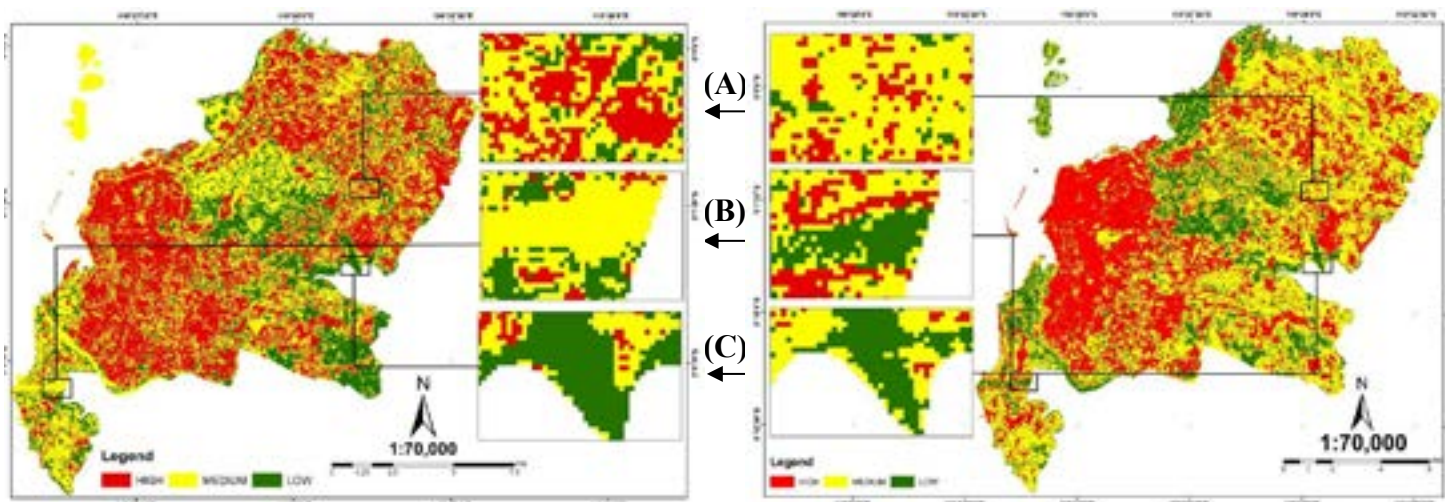

Figure 3. Results of NDBI classification in 1998 using Landsat-5 imagery with acquisition on August 8, 1998 and OLI Landsat-8 imagery for 2018 with acquisition on August 15, 2018. (A) arrow describes that in 1998 the location had built-up area extend with dominantly Medium classification, marked with Yellow colour. Meanwhile by the year 2018,that area has been experiencing increase in built-up area extend into High level, which marked with Red colour. For the direction of (B) arrow, it can be seen that land which previously had very low built-up area index value in 1998 (marked with thick Green colour), has been change into Medium built-up area index value, marked with Yellow. (C) arrow has different result with the previouses, whre land with Low built-up area index (marked with thick green), has been increase in 2018, instead.

Figure 4. Imagery of high resolution from google earth in 2018. A). Urban built-up area dominant, B). less of urban built-up area, C). less vegetation, D). Vegetation area dominant

Validation of vegetation and built-up area

The Normalized Difference Built-up Index (NDBI) has been an effective technique to map built-up areas with accuracy of 92% (Zhang et al. 2013). For assessing accuracy between NDVI and NDBI for Landsat 8 OLI image, defining 3 classes by varying the training pixels, they are low, medium, and high density. The position of each object is also recorded using the *Global Possitioning System (*GPS) with an accuracy of 3 m. Whereas sampling points of objects on the base cover in NDVI of Makassar are 145 sampling and 150 sampling for NDBI. The accuracy of NDVI area is 77.72% and NDBI area is 70.75%.

3.2 Discussion

Remote sensing technology can be used as a method to identify the development of vegetation and built-up area in short time with accountable result accuracy in Makassar city. Extraction of vegetation and built up area transformation from Landsat imagery as moderate spatial resolution have some spectral confusion between other landuse types. There are some missclassification that identified base on ground truth. In fact, There are only 1.01% expansion of the built up area change and 13% of vegetation area has been lost in the capital city between 1998 to 2018 periods. Many forms of development that have been and currently on progress today, mainly the increase of physical development are often related to land limitation. This has become the cause of land use change dynamics from vegetation covered land to built-up land. The increasing demand on land, leads to conflict of interest in land use.

4. CONCLUSIONS

The spatial vegetation cover in Makassar city is decreases continuously for 20 years (1998 to 2018). The use of NDVI shows a low accuracy and ability to classify and discriminate built-up area. Urban industrial, commercial and residential areas are unable to be separated. So in area Makassar city where there is a combination of both industries, commercial and residential area.

Acknowledgments

REFERENCES

Congalton R.G, Green K. 1999. *Assessing the Accuracy of Remotely Sensed Data; Principles and Practices. Florida*: CRC Press, Inc.

E.J. Gago. , J. Roldan, R. Pacheco-Torres, J. Ordóñez. 2013. *The city and urban heat islands: A review of strategies to mitigate adverse effects, Renewable and Sustainable Energy Reviews* 25: 749-758.

H. Z. Zhang , Q.X. Ye, Y, Cai, W. Ma, and M. Chen. 2013. *Analysis of land use/land cover change, population shift, and their effects on spatiotemporal patterns of urban heat islands in metropolitan Shanghai, China*. Applied Geography 44: 121-133.

Nong. D, Miguel. C, Tomoaki. M, Jefferson. F, James. S, and Qi. C. 2014. *Built-Up Area Change Analysis in Hanoi Using Support Vector Machine Classification of Landsat Multi-Temporal Image Stacks*. Environment, Population, and Health Series, No. 1. October 2014.

Zha,Y., Gao, J., Ni, S., 2003. *Use of normalized difference built-up index in automatically mapping urban areas from TM imagery, International Journal of Remote Sensing*, Vol.24, No.3, 2005, pp. 583-594.

Wang. L, Jianghong. Z, Yanqing. X, and Zhanqi. W. 2018. *Urban Built-Up Area Boundary Extraction and Spatial-Temporal Characteristics Based on Land Surface Temperature Retrieval*. Remote Sens. 2018, 10, 473; doi:10.3390/rs10030473

COMPARISON OF LAND COVER CLASSIFICATION USING ROUGH SET THEORY

Yoshie Ishii (1), Hasi Bagan (2), Koki Iwao (3), Tsuguki Kinoshita (4)

[1]Graduate School of Agriculture, Ibaraki University, 300-0393, Ibaraki, Japan
[2]Institute of Urban Studies, Shanghai Normal University, No.100, Guilin Rd. 200234 Shanghai, China
[3]Geological Institute of Geology and Geoinformation Geological Survey of Japan, Advanced Industrial Science and Technology, Ibaraki, 305-8567, Japan
[4]College of Agriculture, Ibaraki University, Ibaraki, 300-0393, Japan
Email: 18am401h@vc.ibaraki.ac.jp; hasibagan@hotmail.com; iwao.koki@aist.go.jp;
tsuguki.kinoshita.00@vc.ibaraki.ac.jp

KEY WORDS: Rough set theory, grade-added rough set model, landcover classification, Landsat 8, Covering Index

ABSTRACT: The objective of this research is to compare the land cover classification methods based on rough set theory which were proposed in the past and to clarify their features respectively. This research focused on the comparison of the original rough set model (ORS) which handle categorical data and the grade-added rough set model (GRS) which was extended ORS to numerical data out of existing land cover classifications using rough set. Also, the effects of Covering Index (C.I.) and β approximation which is defined in the variable precision rough set were examined. In addition, land cover classification in four patterns of the number of training data and two resampling methods (equal pixel count division (EPC) and equal DN interval division (EDI)) were examined. For experiments, Landsat 8 images from band 1 to band 7 were used and southern area of Ibaraki in Japan was selected as the study area. From these experiments, in ORS, approximately κ=0.80 were obtained in the case of 4 bits EPC resampling with C.I. and 7 bits EDI resampling with C.I. Meanwhile, in GRS, there were almost no effects of C.I., resampling, and β approximation, and simple GRS using 16 bits DN was the highest precision. Although high precision results could be obtained in ORS under a certain condition, this condition will not always be highly accurate if the images and training data were changed. Therefore, it is concluded GRS method is higher performance as a land cover classification because it is not necessary to set parameters and resample. However, it was suggested that C.I., applied to land cover classification for the first time in this research, has potential of being effective for estimation of mixed cells.

1. INTRODUCTION

The rough set theory (Pawlak, 1982) is effective for inferring incomplete information (Leung *et al.*, 2007). In recent years, several land cover classification methods using rough set theory have been proposed. The rough set theory originally handles categorical data. On the other hand, condition attribute values in land cover classification are numerical data generally called Digital Number (DN). Therefore, it has been mainly discussed how to handle the DN as the condition attribute value in the development of the land cover classification method using the rough set theory.

Until now, the proposed methods are mainly classified into three patterns. One is a method using original rough set (ORS) proposed by Pawlak. In this method, the focus is on a methodology of DN resampling (Pan *et al.*, 2010) (Leung *et al.*, 2007). Another is a method called grade-added rough set (GRS) by extension of ORS that enables to use DN without resampling (Ishii *et al.*, 2018). By using GRS, information loss caused by grouping can be prevented. The other is the methods using tolerant rough set (Ma and HASI, 2005) (Yun and Ma, 2006). Tolerant rough set is a set that excludes "transitivity" from the properties, "reflectivity", "symmetry" and "transitivity" that are required by ORS (Kim, 2001). Although usefulness of the method was shown, it has a problem that it is difficult to determine the threshold in tolerant rough set.

These methods are based on the rough set theory, but each method has their own characteristics. Comparison studies among several rough set applications don't be conducted on the field of land cover classification in the past. In this research, we conducted comparative experiments to clarify the characteristics of ORS and GRS. For ORS and GRS, the effects of the number of training data, resampling methods, Covering Index (C.I.), and the β approximation were examined. From these results, we clarified the effect of each condition and the most suitable way to land cover classification.

2. THEORY

2.1 The rough set theory

The rough set theory was proposed by Pawlak (Pawlak, 1982). This is a theory that aimed at representing arbitrary feature space approximately by upper and lower approximation using basic sets based on equivalence classes. In the

feature extraction and reasoning, the minimum decision rule is decided by using the decision table and identification matrix proposed by Shan and Ziarko (Shan and Ziarko, 1998).

Defining the target set as U, the condition attribute set C, the decision attribute set as D, the attribute value as VAL, the information table S is expressed by equation (1).

$$S = < U, C \cup D, \{VAL_a\}_{a \in (C \cup D)} >. \tag{1}$$

Using this information table, each element of the discrimination matrix with respect to the decision attribute value v is given as a set by equation (2).

$$M_{ij} = \{(a, a(s_i^v)): a(s_i^v) \neq a(s_j^{\sim v})\}, \tag{2}$$

where $s \in U$, i $(i = 1,2,\cdots \gamma)$ is the number of the sample whose decision attribute value is v, j $(j = 1,2,\cdots \rho)$ is the number of the sample whose determined attribute value is not v ($\sim v$). Also, $a(s_i^v)$ represents the attribute value of attribute a in sample s_i^v. As shown in Equation (3), a disjunction operation is calculated for the set of the identification matrix elements, and a conjunction operation is conducted on the row for the union set of the obtained matrix elements to obtain the minimal decision rules for sample i.

$$B_i^v = \bigwedge_j \bigvee M_{ij}. \tag{3}$$

From Equation (3), if the number of samples whose decision attribute value v is N, N-tuple minimal decision rules are extracted. Using Equation (3), the minimal decision rule for the decision attribute value v is given as the union set for i of B_i^v as shown in Equation (4).

$$RUL(|v|) = \bigcup_i |B_i^v|. \tag{4}$$

In the inference process, it is judged whether the attribute and the attribute value to be inferred are included in the minimal decision rule of Expression (4) or not.

When rough set theory is applied to land cover classification using remote sensing images, the target set corresponds to all training data. The condition attribute corresponds to an image bands, and the condition attribute values correspond to the DN or the converted one. The decision attribute is land cover and the decision attribute values correspond to land cover classes.

The grade-added rough set is a method that was extended from ORS to handle numerical data (Mori and Takanashi, 2000). The basic idea in the grade-added rough set is the same as original rough set. But in grade-added rough set, by given the unidentifiable relation with threshold α, it becomes possible to make an inference such as "above" or "below" that means a difference greater than or equal to the threshold between a sample and another one. The satellite data are numerical data such as 8 bits or 16 bits DN, it is shown that the usefulness of an extended rough set, GRS on land cover classification (Ishii *et al.*, 2018).

2.2 Covering Index (C.I.)

In the rough set theory, the set given by equation (4) is not exclusive for each v. Therefore, there are cases inferring to multiple classes, and it is impossible to specify which class is correctly classified. In this research, Covering Index (C.I.) was introduced (Tsumoto and Tanaka, 1996). C.I. is an index representing the importance of rules in a class of training data, and defined as Equation (5) (Tsumoto and Tanaka, 1996),

$$CI_v = \frac{\sum_{i=1}^{\gamma_v} \delta_i^v}{\gamma_v}, \tag{5}$$

$$\delta_i^v = \begin{cases} 0, & B_i^v = \phi, \\ 1, & B_i^v \neq \phi, \end{cases} \tag{6}$$

where γ_v is the number of training data of class v.

2.3. β approximation

Variable precision rough set model is a method to allow some contradiction data and relax standard of equivalence class (Ziarko, 1993). In the variable precision rough set, degree of misclassification of the set X with respect to set Y was defined as Equation (7),

$$c(X,Y) = \begin{cases} 1 - \dfrac{card(X \cap Y)}{card(X)}, & X \neq \emptyset, \\ 0, & X = \emptyset \text{ or } X \subseteq Y, \end{cases} \tag{7}$$

where $card(X)$ is the number of elements of set X. When $c(X,Y)$ is not 0, in the ordinary rough set theory, the minimal decision rule expressed by equation (3) is an empty set. Therefore, a threshold β is introduced. In the case of $c(X,Y) < \beta$, it is assumed $X \subseteq Y$. That is, if there are a small number of elements that are not included in Y in the set X those elements are ignored as exceptions.

3. MATERIALS AND METHODS

3.1 Data sets

In this research, the southern area of Ibaraki including a part of Kasumigaura in Japan was selected as the study area. The image data consists of band 1 to band 7 of Landsat 8 OLI (Operational Land Imager) acquired on May 31, 2014 (USGS, 2018). The image data is a digital number (DN) obtained by converting the observation value into an integer value. The number of classification classes was seven: urban, cropland, paddy, forest, sparse, grass, and water. The study area and definitions of classification classes in this research and the number of training data and validation data are shown in the Figure 1 and Table 3, respectively. The study area and classes are the same as those in (Ishii *et al.*, 2018), so the details are given there.
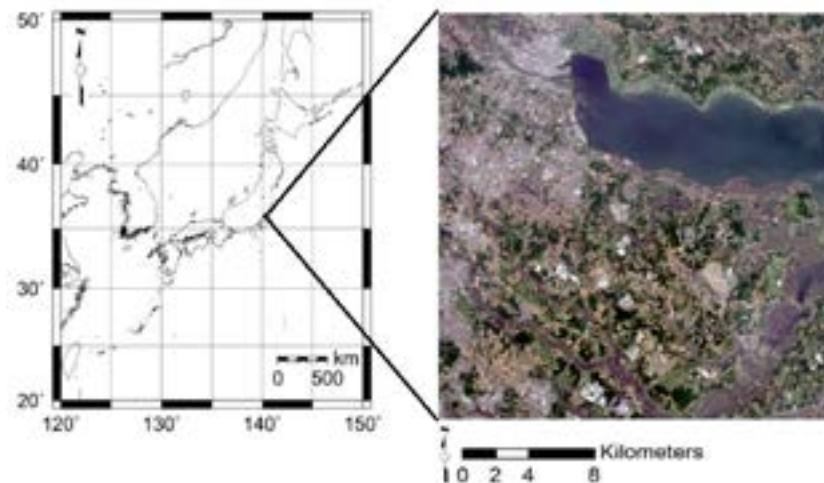
Figure 1 True-color composite Landsat 8 image (RGB = bands 4,3 and 2) of the study area acquired on May 31, 2014, and its location in the southern area of Ibaraki, Japan

Table 1 Class description, and training and validation data set

| Land cover type	Description	Training pixel count				Validation pixel count
		Case 1	Case 2	Case 3	Case 4	
Built-up	Buildings, concrete, and other artificial	30	59	109	209	52
Water	Lakes, rivers and ponds	29	57	107	207	50
Cropland	Dry croplands	25	49	99	199	49
Sparse	Sparse vegetation such as golf courses and	24	47	97	197	48
Grass	Bamboo forest and grass except pf sparse	23	45	95	195	48
Forest	Forests	28	55	105	205	52
Paddy	Rice and lotus paddy	26	50	100	200	50
Total		185	362	712	1412	349

3.2 Methods

The land cover classification methods by ORS and GRS were compared and clarified the differences and characteristics of them. Various classification conditions examined are shown in Table 2.

Table 2 Classification conditions consist of rough set type, the number of training data, resampling method, C.I. and β approximation

| Rough set type | The number of training data (Total) | Resampling | | | C.I. | β |
		Equal pixel count division (EPC)	Equal DN interval division (EDI)	No		
ORS / GRS	Case 1 (185) Case 2 (362) Case 3 (712) Case 4 (1412)	1-bit increments from 3 bit to 15bit	1-bit increments from 3 bit to 15bit	16 bits DN	With / without	0.0 (none) 0.1 0.2 0.3 0.4 0.5

Training data was set to 4 patterns. "Resampling" indicates to convert DN of 16 bits Landsat 8 data to more coarse steps whose range is from 3 bits (8 steps) to 15 bits (32768 steps) using equal pixel count division method (EPC) or equal DN interval division method (EDI). This is mainly aimed at precisely performing land cover classification by ORS. Although GRS does not need resampling, GRS classification were executed in same conditions for references. For C.I., two patterns, "with" and "without" were considered. For β approximation, it was set 6 patterns from 0.0 (none) to 0.5. For these patterns, each land cover classification map was produced, and accuracy evaluation was performed. The classification schematic diagram is shown in Figure 2. However, in the condition of 3 bits resampling by EDI and β approximation, there are some classes which don't include training data resulting from resampling, so the land cover maps under the condition was not produced.
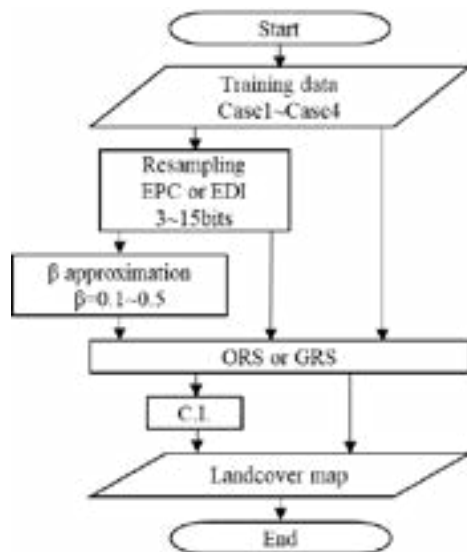
Figure 2 Schematic diagram of land cover classification.

4. RESULTS AND DISCUSSIONS

4.1 ORS

4.1.1 The effect of number of training data: There is usually a positive correlation between the number of training data and classification accuracy. As a result of examining the relation between the number of training data and yhe accuracy derived from classification by ORS under simple conditions using DN (without resampling, CI and β approximation), the accuracy improved as the number of training data increased. However, under all simple conditions, the classification accuracy by ORS was as low as $\kappa = 0.4$, regardless of the number of training data.

4.1.2 The effect of resampling method and the bit number: Graphs of the relation between resampling bit number and the accuracy with the number of training data in ORS are shown in Figure 3. Horizontal axes are bit number and

the vertical axes are κ coefficient. Different trends were shown between EPC and EDI. In resampling by EPC, especially when using C.I., the accuracy is improved as bit number decreases. On the other hand, in resampling by EDI, it peaked at 5 to 6 bits without C.I., and it peaked at 7 bits with C.I. The reason why the accuracy decreased in low bit number is considered that contradiction data were produced due to resampling. Also, same results found in EPC and EDI are that the bit number of the accuracy peaks shifted higher by introducing C.I. From this, it can be seen that optimal division intervals are different between with and without C.I.

In comparison of cases without C.I., for EPC (Figure 3 (a)), 3 bits has the highest accuracy, and 7 to 9 bits accuracies are secondary. On the other hand, for EDI (Figure 3 (c)), the accuracies of 5 to 7 bits are relatively high. From these results, in the case of resampling by EPC, the accuracy improve as the number is closer to the number of classification class. On the other hand, in the case of resampling by EDI, optimal bit number maybe depend on the range of DN, spectral reflection characteristic, number of training data in each class and so on. Because too low bit number produces many contradiction data and too high bit number induces many unclassifiable sets in feature space with limited training data. In addition, optimal bit number may vary from band to band.

In comparison of cases with C.I., tendency of graphs is similar to without C.I. However, the peaks of accuracies shifted to high bit number, because C.I. is effective when many pixels are inferred to multiple classes. Such cases are induced when bit number is high and training data is relatively small, and many pixels are inferred to no classes in such cases.

4.1.3 The effect of C.I.: Under the simple conditions with 16 bits DN, for ORS, the kappa coefficient was improved max 12%. And, the accuracies tend to improve by applying C.I. under some conditions regardless resampling methods (Figure 3). In particular, when the cases the accuracy is high without C.I., the accuracy improvement resulting from C.I is large. In addition, these results show that the synergistic effect by C.I. and resampling is large.
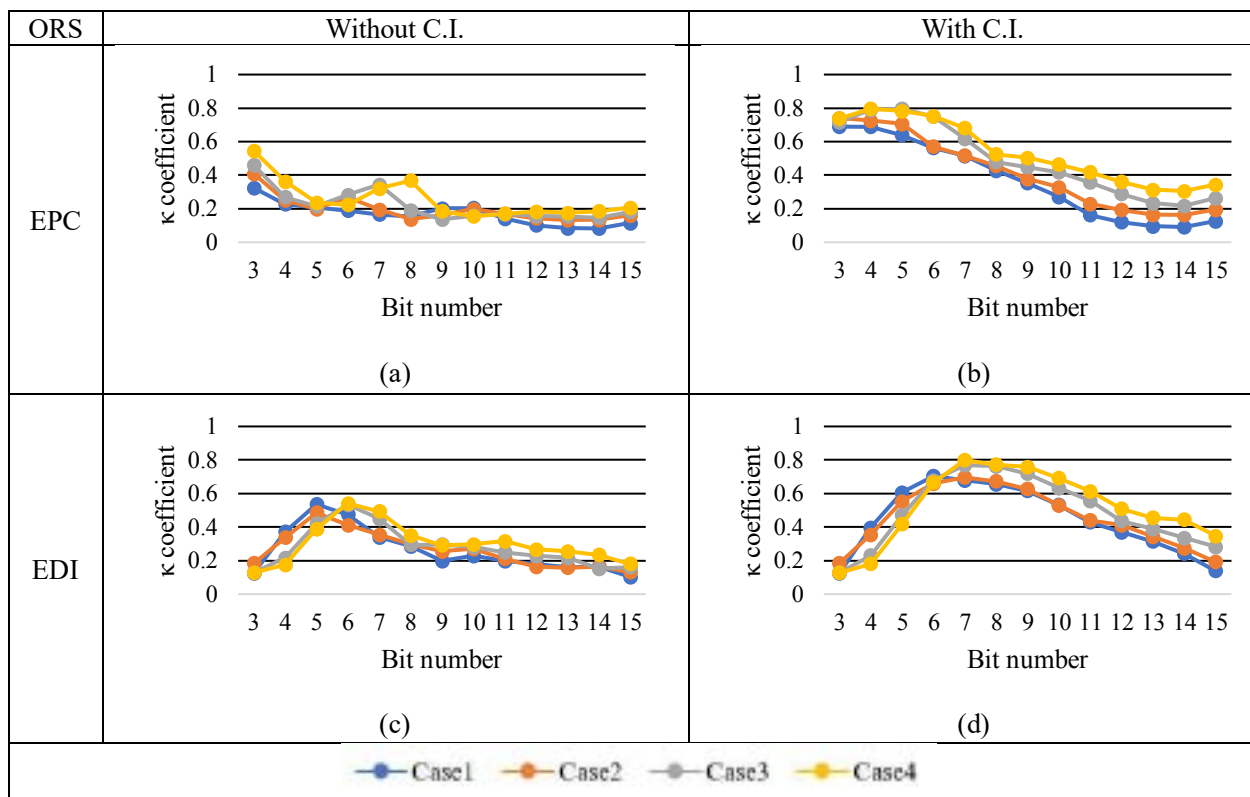

Figure 3 The relation between the resampling number and κ coefficient. Horizontal axes are bit number and the vertical axes are κ coefficient. Legends are the number of training data.

4.1.4 The effect of β approximation: Next, the effect of β approximation was investigated. As a result, effect of β approximation was not found in any resampling by EPC. For the resampling by EDI, the accuracies were improved greatly as the β is from 4 to 6 bits. For the resampling by EDI, since the distribution of the training data in feature space is concentrated in part, many contradiction data were produced when bit number is low. So it seems that the effect of the β approximation appeared. From these results, the effect of β approximation is limited in land cover classification, meanwhile we could find no serious problem of β approximation. If training data include some error data, β approximation will be effective, so there is no need to proactively eliminate the β approximation.

4.1.5 Summary of ORS: When ORS is used for land cover classification, it was found that the β approximation has limited meaning, and it is possible to obtain the same degree of accuracy as the existing classification method by performing appropriate resampling and introducing C.I.

4.2 GRS

4.2.1 The effect of number of training data: The relation between the number of training data and κ coefficients by GRS were examined under simple conditions using DN (without resampling, CI and β approximation). As a result, high accuracies of κ = 0.739 (Case 1) to κ = 0.836 (Case 4) were obtained. As increase of training data, the accuracy tends to be improved, but it seems to be saturate for Case 3 and Case 4. From this, it can be said that it is enough for the GRS to have about 100 to 200 training data per class.

4.2.2 The effect of resampling method and the bit number: The result of comparing the relation between resampling bit number and κ coefficients with the number of training data in GRS is shown in Figure 4. The horizontal axis is the bit number and the vertical axis is κ coefficient. For GRS, when bit number is reduced in the EDI, the accuracy become lower same as ORS. But this is not a serious problem because the accuracies are the highest in high bit number in all cases, and unnecessary do find optimal bit number in GRS. Direct use of DN is the best choice for GRS and highly accurate results around κ = 0.80 can be obtained.
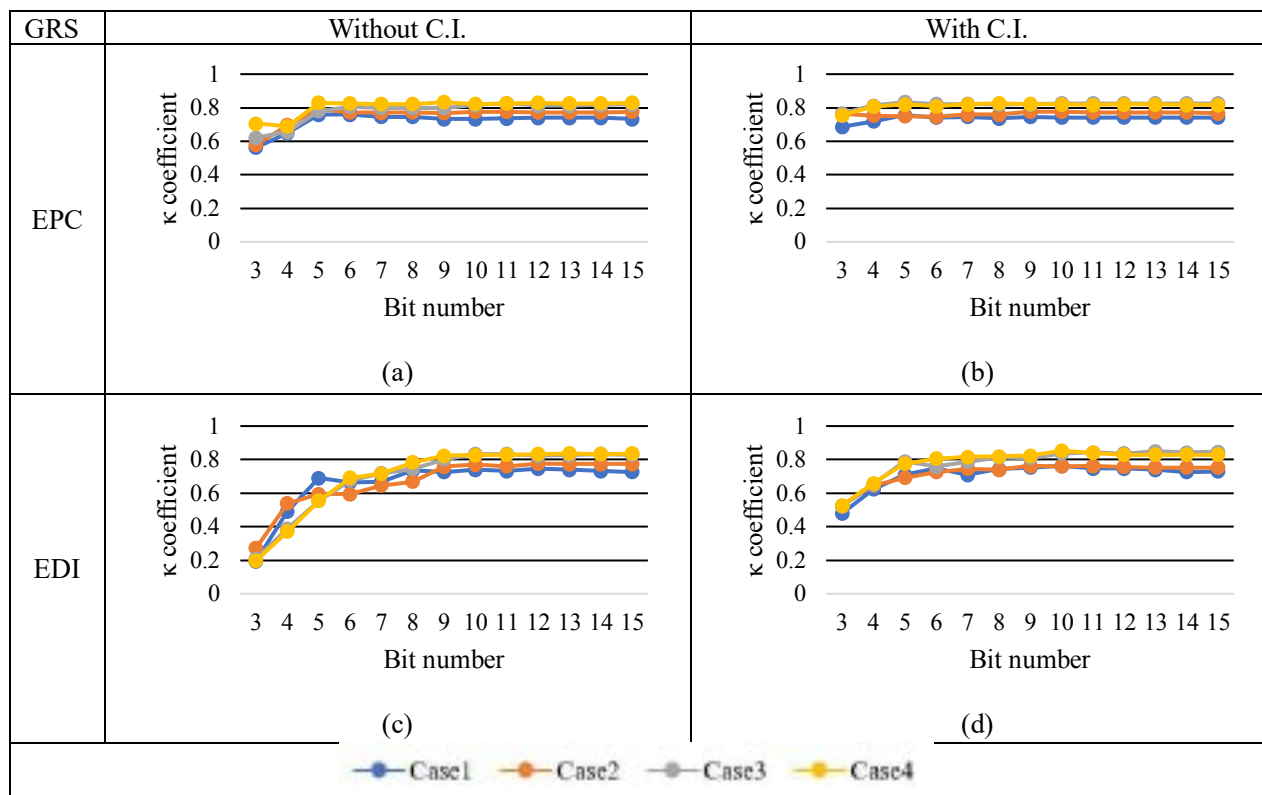

Figure 4 The relation between the bit number and κ coefficient. Horizontal axes are bit number and the vertical axes are κ coefficient. Legends are the number of training data.

4.2.3 The effect of C.I.: In simple condition with DN, there was no change or slight accuracy deterioration by introducing C.I. on GRS. Also, regardless resampling methods, C.I. doesn't affect on relatively higher bit divisions where GRS has meaning.

4.2.4 The effect of β approximation: As mentioned in 4.1.4, there was no contraction in the training data when the 16 bits DN was used. As a result, in simple condition with DN, there was no effect of β approximation also in GRS. And it was almost no effect by β approximation in the condition of resampling.

4.2.5 Summary of GRS: When GRS is used for land cover classification, simple condition without resampling, C.I. and β approximation may be the best choice because there is no parameter setting.

4.3 Overall discussions

In ORS, great synergy was obtained by resampling and C.I. On the other hand, the effect was hardly seen in GRS, or the accuracy declined slightly by using C.I. C.I. was introduced to determine which class to ultimately classify when inferring to multiple classes in land cover classification by ORS. In other words, not only when it is inferred to a single class, but also that it is inferred to multiple classes in some cases in land cover classification by ORS. In the process of ORS, contradiction data (called upper approximation data) of the training data are eliminated. Therefore, inferences are made only from the lower approximation data which are reliable. However, in the following cases, even if the training data are lower approximation, the classification result deduced therefrom is classified into a plurality of classes depending on places, resulting in meaning like an upper approximation.

Figure 5 (a) shows the two-dimensional feature space consist of Band 1 and Band 2. Each band assumes to have from 0 to 6 value. In Figurer 5 (a), a bold diagonal line across the feature space indicates a true boundary of class 1 and class 2, and red and blue numbers enclosed within a circle are training data in each class. Figure 5 (b) and (c) show the difference between ORS classification "without C.I." and "with C.I.", and (d) shows GRS classification. In Figure 5 (b), (c) and (d), left and center matrices are the decision rules resulting from training data about class 1 and class 2, respectively. And the right figures show results of inference, respectively. In results of inference, red cells are class 1, blue cell are class 2 and grey and white cells indicate unclassified. Without C.I., the decision rules are expressed only 0 or 1, and the grey grid cells which are overlapped two classes inference become unclassified. On the other hands, with C.I., the decision rules expressed C.I., and if decision class are overlapped in a cell, a cell is classified lager C.I. class. If C.I. in a cell are equal in two classes, decision class become unclassified. As shown in Figure 5 (b) and (c), number of unclassified cells is decreased by introducing C.I. In GRS, the degrees, differences of grades, are stored in each grid cells, and cells are classified larger degree class if two decision class are overlapped.

(b) ORS classification without C.I.

(a) The two-dimensional feature apace and training data of class 1 (red numbers) and class 2 (blue numbers)

(c) ORS classification with C.I.

(d) GRS classification
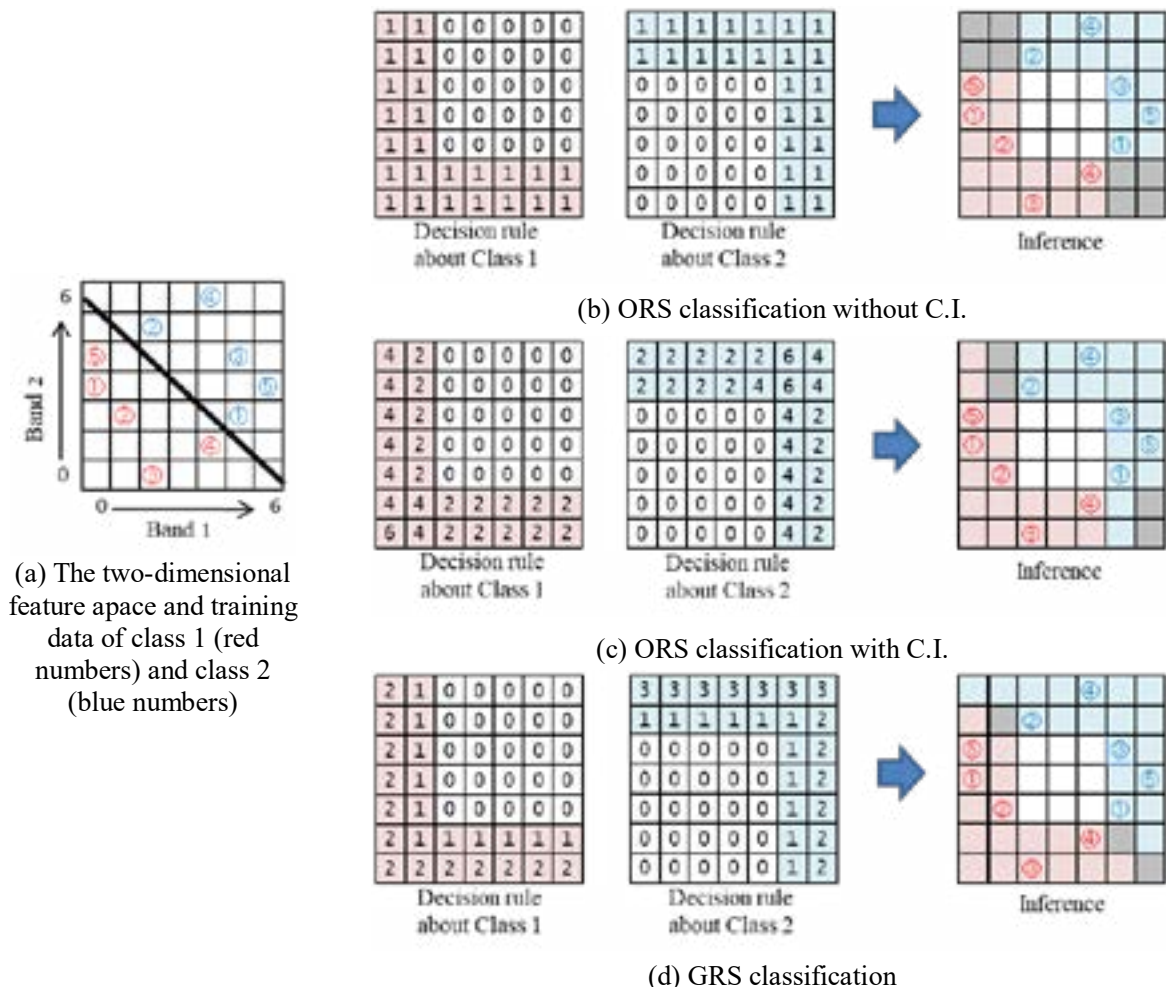
Figure 5 The difference between ORS classification "without C.I.", "with C.I." and GRS classification. In (b), (c) and (d), red or blue areas indicate the rule derived from training data, and "0" areas indicate the other class. In (c), C.I. is multiplied by 10.

From Figure 5, it is not only found out the difference between "without C.I." and "with C.I.", but also the similarity of the effect of C.I. in ORS and the effect of the degree in GRS. Cells inferred in multiple class are classified in a certain class by C.I. or GRS, and they never affect on cells which are inferred in one class or none. This is justified by the results that the accuracy of GRS without C.I. is almost same as that of GRS with C.I.

In addition, there is possibility that the pixels which have multiple C.I, are mixed cell. C.I. may suggest how much proportion of mixed cell is contained in its feature space.

Next, the land cover maps obtained in practical and highest precision conditions by ORS and GRS were compared. The land cover maps are shown in Figure 6, and producer's and user's accuracies are shown in Table 3, respectively., The two maps of Figure 6 tested the difference of κ coefficients by foody (Foody, 2004), as a result, there was no difference under the significance level of 5%, therefore these map accuracies regard as equivalent. Of the total 444889 pixels, 1139 pixels were unclassified in ORS (Figure 6 (a)), while there was not unclassified pixel in GRS (Figure 6 (b)). In Table 3, There was no noticeable difference.

(a) ORS   (b) GRS
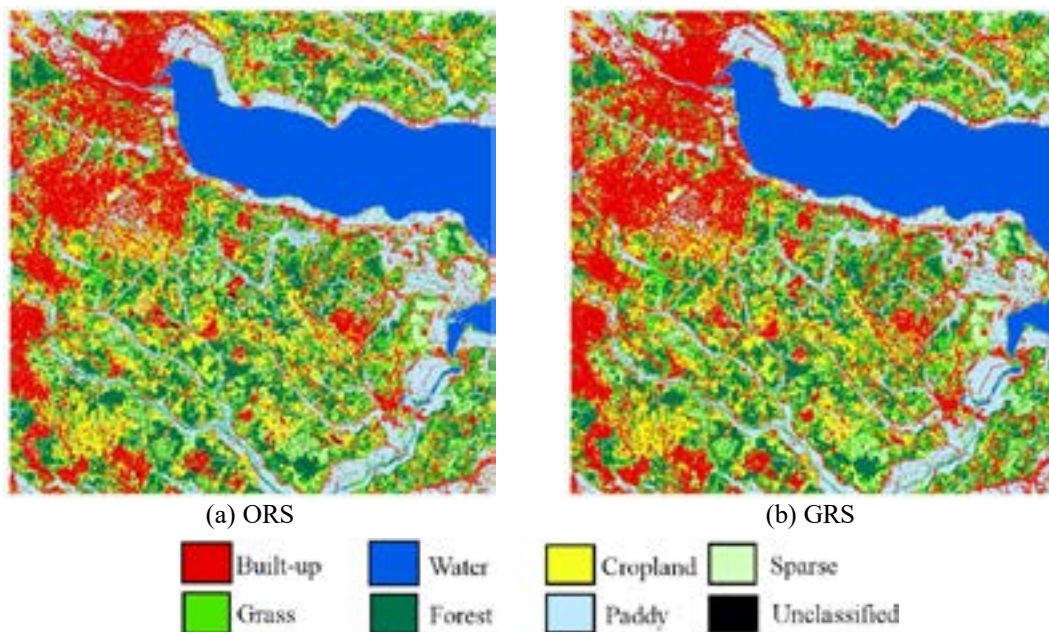
Figure 6 Comparison the high accuracy land cover maps classified by ORS (a) and GRS (b). The map generated under the conditions with C.I., and 7bits EDI resampling and the number of training data Case4 for (a) and without C.I., 16bits DN and the number of training data Case 4 for (b). The accuracies are (a) κ= 0.800 and (b) κ= 0.836.

Table 3 Comparison of producer's and user's accuracies between ORS and GRS corresponding to maps in Figure 6.

	Producer's accuracy (%)		User's accuracy (%)	
	ORS	**GRS**	**ORS**	**GRS**
Built-up	63.5	73.1	91.7	92.7
Water	100.0	100.0	100.0	100.0
Cropland	83.7	89.8	83.7	89.8
Sparse	83.3	85.4	80.0	87.2
Grass	75.0	79.2	65.5	65.5
Forest	82.7	82.7	76.8	81.1
Paddy	92.0	92.0	90.2	90.2

The overall tendency of land cover maps in figure 6 and accuracies in Table 3 are similar, and these results support our hypothesis that GRS includes the effect of C.I. in ORS. It was found that ORS can obtain the almost same accuracy as that of GRS under specific conditions, but the effort to obtain highly accurate results are different. In order to obtain highly accurate results in ORS, in addition to the introduction of C.I., the resampling method and its division number are greatly affected. Although this has been pointed out in existing researches (Pan *et al.*, 2010), it was also confirmed in this research. Furthermore, if the number of training data, land cover class, the image to be classified, the number of bands and so on change, it needs much effort to search for appropriate conditions. On the other hand,

in GRS, high precision results were obtained with a simple method using DN without resampling and C.I. Furthermore, the fact that resampling is unnecessary implies the advantage that GRS is free from information loss. In this research, we used 16 bits Landsat 8 images, but the results in Figure 4 suggest that satellite images observed with 8 bits or 12 bits are sufficiently applicable. Therefore, from a practical point of view, it is concluded that GRS is more effective than ORS.

6. CONCLUSION

In this research, the land cover classification methods by ORS and GRS were compared. As a result, in ORS, high accuracy was obtained near the number of classification classes at EPC, but the number of about 10 bits was high accuracy at EDI. However, if the classification target images and / or the way of taking training data change, optimum conditions of ORS may also change. But, in either case, it was found that the C.I. was effective in ORS. The fact that the accuracy of land cover classification by ORS using resampling and C.I. is equivalent to GRS means that it is the same accuracy as existing methods MLC and SVM (Ishii *et al.*, 2018). There have been no researches showing the usefulness of C.I. in the field of land cover classification. In this research, it was also pointed out that C.I. may be effective in estimating mixed cells.

Next, about GRS, it was demonstrated that the classification by simple GRS using DN is high accuracy. In meaningful range of about 8 bits or more for GRS, the notable effect of C.I. and beta approximation is not obtained. This is, because the degree of GRS includes the effect of C.I. already, and contradiction data don't generate in finer bits conditions.

Finally, ORS and GRS under highly accurate conditions were compared. Similar results were obtained from land cover maps, user's accuracy and producer's accuracy. However, resampling, C.I. and β approximation are not required in GRS, whereas a plurality of conditions have to be set in ORS. Furthermore, GRS has the advantage that there is almost no loss of satellite data information. Therefore, from the viewpoint of practicality and robustness, it is concluded that GRS is more useful as land cover classification method than ORS.

REFERENCES

Foody, G. M., 2004. Thematic map comparison: evaluating the statistical significance of differences in classification accuracy. Photogrammetric Engineering & Remote Sensing, 70(5), pp. 627–633.

Ishii, Y., Bagan, H., Iwao, K. and Kinoshita, T., (submitted). Landcover classification using grade-added rough set theory, pp. 1–16.

Kim, D., 2001. Data classification based on tolerant rough set. Pattern Recognition, 34(8), pp. 1613–1624.

Leung, Y., Fung, T., Mi, J. and Wu, W., 2007. A rough set approach to the discovery of classification rules in spatial data. International Journal of Geographical Information Science, 21(9), pp. 1033–1058.

Ma, J. and HASI, B., 2005. Remote sensing data classification using tolerant rough set and neural networks. Science in China Series D, 48(12), p. 2251.

Mori, N. and Takanashi, R., 2000. Knowledge Acquisition From the Data Consisting of Categories Added with Degrees of Conformity. Kansei Engineering International Vol.1, 1(4), pp. 19–24.

Pan, X., Zhang, S., Zhang, H., Na, X. and Li, X., 2010. A variable precision rough set approach to the remote sensing land use/cover classification. Computers and Geosciences. Elsevier, 36(12), pp. 1466–1473.

Pawlak, Z., 1982. Rough Sets. International Journal of Computer & Information Sciences, 11(5), pp. 341–356.

Tsumoto, S. and Tanaka, H., 1996. Automated Discovery of Medical Expert System Rules from Clinical Databases based on Rough Sets.

USGS, 2018. EarthExplorer. Retrieved September 1, 2018, from https://earthexplorer.usgs.gov/.

Yun, O. Y. and Ma, J. W., 2006. Land cover classification based on tolerant rough set. International Journal of Remote Sensing, 27(14), pp. 3041–3047.

Ziarko, W., 1993. Variable precision rough set model. Journal of Computer and System Sciences, 46(1), pp. 39–59.

PITCH CANKER DAMAGED TREES

Hwa-Seon Lee, YanYan Piao, Kyu-Sung Lee

Inha University, Department of Geoinformatic Engineering, 100 Inharo, Michuhol-Incheon, S. KOREA
Email: hslee89@inha.edu; yanyan213@naver.com; ksung@inha.ac.kr

KEY WORDS: Pitch Canker, multi-temporal, high-resolution, KOMPSAT, NDVI difference, NDVI

ABSTRACT: This study aims to propose a methodology for detecting damaged trees caused by pitch canker using multi-temporal high-resolution KOMPSAT satellite images. NDVI was calculated from each image obtained on March 15, 2015, and April 20, 2011, and then NDVI difference between 2015 and 2011 was also derived. If the spectral reflectance is consistent for two KOMPSAT images, a negative value of NDVI difference indicates foliage discoloration and the decrease of foliage mass in 2015. To detect candidates of damaged trees, suitable threshold was selected from (1) the NDVI of 2015 and (2) both NDVI of 2015 and NDVI difference. The detection accuracy was evaluated by field survey data.

1. INTRODUCTION

Pine pitch canker is a relatively new tree disease found in Korea, which is caused by the fungus Fusarium Circinatum. Considering that pitch canker mainly occurs in mild climate regions, the occurrence of pitch canker in Korea might be an exceptional case and be related to the regional climate changes. Pitch canker is now regarded as an endemic disease that represents small and scattered spatial distribution and mild symptoms.

High-resolution satellite images such as IKONOS (4m), QuickBird (2.8m), GeoEye (1.6m), and Rapideye (5m) allow us to detect forest disease at individual tree level. High-resolution images are useful for detecting forest damage that small and scattered. A multi-temporal analysis has been reported as an effective way of detecting intermediate level damaged tree representing a subtle change in spectral signal (Meddens et al., 2011). The multi-temporal analysis can emphasize the spectral signal resulted from foliage discoloration, the decrease of foliage mass as well as can mitigate environmental effects such as atmosphere, angle, background, and shadow (Hart and Veblen, 2015). This study aims to propose a methodology for detecting damaged trees caused by pitch canker using multi-temporal KOMPSAT images.

2. MATERIALS AND METHODS

Korean Multi-Purpose SATelite (KOMPSAT) that has been developed by Korea is an earth observation satellite equipped with high-resolution multispectral camera range from blue, green, and red to the near infrared. Two multi-temporal KOMPSAT-3 and KOMPSAT-2 images were used. They were acquired on March 15, 2015, and April 20, 2011, over Jeonllanam-do, the southern part of Korea. KOMPSAT-3 and KOMPSAT-2 have 2.8m and 4m spatial resolution, respectively.

To detect any meaningful change from multi-temporal images, their spatial coordinate should be identical and also their spectral signal should be consistent and comparable. As a preprocessing, atmospheric and topographic effects were corrected. NDVI ($NDVI_{2015}$, $NDVI_{2011}$) was calculated from each surface reflectance and then NDVI difference ($\Delta NDVI_{diff}$) between 2015 and 2011 was derived (Figure 1). Only pine forest of Pinus rigida and black pine which are most susceptible species to pitch canker was extracted using digital forest type map.

To detect pitch canker damaged trees in 2015, in single-date approach, a threshold was selected from $NDVI_{2015}$ based on image histogram (Figure 1). In multi-temporal approach, a threshold was also determined from both $NDVI_{2015}$ and $\Delta NDVI_{diff}$ based on scattergram between two images (Figure 1). If the spectral reflectance is consistent for two KOMPSAT images, $\Delta NDVI_{diff}$ would be zero. A negative value of $\Delta NDVI_{diff}$ could be estimated as candidates of damaged trees caused by

pitch canker, which related to foliage discoloration and the decrease of foliage mass and vitality. However, many pixels belonging to negative $\Delta NDVI_{diff}$ were explained as artifacts, harvested and regeneration forest, and crown shadow. Suitable thresholds were selected by trial and error method.
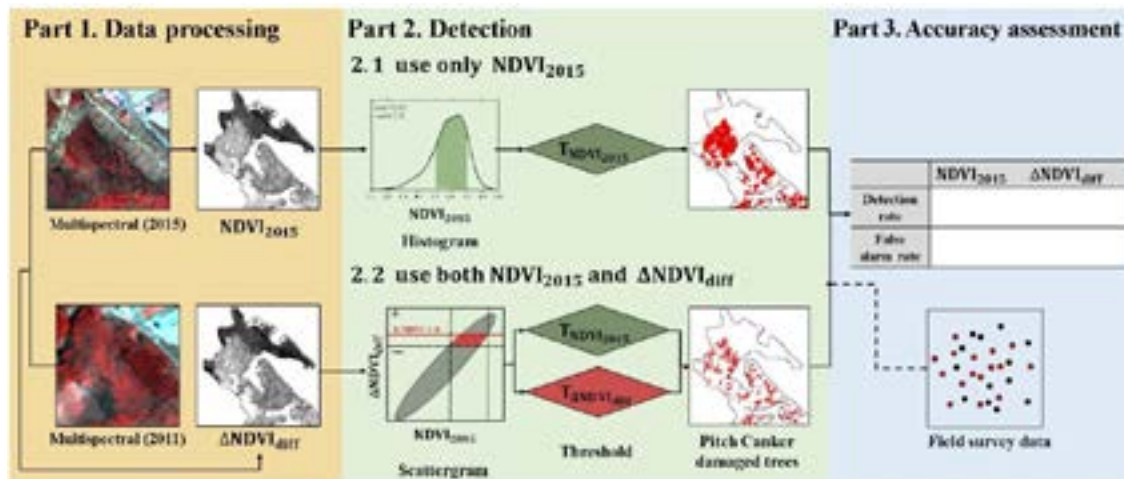
Figure 1. Flowchart of this study for detecting damaged trees by caused by pitch canker using multi-temporal KOMPSAT images.

3. RESULTS AND CONCLUSIONS

To evaluate detection accuracy field survey data was utilized (Figure 1). The field survey was conducted for the area of candidates of damaged trees caused by pitch canker on November 6 and 7, 2015. The twenty-eights field survey sites were classified into two classes: damaged trees caused by pitch canker on pine forest (16 sites) and mixed forest consisting healthy pine forest with deciduous (12 sites). Both two approaches yielded a 100% detection rate (=16/16). A false alarm was observed in mixed forest by their similar spectral signal to damaged trees. In multi-temporal approach using both $NDVI_{2015}$ and $\Delta NDVI_{diff}$, it produced 50% false alarm rate. In single-date approach using $NDVI_{2015}$ alone, it could not distinguish between them (=12/12).

In single-date approach, an area of 4.8ha was detected as damaged trees from the entire pine forest, which is accounts for 6.72 percent out of the entire pine forest. This result is too much and also conflicts with the characteristics on the occurrence of pitch canker in Korea. In multi-temporal approach, an area of 1.8ha was detected as damaged trees from the entire pine forest, which is accounts for only 2.63 percent out of the entire pine forest.

In this study, we have shown a simple and effective method of detecting pine pitch canker using multi-temporal KOMPSAT images. At the detection of mild symptoms caused by pitch canker, the multi-temporal approach using both $NDVI_{2015}$ and $\Delta NDVI_{diff}$ was analyzed as a more effective way rather than the single-date approach using $NDVI_{2015}$ only. Remote sensing detection of forest damages by insect and disease is becoming very important from the aspect of forest management practice and environmental monitoring of forest health problem along with climate changes.

ACKNOWLEDGMENT

REFERENCES

Meddens, A.J., J.A. Hicke, and L.A. Vierling, 2011. Evaluating the potential of multispectral imagery to map multiple stages of tree mortality, Remote Sensing of Environment, 115(7): 1632-1642.

THE EFFECT OF RAINFALL VARIATION ON PHENOLOGY AND PRODUCTION OF OIL PALM IN JOHORE

Amirah Audadi Madzen

Social Environmental and Development Sustainability (SEEDS) Research Centre, Faculty of Social Science and Humanities, Universiti Kebangsaan Malaysia, Selangor, Malaysia
Email: amirahaudadimadzen@gmail.com

KEYWORDS: EVI; oil palm; MODIS; production; vegetation phenology

ABSTRACT: World climate has changed significantly over recent decades and altering earth system. Temperature in Southeast Asia has grown at a rate of 0.14°C to 0.20°C every decade since the 1960s. The IPCC Fifth Assessment Report also projected that global warming and climate change will occur more drastically in the last three decades of the 21st century and temperatures in that region is expected to increase about 1.5°C to 2.0°C in the mid-century (2046-2065). Therefore, the method of tracking and evaluating changes in ecosystems is important in assessing the effects of climate change. Land Surface Phenology (LSP) is a study on plant growth patterns and observed using remote sensing technologies. Variety temporal and spatial resolutions data from remote sensing technologies allow the changes and conditions of vegetation to be studied and monitored in various spatial and time scales. Global climate change is one of the threats to the oil palm industry in Malaysia which plays a major role in the Malaysia's economic development. Therefore, this research is conducted to identify the relationship of rainfall variability on oil palm phenology and productivity in Johore in a period of 11 years (2000 to 2010). Remote sensing data which is Enhanced Vegetation Index (EVI) time series from MODIS-Aqua (product MYD13-Q1), rainfall, temperature and Fresh Fruit Bunch data is use to assess phenological and productivity patterns of oil palm throughout year 2000 to 2010. The result show that rainfall have a significant and medium strong correlation with vegetation's greenness (EVI) and oil palm production (FFB). Then, the EVI value also have a strong relationship with the FFB value of oil palm in Johore. It's show that oil palm plants were responsive and sensitive to changes in quantity of available moisture.

INTRODUCTION

Vegetation phenology refers to the timing of biological occurences in vegetation or its periodic life-cycle which focuses on the onset of growing season to the end of senescence as it relates to both climatic and non-climatic factors (Adole et al. 2016; Moore et al. 2016). Understanding vegetation phenology is very crucial as it is a both sensitive indicator of climate change and also regulates the exchange of carbon, energy and water between land and the atmosphere. Phenological changes in vegetation are considered to be the result of adaptive response to climatic variation on a short or long-term basis as the process in plant cycles is largely rely on the environmental conditions experienced by plants (Adole et al. 2016; Sykes 2009).

Global climate change affects climate elements such as temperature and rainfall patterns. Variation of temperature and rainfall are the major factors affecting the productivity and sustainability of agriculture in the tropics. Temperature in Southeast Asia has grown at a rate of 0.14°C to 0.20°C every decade since the 1960s. The IPCC Fifth Assessment Report also projected that global warming and climate change will occur more drastically in the last three decades of the 21st century and temperatures in that region is expected to increase about 1.5°C to 2.0°C in the mid-century (2046-2065). Therefore, the method of tracking and evaluating changes in ecosystems is important in assessing the effects of climate change. Remote sensing data can contribute significantly to this research. With temporally formatted remote sensing products, it is possible to monitor environmental changes through time and various scale (regions, countries, continents and globally) by analyzing vegetation processes. (Zhang et al. 2004).

Climate change has become one of the threats to the Malaysia's oil palm industry. Although the issue of climate change has attracted many scientists, it's impact on oil palm's growth and productivity are still under study. In Malaysia, oil palm become the most important commercial crop and accounts for almost 35 percents of the total plant-based oil requirements in the world (Corley 2009; Hansen et al. 2015). Until 2014, oil palm plantations occupying the first place in Malaysia's crop sector covering 4.7 million hectares and contributing RM2.3 billion/year to the country's economy. Factors such as the tropical climate and soil suitability placed the Indonesia and Malaysia as the major world producers and exporters. Therefore, it's a need to study the trends and changes of oil palm phenology and expected impact on it's productivity due to climate variability in Malaysia (Suepa et al. 2016).

As climate change issues became topic in the field of plant phenology, there is an urgent need to assess climate variability impact on local vegetation. Therefore, the main goal of this study is to identify intra-annual

changes in oil palm phenology between year 2000 to 2010 using MODIS data. In addition, the oil palm production and phenological response to the average annual rainfall is studied to understand the intra-annual response to the presence of water and to detect long-term changes in the vegetation.

STUDY AREA

The study was conducted in Johore state located between longitude 102º 29 '22 "T to 104º 30' 47" T and latitude 1º 20 '25 "U to 2º 49' 42" U (Figure 1). It covers a total land area of 1,920,885 hectares. Johore has tropical climate with mean annual temperature of 27ºC and mean annual precipitation of 2600 mm. Large areas of Johor consists of plains and low undulating topography of less than 200 m. The northern and central part of Johore is characterised by hilly topography with an altitude of about 180 m to 600 m and exceeding 600 m on the eastern part. As of 2015, more than half the area in Johore was covered by agricultural land use (60.2%), followed by forest (26.1%) (Town and Country Planning Department of Peninsular Malaysia).

Figure 1: Study area

DATA AND METHODS

Data and sources

The major data used for this study includes MODIS Aqua (MYD13Q1) Enhance Vegetation Indices (EVI) with 250 m spatial resolution and 16 days temporal resolution of the study area covering a period of 11 years (2000-2010) which was downloaded from the United States Geological Survey (USGS). EVI was developed to optimize the reflectance signal from vegetation and to correct the distortions caused by the reflection of light by atmospheric particles and the effect of the reflection of soil background under the plants. EVI data does not saturate easily compared to NDVI (Tan et al. 2008), especially in rainforest areas and in areas of high biomass content. Another set of data used for this research is annual rainfall data of Johore spanning from the year 2000 to 2010 and was obtained from the Meteorological Department of Malaysia. Yet, another data used for this study is Fresh Fruit Bunch, FFB (annual) from year 2000 to 2010 are used and derived from Malaysia palm oil statistics published by the Malaysian Palm Oil Board (MPOB).

Image pre-processing

EVI data was extracted from the MODIS Aqua dataset product MYD13Q1 and subjected to some image pre-processing steps such as data quality inspection, geometric transformations from the Sinusoidal projection to GDM

2000 MRSO Peninsular Malaysia projections, image clipping and format conversion. Majority of the image pre-processing steps were done via the Model Builder in ArcGIS 10.3 software.

Identifying and Extracting Oil Palm Plant Phenology

The oil palm plant was identified through visual interpretation of Landsat TM images acquired in year 2000, 2005 and 2010 using a combination of false-color composite image bands 4,5,3. The identified locations of oil palm plant were verified through the Google Earth application. Seasonal and phenological curve for the oil palm were extracted and analysed using Timesat software (Jönsson & Eklundh 2004). Savitzky-Golay filtering method was applied for smoothing the raw EVI data.

Analysis of the Relationship between rainfall-EVI and rainfall-FFB

The Pearson correlation analysis method was applied to investigate the relationship between the annual rainfall with EVI values and also annual rainfall with production of oil palm plantation within 11 years.

RESULT AND DISCUSSION

Oil palm can live with a minimum average monthly rainfall of 150 mm to 420 mm provided that the soil is well drained (Ariffin et al. 2001). The production and harvest of oil palm fruit is expected to increase when there is enough rain and decrease during prolonged dry period (Ariffin et al. 2001; Cadena et al. 2006). In the west coast of Sabah, Puah and Madihah Jaafar Sidek (2011) found that high rainfall and temperatures provide favourable conditions for the production of oil palm fruit. However, if the amount of rainfall causes flooding then it will led to the mortality of the palm trees. This shows that oil palm is responsive to the amount of rainfall received but not to the extent of too extreme or too limited which will affect its growth cycle.

The EVI value for oil palm over 11 years recorded an average of more than 0.5 (Figure 2). This shows that the EVI of oil palm maintains a higher level during this period. High annual rainfall in year 2006 (2578.7 mm), 2007 (2777.44 mm) and 2008 (2488.9 mm) causes the EVI to remains consistent for a period of approximately two years (2009 and 2010) although the average precipitation in year 2009 decreased by 645.7 mm compared to the previous year. This may be explained by the amount of rainfall received within these three years provide enough moisture for the next two years (2009 and 2010). It is believed that the heavy rainfall replenished the soil with plenty of soil moisture which fuelled the continuous raise of EVI values for the next couple of years with low rainfall. The correlation analysis result are significant and medium correlation (r=0.498) occurs between the EVI and annual rainfall from year 2000 to 2010. The significant correlation results shows that there are high confidence to confirm that that the relationship between EVI and annual rainfall in 11 years have a medium strong relationship.
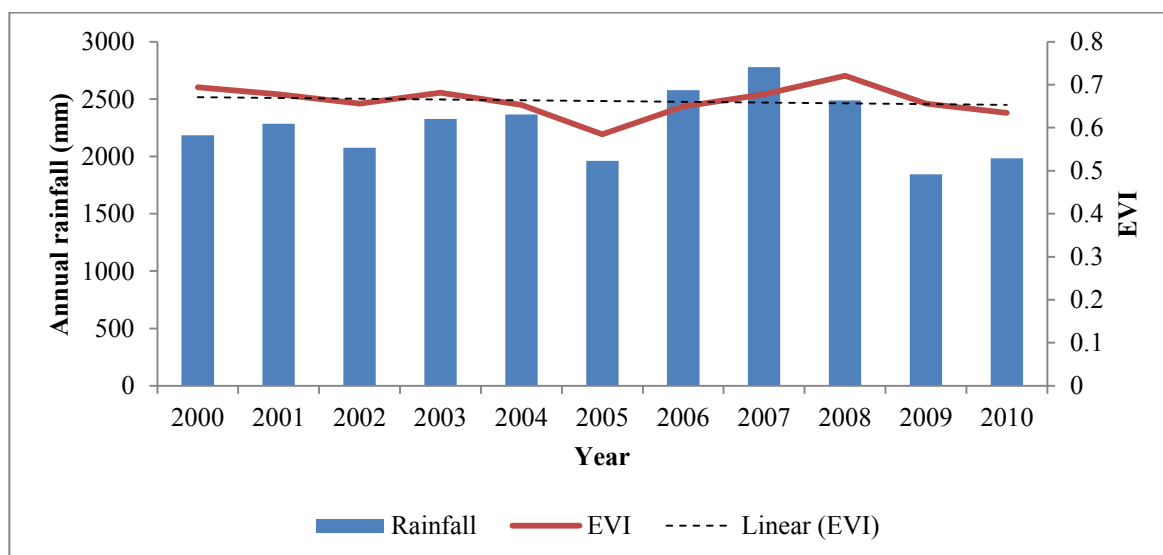

Figure 2: The trend of oil palm phenology and annual rainfall from year 2000 to 2010

The Fresh Fruit Bunch (FFB) production in Johore over 11 years are more than 17 tonnes/hectare and the highest production was captured in year 2006. The FFB production remain constant from year 2000 to 2010. High annual rainfall in year 2006 (2578.7 mm), 2007 (2777.44 mm) and 2008 (2488.9 mm) causes the FFB production to remains consistent for a period of approximately two years (2009 and 2010). It is interesting to note that the FFB values continued to rise from year 2005 to 2006 even rainfall in year 2005 decreased by 405.7 mm compared to the previous year (2004). It is presumed that time-lag effect could be one of the factors which affects the variations of FFB value. Puah and Madihah Jaafar Sidek (2011) also found that time-lag period of up to three months was detected from year 2005 to 2010 in the west coast of Sabah and concludes that the production of oil palm bunches were strongly associated with rain. The correlation analysis results between annual rainfall and FFB value from year 2000 to 2010 are significant and medium correlation ($r=0.429$). The significant correlation results shows that there are high confidence to confirm that that the relationship between EVI and annual rainfall in 11 years have a medium strong relationship.
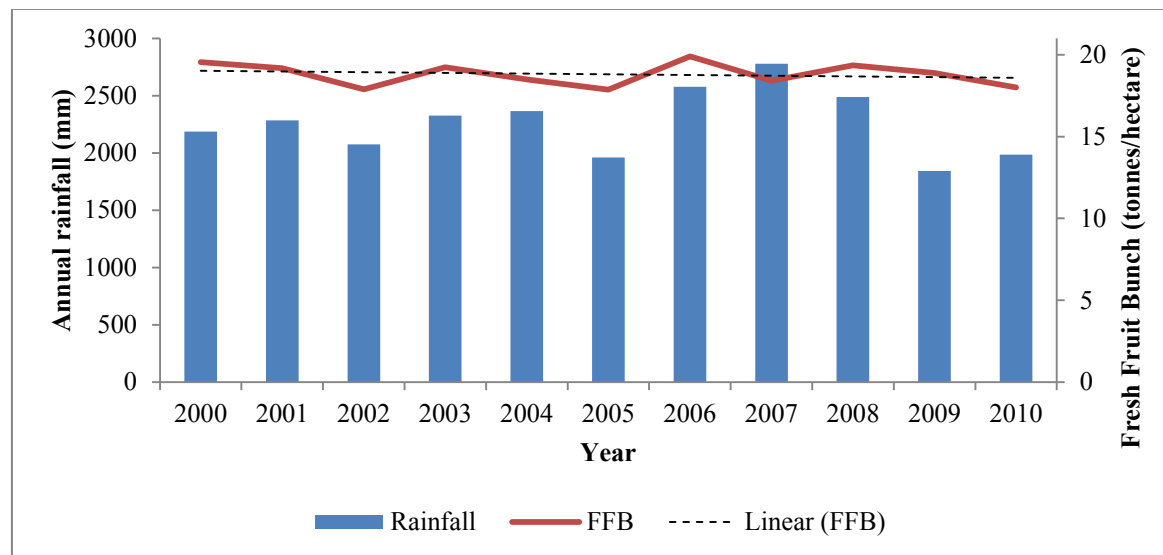

Figure 3: The trend of oil palm Fresh Fruit Bunch and annual rainfall from year 2000 to 2010

Figure 4 shows the trend of EVI and FFB of oil palm from year 2000 to 2010. It can be observed that the fluctuation pattern of EVI and FFB are almost similar. The correlation analysis results between EVI and FFB value of oil palm from year 2000 to 2010 are significant and strong correlation ($r=0.616$). The significant correlation results shows that there are high confidence to confirm that that the relationship between EVI and FFB of oil palm during 11 years have a strong relationship.
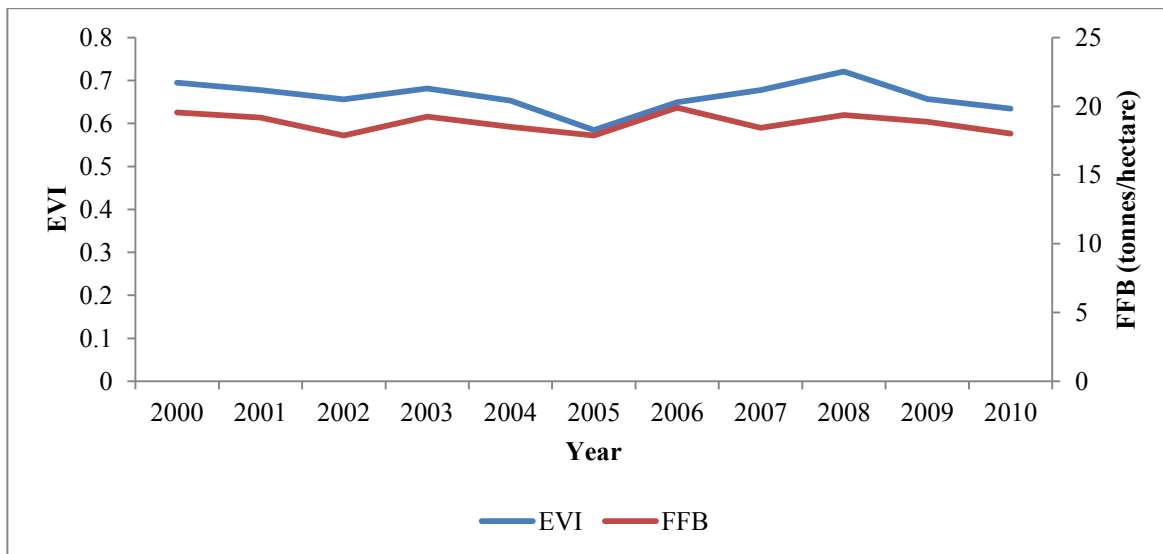
Figure 4: The trend of EVI and Fresh Fruit Bunch of oil palm from year 2000 to 2010

CONCLUSION

The initial results of this research showed phenological and FFB of oil palm response patterns towards annual rainfall throughout year 2000-2010 is positively correlated and have a medium strong relationship. Besides that, the EVI value also have a strong relationship with the FFB value of oil palm in Johore. The effect of time-lag of vegetation's greenness (EVI) and oil palm production (FFB) was detected, mainly after period of heavy rain. It's show that oil palm plants were responsive and sensitive to changes in quantity of available moisture. A longer terms dataset will provide a better understanding of the climate change effects on the phonological and production response of oil palm which will inevitably impacting the socio-economic aspects of oil palm growers.

REFERENCES

Ariffin Tawang, Tengku Ariff Tengku Ahmad & Mohd. Yusof Abdullah. (2001). Stabilization of upland agriculture under El Nino induced climatic risk: impact assessment and mitigation measures in Malaysia. Paperwork of The Regional Co-ordination Centre for Research and Development of Coarse Grains, Pulses, Roots and Tuber Crops in the Humid Tropics of Asia and the Pacific (CGPRT Centre). Organized by CGPRT Centre.

Cadena, M.C., Devis-Morales, A., Pabon, J.D., Malikov, I., Reyna-Moreno,

Adole, T., Dash, J. &Atkinson, P. M. 2016. A systemic review of vegetation phenology in Africa. *Ecological Informatics* 3, 117-128.

Corley R. H. V. 2009. How much palm oil do we need?. *Environment Science Policy* 12, 134–139.

Hansen, S.B., Padfield, R., Syayuti, K., Evers, S., Zakariah, Z., Mastura, S. 2015. Trends in global palm oil sustainability research. *Journal of Cleaner Production* 100: 140 - 149.

IPCC. 2013. Fifth Asessment Report. www.ipcc.ch/report/ar5/wg1 [3 January 2018]

Jönsson, P. & Eklundh, L. 2004. TIMESAT - a program for analysing time-series of satellite sensor data, *Computers and Geosciences* 30, 833-845.

Moore, C. E., Brown, T., Keenan, T. F., Duursma, R. A., Van Dijk, A. I. J. M., Beringer, J., Culvenor, D. 2016. Reviews and syntheses: Australian vegetation phenology; New insight from satellite remote sensing and digital repeat photography. *Biogeosciences* 13(17), 5085-5102.

Puah, Pei Wen & Madihah Jaafar Sidek. (2011). Impacts of rainfall, temperature and recent El Niños on fisheries and agricultural products in the West Coast of Sabah (2000-2010). *Borneo Science* 28(3): 73-85.

Suepa T, Qi J, Lawawirojwong S, Messina JP. 2016. Understanding spatio-temporal variation of vegetation phenology and rainfall seasonality in the monsoon Southeast Asia. *Environmental Research* 147 (2016) 621–629.

Sykes, M.T. (2009). Climate Change Impacts: Vegetation. Encyclopedia of Life Sciences (ELS). John Wiley & Sons, Ltd: Chichester.

Tan, Bin., Morisette, J.T., Wolfe, R.E., Gao, Feng., Ederer, G.A., Nightingale, J & Pedelty, J.A. 2008. Vegetation phenology metrics derived from temporally smoothed and gap-filled MODIS data. IGRSS 2008: 593-596.

Town and Country Planning Department of Peninsular Malaysia. n.d. Land Use Report 2015: Current Land use for Local Planning, Johor.

Zhang, X., Friedl, M.A., Schaaf, C.B. & Strahler, A.H. 2004. Climate controls on vegetation phenological patterns in northern mid and high latitudes inferred from MODIS data. *Global Change Biology* 10: 1133-1145.

Feasibility Study of Normal Height System in Taiwan

Chun-Jia Huang (1), Jen-Wei Hsu (1), Jen-Yu Han (1)

1 Department of Civil Engineering, National Taiwan University, No. 1,

Sec. 4, Roosevelt Rd., Taipei 10617, Taiwan (R.O.C.)
Email: d05521008@ntu.edu.tw; r06521805@ntu.edu.tw; jyhan@ntu.edu.tw

KEY WORDS: Normal Heights, Height datum, Global Navigation Satellite System (GNSS), Earth Gravity Model

ABSTRACT: The normal height system is based on the quasi-geoid, which represents the vertical distance from the quasi-geoid to terrain surface. To make possible an accurate normal height system, the normal gravity should be first determined. This study aims to build the quasi-geoid by using local gravity observations and a global spherical harmonic model in Taiwan. The quasi-geoid undulation was first computed by using the global Earth Gravity Model 2008 (EGM08) with a spherical harmonic model. In addition, the influence of terrain was also considered in the residual terrain model. The hybrid method was then used to construct a high-accurate quasi-geoid component model in conjunction with the remove-compute-restore method, which includes surface curve fitting method. Finally, the normal heights were transformed by calculating the difference between the GNSS-derived geometric heights and the results of quasi-geoid undulation model. To evaluate its practical feasibility, the estimated normal heights were compared to the orthometric heights as adopted in Taiwan's national datum. Based on the numerical results, the mean relative difference to the orthometric heights is about 1.5cm per kilometer. It reaches the accuracy level that fulfils the needs of most engineering applications, but with less cost than that of the traditional approach for maintaining the orthometric height system.

1.INTRODUCTION

The normal heights system is based on the quasi-geoid, which represents the vertical distance from the quasi-geoid to terrain surface. The more comprehensively quasi-geoid model is constructed, the more accurately normal height could be estimated. There are three ways to construct normal heights system, one of which is the mathematical method (Pick,1970). It defines the earth as a rotational ellipsoid, and calculates the ideal geoid by gravity. It is a convenient way, but lack of physical and geometric meanings. Another approach is Global Gravitational Model method, proposed by Heiskanen and Moritz (1967). The method tries to calculate global gravitational potential, and constructs the normal height system by geopotential. The last one is gravity observation method (Torge,1991). It calculates the Geopotentials by gravities and leveling, and obtains the normal height by average gravities.

This study aims to construct normal height system using the Global Gravitational Model method, with an emphasis to build the quasi-geoid by using local gravity observations and a global spherical harmonic model in Taiwan. The hybrid method constructs a high-accurate quasi-geoid component model in conjunction with the remove-compute-restore method, which includes surface curve fitting method. The normal height could be transformed by calculating the difference between the GNSS-derived ellipsoid height and the result of quasi-geoid undulation model.

2.METHODOLOGY

2.1 Spherical harmonic model calculation

The global gravity field model is a spherical harmonic function which represents the true gravitational field of the earth. It is used toestimate global gravity field function values, such as geoidal undulation, gravity anomalies. The conversion formula is as shown in Equation (1). The Cartesian coordinates (x, y, z) of the observation points are converted into spherical coordinates, where (r, θ, λ) are expressed as the geocentric radial, the geocentric latitude, and the geocentric longitude, respectively. The geopotential of point P on the ground surface which can be calculated by EGM08 as following (Heiskanen and Moritz, 1967 ; NGA, 2013).

$$\begin{vmatrix} r \\ \theta \\ \lambda \end{vmatrix} = \begin{vmatrix} \sqrt{x^2 + y^2 + z^2} \\ tan^{-1}\left(\frac{z}{\sqrt{x^2+y^2}}\right) \\ tan^{-1}\left(\frac{y}{x}\right) \end{vmatrix} \tag{1}$$

$$V(r, \theta, \lambda) = \frac{GM}{r}\left[1 + \sum_{n=2}^{N}\left(\frac{a}{r}\right)^n \sum_{m=0}^{n}(\bar{C}_{nm}\cos m\lambda + \bar{S}_{nm}\sin m\lambda) \cdot \bar{P}_{nm}(\cos\theta)\right] \tag{2}$$

In Equation (2), GM is the gravitational constant of $3986004.418 \times 10^{-8}$, where a is the long radius of 6378136.3m, $\bar{C}_{nm}$ and $\bar{S}_{nm}$ are the gravitational spherical harmonic coefficients. $\bar{P}_{nm}$ is a normalized association of the Legendre function. In this Equation, the geopotential W of point P on the surface space which can be calculated by using Earth Gravity Model . The geopotential W(P) is the sum of the gravitational potential and the centrifugal force potential Q(P) (Mortiz,1993):

$$W = V + Q = V + \frac{1}{2}\omega^2(x^2 + y^2) = V + \frac{1}{2}\omega^2 r^2 \sin^2\theta \tag{3}$$

where ω is angle of rotation for the earth, The disturbing potential at point P is defined by the difference between the geopotential W and the normal gravity potential U:

$$T = W - U ; \ U = \frac{GM}{\varepsilon}\tan^{-1}\frac{\varepsilon}{b} + \frac{1}{3}\omega^2 a^2 \tag{4}$$

In a normal height system, the calculation method of normal gravity can be written as Equation(5) through (9), where γ_a is equatorial gravity, γ_b is bipolar gravity, β is gravity flatness, and β_1 is square coefficient of the compression of the earth. The disturbing potential energy T is calculated by Equation (4) and the normal gravity value γ_Q is calculated by Equation (5). The quasi-geoid value of any coordinate Q on the surface can be calculated according to the Bruns formula, as shown in Equation (10) (Heiskanen and Moritz, 1967). Finally, the normal heights were transformed by calculating the difference between the GNSS-derived geometric heights. The following are examples of Equation (11).

$$\gamma_Q = \gamma_0 + \frac{\partial\gamma}{\partial h} \cdot H_P + \left(\frac{1}{2!}\right) \cdot \left(\frac{\partial^2\gamma}{\partial h^2}\right) \cdot H_\propto{}^2 \tag{5}$$

$$\gamma_0 = \frac{a\gamma_a\cos^2\varphi + b\gamma_b\sin^2\varphi}{\sqrt{a^2\cos^2\varphi + b^2\sin^2\varphi}} \tag{6}$$

$$\gamma_0 = \gamma_a(1 + \beta\sin^2\varphi + \beta_1\sin^2 2\varphi) \tag{7}$$

$$\beta = \frac{\gamma_b - \gamma_a}{\gamma_a} \tag{8}$$

$$\beta_1 = \frac{1}{8}f^2 + \frac{1}{4}f\beta \tag{9}$$

$$N = \frac{T}{\gamma_Q} \tag{10}$$

$$H_{normal\ heights} = h_{GNSS} - N_{quasi-geoid} \tag{11}$$

2.2 Residual Terrain Model

While using the Erath gravity model to calculate the quasi-geoid undulation model, it is impossible to accurately describe the quasi-geoid undulation complete signal. Especially in mountainous areas, height differences makes much significant inaccuracy, which could reach the error level of more than 10 cm. Therefore, it is also necessary to consider the detailed differences caused by the terrain and make corrections. The residual terrain model is constructed on the effect of the terrain, and the error caused by the short-wavelength component can be improved (Forsberg, 1984). As shown in Figure 1, the diagonal line is the residual terrain and considers the high-frequency terrain mass effect between the ground surface and the average terrain reference plane. The method for calculating the residual terrain model is the Fast Fourier transform Method (Schwarz et al.,1990). The short-wavelength component N^{RTM} generated for the residual topographic effect can be obtained using Equation (12):

$$N^{RTM}(x_P, y_P) = \frac{G}{\gamma}\int\frac{\rho(x,y)\lfloor h(x,y) - h_{ref}(x,y)\rfloor}{\sqrt{(x-x_a)^2 + (y-y_a)^2}}dxdy = \frac{G}{\gamma}\left[\rho(h - h_{ref})\right] * \frac{1}{r} \tag{12}$$
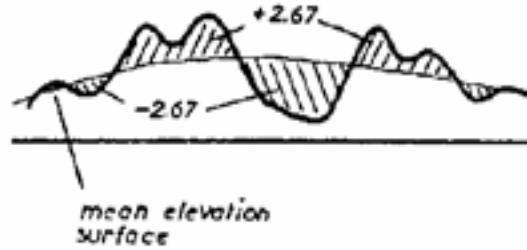
Figure 1. Residual Terrain Model (Forsberg, 1984)

where x_a, y_a are the points to be solved; h is the point elevation value of each integral element; h_{ref} is the reference height value of each integral element; ρ is the geological density of each integral element; γ is the normal gravity value of the points. In general, the density of the formation will be based on the mass of 2670 kg/m^3. Taiwan has a variety of geological features with a geological density of 1800 kg/m^3 to 3000 kg/m^3. This study used a 1/250,000 geological map and constructed a digital geological density map with reference to geological property data. Finally, the 5-m high-resolution digital terrain model is used and the residual terrain estimation is constructed.

2.3 Remove-Restore Method

The long-wavelength component can be calculated from the global spherical harmonic, and the short-wavelength component is obtained from the residual terrain model. However, in the mid-wavelength component, the required observation data needs to be obtained through the measured gravity observation data, which could incur relatively high cost. Therefore, in this study, the known GNSS observations on the first-order level and the normal height calculated from the height difference data on the levelling course are used to obtain the mid-wavelength component (Zhu et al., 2011). The mathematical form is expressed as Equation (13), where N^{GPS} is the difference between the ellipsoid height and the normal height, which is used as the true value in this study.

$$N^{res} = N^{GPS} - N^{ref} - N^{RTM} \tag{13}$$

According to the calculation and obtaining N^{res} and using the surface fitting method to build a model of N^{res} in Taiwan. This study applied quadric surface fitting Equation (14) and cubic surface fitting Equation (15) to fit the surface as a mid-wavelength model. The calculation flow chart is shown in Figure 2.

$$N^{res}(x,y) = a_0 + a_1 x_i + a_2 y_i + a_3 x_i^2 + a_4 y_i^2 + a_5 x_i y_i \tag{14}$$

$$N^{res}(x,y) = a_0 + a_1 x_i + a_2 y_i + a_3 x_i y_i + a_4 x_i^2 + a_5 y_i^2 + a_6 x_i^3 + a_7 y_i^3 + a_8 x_i^2 y_i + a_9 x_i y_i^2 \tag{15}$$

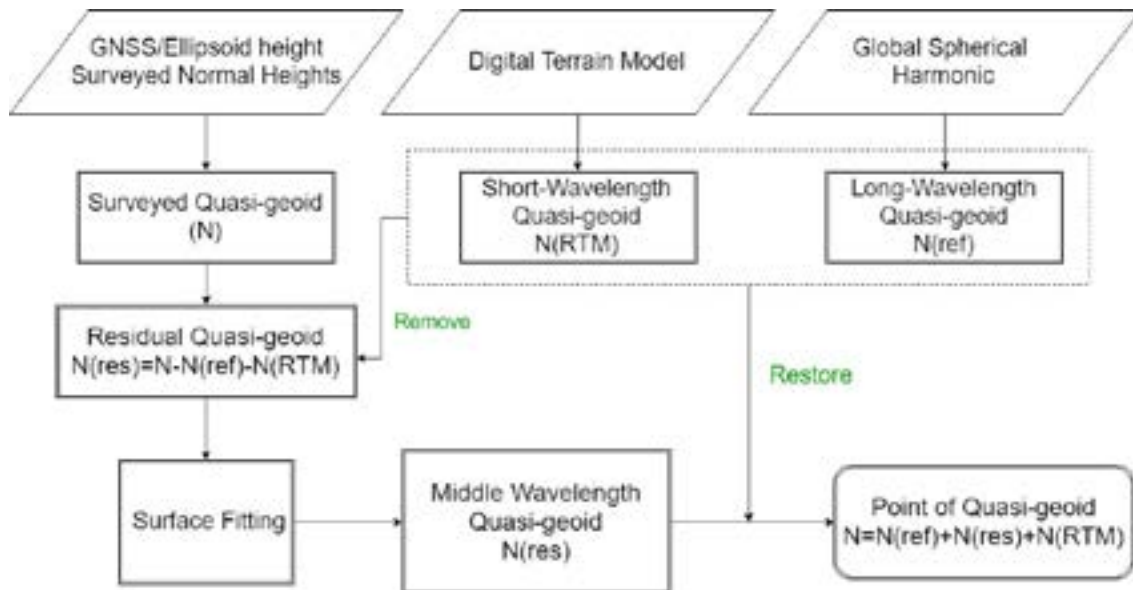Figure 2. Remove-Restore Method Calculation Process

3. RESULTS ANALYSIS

3.1 Experimental Setup

After obtaining the orthometric heights and ellipsoid heights of first order benchmarks, the quasi-geoid model according to the 1′×1′ grid of global Earth Gravity Model 2008(EGM08) was first constructed. Then ellipsoid heights were transformed into normal heights using the approach described in this study. The result of the normal heights as test group, and the orthometric heights as comparison group. Each of group calculates the height differences separately, and estimates the average value and standard deviation. Table 1 lists the evaluation methods of this study. The result is compared to the orthometric heights of first order benchmarks, and divides into (a)absolute height differences and (b)normalized relative height differences to analyze the results.

Table1. Evaluation Methods

Height Datum: Orthometric Heights		Methods		
		EGM08	EGM08+RTM	EGM08+RTM+Fitting
Absolute Height Differences	(a)	$\Delta_{H,HN} = HN - H$		
Normalized Relative Height Differences	(b)	$\bar{\delta}_{H,HN} = \dfrac{\Delta HN - \Delta H}{\sqrt{s}}$		

3.2 Quasi-Geoid Model

This study uses 1784 first-order benchmarks in Taiwan as the height datum, with a total of 1441 leveling course. The quasi-geoid undulation can be estimated by the global spherical harmonic model. The calculation of the quasi-geoid undulation is shown in Figure 3(a). In order to incorporate the calculation of the residual terrain model, this study uses 5m × 5m resolution grid interpolation. The residual terrain model calculated using fast Fourier transform is represented as shown in the figure 3(b). The mid-wavelength fitting model is shown in Figure 4.

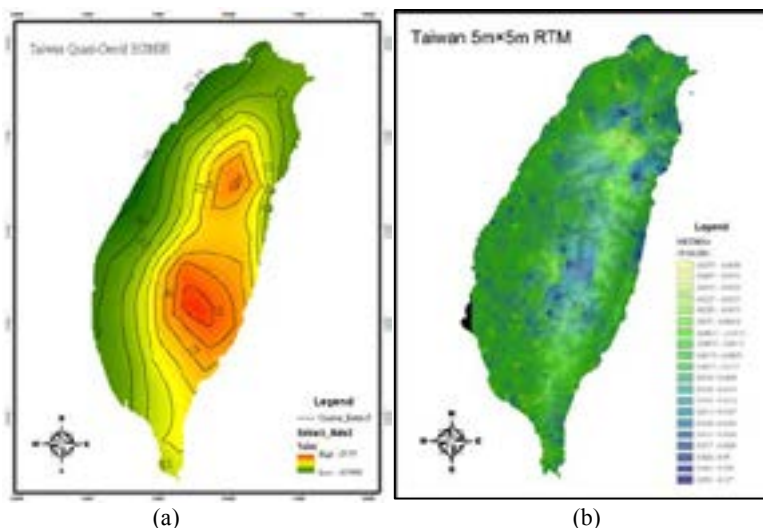(a)   (b)

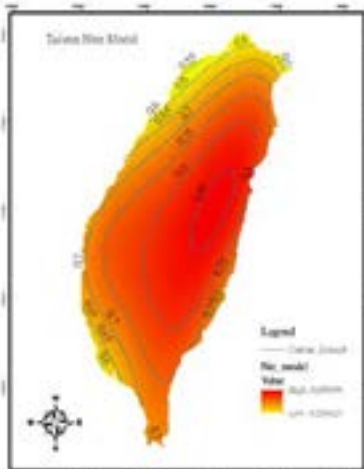Figure 3. (a) Taiwan Quasi-Geoid Model (EGM08) (b) Taiwan RTM Model

Figure 4. Taiwan N^{res} Model (surface fitting)

3.3 Normal Heights and Orthometric Heights Analysis

In the absolute height difference, the difference between the normal heights of 1784 points (global spherical harmonic + residual terrain model+ surface fitting) and the orthometric heights are obtained, and then interpolated map as shown in Figure 5. The difference value range is about 0.5~1.5 m, indicating that the heights difference is greater than 0; However, the color of each bench marks in the figure indicates the interval corresponding to the orthometric heights. It can be seen that there is no significant correlation between the absolute of between the normal heights (global spherical harmonic + residual terrain model+ surface fitting) and the absolute difference of orthometric heights. This relationship can also be verified by Figure 6(a). (representing the difference and orthometric heights relationship). In addition, the statistical indicators of the elevation difference are shown in Figure 6(b) and Table 2. The RMES value of the elevation difference is 0.730 m, the average value is 0.723 m, and the elevation difference is mostly around 0.6~0.8 m (plain and hilly area).
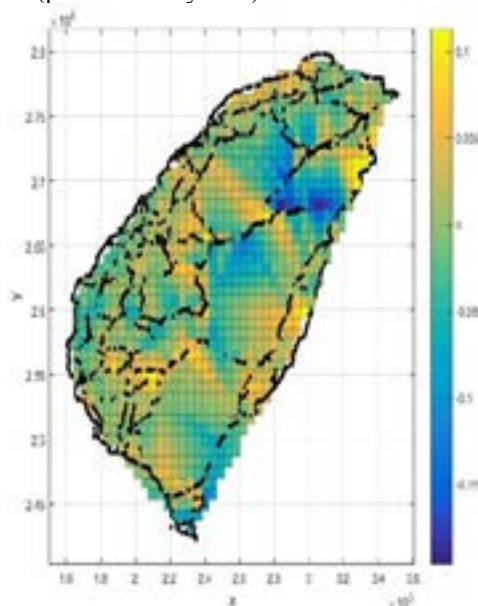

Figure 5. Height difference between HN and HO (Interpolation Map)
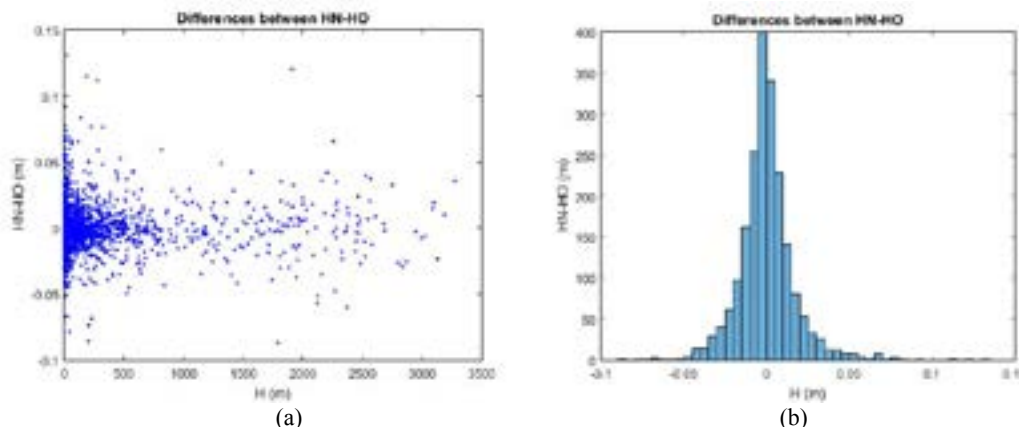

	(a)		(b)

Figure 6. Height difference between HN and HO (Scatter map & Histogram)

Table2. Normal heights(absolute heights difference statistics)

Topography	Heights (m)		Normal Heights(HN)−Orthometric Height(HO)(m)		
	Interval		Mean	Standard Deviation	RMSE
Plain	0	100	-0.002	0.038	0.038
Hills	100	1000	0.009	0.048	0.049
Mountain	1000	2000	-0.035	0.042	0.055
Mountain	2000	3500	-0.002	0.105	0.105
All	**0**	**3500**	**0.007**	**0.046**	**0.0461**

For the relative height difference per unit distance, the height difference between the normal heights of the 1441 levelling course (global spherical harmonic + residual terrain model+ surface fitting) and the orthometric heights difference is calculated. In addition to the corresponding leveling course (unit: km), interpolated as shown in Figure 7, and calculate the difference between the two height differences, and divide the difference by the distance of the leveling course (unit: km). The range of the difference value range is about $-0.5 \sim 0.5 \text{m}/\sqrt{km}$, which means that the relative height difference (normalization) is positive and negative, and the average is distributed in the figure 8(a). In the figure, the color of bench marks in the map indicates its orthometric height corresponding interval. It can be seen that there is no significant correlation between the normal heights (global spherical harmonic + residual terrain model+ surface fitting) and the orthometric height (after normalization) and the orthometric height of the point. It can be verified by Figure (representing the normalized relative difference and orthometric heights relationship). In addition, the statistical indicators of the relative height difference (normalization) are shown in Figure 8(b)and Table 3. The RMES value of the relative height difference (normalization) is 0.015 m/$\sqrt{km}$, and the average value is 0.0001 m/$\sqrt{km}$,. The relative height difference (normalization) mostly around near $-0.01 \sim 0.01$m/km (plain and hilly area).
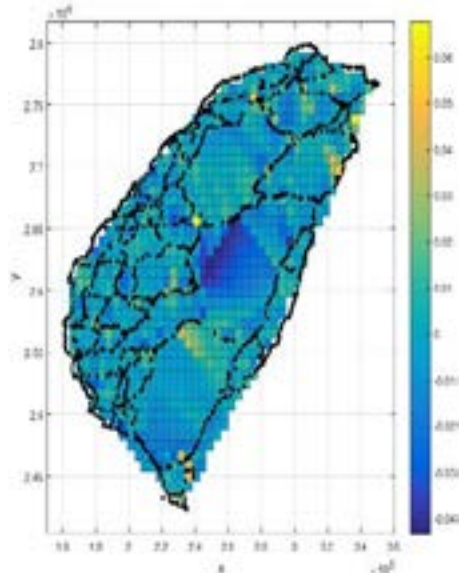

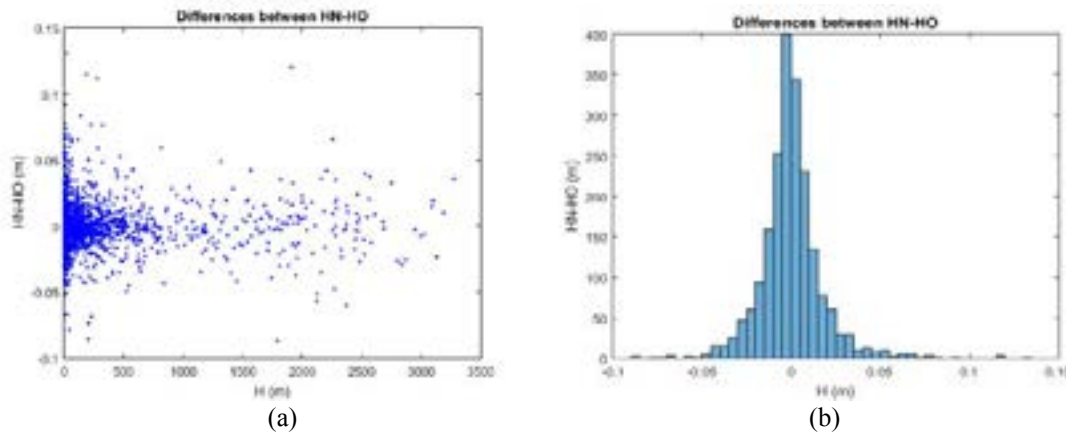Figure 7. Height difference between HN and HO (Interpolation Map)

| (a) | (b) |

Figure 8. Height difference between HN and HO (Scatter map & Histogram)

Table3. Normal heights(relative heights difference statistics)

Topography	Heights (m)		Normal Heights(HN)−Orthometric Height(HO)(m)		
	Interval		Mean	Standard Deviation	RMSE
Plain	0	100	0.001	0.011	0.017
Hills	100	1000	0.001	0.012	0.018
Mountain	1000	2000	-0.001	0.013	0.019
Mountain	2000	3500	0.002	0.020	0.021
All	**0**	**3500**	**0.0001**	**0.015**	**0.018**

4. CONCLUSION

According to the result of the proposed methods, in the normal height system The mean relative difference to the orthometric heights is about 0.018 meters per kilometer. The results of this study are compared to specification of survey, and the accuracy of the engineering is 20mm$\sqrt{km}$ in the specification of leveling surveying, obviously, the study shows results better than engineering accuracy in the relative height differences. Therefore, the methods can reach the accuracy level that fulfils the needs of most engineering applications.

In most engineering applications, such as Hydraulic engineering or Geotechnical engineering. The transformation between different height systems is often used. The hybrid method and the gravity observation method could meet the need of engineering accuracy. In the future, the study would try to use artificial intelligence method to improve the accuracy of the model, and optimize the model with different methods.

5. REFERENCE

Filmer, M. S., Featherstone, W. E., and Kuhn, M, 2010. The effect of EGM08-based normal, normal-orthometric and Helmert orthometric height systems on the Australian levelling network, Journal of Geodesy,84(8),pp.501-513.

Forsberg, R., 1984. A Study of Terrain Reductions, Dendity Anomalies and Geophysical Inversion Methods in Gravity Field Modellingm. Ph.D. Dissertation, The Ohio State University, Columbus.

Heiskanen, W. A., and Moritz, H,1967. Physical Geodesy, W. H. Freeman Publishers, San Francisco, 364p.

Hirt, C., Featherstone, W.E., and Marti, U, 2010 Combining EGM08 and SRTM/DTM2006.0 residual terrain model data to improve quasigeoid computations in mountainous areas devoid of gravity data, Journal of Geodesy,84,557-597.

Moritz, H, 1993.The Figure of the Earth : Geodesy and the Earth's Interior, Wichmann Publishers,292p.

NGA, 2013, EGM08 - WGS 84 Version, URL: http://earth-info.nga.mil/GandG/wgs84/gravitymod/EGM08/egm08_wgs84.html (last date accessed: 14 Oct 2016).

Patroba, A. O., Yoichi F., and Yuki, K, 2012. A high-resolution gravimetric geoid model for Japan from EGM08 and local gravity data, Earth Planets Space, 64, 361-368.

Pavlis, N. K., Simon, A. H., Steve C. K., and John, K. F, 2012. The development and evaluation of the Earth Gravitational Model 2008 (EGM08). Journal of Geophysical Research, 117(4).

Ramazan, A., Bihter, E., and Aydin, U, 2012. Comparison of the kth and remove–cmpute– rstore tchniques to geoid modelling in a mountainous area, Computers & Geosciences, 48, 34-40.

Schwarz, K. P., Sideris, M. G., and Forsberg, R, 1990. The Use of FFT Techniques in Physical Geodesy, Geophys. J. Int,100, 485-514.

Zhu, Y., Gao, X., Liu, Y., et al, 2011. Study on the elevation determination based on EGM08 model. journal of university of jinan, 25(4), 410-413.

ACKNOWLEDGEMENT

MONITORING AND MEASURING THE WATER SURFACE LEVEL AREA OF MAE KHAM DAM IN NORTHERN THAILAND USING POLARIZATION SAR IMAGES

Kamolratn Chureesampant (1), Maitree Foitong (1), Wiwat Khlairasamee (1)

[1]Electricity Generating Authority of Thailand (EGAT), Survey Division, Map and Geographic Information System Department, Photogrammetry and Remote Sensing Section,
No. 53 Moo 2, Charunsanitwong Road, Bang Kruai, 11130, Nonthaburi, Thailand
Email: kamolratn.c@egat.co.th; maitree.f@egat.co.th; wiwat.k@egat.co.th

KEY WORDS: Selection Synthetic Aperture Radar (SAR); Polarization Combination; Gray Level Co-occurrence Matrix (GLCM); Adaptive Filtering; Water Surface Level Area

ABSTRACT: According to the traditional on-site hydrographic survey for monitoring and measuring water surface area extent is time consuming, labor-intensive and costly, while the satellite remote sensing resources that are attractive tool and provide the opportunity to monitor hydrological process. Therefore, this paper addresses the measuring surface area of Mae Kham dam in Northern Thailand from Synthetic Aperture Radar (SAR) for the Advanced Land Observing Satellite (ALOS)/Phased Array type L-band Synthetic Aperture Radar (PALSAR) in single- and dual-polarization and fully polarimetric data obtained from different temporal variation. All polarization combinations are investigated quantitatively by supervised classification in order to generate the water surface area automatically. Within this framework, the combination with gray level co-occurrence matrix (GLCM)-based mean textural measure and enhanced frost adaptive filtering is considered in order to remove multiplicative speckle noise. The fusion of measured daily data from telemetry system for water level measurement with SAR satellite imagery is taken into account. Because it corresponds to spatial change in an appropriate time interval. Classification results were generated by taking water surface level area using multi-temporal SAR data and telemetry data. The Geographic Information System (GIS) process involved in creating upper depth contour. Experimental results reveal that the combined cross-polarized (HV+VH) power data with the mean textural is the most suitable. Because the supplement of cross-polarization data used as the characteristics for the HV and VH data are mostly similar with the smoothing effect on the image of the texture. This operational approach enhances water surface area monitoring and measurement. It supports several applications e.g., hydrological modeling, drought/flood prediction, and reservoir area utilization planning.

1. INTRODUCTION

According to the traditional on-site hydrographic survey for monitoring and measuring water surface level area, it is time consuming, labor-intensive and costly. This survey can generate water depth which measured by soundings. Water depths connect with a line known as a depth contours. While the satellite remote sensing resources that are attractive tool and provide the opportunity to monitor hydrological process e.g., the spatial information change of dams in timely and cost effective manner. At the present time, classification applications are widely used in natural and man-made resources mapping. Measuring the water surface level area by remote sensing is challenge by using classification basis. It involves acquiring multi-temporal co-registered images of the same geographic area at different times. Because monitoring the spatial change in dams can determine the water extent in an appropriate time interval. Two classification techniques are popularly categorized. Supervised techniques require a training set for the learning process of the classifiers. In contrast, unsupervised techniques merely discriminate without a priori knowledge of the scene [1].

With the satellite remote sensing, satellite-based Earth observation involves optical and microwave sensors. The satellite-based SAR sensor data is considered to provide additional information on the image surface. The apparent strength of SAR data is all weather imaging, day and night independence, and cloud-free which enable to acquire the desired area of interest explicitly [2]. However speckle noise and geometrical features are the limitations of using SAR data for classification [3], therefore a suitable technique for removing noise is inquisitiveness. Furthermore, the selection of an optimal signal polarization is an essential criteria in SAR image classification, which depends on kinds of detected objects. In addition, the curiosity is to compare the performance of the signal polarizations in single- and dual-polarization and fully polarimetric data including their combination.

Hence, the main objective of this paper is to study the performance of using multi-temporal polarization SAR images to measuring the water surface level area of Mae Kham dam for the L-band frequency, to compare the performance of the combinations of signal polarizations in accordance with different processing modes before supervised classification. Thus, all multi-temporal polarization SAR images are classified to generate the upper depth contour lines that provides the approach for monitoring hydrological process.

2. STUDY AREA AND DATA DESCRIPTION

The study area is the Mae Kham dam in Northern Thailand, as shown in Figure 1. The data sources are the multi-temporal ALOS/PALSAR (L-band) Level 1.5 data. PALSAR in single- and dual-polarization and fully polarimetric data of the area were used. The properties of SAR data were shown in Table 1.
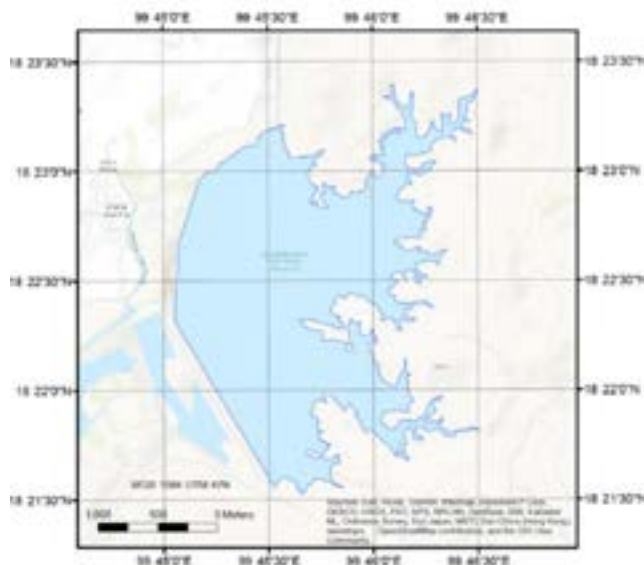

Figure 1. Location of the Mae Kham dam in Northern Thailand

Table 1. Properties of single- and dual-polarization and fully polarimetric SAR images acquired by the different satellites.

No.	Acquisition Date	Image center (Lat / Long)	Polarization	Observation orbit	Off-nadir angle	Pixel Spacing (m.)
1	23 Mar 2011	18.431 / 99.792	Quadrature	Ascending	21.5°	12.5
2	14 Feb 2011	18.308 / 99.558	Single: HH	Descending	34.3°	6.25
3	3 Dec 2011	18.309 / 99.716	Dual: HH+HV	Ascending	34.3°	12.5
4	18 Oct 2010	18.307 / 99.719	Dual: HH+HV	Ascending	34.3°	12.5
5	27 Nov 2008	18.312 / 99.701	Single: HH	Ascending	34.3°	12.5
6	8 Nov 2008	18.311 / 99.584	Single: HH	Descending	34.3°	6.25
7	23 Sep 2008	18.311 / 99.586	Single: HH	Descending	34.3°	6.25
8	27 Aug 2008	18.316 / 99.684	Dual: HH+HV	Ascending	34.3°	12.5
9	12 Jul 2008	18.314 / 99.701	Dual: HH+HV	Ascending	34.3°	12.5
10	27 May 2008	18.312 / 99.718	Dual: HH+HV	Ascending	34.3°	12.5
11	25 Feb 2008	18.311 / 99.721	Single: HH	Ascending	34.3°	6.25
12	10 Jan2008	18.310 / 99.718	Single: HH	Ascending	34.3°	6.25
13	25 Nov 2007	18.307 / 99.715	Dual: HH+HV	Ascending	34.3°	12.5
14	22 Feb 2007	18.313 / 99.709	Single: HH	Ascending	34.3°	6.25

3. PRE-PROCESSING TECHNIQUES

According to ALOS/PALSAR Level 1.5 data, the radiometric and geometric corrections are performed to the map projection [4] in grid zones 47 North of the Universal Transverse Mercator (UTM) projection. In this research, SAR images were resampled at a pixel size of 12.5 m. Furthermore, the images were cropped to a size of 450 × 450 pixels. PALSAR in single- and dual-polarization and fully polarimetric data are considered and coordinated with the polarization combination. The six signal polarizations were tested: the amplitudes of the single-polarization SAR (HH) data, the HV data, the combined co-polarization (HH + VV) data (represented as CO), the combined cross-polarization (HV+VH) data (represented as CS), the combined dual-polarization (HH + HV) data (represented as DUAL) data, and the combined fully polarimetric data (represented as FP). The FP received by the four channels of a polarimetric radar system is then calculated as the sum of the amplitudes of all polarization data.

$$HH = |HH_{amp}| \; . \tag{1}$$

$$HV = |HV_{amp}| \; . \tag{2}$$

$$CO = |HH_{amp}| + |VV_{amp}| . \qquad (3)$$

$$CS = |HH_{amp}| + |HV_{amp}| . \qquad (4)$$

$$DUAL = |HH_{amp}| + |HV_{amp}|. \qquad (5)$$

$$FP = |HH_{amp}| + |HV_{amp}| + |VH_{amp}| + |VV_{amp}| . \qquad (6)$$

4. METHODOLOGY

The framework (Figure 2) starts with multi-temporal co-registered SAR amplitude images of the same area acquired at different times. The six signal polarizations described in Section 3 are investigated in four processing modes to determine the optimal step of the information fission. Raw data mode (Mode 1) is the using the original source of SAR images. Filtering mode (Mode 2) is to remove speckle noise [5], which the adaptive enhanced Frost filtering is applied. The filter parameters are set as follows. The 3×3 filter size with 1.0 of damping factor and the default for the coefficient of variation cutoffs which includes 0.523 of the homogenous areas (Cu) and 1.732 of the heterogeneous area (Cmax). The mean texture measure from the Gray Level Co-occurrence Matrix (GLCM) is applied to the SAR images in texture mode (Mode 3) with the 3×3 processing window and 1x1 co-occurrence shift. And the combination of GLCM and filtering mode (Mode 4) is examined. The supervised classification is performed with the water body of Mae Kham dam from the information fission for multi-temporal SAR images to generate the upper depth contour lines according the measured daily data from telemetry system for water level measurement. The measured daily data from telemetry system are listed in Table 2. Next, the generated contour lines from the surveyed sounding was selected to validate in accuracy assessment.
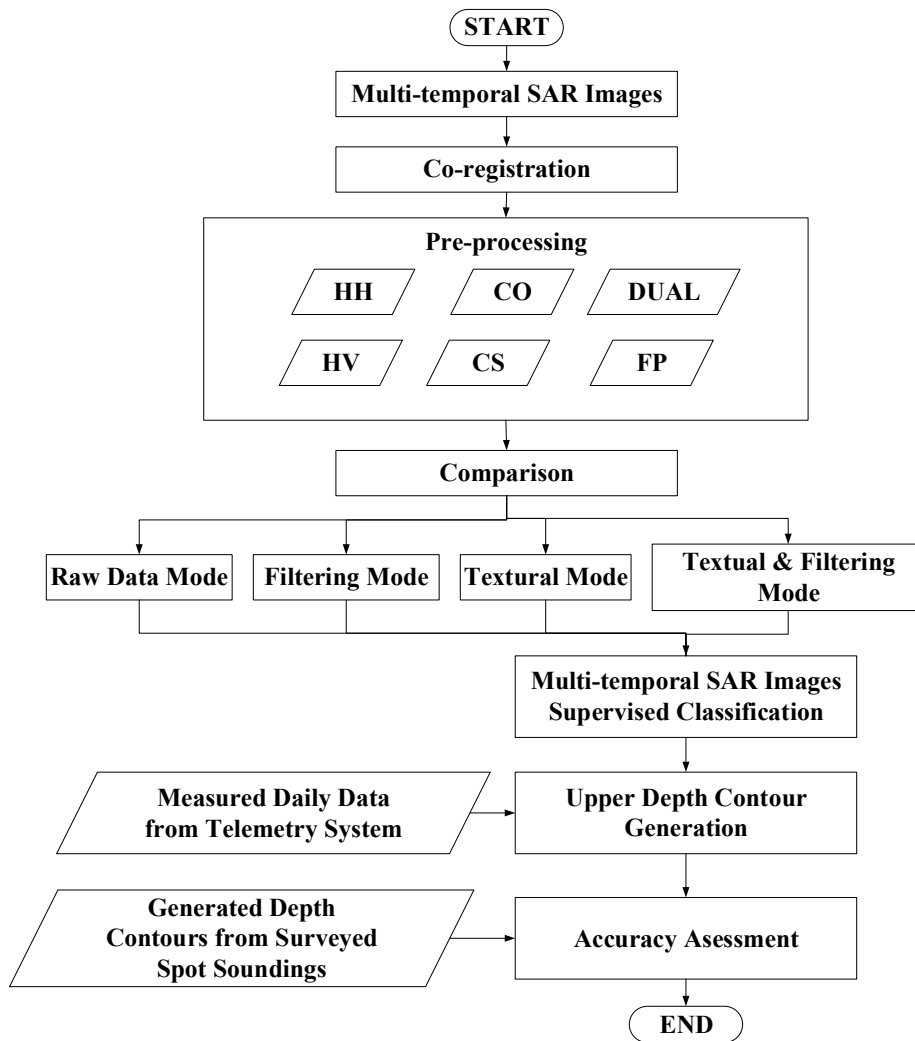

Figure 2. Framework overview.

Table 2. Water level measurement by measured daily data from telemetry system in correspondence to imagery acquisition date.

No.	Measured Daily Data from Telemetry System in Correspondence to Acquisition Date	Water level at Mean Sea-Level (Meter)
1.	12 Jul 2008	341.05
2.	27 Aug 2008	341.38
3.	27 May 2008	341.46
4.	23 Sep 2008	342.49
5.	22 Feb 2007	342.64
6.	25 Feb 2008	343.27
7.	10 Jan2008	343.82
8.	25 Nov 2007	344.44
9.	27 Nov 2008	346.28
10.	8 Nov 2008	346.37
11.	23 Mar 2011	347.79
12.	14 Feb 2011	348.23
13.	3 Dec 2011	349.21
14.	18 Oct 2010	349.9

Source: Electricity Generating Authority of Thailand (EGAT), 2018

4.1 Accuracy Assessment

To realize the accuracy, the accuracy assessment is therefore necessary. The measurements of area for contour lines were selected to determine the accuracies. Since surveyed sounding data is available by EGAT, the digital elevation model (DEM) is produced by using ArcGIS software version 10.3, as input data for accuracy evaluation (Figure 3(a)). The model builder is built to generate tool for producing contour lines automatically. The surface volume (3D analyst) of ArcGIS is used as a tool, with defined plane heights (or water level by measured daily data from telemetry system), as shown in Figure 3(b.).
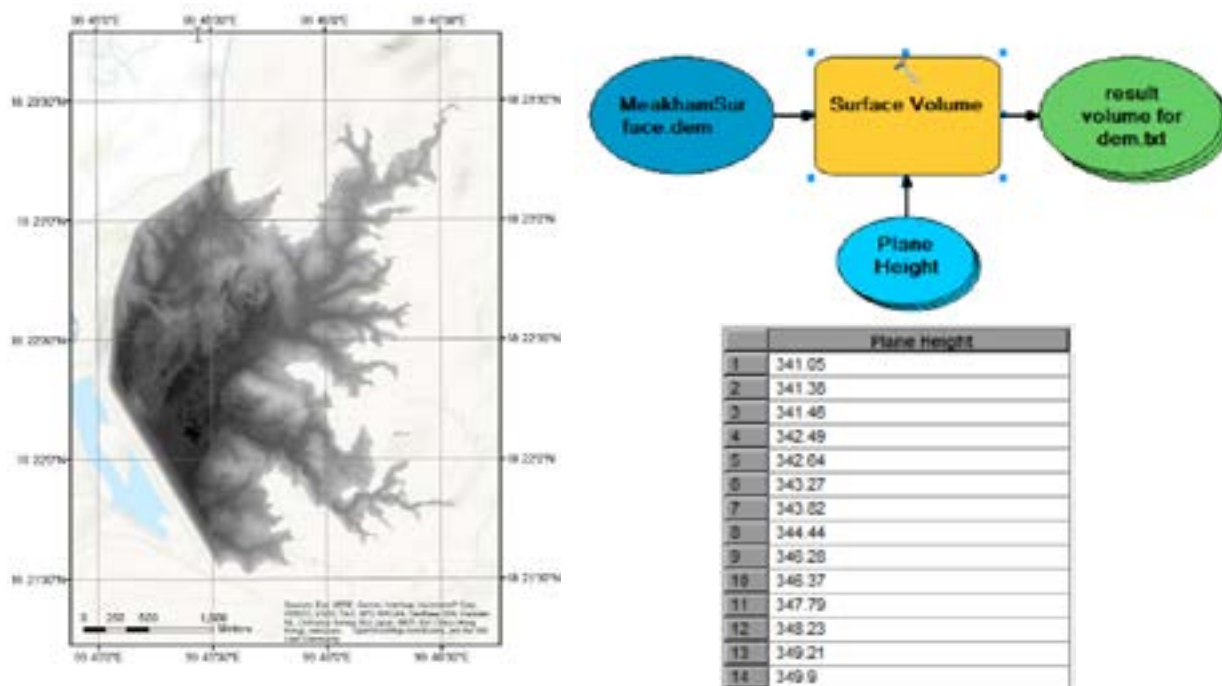
(a) Digital elevation model of Mae Kham dam.　　　　(a) Model builder and plane height list.
Figure 3 Model builder of surface volume.

5. EXPERIMENT RESULTS AND DISCUSSION

The proposed framework (Figure 2) was applied to the study area of Mae Kham dam. The six signal polarizations are analyzed with the four processing modes.

5.1 Results Obtained from the Six Signal Polarizations

The six signal polarizations were shown in Figure 4. Figure 4(a) and 4(b) show the amplitudes of the single-polarization HH and HV, respectively. As we known, the water surface appears dark in a SAR images. With visual interpretation, the results showed that the HV data was better than HH data for water body of Mae Kham dam. However HH is always show the best result in mapping surface water [6], whereas the surface becomes rougher e.g., wind and waves; the water surface has many facets in many direction causing the reflection becomes more diffuse [7]. It made HV often demonstrates the best result for surface water mapping. This result is consistent with other researches [8], [9]. Because the backscatter is dependent on the look angle to the surface roughness, orientation and polarization. Therefore, it can be concluded that the most appropriate signal polarization is strongly dependent on weather condition or scene to the surface water mapping.

The polarization combinations are also investigated namely the DUAL (HH + HV) data, the CO (HH + VV) data, the CS (HV + VH) data, and the FP (HH + HV + VH + VV) data as shown in Figs 4(c) – 3(f), respectively. It was found that the CS (HV + VH) data (Figure 4(e)) showed the best result in the scene which has more clear water body of Mae Kham dam than others. Because the supplement of cross-polarization data used as the characteristics for the HV and VH data are mostly similar. While the others have the combinations of HH, multiplicative speckle noise were found in the scenes. Thus, the CS data is found to have the appropriate signal polarization for the surface water mapping. However most of SAR images are dual-polarization data, the HV data is preferable to classification.
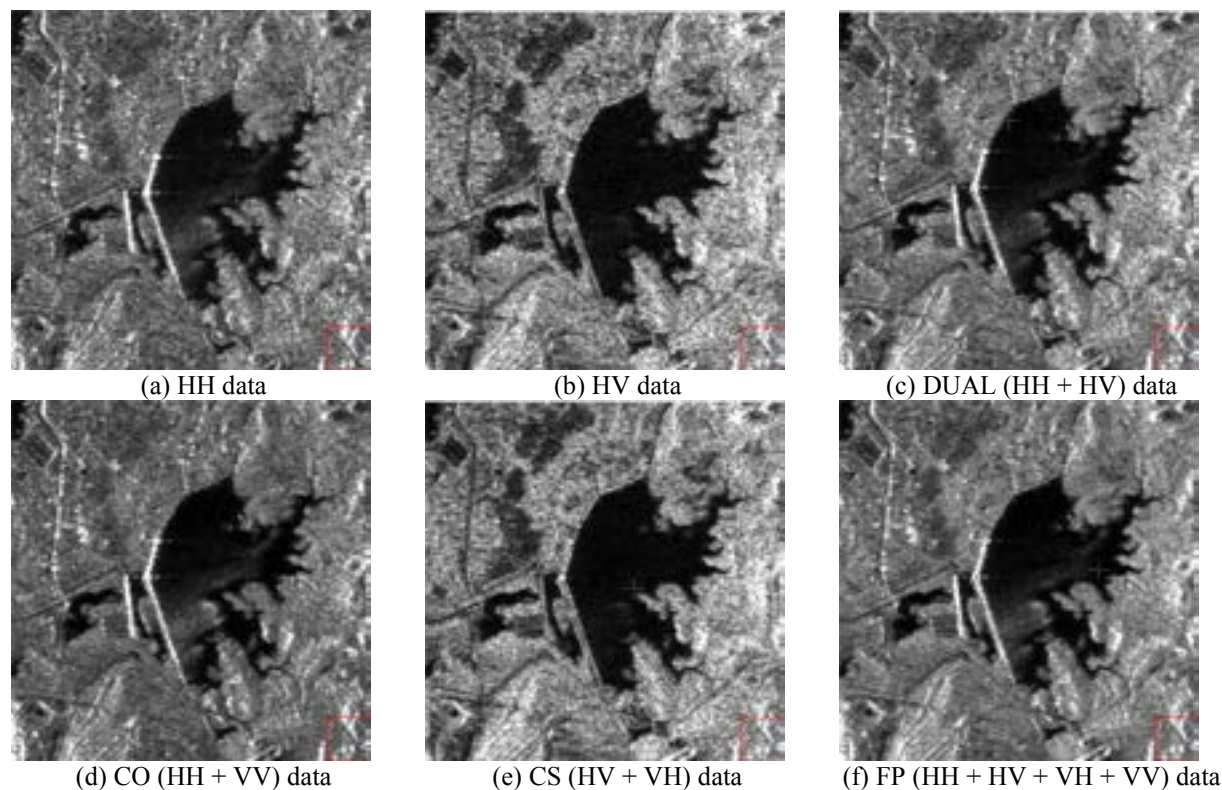

(a) HH data	(b) HV data	(c) DUAL (HH + HV) data
(d) CO (HH + VV) data	(e) CS (HV + VH) data	(f) FP (HH + HV + VH + VV) data

Figure 4. The six signal polarizations.

5.2 Results Obtained from the Four Processing Modes

The suitable CS data is used for examining the information fission in four processing modes (Figure 5). The original source of SAR image in raw data mode (Mode 1) is shown in Figure 5(a). The adaptive enhanced Frost filtering was applied in filtering mode (Mode 2) as shown in Figure 5(b). In Figure 5(c), the mean texture measure from the GLCM was employed in textural mode (Mode 3). And the combination of adaptive enhanced Frost filtering and GLCM mean texture measure was experimented in filtering and textural mode (Mode 4) (Figure 5(d)). It look seems similar among these results. To acquire more explicit results, the zoomed noise area is considered to determine the optimal mode of the information fission. It is represent as the point of interest (POI) located at 571739.8830E and 2028407.1620N meters of WGS 1984 and UTM Zone 47 North. The grayscale quantization intensity of the images of four processing mode were computed (i.e., 58, 56, 55, and 52) and demonstrated in Figs 5(e) – 4(h) with regard to Mode 1 to Mode 4. The results reveals that the grayscale quantization intensity of POI for the CS data with the combination of adaptive enhanced Frost filtering and GLCM mean texture measure (Mode 4) showed the lowest value. It leads to detect water bodies more accurate than other processing modes.
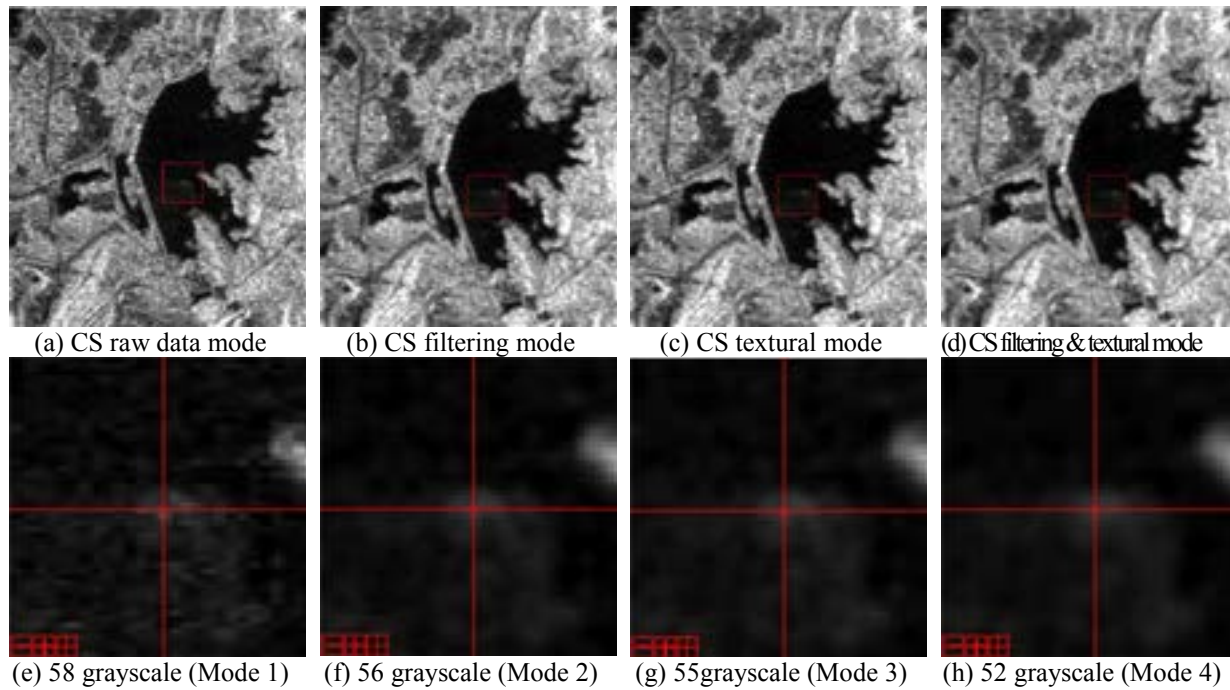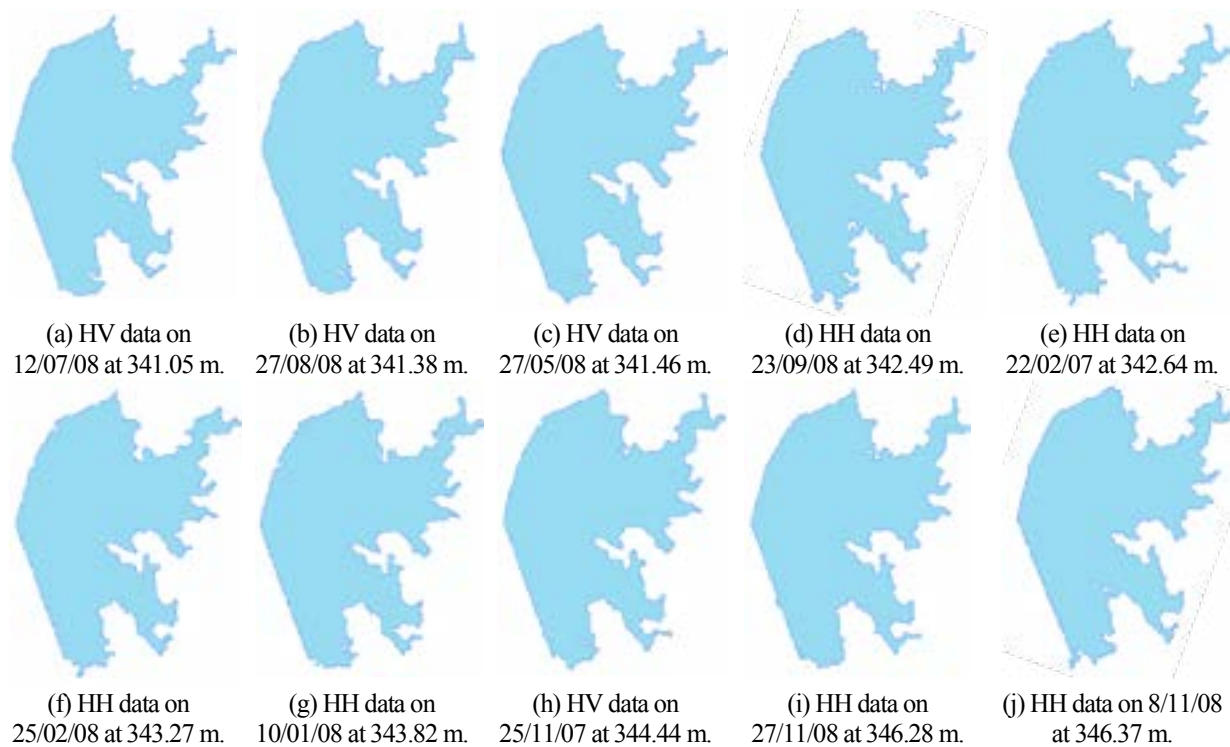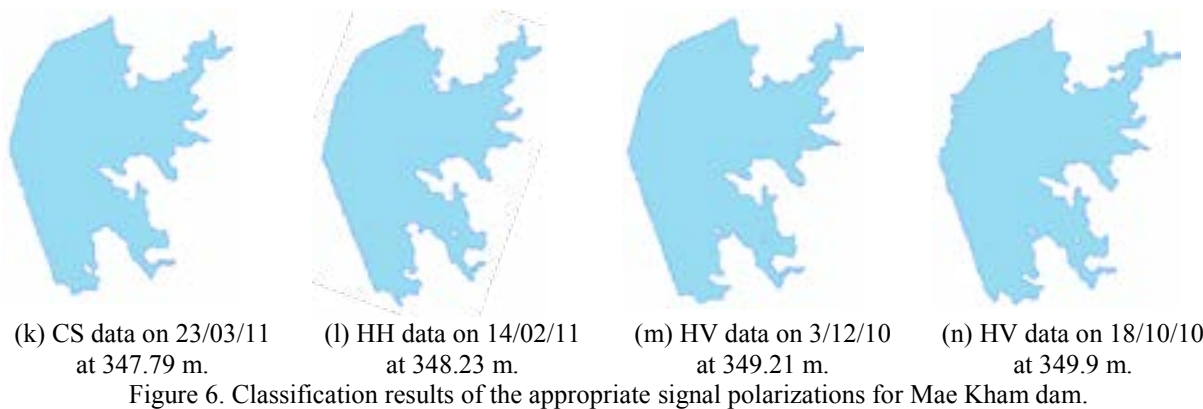
| (a) CS raw data mode | (b) CS filtering mode | (c) CS textural mode | (d) CS filtering & textural mode |

| (e) 58 grayscale (Mode 1) | (f) 56 grayscale (Mode 2) | (g) 55grayscale (Mode 3) | (h) 52 grayscale (Mode 4) |

Figure 5. The CS (HV + VH) data with four processing modes.

5.3 Classification Results Obtained from the Appropriate Signal Polarizations with the Combination of Filtering and Textural Mode

It was found that the CS data and the HV data are the suitable signal polarization for classification. The HV data and the HH data would rather use in case of dual- and single-polarization data are provided, respectively. These proper signal polarization data were analyzed with the combination of adaptive enhanced Frost filtering and GLCM mean texture measure in (Mode 4). Then the supervised classification was proceeded. Figure 6 illustrates the classification results of appropriate signal polarizations for multi-temporal SAR images of the Mae Kham dam. These layers display 1:25,000 scale.

| (a) HV data on 12/07/08 at 341.05 m. | (b) HV data on 27/08/08 at 341.38 m. | (c) HV data on 27/05/08 at 341.46 m. | (d) HH data on 23/09/08 at 342.49 m. | (e) HH data on 22/02/07 at 342.64 m. |

| (f) HH data on 25/02/08 at 343.27 m. | (g) HH data on 10/01/08 at 343.82 m. | (h) HV data on 25/11/07 at 344.44 m. | (i) HH data on 27/11/08 at 346.28 m. | (j) HH data on 8/11/08 at 346.37 m. |

| (k) CS data on 23/03/11 at 347.79 m. | (l) HH data on 14/02/11 at 348.23 m. | (m) HV data on 3/12/10 at 349.21 m. | (n) HV data on 18/10/10 at 349.9 m. |

Figure 6. Classification results of the appropriate signal polarizations for Mae Kham dam.

5.4 Accuracy Assessment

The upper depth contour lines at 341.05, 341.38, 341.46, 342.49, 342.64, 343.27, 343.82, 344.44, 346.28, 346.37, 347.79, 348.23, 349.21, and 349.9 meters were produced from DEM of Mae Kham dam in Section 4.1, as shown in Figure 7. The areas of each water level were computed as shown in Table 3.
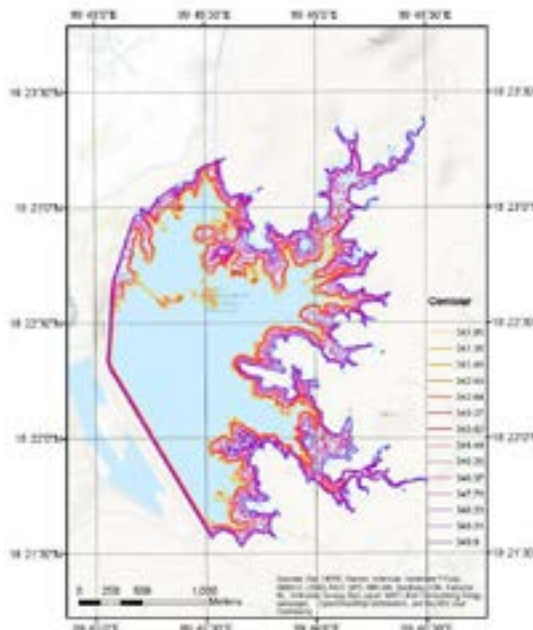
Figure 7. Upper level contour lines of Mae Kham dam by volume surface tool in ArcGIS 10.3.

Table 3 compares the area results (in particular, differential percentage) for the classified area from multi-temporal SAR images and the measured area from the contour lines. The average of differential percentage between area from the classification result and the measured contour lines was 0.83%. It shows the slightly discrepancy of the classification. Here, the results of classified area are considered. It was found that the area of the classification results and measured contour lines regarding to water levels show similar trends, with the rates increase slightly. It is proved that the water level area of dam is directly related to the utilization of multi-temporal SAR images.

Table 3. Comparison of water level area measurement for the classified area from multi-temporal SAR images, and the measured area from contour characteristic in correspondence to measured daily data from telemetry system.

No.	Acquisition Date	Water level at Mean Sea-Level (Meter)	Classified Area from SAR images (Square Meters)	Measured Area from Contour lines (Square Meters)	Differential Percentage (%)
1.	12 Jul 2008	341.05	2,175,960.22	2,174,380.72	0.07
2.	27 Aug 2008	341.38	2,184,744.57	2,182,877.74	0.09
3.	27 May 2008	341.46	2,186,472.50	2,184,543.14	0.09
4.	23 Sep 2008	342.49	2,375,607.37	2,365,265.60	0.44
5.	22 Feb 2007	342.64	2,378,861.19	2,368,316.83	0.44
6.	25 Feb 2008	343.27	2,562,944.35	2,556,450.58	0.25

7.	10 Jan2008	343.82	2,575,547.82	2,568,159.35	0.29
8.	25 Nov 2007	344.44	2,763,328.12	2,749,555.52	0.50
9.	27 Nov 2008	346.28	3,191,949.39	3,160,983.40	0.97
10.	8 Nov 2008	346.37	3,194,411.52	3,163,120.18	0.98
11.	23 Mar 2011	347.79	3,433,663.28	3,397,418.22	1.06
12.	14 Feb 2011	348.23	3,648,702.39	3,582,653.51	1.81
13.	3 Dec 2011	349.21	3,875,557.70	3,792,158.04	2.15
14.	18 Oct 2010	349.9	3,898,634.17	3,804,030.66	2.43

7. CONCLUSION

The effectiveness of measuring the water surface level area of Mae Kham dam using multi-temporal SAR images based on an optimal signal polarization for quantitatively evaluating the classification capabilities of fully polarimetric, dual-polarization, and single-polarization SAR were investigated. The quantitative comparisons were made with six signal polarizations (i.e., HH data, HV data, CO data, CS data, DUAL data, and FP data) in perspective of different processing modes namely raw data mode, filtering mode, textural mode, and texture & filtering combination mode. The supervised classification was applied to discriminate the water body area. The optimal combination of GLCM-based mean textural and enhanced frost adaptive filtering mode was indicated for removing multiplicative speckle noise significantly due to the smoothing effect on the image of the texture. From the aspect of signal polarizations, the combined cross-polarized (HV+VH) data or (CS data) showed high potential for generating accurate classification. Because the supplement of cross-polarization data used as the characteristics for the HV and VH data. In addition, the fusion of measured daily data from telemetry system for water level measurement with SAR satellite imagery is practical for creating upper depth contour lines. Forasmuch as it corresponds to spatial change in an appropriate time interval.

REFERENCES

[1] Chureesampant, K. and Susaki, J., 2012. Automatic unsupervised change detection using multi-temporal polarimetric SAR data. In Proceedings of the IEEE International Geoscience and Remote Sensing Symposium (IGARSS 2012), Munich, Germany, pp. 6192-6195.

[2] Parker, W. V., 2012. Discover the benefits of radar imaging, Retrieved July 13, 2018, from https://eijournal.com/print/articles/discover-the-benefits-of-radar-imaging.

[3] Bruzzone, L., Marconcini, M., Wegmuller, U., and Wiesmann, A., 2004. An advanced system for the automatic classification of multi-temporal SAR images. IEEE Transactions on Geoscience and Remote Sensing, 42(6), pp. 1321-1334.

[4] Japan Aerospace Exploration Agency (JAXA), 2007. ALOS/PALSAR level 1.1/1.5 product format description <English Version> version NEB-070062A.

[5] Lopes, A., Touzi, R., Nezry, E., 1990. Adaptive speckle filters and scene heterogeneity. IEEE Transactions on Geoscience Remote Sensing, 28, pp. 992-1000.

[6] White, L., Brisco, B., Pregitzer, M., Tedford, B., and Boychuk, L. 2014. RADARSAT-2 Beam Mode Selection for Surface Water and Flooded Vegetation Mapping in Canadian Journal of Remote Sensing, 40(2), pp. 135-151.

[7] White, L., Brisco, B., Dabboor, M., Schmitt, A., Pratt, A., 2015. Collection of SAR Methodologies for Monitoring Wetlands, MDPI Remote Sensing, 7, pp. 7615-7645.

[8] Manore, M., Flett, D. G., Abreau, R. A. D., Ramsay, B. R., and van der Sanden, J. 2001. Multi-polarization SAR data for operational ice monitoring. In Proceedings of the IEEE International Geoscience and Remote Sensing Symposium (IGARSS 2011), Sydney Australia, pp. 1246–1248.

[9] Scheuchl, B., Flett, D., Caves, R., and Cumming, I. 2004. Potential ofRADARSAT-2 Data for operational sea ice monitoring. Canadian Journal of Remote Sensing, 30(3), pp. 448–461.

UAV REMOTE SENSING TECHNOLOGY FOR BIOGEOGRAPHY AND BIODIVERSITY MAPPING OF PADAKEMBANG VILLAGE, WEST JAVA, INDONESIA

Lissa Fajri Yayusman[1], Muhammad Fakhriy Ramadhan[1], Deni Suwardhi[1,2], Ketut Wikantika[1,2]

[1]Center for Remote Sensing, Institut Teknologi Bandung, Bandung, Indonesia
[2]Remote Sensing and GIS Research Group, Institut Teknologi Bandung, Bandung, Indonesia
Email: lissafajri@gmail.com , fakhriyramadhan25@students.itb.ac.id , deni@gd.itb.ac.id , ketut@gd.itb.ac.id

KEY WORDS: UAV, photogrammetry, biogeography, biodiversity

ABSTRACT: Padakembang Village is located at the foot of Mount Galunggung, an active stratovolcano in Tasikmalaya Regency, Indonesia. Supported by its temperature, water resource, and fertile soil, this village possesses high biodiversity of various vegetation and become a potential area of ecotourism. However, the village development and natural resource management have not been optimized because of the lack information about the biogeography and land cover condition. To support this program, Unmanned Aerial Vehicle (UAV) was used for high resolution mapping of the Padakembang Village. Aerial photos were taken using a fixed-wing UAV covering 500.1 Ha area. Because of the large area coverage and hilly topography, data acquisition was performed in four blocks area divided based on the similar elevation to maintain spatial resolution. Geo-referencing process was performed using sixteen Ground Control Points (GCPs) measured in rapid-static method with radial baseline. Methodology and the obtained results are shown and discussed in this paper. The results presented as ortho-image and Digital Elevation Model of the village could be employed by the local government as the main reference for natural resource management, development, and monitoring of Padakembang Village.

1. INTRODUCTION

Sustainable rural development is considered as an important element to the social, economic, and environmental sectors of a nation. As mentioned in the report of the 7th session of CSD, the strategy to carry out the rural development should consider both the location and potentials in rural areas, so that proper approaches can be implemented (UN, 2009; Trukhachev, 2015). Padakembang Village in Tasikmalaya Regency, Indonesia possesses high biodiversity and agricultural potentials. On the other hand, the farmers are known to be both users and custodians of biodiversity (FAO, 2008). They take the advantages but also need to protect those natural resources. Therefore, high natural potentiality in this village should be managed and optimized in effective ways to develop the socio-economic condition as well as to conserve biodiversity. A fundamental step to support this process is the knowledge improvement of spatial distribution and land cover condition of the village itself.

UAV photogrammetry has been widely used to extract spatial information of objects on the Earth (Graca, et al. 2014; Remondino et al. 2011). This technology was introduced as the low-cost alternative to the conventional aerial photogrammetry which is very expensive and has limited image resolution. The UAV photogrammetry offers higher flexibility to acquire the data from closer range in autonomous flight with lower cost flight mission and platform (Eisenbeiss, 2009; Perez, 2013). These advantages make the mapping process become much easier and give higher resolution of image results. Therefore, this technology will be useful to identify the biodiversity in Padakembang Village as part of the efforts to develop the socio-economic condition of this village. The aims of this study were to assess the methodology of data acquisition in the hilly topography, and to obtain the high resolution photo map and Digital Elevation Model of Padakembang Village, Tasikmalaya, Indonesia as a preliminary study to identify the spatial distribution of biodiversity in the village.

2. STUDY AREA AND DATA ACQUISTION

2.1 Study Area
The photogrammetric data acquisition was performed in Padakembang Village, Tasikmalaya Regency, West Java, Indonesia. This village is located at the foot of an active stratovolcano, Mount Galunggung. Since the mountain's last major eruption in 1982, this area has been developed as a promising site for agricultural activities and ecotourism. Supported by its favorable temperature, sufficient water resource, and fertile soil, the village possesses abundant natural resources, such as high biodiversity of various vegetation that has potentiality as the main commodities. The

total about 500.1 Ha area of this village are mainly covered by agricultural land and settlement in the lower part (Fig. 1), and forest area in the higher part. While paddy is known as the major commodity, other potential biodiversity such as coconut and various cultivars of bananas also known as the unique resource of this village.

Figure 1 Preview of landscape condition in Padakembang Village taken by UAV

2.2 Flight Plan

Aerial photos were taken using a Sky Walker fixed-wing UAV. The flight altitude was set at 300 m from the base to obtain a 1:1000 scale of photo map. Because of the large area coverage and hilly topographic condition, the flight plan was divided into four blocks, with the first block located at the lowest altitude, and the last block at the highest part (Fig.2). The photos were taken in 80% overlap and 60% sidelap for about 150 Ha area with an hour flight duration for each block. A Sony Alfa 6000 camera with 16 mm E mount fixed lens was used for RGB data acquisition.

2.3 Ground Control Points (GCPs)

Total of sixteen (16) GCPs were installed over the whole area, with seven GCPs for each block (Fig. 3). The GCPs distributed in the corner parts of each block, in the center part, and in the overlap between blocks. GCP positions were measured using Global Navigation Satellite System (GNSS) receivers with radial baseline. The base point position was measured for 24 hours using ITRF2014 as the reference, while each GCP was measured for 15 minutes in rapid-static method.
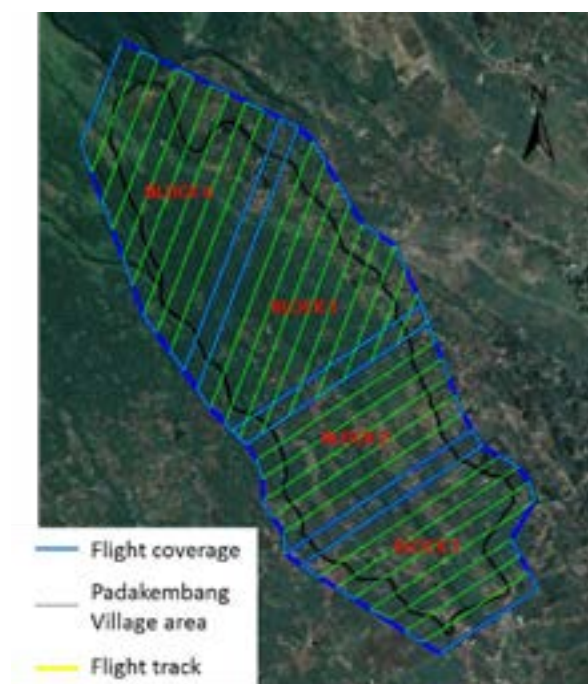

Figure 2 Flight tracks and blocks area

Figure 3 GCP distributions

3.   METHODS

3.1   Aerial Triangulation

Aerial triangulation (bundle adjustment) was performed to determine the exterior parameters of the image block. In this study, bundle adjustment was executed using the sixteen control points in the blocks. The results of root means square errors of the measurement's residuals (Table 1) show acceptable values of the precision from bundle adjustment. The RMSE in horizontal coordinates are 4 mm and 5 cm in X and Y, respectively, while the RMSE in vertical coordinates is 7 cm. The error values are smaller than the resolution between two pixels, therefore the error value is considered to be acceptable.

Table 1 RMSE of control points and check points

Flight Block	Control Point Coordinate Residual (m)			Check Point Disprepancies(m)		
	RMSE x	RMSE y	RMSE z	RMSE x	RMSE y	RMSE z
block 1	0,00722	0,11926	0,005795	0,006415	0,116544	0,175062
block 2	0,005542	0,001607	0,003794	0,010929	0,08343	0,135714
block 3	0,000185	0,000129	0,000086	0,000372	0,000031	0,00003
block 4	0,000362	0,000419	0,000134	0,000253	0,000663	0,000321
Total Merge block	0,003327	0,030354	0,002452	0,004492	0,050167	0,077782

3.2   Digital Surface Model and Orthoimage Generation

Digital Surface Model (DSM) were processed from the dense cloud generated from the interpolation of tie points between photos. DSM shows the 3D elevation model of each object taken in the photos. Agisoft Photoscan version 1.3.3 software was used to produce and export the DSM and a 3 bands (Red, Green, Blue) orthoimage. Orthomosaic was then generated from the 4-blocks orthoimage to obtain an orthoimage for the whole area of Padakembang Village.

4.   RESULT AND DISCUSSION

The DSM of each block were generated for each 100 m elevation change (Fig. 4). DSM shows the pixel representing 480 m elevation from as the lowest point, and 600 m as the highest point. Large elevation gap was obtained due to the hilly topographic condition and the generated model which is representing the surface of objects. The elevation between 575 – 600 m were identified as the forest area close to the pick of the mountain.
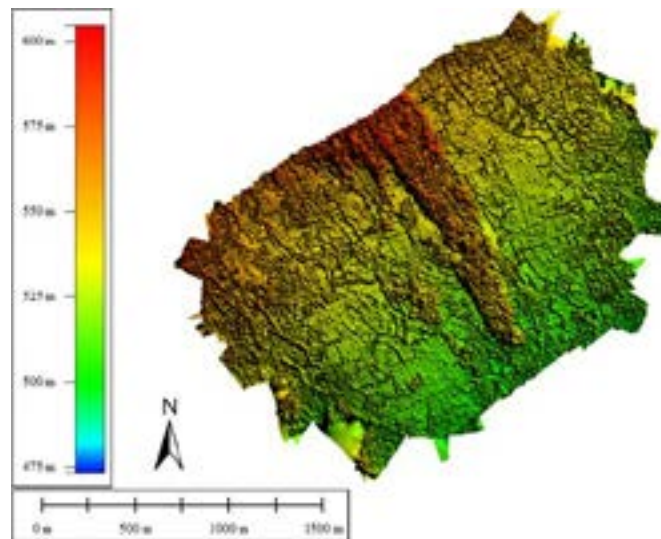
Figure 4 DSM of Block 4 area

The orthoimage of the whole area of Padakembang Village was generated in 7 cm resolution (Fig. 5). However, the image result shows different color tone of same objects in different blocks because of the different time of data acquisition. Several factors such as weather condition (haze) particularly in the upper part of the mountain, and sun angle effects make some areas in the image become darker, while the other areas become too bright. To overcome this problem, image enhancement process was carried out using four parameters: color balance, brightness, contrast,

and exposure, by taking some color representing each object from one of the block which is close enough to the original color. These colors then used as the reference for the same objects in the other blocks. This process was done to improve the further analysis which mainly use the vegetation cover as the main objects. The high resolution of the orthoimage combined with the generated DSM will be very useful to identify the spatial distribution of biodiversity in the village. These result also can be employed by the local government as the main reference for natural resource management, development, and monitoring of Padakembang Village.

Figure 5 Orthoimage of Padakembang Village

5. CONCLUSIONS

The UAV photogrammetry has been successfully employed to produce the 3D elevation model and high resolution photo map of Padakembang Village. The data acquisition methods in this study were mainly considered based on the topographic condition and coverage area. The results showed acceptable geometric RMSE but still strongly affected by the weather condition which is one of the limitation of this technology. Therefore, better flight plan to minimize this effects is necessary. Further analysis to identify the biodiversity automatically from the image are also recommended for the future study.

References

Eisenbeiss, H., 2009. UAV Photogrammetry. Diss. ETH No. 18515, Institute of Geodesy and Photogrammetry, Zurich: ETH Zurich.

FAO. 2008. Agriculture for Biodiversity for Agriculture. FAO, pp. 1-46.

Graca, N., Mitishita, E., & Goncalves, J., 2014. Photogrammetric Mapping Using Unmanned Aerial Vehicle. ISPRS Technical Commission I Symposium. Denver, Colorado, USA: ISPRS, pp. 129 – 133.

Perez, M., Aguera, F., & Carvajal, F. (2013). Low Cost Surveying Using An Unmanned Aerial Vehicle. International Archives of the Photogrammetry, Remote Sensing and Spatial Information Sciences, Rostock, Germany, pp. 311-315.

Remondino, F., Barazzetti, L., Nex, F., Scaioni, M., Sarazzi, D., 2011. ISPRS Zurich 2011. Zurich, Switzerland: ISPRS, pp. 25–31.

Trukhachev, A. (2015). Methodology for Evaluating the Rural Tourism Potentials: A Tool to Ensure Sustainable Development of Rural Settlements. Sustainability, pp. 3052-3070. doi:10.3390/su7033052.

United Nation., 2009. E/2009/29-E/CN.17/2009/19 - Report on the 17th session of CSD.

ATMOSPHERICALLY CORRECTED D-INSAR TO DETECT TIME SERIES DEFORMATION AT AGUNG VOLCANO USING SENTINEL-1A SAR DATA

Dina Noviana Rahmawati (1,2), Asep Saepuloh (1,3), Ketut Wikantika (1,2)

[1]Center for Remote Sensing, Bandung Institute of Technology (ITB), Labtek IX-C Jl. Ganesha No. 10, 40132 Bandung, West Java, Indonesia
[2]Research Group of Remote Sensing and Geographic Information Science, Faculty of Earth Sciences and Technology, Bandung Institute of Technology (ITB), Labtek IX-C Jl. Ganesha No. 10, 40132 Bandung, West Java, Indonesia
[3]Research Group of Petrology, Volcanology, and Geochemistry, Faculty of Earth Sciences and Technology, Bandung Institute of Technology (ITB), Labtek IV Gedung Teknik Geologi Jl. Ganesha No. 10, 40132 Bandung, West Java, Indonesia
Email: dinanovr@students.itb.ac.id; saepuloh@gl.itb.ac.id; ketut@gd.itb.ac.id

KEY WORDS: Agung volcano, deformation, D-InSAR, pairwise logic technique, Sentinel-1A

ABSTRACT

Agung volcano located in the far east of Bali Island, Indonesia is one of the active volcanoes parts of Circum-Pacific ring of fire. Following the large eruption of 1963, the seismicity of Agung volcano increased significantly and put into alert level IV in September 22nd, 2017. Then, the early eruptions had occurred in November 25th and 26th, 2017. Regarding the eruptions, this research was aimed to observe the deformation series of Agung volcano from August 2017 to January 2018 using the atmospherically corrected Differential Interferometric Synthetic Aperture Radar (D-InSAR) of multiplatform Sentinel-1A data. The D-InSAR techniques were commonly used for surface deformation monitoring by eliminating the topographical influence of the interferogram's phase. The Pairwise Logic Technique as termed as PLT was applied following the D-InSAR processing to eliminate atmospheric phase delay. The common image selection for D-InSAR pair served as the basis of the PLT. The method was adopted to Sentinel-1A data in ascending and descending orbits to observe the deformation change in Line-of-Sight (LOS). The deformation velocity was then calculated on the daily basis to omit the variation of temporal baseline. According to the PLT in ascending orbit, the surface velocity near the summit was calculated from -4.1 mm/day to 2.9 mm/day. The velocity obtained from the descending orbits was slightly different than the ascending orbit, from -2.5 mm/day to 3.6 mm/day due to different LOS orientation and time reference of the data. The deformation patterns formed from the deformation magnitude showed that the inflation occurred near the time of the eruption and the subsidence followed the eruption due to changes of pressure in the reservoir.

INTRODUCTION

Agung volcano is a stratovolcano, located in the far east of Bali Island, Indonesia. Based on the historical texts and notes, Agung volcano had erupted in 1711, 1808, 1821, and 1843 (Fontijn et al., 2015). After resting about 120-years, in 1963, the Agung volcano erupted with VEI 4 and became one of the largest eruptions in the 20th century (Geiger, 2014). Later in 2017, Agung volcano had a significant increase of seismicity, raising the alert level to level IV in September 22nd, and followed by eruptions on November 25th and 26th, 2017.

Deformation derived by magma is the displacement caused by the movement of the fluids or the changes of the hydrostatic pressure of spherical source in the depth of the Earth's crust (Mogi, 1958). The displacement has been occurred in deflation and inflation of the ground. The deflation could be occurred by the decreasing of volume and/or pressure of the magma in the reservoir as the result of emptying or solidifying magma. Meanwhile, the inflation could be occurred by increasing of volume and/or pressure of magma in the reservoir due to injection of new magma or second boiling process. According to the Global Navigation Satellite System (GNSS) observation conducted by the Indonesian Centre for Volcanology and Geological Hazard Mitigations (CVGHM), the inflation of Agung volcano has occurred in August to September 2017 and followed by the deflation in October 2017.

Terrestrial methods, such as triangulation and GNSS as well as remotely sensed methods are commonly used for accurate deformation measurements. Interferometric Synthetic Aperture Radar termed as InSAR is one of the remotely sensed methods. The InSAR method uses a multiplication of SAR (Synthetic Aperture Radar) phase data to produce interferograms. The interferogram presents the range and elevation of the ground object. Removing topographic by differentiating the phases, the Differential InSAR termed as (D-InSAR) produce the displacement vector in a Line-of-Sight (LOS). The D-InSAR was applied to this method to calculate the time-dependent ground deformation of the Trans-Mexican Volcanic Belt (TMVB) and 4-four Indonesian volcanoes, including Agung volcano in the 2007-2009 (Chaussard et al., 2013). The displacement time series showed a movement of Agung volcano with velocity about 7.8 cm/year towards the satellite in 2007-2009 and 1.9 cm/year away from the satellite after 2009 (Chaussard et al., 2013). Saepuloh, et al. (2013) was also demonstrated the D-InSAR method using the ALOS/PALSAR data to measure the time-series of ground displacement of Merapi volcano in 2006 to 2010. The Pairwise Logic Technique (PLT) was also used to eliminate the atmospheric delay effects in the D-InSAR interferograms (Saepuloh et al., 2013).

PAIRWISE LOGIC TECHNIQUE TO REDUCE ATMOSPHERIC PHASE DELAY

The data used in total was 29-imageries of Sentinel-1A in both ascending and descending orbit with IW-mode and SLC-format in the period of August 2017 to January 2018. Interferometric Wide-swath (IW) mode is one of the platform operational mode, commonly used in InSAR methods (European Space Agency, 2012). IW-mode imageries are 5 m in cross-track resolution and 20 m in along-track resolution. Single Look Complex (SLC) data are in slant coordinate system and contains both phase and magnitude of the radar echoes (Sircar et al., 2003). The temporal resolution are 12-days in each imagery of the same orbit. DEM data of SRTM 1-sec HGT is also used in the process for removing topographical phase and terrain correction.

InSAR is a technique that combines two SAR images and use its phase information to determine the phase difference, thus producing a radar interferogram (Bürgmann et al., 2000). If the ground surface moves towards or away from the satellite during the time difference, it will produce a shift in the returned phase as the result of the phase difference. This technique is widely used in ground displacement and shifts monitoring, such as inter-eruptive and post-eruptive stages of volcanoes, earthquakes, land subsidence, and glacier monitoring.

Coregistration of each image is an essential step in InSAR processing. Coregistration is a shifting of two image signals by cross-correlating an image to a reference image in SAR image pairs (Li & Bethel, 2008; Rosen et al., 2000). The process will be a pixel-to-pixel matching between two images for the accurate phase difference determination and noise reduction (Li & Bethel, 2008). The coregistration process will produce 13-thirteen stacks of ascending data and 12-twelve stacks of descending data. Each stack will contain coregistered slave image to the master image and produce one interferogram in interferogram formation processing. Interferogram formation will be a complex multiplication of the reference image and the slave image consists of magnitude (correlation between images) and phase difference (Gamma Remote Sensing, 2007; Hanssen, 2001). The correlation indicates the fringe visibility; meanwhile, the phase difference produced will be the sum of Earth's curvature phase, topographical phase, atmospheric delay phase, the noise phase, and the deformation phase (Gamma Remote Sensing, 2007). Thus, filtering and corrections are used to eliminate others phase and maintaining only the deformation phase.
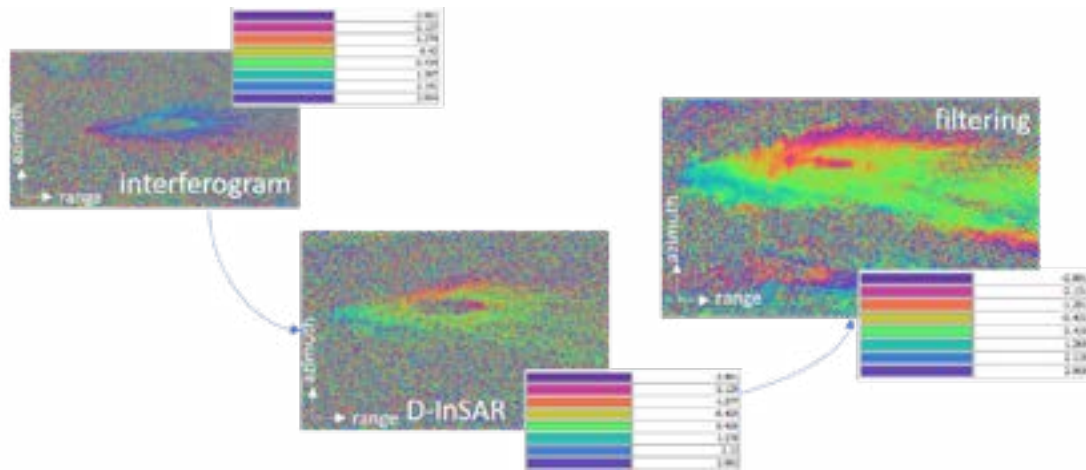
Figure 1. Changes of Agung volcano interferograms within Interferogram formation (left), D-InSAR (middle), and Goldstein Phase Filtering process (right)

D-InSAR is a process required to separate topographic and displacement phase from the interferograms (Gamma Remote Sensing, 2007). The generation of D-InSAR interferograms was performed by removal of topographical phase using DEM SRTM 30 m resolution. The D-InSAR data reveal the component of ground deformation that occurred in between two observations along the LOS between the ground and satellite (Saepuloh et al., 2013). Goldstein Phase Filtering is an adaptive filtering algorithm that is sensitive to the local phase noise and fringe rate of an interferogram to help reduce the noise (Goldstein & Werner, 1998). The phase filtering is performed next after the D-InSAR. Multilooking is an averaging process of neighbouring pixels to reduce speckles and allow us to obtain a square pixel (Alaska Satellite Facility, 2017; Masonnet & Fiegl, 1998). It will also improve the signal-to-noise ratio (SNR) (Masonnet & Fiegl, 1998). After multilooking, terrain correction was applied as the last D-InSAR processing. The terrain correction will geocode the interferograms into the geographic coordinate system and eliminate geometric distortion, such as shortening, layover, and shadow (Tănase, 2011).
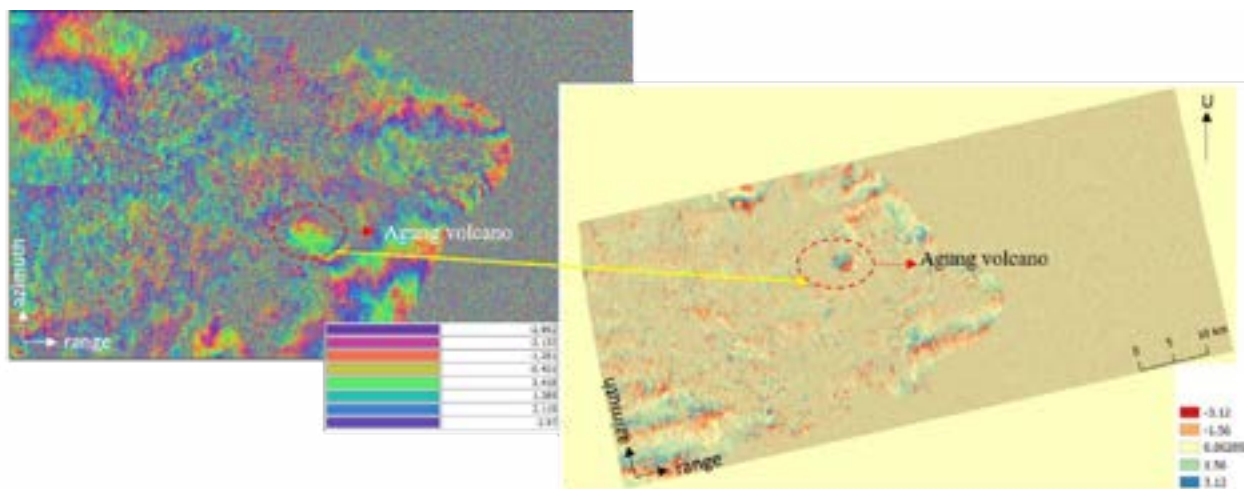
Figure 2. Changes in Multilooking (left) and Terrain Correction (right) interferograms; the terrain correction interferogram was rotated following reference from DEM SRTM 30 m resolution

The atmospheric delay is caused by the water vapour interrupting the reflection of the electromagnetic waves. It will lead to the mixing effect of refractive index variability and vertical stratification which causes differences in vertical refractivity on two SAR acquisitions (Hanssen, 2001). Thus, a correction is required to remove the phase with the Pairwise Logic Technique (PLT). This method will sum two interferograms within an overlapping time interval, with the assumption of having the same atmospheric condition (Saepuloh et al., 2013). PLT will produce deformation fringes in 2π cycles and must be unwrapped. The phase unwrapping is done manually by counting the fringes and multiply it with the half-wavelength (Syahreza et al., 2017).
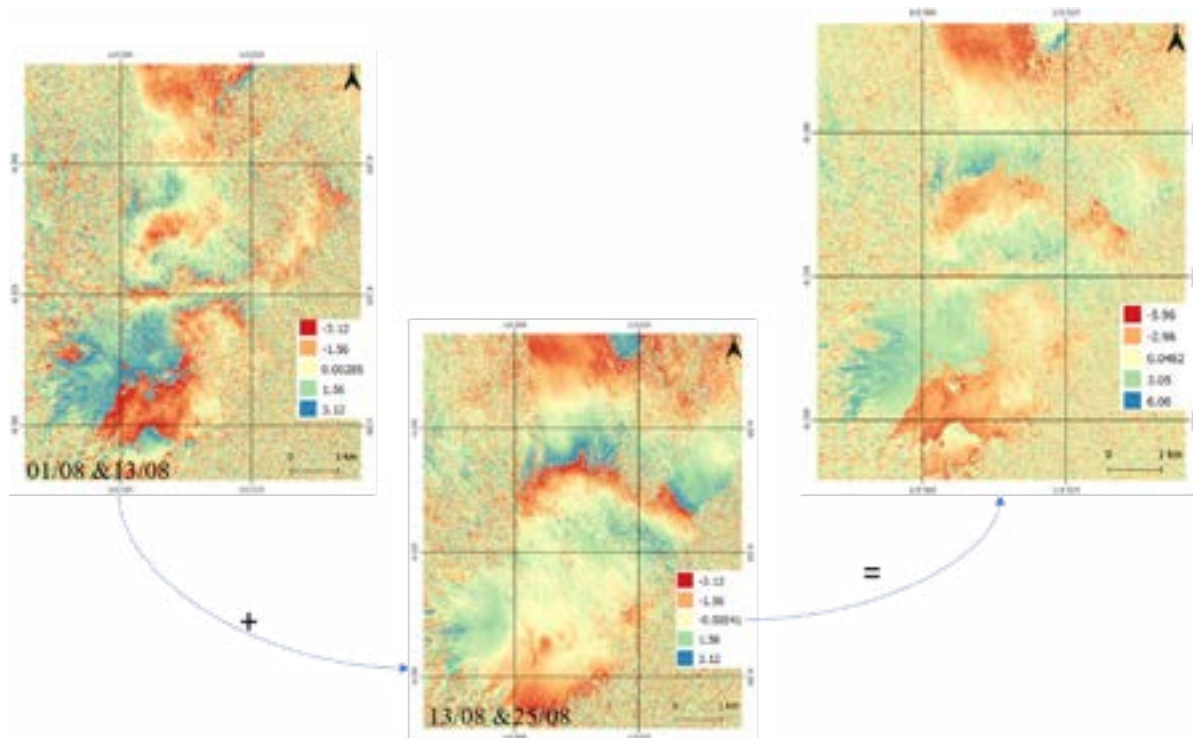
Figure 3. Summarizing interferogram of August 1st and 13th (left) with interferogram of August 13th and 25th (middle) resulted in PWL images of August 1st and 25th (right)

From Figure 3, PLT processing summarized interferogram of August 1st and 13th with interferogram of August 13th and 25th. The overlapping pair was at August 13th, that created an assumption of both interferograms had the same atmospheric condition. The addition of both August 13th images as a Slave image and Master image eliminated the atmospheric delay effect. The resulted PLT image duration was prolonged from 1st to 25th of August. Therefore, the deformation date was August 25th.

RESULT AND DISCUSSION

Table 1. Statistics of deformation and the velocity of Aung volcano

Descending				Ascending			
Deformation date	Fringes (π)	Deformation (cm)	Deformation Velocity (mm/day)	Deformation date	Fringes (π)	Deformation (cm)	Deformation Velocity (mm/day)
28/08/2017	-1,4	-4,228	-1,762	25/08/2017	-2,6	-7,748	-3,228
09/09/2017	2,7	8,249	3,437	06/09/2017	1,6	4,48	1,867
21/09/2017	2,8	8,554	3,564	18/09/2017	-2,7	-7,898	-3,291
03/10/2017	1,2	3,66	1,525	30/09/2017	-2,7	-7,992	-3,33
15/10/2017	1,8	5,373	2,239	12/10/2017	1,4	4,158	1,733
27/10/2017	-1,2	-3,402	-1,418	24/10/2017	1,4	4,186	1,744
08/11/2017	-1	-3,065	-1,277	05/11/2017	-3,3	-9,867	-4,111
20/11/2017	1,9	5,757	2,399	17/11/2017	-2,8	-8,61	-3,588
02/12/2017	-0,9	-2,714	-1,131	29/11/2017	2,4	6,9	2,875
14/12/2017	-2	-6,09	-2,538	11/12/2017	-0,8	-2,304	-0,36
26/12/2017	-0,7	-2,139	-0,891	23/12/2017	-1,1	-3,234	-1,348
07/01/2017	0,5	1,493	0,622	04/01/2017	-0,1	-0,3	-0,125
				16/01/2017	-1,1	-3,322	-1,384

The positive value indicates the shift happens towards the satellite and the negative indicates the movement away from the satellite. The deformation rates will be calculated by dividing the deformation with the temporal baseline of 24 days. The tabular data were then presented by a graph to show the temporal deformation pattern of Aung volcano.

The X-axis is the deformation dates; meanwhile, the Y-axis is the magnitude of deformation. Each of the deformation dates of two acquisitions will be drawn as one line as it complements each other. The eruption date from the Indonesian Centre for Volcanology and Disaster Hazard Mitigations was also included in the graph.
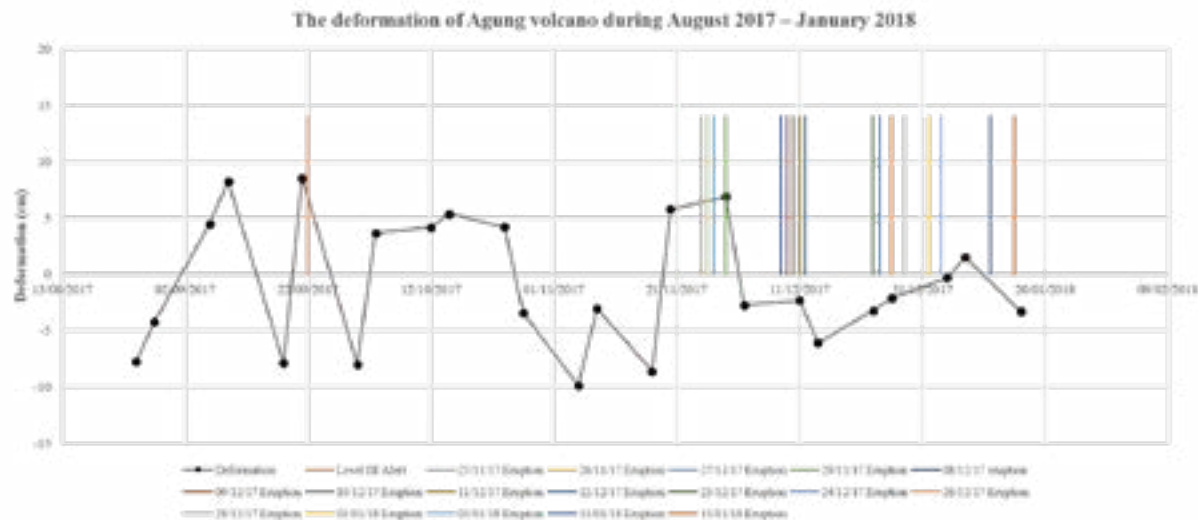

Figure 4. The deformation pattern of Agung volcano

The deformation in ascending and descending modes has a considerable difference, with a maximum value of 16.45 cm in between 18th and 21st of September 2017 and an average difference of 6.5 cm. It can be caused by different orientation angle of LOS and different time reference of the way it's compared. The difference of LOS orientation angles can lead to the different power of the ground echo and different incident angle of the same object. Those geometrical effects may affect the interferogram (Moore, 1990). To reduce this effect, the combination algorithm of two acquisition method is recommended as it will obtain deformation vectors in east-west (EW), up-down (UD), and north-south (NS) direction (Pepe & Calò, 2017). Furthermore, the deformation value compared was not at the same date of deformation. Changes was very likely happened in the reservoir at an unknown pace in this time difference.

From Figure 4, a deflation happened at September 18th and followed by an inflation until September 21st and then an increase of alert level to Level IV by September 22nd occurred. This shows an increase of pressure within the reservoir in the time span but hasn't reached the critical point of eruptions. This increase of pressure is indicated by an increase of deep volcanic earthquakes to 2533 times based on CVHGM observations. After the September 22nd, the deflation occurred, and an inflation occurred until mid-October and deflation until early November, respectively. We interpreted that the increase of pressure in the reservoir, as indicated by an increase of deep volcanic earthquakes statistics up to 15857 times was followed by a decreasing pressure, as indicated by a lowering statistic of deep volcanic earthquakes to 599 times based on CVHGM observations.

The inflation recurred in mid-November until the first eruption of Agung volcano, marked on November 25th, 2017. This eruption shows that the increase of magma within the reservoir has reached its critical point and starts to breach the peak as it erupts. This inflation immediately followed by deflation until the end of December 2017, before the inflation recurred until the beginning of January 2018. The deflation marks the decreasing pressure in the reservoir as an out-flow lava has been occurred continuously; marked by the eruption at 9th – 12th until December 23rd and 24th. The inflation happened was minor and followed simultaneously by deflation, marked by the eruption on December 28th, 2017 and January 1st, 2018.
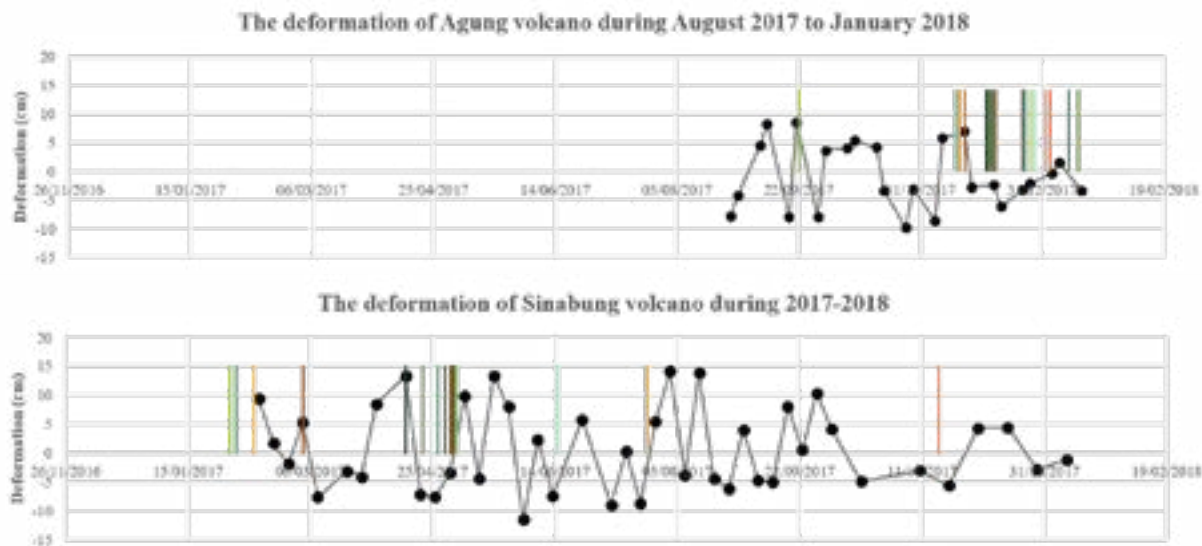
Figure 5. Comparison between Sinabung and Agung deformation graphs; vertical bars indicated eruption dates

The temporal deformation was then compared with Sinabung volcano, as it is tremendously active from 2010 until now, as shown in Figure 5. The deformation acquisition dates were in the same period, from 2017 until early 2018. The vertical bars marked the eruption dates. The bars presented eruption times more than 7, in total 18 dates. The temporal deformation pattern at Agung volcano is not as fluctuated as the Sinabung volcano because in 2017, Sinabung volcano 1246 times in 331 eruption dates based on CVGHM observations. Therefore, it leads to drastic changes of pressure within the reservoir continuously as the frequent eruptions or multi-period eruptions.

CONCLUSION

The deformations have been detected at Agung volcano from August 2017 to January 2018 at ascending orbit from -9.8 to 6.9 cm and descending from -6.1 to 8.5 cm. The deformation at two orbits is slightly different due to different LOS orientation angle and time reference. The deformation velocity has been calculated for ascending orbit from -4.1 to 2.8 mm/day and descending orbit from -2.5 to 3.5 mm/day. The detected deformation at the summit included deflation and inflation was interpreted as pressure decrease and increase in the magma reservoir, respectively. The inflation was occurred before the eruptions and followed by deflation. Comparing to the deformation at Sinabung volcano, the pattern of temporal deformation at Agung volcano showed a single eruption period.

ACKNOWLEDGEMENT

REFERENCES

Alaska Satellite Facility. (2017, June 16). *Sentinel-1 InSAR Processing using the SNAP Toolbox.* Retrieved June 27, 2018, from STEP Science Toolbox Exploitation Platform: https://step.esa.int/docs/tutorials/S1TBX%20TOPSAR%20Interferometry%20with%20Sentinel-1%20Tutorial.pdf

Bürgmann, R., Rosen, P. A., & Fielding, E. J. (2000). Synthetic Aperture Radar Interferometry. *Annual Review of Earth and Planetary Science*, pp. 169-209.

Chaussard, E., Amelung, F., & Aoki, Y. (2013, August 6). Characterization of open and closed volcanic systems in Indonesia and Mexico using InSAR time series. *Journal of Geophysical Research: Solid Earth*, pp. 3957-3969.

European Space Agency. (2012). *Sentinel-1: ESA's Radar Observatory Mission for GMES Operational Services.* Noordwijk, The Netherlands: ESA Communications.

Fontijn, K., Costa, F., Sutawidjaja, I., Newhall, C. G., & Herrin, J. S. (2015, Juli). A 5000-year record of multiple highly explosive mafic eruptions from Gunung Agung (Bali, Indonesia): implications for eruption frequency and volcanic hazards. *Bulletin of Vulcanology*, hal. 59.

Gamma Remote Sensing. (2007). *Interferometric SAR Processing.* Gümligen, Swiss: GAMMA Remote Sensing AG.

Geiger, H. (2014). *Characterising the magma supply system of Agung and Batur Volcanoes on Bali, Indonesia.* Uppsala: Uppsala University.

Goldstein, R. M., & Werner, C. L. (1998). Radar interferogram filtering for geophysical applications. *Geophysical Research Letters*, 4035-4038.

Hanssen, R. F. (2001). *Radar Interferometry* (Vol. 2). New York, US: Kluwer Academic Publishers.

Li, Z., & Bethel, J. (2008). Image Coregistration in SAR Interferometry. *The International Archives of the Photogrammetry, Remote Sensing and Spatial Information Sciences*, 433-438.

Masonnet, D., & Fiegl, K. L. (1998, November). Radar Interferometry and Its Application to Changes in the Earth's Surface. *Reviews of Geophysics*, pp. 441-500.

Mogi, K. (1958, March 31). Relations between the Eruptions of Various Volcanoes and the Deformations of the Ground Surfaces around them. *Bulletin of Earthquake*, pp. 99-134.

Moore, R. K. (1990). Ground Echo. In M. I. Skolnik, *Radar Handbook* (pp. 12.1-12.35). United States: McGraw-Hill.

Pepe, A., & Calò, F. (2017). A Review of Interferometric Synthetic Aperture RADAR (InSAR) Multi-Track Approaches for the Retrieval of Earth's Surface Displacements. *Applied Science*, 1264 (39).

Rosen, P. A., Hensley, S., Joughin, I. R., Li, F. K., Madsen, S. N., Rodríguez, E., & Goldstein, R. M. (2000, March). Synthetic Aperture Radar Interferometry. *Proceedings of IEEE, 88*, 333-382.

Saepuloh, A., Urai, M., Aisyah, N., Sunarta, Widiwijayanti, C., Subandriyo, & Jousset, P. (2013). Interpretation of ground surface changes prior to the 2010 large eruption of Merapi volcano using ALOS/PALSAR, ASTER TIR, and gas emission data. *Journal of Volcanology and Geothermal Research*, 130-143.

Sircar, S., Randell, C., Power, D., Youden, J., & Gill, E. (2003). Measuring 3D Ground Movement by Differential Interferometry: Technique and Validation. *IEEE NECEC*. Newfoundland & Labrador: IEEE.

Syahreza, S., Siddieq, H. H., Saepuloh, A., & Meilano, I. (2017). Deformation Monitoring of Pidie Jaya Earthquake using Pairwise Logic of Multitemporal Sentinel-1 SAR Data. *International Symposium on Earth Hazard and Disaster Mitigation (IESDM) 2017* (p. 020098 (7)). Bandung, Indonesia: AIP Publishing.

Tănase, R. (2011). *Unsupervised Segmentation in Heterogeneous Clutter Applied to Polarimetric SAR Interferometry.* Grenoble, France dan Bucharest, Romania: GIPSA Lab and Military Technical Academy.

TEMPORAL SURFACE TEMPERATURE OF AGUNG VOLCANO USING DAY AND NIGHTTIME OBSERVATIONS OF ASTER TIR

Adelina Nur Afiani[1,2], Asep Saepuloh[1,3], Ketut Wikantika[1,2]

[1]Center for Remote Sensing, Bandung Institute of Technology (ITB), Labtek IX-C Jl. Ganesha No. 10, 40132 Bandung, West Java, Indonesia
[2]Research Group of Remote Sensing and Geographic Information Science, Faculty of Earth Sciences and Technology, Bandung Institute of Technology (ITB), Labtek IX-C Jl. Ganesha No. 10, 40132 Bandung, West Java, Indonesia
[3]Research Group of Petrology, Volcanology, and Geochemistry, Faculty of Earth Sciences and Technology, Bandung Institute of Technology (ITB), Labtek IV Gedung Teknik Geologi Jl. Ganesha No. 10, 40132 Bandung, West Java, Indonesia

Email: adelinanurafiani@students.itb.ac.id; ketut@gd.itb.ac.id; saepuloh@gl.itb.ac.id

KEYWORDS: ASTER, thermal infrared, surface temperature, Agung volcano

ABSTRACT: A research using Thermal Infrared (TIR) remote sensing have been conducted at Agung volcano to analyze the temporal thermal characteristics in the crater. We collected and identified the surface temperature of Agung volcano prolong prior and post eruptions in 2017-2018. The land surface temperature is one of the crucial parameters for observing volcanic activities by the occurrence of temperature change anomalies in the crater surface. We used the Advanced Spaceborne Thermal Emission and Reflection Radiometer (ASTER) day and nighttime thermal infrared observations over Agung volcano for 18 years from February 2001 to July 2018. The surface temperature was obtained by Temperature and Emissivity Separation (TES) method. This method was also applied to reduce the effect of thermal inertia from the objects. According to the proposed method, the surface temperature of the ASTER nighttime observation at Agung volcano is 15 to 20°C in an intra-eruption period between 2001-2016. However, three months preceding the 21 November 2017 eruption, the maximum surface temperature at the summit increased to 34.93°C. Interestingly, the temperature decreased a week before the eruption to 28.41°C. Contrary, the highest surface temperature was obtained one day before the eruption on 28 June 2018 about 104.12°C. According to the visual interpretation of LANDSAT 8 image, a new incandescent lava extruded on 2 July 2018. Meanwhile, the ASTER daytime observed two weeks after the eruption of 25 November 2017 showed surface temperature at the summit about 105.99°C. The derived temporal surface temperature based on ASTER TIR provided prolong prior and post thermal signature to a new eruption phase of an active volcano.

INTRODUCTION

Agung Volcano is a strato-composite volcano located at 8º 20.5 ' LS and 115º 30.5' BT. The volcano is part of the Sunda Arc a and one of the active volcano that was recorded to have experienced the largest eruption in the past 1963-1964 after Krakatau in 1883 (Zen & Hadikusumo, 1964; Geiger, 2014). The 1963-1964 eruptions are considered as an important volcanic event of the 20th century since damaged extensive surface, included villages and cultivated areas and took thousands of lives. The 1963-1964 eruption emitted 0.95 km³ dense rock equivalent (DRE) of basaltic andesite tephra and andesite lava, which gained eruptive column height reached 28 km (Geiger,2014). Besides, the high amount of SO2 gas emitted during the 1963 eruption formed 11-12 million metric tons of H_2SO_4 aerosols in the stratosphere, which might be involved to the fall of 0.3°C in average temperatures in the northern hemisphere (Geiger, 2014). This eruption was started from 18 February 1963 and ended on the 27 January 1964 (Pratomo, 2006). According to the reports of Center for Volcanology and Geological Hazard Mitigation of Indonesia (CVGHM), after 54 years of quiescent period, Mount Agung again indicated an increase in seismic and volcanic activity in 2017 to 2018. At its peak, several eruptions were occurred on 21, 25, November and 24 December 2017 and 11 January, 11 March, 13 and 28 June 2018, and 2 July 2018 (Table 1).

Surface temperature is one of the crucial parameters for observing volcanic activities by the occurrence of temperature change anomalies on the crater surface (Saepuloh et al., 2013). Such anomalies may occur for many reasons, such as high reflected sunlight on surface, or natural (anthropogenic) signals (e.g., fires, smoke stacks), but at volcano this can be an indicator of volcanic activity or even a precursor to more explosive activity (Dehn & Harris, 2015). The anomalies occur when a pixel in a satellite image shows a higher temperature than is expected relative to its neighbors. This research was focused on the Mount Agung summit area in order to monitor and detect changes in the surface temperature during both quiescent and eruptive periods as shown in Figure 1.
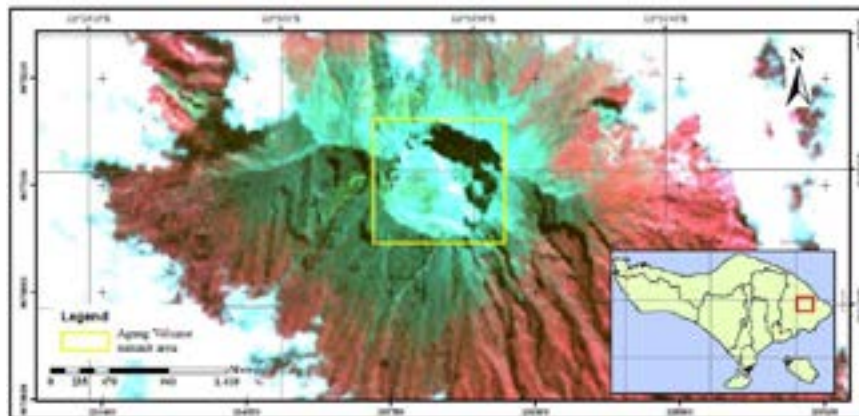
Figure 1. ASTER image acquired on 6 August 2012 shows Mount Agung, Bali summit crater area from RGB composite of ASTER VNIR bands. The yellow rectangle is the selected area for surface temperature analysis.

Table 1. Eruptive dates of Agung Volcano in 2017-2018

Eruptive events	
2017	21 November
	25 November
	24 December
2018	11 January
	11March
	28 June
	29 June
	2 July

In this research, surface temperature was obtained by processing ASTER (Advanced Spaceborne Thermal Emission and Reflection Radiometer) satellite imagery data. ASTER is one of the five sensors systems on-board the Terra platform launched in December 1999 as part of the NASA Earth Observing System (EOS). ASTER was provided by cooperative project of NASA, Japan's Ministry of Economy, Trade and Industry (METI), the National Institute of Advanced Industrial Science and Technology (AIST) in Japan, and Japan Space Systems (J-spacesystems) (Abrams, & Hook, 2000). It is known as available sensor acquiring images at high spatial resolution bands as shows in Table 2. From EOS-1 Terra Satellite, images have been acquired over the 18 year period between 2001 and 2018 for Mount Agung area. During this period number of eruptions have occurred with substantially different intensity and durations started by the quarter end of 2017 until mid-year 2018. Here we focus on the changes of temperature in the crater summit area of Agung Volcano as analyzed in 130 ASTER images, including 35 day and 95 nighttime observed images. Table 3 shows the entire ASTER Agung Volcano data collection reported in number of images per year, divided into day and nighttime acquisitions. The derived temporal surface temperature based on ASTER TIR provided prolong prior and post thermal signature to a new eruption phase of an active volcano.

Table 2. ASTER instrument characteristics (Buongiorno et al., 2013)

Instrument	VNIR		SWIR		TIR	
Bands and spectral range (μm)	1	0.52-0.60	4	1.60-1.70	10	8.125-8.475
	2	0.63-0.69	5	2.145-2.185	11	8.475-8.825
	3N	0.78-0.86	6	2.185-2.225	12	8.925-9.275
			7	2.235-2.285	13	10.25-10.95
			8	2.295-2.365	14	10.95-11.65
			9	2.360-2.430		
Spatial resolution (m)	15		30		90	
Swath width (km)	60		60		60	
Cross track pointing	± 318 km		± 116 km		± 116 km	
Quantisations (bits)	8		8		12	
Revisit time (days)	16		16		16	

Table 3. ASTER Data, Daytime and Nighttime Images

Year	Number of ASTER images daytime	Number of ASTER images nighttime	Year	Number of ASTER images daytime	Number of ASTER images nighttime	Year	Number of ASTER images daytime	Number of ASTER images nighttime
2001	1	2	2007	-	5	2013	1	4
2002	3	5	2008	1	7	2014	1	6
2003	4	3	2009	6	10	2015	3	5
2004	-	5	2010	1	5	2016	1	4
2005	-	8	2011	2	9	2017	6	4
2006	3	2	2012	2	8	2018	-	3

DATA PROCESSING METHOD

The ASTER data product that we used was ASTER L1B data (i.e., radiance at the sensor). The L1B was used because the images already resampled to the geometry of the appropriate UTM projection with the WGS84 Datum. In fact the ASTER Level-1B Registered Radiance at the Sensor product already contains radiometrically calibrated and geometrically co-registered data for the acquired channels of the three different telescopes of Level-1A data. In the other words, the Level-1B data set is produced by applying the radiometric calibration and geometric correction coefficients to the Level-1A (Buongiorno et al., 2013).

The suitable data for analysis was extracted, selecting 35 daytime and 95 nighttime cloud free ASTER images. The daytime data has less number of images than the nighttime data because the infrequent revisit time of ASTER's and cloud occurrence thus reduced the number of available ASTER observations for the assessments. To obtain the surface temperature of Mount Agung summit, several steps were conducted on TIR bands of ASTER data:

Orbital Correction – ASTER Level 1B image is an image that has georeferenced and has an orientation in the direction of the satellite path. However, even though this data has been georeferenced properly, ASTER has not been oriented to the north of the image so that it needs correction of the orbit value to adjust the direction of the image to face north precisely (True North). Orbital correction is done by rotating image data with a certain angle value. The angle used can be known from the header information in the ASTER image (Harris, 2013).

Thermal Atmospheric Correction – Radiation values received by the sensor not only come from the interaction of solar energy and objects, but also by atmospheric influences (e.g. absorption, scattering), so that the radiance values received by the sensor are likely to be distorted and do not reflect the radiant values emitted by the object. Therefore, to get the estimated temperature value that corresponds to the radiated emission of the object, it is necessary to conduct an atmospheric correction. In the case of thermal infrared data, the reflection and or scattering of solar radiation makes a negligible contribution to the total at-satellite radiance, thus, the at-sensor signal has to be corrected just for atmospheric up-welling radiation and atmospheric attenuation (Gonzales, 2018). This step was proceed using module generated by ENVI® 5.2. Since this research interested in surface temperature, the formula was (Harris, 2013):

$$L(\lambda, T_s) = \frac{[L(\lambda, T*) - L\_u\,(\lambda)]}{[\tau(\lambda)\varepsilon(\lambda)]} \dots\dots\dots\dots\dots\dots\dots\dots(1)$$

Where $L(\lambda, T_s)$ is the radiance of a black body at the surface, $L(\lambda, T*)$ is the radiance arriving to the sensor (corresponding to brightness temperature), $L_u(\lambda)$ the up-welling radiance from the atmosphere, and $\tau(\lambda)\varepsilon(\lambda)$ the transmissivity and emissivity. Transmissivity is the attenuation effect from the atmosphere, having a value of one for a perfectly transparent atmosphere, and zero for an opaque atmosphere; the radiance emitted by the surface and arriving at the sensor will be reduced by a factor described by the atmospheric transmissivity (Harris, 2013; Gonzales, 2018).
To estimate the upwelling atmospheric radiance and the atmospheric transmission, the module first estimates the temperature value for each pixel, then, a trend line is equipped to a scatter plot of radiance towards brightness temperature. The atmospheric upwelling and transmission are then derived from the slope and offset of this line (Gonzales, 2018).

Temperature Emissivity Separation, Emissivity Normalization – The surface temperature is retrieved by the Emissivity Normalization Method (Kealy and Hook, 1993) by using ENVI® 5.4. This method is applied because it can

separate the emissivity and temperature information in the data from the infrared thermal sensor. In addition, this method is a good choice to the images that have type of surfaces dominated by soil, and rocks (Kealy and Hook, 1993), while soil and rocks are the dominant types of surfaces area used in this study. The emissivity normalization method assumes a fixed emissivity value or an emissivity constant as an approach to produce output or output in the form of model emissivity and radiance temperature by calculating the temperature in each pixel on the thermal infrared channel of the iteration image. Furthermore, the highest temperature value for each pixel is used to calculate the emissivity value through the Planck equation. The emissivity constant used is 0.96 (Harris, 2018).

DETECTED SURFACE TEMPERATURES AT AGUNG VOLCANO

Using the described methods above, surface temperature were calculated for the area at the summit crater of Mount Agung from both the data sets. Figure 2 shows detected hot spot by ASTER TIR with TES method compared to visible band of Sentinel 2 and Landsat 8.
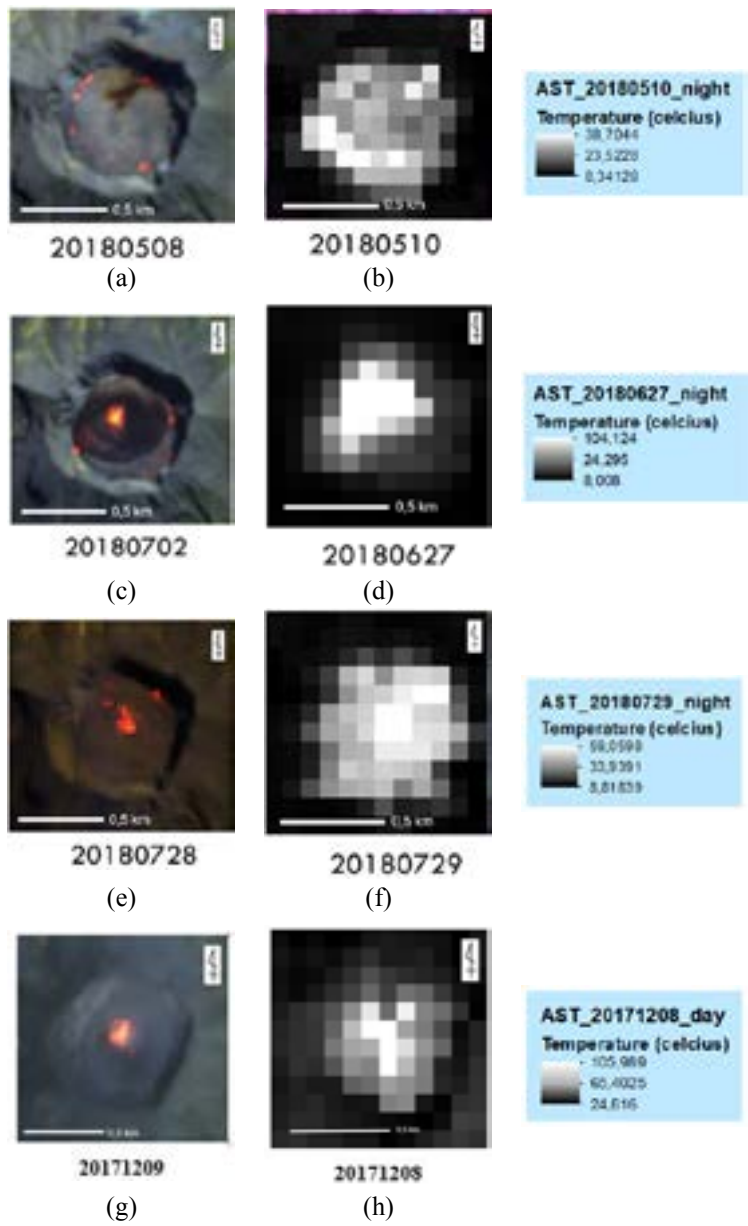
Figure 2. Hot spots detected by ASTER TIR with TES method (b; d; f; h) and compared to visible band of Sentinel 2 (a; c) and Landsat 8 (e; g) images.

Temperature in the summit crater from the nighttime data has constant temperature ranging from 15º to 20º celsius in 2001 until 2016 but began to experience a drastic increase beginning in 2017, August 11, reached $29,73^0$ celsius and still continues to increase until September 11, 2017 reached $34,93^0$ celsius. On November 15, 2017 or one week before the first eruption on November 21, 2017, the surface temperature has decreased back to $28,41^0$ celsius. This is probably due to the presence of scattered thin clouds over the summit crater area which may absorbs part of the emitted radiance toward the sensor. Meanwhile, the crater temperature has increased again on May 10, 2018 reaching $38,7^0$ celsius, until the highest temperature is reached on June 27, 2018, with 105.53º celsius or a day before the eruption of June 28, 2018. After compared the ASTER derived images with other satellite images (Sentinel 2 and Landsat 8) that can detect hot surfaces visually, it shows that the increase in temperature is caused by the presence of hot spots scattered in the crater wall and incandescent lava in the middle of the crater, as shown in the Figure 2.

As with the ASTER image acquisition on July 29, 2018, despite experiencing a decrease in temperature, the detected temperature is still above the average temperature with 59.06º celsius. This is due to the presence of lava areas after compared the visual with Landsat 8 image.

Figure 3 shows the graphic of the overall surface temperature on Gunung Agung crater as a result of the ASTER image temperature extraction during the day and nighttime . From the graph, the result of daytime data does not indicate a significant temperature change until December 8, 2017, where on 21 and 25 November 2017 Agung Volcano erupted. While significant temperature anomalies only seen on December 8, 2018 or two weeks after the eruption of November 28, 2017, showed that the surface temperature of the crater reached 105,989º celsius. Unfortunately, the surface temperature from daytime data in 2018 can't be obtained due to the high cloud coverage on the summit.

Besides that, the surface temperature obtained from ASTER images during the day shows more varied than the results from nighttime data, where temperature anomalies were detected and didn't relate to any volcanic activity of Mount Agung. Campbell et al. (2011), point out that variations of surface temperature on the daytime thermal acquisition image can be influenced by several things. First, the temperature anomaly rises due to the effects of solar heating, where during the day the surface of the crater absorbs and emits maximum heat from the sun to be received again by the sensor compared to night, so that the obtained temperature is higher than the average temperature. Second, low temperature anomalies can be caused by shadowing (shadow effects) formed by the topography of the object's surface or due to cloud cover when satellite coverage passes through the object's surface. This will block the direct sunrays and form darker observed areas thus reduce the surface temperature value.

Figure 3 shows the time series of ASTER derived surface temperature from nighttime and daytime observation:
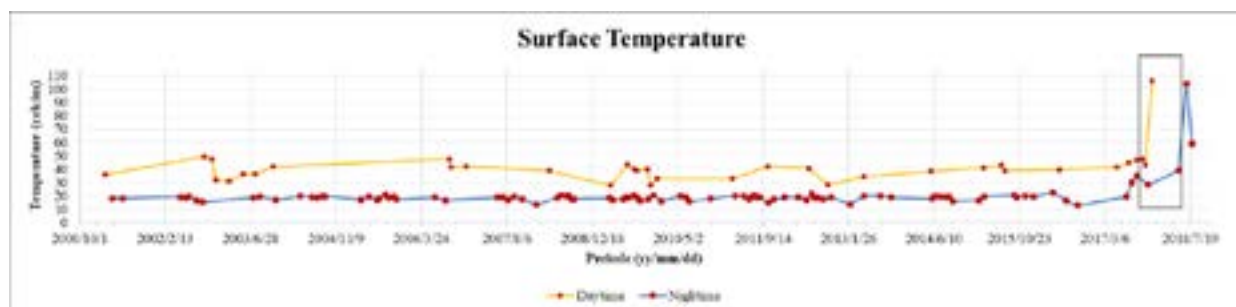

Figure 3. Time series of ASTER derived surface temperature from nighttime and daytime observation. The black rectangle describes for the main eruptive events as reported in Table 1.

CONCLUSIONS

From the results of the surface temperatures processing from 2001 to 2018 for ASTER daytime and nighttime images, shows that there are anomalies in the crater in 2017 and 2018, where at night images, the surface temperature continues to rise September 2017 to July 2018. As for the daytime images, temperature anomalies occur in the acquisition of December 2017. This is due to an increase in volcanic activity of Mount Agung which is marked by the appearance of hot spots on the surface of the crater. By comparing with Landsat 8 and Sentinel 2 satellite images, these hot spots were identified as incandescent lava that appears after eruptions occurred.

ACKNOWLEDGMENTS

REFERENCES

Abrams, M. and Hook, S., 2000. ASTER User Handbook. Version 2. Jet Propulsion Laboratory.

Buongiorno, M.F., Pieri D., Silvestri M., 2013. Thermal Analysis of Volcanoes Based on 10 Years of ASTER Data on Mt. Etna. Thermal Infrared Remote Sensing, pp.409-428.

Campbell, James B., & Wyne, R.H., 2011. Introduction to Remote Sensing Fifth Edition. London, Guilford Press.

Dehn, Jonathan, and Andrew J. L. Harris. Thermal Anomalies at Volcanoes. In: Monitoring Volcanoes in the North Pacific, 2015, pp.49–78

Geiger, Harri, 2014. Characterising the magma supply system of Agung and Batur Volcanoes on Bali, Indonesia. Uppsala, Department of Earth Sciences, Geotryckeriet.

González, L.M. Ramírez, 2018. Remote sensing of surface hydrothermal alteration, identification of minerals and thermal anomalies at Sveifluháls-Krýsuvík high-temperature geothermal field, SW Iceland. Iceland, University of Iceland.

Harris Geospatial Solutions, Documentation Center Using ENVI. Retrieved 29 January 2018, from https://www.harrisgeospatial.com/docs/AtmosphericCorrection.html

Kealy, P.S., dan Hook, S.K. 2013. *Separating Temperature and Emissivity in Thermal Infrared Multispectral Scanner Data: Implications for Recovering Land Surface Temperatures.* IEEE Transactions on Geoscience and Remote Sensing, Vol. 31, No. 6.

Saepuloh A., Urai M., Aisyah N., Sunarta, Widiwijayanti C., Subandriyo, Jousset P., 2013. Interpretation Of Ground Surface Changes Prior To The 2010 Large Eruption Of Merapi Volcano Using ALOS/PALSAR, ASTER TIR And Gas Emission Data. Journal of Volcanology and Geothermal Research, Vol. 261, pp.130-143.

Zen, M. T. & Hadikusumo, D., 1964. Preliminary report on the 1963 eruption of Mt. Agung in Bali (Indonesia). Bulletin of Volcanology, 27, pp.269-300.

LANDSAT 8 SATELLITE DATA-BASED HIGH-RESOLUTION VEGETATION MAPPING IN HOKKAIDO, JAPAN

Ram C. Sharma (1), Hidetake Hirayama (2) and Keitarou Hara (1)

[1] Department of Informatics, Tokyo University of Information Sciences, 4-1 Onaridai, Wakaba-ku, Chiba 265-8501, Japan
[2] Graduate School of Tokyo University of Information Sciences, 4-1 Onaridai, Wakaba-ku, Chiba 265-8501, Japan
Email: sharma@rsch.tuis.ac.jp; h17002hh@edu.tuis.ac.jp; hara@rsch.tuis.ac.jp

KEY WORDS: Vegetation; Mapping; BIC; Landsat 8; Machine learning; Hokkaido

ABSTRACT: High resolution satellite data are important source of information for assessing and monitoring of vegetation conditions. This research assesses potential of the Biophysical Image Composite (BIC) for the classification and mapping of vegetation types in the eastern part of the island of Hokkaido, Japan. The island of Hokkaido, Japan's coldest region, is located at the north end of Japanese archipelago. It is one of the most affected region by the effect of global warming in Japan. This research deals with the classification of major vegetation types: forests, crops, grasses, and non-vegetation (urban, water, and barren) of the study area. Ground truth data were prepared with reference to the Google Earth imagery. Four machine learning classifiers, k-Nearest Neighbors, Random Forests, Support Vector Machines, and Multi-layer Perceptron, were assessed for the classification of vegetation types with the support of ground truth data. Confusion matrix, overall accuracy, and kappa coefficient calculated with the validation data were used as the metrics for quantitative evaluation. The best performed classifier was employed for the production of vegetation map in the study area. The methodology and the results presented in the research are expected to contribute to the mapping of vegetation types in other regions as well.

1. INTRODUCTION

While massive volumes of multi-temporal satellite images are being collecting with the increase in Earth-observing satellites, image compositing techniques are vital to the extraction of concise biophysical information from the massive volume of satellite data (Sharma et al., 2018).

Landsat 8, an Earth observation satellite, has been collecting high resolution (15-100m) multi-spectral images over the global land surface with a standard 16-day repeat cycle (Irons et al., 2012; Roy et al., 2014). Landsat 8 consists of two sensors, Operational Land Imager (OLI) and Thermal InfraRed Sensor (TIRS); and collects image data for nine visible-shortwave bands and two thermal bands (www1). Landsat data archives have been re-organized into a tiered collection to ensure a consistent archive of known data quality to support time-series analyses and data stacking, and the collection consists of three categories, Tier 1, Tier 2, and Real-Time (www1). Data in Tier 1 are the highest quality data available, and they are considered suitable for time-series analysis. The geo-registration of Tier 1 scenes is consistent and within prescribed image-to-image tolerances of $\leqq$ 12-meter radial root mean square error (www1). Earth Explorer (www2) is the primary search interface to access Landsat data products.

The Normalized Difference Vegetation Index (NDVI) is a common technique for the detection and discrimination of vegetation types (Rouse et al., 1974; Tucker, 1979). The NDVI is the normalized difference between the near infrared (Nir) and red (Red) reflectance. However, only the NDVI may not be sufficient to derive biophysical information about the surface of Earth. In our previous, we developed a Biophysical Image Composite (BIC) for simultaneous visualization and extraction of the major biophysical components, barren/urban, vegetation, and snow/water areas, on the surface of Earth (Sharma et al., 2016). The BIC is a RGB (red, green, blue) color composite image made up of Normalized Difference Vegetation Index (NDVI), short wave infrared reflectance, and green reflectance, which were specially selected from the day of highest vegetation activity over an entire year. The procedure of deriving the Biophysical Image Composite (BIC has been illustrated in Figure 1.
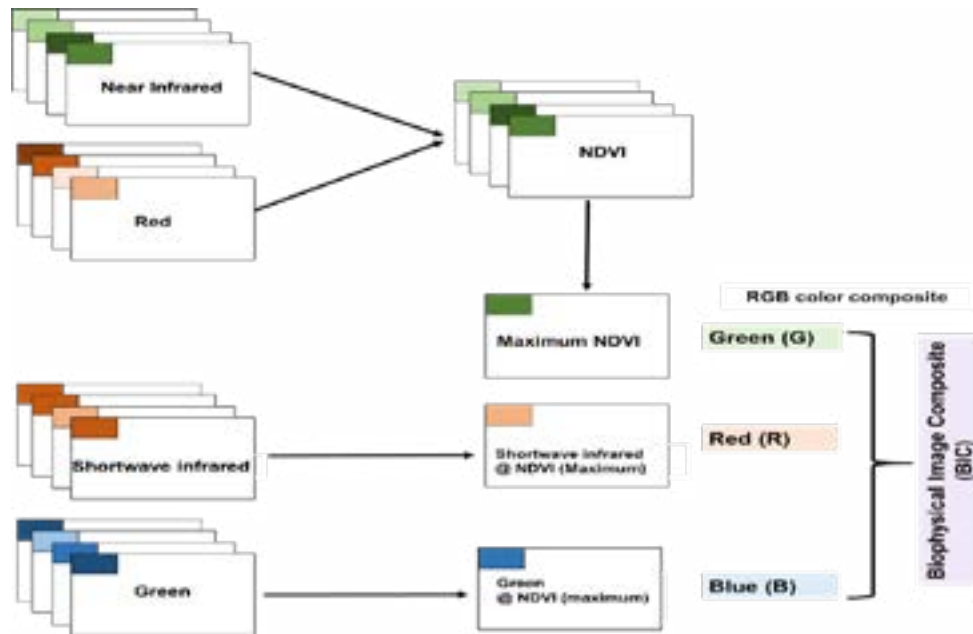
Figure 1. The procedure of creating the Biophysical Image Composite (BIC) using time-series of the Landsat 8 data over an entire year (Sharma et al., 2016).

The major objectives of the research were as follows:

    i.   Evaluate the potential of the BIC for the classification and mapping of vegetation types in Hokkaido

    ii.   Assess the performance of different machine learning classifiers for vegetation classification using the BIC

    iii.   Produce vegetation map for the study area using the BIC

2. MATERIALS AND METHODS

2.1 Study Area

This research was carried out in the eastern part of the island of Hokkaido, Japan. The island of Hokkaido, Japan's coldest region, is located at the north end of Japanese archipelago. It is one of the most affected region by the effect of global warming in Japan. Compared to the national average of 1.09°C, the average winter temperatures have risen by 1.33°C over the last century (www3). It represents a transitional zone between cool temperate forests, consisting of oaks, ashes, and conifers to the south, and the sub-arctic ecosystems to the north (www4). In the context of global warming, study of distribution and mapping of vegetation is relevant in the region which is dominated by subarctic climate. The location of the study area is shown in Figure 2.
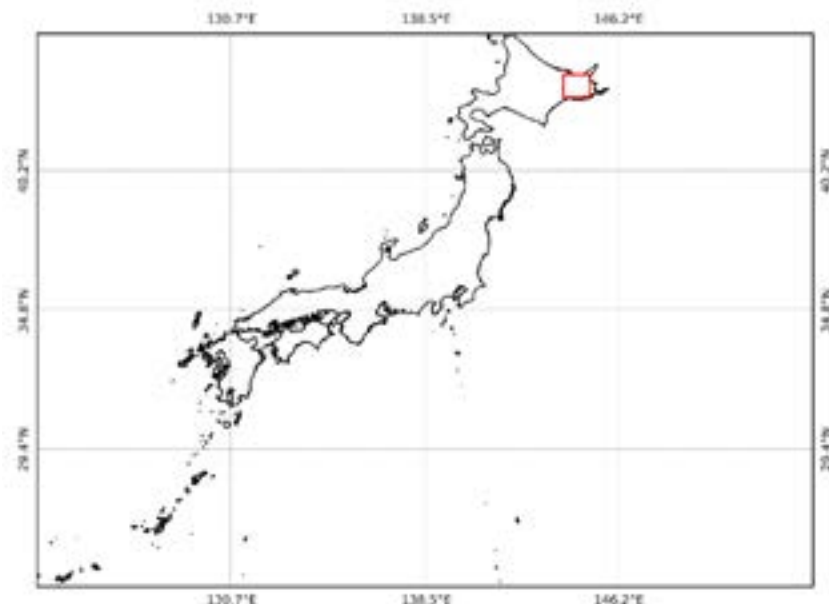
Figure 2. Location of the study area (red polygon) displayed over the country map of Japan.

2.2 Preparation of ground truth data

This research deals with the classification of the following major vegetation types of the study area: forests, grasses, crops, and non-vegetation (water, urban, and barren). In the research, the crops refers to dry crops, paddy, and grazing pastures. Ground truth data were prepared with reference to the Google Earth Imagery (www5). In total, 500 reference points, representing a homogenous area of 90×90m, were prepared for each class.

2.3 Processing of Landsat 8 data

We used all Landsat-8 scenes under the Tier 1 collections, available for the study area in 2017, to generate the BIC. Landsat-8 data were converted into top-of-atmosphere (TOA) spectral reflectance using the rescaling coefficients found in the metadata file; and the clouds were removed by using separate quality assessment (QA) band information available in the Landsat-8 data. The procedure of generating the BIC has been illustrated in Figure 1.

2.4 Machine learning and mapping

Four machine learning classifiers: k-Nearest Neighbors, Random Forests, Support Vector Machines, and Multi-layer Perceptron (www6), were assessed for the classification of vegetation types. Out of 500 ground truth points, 280 points were used as the training data, whereas remaining 220 points were used as the validation data. Confusion matrix, overall accuracy, and kappa coefficient calculated with the validation data were used as the metrics for quantitative evaluation. Further details on the machine learning and mapping have been described in previous study (Sharma et al., 2017). The best performed classifier was employed for the production of vegetation map in the study area.

3. MATERIALS AND METHODS

3.1 Biophysical Image Composite (BIC)

The BIC generated for the study area is shown in Figure 3. With reference to the Google Map Image (Figure 4), the BIC is capable of discriminating forest (greenest), grass (red/yellow), crops (greener), and non-vegetation (reddest/bluest) classes.

**Figure 3.** 30m resolution Biophysical Image Composite (BIC) of the study area of 2017.

The Google Map based true-color image (Figure 4) was provided for the visual discrimination between vegetation types as our eyes are intrinsically trained for distinguishing the vegetation types in nature.

Figure 4. Google Map Image (2017-10-06), © CNES/Airbus, DigitalGlobe, of the study area.

3.2 Performance of the classifiers

The performance of different machine learning classifiers: k-Nearest Neighbors, Random Forests, Support Vector Machines, and Multi-layer Perceptron for the classification of vegetation types using the BIC has been demonstrated in Figure 5. Among the classifiers tested, the Random Forests (RF) classifier provided the best performance (Overall accuracy=0.82; Kappa coefficient=0.76) with the validation data.
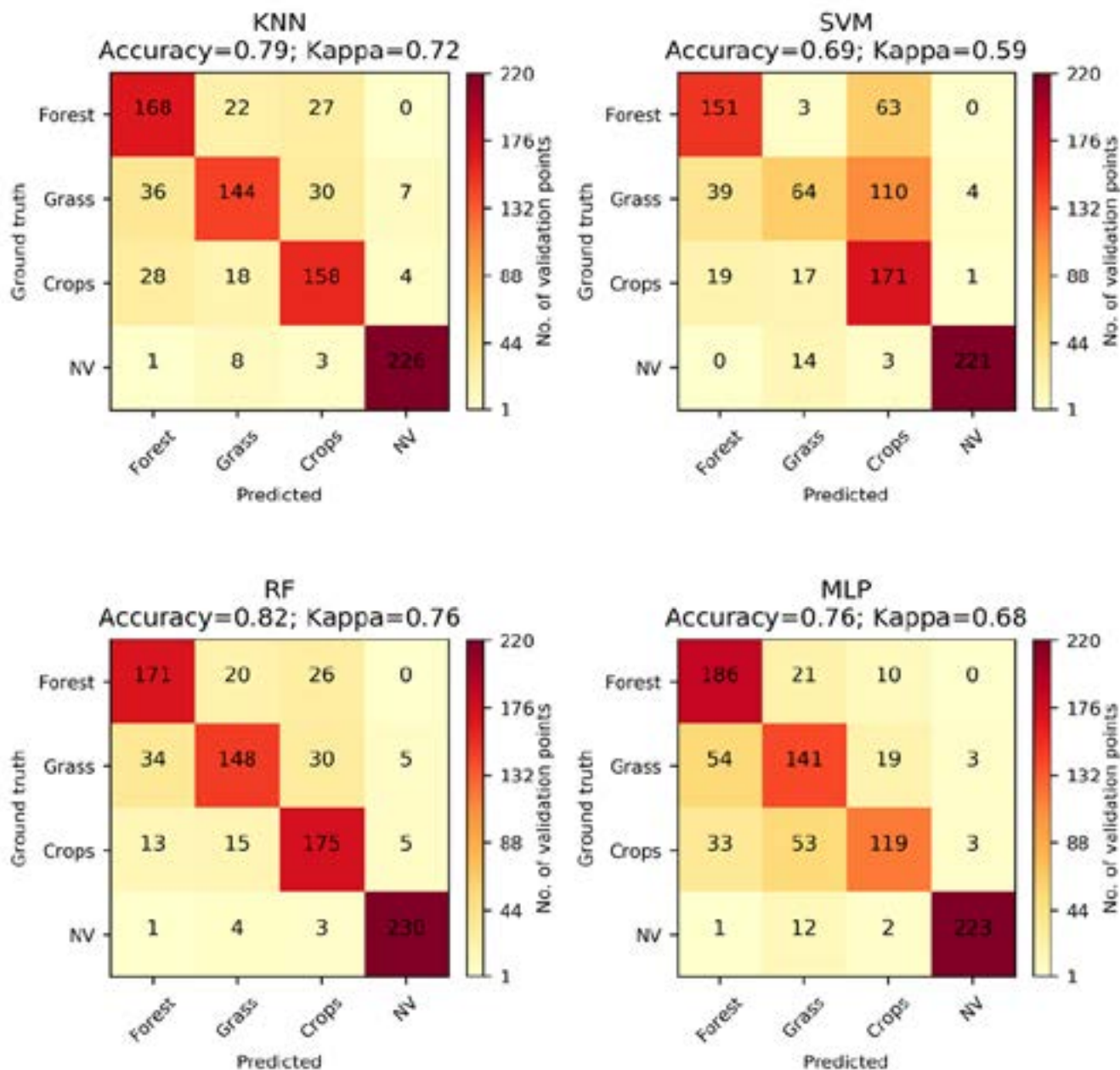
Figure 5. Performance of different machine learning classifiers: k-Nearest Neighbors (KNN), Random Forests (RF), Support Vector Machines (SVM), and Multi-layer Perceptron (MLP) for the classification of vegetation types, forests, grasses, crops, and non-vegetation using the BIC.

3.3. Vegetation map of the study area

The Random Forests classifier was employed for the production of vegetation map in the study area. The resulted vegetation map has been plotted in Figure 6. The map was capable of even visualizing the minor details on the distribution of small patches of forests and urban built-up areas. Such a finer mapping of the land cover types is suitable for landscape connectivity analysis.
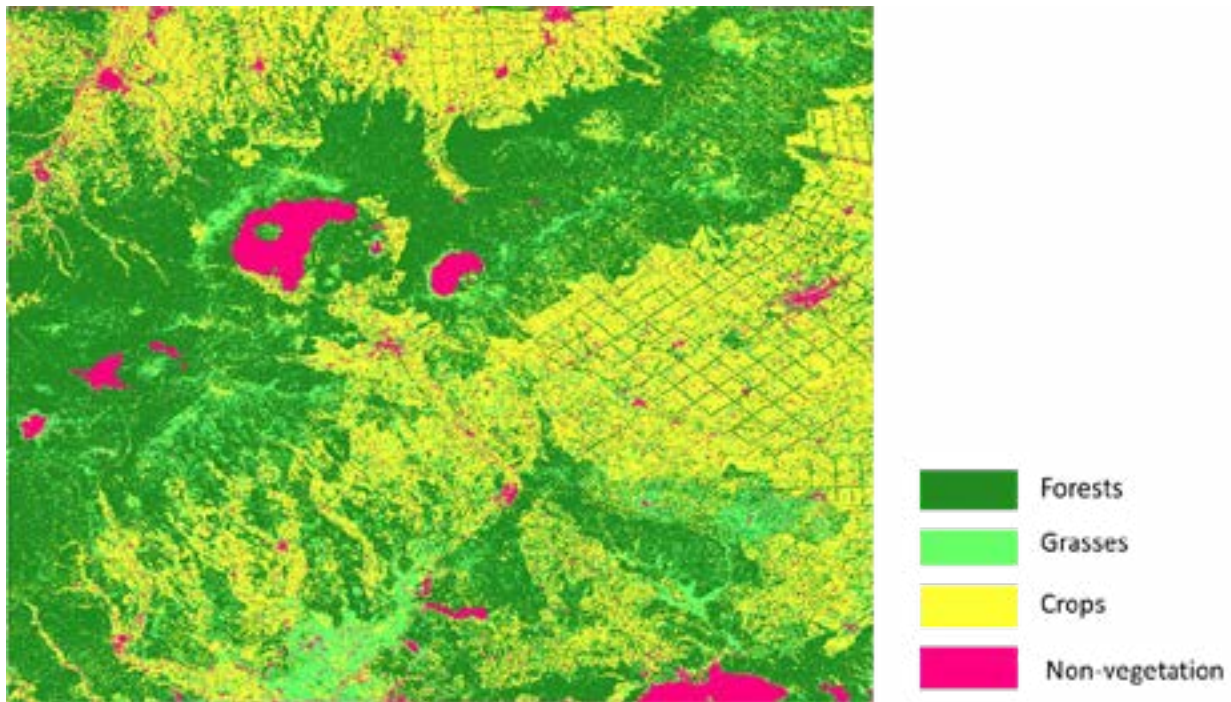
Figure 6. 30m resolution Vegetation Map of 2017 produced in the research by using the BIC.

4. CONCLUSION

The BIC offers an opportunity of reducing massive volumes of the satellite data into a concise (3-layered seamless mosaic) output. In this research, the potentiality of the BIC for the classification and mapping of vegetation types in the eastern part of the island of Hokkaido, Japan was assessed with the support of reference data prepared in the research. Among the four machine learning classifiers, k-Nearest Neighbors, Random Forests, Support Vector Machines, and Multi-layer Perceptron Neural Networks examined for vegetation classification using the BIC, the Random Forests (RF) classifier provided the best performance (Overall accuracy=0.82; Kappa coefficient=0.76).The BIC was developed for discrimination of the barren/built-up areas from vegetative and water/snow areas; and it was successfully applied for the extraction of barren areas on the global level (Sharma et al., 2016). However, results from this research presents applicability of the BIC for the classification and mapping of major vegetation types (forests, grasses, crops, and non-vegetation) as well. Nevertheless, its applicability in different climatic zones for the mapping of vegetation types is a subject of future research. Further improvement of the classification accuracy by reducing salt-and-pepper noise with aggregation of multiple classifiers is recommended.

Acknowledgements

References

Irons, J.R., Dwyer, J.L., Barsi, J.A., 2012. The next Landsat satellite: The Landsat Data Continuity Mission. Remote Sensing of Environment 122, 11–21. https://doi.org/10.1016/j.rse.2011.08.026

Rouse Jr, J., Haas, R., Schell, J., Deering, D., 1974. Monitoring vegetation systems in the Great Plains with ERTS

Roy, D.P., Wulder, M.A., Loveland, T.R., C.E., W., Allen, R.G., Anderson, M.C., Helder, D., Irons, J.R., et al., 2014. Landsat-8: Science and product vision for terrestrial global change research. Remote Sensing of Environment 145, 154–172. https://doi.org/10.1016/j.rse.2014.02.001

Sharma, R., Tateishi, R., Hara, K., 2016. A Biophysical Image Compositing Technique for the Global-Scale Extraction and Mapping of Barren Lands. ISPRS International Journal of Geo-Information 5, 225. https://doi.org/10.3390/ijgi5120225

Sharma, R.C., Hara, K., Hirayama, H., 2017. A Machine Learning and Cross-Validation Approach for the Discrimination of Vegetation Physiognomic Types Using Satellite Based Multispectral and Multitemporal Data. Scientifica 2017, 1–8. https://doi.org/10.1155/2017/9806479

Sharma, R., Hara, K., Tateishi, R., 2018. Developing Forest Cover Composites through a Combination of Landsat-8 Optical and Sentinel-1 SAR Data for the Visualization and Extraction of Forested Areas. Journal of Imaging 4, 105. https://doi.org/10.3390/jimaging4090105

Tucker, C.J., 1979. Red and photographic infrared linear combinations for monitoring vegetation. Remote sensing of Environment 8, 127–150

www1. https://landsat.usgs.gov/landsat-8-data-users-handbook

www2. https://earthexplorer.usgs.gov/

www3. https://www.wwf.or.jp/activities/lib/pdf_climate/environment/WWF_NipponChanges_lores.pdf

www4. https://www.worldwildlife.org/ecoregions/pa0423

www5. http://earth.google.com/

www6. http://opencv.org

SUSTAINABLE WATER MANAGEMENT IN SERAYU CATHMENT AREA IN SUPPORTING POTENCY OF ELECTRICAL ENERGY MICROHYDRO BANJARNEGARA REGENCY CENTRAL JAVA PROVINCE

By

Jaka Suryanta[1], Rizka Windiastuti[2], Tia Rizka N. Rachma[3] and Irmadi Nahib[4]

Researcher in Badan Informasi Geospasial (BIG)
E-mail: jakaeriko@gmail.com ,
Jalan Raya Jakarta – Bogor KM 46 Cibinong - Indonesia
Telp/Fax: +62-21-8790-6041

ABSTRACT

There are 94 points of licensing of microhydro power plant (PLTMH) in Banjarnegara District from 100 KW to thousands KW, both operational and non operational, excluding larger ones such as in Mrica reservoir. The principle of hydroelectricity is the existence of a stable water flow throughout the year and a sufficient height difference for turbine power. To support these conditions, sustainable land management is needed to ensure that water is always available. Kabupaten Banjar Negara has 18655.78 ha of forest area but 40.56% has become plantation even in its 6.3% protected forest area changed function for seasonal crops, vegetables and caribou trees and other plants, it is feared to affect the flow stability water. Agroforestry is an efficient and ecologically beneficial agroforestry example but not significant percentage needs to be improved in order to maintain the land. This study aims to calculate the area of deviation of land use in forest area and to estimate water availability for microhido. The method used is overlay map of forest area and landuse map whereas to calculate the potential of water flow used Wflow. The results of the study indicate the existence of vegetation types and other uses that deviate from the function of forest area. Forest cover in protected areas remained 2.5% and 6% in the form of plantations, whereas in forest HPT-HPK still 13%, shrubs 20.4%, plantations 40.6% in KSPA estates 0.3%, other shrubs and bushes. Runnof flow reaches 345mm in december down to 100 mm in June. River flow in order 3 and the height difference (head) is still potential for micro hydro power (100 kw). The Wanatani management model can help community and environmental management, strict supervision is required where slope above 40% is not recommended for potato plantations. Meanwhile, the area under it can be processed with the principle of agroforestry that is by mixing potato plantations with other perennials.

Keyword : PLTHM, watershed, wanatani, potatoes.

Background

Banjarnegara regency covers an area of 1,023.73 km², and it had a population of 1.170.292 at the 2016 Census [1] (BPS Banjarnegara 2016); the latest official estimate is more than 1,2 millions. The disturbance of the ecological balance of Serayu watershed upstream has an impact on watershed environmental degradation which is indicated by the large fluctuation of water balance between season and river contamination by chemicals. The problem of water quantity and quality is known as 3T namely; too much (too much flood, erosion and landslide), too little (drought) and too dirty (water pollution by chemicals

and sedimentation). The occurrence of extensification of land with seasonal crops not accompanied by reforestation or rejuvenation has led to massive deforestation resulting in environmental degradation [2] (Biswas, A. K. 2004). The forest vegetation is diminishing due to land conversion for agriculture, it has also resulted in ecosystem destruction and reduced levels of upstream biodiversity. Whereas forest areas have unique characteristics that can provide protection to the surrounding area and below, as a regulator of water systems, flood prevention and erosion and maintaining soil fertility.

The abundance of plantations in the upper of Serayu watershed with parallel slope planting methods has been applied by farmers resulting in the rapid flow of rainwater down and transporting more materials and accelerating the rate of erosion. The soil's ability to infiltrate and percolate decreases thus increasing surface runoff. The subsequent impacts are the decrease of land productivity, as well as the ability of the soil to retain water as a result of the Upper Serayu basin area prone to landslides and flash floods. Even the great flash floods once hit the Tieng Village, Kejajar Subdistrict, Wonosobo in 2011, flooding occurred in the flow of the river Grobok (tributary of Serayu). A flash flood from the hill that hit the village caused loss of property and loss of life, and caused 75 families to evacuate. While landslides, often every rainy season on the other side during the dry season, ground water is not enough to meet the needs of the community due to less storage in the rainy season. The impact already felt by farmers is the increasingly limited water resources because the groundwater reserves continue to decrease. The high population density (approximately 1000 inhabitants / km²) with low land tenure has caused pressure on protected areas and resulted in a significant shifting of land functions. This land conversion resulted in land degradation, of which around 4,758 hectares in Banjarnegara and 3,000 hectares in Wonosobo have become critical land. Potatoes are grown on thin soil solum but the land is still capable of producing because it is fueled by chemical fertilizers and pesticides in large doses. In addition to polluting the environment, the use of chemical fertilizers and excessive pesticides also poison potato crops so that many potatoes contain chemicals. The slope of the upland serayu basin is between 35% and more than 45% so farmers use terracing system. However, excessive tillage even reaching the tops of the hills, some using the contour parallel system in the absence of perennial crops have made the Dieng farmland also prone to erosion. The erosion rate has reached 161 tons / hectare / year and caused the sedimentation to flow into the river. Erosion in the Upper Serayu watershed caused sediments in the Sudirman, Mrica, Banjarnegara, reservoir since 1989. The sinking level in this reservoir has reached 60.106 m3 or 40% of the reservoir capacity. Addition of sediment in 2000 reached 7.106m3 in the event of massive deforestation in the Dieng plateau. This sedimentation has even decreased the productivity of Sudirman water power plant (Banjarnegara) and Garung water power plant (Wonosobo), another impact that will happen is the unstable supply of water in hundreds of PLTMH in Banjar Negara area. The upstream Serayu watershed currently represents social, economic and environmental problems [3]   (Widayati, T et al 2017), but it must be sought to solve the problem with the hope that the community still exists economically and minimizes the environmental damage. Other agro-forestry and plantation systems use much of the forest area which is a collaboration between the community and the owners of capital, but it is necessary to increase the obligation to maintain timber stands for each potato garden plot, in order to reduce erosion and maintain groundwater filling. Land cover conditions in forest areas are an indication of the success of Serayu watershed management, as it greatly affects groundwater storage and surface flow.

Research purposes

> • Calculate non-synchronized land use/cover in forest areas.

> • Calculate the potential runoff in supporting Micro Hidro Serayu Sub_watershed, especially in

Banjar Negara State.

Method

Tools and materials
Map of RBI scale 1: 25.000
Map of forest area
Rainfall data
Satellite Landsat data 2015
Landuse / cover map scale 1: 25.000
Distribution of microhydro potential points
Watershed Management adheres to the principle of integration of "one planning system within a watershed [4] (Suprapto, M. (2010). Highly related components are hydrological, vegetation, environmental, socioeconomic and institutional governance conditions among sectors. The SCS method uses these variables and is suitable for calculating surface flow.
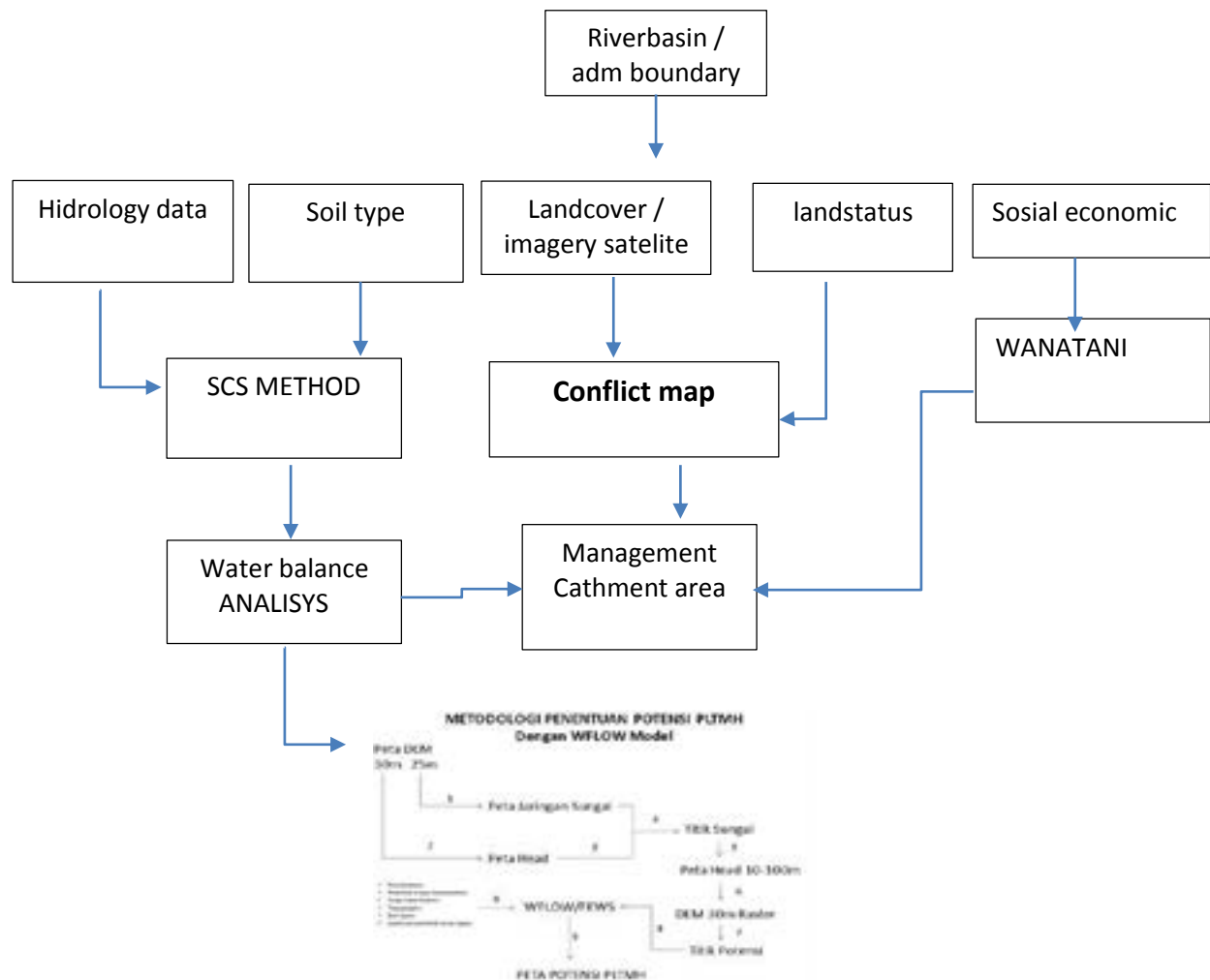
Figure 1.1 Research flow diagram

The existence of the forest sector in the upstream areas that are well managed and sustainably maintained and supported by central infrastructure and facilities will be sufficient for downstream watershed and

non-basin needs [5] (Laila, N.et al, 2015). To maintain the balance is required Government and private institutions that regulate the mechanism of maintenance and compensation to meet the social economic needs of the upstream. In principle, this institution can regulate how the upstream part of the forest and water and get compensation from downstream and outside the watershed that utilize water. This institution also maintains the administrative and consistency of spatial implementation so that it is necessary to coordinate various stakeholders in cross-sectoral and trans-regional areas actively. In this series of processes satellite imagery can be utilized to monitor land cover especially in conservation areas and assisted equipment Geographic information systems [6]   (Gauzan, H. 2009) will facilitate the identification of vital objects that change within the watershed. To identify conflicts of interest that can degrade environmental conditions an overlay analysis is made between the status map of the area and the land cover map. Furthermore, these findings provide input for policy makers in managing the Watershed.

Results and Discussion

- Land conflicts

Banjarnegara regency covers an area of 1,023.73 km², has a cultivated area of 83717.2163 ha (81.88%) with forest area of 18655,7837 ha (18.22%) has occurred land use less suitable for its purpose. To know the type of plant in the forest area, intersect between land use map resulted from satellite image interpretation with map of forest area and the result showed in limited production forest (HPT) and conversion forest even in asylum area (KSPA) and protected forest area (HL) many utilization which is less functional. The existence of moor, settlement and plantation including in potato, karika and other plantations, table 3.1 below the data of land use area in forest area and picture 3.1 shows the result of landuse overlay with forest area.

Figure 3.1 overlay forest area and landuse map

Table 3.1. Area of land use in Upper Serayu forest zone

No	forest zone	land use	area (ha)	area (%)
1	HL	bushes	355,6356	1,906302

2	HL	forest	464,1357	2,487892
3	HL	waters / rivers	2,6912	0,014425
4	HL	plantation	1177,8659	6,313677
5	HL	settlement	0,2558	0,001371
6	HL	regular settlements	1,5999	0,008576
7	HL	swamp	3,4674	0,018586
8	HL	grass	71,0721	0,380966
9	HL	rice fields	7,9372	0,042545
10	HL	rain-fed rice fields	5,6578	0,030327
11	HL	moor	340,5590	1,825488
12	HPT-HP-HPK	bushes	3814,8895	20,44883
13	HPT-HP-HPK	forest	2425,8842	13,00339
14	HPT-HP-HPK	waters / rivers	44,5909	0,239019
15	HPT-HP-HPK	plantation	7571,8050	40,5869
16	HPT-HP-HPK	settlement	1,6776	0,008992
17	HPT-HP-HPK	regular settlements	8,1593	0,043736
18	HPT-HP-HPK	grass	112,7882	0,604575
19	HPT-HP-HPK	rice fields	17,7524	0,095158
20	HPT-HP-HPK	rain-fed rice fields	81,8055	0,438499
21	HPT-HP-HPK	moor	2034,8504	10,90734
22	KSPA	bushes	16,2105	0,086893
23	KSPA	lake/setu	9,8528	0,052814
24	KSPA	plantation	56,1186	0,300811
25	KSPA	grass	26,6353	0,142772
26	KSPA	moor	1,8859	0,010109
		amount	**18655,7837**	**100**

Source: analysis 2017

Forest cover in protected areas is only 2.5% and 6% in the form of plantations, whereas in HPT-HP-HPK forest is still 13%, shrubs 20.4%, plantations 40.6% in KSPA estates 0.3%, others are shrubs and bushes.

Distribution of rainfall

Rainfall in banjarnegara reaches 100 - 500 mm / month in wet season ie november to end of maret, while when dry season drop to under 50mm / month even no rain. This fluctuating condition greatly affects runoff and groundwater filling, so the role of forests and other vegetation is essential in maintaining the flow of surface and groundwater filling.

Isohyet map Figure 3.2 below shows a fairly wet annual rainfall where in the upper watershed reaches an average of a maximum of 4000mm / year, this is also reflected in the permanent river flow for most of the year despite fluctuations.

Figure 3.2. map The annual rainfall distribution of Serayu watershed (Isohyet)

Runoff calculation

Based on the precipitation conditions above then calculated the surface flow by the SCS- CN method, because the method is quite simple but the result shows a strong relation between rain and surface flow [7] (Tikno.S et al 2016). SCS-CN method uses several variables such as soil conditions, rainfall, and vegetation type of land cover, in this case the result shows fluctuations between 0.0 - 200 mm or when multiplied by the cachment area of 0.0 – 189,6 m3 / s shown in Figure 3.3. The discharge data of small rivers is not recorded by the relevant authorities, in this case attempting to calculate the current in the 3rd order sub-watershed with a result of 0.02-0.4 m3 / s depending on the area of each sub-catchment, shown in Figure 3.4 below.
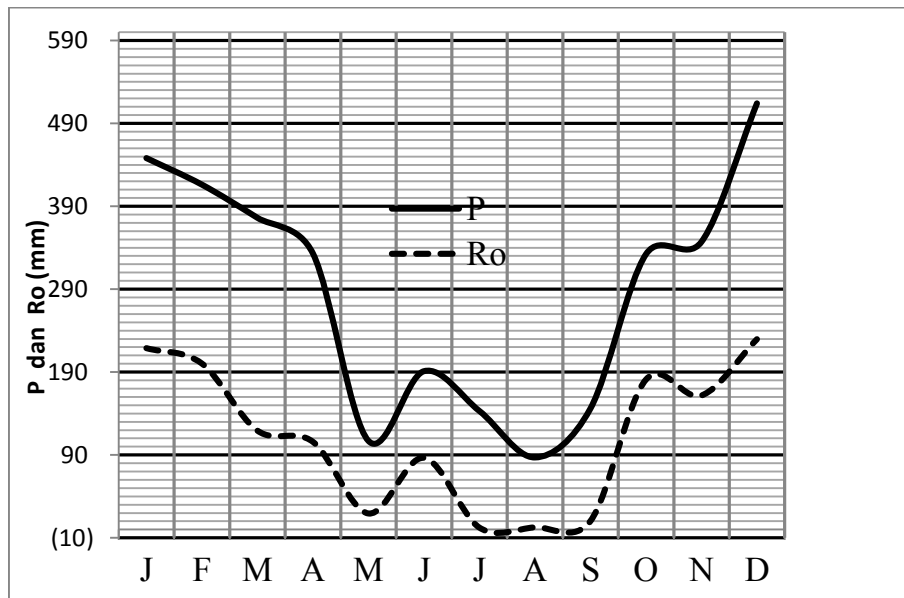
Source: analysis 2017

Figure 3.3 Serayu River Basin runoff with SCS method

Figure 3.4. surface flow discharge on the river of orde 3 Serayu River Basin

The potential surface flow of calculations on the sub watershed of the ordo3 river is equivalent to the water power of the PLTM turbine player with a capacity of approximately 100 Kw- 1MW. In real terms based on the data distribution field has been shown in Figure 3.5. in the form of distribution of PLTM position points, capacity and permissions.

Figure 3.5. distribution of PLTM points in Banjarnegara regency

Table 3.2. PLTMH name and capacity and Permission note number.

Discussion

No	Name	Type	River	Capacity (kwh)	Company	Permission Note number
10	PLTM Ambal	PLTM		2100	PT Nureco Tirta Banjarnegara	503.01/214/KP2T/2015 Tgl 5 Feb 2015
12	PLTMh Singgi	PLTMH		400	PT Naluri Energi Utama	503.1/3938/09
24	PLTM Tanjungtirta	PLTM		9000	PT Maji Baru Pusaka	503.1/2857/2012 Tgl 28 Agu 2012
25	PLTM Majasari	PLTM		6600	PT Aqua Hidro Perkasa	503.01/2596/KP2T/2013 Tgl 22 Juli 2013
26	PLTM Tegaljeruk	PLTM	S Jawar	8000	PT Illanur Hidro	503.01/1030/2014 Tgl 18 Des 2014
27	PLTM Tempuran	PLTM	S Merawu, Bojong	1500	PT Putra Tirta Nusantara	503.01/4344/2013 Tgl 19 Des 2012
28	PLTM Panaraban	PLTM	S Panaraban	5000	PT Daya Hidro Energi	503.01/2997/KP2T/2019 Tgl 31 Agu 2013
29	PLTM Sirukem	PLTM	Merawu	1000	PT Istana Niaga Pratama	503.1/791/KP2T/2014 Tgl 14 Nov 2014
30	PLTMH Kalipelus	PLTMH		450	PT Bina Pertiwi	503.01/651/KP2T/2013 Tgl 29 Feb 2013
31	PLTM Pandanarum	PLTM	K Gintung	8000	PT Hidro Berkah Energi	503.1/651/KP2T/2013 Tgl 28 feb 2013
32	PLTM Pandansari	PLTM	K Merawu	6000	PT Putra Tirta Nusantara	503.01/3197/KP2T/2013 Tgl 14 Sep 2013
33	PLTM Watupayung	PLTM		2400	PT Putra Tirta Nusantara	503.01/3197/KP2T/2013 Tgl 14 Sep 2013
35	PLTM Kaliurip	PLTM	S Merawu	9960	PT Air Besar Energi	MERAH - 503.01/1958/KP2T/2014 Tgl 4 Agu 2014
36	PLTM Tlaga	PLTM	S Brukah	9000	PT Daya Air Energi	MERAH - 503.01/1533/KP2T/2014 Tgl 5 Jun 2014
37	PLTM Bunderan 1	PLTM	S Pekacangan	3000	PT Darma Putra Mandiri	MERAH - 503.01/1959/KP2T/2014 Tgl 4 Agu 2014
38	PLTMH Plipiran	PLTMH	K Tulis	1500	PT Persada Karya Tama	MERAH - 503.01/2166/KP2T/2014 Tgl 23 Sep 2014
39	PLTM Sarwodadi	PLTM	K Panaraban	6000	PT Sumber Energi Mikro Indonesia	MERAH - 503.1/1078/KP2T/2014 Tgl 30 Des 2014
41	PLTMH Limbangan	PLTMH	K Tulis	550	PT Persada Karya Tama	MERAH - 503.01/1070/KP2T/2014 Tgl 29 Des 2014
42	PLTMH Siwedung	PLTMH	K Tulis	818	PT Persada Karya Tama	MERAH - 503.1/1923/KP2T/2014 Tgl 16 Jul 2014
43	PLTM Mandiraja	PLTM	S Serayu	60000	PT Indonesia Power UBP Mrica	MERAH - 503.1/262/KP2T/2015 Tgl 11 Feb 2015
44	PLTM Kalibening	PLTM	S Brukah	3200	PT Indonesia Power UBP Mrica	503.1/279/KP2T/2015 Tgl 12 Feb 2015
45	PLTM Kalisapi	PLTM		1050	PT Sinar Anugrah Nusantara	503.1/768KP2T/2015 Tgl 22 Apr 2015
48	PLTM Sembawa	PLTM		2000	PT Bumi Iriano Energi	503.1/1073/KP2T/2015 Tgl 13 Jan 2015
49	PLTM Jawan	PLTM	S Dolog & S Tulis	5000	PT Telaga Petrogas Sejahtera	503.1/1110/KP2T/2015 Tgl 4 Jun 2015
50	PLTMH Pucang Bw	PLTMH	Sal Irigasi Siwuluh	200	PT Tirtanusa	
51	PLTM Pagerpelah	PLTM	S Urang	2100	PT Tekindo Karya Lestari	503.1/1408/KP2T/2015 Tgl 23 Jul 2015

| 54 PLTMH Aries | PLTMH | 400 | PT Gading Mitra Energi | 503.1/2588/KP2T/2015 Tgl 8 Des 2015 |

The principle of maintaining the condition of Watersheds is to stabilize the river flow throughout the region, so that must be done is to increase the flow in the dry season and reduce the amount of flow in the rainy season [8] (Kartodihardjo, H.et al 2004). The rain given are relatively stable throughout the year so that can be arranged is the type of plant and land processing systems that affect the water storage.

Efforts to restore the Upper Serayu watershed is not an easy issue because it is multisectoral that involves many aspects. Agriculture accounts for about 38.98% of Wonosobo and Banjar Regency GRDP, potato farming has also made the living standards of upstream Serayu River Basin growers. Upper Serayu River Basin Management becomes a dilemma, between ecological interests and economic interests. Thus, in the upstream area of Serayu management should use the principle of balancing the interests of both, in addition to the necessary role of social interest and environment Serayu watershed. Land management also means maintaining a sustainable water system must underlie the recovery solution of the region. Water spatial pattern is the distribution of the designation of water spaces within a region, including the Groundwater Basin (CAT), the conservation area within the watershed and the space allocation for the cultivation function (Roestam et al, 2010).

From the analysis results indicated the deviation of land use in the forest area (conservation area), this is where the region must be restored with the appropriate plant designation. The existence of a conflict of interest requires the re-enactment of an integrated zonation of the upstream region of Serayu. The principle of a single map policy needs to be applied in protected area zoning and cultivation to avoid errors due to position reference will certainly help accuracy in the mapping. Recovery of conservation areas will further strengthen the flow of surface, ground flow and groundwater reserves, because the rainfall of this area is very potential that is between 3000 to 4000 mm / year. The restoration of vegetation is expected to raise the base flows in May through November to rise above 100 mm. The 3rd order river is currently capable of supporting microhydro power, but its existence will be sustainable if the conservation area function is upheld consistently. River as a pool of flowing resources, not knowing the administrative boundaries, upstream water use will reduce the opportunity value, upstream contamination will cause externality effect and upstream conservation will give benefits downstream. Consequences need to be taken into consideration in the decentralized management of integrated river basin upstream, middle and downstream [9] (Lisdiyanta, T. 2004) , through the coordination of each stakeholder concerned. Protected areas are intended to achieve ecosystem sustainability, including land with slopes of more than 40%, natural reserve areas and cultural reserves, protected forests and water catchment areas while cultivation areas cover agricultural land and residential areas. The development of community based development based recovery programs that require community participation in watershed management should be well socialized as this will also have a positive impact on the environment-related societies. In order to make the water spatial more robust, it needs to be poured into a legal product in the form of local regulations at the provincial and regency / municipal levels in certain watersheds, while the visual representation of zoning data is set forth in the form of a one-rule spatial map. Besides the regulation, the government can also utilize concept of willingness to accept payment for environmental service of water [10] (Arafat, F. et al 2015) to contribute the upstream area. The existing reality condition, the area of potato plantation has now penetrated almost most of the protected areas. This causes an ecological and economic dilemma,

then agroforestry can be used as one of the solutions in the upper watershed of Serayu. Wanatani is a form of resource management that combines forest management activities or timber trees by planting commodities or short-term crops, such as agricultural crops. Management of potato plantation land with agro-forestry concept should be done according to the established zonation. Land with a slope of more than 40% should not be used as an agroforestry area but only for protected forest. Meanwhile, the area under it can be processed with the principle of agroforestry that is combining potato plantations with other perennials. This concept is very efficient to produce ecologically and economically profitable plantations. The planting of perennials around the open potato plantation can reduce the rate of erosion, because the tree stand will minimize the rainwater energy that is in the soil, slow the surface runoff rate and increase the potential for infiltration and interception. Tree stands can act as a windbreaker, to prevent erosion by wind and prevent the destruction of plantation land during heavy rains accompanied by strong winds. Wanatani also supports soil conservation efforts whereas plantations are generally only applied monoculture principles using potato commodities for years. The application of agroforestry that also acts like the principle of intercropping, is able to regulate soil nutrient content and increase fertility by preventing further erosion and adding to the soil biotic element.

Conclusions

From the above discussion can be concluded that the management of Serayu watershed needs to be done seriously considering the many conflicts of interest, and the absence of spatial landused planning synergy with water spatial planning. Conflicts of interest can be identified through map conflict, in which case forest cover in protected areas (HL) is only 2.5% and 6% in the form of plantations and even settlements. While in the HPT-HP-HPK forest cover area only 13%, shrubs 20.4%, plantations 40.6% in KSPA estates 0.3%, other shrubs and bushes. Based on runoff calculations, the potential is still able to support micro hydro energy even mini hydro. Upstream areas that play a supporting role under it need immediate recovery of plants according to their function and required a water spatial with the principle of sustainable development, so that the stability of water is maintained. The Wanatani Principles will support the empowerment of the environment but also keep in mind the economic condition of the community so that its institutional needs to be further strengthened.

Bibliography

[1] BPS Banjarnegara.. Banyaknya Desa/Kelurahan, Luas, Penduduk, dan Kepadatan Kabupaten Banjarnegara 2016

[2] Biswas, A. K. Integrated water resources management: a reassessment: a water forum contribution. *Water international*, *29*(2), 248-256. (2004).

[3] Widayati, T., & Yusuf, E. (2017). Strategies for Environmental, Economic, and Social Sustainability of Potato Agriculture in Dieng plateau Central Java Indonesia. *Journal of Environmental Management & Tourism*, *8*(1 (17)), 259. 2017

[4] Suprapto, M.. Concept of Sustainable Water Resources Management in Notog Irrigation Area. (2010).

[5] Laila, N., Murtilaksono, K. and Nugroho, B., 2015. Kelembagaan Kemitraan Hulu Hilir Untuk Pasokan Air Das Cidanau, Provinsi Banten. Jurnal Penelitian Sosial dan Ekonomi Kehutanan, 11(2), p.16. 2015

[6] Gauzan, H.. Sistem Informasi Geografis Erosi DAS Cidanau Menggunakan Framework Pmapper. 2009

[7] Tikno, S., Hariyanto, T., Anwar, N., Karsidi, A., & Aldrian, E. .. Aplikasi Metode Curve Number Untuk Mempresentasikan Hubungan Curah Hujan Dan Aliran Permukaan Di Das Ciliwung Hulu–Jawa Barat. Jurnal Teknologi Lingkungan, 13(1), 25-36. 2016

[8] Kartodihardjo, H., Murtilaksono, K., & Sudadi, U. (2004). *Institusi pengelolaan daerah aliran sungai: konsep dan pengantar analisis kebijakan*. 2004

[9] Lisdiyanta, T. Peranserta masyarakat hulu dalam membangun mekanisme hubungan hulu hilir pengelolaan DAS (studi kasus: Daerah Aliran Sungai (DAS) Cidanau di desa Citaman, Kecamatan Ciomas, Kabupaten Serang, Propinsi Banten). (2004).

[10] Arafat, F., Wulandari, C., & Qurniati, R. (2015). Willingness To Accept Payment For Environmental Service Of Water Sub Das Way Betung Upstream By Society Forest Area Register 19 (Case Study In Talang Mulya Village District Of Padang Cermin Sub Province Pesawaran. *Jurnal Sylva Lestari*, *3*(1). 2015

[11] Wasson, R. J. Application of the catchment concept for integrated rural development. In *ACIAR PROCEEDINGS* (Vol. 126, p. 86). ACIAR; 1998. 2015

[12] Maulana, E., & Subanu, I. L. P. (2012). *The Impact Of Payment For Environmental Services (Pes) Program In The Cidanau Collaborative Watershed Management* (Doctoral Dissertation, Universitas Gadjah Mada). 2015

Acknowledgement

SEASONALITY TRENDS OF RUBBER TREE CANOPY OBSERVED BY X-BAND SYNTHETIC APERTURE RADAR

Bambang H. Trisasongko (1,2), David J. Paull (1), Dyah R. Panuju (1,2)

[1] School of Physical, Environmental and Mathematical Sciences, UNSW Canberra, Northcott Drive, Campbell ACT 2600, Australia

[2] Department of Soil Science and Land Resources, Bogor Agricultural University, Jalan Meranti, Bogor 16680, Indonesia

Email: trisasongko@apps.ipb.ac.id

KEY WORDS: canopy; Cosmo/SkyMed; rubber plantation; seasonality; X-band

ABSTRACT: Understanding seasonality is critical for many remote sensing applications since the role of local weather events associated with particular seasons may impact information retrieval. Unfortunately, the issue has been inadequately assessed; hence, various outcomes could be expected when a single date of observation is employed for a specific task. This article considers seasonal discrepancies in SAR data backscatters returned by different ages of rubber trees. We selected Jalupang rubber plantation situated in Subang, Indonesia to illustrate the problem using dense multi-temporal Cosmo/SkyMed X-band SAR data. Large variation occurs amongst young trees of 1–4 years age indicating a strong contribution of non-tree scatterers. Mature stands < 20 years act as stable scattering objects, which could serve as a potential natural entity for SAR calibration. Backscatter from old growth > 25 years appears less stable, perhaps due to increasing canopy gaps. Extreme variation due to season was observed in young trees, with the discrepancy being about 4 db in HH polarization between observations in wet and dry seasons. The ambiguity tends to be lower for maturing trees (6–20 years) to ca. 1.5 db. The research suggests that variations due to associated seasonal events could be significant in X-band, which is an important issue for long-term monitoring of tropical woodlands.

1. INTRODUCTION

Remotely-sensed data have been implemented for tropical forest monitoring for decades. Given the nature of the tropical zone, Synthetic Aperture Radar (SAR) has increasingly gained attention for obtaining environmental information under the presence of atmospheric disturbances, particularly persistent cloud cover. While in-depth research and analyses are continually sought, a recent focus has increasingly been given to plantations, as the major outcome of deforestation in the tropics. Rapid land cover change in tropical countries necessitates frequent updating of land cover maps; this is a situation where remote sensing data can significantly contribute. The main plantation types in tropical regions include timber, oil palm and rubber estates. In the SAR domain, they have been studied within the context of land cover discrimination and mapping. Much of the research in this domain is related to the use of dual polarimetric data, considering the abundance of datasets (see for instance, Longépé et al.

(2011)). Recently, Trisasongko et al. (2017) provided an experiment on the use of fully polarimetric L-band SAR for separating oil palm, tea and rubber plantation in the complex landscape of West Java, Indonesia.

Similar to teak, rubber trees have distinctive features; they exfoliate in dry seasons at different intensities in relation to the local availability of soil moisture. Hence, the effect somewhat differs between locations. This situation makes mapping procedures fairly difficult to conduct and, therefore, external information such as climatic data is likely to be required during the process. Complexity arises in terms of using SAR data for this purpose since short and long wavelength sensors behave differently to targeted objects. An abundance of C- and L-band data have been under examination. Pioneers to this domain include Rosenqvist (1996) who analyzed Japanese Earth Resources Satellite (JERS-1) SAR, Erath Resource Satellite (ERS-1) and Almaz SAR, with each representing single-polarized L-, C- and S-band SAR data, for rubber monitoring in Malaysia. Using L-band Phased Array-type L-band Synthetic Aperture Radar (PALSAR) data, Trisasongko and Panuju (2015) summarized that a large temporal change was observable using dual polarization HH-HV data in juvenile trees, while variation in maturing trees could only be seen using HH polarization.

Studies by X-band SAR, unfortunately, are severely limited, perhaps due to limited data availability. This research attempts to minimize the gap by exploring X-band data taken from Cosmo/SkyMed data to understand varying properties of HH polarization over different age classes of rubber plantation. In addition, we are interested in the behavior of HH scattering affected by tropical weather as observed from a dense stack of SAR data.

2. METHODOLOGY

2.1 Test Site and Dataset

The test site is situated in Jalupang rubber plantation, Subang, West Java, Indonesia (Figure 1). This plantation was selected due to its high performance in terms of rubber productivity with superior ground and ancillary datasets available (Trisasongko 2017). Relatively flat terrain, with some inclusion of undulating topography, is found in the region, making the area a suitable site for research related to long-term monitoring from Earth observing satellites.

The main dataset used in this research is a collection of Cosmo/SkyMed scenes, obtained from the Italian Space Agency (Agenzia Spatiale Italiana, ASI) under a European Space Agency Category-1 (ESA Cat-1) project. Ten scenes were taken from November 2013 to October 2014 on a monthly basis, except two missing collections in May and June (the beginning of dry season). All datasets were provided in slant range geometry (single look complex, SLC).
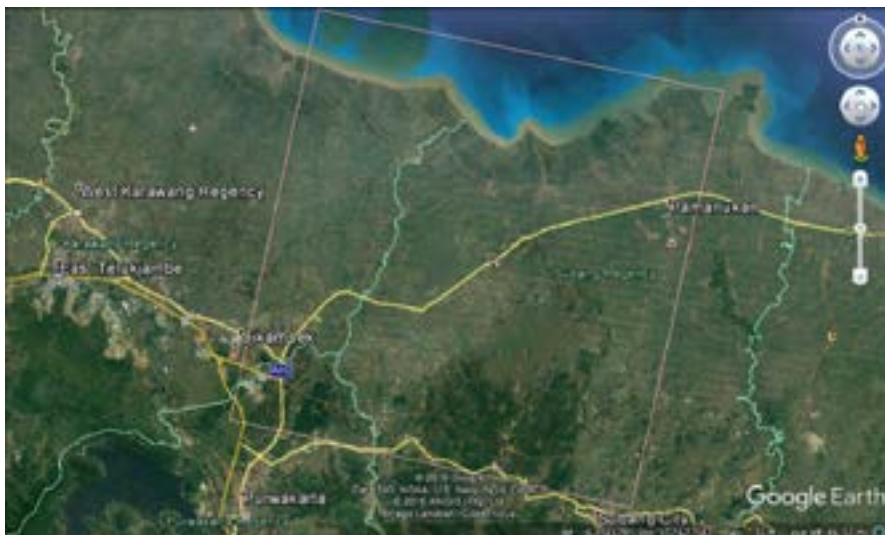
Figure 1. Cosmo/SkyMed scene coverage. Rubber plantation is situated in the lower part of the scene.

2.2 Preprocessing and Analysis

All images were calibrated using SNAP 6 software, provided by ESA. To compensate for undulating topography in the southern part of the region, we used a procedure to flatten terrain and subsequently applied the Range-Doppler Terrain Correction module in the same software. The digital elevation model used in this research was taken from 1 arc-second Shuttle Radar Topography Mission (SRTM). All scenes were then co-registered to facilitate the analysis. In this research, statistical analysis and graphing employed the R statistical environment.

Ancillary datasets to support the analysis and interpretation included a stand age map and ground surveys taken in January 2013 and 2016. Samples were taken in the northern site of the estate as the southern part was not covered by Cosmo/SkyMed scenes. Consequently, stands with mature rubber trees (between 11 and 20 years) were absent. Figure 2 represents a variety of rubber tree ages present in the scene, with the youngest being 1 year old. The oldest tree stand recorded was 30 years.
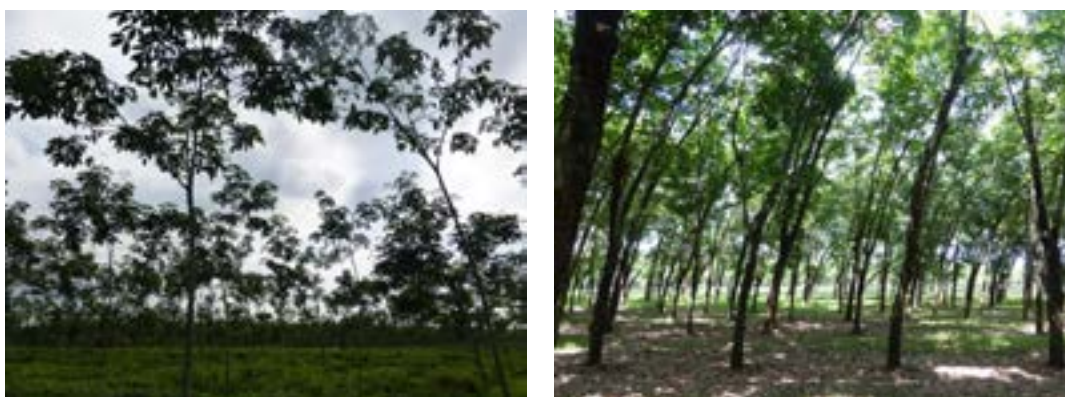
Figure 2. Field photographs: (left) juvenile; (right) mature rubber trees.

3. RESULTS AND DISCUSSION

Figure 3 presents a violin plot describing the behavior of HH backscatter coefficients taken from different tree ages. Rubber trees aged 1 year old have a slightly higher backscatter coefficient compared to slightly older trees. This is due to a stronger return as a result of wave-tree interaction, following a bounce from the ground. With the meagre canopy layer at this age, incident waves firstly interact with the ground surface, which is often barren, and then bounce to the nearby tree stems and return back to the SAR antenna. This phenomenon is somewhat similar to the double-bounce mechanism applied to urban settings. This was previously reported in the case of L-band radar by Trisasongko and Panuju (2015), although it appears that the attenuation at X-band is slightly lower than the case of PALSAR. Amplification of X-band HH backscatter by very young tree is about 1.5 dB, while the number almost doubles in L-band SAR (Trisasongko and Panuju 2015). This phenomenon is likely to be similar to regular rice planting as observed by Ouchi et al. (2006), where water served as a critical component to a bounce to rice stalks. Ouchi et al. (2006) further suggest the phenomenon is a form of the Bragg scattering mechanism.
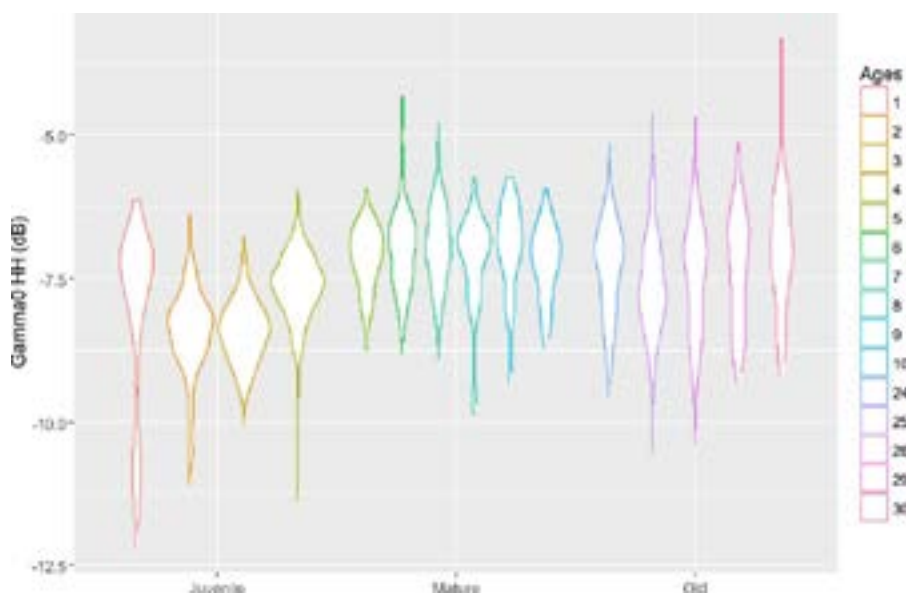
Figure 3. Variability of backscatter coefficients after the interaction with rubber trees.

With the expansion of canopy cover, the attenuation effect fades. Scattering at juvenile ages tends to rise until rubber trees approach 6 years old when the canopies between rows are totally closed. As shown in Figure 3, backscatter coefficients appear stabilized with mature rubber trees. This information is essential for SAR calibration purposes without the necessity to establish passive or active calibration devices. The issue of finding suitable natural objects for improving SAR calibration networks has been raised in previous publications related to L-band (Shimada 2005) or C-band sensors (El Hajj et al. 2016). The present research contributes to previous knowledge by demonstrating that a similar situation could occur for X-band datasets.

Unfortunately, the stability of X-band SAR signals weakened on old growth rubber trees. It is suspected that the primary cause for this issue was canopy gaps. Field observations suggested that the gaps were due to many sources, including lightning strike and diseases. Nonetheless, the variation appears insignificant compared to L-band (Trisasongko 2017), perhaps due to the nature of X-band being more sensitive to the presence of a canopy layer. Comparison of multi-frequency SAR data at this growth stage is therefore an interesting topic for future research.

Figure 4 shows temporal variation of several sample pixels taken from three different tree ages. As shown, variation in juvenile trees was clearly high. Horizontal co-polarization varies greatly with the lowest occurrence at the peak of the dry season (August), i.e. about −11 db, which shifted ca. 4 db lower than the average of the wet season. The figure suggests that moisture contributes to the returning wave more than the actual canopy. Field observations suggested that the leaf-off phenomenon often seen in rubber plantation was not entirely significant at this test site.

With maturing trees, an extreme drop-off related to the different season was not clearly observed. The disparity between backscatter coefficients retrieved from wet and dry seasons was about 1 db, suggesting that signals were generally stabilized. This figure reinforces previous discussion that maturing rubber trees could serve as an excellent natural calibrator for SAR sensors. Variation in backscatter pattern was again observed in old growth rubber plantation.

4. CONCLUSION

Although seasonality has increasingly been examined in recent remote sensing studies, its effect on data analysis is largely unknown. This issue is particularly important to tropical regions where significant differences of weather could potentially disturb the expected outcome, even with regard to SAR data, which tend to be 'weather-proof'. Our findings suggest that weather implications to the detection of woody vegetated cover, especially rubber plantation, should be considered. Effects on vegetation differ depending on the stand age of rubber plantation. Young trees and old-growth tended to behave variably, perhaps due to the contribution of soil background to the total backscatter. Mature rubber trees appeared similar in horizontal co-polarization with the average backscatter around −7 db. Further investigation into the effect of weather suggests that variability of HH polarization occurred in young and old growths, although the latter had about 2 db shifts between dry and wet season datasets. Our research found that mature rubber plantation revealed a small deviation of about 1 db within the course of observation. This suggests that this type of vegetation could be employed as a potential natural SAR calibration target.
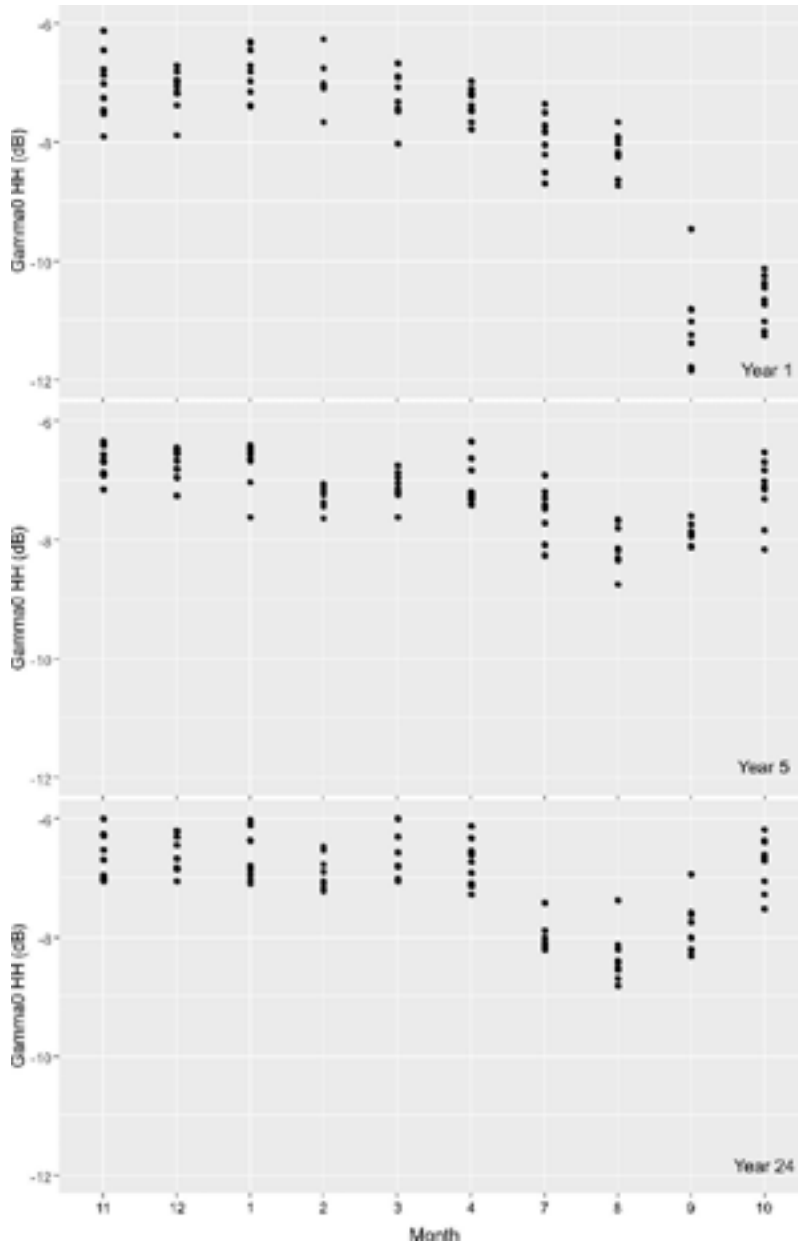
Figure 4. Temporal variation of horizontal co-polarization backscatter coefficient.

ACKNOWLEDGEMENTS

REFERENCES

El Hajj, M., N. Baghdadi, M. Zribi, and S. Angelliaume. 2016. Analysis of Sentinel-1 radiometric stability and quality for land surface applications.   Remote Sensing 8 (5), pp.

Longépé, N., P. Rakwatin, O. Isoguchi, M. Shimada, Y. Uryu, and K. Yulianto. 2011. Assessment of ALOS PALSAR 50 m orthorectified FBD data for regional land cover classification by support vector machines.   IEEE Transactions on Geoscience and Remote Sensing 49 (6 PART 1), pp. 2135-50.

Ouchi, K., H. Wang, N. Ishitsuka, G. Saito, and K. Mohri. 2006. On the Bragg scattering observed in L-band synthetic aperture radar images of flooded rice fields.   IEICE Transactions on Communications E89-B (8), pp. 2218-25.

Rosenqvist, Å. 1996. Evaluation of JERS-1, ERS-1 and Almaz SAR backscatter for rubber and oil palm stands in West Malaysia.   International Journal of Remote Sensing 17 (16), pp. 3219-31.

Shimada, M. 2005. Long-term stability of L-band normalized radar cross section of Amazon rainforest using the JERS-1 SAR. Canadian Journal of Remote Sensing 31 (1), pp. 132-7.

Trisasongko, B. H. 2017. Mapping stand age of rubber plantation using ALOS-2 polarimetric SAR data.   European Journal of Remote Sensing 50 (1), pp. 64-76.

Trisasongko, B. H., and D. R. Panuju. 2015. Characteristics of L-band backscatter coefficients of rubber plantation and their seasonal dynamics.   AIP Conference Proceedings 1677, pp. 060006.

Trisasongko, B. H., D. R. Panuju, D. J. Paull, X. Jia, and A. L. Griffin. 2017. Comparing six pixel-wise classifiers for tropical rural land cover mapping using four forms of fully polarimetric SAR data.   International Journal of Remote Sensing 38 (11), pp. 3274-93.

BI-TEMPORAL ANALYSIS OF VEGETATIVE COVER AT HALIMUN SALAK NATIONAL PARK BY USING ALOS PALSAR

Dyah R. Panuju[1,2], David J. Paull[1], Bambang H. Trisasongko[1,2]

[1] School of Physical, Environmental and Mathematical Sciences, UNSW Canberra, Northcott Drive, Campbell, ACT 2600, Australia

[2] Department of Soil Science and Land Resource, Bogor Agricultural University, Jalan Meranti, Kampus IPB Darmaga, Bogor 16680, Indonesia

Email: panuju@apps.ipb.ac.id

KEY WORDS: ALOS PALSAR, change detection, Halimun Salak, IRMAD, post-classification

ABSTRACT: The implementation of bi-temporal change analysis using optical and microwave datasets has assisted management of rural and urban land use, including forest areas. Forests in tropical regions such as Indonesia are often situated in mountainous terrain and their monitoring needs to cope with persistent cloud cover. This research applied an Iteratively Reweighted Multivariate Alteration Detection (IRMAD) and post-classification change analysis on a pair of dual polarimetric ALOS PALSAR datasets to detect vegetation dynamics in the vicinity of Taman Nasional Gunung Halimun Salak for the years 2007 and 2010. Employing Gamma Map filtering for the second MAD variate and differencing of cross-polarization data of the pair enabled the detection of subtle changes related to maturing oil palm plantations as well as land clearing and replanting. The result indicated successful detection of typical dynamic change of maturing vegetation and land clearing as well as discrimination of vegetated and non-vegetated areas. By comparing combinations of the datasets, it appears that differencing of cross-polarisation yielded clearer change detection while secondary MAD variates with Gamma Map filtering generated comparable results. The accuracy of classification may also be improved by additional synthetic data. When examining four pixel-based classifiers for pre-change detection, a gradient boosting tree of datasets injected with three texture components, i.e. mean, variance, and correlation, yielded the highest accuracy at 71%. Google Earth imagery assisted in interpreting binary change that resulted from MAD variates or differencing cross-polarisation whereas post-classification detection was unable to detect the subtle changes.

1 INTRODUCTION

1.1 Background

The application of bi-temporal change detection on optical and synthetic aperture radar (SAR) has provided invaluable information for managing rural and urban land use, including forest areas. Monitoring rain forest in tropical regions has to deal with the challenges of poor accessibility to the area and persistent cloud cover (Bijker, 1997). Microwave remote sensing such as SAR is an option for monitoring remote areas while coping with the cloud problem.

The difference of log images or ratio of intensity images and determining thresholds to differentiate changed from unchanged land was a standard approach to change detection with SAR data for forested areas (Grover et al., 1999). An alternative technique includes the combined use of radar backscatter and optical images to study earthquake damage detection (Stramondo et al., 2006) or to assess tsunami-damage (Bovolo and Bruzzone, 2007).

A common technique for change detection employing optical images that provides "from-to" information is post-classification comparison. However, a limited number of predictors in single or dual polarisation radar data may limit the accuracy of classification while error detection is proliferated by each classification. Injecting synthetic data may enrich information to improve the accuracy of change detection based on radar data. The synthetic data may be generated from simple algebra such as differencing and ratioing or from more advanced techniques such as decomposition and texture analyses. This strategy was implemented by Kuntz and Siegert (1999) to monitor deforestation and land use at the Samarinda rain forest, Arzandeh and Wang (2003) to detect *Phragmites*, and Yayusman and Nagasawa (2015) to identify smallholder oil palm plantation.

A recent development in binary change analysis, i.e. Iteratively Reweighted Multivariate Alteration Detection (IRMAD), provides an alternative to identify change while performing relative radiometric calibration. This method has been applied to analyse optical images, including Landsat (Nielsen, 2007), ASTER (Crocetto and Tarantino, 2009) and hyperspectral images (Wang et al., 2015). However, we are not aware of the employment of IRMAD for radar data.

By performing binary change identification combined with post-classification detection, this research aims to identify the dynamics of vegetative cover at Halimun Salak National Park, which is one of the last remaining rain forests in Java.

1.2   Bi-temporal change detection by using IRMAD and post classification detection

Bi-temporal change detection performs change analysis on a pair of datasets of the same extent taken at two acquisition times (Singh, 1989). Bi-temporal change detection may be performed based on comparative-based analysis or simultaneously on spectral images. The comparative-based analysis detects change from post-classified images. The procedure has been applied to various ecosystems, including forest, coastal, agriculture and urban systems. The detection provides "from-to" information on pre- and post- land use maps, which cannot be provided by binary change detection containing changed and unchanged classes (Mas, 1999). However, the quality of post-classification detection relies on the accuracy of each classification process. Sufficiently high accuracy of classification is the main challenge in obtaining adequate change accuracy.

Simultaneous change analysis is an alternative technique that firstly transforms data into a biophysical representation or into new data structures before the analysis. Transformation into biophysical characteristics is achieved by measuring indices to represent vegetation abundance, water extent or reflectivity of the land surfaces (Lambin and Strahler, 1994). The new structures can be generated by statistical analyses such as principal components analysis (PCA), which transforms original vector images into new linear combinations of vector images or the tasselled cap.

Either post-classification or simultaneous change analysis requires pre-processing that involves geo-registration, atmospheric and radiometric correction. These procedures are considered mandatory to result in accurate change detection. It has been shown that mis-registration contributes up to 50% of error detection (Townshend et al., 1992). Meanwhile, atmospheric and radiometric correction is vital for ensuring the homogeneity of multi-temporal change analysis of optical images such as MODIS and Landsat (Vicente-Serrano et al., 2008).

Multivariate Alteration Detection (MAD) is a technique based on Hotteling's (1936) canonical correlation, by transforming two sets of vector images of the same place, acquired at two time points, $M=(M_1, \ldots, M_k)$ and $N=(N_1, \ldots, N_k)$ into new images $Q= a^T M$ and $R= b^T N$. From p spectral bands in the original bi-temporal images, two images can be generated where each new image is composed of p MAD-variates. The MAD-variates are ordered by descending variance. Standardising values by computing their correlation helps to cope with differing scales that result from different gain factors and atmospheric conditions. The improvement of MAD by iterative processing, which is IRMAD, is performed to improve separation among classes by adding more weight to no-change probabilities during the process (Nielsen, 2007).

Compared to post-classification and transformation-based analysis, MAD does not strictly demand pre-processing to produce an accurate change map. This advantage is rooted to a process that selects pseudo-invariant features (PIF) or invariant pixels as non-change samples for relative normalisation of images (Canty and Nielsen, 2008). PIF are selected from features such as buildings or constructions that are relatively constant in their reflectance over acquisitions, albeit with minor effects of seasonal conditions.

MAD is frequently used for change detection employing optical images. For instance, IRMAD was applied to characterise decadal change processes by employing Landsat images (Alaibakhsh et al., 2015). A comparison of the performance of IRMAD using original surface reflectance and tasselled cap transformed Landsat images demonstrated comparable change results (Panuju et al., 2017). Nonetheless, IRMAD analysis employing radar data to analyse change needs to be explored.

2   METHODS

2.1   Site

Taman Nasional Gunung Halimun Salak is situated approximately 65 km south of Jakarta, the capital city of Indonesia (Figure 1). The park is the last montane rain forest on the island of Java, hosting several endangered species including the Javan eagle. Threats to the park in the form of land cover change compromise the conservation of protected species as well as downstream water provision. Land cover dynamics of this critically important area and its surroundings threaten numerous ecosystem services.
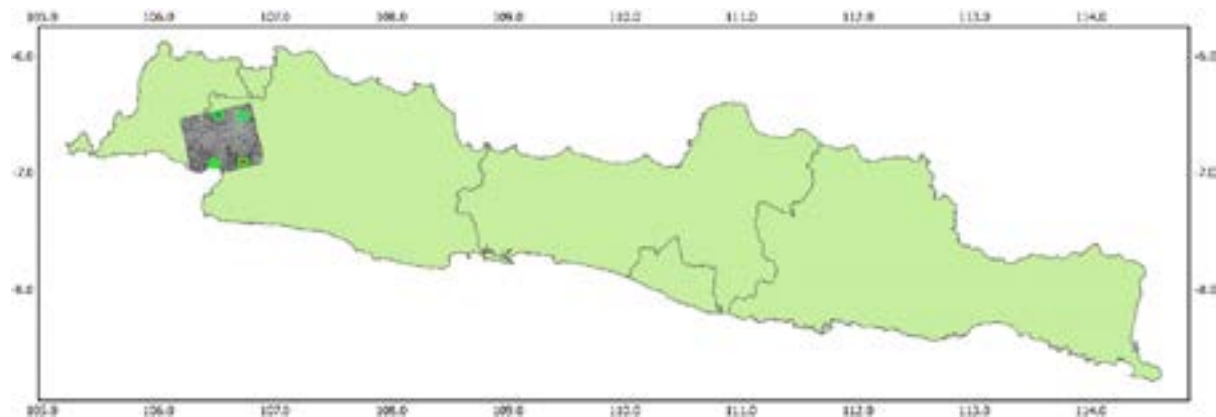
Figure 1. Sites for change detection using dual polarimetric ALOS PALSAR

2.2   The procedure of change detection and its validation

Prior to change detection, all images were calibrated, terrain corrected, de-speckled, and converted to dB (sigma0). Synthetic data were then generated, comprising of differencing of HH-HV, ratioing of HH/HV, radar vegetation index (RVI), entropy alpha decomposition and texture analysis. RVI for dual polarization data was determined following Trudel et al. (2012). Considering the contribution of texture components for classification as suggested by Yayusman and Nagasawa (2015), only the result of GLCM, i.e. mean, variance, and correlation, were utilised for post-classification.

Change detection was performed by employing differencing of dual polarisation images and RVI, as well as IRMAD onto a pair of dual polarimetric ALOS PALSAR for the years 2007 and 2010. The IRMAD processing result binary maps that was used to identify change process. Gamma Map filtering was then applied to MAD variates.

The post-classification was performed to provide "from-to" information by employing supervised classification techniques. A set of combinations was tested to yield the highest possible accuracy, comprising of horizontal co-polarisation, cross-polarisation and synthetic data. Dual polarisation data were the control treatment to evaluate the robustness of data injection. Simple synthetic bands resulted from map algebra including differencing and ratioing of cross-polarisation images that were injected. Other synthetic injection occurred by adding RVI, entropy alpha decomposition and three selected textures. The entropy-alpha decomposition was determined based on Cloude and Pottier (1997). A summary of these data combinations is presented in Table 1.

Table 1. Data combinations for IRMAD processing and post-classification detection

Method	Data	Additional synthetic layer
Differencing	$HH_{t1}-HH_{t0}$	-
	$HV_{t1}-HV_{t0}$	-
	$RVI_{t1}-RVI_{t0}$	-
IRMAD	HH & HV	-
Post-classification	HH & HV	-
	HH & HV	Differencing HH-HV
	HH & HV	Ratioing HH/HV
	HH & HV	Radar Vegetation Index (RVI)
	HH & HV	Decomposition H-Alpha
	HH & HV	Texture (mean, variance, correlation)

Four pixel-based classifications including support vector machine (SVM), classification and regression tree (CART), random forest (RF), and gradient boosting tree (GBT) were employed. The selection was based on previous results that suggested the employment of pixel-based methods with tuning can result in enhanced accuracy (Trisasongko et al., 2017). The imagery was classified into five classes, i.e. oil palm, paddy field/crop, built-up, forest, and other broad-leaf vegetation.

The validation of change may be performed by using other image products, employing other available mapping, or via ground truth. In this research, freely accessible high-resolution images provided by Google Earth were employed as a reference. We used Google Earth to validate the change map that resulted from IRMAD processing. For each extent, at least two images were examined, captured at times that were proximate to the first and second dates. The accuracy between classification methods was then compared to identify the best method.

3   RESULTS

3.1   Detected change using differencing and IRMAD of the backscatter of dual polarimetric ALOS PALSAR

As a common technique to derive change, differencing of dual polarisation backscatter was compared with the differencing of RVI and IRMAD processing. The binary map describes the location of change occurrences between the data span. Figure 2 shows the result of change detection from differencing of horizontal polarisation, cross-polarisation, RVI, 1st MAD variate, 2nd MAD variate and Gamma Map filtered of the 2nd MAD variate.

The figure indicates that differencing of cross-polarisation generated a clearer sign of where change occurred during the time span than the differencing of horizontal polarisation, RVI or MAD variates. The RVI differencing appears to have been ineffective for detecting where change occurred within the span. The second MAD variate detected the change as the differencing yielded a smaller intensity. Applying the Gamma Map to filter MAD variate-2 improved the result in a similar way to differencing of cross-polarisation, which clearly pointed out the location of change. It appears that filtering increased the contrast between changed and unchanged areas.
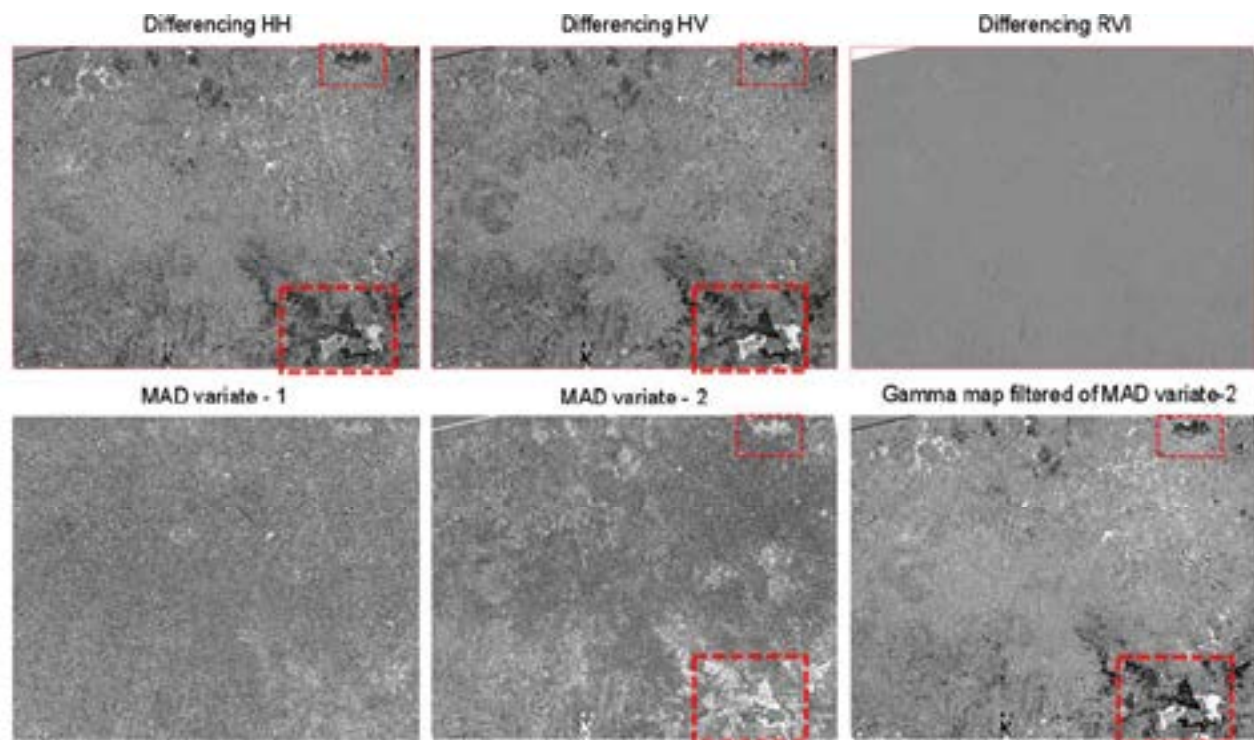
Figure 2. Results of image differencing of horizontal polarisation, cross-polarisation, radar vegetation index, 1st MAD variate, 2nd MAD variate and Gamma Map filtered of MAD variate-2 from IRMAD processing

3.2   Comparing accuracies of data combinations for post-classification detection

The outcome of a single classification should be sufficiently accurate to generate reliable change detection. The injection of various synthetic datasets to original backscatter data was expected to improve the accuracy of classification. The results of synthetic data injection to the accuracy of classification is presented in Table 2.

Table 2 shows that CART was unable to generate five classes as expected. The technique failed to differentiate broad-leaf vegetation as the fifth class even when the dual polarimetric backscatter was added with synthetic data. However,

data injection appears to have improved the ability of CART to produce an expected land cover map. The maximum number of classes was four produced by texture amendment.

Table 2. *Overall accuracy of six data combinations derived from ALOS dual polarimetric radar data for land cover classification. The classes comprised of built-up, forest, paddy field, oil palm, and other broad-leaf cover. Bold text signifies the highest accuracy. Asterisk refers to classes' generation, i.e. * generated 2 classes: forest, oil palm, ** generated 3 classes: forest, oil palm, crops, *** generated 4 classes: forest, oil palm, built-up, crops.*

Methods	Datasets	Accuracy 2007	Accuracy 2010	
CART	dB	0.645	0.645	*
	dB_Dif	0.645	0.645	*
	dB_Rat	0.645	0.645	*
	dB_HAlpha	0.645	0.619	**
	dB_RVI	0.645	0.645	*
	dB_Texture	0.366	0.366	***
GBT	dB	0.608	0.608	
	dB_Dif	0.649	0.649	
	dB_Rat	0.638	0.638	
	dB_HAlpha	0.635	0.634	
	dB_RVI	0.638	0.638	
	dB_Texture	**0.712**	**0.712**	
RF	dB	0.638	0.638	
	dB_Dif	0.661	0.661	
	dB_Rat	0.656	0.656	
	dB_HAlpha	0.638	0.624	
	dB_RVI	0.656	0.656	
	dB_Texture	0.562	0.562	
SVM	dB	0.641	0.641	
	dB_Dif	0.635	0.635	
	dB_Rat	0.641	0.641	
	dB_HAlpha	0.551	0.587	
	dB_RVI	0.641	0.641	
	dB_Texture	0.607	0.607	

Different techniques responded variably with data injection. GBT appears to have resulted in the best trend for describing the importance of supplementary synthetic data to improve accuracy. The greatest improvement was demonstrated by adding texture parameters that resulted in an accuracy of 71%. The use of the RF classifier suggested that additional data may increase or decrease the accuracy compared to the standard, dual polarisation backscatter. Injecting synthetic layers of differencing, ratioing, and RVI appears to have improved the accuracy. Nonetheless, adding more advanced synthetic data produced by entropy alpha decomposition and texture analysis generated lower accuracy than the standard data. The result of SVM contrasted with the other methods by either preserving or reducing the accuracy. Adding images derived from ratioing of cross-polarisation or RVI generated accuracy that was the same as the standard, while other synthetic data reduced it. Post-classification change analysis resulted in none of the area experiencing change. Figure 3 presents the map that resulted from the highest accuracy of GBT for five land cover classes either for the year 2007 or 2010. The map assisted in interpreting the change that was indicated by the binary change map.

3.3 Interpretation of Change using Google Earth

The validation of change through ground truth or by using higher spatial resolution images is a qualitative way to assess the robustness of change detection procedures. The explanation regarding the detected change can be visually described by referring to the finer resolution data. Figures 4 and 5 demonstrate how Google Earth can assist in IRMAD processing, where different tones of the grey-colour images are evaluated.
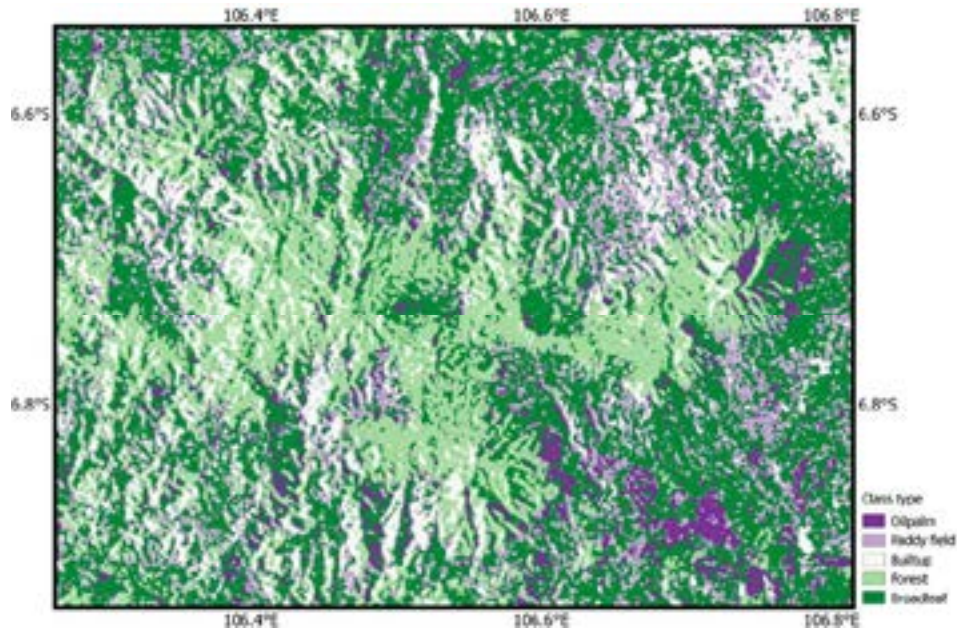
Figure 3. The map of GBT classification for five classes including oil palm, paddy field, built-up, forest, other broad leaf plants

Post-classification detection may describe the type of change. However, when the change is subtle like maturing vegetation or semi-bare land of juvenile plantation, the procedure might not be effective. In humid tropics, weeds and plants grows faster than dry areas. For rubber plantation, a cover crop is usually planted to minimise erosion and to provide a source of nitrogen. In places with less-controlled land management, within weeks cleared land might be fully covered by weeds and plants.
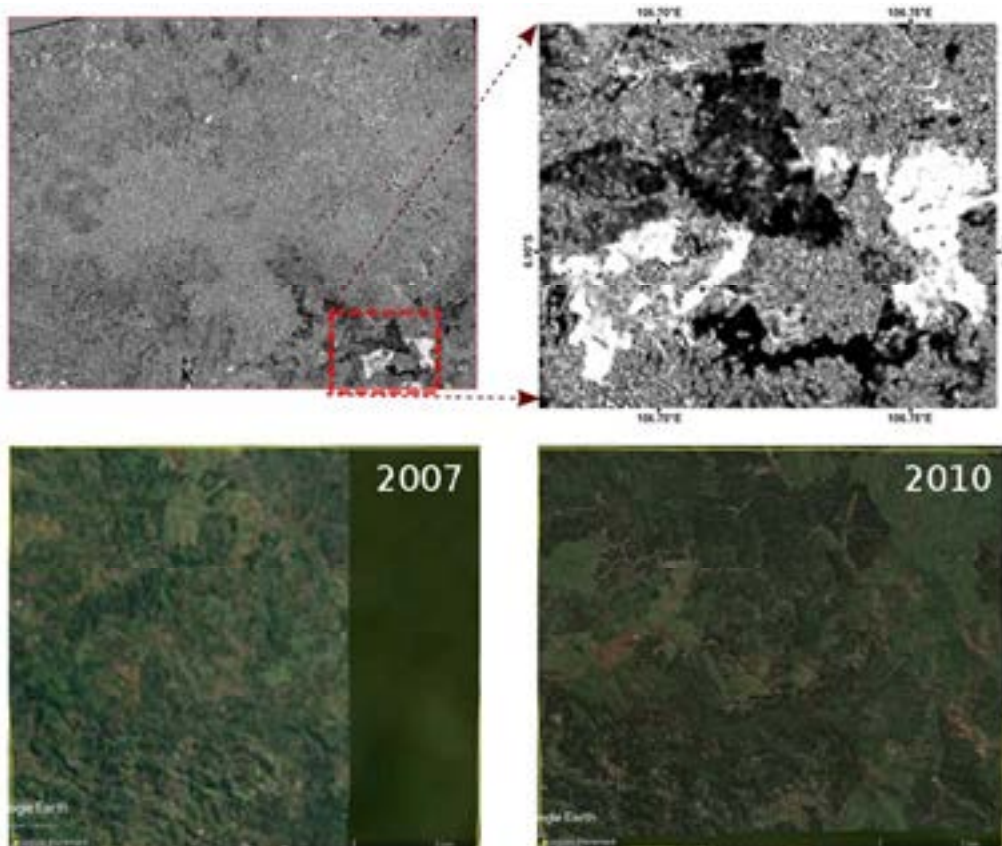
Figure 4. Detected change from MAD variate 2 by using ALOS dual polarimetric, validated with historical images of Google Earth. Black indicates maturing oil palm, white signifies changing plants from rubber to oil palm, grey shows unchanged condition from t1 (2007) to t2 (2010)

Figure 4 shows that either differencing of cross-polarisation or IRMAD detected the subtle change related to maturing vegetation and the conversion from oil palm to rubber plantation, which was undetected by post-classification analysis. Since the classification scheme combined all the vegetation types other than primary forest and oil palm plantation into broad-leaf plants, it appears that the classification could not identify this change. Meanwhile, Google Earth imagery assisted in interpreting the difference of tone indicated by differencing of dual polarisation backscatter or IRMAD processing.

Similarly, Figure 5 describes the differing change that occurred in the location with the assistance of Google Earth for a better interpretation of change analysis. The figure shows the change of semi-bare land to oil palm plantation, vegetated to non-vegetated paddy fields, and juvenile to mature oil palm plantation. Land alteration of the vegetated from non-vegetated areas is clearly seen by a different colour tone.
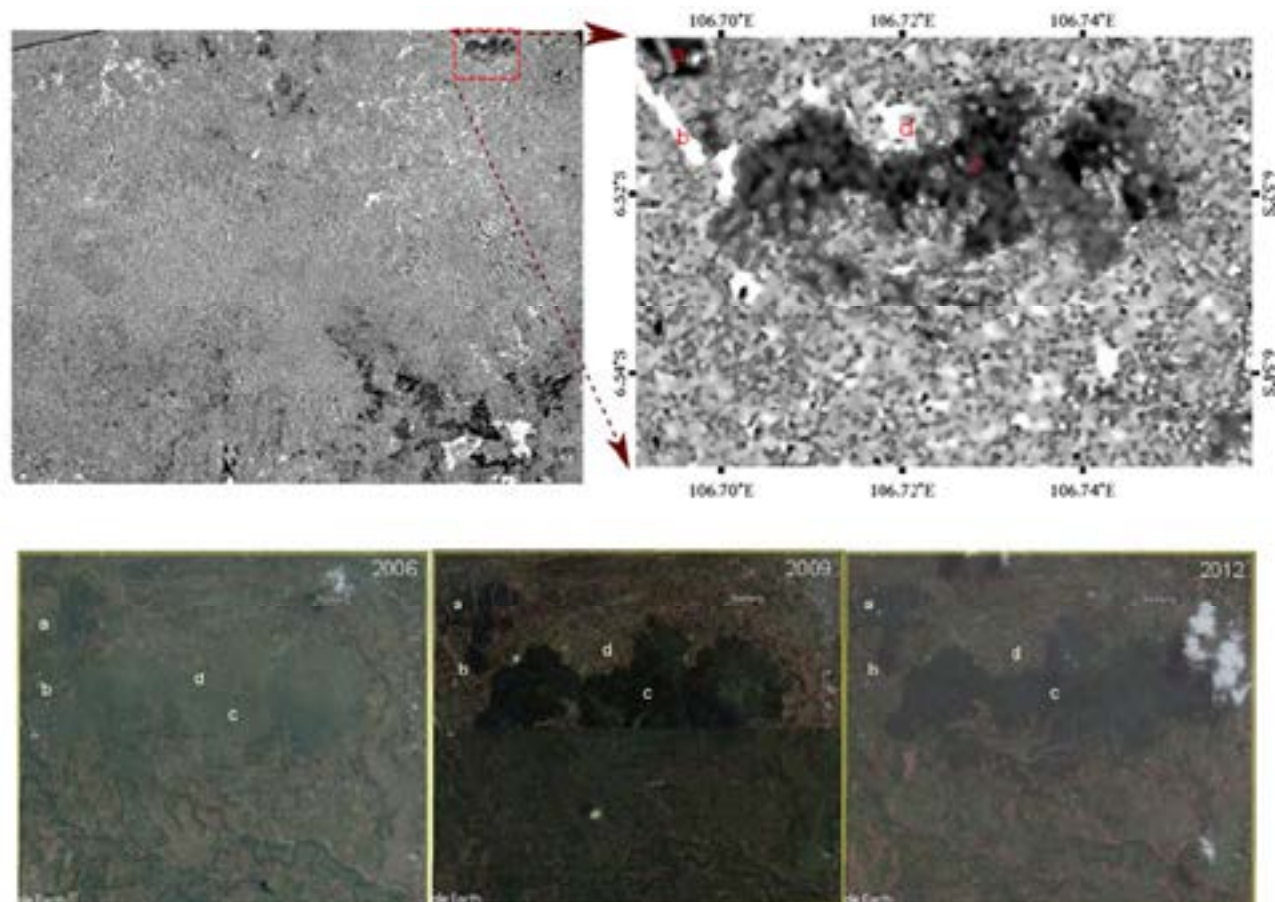
Figure 5. Change detection by using ALOS PALSAR Dual Polarimetric 2007 and 2010 (top right) with image crops of Google Earth for the years 2006, 2009 and 2012. Different change samples: (a) open area to vegetated area (oil palm), (b) vegetated to non-vegetated paddy fields, (c) juvenile to mature oil palm, (d) vegetated to non-vegetated crop areas.

4   CONCLUSION

Employing microwave satellite images is an option for monitoring areas with poor accessibility that are severely affected by persistent cloud cover. Employing the difference of log images of dual polarisation ALOS radar backscatter demonstrated the potential of monitoring such areas. Differencing of HH, HV backscatter and MAD variates pointed to the location of change with the clearest indication being demonstrated by the difference of HV. Filtering the second MAD variate produced a similar result to differencing of log HV.

The employment of post-classification change analysis informs "form-to" change. Dual layers of ALOS FBD images may limit capabilities for classification of complex classes, hence injecting synthetic images enriches information that may improve the accuracy. In post-classification change detection, error detection is proliferated by each classification. The increment of accuracy by data injection was demonstrated by employing GBT. The greatest accuracy was yielded from texture injection comprising of GLCM layers, i.e. mean, variance and correlation. However, a limited number of classes across a three-year time span could not indicate any change occurrence in the

location. Google Earth imagery assisted in the interpretation of binary change detection. The different tone resulted from differencing and IRMAD indicated subtle changes due to the change of vegetation type or growth phases such as from juvenile to maturing oil palm or unvegetated to vegetated paddy fields.

5 ACKNOWLEDGEMENTS

6 REFERENCES

Alaibakhsh, M., Emelyanova, I., Barron, O., Mohyeddin, A. and Khiadani, M., 2015. Multivariate detection and attribution of land-cover changes in the Central Pilbara, Western Australia. International Journal of Remote Sensing, 36 (10), pp. 2599-2621.

Arzandeh, S. and Wang, J.F., 2003. Monitoring the change of Phragmites distribution using satellite data. Canadian Journal of Remote Sensing, 29 (1), pp. 24-35.

Bijker, W., 1997. Radar for rainforest - A monitoring system for land cover change in the Colombian Amazon. European Space Agency, (Special Publication) ESA SP(405), pp. 53-60.

Bovolo, F. and Bruzzone, L., 2007. A split-based approach to unsupervised change detection in large-size multitemporal images: Application to tsunami-damage assessment. IEEE Transactions on Geoscience and Remote Sensing, 45 (6), pp. 1658-1670.

Canty, M.J. and Nielsen, A.A., 2008. Automatic radiometric normalization of multitemporal satellite imagery with the iteratively re-weighted MAD transformation. Remote Sensing of Environment, 112 (3), pp. 1025-1036.

Cloude, S.R. and Pottier, E., 1997. An entropy based classification scheme for land applications of polarimetric SAR. IEEE Transactions on Geoscience and Remote Sensing, 35 (1), pp. 68-78.

Crocetto, N. and Tarantino, E., 2009. A class-oriented strategy for features extraction from multidate ASTER imagery. Remote Sensing, 1 (4), pp. 1171-1189.

Grover, K., Quegan, S. and Da Costa Freitas, C., 1999. Quantitative estimation of tropical forest cover by SAR. IEEE Transactions on Geoscience and Remote Sensing, 37 (1 II), pp. 479-490.

Kuntz, S. and Siegert, F., 1999. Monitoring of deforestation and land use in Indonesia with multitemporal ERS data. International Journal of Remote Sensing, 20 (14), pp. 2835-2853.

Lambin, E.F. and Strahler, A.H., 1994. Change-vector analysis in multitemporal space: A tool to detect and categorize land-cover change processes using high temporal-resolution satellite data. Remote Sensing of Environment, 48 (2), pp. 231-244.

Mas, J.F., 1999. Monitoring land-cover changes: a comparison of change detection techniques. International Journal of Remote Sensing, 20 (1), pp. 139-152.

Nielsen, A.A., 2007. The regularized iteratively reweighted MAD method for change detection in multi- and hyperspectral data. IEEE Transactions on Image Processing, 16 (2), pp. 463-478.

Panuju, D.R., Paull, D.J., Griffin, A.L. and Trisasongko, B.H., 2017. The performance of iteratively reweighted multivariate alteration detection (IRMAD) applied on untransformed and transformed Landsat surface reflectance, 38th Asian Conference on Remote Sensing - Space Applications: Touching Human Lives. Asian Association on Remote Sensing, New Delhi, India, pp. 317-325.

Singh, A.N., 1989. Review Article Digital change detection techniques using remotely-sensed data. International Journal of Remote Sensing, 10 (6), pp. 989-1003.

Stramondo, S., Bignami, C., Chini, M., Pierdicca, N. and Tertulliani, A., 2006. Satellite radar and optical remote sensing for earthquake damage detection: results from different case studies. International Journal of Remote Sensing, 27 (20), pp. 4433-4447.

Townshend, J.R., Justice, C.O., Gurney, C. and McManus, J., 1992. The impact of misregistration on change detection. IEEE Transactions on Geoscience and Remote Sensing, 30 (5), pp. 1054-1060.

Trisasongko, B.H., Panuju, D.R., Paull, D.J., Jia, X. and Griffin, A.L., 2017. Comparing six pixel-wise classifiers for tropical rural land cover mapping using four forms of fully polarimetric SAR data. International Journal of Remote Sensing, 38 (11), pp. 3274-3293.

Trudel, M., Charbonneau, F.J. and Leconte, R., 2012. Using RADARSAT-2 polarimetric and ENVISAT-ASAR dual-polarization data for estimating soil moisture over agricultural fields. Canadian Journal of Remote Sensing, 38 (4), pp. 514-527.

Vicente-Serrano, S.M., Perez-Cabello, F. and Lasanta, T., 2008. Assessment of radiometric correction techniques in analyzing vegetation variability and change using time series of Landsat images. Remote Sensing of Environment, 112 (10), pp. 3916-3934.

Wang, B., Choi, S.K., Han, Y.K., Lee, S.K. and Choi, J.W., 2015. Application of IRMAD using synthetically fused images for change detection in hyperspectral data. Remote Sensing Letters, 6 (8), pp. 578-586.

Yayusman, L.F. and Nagasawa, R., 2015. ALOS-Sensor data integration for the detection of smallholder's oil palm plantation in Southern Sumatra, Indonesia. J. JASS, 31 (2), pp. 27-40.

THE DETERMINATION OF THE EFFECT OF SOIL HYPERTROPHICATION WITH RESPECT TO MUNG BEAN MORPHOLOGY USING RGB ANALYSIS AND CANNY EDGE DETECTION

Jennifer C. Dela Cruz, Jessie R. Balbin, Julius T. Sese,
Ivan Jason A. Inmenzo, Jean Rene D. Kalaw, Ryann David C. Paglinawan, Ian Gabriel W. Sumague

School of Electrical, Electronics, and Computer Engineering, Mapúa University, 658 Muralla St., Intramuros, Manila 1002, Philippines
Email: jcdelacruz@mapua.edu.ph; jrbalbin@mapua.edu.ph; jtsese@mapua.edu.ph

KEYWRORDS: hypertrophication, plant morphology, Mung Bean, RGB analysis

ABSTRACT: The study utilized a microcontroller based prototype for assessing the effects of soil hypertrophication on Mung Bean Plants. Canny Edge detection and RGB analysis were used for analyzing the morphology of the plant. Rapitest Soil Test Kit was used to determine the nutrient levels, specifically, the NPK levels present in the soil. The study shows that NPK Hypertrophication results in smaller morphology and slower growth as compared to the recommended set-up. Nutrients were varied to assess the effects of specific nutrients on the plant morphology. With the results of the research, other studies will be able to make use of the data and find ways to improve the situation in the plantations and farmlands. The study will also be useful for agriculture students who wish to conduct research regarding plant morphology.

1. INTRODUCTION

Hypertrophication, otherwise known as Eutrophication in known to be the dramatic increase in the nutrient levels, specifically Phosphorus and Nitrogen in a body of water (Szekielda et al,2014). Soil Hypertrophication occurs when the land or plantation is exposed to eutrophicated water, or perhaps due to the overuse of fertilizers. According to the National Economic and Development Authority in 2008, the agricultural practices result to 37% of the total water pollution in the Philippines, the polluted water used as well as the high nutrient content of soil affects the characteristics of the plant in agricultural lands (Lauffer et.al, 2015). The growth and development of a plant may be used as a part of the analysis of the soil quality and soil nutrients. When there is an excessive abundance of nutrients in the soil, it could lead to abnormal growth of qualities of the plant, as well as cause some soil-borne plant diseases and attract unwanted algae (Shiva Kumar et.al, 2014). Knowing these conditions, the problem arise is the occurring immoderate eutrophication on the agricultural sectors, manifesting the quality of the soil thus affecting the overall condition of the plant.

Previous studies stated that manmade Nitrogen and Phosphorus discharge results in an accelerated eutrophication process. In their research regarding the eutrophication in Manila Bay (Raven, et.al, 2005), they have found using chlorophyll estimates and Satellite measurements that Eutrophication is present throughout the year, yet is decoupled from the monsoon seasons. Another research used the method of a colorimetry based test kit utilizing ascorbic acid was used to measure the levels of phosphorus and potassium .Another study that focuses on rice plant nitrogen level assessment published in 2013 determined the nitrogen level in rice plants, the researchers made use of a Leaf Color Chart specifically made for rice plants with the supposed corresponding nitrogen level, using the image processing algorithm, they were able to use basic statistical methods (James, D. W, 1993). These studies show that data acquired regarding plant morphology can be used for the analysis of the development and nutritional conditions of a plant.

Currently, the method of determining the soil quality is through laboratory testing of soil samples, which requires complex equipment and is economically impractical considering the need for frequent monitoring (Khirade and Patil, 2015). Another method is the use of a colorimetric test kit which relies on a reference chart and manual identification. Previous researchers did not make use of the test kit and morphology image processing to determine the effects of soil Hypertrophication on certain plants, as to whether it would have purely negative effects or if it may have any positive effects on the growth of the plant (Regalado and Dela Cruz,2016).Using either manual ocular inspection or image Processing, researchers were able to determine and estimate the plant nutrients using either official leaf color charts and other reference materials, or with the use of artificial neural networks for automated analysis (Orillo, et.al,2014). In order to address this problem the researchers would observe the soil quality, and determine its effects to the growth of the plant to find out the exact effects of Soil Hypertrophication to the Mung Bean morphology, and determine what variations to the soil condition may be done to improve the growth of the plant.

The main objective of the study is to determine the effect of Soil Hypertrophication with respect to Mung Bean morphology using RGB Analysis and Canny Edge Detection. Particularly, the researchers aim to (1) develop a microcontroller based prototype which utilizes a color based Soil NPK Test kit and a camera for the analysis of the soil NPK values and the morphology of the plant, (2) develop a program utilizing image processing algorithms such as RGB analysis, which would be able to determine the Soil NPK levels, and Canny edge detection to determine the change in morphology of the plant, (3) to test different soil conditions and determine the effects of the variation, by changing the concentration fertilizer to determine the ideal soil condition to increase the growth of the plant, (4) to verify the results of the testing by replicating the ideal condition found to yield similar plant growth.

composed of their respective red, green and blue color values which makes it suitable for analysis. The colors are interpreted individually because analysing all the colors at once would produce inaccurate results. Averaging of respective Red, Green and Blue intensities are made in order to get the ratio of the colors.

1.2 Canny Edge Detection

Canny edge detection is a multi-step algorithm that can detect edges with noise supressed at the same time.

There are three issues the edge detector must address:

- **Error Rate** – the detector must only find edges and must not miss any edges.
- **Localization** – the actual edge must be as small as possible and the distances between pixels should be determined.
- **Response** – the detector should only identify one edge pixel when only one edge pixel actually exists.

$$(x) = e^{-2\sigma^2} \quad , \quad (y) = e^{-2\sigma^2} \qquad (1)$$

As shown in equation 1, the Canny Edge Detector makes use of a Gaussian function as well as the first derivative of the said Gaussian Function, for the x dimension and y dimension

The Algorithm for edge detection now focuses on the following instructions,

1) Create a one-dimensional Gaussian Mask G to convolve with g in which g is the image. Using σ as the standard deviation. This is shown in equation (2).

$$g(x, y) = Go(x, y) * f(m, n) \qquad (2)$$

Where:

$$Go = \frac{1}{\sqrt{2\pi\partial^2}} exp\left(-\frac{x^2+y^2}{2\partial^2}\right) \qquad (3)$$

Equation (3), the Gaussian Filter Equation shows smoothening the image with a Gaussian filter to reduce noise and unwanted details and textures.

2) Convolve I with G along the x direction to obtain gx and along y to obtain gy .Afterwards, convolve gx with Gx to obtain g'x, and Convolve gy with Gy to obtain g'y

$$(x, y) = \sqrt{g'(x, y)^2 + g'(x, y)^2} \qquad (4)$$

Equation (4) shows the computation for the magnitude of the Gaussian function in which it corresponds to the Canny Edge Detection.

Furthermore the direction of the gradient is to be computed using equation (5).

$$\theta(x, y) = arctan\frac{g'x(x,y)}{g'y(x,y)} \qquad (5)$$

As shown in equation (5), the direction of the gradient is computed using an inverse tangent function of the convolution functions g'x over g'y.

3) The Final step is called *non-maximum suppression step*, where pixels that are not local maxima are removed.

$$M_T(x, y) = \begin{cases} M(x, y), & if\ M(x, y) > T \\ 0, & otherwise \end{cases} \qquad (6)$$

Equation (6), the threshold value function, suppresses non-maxima pixels in the edges in M_T obtained above to thin the edge ridges (as the edges might have been broadened in step 1). To do so, check to see whether each non-zero $M_T(x,y)$ is greater than its two neighbors along the gradient direction (x, y) . If so, keep $M_T(x,y)$ unchanged, otherwise, set it to 0.

2. METHODOLOGY

The study will make use of images of the soil test kit and the plant itself as inputs to the image processing algorithms such as RGB Color Analysis and Canny Edge Detection. With the proper calibration and adjustments, the results shall provide the soil NPK levels and the plant growth parameters such as average height, average growth rate, and leaf coverage area.

As shown in figure 1, the process makes use of the Raspberry Pi for Image Acquisition and image pre- processing. The images are

Pi GUI.
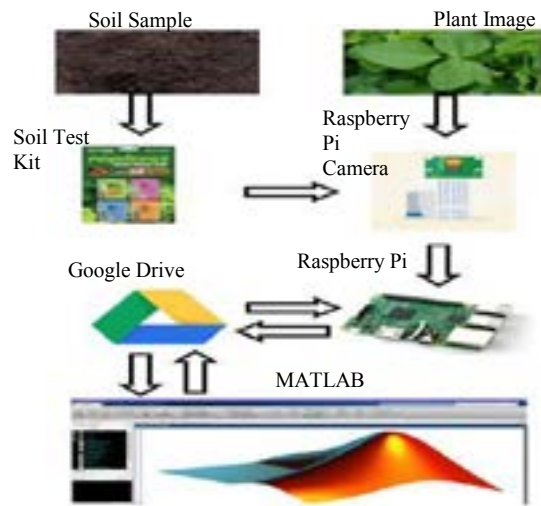
Fig. 1. Conceptual Framework of Data Transmission

2.1 Soil Test Kit Image Acquisition

As shown in Figure 2 and 3, after the soil testing procedures are performed and the soil test kit solution have shown the resulting color of the corresponding NPK levels, the test tubes are placed inside the casing for calibrated lighting and also for their images to be taken by the Raspberry Pi camera. Where the results of the image processing are seen in Figure 4.
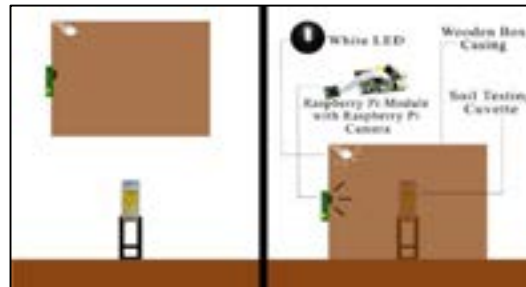
Fig. 2. Image Acquisition set-up of Test Kit

Fig. 3. Actual Setup for Soil Test Kit Image Acquisition
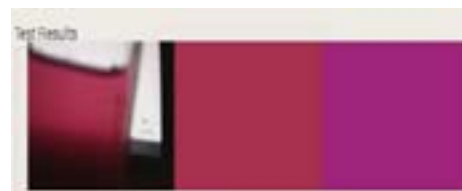
Fig. 4. RGB Analysis results on Rapitest Soil Kit

2.2 Plant Image Acquisition

As shown in Figure 5 and 6,, for the image acquisition of a single potted plant, the plant is placed inside the casing for calibrated lighting and for its image to be taken by the Raspberry Pi camera. Canny Edge detection result is shown in Fig.7
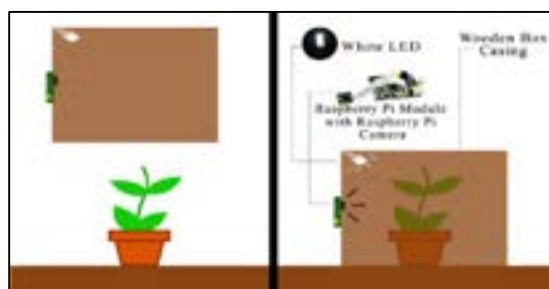
Fig. 6. Actual Plant Image Acquisition Set-up

(a)   (b)
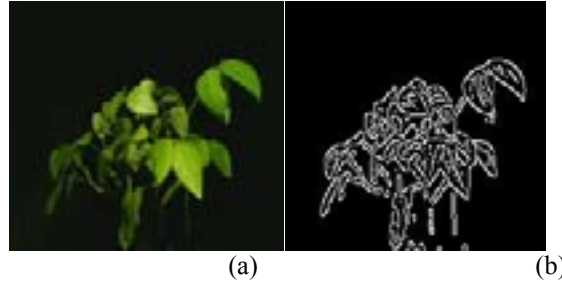
Fig. 7. Canny Edge Filtering on Mung bean leaves using OpenCV

(a) Original Image (b) Canny Operation Output

Image comparison of the canny processed plant images will be used to determine the plant height. The plant leaf coverage will also be determined by the segmented image and the result of the Canny operation. The leaf coverage area will be approximated in cm^2. The formula used in the computation of the height and leaf coverage area are shown in equations (7) and (8), where the number of pixels in an image is 28341 pixels. The resolution of the image is 400 x 800 , with a calibration height of 75 cm and width of 150 cm, resulting in an captured area of 11250 cm^2.

$$\text{Height(h)} = (\text{Highest white pixel} - \text{lowest white pixel}) \times (\text{Pixel height}) \quad (7)$$

$$\text{Leaf Coverage Area} = (\text{Green Pixels}) \times (\text{Unit Pixel Area}) \quad (8)$$

The formula used in the computation of the height and leaf coverage area are shown in equations (7) and (8), where the number of pixels in an image is 28341 pixels. The resolution of the image is 800 x 400, with a calibration height of 75 cm.

2.3 Software Development

Fig. 8. Software Data Transmission

The study makes use of google drive for data storage and OpenCV for image processing where the software data transmission is shown if Fig. 8.

In this study, the obtained NPK levels through RGB analysis are used for the analysis of the plant morphology. In order to study the plant morphology, the image processing algorithm called Canny Edge Detection is used. This algorithm is used to identify the edges of the plant in the image for analysis and data comparison with the NPK levels. For the pre-processing of the image it will require some minor morph operation for feature enhancement and noise reduction using binary erosion and dilation of the image.

Soil testing kits were also used in order to determine the NPK levels of soil. These test kits however, do not give exact quantities of data but only produce colors from the reaction of the testing reagents with the soil. The soil test kit provides a reference color chart in order for the user to interpret the level of NPK present in the soil. In this study, RGB Analysis is used to interpret the NPK levels of the soil. The raspberry pi camera will take an image of the cuvette from the soil test kit where the color of the nutrient level is produced, then the Raspberry Pi will perform the RGB analysis algorithm upon the image and display results. The image is also uploaded to google drive for storage and backup purposes.

different combinations of NPK levels were observed as the mungbean plant grows in a span of 60 days. The plants' morphology was measured every five days and the resulting values of height and area were recorded.
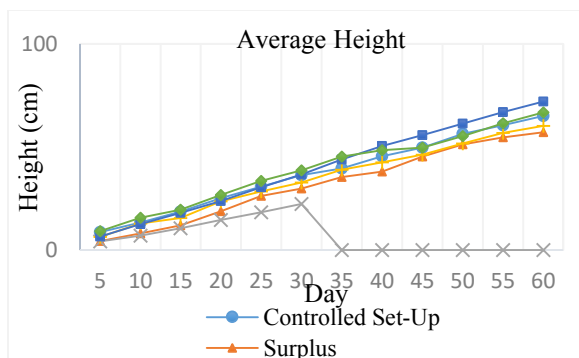
Fig. 9. Graph of Average Height for all Set-ups

Figure 9 shows the height of each plant setup where the High P setup has produced the tallest height. The increase in height in every setup is relatively linear except for the deficient setup as the plant started to wilt after thirty days.
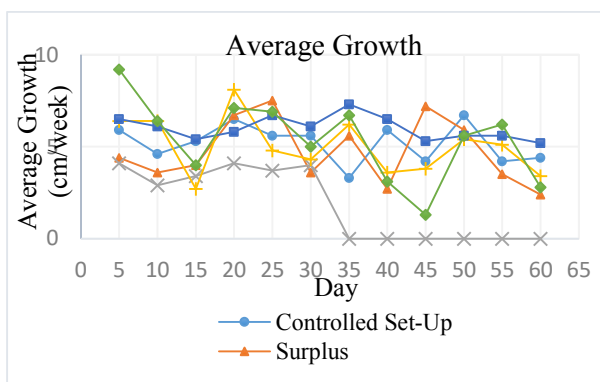
Fig. 10. Graph of Average Growth for all Set-ups

Figure 10 shows the average growth rate of each setup. The growth rate is determined by the difference in height per week. The maximum growth rate is achieved by the high K setup after five days, followed by the high N setup at twenty days.
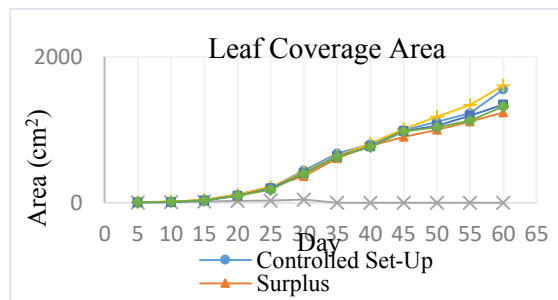
Fig. 11. Graph of Leaf Coverage Area for all Set-ups

Figure 11 shows the graph of each setup's leaf coverage area. The setup that covered the most area was the high N setup followed by the controlled setup with only a slight difference. The setups followed a relatively alike trend with evident differences.

Table 1. Seed number per setup

Set-Up	Seed Number (average number per group)
Controlled	32
Hypertrophicated	27
Deficient NPK	0
N-Variation	25
P-Variation	23

After the maturity of the plant, when the seeds are available, the seeds for each setup is obtained as shown in Table 1 and averaged per group to determine which soil condition resulted in a higher number of seeds compared to the controlled setup.

It was found that the recommended values of NPK still manages to result in a higher average seed count, with the hypertrophicated set-up having the second highest count. Though the data shows that the difference in the seed number is not quite large as compared to the other set-ups were the number of matured seeds pale in comparison to the quantity yielded by the recommended set-up.

4.   CONCLUSION

The prototype was able to obtain, analyze and record the morphological characteristics of the plant through image acquisition and image processing. The prototype was also able to use RGB analysis on the soil test result to determine the levels of the nutrients in the soil.

Experimental results show that Soil Hypertrophication causes the plant to have a decrease in its morphological growth, especially considering the height and leaf area. The data is significantly lower compared to that of the recommended values of NPK. It was also determined that the characteristics of the samples in the recommended set-up did not necessarily meet the highest values for the height and the leaf coverage area, but rather, the results were average. Considering the effects of the variation set-ups for the plant, it was found that increasing the Nitrogen levels resulted in an increase in Leaf coverage area, but lower height compared to the other set-ups. Increasing the Phosphorus level on the other hand shows greater height among all the samples but inhibits the growth of leaves, resulting in lower leaf coverage area. When all levels of NPK are elevated to surplus, it was found that the desirable effects of the exclusive set-ups were not present. The researchers determined through the data that the recommended set-up positively affected the growth of the plant best.

After maturity, it was found that the controlled set-up yielded the most number of seeds, with the hypertrophicated set-up having the second highest seed count. The researchers were also able to verify the results by replicating the conditions for the N-Variation set-up, and obtaining similar growth rates and morphological characteristics.

5.   RECOMMENDATIONS

In the study, the researchers focused on using image processing to analyze the height and leaf coverage area of the plant given a certain soil nutrient level. It is recommended to add other image processing algorithms to further increase the reliability of the data. Furthermore, the researchers recommend that future studies make use of other means of determining the soil nutrient level, considering that as of present, the most reliable method of determining the NPK values of the soil are through soil test kits or laboratory testing.

It is also recommended that future studies make use of the data for comparison for other parameters that may affect the morphology of Mung Beans. A similar set-up may also be used on other plants for different studies concerning the effects of Soil Hypertrophication on other plants.

6.   REFERENCES

Szekielda, Karl H., Emilyn Espiritu, and Nofel Lagrosas. *"EUTROPHICATION OF MANILA REGION, PHILIPPINES".* International Journal of Geology, Earth & Environmental Sciences 4.3 (2014): 38-50.

M. Lauffer, F. Genty, J. L. Collette and S. Margueron, *"Phytoplankton identification by combined methods of morphological processing and fluorescence imaging,"* 2015

G. Shiva Kumar, P. Lakshmi Sruthi, P. Rajasekhar and F. Karaer, *"Eutrophication assessment of a shallow lake using GIS,"* International Conference on Computing and Communication Technologies, Hyderabad, 2014, pp. 1-6.

Raven, Peter H., Ray F. Evert, and Susan E. Eichhorn. *Biology Of Plants.* 7th ed. W H Freeman, 2005. P

James, D. W., "*Diagnostic Testing for Nitrogen Soil Fertility"* (1993). All Archived Publications

S. D. Khirade and A. B. Patil, "Plant Disease Detection Using Image Processing," 2015 International Conference on Computing Communication Control and Automation, Pune, 2015, pp. 768-771.

G. Regalado and J. C. Dela Cruz, *"Soil pH and nutrient (Nitrogen, Phosphorus and Potassium) analyzer using colorimetry,"* 2016 IEEE Region 10 Conference (TENCON), Singapore, 2016, pp. 2387-2391.

J. W. Orillo, G. J. Emperador, M. G. Gasgonia, M. Parpan and J. Yang, *"Rice plant nitrogen level assessment through image processing using artificial neural network,"* 2014 International Conference on Humanoid, Nanotechnology, Information Technology, Communication and Control, Environment and Management (HNICEM), Palawan, 2014, pp. 1-6.

EVALUATION OF INTENSITY AND RGB VALUES ON 3D POINT CLOUD CLASSIFICATION

Quan Li (1), Xiaojun Cheng (1)

[1] College of Surveying and Geo-Informatics, Tongji University, No. 1239, Siping Road, Shanghai 200092, China

Email: 329yvonnelee@tongji.edu.cn; cxj@tongji.edu.cn

KEYWORDS: Point Cloud; Classification; Supervoxel; Intensity; RGB

ABSTRACT: 3D point cloud classification has become an issue of major interest in recent years. The common workflow of 3D point cloud classification involves neighborhood selection, feature selection and extraction and the classification of points based on the respective features. The feature selection and extraction has been the focus of many studies. In most previous studies, only geometric features are used for classification and there are limited studies which have investigated the potential of both intensity and RGB values on classification using TLS (Terrestrial Laser Scanner) point cloud. Therefore, the main objective of this study is to carefully investigate the influence of intensity and RGB values on the classification performance. Firstly, the point cloud data are over-segmented into spatially consistent supervoxels. The supervoxel based neighborhood is utilized to improve computational efficiency. Then four feature sets, namely the geometric features, the geometric features combined with the intensity features, the geometric features combined with RGB features and the geometric features combined with both intensity and RGB features are extracted. These features are then used for training four Random Forest classifiers in the training stage and for classification in the prediction stage. Finally, the recall, precision and overall accuracy are used to evaluate the classification results. The designed experiments are implemented on two real-world datasets. To train the classifiers and evaluate the classification results, these two datasets are manually labeled and classified into six classes which involve ground, façade, pole-like object, tree, vegetation and curb. The experimental results show that the overall classification accuracy has been improved when either intensity or RGB features is involved and the geometric features combined with both intensity and RGB features achieves the highest overall accuracy.

1. INTRODUCTION

With the advances of 3D data acquisition technology like TLS which can obtain huge amount of points in a short time, the automatic classification of 3D point cloud has gained widespread interest and importance in recent years. The common workflow of point cloud classification involves neighborhood selection, feature extraction and the classification of points based on the respective features (Weinmann et al., 2015). The feature selection and extraction has long been the research interest for many previous studies. The features often used in TLS point cloud classification is related to the geometric information (Weinmann et al., 2017; Hackel et al., 2017). Besides the geometric information, most TLS systems also record the intensity information, which is considered as an important measurement of the spectral property of the scanned surface. And many TLS systems are also equipped with digital cameras which can acquire corresponding color information for each point. Several previous studies

have also utilized one of these two information for TLS point cloud classification. Li et al. (2016) have used the mean RGB color and the LAB values of that mean RGB as features in their study. In the study of Babahajiani et al. (2014), they have utilized the median intensity of points in feature extraction. Only few studies have used both intensity and RGB values for classification. In the study of Aijazi et al. (2013), they have incorporated RGB and intensity values on classification and find that intensity with RGB value performs better in classification than RGB color alone. However, they evaluate the classification result with only the overall accuracy for a whole test case. In this paper, we carefully analyze the impact of both intensity and RGB values on the 3D point cloud classification performance for the whole test case. In addition, we also analyze the impact on individual objects and the evaluation measures also includes precision and recall values for each class.

The paper is organized as follows. We first introduce the proposed method in Section 2. Then in Section 3, the experiments conducted are described and the experimental results are carefully discussed. Finally, conclusions follow in Section 4.

2. PROPOSED METHOD

Figure 1 provides an outline of the proposed method. The original point cloud obtained is first processed to eliminate noises. Afterwards, the point cloud is over-segmented into supervoxels. Based on the supervoxel neighborhood, the feature sets related to geometric information, intensity and RGB values are extracted, which are then used for training the Random Forest classifiers in the training stage and for classification in the prediction stage. To evaluate the classification performance, the recall, precision and overall accuracy are used.
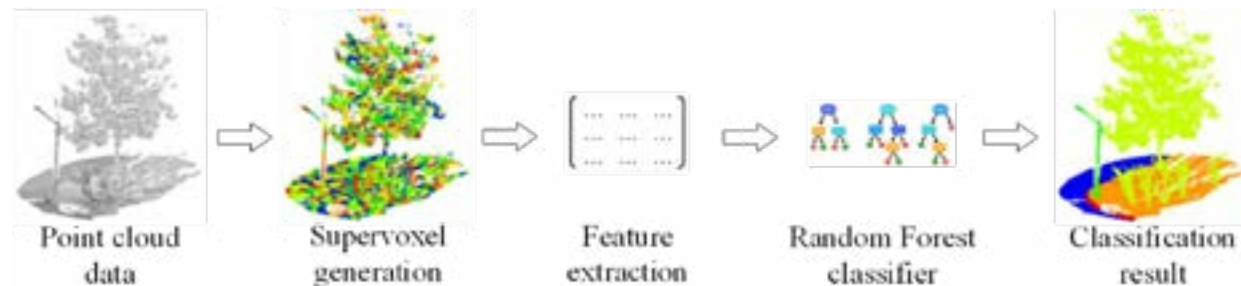
Figure 1 The outline of the proposed method

2.1 Supervoxel Neighborhood Generation

The neighborhood selection problem is also an interest of many studies. Many researchers focused on point-wise classification approaches, in which features for every point are calculated by using the points within its neighborhood. The spherical neighborhood and K-Nearest neighborhood are two commonly used neighborhood. The spherical neighborhood which has fix-bound radius is inappropriate for TLS point cloud for its varying point density. Although the K-Nearest neighborhood can provide irregular neighborhood size depends on the density of point cloud, it requires high computational complexity. To improve the computational efficiency, some authors have proposed the voxel-based neighborhood. In the study of Lin and Suter (2009), they first segment the point

cloud into supervoxels as support regions and then multiscale conditional random field method is used to classify TLS point cloud. In this study, we also utilized supervoxel neighborhood for feature extraction. Supervoxels group 3D points into perceptually meaningful clusters with high efficiency. The commonly used method for supervoxel generation is VCCS (Voxel Cloud Connectivity Segmentation) (Papon et al., 2013). However, for point cloud with varying density, it cannot preserve object boundaries well and may then leads to under-segment errors. Therefore, in this paper the supervoxel generation method proposed by Lin et al. (2018) is used. Their method provides better-preserved boundaries and lower under-segment errors. Besides, their method is more computationally efficient than most of the state-of-the-art supervoxel methods.

2.2 Feature Extraction

Formally, a point cloud can be written as $P = \{x_i, y_i, z_i, I_i, R_i, G_i, B_i\}$, consisting of the coordinates x_i, y_i, z_i of the 3D point, the intensity data I_i and the RGB values R_i, G_i, B_i. The derived supervoxel neighborhood serves as the basis for feature extraction. In this study, we extract three types of features, namely geometric features, intensity features and color features. The geometric features are mainly comprised with covariance features which are derived from the normalized eigenvalues $\lambda_{1,2,3}$ of the 3D structure tensor (Demantké et al., 2011; Weinmann et al., 2014). These eigenvalues are sorted as $\lambda_1 \geq \lambda_2 \geq \lambda_3$ and all these features are listed in equation (1).

$$
\begin{aligned}
\text{Linearity:} \quad & (\lambda_1 - \lambda_2)/\lambda_1 \\
\text{Planarity:} \quad & (\lambda_2 - \lambda_3)/\lambda_1 \\
\text{Sphericity:} \quad & \lambda_3/\lambda_1 \\
\text{Omnivariance:} \quad & (\lambda_1 \cdot \lambda_2 \cdot \lambda_3)^{1/3} \\
\text{Anisotropy:} \quad & (\lambda_1 - \lambda_3)/\lambda_1 \\
\text{Eigenentropy:} \quad & -\sum_{i=1}^{3} \lambda_i \cdot \ln(\lambda_i) \\
\text{Sum of eigenvalues:} \quad & \lambda_1 + \lambda_2 + \lambda_3 \\
\text{Change of curvature:} \quad & \lambda_3/(\lambda_1 + \lambda_2 + \lambda_3)
\end{aligned}
\tag{1}
$$

Besides covariance features, three other features derived from the supervoxel neighborhood are given by mean z value, z variance and maximum z difference which are listed below in equation (2).

$$
\begin{aligned}
\text{Mean } z: \quad & \left(\sum_{i=1}^{n} z_i\right)/n \\
z \text{ variance:} \quad & \left(\sum_{i=1}^{n} z_i - \bar{z}\right)/n \\
\text{Maximum } z \text{ difference:} \quad & z_{max} - z_{min}
\end{aligned}
\tag{2}
$$

The considered intensity feature set comprises three features which involve mean intensity, intensity variance and maximum intensity difference. The three features are listed in equation (3).

$$
\begin{aligned}
\text{Mean intensity:} \quad & \left(\sum_{i=1}^{n} I_i\right)/n \\
\text{Intensity variance:} \quad & \left(\sum_{i=1}^{n} I_i - \bar{I}\right)/n
\end{aligned}
\tag{3}
$$

$$\text{Maximum intensity difference:} \quad I_{max} - I_{min}$$

The considered color feature set comprises 12 features. There are mean R, G, B, R, G, B ratio, R, G, B variance and maximum R, G, B difference, which are listed in equation (4).

$$
\begin{aligned}
\text{Mean R:} \quad & (\textstyle\sum_{i=1}^{n} R_i)/n \\
\text{Mean G:} \quad & (\textstyle\sum_{i=1}^{n} G_i)/n \\
\text{Mean B:} \quad & (\textstyle\sum_{i=1}^{n} B_i)/n \\
\text{R ratio:} \quad & \overline{R}/\textstyle\sum_{i=1}^{n}(\overline{R} + \overline{G} + \overline{B}) \\
\text{G ratio:} \quad & \overline{G}/\textstyle\sum_{i=1}^{n}(\overline{R} + \overline{G} + \overline{B}) \\
\text{B ratio:} \quad & \overline{B}/\textstyle\sum_{i=1}^{n}(\overline{R} + \overline{G} + \overline{B}) \\
\text{R variance:} \quad & (\textstyle\sum_{i=1}^{n} R_i - \overline{R})/n \\
\text{G variance:} \quad & (\textstyle\sum_{i=1}^{n} G_i - \overline{G})/n \\
\text{B variance:} \quad & (\textstyle\sum_{i=1}^{n} B_i - \overline{B})/n \\
\text{Maximum R difference:} \quad & R_{max} - R_{min} \\
\text{Maximum G difference:} \quad & G_{max} - G_{min} \\
\text{Maximum B difference:} \quad & B_{max} - B_{min}
\end{aligned}
\tag{4}
$$

2.3 Classification and Evaluation

After feature extraction, these feature sets are used as the inputs for the Random Forest classifier. Random Forest classifier has been proved to be successfully applied to point cloud classification in many previous studies due to the fact that it can provide a good trade-off with respect to both accuracy and computational efficiency (Chehata et al., 2009; Hackel et al., 2016). Random Forest creates a set of decision trees from randomly selected subset of training set and then combine these decision trees with model averaging to reduce the generalization errors of individual trees.

To assess the quality of the classification, the precision, recall and overall accuracy are estimated. Precision represents a measure of exactness or quality, recall represents a measure of completeness or quantity and overall accuracy represents a measure of the overall performance of the classification results. These evaluation measures are described below in equation to equation.

$$\text{Precision} = \frac{TP}{TP+FP} \tag{5}$$

$$\text{Recall} = \frac{TP}{TP+FN} \tag{6}$$

$$\text{Overall accuracy} = \frac{TP+FN}{TP+FP+TN+FN} \tag{7}$$

where TP, TN, FP and FN are the number of true positive, true negative, false positive and false negative counts.

3. EXPERIMENT AND DISCUSSION

3.1 Datasets

The point clouds involved in this study were obtained by a Faro Focus³ᴰ scanner on a campus. After preprocessing, two test cases contain 1,250,733 points and 835,482 points respectively. In order to train the classifier and evaluate classification performance, we manually labelled two test cases into six classes: ground, façade, pole-like object (note: we use pole for short in the following paper), tree, vegetation and curb. Figure 2 shows the ground truth labeling of two test cases. For each case, we randomly select a training set with 500 training examples per class and the remaining is used as test case. Both test cases are first over-segmented into supervoxels. The resolution of supervoxels is set to be 0.5m in our application.
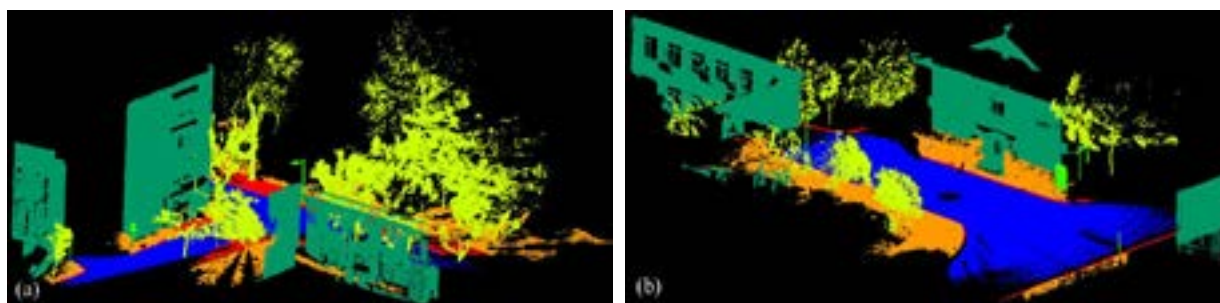
Figure 2 Ground truth labeling of both test cases: (a) test case 1, (b) test case 2. Legend for labels: ground façade pole tree vegetation curb.

3.2 Results and Discussions

After feature extraction, the Random Forest classifier is used for training and predicting. In this study, Matlab's Random Forest classifier implementation is used. A total of 100 trees are used for our application. The overall accuracy, recall and precision values for both cases are listed in table 1 and table 2. The visualization of the classification results with four feature sets are illustrated in Figure 3 and Figure 4. In the tables and figures, Geo stands for geometric features, Geo & I stands for geometric features combined with intensity features, Geo & C stands for geometric features combined with color features and Geo & I & C stands for geometric features combined with both intensity and color features.

Table 1 Overall accuracy (in %) of two test cases for different feature sets

Feature set	Test case 1	Test case 2
Geo	92.6	93.0
Geo & I	93.2	94.4
Geo & C	96.0	95.9
Geo & I & C	**96.2**	**96.1**

From the experiment results, we can see that the overall accuracy of geometric features combined either with intensity or color features is higher than geometric features alone. Moreover, geometric features combined with both intensity and color features achieves the highest overall accuracy. Compared with intensity features, when color features are considered, the overall accuracy improves much more. And compared with geometric features combined with color features, the overall accuracy only improves slightly when additional intensity features are combined. This may be due to the fact that the original intensity is affected by several factors such as range, incidence angle thus influencing the classification results. Further studies may need to consider correcting the original intensity to improve the classification accuracy.

Table 2 Recall and precision values (in %) of three test cases for different feature sets

Class	Feature set	Test case 1		Test case 2	
		Recall	Precision	Recall	Precision
Ground	Geo	**99.0**	99.6	98.5	99.6
	Geo & I	98.9	99.5	**98.7**	99.6
	Geo & C	98.6	**99.7**	98.5	99.9
	Geo & I & C	98.9	**99.7**	**98.7**	**100.0**
Façade	Geo	89.2	95.6	91.5	98.7
	Geo & I	89.7	96.7	93.4	99.1
	Geo & C	94.4	**98.6**	96.3	99.4
	Geo & I & C	**94.7**	98.5	**96.3**	**99.6**
Pole	Geo	**99.6**	21.2	**99.4**	27.9
	Geo & I	**99.6**	23.7	**99.4**	48.2
	Geo & C	**99.6**	30.4	**99.4**	66.1
	Geo & I & C	**99.6**	**35.8**	**99.4**	**72.1**
Tree	Geo	92.0	92.4	87.0	84.9
	Geo & I	93.2	92.7	90.9	87.2
	Geo & C	96.1	**96.2**	94.9	89.8
	Geo & I & C	**96.2**	**96.2**	**95.5**	**90.0**
Vegetation	Geo	94.6	89.4	89.7	93.5
	Geo & I	95.4	89.5	91.0	92.8
	Geo & C	**96.6**	92.6	91.0	**95.9**
	Geo & I & C	96.5	**92.8**	**91.5**	95.8
Curb	Geo	96.7	85.3	95.9	48.4
	Geo & I	96.2	85.6	95.5	**50.3**
	Geo & C	96.9	89.2	**96.2**	48.5
	Geo & I & C	**97.1**	**89.9**	95.4	49.4

The recall values of six classes for both test cases are relatively high. And the pole achieves the highest for both test cases with over 99%. Ground and curb are the next highest with over 98% and 95% for two cases. The recall values for these three classes with four different feature sets are really close and with additional intensity and color features, the recall values do not improve much. Because these three objects have relatively regular geometric shapes thus can be classified correctly with only geometric features. The recall values of other three classes have all been improved with additional intensity and color features. The precision values differ a lot among different classes. Ground is detected with the highest precision with over 99% for both test cases. Façade achieves the next highest with over 95% for both cases. Geometric features combined with both intensity and color features are the most distinctive features for pole classification. Compared with other features, the precision values have been greatly improved. Because poles are similar to tree trunks and some window frames in geometric shape. With only geometric features, lots of tree trunk points and window frame points are wrongly classified as pole points. Tree trunk are rather different from pole in color and intensity, so the classification results have been improved when intensity and color features are considered. Curb in test case 2 has a relatively low precision value. This is mainly due to the fact that curbs in test case 2 are all connected with vegetation and ground and some features of these three are similar. Therefore, many vegetation and ground points are wrongly classified as curb points. Note that when intensity and color features are involved, the precision value has improved a little. Above all, the recall and precision values have all been improved with additional intensity and RGB values which demonstrates that both intensity and RGB values have a positive impact on 3D point cloud classification.
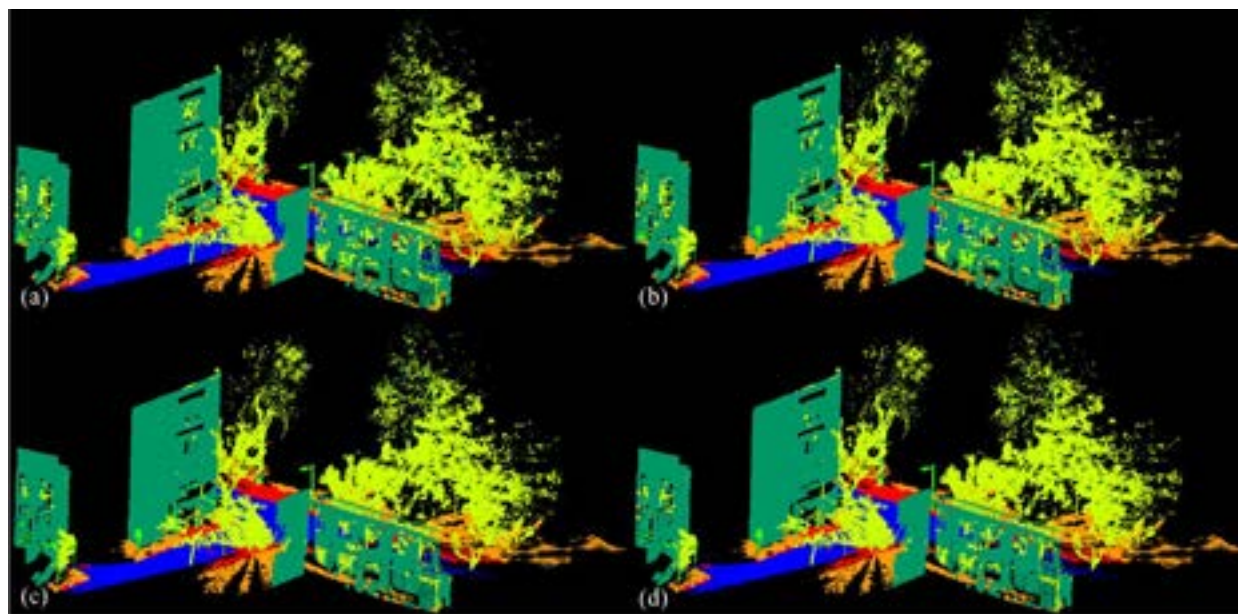
Figure 3 Visualization of classification results for test case 1 with four feature sets: (a) Geo, (b) Geo & I, (c) Geo & C, (d) Geo &I &C. Legend for labels: ground façade pole tree vegetation curb.
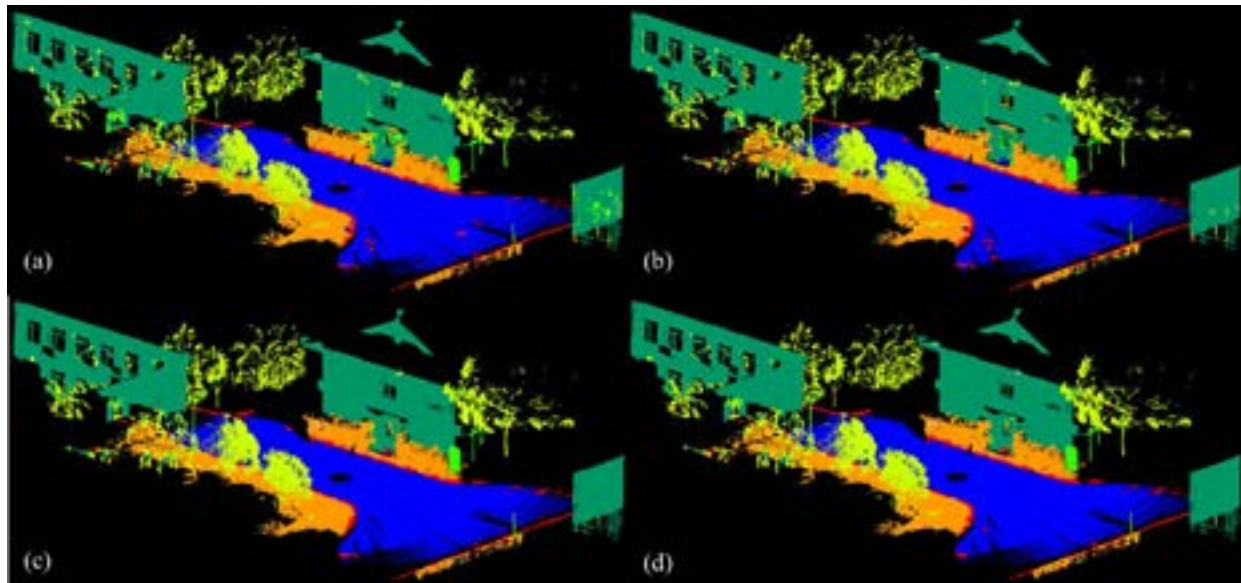
Figure 4 Visualization of classification results for test case 2 with four feature sets: (a) Geo, (b) Geo & I, (c) Geo & C, (d) Geo &I &C. Legend for labels: ground façade pole tree vegetation curb.

4. CONCLUSIONS

In this paper, we carefully evaluate the impact of both intensity and RGB values on 3D point cloud classification. The overall accuracy has been improved when either intensity or RGB features are involved which demonstrates that both intensity and RGB have positive impact on point cloud classification. Especially for pole-like objects, with additional intensity and RGB features, its classification precision has been greatly improved. However, compare with RGB features, classification accuracy only improves slightly when intensity features are involved. This may be due to the fact that the original intensity data is affected by several factors thus making it less applicable. Further study will investigate the impact of corrected intensity features on 3D point cloud classification.

ACKNOWLEDGEMENT

REFERENCES

Aijazi, A. K., Checchin, P., & Trassoudaine, L., 2013. Segmentation based classification of 3D urban point clouds: A super-voxel based approach with evaluation. Remote Sensing, 5(4), 1624-1650.

Babahajiani, P., Fan, L., & Gabbouj, M., 2014. Object recognition in 3d point cloud of urban street scene. In Asian Conference on Computer Vision (pp. 177-190). Springer, Cham.

Chehata, N., Guo, L., & Mallet, C., 2009. Airborne lidar feature selection for urban classification using random forests. International Archives of Photogrammetry, Remote Sensing and Spatial Information Sciences, 38(Part 3), W8.

Demantké, J., Mallet, C., David, N., & Vallet, B., 2011. Dimensionality based scale selection in 3D lidar point clouds. International Archives of the Photogrammetry, Remote Sensing and Spatial Information Sciences, 3812(5), pp. 97-102.

Hackel, T., Wegner, J. D., & Schindler, K., 2016. FAST SEMANTIC SEGMENTATION OF 3D POINT CLOUDS WITH STRONGLY VARYING DENSITY. ISPRS Annals of Photogrammetry, Remote Sensing & Spatial Information Sciences, III-3, pp. 177-184.

Hackel, T., Wegner, J. D., & Schindler, K., 2017. Joint classification and contour extraction of large 3D point clouds. ISPRS Journal of Photogrammetry and Remote Sensing, 130, 231-245.

Li, Z., Zhang, L., Tong, X., Du, B., Wang, Y., Zhang, L., ... & Mathiopoulos, P. T., 2016. A three-step approach for TLS point cloud classification. IEEE Transactions on Geoscience and Remote Sensing, 54(9), 5412-5424.

Lim, E. H., & Suter, D., 2009. 3D terrestrial LIDAR classifications with super-voxels and multi-scale conditional random fields. Computer-Aided Design, 41(10), pp. 701-710.

Lin, Y., Wang, C., Zhai, D., Li, W., & Li, J., 2018. Toward better boundary preserved supervoxel segmentation for 3D point clouds. ISPRS Journal of Photogrammetry and Remote Sensing.

Papon, J., Abramov, A., Schoeler, M., & Worgotter, F., 2013. Voxel cloud connectivity segmentation-supervoxels for point clouds. In Proceedings of the IEEE conference on computer vision and pattern recognition (pp. 2027-2034).

Weinmann, M., Jutzi, B., & Mallet, C., 2014. Semantic 3D scene interpretation: a framework combining optimal neighborhood size selection with relevant features. ISPRS Annals of the Photogrammetry, Remote Sensing and Spatial Information Sciences, 2(3), 181.

Weinmann, M., Jutzi, B., Hinz, S., & Mallet, C., 2015. Semantic point cloud interpretation based on optimal neighborhoods, relevant features and efficient classifiers. ISPRS Journal of Photogrammetry and Remote Sensing, 105, 286-304.

Weinmann, M., Hinz, S., & Weinmann, M., 2017. A hybrid semantic point cloud classification-segmentation framework based on geometric features and semantic rules. PFG–Journal of Photogrammetry, Remote Sensing and Geoinformation Science, 85(3), 183-194.

THE GUIDANCE SEEKER ONBOARD ROMOTE SENSING SATELLITE TO ENHANCE MISSION EFFECTIVENESS

Pei-Hsuan Wu, Jer Ling and Po-Yen Huang

National Space Organization (NSPO), Hsin-Chu, Taiwan, 30078

Email: phyllis@nspo.narl.org.tw ; jl@nspo.narl.org.tw ; mikehuang@nspo.narl.org.tw

KEY WORDS: AI Target-Seeking, Seeker, Machine Learning, Fine-tuned

ABSTRACT

Nowadays, the swath has trend to get smaller with the development of high-resolution satellite for fixed number of pixels. So it is getting more important to capture clear target image efficiently. Otherwise, it might take several times to have a clear image if there is cloud between the remote sensing instrument (RSI) and target image. The objective of this paper is to develop an on-board guidance seeker on RSI. The on-board guidance seeker is used to get wide-angle images and detect target before the task target is captured. Based on wide-angle images and detected-target, the path of satellite can be fine turned to direct ground target without cloud blocking ground target to get clear image or to find target ships and so on. The on-board guidance seeker includes a wide-angle camera, an on-board machine learning unit and an on-board real time path fine-tuning unit. This kind of on-board AI-driven design can enhance the mission effectiveness. It also can be applied to rescue in the open sea.

1. INTRODUCTION

According to the experience on the RSI of FS2 and FS5, it depends on weather and cloud to get a clear image. If the weather is cloudy, the information is hard to get from the satellite imagery. If cloud blocks task target, we have to execute imagery task at next time while satellite passes through the ground target. The ground target imagery usually needs to take several times to complete the whole imagery. The times of image-captured is relative to the swath width. For example, it takes at least two times of image-capturing for the whole island of Taiwan by FS5 on a sun synchronous orbit of 720 km altitude. If the image is not clear, it needs to image the ground target again. For fixed number of pixels, the shorter swath width takes much more times to accomplish the entire ground target than the longer one. Therefore, it is important to capture the clear target image efficiently.

The consists of a wide-angle camera, an on-board unit which has the function of the machine learning and an on-board, real-time path fine-tuning unit. The wide-angle camera provides larger image to the unit to identify the object. Satellite computer defines fine-tuned angle, so that the on-board unit can fine tune path. Fine-tuned path enhances the mission effectiveness. The guidance seeker has two operation modes. One is the image task mode and the other is the target-searching mode, as shown in Fig. 1.

THE EFFECT OF LAND USE CHANGE ON LAND SURFACE TEMPERATURE OF DEPOK CITY, WEST JAVA USING LANDSAT IMAGE DATA

Perlita Angelika (1), Pricilia Chika Alexandra (1), Yerisca Adriani Dethan (1)

¹Departement of Geography, Faculty of Mathematics and Natural Science, University of Indonesia Jl. Margonda Raya, Beji, Pondok Cina, 16424, Depok, Indonesia
Email: perlita.angelika@ui.ac.id, pricilia.chika@ui.ac.id, yerisca.adriani@ui.ac.id

KEY WORDS : City Development, Supervised, Remote Sensing

ABSTRACT : The detection of change in land use digitally by using multi-spectral satellite imagery in the form of Landsat imagery helps in understanding the dynamics of the usage of land use. Moreover, the Landsat image can also be used to detect the surface temperature or LST (Land Surface Temperature) of an area. The land used is closely related to the surface temperature or LST of a region. The development of Depok City makes the use of land that is used as constructed area become higher. It affects the surface temperature because the more constructed an area, the temperature around it will increase. The purpose of this research is to see the relation between the changes of land used in Depok City and the surface temperature of Depok City in 2005-2017. The land used data is obtained from the supervised classification of Landsat 8 OLI/TIRS imager for year 2017 and 5 TM landscapes for year 2005. The surface temperature or LST is obtained from Landsat 8 OLI/TIRS and 5 TM Landsat processing so that obtaining the surface temperature data of Depok City.

INTRODUCTION

The high level of urbanization could induce the change of Land Use / Land Cover (LULC), that affect the process of ecological environment on local and regional stage (Gall and Owen, 1998). The city temperature can be pictured through distribution of Land Surface Temperature (LST). Over the past few years, many satellite image-based studies have focused on the effects of LULC on LST (Xiao and Weng, 2007). Weng (2001) implemented a remote sensing system and geographic information system (GIS) to examine the impact of urban growth on surface temperature and find the urban land could increase the local temperature.

Depok City, aside from being as a goverment center that directly adjacent to the Special Capital Territory of Jakarta, is also a buffer zone of the State Capital City that is directed to residential cities, student city, center of trade and service, city of tourism, and also as a water infiltration area. Depok City's land resources encounter a strain, together with the rapid development of the city. As we all know based on the data analysis of Depok City Spatial Plan (2000-2010) in urban space utilization, residential areas in 2005 reached 8,915.09 ha (44.31%) of the total spatial use of Depok City (Depok City Government, 2015). In 2005, the green area recorded 10,106.14 ha (50.23%) of the area of Depok or depreciation of 0.93% from 2000 data. The increase in land surface cover, affecting the decrease of natural environment in Depok City, mainly due to pressure from land use for residential activities that reach more than 44.31% of the city area. While the width of built area in 2005 reached 10,013.86 ha (49.77%) from the area of Depok City or increased by 3.59% from the data in 2000 (Depok City Government, 2015).

Remote sensing can provide information about parameters such as surface albedo, emissivity and temperature and also NDVI (Chakraborty et al., 2015). Liu and Weng (2008) use landscape matrices to test the relationship between LULC and LST patterns. Liu et al. (2017) apply remote sensing and GIS to examine the impact of urban expansion on surface temperature and to find that urban development benefits have resulted an increase in radiation temperatures above 3K in urban areas. They consider ecological landscape as an effective tool that can be used to measure the LULC and LST patterns. Based on satellite imagery, the vegetation index is used to estimate the percentage of vegetation cover in each pixel as NDVI (Purevdorj et al 1998). Xu (2005) developed a Modified Normalized Difference Water Index (MNDWI) to explain the water purity level and detect the changes of water content. This index can be used to classify various types of land use / cover by determine an appropriate threshold value. They also have the potential to provide qualitative descriptions of LULC conditions in each place (Chen et al 2006).

The most commonly used method use remote sensing data to learn the surface temperature / ambient temperature including NOAA / AVHRR images, Landsat TM / ETM +, MODIS and ASTER. Among multi-source image images, Landsat TM / ETM + images has the highest resolution and are easily obtained from http://www.earthexplorer.usgs.gov/. With the efficiency to produce results that mean to evaluate the surface

temperature, this method is widely used in various research projects in this sector. But in this research, LULC was obtained through Supervised Classification method using Maximum Likelihood Classification. This research was conducted to explain the changes of land use / land cover in Depok City and its relationship to the soil surface temperature.

STUDY AREA

Geographically Depok City is located at coordinates 6º 19 '00 "- 6º 28' 00" South Latitude and 106º 43' 00"- 106º 55' 30" East Longitude. Geographically, Depok City is directly adjacent to Jakarta City or is in the Greater Jakarta area. The Depok City landscape from South to North is a lowland area untill the hills are weakly undulating, with the elevations between 50 - 140 meters above sea level and the slopes of less than 15%. Depok City as the youngest region in West Java, has an area of about 200.29 km^2. The geographical conditions are flooded by large rivers, like the Ciliwung and Cisadane Rivers and 13 sub-watersheds. Besides that there are also 25 lakes. Data of the lakes in 2005 is about 169.68 Ha, with poor average water quality due to contamination. Topographic conditions in the form of undulating lowlands with gentle slope causes flooding problems in some areas, especially the basin between the several rivers that flows from the south to the north: Angke River, Ciliwung River, Pesanggrahan River and Cikeas River (Depok City Government, 2015).
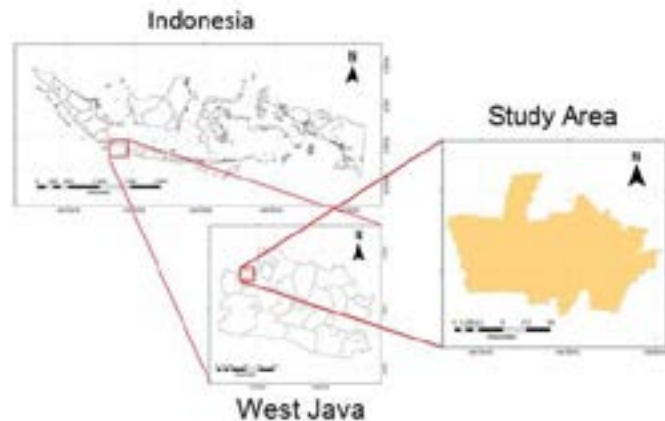
Figure 2.1 : Study Area

METHOD

The images processed were Landsat-5 TM images for 2005 data and Landsat-8 OLI / TIRS imagery for data for 2017. Both images have the same line / line of 122/64. Landsat-5 TM imagery which is the recording data on 2 June 2005 at 02:47:42 with cloud cover as much as 7.0% and 1.0% cloud cover on the island area. Whereas Landsat-8 OLI / TIRS imagery which is the recording data on June 19, 2017 at 02:59:56 with cloud cover as much as 11.47% and 12.73 cloud cover on the island area. Both images have values on sensors and wavelengths available for each band. The following ranks between Landsat-5 TM images and Landsat-8 OLI / TIRS.

Satellite	Sensor	Path / Row	Years	Resolution(m)	Wavelength (μm)
Landsat-5	TM (ThematicMapper)	122 / 64	2005	30	Band 1 : 0,45-0,52
					Band 2 : 0,52-0,60
					Band 3 : 0,63-0,69
					Band 4 : 0,76-0,90
					Band 5 : 1,55-1,75
					Band 6 : 10,40-12,50 (Band

					Thermal)
Landsat-8	OLI (Operational Land Imager) and TIRS (Thermal InfraredSensor)	122 / 64	2017	30 (15 for band 8)	Band 1 : 0,435-0,451
					Band 2 : 0,452-0,512
					Band 3 : 0,533-0,590
					Band 4 : 0,636-0,673
					Band 5 : 0,851-0,879
					Band 6 : 1,566-1,651
					Band 7 : 2,107-2,294
					Band 8 : 0,50-0,68
					Band 9 : 1,363-1,384
					Band 10 : 10,60-11,19 (Band Thermal)
					Band 11 : 11,50-12,51 (Band Thermal)

Table 1. Differences in Landsat-5 TM and Landsat-8 OLI / TIRS imagery

Before starting to process the image, re-sizel image was made so that the size would be smaller and in line with the study area so that the processing would be lighter and faster. To obtain land use / cover data from Landsat imagery, this research conducted Supervised Classification using the Maximum Likelihood Classification method. The first process is the stacking image layer to combine all bands in the image. After the ENVI 5.1 Software Stacking Layer was performed, the classification was done on ArcGIS 10.4 Software using the Maximum Likelihood Classification toolbox. Previously it is necessary to make a signature for each classification that will be used as a guide to the classification process by Software.

To obtain surface temperature / LST data, the researcher performed 3 times the calculation process in ENVI 5.1 using the Math Band. These steps are:

1. Change the value of DN (Digital Number) to radians value, the formula (Radian Multiband * Thermal Band) + Radian Add Band

   For the Multiband Radian value and the Add Band Radian can be seen in the metadata of each image. For the Thermal Band Landsat-5 TM is translated into Band 6 while the Thermal Band Landsat-8 OLI / TIRS translates to Band 10.

2. Change the Radian value to Kelvin temperature data, the formula Constants 2 / alog (Constants 1 / Band Radian + 1) Constants 1 and Constants 2 can be seen in the metadata of each image. For the Radian Band, use the data from the first step.

3. Changing Kelvin to degrees Celsius, the formula is Band Kelvin - 272.15

   The Kelvin band in question is the result of processing the second step. After the three steps are carried out, open the LST raster data on ArcGIS software to facilitate the classification of the temperature class and LST map layout.
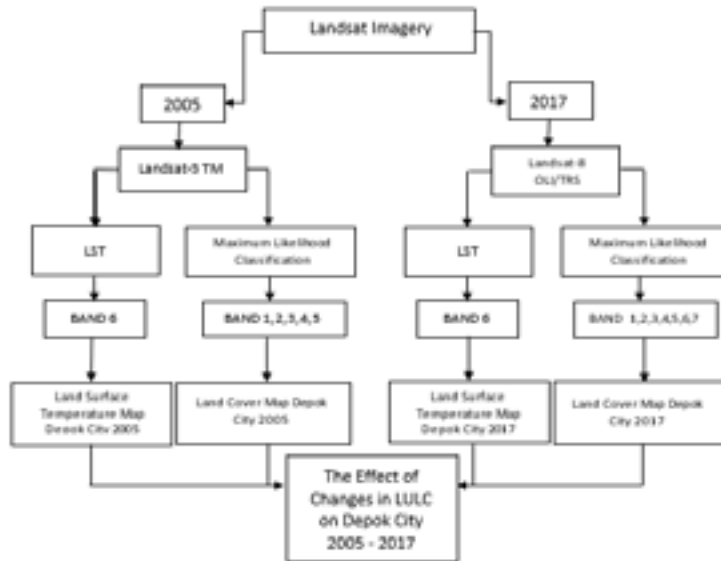
Figure 1. Research Mindset

RESULT AND DISCUSSION
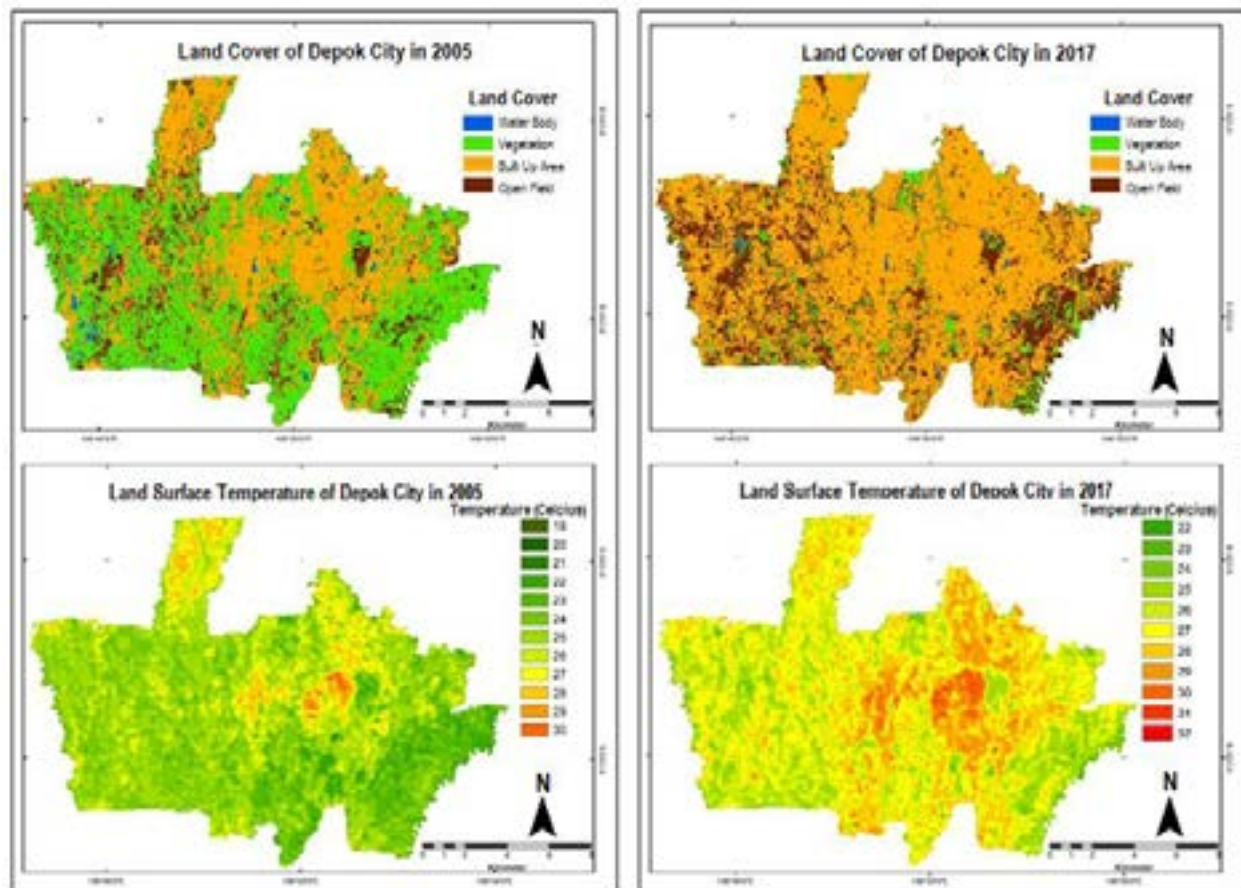
Changes in land use and cover in Depok city which during 2005-2017 continued to develop into built-up land were seen based on the results of supervised classification using the Maximum Likelihood Classifcation method in ArcGIS 10.4. Changes in land use and cover in the city of Depok which was previously dominated by vegetation (in

2005) into a built-up land are the result of rapid and continuous urbanization. This is inseparable from the status of Depok City as a Government Center that is directly adjacent to the Special Capital Territory of Jakarta, which is also a buffer zone of the State Capital City which is directed to residential cities, City of Education, Center for trade and service services, City of tourism and as City of water catchment. Based on the results of the supervised classification using the Maximum Likelihood Classifcation method in ArcGIS 10.4, in 2005, 47.08% of the total area of Depok City was used as a vegetation area, in the form of forests, gardens, parks and river banks. The area identified as built land is only 37.89% of the total area of Depok City, the area identified as a water body in the form of situ, lake and pond covering an area of 1.21% and an open area of land identified 13.82% of the total area of Depok City .

But in 2017, a very high increase occurred in the area of built land which in 2005 identified only 37.89% of the total area of Depok City changed to 67.71% of the area of Depok City. As for the use / cover of other land in the form of vegetation and water bodies reduced. The area that became the place to grow vegetation which in 2005 dominated 47.08% of the area of Depok City, now there is only 7.93% of the total area of Depok City. While for water bodies decreased from 1.21% in 2005, only 0.41% remained in 2017. One interesting thing is the expansion of open land which in 2005 occupied 13.82% of the total area of Depok City now increased to 23.95% of Depok City.
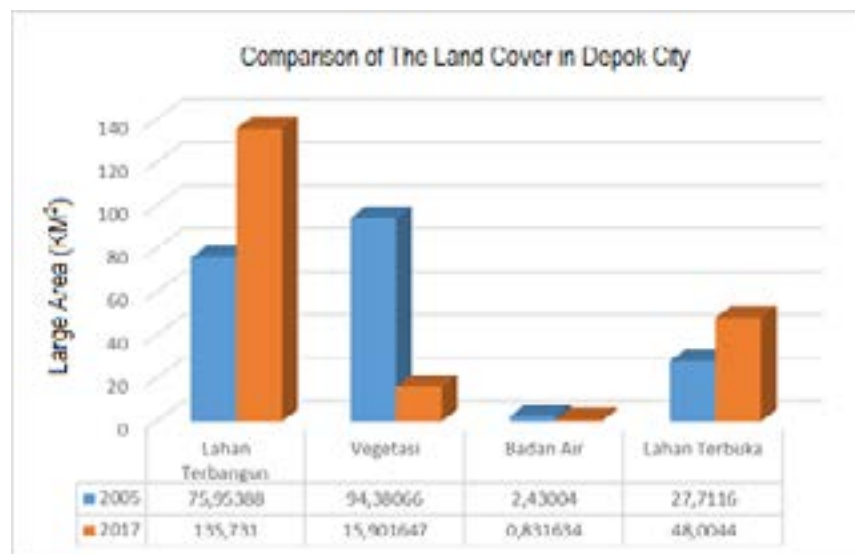
Graph 1. Changes in The Land Use / cover area of Depok City in 2005 – 2017

The change in land use / cover changes due to urbanization and the status of Depok City as a City of Settlement, City of Education, Center for trade and service services, City of tourism and as a city of water catchment, causes the conversion of land previously in the form of a green open area or land vegetation, turned into built land in the form of settlements, apartments, malls, shopping areas and other built areas, resulting in an increase in the surface temperature of Depok City. The results of thermal band image processing data (band 6 on Landsat-5 TM (2005) and band 10 on Landsat-8 OLI / TIRS) indicate an increase in surface temperature or LST in the city of Depok. This can be seen from the existing temperature range, in 2005 the surface temperature of Depok city was in the range of 19^0C - 30^0C and in 2017 the surface temperature of Depok city was in the range of 22^0C -32^0C. This shows the drinking temperature of Depok city rose 3^0C and the maximum temperature of Depok city increased by 2^0C in the period 2005-2017.
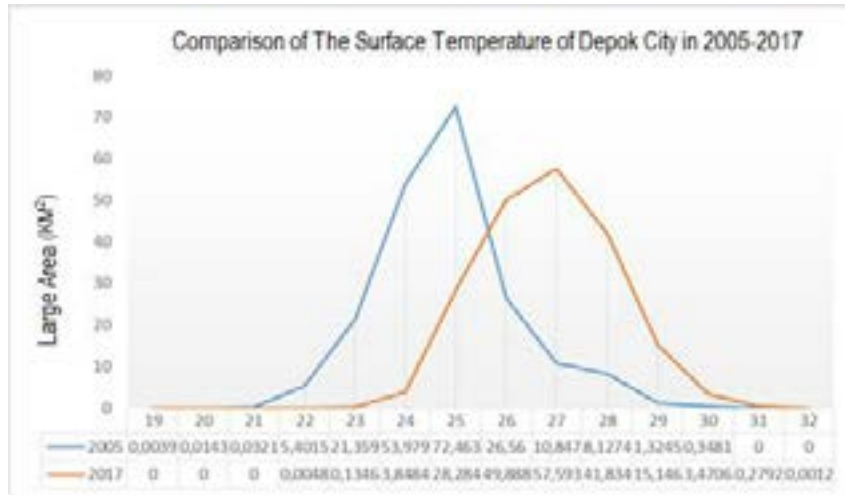
Graph 2. Comparison of the surface temperature of Depok City in 2005-2017

This is as a result of reduced green open areas and increased area of built land. Built land has the highest surface temperature compared to other types of land cover / use. While the forest or in this study is written as vegetation, has the lowest surface temperature compared to other land uses / cover. Based on previous research by Qinqin Sun, Zhifeng Wu and Jianjun Tan (2012) the following is the relationship between LST and land use / cover. (Conversion of Kelvin to Celsius with a reduction of 272.15 K).
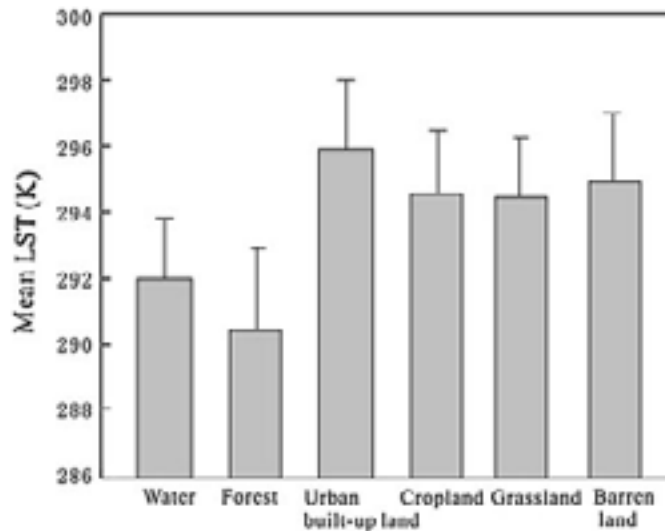
Graph 3. Relationship between LST and land use / cover
Source: Qinqin Sun, Zhifeng Wu and Jianjun Tan (2012)

This is in accordance with the existing reality, that the increase in surface temperature in the city of Depok which is most evident in the area that was previously in the form of green open land and turned into a built-up land, has increased the temperature from 21^0C to 28^0C. At another point there is a temperature change that is initially 20^0C to 27^0C. While for the use / land cover is still maintained as green open land / vegetation the temperature rise that occurs is not as high as the area changed to built land, temperature changes occur from the temperature of 2005 21^0C changes become 23^0C.

CONCLUSION

The Changes in land use and land cover in Depok city which during in 2005 until 2017 continued to develop into built-up land were seen based on the results of supervised classification using the Maximum Likelihood Classifcation method in ArcGIS 10.4. The changes in land use and land cover in Depok City which was previously dominated by vegetation (in 2005) into a built-up land are the result of rapid and continuous urbanization. The change in land use or land cover that changes due to the urbanization status and status of Depok City as a City of Settlement, City of Education, Service Centers and Labor, cities and towns that exist before is green open land or vegetated land, is transformed into land built into settlements, apartments , malls, shopping areas or other built zones also result in an increase in surface temperature. The increase in surface temperature in Depok City which is most clearly seen in the area that was previously in the form of green open land and turned into a built-up area, it has an increase in temperature from 21°C to 28°C. At another point there is a temperature change that is initially 20°C to 27°C. While for the land use and land cover is still maintained as green open land or vegetated land, the temperature rise that occurs is not as high as the area changed to built land, temperature changes occur from the temperature in 2005 from 21°C changes become 23°C.

REFERENCES

Ahmad, Asmala. (2012). Analysis of Maximum Likelihood Classification on Multispectral Data. Applied Mathematical Sciences, Vol. 6, 2012, no. 129, 6425 – 6436

Devadas. D Monsingh dan A Rose L. (2009). ANALYSIS OF LAND SURFACE TEMPERATURE AND LAND USE / LAND COVER TYPES USING REMOTE SENSING IMAGERY – A CASE IN CHENNAI CITY, INDIA. ,The Seventh International Conference on Urban Climate, 29 June – 3 July 2009, Yokohama,Japan

Fei Zhang, Hsiangte Kung, Verner Carl Johnson, Bethany Iris LaGrone dan Juan Wang. (2017). Change Detection of Land Surface Temperature (LST) and some Related Parameters Using Landsat Image: a Case Study of the Ebinur Lake Watershed, Xinjiang, China. Wetlands https://doi.org/10.1007/s13157-017-0957-6

Hero Marhaento. (2009). Tutorial ENVI 4.1. untuk Terapan Kehutanan Tingkat Dasar. https://www.researchgate.net/publication/272833179

J.S. Rawat dan Manish Kumar. (2015). Monitoring land use/cover change using remote sensing and GIS techniques: A case study of Hawalbagh block, district Almora, Uttarakhand, India. The Egyptian Journal of Remote Sensing and Space Sciences (2015) 18, 77–84

Kun Jia, Shunlin Liang, Xiangqin Wei, Yunjun Yao, Yingru Su, Bo Jiang dan Xiaoxia Wang. (2014). Land Cover Classification of Landsat Data with Phenological Features Extracted from Time Series MODIS NDVI Data. www.mdpi.com/journal/remotesensing doi:10.3390/rs61111518

PUSAT PEMANFAATAN PENGINDERAAN JAUH. (2015). Pedoman Pengolahan Data Penginderaan Jauh Landsat 8 untuk MPT. LAPAN

Qinqin Sun, Zhifeng Wu dan Jianjun Tan. (2012). The relationship between land surface temperature and land use/land cover in Guangzhou, China. Environ Earth Sci (2012) 65:1687–1694

Ramita Manandhar, Inakwu O. A. Odeh dan Tiho Ancev. (2009). Improving the Accuracy of Land Use and Land Cover Classification of Landsat Data Using Post-Classification Enhancement. www.mdpi.com/journal/remotesensing doi:10.3390/rs1030330

Rizky Mulya Sampurno dan Ahmad Thoriq. (2016). KLASIFIKASI TUTUPAN LAHAN MENGGUNAKAN CITRA LANDSAT 8 OPERATIONAL LAND IMAGER (OLI) DI KABUPATEN SUMEDANG. Jurnal Teknotan Vol. 10 No. 2, November 2016

Swades Pal a dan Sk. Ziaul. (2017). Detection of land use and land cover change and land surface temperature in English Bazar urban centre. The Egyptian Journal of Remote Sensing and Space Sciences 20 (2017) 125–145

Xiao-Ling Chen, Hong-Mei Zhao, Ping-Xiang Li dan Zhi-Yong Yin. (2006). Remote sensing image-based analysis of the relationship between urban heat island and land use/cover changes. Remote Sensing of Environment 104 (2006) 133–146

Zi-Qi Zhao, Bao-Jie He, Li-Guang Li, Hong-Bo Wang dan Amos Darko. (2017). Profile and concentric zonal analysis of relationships between land use/land cover and land surface temperature: Case study of Shenyangs, China. Energy and Buildings 155 (2017) 282–295

2	2014	4,337.2	6.56	5.86	6.38
	2015	5,144.7	5.24	12.28	10.04
	2016	7,157.1	9.94	9.75	13.90
	2017	5,098.0	3.05	14.98	6.38
	2018	5,896.8	14.99	11.84	13.28
1	2013	17,409.3			
	2014	17,252.1	7.06	12.76	13.47
	2015	23,170.4	8.42	12.76	13.48
	2016	24,764.1	11.13	13.91	0
	2017	23,951.6	0	9.72	13.48
	2018	27,916.7	11.97	13.68	3.27
2	2013	11,178.3			
	2014	12,072.1	8.38	12.87	5.97
	2015	13,137.9	10.42	18.57	9.73
	2016	15,074.6	36.75	7.51	3.02
	2017	14,278.7	4.75	5.02	3.02
	2018	15,866.9	11.44	5.92	5.03

nd speed analysis of the GLDAS monthly data was extracted from the NOAH
 its spatial coverage is a quarter of a degree approximately 27 km. The data for the
d Qassim were taken and tested with the GLDAS data to ascertain the feasibility of
The data for the period 2013 to 2016 were analyzed and registered a positive cor
efficient of 0.86 (Figure 5).

Figure 5, the relationship between GLDAS and weather station.
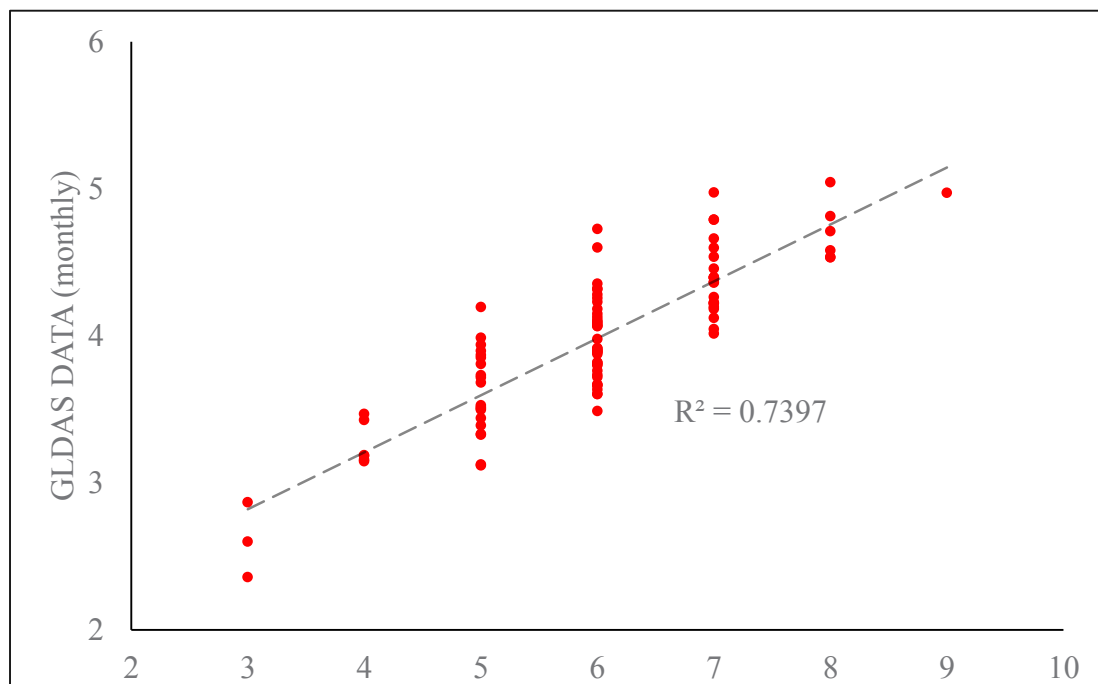
LOCAL STRAIN BEHAVIOR IN TAIPEI BASIN BASED ON CONTINUOUS GNSS OBSERVATIONS

Chun-Yun Chou (1), Jen-Yu Han (1)

[1] Department of Civil Engineering, National Taiwan University,
No. 1, Sec. 4, Roosevelt Rd., Taipei 10617, Taiwan (R.O.C.)
Email: d02521001@ntu.edu.tw; jyhan@ntu.edu.tw

KEYWORDS: Surface Displacement, Global Navigation Satellite System (GNSS), Time Series Analysis, Strain Analysis.

ABSTRACT: Taipei City is densely populated and it is located in Taipei Basin. It is not only the political, economic, and cultural center of Taiwan, but also one of the most important commercial and financial hubs in Asia. However, the location of Taipei Basin is around several faults and the Tatun volcano group which could be active. Additionally, with the severe climate change, earthquakes and rainstorms happen frequently and pose threats to the life and property of the residents. Therefore, it is essential to monitor surface displacements immediately for protecting the life and property of the people in the metropolitan area. The common practice is to establish the GNSS (Global Navigation Satellite System) stations in the monitored area and to record positions of the stations through time. Consequently, for the deformation analysis, this research will estimate the velocities of observations through the time series data of the GNSS continuously operating reference stations in Taipei Basin and interpret the corresponding strain rates in recent years. Finally, according to the obtained results, surface dynamic behavior in Taipei Basin could be provided for monitoring and deformation analyses, and even referred to concerned departments for developments, constructions, and disaster preventions.

1. INTRODUCTION

Taipei is the major political and economic city in Taiwan; it is not only the seat of Taiwan's central government, but also as Taiwan's business, financial, and technology hub. Many important establishments are located in Taipei, such as foreign consulates, international financial institutions, and multi-national corporations with offices or regional headquarters. Similarly, technology and electronics companies are often clustered in the Neihu Technology Park or the Nankang Software Park. Population growth, high-land value, and surging house prices are accompanied by the rapid development of the city. However, behind the prosperity of the city are risks in natural disasters which may endanger the safety and property of people. Close to the convergence of tectonic plates, earthquakes frequently occur in Taiwan and bring potential destruction. In the vicinity of active the Tatun volcano group and the Shanchiao fault, Taipei must be well prepared for disaster prevention in response to earthquakes. In addition, the dramatic climate change leads to short-term disaster rainfall. The various factors reveal the importance and necessity of deformation monitoring for the safety of people's lives and property in the metropolitan area.

For decades, the well-developed technology of Global Navigation Satellite System (GNSS) has been facilitated 24-hour observations, high frequency, and high precision of positioning measurements applied deformation monitoring widely (Betti *et al.*, 1999). In the 1990s, with the extensive application of satellite positioning measurement, the Taiwan Geodetic Datum 1997 was established to update the national coordinate system (Yang *et al.*, 2001). The eight satellite stations were set up to obtain 24-hour observations and to obtain coordinates for the datum. Currently, as many as five hundred GNSS satellite stations have been constructed and deployed by industry, government and academic unit in Taiwan to observe surface displacements and to collect deformation data for analysis. Therefore, this research would estimate the velocities and strain rates of GNSS satellite stations in Taipei Basin by their time series data. Furthermore, Regulations of Implement for Fundamental Surveying would be referred to in order to examine the surface strain rates and to analyze the surface dynamic behavior. The results of this study would be provided for developments, constructions, and disaster preventions.

2. METHOD

Figure 1 shows the flowchart in this research. First, the historical time series data of GNSS satellite stations in Taipei Basin would be used to estimate the velocity field and then to output position coordinates of different periods. Second, the triangulated irregular networks (TIN) could be formed by the position coordinates of stations to calculate the strain rates. After that, the strain rate field would be interpolated in Taipei Basin. Finally, the scale deformation and angle distortion would be examined by Regulations of Implement for Fundamental Surveying. Velocity field

fitting and strain analysis are the major methods in this study and would be introduced separately in the following sections.
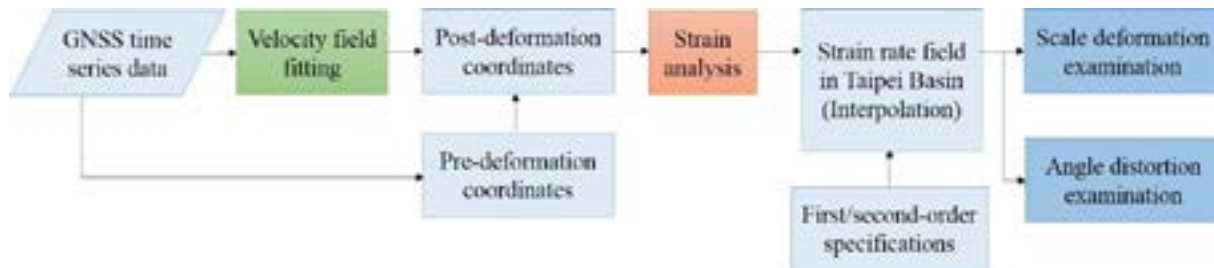

Figure 1. Flowchart in this research.

2.1 Velocity Field Fitting

The procedures of velocity field fitting by the historical time series data include discontinuous point detection, trend line fitting, gross error detection, optimized line fitting and statistical testing (Figure 2). The method could completely and reasonably process the historical time series data of GNSS satellite stations and output higher-quality and reliable position coordinates, velocity coordinates, and the corresponding standard deviations (Chou and Han, 2018).

First, the observed times and coordinates in a single direction (e.g., east direction) of the historical time series data in a station are inputted to fit the line by slop-intercept form with indirect linear adjustment and then to accumulate the residuals at different epochs. When the residuals are randomly uniform positive and negative, the accumulated line is a straight line. Otherwise, a significant turning point would show in the curve, and it means the position of a discontinuous point. Second, the continuous data which was not included the discontinuous point is inputted to fit the trend line by point-slope form and to detect gross errors. The optimized line is fit after removing gross errors. The slope and its precision as the results are outputted. Third, the discontinuous data were grouped by the discontinuous point and the second step is repeated in every group. Every two groups should take the statistical testing. If the test passes, the data of the two groups are combined for fitting the optimized line again, and the results are outputted. If not, the slopes and its precision in every group immediately are outputted. In those groups, the longer data means more credibility. Finally, after repeating the direction in east, north and up, the base model of surface motion in the satellite station is established.
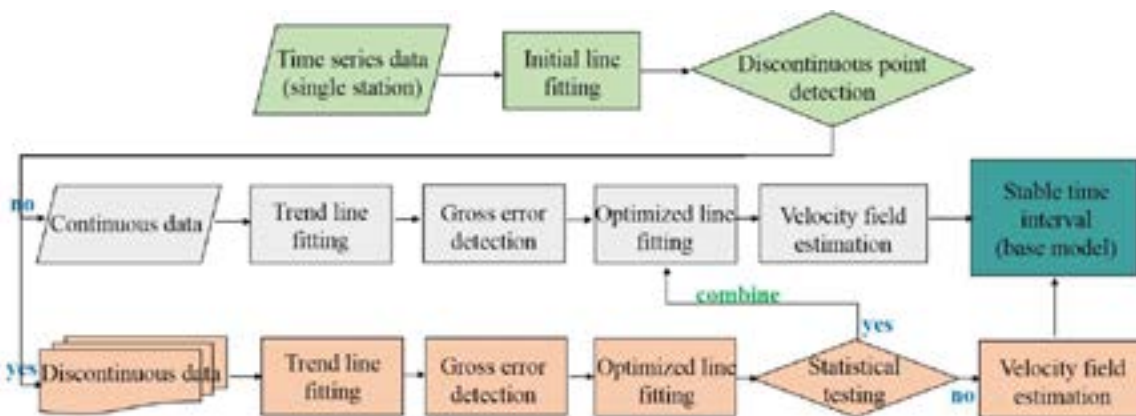
Figure 2. Flowchart of velocity field fitting.

2.2 Strain Analysis

The velocity field in Taipei Basin could be estimated by section 2.1, and to further calculate the local deformation behavior, the strain analysis needs to be introduced.

In engineering mechanics, stress means the strength of the force, and strain represents the deformation behavior of an object after it is subjected to stress, could be defined as the amount of deformation per unit length of the object (Billington & Tate, 1981). When the object is subjected to stress, the strain generated can be divided into the forward

strains (ε_x, ε_y) and the shear strains (γ_{xy}, γ_{yx}). The former cause the scale deformation, and the latter distort the shape. Through the forward strains and the shear strains, a strain tensor matrix E can be formed to describe the deformation behavior of the whole object.

$$\mathbf{E} = \begin{bmatrix} e_{11} & e_{12} \\ e_{21} & e_{22} \end{bmatrix} = \begin{bmatrix} \varepsilon_x + 1 & \dfrac{\gamma_{xy}}{2} \\ \dfrac{\gamma_{yx}}{2} & \varepsilon_y + 1 \end{bmatrix} \tag{1}$$

In general, γ_{xy} is equal to γ_{yx}, so **E** is a symmetric matrix, which is decomposed with eigenvalue decomposition. **E** can be expressed by the product of the orthogonal matrix **S** and the diagonal matrix $\mathbf{\Lambda}$, where λ_1 and λ_2 are the eigenvalues of **E**. The λ_1 and λ_2 are also known as the main parameters of strain which are composed of the principal strains ε_1 and ε_2. The principal strain ε_1 and ε_2 is the maximum and minimum forward strain on the principal plane passing through the zero shear strain of the object, which is orthogonal to each other. The row vectors in the matrix **S** are the eigenvectors of **E**, which are composed of the angle θ_1. The X_1-axis is rotated counterclockwise through θ_1 with respect to the X-axis, which called the main strain direction corresponding to the principal strain ε_1.

$$\mathbf{E} = \mathbf{S}^T \mathbf{\Lambda} \mathbf{S} \tag{2}$$

$$\mathbf{\Lambda} = \begin{bmatrix} \lambda_1 & 0 \\ 0 & \lambda_2 \end{bmatrix} = \begin{bmatrix} \varepsilon_1 + 1 & 0 \\ 0 & \varepsilon_2 + 1 \end{bmatrix} \tag{3}$$

$$\mathbf{S} = \begin{bmatrix} s_{11} & s_{12} \\ s_{21} & s_{22} \end{bmatrix} = \begin{bmatrix} \cos\theta_1 & \sin\theta_1 \\ -\sin\theta_1 & \cos\theta_1 \end{bmatrix} \tag{4}$$
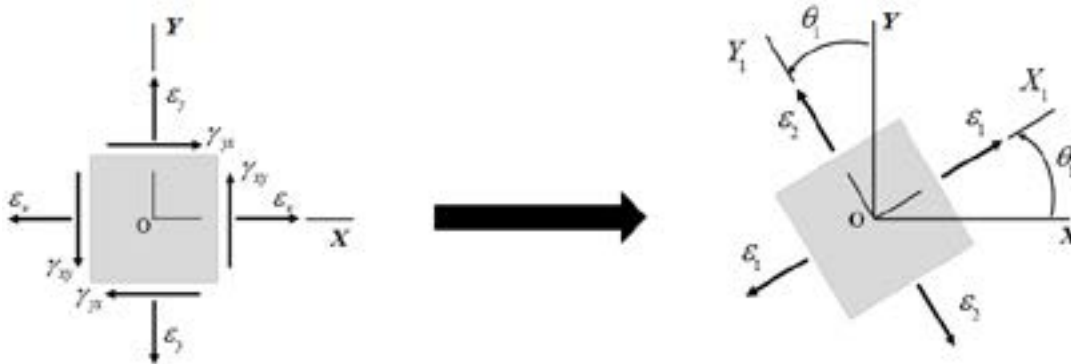
Figure 3. The relationship between strain tensor elements and the principal strains.
Modified from Gere and Timoshenko (1991)

The strain tensor **E** could be estimated by the pre-deformation coordinates **x** and the post-deformation coordinates **x'**. Due to the non-uniform deformations in the target area, the surface points should form the triangulated irregular networks, and then the strain analysis in every triangular network is performed (Zheng, 2009). Besides deformation signals, tectonic motions and the defined reference frame which is time-variant cause the movement of the observed points in long-term deformation monitoring and influence the deformation parameter estimation (Vaníček *et al.*, 2008; Han *et al.*, 2009).

The main purpose of strain analysis is to estimate the matrix **E** and the principal strains. Therefore, this study refers to the concept of Han (2006) about the invariant function and uses the characteristics of the translation matrix and the rotation matrix. Not only modify the model for the traditional strain analysis without estimating the parameters of the translation and rotation to obtain the correct strain tensor E, but also effectively eliminate the effects in active motion and passive motion as so to estimate the proper deformation parameters. The equations in the model are as the following.

$$(\bar{e}_{11}\Delta x'_{ij} + \bar{e}_{12}\Delta y'_{ij})^2 + (\bar{e}_{12}\Delta x'_{ij} + \bar{e}_{22}\Delta y'_{ij})^2 = \Delta x_{ij}^2 + \Delta y_{ij}^2 \tag{5}$$

$$\mathbf{E}^{-1} = \begin{bmatrix} \bar{e}_{11} & \bar{e}_{12} \\ \text{sym.} & \bar{e}_{22} \end{bmatrix} \tag{6}$$

In equation (5), the unknown parameters could be estimated by the differences of the positional observables, where Δx_{ij} represents the differences of pre-deformation coordinates by any two points i, j (i ≠ j), and $\Delta x'_{ij}$ represents the differences of post-deformation coordinates by any two points i, j (i ≠ j). After adjusting the strain tensor inverse matrix $\mathbf{E}^{-1}$, the $\mathbf{E}$ which was calculated by inversing the matrix $\mathbf{E}^{-1}$ would be decomposed with eigenvalue decomposition to obtain the eigenvalues (λ_1, λ_2), and then to estimate the principal strains (ε_1, ε_2).

3. NUMERICAL RESULTS AND DISCUSSION

This study referred to the time series data in the automatic GNSS data processing system created by Dr. Guo in the Institute of Earth Sciences, Academia Sinica. The time series data was the existing long-term solutions for the ground stations and could be downloaded on the GPS LAB data platform (GPS LAB, 2018). The downloaded material contained more than 500 files (*.cor) named by the station name, and each file consisted of multiple latitudes, longitudes, and ellipsoid heights at corresponding times. This research took twenty-six satellite stations in Taipei Basin, using the time series data for solving and analyzing. The range of latitude and longitude distributed in the stations was shown in Figure 4, and the interpolation of ellipsoidal elevation was shown in Figure 5, that the ups and downs in the terrain could be observed.
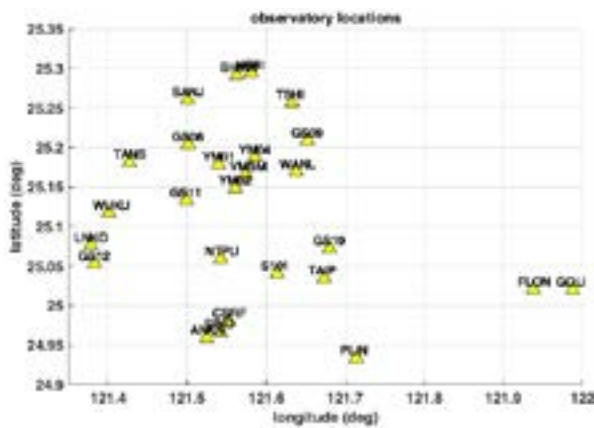
Figure 4. Observatory locations and the corresponding station names.
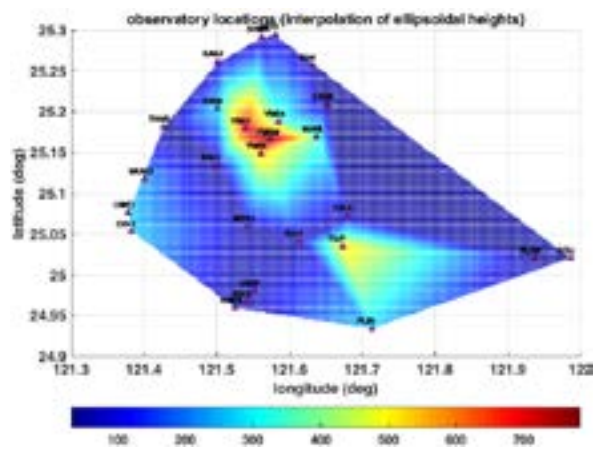
Figure 5. Observatory locations and the interpolation of the ellipsoidal elevations.

3.1 The Performance of Velocity Field Fitting

Figure 6 revealed that the observed years of all satellite stations were more than three years. The observations were used for fitting velocities. The results were shown in Figure 7, and it can be seen that the estimated values and directions of velocities in all the satellite stations were similar, consistent and stable. In the X direction, the maximum value was -0.026 m/yr, the minimum value was -0.034 m/yr, and the average value was -0.031 m/yr. In the Y direction, the maximum value was -0.012 m/yr, the minimum value was -0.018 m/yr, and the average value was -0.014 m/yr.
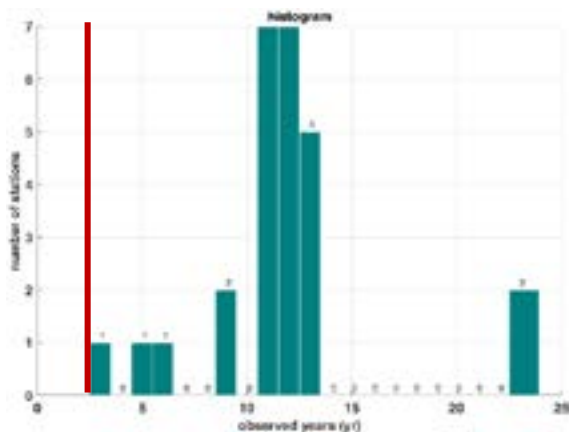
Figure 6. Histogram of the number of stations with the observed years.
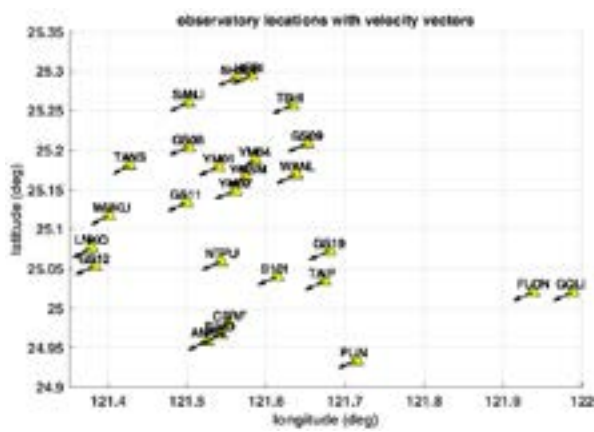
Figure 7. Observatory locations and the corresponding velocity vectors.

The statistic data of the velocity precision was shown in Figure 8. The number of the velocity precision which was better than 10^{-4} m was 22, accounting for 85% of the total.

Figure 9 was drawn to investigate the relationship between the observed years and the velocity precision, showing that the value of the velocity precision was roughly inversely proportional to the number of the observed years. In other words, the larger number of the observed years was, the higher the velocity precision would be.
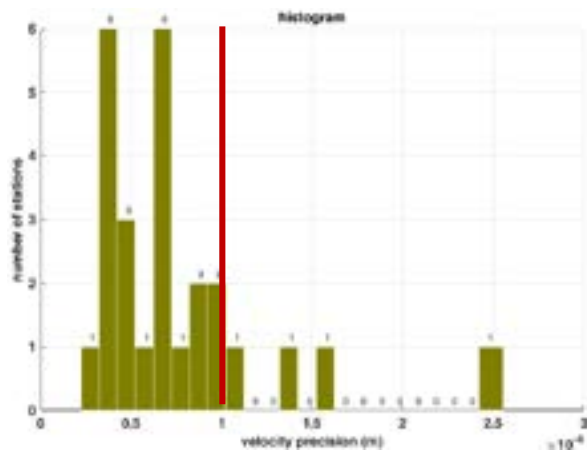
Figure 8. Histogram of the number of stations with the velocity precision.
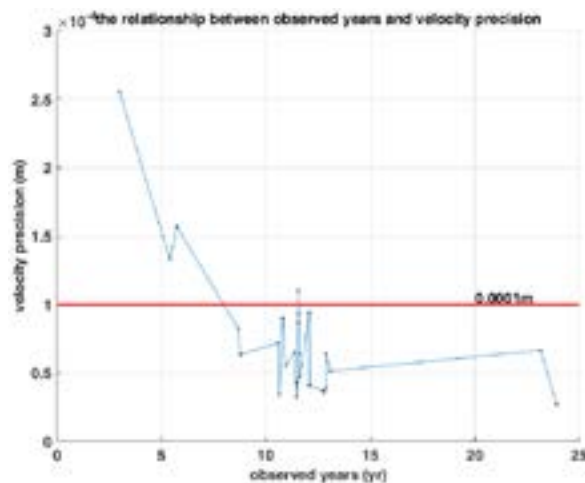
Figure 9. The relationship between the observed years and the velocity precision.

3.2 Strain Analysis and Survey Standard Inspection

Figure 10 showed the results of the triangulated irregular networks (TIN) composed of the point coordinates, where the yellow point meant the center of gravity in each triangle. The interpolated strain results such as the shear strain rates, the first principal strain rates, and the second principal strain rates were shown in Figures 11, 12 and 13. The maximum of the shear strain rates γ_{xy} was 1.88 μstrain/yr, and the minimum value was -1.99 μstrain/yr. The maximum of the first principal strain rates ε_1 was 1.70 μstrain/yr, and the minimum value was -0.01 μstrain/yr. The maximum of the second principal strain rates ε_2 was 0.10 μstrain/yr, and the minimum value was -1.97 μstrain/yr. For the scale deformation, it was 2 mm per kilometer per year in Taipei Basin. The area with the larger strain rate was in the highest level of the terrain, where was around the Tatun volcano group.
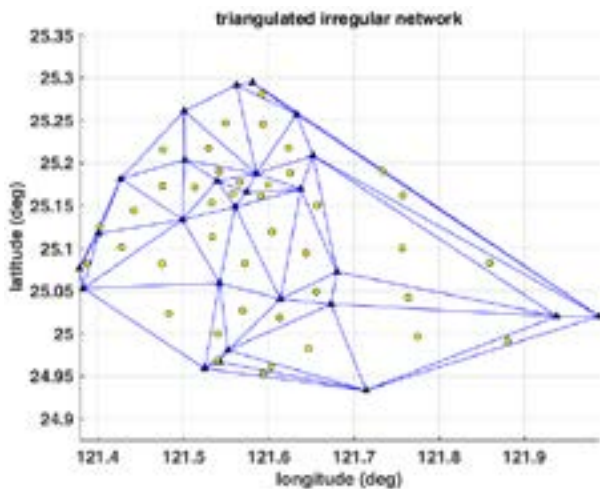
Figure 10. The distribution of the triangular network and the corresponding centers of gravity.
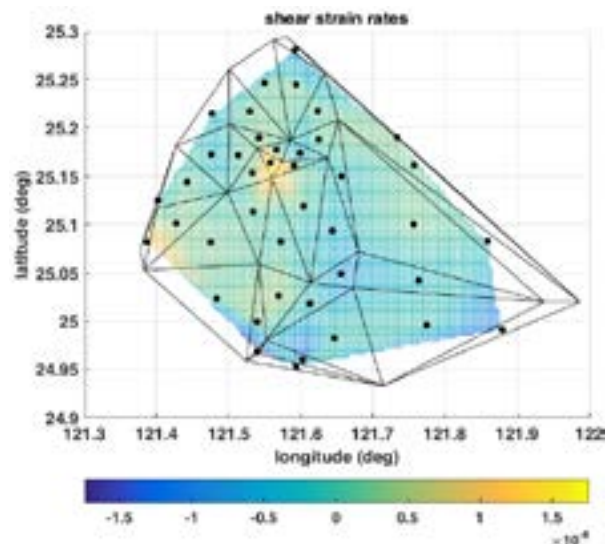
Figure 11. Interpolation of the shear strain rates.
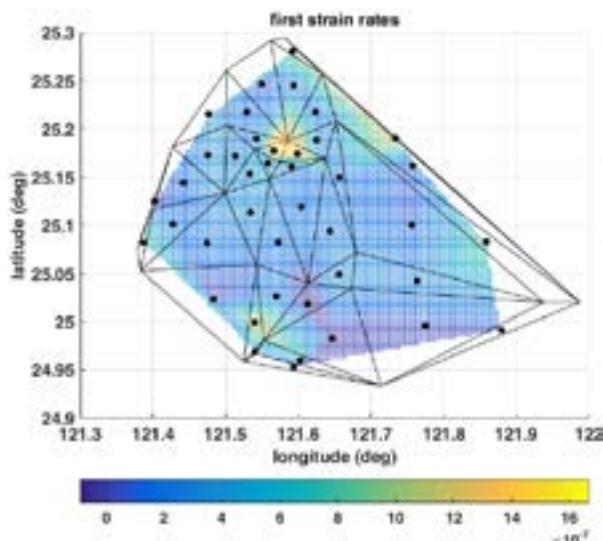
Figure 12. Interpolation of the first principal strain rates.
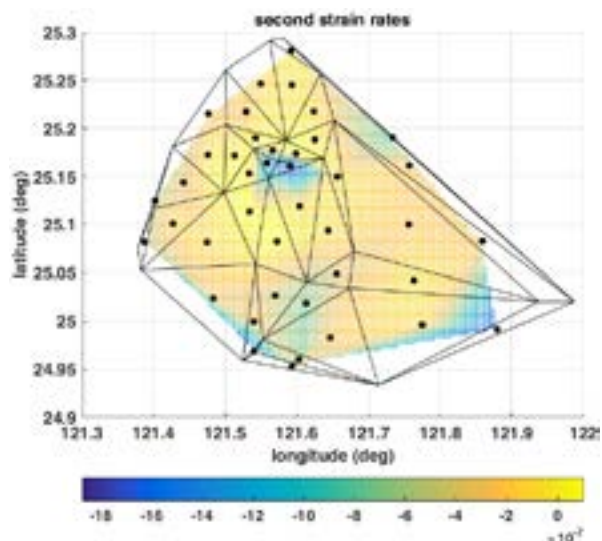
Figure 13. Interpolation of the second principal strain rates.

In order to examine the principal strain results, Regulations of Implement for Fundamental Surveying: the accuracy specification for the first and second-order basic control surveys implemented by satellite positioning measurement were referred to (MOJ, 2018). The distance tolerance in the first-order specification was 5mm+1ppm × k, where k was the length of the baseline (km), and the value in the second-order specification was 10mm+2ppm × k. The allowable deformation of each baseline could be calculated by the specification, and the corresponding actual deformation could be estimated by the principal strain rates. The allowable year of each baseline was that the allowable deformation divided by the actual deformation.
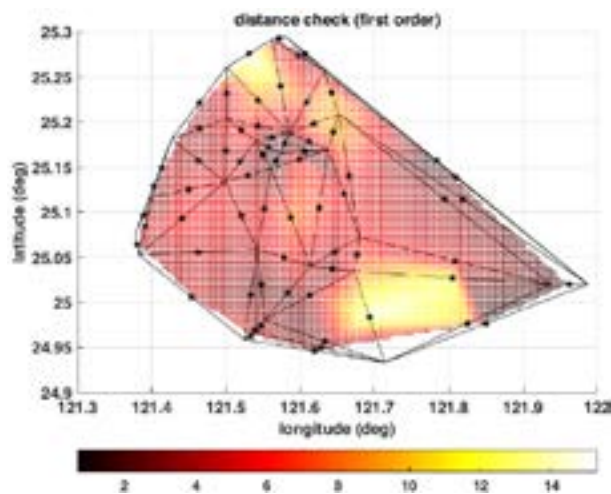
Figure 14. Interpolation of the allowable years in the first-order specification.
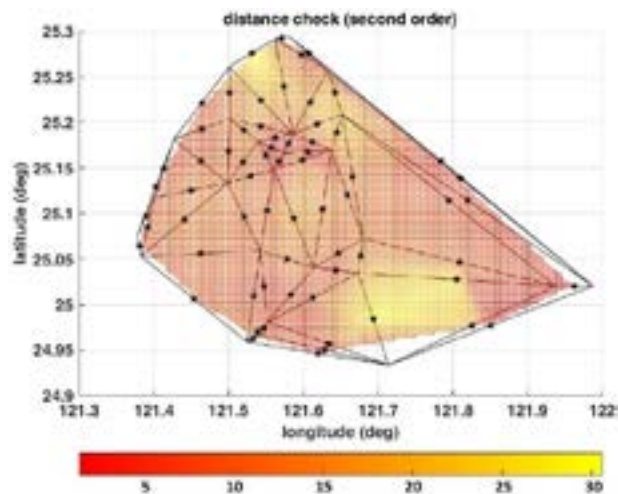
Figure 15. Interpolation of the allowable years in the second-order specification.

The maximum allowable year in the first-order specification was 23yr, and the minimum one was 0.6yr. The maximum allowable year in the second-order specification was 46yr, and the minimum allowable one was 1.2yr. The allowable year of each baseline in the first-order and the second-order specification were interpolated respectively to draw Figure 14 and Figure 15.

Furthermore, the number of baselines per five years in the first-order and second-order specification was counted separately. In the first-order specification, the number of baselines from 0 to 5 years accounted for 57.6% in total and the one from 6 to 10 years accounted for 36.4% in total. In the second-order specification, the number of baselines from 0 to 5 years accounted for the overall 24.2% and the one from 6 to 10 years accounted for the overall 30.3%. It can be seen that within ten years, the actual deformation exceeding the first-class specification was more than 94% of the baselines, and exceeding the second-class specification was about 54.5%.
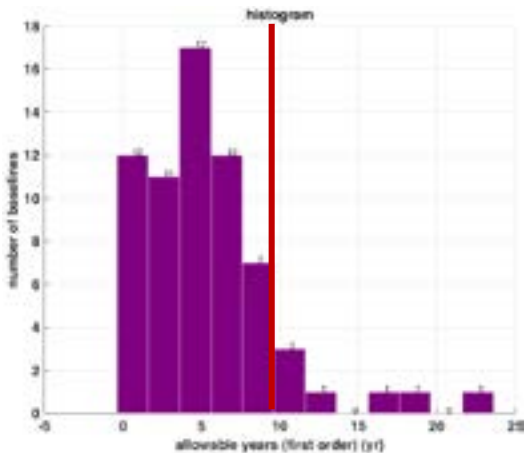
Figure 16. Histogram of the number of baselines with the allowable years in the first-order specification.
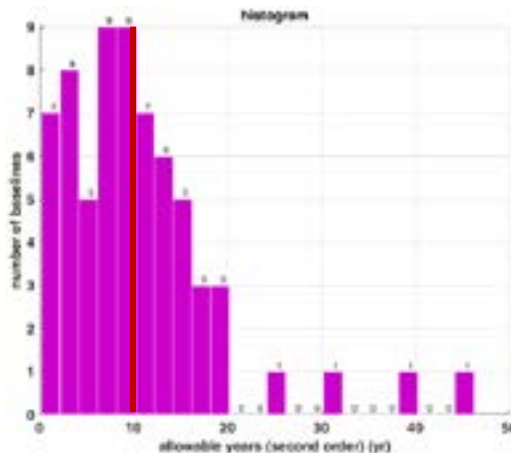
Figure 17. Histogram of the number of baselines with the allowable years in the second-order specification.

For angle distortion, there was a maximum deformation of about 0.35 seconds per year in Taipei Basin. The area with a larger shear strain rate was in the highest level of the terrain, where was around the Tatun volcano group, as shown in Figure 18.

In order to examine the shear strain results, Regulations of Implement for Fundamental Surveying: the accuracy specification for the first and second-order basic control surveys implemented by the precise traversing measurement were referred to (MOJ, 2018). In the first-order specification, the observed differences in horizontal angles cannot be larger than 4 seconds. Moreover, another specification could be referred to such as Regulations of Implement for Fundamental Surveying: the accuracy specification for the first and second-order basic control surveys implemented by the triangulation measurement (MOJ, 2018). The closing error in a single triangle shall not exceed 3 seconds in the first-order specification.

The number of the shear strain rates every 0.1 seconds was counted, and the number fewer than 0.3 seconds was 39, which was for 95% in total (as shown in Figure 19). It can be seen that the maximum angle distortion would exceed the specification value after ten years.
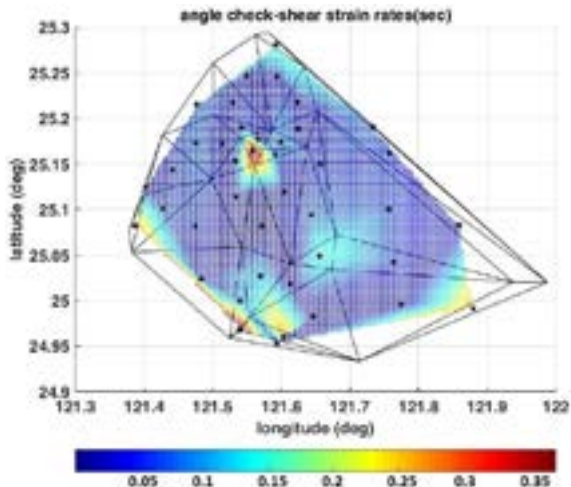
Figure 18. Interpolation of the shear strain rates. (The original values took the absolute values and then converted to seconds)
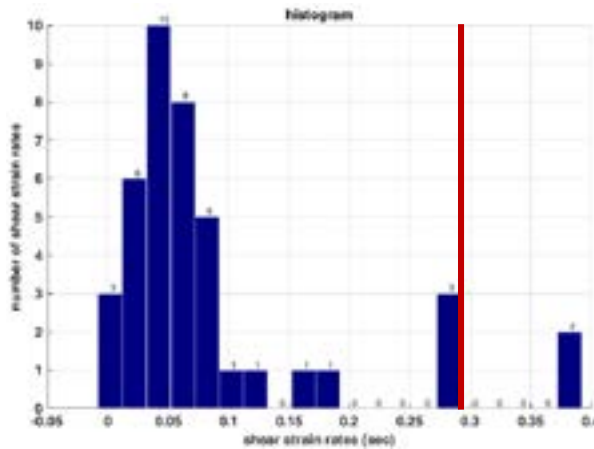
Figure 19. Histogram of the number of the shear strain rates.

4. CONCLUSION

The observed years of the GNSS satellite stations are highly related to the velocities precision, indicating that the longer the observed years are, the higher the velocity precision can be expected. The current observed years of the GNSS satellite stations in Taipei Basin are over three years so that the stable velocity precision can be obtained. In Taipei Basin, the velocity results of the GNSS observation stations are: in the X direction, the maximum value is -0.026m/yr and the minimum value is -0.034m/yr; in the Y direction, the maximum value is -0.012m/yr, and the

minimum value is -0.018m/yr, showing the stable and consistent velocity vectors.

The area with a larger strain rate in Taipei Basin is in the highest position, surrounded by the Tatun volcano group. The major strain rates in this area are about ±2μstrain/yr. In other words, for a 1-km baseline, the maximum linear deformation is 2mm. According to the first-order specification by satellite positioning measurement, which is 5mm+1ppm × k, where k is the length of the baseline (km); therefore, the longer the baseline is, the smaller the allowable year is. For the triangulation baseline consisting of the GNSS stations in this study, within ten years, the number of the actual deformation exceeding the first-order specification is more than 94% in total, and exceeding the second-order specification is about 54.5%. The shear strain rates have a maximum value of about 0.35 sec/yr. In the light of the 3 seconds of the closing error in horizontal angle in the first-order specification by triangulation, the maximum angular distortion will exceed the specification value after ten years.

5. REFERENCE

Betti, B., Biagi, L., Crespi, M., & Riguzzi, F. (1999). GPS sensitivity analysis applied to non-permanent deformation control networks. *Journal of Geodesy*, *73*(3), 158-167.

Billington, E. W., & Tate, A. (1981). *The physics of deformation and flow* (pp. 51-54 & pp. 269-283), McGraw-Hill, New York.

Chou, C. Y., & Han, J. Y. (2018). The implementation for processing and analyzing GNSS time series data. In: The 37th Conference on Surveying and Geoinformatics, 4-5 Sep., Taoyuan, Taiwan.

Gere, J. M., & Timoshenko, S. P. (1991). *Mechanics of Materials* (pp. 378-394), 3rd SI edition, PWS-KENT Publishing Company.

GPS LAB. (2018). GPS LAB data platform, Retrieved Aug. 10, 2018, from http://gps.earth.sinica.edu.tw/main.jsp .

Han, J. Y. (2006). Time-variant transformations for modern terrestrial reference frame. Ph.D. Dissertation, Purdue University, West Lafayette, Indiana, U.S.A.

Han, J. Y., van Gelder, B. H., & Lin, S. L. (2009). Rotation-and translation-free estimations of symmetric, rank-two tensors with a case study in LIDAR surveying. *Journal of surveying engineering*, *136*(1), 23-28.

Ministry of Justice. (2018). Laws & regulations database of the Republic of China: Regulations of Implement for Fundamental Surveying, Retrieved Aug. 10, 2018, from https://law.moj.gov.tw/LawClass/LawContent.aspx?pcode=D0060096 .

Vaníček, P., Grafarend, E. W., & Berber, M. (2008). Short note: strain invariants. *Journal of Geodesy*, *82*(4-5), 263-268.

Yang, M., Tseng, C. L., & Yu, J. Y. (2001). Establishment and maintenance of Taiwan geodetic datum 1997. *Journal of surveying engineering*, *127*(4), 119-132.

Zheng, Z. Y. (2009). A sensitivity analysis for the principal strain parameters of a 2D trilateration network. Master Thesis, Department of civil engineering, National Taiwan University, Taipei, Taiwan.

6. ACKNOWLEDGMENT

TIME SERIES IMAGE FUSION FOR FORMOSAT-2 AND LANDSAT-8 IMAGES

Tee-Ann Teo [1], Yu-Ju Fu [2]

[1] Professor, Dept. of Civil Engineering, National Chiao Tung University, Hsinchu, Taiwan 30010.
[2] Master Student, Dept. of Civil Engineering, National Chiao Tung University, Hsinchu, Taiwan 30010.
Email: tateo@mail.nctu.edu.tw; fcud0271929@gmail.com

KEY WORDS: Image fusion, time-series, satellite, image

ABSTRACT: The aim of this study is to construct time series images from multi-sensor images. This study compares different time series image fusion techniques for Formosat-2 (FS-2) and Landsat-8 (LS-8) images. Three different image fusion approaches are included to generate time series images from Formosat-2 and Landsat-8 images, including bi-cubic image resampling, high pass filter pan-sharpening and spatial and temporal adaptive reflectance fusion model (STARFM). The goal is to integrate satellite images from different sensors with different spatial and temporal characteristics. In order to assess the quality of simulated images, this study calculates the biases between the observed and the synthetic reflectance for Formosat-2 image. Also, this study demonstrates the simulation of Formosat-2 image from Landsat-8 image through different approaches. In qualitative analysis, the STARFM approach provides better results than other approaches. The quantitative results also indicated that the difference between simulated and real image via STARFM has the lowest bias. In summary, the time series satellite images can be constructed from multi-sensor satellite images successfully.

1. INTRODUCTION

Time series image fusion is a technology generating sequential images from multi-sensor and multi-temporal images (Wu et al., 2015). The data with high temporal resolution are usually with coarse spatial resolution, while the data with high spatial resolution are usually with low temporal resolution. For example, daily Modis image in 500m spatial resolution and every 16days Landsat image in 30m spatial resolution. Multi-sensor image fusion simulates high spatial resolution time series images in dates where only low spatial resolution images are available. Therefore, multi-sensor image fusion is an important technology for generating time-series images from different sensors at different time (Weng, 2018).

Time series image fusion approaches between high spatial resolution systems and high revisit frequency systems have been proved to be an effective way to mitigate the constraint caused by low spatial resolution, low temporal resolution, or unpredicted cloud coverages. Landsat-8 satellite acquires 15m panchromatic and 30m multispectral images at a fixed view angle while Formosat-2 provides 8m multispectral images. The time interval of Landsat-8's time series images in a specific location is 16 days. Although Formosat-2 has higher spatial resolution than Landsat-8, it acquires imagery in different view angles in the way of body rotation, and consequently, the time interval of time series Formosat-2 images is not a fixed time interval. Hence, the fusion of Formosat-2 and Landsat-8 images may improve both spatial and temporal resolutions for constructing the time series satellite images in same spatial resolution.

2. METHODOLOGY

The study generates time series satellite image from 8m FS-2 and 30m LS-8 using three different approaches, including bi-cubic image resampling, high pass filter (HPF) pan-sharpening (Metwalli et al., 2009) and STARFM (Gao et al., 2006). The bi-cubic image resampling method directly interpolates a 30m LS-8 image into a new 8m LS-8 image by operating on 4×4 cell of pixels surrounding each new pixel location. This interpolated 8m LS-8 image only consider the information from LS-8 image itself. This bi-cubic interpolation interpolates a LS-8 images into a new image with the same resolution as Formosat-2 images. The HPF pan-sharpening technique

replaces the spatial frequency of LS-8 image from FS-2 image. The high spatial content of the 8m FS-2 image is extracted by a high pass filter and injected the high spatial information to LS-8 image. Therefore, the simulated 8m LS-8 image is blended by high spatial frequency of FS-2 and high spectral frequency of LS-8. The STARFM used coarse-resolution images to obtain a synthetic high-resolution image. This method was originally developed for Modis and Landsat images; however, it can also be applied to other sensors, for instance, Formosat-2 and Landsat-8 images. The idea of STARFM is to determine a weighting function to convert a LS-8 image to FS-2 image from a homogeneous area. In this study, Landsat-8 offered the medium-resolution imagery and the Formosat-2 offered the high-resolution imagery to simulate high-resolution image by producing synthetic surface reflectance data from two base pairs of LS-8 and FS-2 images and a single LS-8 image collected on the simulation date.

3. EXPERIMENTAL RESULTS

3.1 Test Data

The test data are FS-2 and LS-8 satellite imagery covered a crop area. Formosat-2 multispectral images have a spatial resolution of 8m and consists of four multispectral bands. Landsat-8 multispectral images have a spatial resolution of 30m and consists of eleven bands. Only the identical bands such as blue, green, red and near are selected from both FS-2 and LS-8 images. In the study, we select 15 FS-2 standard scenes (i.e. 2014/01/29, 02/23, 03/26, 08/03, 08/23, 08/29, 09/04, 10/09, 10/18, 11/22, 11/26, 11/30, 12/01, 12/06; 2015/02/01) and 21 LS-8 images (i.e. 2014/01/29, 02/21, 03/18, 04/10, 05/12, 06/13, 07/15, 08/16, 08/25, 09/01, 09/10, 09/17, 09/26, 10/12, 10/19, 10/28, 11/04, 11/20, 11/29, 12/06, 12/22; 2015/02/01) over the study area from January 2014 to February 2015. Among these images, only three images (i.e., 2014/01/29, 2014/12/06 and 2015/02/01) are taken on the same date. Notice that, the LS-8 and FS-2 images have been co-registred and converted to Top of the Atmosphere (TOA) reflectance.

| (a) 2m FS-2 (PAN) | (b) 8m FS-2 (MSI) | (c) 30m LS-8 |
| (d) 8m interpolated LS-8 | (e) 8m fused LS-8 | (f) 8m synthesized LS-8 |
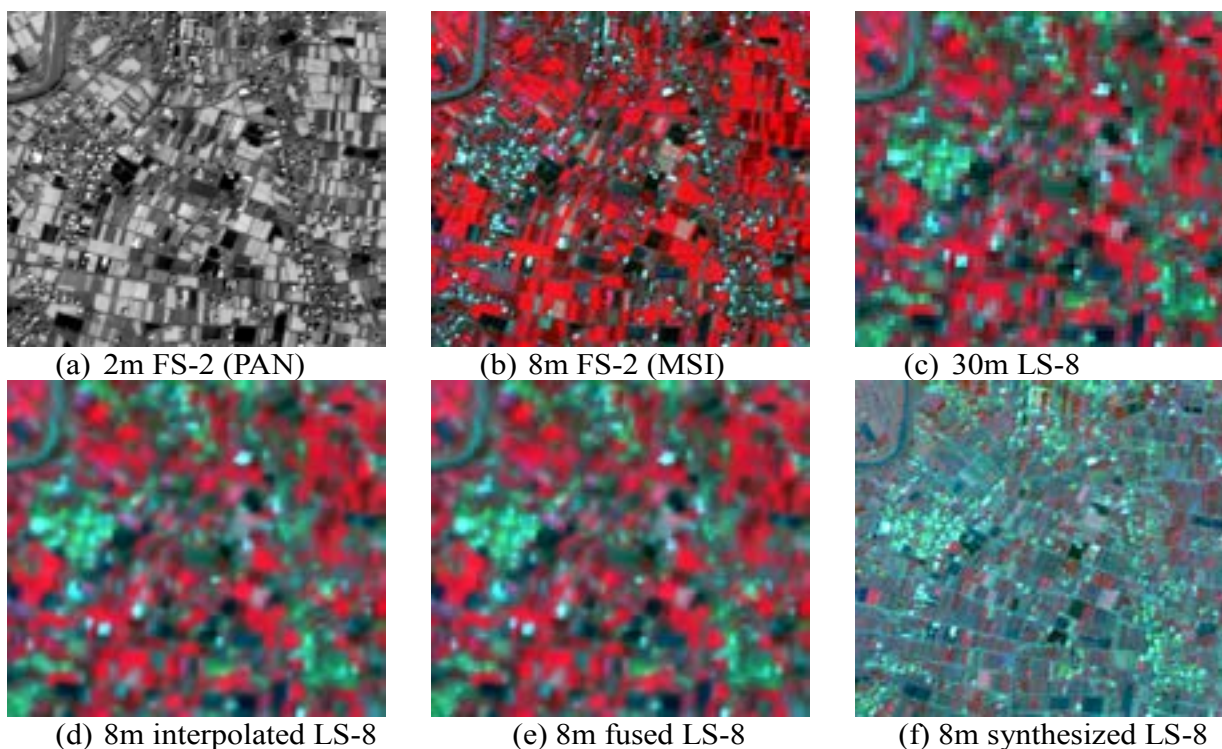
Figure 1. Comparison of different images in 2014/12/06

3.2 Results and Discussions

This study integrates satellite images taken from different sensors for the generation of time series satellite images. The total number of time series image was 33 images (i.e. 15 images from FS-2 and 18 images from LS-8). Figure 1 shows the original, interpolated, fused, and synthesized images.

The evaluation was divided into three parts. The first part analyzed the accuracy of simulated reflectance values by calculating the mean deviation between the real observed and generated images. As shown in Table 1, the reflectance of fused images that simulated by STARFM method are most similar with the observed image. Therefore, this approach is the best one to generate a simulated image when compared to other methods.

Table 1. The mean deviation of reflectance between the Formosat-2 and the synthesized image (2014/12/06)(Unit: reflectance x 10000)

Band	with/without cloud area	STARFM	Pan-sharpening	Resampling
Blue	with cloud area	52.58	62.23	63.67
	without cloud area	46.69	49.40	50.84
Green	with cloud area	67.43	81.36	83.39
	without cloud area	59.76	66.53	68.55
Red	with cloud area	105.00	115.36	118.07
	without cloud area	95.03	97.28	99.98
NIR	with cloud area	368.77	476.25	480.26
	without cloud area	360.41	455.21	459.29

The second evaluation utilized the entropy (Gonzalez et al., 2003) to measure the amount of information contained in images. The comparisons of the entropy value between Landsat-8 images and simulated images are shown in Table 2. The mean entropy of generated images was higher than the original images, which means, the generated 8m images gain better information than original 30m LS-8 images. Hence image fusion technology can increase the complementary information of the image.

Table 2. Mean and standard deviation of entropy from 22 LS-8 images

	Bands	Original LS-8 (30m)	STARFM	Pan-sharpening	Image resampling
Mean entropy	Blue	3.062	3.111	3.311	4.220
	Green	2.824	2.620	3.058	3.914
	Red	2.714	2.856	3.141	4.040
	NIR	2.715	2.856	3.143	4.037
Std. entropy	Blue	0.657	0.607	0.550	0.309
	Green	0.718	0.621	0.645	0.417
	Red	0.511	0.484	0.463	0.388
	NIR	0.511	0.485	0.462	0.387

The last part discussed the advantages and disadvantages of three different approaches. The advantage of STARFM method is to provide better performance in the cloudy area. In Figure 2, although the observed image of Formosat-2 contains cloud area, the synthesized image of STARFM still can simulate the area with the cloud. In contrast to the STARFM, the simulation images of Pan-sharpening and image resampling were easily affected by observed images of Landsat-8 (Figures 2c and 2d). However, the STARFM needs to have at least a pair of Landsat-8 and Formosat-2 images on the same day, it might cause a significant difference between the date of input images and predict day. Consequently, the time interval is the limitation of STARFM. The advantage of image resampling method is that it does not need the temporal information from other images. Nevertheless, the result of image resampling does not contain the information of Formosat-2. Although the ground sampling resolution of images is increased, the resulting images still look blurry when compared to other simulated images.
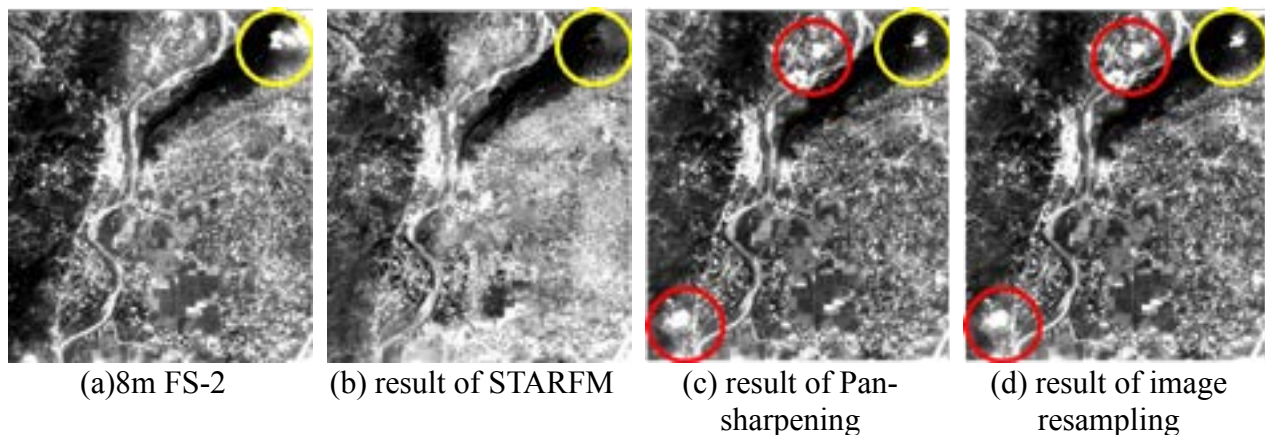
| (a)8m FS-2 | (b) result of STARFM | (c) result of Pan-sharpening | (d) result of image resampling |

Figure 2. Comparison of different blue band images in 2014/12/06

4. CONCLUSIONS

The study demonstrates the simulation of Formosat-2 image from Landsat-8 image through different methods. In qualitative analysis, the STARFM approach provides better results than other approaches. STARFM method is the most promising method to generate sequential images from multi-sensor and multi-temporal images. The quantitative results also indicated that, the difference between simulated and real image via STARFM has the lowest bias. In summary, the time series satellite images can be constructed from multi-sensor satellite images successfully. In addition, integrating satellite images from sensors with different spatial or temporal characteristics is able to improve the quantity of time series images and increase the information of observed images (Jönsson and Eklundh, 2004).

ACKNOWLEDGMENTS

REFERENCES
1. Gao, F., Masek, J., Schwaller, M. and Hall, F., 2006. On the blending of the Landsat and MODIS surface reflectance: Predicting daily Landsat surface reflectance. IEEE Transactions on Geoscience and Remote Sensing, 44(8), 2207–2218.
2. Gonzalez, R.C., Woods, R.E. and Eddins, S.L., 2003. Digital image processing using MATLAB, New Jersey, Prentice Hall, 2003, Chapter 11.
3. Jönsson, P. and Eklundh, L. 2004. TIMESAT—a program for analyzing time-series of satellite sensor data. Computers & Geosciences, 30(8), 833-845.
4. Metwalli, M.R., Nasr, A.H., Allah, O.S.F. and El-Rabaie, S., 2009. Image fusion based on principal component analysis and high-pass filter. IEEE International Conference on Computer Engineering and Systems 2009.63-70.
5. Weng, Q., 2018. Remote sensing time series image processing, CRC Press. 243 pages.
6. Wu, M., Huang, W., Niu, Z. and Wang, C. 2015. Generating daily synthetic Landsat imagery by combining Landsat and MODIS data. Sensors, 15(9), 24002-24025.

Improving CityGML LOD-1 building models using terrestrial point cloud data

Fuan Tsai (1), Jhe-Syuan Lai (2), Yu-Ching Liu (1)

[1] Center for Space and Remote Sensing Research, National Central University, Taoyuan 32001, Taiwan.
[2] Department of Civil Engineering, Feng Chia University, Taichung 40724, Taiwan.
Email: ftsai@csrsr.ncu.edu.tw

KEY WORDS: 3D building model, dense matching, level of detail, OGC CityGML, point cloud.

ABSTRACT: The elevation of the generated OGC CityGML LOD-1 models is usually determined as the height of the roof from ground. However, this criterion might result in significant discrepancies between the generated models and some real buildings, such as arcades and open spaces on first floors. This study develops a procedure to improve the OGC CityGML LOD-1 building models based on terrestrial point clouds derived from close-range images. The point clouds are generated from multiple photos acquired using non-metric cameras (including cell phones), and analyzed by the CMVS (Clustering Views for Multi-view Stereo) algorithm which is one of the dense matching methods for point cloud generation. Experimental results presented in this paper demonstrate the effectiveness of the developed procedure, and show that the improved LOD-1 building models are more close to real buildings in terms of shapes and appearances. In addition, this study also briefly compares the developed method with other conventional approaches (e.g., laser scanning and total station) for improving OGC CityGML LOD-1 building models.

1. INTRODUCTION

Open Geo-spatial Consortium (OGC) suggests five LODs (Level of Details) for building models in the CityGML Specification (OGC, 2006). Among them, OGC CityGML LOD-1 defines buildings as block-based, cube-shaped, and flat-floor models. The elevation of the generated LOD-1 models is usually determined as the height of the roof from ground. However, this criterion might result in significant discrepancies between the generated models and some real buildings, such as arcades and open spaces on first floors (Fig. 1, for example). To address this issue, this study develops a procedure to improve the CityGML LOD-1 building models based on terrestrial point clouds derived from close-range images. The point clouds are generated from multiple photos acquired using non-metric cameras (including cell phones), and analyzed by the CMVS (Clustering Views for Multi-view Stereo) algorithm (Furukawa and Ponce, 2010) which is one of the dense matching methods for point cloud generation.

Fig. 1. Arcades or open spaces on first floors resulting insignificant discrepancies between the reality (left) and the generated CityGML LOD-1 building model (right)

2. METHODOLOGY

Fig. 2 shows the proposed procedure to improve the OGC CityGML LOD-1 building models for the cases such as arcades and open spaces on first floors. Firstly, this study acquires multiple, oblique and overlap close-range images captured from non-metric cameras (including cell phones). These images are analyzed using the Clustering Views for Multi-view Stereo (CMVS) dense matching algorithm under the Visual SFM platform (Wu, 2011) to generate image-based point cloud data. Among the procedure of image-based point cloud generation, the Scale-Invariant Feature Transform (SIFT) algorithm for feature detection and image matching, the sparse reconstruction, and the Multi-core Bundle Adjustment method are included. The detailed theories and procedures can be found in Wu (2011). This study further overlaps (registers) the generated point cloud data with the LOD-1 models (MOI, 2015) in order to

adjust the heights of individual models from ground. An example of the adjustment is shown in Fig. 3.
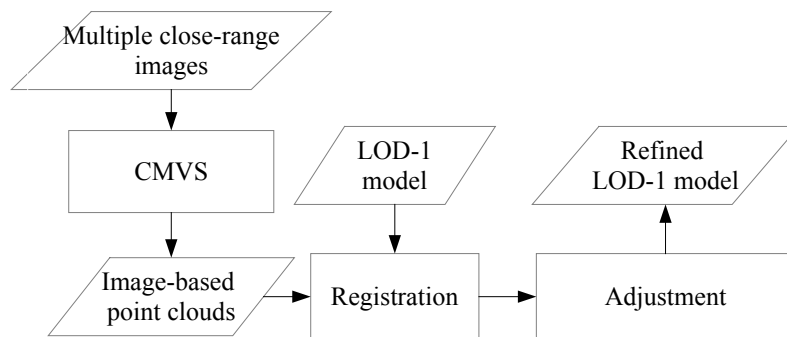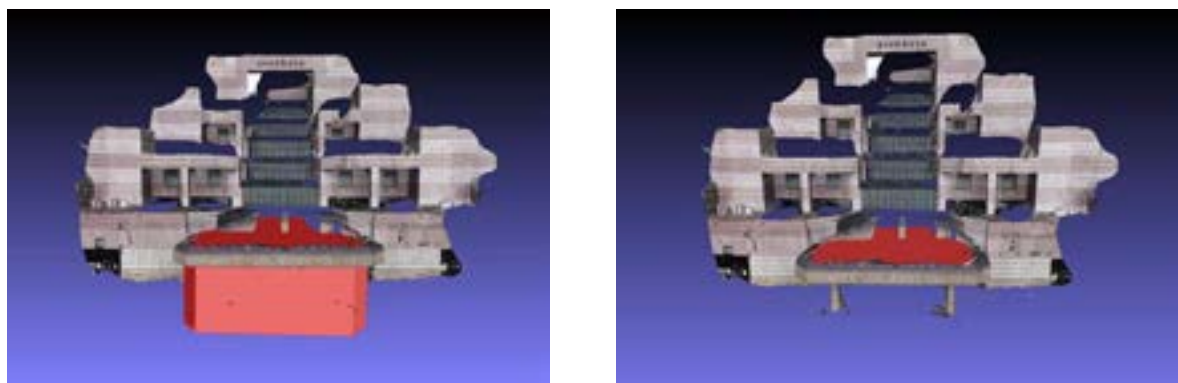

Fig. 2. Study procedure

(a) before adjustment   (b) after adjustment

Fig. 3. The concept of improving the OGC CityGML LOD-1 building models (the red object)

3. RESULTS

Three buildings located in Xinyi District, Taipei, Taiwan are selected as the test cases. Figs. 4 to 6 show the street view images and the results based on traditional and the proposed methods, respectively. Based on these figures, it is obvious that the adjusted LOD-1 building models in this study not only provide a better presentation to be close to the reality, but also include the attributes as shown in these figures. For comparing the develop method with laser scanning and total station based approaches for improvement of LOD-1 building models, Table 1 lists their characteristics.

Table 1. Comparisons of potential approaches for improving LOD-1 building models

Instrument	Advantages	Disadvantages
Close-range images (proposed method)	● Easy to learn ● Instrument is relatively cheaper ● Provide field images (texture) ● Remote data acquirement ● Short time for data acquirement	● Long time for data processing ● High demand for computer hardware
Laser scanner (handheld)	● Easy to learn ● Instrument is relatively cheaper ● Short time for data acquirement ● Short time for data processing ● No demand for computer hardware	● Near data acquirement ● Only height information
Laser scanner (terrestrial LiDAR)	● Directly provide point clouds ● Remote data acquirement ● Accurate measurement	● Difficult to learn ● Instrument is relatively expensive ● Long time for data acquirement ● Long time for data processing ● High demand for computer hardware

Instrument	Advantages	Disadvantages
Total station	• No demand for computer hardware • Accurate measurement	• Difficult to learn • Instrument is relatively expensive • Long time for data acquirement • Long time for data processing • Near data acquirement • Only height information

(a) street view
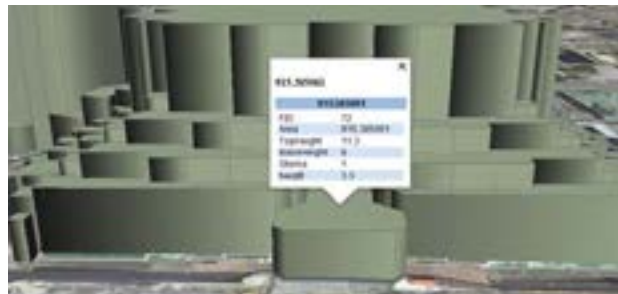
(b) Traditional method

(c) Proposed method

Fig. 4. Case 1

(a) street view

(b) Traditional method
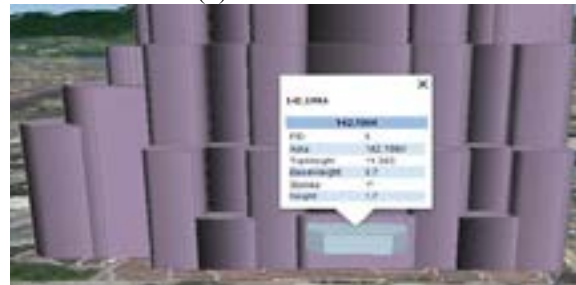
(c) Proposed method

Fig. 5. Case 2

(a) street view

(b) Traditional method

(c) Proposed method

Fig. 6. Case 3

4. CONCLUSION

A procedure to improve the CityGML LOD-1 building model presentation is presented in this study. The LOD-1 building models can be improved according to the terrestrial point cloud data derived from close-range images processed with a dense matching algorithm. Experimental results show that the improved LOD-1 building models are more resemblance to the real buildings than the traditional presentation from in terms of shape and appearance. Furthermore, the characteristics of the developed method and other approaches such as laser scanner and total station based approaches for improvement of OGC CityGML LOD-1 building models are also compared in this study. Users can choose a suitable way to implement depending on their costs and requirements.

REFERENCES

- Furukawa, Y., Ponce, J., 2010. Accurate, Dense, and Robust Multi-view Stereopsis, IEEE Transactions on Pattern Analysis and Machine Intelligence, Vol. 32, No. 8, pp. 1362-1376.
- MOI, 2015. Integration of 3D Digital City and Architectural Models (II), Final Report, p. 321 (in Chinese with English abstract).
- OGC, 2006. Candidate OpenGIS CityGML Implementation Specification (City Geography Markup Language), p. 120.
- Wu, C., 2011. VisualSFM: A Visual Structure from Motion System, URL: http://ccwu.me/vsfm/, Last Access: 15 August, 2018.

LINEAR SOLUTION OF OVERDETERMINATED SEVEN-PARAMETER TRANSFORMATION

Tsai ,Ta Tzu [1]   and You, Rey-Jer [2]

[1] Graduated student, National Cheng Kung University,No. 1, University Rd., East District, 70101 Tainan City, Taiwan

[2] Professor, National Cheng Kung University, No. 1, University Rd., East District, 70101 Tainan City, Taiwan

Email: klnes5218@gmail.com; rjyou@mail.ncku.edu.tw

KEY WORDS:: Nonlinear seven-parameter transformation, Cayley transformation, linear solution, Photogrammetry, Mobile mapping systems.

ABSTRACT: The current applications in Photogrammetry and mobile mapping systems (MMSs) use normally the centric perspective projection to construct the mathematic relationship of images and their corresponding ground points. The relationship is based on a three dimensional seven-parameter similarity transformation which is generally nonlinear. Traditionally, to solve these kinds of transformation problems, we have to first use the linearization method and give the initial values of unknowns together with iterative processing to solve the transformation parameters. Linearized solution procedures need relative good initial values of orientation elements and approximated ground coordinates of object points which may lead to some instable problems and computation-effectiveness.

In this paper, we transform the nonlinear seven-parameter similarity transformation to a linear one by a special transformation, namely the Cayley transformation. In this model, we do not need the initial values and linearization. The solution procedures of the linear model here will be suggested by three step stages. The algebra formulation will be given. In this paper, a set of three coordinates is simulated with random errors for analysis. The results of the linear method including Helmert method and Molodensky method will be compared with those of the iteratively linearized method. Finally, we will discuss the application possibility of the linear model for Photogrammetry and MMSs.

1. INTRODUCTION

The seven-parameter similarity transformation is a common transformation model in many engineering fields when a coordinate set is needed to be transformed to other coordinate systems, e.g. robot dynamics control and geodetic datum transformation problems, and MMS positioning problems etc. The seven-parameter similarity transformation is also widely used in Photogrammetry to solve the relative or absolute orientation between image coordinate systems and object coordinate systems. This similarity transformation includes seven parameters, namely one scale factor, three rotation parameters, and three translation parameters, which describe the transformation relationship between two coordinate systems.

A number of researches have studied the inversion solution of the seven-parameter transformation model to determine the transformation parameters. Most of them have used the linearization and iteration processing mothed to solve the transformation problems. Since 1970s, there were some works using the algebraic algorithms or the

adjustment concepts to separate the whole solution processing to several stages for solution of the seven-paremeter transformation problem step by step to instead using linearization way like using partial least square method and Groebner basis algorithm etc., such that it can prevent the instable problems.

As examples, Awange and Grafareand (2002) applied the Gauss-Jacobi combinatorial algorithm and the Groebner basis algorithm to solve the seven-parameter similarity transformation problem instead of using the traditional linearization way. They solved the overdetermined transformation problem by using a combinatorial solutions. Awange and Fukuda (2004) selected the minimal sufficient points to solve the nonlinear transformation problems using the Groebner basis (see also Zavoti and Jancso, 2006) , while Hashemi et al. (2013) also adopted the Groebner basis technique to solve the problem in a direct manner. With the approach of Groebner basis, they either used a minimal case to solve the exact solution or had to calculate the combinatorial solutions for overdetermined problems. However, it may have trouble if we want to apply the methods to solve the huge point data cases in reality. In Zavoti's paper (2012), he used another method by incorporating the concept of the centroids into the problem to reduce the number of parameters first, then to derive the linear solution by steps. In this study, we take advantages of the usage of the centroids to find the linear solutions with the Helmert transformation model and the Molodensky transformation model respectively.

In the section 2, the basic nonlinear seven-parameter similarity transformation is introduced, and the derived linear transformation models is also given. In the section 3, numerical examples are simulated and analyzed. Finally, conclusion is drawn in the section 4.

2. BASIC CONFIGURATION OF 7-PARAMETER TRANSFORMATION

The seven-parameter Helmert similarity transformation model is expressed as follows:

$$\mathbf{Y}_i = \lambda \cdot R\boldsymbol{x}_i + \mathbf{Y}_0 \ , \qquad\qquad i = 1,2,3,\dots,n, \qquad\qquad (1)$$

where $\boldsymbol{x}_i = [x_i, y_i, z_i]^T$ are the coordinates in a local system and $\mathbf{Y}_i = [X_i, Y_i, Z_i]^T$ are the coordinates in the global system, like WGS84 system; λ is the scale factor, R is the rotation matrix, and $\mathbf{Y}_0 = [X_0, Y_0, Z_0]^T$ denotes the translation vector which is the shift vector from the origin of WGS84 coordinate system to the origin of the local system. The rotation matrix R is defined as $R = R_1(\omega)R_2(\varphi)R_3(\kappa)$ expressed by the Cardan angles:

$$R = \begin{bmatrix} \cos\varphi\cos\kappa & \cos\varphi\sin\kappa & -\sin\varphi \\ \sin\omega\sin\varphi\cos\kappa - \cos\omega\sin\kappa & \sin\omega\sin\varphi\sin\kappa + \cos\omega\cos\kappa & \sin\omega\cos\varphi \\ \cos\omega\sin\varphi\cos\kappa + \sin\omega\sin\kappa & \cos\omega\sin\varphi\sin\kappa - \sin\omega\cos\kappa & \cos\omega\cos\varphi \end{bmatrix} . \qquad (2)$$

It's obvious that the rotational angles can be derived by the following formulas

$$\omega = \arctan\left(\frac{r_{23}}{r_{33}}\right), \qquad \varphi = -\arcsin(r_{13}), \qquad \kappa = \arctan(\frac{r_{12}}{r_{11}}) \qquad\qquad (3)$$

As seen in Eq. (1), the equation with respect to the transformation parameters is nonlinear. The problem of the transformation parameter determination is commonly solved by the linearization and iteration.

2.1 Helmert Transformation in Three-Step Stages

Our problem is that the two sets of coordinates in different datums are given and the unknown transformation parameters have to be determined, namely to find the scale factor λ, the rotation matrix R, as well as the translation vector $\mathbf{Y}_0$. The centroids are compute by following formulas:

$$x_s = \frac{\sum_{i=1}^{n} x_i}{n}, \qquad Y_s = \frac{\sum_{i=1}^{n} Y_i}{n}. \qquad (4)$$

Using the centroid systems, it is explicitly that the translation parameters are eliminated and the transformation equation (1) becomes the following form:

$$Y_{is} = \lambda \cdot R x_{is}, \qquad i = 1,2,3,\dots,n, \qquad (5)$$

where the index is means the coordinates of point i referred to the gravity center coordinate system.

The inversion problem of the transformation is now solved in three steps. First, based on the orthogonality of the rotational matrix, the scale factor λ is easily to be determined as follows:

$$\lambda^2 x_{is}{}^T x_{is} = Y_{is}{}^T Y_{is}, \qquad i = 1,2,3,\dots,n. \qquad (6)$$

The solution for the positive scale factor is

$$\lambda = \frac{\sum_{i=1}^{n} \sqrt{Y_{is}^T Y_{is}}}{\sum_{i=1}^{n} \sqrt{x_{is}^T x_{is}}}. \qquad (7)$$

Next, we make use of the Cayley transformation due to the orthogonal characteristic of rotational matrix such that the matrix can be expressed by a skew-symmetric matrix **S** as follows:

$$R = (I - S)^{-1}(I + S), \qquad \text{which } S = \begin{bmatrix} 0 & -c & b \\ c & 0 & -a \\ -b & a & 0 \end{bmatrix}. \qquad (8)$$

Consequently, we have the following equation after rearrangement.

$$(I - S)Y_{is} = \lambda \cdot (I + S)x_{is}, \qquad i = 1,2,3,\dots,n. \qquad (9)$$

Since the scale factor is already solved in Eq. (7), the above equation is therefore linear and the parameters can be determined by the least squares.

At last, putting the coordinates x_s and Y_s into Eq. (1) to find the shift parameters Y_0, we can carry out our Helmert transformation problem without linearization and iteration in three-step stages mentioned above.

2.2 Molodensky Transformation in Three-Step Stages

The Molodensky transformation model is normally used to overcome the correlation problems between the transformation parameters in the Helmert transformation model. The significant difference between the Molodensky model and the Helmert model is the processing method of the translation parameters. In the Helmert transformation model, the translation parameters expressed as the $Y_0 = [X_0, Y_0, Z_0]^T$ (see Eq. (1)) are the shift magnitudes between the origins of two coordinate systems. In contrast to the Helmert model, the translation parameters are expressed by the differences of the coordinate of centroids in the two coordinate systems. The Molodensky model is written as

$$Y'_{is} = \lambda \cdot R x'_{is} + \delta x_s \ , i = 1,2,3, \dots, n, \tag{10}$$

where $Y'_{is} = Y_i - x_s$ and $x'_{is} = x_i - x_s$.

The three-step stages for the solution are similar as those of the Helmert model. The Molodensky model (10) plays the role of our solution stages as the Helmert model (1). The shift can be determined as follows.

$$Y_0 = x_s + \delta x_s - \hat{\lambda} \cdot \widehat{R} x_s \tag{11}$$

3.   CASE STUDY

In this section, two sets of coordinates referred to two different datums were simulated and three solution methods were analyzed, namely linearization and iteration method for the Helmert model, three-stage method for the Helmert model,, and three-stage method for the Molodensky model mentioned above. The distribution of points is illustrated in Figure 1. One set of coordinates was introduced by the normal distributed random errors. The results are shown in Table 1.
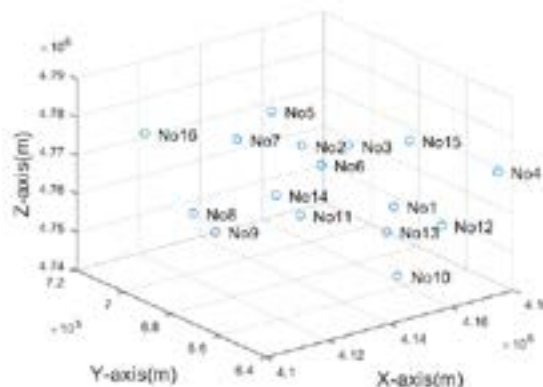
Figure 1. Simulated points.

Table 1. Comparison of results

Parameter	Linearization & iteration	3-stage Helmert method	3-stage Molodensiky method
λ	1.00004981	1.00004981	1.00004981
ω(degree)	0.98253	0.99998	0.99998
φ(degree)	1.01717	1.00002	1.00002
κ(degree)	0.98257	1.00001	1.00001
X_0(m)	12.1318	12.1228	12.1228
Y_0(m)	12.9103	12.8930	12.8930
Z_0(m)	9.3546	9.3658	9.3658

As seen in Table 1, the results of both linear methods are the same, but there is a little difference with the linearization and iteration methods, especially in rotational angles. The reason is obvious that the seven parameters have high correlation between rotational angles and the rest parameters. The solutions by the linear models can overcome the correlation problems. Based on the study (Fu, 2018), the linear methods have a significant advantage in computational efficiency compared to the linearization and iteration method, in particular, in the case of a number of transformed common points. His conclusion was that the computational efficiency can be increasing about 100 times than that of linearization and iteration method in case of 1000 common points. We obtained the similar results.

4. CONCLUSION

In this study, we have shown two linear models for the seven-parameter similarity transformation that lead to fast solutions. The linear methods do not need the initial values of unknowns that are big different with the linearization and iteration method. The developed methods here can be used to the modern positioning by GNSS/IMU and MMSs. The results of this part will be published in the near future.

5. REFERENCE

Awange, J.L., and Grafarend, E.W., 2002. Linearized Least Squares and nonlinear Gauss-Jacobi combinatorial algorithm applied to the 7-parameter datum transformation C_7 (3) problem. zfv, 2, pp. 109-116.

Awange, J.L., and Fukuda, Y., 2004. Exact solution of the nonlinear 7 parameter datum transformation by Groebner basis. Bollettino Di Geodesia Science Affini, N.1, pp. 117-127.

Fu , M.-H., 2018. Non-iterative Method of Seven-Parameter Similarity Transformation and Gross Error Detection. Master-degree thesis, department of Geomatics, National Cheng Kung University, Tainan City, Taiwan.

Hashemi, A., Kalantari, M., and Kasser, M.,2013. Direct solution of 7 parameters transformation problem. Appl. Math. Inf. Sci., 7(4), pp. 1375-1382.

Deakin, R.E., 2006. A note on the Bursa-Wolf and Molodensky-Badekas Transformation. School of Mathematical & Geospatial Sciences, RMIT University.

Závoti, J., and Jancsó, T., 2006. The solution of the 7-parameter datum transformation problem with- and without the Grobner Basis. Acta Geod. Geoph. Hung., 41(1), pp. 87-100.

Závoti, J., 2012. Simple proof of the solutions of the Helmert-and the overdetermined nonlinear 7-parameter datum transformation. Acta Geod. Geoph. Hung, 47(4), pp. 453–464.

AUTOMATIC SCALING OF CRITICAL FREQUENCY foF2 FROM IONOGRAMS BASED ON A PIXEL-FOLLOWING TECHNIQUE

Yuttapong Rangsanseri, Weeranat Phasamak

Faculty of Engineering, King Mongkut's Institute of Technology Ladkrabang (KMITL),
Bangkok 10520, Thailand
Email: yuttapong.ra@kmitl.ac.th, 59601303@kmitl.ac.th

KEY WORDS: foF2 Automatic Scaling, Ionogram, Pixel-Following

ABSTRACT: This paper proposes a new technique for automatic scaling of critical frequency foF2 parameter of F2-layer from ionograms. Scaling of ionograms initially had to rely on experienced staff for manual operation. In this paper, we have examined ionograms data collected at Chumphon, Thailand, in March 2015, during the period that the observed F2 layer traces can be identified. Our method extracts foF2 value by finding a pixel on the beginning of the trace line and will use this pixel as the starting point for finding the ends of the traces by scanning either one or two lines. In each step we need to prepare the ionogram image, remove unnecessary part of image then remove noise, and refill the trace line before final scanning process. Based on a pixel-following technique, the method produces high accuracy results because it can scan until the final pixel of the trace line. The proposed method has been successfully tested on various ionograms, the results match with a single-pixel accuracy comparing to manual scaling.

1. INTRODUCTION

Ionosphere is the name of atmosphere layer lying above Ozonosphere and is the furthest atmospheric layer from the earth surface. It helps reflecting HF radio signal for telecommunication purpose, it is observed that radio signal can be sent all over the globe. Ionosphere affected directly the propagation of radio waves. Ionograms are generated by ionosondes. An ionogram showing the radio wave propagation time delay against operating frequency can be got when using high frequency radio waves to detect the ionosphere. There are many parameters related to the ionosphere from ionogram such as fmin foE h'E foEs h'Es Es fbEs foF1 h'F h'F2 foF2 ans fxI. The process for extracting the related ionospheric parameters is called scaling. Scaling of ionograms initially had to rely on experienced staff for manual operation, this method can provide more accurate results but need a lot of time to do this task. Automatic scaling the parameters from ionograms will therefore be very helpful in many research works on this data. With the development of computer and image processing techniques, much effort has been focused on the development of techniques that will automatically scale ionograms (Wright et al, 1972), (Mazzetti and Perona, 1978), (Fox and Blundell, 1989), (Tsai and Berkey, 2000). Most of these methods firstly emphasize the accurate recognition of ionogram traces and then make an inversion of the density profile using ionospheric inversion techniques (Huang, 2001). However, automatic scaling algorithm of ionogram cannot be directly applied in the ionogram because there are very differences between form of ionogram and noise.

This paper will focus on the extraction of the critical frequency of F2 layer, foF2, because it is the ordinary wave critical frequency of the highest stratification in the F region and therefore is one of the most important parameters for telecommunication application. Our foF2 scaling method uses image-processing techniques performed on the ionogram image. The first step is finding the pixel on the left side of the trace line, starting at low frequency that is not lower than the least frequency of foF2. This point is used for starting point to scanning the trace to the end of the trace line. This will result in the critical frequency foF2 at the end of the trace and the leftmost traces in the case of two lines. This method provides high accuracy because it can scan up to the last pixel of the signal that is still present in an ionogram image.

2. IONOSONDE AND TEST DATA

An ionosonde is a swept frequency vertical-incidence high frequency radar. The time delay of the echoes from the ionosphere give information on the electron density in the ionosphere. The ionogram, picture produced by an ionosonde, display the time to receipt of an echo on the vertical axis against frequency on the horizontal axis. Ionograms are recorded typically every 5 minutes for good temporal resolution. The ionogram data used in this paper was collected at ionosonde station in Chumphon, Thailand ($10.72°$N, $99.37°$E, dip angle $3.0°$N) during March 2015.

The data was collected from the frequency range of 2-30 MHz. This ionosonde installed by the National Institute of Information and Communications Technology (NICT) of Japan. It provides Frequency Modulated Continuous Wave (FMCW) versatile ionosonde consisting of SKI-02098T amplifier/low pass filter bank and SKI-02098RC controller/dual channel receiver. FMCW is one of strong pulse compression technique and data processing gain reaches as much as 10^5. When only 20W transmitting power is fed to a wide band antenna, clear ionogram is obtained equivalent to 10 kW pulse ionosonde. Frequency range, sweep rate, and many observation parameters are programmable in the host PC. Vertical and oblique incidence observations are supported. GPS clock keeps fine synchronization between transmitting and receiving station in oblique sounding.

The test ionogram data from day time recorded by SKI-02098T/RC installed at Chumphon, March 2015 are shown in Figure 1.

3. THE PROPOSED ALGORITHM

Ionograms acquired during a day are significantly different in term of shaping and amount of noise, making it difficult to identify the desired critical frequency because normal filtering during the process will lose other important information. In this paper, we used the method to find the point on trace line. This will reduce the problem of noise elimination. This point will used as the starting point for following the pixels on trace line till the end of the line, most left line in case two lines. This will be the value of the critical frequency foF2, which will result in a very accurate critical frequency because this method used point-to-point scan to the end of trace. The process of preparing an ionogram image for a starting point and the method is used for pixel following technique will be explained later. For the first step, the daytime ionogram shown in Figure 1 contains an unnecessary information for calculating foF2. A manual scaling performed on a long-term ionograms data from Chumphon (Thailand) station (Wichaipanich and Supnithi, 2013) showed that the foF2 values never exceed 13 MHz. Hence we can limit the area of ionogram image by discarding the area beyond this frequency as shown in Figure 2.
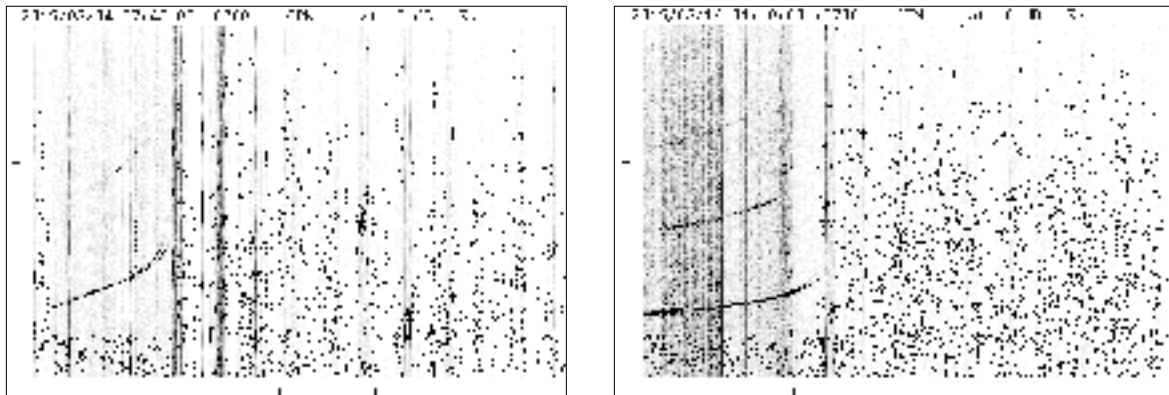
Figure 1. Ionogram recorded by SKI-02098T/RC installed at Chumphon, March 2015 (size: 500 x 738)
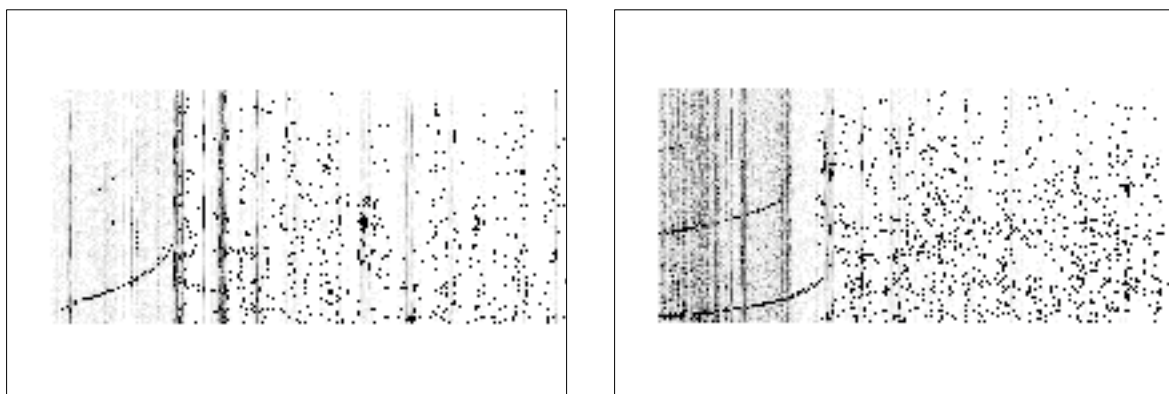
Figure 2. Clear the area outside trace (top buttom and left sides)

After the ionogram image is cropped, we proceed to threshold image to eliminate background noise and prepare the image for further processing. As shown in Figure 3, there is still a lot of noise in the image. Most of noise in trace range is in the form of vertical line. To eliminate this noise in the range of images with lines of trace. After the ionogram image is thresholded, we proceed to remove the noise in the form of a vertical line. By scanning on each column of the ionogram image, the column will be totally removed if it has a pixel summation above a threshold value. In during this procedure, each pixel of the row in the column will be scanned once again to prevent information loss. The rule is to monitor pixel beside the processing pixel as shown in Figure 4. For each position processed by this method the value of each pixel will be restored into its original position as show in Figure 4 for further processing. To be processed in the next step. This step will remove this vertical line only scans half of the ionogram image and no need to scan the whole because the rest will be at a higher frequency than the trace. The range is set to cover all traces.
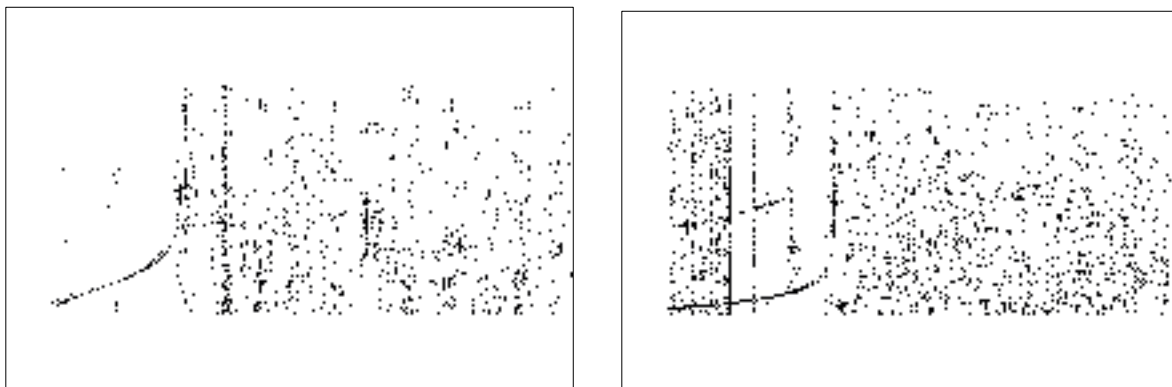
Figure 3. Ionogram image after thresholding

The next step from the main idea of this algorithm. The point is on the line of the trace to be the starting point for scanning by following pixel on trace to the end of the trace. The purpose of noise reduction is to provide the most accurate point of starting scan. To find this starting point, we will find the point at the beginning of the trace line, the left side of the trace at low frequency. There are remain some noise in trace range as show in Figure 4, this may result in error for finding starting point. The traces begin with low frequencies and heights. So we can crop the parts that are not in this range. Then scan for points at the ends of the trace lines. This will be used as the starting point for future critical frequency scans as shown in Figure 5.
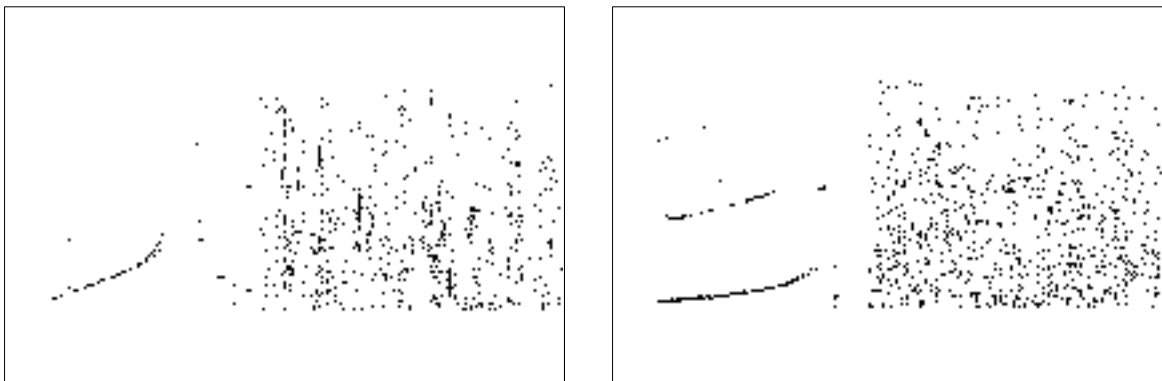
Figure 4. Remove vertical lines and refill deleted points belonging to the line parts
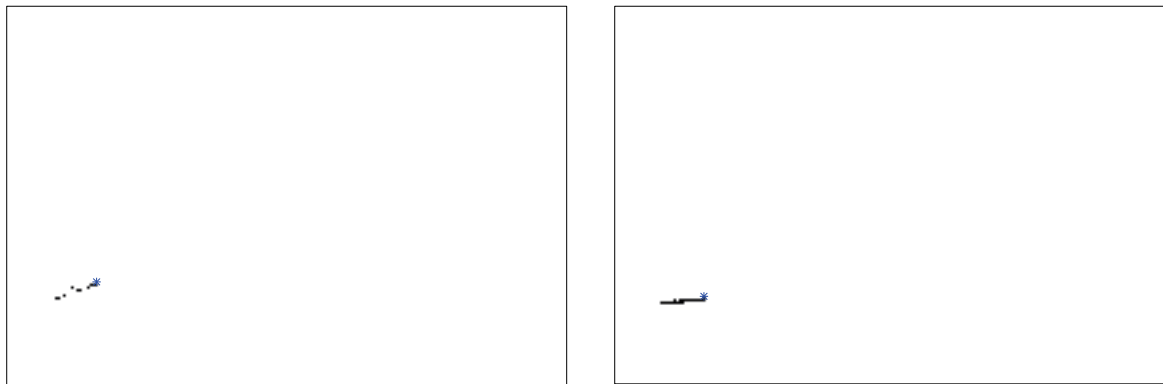
Figure 5. Crop the image to the left and find last point of line

The last point was plotted in Figure 4 and was shown in Figure 6, the prepared ionogram image for scanning the end of the line. To make the scan from this point more accurate, it is necessary to improve the image or line of the trace again. By scanning the trace lines to determine whether there is a missing range or not, this process will fill the pixel to keep the line continuity. It makes scanning to the end of the line more efficient, because it is a pixel to pixel scanning.

The last step is to scan from the starting point on the traces, by scanning from right to left and set the condition to scan to the top neighborhood and then in clockwise direction because of some ionogram images, there may be only one line in the image. In case of ionogram images with two overlapping lines at the end, if this condition is not met, the scan will fail. The point that we need is that the end of the line on the left side is the critical frequency foF2. The effect of scanning the trace is shown in Figure 7 (Top).
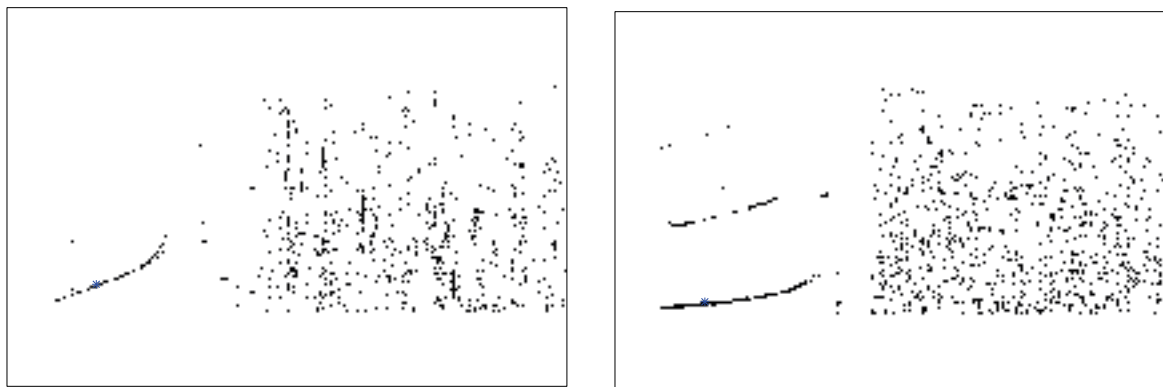
Figure 6. Displays the starting point for scan the prepared ionogram image

When the position of the last point of the trace is reached, the frequency of the foF2 will be calculated. Finally, the values for the parameters foF2 are 8.92 MHz and 11.04 MHz, respectively, as shown in Figure 7 (Bottom). Compared to manual scaling as shown in Figure 8, the results are the same values of foF2 from this method.

4. ANALYSIS

The automatic scaling technique described above has been tested on many ionogram images, the results are mostly consistent with manual scaling by human expert. From the image that used in this experiment, our algorithm gives foF2 values at exactly same values as those marked by manual scaling. Different people may give different result depending on perspective and spot that collect the data, only one pixel difference can change the frequency to about 0.04 MHz according to the calculation base on the standard size of 500x738 pixels images produced from the ionosonde at Chumpon station.
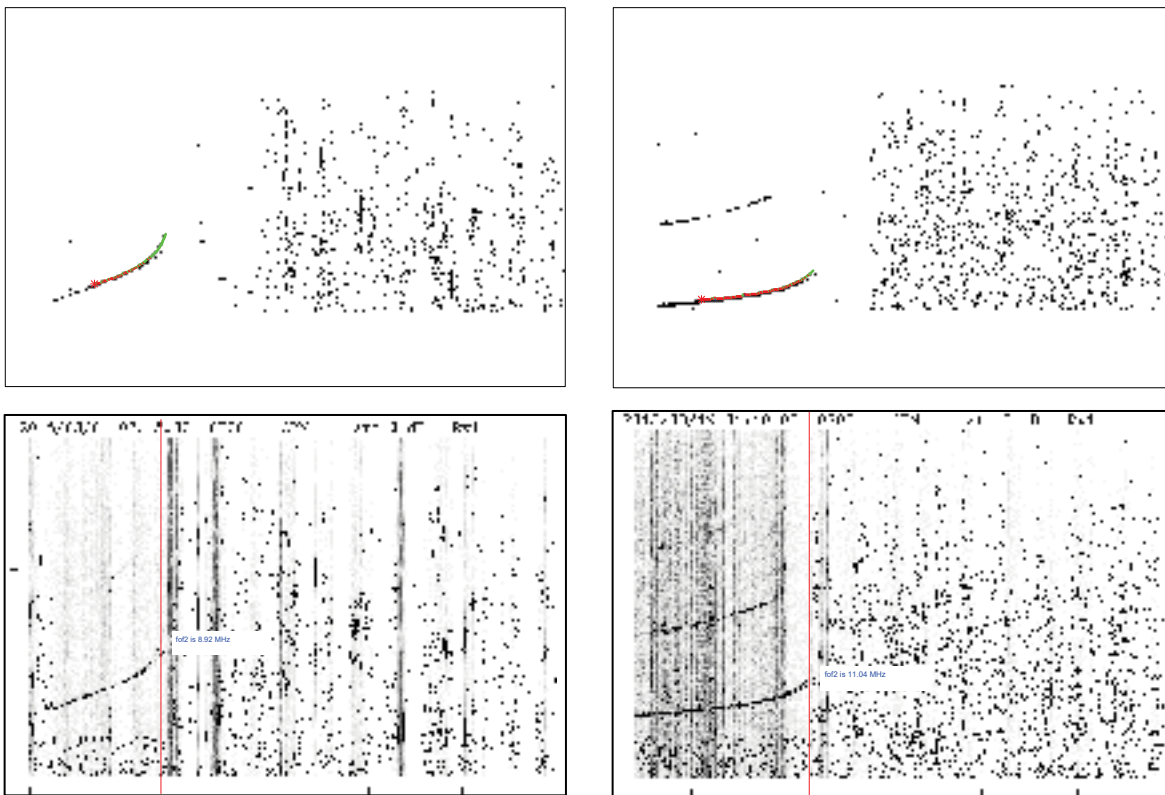
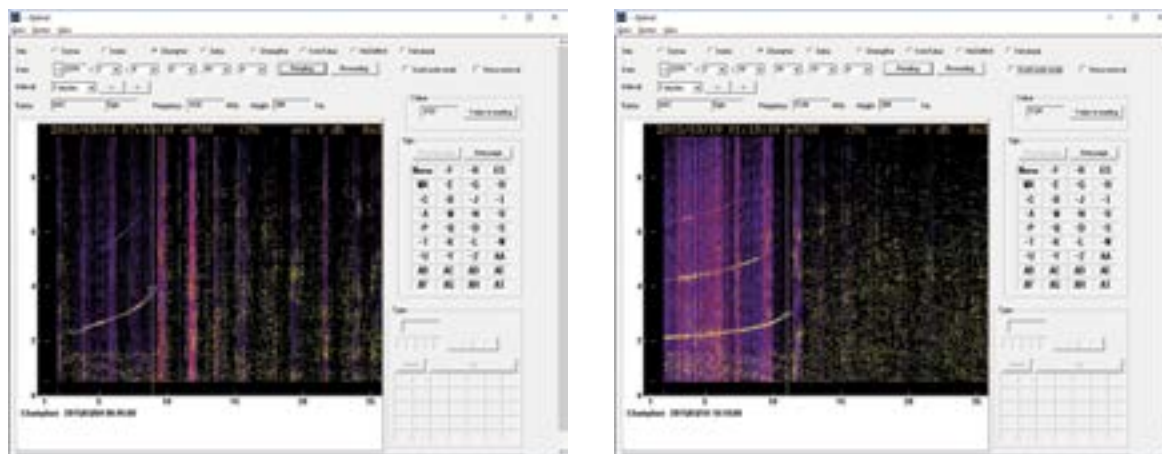Figure 7. Scan from the last point to the end of the line at the far left (Top), result of foF2 (Bottom)

Figure 8. Result of foF2 from manual scaling (foF2 = 8.92 MHz and 11.04 MHz)

5. CONCLUSION

We have proposed a method for automatic scaling critical frequency foF2 parameter in F2 layer from ionogram images based on a pixel-following technique by processing directly with the ionogram image. The main idea is that if we can find any points that are part of the trace line, we can find the next point of this line. The most important part for this method is to find the starting point for the scan to be on the trace line. It is necessary to eliminate the noise that may cause this error to occur as proposed. It will be possible to find the critical frequency foF2 as the last pixel of the trace line accurately.

ACKNOWLEDGMENTS

REFERENCES

Fox, M. W., and Blundell, C., 1989. Automatic scaling of digital ionograms., Radio Science, 24, pp. 747-761.

Huang, X. Q., and Reinisch, B. W., 2001. Vertical electron content from ionograms in real-time. Radio Science, 36, pp. 335-342.

Mazzetti, B. and Perona, G. E., 1978. Automatic analysis of diurnal digital ionograms. Alta Frequenza, 47, pp. 495-500.

Tsai, L. C., and Berkey, F. T., 2000. Ionogram analysis using fuzzy segmentation and connectedness techniques. Radio Science, 35, pp. 1173-1186.

Wichaipanich, N., and Supnithi, P., 2013. Comparison of ionosphere characteristic parameters obtained by ionosonde with IRI-2007 model over Southeast Asia. Advances in Space Research, 52, pp. 1748-1755.

Wright, J. W., Laird, A. R., Obitts, D., Violette, E. J., and McKinnis, D., 1972. Automatic N(h,t) profiles of the ionosphere with a digital ionosonde. Radio Science, 7, pp. 1033-1043.

FORMOSAT-5 Satellite Image Data Transferring Mechanism from Norway Receiving Station

Chin-Yin Chen (1), Hsin-Yen Chen (2), Sheng-Yun Yan (1)

[1] National Space Organization,

8F, 9 Prosperity 1st Road, Hsinchu Science Park, HsinChu, Taiwan
[2] Academis Sinica Grid Computing Center, Research Center for Information Technogly Innovation, Academia Sinica
128, Sec. 2, Academia Rd. Nankang, Taipei 11529, Taiwan
Email: fifi@nspo.narl.org.tw; hychen@sinica.edu.tw; ysyun@nspo.narl.org.tw

ABSTRACT: The path for the remote sensing data, from the FORMOSAT-5 satellite to the receiving station at Svalbard, through data processing and then long-distance file transfer to NSPO in Taiwan, is a complex one. Due to the limited network bandwidth and long latency, NSPO used the tape storage for FORMOSAT-2 image data and delivered the media via airline logistics for a long time. The critical issue is whether one may download the data sets including the raw data as fast as possible to the user communities in Taiwan. NSPO have thus developed the automatic long distance file transferring platform. Taking advantage of the Taiwan Academia Grid Computing Center's research network infrastructure and secure long distance transferring technology, we could ensure the data sets up to 30GB would be transferred to Taiwan in 2 hours. It is much shorter than one manually does it using the ad-hoc network service in 4 hours. We have optimized the network parameters in the file transferring platform since the beginning of the project. Now, we could receive the data sets in Taiwan within 1 hour after parameters adjustment

This long-distance data transferring mechanism could help us to develop the applications which need fast delivery of satellite image production, such as the identification of earthquake, flood, and forest fires disaster area. It could greatly improve the international emergency rescue services. The experience of long distance file transferring mechanism could help the other countries to receive image data at the Norway receiving station and to quickly transmit relevant data back to their countries.

KEY WORDS: remote sensing, satellite image data, emergency rescue service, long distance data transferring

1. Introduction

FORMOSAT-5 operates in a sun synchronous orbit at 720-km altitude with 2 day revisit property., and its field of regard can cover most area of the world. Therefore, NSPO contracts with the Kongsberg Satellite Services (KSAT) on Svalbard in Norway to receive image data from FORMOSAT-5 11 passes every day.

The data flow with long-distance transmission from receiving satellite signal on oversea station to local image processing center is a complex issue. Due to the limitation of network bandwidth and long latency, NSPO used the tape to store the satellite raw data and delivered these tapes via airline logistics to NSPO from oversea station for FORMOSAT-2 operation. To use tape transmission, it takes two weeks to get the satellite data. Another way is to transfer satellite data through a traditional internet network, and this only took 4 hours, more efficiently than previous one. But the data delivery timeline shall be improved and get faster with the times. Therefore, NSPO has developed the Nordic Academic network data transmission mechanism. The mechanism takes advantage of the Taiwan Academia Grid Computing Center's research network infrastructure and secure long distance transferring technology, that guarantee the 30GB satellite raw data (includes Date Raw Data, DRD and Virtual Channel Data Unit, VCDU) would be transferred to NSPO from Norway receiving station within 2 hours. (see the Figure 1.)
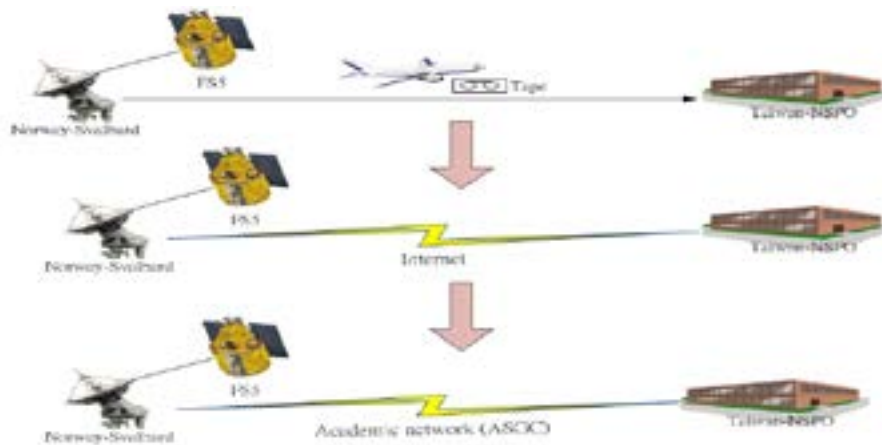
Figure 1. The Evolution of Transfer medium from Norway Receiving Station to NSPO

2. The processing procedure and data volumes of FORMOSAT-5 image

FORMOSAT-5 satellite was launched successfully by SpaceX Falcon 9 rocket on August 25, 2017 from the U.S. Vandenberg Air Force Base. Before FORMOSAT-5 launch, NSPO conducted serval data transmission tests including the transfer the multiple 10GB simulated raw data from Norway receiving station to NSPO.

 FORMOSAT-5 remote sensing image data are downloaded by X-band antenna system (XAS), the image data are protected by on-board encoding and data scrambling on satellite. The main function of the image-processing center is to further process and display the original image data received by X-band antenna system. The image processes include: frame synchronization, image decoding, optimal proximal correction, and geometry correction. Data Ingestion System (DIS) is in charge of retrieving and decoding image, hence the encoding algorithm and scrambling rules are needed to involve in developing DIS system. After RT-STPS and DIS system processing, the DRD will decode into VCDU and Gerald files. The original 10GB DRD file size, will decode to approximately10GB VCDU and 100GB Gerald file size (compression ratio is 7.5). (see Figure 2.)

Figure 2. The Data Flow of DIS System and Their File Format

This mechanism has to make sure those files are ready and successfully transferred back to Taiwan. It is setting up to 10 minutes that each data from receiving station at Svalbard, it could be processed and analyzed to image product. Moreover, it also optimized the network transferring performance using the dedicated 100M bit/sec between Svalbard and Tromso data center. It will take 15 minutes to complete the file transmission. Then, this paper could use the optimized long distance file transferring platform which is implemented with Globus GridFTP program and using the AGGC research network infrastructure. The file transferring rate of the 10GB data file is more than 60 MB/sec. Then, the data file is transferred to Taiwan NSPO data center. It will take 10 minutes in transferring time. Therefore, each orbit data from receiving station at Svalbard to NSPO data center, it totally needs 45 minutes.
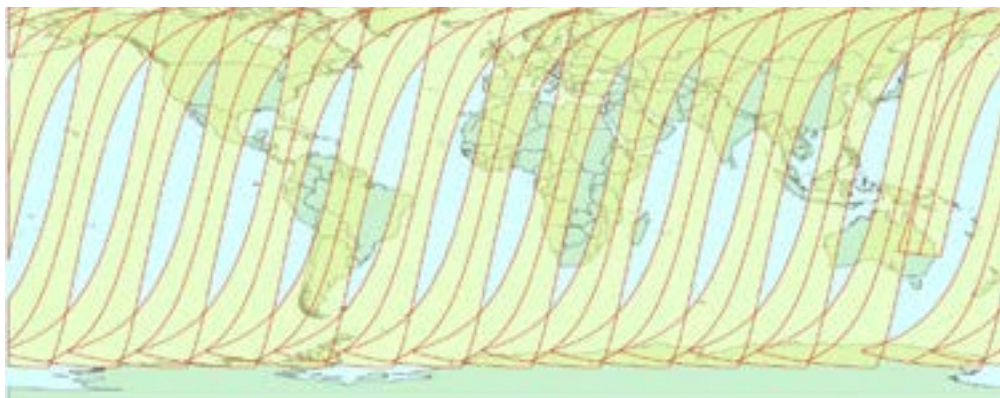
Figure 3. FORMOSAT-5 Imaging Coverage

The FORMOSAT-5 one-day imaging coverage is shown in Figure 3. The data of the FORMOSAT-5 was received 14 times a day, it was received twice times in Taiwan, and was received 12 times in Norway receiving station. The time interval of downloading data in KSAT between adjacent orbit is 100 minutes. According to last description, in the case of only transferring the Gerald files from Norway receiving station to NSPO, it will take more than100 minutes. The means that the raw data of next pass will transfer with previous one at the same time, and this situation will affect the latency transmission efficiency, Therefore, it is the best way to select the VCDU files be the first transmission target instead of Gerald files, and the DRD is second.

3. Implementation

For the network performance of the long distance file transferring, there are three major factors that could affect the TCP performance. There are the packet loss, latency and buffer/window size and those three are interrelated. The TCP RTT network latency is the amount of time it takes for a packet to go from the sender to the receiver and back (a "round trip"). This is the amount of time for one host to get information back from the other host about data that was sent.

And the buffer and window size determine both the amount of data that the kernel will keep in buffers for the connection, and the "window" that is advertised over the TCP connection. The original TCP configurations supported the TCP window size buffers up to 64 KB. The network buffer is used throughout high performance network systems to handle delays in the system. In general, buffer size will need to be scaled proportionally to the amount of data "in flight" at any time. The larger the window, the more data can be in flight between the two hosts. If the window is smaller than the available bandwidth multiplied by the latency, therefore, the sender will send a full window of data and then sit and wait for the receiver to acknowledge the data. This results in lower performance. You could set system-global parameters to optimize for each destination, or the application has to have knowledge of the underlying network to set its buffers correctly.

 When TCP encounters loss, it has to recover - but it starts with a small window and opens it back up again over time. The longer the latency, the longer the control loop is for doing this. So, all other things being equal, the time necessary for a TCP connection to recover from loss goes up as the round-trip time goes up. TCP then ramps its sending rate back up again, in hopes that the loss was transitory. Today, there are algorithms such as htcp and cubic are much more aggressive about ramping back up again than the old scheme (TCP Reno).

Generally, the latency between Tromso and Taiwan is about 322 ms using the ASGC worldwide network infrastructure. For the file transferring requirement of the FORMOSAT-5, It have to transfer each orbit's data including the VCDU and DRD files in 100 minutes. It is about 30GB for

Taiwan ASGC data center. There are the different OS on the two client systems. For those systems, this study increases the tcp shared memory up 64 MB on the kernel file sysctl.conf. Then, we do the ad-hoc benchmark using the scp, transferring the 10GB data, the network performance is about 6MB/sec. Therefore, this study tries to use the globus grid-ftp program to investigate the network transferring performance using the different block size and parallel sessions. Firstly, this study keeps the single TCP stream and to verify the block size from 1MB to 16 MB. This paper does the 10GB file transferring tests. From the results of the Table 1, the larger block size, the better network transferring performance. And it almost could be scale up. Secondly, it fixes the grid-ftp block size, 1MB, and to do the tests using the different parallel sessions. From the results of the Table 2, this mechanism has the better performance using the more current sessions.

In general, the current file transferring mechanism implemented with globus grid ftp program, it could have the very good platform to transfer the FORMSAT 5 data from Norway Tromso data center do Taiwan ASGC data center. the advanced research network infrastructure is not only reduced the network transferring nodes and but also has the more bandwidth. Therefore, this mechanism could use the more parallel session to keep the stable transferring rate.

Table 1: The network transferring performance using one Globus Grid-FTP session vs the different block size

Block Size	1M	2M	4M	8M	16M
Gw0	4.39	8.8	16.96	29.47	57.41
Gw1	4.39	8.93	18	27.84	62.31

Table 2: The network transferring performance of the Globus Grid-FTP block size equal to 1MB vs. the different parallel sessions:

Parallel Sessions	1	2	4	8	12	16
Gw0	4.39	8.59	16.65	38.16	55.44	71.62
Gw1	4.39	8.49	16.96	38	58.88	76.85

4. The case study of FORMOSAT-5's emergency observation

After almost half year calibration for satellite component, orbit maintenance and image processing, the quality of satellite images have already proven sufficient in supporting the disaster prevention mission and diverse civilian applications. The event of observation was including California wildfire in December 2017, oil spill in East China Sea in January 2018, monitoring of Agung volcano in Indonesia and Hualien earthquake in February 2018. FORMOSAT-5 is scheduled to enter service to support the nation's disaster during the flood season of Taiwan and support global disaster events (see Figure 4).

Oil spill occurred in southern of Thailand during 7-9 July 2018. It need to monitor oil spill in Pangan Province.FORMOSAT-5 supported Sentinel Asia to take the image of the oil spill on the coast of Phangan island in the southeastern gulf of Thailand. The Phangan island is renowned for its boisterous and fun-filled Full Moon Parties held every month, it is also a sightseeing spot for many self-help travelers. The oil pollution range is 10 meters wide and 200 meters long, it could be affect the ecological conservation and sightseeing. The basic characteristics of FORMOSAT-5 are similar to FORMOSAT-2, the swath width is 24 km @ nadir, which can effectively help monitor the spread of coastal oil spills and provide imagery for national disaster prevention center to control the impact on ecological conservation and sightseeing.

The raw data of FORMOSAT-5 image received by the Norway receiving station is transmitted quickly to NSPO's Image Processing Center via Nordic academic network mechanism. The FORMOSAT-5's Image Processing System (IPS) is independently developed by NSPO. It is designed to process images by tasking the satellite according to the user's needs. Images are then taken and downloaded through X-band antenna, then processed by through IPS such as radiometric correction image product and stored in computers. Finally, the panchromatic and multispectral disaster imagery was provided to the Sentinel Asia and the end users in Thailand after 8 hours of receiving the satellite data. (see Figure 5).

Figure 5. FORMOSAT-5 Multispectral Imagery, Oil Spill in Phangan Island

The another case of application of FORMOSAT-5 image is: At 6:00 am on September 6, 2018, a 6.7 strong earthquake was observed in the Japan's Hokkaido island. The heavy landslides buried a large number of homes at the foot of a ridge. At least 28 people were injured in the region and 20 residents in the town of Atsuma may be unaccounted for, officials said. The operation team of NSPO immediately began to plan FORMOSAT-5 imaging to take the disaster area after receiving the emergency observation request from Sentinel Asia.

On September 7th, the first disaster area image was receiving at Taiwan Standard Time (TST) in the afternoon. The image data are arranged for reception and return at the Kongsberg Satellite Services AS, and the radiometric calibration image product was provided and notified to Sentinel Asia after 8 hours of receiving the image at Norway receiving station.

With the practiced imaging experiences of the last 12 years of FORMOSAT-2 satellite, the imaging operation team is rapidly reacting to support the global disaster events and requests. For the data transmission, with the high efficiency of the Nordic Academic network data transmission mechanism, so that FORMOSAT-5's imagery can timely and quickly transmitted to NSPO, and can provide image product for disaster prevention and rescue tasks.

5. Conclusion and Future Work

To establish the long-distance rapid image data transmission mechanism from oversea receiving station to NSPO through the ASGC network architecture, the automatic backhaul is necessary and effective, which improve the data transmission time from 4 to 1 hours, thereby increasing

production rate. At the application level, it helps to facilitate rapid product delivery time, and supports disaster relief. FORMOSAT-5 imagery has been used provided in earthquake, fire and forest fire applications and international emergency relief supporting.

The establishment of high efficiently long-distance satellite data transmission mechanism can be applied and packaged into a reliable and practical service in the future. This mechanism is able to the data transmission form polar station to the local processing center for any satellite depending on the customer needed.

6. Reference

Tony Tsai ,Feng-Tai Huang, 2016. FORMOSAT-5 System & The initiator of FORMOSAT-series Remote Satellite Mission. Science Development, pp.518

Sentinel Asia , Emergency Observation Request Information , from
https://sentinel.tksc.jaxa.jp/sentinel2/emobSelect.jsp

Satellite Imaging Corporation ,Satellite Image Application and Corporation , from
https://www.satimagingcorp.com/

NSPO, Image Processing System and Image Application, from
http://www.nspo.narl.org.tw/en2016/projects/FORMOSAT-5/ipc.html.

Wetland Change Detection Using Long-Term (15 years) Multi-Temporal Landsat TM Data

Maslina Natar and Mazlan Hashim,
Geoscience and Digital Earth Centre (INSTeG),
Research Institute of Sustainable Environment
Universiti Teknologi Malaysia, 81310 UTM Johor Bahru, Malaysia.
Tel.: +60-7-555-7661; Fax: +60-7-555-7662.

Abstracts: Wetlands plays significant role to sustain the natural ecosystems, control the global climate regulation and acts as natural protector from pollutants and flood events. However, rapid growth of urban planning and agricultural development has affected the wetland ecosystems distribution in this country. This study was carried out to assess the changes of wetlands area in Pahang using Landsat TM satellite images. Six bands were used as input data along 15 years observation. Supervised maximum likelihood classifier were utilized to classify the images into seven classes; wetland, water, urban, oil palm, paddy, rubber and forest. The classification accuracy was assess using the reference data by a confusion matrix. The result shows higher overall accuracy of 85.20%, 79.15% and 90.60% for year 2000, 2008 and 2015 respectively. The post classification change detection analysis over wetland conversion areas were successfully presented. The result revealed the wetlands area has decrease and facing some changes for the incoming years. As a conclusion, change detection technique with satellite data images perform a great result to evaluate the land use cover changes by spatial and temporal studies.

KEYWORDS: Wetland, Change detection, Maximum likelihood, Supervised classification, Landsat TM

1. Introduction

Wetlands provide habitat for flora and fauna, supporting numerous biodiversity, acts as natural flood protector and control the climate regulation. Since last decades, more than half wetlands around the world have been converted for agricultural production and infrastructure development (Schuyt et al., 2005). To prevent the loss of wetland areas, it is crucial to monitor and assess the wetland inventory. The aim of this study is to assess wetland changes using long-term multi-temporal landsat TM data within 15 years observation. To achieve the purpose, maximum likelihood supervised classification was used based on spectral images of Landsat 5 TM.

Remote sensing and GIS tools are able to detect land use land cover changes at various spatial and temporal resolution. Satellite remote sensing is suitable to monitor wetland changes due to redundant in coverage by seasonal and year (Ozesmi and Bauer, 2002). Change detection using remote sensing sources has extensively used in recent decades. Past studies were revealed that the most common method for change detection includes image differencing, principle component analysis and post-classification comparison produce the great result. Image classification is one of the most significant method in remote sensing, and widely used for monitoring and mapping land cover changes (Lawrence and Chase, 2010). Land-cover classification normally evaluated using hard and soft classifications. By hard classifications, each pixel is assigned to a single class, meanwhile in soft classification, a pixel may belong to many classes and different levels of class membership or proportion are assigned. Wetland classification is difficult because of spectral confusion with other land cover classes and other types of wetlands. However, multi-temporal imagery and ancillary information for certain parameter will improved

the wetland classification accuracy (Ozesmi and Bauer, 2002). Many classification techniques have been used to map vegetation land cover across around the world from coarser to medium spatial resolution data. Common techniques for mapping involve unsupervised or supervised classification of the images for extraction of the various features.

It is often difficult to acknowledge the best classifier for image classification due to lack of selection guidelines and the availability of suitable classification algorithm for each band. Therefore, researchers have conducted some practice and comparison to improve classification accuracy. Most of them has suggested supervised, semi-supervised and unsupervised among the three popular techniques for remote sensing image classification, such as, maximum-likelihood classifiers, neural networks and neuro-fuzzy models (Melgani et al., 2002; Bardossy et al, 2002; Bruzzone et al, 2002). Maximum likelihood is the most common supervised classification method. These method evaluating a known class of distributions while the unclassified pixels are assigned membership based on the probability of that pixel occurring within each category's probability density function (Hagner and Reese, 2007).

2.Material and method

2.1 Study Area

Pahang state lies between 3.8126ºN and 103.3256º E and is the largest state in Peninsula Malaysia an area of 35,840km^2. More than half of this state occupy with densely forest area. It is divided into freshwater, lowlands and highlands rainforest and coastline. Peat swamp forest in Southeast Pahang is the largest and undisturbed. The forest is highly diverse with mixed swamp forest on the eastern side and deep peat in the center are interspersed with dry land hills and slow-flowing rivers. The highlands are covered with tropical rainforest. Although most of the region is dense forest, its central plains are intersected by important riverine systems such Bera and Chini lakes. The lake environment surrounded by dry lowland dipterocarp forests that connected to peat swamp forest. The study area facing humid tropical climate with two monsoon seasons. It is warm and humid throughout the year with temperature range from 21°C to 32°C. Annual mean rainfall intensity received is at 2170mm.
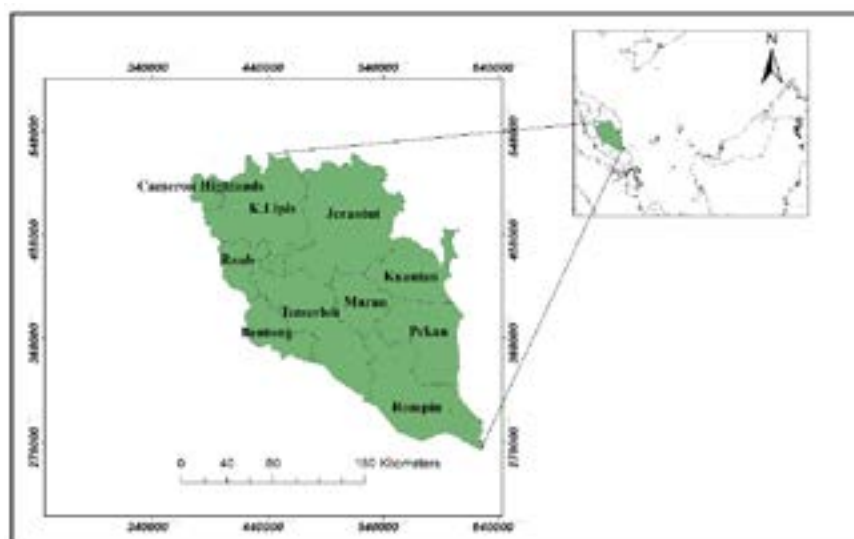
Figure 1: Location of Study area

2.2 Data Acquisition and Processing

Moderate resolution of Landsat 5 TM images were freely downloaded from USGS Global Visualization viewer (http://glovis.usgs.gov). The selected image was filter by less than 20% of cloud cover to get better accuracy. All the datasets went through Image enhancement by image georectification and atmospheric correction. Then, layer stack were used to combine all the different bands. The satellite consisting of 7 bands including visible, near-infrared and thermal band. Landsat 5 TM has spatial resolution of 30×30 m for each band except 120×120 m for band 6. In this study, thermal band are being neglected. A shapefile of the study area was then overlaid on each image as the area of interest (AOI) and a subset obtained. Topographical map of study area where used to established ground control points (GCP) that links many features on the satellite images to true location of corresponding features on the Earth's surface based on local mapping coordinate system and World Geodetic System (WGS-84) as the datum.

Seven classes were developed in this study namely wetland, water, urban/settlement, oil palm, paddy, rubber, and forest area. Supervised classification using the Maximum likelihood Classification algorithm was used to classify the images, after generate the spectral signature of each classes. Land use land cover topographic map obtained from Department of Environment (DOE) were used for training and evaluation the map accuracy. Envi 5.3 and ArcGis software were used during the process. A confusion matrix was applied to the classified image for each year. A confusion matrix was used to evaluate the overall accuracy, kappa coefficient, user's and the producer's accuracy. The overall accuracy represents the percentage of correctly classified pixels by divide the number of correct observation and actual observation. At Final stage, change detection were calculated based on image differencing method. Digital number in the resultant different image assume to be normally distributed where pixel with less changes are observed based on mean. The changes detected by subtraction of pixel between two co-registered datasets to see the changes of the area.

3. Result and Discussion

The maximum likelihood supervised classification technique produces reliable result, above 79% accuracy during the assessment. The result of confusion matrix, overall accuracy and kappa coefficient were shown in table 1. Figure 2 illustrates the visual changes. Table 2 shows the change detection from 2000, 2008 and 2015. Based on the changes, wetland area has decrease from 2000 to 2008 until 3384.85km^2. Wetland possess big changes during this phase. However, for the second phase, wetland hectarage has increase dramatically even facing the small class changes. The increment might be from other type of land converted to develop new wetland area. This is might be as a consequences of climate change issue which tend to rise up the global temperature around the world.

Table 1: Confusion matrix, overall accuracy and kappa coefficient

Class	2000		2008		2015	
	Prod. Acc. (%)	User Acc. (%)	Prod. Acc. (%)	User Acc. (%)	Prod. Acc. (%)	User Acc. (%)
wetland	44.42	82.23	96.90	65.19	63.14	39.61
water	96.51	96.12	95.45	83.80	98.68	65.69
urban	97.72	97.80	87.43	95.47	95.02	85.42

oil palm	94.87	91.30	81.21	69.81	90.88	93.34
paddy	83.98	96.52	55.68	76.56	65.07	72.65
rubber	89.85	93.51	64.29	65.58	85.00	64.77
forest	96.60	87.65	77.86	90.40	85.50	97.06
Overall Accuracy (%)	90.60		79.15		85.20	
Kappa Coefficient	0.8739		0.7295		0.7916	
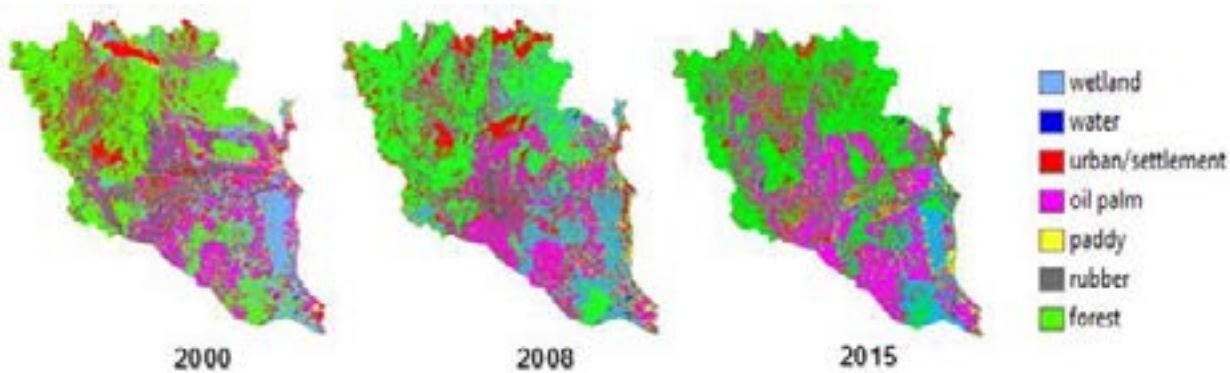
Figure 2: Land cover classification using maximum likelihood classification method

Table 2: Change detection a) from 2000 to 2008 b) from 2008 to 2015

changes area(km2):2000 to 2008

	wetland	water	urban	oil palm	paddy	rubber	forest	Row Total	Class Total
nclassified	13.99	0.4	25.28	8.34	1.99	6.88	30.5	87.39	47728.
etland	1850.1	24.48	157.62	224.61	167.71	268.66	572.9	3266.07	3273.
ater	23.49	67.18	19.47	13.37	11.86	10.61	42.63	188.6	195.
ban	396.47	50.77	678.15	359.14	134.69	320.77	1056.48	2996.48	3016.
l palm	493.34	21.33	697.46	3406.39	371.8	1918.91	1576.12	8485.36	8489.
ddy	338.24	18.3	207.94	280.43	190.75	275.3	336.82	1647.78	1657.
bber	646.93	17.63	357.41	851.05	254.87	925.65	848.28	3901.84	3908.
rest	2895.87	74.99	2046.52	966.35	251.26	771.96	8420.31	15427.26	15472
ass Total	6658.43	275.08	4189.86	6109.68	1384.94	4498.74	12884.05	0	
ass Changes	4808.33	207.9	3511.71	2703.29	1194.19	3573.09	4463.74	0	
age fference	-3384.85	-79.72	-1173.23	2380.23	272.21	-589.9	2588.05	0	

changes area(km2):2008 to 2015

	wetland	water	urban	oil palm	paddy	rubber	forest	Row Total	Class Total
nclassified	5.79	5.39	10.79	1.53	13.59	1.28	6.96	45.33	47723.
etland	669.82	154.97	295.41	802.91	328.33	233.82	4172.21	6657.46	6658.
ater	17.01	71.38	20.9	25.69	36.88	26.57	76.45	274.87	275.

ban	134.61	159.46	658.55	646.64	371.28	433.94	1784.06	4188.54	4189.
l palm	155.72	107.54	272.52	2712.15	393.25	1358.16	1109.75	6109.1	6109.
ddy	91.7	38.05	71.36	265.11	236.63	252.78	429.13	1384.76	1384.
bber	104.23	143.22	270.31	1271.43	363.18	1380.6	965.28	4498.25	4498.
rest	266.36	418.89	1190.19	2082.23	654.58	863.73	7405.8	12881.77	12884.
ass Total	**1445.24**	**1098.89**	**2790.03**	**7807.7**	**2397.72**	**4550.88**	**15949.64**	**0**	
ass Changes	**775.42**	**1027.51**	**2131.48**	**5095.54**	**2161.09**	**3170.28**	**8543.84**	**0**	
iage									
fference	**5213.19**	**-823.81**	**1399.84**	**-1698.01**	**-1012.79**	**-52.14**	**-3065.59**	**0**	

Pahang facing important economic growth with main activities in services, agricultural sector and manufacturing. As part of East Coast economic region, this state become the main region for manufacturing sector. The largest settlements in Pahang located in Kuantan and Pekan. Rubber plantation are widely farmed along the Pahang river and the major roads. Paddy also extensively farmed along the coastal river. The highly demand for herbal products in Malaysia has urge Pahang interrupt the natural sources by harvesting the natural forest area to support raw material need. To support the agricultural demand, deforestation and clearing the wetland area were seriously occurred. The conversion activity may interrupt the surrounding agricultural plantation and eco-tourism area because the shrinkage of water quality due to existence of nutrients and heavy metals (Rendana et al., 2017).

The decision makers convince that wetlands ecosystem is invaluable and the total cost to sustain the wetland services may exceed the beneficial value (Schuyt et al., 2005). So that they decide to convert the area for monocultural agricultural and industrial activity. The most promising market is by the widespread the oil palm plantation area. The ecological factor of wetlands area suitable for oil palm growth rather than rubber plantation. The oil palm trees are easy handling, less human dependence and high market price compare to paddy cultivation which need labor-intensive and gives less market price. Oil palm planted in wetland areas brings greater output compare to other land type. Most of wetlands in Pahang have been reclaim for oil palm plantations by a legal project. The cultivation activity is registered with the District Office Agriculture Department where there is a comprehensive list of proposals (Olorunfemi et al., 2017). In spite of active land conversion activity, rapid industrialization and rising population, this state provides the systems for protected and managed areas of natural resources. There are some 74 forest reserves, including 10 spot of undisturbed forest reserves and 13 amenity forests, wildlife reserves, parks and marine parks. Depletion of natural sources is happening at an alarming rate and without proper action these materials will be lost.

4.Conclusion

Remote sensing and GIS technique provides more reliable and cost-effective data quantification as compared to other conventional surveying methods. Assessment of wetland area has successfully observed using multiple band of Landsat 5 TM. Seven classes has been identified using maximum likelihood supervised classification method shown high accuracy. Wetland area facing reclamation activity in order to support agricultural based industry especially oil palm

plantation. The use of multi-temporal imagery and ancillary data will improve the result of wetland classification.

Acknowledgements

References

Bardossy A, Samaniego L. Fuzzy rule-based classification of remotely sensed imagery. IEEE Trans Geosci Remote Sens 2002;40(2):362–74.

Bruzzone L, Cossu R. A multiple-cascade-classifier system for a robust and partially unsupervised updating of land-cover maps. IEEE Trans Geosci Remote Sens 2002;40(9):1984–96.

Clean Malaysia. "Malaysia's Wetlands: The Silent Crisis." November 28, 2015. Accessed November 17, 2016. http://cleanmalaysia.com/2015/11/28/malaysias-wetlands-thesilent-crisis/

Congalton R.A., Review of assessing the accuracy of classifications of remotely sensed data, Remote Sens. Environ 1991, 37, 35–46.

Gurgel H.C., Ferreira N.J., Annual and international variability of NDVI in Brazil and its connections with climate, International Journal of Remote Sensing 2003, 24, 3595–3609.

Hagner O., Reese, H. (2007). A method for calibrated maximum likelihood classification of forest types, Remote Sensing of Environment 110 (4) (2007) 438–444.

J.N. Nilsson (1965).Learning Machines Foundations of Trainable Pattern-Classifying Systems, in: McGraw-Hill Series in Systems Science, McGraw-Hill Book Company, New York, 1965.

Lawrence, P.J., Chase, T.N., (2010). Investigating the climate impacts of global land cover change in the community climate system model. Int. J. Climatol. 30, 2066–2087.

Melgani F, Serpico SB. A statistical approach to the fusion of spectral and spatiotemporal contextual information for the classification of remote-sensing images. Pattern Recognit Lett 2002;23(9):1053–61.

Mohd, Kher Hussein and Noorzan Mohamed. (2007) "Wetland Landscape Conservation and Ecotourism in Malaysia. Pertanika Journal of Social Science and Humanities 5 (2) (2007): 159-168.

Olorunfemi. F. (2017). The Drivers Of Wetland Use in Temerloh District, Pahang,Malaysia. Malaysia Sustainable Cities Program, Working Paper Series 2

Ozesmi S. L., Baueri M. E (2002). Satellite Remote sensing of wetlands.Wetland Ecology and Management 10: 381-402.

Rendana M, Rahim S. A., Idris. W. M.R, Lihan. T. (2017). Soil Erosion Assessment in Tasik Chini Catchment using Remote Sensing and GIS Techniques. Sains Malaysiana 46(4): 529–535 ://dx.doi.org/10.17576/jsm-2017-4604-03

Schuyt, D.K. "Economic Consequences of Wetland Degradation for Local Population in Africa." Ecological Economics 53 (2005): 177–190.

Vliet V., Bregt J., Hagen-Zanker A., Revisiting Kappa to account for change in the accuracy assessment of land-use change models, Ecological Modelling 2011, 222, 1367–1375.

Xie, Y., Sha, Z., & Yu, M. (2008). Remote sensing imagery in vegetation mapping: A review. Journal of Plant Ecology, 1(1), 9–23. doi:10.1093/jpe/rtm005

PRELIMINARY ORBIT DESIGN AND SIMULATION FOR THE FIRST SMALL SATELLITE REMOTE SENSING CONSTELLATION MISSION OF TAIWAN

Chuang-Wei Hsueh (1), Feng-Tai Hwang (1),

[1] National Space Organization, 8F, 9, Prosperity 1st Road, Hsinchu Science Park, Hsinchu City, Taiwan, R.O.C.

Email: chuangwei@narlabs.org.tw; fthwang@narlabs.org.tw

KEY WORDS: NSPO, LEO, STK, SSO, LOP

Abstract: After the successful launch of FORMOSAT-5 on August 25, 2017, National Space Organization (NSPO) focuses on the first self-reliant small satellite remote sensing constellation mission of Taiwan. The paper presents the preliminary orbit design and simulation for the satellite constellation mission, and the main objective of this paper is to provide the feasibility study on different conditional parameters to increase the temporal resolution of overall constellation system. The mission orbit is a sun-synchronous orbit (SSO) of 561 km altitude with repeating ground tracks every day. Depending on the design for different number of satellites in constellation, the mission could reach the goal of the global coverage with a 45 degree field of regard (FOR) and have the capability of revisiting Taiwan area many times per day. Some different scenarios are proposed in this paper. For each scenario, the orbit of satellite constellation is performed and analyzed by AGI's Systems Tool Kit (STK). Finally, comparisons of the advantages and disadvantages for each circumstance will be described in detail.

1. INTRODUCTION

FORMOSAT-5, operating in a SSO of 720 km altitude, is Taiwan's first space program that NSPO takes full responsibility for the complete satellite system design, manufacturing, assembly, integration and test. After the successful launch of FORMOSAT-5 on August 25, 2017, NSPO focuses on the first self-reliant small satellite remote sensing constellation mission of Taiwan. The remote sensing constellation mission is scheduled to take place during the third-phase space program of Taiwan, and the mission orbit is defined by a SSO of 561 km altitude with repeating ground tracks every day. The actual numbers of satellites and orbit planes are critically based on the government's funding and NSPO's long term planning in the future. In order to reach the goal of global coverage and increase the temporal resolution for specific regions at specific times (e.g., revisiting Taiwan area five times per day). This paper proposes five preliminary constellation designs with three to six satellites on three orbit planes at the current stage.

The remainder of this paper is structured as follows. Section 2 presents some related theories for preliminary orbit design. Section 3 describes five scenarios of preliminary constellation design with comparisons of their advantages and disadvantages. Finally, Section 4 provides some conclusions.

2. RELATED THEORY FOR PRELIMINARY ORBIT DESIGN

2.1 Sun-Synchronous Orbit (SSO)

The rate of change of right ascension of the ascending node (RAAN) Ω due to J_2 is

$$\dot{\Omega} = -\frac{3}{2(1-e^2)^2}J_2 n \left(\frac{R_\oplus}{a}\right)^2 \cos i \quad, \tag{1}$$

where n is mean motion, $R_\oplus$ is Earth's equatorial radius, a is semimajor axis, e is eccentricity, i is inclination angle, and J_2 is the second-order zonal harmonic of Earth's gravitational field.

The mean motion is determined by the semimajor axis of the orbit, and can be expressed as

$$n = \sqrt{\frac{\mu}{a^3}} \quad, \tag{2}$$

where μ is the gravitational parameter of Earth.

For a circular sun-synchronous orbit($e \approx 0$), the nodal precession rate of the satellite orbit is

$$\dot{\Omega} = -\frac{3}{2}J_2 n \left(\frac{R_\oplus}{a}\right)^2 \cos i \approx 0.9856 \quad. \tag{3}$$

The rate of nodal regression for SSO is a function of inclination and altitude. Moreover, a sun-synchronous satellite passes over any given latitude at almost the same local mean time.

2.2 Repeating Ground-Track Orbit

For a repeating ground-track orbit, the period of repetition T_r is

$$T_r = NT_\Omega = DT_G \quad, \tag{4}$$

where N is the number of revolutions along the orbit in one period of repetition, D is the number of sidereal days Earth completes during the period of repetition, and T_Ω is the nodal period, defined as the time interval elapsed between successive passages of a satellite through consecutive ascending nodes (Michel Capderou, 2006; Sharon D. Vtipil1 and Brett Newman, 2010). It means that a ground track will be repeated after the satellite completes N revolutions over D days.

The nodal period of Greenwich T_G is

$$T_G = \frac{2\pi}{\omega_\oplus - \dot{\Omega}} \quad , \tag{5}$$

where $\omega_\oplus$ is Earth's rotation rate.

Substituting Eq. (3) into Eq. (5), if there exit two coprime integers, N and D, with

$$\frac{N}{D} = \frac{1440}{T_\Omega} \quad , \tag{6}$$

then the orbit will satisfy both sun-synchronous and repeating ground-track properties.

The ground shift λ_S can be defined as

$$\lambda_S = T_\Omega \left(\omega_\oplus - \dot{\Omega} \right) R_\oplus = \frac{2\pi R_\oplus}{\left(\frac{N}{D}\right)} \quad , \tag{7}$$

which is the difference between successive passages of a satellite through consecutive ascending nodes. The difference between the consecutive ascending nodes in the period of repetition is

$$\triangle \lambda = \frac{\lambda_S}{D} \quad . \tag{8}$$

Let d be the FOR width at equatorial for a satellite. If $d > \triangle \lambda$, then the satellite can reach the goal of global coverage in the period of repetition. (Chuang-Wei Hsueh, Feng-Tai Hwang, 2013)

Based on the orbital equations mentioned, a single satellite in a SSO of 561 km altitude with a FOR of ±45º cannot achieve global coverage, and the related parameters for the satellite are listed in Table 1.

Table 1: The related orbital parameters

D	N	a (km)	i (deg)	d (km)	λ_S (km)	$\triangle \lambda$ (km)	Global Coverage
1	15	6939.13	97.64	1178.03	2671.67	2671.67	No

2.3 Perturbations from Atmospheric Drag

The equation for acceleration due to drag on a satellite can be defined as

$$a_D = -\frac{1}{2}\rho \left(\frac{C_D A}{m}\right) V_r^2 \quad , \tag{9}$$

where ρ is atmospheric density, A stands for the cross-sectional area of the satellite, m represents the mass of the satellite, V_r is the velocity of the satellite with respect to the atmosphere, and C_D is the drag coefficient.

2.4   Perturbations from Third-body Attractions

The equation for the secular change in inclination of sun-synchronous orbit is

$$\frac{di}{dt} = \frac{3}{8}\left(\frac{n_{\odot}^2}{n}\right)\left(\frac{a_{\odot}}{r_{\odot}}\right)^3 \sin i \left(1 + \cos i_{\odot} - \frac{\sin^2 i_{\odot}}{2}\right) \sin 2(\Omega - \alpha_{\odot}) \ , \tag{10}$$

where $n_{\odot}$ is the mean motion of the sun, $\frac{a_{\odot}}{r_{\odot}}$ is the ratio of the semimajor axis to the radius of the orbit of the sun, $i_{\odot}$ represents the obliquity of the ecliptic, and $\alpha_{\odot}$ is the right ascension of the mean sun. (Chia-Chun Chao, 2005)

Based on the equation mentioned above, the rate of change in inclination is shown in Figure 1. The maximum rates occur at local times of 3, 9, 15, and 21 hours, while the minimum rates occur at 0, 6, 12, and 18 hours.

3   CASE STUDIES AND SIMULATED RESULTS

There are no absolute rules to design a perfect constellation. Satellites randomly deployed in low Earth orbit (LEO) may reduce the overall constellation performance for a remote sensing mission. The goal of designing a suitable orbit for the satellite constellation mission is to increase the temporal resolution of constellation system, especially for Taiwan area. In order to assess advantages and disadvantages for different constellation designs, five different scenarios are proposed and discussed. To begin with, some constraints/conditions for constellation designs are described below:

(1) All satellites will be operated in circle SSOs with altitude of 561 km and daily repeating ground tracks.
(2) All satellites have the same semimajor axis (6939.13 km), eccentricity (zero), inclination (97.64 deg), and specifications except the geometry position of each satellite deployed in the constellation.
(3) Each satellite is box-shaped with dimension of 1200x1200x1250 (mm^3) and a wet mass of about 300 kg, as shown in Figure 2.
(4) The long-term orbit predictor (LOP) provided by STK is used for orbit decay prediction on the inclination and the semimajor axis. The orbit epoch starts from 1 Jan 2021 00:00:00.000 UTCG, and the simulation duration is one year.
(5) The Chung-li station (25º N, 121.3º E) is used for counting the number of revisits per day if the Chung-li station is within the satellite FOR of ±45º during daylight hours.

Scenario 1: The three satellites of the constellation will be operated on three different orbit planes, and the Local Time of Descending Nodes (LTDN) of these planes are 10:00 A.M. (green line), 11:00 A.M. (yellow line), and 01:00 P.M. (red line), respectively, as shown in Figure 3. Each satellite will be deployed with proper orbit phase to keep the three satellites having the same ground tracks. The initial orbital elements are listed in Table 2, and the ground track and coverage area of Scenario 1 are shown in Figure 4.

Scenario 2: Similar to Scenario 1, Scenario 2 deploys each satellite with proper orbit phase to keep the three satellites having the property of global coverage, as shown in Figure 5. The initial orbital elements are listed in Table 3.

Scenario 3: Similar to Scenario 1, Scenario 3 deploys each satellite with proper orbit phase to keep the three satellites having the property of revisiting Taiwan area three times per day by using different ground tracks, as shown in Figure 6. The initial orbital elements are listed in Table 4.

Scenario 4: Similar to Scenario 3, Scenario 4 adds another satellite in the orbit plane with LTDN 10:00 A.M. to keep the four satellites having the two properties of global coverage and revisiting Taiwan area three times per day, as shown in Figure 7. The initial orbital elements are listed in Table 5.

Scenario 5: Combining Scenario 1 and Scenario 4 keeps six satellites not only having the two properties of both global coverage and revisiting Taiwan area three times per day, but also enhancing the number of revisit times of Taiwan area from three to five times per day, as shown in Figure 8. The initial orbital elements are listed in Table 6. From Scenarios 5, the behaviour of secular change in altitude is almost the same for each satellite, as shown in Figure 9. That means the constellation geometry can be preserved without additional orbit maintenance, which fact can reduce the fuel usage and thereby extend the lifetime of the satellites. Otherwise, the behaviours of secular changes in inclination are different due to the different RAANs of the satellites, as shown in Figure 10. It is important to notice that although the rate of inclination change is small, the accumulated deviation in RAAN will be significant in a few years, and the local mean time will no longer satisfy the mission requirement. (Chia-Chun Chao, 2005)

The comparisons of advantages and disadvantages of the five scenarios are listed in Table 7.

Table 2: The orbital elements of Scenario 1

Parameter	Sat 1 (LTDN 10 A.M.)	Sat 1 (LTDN 11 A.M.)	Sat 1 (LTDN 1 P.M.)
RAAN (deg)	70.865	85.865	115.865
Arg of Perigee (deg)	0	0	0
True Anomaly (deg)	29.374	164.374	74.374

Table 3: The orbital elements of Scenario 2

Parameter	Sat 1 (LTDN 10 A.M.)	Sat 2 (LTDN 11 A.M.)	Sat 2 (LTDN 1 P.M.)

RAAN (deg)	70.865	85.865	115.865
Arg of Perigee (deg)	0	0	0
True Anomaly (deg)	29.374	284.374	314.374

Table 4: The orbital elements of Scenario 3

Parameter	Sat 1 (LTDN 10 A.M.)	Sat 3 (LTDN 11 A.M.)	Sat 3 (LTDN 1 P.M.)
RAAN (deg)	70.865	85.865	115.865
Arg of Perigee (deg)	0	0	0
True Anomaly (deg)	29.374	214.374	24.374

Table 5: The orbital elements of Scenario 4

Parameter	Sat 1 LTDN 10 A.M.	Sat 2 LTDN 10 A.M.	Sat 3 LTDN 11 A.M.	Sat 3 LTDN 1 P.M.
RAAN (deg)	70.865	70.865	85.865	115.865
Arg of Perigee (deg)	0	0	0	0
True Anomaly (deg)	29.374	209.374	214.374	24.374

Table 6: The orbital elements of Scenario 5

Parameter	Sat 1 LTDN 10 A.M.	Sat 2 LTDN 10 A.M.	Sat 1 LTDN 11 A.M.	Sat 3 LTDN 11 A.M.	Sat 1 LTDN 1 P.M.	Sat 3 LTDN 1 P.M.
RAAN (deg)	70.865	70.865	85.865	85.865	115.865	115.865
Arg of Perigee (deg)	0	0	0	0	0	0
True Anomaly (deg)	29.374	209.374	164.374	214.374	74.374	24.374

Table 7: Comparisons of the five scenarios

Scenario	Advantages	Disadvantages	Global Coverage	The number of revisiting Taiwan area per day	The number of satellites
1	It has three imaging opportunities per day for the Chung-li station.	It cannot attain the goal of global coverage.	No	3	3
2	It can reach the goals of global coverage and daily revisit for the Chung-li station.	It has least imaging times.	Yes	1	3
3	It has three imaging opportunities per day for the Chung-li station, and the imaging area is greater than the scenario 1.	It cannot attain the goal of global coverage.	No	3	3
4	It can reach the goal of global coverage. If a satellite of LTDN 10:00 fails, it has the capability	The cost to build up the Scenario 4 is more expensive than the previous three	Yes	3	4

	of rephrasing the rest satellite to meet the constellation of Scenario 3.	scenarios.			
5	It can reach the goal of global coverage with the highest temporal resolution for Taiwan area.	The cost to build up Scenario 5 is the most expensive.	Yes	5	6

4   CONCLUSIONS

The paper presented the preliminary orbit design as well as simulation for the first small satellite remote sensing constellation mission of Taiwan, and provides the feasibility study on different conditional parameters to increase the temporal resolution of overall constellation system. The paper described the comparisons of advantages and disadvantages for the five different scenarios based on the STK simulations in the end.

5   REFERENCES

[1]   Chia-Chun Chao, 2005. Applied orbit perturbation and maintenance, Aerospace Press.
[2]   Chuang-Wei Hsueh, Feng-Tai Hwang, 2013. Preliminary constellation design of Taiwan remote sensing satellites, 2013 AASRC Conference.
[3]   Michel Capderou, 2006. Satellites: Orbits and Missions, translated from French by Stephen Lyle, Springer.
[4]   NSPO, 2017. Program Description from
http://www.nspo.narl.org.tw/tw2015/projects/FORMOSAT-5/status.html
[5]   Sharon D. Vtipil1 and Brett Newman, 2010. Determining an Efficient Repeat Ground Track Method for Earth Observation Satellites: For Use in. Optimization Algorithms, 2010 AIAA/AAS Astrodynamics Specialist Conference.
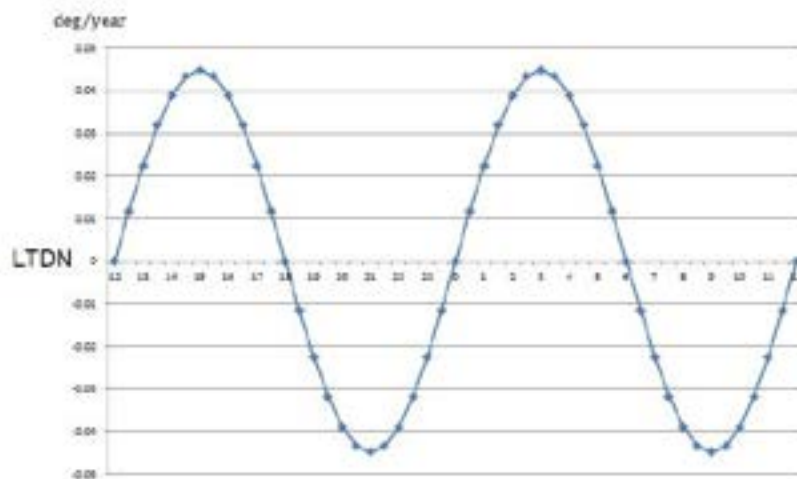
Figure 1: Inclination change rate

Figure 2: The preliminary satellite configuration
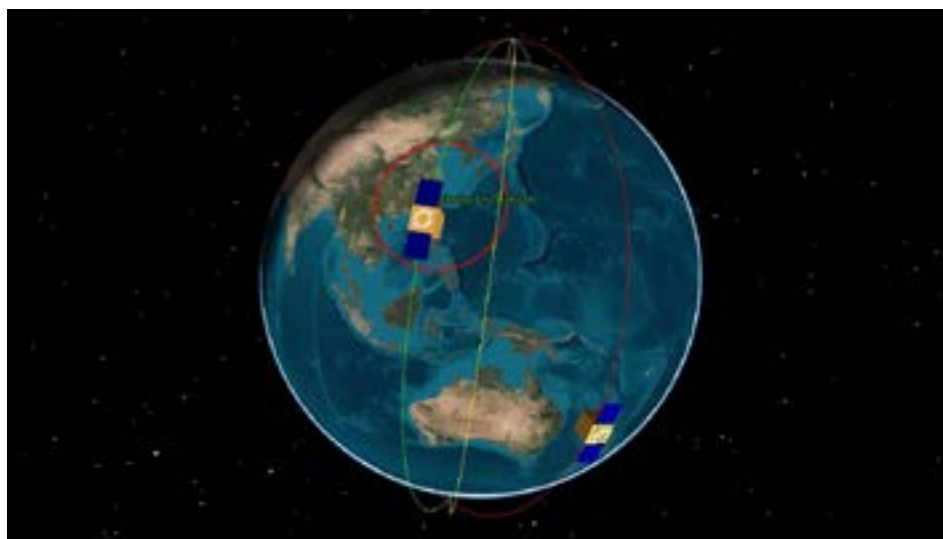
Figure 3: The constellation of Scenario 1
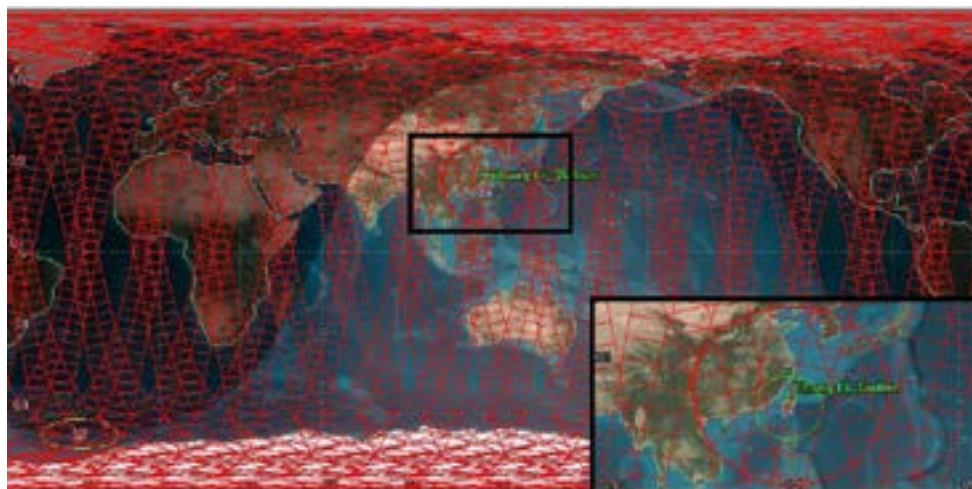
Figure 4: The ground track and coverage area of Scenario 1
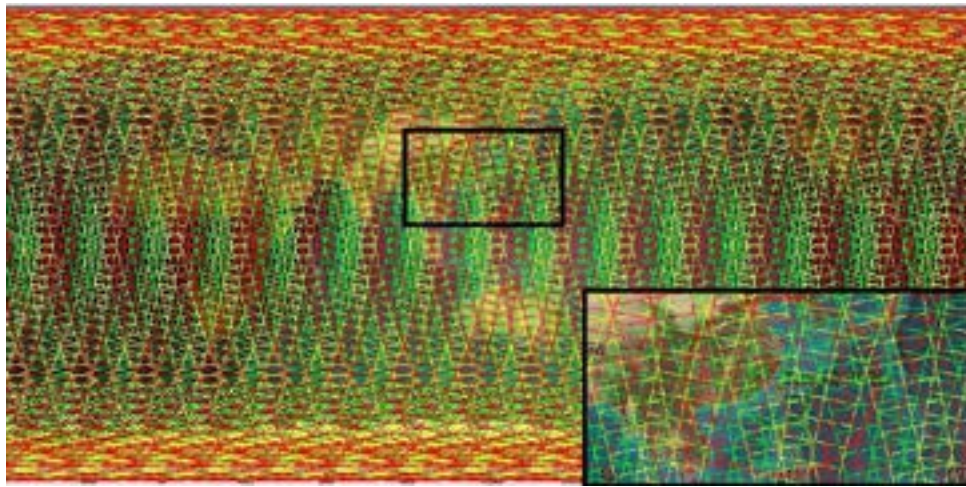
Figure 5: The ground track and coverage area of Scenario 2
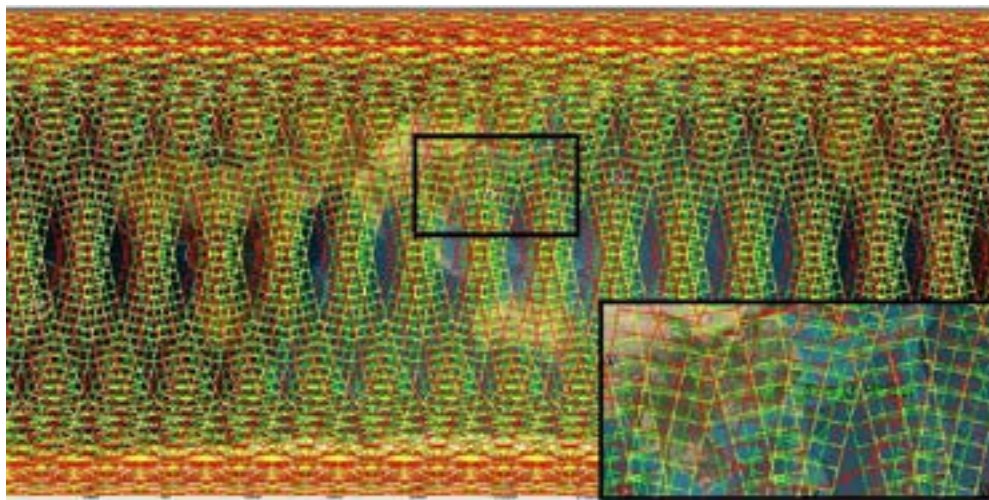
Figure 6: The ground track and coverage area of Scenario 3
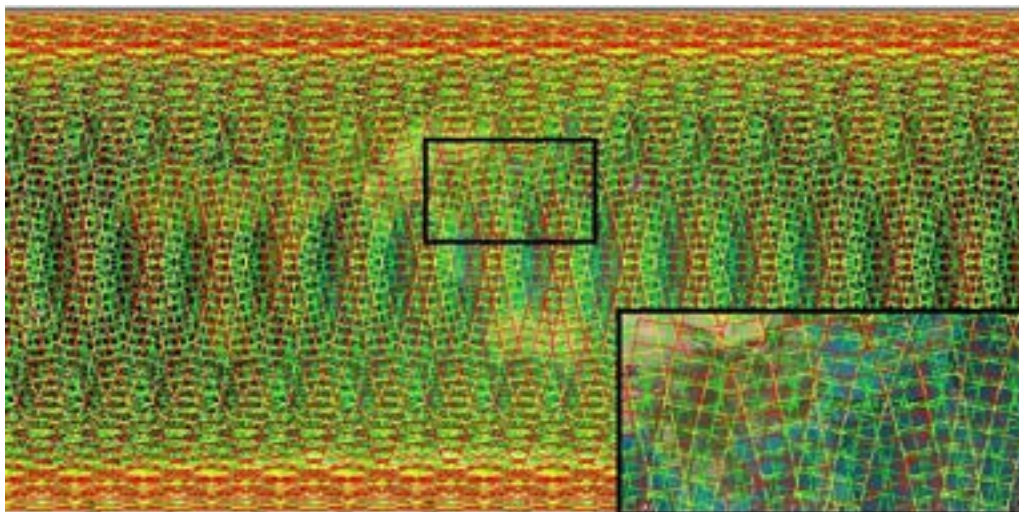
Figure 7: The ground track and coverage area of scenario 4
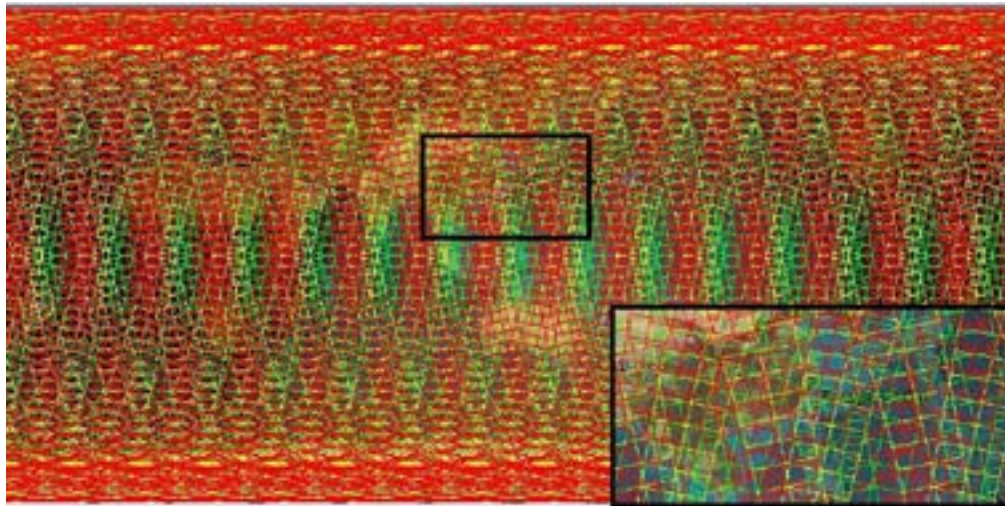
Figure 8: The ground track and coverage area of Scenario 5
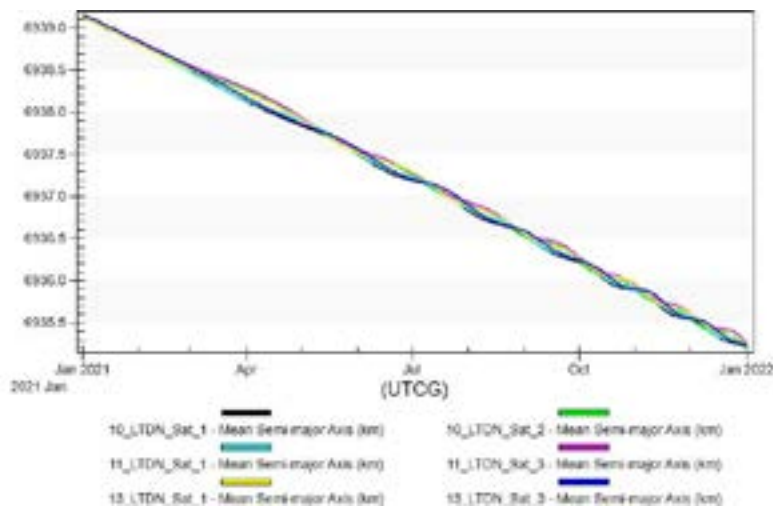
Figure 9: One-year altitude histories of the six satellites of Scenario 5 without orbit maintenance.
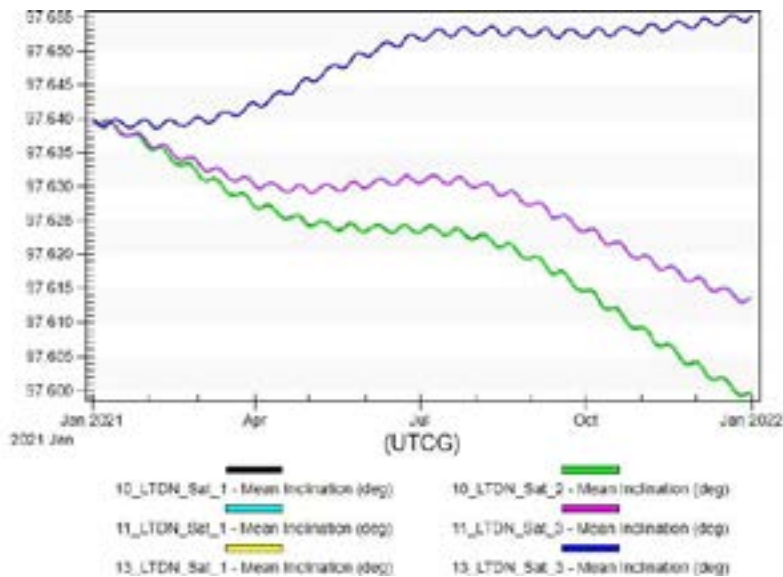
Figure 10: One-year inclination histories of the six satellites of Scenario 5 without orbit maintenance.

3049

THE GUIDANCE SEEKER ONBOARD ROMOTE SENSING SATELLITE TO ENHANCE MISSION EFFECTIVENESS

Pei-Hsuan Wu, Jer Ling and Po-Yen Huang

National Space Organization (NSPO), Hsin-Chu, Taiwan, 30078

Email: phyllis@nspo.narl.org.tw ; jl@nspo.narl.org.tw ; mikehuang@nspo.narl.org.tw

KEY WORDS: AI Target-Seeking, Seeker, Machine Learning, Fine-tuned

ABSTRACT

Nowadays, the swath has trend to get smaller with the development of high-resolution satellite for fixed number of pixels. So it is getting more important to capture clear target image efficiently. Otherwise, it might take several times to have a clear image if there is cloud between the remote sensing instrument (RSI) and target image. The objective of this paper is to develop an on-board guidance seeker on RSI. The on-board guidance seeker is used to get wide-angle images and detect target before the task target is captured. Based on wide-angle images and detected-target, the path of satellite can be fine turned to direct ground target without cloud blocking ground target to get clear image or to find target ships and so on. The on-board guidance seeker includes a wide-angle camera, an on-board machine learning unit and an on-board real time path fine-tuning unit. This kind of on-board AI-driven design can enhance the mission effectiveness. It also can be applied to rescue in the open sea.

1. INTRODUCTION

According to the experience on the RSI of FS2 and FS5, it depends on weather and cloud to get a clear image. If the weather is cloudy, the information is hard to get from the satellite imagery. If cloud blocks task target, we have to execute imagery task at next time while satellite passes through the ground target. The ground target imagery usually needs to take several times to complete the whole imagery. The times of image-captured is relative to the swath width. For example, it takes at least two times of image-capturing for the whole island of Taiwan by FS5 on a sun synchronous orbit of 720 km altitude. If the image is not clear, it needs to image the ground target again. For fixed number of pixels, the shorter swath width takes much more times to accomplish the entire ground target than the longer one. Therefore, it is important to capture the clear target image efficiently.

The consists of a wide-angle camera, an on-board unit which has the function of the machine learning and an on-board, real-time path fine-tuning unit. The wide-angle camera provides larger image to the unit to identify the object. Satellite computer defines fine-tuned angle, so that the on-board unit can fine tune path. Fine-tuned path enhances the mission effectiveness. The guidance seeker has two operation modes. One is the image task mode and the other is the target-searching mode, as shown in Fig. 1.

Fig. 1. Operation algorithm flow chart

2. METHODOLOGY

2.1 The time difference between seeker and payload capturing at the same position

The seeker gets information from the imagery and defines the path-corrected angle ΔT earlier than the payload images of ground target, as shown in Fig. 2. The time difference between seeker and payload capturing at the same position can be defined with a two-dimensional relation, as shown in Fig. 3. The time difference, ΔT, can be calculated using Eq. (1).

$$\Delta T = T_2 - T_1$$
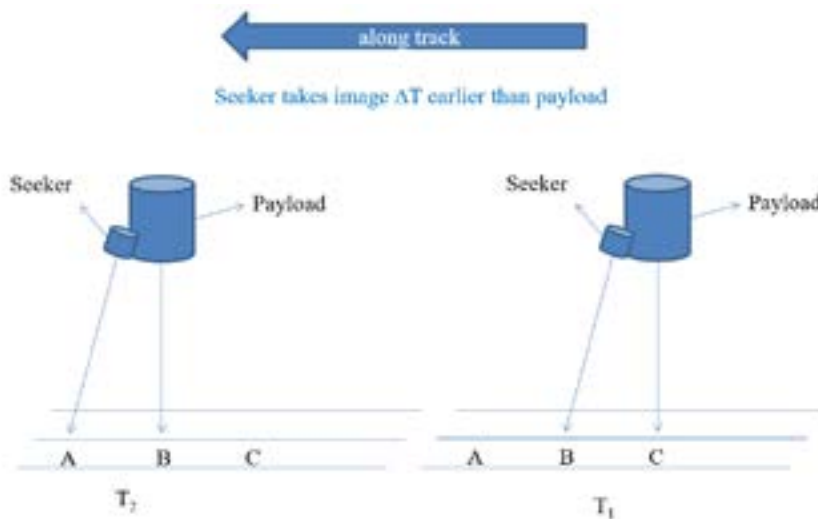
Fig. 2. The direction of flight and time difference

H : orbit height (km)
Θ : angle (°)
V_{sat} : satellite flight speed (km/sec)
ΔT : time difference (sec)

$H\tan\Theta / V_{sat} = \Delta T$
$V_{sat} : 7$
$\Delta T = H \tan \Theta / 7$
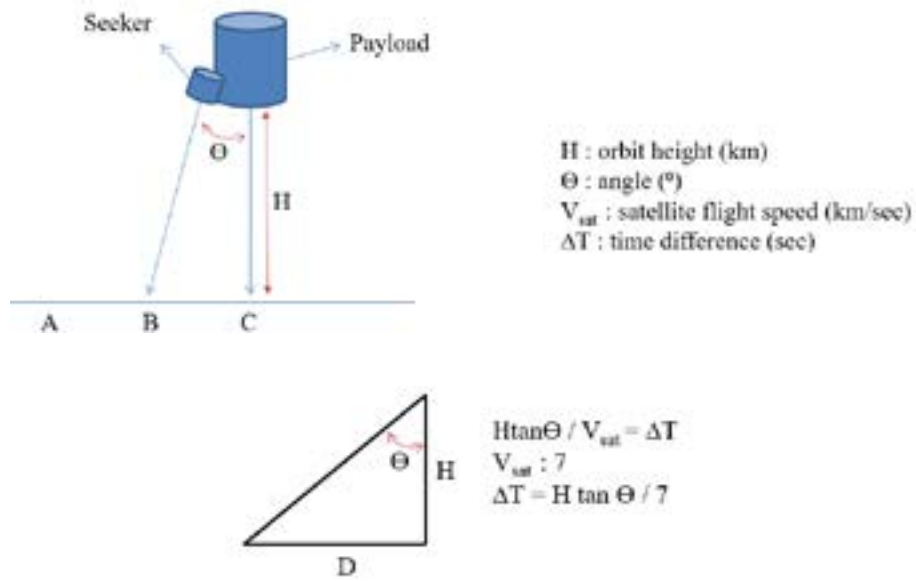
Fig. 3. The time difference between seeker and payload capturing at the same position

$\Delta T = H \tan \Theta / 7$ (sec)   (1)

2.2 Fine-tuned angle β and fine-tuned distance D

The guidance seeker captures images, and identifies the object like cloud and calculates the fine-tuned angle β in ΔT, where, β is the rotation angle in Y-axis direction. The β and fine-tuned distance D can be defined by the two-dimensional relation, as shown in Fig. 4. The β can be calculated by using Eq. (2).

H : orbit height (km)
β : fine-tuned angle (°)
D : fine-tuned distance (km)
$D = H \tan \beta$
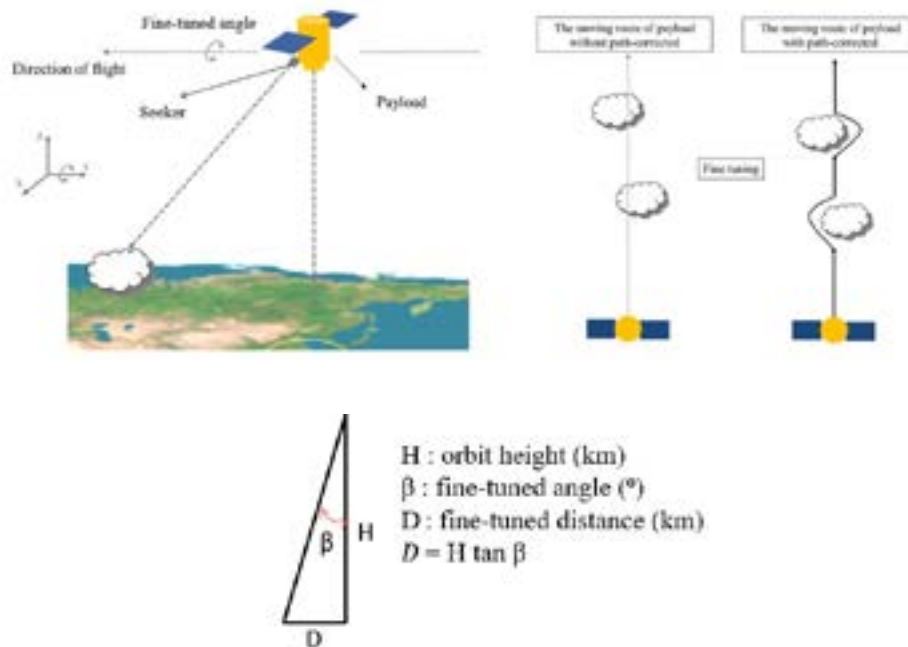
Fig. 4. Fine-tuned angle β and fine-turned distance D

$$\beta = \tan^{-1}(D/H) \ (^{\circ}) \tag{2}$$

2.3 The guidance seeker operation mode

The guidance seeker has two modes. One is the image task and the other is the target searching. Target searching mode can be applied to the rescue in the open sea. Image task (cloud detection) mode algorithm flow chart is shown as Fig. 5. Target seeking task (ship detection) mode algorithm flow chart is shown in the Fig 6.
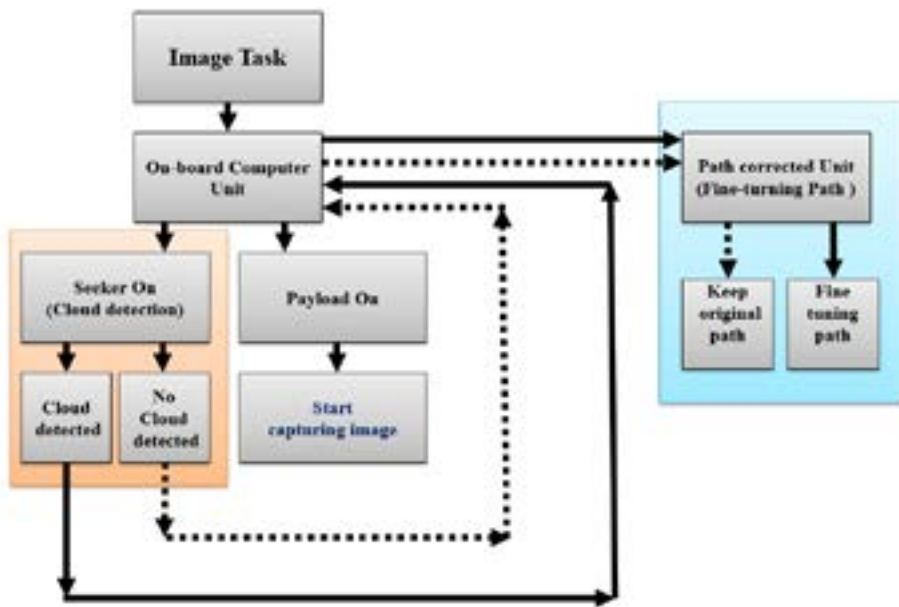
Fig. 5. Image task (cloud detection) algorithm flow chart
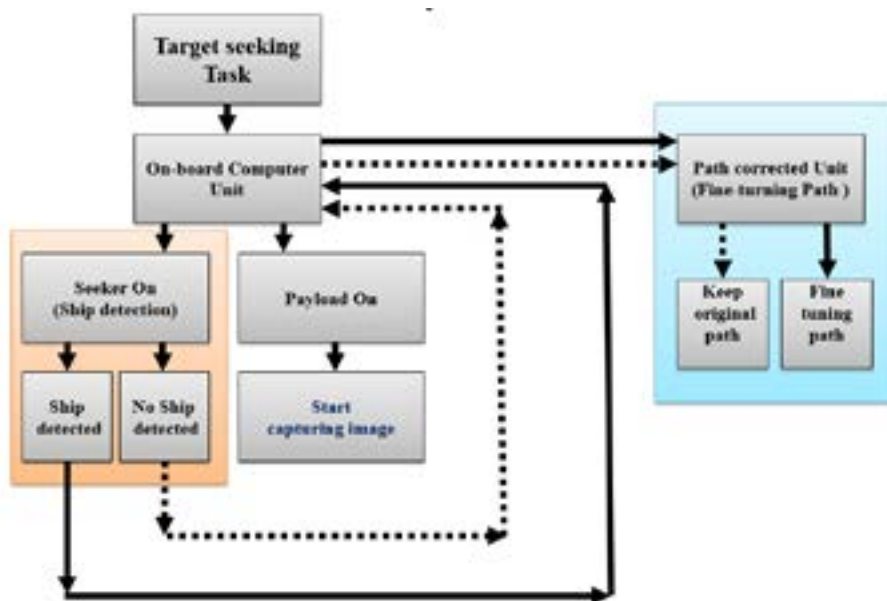
Fig. 6. Target seeking task algorithm flow chart (ship detection)

3   RESULT

3.1 The time difference between the seeker and payload capturing at the same position calculation

Using the Eq. (1) as defined in section 2.1 with the satellite design parameters to calculate time difference. The time difference is the response time for the seeker to define the fine-tuned angle β. The response time is corresponding to the satellite orbit. Table 1 shows the response time with a design angle Θ = 60º on the orbit of FS-2, FS-5 and height at 561 km .

Table 1. ΔT (sec)

Orbit Height (km)	561	720 (FS-5)	891 (FS-2)
ΔT (sec)	138	178	220

3.2 Fine-tuned angle β calculation

Using the Eq. (2) as defined in the section 2.2 with fine-tuned distance D to calculate fine-tuned angle β, as shown in Table 2. Where D is identified by machine-learning unit and calculated by satellite computer from the wide-angle image, as shown in Fig. 7.

Fine-tuning angle β
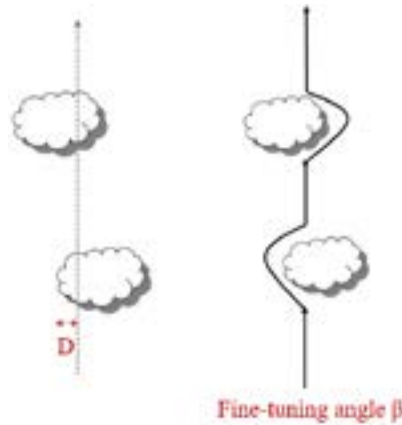
Fig. 7. Fine-tuned distance D and fine-tuned angle β

Table 2. Fine-tuned angle β calculation

D (km) (Cloud position)	β(º) Orbit Height 561 km	β(º) Orbit Height 720 km	β(º) Orbit Height 891 km
1	0.102	0.080	0.064
2	0.204	0.159	0.129
3	0.306	0.239	0.193
4	0.409	0.318	0.257
5	0.511	0.398	0.322

3.3 The guidance seeker operation mode flow

To carry out the image task, the algorithm will be switched to image task (cloud detection) algorithm as defined in section 2.3. The guidance seeker will detect cloud first to calculate fine-tuned angle β, as discussed in section 3.2. If no cloud is over the along-track, the payload will keep the original path to collect imagery. If cloud is over the along-track, according to image task (cloud detection) algorithm and fine-tuned angle β, the payload will be rotated to fine-tuned path with minimum cloud.

To execute target seeking task (ship detection), the algorithm will be switched to the target seeking task (ship detection) algorithm as defined in section 2.3. The following procedure is the same as image task.

4. CONCLUTION

Combining the wide-angle camera, machine learning function and imaging path fine-tuning function with satellite to decrease the amount of null satellite images is studied. This on-board AI-driven design is an innovation design that can obtain more available satellite images. The machine learning function is widely developed and used in commercial product. The advanced study is to combine the function with satellite in space. The goal of this design is able to minimize cloud on flight path. Changing cloud detection to ship detection by machine learning can be applied to rescue in the open sea. The high-resolution satellite in the future will have smaller swath tendency than the present one. Based on the imagery experience of FS-2 and FS-5, the on-board guidance seeker is a good application in the high-resolution satellite.

REFERENCE

[1] Tang, J., Deng, C., Huang, G. B., and Zhao, B., 2015. Compressed-domain ship detection on spaceborne optical image using deep neural network and extreme learning machine. IEEE Transactions on Geoscience and Remote Sensing, 53(3), pp. 1174-1185.

[2] Geng, F., and Zhu, X. P., 2007. The Research of Accuracy Guidance Weapon Infrared Imaging Seeker Control System [J]. Journal of Astronautics, 3, pp. 4.

[3] N. S. Keskar, D. Mudigere, J. Nocedal, M. Smelyanskiy and P. T. P. Tang, 2016, On Large-Batch Training for Deep Learning: Generalization Gap and Sharp Minima, technical Report, arXiv:1609.04836.

SHIP WATERLINE AND DISPLACEMENT TONNAGE MEASUREMENTS USING TERRESTRIAL LASER SCANNING DATA

Xiaojun Cheng (1), Zexin Yang (1), Jixing Zhang (2), Zhenlun Wu (1), Wang Guo (3), Xiaolong Cheng (4)

[1] College of Surveying and Geo-Informatics, Tongji University, No. 1239, Siping Road, Shanghai 200092, China

[2] SAIC General Motors Corporation, No. 1500, Shenjiang Road, Pudong New Area, Shanghai 201206, China

[3] Shanghai Huace Navigation Technology Ltd., No. 599, Gaojing Road, Shanghai 201702, China

[4] College of Architecture and Surveying and Mapping Engineering, Jiangxi University of Science and Technology, No.86, Hongqi Ave., Ganzhou 341000, China

Email: cxj@tongji.edu.cn; zexinyang@tongji.edu.cn; 15900522279@163.com; 1633313@tongji.edu.cn; wang_guo@huace.cn; 494322312@qq.com

KEYWORDS: Ship Waterline Generation; Ship Displacement Tonnage Calculation; TLS; Point Cloud

ABSTRACT: The problem of how to measure the waterlines and displacements of a ship is of great significance. The common methods are time-consuming, labor-intensive, expensive but imprecise. Therefore, the main objective of this paper is to measure the ship waterlines and displacements much faster and more accurate by using TLS (Terrestrial Laser Scanning) point cloud data. First, raw scans are acquired and automatically registered with the help of our custom-designed devices. After point cloud preprocessing, the ship hull data are sectioned into thin point cloud slices along the z-axis direction. For each point cloud slice, offsets are extracted by the 2D voxel grid method and ordered based on polar angles. The waterlines are then reconstructed using NURBS. The area of each slice, meanwhile, is calculated by the coordinate analytic method. Accordingly, the volume of every polyhedron formed from two neighbor waterlines is calculated. Finally, the displacement table can be acquired by accumulating the volume of every polyhedron. To evaluate the result of our proposed method, we calculate the difference between the experimental results and the results generated by the Geomagic Studio - a leading commercial software. The difference is generally slight which has proven that the proposed method is effective.

1. INTRODUCTION

Waterline (or load line), the line where the hull of a ship meets the surface of the water, and displacement tonnage (or displacement), the weight of a ship expressed in tons of water its hull displaces, are two vital parameters of a ship. However, the common workflows to measure these two parameters remain comparative labor-intensive, time-consuming, expensive but imprecise. In terms of the ship waterline measurement, usually a total station is used to measure offsets and then waterlines are reconstructed based on these observed points. As for ship displacement measurement, there are two common methods: the geometric measurement method and the capacity comparison method. The former method uses a total station to capture data points of the ship hull and then reconstruct the hull model for displacement calculation, but it is inefficient and imprecise due to the low data

density. In the latter method, water is poured into the ship and the weight of the water is calculated as the displacement at the same time. It is noticeable that the capacity comparison method is quite expensive, labor-intensive and impracticable for large ships.

The waterline and displacement measurements of ships should be performed in the shortest time with the lowest costs and highest precision. With the development of photogrammetric algorithms, recently there has been an increase in the popularity of maritime applications using photogrammetric techniques. Menna and Troisi (2007) integrated different photogrammetric software to model a small sailing boat's hull, while Tang et al. (2016) reconstructed the 3D hull model of a larger anchor handing tug (40m). Although most ship survey projects are carried out in dock or shipyards, Menna et al. (2011) proposed a method for modeling floating objects based on photogrammetry both terrestrial and underwater. In spite of the effectiveness of photogrammetry used for data acquisition, the surveyed object has to be not uniformly painted. Unfortunately, usually there is not enough texture on hulls. Hence, for adequate accuracy, a large number of Ringed Automatically Detected (RAD) targets needed to be temporarily and evenly attached to the hull body, with a gap between each target of approximately 0.5 m for complex hull surface (bow and stern) and approximately 1 m for simpler ship's body surface (Menna & Troisi, 2007).

To avoid this cumbersome process, Terrestrial Laser Scanning (TLS), an active technique provided high-resolution spatial data, has been used for ship measurement (Abbas et al., 2017; Jawor et al., 2012; Paoli & Razionale, 2012; Wujanz et al., 2013). Additionally, some research which focused on the integration of TLS with close range photogrammetry for ship model generation and maritime heritage recording was carried out (Menna and Nocerino, 2014; Menna et al., 2011; Wujanz et al., 2013). At the moment TLS is not as widely used in marine applications as it should be, especially waterline and displacement measurement. Biskup et al. (2007) calculated the volume of the underbody of a boat based on a waterline, but the waterline is marked with artificial targets which make it less precise. A study was performed by Edessa and Bronsart (2015), which presented a practical and efficient ship hull form reconstruction strategy. However, the data they used was generated from an existing hull form CAD data with some extra random noise, which is much simpler than that acquired from a real ship. In order to measure waterlines and displacements much faster and more accurate, this paper presents a TLS data-based method. In addition, the presented methodology has been finally tested by measuring a 172 m ship.

2. METHODOLOGY

The proposed methodology broadly consists of four parts (point cloud data acquisition, point cloud data preprocessing, waterline generation and displacement tonnage calculation) as shown in Figure 1. The method proceeds as follows. First, several scans are captured via a terrestrial laser scanner. Second, the integrated hull point cloud is produced by registering scans, removing outliers as well as unwanted points and down-sampling. In the next step, waterlines are generated by fitting the extracted offsets into Non-Uniform Rational B-Splines (NURBS) curves. Finally, the displacement tonnage is calculated by accumulating the volume of every polyhedron between two neighbor slices. In the following, we explain the steps of our method in detail.
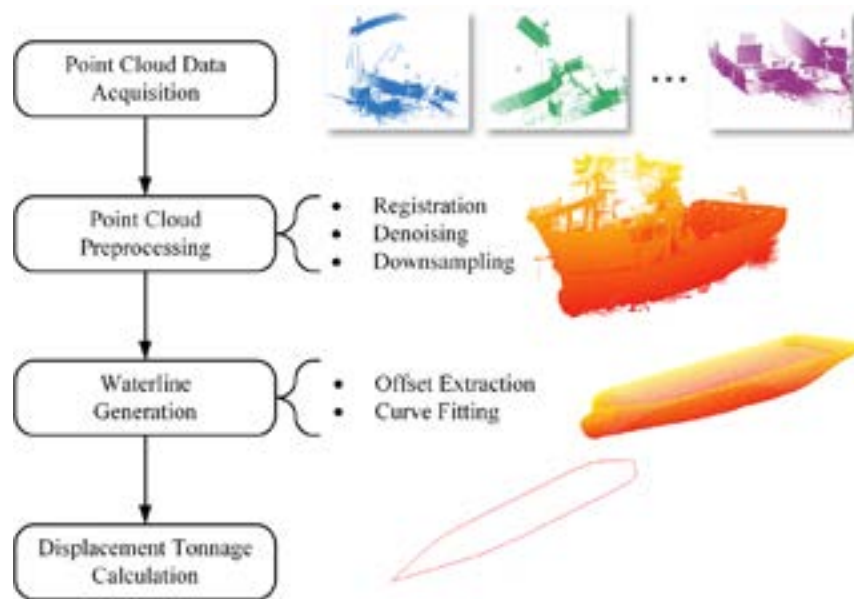
Figure 1. Overview of the proposed pipeline.

2.1 Point Cloud Data Acquisition

For obtaining the high-quality waterlines and displacement tonnage table, the precision and accuracy of the integrated hull point cloud are of great importance. Therefore, we designed and built a positioning pedestal for the scanner and two orientation pedestals for reference spheres (see Figure 2) in the previous research (Jia et al., 2014). With these devices, for every scan, the precise scan position and initial scan direction can be easily measured and determined by conducting a closed traverse survey surrounding the ship. Afterward, a precise scan registration can be performed automatically.

(a) The scanner positioning pedestal;   (b) the orientation pedestal
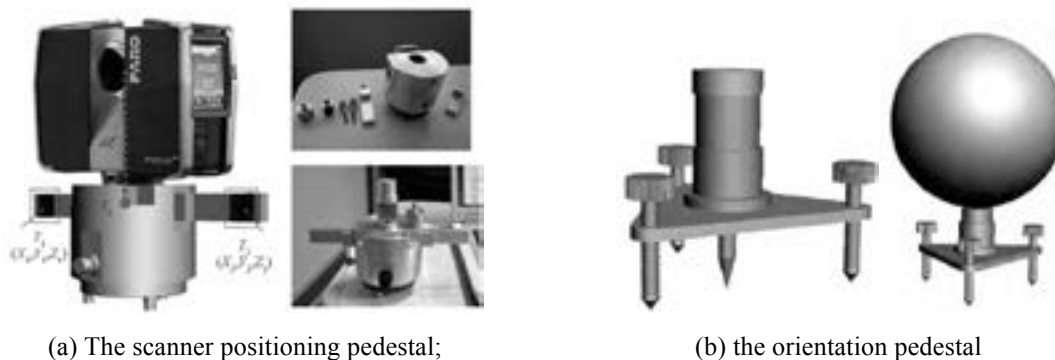
Figure 2. The custom-designed devices.

2.2 Point Cloud Preprocessing

The focus of this step is to obtain a complete and integrated hull point cloud. The work can be divided into three parts:

Scan Registration: Registering scans is, in essence, coordinate transformation: this necessary step rebuilds the spatial relationship between different scans and transforms these data from the scan coordinate system into the overall coordinate system. There are generally two categories of common registration methods: target-free and target-based. Nevertheless, either category of methods has its own limitations. For target-free registration methods, the overlap area of two scans must be considerable and these algorithms seem to be slow and computationally expensive. When it comes to the target-based methods which are widely used in most scanning projects, if planar targets (checkerboards) are chosen, data acquisition error occurs if the incident angle of laser is non-zero and the error would increase as the angle enlarge. Spherical targets (reference spheres) do not have this disadvantage since they are always the same solid circle when viewed from any angle. However, placing man-made targets is a time-consuming and demanding process because the targets should be uniformly distributed: not in a line and with different heights. Moreover, the precision of registration will suffer because of error propagation if there is no loop closure scanning: the first scan and the last one does not contain matching targets. In order to overcome the drawbacks of current registration methods, we designed the scan positioning and orientation devices (Jia et al., 2014). In our method, a closed traverse is first surveyed. Subsequently, for every scan, the scanner position can be measured precisely by a total station and two reference spheres are placed on the neighbor control points to determine the initial scan direction. After inclination correction using the inclinometer data of the scanner, the problem can be simplified to 2D coordinate transformation (see Figure 3). Thus, the rotation angle α between each independent scan coordinate and the overall coordinate can be calculated by Equation 1 and then each scan can be registered using Equation 2.

$$\alpha = \arctan \frac{-y_p(X_p - X_0) + x_p(Y_p - Y_0)}{x_p(X_p - X_0) + y_p(Y_p - Y_0)} \tag{1}$$

$$\begin{bmatrix} X_p \\ Y_p \\ Z_p \end{bmatrix} = \begin{bmatrix} X_0 \\ Y_0 \\ Z_0 \end{bmatrix} + \begin{bmatrix} \cos\alpha & -\sin\alpha & 0 \\ \sin\alpha & \cos\alpha & 0 \\ 0 & 0 & 1 \end{bmatrix} \begin{bmatrix} x_p \\ y_p \\ z_p \end{bmatrix} \tag{2}$$
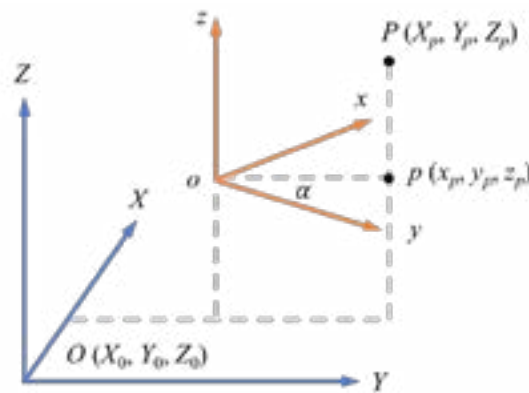
Figure 3. The overall coordinate system (blue) and scan coordinate system (orange).

Noise Reduction: Raw point clouds generally contain sparse outliers because data can be easily affected by environmental interference and systematic errors (the sensor itself). In addition, commonly, there are numerous

unwanted points in raw scans. Whether a point is unwanted or not depends on the objective of the project. This research, for instance, focuses on waterline generation as well as displacement calculation and therefore all points except those of the ship hull are considered as unwanted points. A statistical analysis algorithm (Rusu et al., 2008) is performed for irregularities removal whereas unwanted points such as crossers, scaffolding, transporters and workers in the open-space shipyard are eliminated manually. The reason why these points cannot be deleted automatically is that they are of high density and quality. Besides some of them are attached to the ship hull.

Data Compression: Because the following steps of the proposed method are point-based, large input data can make them extremely slow. Hence, down-sampling should be done to speed them up. Note that some common down-sampling methods will create a new cloud with points that are not at the same position in space as the input cloud such as Voxel- and Octree-based algorithms. These methods are not suitable for our work since the original point positions should be reserved to fit waterlines and calculate displacement tonnage. In this work, the spatial method within CloudCompare is performed for data compression.

2.3 Waterline Generation

Offset Extraction: Once the integrated hull cloud is produced, it is sectioned from the bottom up according to the Z-axis to extract offsets. The waterline points extracted by each waterline plane – the plane perpendiculars to the Z-axis – could be insufficient and unevenly distributed because of unwanted points removal. In order to address this situation, points around each waterline plane within a defined tolerance are projected to the plane. The next step is to filter the waterline points for generating smooth curves. In the proposed method, the 2D voxel grid (Rusu & Cousins, 2011) is simply performed to regularize waterline points and extract offsets (see Figure 4). Afterward, a polar angle based method is implemented to order the offsets since the curve fitting process needs strictly ordered points. In terms of each offset point cloud, the proposed sorting algorithm defines a polar coordinate system where the pole is the center of gravity of the point cloud and orders the points into clockwise based on the polar angles of each point. This method is efficient for convex polygons which the shapes of waterlines are.
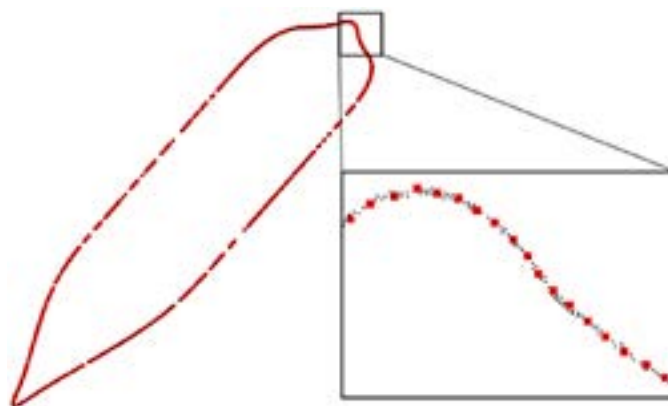
Figure 4. The extracted offsets of a waterline.

Curve Fitting: Usually in curve fitting, a set of data points is fitted with a curve defined by some mathematical functions such as polynomial or exponential functions. Nonetheless, there is no theoretical basis for choosing a function to fit waterlines due to the complex shape of ship hull form. Non-Uniform Rational Basis Spline (NURBS) can offer great flexibility and precision for handling both analytic and modeled shapes and thus it is commonly used in the maritime industry (Wang & Zou, 2008; Edessa & Dronsart, 2015). Curve fitting can involve either interpolation (see Figure 5(a)), which requires the curve to contain all data points, or approximation (see Figure 5(b)), in which a "smooth" function is constructed that approximately fits the data. An interpolating curve may wiggle through all data points rather than following the data polygon closely. Therefore, the approximation technique which can overcome this problem is chosen to generate waterlines.

(a) Curve interpolation;   (b) curve approximation
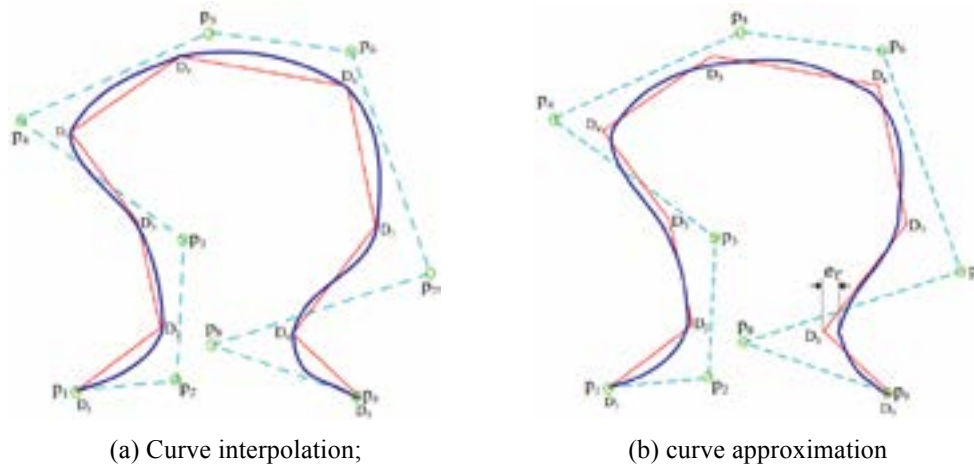
Figure 5. Demonstration of curve interpolation and approximation (Edessa & Bronsart, 2015).

2.4 Displacement Tonnage Calculation

Displacement is the weight of the water displaced by the hull of a ship up to the waterline. Therefore, it can be measured by first calculating the volume of water displaced by the ship then converting that value into tons. We first apply the coordinate analytic method to calculate the area surrounded with each waterline (Equation 3). The volume of every polyhedron formed from two neighbor waterlines is then calculated using Equation 4. Finally, the displacement table can be acquired by simply accumulating the volume of every polyhedron from the bottom up since the density of fresh water is 1000 kg/m^3.

$$S = \frac{1}{2}\sum_{i=1}^{n}(x_i y_{i+1} - x_{i+1}y_i)$$ (3)

$$V = \frac{1}{3}h(S_{\text{bottom}} + S_{\text{top}} + \sqrt{S_{\text{bottom}}S_{\text{top}}})$$ (4)

In the Equation 3, element S refers to the area surrounded with the waterline whereas (x_i, y_i), $i = 1,…,n$ represents the coordinates of the ordered offsets. Furthermore, the V and h element in the Equation 4 are the volume of polyhedrons and the gap between two neighbor waterline planes, respectively.

3. EXPERIMENT

3.1 Material

To demonstrate the performance of the proposed method, experiments were conducted of a ship with an overall length of 172m, a maximum width of 35m and a height of 16m. We collected 13 scans of the ship using a FARO Focus^{3D} X330 terrestrial laser scanner at a spatial resolution 6.28mm/10m, resulting in a ship hull of 947,167 points after point cloud preprocessing. Figure 6(a) shows the registered point cloud while Figure 6(b) reports the ship hull point cloud after noise reduction and down-sampling.
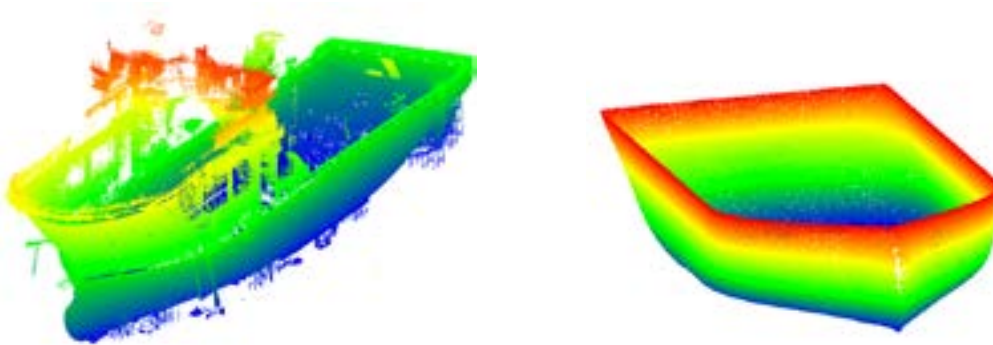
(a) The registered point cloud;   (b) the preprocessed point cloud

Figure 6. Point cloud visualization of the ship (colored by height).

3.2 Results

In the current experiment, the preprocessed point cloud is sectioned from the bottom up according to the Z-axis with a gap between each slice of 5 cm. In addition, points around each waterline plane within a tolerance of 5 mm are projected to the plane. The waterline result and displacement table are acquired as shown in Figure 7 and Table 1, respectively. Note that only some of the waterlines are visualized in Figure 7 for a better visual effect.
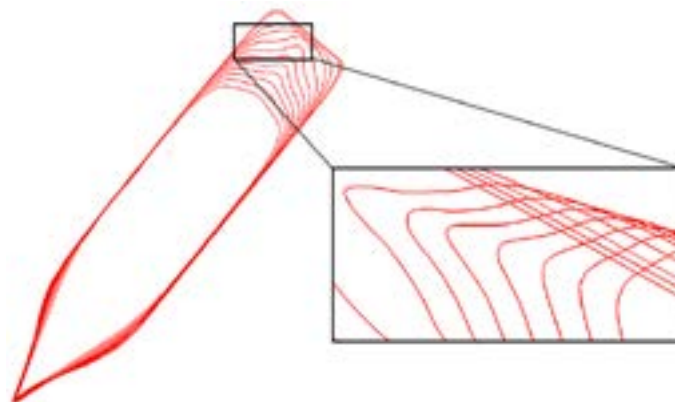
Figure 7. The generated waterlines.

In order to evaluate the performance of our method, the ship hull surface is reconstructed and used for calculating the reference displacements by means of the Geomagic Studio. We use the relative error to assess the accuracy of the calculated displacements. It is clear from Table 1 that the difference between calculated and reference displacements is barely noticeable, with all the relative errors below 0.1‰.

Table 1. Displacement tonnage table (fresh water)

Height (m)	Calculated displacement (t)	Reference displacement (t)	Relative error (‰)
0.74	822.710	822.713	0.003
0.79	906.098	906.113	0.016
0.84	990.286	990.307	0.020
0.89	1075.236	1075.261	0.024
0.94	1160.914	1160.949	0.031
0.99	1247.302	1247.349	0.037
6.04	12401.528	12402.49	0.078
6.24	12916.404	12917.41	0.078
6.34	13174.872	13175.90	0.078
8.74	19492.808	19494.41	0.082
8.84	19758.964	19760.63	0.084
8.94	20025.326	20027.03	0.085
9.04	20291.878	20293.61	0.085

5. CONCLUSIONS

In this study, a novel method for measuring the ship waterlines and displacement tonnages based on the TLS data has been presented and applied on a 172×35×16 m ship. Our results demonstrate that all the relative errors of generated and reference displacements are less than 0.1‰, which shows that the accuracy of our method is high enough for ship surveying. In future work, we would like to utilize the waterlines obtained from the proposed method to reconstruct the ship hull surface.

ACKNOWLEDGEMENT

REFERENCES

Abbas, M., Lichti, D., Chong, A., Setan, H., Majid, Z., Lau, C., … Ariff, M., 2017. Improvements to the accuracy of prototype ship models measurement method using terrestrial laser scanner. Measurement, 100, pp. 301–31.

Biskup, K., 2007. Application of terrestrial laser scanning for shipbuilding. In: ISPRS Workshop on Laser Scanning 2007 and SilviLaser 2007, Espoo, pp. 56-61.

Edessa, D., & Bronsart, R., 2015. A contribution to curves network based ship hull form reverse engineering. International Shipbuilding Progress, 62, pp. 17–42.

Jawor, J., Luft, M., Łukasik, Zbigniew, & Szychta, E, 2012. Integration of Cloud Computing and Reverse Engineering 3D Scanning for marine applications. Scientific Journals, 30(102), pp. 66–69.

Jia, D., Cheng, X., Liu, Y., & Cheng, X., 2014. The orientation method of terrestrial 3D laser scanner. Geotechnical Investigation & Surveying, 10, pp. 60-65.

Koelman, H., 2010. Application of a photogrammetry-based system to measure and re-engineer ship hulls and ship parts: An industrial practices-based report. Computer-Aided Design, 42(8), pp. 731–743.

Menna, F., & Nocerino, E, 2014. Hybrid survey method for 3D digital recording and documentation of maritime heritage. Applied Geomatics, 6(2), pp. 81–93.

Menna, F., Nocerino, E., Del Pizzo, S., Ackermann, S., & Scamardella, A., 2011. Underwater photogrammetry for 3D modeling of floating objects: the case study of a 19-foot motor boat. Sustainable Maritime Transportation and Exploitation of Sea Resources, 537(544), pp. 537-544.

Menna, Nocerino, & Scamardella., 2011. Reverse engineering and 3d modelling for digital documentation of maritime heritage. In: ISPRS-International Archives of the Photogrammetry, Remote Sensing and Spatial Information Sciences, Trento, Vol.XXXVIII-5-W16(1), pp. 245–252.

Menna, F., & Troisi, S., 2007. Photogrammetric 3D modelling of a boat's hull. In: Proceedings of Optical 3D Measurement Techniques Conference, Vol.2, pp. 347-354.

Paoli, A., & Razionale, A., 2012. Large yacht hull measurement by integrating optical scanning with mechanical tracking-based methodologies. Robotics and Computer-Integrated Manufacturing, 28(5), pp. 592–601.

Rusu, R., & Cousins, S., 2011. 3D is here: Point Cloud Library (PCL). IEEE International Conference on Robotics and Automation, 47, pp. 1-4.

Rusu, R., Marton, Z., Blodow, N., Dolha, M., & Beetz, M., 2008. Towards 3D point cloud based object maps for household environments. Robotics & Autonomous Systems, 56(11), pp. 927-941.

Tang, C., Tang, H., & Tay, P., 2016. Low cost digital close range photogrammetric measurement of an as-built anchor handling tug hull. Ocean Engineering, 119, pp. 67–74.

Wang, H., & Zou, Z., 2008. Geometry modeling of ship hull based on non-uniform B-spline. Journal of Shanghai Jiaotong University (Science), 13(2), pp. 189–192.

Wujanz, D., Weisbrich, S., Neitzel, F., Gaitanis, C., Arani, R., Krueger, D., & Petrovic, S., 2013. Fusion of point clouds from TLS and MVS for the generation of a 3D ship model. Proceedings of the oldenburger 3D Tage. 120, pp. 83-89.

ENVIRONMENTAL MONITORING USING LISAT (LAPAN-IPB SATELLITE) AND LANDSAT 8 SATELLITE IMAGERY OVER PATI REGENCY, CENTRAL JAVA, INDONESIA

Luisa Febrina Amalo (1), Irza Arnita Nur (1), Nur Riana Rochimawati (1)

[1]Environmental Research Center, Bogor Agricultural University, Lingkar Akademik St., PPLH Building 4th Floor 1680 West Java, Indonesia
Email: luisafebrina@gmail.com; irzaarnitanur@gmail.com; neineiku@gmail.com

KEY WORDS: LAPAN-IPB Satellite, LANDSAT, NDVI, Drought

ABSTRACT: The LAPAN-IPB Satellite called "LISAT" is designed and developed by LAPAN Indonesia. Not so many papers are addressing LISAT data application for environmental monitoring. Therefore, it is important to evaluate whether or not LISAT data can be used for environmental monitoring compared to LANDSAT 8 OLI/TIRS satellite imagery. The objectives of this research are (1) to compare LISAT and LANDSAT 8 Satellite by identifying the landuse (settlements and vegetation ar) through composite band images visually, (2) NDVI values from two different satellites over Pati Regency in specific time of study. The result showed similar spatial data view because the spatial resolution for both data were relatively similar (LISAT: 18 m; LANDSAT 8: 30 m). But LANDSAT 8 had more sharp image compared to LISAT. Moreover, LISAT image was not too focused (blur) compared to LANDSAT 8. However, the spatial data produced from LISAT was good enough as it is a new launched satellite, where LANDSAT is a well-known satellite. LISAT can be used for land monitoring because of its 30 m resolution images compared to others moderate resolution images. Nevertheless, NDVI data showed different range values between LISAT and LANDSAT 8. Value of NDVI derived from LISAT data was ranging between -1 to -0.006, while LANDSAT 8 was ranging -0.38 to 0.7. Minus value of NDVI derived from LISAT data was produced because LISAT data provided by LAPAN did not have absolute radiance values, only raw digital values. The next plan of this study is to normalized the digital number value and the information wiill be given from LAPAN.

1. INTRODUCTION

Since 2010, Bogor Agricultural University (IPB) and the National Institute of Aeronautics and Space of Indonesia (LAPAN) have committed to work together in developing satellite in order to support the food security and environmental monitoring program in Indonesia. The LAPAN-IPB Satellite called "LISAT" is designed and developed by LAPAN, and IPB will be responsible for developing algorithm and datasets application, in order to support the food security and environmental monitoring program. Not so many papers are addressing LISAT data application for environmental monitoring. Therefore, it is important to evaluate whether or not LISAT data can be used for environmental monitoring compared to LANDSAT 8 OLI/TIRS satellite imagery.

In this study, Normalized Difference Vegetation Index (NDVI) were conducted for environmental monitorng (Maselli, 1992). Environmental monitoring can be measured by vegetation condition. NDVI has higher sensitivity corresponding with crown density change than other vegetation index (Zaitunah et al., 2018). NDVI is calculated by using Near Infrared and Red Band from LISAT (LAPAN-IPB Satellite) and LANDSAT 8 Satellite imagery. Lower NDVI indicates areas of barren rock and sand and higher NDVI reflects dense vegetation. The objectives of this research are (1) to compare LISAT and LANDSAT 8 Satellite by identifying the landuse (settlements and vegetation ar) through composite band images visually, (2) NDVI values from two different satellites as LISAT is a new launched-satellite, while LANDSAT is well-established and developed satellite which has been widely used for many scientific researches over Pati Regency in specific time of study.

2. DATA AND METHODS
2.1 Study Area

The study area will focus in Pati Regency, Central Java, one of Central Java agricultural production center (Figure 1). Pati itself is known as a productive rice producing area in six districts such as Sukolilo subdistrict 3,398 hectares, Pucakwangi subdistrict 3,150 hectares, Jakenan subdistrict 2,987 hectares, Winong district 2,987 hectares, Jaken subdistrict 2,639 hectares and Tambakromo 2,589 hectares.

Figure 1. Study location

2.2 Data

The data used in this project LAPAN A3/LAPAN-IPB Satellite (LISAT) and LANDSAT 8 TIRS/OLI. Acquisition time for LISAT images was retreived on 12th October 2017 while LANDSAT 8 images was retrieved on 18th October 2017. October 2017 was chosen because it covered less haze and clouds for both LISAT and LANDSAT 8 Satellite data (dry season).

Table 1. LAPAN A3/LAPAN-IPB Satellite (LISAT) and LANDSAT 8 TIRS/OLI Satellite Specification

Specification		LISAT	LANDSAT 8
Spectral resolution	Blue	Band 1 (0.41 – 0.49 μm)	Band 2 (0.45 – 0.51 μm)
	Green	Band 2 (0.51 – 0.58 μm)	Band 4 (0.53 – 0.59 μm)
	Red	Band 3 (0.63 – 0.70 μm)	Band 2 (0.63 – 0.67 μm)
	Near Infrared	Band 4 (0.77 – 0.99 μm)	Band 5 (0.85 – 0.88 μm)
Spatial resolution		18 m	30 m

These data were downloaded from LISAT.ipb.ac.id and glovis.usgs.gov

2.3 Methods
2.3.1. Compositing Images
    a. LISAT image by compositing band 432
    b. LANDSAT 8 image by compositing band 234

2.3.2. Normalized Difference Vegetation Index (NDVI) (Ganie and Nusrath, 2016)
    a. Calculating radiance value from satellite data

$$\rho\lambda' = M \rho Q\, cal + A\, \rho$$

Where:
$\rho\lambda'$ = TOA planetary reflectance, without correction for solar angle.
$M\rho$ = Band-specific multiplicative rescaling factor from the metadata (Reflectance_Mult_Band_x, where x is the band number)
$A\,\rho$ = Band-specific additive rescaling factor from the metadata (Reflectance_Add_Band_x, where x is the band number)
$Q\, cal$ = Quantized and calibrated standard product pixel values (DN).

    b. Correcting reflectance value with sun angle

$$\rho\lambda = \rho\lambda\,'/\cos\,\theta SZ = \rho\lambda\,'/\sin\,\theta SE$$

$\rho\lambda$ = TOA planetary reflectance

θSZ = Local solar zenith angle; θSZ = 90° - θSE.

c. Calculating NDVI

$$NDVI = \frac{NIR - Red}{NIR + Red}$$
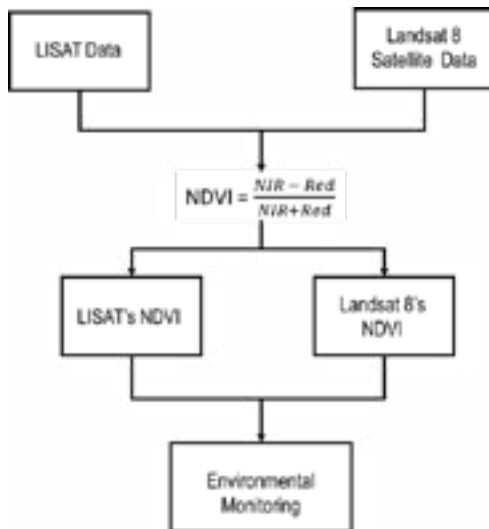
Figure 2. Flow Diagram

3. RESULT AND DISCUSSION

LISAT and LANDSAT Imagery composite bands are presented in Figure 3. Different color from those images was made from different band and wavelength of each satellite. LISAT image was done by compositing band 432, whereas LANDSAT image was done by compositing band 234. Compositing images is needed to see the true color of each scene. Therefore, landuse cover can be seen by using compositing images.

(a)　　　　　　　　　　　　　　　　　　　　(b)
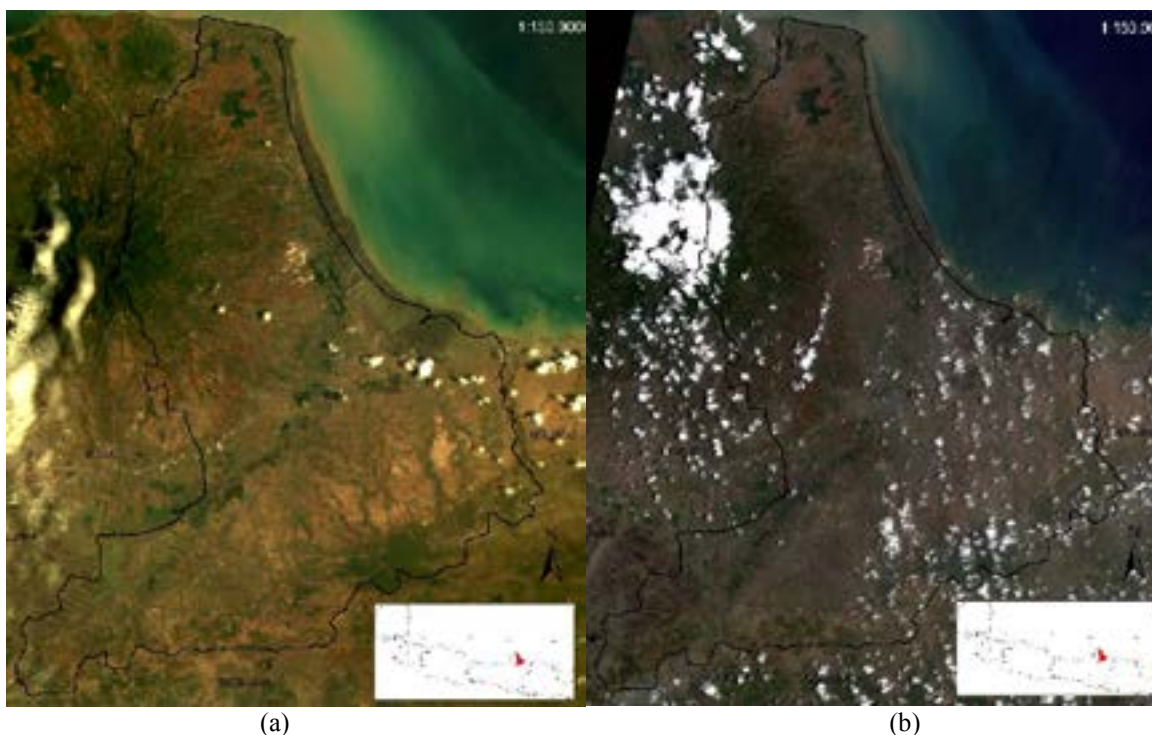
Figure 3. (a) LAPAN-IPB Satellite (LISAT) (b) LANDSAT 8 TIRS/OLI view in Pati Regency, October 2017

3067

it showed similar spatial data view because the spatial resolution for both data were relatively similar (LISAT: 18 m; LANDSAT 8: 30 m). But of course, LANDSAT 8 had more sharp image compared to LISAT. Moreover, LISAT image was not too focused (blur) compared to LANDSAT 8. However, the spatial data produced from LISAT was good enough as it is a new launched satellite, where LANDSAT is a well known satellite. LISAT can be used for land monitoring because of its 30 m resolution images compared to others moderate resolution images.

Figure 4. LANDSAT 8 TIRS/OLI view in Pati Regency, October 2017

Figure 5. LANDSAT 8 TIRS/OLI view in Pati Regency, October 2017

NDVI calculation had been done for environmental monitoring. It is important to see if LISAT data result is similar with LANDSAT 8 which there were numerous study using LANDSAT imagery for calculating NDVI (Mushtaq et al., 2016). Besides environmental monitoring, particularly vegetation cover monitoring, NDVI also can be used as drought indices (Zargar et al., 2011). Pati Regency is one of the largest Agricultural production in Indonesia. Therefore, NDVI result can be used as drought monitoring for multi-year monitoring which combined with field observation on next research plan.
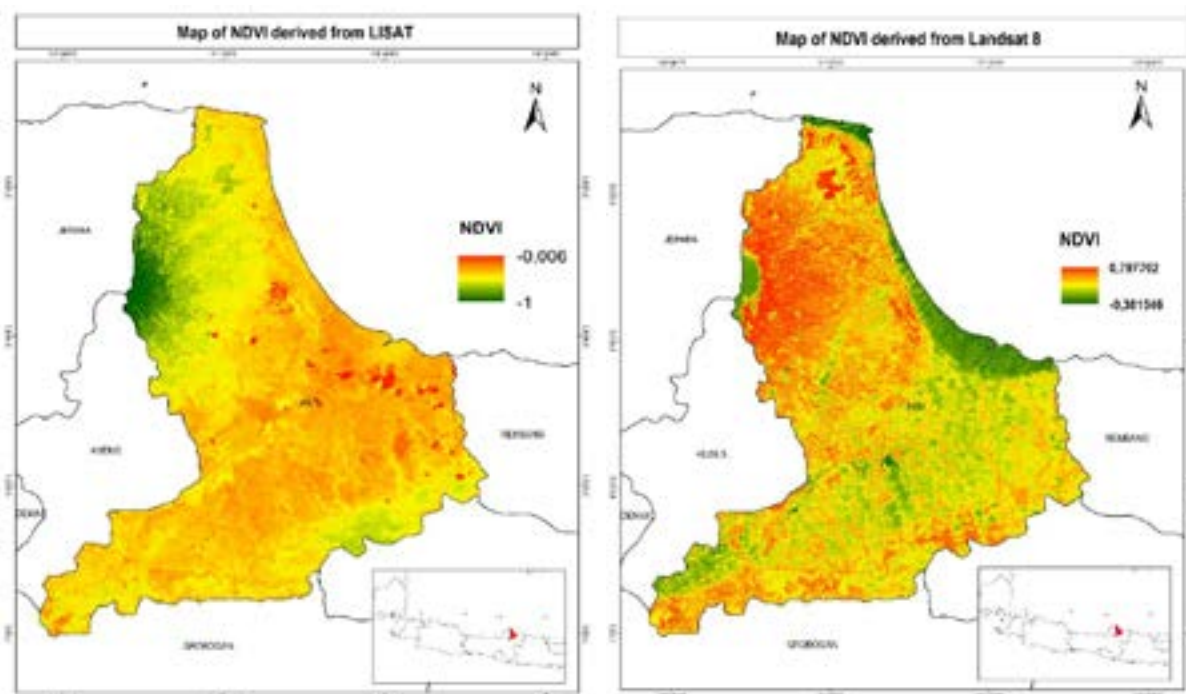
Figure 6. NDVI Data derived from LAPAN-IPB Satellite (LISAT), October 2017

Preliminary result of NDVI were presented in Figure 6. Nevertheless, NDVI data showed different range values between LISAT and LANDSAT 8. Value of NDVI derived from LISAT data was ranging between -1 to -0.006, while LANDSAT 8 was ranging -0.38 to 0.7. Refers to literature, NDVI value was to low even when dry season occurred. There has been some error or miscalculated within NDVI from LISAT data calculation because lack of metadata information. Minus value of NDVI derived from LISAT data was produced because LISAT data provided by LAPAN did not have absolute radiance values, only raw digital values.

4. CONCLUSION

The result showed similar spatial data view because the spatial resolution for both data were relatively similar (LISAT: 18 m; LANDSAT 8: 30 m). But LANDSAT 8 had more sharp image compared to LISAT. Moreover, LISAT image was not too focused (blur) compared to LANDSAT 8. However, the spatial data produced from LISAT was good enough as it is a new launched satellite, where LANDSAT is a well-known satellite. LISAT can be used for land monitoring because of its 30 m resolution images compared to others moderate resolution images. Nevertheless, NDVI data showed different range values between LISAT and LANDSAT 8. Value of NDVI derived from LISAT data was ranging between -1 to -0.006, while LANDSAT 8 was ranging -0.38 to 0.7. The next plan of this study is to normalized the digital number value and the information will be given from LAPAN.

5. ACKNOWLEDGMENT

6. REFERENCES

F. Maselli, Conese, C., Petkov, L., and Gilabert, M. A. 1992 Use of NOAA-AVHRR NDVI data for environmental monitoring and crop forecasting in the Sahel. International Journal of Remote Sensing, 13:14, pp. 2743-2749, DOI: 10.1080/01431169208904076.

Ganie, M.A., Nusrath, A. 2016. Determining the Vegetation Indices (NDVI) from LANDSAT 8 Satellite Data. International Journal of Advanced Research, 4(8), pp. 1459-1463.

Mushtaq, A.G., and Asima, N., 2016. Determining the Vegetation Indices (NDVI) from LANDSAT 8 Satellite Data. Int. J. of Adv. Res. **4** (8), pp. 1459-146, ISSN 2320-5407.

Zargar, A., Sadiq, R., Naser, B., and Khan, F. I. 2011. A review of drought indices. Environmental Reviews, 19, pp. 333–349.

QUALITY OF NOAA-20 SATELLITE TRACKING SIGNAL RECEIVED IN MRSA GROUND STATION TEMERLOH PAHANG

Muhammad Fakhrul Razi Mohamed Mokhtar, Siti Rohana Adi,
Mohd Najib En, Siti Aishah Mohd Said

Malaysian Remote Sensing Agency (MRSA),
Ministry of Energy, Science, Technology, Environment and Climate Change (MESTECC)
No. 13, Jalan Tun Ismail, 50480 Kuala Lumpur, Malaysia
fakhrul@remotesensing.gov.my; rohana@remotesensing.gov.my;
najib@remotesensing.gov.my; aishah@remotesensing.gov.my

KEY WORDS: Antenna, Signal Gain, Receiving Signal, Elevation Angle, Spectrum Analyser.

ABSTRACT: The new NOAA-20 Satellite data will be the best option in the future for continuity of Suomi NPP Satellite data that been used in various projects in Malaysia. The quality of NOAA-20 satellite tracking signal in low and high elevation angles in MRSA Ground Station Temerloh Pahang is important to be verified to ensure the receiving operation of NOAA-20 Satellite data in the future could be determined. Using the existing MRSA Ground Station 3.6 meter Antenna to track NOAA-20 satellite at both low and high elevation angles and record the signal gain based on spectrum analyser data in certain period that cover all orbit path of the satellite in Malaysia region are the collection of data to be analysed. From the results, NOAA-20 Satellite tracking signal is well received in MRSA Ground Station Temerloh Pahang and receiving operation in the future could be determined. Various projects in Malaysia that using Suomi NPP Satellite data could continue with NOAA-20 Satellite data for sustainable operation in the future.

1. INTRODUCTION

NOAA-20 Satellite or formerly JPSS-1 launched into space on November 18, 2017, joined its predecessor, the Suomi NPP Satellite in the same polar orbit, as the continuity satellite. Both NOAA-20 and Suomi NPP imagers and sensors that observing Earth's land and oceans could be utilised widely for various remote sensing applications. In Malaysia, Suomi NPP Satellite data had been utilised for oceanography and forestry applications. As Suomi NPP Satellite's end of life could never be predicted, future planning for data continuity must be determined using the best option for that purpose, NOAA-20 Satellite data.

The ideal signal gain could be measured by flux density or link analysis that relates the transmit power from satellite's antenna and the receive power by ground station's antenna which shows in detail how the difference between these two is accounted for. By assuming the ideal parameters as references, it is expected that the real signal gain on the receive power value will be different due to various loss components such as losses in the atmosphere due to attenuation by air, water vapour and rain, losses at the antenna at each side of the link and possible reduction in antenna gain due to antenna misalignment (Atayero *et al*., 2011).

The quality of NOAA-20 satellite tracking signal received in MRSA Ground Station Temerloh Pahang will also affected by various transmission parameters and loss components which will not covered in details in this study. The study only focus in the quality of signal gain received by ground station antenna over tracking the NOAA-20 satellite at low and high elevation angles that cover orbit path of the satellite in Malaysia region.

2. METHODOLOGY

The Friis Transmission Formula (IEEE, 1979) which states that the power received at a matched load connected to the receiving antenna is given by

$$P_r = P_t\,G_t\,G_r\left(\frac{\lambda}{4\pi R}\right)^2 \tag{1}$$

Where P_r is the power received, P_t is the power accepted by the transmitting antenna, G_t is the power gain of the transmitting antenna, G_r is the power gain of the receiving antenna, λ is satellite signal wavelength and R is the distance between the receiving and the transmitting antenna (Balanis, 2005).

The product P_tG_t is called *Effective Isotropic Radiated Power* (EIRP) and the $(4\pi R/\lambda)^2$ is known as the *Path Loss* (L_P) may be read as

$$\text{Power received} = \frac{\text{EIRP x Receive antenna gain}}{\text{Path Loss}} \text{ [Watts]} \qquad (2)$$

Using decibel notation, equation 2 can be simplified to:

$$P_r = EIRP + G_r - L_P \text{[dB]} \qquad (3)$$

MRSA Ground Station 3.6 meter antenna with antenna gain, 46.55 dB (Young, 2014) used to received NOAA-20 satellite with EIRP, 42.9 dB, signal of frequency, 7.812 GHz (Charlson, 2012) and speed of light, 3×10^8 ms-^{1} will determine the ideal received power, P_r, by

i.   Low elevation (5^0 elevation angle) distance R, 2835 km:

$$P_r = EIRP + G_r - L_P$$

$$= 42.9 + 46.55 - 20 \log ((4\pi \times 2835 \times 10^3) / (3 \times 10^8/7.812 \times 10^9))$$

$$= -89.9 \text{ dB} \qquad (4)$$

ii.   High elevation (90^0 elevation angle) distance R, 824 km:

$$P_r = EIRP + G_r - L_P$$

$$= 42.9 + 46.55 - 20 \log ((4\pi \times 824 \times 10^3) / (3 \times 10^8/7.812 \times 10^9))$$

$$= -79.2 \text{ dB} \qquad (5)$$

The signal received by MRSA Ground Station 3.6 meter antenna will be amplified by low-noise amplifier (LNA) which had typical gain of 54 dB (Young, 2014). After adding this gain, the ideal of value in equation 4 will be -35.9 dB and value in equation 5 will be -25.2 dB. The ideal received power value in equation 4 and 5 are the foundation of this study which indicates that the higher elevation tracking by the antenna, the power loss will be less as path loss during tracking operation.

In this study, the data that have been recorded will be vice versa by the spectrum analyser built in the MRSA Ground Station 3.6 meter Antenna Tracking System. The better tracking signal received by the antenna, the stronger power that have been collected, the higher signal strength will be recorded and plotted automatically into graphs. Threshold of the Pedestal Control Unit (PCU) that keeps the antenna tracking the satellite with auto tracking is 1800mW or 32.6 dBm gain.

3. RESULTS AND DISCUSSION

Figure 1 and Figure 2 are the two samples of the results that have been recorded in September 2018. Figure 1 shows NOAA-20 satellite tracking at low elevation orbit path with coverage of North Peninsular of West Malaysia on September 5, 2018, tracking start time at 19.31 UTC. Figure 2 shows NOAA-20 satellite tracking at higher elevation orbit path with coverage of all Peninsular of West Malaysia and Sarawak of East Malaysia on September 6, 2018, tracking start time at 06.32 UTC.
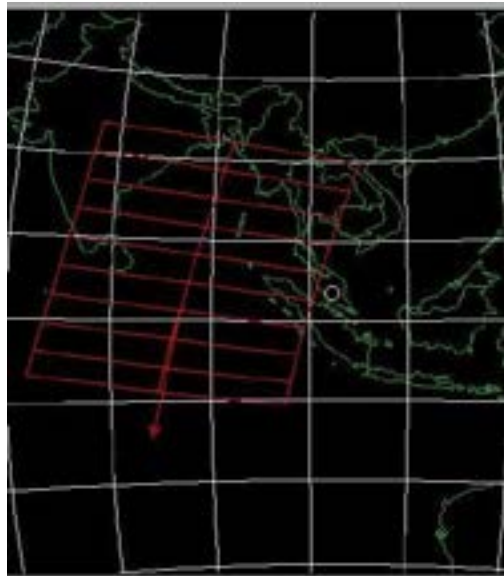
Figure 1: Descending low path orbit of NOAA-20 coverage over North of Peninsular of West Malaysia (September 5, 2018 at 19.31 UTC)
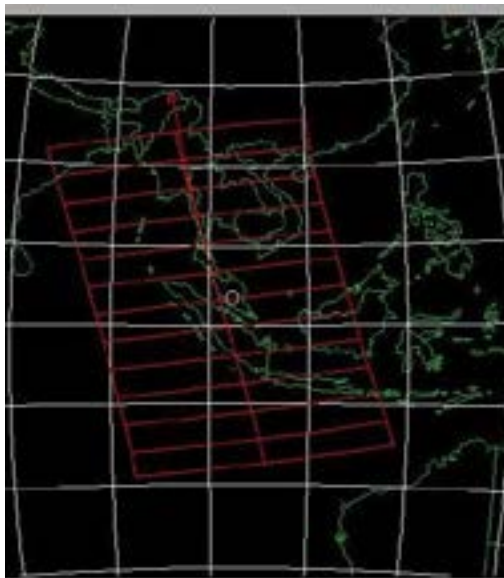
Figure 2: Ascending high path orbit of NOAA-20 coverage over all Peninsular of West Malaysia and Sarawak of East Malaysia (September 6, 2018 at 06.32 UTC)

Figure 3 shows signal strength (upper graph) plotted during tracking at elevation angles of 10 to 22 degrees over time (lower graph) for the sample of descending orbit from Figure 1. Figure 4 shows signal strength (upper graph) plotted during tracking at elevation angles of 10 to 80 degrees over time (lower graph) for the sample of ascending orbit from Figure 2.

From the results and the graphs that have been plotted in Figure 3 and Figure 4 for both descending and ascending, at low and high elevation, signal strength of both tracking signal are shown between 1800 to 2100 mW.
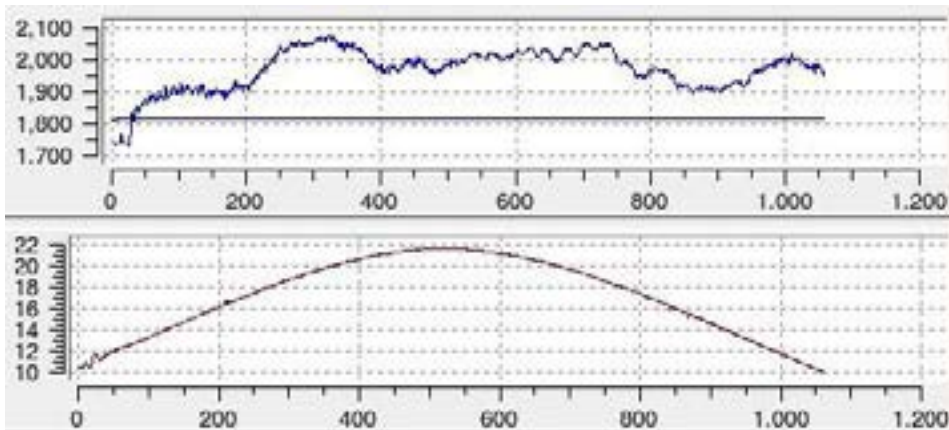
Figure 3: Signal strength (upper graph) and elevation angles of 10 to 22 degrees tracking over time (lower graph) of low path orbit (September 5, 2018 at 19.31 UTC)
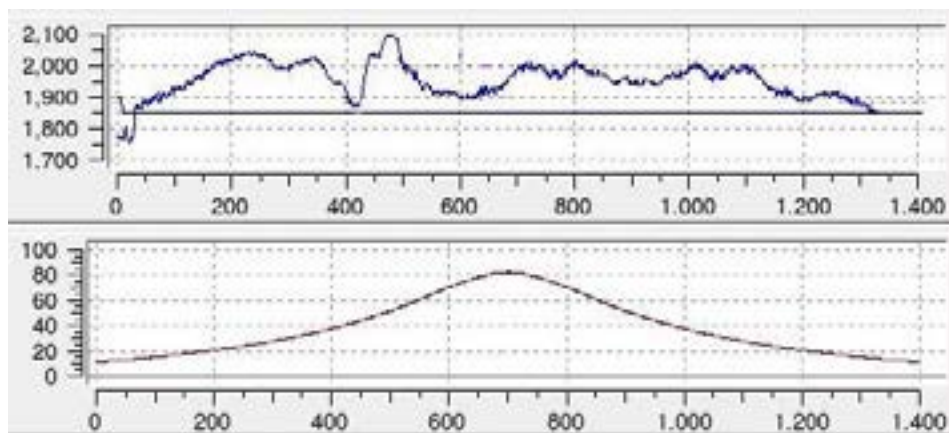
Figure 4: Signal strength (upper graph) and elevation angles of 10 to 80 degrees antenna tracking over time (lower graph) of high path orbit (September 6, 2018 at 06.32 UTC)

The signal strength in both Figure 3 and Figure 4 have pattern of going down at certain period of time although the antenna moving from lower elevation angles to the higher elevation angles. These results are different pattern compared to the ideal value of received power, P_r in equation 4 and 5 which indicate signal strength should be higher at higher elevation angles and lower at lower elevation angles.

The results indicate possibility of degraded efficiency of receiving antenna which involve pointing accuracy, reduction of antenna gain and various loss components. In this case, the results shows high signal strength captured above the threshold, both at low and high elevation indicates, at the minimum capabilities of receiving antenna, NOAA-20 satellite tracking signals are still being received above threshold of the system in MRSA Ground Station Temerloh Pahang.

4. CONCLUSION

From the results, although the quality of NOAA-20 satellite tracking signal received in MRSA Ground Station Temerloh Pahang less than expected due to degraded efficiency of receiving antenna, the signals are above minimum threshold of lock signal at low and high elevation of tracking signal. This could determine the NOAA-20 satellite tracking signal quality in MRSA Ground Station and to conclude the utilisation of NOAA-20 Satellite data as continuity of Suomi NPP Satellite data for sustainable operation in Malaysia in the future.

5. ACKNOWLEDGEMENTS

6. REFERENCES

Atayero, A.A, Luka, M.K, Alatishe, A.A, 2011. Satellite Link Design: A Tutorial, IJECS-IJENS 11 (4), pp.1-6.

Balanis, C.A., 2005. Antenna Theory: Analysis and Design, 3rd Edition, John Wiley & Sons, New Jersey, pp. 89-96.

Charlson, D., 2012. Joint Polar Satellite System 1 (JPSS-1) Spacecraft High Rate Data (HRD) to Direct Broadcast Stations (DBS) Radio Frequency (RF) Interface Control Document (ICD), Goddard Space Flight Center, National Aeronautics and Space Administration (NASA), Maryland, pp. 15-19.

IEEE, 1979.IEEE Standard Test Procedures for Antennas, IEEE Std 149-1979, pp. 96-97.

Young, T., 2014. TeraScan 2.4m/3.6m/4.4m/4.5m Polar Satellite Tracking Antenna Operations and Maintenance Manual, SeaSpace Corporation, California, pp. 12-281.

Characterization and Correction of Line-wise Stripes for Remote Sensing Imagery Using Wavelet Filtering Method

Kuo-Hsien Hsu, Sunny Lee, Yu-Lin Tsai

National Space Organization, 8F, 9 Prosperity 1st Road, HsinChu, Taiwan

Email: khhsu@nspo.narl.org.tw; sunnylee@nspo.narl.org.tw; morphling@nspo.narl.org.tw

Abstract: The primary objective of this paper is to implement a wavelet filtering method [Shresha, 2010] to remove the line-wise stripes of remote sensing imagery. This work concentrates on dealing with such kind of stripe removal and image detail preservation for remote sensing image. The wavelet filtering method invokes three different approaches. Low Frequency Sub-band (LFSB), High Frequency Sub-band (HFSB), and All Frequency Sub-band (AFSB) are used to decompose the image with different level of sub-banding. Then, we apply an identical filter on various component imagery to remove isolated stripes. Finally, we reconstruct the image using an inverse wavelet transform. The corrected image is evaluated qualitatively and quantitatively by Modulation Transfer Function (MTF) estimation. The result recommends that AFSB/Coiflets approach with one-level sub-banding is sufficient in removing the stripes and retaining most of the information of image at the same time.

KEY WORDS: wavelet filtering, remote sensing imagery, line-wise stripes

1. Introduction

Due to non-uniform response between odd and even lines of remote sensing image in along-track direction, this kind of difference therefore results in visual line-wise stripes in the image. In order to recover the accuracy of image data without adversely affecting the image, this work essentially concentrates on dealing with such kind of stripe removal and image detail preservation. The remainder of this work is organized as follows. Section 2 provides the algorithms used for de-striping and sharpness estimation. Section 3 conducts the observations based on the qualitative/quantitative evaluation and analysis. Section 4 concludes some remarks.

2. Algorithm

As shown in Fig. 1, this section covers the de-striping algorithms and procedures [Shresha, 2010] using three major steps: image decomposition, filter application, and image reconstruction. The approach of each step is provided briefly in the following:
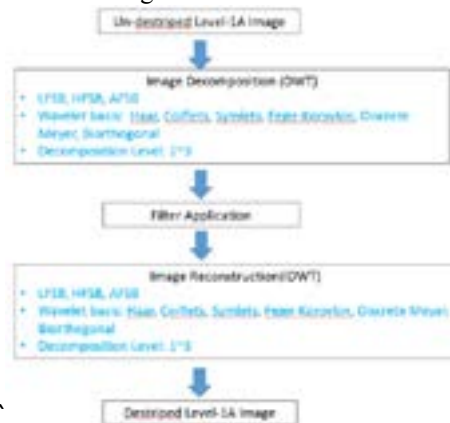
Figure 1. Flowchart of characterization and correction of stripes using wavelet filtering method

(1) Image Decomposition: The purpose of this step is to decompose an image into different frequency components (low-, high-, and both frequency) with multi-resolution (1~3 levels). The resulting two-dimensional array of DWT coefficients contains four bands of data, each labelled as LL (low-low), HL (high-low), LH (low-high) and HH (high-high). Three kinds of image decomposition, Low Frequency Sub-band (LFSB), High Frequency Sub-band (HFSB) and All Frequency Sub-band (AFSB), are used to identify the stripes in different frequency components. The LL and LH bands can be decomposed once again up to the third level in the same manner to produce more sub-bands in a pyramidal decomposition as shown in Fig. 2. In each sub-figure of Fig. 2, the red sub-band

domain is where each of decomposition approach attempts to identify stripes. For LHSB approach, we remove the stripes which are located only in the low frequency domain. The stripes located only in the high frequency domain can be removed by HFSB approach. The AFSB approach deals with stripes both located in low and high domains.

(2) Filter Application: The purpose of this step is to apply an identical filter to remove the stripes which are already identified at different frequency from previous step. For each selected wavelet sliding image $W(i,j)$, the line-wise averaged image ($Avg(i,j)$), line-wise difference image ($Diff(i,j)$), and pixel-wise averaged $Avg(i,j)$ are defined by

$$Avg(i,j) = W(i,j) + W(i+1,j), \quad (1)$$

$$Diff(i,j) = W(i,j) - W(i+1,j), \quad (2)$$

$$\text{and} \quad v(j) = \sum_i Avg(i,j). \quad (3)$$

For extracting the stripe noise information n, we apply a smoothing kernel k to the v

$$n = k \otimes v - v. \quad (4)$$

The de-striping wavelet sliding image $\overline{W}$ can be obtained by

$$\overline{W}(2i-1,j) = Avg(i,j) + n(j) + Diff(i,j) - \sum_{j'} k(j')Diff(i,j-j'), \quad (5)$$

$$\text{and} \quad \overline{W}(2i,j) = Avg(i,j) + n(j) - Diff(i,j) + \sum_{j'} k(j')Diff(i,j-j'). \quad (6)$$

(3) Image Reconstruction: The purpose of this step is to reconstruct an image based on the approach and wavelet basis that are used in image decomposition. Basically, this step depends on the level of decompositions and the types of decompositions which are used in step (1). Fig. 3 shows LFSB, HFSB, and AFSB reconstruction of an image using different components obtained by different stages. In general, four low resolution components located in low frequency domain are combined together to generate next higher resolution component at the first step of reconstruction process. At the second step, this new higher resolution component is combined with other three components to form the final reconstructed image. Therefore, the reconstructed image represents a resulting image, and most of its stripes are removed.

(a)　　　　　　　　(b)　　　　　　　　(c)

(d)　　　　　　　　(e)　　　　　　　　(f)

<div align="center">(g)   (h)   (i)</div>
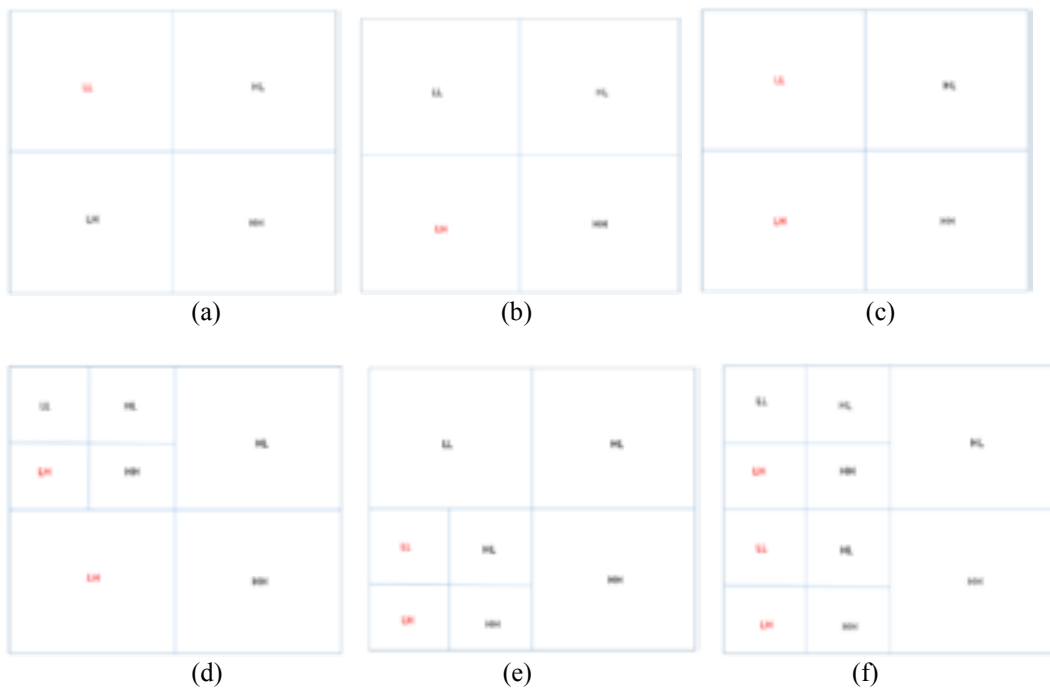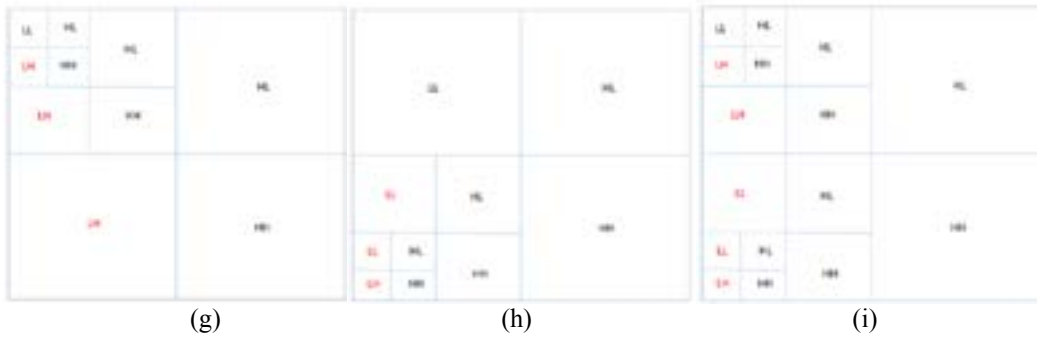
Figure 2. Pyramidal decomposition of an image: (a) 1-level LFSB, (b) 1-level HFSB, (c) 1-level AFSB, (d) 2-level LFSB, (e) 2-level HFSB, (f) 2-level AFSB, (g) 3-level LFSB, (h) 3-level HFSB, and (i) 3-level AFSB. The red sub-band domain is where each of decomposition approach attempts to identify and remove stripes.

<div align="center">(a)</div>

<div align="center">(b)</div>

<div align="center">(c)</div>
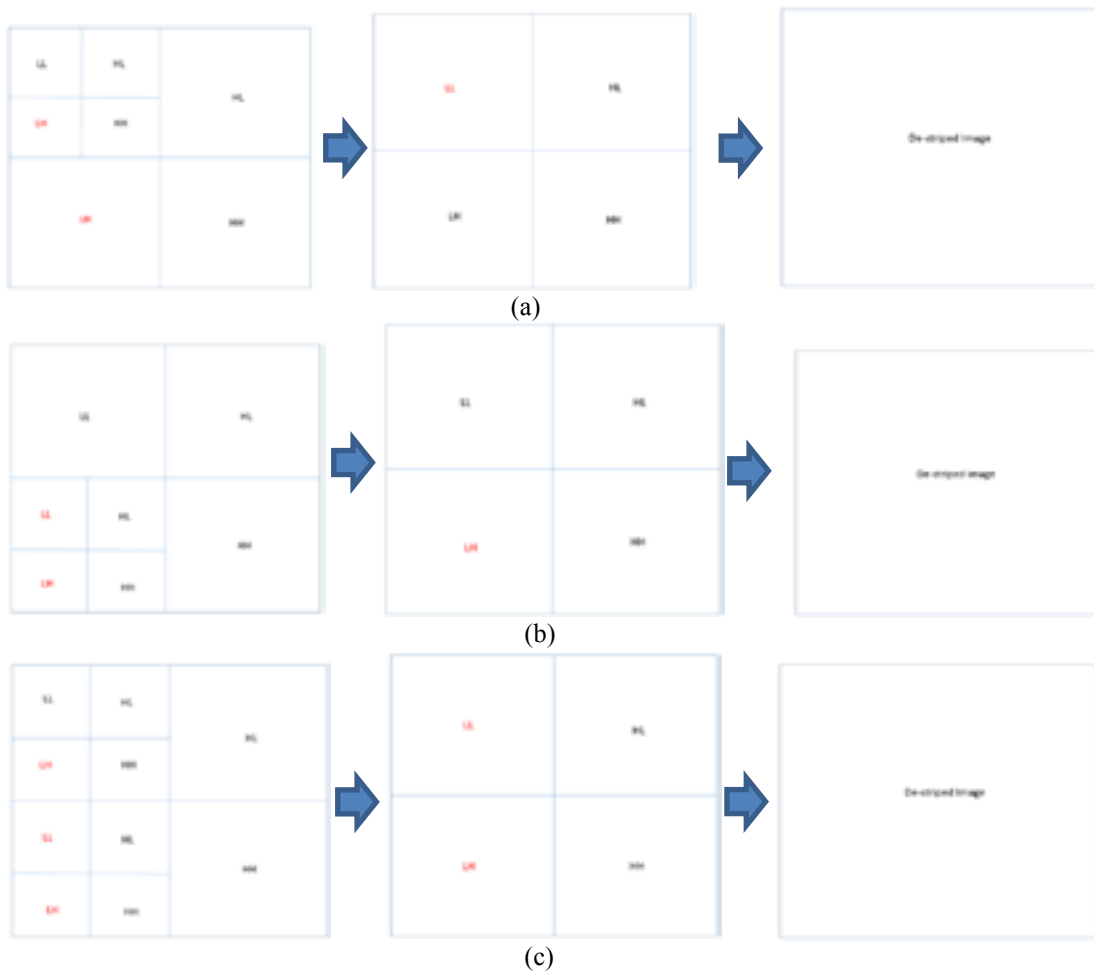
Figure 3. Image components at different stages of (a) LFSB, (b) HFSB, and (c) AFSB reconstruction process

The corrected images obtained from the de-striping approaches are evaluated qualitatively by visual assessment and quantitatively using Modulation Transfer Function (MTF) estimation. Typically, measurement of spatial quality is performed by calculating MTF or, equivalently, Contrast Transfer Function (CTF) of targets. As shown in Fig. 4, MTF is the normalized spatial frequency response of an imaging system, and it is defined as the normalized magnitude of the Fast Fourier Transform (FFT) of the Line Spread Function (LSF). As shown in Fig. 5, the pattern of target site is specifically designed to measure the sharpness in the along-track (ALT) and across-track (ACT) directions using MTF estimation. The steps of MTF estimation are:

1. Calculate the Edge Spread Function (ESF) from the Digital Number (DN) of MTF target image;
2. Calculate LSF by taking the first-derivative of ESF;
3. Calculate the FFT of the LSF;
4. Check the MTF value at the one half the sampling rate of the system (*i.e.*, Nyquist frequency).
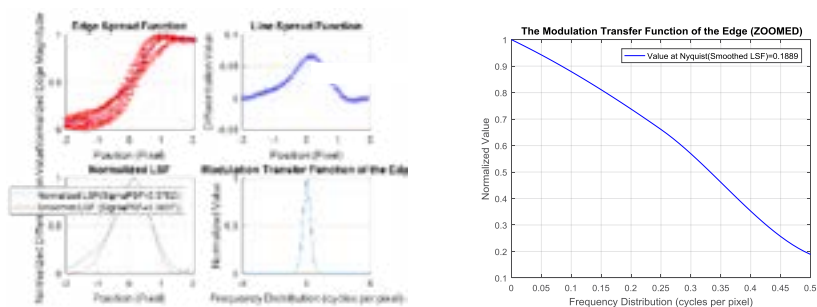
Figure 4. Steps of MTF estimation method: Modulation Transfer Function (MTF) is the normalized spatial frequency response of an imaging system, and it is defined as the normalized magnitude of the Fast Fourier Transform (FFT) of the Line Spread Function (LSF).
.

| (a) | (b) |

Figure 5. MTF pattern of (a) permanent and (b) portable target sites

3. Results and Analysis

This section evaluates and compares quantitatively/qualitatively the results obtained from different approaches, various wavelet bases, and multiple sub-banding levels. Ideally, a best approach should not only have the capability of removing stripes, but also need to keep radiometric quality in images as good as possible. As shown in Fig. 6 and Fig. 7, we begin to evaluate the effect of different level of different decomposition approaches using two wavelet bases. A remote sensing image contains MTF site is selected to be used as the test scene. The results obviously reveal that some observations are witnessed and interesting: First, 2-/3-level sub-banding with LFSB(Haar)/LFSB(bior6.8) and AFSB(Haar)/AFSB(bior6.8) results in a blurring image. Second, different level of sub-banding with LFSB(Haar)/HFSB(Haar)/AFSB(Haar) results in unexpected low-frequency stripes. Third, different levels of sub-banding of HFSB(Haar) and HFSB(bior6.8) have similar performance of stripe removal and detail preservation, but they are not good enough compared with 1-level sub-banding with AFSB(bior6.8). This also suggests that one level sub-banding is adequate to correct the image.
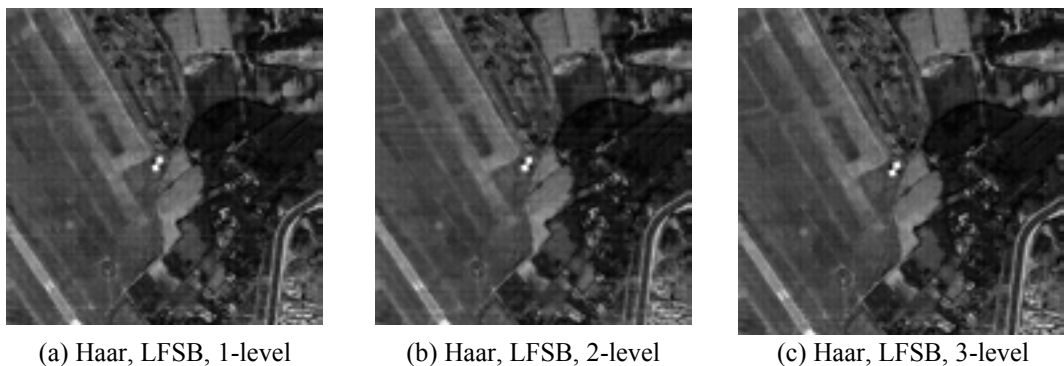
| (a) Haar, LFSB, 1-level | (b) Haar, LFSB, 2-level | (c) Haar, LFSB, 3-level |

(d) Haar, HFSB, 1-level

(e) Haar, HFSB, 2-level

(f) Haar, HFSB, 3-level

(g) Haar, AFSB, 1-level

(h) Haar, AFSB, 2-level
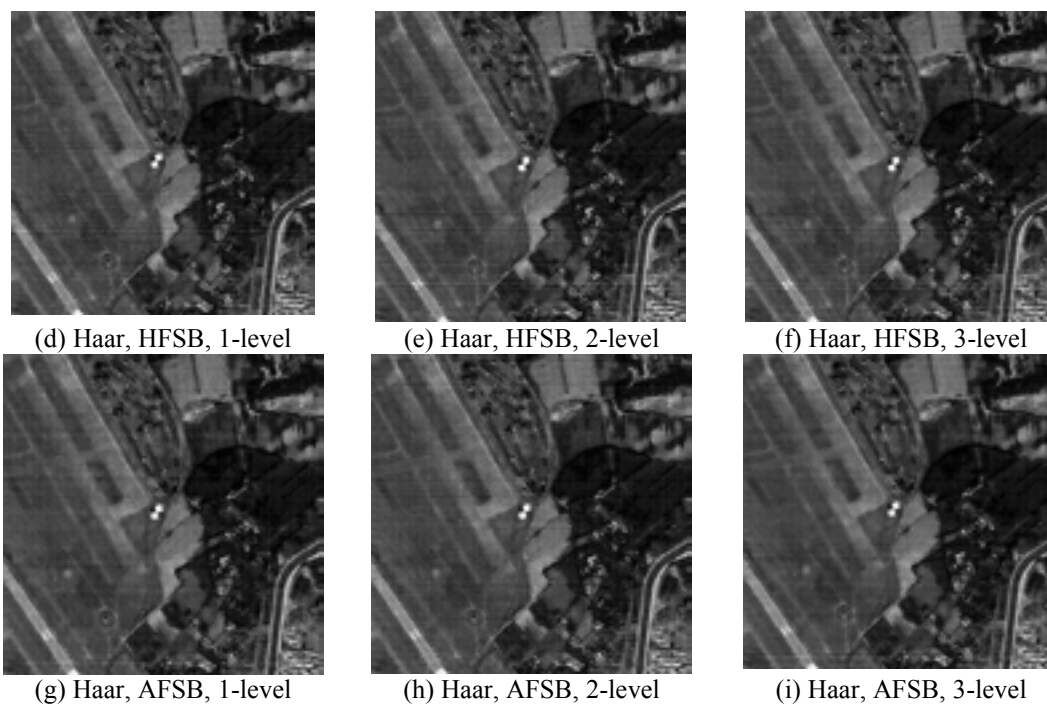
(i) Haar, AFSB, 3-level

Figure 6. Corrected images with wavelet basis (Haar) and three different decomposition levels using (a)~(c) LFSB, (d)~(f) HFSB, and (g)~(i) AFSB approaches

(a) Bior6.8, LFSB, 1-level

(b) Bior6.8, LFSB, 2-level

(c) Bior6.8, LFSB, 3-level

(d) Bior6.8, HFSB, 1-level

(e) Bior6.8, HFSB, 2-level

(f) Bior6.8, HFSB, 3-level
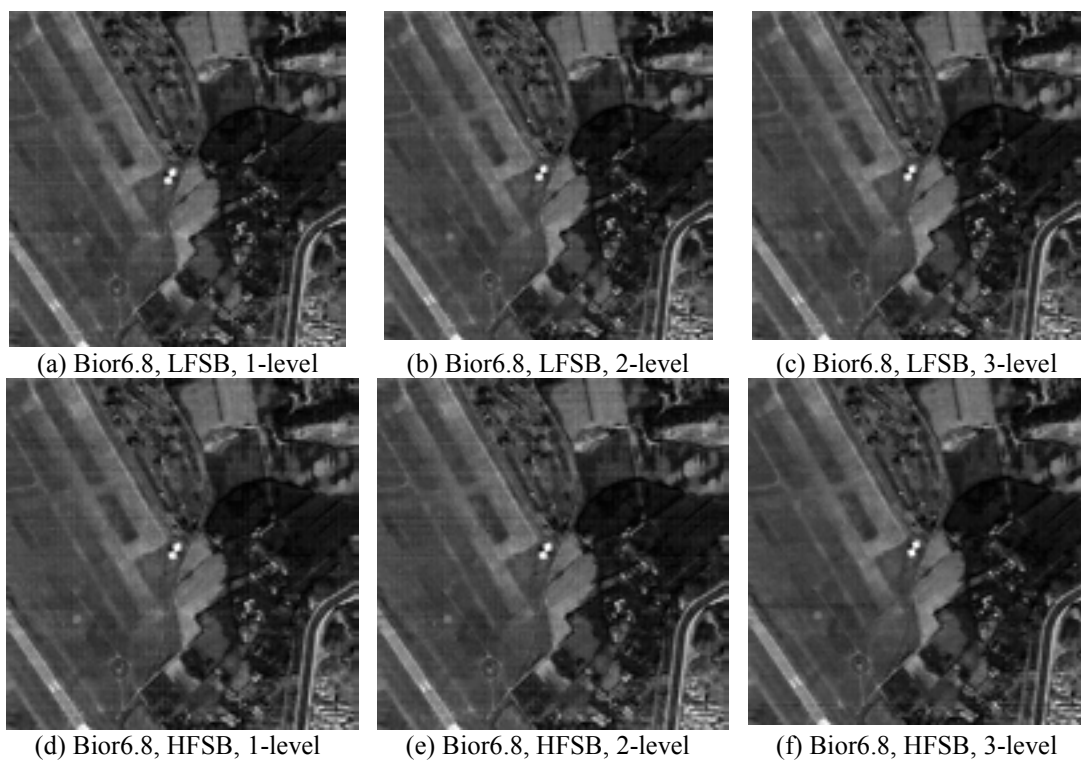
| (g) Bior6.8, AFSB, 1-level | (h) Bior6.8, AFSB, 2-level | (i) Bior6.8, AFSB, 3-level |

Figure 7. Corrected images with wavelet basis (Biorthogonal (bior6.8)), and three different decomposition levels using (a)~(c) LFSB, (d)~(f) HFSB, and (g)~(i) AFSB approaches

Thus, the effect of using different wavelet bases (such as Coiflets, Discrete Meyer, Fejer-Korovkin, and Symlets) of the 1-level sub-banding with AFSB approach is then evaluated. As shown in Fig. 8, it can be observed that these approaches provide similar removal performance in stripes according to the visual assessment. MTF is calculated as a quantitative approach to quantify the radiometric quality preservation for all corrected images. Table 1 records the normalized MTF index for the five different wavelet bases with 1-level sub-banding of AFSB approach.   Here, this index value does not present a real MTF value. It is just a normalized value of real MTF value for sharpness comparison. Higher index value indicates that higher performance of sharpness. Based on this comparison, the use of 1-level sub-banding with AFSB/Coiflets approach is recommended.

| (a) coif5 | (b) Dmey | (c) Fk22 |

(d) Sym45

Figure 8. De-striped images with wavelet bases (a) Coiflets(coif5), (b) Discrete Meyer(Dmey),   (c) Fejer-Korovkin(Fk22), and (d) Symlets(Sym45) of the 1-level sub-banding with AFSB approach.

Table 1. Normalized MTF index derived from corrected MTF scene using different wavelet bases with 1-level sub-banding of AFSB approach.

Normalized MTF index			
Across-track direction		Along-track direction	
Region Wavelet basis			
Lower	Upper	Right hand side	Left hand side

bior6.8,	0.3327	0.4333	0.2593	0.2452
Coif5	1	1	1	1
dmey	0.5448	0.9036	N/A	0.8143
fk22	0.4110	0.6854	0.1133	0.6178
sym45	N/A	0.4965	1.0179	0.7182
Notice: The index value does not present a real MTF value. It is just a normalized value of real MTF value for sharpness comparison.				

.
4. CONCLUSIONS

In this work, the line-wise stripes of remote sensing image is identified and removed based on de-striping algorithm using different approaches (LFSB, HFSB, AFSB), various wavelet bases (Coiflets, Discrete Meyer, Fejer-Korovkin, and Symlets), and multiple decomposition levels (1~3). From the qualitative and quantitative evaluation, all these approaches are able to remove stripes from image, but each of them is observed to have its own performance of de-striping and detail preservation. The results suggest that lower level decompositions of AFSB can be used to remove stipes from image without blurring the image by removing high frequency information. In addition, it concludes that the images corrected with Haar, Biorthogonal, Discrete Meyer, Fejer-Korovkin, and Symlets are blurred compared to the image corrected with Coiflets. Overall speaking, the AFSB with one-level sub-banding is adequate to correct remote sensing imagery since it removes amount of stripes from image, and retains detailed information at the same time.

References:

1. Shrestha, A. K., 2010, Relative Gain Characterization and Correction for Push-broom Sensors Based on Lifetime Image Statistics and Wavelet Filtering. Master Thesis, South Dakota State University.

3D LASER SCANNING IN THE RENOVATION OF WATPASATHARUAM, NAKHON RATCHASIMA, THAILAND

Intareeya Sutthivanich (1), Udomvit Maneewan (1), Punya Suamkumpung (1), Sirilak Tanang (1),
Suriporn Charungthanakij (2), Anucha Prangsungneon (1), Benja Klinjundaeng (1),

1 Suranaree University of Technology, Center for Scientific and Technological Equipment,
Mueang District, Nakhon Ratchasima, Thailand, 30000
2 Silpakorn University, Mueang Nakhon Pathom District, Nakhon Pathom, Thailand, 73000

Email: suttin1@sut.ac.th; udomvit@sut.ac.th; sevennight2009@gmail.com; sirilak@sut.ac.th;
scharung@hotmail.com; anucha@sut.ac.th; 236080@sut.ac.th

KEY WORDS: 3D laser scanning, point cloud, 3D modelling, renovation, preservation

ABSTRACT: Watpasatharuam is a long historic temple of Buddhism and is located in Nakhon Ratchasima province, northeast region of Thailand. The temple was established in 2475 B.E (1932 A.D.) and covered the area of 0.25 sq.km. (134 rai). It is a significant center of spiritual and religious practices for the surrounding local communities. The temple nourishes the natural landscape and traditional architecture building. Up to date, new technology takes part in renovation and preservation of historic temple processes. A 3D laser scanning can play an important role in the renovation and preservation of historic architecture. It can be expanded beyond the traditional dependence on 2D representations. The products from 3D laser scanning can be integrated into commercial Building Information Model (BIM)/ Computer Aided Design (CAD) and modeling applications that can be used from initial concept, throughout the design process to construction drawing. This paper discusses how 3D laser scanning is used to record the temple features and its 3D point cloud data set can assist the architect exploring potential alternative design. The design solutions can be established within an accurate framework. Along with cost estimation can be calculated in the renovation process. 3D models built from laser scanning data set ultimately improve the quality and understanding of a planned design for architectural reconstruction. A proposed renovation of the Watpasatharuam temple provides a case study illustrating how data derived from 3D laser scanning can form the basis of an accurate 3D model which can be integrated seamlessly into the architectural design process.

1. INTRODUCTION

Laser scanning is a relatively new technology. The scanning systems are used for the rapid acquisition of spatial data with a laser beam to obtain dense and accurate point clouds. Many researcher have been applied this new technology to their works, for instant, Wilson et al. 2013, Cardaci et al. 2011, Nettley et al. 2013, Ruther et al. 2009, Matias et al. 2013, and Lerma et al. 2010. Laser scanning systems can be utilized to model terrestrial features such as topography, structures, and objects. The 3D laser scanner is also called an active remote sensing system because no additional personnel is required for measuring any surfaces. The scanner records thousands of points per second and each point has location coordinates and elevation information. All of these points are placed into the same local coordinate system to make up a point cloud which represents the area, building, or object being scanned in a 3D space. Most modern scanners have their best accuracy at distances to 100-130 meters. The typical scanners are available and can scan in horizontal and vertical direction which allows large amount of data to be collected from one location. This makes the technique more practical for an urban plane sites. Many advantages of laser scanning are better quality of the results in terms of accuracy and precision of final result, no interference with construction and operations activities, simple and easy equipment operating and data processing. The geometric 3D data acquired by laser scanners can be generated by imposing real color textures simultaneously captured by a color camera images. The 3D visualization model, thus created, plays an important role in wide variety of field to support various applications like campus planning, city planning, reverse engineering, facility management, crime investigation, cultural heritage documentation, and documentation of the historical buildings and sites. (El-Hakim et al. 2005, Boehler 2002, El-Hakim et al. 2002, and Susan and Megan 2012)

In recent years, the use of 3D terrestrial laser scanning (TLS) seem to be increasing as its effectiveness in recording and documenting cultural heritage is widely documented. This is due to its capability to provide users with better

spatial information of structure in complex 3D scenes in a short period of time. The 3D colored point clouds data produced by the laser scanner can be used to give a realistic impression of a building or structure for users to interactively navigate the viewpoint around it. Moreover, it can be viewed from all the angles and position desired. In heritage and architecture, laser scanning has been adopted first for projects of major significant cultural value (Addison 2001, Eakin 2001, Levoy 2000, and Molenbrey 2001).

In this study, the practical use of 3D TLS in documentation of Watpasatharuam building structure will be demonstrated. The terrestrial laser scanner system used for this project is a laser scanner based, FARO Focus 3D. This system includes color digital camera to capture the high resolution images of the geometric model. This work evaluates the capability of FARO terrestrial laser scanner system for capturing high detailed architectural geometric data. The combination of 3D point clouds with the RGB information yield by photogrammetry technique will be presented. The 3D colored visualization model of Watpasatharuam was produced using FARO Scene. Further, this model will be used to plan effectively and efficiently renovation and interior design of the Watpasatharuam building structure.

2. METHODOLOGY

1. Terrestrial Laser Scanner	2. Data Registration and Texture Editing	3. 3D Visualization and Exporting
• Planning Scan Point • Scanning the Exterior and interior • Laser Scanning and Photographing	• Registration of 3D point cloud data • Applying RGB values • Editing texture and noises	• Visualizing 3D point cloud through FARO Scence • Rendering virtual model • Export for architecture designing and documenting

Figure 1 Methodology Workflow

2.1 Study Site Information and Project Plan

Nakhon Ratchasima is one of the northeastern provinces of Thailand. It is located on Korat plateau and mountainous terrain, covering an area of 20,494 sq. km. It is the largest Thai province and serves as the gateway to the lower northeastern region. The area is mainly within the high level plain, average range of elevations is 130-300 meters. The province is subdivided into 32 districts, 263 sub-districts, and 3,743 villages (http://www.tourismthailand.org/). Watpasatharuam is a long historic temple of Buddhism and is located in Nakhon Ratchasima province, Thailand. The temple was established in 2475 B.E (1932 A.D.) and covered the area of 0.25 sq.km. (134 rai). It is a significant center of spiritual and religious practices for the surrounding local communities. The temple nourishes the natural landscape and traditional architecture building. Up to date, the digital preservation of architectural information, historical building using advanced 3D measurement technologies is becoming an efficient tool. 3 Dimensional terrestrial laser scanning is rapidly becoming one of the most commonly used techniques due to its completeness, accuracy and fastness characteristics for data acquisition (Ong Chee Wei 2010, Naif Adel Haddad 2011, and Tredinnick et al. 2016).
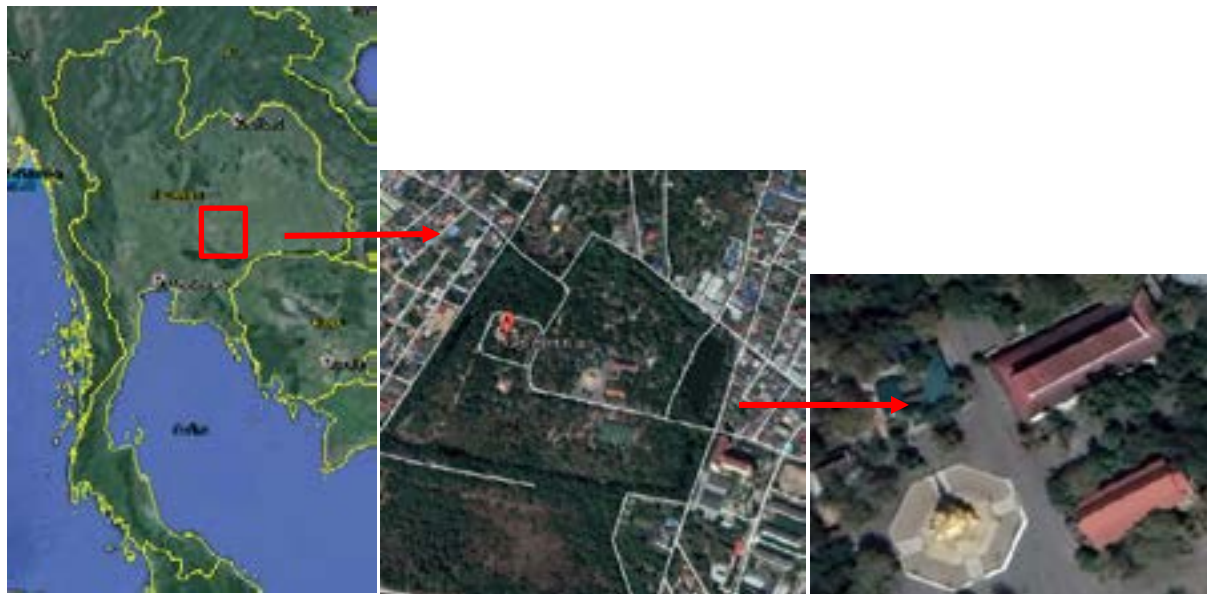
Figure 2 Study Site location and boundary: Watpasatharuam temple, Nakhon Ratchasima, Thailand

2.2 Data Acquisition

FARO Focus 3D Laser Scanner system (Figure 3), which uses laser, capable of capturing up to 976,000 points per second. The maximum captured range for this scanner is 150 meters with low ambient light on 90 percent reflective surface. The system is based on measuring principle and it provides a larger field of view of 360 degrees in horizontal direction and 300 degrees in vertical direction with 0.009 degrees accuracy, and allows the collection of full panoramic views, including color camera.

Figure 3 FARO Focus 3D Laser Scanner and Ancillary Equipment

The TLS data acquisition at the Watpasatharuam was carried out with the FARO Focus 3D laser scanner. The data capturing procedure was executed in two phase steps, laser scanning and photographing. The geometry and the intensity of frontage data were captured by the terrestrial laser scanner while the RGB values of the geometric object were captured by a high resolution digital camera. The Watpasatharuam has a detail features for its inner and outer shape. Hence, an appropriate scanning positions need to be established to capture the full coverage of the data. There were 16 captured scans to cover the whole Watpasatharuam structure. There were 4-6 sphere targets (reference target or control point) placed around the 3D space. The placing of the spheres targets must meet the requirement of minimum 3 corresponding points in two different station. Besides, the numbers of total scan station depends on the size and complexity of the structure of the building. Hence, appropriate scan station needs to be established for better coverage to cover all the details of the building. The distribution of the sphere targets has to be located at a distance around 2 meters to 5 meters from the scanner to obtain a good geometry network. The distribution of the sphere targets is very crucial in merging all images properly. The sphere targets need to set in a position that could be seen and corresponded between two scan stations which require minimum 3 common targets (Figure 4: a, b, c, d).

(a)   (b)

(c)   (d)

Figure 4 (a, b, c, d) Data Capturing Processes

2.3 Processing

The point cloud processing stage involves the basic checking of data, removal of bad point cloud caused by blocking object or false returns. FARO Scene was used to mesh the point clouds. The registration involved point clouds from a total of 16 scans location covered the whole Watpasatharuam structure with planned scan direction. There were 14 scans positions at the exterior part and 2 scans in the interior part of the Watpasatharuam. These point clouds have to be registered into one coordinate system in order to achieve a complete visualization model of the Watpasatharuam structure. Millions of points have been merged to get an integrated view. Before starting to mesh the point clouds, data filtering process need to be done to correct or remove the selected scan point from the raw data. This was determined by the selection criteria. The filters differ according to which method they identify an inaccurate scan point and which counter measure was then taken. The FARO Scene software was used to register the range data and produce a 3D visualization model based on registered point clouds. The registration of all scans were performed pair by pair by means of minimum 3 control points required to match two different data sets in one common coordinate system. Once

the scan registration was completed, a partial 3D model view of the Watpasatharuam structure was loaded in 3D form to check whether the two scans were correctly registered. The color information from the high resolution digital images would be fused with the 3D registered point clouds after the geometric object had correctly meshed (Figure 5: a, b, c, d, e, f, g).

(a)

(b)

(c)

(d)

(e)

(f)

(g)
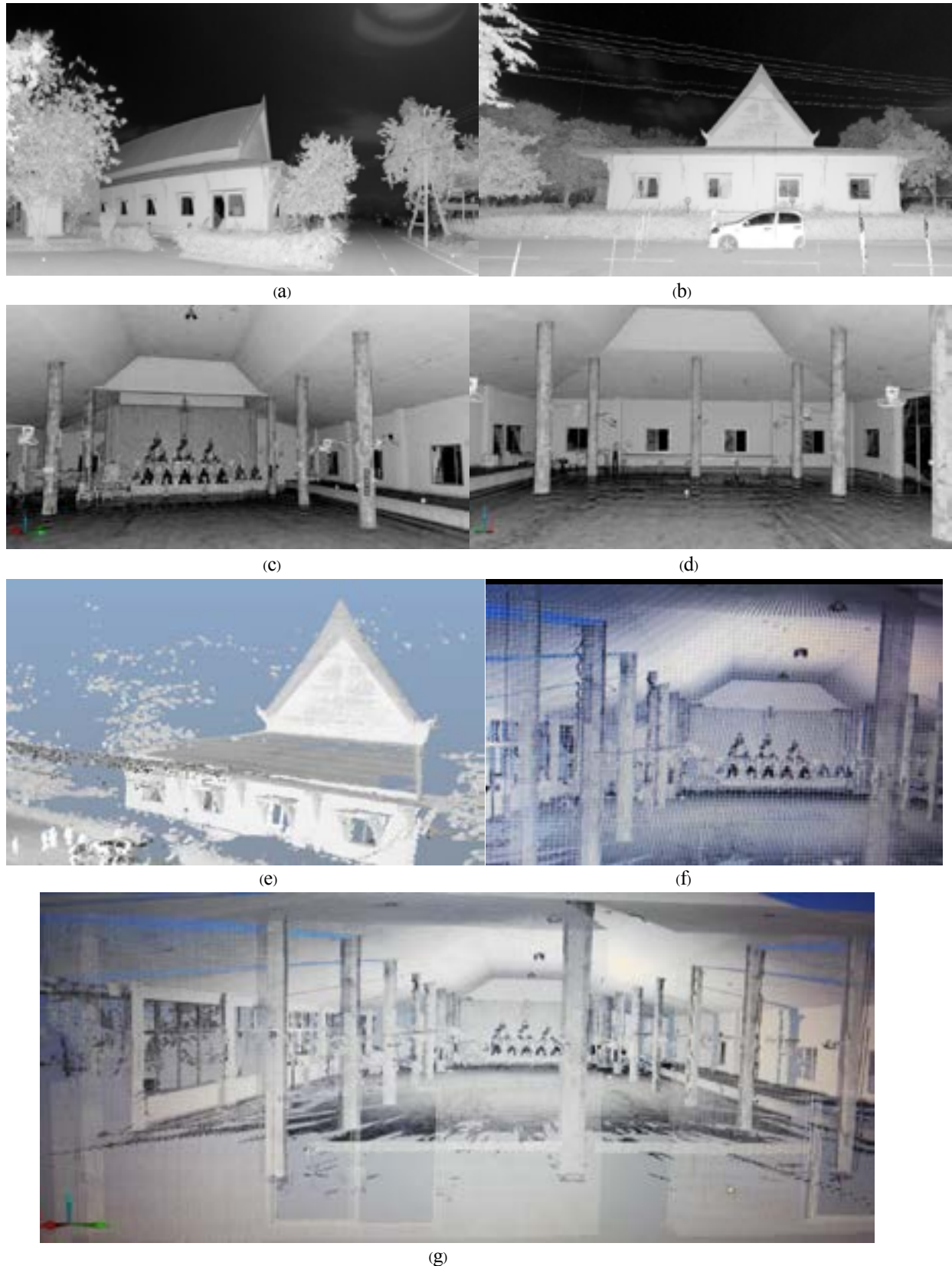
Figure 5 (a, b, c, d, e, f, g) Point Cloud Processing

2.4 3D Visualization

3D visualization and creation of walkthrough animation is followed by rendering of animation of the complete 3D registered colorized model was done through rendering software (Figure 6: a, b, c, d).

(a)

(b)

(c)

(d)
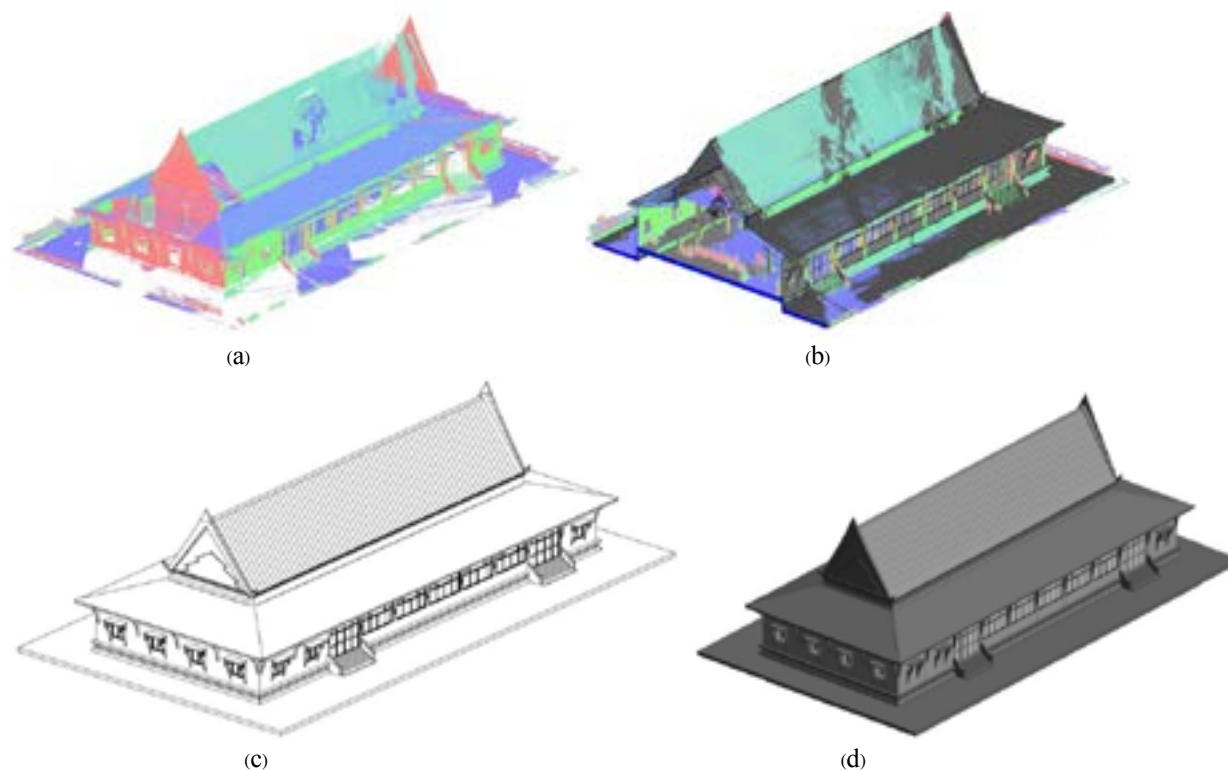
Figure 6 (a, b, c, d) 3D Visualization

3. RESULTS AND DISCUSSION

The use of 3D laser scanning has proven to be fastest in reconstructing the 3D buildings. More advantage of this method is the fact that not only buildings, but also others bodies, that would have been impossible to get their real shape using other methods can be scanned. It is important to note that during the scanning process, moving objects like vehicles and people can affect the real color of certain stationary and/or needed objects. This needs to be removed from the final data. The model provided very beneficial way for planning renovation and preservation of the building and depicting idea for applying interior decoration. This has proved efficient way for rendering large information into 3D model (Figure 7: a, b, c, d, e, f, g, h)
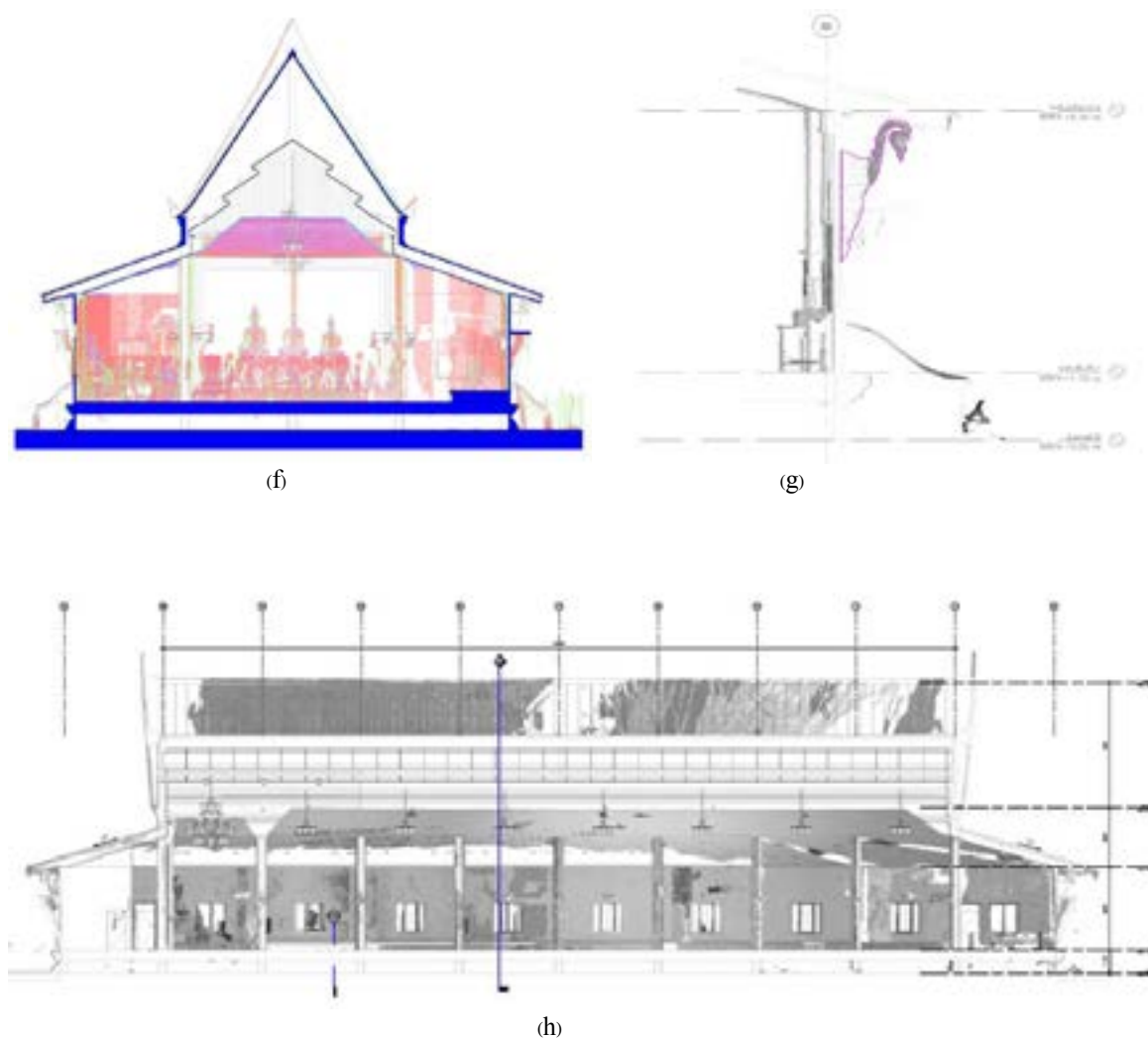

(a)

(b)

(c)

(d)

(e)

(f)

(g)

(h)

Figure 7 (a, b, c, d, e, f, g, h) Architectural Design Process

4. CONCLUSIONS

3D laser scanning technology makes it possible to provide real design and construction of buildings as well as, gaining survey information about a location or existing building to make well-informed calculations and designs. It used to document existing conditions in order to plan a project and create the initial design. It allows all the designers and architects to see closely what the actual conditions of the selected site study look like in full 3D. The benefits of 3D laser scanning technology are decreased field time, increased visibility and understanding, accurate spatial reconstruction and higher precision data that can be manipulated and applied to other processes via a computer. This takes less time and provides more accurate results when designing a building, planning construction and taking on a preservation and renovation project. Extracting data from these spatial models for statistical analyses could then be done within a GIS or CAD application. Virtual construction in 3D space will be required throughout the design process.

In conclusion, the study shows that 3D laser scanning technology provides effectively method of creating a 3D digital data collections for their archives. The initial 3D model provided very beneficial way for planning renovation preservation and documentation of the historic site, develop research ideas in other fields, and increase the potential of collaboration.

REFERENCES a cost-effective

Addison, A.C. 2001. Emerging Trends in Virtual Heritage. IEEE Multimedia, April –June, pp. 22-25.

Boehler, W. and Marbs, A. 2002. Investigating Laser Scanner Accuracy. Retrieved at http://scanning.fhmainz.de/scannertest/results300305.pdf on 02 September 2009

Cardaci, A., G. M. Roberti, and A. Versaci, 2011. From the Continuous to the Discrete Model: a Laser Scanning Application to Conservation Projects, Proceedings of the Congress of the International Society for Photogrammetry and Remote Sensing (ISPRS), pp. 437–444.

Eakin, E. 2001. Cyberslueths take on the mystery of the collapsing colossus. The New York Times, Saturday, October 27, 2001.

El-Hakim, S., Beraldin, A. and Picard, M., 2002. Detailed 3D Reconstruction of Monuments using Multiple Techniques. ISPRS/CIPA International Workshop on Scanning for Cultural Heritage Recording, Corfu, Greece, pp.58-64.

El-Hakim, S., Whiting, E., Gonzo, L., and Girardi, S., 2005. 3-D reconstruction of complex architectures from mltiple data. 3D Virtual Reconstruction and Visualization of Complex Architectures (3D-Arch'2005), August 22-24, Venice-Mestre, Italy, 8 pages. www.3dphotomodeling.org/3d-arch-05.pdf

Faro Technologies Inc. Faro Focus 3D Laser Scanner. Retrieved on April 2013, from http://www.faro.com/

Ruther H., Chazan M., Schroeder R., Neeser R., Held C., Walker S. J., Matmon A., and Horwitz L. K., 2009. Laser scanning for conservation and research of african cultural heritage sites: the case study of wonderwerk cave, south africa, Journal of Archaeological Science, vol. 36, no. 9, pp. 1847–1856.

Lerma J., Navarro S., Cabrelles M., and Villaverde V., 2010. Terrestrial laser scanning and close range photogrammetry for 3d archaeological documentation: the upper palaeolithic cave of parpall´o as a case study, Journal of Archaeological Science, vol. 37, no. 3, pp. 499–507.

Levoy, M., K. Pulli, B. Curless, S. Rusinkiewicz, D. Koller, L. Pereira, M. Ginzton, S. Anderson, J. Davis, J. Ginsberg, J. Shade, and D. Fulk., 2000. The Digital Michelangelo Project: 3D scanning of large statues, Proceedings SIGGRPAH 2000 (New Orleans, Louisiana, July 23-28, 2000), ACM SIGGRAPH, pp. 131–144.

Matías, J. D., F. Berenguer, J. Cortés, J. D. Sanjosé, and A. Atkinson, 2013. Laser Scanning for the Geometric Study of the Alcántara Bridge and Coria Cathedral, Proceedings of 3D-ARCH 2013 - 3D Virtual Reconstruction and Visualization of Complex Architectures, Trento, Italy, pp. 51–56.

Molenbrey, K., 2001. Preserving the Past. Computer Graphics World, pp. 24-30.

Naif Adel Haddad, 2011. From ground surveying to 3D laser scanner: A review of techniques used for spatial documentation of historic sites, Journal of King Saud University – Engineering Sciences.

Nakhon Ratchasima general information. Retrieved July 4, 2015 from http://www.tourismthailand.org/

Nettley, A., K. Anderson, C. DeSilvey, and C. Caseldine, 2013. Using Terrestrial Laser Scanning and LIDAR Data for Photo-Realistic Visualization of Climate Impacts at Heritage Sites, in Proceedings of the International Symposium on Photogrammetry, Remote Sensing and Spatial Information Sciences, pp. 223–229.

Ong Chee Wei, Cheong Siew Chin, Zulkepli Majid, Halim Setan, 2010. 3D Documentation and Preservation of Historical Monument using Terrestrial Laser Scanning, Geoinformation Science Journal, Vol. 10, No. 1, pp: 73-90.

Susan C. Kuzminsky and Megan S. Gardiner, 2012. Three-dimensional laser scanning: potential uses for museum conservation and scientific research, Journal of Archaeological Science 39: pp. 2744-2751.

Tredinnick R., Broecker M., and Ponto K., 2016. Progressive feedback point cloud rendering for virtual reality display,

in Virtual Reality (VR), IEEE, pp. 301–302.

Wang J., Zhang J., and Xu Q., 2014. Research on 3d laser scanning technology based on point cloud data acquisition, in Audio, Language and Image Processing (ICALIP), International Conference. pp. 631–634.

Wilson, L., A. Rawlinson, D. Mitchell, H. McGregor, and R. Parsons, 2013. The Scottish Ten Project: Collaborative Heritage Documentation, International Archives of the Photogrammetry, Remote Sensing and Spatial Information Sciences, Volume XL-5/W2. XIV International CIPA Symposium, Strasbourg.

Upgrading CityGML LOD-1 building models using airborne LiDAR data

Jhe-Syuan Lai (1), Fuan Tsai (2), Yu-Ching Liu (2), Ching-Sung Yang (2)

[1] Department of Civil Engineering, Feng Chia University, Taichung 40724, Taiwan.
[2] Center for Space and Remote Sensing Research, National Central University, Taoyuan 32001, Taiwan.
Email: jslai@fcu.edu.tw

KEY WORDS: 3D building model, level of detail, LiDAR, OGC CityGML, point cloud.

ABSTRACT: This study integrates OGC CityGML LOD-1 (Level of Detail) building models with airborne LiDAR (Light Detection and Ranging) data to refine the models to be conforming to the LOD-2 requirements. For reconstructing LOD-2 flat-roof building models, this study develops an automatic algorithm based on a majority operator to extract the heights of stories from point cloud data. Subsequently, the elevation of building models can be adjusted to be close to real height. For pitched roof buildings, a semi-automatic procedure is developed to adjust the elevation of building models vertex by vertex. Experimental results indicate that the averages and standard deviations of elevation differences, and the Root Mean Squared errors (RMSE) of the constructed models are 0.712, 0.489 and 0.964 meters, respectively. Further exploring the reconstructed results reveals an inconsistent building height criterion between the generated models and reference data. The elevation of a generated model is determined as the height of the roof floor (because of the majority of point cloud) from ground. However, the reference data is measured from ground to the top of parapet walls for better mapping texture façades using in-situ images, representing different viewpoints between data-acquisition process, geometric modeling and visualization. However, the quantitative validation results, from a technical perspective, are reasonable and conform to OGC CityGML LOD-2 building model requirements.

1. INTRODUCTION

Large-scale (1/1000) topographic map is an important geo-spatial dataset in Taiwan. The vector-based topographic maps provide detailed two-dimensional (2D) outlines of buildings, roads, infrastructures and other ground objects in urban areas. The OGC CityGML LOD-1 (Level of Detail) building models can be automatically and fast reconstructed from 1/1000 topographic maps but with limited or approximated height information of the reconstructed models (MOI, 2017). The objective of this study is to integrate point cloud data generated from LiDAR (Light Detection and Ranging) or close-range photographs and 1/1000 topographic maps to reconstruct building models conforming to OGC CityGML LOD-2 requirements (OGC, 2006). Four roof types in the study site are included (Fig. 1), i.e., flat, pitched, complex and cupola. The degree of reconstruction automation and difficulty is dependent on the roof type. Reconstructing flat and pitched roof based buildings is the scope of this study. In order to reconstruct LOD-2 flat-roof building models, this study develops an automatic algorithm based on a majority operator to extract the heights of stories from point cloud data. After that, the elevation of building models can be adjusted to be close to real height. To produce pitched roof buildings, this study develops a semi-automatic procedure to adjust the elevation of building models vertex by vertex. For model validation, this study compares the generated models with reference data, and calculates the averages and standard deviations of elevation differences and RMSEs (Root Mean Squared errors).
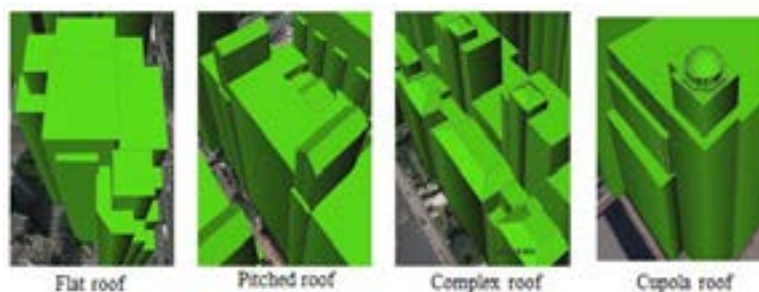

Fig. 1. Roof types in the study site

2. METHODOLOGY

The developed procedure is divided into two parts, i.e., the automatic and semi-automatic schemes to adjust the elevation and shape of the constructed LOD-1 building models (MOI, 2015) for the upgrade into the LOD-2

requirements. The automatic scheme is to determine the height of a flat roof based on the majority of point clouds as shown in Fig. 2. For the pitched roof, the semi-automatic procedure is designed to assign the height vertex by vertex as shown in Fig. 3. This study further compares the generated models of flat roof with reference data, and the averages (AVG) and standard deviations (SD) of elevation differences and RMSE are calculated. Equations of 1 to 3 show the formulas of AVG and SD of elevation differences, and RMSEs, respectively, where Z'_i and Z_i represent the elevations of the reference data and generated models, n indicates the number of vertices.

$$AVG = \frac{\sum_{i=1}^{n}(Z'_i - Z_i)}{n}$$

Eq. (1)

$$SD = \sqrt{\frac{\sum_{i=1}^{n}[(Z'_i - Z_i) - AVG]^2}{n-1}}$$

Eq. (2)

$$RMSE = \sqrt{\frac{\sum_{i=1}^{n}(Z'_i - Z_i)^2}{n}}$$

Eq. (3)
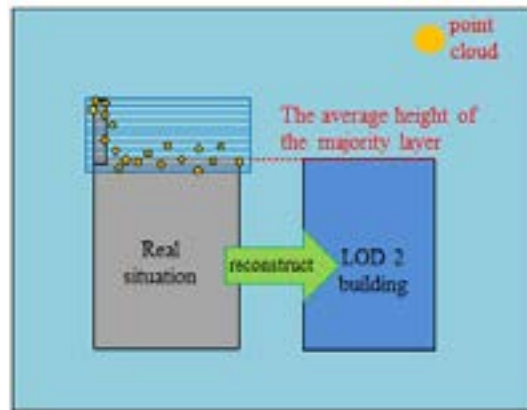
Fig. 2. The automatic scheme for flat roof
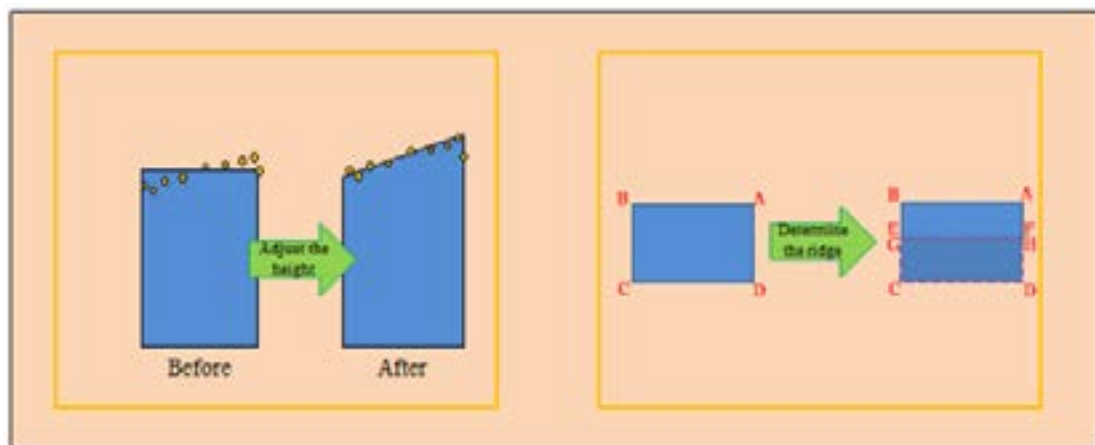
Fig. 3. The semi-automatic scheme for the pitched roof types

3. RESULTS

The purple area in Fig. 4 located in the Xinyi District, Taipei, Taiwan is selected as the study site. Based on MOI (2009), this study separates the study site into 100 by 100 meters grids, and randomly selects one of the buildings as check data in each grid. Fig. 4 shows the distribution of reference data for checking the constructed flat-roof models. For validation, Table 1 lists the total averages (AVG) and standard deviations (SD) of elevation differences, and RMSEs, which are 0.146, 1.705 and 2.198 meters, respectively. Among them, it should be noted that the cases of building 21, 23, 24 and 25 have large errors. To further explore, this study concludes three error sources in the study

cases as shown in Fig. 5. Firstly, Fig. 5(a) reveals an inconsistent building height criterion between the generated models and reference data. The elevation of a generated model is determined as the height of the majority of point cloud from ground. However, the reference data is measured from ground to the top of parapet walls for better mapping texture façades using in-situ images (so the top height of the constructed model covers some point clouds of top floor as shown in Fig. 5(a)). Secondly, the majority-based results are affected by other objects (e.g., water tower) and broad parapet walls as shown in Fig. 5(b). Finally, the point clouds are too insufficient to construct the small objects such as Fig. 5(c). The cases of building 21, 23, 24 and 25 belong to the third situation (i.e., Fig. 5(c)). To address this issue, this study adjusts the building height manually, and re-validates the developed models. Table 2 shows the improvements, and the overall results after adjustment are shown in Table 3. On the other hand, the results of pitched roof are also shown in Fig. 6. Based on visual analysis, the shape of constructed models are close to the reference data.

Fig. 4. Distribution of reference data for the flat-roof buildings

Table 1. Validation results of the averages (AVG) and standard deviations (SD) of elevation differences and RMSEs

Building ID	AVG (m)	SD (m)	RMSE (m)
1	0.452	0.202	0.494
2	1.247	0.295	1.281
3	0.216	0.408	0.461
4	0.679	0.382	0.778
5	0.420	0.834	0.920
6	0.704	0.423	0.818
7	1.308	0.724	1.488
8	0.402	0	0.402
9	0.921	0.863	1.252
10	0.739	0.651	0.980
11	1.110	0.429	1.188
12	0.628	0	0.628
13	1.277	0.463	1.355
14	0.579	0.423	0.713

Building ID	AVG (m)	SD (m)	RMSE (m)
15	-0.525	0.741	0.896
16	0.991	0.507	1.112
17	0.359	0.356	0.504
18	1.238	0.361	1.289
19	-0.399	0.634	0.744
20	1.472	0.554	1.572
21	-4.923	14.589	15.287
22	1.276	1.455	1.921
23	-2.395	2.371	3.357
24	-1.460	9.047	9.084
25	-2.665	5.907	6.420
Total AVG	0.146	1.705	2.198
Max value	1.472	14.589	15.287
Min value	-4.923	0	0.402

Table 2. Improvement of the building 21, 23, 24 and 25

Building ID	Adjustment	AVG (m)	SD (m)	RMSE (m)
21	Before	-4.923	14.589	15.287
	After	1.23	0.363	1.282
23	Before	-2.395	2.371	3.357
	After	0.315	0.227	0.387
24	Before	-1.460	9.047	9.084
	After	1.094	0.504	1.203
25	Before	-2.665	5.907	6.420
	After	0.071	0.426	0.427

Table 3. Overall evaluations after manually adjusting the building 21, 23, 24 and 25

	AVG (m)	SD (m)	RMSE (m)
Total AVG	0.712	0.489	0.964
Max value	1.472	1.455	1.921
Min value	-0.525	0	0.387
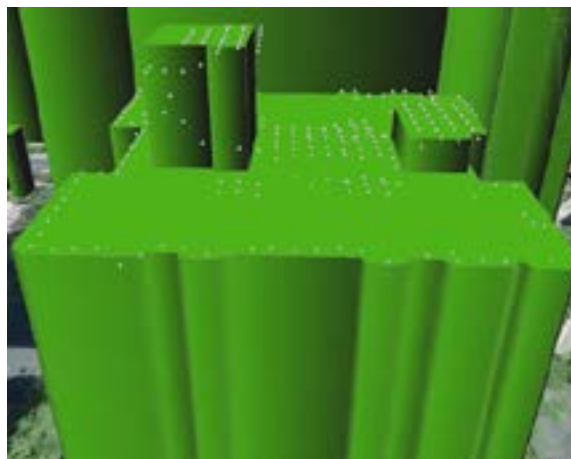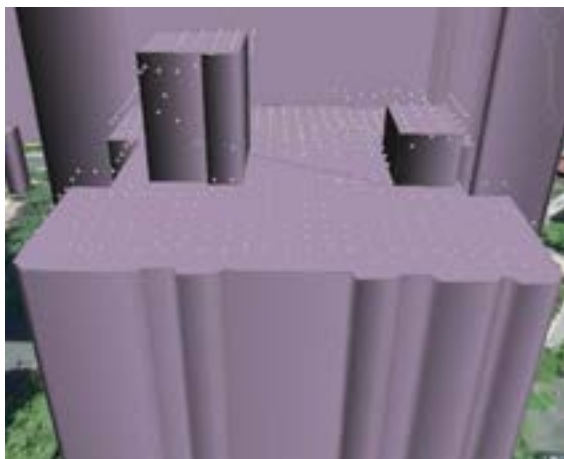
(a) different criteria for determining the top height of buildings overlap with the point clouds (left: from ground to the majority-based height; right: from ground to the top of parapet walls)

(b) the majority-based results are affected by other objects (e.g., water tower) and broad parapet walls

(c) insufficient LiDAR point clouds for construction of the small objects (left: reference data; middle: the constructed model based on the point clouds; right: adjust the constructed model manually)
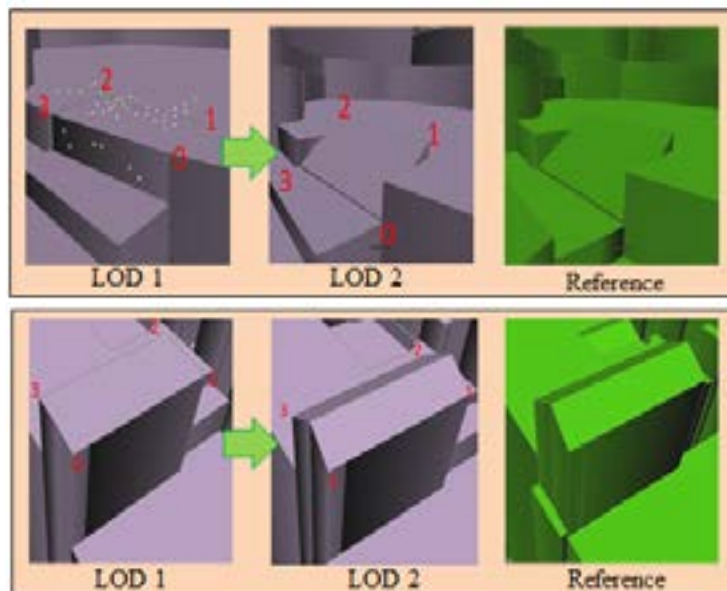
Fig. 5. Error sources in the study cases

Fig. 6. Constructed models of the pitched roof types

4. CONCLUSION

This study combines the OGC CityGML LOD-1 building models with airborne LiDAR data to upgrade the models to LOD-2. The case study demonstrates that the total AVG, SD of elevation differences and RMSEs of the constructed flat-roof models, after reducing the large errors in the special cases, are 0.71, 0.49 and 0.96 meters, respectively. Further exploring the reconstructed results discovers that these errors include an inconsistent building high criterion between the generated models and reference data. This inconsistence represents different points of view between data-acquisition process, geometric modeling and visualization. Nevertheless, from a technical perspective, the quantitative validation results are acceptable. The results of the flat and pitched roof building reconstructions also demonstrate the feasibility of proposed procedure for the OGC CityGML LOD-2 building model generation.

REFERENCES

- MOI, 2009. Standard Operation Document for 3D Building Model Reconstruction, 1st Version Report, p. 17 (in Chinese).
- MOI, 2015. Integration of 3D Digital City and Architectural Models (II), Final Report, p. 321 (in Chinese with English abstract).
- MOI, 2017. Development of 3D Topographic Mapping Technology, Final Report, p. 211 (in Chinese with English abstract).
- OGC, 2006. Candidate OpenGIS CityGML Implementation Specification (City Geography Markup Language), p. 120.

AN ALGORITHM OF PIPELINE POINT CLOUD EXTRACTION USING L$_1$-MEDIAL SKELETON

Kai Huang(1), Xiaojun Cheng(1), Yanping Liu (2), Lishuo Zhang (1), Danhua Hu (3)

[1] College of Surveying and Geo-Information, Tongji University, Shanghai 200092, China

[2] Department of Civil Engineering, Tongji Zhejiang College, Jiaxing,Zhejiang 314051, China

[3] Fujian Electric Power Survey & Design Institute Co.,Ltd, Fuzhou, Fujian 350003, China

Email: 1633312@tongji.edu.cn

KEY WORDS: Lidar; L$_1$-Medial Skeleton; Random sample consensus algorithm; Dense pipeline

ABSTRACT: In order to solve the problem of pipeline extraction in massive point cloud, we propose a new method for automatic segmentation of dense pipeline with circular section based on the algorithm of L$_1$-medial skeleton construction. The algorithm mainly consists of four steps. First, the point cloud of plane is filtered out based on general algorithms such as RANSAC to obtain high quality data. Then, the point cloud is downsampled using octree decomposition and the L$_1$-medial skeleton is calculated in parallel by the neighborhood point set of the sample points which is extracted using the Euclidean cluster extraction according to the spatial distribution of the point cloud. Finally, we reorient the skeleton to the cylinder axis along the direction of the skeleton, and analyze the connectivity of the skeleton to get the result. We apply this algorithm to scenarios such as simulation data and power plants with incomplete cloud data and dense pipelines. The experimental results show that the algorithm proposed in this paper can extract pipeline and obtain skeleton quickly and accurately when the data is incomplete.

1. INTRODUCTION

Because of the depreciation and limited lifespans of industrial products, the renewal of plant equipment is inevitable. It is necessary to collect the current data and generate the necessary spatial information before renovating the power plant and updating facilities. Pipelines play an important role in the operation of existing refinery, chemical and power plants. However, there are usually a large number of floors, walls, steel structures and many temporarily stacked items in plants besides various types of pipes. Therefore, the accurate extraction of the location of the pipeline is very important for the transformation of plants.

Light detection and ranging (LiDAR) originated in the early 1960s. With the rapid development of the theory and the technology of processing of massive point cloud, 3D laser scanning has become a common means of surveying. 3D laser scanner can quickly and comprehensively collect spatial data of shapes. At the same time, data redundancy has become a difficult problem in reconstruction of objects. The traditional pipeline segmentation method is mainly through human-machine interactive extraction, which has a large workload and extremely low efficiency especially

in scenes with enormous and complex laser-scanned data Therefore, a method of pipeline point cloud segmentation and fast extraction of valid information needs to be proposed.

Point cloud segmentation methods generally categorized into five classes (Nguyen et al. 2013) : edge based methods, region based methods, attributes based methods, model based methods and graph based methods. Circular pipeline can be segmented by the method of cylindrical fitting and the method of surface fitting. The method of cylindrical fitting can directly obtain the axis direction and radius of the pipeline. The method of surface fitting calculates the radius and axis direction of the pipeline by the curvature and covariance matrix of the surface (Son et al. 2013; Kawashima et al. 2014; Su et al. 2016). Surface fitting can be used to segment the pipe and plane by the curvature of the surface, but this method is cumbersome and sensitive to noise.

Vosselman et al. (2008) used the surface growing technique to segment point cloud into planes and cylinders, then they analyzed the surface smoothness to group all points on a series of connected cylinders to one segment where the pipes were extracted by fitting the cylinders. The method of cylindrical fitting is to plotted the normal vector of the point cloud on the Gaussian sphere, thereby extracting the cylinder axis directions and transforming the cylindrical fitting into circular fitting (Chaperon et al. 2001; Vosselman et al. 2008).Rabbani et al. (2012) proposed a region growing segmentation algorithm using smoothness constraint. The algorithm uses only surface normal as a measure of local geometry, which are estimated by fitting a plane to the neighborhood of the point. This algorithm can segment the point cloud into collections of similar local geometric features, but cannot distinguish between planes and surfaces.

The skeleton of an object is a 1D representation providing an intuitive and topological abstraction that helps shape understanding and manipulation. The best known example is Blum's medial axis transform(MAT) (Blum, 1967). Tagliasacchi et al. (2009) proposed an algorithm for extracting curve skeleton from incomplete point cloud. Their construction is primarily based on rotational symmetry axis (ROSA) of an oriented point set. They presented an iterative algorithm via planar cuts to compute the ROSA of a point cloud. The calculation of Mahalanobis distance (Daszykowski, 2007) and the normal vector of the point cloud are needed in the construction process. Its calculation process is cumbersome and it means that noise and outliers need to be filtered out before extracting the skeleton.

Compared to Tagliasacchi's skeleton extraction, the L_1-medial skeleton (Huang et al. 2013) can be directly applied to unorganized and unoriented point cloud with noise, outliers and areas of missing data. The algorithm computes the position of the skeleton point by iteration and only requires the spatial position of the neighborhood in the calculation process without using normal vectors of the point cloud. The robust characteristics of the L_1-medial skeleton and its simple iterative process make it ideal for the extraction of dense pipeline skeletons from point cloud.

In this paper, we propose an algorithm for extracting pipeline from massive point cloud. We first try to filter out the non-pipeline data in the point cloud to reduce the amount of data that needs to be processed in subsequent calculations. The approximate direction of the pipeline is obtained by calculating the skeleton of point cloud using the algorithm of L_1-medial skeleton extraction. The L_1-medial skeleton is then reoriented using RANSAC according to the local

point cloud along the skeleton direction. Finally, by analyzing the local connectivity of the skeleton points, we merge and join some pipeline skeletons to get the final outputs

2. OVERVIEW

As shown in Figure 1, the algorithm of pipeline skeleton extraction proposed in this paper mainly includes four steps: plane filtration, skeleton extraction, skeleton reorientation, and connectivity analysis.
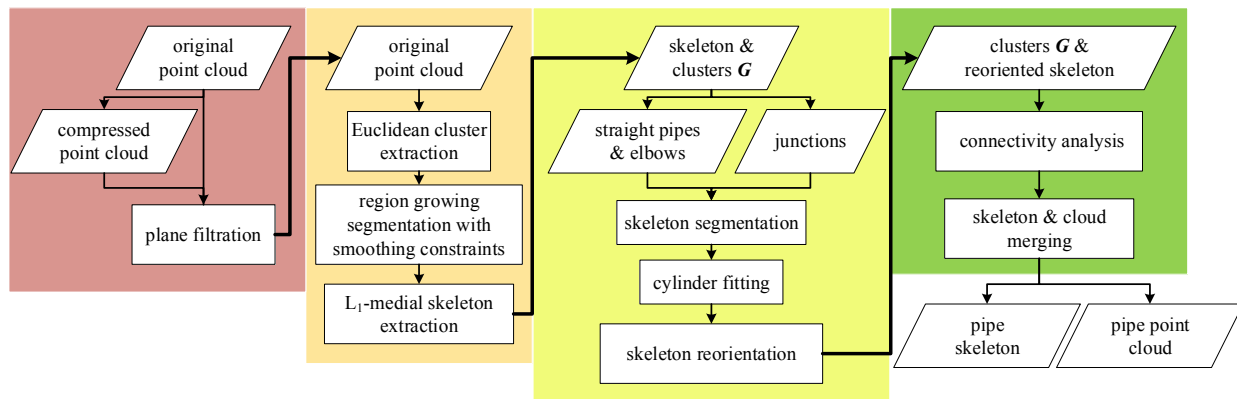

Figure 1. Algorithm flow chart

2.1 Plane Filtration

The local geometrical characteristics of point cloud of pillars, slabs and walls in plants are mostly flat, which means that these structures can be divided into several planes. Unlike planar structures, the point cloud of pipeline is curved surface. If the skeleton extraction of the pipeline from point cloud is performed without pre-processing, the execution time of the algorithm will be greatly increased due to the excessive amount of data, and the point cloud irrelevant to the pipeline will have great influence on the extraction of pipeline skeleton. To solve this problem, the first step in point cloud processing is to filter out the irrelevant data as much as possible. We remove the point cloud of plane using RANSAC (Schnabel et al. 2010) to reduce the amount of data that needs to be processed later. Given an unorganized and unoriented point cloud $P=\{p_i\}$, in order to speed up the plane fitting and improve the local accuracy, we compress P by the distance between the points to obtain the compressed point cloud $W=\{w_i\}$, and then splitting the dataset P and W into bins using octree decomposition with the same resolution d_1. For each of the subsets an octree is constructed, so that during the plane fitting only the points lying in cells and distance within ε_1 to the plane have to be considered. The point cloud of plane in the subsets of P will be filtered out by plane parameters, which is calculated in the corresponding subsets of W.

Various components in plants are directly or indirectly connected through large planes such as floors, walls, etc. After filtering out the point cloud of large planar, the individual components are spatially separated from each other. In order to ensure a better result of the skeleton extraction of pipeline, it is necessary to filter out the small planes still existing in the point cloud. Using Euclidean cluster extraction (Rusu, 2008) with distance threshold ε_2, point cloud

separated from each other in space are clustered into $C=\{c_i\}$. Then, using the region growing segmentation with smoothing constraints (Rabbani et al. 2012), C is subdivided into several clusters $R=\{r_i\}$ with similar local geometric features. The point cloud of plane is filtered out by analyzing the covariance matrix (Rusu, 2008) of the point cloud in each cluster of $R=\{r_i\}$:

$$
\begin{cases}
D = \dfrac{1}{k}\sum_{i=1}^{k}(p_i - \bar{p})(p_i - \bar{p})^{\mathsf{T}}, \; D \bullet v_j = \lambda_j v_j, \; j \in \{0,1,2\} \\[2mm]
\sigma_j = \dfrac{|\lambda_0|}{|\lambda_0| + |\lambda_1| + |\lambda_2|}, \qquad\quad \text{if } 0 \le \lambda_0 \le \lambda_1 \le \lambda_2
\end{cases}
\tag{1}
$$

where k is the total number of cluster r_j, p_i is the position (column vector) of the i-th point in cluster r_j, D is the covariance matrix of cluster r_j, λ_n and v_n are the n-th eigenvalue and eigenvector of the covariance matrix. Based on the value of σ_j, determine whether the cluster r_j is approximate to a plane and whether it needs to be filtered out. To get high quality point cloud $U=\{u_i\}$, Sparse Outlier Removal (SOR) (Rusu, 2008) is used for point cloud filtering after removing the point cloud of plane. The effect of the removal of the planar area is very important for skeleton extraction. Because the planar structure usually occupies the majority of scanned data in plants, and the skeleton extraction of plane is meaningless.

2.2 Skeleton Extraction

After planar filtration, if RANSAC is used to fit the cylinder to extract the pipeline, although it can quickly fit the straight section of the pipeline, it is difficult to judge the connection relationship between the pipelines from the fitted straight section. In addition, the original data need to be compressed to speed up the fitting of geometric model in massive point cloud. However, excessive compression will weaken the cylindrical geometric characteristics of point cloud on pipeline surface and affect the fitting accuracy.

We extract the skeleton of the point cloud and then fit the cylinder using RANSAC follow the direction of the skeleton. As mentioned in Section 1, the extraction of L$_1$-medial skeleton does not need to estimate normal vectors of the point cloud, but directly uses the position of the original point cloud for iterative calculation (Huang et al. 2013):

$$
\underset{\mathrm{x}}{\text{argmin}} \sum_{i \in I} \sum_{j \in J} \left\| x_i - q_j \right\| \theta\!\left(\left\| x_i - q_j \right\| \right) + R(x)
\tag{2}
$$

where the first term is a localized L$_1$-median of Q, the second term $R(x)$ regularizes the local point distribution of x, I indexes the set of projected points X, and J indexes the set of input points Q. The weight function $\theta(r) = e^{-r^2/(h/2)^2}$ is a fast decaying smooth function with support radius h defining the size of the supporting local neighborhood for L$_1$-medial skeleton construction.

3101

In order to distribute the seed points evenly, we splitting the dataset U into smaller bins using octree decomposition with a smaller resolution d_2. Select the nearest points of the center of bins as the set of seed points $S=\{s_i\}$, if there is point cloud in the bin.

In the extraction of L_1-medial skeleton $X=\{x_i\}$, every seed point needs to search the neighborhood in point cloud for each iteration. Since U was split into bins using octree decomposition with resolution d_1 in Section 2.1, the algorithm proposed in this paper searches only the neighborhood of the seed point in the subset of U where the seed point is located. To reduce the interference of external points, Euclidean cluster extraction is carried out with threshold ε_3, which is preferably smaller than the distance between two pipes, in the neighborhood of seed points, and then the position of skeleton points is calculated using the equation (2) by the clusters where the nearest points of seed points are located. Record the nearest neighbor cluster corresponding to the skeleton point $X=\{x_i\}$ as $G=\{g_i\}$
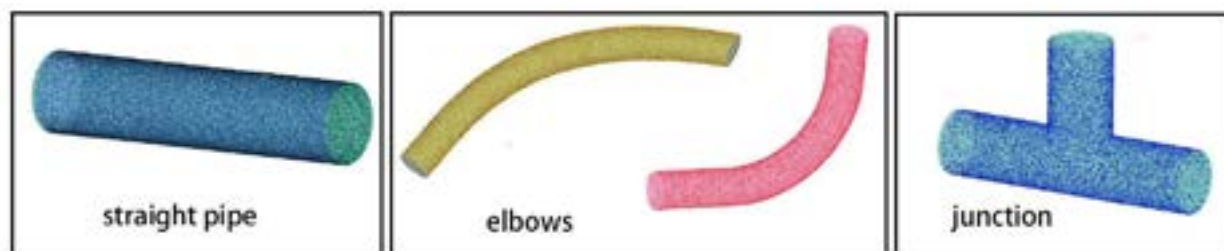
Figure 2. Type of pipe segmentation

As shown in Figure 2, the types of pipeline is divided into straight pipes, elbows and junctions. Since the L_1-medial skeleton is calculated by the equation (2), the L_1-medial skeleton is actually not the geometric axis of the cylinder. Seed point selection and L_1-medial skeleton extraction are both random But the L_1-medial skeleton can provide us with an approximate direction of the pipeline, along which we can reorient the L_1-medial skeleton to the geometric axis of the pipeline.
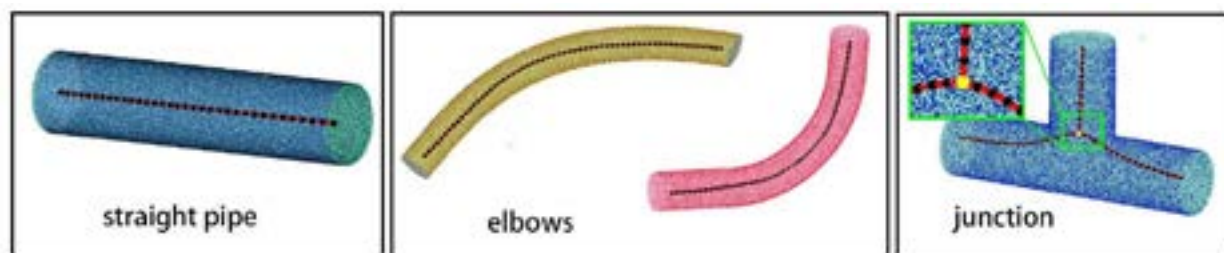
Figure 3. Skeleton of pipe segmentation (branch points are labeled in black and bridge points in yellow).

2.3 Skeleton Reorientation

For the straight pipes, we reorient the L_1-medial skeleton by cylindrical fitting using RANSAC along the direction of L_1-medial skeleton. For the elbows, the skeletons are approximated by piecewise cylindrical fitting. For the junctions, the skeletons are reoriented by calculating the intersection points of the axes of the pipes. The points in L_1-medial

skeleton can be divided into branch points and bridge points (points with more than two connected points, as the yellow point in Figure 3). We classify L₁-medial skeleton into two categories: with bridge points (pipeline with junctions) and without bridge points (pipeline without junctions).
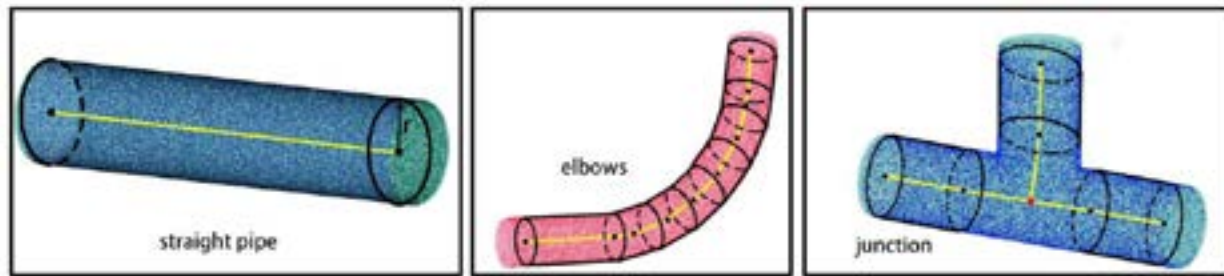
Figure 4. Skeleton after reorientation

Skeleton without bridge points (pipeline without junctions): Calculate the angle of the skeleton point from the start point to the end point along each skeleton:

$$\theta_i = \arccos(\frac{|\overrightarrow{x_i x_{i-1}} \bullet \overrightarrow{x_i x_{i+1}}|}{|\overrightarrow{x_i x_{i-1}}||\overrightarrow{x_i x_{i+1}}|}) \ , 2 \leq i \leq max\{I\} - 1 \tag{3}$$

Where I indexes the set of skeleton points X. Set an angle threshold θ_t (<10°) and track from θ_1 to the end point along the skeleton direction.

(a) If the angle between θ_A and θ_B is all smaller than θ_t, it is considered that the segmentation of the skeleton from x_A to x_B is a straight pipe. The cylinder is fitted using RANSAC by clusters G where the nearest points of x_A to x_B are located. Project x_A and x_B onto the cylinder axis, and the two projection points serve as the new skeleton points of this section of the pipeline.

(b) If the angle θ_i is greater than θ_t, the planes are constructed by the normal direction of $\overrightarrow{x_{i-2}x_{i-1}}$ at x_{i-1} and $\overrightarrow{x_{i-1}x_i}$ at x_i. The cylinder is fitted using RANSAC by clusters G where the nearest points of x_A and x_B are located. Project the midpoint of x_A and x_B to the axis of the cylinder, and projection point is taken as a new skeleton point.

Skeleton with bridge points (pipeline with junctions): Take bridge points as the starting points. Calculate the angle of the skeleton point from the bridge point to the end point along each skeleton using equation (3). Tracking from the bridge point to end points along direction of each skeleton until the segmentation with k (k =5 by default) connected skeleton points whose angles are all smaller than θ_t is obtained. Treat the segmentation of the connected k skeleton points as three straight pipes and process each of them according to the above method of skeleton without bridge points. Compute the angle between the three pipe axis directions, and consider that the two pipes with smaller angles are the main pipeline of the junction. Connect the two points of mail pipeline closer to the bridge point as the junction

axis. We construct a plane parallel to the axis of the branch pipe through the junction axis, and then project the axis of the branch pipe to the plane, so we can get the intersection point x_S on the junction axis. Connect x_S and the nearest point to the bridge point on the axis of the branch as the branch axis of the junction. The rest of the skeleton is reoriented according to the above method of skeleton without bridge points.
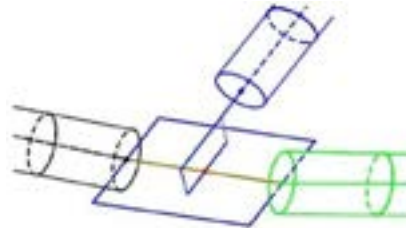

Figure 5. Junction reorientation

2.4 Connectivity Analysis

After reorienting the axes of the pipes, we can predict some missing parts of the data based on the spatial relationship of the skeleton. Compared with point cloud, the total number of skeleton points is very small, so it is easier to predict the missing part of pipeline based on skeleton points. Set the distance threshold to ε_S, the radius difference threshold to ε_R, and the angle threshold to ε_β. If the distance between the endpoints of the skeleton, the difference in the radius of the pipe and the angle between the axes are all smaller than the thresholds, it is considered that the two pipes are connected, then the two ends are connected and the data is merged into one pipe.

3. RESULTS AND APPLICATIONS

We scanned some areas in a power plant with dense pipelines. After registration, the point cloud is shown in Figure 6. It can be seen that the data of the pipeline point cloud is incomplete. To test the effectiveness of the algorithm of the pipeline extraction proposed in this paper, we extract the skeleton of dense pipeline in the cloud. Since the ground and wall flatness of the power plant is low, the distance threshold ε_1 is set to 0.025 m, and the remaining parameters are shown in Table 1. As shown in Figure 7, after plane filtering, the planar point cloud is mostly removed, but there is still some non-pipeline data in the point cloud. In order to present the experimental results, we extract a subset of point cloud using octree decomposition to show the effect of each step in Figure 8.
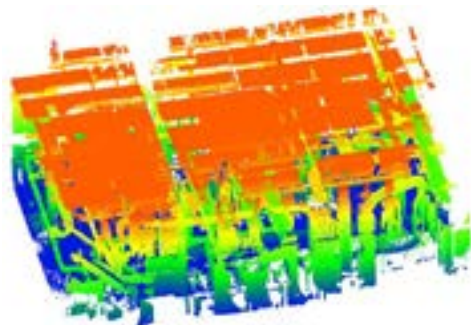

Figure 6. Point cloud after registration

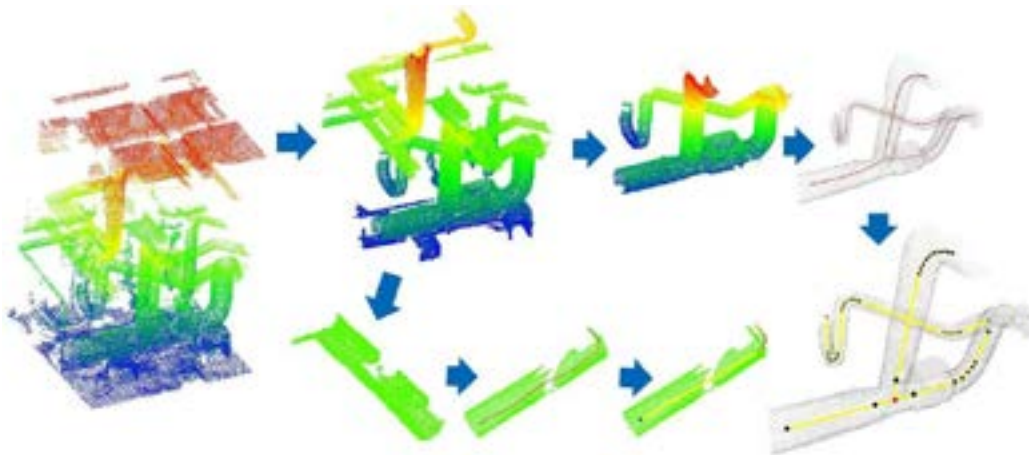Figure 7. Point cloud after plane filtering

Figure 8. The effect of each step in the subset

As shown in Figure 8, the L_1-medial skeleton is not coincided with the axis of the pipeline. After reorientation, the skeletons of the pipeline approach the axes of the pipeline at the elbows, coincide with the axes at the straight pipe and well represent the spatial topological relationship of the pipe at the junctions.

Table 1. Parameters in experiment

Parameter	d_1(m)	ε_1(m)	ε_2(m)	d_2(m)	θ_t(°)	k	ε_S(m)	ε_R(m)	ε_β(°)
value	4	0.025	0.1	0.05	4	5	0.3	0.08	7

3.1 Limitations

When there is too much noise or missing data in the point cloud, the skeleton we extracted using L_1-medial skeleton may not be accurate enough, which will have a bad influence on the subsequent skeleton reorientation and connectivity analysis, and eventually lead to erroneous outputs.

4. CONCLUSION AND FUTURE WORK

We demonstrate the effectiveness of our algorithms which based on L_1-medial skeleton extraction to extract pipeline from noisy and incomplete point cloud. L_1-medial skeleton can provide us with the spatial geometry information of shapes, especially for artificial objects with cylindrical components, which provide a more intuitive abstraction. But the L_1-medial skeleton is not the axis of the pipeline. The more the pipeline data is missing, the greater the deviation between the L_1-medial skeleton and the pipeline axis. However, it is inevitable that the pipe point cloud is incomplete due to obstruction when scanning in plants, and the noise cannot be completely filtered out during data preprocessing. We get the axis of the pipeline through skeleton correction and connectivity analysis and the axis accurately represents the location of the pipeline.

As for future work, we would like to apply our technique to more places, more objects, such as steel structures and towers. We would also like to explore the possibility of using the extracted skeletons to assist point cloud repair and model reconstruction.

References

Blum, H. 1967. A transformation for extracting new descriptors of shape. Models for the Preception of Speech & Visual Form, 19, 362-380.

Chaperon, T., & Goulette, F. 2001. Extracting Cylinders in Full 3D Data Using a Random Sampling Method and the Gaussian Image. Vision Modeling and Visualization Conference (pp.35-42). DBLP.

Daszykowski, M., Kaczmarek, K., Heyden, Y. V., & Walczak, B. 2007. Robust statistics in data analysis — a review : basic concepts. Chemometrics & Intelligent Laboratory Systems, 85(2), 203-219.

Huang, H., Wu, S., Cohen-Or, D., Gong, M., Zhang, H., & Li, G., et al. 2013. L1-medial skeleton of point cloud. Acm Transactions on Graphics, 32(4), 1-8.

Kawashima, K., Kanai, S., & Date, H. 2014. As-built modeling of piping system from terrestrial laser-scanned point clouds using normal-based region growing. Journal of Computational Design & Engineering, 1(1), 13-26.

Nguyen, A., & Le, B. 2013, November. 3D point cloud segmentation: A survey. In RAM (pp. 225-230).

Rabbani, T., Heuvel, F. A. V. D., & Vosselman, G. 2012. Segmentation of point clouds using smoothness constraint. International Archives of Photogrammetry, Remote Sensing & Spatial Information Sciences (Vol.36).

Rusu, R. B., Marton, Z. C., Blodow, N., Dolha, M., & Beetz, M. 2008. Towards 3d point cloud based object maps for household environments. Robotics & Autonomous Systems, 56(11), 927-941.

Schnabel, R., Wahl, R., & Klein, R. 2010. Efficient ransac for point‐cloud shape detection. Computer Graphics Forum, 26(2), 214-226.

Son, H., & Kim, C. 2013. Fully automated as-built 3d pipeline segmentation based on curvature computation from laser-scanned data. American Society of Civil Engineers, 765-772.

Su, Y. T., Bethel, J., & Hu, S. 2016. Octree-based segmentation for terrestrial lidar point cloud data in industrial applications. Isprs Journal of Photogrammetry & Remote Sensing, 113, 59-74.

Tagliasacchi, A., Zhang, H., & Cohen-Or, D. 2009. Curve skeleton extraction from incomplete point cloud. (Vol.28, pp.1-9). ACM.

Vosselman, G., Gorte, B. G. H., Sithole, G., & Rabbani, T. 2008. Recognising structure in laser scanner point clouds. International Archives of Photogrammetry Remote Sensing & Spatial Information Sciences, págs. 94-95.

ESTABLISHING METHOD OF 3D GEOLOGICAL MODELS BASED ON AIRBORNE LIDAR DATA AND BIM TECHNOLOGY

Zhenlun Wu (1), Xiaojun Cheng (1), Huanqiang Li (2), Zexin Yang (1)

[1] College of Surveying and Geo-Informatics, Tongji University, No. 1239, Siping Road, Shanghai 200092, China

[2] Institute of Design&Research, Zhejiang Province, No. 89, Huanchen Western Road, Hangzhou 310006, China

Email: 1633313@tongji.edu.cn; cxj@tongji.edu.cn; li.huanqiang@qq.com; zexinyang@tongji.edu.cn

KEYWORDS: Airborne LiDAR; Point Cloud Filtering; Surface Fitting; DTM; BIM

ABSTRACT: BIM (Building information model) technology has played a significant role in infrastructure engineering design in recent years. The common 2D topographic map measured by digital mapping cannot satisfy the requirement of BIM 3D design. Therefore, the main objective of this study is to establish 3D geological models for BIM 3D design based on Airborne LiDAR data and geophysical data. ALS (Airborne Laser Scanners) is one of the most effective and reliable means of terrain data collection, using LiDAR data for DTM (Digital Terrain Model) generation is becoming a standard practice in spatial related areas. However, original ALS point cloud cannot be used directly due to the low elevation precision and the influence of non-ground data, while this method is more effective in filtering LiDAR ground point cloud, retaining continuous undulate topography at the same time, and obtaining high precision DTM and 3D geological models through 3D point cloud and geophysical data. Firstly, selecting CSF (Cloth Simulation Filtering) algorithm which constructs virtual grid to simulate terrain surface and filter the residual highway and bridge point cloud by RGB features. Next, by fitting the quadric surface by the RTK (Real-Time Kinematic) control points and using the quadric surface equation to correct the elevation value of point cloud, the high precision DTM can be obtained via revised point cloud data. Then, 3D geological models can be established by geophysical data and DTM. The experimental results show that the 3D geological models generated basing on ALS data and geophysical data can satisfy the requirement of BIM 3D design.

1. INTRODUCTION

Terrain data is the basis of BIM 3D design and the traditional highway and survey design is based on 2D topographic map, while BIM highway and survey design needs to transform from 2D drawings to 3D models. Therefore, it is essential to establish 3D geological models by LiDAR data and geophysical data to assist with BIM 3D design. DTM, as a significant topographic product, is important for establishing 3D geological models, which represents the earth's surface without any additional objects on its plane. The common methods for DTM creation are very costly and time consuming due to terrain points surveying (Drăguţ, L et al., 2006; Niekerk, A. V., 2010). Recently, ALS has become one of the most effective and reliable means of terrain data collection (Liu, X., 2008), using LiDAR data for DTM generation is becoming a standard practice due to merit of collecting 3D information very effectively over a large area by means of precision and time. The common workflow of DTM generation involves point cloud coordinate conversion, filtration of the ground points and interpolation of the

DTM surface, therefore, the methods of coordinate conversion, filtration and interpolation will influence precision of DTM (Aguilar, F. J et al., 2005). The methods of point cloud filtering and interpolation has long been the research interests for many previous studies. The main filtering approaches of point cloud can be categorized into the following four classifications which are statistical-based, neighborhood-based, projection-based and PDEs-based filtering (Schall, O et al., 2008). Besides, Digne et al. (2012) proposed a similarity based on filtering to denoise point cloud and quadtree-based filtering method has been used for filtering point cloud which creates a quadtree as a data structure to organize a point cloud. Several previous studies have also utilized interpolation algorithms to fill holes of filtered ALS data. Brovelli, M. A et al. (2002) have utilized spline interpolation to repair the DTM of hilly area. In the study of Kraus et al. (2001), they have utilized hierarchical robust interpolation for vegetation points. However, only few studies proposed a DTM generation for 3D Geological Models requested by BIM 3D design. In this paper, we carefully propose an establishing method of geological models for highway and survey BIM 3D design which is based on geophysical data and DTM generated by ALS data. In addition, we also analyze whether the model precision meets the design specification requirements.

The paper is organized as follows. We first introduce the proposed method in Section 2. Then in Section 3, the experiments conductions are described and the experimental results are carefully discussed. Finally, conclusions follow in Section 4.

2. PROPOSED METHOD

Figure 1 provides an outline of proposed method. The original ALS data obtained is firstly conversed to independent engineering coordinate system. Then, divide the point cloud into two classes (highway and bridge point cloud, residual point cloud) by RGB features, and select CSF algorithm to filter the non-ground points of two classifications respectively. Based on quadric surface fitting, the elevation correction model related to RTK control points and terrain point cloud is established, which is used for generating high precision DTM. Afterwards, geological models can be established by geophysical data and DTM with the BIM design software.
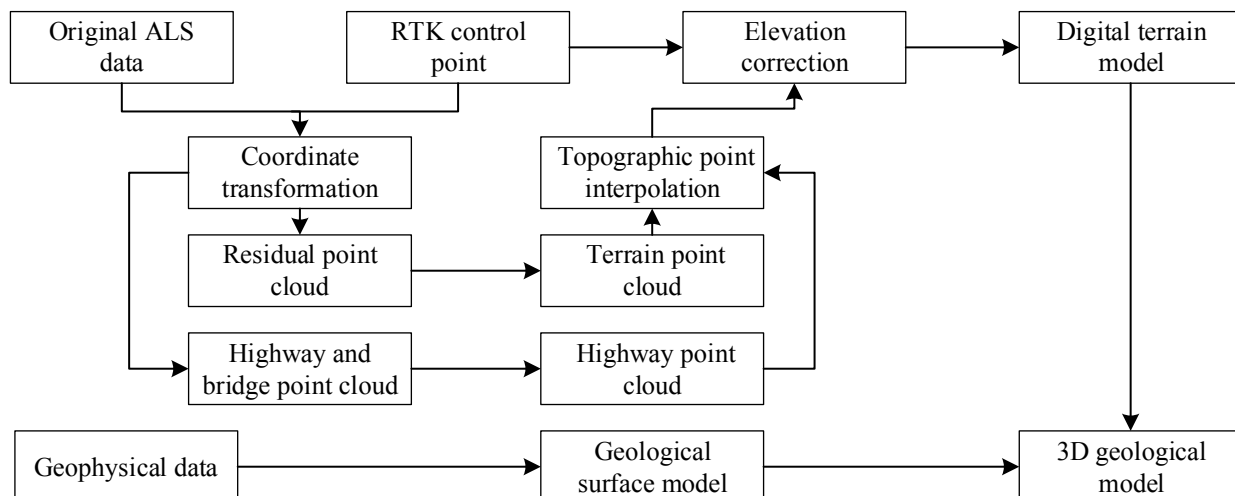

Figure 1 The outline of the proposed method

2.1 Coordinate transformation

Formally, a point cloud can be written as $P = (x, y, z, R, G, B)$, consisting of the coordinates x, y, z of the 3D point, and the RGB values R, G, B. The original point cloud obtained by LiDAR system is based on scanner coordinate system, while in real projects, the highway designs are always processed under the independent engineering coordinate system (Wang, J., 2015). Therefore, the original ALS data is needed to converted from scanner coordinate system to independent engineering coordinate system, in order to fulfill the requirements of engineering design and construction. Bursa Model is a common coordinate transformation model, it can finish transformation between scanner coordinate system and body system via three space transformation methods of translation, rotation and scaling. To calculate the seven transformation parameters, substituting control points measured by RTK and same points of original point cloud into equation (1), and substituting original ALS data into Bursa model to complete the program of point cloud coordinate system.

$$\begin{bmatrix} X \\ Y \\ Z \end{bmatrix} = \begin{bmatrix} \delta x \\ \delta y \\ \delta z \end{bmatrix} + k\boldsymbol{R}_z(\alpha)\boldsymbol{R}_z(\beta)\boldsymbol{R}_z(\gamma)\begin{bmatrix} x \\ y \\ z \end{bmatrix} \tag{1}$$

Where (X, Y, Z) is independent engineering coordinate, (x, y, z) is original ALS coordinate, δx, δy, δz is translation parameters, $\boldsymbol{R}_z(\alpha)$, $\boldsymbol{R}_z(\beta)$, $\boldsymbol{R}_z(\gamma)$ is rotation matrix, k is scaling parameter.

2.2 Data filtering

DTM generation using ALS data can be simplified to be the process of filtering non-ground points. Many filtering algorithms have been proposed and some of them have been compared by Sithole, G et al. (2004). Considering previous studies, in this paper, RGB features of point cloud and CSF filtering (Zhang, W et al., 2016) are used to filter raw LiDAR data in order to generate DTM. The filtration algorithm has two main steps. Firstly, dividing raw point cloud into two classes (highway and bridge point cloud, residual point cloud) by RGB features, and then filtering the non-ground points of two classes respectively by CSF algorithm.

Regarding the particularity of BIM designs in highway projects that often involve in old road and bridge reconstruction, extracting the highway and bridge point cloud separately to support the subsequent design becomes a necessary process in data filtering. Traditional filtering methods are based on spatial pattern recognition, which are not suitable for highway and bridge point cloud extraction. However, filtering methods based on RGB features, which is similar to Spectral Pattern Recognition, usually get the results by scanning the color difference of the points rather than the spatial position between points. To be more specific, select representative training areas manually to determine the RGB value of each class and the average RGB value of each class; then calculate the distance between each point and the average RGB value of each class and the nearest is the class to which the point belongs.

After point cloud classification, selecting CSF algorithm to filter the non-ground points of two classes respectively. CSF algorithm is based on a simple physical process simulation. It assumes that a piece of suppositional cloth drops on a terrain due to gravity. If the hardness of the cloth is small enough, it will stick to the surface and the final shape of the cloth will be the DSM (Digital Surface Model). However, if the terrain is turned upside down and the cloth is defined with rigidness, then the final shape of the cloth is the DTM, which is showed in Figure 1 (a). Based on this technique, in the cloth simulation calculation, cloth used in the CSF modeling can be regarded as a grid that consists of particles with mass and interconnections, as shown in Figure 1 (b), which can also be called a Mass-Spring Model. In this model, points and points are interrelated by 'virtual springs', and their interactions obeys Hooke's law (Provot, X., 1995).
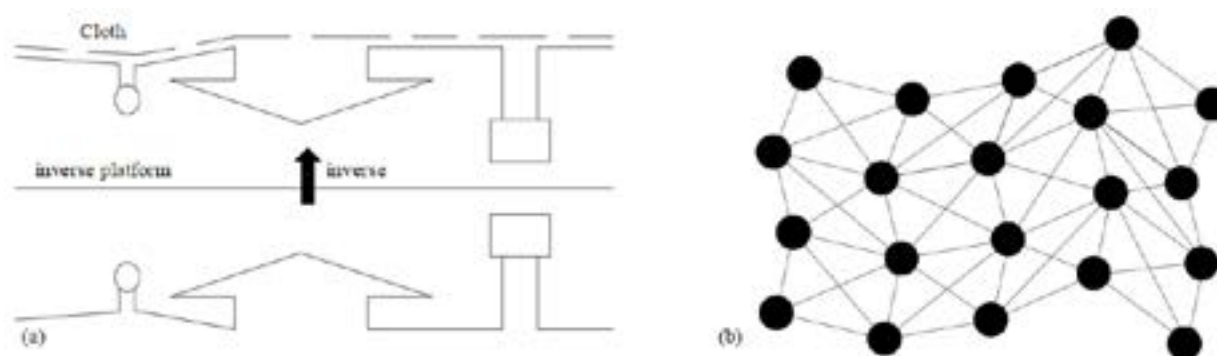

Figure 1 Overview of CSF algorithm: (a) schematic illustration of CSF, (b) schematic illustration of the CSF grid.

CSF used in the paper mainly consists of four user-defined parameters: grid resolution, which represents the horizontal distance between two neighboring particles; cloth rigidness, which controls the rigidness of the cloth, the higher the rigidness is, the more compact the cloth is. It can be divided into three grades, the plain area is defined as 1, the hill area is as 2, and 3 for the steep area; height threshold, which is used to determine whether a point should be moved to ground points or not, usually set to 0.5m can meets most of the data filtering requirements; iteration times, this parameter is set between 100 and 150 for all of the datasets. In addition, steep slope fit factor is an optional parameter, it is suggested to be selected by users for hill area datasets.

To evaluate the quality of the filtration, the precision, recall are estimated. Precision represents a measure of exactness or quality and recall represents a measure of completeness or quantity. These evaluation measures are described below in equation (2).

$$\begin{cases} Q_p = \dfrac{n_{TP}}{n_{TP} + n_{FP}} \times 100\% \\ Q_R = \dfrac{n_{TP}}{n_{TP} + n_{FN}} \times 100\% \end{cases} \tag{2}$$

Where Q_p, Q_R are precision and recall, n_{TP}, n_{FP} and n_{FN} are the number of true positive, false positive and false negative counts.

3110

2.3 Interpolation methods

The filtered LiDAR data will be random and irregular due to the existence of sampling blind area and the observation data filtered by CSF. Therefore, the filtered point cloud should be processed by interpolation methods. Krige (1976) proposed Kriging interpolation method of geostatistics, which has capability of producting high correlation between observed and input points. Compared with other deterministic interpolation methods, Kriging is a geostatistical interpolation method with the advantage of autocorrelation. Ordinary Kriging interpolation method is used in this paper to process point clouds. In other words, it defines the surface variation via the distance and the direction among the sample points.

2.4 Elevation correction

With the influence of surveying environment, such as the light, temperature, and flying height, the original ALS data always shows low elevation precision. In order to generate DTM model with high precision, in this paper, high precision control points measured by RTK in surveying area are used to correct the elevation values of point clouds. In partial range, there is only elevation difference between the filtered point cloud and terrain, and the terrain relief tends to be a general smooth trend surface, therefore, the elevation corrected value can be fitted as a function of plane coordinates based on quadric surface equation. The quadric surface fitting model is listed in equation (3).

$$\zeta_k = \alpha_0 + \alpha_1 \Delta x_k + \alpha_2 \Delta y_k + \alpha_3 \Delta x_k^2 + \alpha_4 \Delta y_k^2 + \alpha_5 \Delta x_k \Delta y_k - \varepsilon_k \tag{3}$$

Where $\Delta x_k = x_k - x_0$, $\Delta y_k = y_k - y_0$; x_0, y_0 is plane coordinate of the central control point; x_k, y_k is the plane coordinate of control point; ζ_k is the elevation corrected value of control point; ε_k is fitting residual. The least square method is used to minimize the ε_k, in order to fit the quadric surface optimally. Fitting coefficients can be solved by equation (4).

$$\boldsymbol{\alpha} = (A^T A)^{-1} A^T \zeta \tag{4}$$

Where:

$$\boldsymbol{\alpha} = (\alpha_0 \alpha_1 \cdots \alpha_5)^T, \zeta = (\zeta_0 \zeta_1 \cdots \zeta_m)^T$$

$$[A] = \begin{bmatrix} 1 & \Delta x_1 & \Delta y_1 & \Delta x_1^2 & \Delta y_1^2 & \Delta x_1 \Delta y_1 \\ 1 & \Delta x_2 & \Delta y_2 & \Delta x_2^2 & \Delta y_2^2 & \Delta x_2 \Delta y_2 \\ . & . & \vdots & . & \vdots & . \\ 1 & \Delta x_m & \Delta y_m & \Delta x_m^2 & \Delta y_m^2 & \Delta x_m \Delta y_m \end{bmatrix}$$

Equation (3) indicates six groups of control points and their same points are required to solve the fitting coefficients, and after getting the fitting coefficients, the elevation corrected value of any point can be generated by equation (5).

$$\zeta_i = \alpha_0 + \alpha_1 \Delta x_i + \alpha_2 \Delta y_i + \alpha_3 \Delta x_i^2 + \alpha_4 \Delta y_i^2 + \alpha_5 \Delta x_i \Delta y_i \tag{5}$$

2.5 3D geological model established method

Autodesk Civil 3D software is a BIM solution for civil engineering design and documentation, which helps civil engineers who engaged in transportation, land development and water conservancy projects to explore design schemes more easily and efficiently, analyse project features, and provide consistent and higher quality documents. In this paper, Civil 3D software is used to establish the 3D geological model by generating the triangulated terrain surface and geological surface based on 3D point cloud and geophysical data, and enclosing the geological solid by geological surface.

3. EXPERIMENT AND DISCUSSION

3.1 Datasets

The point cloud and control points involved in this study were obtained by an Airborne LiDAR system and RTK on a plain area of Zhejiang Province in southeastern China. The original point cloud contains 9,759,112 points and RTK control points contains 120 points, which are showed in Figure 2 respectively.
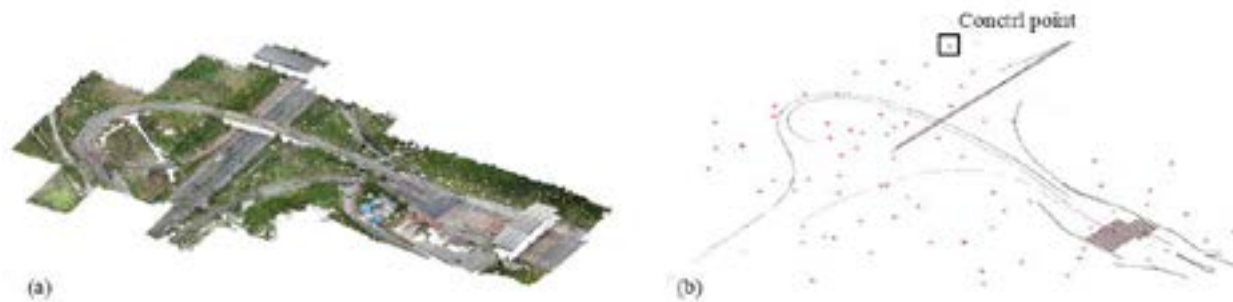
Figure 2 Original data: (a) ALS data, (b) Control points.

3.2 Results and Discussions

After conversing the point cloud to independent engineering coordinate system by Bruse model, the RGB features is used for classification. In this study, original point cloud is divided into two classes (highway and bridge point cloud, residual point cloud). Filtering the point cloud of two classes by CSF algorithm respectively to extract the ground point cloud and highway point cloud. Considering the surveying area is plain, the grid resolution is set to 0.5m, the cloth rigidness is defined 1, the height threshold is set to 0.5m and iteration times is set to 100. The

visualizations of the filtration results are illustrated in Figure 3 and Figure 4. The recall and precision values for two filtering algorithms are listed in table 1.
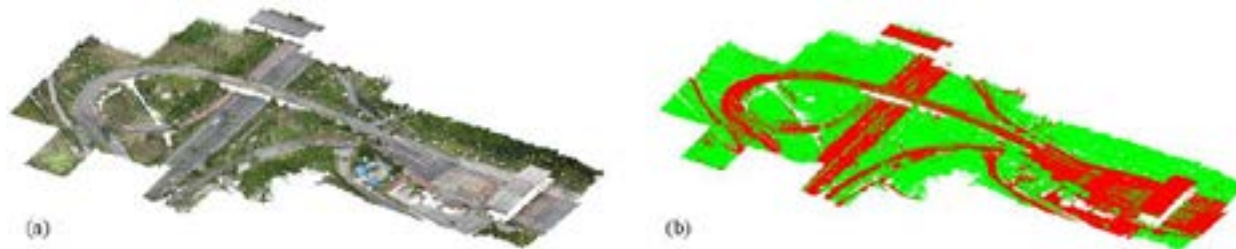
Figure 3 Visualization of classification results for surveying area: (a) Original point cloud, (b) Classified point cloud. Legend for labels: red stands for highway and bridge point cloud and green stands for residual point cloud
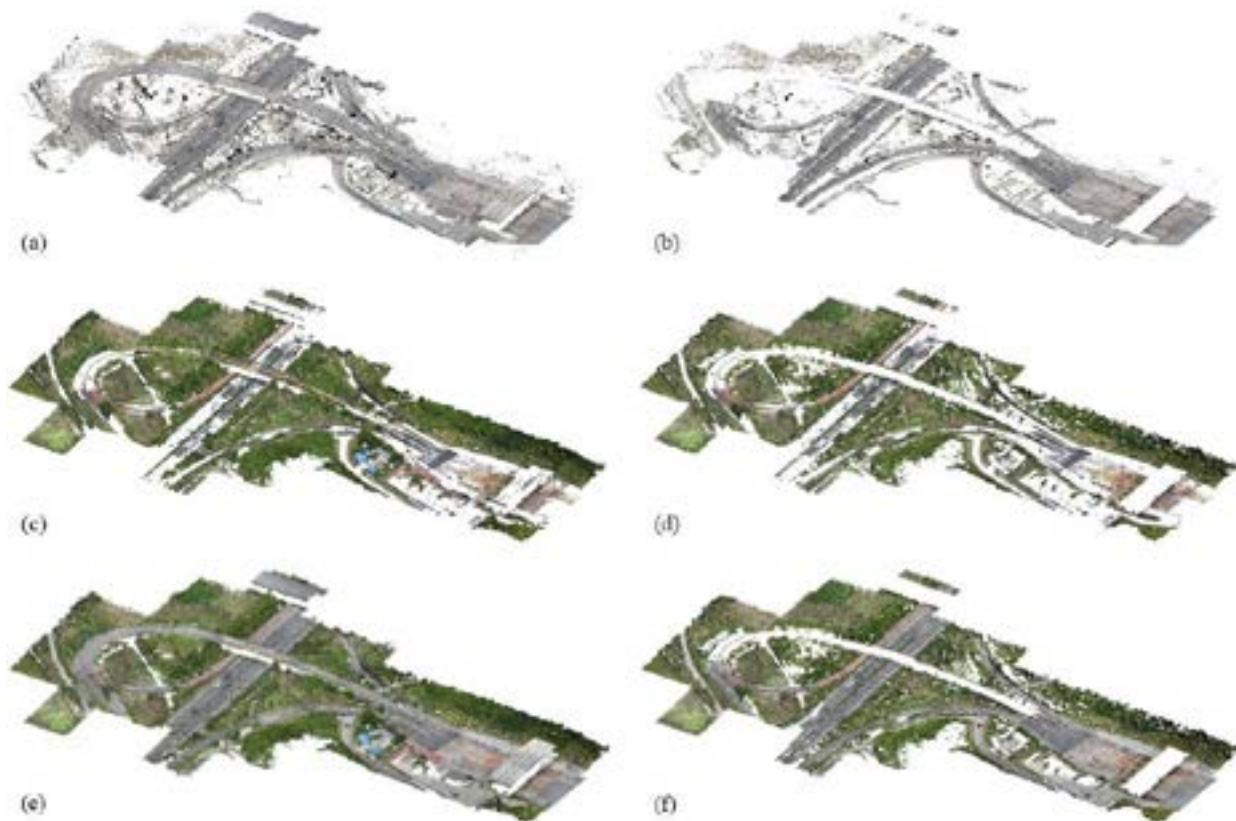
Figure 4 Visualization of filtration results: (a) highway and bridge point cloud, (b) highway point cloud, (c) residual point cloud, (d) residual ground point cloud, (e) original point cloud, (f) ground point cloud

Table 1 Recall and precision values (in %) of two filtering algorithms

Filtering algorithm	Class	Recall	Precision
RGB algorithm	High way and bridge point cloud	94.6	96.2
	Residual point cloud	97.6	96.6
CSF algorithm	Ground point cloud	97.2	96.3
	Feature point cloud	92.7	94.4

From the filtration results, we can see that the features points, which are vegetation, buildings and bridges, are filtered, while the topographic features such as gullies, steep slopes and roads are well preserved. The recall values and precision values are relatively higher than 96%, which indicates that the filtering algorithms can filter the feature points and remain ground point effectively and robustly. Interpolating the filtered point cloud by Kriging method in ArcGIS software and the interpolation result is illustrated in Figure 5.

Figure 5 Visualization of interpolation results: (a) filtered point cloud (b) interpolated ground point

To correct the elevation values of interpolated point cloud following the correction process in section 2.4, 80 control points are selected from 120 RTK control points regard as the control points, and the remaining 40 as t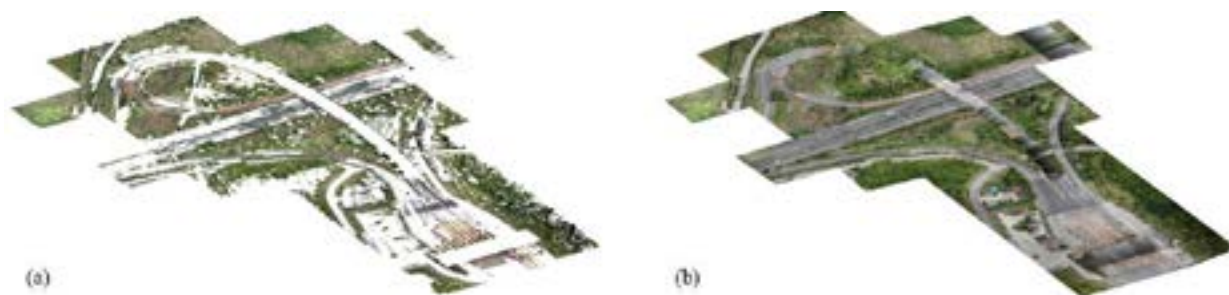he check points for evaluating the method precision. The coefficient values of the corrected model are listed in table 2, and calculate the height difference between corrected points and check points, the precision statistical results of average error, maximum error, minimum error and mean square error are listed in Table 3. Establishing the 3D geological model based on corrected point cloud and geophysical data listed in Table 4 in Civil3D software by the process mentioned in section 2.5. The visualization of the 3D geological model for BIM 3D design is illustrated in Figure 6.

Table 2 Coefficient value of the corrected model

α_0	α_1	α_2	α_3	α_4	α_5
5.438	0.005	-0.002	$8.943*10^{-5}$	$8.943*10^{-5}$	$9.409*10^{-4}$

Table 3 Statistical result values (in m) of the corrected point cloud

AVG	MAX	MIN	RMS
0.129	0.173	0.003	0.119

Table 3 shows that the mean square error value of corrected model is 0.119m, which satisfies the requirement of elevation mean square error of topographic map in flat area under 1:500 scale is 0.15m. Above all, the establishing method of the 3D geological model can make full use of the advantages of data collection by ALS, reflect the topographic and geological features and provide terrain data support for BIM 3D design under the condition of meeting the requirements of design specifications.

Table 4 Geophysical data

Strata number	Depth (m)	Thickness (m)	Strata feature
1	2.1	2.1	Silty clay: brown, medium dry strength and toughness, no shaking reaction, knife cutting surface gloss, the top contains a small number of plant rhizomes.
2	8.3	6.2	Fine sand: grey-brown, wet, slightly dense, the main components of feldspar, quartz, etc, particle size greater than 0.075 mm accounted for about 85%.
3	20.5	12.3	Limestone: grey, moderately weathered, harder, the main mineral components of calcite, rock mass quality basic grade IV.
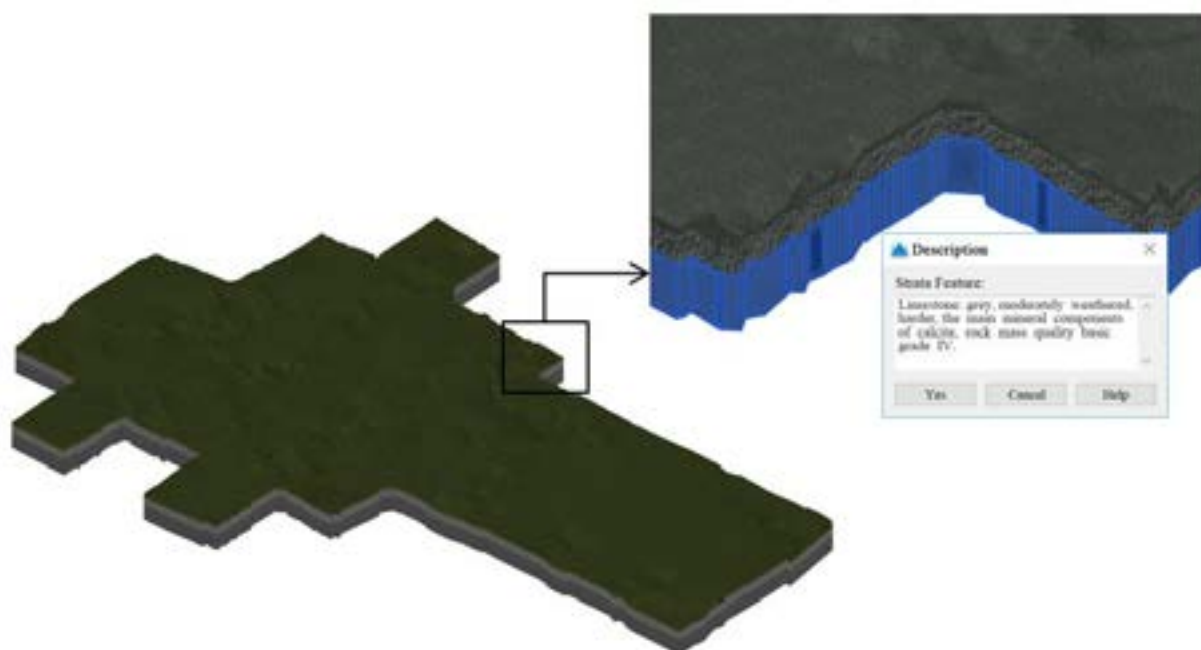
Figure 6 Visualization of 3D geological model

4. CONCLUSIONS

In this paper, in order to obtain the high precision 3D geological model for 3D BIM design, the ALS data was filtered and after processes of data interpolation and elevation correction, processed point cloud data are used to generate DTM, and model creation is finished by combining DTM and geophysical data in Civil 3D software. The results show that the method can make full use of the advantages of data collection by ALS, reflect the topographic and geological features and provide terrain data support for BIM 3D design under the condition of meeting the requirements of design specifications. However, this method is not very applicable in complicated

terrain areas which may due to the filtering algorithm parameters cannot adapt to areas with diverse terrain. Further study will investigate a more applicable filtering algorithm for complicated area.

REFERENCES

Aguilar, F. J., Agüera, F., Aguilar, M. A., & Carvajal, F., 2005. Effects of terrain morphology, sampling density, and interpolation methods on grid dem accuracy. Photogrammetric Engineering & Remote Sensing, 71(7), pp. 805-816.

Brovelli, M. A., Cannata, M., & Longoni, U. M., 2002. Managing and processing lidar data within grass. Proceedings of the Open source GIS - GRASS users conference 2002 Trento, Italy.

Digne, J., 2012. Similarity based filtering of point clouds. Computer Vision and Pattern Recognition Workshops (pp.73-79). IEEE.

Drăguţ, L., & Blaschke, T., 2006. Automated classification of landform elements using object-based image analysis. Geomorphology, 81(3), pp. 330-344.

Krige, D. G., 1976. A review of the development of geostatistics in south africa.

Kraus, K., & Pfeifer, N., 2001. Advanced DTM generation from LIDAR data. International Archivers of the Photogrammetry, Remote Sensing and Spatial Information Sciences, XXXIV(3/W4), pp. 23-30.

Liu, X., 2008. Airborne lidar for dem generation: some critical issues. progress in physical geography. Progress in Physical Geography, 32(1), pp. 31-49.

Niekerk, A. V., 2010. A comparison of land unit delineation techniques for land evaluation in the western cape, south africa. Land Use Policy, 27(3), pp. 937-945.

Provot, X., 1995. Deformation constraints in a mass-spring model to describe rigid cloth behavior. Proceedings of Graphics Interface, 23(19), pp.147-154.

Sithole, G., & Vosselman, G., 2004. Experimental comparison of filter algorithms for bare-earth extraction from airborne laser scanning point clouds. Isprs Journal of Photogrammetry & Remote Sensing, 59(1), pp. 85-101.

Schall, O., Belyaev, A., & Seidel, H. P., 2008. Adaptive feature-preserving non-local denoising of static and time-varying range data. Computer-Aided Design, 40(6), pp. 701-707.

Wang, J., Sun, W., Shou, W., Wang, X., Wu, C., & Chong, H. Y., et al. 2015. Integrating bim and lidar for real-time construction quality control. Journal of Intelligent & Robotic Systems, 79(3-4), pp. 417-432.

Zhang, W., Qi, J., Wan, P., Wang, H., Xie, D., & Wang, X., et al., 2016. An easy-to-use airborne lidar data filtering method based on cloth simulation. Remote Sensing, 8(6), pp. 501.

Mobile Application for Geographical Information System (GIS) Information Dissemination

Syahidah Fariza Moh Esa, Norhayati Che Musa

Malaysian Remote Sensing Agency (MRSA), Ministry of Energy, Science, Technology, Environment and Climate Change (MESTECC)

No. 13, Jalan Tun Ismail, 50480 Kuala Lumpur, Malaysia

Email: syahidah@remotesensing.gov.my ; norhayati@remotesenisng.gov.my

KEY WORDS: **mobile application, GIS, information dissemination, cross platform framework**

ABSTRACT: A web application is developed with complete modules to serve targeted users. It provides a number of modules and functions according to the user requirement. However, some of the modules are rarely utilized or not of the utmost importance to the user. Therefore, a mobile application is built mainly to focus on the main module to provide express information access to the user. This paper will discuss on development using cross platform framework to develop a mobile application since it provides faster coding/programming solution to the developers. Our main focus is to build a mobile app containing a page that shows Geographical Information System (GIS) like coordinates location on a Malaysia map and also other information to complete the development of this app. This mobile application enables user to get the information faster and easier as they can reach it anytime and everywhere which will increase the effectiveness of information dissemination.

1. INTRODUCTION

Mobile application development is becoming more challenging as today it receives high demand from user. People are now more comfortable to open and surf application from their smartphone or personal device. Mobile applications are evolving at a meteor pace to give user a rich and fast user experience [1].

Living in the high speed moving world, quick information dissemination is highly demanded. Searching information via web-based application sometimes can be time consuming as user has to browse through the web to find the exact page that contains specific information that they want. The situation can be worsening whenever a user switching to different computer, since URL bookmark is locally residing in the user computer.

Report by Department of Statistic Malaysia (DOSM), 'ICT Use and Access By Individuals and Households Survey Report, Malaysia, 2015' shows that 97.5% individuals were using mobile phones in 2015 compared to 2013 [2], and this trend is increasing by year.

Due to that reason we decided to develop in-house a mobile application that contains specific business information that helps to disseminate information. In this paper, we will present mobile application

development using hybrid cross platform apps. As stated by Esteban et al, we choose to build our apps using cross platform since the advantages of these tools for software development organizations include the potential to: reuse developer skills; share codebases; synchronize releases; and reduce support costs [3].

The objective of this paper is to introduce a mobile application as information dissemination tool and its benefit to the user.

2.   FRAMEWORKS

A lot of discussions have been made on advantages / disadvantages for mobile application development using either native or cross platform. Developing native apps refers to developing your application on just one platform. This means that the app is built from scratch without applying any existing coding properties; built from the ground up to suit just one platform. This also means that careful attention must be paid to the language of choice, be it Java, Swift and so on. On the other hand, cross platform involves developing applications over a variety of platforms. This means that a code is usually created to run on multiple devices or platforms such as iOS, Android and even Windows using languages such as JavaScript or HTML. This method of development is more suitable to those applications that usually require simple interaction and doesn't need to access other peripherals [5]. Since we have experiences in developing web makes us familiar with languages such as HTML and JavaScript, plus our apps only contains simple interaction, therefore we decided to build our mobile app on cross platform.

There are numerous cross platform frameworks available on the net either open source or proprietary. A few examples of the platforms are:

  2.1 AppyPie [6]
  - HTML5 based hybrid app that works with Android, iPhone, iPad, Windows Phone and Blackberry.

  2.2 Ionic Framework [7]
  - Open source SDK using HTML, CSS, and JavaScript.

  2.3 Alpha Anywhere [8]
  - Combinations of HTML5, CSS3 and JavaScript.

  2.4 PhoneGap [9]
  - Open source framework that built hybrid applications built with HTML, CSS and JavaScript.

  2.5 Angular [10]
  - Open source platform and framework for building client applications in HTML and TypeScript.

  2.6 Apache Cordova [11]
  - Open source platform using HTML5, CSS3 and JavaScript.

  2.7 Backbone Bits [12]
  - Open source platform using PHP.

3.   METHODOLOGY AND RESULTS

The Potential Fishing Zone System was established in 2010. The system contains a few modules, and we have narrowed down to three modules to be published in mobile apps; fisherman profile, coordinate of potential fishing zone (PFZ) and marine weather forecast.

PFZ map is generated using satellite image from Moderate Resolution Imaging Spectroradiometer (MODIS). The image is pre-processed to produce maps of sea surface temperature (SST) and chlorophyll. Both map products are then analysed to obtain the thermal front to determine the location of PFZ. The daily generated latitude and longitude of PFZ points are stored in relational database management system along with other supporting details to ensure systematic data storage and safekeeping as shown in Figure 1.

Figure 1: PFZ points stored in database.

Our mobile app was built using JQuery mobile. It is a free open source cross platform framework. The backend scripting uses PHP to grab data from database. The script was compiled using integrated development environment (IDE) Intel XDK. The app was created and simulated using the IDE then exported to Adobe PhoneGap Build for compilation. The app comprises of four main pages which are:

3.1 Main Menu
- Contains listview of the main menu

3.2 Fisherman profile
- Portrays name and vessel type

3.3 PFZ Coordinates
- Latitude and longitude of valid PFZ points with its fishing zone area in table format. These data can be used for a period of three days from the date of satellite image received.

3.4 Marine Weather Forecast
- Weekly weather forecast.

The main objective of this app is to disseminate the potential fishing area location anywhere at any time provided that the user mobile device has access to the internet. Compared to the traditional fishing method where they searched for fish following their hunch, the coordinates provided in the system help them to plan their fishing trip. They can save searching time and fuel usage by heading directly to the potential fishing area.

The weather forecast also helps the fisherman to decide their fishing trip in case of any bad weather coming their way. Below is the screenshot of the mobile app (Picture 1).
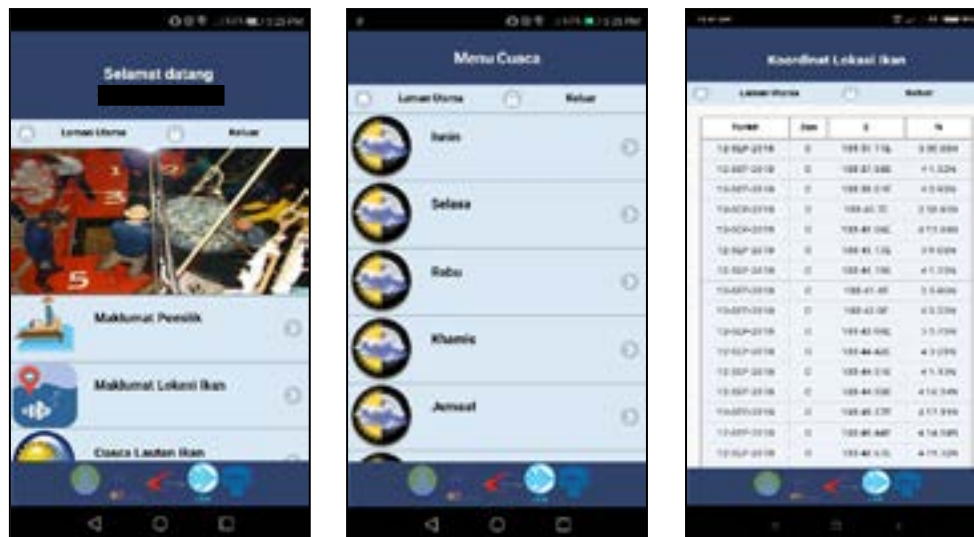
Picture 1: Pages of the mobile app.

4.   CONCLUSION

By having this mobile app, information dissemination for PFZ data becomes more broad. User can easily open the app installed in their mobile device by the tip of their finger. PFZ data helps them to minimize fuel usage and searching time. Hence this will also indirectly help them to save cost.

5.   REFERENCE

[1] Suhas Holla, Mahima M Katti, 2012. Android based mobile application development and its security, pp 490. http://ijcttjournal.org/Volume3/issue-3/IJCTT-V3I3P130.pdf

[2] Department of Statistics, 2016. Press Release Ict Use And Access By Individuals And Households Survey Report, Malaysia, 2015.
https://www.dosm.gov.my/v1/index.php?r=column/pdfPrev&id=Q3l3WXJFbG1PNjRwcHZQTVlSR1UrQT09

[3] Esteban Angulo, Xavier Ferre, 2014. A Case Study on Cross-Platform Development Frameworks for Mobile Applications and UX. http://oa.upm.es/37164/1/INVE_MEM_2014_199184.pdf

[4] Anirudh Nagesh, Carlos E. Caicedo, 2012. Cross-Platform Mobile Application Development.
https://www.researchgate.net/publication/263416908_Cross-Platform_Mobile_Application_Development

[5] Shaistha Farheen, 2016. Native Mobile Application Development Vs Cross Platform App Development. [Online] https://yourstory.com/mystory/b446d9c74e-native-mobile-applicat

[6] AppyPie, About App Builder Appy Pie. [Online] https://www.appypie.com/about-us

[7] Ionic, What is Ionic? [Online] https://ionicframework.com/what-is-ionic

[8] Alpha Anywhere, Alpha Anywhere Technical Overview. [Online]

https://documentation.alphasoftware.com/documentation/pages/GettingStarted/Overview/index.html

[9] PhoneGap [Online] https://phonegap.com/

[10] Angular, Architecture Overview. [Online] https://angular.io/guide/architecture

[11] Apache Cordova, Overview. [Online] https://cordova.apache.org/docs/en/latest/guide/overview/index.html

[12] Backbone Bits, About. [Online] http://www.backbonebits.com/about

ROBUST FUNDAMENTAL MATRIX ESTIMATION USING GENETIC ALGORITHM BASED APPROACH WITH MULTI-OBJECTIVE FITNESS FUNCTION FOR STEREO IMAGES

Manimala Mahato[1] , Shirishkumar Gedam[2]

[1,2]Centre of Studies in Resources Engineering, Indian Institute of Technology Bombay,
Mumbai 400076, India
Email: [1]manimala.mahato@iitb.ac.in; [2]shirish@iitb.ac.in

KEY WORDS: Fundamental matrix; genetic algorithm; multi-objective function; stereo vision.

ABSTRACT: A novel approach for the estimation of 3 X 3 fundamental matrix using genetic algorithm with multi-objective fitness function is proposed and implemented despite of false matches due to noise, occlusion, geometric and radiometric distortion present in stereo images by analyzing the stereo image pair. In stereo vision, fundamental matrix is the only geometrical constraint available for outlier removal in order to prune the stereo correspondences by relating the two perspective projections of the same point in the scene thus a core research area and received a large attention in the last two decades. Here, the genetic algorithm steps such as initialization of the population, fitness function, crossover and mutation operation are customized and implemented to estimate the optimal fundamental matrix. Each candidate in the population has a 2D structure representing the fundamental matrix for the input stereo image pair. To solve the complex real-world optimization problem of fundamental matrix estimation, improved initialization of population is used instead of randomly selected population, because it leads to more accurate and faster convergence. The proposed algorithm is divided into two parts. First part is the initialization of the population needed for the genetic algorithm. The second part is to improve the population using multi-objective genetic algorithm through iterations for finding the optimal solution. The set of correspondence points are obtained by extracting and matching the Scale Invariant Feature Transform (SIFT) feature points from the stereo image pair and are pruned by enforcing bidirectional constraints. The initial population is filled by the fundamental matrices computed from the set of pruned correspondence points using Random Sample Consensus (RANSAC) through random sampling. The most suitable fundamental matrices are chosen based on the evaluated parameter values using the designed fitness functions considering the constraints related to the epipolar geometry of the stereo image pair. Here, two objective functions are: maximization of number of inliers computed using each candidate and minimization of the distances between the points and its epipolar lines. The usefulness of this approach for is demonstrated by improving the number of inliers and comparing with state-of-the-art dense stereo image matching method.

1. INTRODUCTION

In computer vision and computer graphics, one of the most difficult problems is to find the geometrical constraint available between the two images of a stereo image pair irrespective of the specific objects in the scene. The two different views of the same scene are related by the epipolar constraint, which plays very important role in various applications such as 3D reconstruction, stereo analysis, camera self-calibration, motion segmentation etc. Epipolar geometry of a stereo image pair is expressed mathematically by a 3 X 3 matrix, known as fundamental matrix. There are two ways by which fundamental matrix can be computed. If the camera parameters are known, then the fundamental matrix can be computed using the camera parameters. In this case, the complexity of the estimation problem is not so severe. However, the complexity increases if the camera parameters are unknown. In that case, the epipolar geometry can be computed using the image characteristics of the stereo image pair. A great deal of literature exists on this subject (Longuet-Higgins 1981), (Xu and Zhang 1996). In order to estimate the fundamental matrix, a certain number of corresponding points need to be extracted from the stereo image pair. Considering, the stereo image pair I and I' are the images of the same scene which are captured from two different view. The projected location of a point P in the scene is X in the left image I and X' in the right image I'. The points X and X' are known as correspondence points.Therefore, the accuracy of the fundamental matrix depends on the accuracy of the correspondence points. In general, the feature correspondence points are extracted and matched using feature matching algorithms. However, the presence of outliers and noise may corrupt the correspondence point. Hence, the goal of the researchers is to build the fundamental matrix estimation method robust to outliers and noise in the correspondence points.

Some well known robust methods for fundamental matrix estimation are M-estimator, LMedS, RANSAC etc. These methods have in-built mechanism to reduce the influence of outliers. However, their performance degrades if the

proportion of outliers is higher than half. Most of the highly robust estimator is best on the principle of random sampling of the input correspondences. Random sampling can avoid to converge in the local minima in some extent. However, as the proportion of outliers in the input correspondences increases, the execution time for the convergence of the algorithm also increases and the chances to converge to the global minima decreases. This is due to the fact that the proportion of outliers in the input correspondences are not known in advanced(Jinxiang and Song 1998).

The aim of this paper is to use genetic algorithm (GA) for the estimation of robust fundamental matrix for the given stereo image pair. Inspired by the effectiveness of genetic algorithm converging to the global optima, a novel approach using population based evolutionary multi-objective optimization strategy is proposed in this paper. The block diagram in Fig. 1 shows the genetic algorithm steps such as initialization of the population, fitness function, crossover and mutation operation. The initial population is evolved through generations iteratively till the convergence condition satisfied.
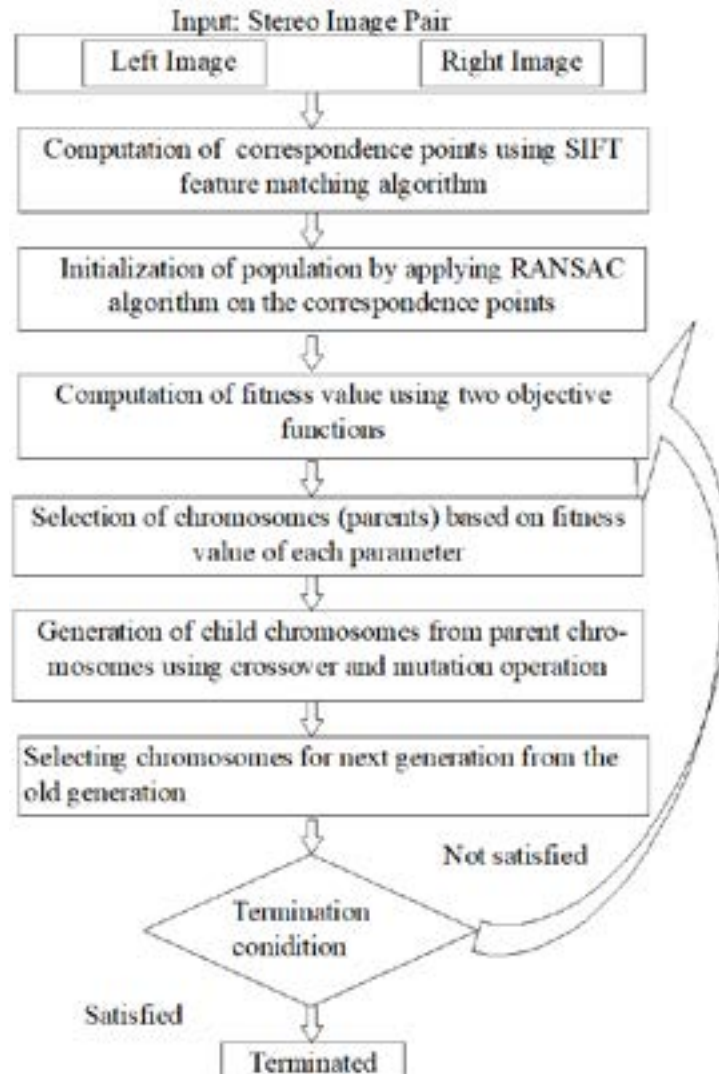
Fig. 1: Block diagram of the proposed method

2. ESTIMATION OF FUNDAMENTAL MATRIX USING MULTI-OBJECTIVE GENETIC ALGORITHM

In general, genetic algorithm starts with randomly generated initial population and gradually optimizes the population through iterative process. In the process of optimization, a new population of next generation is created using crossover and mutation operation from the old population of previous generation. In order to evolve the populations through generations, the chromosomes are evaluated based on the fitness functions and best chromosomes are selected for the next generation. The iterative process is continued till the convergence condition

satisfied. Next, the genetic algorithm is discussed for the estimation of fundamental matrix.

2.1. Encoding scheme for chromosomes

Encoding scheme for representing the chromosome in the genetic optimization algorithm plays very important role and is application dependent. Thus, 2-D fundamental matrix is simply encoded as a chromosome with size of 3 X 3 and the value of each parameter in the, matrix becomes a gene value of the chromosome.

2.2. Multi-objective fitness functions

In the process of optimization, each chromosome is evaluated using fitness function by assigning a scalar value to each chromosome. Larger scalar value represents higher degree of fitness. In this work, the fitness of each chromosome is evaluated based on two objective functions. The objective functions are: maximization of number of inliers computed using each chromosome and minimization of the distances between the points and its epipolar lines. The input to the genetic algorithm is the set of correspondence points. The set of correspondence points are obtained by extracting and matching the Scale Invariant Feature Transform (SIFT) (Lowe 2004) feature points from the stereo image pair and are pruned by enforcing bidirectional constraints.

The first fitness value is defined by the number of inliers which are validated by the chromosomes among the set of correspondence points. In this work, matching error is computed for each estimated corresponding pair by applying the fundamental matrix (Trucco and Verri 1998), respecting the epipolar constraint of stereo matching as in equation (4).

$$X^T F X = \varepsilon_X \tag{1}$$

Where F is the fundamental matrix represented by each chromosome, (X, X') is the corresponding pair between the left image and right image of stereo image pair and ε_X is the matching error. Ideally, ε_X should be zero, but practically, this value does not come exactly zero. Therefore, we have decided a threshold value ε_0 and the corresponding pairs, which give matching error less than ε_0 are considered as inliers i.e.

$$X^T F X < \varepsilon_0 \tag{2}$$

However, the fitness value f_1 is computed as the proportion of inliers of the set of correspondence points of size N using equation (6).

$$f_1 = \frac{c}{N} \tag{3}$$

Where c is the number of inliers found using each chromosome. Hence, our goal is to maximize the fitness value f_1 of each chromosome by maximizing the number of inliers c.

The second fitness value is defined by the sum of distances between the points in the left image and its corresponding epipolar lines in the right image and vice versa using equation (4).

$$f_2 = \sum_{i=1}^{N} (dis(X_i, FX'_i) + dis(X'_i, FX_i)) \tag{4}$$

Where dis is the distance between the point and its epipolar line. Our goal is to minimize the fitness value f_2 of each chromosome.

2.3. Generation of initial population

Genetic algorithm starts its optimization process with a population of initial chromosomes. The size of the population and the generation of the initial population are very important factors of the genetic algorithm as it controls the speed of the convergence of the algorithm. The size of the population represents by the number of chromosomes at each generation. Use of too large population is advantageous as it reduces the chance to converge to local optima by searching the solution space more thoroughly, but at a cost of larger time to converge. On the other hand, use of too small population may converge to local optima very quickly and may not be able to produce the optimal solution. In this work, the size of the population is empirically decided to be 40.

In order to generate the chromosomes in the initial population, use of random function is very common in the literature, due to which the time to converge is high. The converging time can be reduced by using the informed population as the initial population. In this way, the chromosomes are seeded in the area of search space where the optimal solution is most likely to be found. Since the camera parameters are unknown for the given stereo image pair, the most feasible way to compute the fundamental matrix is through feature matching algorithm (Joglekar, Gedam, and Krishna Mohan 2014). In this work, SIFT feature matching algorithm (Lowe 2004) is used for the computation of the corresponding matching points. Further, the fundamental matrix is determined from the best matching pairs using RANSAC algorithm (Fischler and Bolles 1981). Chromosomes are initialized by computing fundamental matrices by applying RANSAC algorithm several times on the same set of corresponding points.

2.4. Selection function

Child chromosomes are computed from the parent chromosomes using crossover and mutation operators. The chromosomes in the population are selected as parents based on their fitness value using tournament selection function. Tournament selection chooses two parents randomly and selects the chromosome with better fitness value among them. This way the required number of chromosomes for crossover and mutation operations are selected. Chromosomes with high quality genes have better fitness value. In order to generate improved population using crossover and mutation operation chromosomes with better fitness value are selected multiple times.

2.5. Crossover operation

The search mechanism of genetic algorithmis based on two main operators such as crossover and mutation. These operators are useful to explore the entire search space in order to converge to global optimum. In this work, one point crossover operator has been used with a probability of p_c. Two children chromosome is computed from two parents. For each gene of the parent chromosome random number between 0 to 1 is generated. If the generated number is more than the crossover probability p_c, then crossover operation takes place. Fig. 2 shows as example of crossover operation in which $p_c = 0.6$.

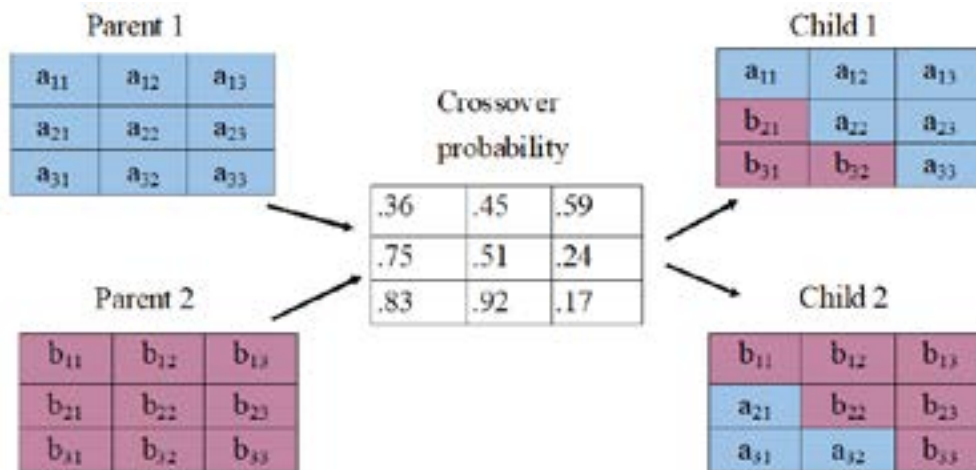Figure 2: The crossover operation
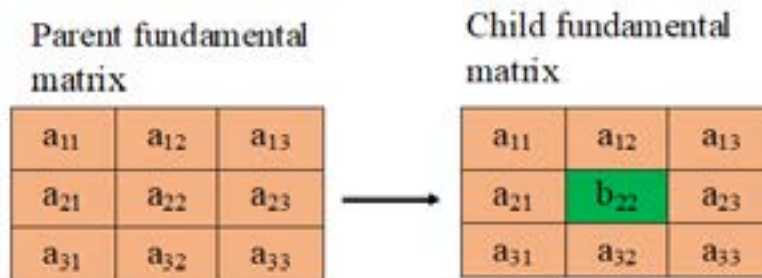
Figure 3: Mutation operation

3125

2.6. Mutation operation

The goal of the mutation operation is to reduce the possibility of being converged into the local minima by exploring the search space independent of the location of other chromosomes. Child chromosome is computed from the parent chromosome by introducing new genetic material through the mutation operation. Fig. 3 shows an example of mutation operation in which the middle value of the parent fundamental matrix is modified.

3. RESULT AND ANALYSIS

To demonstrate the effectiveness of the proposed approach, the results are obtained using the proposed method on *Corridor* stereo image pair. The left image and right image of the stereo pair is shown in Fig. 4. The correspondence points are computed using the SIFT feature matching algorithm. As shown in Table I, 167 correspondence points are extracted. Further, the correspondence points are pruned using left-right consistency stereo constraints. After pruning, there are 104 correspondence points for the stereo image pair. Using these 104 correspondence points, RANSAC algorithm estimates the fundamental matrix which validates only 54 points as inliers. Whereas, the fundamental matrix computed by the proposed method validates 70 points as inliers. The comparison in Table I shows that, the proposed method computes better fundamental matrix compared to the state-of-the-art RANSAC algorithm by improving the number of inliers. Fig. 5 is showing the inliers validated by the fundamental matrix computed by our proposed method.

(a)   (b)

Figure 4: *Corridor* stereo image pair (a): Left Image (b): Right Image

Figure 5: Inliers pruned by the fundamental matrix computed using the proposed method

Table I: Comparison of the proposed method with state-of-the-art RANSAC algorithm

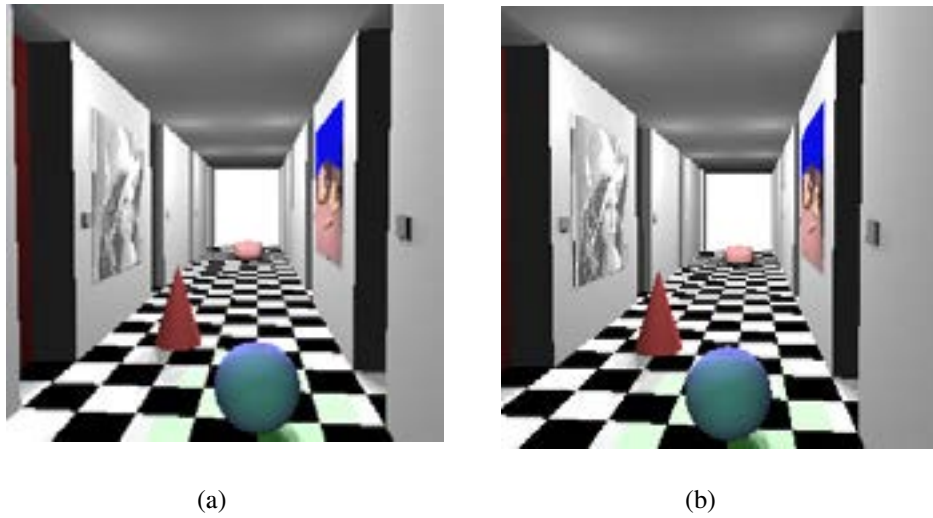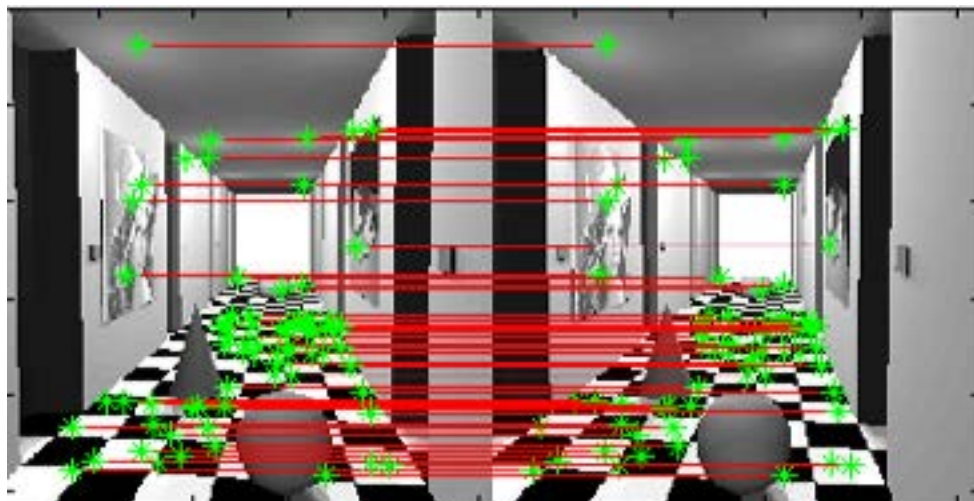| Number of Inliers computed by SIFT feature matching algorithm	Number of Inliers after pruning using LRC consistency	Number of Inliers pruned using fundamental matrix computed by RANSAC algorithm	Number of Inliers pruned using fundamental matrix computed by the proposed method
167	104	54	70

4. CONCLUSION

The fundamental matrix obtained by the proposed genetic algorithm based algorithm with multi-objective fitness function is useful to validate the correspondence points for stereo image pair. The estimation of fundamental matrix is a challenging problem due to noise, occlusion, geometric and radiometric distortion. The proposed algorithm estimates optimal fundamental matrix for the stereo image pair despite of the above mentioned issues. Multiple objective functions used in the proposed algorithm are based on epipolar constraint which is the only geometrical constraint available for stereo image pair. Various steps of genetic algorithm are designed to solve the optimization problem. The effectiveness of the proposed method is demonstrated and verified with state-of the-art algorithms.

5. REFERENCES

Fischler, Martin A, and Robert C Bolles. 1981. "Random Sample Consensus: A Paradigm for Model Fitting with Applications to Image Analysis and Automated Cartography." *Communications of the ACM* 24 (6): 381–95.

Jinxiang, Chai, and De Ma Song. 1998. "Robust Epipolar Geometry Estimation Using Genetic Algorithm." *Pattern Recognition Letter*, no. 19: 829–38.

Joglekar, Jyoti, Shirish S. Gedam, and B. Krishna Mohan. 2014. "Image Matching Using SIFT Features and Relaxation Labeling Technique -A Constraint Initializing Method for Dense Stereo Matching." *IEEE Transactions on Geoscience and Remote Sensing* 52 (9): 5643–52.

Longuet-Higgins, H. C. 1981. "A Computer Algorithm for Reconstruction a Scene from Two Projection." *Nature* 293: 133–35.

Lowe, David G. 2004. "Distinctive Image Features from Scale-Invariant Keypoints." *International Journal of Computer Vision* 60 (2): 91–110.

Trucco, Emanuele, and Alessandro Verri. 1998. *Introductory Techniques for 3-D Computer Vision. Introductory Techniques for 3-D Computer Vision*. Prentice Hall Englewood Cliffs.

Xu, G., and Z. Zhang. 1996. *Epipolar Geometry in Stereo, Motion and Object Recognition*. Kluwer Academic Publishers.

Comparison of land cover classification methods for economic crops in Thailand

Tanakorn Sritarapipat (1), Siam Lawawirojwong (2), Panu Srestasathiern (2)

[1] School of Geoinformatics, Institute of Science, Suranaree University of Technology,
Nakhon Ratchasima 30000, Thailand
[2] GISTDA Academy, Geo-Informatics & Space Technology Development Agency,
Bangkok 10210, Thailand

Email: tanakorn.s@sut.ac.th; siam@gistda.or.th; panu@gistda.or.th

KEYWORDS: Economic Crop, Maximum Likelihood, Support Vector Machine, Neural Network, Landsat 8

ABSTRACT: Thailand is the large exporter for agricultural products and the main economic agricultural products are rice, cassava, maize, para-rubber, sugar cane and oil palm. Updated and reliable economic crop areas at the country level are necessary for planning and management for Thailand's government, and relevant organizations. This research aims to find a suitable classification method for land cover types with economic crops; urban, water, forest, rice, cassava, maize, para rubber, sugar cane, and oil palm in Thailand. Multiple Landsat-8 (OLI) images were used as dataset. We systematically sampled the data covering almost parts of Thailand. Supervised classification methods including; maximum likelihood, support vector machine, and neural network, were employed to classify the land cover types. In the experiments, the comparisons of the results of the classification methods were described with the accuracy and processing time. In the experiments, the results indicated that the land cover classification using neural network with multi-layers perceptron provided the highest accuracy with the overall accuracy of 91.83%, the Kappa coefficient of 0.7552, and the lowest accuracy in each class of 56% and computing time of 51 minutes. While, maximum likelihood method provided the lowest accuracy with the overall accuracy of 60.29%, the Kappa coefficient of 0.3108, and the lowest accuracy in each class of 7% and computing time of 35 second.

1. INTRODUCTION

Agriculture in Thailand is highly competitive, and diversified. The agriculture exports are very prosperous. Rice is the country's most important crop, with around 60% of 13 million farmers and it is totally half of cultivated land (Bangkok post, 2017). In 2014, rice exports amounted to 1.3% of GDP. Agricultural production as a whole estimated about 9-10.5% of GDP. Around 40% of the population work in agriculture-related occupations (The world bank, 2016). Thailand is considered as the large exporter for agricultural products. The core economic agricultural products are rice, cassava, maize, para-rubber, sugar cane and oil palm. As a result, updated and reliable economic crop areas at the country level are necessary for planning and management for Thailand's government, and relevant organizations in enhancing Thailand's economic growth.

The image analysis of remotely sensed data is very important in several practical applications, especially land cover classification. Based on the pixel based analysis, the land cover classification consider the given spectrum to assign it to a certain class. A variety of classification algorithms have been developed such as maximum likelihood (Le Cam, 1990), Mahalanobis distance (De Maesschalck et.al, 2000), random forest (Breiman, 2001), support vector machine (Meyer, 2003), and neural network (Graupe, 2013). For example, Al-Razzaq Abd used Maximum likelihood classification to produce land use and land cover map. The mahanobis distance was applied to classify land cover areas (Sritarapipat, 2015). Pal and Mather (, 2015) employed support vector machine to obtain land cover map. Neural network with multi-layer perceptron were performed to provide land cover images (Civco, 1993).

However, classification results are often effected by various factors such as (1) ground truth data and ancillary data available; (2) the complexity of landscape and analyst's knowledge about the study area; (3) image band selection and processing; and (4) the classification algorithm and analysts experience with the classifiers used (Lu et.al, 2004). In general, to improve the land cover classification results, several classifiers can be investigated to find the suitable classifier.

In this research, we proposed the comparison of land cover classification methods for economic crop in Thailand using multispectral images acquired by Landsat-8 satellite. We applied three classification methods including maximum likelihood, support vector machine, and neural network with varying the parameters. The land cover area is classified into nine classes; urban, water, forest, rice, cassava, maize, para rubber, sugar cane, and oil palm.

2. MATERIALS AND METHODS

2.1 Study area and materials

In this research, we focused on the area of Thailand. Thailand has the land area of 510,890 square kilometers and the water area of 2,230 square kilometers also the total area of 513,120 square kilometers (the 51st largest nation in the world). Thailand is the large exporter for agricultural products with the main economic agricultural products of rice, cassava, maize, para-rubber, sugar cane and oil palm. In this research, 43 multispectral images during 2015-2017 acquired by Landsat 8 satellite (OLI) that covers almost parts of Thailand were used as dataset. The images has the spatial resolution of 30 m. and 11 spectral bands. However, we only used 7 spectral bands with Band 1 – Coastal Aerosol, Band 2 – Blue, Band 3 - Green, Band 4 - Red, Band 5 - Near Infrared (NIR), Band 6 - Short-wave Infrared (SWIR) 1, Band 7 - Short-wave Infrared (SWIR) 2.

2.2 Methods

For the methods to obtain the accuracies of land cover classification methods, firstly, we sampled the data of nine classes from 43 Landsat 8 images. Then, the data are separated into two groups; training data and testing data. In some methods, we used the feature extraction by using principle component analysis to transform the data from original space into the other space. Then, we applied the testing data with the supervised classification methods with (1) maximum likelihood, (2) support vector machine, (3) neural network with multi-layers perceptron to provide the several classifiers. We employed the testing data with the classifiers to obtain the results of land cover areas. Next, we validate the results of land cover areas with the referenced land cover areas as testing data to calculate the accuracies. The flowchart of our methods to obtain the accuracies of land cover classification methods is illustrated in figure 1.

Figure 1 The flowchart of our methods to obtain the accuracies of land cover classification methods.

2.2.1 Sampling data

We sampled the data of nine classes with urban, water, forest, rice, cassava, maize, para-rubber, sugar cane, and oil palm with the systematic regions from 43 multi-spectral images acquired by Landsat 8 by using visual interpretation. The total sampling pixels are 20,132,734. The regions of sampling data is showed in figure 2.

Figure 2 The regions of sampling data that covers Thailand.

2.2.2 Splitting training data and testing data

The sampling data was separated into two groups with (1) training data with 20% and (2) testing data with 80%. The training data are 4,026,547 pixels and the testing data are 16,106,187pixels.

2.2.3 Feature extraction

In some cases, we used principle component analysis with data to transform the data from original space into the other space. Principal component analysis (PCA) is a statistical process that uses an orthogonal transformation to convert a set of observations of possibly correlated variables into a set of values of linearly uncorrelated variables (Jackson, 1991). The first principal component describes the highest variability in the data and each next component describes the remaining lower variability in the data.

2.2.4 Supervised classifications

We used the supervised classification methods with (1) maximum likelihood, (2) support vector machine, (3) neural network with multi-layers perceptron with the testing data with to provide the several classifiers.

Maximum likelihood estimation (Millar, 2011) is a statistical method of estimating the parameters of a statistical model, given observations. Maximum likelihood estimation tries to find the parameter values that maximize the likelihood function, given the observations. Maximum likelihood classification (Sisodia, 2014) is a parametric classifier that assumes normal distribution for the training data statistics for each class in each band. It is based on the probability that a pixel belongs to a particular class. Here, we have one experiment of land cover classification by using maximum likelihood classifier.

Support vector machine (Cortes and Vapnik, 1995) is supervised learning model with associated learning algorithm that analyze data used for classification and regression analysis. A Support Vector Machine model is a representation of the examples as points in space, mapped so that the examples of the separate categories are divided by a clear gap

that is as wide as possible. A Support Vector Machine performs classification by finding the hyperplane that maximizes the hyperplane margin between the two classes. The vectors that define the hyperplane are the support vectors. Here, we have two experiments of land cover classification by using (1) support vector machine with linear kernel and (2) support vector machine with linear kernel and principle component analysis.

Artificial neural networks (Haykin, 2008) are computing systems inspired by the biological neural networks that constitute animal brains. An Artificial neural network is based on a collection of connected units or nodes called artificial neurons which loosely model the neurons in a biological brain. A multilayer perceptron (Mizutani, 2000) is a class of feedforward artificial neural network. An multilayer perceptron consists of at least three layers of nodes. Except for the input nodes, each node is a neuron that uses a nonlinear activation function. Multilayer perceptron utilizes a supervised learning technique called backpropagation for training. Its multiple layers and non-linear activation distinguish multilayer perceptron from a linear perceptron. It can distinguish data that is not linearly separable. Here, we have five experiments of land cover classification by using (1) neural network using multi-layer perceptron with 1 hidden layer composed of 100 nodes (2) neural network using multi-layer perceptron with 2 hidden layer composed of 100 nodes in each hidden layer, (3) neural network using multi-layer perceptron with 3 hidden layers composed of 100 nodes in each hidden layer, (4) neural network using multi-layer perceptron with 4 hidden layer composed of 100 nodes in each hidden layers, (5) neural network using multi-layer perceptron with 4 hidden layer composed of 100 nodes in each hidden layers that was calculated by using graphic processing unit.

2.2.5 Results of land cover classifications

After we got the all classifiers, we applied the classifiers with the testing data to obtain the all results of land cover classification methods.

2.2.6 Accuracy assessments

To validate the results, we compared the results of land cover classifications with the referenced land cover area as the testing data. For accuracy assessments, we calculated the multiple indexes with (1) overall accuracy, kappa coefficient, confusion matrix, accuracy in each class, and time computing process.

3. RESULTS AND DISCUSSION

In the experiments, there are eight experiments with (1) maxim likelihood, (2) support vector machine using linear kernel (3) support vector machine using linear kernel, and principle component analysis, (4) neural network using multi-layer perceptron with 1 hidden layer composed of 100 nodes (5) neural network using multi-layer perceptron with 2 hidden layer composed of 100 nodes in each hidden layer, (6) neural network using multi-layer perceptron with 3 hidden layers composed of 100 nodes in each hidden layer, (7) neural network using multi-layer perceptron with 4 hidden layer composed of 100 nodes in each hidden layer, (8) neural network using multi-layer perceptron with 4 hidden layer composed of 100 nodes in each hidden layer that was calculated by using graphic processing unit.

3.1 Results of the accuracies of land cover classifications

Table 1 shows the comparison of the overall accuracies of land cover classification methods and the Kappa coefficients and the computing times. The bar graph in figure 3 illustrates the comparison of the overall accuracies of land cover classification methods. The bar graph in figure 4 demonstrates the comparison of the Kappa coefficients of land cover classification methods. The bar graph in figure 5 shows the comparison of the computing times of land cover classification methods.

Table 1 The comparison of the overall accuracies, the Kappa coefficients and the computing times of land cover classification methods

No	Method	Overall accuracy	Kappa coefficient	Computing time
1	Maximum likelihood	29.60%	. 0.3108	0 min. 35 sec.
2	SVM linear	87.10%	0.5705	43 min. 42 sec.
3	PCA + SVM linear	86.96%	0.5387	28 min. 12 sec.
4	Neural network MLP 1 layer	89.56%	0.6657	7 min. 6 sec.
5	Neural network MLP 2 layers	90.87%	0.7294	27 min. 14 sec.
6	Neural network MLP 3 layers	91.26%	0.7288	27 min. 41 sec.
7	Neural network MLP 4 layers	91.83%	0.7552	51 min. 11 sec.
8	Neural network MLP 4 layers (GPU)	90.16%	0.6959	20 min. 58 sec.
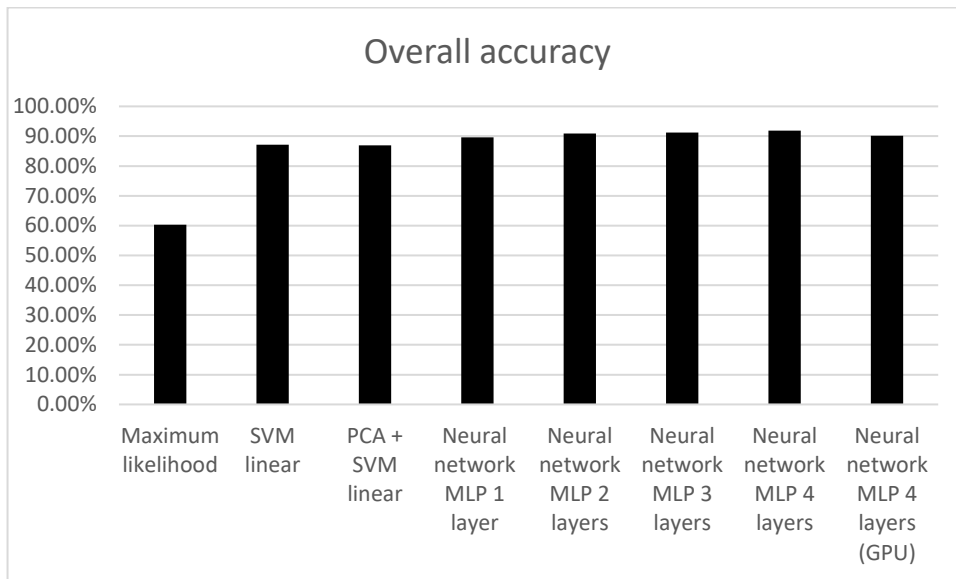
Figure 3 The comparison of the overall accuracies of land cover classification methods
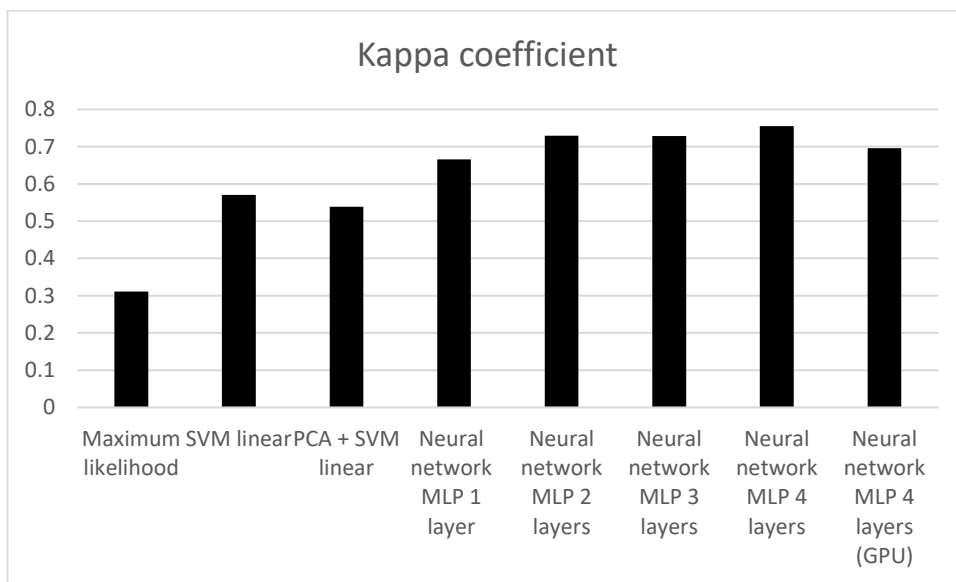
Figure 4 The comparison of the Kappa coefficients of land cover classification methods

3132
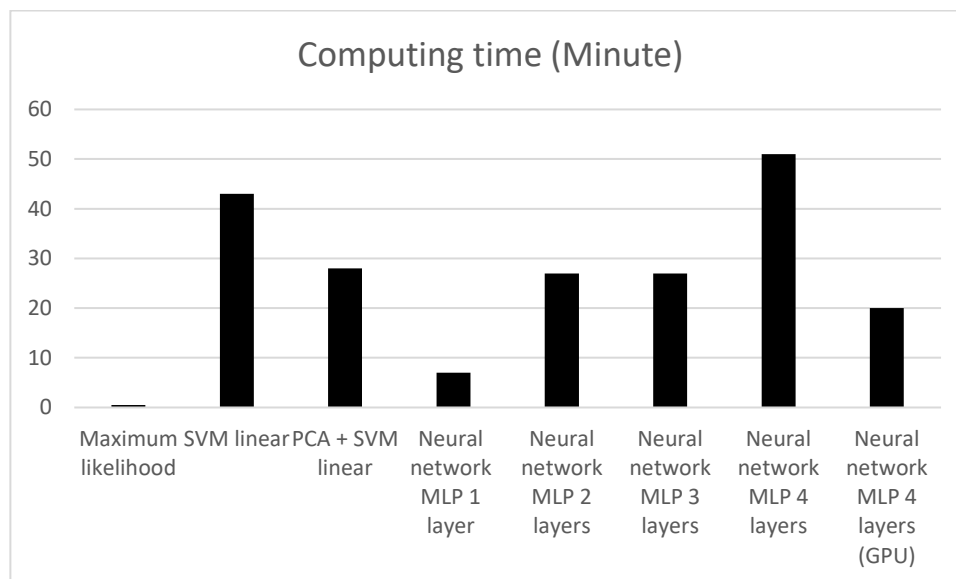
Figure 5 The comparison of the computing times of land cover classification methods

The comparison of the precision in each class of land cover classification methods demonstrates in table 2. The bar graph in figure 6 shows the precision in each class of land cover classification methods.

Table 2 The comparison of the precision in each class of land cover classification methods

No	Method	Urban	Paddy	Maize	Cassava	Sugarcane	Rubber	Oil palm	Forest	Water
1	Maximum likelihood	0.65	0.46	0.07	0.22	0.44	0.16	0.09	0.95	0.82
2	SVM linear	0.77	0.66	0.05	0.61	0.76	0.64	0.17	0.89	0.97
3	PCA + SVM linear	0.84	0.66	0.02	0.69	0.68	0.71	0.03	0.88	0.97
4	Neural network MLP 1 layer	0.85	0.76	0.56	0.77	0.77	0.73	0.74	0.91	0.97
5	Neural network MLP 2 layers	0.87	0.78	0.33	0.78	0.77	0.67	0.76	0.93	0.95
6	Neural network MLP 3 layers	0.84	0.81	0.37	0.68	0.85	0.84	0.76	0.92	0.98
7	Neural network MLP 4 layers	0.9	0.77	0.56	0.76	0.77	0.77	0.79	0.94	0.98
8	Neural network MLP 4 layers (GPU)	0.88	0.77	0	0.72	0.63	0.74	0.68	0.92	0.98
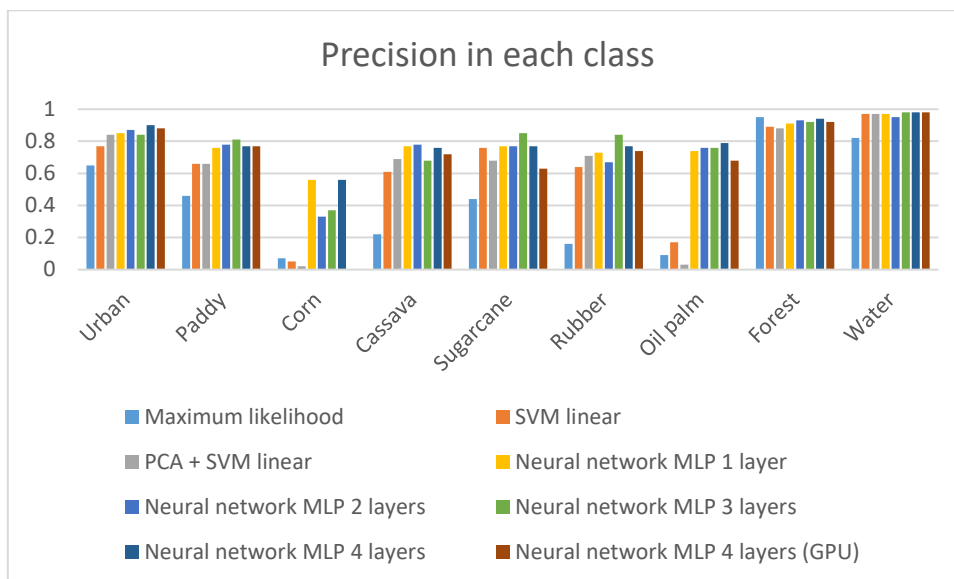
Figure 6 The comparison of the precision in each class of land cover classification methods

The confusion matrix of land cover classification method by using (1) maxim likelihood shows in table 3. The confusion matrix of land cover classification method by using (7) neural network using multi-layer perceptron with 4 hidden layer composed of 100 nodes in each hidden layer shows in table 4.

Table 3 The confusion matrix of land cover classification method by using maxim likelihood

		Predicted class							
		Urban	Paddy	maize	Cassava	Sugarcane	Rubber	Oil palm	Forest	Water
True class	Urban	253345	21909	705	36147	755	16765	1949	29906	10282
	Paddy	13602	138032	3300	16504	96935	112536	40587	97189	309
	maize	406	2348	11521	8405	2517	22774	2494	1390	0
	Cassava	9231	6280	37352	61303	2765	55503	3804	5117	59
	Sugarcane	2386	33225	1675	4877	129225	30586	23467	22772	96
	Rubber	3832	27460	24288	44796	43915	636579	88849	175906	108
	Oil palm	424	2115	621	1198	620	55094	179243	54722	59
	Forest	86747	69692	79166	98991	18031	2979436	1600141	7750878	106547
	Water	19951	1090	26	458	52	883	306	30156	551472

Table 4 The confusion matrix of land cover classification method by using neural network using multi-layer perceptron with 4 hidden layer composed of 100 nodes in each hidden layer

		Predicted class							
		Urban	Paddy	maize	Cassava	Sugarcane	Rubber	Oil palm	Forest	Water
True class	Urban	302145	14327	77	1112	1380	2257	459	44368	5638
	Paddy	4969	399535	172	1572	32770	8165	1340	68648	1823
	maize	387	3624	2558	10456	2090	4049	875	27808	8
	Cassava	1997	3033	695	93182	5145	11477	506	65214	165
	Sugarcane	2019	21319	18	2141	194051	3117	504	24883	257
	Rubber	2460	6454	91	4448	3623	559454	2140	466783	280
	Oil palm	700	4665	14	446	821	3299	133067	150961	123
	Forest	17603	61951	894	8768	11868	130373	28941	12524279	4952
	Water	2550	3282	18	107	203	180	25	15164	582865

3.2 Discussions of land cover classifications

From the experimental results as table 1-4 and figure 3-6, we investigated that the land cover classification using (1) maxim likelihood gave the lowest overall accuracy (the overall accuracy of 60.29%) but it took the fastest computing time (the computing time of 35 seconds).

While, the land cover classification using (2) support vector machine using linear kernel provided high overall accuracy (the overall accuracy of 87.10%) but it gave low value of the precision in each class especially; the class of maize (the accuracy of 5%). Also, it took the slow computing time (the computing time of 43 minutes).

Then, the land cover classification using (3) support vector machine using linear kernel, and principle component analysis did not give higher overall accuracy (the overall accuracy of 86.96%) than using support vector machine using linear kernel but it took the faster computing time (the computing time of 28 minutes).

Next, the land cover classification using (4) neural network using multi-layer perceptron with 1 hidden layer composed of 100 nodes provided high accuracy (the overall accuracy of 89.56%) and gave the acceptable value of the precision in each class. Also, it took the fast computing time (the computing time of 7 minutes).

Then, we found that when the number of hidden layer increases, the accuracy will be higher such as the land cover classifications using (5) neural network using multi-layer perceptron with 2 hidden layer composed of 100 nodes in each hidden layer, (6) neural network using multi-layer perceptron with 3 hidden layers composed of 100 nodes in each hidden layer but it takes the slower computing time.

Here, we explored that the land cover classification using (7) neural network using multi-layer perceptron with 4 hidden layer composed of 100 nodes in each hidden layer gave the highest accuracy (the overall accuracy of 91.83%). It provided the high accuracy in each class such as the three highest ranks including water (the accuracy of 98%), forest (the accuracy of 94%), urban (the accuracy of 90%) and the three lowest ranks including maize (the accuracy of 56%), cassava (the accuracy of 76%), para-rubber (the accuracy of 77%). However, it took the slow computing time (the computing time of 51 minutes).

Moreover, when the graphic processing unit was employed such as the land cover classifications using (8) neural network using multi-layer perceptron with 4 hidden layer composed of 100 nodes in each hidden layer, it took the faster computing processing time (the computing time of 21 minutes). However, we found that the overall accuracy was reduced (the overall accuracy of 90.16%) since it may be incorrect in setting the parameters.

4. CONCLUSIONS

We proposed the comparison of land cover classification methods to find a suitable classification method for land cover types with economic crops; urban, water, forest, rice, cassava, maize, para rubber, sugar cane, and oil palm in Thailand. Multiple Landsat-8 (OLI) images were used as dataset. Supervised classification methods; maximum likelihood, support vector machine, and neural network, were employed to classify the land cover types. In the experiments, the results showed that the land cover classification using neural network using multi-layer perceptron with 4 hidden layer composed of 100 nodes in each hidden layer the highest accuracy with the overall accuracy of 91.83%, the kappa coefficient of 0.7552, and the lowest accuracy in each class of 56% and computing time of 51 minutes. While, maximum likelihood method provided the lowest accuracy with the overall accuracy of 60.29%, the kappa coefficient of 0.3108, and the lowest accuracy in each class of 7% and computing time of 35 second.

ACKKNOWLEDGEMENT

REFERENCES

Al-Razzaq Abd, H. A., Alnajjar, H. A. (2013) Maximum Likelihood for Land-Use/Land-Cover Mapping and Change Detection Using Landsat Satellite Images: A Case Study "South Of Johor", International Journal of Computational Engineering Research, 3(6), PP. 26-33.

Bangkok Post. (2017), Thai organic foods have healthy growth potential. SCB Economic Intellignce Center, Retrieved 7 February 2017.

Civco, D. L. (1993). Artificial neural networks for land-cover classification and mapping. International Journal of Geographical Information Systems, 7(2), PP. 173-186.

Cortes, C.; Vapnik, V. N. (1995). Support-vector networks. Machine Learning, 20(3), PP. 273–297.

De Maesschalck, R., Jouan-Rimbaud, D., Massart, D.L. (2000). The Mahalanobis distance. Chemometrics and Intelligent Laboratory Systems, 50 (1), PP. 1–18.

Graupe, D., (2013) Principles of Artificial Neural Networks.3rd Edition. World Scientific Publishers, pp. 203–274.

Haykin, S. O. (2008). Neural Networks and Learning Machines (3rd Edition). Pearson.

Jackson, J. E. (1991). A user's guide to principal components. New York, NY: Wiley.

Le Cam, L. (1990). Maximum likelihood — an introduction. ISI Review, 58 (2), PP. 153–171.

Lu, D., Mausel, P., Batistella, M., Moran, E. (2004). Comparison of land-cover classification methods in the Brazilian Amazon basin. Photogrammetric Engineering and Remote Sensing, 70(6), PP. 723-731.

Meyer, D., Leisch, F., Hornik, K. (2003). The support vector machine under test. Neurocomputing, 55, PP. 169-186.

Millar, R. B. (2011). Maximum Likelihood Estimation and Inference. Wiley.

Mizutani, E., Dreyfus, S., Nishio, K. (2000). On derivation of MLP backpropagation from the Kelley-Bryson optimal-control gradient formula and its application. Proceedings of the IEEE International Joint Conference on Neural Networks (IJCNN 2000), Como Italy, July.

Pal, M., Mather, P. M. (2005). Support vector machines for classification in remote sensing, International Journal of Remote Sensing, 26(5), PP. 1007-1011.

Sisodia, P. S., Tiwari, V., Kumar, A. (2014). Analysis of Supervised Maximum Likelihood Classification for remote sensing image. International Conference on Recent Advances and Innovations in Engineering (ICRAIE-2014), Jaipur, pp. 1-4.

Sritarapipat, T. Takeuchi, W. (2015). Estimating land value and disaster risk in urban area in Yangon, Myanmar using stereo high-resolution images and multi-temporal Landsat images, Asian conference on remote sensing 2015, Philippines, October 19-23.

The World Bank. (2016). Agriculture, value added (% of GDP). Retrieved 26 November 2016.

Development of Low-Cost Remote Control Photometer for Solution Concentration Determination

Po-Jui Chen, Chun-Chieh Lien, Yi-Hao Lin, Ming-Fu Chen

Instrument Technology Research Center, National Applied Research Laboratories,
20, R&D Rd. VI, Hsinchu Science Park, Hsinchu, Taiwan
Email: proray@itrc.narl.org.tw; 1209645@narlabs.org.tw; 1609809@narlabs.org.tw; mfchen@itrc.narl.org.tw

KEY WORDS: Beer Lambert law, LED, Bluetooth

ABSTRACT: Researchers usually use spectrophotometers to analyze the compositions of the unknown solution and estimate the concentration according to its light absorbance. Although spectrophotometers could provide a wide range of spectrum for "spectro-scanning" purposes, most spectrophotometers were not suitable for outdoor measurements and expensive because of elaborate optical components. For some biochemical inspection or clinical analysis applications, only a few specific wavelengths of light are applied to examine the light absorbance of ascertaining chemical analyte regularly. The light emitting diode (LED) is a kind of superior light source that brings an excellent monochromatic light beam profile and delivers wavelengths from ultraviolet to near infrared. In this work, a low-cost and remote control photometer is developed by use of the LED. Four different wavelengths of LEDs are installed inside the photometer as the inspecting light directly to substitute for the complicated diffraction grids or the delicate optical components to low down the cost of the photometer. These four LEDs are collimated by a single collimator lens to make all the light beams be able to irradiate the analyte entirely in the cuvette. Each time only one LED can be switched on, according to the wavelength requirements of the inspections. The proposed photometer is controlled by personal handheld devices, such as smartphones and tablets that are equipped the exclusive application program (APP). The APP is designated to communicate with the photometer via the interface of Bluetooth Low Energy protocol (BLE). The photometer establishes the excellent linearity relationship between sample concentrations and their absorbance in the testing experiments. As a result, the low cost photometer proves itself to determine the concentration of the sample preliminarily for industrial inspections as well as to be basic tutorial equipment in laboratory courses.

1. INTRODUCTION

The spectral characteristics of substances are significant for scientists to analyze their compositions and the studies on the feature of the spectrum have been persisted for centuries. Many principles of non-destructive inspection have been proposed base on the behaviors of spectrum, e.g. sugar content and acidity diagnosis in fruits. The methods about spectrum analysis can be divided into active and passive types. The active type of the spectrum inspection is to analyze the spectrum distribution of self-illumination objects, whereas the passive type is to illuminate the objects with different wavelengths of monochromatic light and detect the corresponding light intensity. According to the previous researches, every substance only can absorb the certain spectrum when its molecule encounters the photons progressing with the specific wavelength. As for the remainder wavelengths of radiant photons, they have no reaction with that substance but just pass through it directly. Thus, the light intensity of transmitting light is relatively lower than the original incident light due to the effect of photon absorption. If the primary intensity of the incident light is assumed to be I_0, and the power of transmitting light is I, the light transmittance of the substance illuminating by the monochromatic light is defined as follows:

$$T = \frac{I}{I_0} \tag{1}$$

Apparently, the light transmittance T is less than 1 because I_0 is always larger than I. The Beer Lambert law (Gupta, 2015) (Shi, 2003) is the well-known theory in the field of biochemistry to describe the relationship between the solution concentration and the light transmittance. The theory states that dense solution usually absorbs more light energy and releases less light transmittance than sparse solution. Equation (2) lists the Beer Lambert function, where Abs is the absorbance, $\varepsilon(\lambda)$ is a wavelength dependent extinction coefficient, L is the total length of the light path, and C is the solution concentration. The light absorbance Abs can also be called as optical density (OD).

$$Abs = log_{10}\left(\frac{1}{T}\right) = \varepsilon(\lambda) \cdot L \cdot C \tag{2}$$

According to the Beer Lambert equation, the light absorbance of the solution equates to a logarithm ratio of the

reciprocal transmittance and is directly proportional to the concentration of the analyte. Thus, if the inspection light path is fixed, the analyte concentration and the transmission ratio of light present a perfect linear relation with each other.

Traditional spectrophotometer is the common instrument that can resolve the complex light into individual spectrums for scientific researches or material inspections. The first spectrophotometer was developed by Arnold J. Beckman and his colleagues in 1941 (Cary, 1941). The Beckman spectrophotometer adopts the incandescent lamp as the illuminant of the instrument and integrates the phototube to detect the light response. Until today, most spectrophotometers still follow the basic structure of the Beckman spectrophotometer, including a slit, a diffraction grid and focusing lens, and the grid is spun by a motor to diffract the incident light (Chen, 1999). Because of the complicated optical mechanism, traditional spectrophotometers are delicate and expensive. Besides, most spectrophotometers must collocate with a computer to acquire, display and store the dispersing spectrum data. Consequently, it is rare to be teaching aids in high school education or even in the teaching of laboratory courses at university level. Moreover, for some industrial applications, the function of "spectro-scanning" is redundant because only a few wavelengths of spectra are implemented for analysis regularly. It merely requires some narrow-band inspecting light rather than a wide range of wavelengths since the compositions of the analyte have been ascertained.

In the 20th century, the rapid growth in semiconducting manufacture technologies facilitate the LED to produce excellent light beam profile and emit peak wavelengths spreading from ultraviolet to near infrared (Holonyak, 1962). Low power consumption and distinct distribution of output wavelength prompt LEDs to be the prime inspection light source in many researches (Le, 2011) (Veras, 2009). Liao et al. design a portable digital microscope that utilizes a commercial digital camera embedding with specific magnifying lens and a ring shape of LED light (Liao, 2008). The microscope can magnify the image of a tiny object up to 150x under the adequate illumination of the LED light. Zhang introduces an effective method to capture the particle image of drug solution on the pharmaceutical injection system (Zhang, 2018). By means of synchronizing the high-speed image acquisition device with the novel LED illumination techniques, including light transmission and reflection mechanisms, the system can get a sequence of particle images from the same reagent container. Tumas and Serackis propose an algorithm about food quality inspection based on background subtraction on multi-spectral images. A low cost near infrared camera is designated to acquire the spectral images of food samples under the illumination by four different peak wavelengths of LEDs separately. LED has become the most superior and popular light source nowadays.

In this work, a low-cost and remote control photometer is proposed by use of the LED as the main inspection light. Comparing with other commercial spectrophotometers that are equipped with a halogen bulb, the proposed photometer uses LED as the monochromatic wavelength of the inspecting light directly without any elaborate optical components. Since discarding the precise dispersing configuration, the cost of the photometer can be dropped drastically. Four LEDs are set in a light module and collimated by a single collimator lens that is placed as close as to the cuvette holder to keep light losses at a minimum. The kinds of LEDs which are set in the photometer depend on the wavelength requirements of the inspections. Besides, in order to improve the limitation of measurement in the laboratory, personal handheld devices, such as smartphones or tablets, replaces desktop computers to control the photometer as long as the devices are equipped the exclusive control APP of the photometer. All measuring data are sent to the APP for storage and further analysis via the interface of BLE protocol. A common 9V battery is responsible for the entire power supplement to avoid the restriction of usage in the outdoors or other critical environments. Therefore, the photometer can be used for solution preliminary analysis anytime and anywhere. Although the photometer is still at the stage of development, it establishes the excellent linearity relationship between sample concentrations and their absorbance in the testing experiments. This novel photometer is expected to implement either in the teaching of laboratory courses or for industrial preliminary inspections.

2. SYSTEM ARCHITECTURE

The similar design idea has been brought up by the author in 2017 (Chen, 2017). That portable photometer also uses LEDs as inspection light source directly and leaves out complicated optical assemblies. The photometer consists of three independent parts, i.e. the LED driver module, the cuvette holder module, and the light sensing module. It provides the functions for solution transmittance measurement as well as substance fluorescence inspection simply by shifting the location of the LED driver module. Eight LEDs with different wavelengths are dispatched symmetrically within the knob of the LED driver module. By twisting the knob, operator can select the desired wavelength of LED depending on the compositions of the testing samples. The LED intensity can be adjusted simply by altering the resistance of the potentiometer manually. The photometer is equipped with two cell rechargeable lithium-ion batteries and a battery charge protection circuit is involved in it as well. Thus, all these facilities increase the manufacturing cost of the LED type photometer and some functions must be simplified if the total cost is expecting to be restricted within 100 USD.

Figure 1 is the detail system framework of the low cost photometer. The device also comprises three primary

parts, including LED current driver, photoelectric signal amplifier, and signal processing module. The system architecture is similar to the previous photometer which is proposed by the former research team but has some modifications. The differences are listed as follows:

1. The photometer is a single-function facility providing for transmittance measurement only. No any side-lights are arranged to excite the sample to generate fluorescence reaction.
2. Rather than using the complicated rotatable mechanism to switch different LEDs, only four LEDs are fixed on the brace board that erects in the front of the cuvette holder. These four LEDs and the intensity are controlled by the corresponding electric switch.
3. All the setting parameters of the photometer are varied by the exclusive APP via BLE communication interface instead of entity knobs or switches. The light intensity can be explicitly assigned by means of specific digital commands to avoid unnecessary trial and error regulation.
4. The photometer has no battery charge circuit or any rechargeable lithium batteries inside. It must connect an extra regular 9V battery to supply the sufficient power consumption for the whole device.
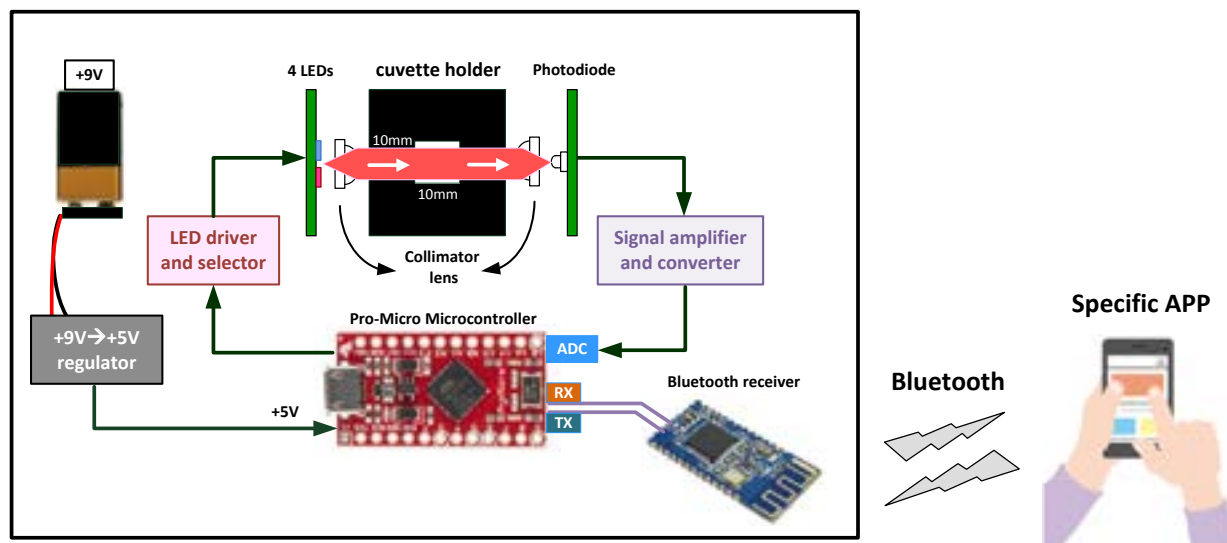

Figure 1. System configuration of the low cost photometer.

As the function block diagram shows in figure 1, the Arduino controller is the major "brain" which is in charge of the data processing and transmission. The controller is operated under the voltage of +5V, and therefore an additional voltage regulator is essential to depress the input power from +9V to +5V. In order to promote measurement accuracy, the LED current driver and the photoelectric signal amplifier regulate the steady current to drive LED and convert the transmitted light to electric signal, respectively. The device takes a high sensitive photodiode to sense the slight variation of transmitted light. The cuvette holder is placed in the middle of four LEDs and the photodiode, and used to settle a 10mm x 10mm cuvette. In the next paragraphs, detailed descriptions will explain how the individual module works and its design principle.

2.1 Mechanical Design

The photometer is designed in the shape of a saddle whose dimension is 125mm x 100mm x 66mm. Figure 2(a) is the mechanic design graph of the photometer in perspective. The cuvette holder pedestal locates in the central part of the photometer, and the holder cavity is covered over by a shiftable cap to prevent the transmittance measurement from the interference of environmental stray light. Figure 2(b) is the component assembly photograph of the photometer under its saddle-shape shell. All components are mounted on the mother board, including the cuvette holder pedestal, LED brace board, photoelectric signal amplifier, and the other electronic parts. The red printed circuit board (PCB) on the rear of figure 2(b) is the commercial Arduino-compatible microcontroller board, Sparkfun Pro-Micro, while the blue board in the front is the Bluetooth transceiver, HM-10. Both LED brace board and photoelectric signal amplifier stand erectly on either side of the cuvette holder pedestal, and are welded firmly on the mother board to make sure the inspection light path is fixed. Hence, the photometer can be qualified to determine unknown concentration of the testing sample based on the Beer Lambert law. Besides, two individual collimator lenses are mounted on the entrance and exit window of the transmittance light inside the cuvette holder pedestal. The first lens collimates the spreading angle of LED light and lets the angle of light irradiate into the cuvette identically even the light emit from different LEDs. All light will converge on the sensing area of the photodiode which is placed at the focal point of the last collimator lens.
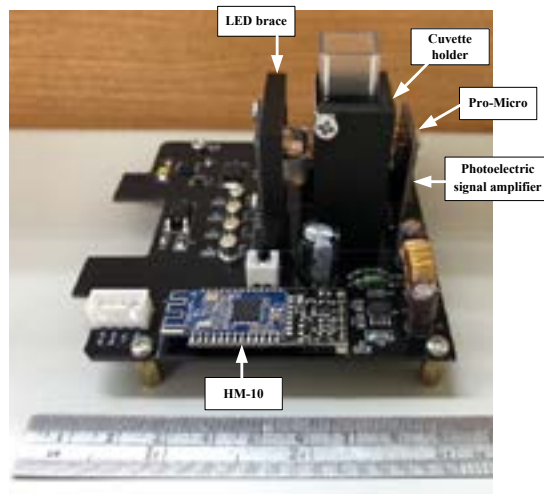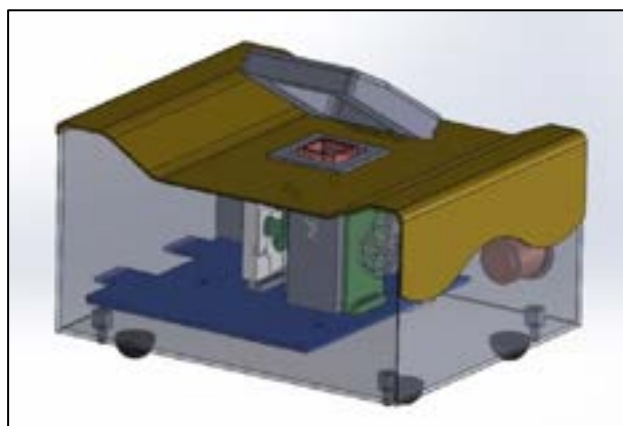
(a) The prime mechanic design chart   (b) Component assemblies inside the photometer
Figure 2. The mechanic design and component assemblies of the photometer.

The cuvette holder pedestal is a specific mechanism which is used to place a standard plastic or quartz cuvette. As the pictures shown in figure 3(a), the cuvette holder pedestal is a hollow cuboid with two windows on its either sides. The pedestal is screwed on the mother board between the LED brace board and the photoelectric signal amplifier. A particular leaf spring is fastened on the pedestal top and it presses the cuvette to adhere to the holder wall steadily avoiding slight sway. General plastic cuvettes are not identical exactly in dimension due to the tolerance of injection molding processing. The leaf spring can ensure that the cuvette is fixed at the same location whenever the cuvette is plugged in. The two windows on the cuvette holder are designed to let the inspecting light pass though thoroughly. Since the sample solution may spill out and damage the electric components below, two glasses are seal on the light entrance and exit window to prevent water outflow.
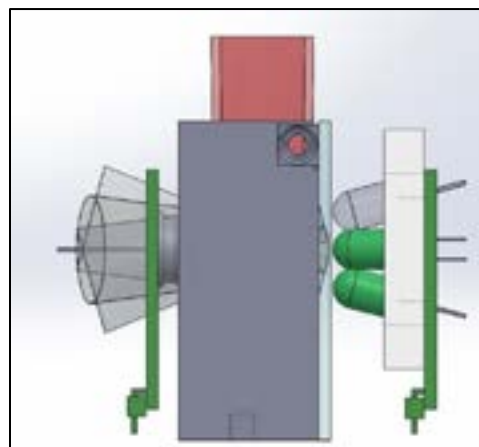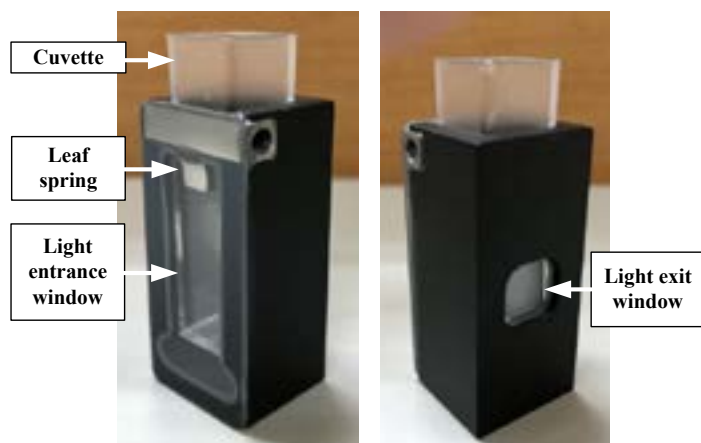
(a) The entity of the cuvette holder pedestal   (b) The simulation of LED light path
Figure 3. The cuvette holder pedestal and the light path simulation of the photometer.

Another special mechanical design deserves to be mentioned in this work is the LED brace board. Because of space limitation in the photometer, only four LEDs are allowed to install in the device for the transmittance measurement. Every time only one LED can be turned on depending on the wavelength requirements. All these LEDs are 5mm in diameter and their dies are encased in an epoxy dome case for protection. The crystal epoxy case functions as a light beam condenser, and therefore the effective viewing angle of this LED type rarely exceeds 30 degree. By considering optimizing the optical path length of different inspecting light, four LEDs are deployed in a crisscross orientation on the plastic brace. The special ramps which are fabricated on each LED socket of the brace tilt the central points of LEDs to aim at the photodiode on the opposite side. The inclined angle of the LED deviates from the central optical axis of the photodiode is around 15 degree. According to the light propagation simulation in figure 3(b), the LED emitting light can cover the whole photodiode sensing area whatever sockets LED is welded on. The brace is locked on a PCB and then the PCB is mounted on the mother board by a five pin connector to acquire respective current power to drive the four LEDs.

2.2 LED driver and selector

The inspection light stability is a critical factor that affects the measurement accuracy significantly. In order to prevent LED from slight flicker, a reliable current source is responsible to stabilize light intensity as long as the LED is powered on. As the behaviors of most illuminators, the larger the driving current supply, the brighter the LED will appear. Figure 4 is the circuit schematic of the current source and LED switching selector. According to the circuit design, the voltage V_{set} remains constant due to the negative feedback complement by the operation amplifier U_{IB}. Since V_{in} is also a stationary voltage, I_O can be regarded as a constant current and is calculated as:

$$I_o = \frac{V_{in} - V_{set}}{R} = \frac{(5 - V_f) - V_{set}}{R} \tag{3}$$

Where V_f is the constant voltage drop of diode (D_1) under a forward bias. Afterward the driving current is steadied by a PNP transistor, MJD42CG, and distributes over four LED selectors. The current flow through the LED and halt at the switching selector until the selector is activated. Four I/O pins of the Pro-Micro microcontroller which are labeled from "LED1_SW" to "LED4_SW" in sequence control individual LED switching selector. If the pin outputs low signal ($\approx$ 0V) at the base of transistor (2N2907A), then the driving current can pass through the transistor to ground and consequentially the corresponding LED will be turned on. These four I/O pins keep at high ($\approx$ +5V) level in the initial state and no LEDs are active when the photometer is powered on. It merely demands a single wavelength to be the inspecting light for each testing analyte. Hence, each time the control firmware permits the microcontroller to pull one of four pin levels down during the transmittance measurement processing.
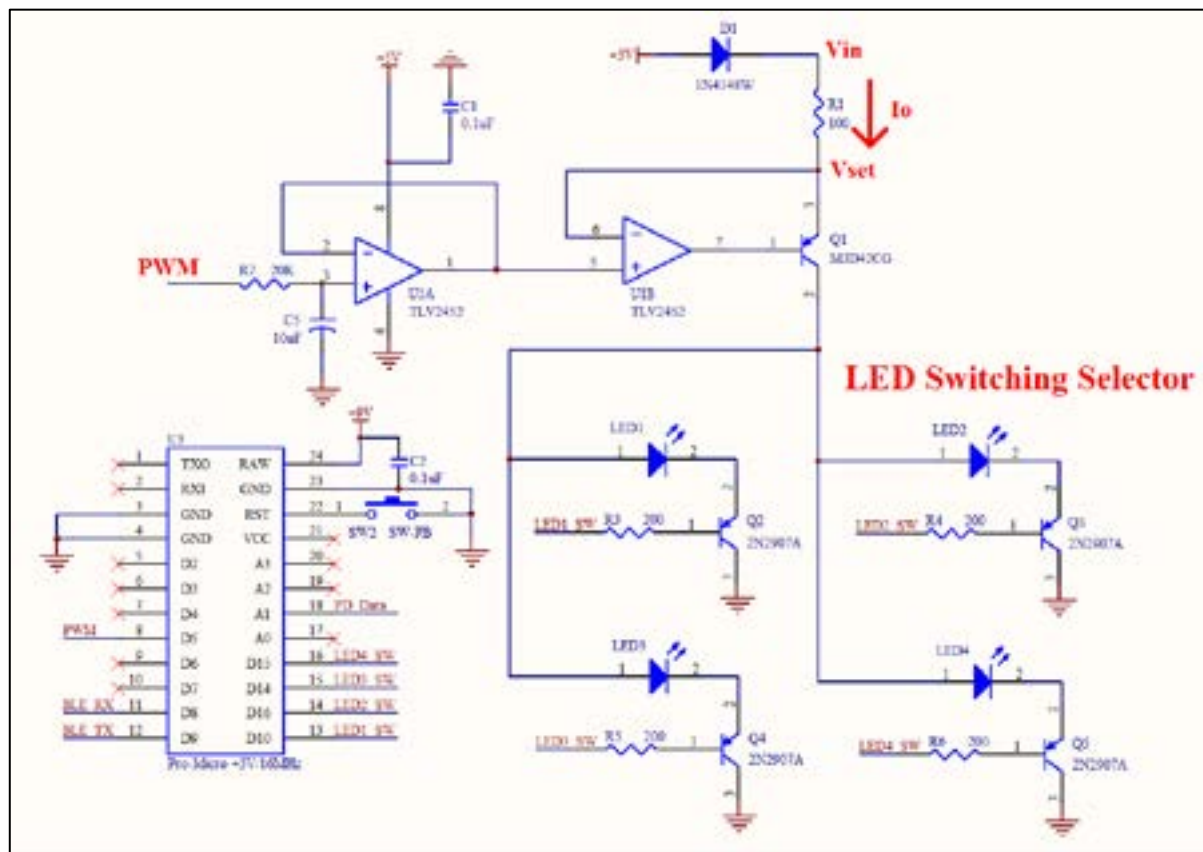

Figure 4. LED driving current source and selector circuit.

According to equation (3), the brightness of LED is adjustable simply by altering the voltage, V_{set}. Increasing V_{set} will reduce the magnitude of the current, I_O, and dim the light intensity. On the contrary, decreasing V_{set} can bring more current to the LED and make it brighter. However, it should notice that voltage, V_{set}, must exceed the forward voltage of the LED specification. Otherwise, the LED can't irradiate any more even though the sufficient current has been applied to it. The most common way to generate a variable voltage signal in the automatic control system is to integrate a digital-to-analog converter (DAC) with a microcontroller. In order to cut down the cost, a low precise DAC-like circuit is built by implementing the pulse width modulation (PWM) function of Pro-Micro microcontroller with a few components instead of using external DAC chips (Scuola, 2016).

PWM is a sequence of a square wave delivering with alternate full high (+5V) and full low (0V) signal repeatedly. The durations of the full high and full low signal are variable in each pulse, and the duration ratio of full high signal to the wave period is defined as the duty cycle of PWM. The duty cycle represents the percentage of the period time in which the wave keeps at maximum amplitude, i.e. +5V voltage. If the frequency of the PWM is fast enough, the high-low pattern can be seemed as a speedy ON-OFF mechanism to simulate various analog signals in between 0V and +5V by changing the duty cycle. The equivalent output voltage providing from the PWM is the average of the voltage that arises over a period time of the wave. In other words, the output voltage is equal to the amplitude (+5V) multiplied by the duty-cycle and is also called the mean value of the PWM. For example, the PWM has a mean value of 2.5V if the duty cycle is set at 50% while the voltage appears 5V when the duty cycle is modified to100%.

According to the signal processing theory, every signal is comprised of various basic waves with different frequencies and amplitudes. The mean value of PWM is exactly preserved at the part of zero frequency (or call as DC value). Hence, a low pass filter is attached to the PWM output pin of the Pro-Micro microcontroller to reserve its DC part and block the remnant frequencies of the PWM. As the LED driver circuit shows in figure 4, resistance R_7 and capacitor C_5 are used to compose a simple low pass filter whose cut-off frequency f_c is set as follows:

$$f_c = \frac{1}{2\pi R_7 C_5} = \frac{1}{2\pi \times 2 \times 10^4 \times 1 \times 10^{-5}} = 0.796 (H_z) \tag{4}$$

Since the cut-off frequency f_c is lower than 1, the low pass filter extracts the DC value of the PWM signal and restrains almost the other parts. This DC value is what the device desires to be taken as the setting signal of driving current for the LED brightness adjustment. Although this configuration could not compete against high precision and high speed DAC chips, it was good enough for the low cost photometer to deal with the process of concentration preliminary measurement.

2.3 Signal converter and control module

In order to estimate the light absorbance of the testing solution, the transmitting light intensity must be transferred into the electric format for further data processing and transmission. The high sensitive semiconductor detector which is adopted in the photometer to sense light intensity is the Hamamatsu S1087-01 photodiode. This model of photodiode can detect the slight variation of light intensity whose wavelength distributing from 320nm to 1100nm. When the photon strikes on the photosensitive area of the photodiode, it will create an electron-hole pair at the internal P-N or PIN junction due to the inner photoelectric effect. If the photon absorption occurs in the barrier region of the junction, the holes and the electrons will move toward the anode and the cathode, respectively. A photocurrent is produced owing to the phenomenon of the electron-hole movement. The amount of photocurrent generated from the photodiode depends on the energy of the photon absorbed on the active area.
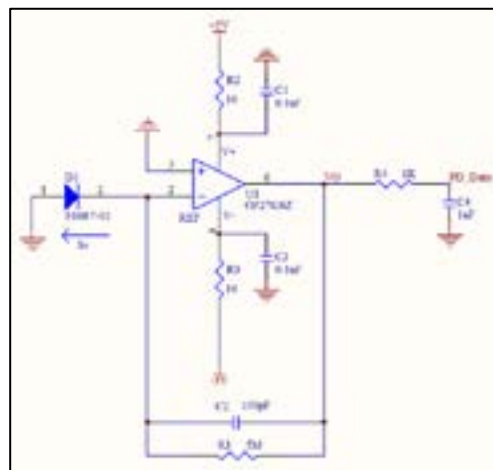

Figure 5. The photoelectric signal converter and amplifier circuit.

Most electrical control system handles signals in voltage mode rather than current type, hence the photocurrent signal must be converted into voltage format and get digitization for data computing and storage. Figure 5 is the photoelectric signal converter circuit with the amplitude amplifier utility. The circuit is the ordinary transimpedance amplifier that operates the photodiode in photovoltaic mode. The anode of S1087-01 is connected to the ground and the cathode attach to the negative input terminal of the operational amplifier, OP27GSZ. Obviously, no reverse bias is applied to the photodiode and keeps the voltage drop zero because the positive input of OP27GSZ is put at the

ground as well. A feedback resistor, R_1, is arranged between the negative input and the output terminal of the operational amplifier. When the photocurrent derived from the photodiode, the current flows from the cathode to its anode and causes a plain voltage drop across the resistor, R_1. The voltage drop is just the result of the photocurrent conversion that reflects the transmitting light intensity in voltage. According to the basic Ohm's law, the voltage drop equals to the photocurrent multiplied by R_1, i.e.

$$V_o = I_o \times R_1 = 5 \times 10^6 \times I_o (V) \tag{5}$$

As the I-V correlation shows in the above relations, the feedback resistor not only translates the photocurrent into voltage format but also amplifies the amplitude of the photocurrent at the same time. Therefore, R_1 can be seemed as the gain of the transimpedance amplifier. Since the power of LED light is quite weaker than laser light, the R_1 resistance must be large enough to magnify light variation either for high concentration or low concentration solution. Besides, an additional capacitor, C_2, which is in parallel with R_1 is used as a complementary buffer to minimize gain peaking. Before getting digitization, another low pass filter is designated to expel unnecessary noise induced from the conversion to improve signal-to-noise ratio (SNR). Eventually the Pro-Micro microcontroller translates the processed signal into digital format through its own analog-to-digital converter (ADC) with 10 bits resolution. Once the application program asks for the present light intensity, the Pro-Micro microcontroller will send the two bytes digital data back to the program via HM-10 Bluetooth transceiver.

Rather than furnishing the photometer with versatile data analysis function, all measurement data have to transfer for outside devices to calculate the light absorbance and determine the correlation between optical density and solution concentration. Considering making the photometer available to the public, an exclusive Android-based application program is provided for users to install in their own smart handheld devices themselves. Smart handheld devices, such as smartphones and tablets, can offer high performance computing ability for the program to analyze the absorbance data in real time. Figure 6 shows the graphical user interface of the control program. User can download this APP directly from the Google Play store without paying any fees. Both automatic and manual measurement modes are embedded in the APP to cope with different inspecting scenarios. Besides, the APP has a capacity of evaluating the linearity of the analyte concentration versus the light absorbance instantaneously and establishes relative linear regression curves on the screen. In addition to data analysis and storage, the program dominates the photometer thoroughly so that users must use it to manipulate the photometer, e.g. to select the LED for the inspection, to adjust LED brightness, or to monitor the sysyem status etc. The signal communicating medium between the control APP and the photometer is through the commercial Bluetooth Low Energy transceiver, HM-10, that requires very low power consumption for data transmission. Compared with traditional spectrophotometers, all these utilities make the photometer more practical and flexible on the usage of field measurement in extreme environments.

Figure 6. The user control interface of the Android application program.

3. EXPERIMENTS

The Beer Lambert law tells that the concentration of the solution is proportional to its light absorbance if the light path length is fixed and the wavelength conforms to the spectrum characteristic of the substance. Due to the one-to-one relationship, the photometer can determine solution concentration once the linear relation of absorbance versus the corresponding concentration has been established. Thus, the linear regression determination of these two

variables is the critical reference to evaluate the performance of the photometer. In this work, six dilutions of standard bovine serum albumin reagents (BSA, a kind of serum albumin protein derived from cows) are setup for linearity testing of the proposed photometer. In order to let these protein solutions produce differential reaction in color, the Bio-Rad Protein Assay is adopted to dye the protein reagents. The Bio-Rad Protein Assay is a kind of biochemical dye assay that consists of dye, phosphoric acid, and methanol. The dye reagent can bind with protein molecules and brings differential color changes associating with various concentrations of protein. Table 1 lists the compositions of the six testing protein reagents. The amount of BSA solutions are proportioned and diluted with appropriate distilled-deionized water (DD water) to compose six relative concentrations in the range from 0.5x to 8x. Each tube of BSA solutions is added 2ml Bio-Rad Protein Assay and the reagents are sent to a vortex mixer afterward. After incubating at room temperature for 20 minutes, the phenomenon of absorbance is getting obvious over that time.

Table 1. The compositions of the protein reagents for linearity testing.

Relative concentration	0.5x	1x	2x	4x	6x	8x
Bio-Rad Protein Assay (ml)	2	2	2	2	2	2
0.01% BSA (ml)	0.05	0.1	0.2	0.4	0.6	0.8
Distilled-deionized water (ml)	7.95	7.9	7.8	7.6	7.4	7.2
Total (ml)	10	10	10	10	10	10

There are three sets of six diluted protein solutions prepared for the experiment to compare the results with each other. The 590nm LED is selected to be the inspection light source in the photometer to match the characteristic of the dyed reagent under testing exactly. Table 2 lists the results of the linearity testing with respect to light absorbance. The curves of the three sets of relative concentration versus the corresponding light absorbance are plotted in figure 7. Analyzing the data with the linear regression algorithm, the regression equations of the three testing sets are listed as follows:

$$\text{BSA} - 01: ABS = 0.0260C + 0.3172$$
$$\text{BSA} - 02: ABS = 0.0250C + 0.3434 \tag{6}$$
$$\text{BSA} - 03: ABS = 0.0272C + 0.3350$$

Where the parameter, C, represents the relative concentration of the BSA reagent and ABS is the light absorbance. The coefficients of determination, R_2, of the group BSA-01, BSA-02, and BSA-03 are 0.9854, 0.974 and 0.9761, respectively. Moreover, all the standard deviations of the absorbance derived from the same concentration are less than 0.02. Although all the coefficients of determination were not over 0.99, the photometer was still discriminative and reproducible enough for concentration evaluation.

Table 2. Result of relative concentration of BSA solutions with light absorbance.

Relative concentration	0.5x	1x	2x	4x	6x	8x
BSA-01 absorbance	0.318	0.342	0.378	0.430	0.479	0.515
BSA-02 absorbance	0.354	0.366	0.406	0.425	0.508	0.539
BSA-03 absorbance	0.337	0.358	0.395	0.458	0.510	0.536
Standard deviation	0.018	0.012	0.014	0.018	0.017	0.013

4. CONCLUSION AND DISSCUSSION

In terms of basic function validation, the experiment verifies that the photometer possesses adequate capacity for reagent concentration determination. Compared with the traditional spectrophotometers, four LEDs are assembled in the photometer and used as the inspecting light directly without any expensive dispersers or sophisticated optical components. The cost of the device is markedly reduced so that the novel photometer has a great advantage of replacing regular spectrophotometer equipment in the teaching of photoelectric colorimetry. In this paper, the authors have presented detailed descriptions about the working principle and system architecture of the photometer. The peak wavelength of the LED is the major factor to decide which kind of LED shall be taken for the measurement in order to induce the necessary phenomenon of photon absorbance. By considering optimizing and

simplifying the illumination configuration, all LEDs are mounted on the particular surface of the brace that tilts LEDs to aim at the light detector on the opposite side. By means of the specific inclined angle, the emitting light of the LED is guaranteed to cover the photodiode sensing area entirely. Both the LED brace and the light detector are welded firmly inside the photometer to make the inspection light path fixed and meet the inspection condition of the Beer Lambert law. A reliable current driver and a high sensitive detector play an important role in stabilizing light intensity and translating the transmitted light intensity into electric signal, respectively. Moreover, a unique cuvette holder pedestal and a special leaf spring are also proposed in this work to let the cuvette stay steadily avoiding slight sway. Based on the design information, the photometer can be reconstructed easily for the feasibility of cross-validation in the study of solution concentration determination.

Unlike general instruments, there are no any entity potentiometers or switches assembling on the novel photometer except the power switch. All the setting parameters of the photometer are controlled by the APP which is installed on the Android operating system. According to personal preferences, users can choose any appropriate handheld devices to manipulate the photometer as well as proceeding data analysis and storage. The APP is designated to communicate with the photometer through the wireless interface of BLE. Thus, the remote control photometer is more flexible than standard spectrometers for outdoor measurements in the extreme environment. In the future, the research group plan to collect large amount of absorbance data from various standard reagent solution and then build up a database for the on-line query. The absorbance values are stored in the cloud database referring to the corresponding solution concentration and chemical category. As long as the handheld device connects to the Internet, user can compare the measurement data with the reference data to inquire the possible concentration from the optimal linear curve of the database.
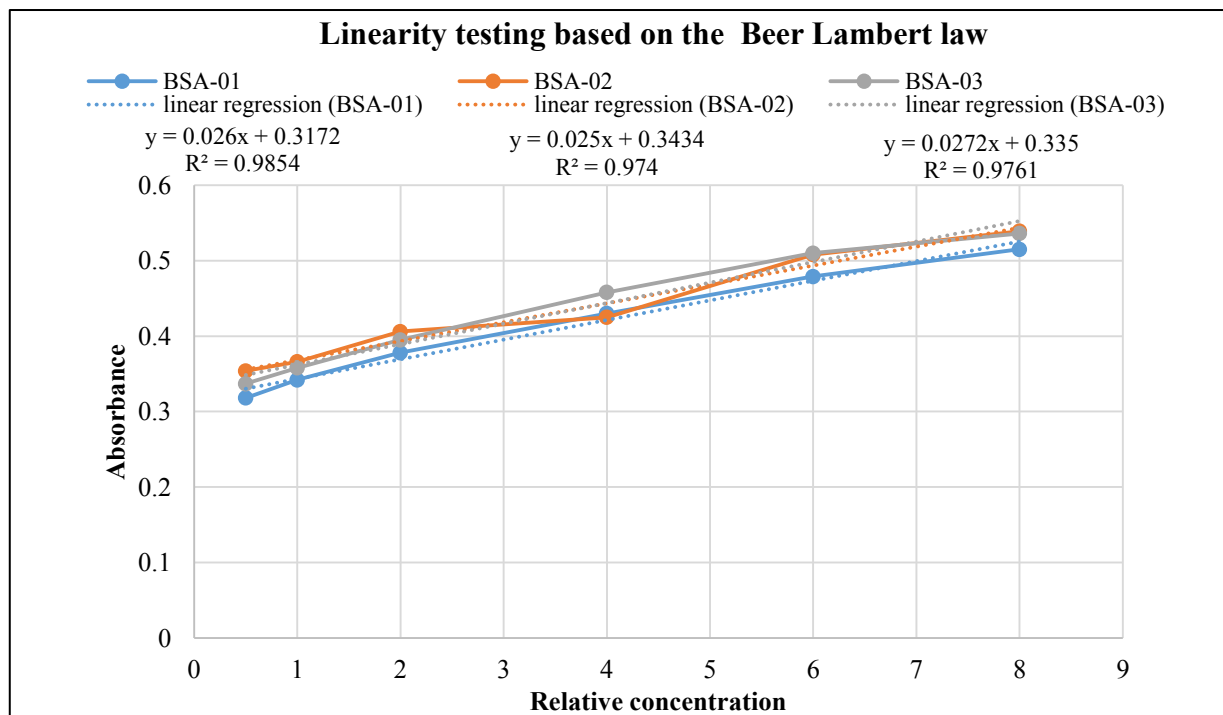

Figure 7. Relative concentrations versus the photometer voltage and the light absorbance..

REFERNCES

Cary, H. H. and Beckman, A. O., 1941. A Quartz photoelectric speetrophotometer. J. Opt. Soc. Am., (31), pp. 682.

Chen L. Q. and Juan J. Y., 1999. Principle of Spectrometers. Beijing:Beijing Institute of Technology Press.

Chen, H. Y., Nieh, H. M., Yang, M. F., Chou, Y., Chung, K., J. H., and Liou, J. W., 2016. Implementation of a Low-Cost Automated LED Photometer for Enzymatic Reaction Detection to Teach Basic Bioelectronics Technologies in Vocational High Schools. In: IEEE Transactions on Education, 59(3), pp. 194–201.

Chen, P. J., Wang, H. T., Lin, L. Y., Hsu, B. D., Liu, D. R., Hwang, C. H., Wu, W. H., 2017. A practical portable photometer using LEDs as inspection light source. In: IEEE International Instrumentation and Measurement Technology Conference (I2MTC), pp. 1-6.

Gupta, S., Liaw, H. C., Vadakkepat, P., and Starmer, C. F., 2015. Smartphone spectrophotometer for point-of-care diagnostics in low-resource settings. In: Humanitarian Technology Conference.

Holonyak Jr. and Bevaqua N., 1962. S.F. Coherent (visible) light emission from Ga(As1-xPx) junctions. Applied Physics Letters, 1, pp. 82-83.

Liao, T. S., Hsu, F. C., Lee, C. S., Huang, K. C., Chen, P. J., Chen, F. Z., 2008. The development of Portable digital microscope inspecting instrument. In: International Conference on Smart Manufacturing Application, pp. 474 – 476.

Le, J., Li Y., Hua, D., Tan, L., and Cao, N., 2011. Research on method of LED-induced chlorophyll fluorescence spectrum and image information acquisition. In: International Conference on Electronic Measurement & Instruments.

Scuola, A., 2016. Build a simple DAC for your Arduino, Retrieved July 8, 2016, from https://create.arduino.cc/projecthub/Arduino_Scuola/build-a-simple-dac-for-your-arduino-4c00bd.

Shi, J. f. and Hui, M., 2003. Micromation and applications of spectrometers. Optical Technique, 29(1), pp.13-16.

Veras, G., Silva, E.C., Silva, Lyra W., Soares, S. F., Guerreiro, T. B., and Santos, S. R., 2009. A portable, inexpensive and microcontrolled spectrophotometer based on white LED as light source and CD media as diffraction grid. Talanta, 77(3).

Tumas, P. and Serackis, A., 2017. Effective background subtraction algorithm for food inspection using a low-cost near infrared camera. In: Open Conference of Electrical, Electronic and Information Sciences (eStream), pp. 1-4.

Zhang, H., Li, X. L., Zhong, H., Yang, Y. M., Wu, Q. M. J., Ge, J., Wang, Y. N., 2018. Automated Machine Vision System for Liquid Particle Inspection of Pharmaceutical Injection. In:IEEE Transactions on Instrumentation and Measurement, 67(6), pp. 1278 – 1297.

Adjustment method of MMS point clouds using aerial photogrammetry

Takehiko Ogami [a*], Tatsuma Jahana [a], Toshiki Mitsuyasu [a], Taeko Hattori [a]

[a] Higashi-Nihon Spatial Data Center Asia Air Survey Co.,Ltd 1-2-2 Mampukuji Asao-ku
Kawasaki-shi Kanagawa, Japan 215-0004
(tak.ogami, ttm.jyahana, tsk.mitsuyasu, tae.hattori)@ajiko.co.jp

Keywords: MMS (Mobile Mapping System) / Aerial photogrammetry /Autonomous-driving / point cloud accuracy /GNSS

ABSTRACT:
Autonomous-driving technologies have received broad attention. In Japan, Dynamic map is created for autonomous-driving map. Point clouds generated by MMS (Mobile Mapping System) are suitable for building the basic information of the Dynamic map. In order to maintain the accuracy of the MMS point clouds, GCP (ground control point) by GNSS positioning is necessary. In this study, we adjusted MMS point clouds by using GCP acquired by aerial photogrammetry. And, the accuracy of point cloud data was verified according to the rules of Geospatial Information Authority of Japan (GSI). As a result, the accuracy of point cloud data was less than the allowable value of the map level 500 stipulated by the GSI. The results clearly prove that the adjustment by GCP is capable of position accuracy (Map Information Level 500) in good status of GNSS radio waves.

1 Introduction

In recent years, autonomous-driving technologies have received broad attention. In Japan, Dynamic map is created for autonomous-driving map. MMS point clouds were suitable for building the basic information of the Dynamic map. In order to integrate Dynamic map and various data, it is important to maintain position accuracy of Dynamic map. It is as important as ensuring the accuracy of MMS point clouds.

2 Characteristics of the Combination method

In order to maintain the accuracy of the MMS point clouds, GCP (ground control point) by GNSS positioning is necessary. However, it is difficult for the surveyors to observe directly on the express-way. Pedestrians are prohibited from entering the expressway. Aerial photogrammetry was used as a solution to this problem. The solution method is called the combination method with aerial photogrammetry. We explain the combination method of aerial photogrammetry. Figure.1 shows a schematic diagram of combination method.Figure.2 shows Work Flow of Combination Method. In the conventional method, XYZ coordinates with Terrestrial survey are used.

In the combination method, we use XYZ coordinate by aerial photogrammetry as GCP. We adjusted MMS point clouds by using GCP acquired by aerial photogrammetry. And the accuracy of point cloud data is verified according to the rules of GSI of Japan with RTK-GNSS. The merits of using the combination method are listed below.

Merit 1: It is possible to remote sensing places where entry is difficult.
Merit 2: Multiple times surveying are possible by aerial photogrammetry.
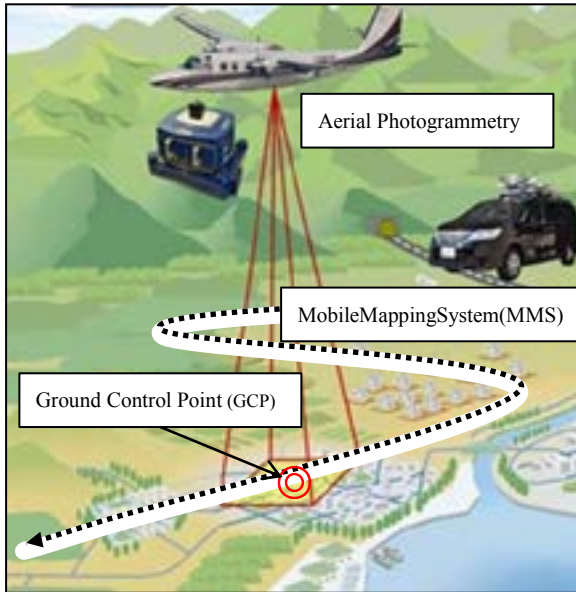

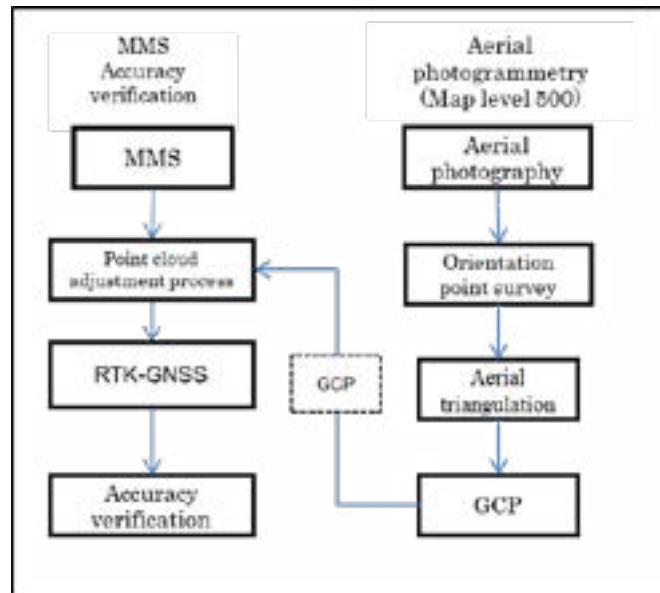Figure1 Combination Method by Aerial Photogrammetry and Mobile Mapping System(MMS)

Figure2 Work Flow of Combination Method

3. Specifications of MMS measurement and aerial photogrammetry

Table 1 show that the measuring equipment used and the Map Information Level.

Table1 Specifications of MMS Measurement and Aerial Photogrammetry

	Map information level	Measuring equipment	Distance measurement accuracy/ Photography resolution
MMS	500	Street Mapper360	(1σ) 10mm
Aerial photogrammetry	500	DMC II	80mm

4. Reasons for selection verification site

In this study, we selected the curve section of Japan National Route 246 in Hadano City as a verification site of the combination method. There is the Government Order on Road Design Standards as Japan's road design guidelines. According to this guideline, the difference

3148

between the national highway and the expressway is the design speed and the access function of the road. In depending with this guideline, we decided that the Route 246 is suitable as a place where the expressway was simulated. Figure.3 shows verification sites. The verification site.1 was selected as sample the junction of the interchange. The verification site.2 was selected as sample the cant of curve road.

Figure3 SITE.1 and SITE.2 on Route 246

5. Placement of Ground Control Points

In the placement of GCP, two points are placed at both ends of the verification site. We selected corners of grating on the road and corners of white lines. Figure.4 shows placements of GCP on SITE.1's map.

Figure 4 Corners of Grating and White Lines on the road (SITE.1)

6. Results

Table 2 shows the measured values and the results of accuracy verification by the combination method. Figure.5 shows a comparative image. The allowable error of Map Information Level 500 is in root mean square error 25cm.Both SITE.1 and SITE.2 were within the allowable error of Map Information Level 500.If accuracy of GCP is within Map Information Level 500,the horizontal and the altitude difference of adjusted point cloud data fall within the tolerance of the Map Information Level 500.
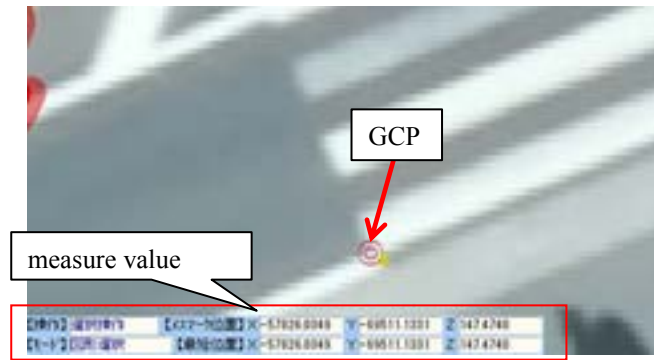
Figure 5 Comparison between GCP and measured value

Table 2 Result of accuracy verification

		count	Max(cm)	Avg(cm)	RMSE
SITE.1	MMS (Adjusted)	17	14.6	9.4	8.7
	GCP	17	29.3	12.7	14.4
SITE.2	MMS (Adjusted)	10	11.6	6.2	5.4
	GCP	10	19.9	10.5	10.9
		count	Max(cm)	Avg(cm)	RMSE
SITE.1	MMS (Adjusted)	17	10.9	3.7	5.5
	GCP	17	17.1	4.6	6.7
SITE.2	MMS (Adjusted)	10	6.5	2.6	3.4
	GCP	10	7.5	3.3	3.4
		count	Max(cm)	Avg(cm)	RMSE
SITE.1	Horizontal difference	13	17.6	10.5	11.0
	Altitude difference	13	17.8	9.3	11.5
SITE.2	Horizontal difference	6	14.5	10.1	10.2
	Altitude difference	6	6.1	3.3	6

7. Conclusions

The results clearly prove that the adjustment by GCP is capable for position accuracy (Map Information Level 500). In this research, the reception status of GNSS radio waves was good. In the future, it is necessary to consider a method in a place where the reception status is bad (city area, under the bridge, tunnel etc.)

ACKNOWLEDGEMENTS

REFERECES

Geospatial Information Authority of Japan (GSI) has produced and published operating manual and safety guidance for survey in March, 2016. http://psgsv2.gsi.go.jp/koukyou/jyunsoku/index.html

MULTI-OBJECTIVE EVOLUTIONARY ALGORITHM FOR OIL SPILL DETECTION FROM COSMO-SKYMED SATELLITE DATA

Maged Marghany
[1]School of Humanities, Geography Section,
Universiti Sains Malaysia,
11800 USM Penang, Malaysia
[2]Faculty Geospatial and Real Estate,
Geomatika University College,
Kuala Lumpur

Email :magedupm@hotmail.com

KEYWORDS: Multi-Objective Evolutionary Algorithm, Entropy-based Multi-Objective Evolutionary Algorithm, Non-dominated Sorting Genetic algorithm-II, oil spill spreading, Cosmo-SkyMed satellite.

ABSTRACT: This study has demonstrated work to optimize the oil spill footprint detection in synthetic aperture radar (SAR) data. Therefore, Entropy-based Multi-objective Evolutionary Algorithm (E-MMGA) and non-dominated sorting genetic algorithm-II (NSGA-II) have implemented with COSMO-SkyMed data during the oil spill event along the coastal water of along the Koh Samet Island, Thailand. Besides, Pareto optimal solution is implemented with both E-MMGA and NSGA-II to minimize the difficulties of oil spill footprint boundary detection because of the existence of a look-alike in SAR data. The study shows that the implementation of a Pareto optimal solution and weight sum in E-MMGA and NSGA-II generated an accurate pattern of an oil slick. The NSGA-II has the highest performance as compared to E-MMGA, which is able to preserve the morphology of oil spill footprint boundaries i.e. thick, medium, and light. In conclusion, NSGA-II is considered as an excellent algorithm to discriminate oil spill from look-alikes and also to identify thick oil spill from the thin one within the shortest computing time.

1. INTRODUCTION

Intelligent, learning machine algorithms such as genetic algorithm and multi-objective algorithms have been used for oil spill automatic detection from SAR data (Topouzelis et al. 2009 and Marghany 2014b). Recently, Marghany (2014a) utilized the Genetic algorithm (GA) as an automatic detection algorithm for the oil spill in RADARSAT-2 SAR data. Marghany (2014a) confirmed the work of Topouzelis et al. (2009). Further, The GA is shown to be able to identify and remove pixels that do not significantly contribute to oil slick footprint in SAR data. This conclusion has approved the findings of Mohanta and Sethi (2012); Skrunes et al. (2012) and Marghany (2014a).

Recently, there are several advanced in developing new algorithms that improve the efficiency of GA. These algorithms are an Evolutionary algorithm and non-dominated sorting genetic algorithm-II (NSGA-II). For two decades, evolutionary algorithms have played a tremendous role for accurately solving optimization problems in the area of computational engineering and image processing. One of the popular optimization algorithm is NSGA. Indeed, NSGA has the effective performance to determine the Pareto front of problems which predict low computational costs to evaluate the objective functions under the circumstance of the objective functions are explained by simple analytical models. Consequently, NSGA algorithm simulates the evolution of the evolution of a population with an internal selection of the most excellent individuals. Truthfully, NSGA has excellent performance when the evaluation of objective functions is less time-consuming, which is managing a huge number of individuals (Deb et al., 2000 and Deb 2001).

The novelty of this work is designing an optimization tool based on Pareto optimal for the real-time oil spill automatic detection by comparing between Entropy-Based Multi-objective Evolutionary algorithm and non-dominated sorting genetic algorithm-II (NSGA-II) without involving others tools such as neural network or any image processing classification tools. Indeed, previous studies have executed artificial neural networks (Topouzelis et al., 2009; Mohanta and Sethi, 2012) or post-classification techniques (Barni et al., 1995; Calabresi et al., 1999), which are considered to be semi-automatic techniques (Marghany 2001). In addition, Pareto optimal can be a new approach to determine oil spill morphology features, i.e. thick, medium, and light oil spill. Yet, advanced previous work which, is based on artificial neural networks and post-classification techniques are not able to identify the oil spill morphology features. In addition, artificial neural networks and post-classification techniques are

time-consuming and the probability of misclassification does not always decrease as the number of feature increases, especially when sample data are insufficient (Marghany 2014d and Marghany 2016).

2. NON-DOMINATED SORTING GENETIC ALGORITHM NSGA-II

This section presents a brief description of NSGA-II relevant to this study. NSGA-II is the second version of the famous "*Non-dominated Sorting Genetic Algorithm*". Its main features are: (i) A sorting non-dominated procedure where all the individual are sorted according to the level of non-domination; (ii) It implements elitism which stores all non-dominated solutions, and hence enhancing convergence properties; (iii) It adapts a suitable automatic mechanics based on the crowding distance in order to guarantee diversity and spread of solutions; and (iv) Constraints are implemented using a modified definition of dominance without the use of penalty functions.

In order to sort a population of size N for $E(\beta_1),................,E(\beta_N)$ according to the level of non-domination, each solution m must be compared with every other solution in the population to find if it is dominated. This requires comparisons $O(E(\beta_m))_N$ for each solution, where is m is the number of different pixels belongs to the oil spill, look-alikes, and sea roughness, and low wind zones.

The initialized population N of $E(\beta_1),................,E(\beta_N)$ is sorted based on the level of non-domination for each individual $E(\beta_1)$ in the main population P do the following

Initialize $S_{E(\beta_1)} = \Phi$. This set Φ would include all the individuals of $E(\beta_n)_N$ which is being dominated by $E(\beta_1)$.

Initialize $n_{E(\beta_1)} = 0$. This would be the number of individuals that dominate $E(\beta_1)$ i.e. no individuals dominate, $E(\beta_1)$ then $E(\beta_1)$ belongs to the first front; set rank for an individual $E(\beta_1)$ to one i.e. $E(\beta_1)_{rank} = 1$. For each individual m in P if $E(\beta_1)$ dominated m then add m to the set Φ i.e. $\Phi = \Phi \sqcup \{m\}$ *else if m dominates $E(\beta_1)$ then increment for domination counter for $E(\beta_1)$ i.e. $n_{E(\beta_1)} = n_{E(\beta_1)} + 1$.

Selection. Once the individuals $E(\beta_j)$ are sorted based on non-domination and

with crowding distance $E(\beta_{d_K})$ assigned, the selection is carried out using a crowded comparison operator $\prec_n$ which is based on
   (1) non-domination rank $E(\beta_1)_{rank}$ i.e. individuals $E(\beta_j)$ in front F_i will have their rank as $E(\beta_1)_{rank}$=i.
   (2) crowding distance $E(\beta_{d_K})$

   • $E(\beta_1) \prec_n m$
      - $E(\beta_1)_{rank} < m_{rank}$
      - or if $E(\beta_1)$ and m belongs to the same front F_i then $F_i(E(\beta_{d_K}) > F_i(d_m)$ i.e. the crowing distance should be more.

The individuals $E(\beta_1)$ are chosen by exercising a binary contest selection with crowed comparison-operator $\prec_n$.

2.1 Recombination and Selection

The offspring population is merged with the current generation population and variety is completed to set the individuals of the next generation. Elitism is confirmed, subsequently, all best individuals are included in the population. In this context, the population is now sorted based on non-domination and function of wind speed (*V*). Subsequently, the new generation is filled by each front till the population size surpasses the existing population size. For instance, the population exceeds N when adding all the individuals in front F_i, then the individuals in front F_i is chosen based on their crowding distance in the descending order until the population size is N.

3. RESULTS AND DISCUSSION

In this study, the COSMO-SkyMed image is acquired on July 29, 2010, at 11:23:33 UTC which is implemented for oil spill detection in the Koh Samet island, Thailand. This data covered 12° 31´48" N to 12° 37´ 48" N latitude and 101° 2´24" E to 101 33 37" E longitude (Figure 1). According to Marghany (2014b), the oil spill has moved away from the mainland and has started to disperse to an extent within 6.59 km (Figure 2).

Figure 1. Geographical location of the oil spill in the Gulf of Thailand.

Figure 2. Massive oil pollution along the coastal water of Ko Samet.

Figure 3 shows the variation in the average backscatter intensity along the oil slick footprint. The average backscatter intensity was dumped by -20 dB to -9 dB and decreased over time as the oil slick footprint gradually increased (Figure 3). Besides, the sea surface roughness have highest backscatter values of -10 dB than oil spill footprint pixels. Consistent with and Trivero et al., (2007) and Marghany (2014b), the wind speed is recorded on July 29, 2013, was ranged between 1 to 7 m/s. Besides, the measured reductions of backscattered radar power at X-band could be impacted by instrumental limitations, i.e. by the fact that the backscattered radar power reaches the noise floor (Trivero et al., 2007;Marghany 2014b).
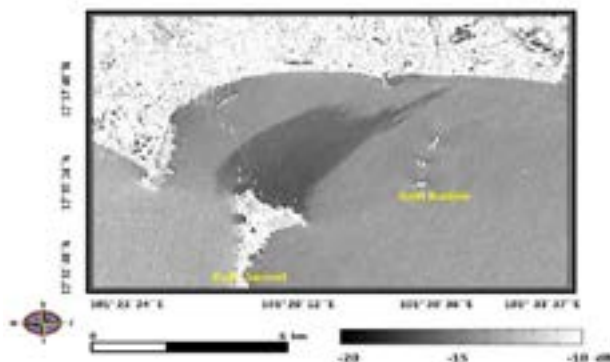

Figure 3: Average backscatter variations in COSMO-SkyMed.

3153

Figures 4b and 4c show the output result of E-MMGA and NSGA-II. Clearly, E-MMGA is able to produce four different segmentation boundaries. However, NSGA-II can produce sharper segmentation boundaries than E-MMGA. In the NSGA-II algorithm, oil spill footprint discriminated and identified by a sharp vector that separates it from surrounding features, i.e., sea surface, look-alikes and land boundaries (Figure 4c). Besides, Figure 5a shows that the thick oil spill footprint has highest E-MMGA value of 2 than a medium and light oil spill. Nevertheless, NSGA-II is able to produce different clusters of oil spill footprint thickness as compared to E-MMGA with the highest value of NSGA-II of 2.5. This indicates that NSGA-II can identify clearly the level of oil spill footprint spreading accurately than E-MMGA due to the accurate Pareto frontier of NSGA-II.

(a)   **(b)**

(c)
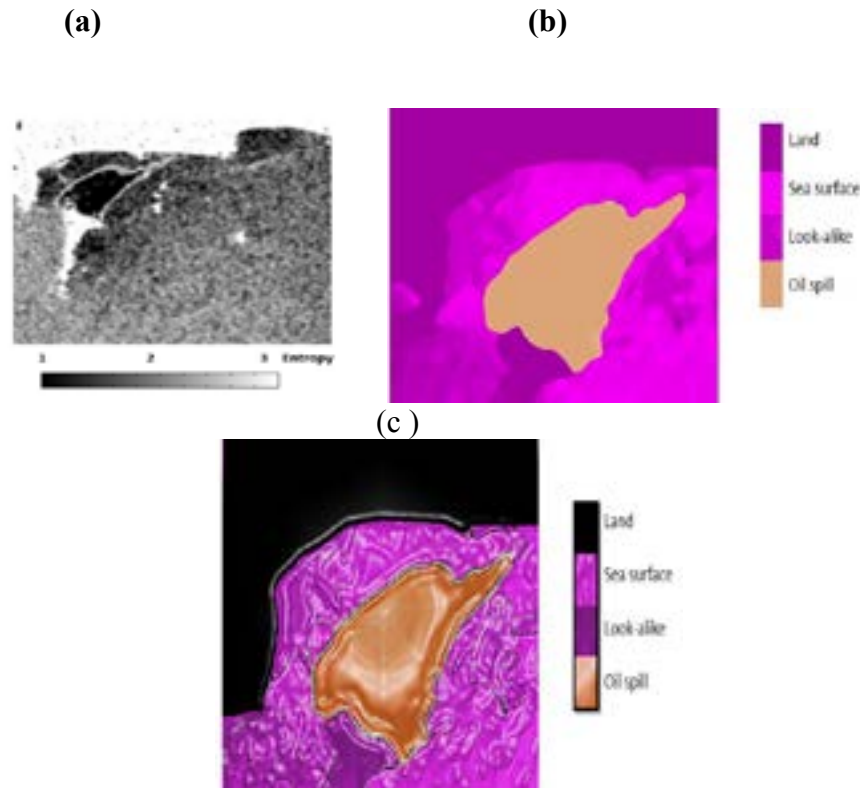
Figure 4.   Results of   (a) entropy (b) E-MMGA and (c) NSGA-II for oil spill discrimination in COSMO-SkyMed.

NSGA-II can accurately identify the sharpest morphological boundary of the oil spill and assigned by different segmentation layers in COSMO-SkyMed satellite data as compared to Entropy algorithm and E-MMGA. In fact, NSGA-II provides a set of compromised solutions called Pareto optimal solution since no single solution can optimize each of the objectives separately. The decision maker is provided with the set of Pareto optimal solutions in order to choose a solution based on the decision maker's criteria.

This sort of NSGA-II solution technique is called nondominated since the decision is taken after searching is finished. This confirms the work done by Deb (2000) and Deb et al., (2001). In this context, the Pareto-optimization approach does not require any a priori preference decision between the conflicting of the oil spill, look-alike, land, and surrounding sea footprint boundaries.

Further, Pareto-optimal points have formed Pareto-front as shown in Figure 4 in the multi-objective function of the COSMO-SkyMed data space. Finally, NGSA-II has advantages on Entropy and   E-MMGA because (i) NGSA-II explicit diversity preservation mechanism;(ii) overall complexity of NSGA-II is at most $O(MN^2)$ and;(iii) elitism does not allow an already found Pareto optimal solution to be deleted. This agreed with Deb et al., (2001).

In general, the NSGA-II algorithm was able to automatically extract oil spill pixels from the surrounding pixels without using a separate segmentation algorithm, as was done by Skrunes et al. (2012). Further, all the algorithms have been introduced are effectively depended on wind speed conditions. Nonetheless,   the NSGA-II can automatically discriminate oil spill from the surrounding pixels even under wind speed of 6 ms^{-1} . Further, the TCNNA algorithm of Garcia et al., (2013b) is based on entropy, which first introduced by Marghany (2001) as an excellent tool for oil spill detection in SAR data. In fact, entropy algorithm was automatically determined the graduate changes of sea surface backscatters along the boundary layers of the oil spill in SAR data. This helps to identify oil spill footprint in SAR data.

Indeed, the capability of a SAR satellite to differentiate between oil, low wind areas, look-alikes is restrained by the noise floor of SAR. However, NGSA-II explicit diversity preservation mechanism is involved in NSGA-II is able to overcome this issue. The Support Vector Machine (SVM) was implemented by Matkan et al., (2013) for automatic detection of the oil spill is based on thresholding. Finally, the recent work done by using a genetic algorithm (Marghany 2014c and Marghany 2017) is not able to provide any information regarding the level of oil spill footprint spatial variations from thickness to lightness levels as compared to NGSA-II.

5. CONCLUSIONS

This investigation has validated work to optimize the oil spill footprint detection in synthetic aperture radar (SAR) data. Consequently, Entropy-based Multi-objective Evolutionary Algorithm (E-MMGA) and non-dominated sorting genetic algorithm-II (NSGA-II) have applied with COSMO-SkyMed facts throughout the oil spill match along the coastal water of alongside Koh Samet Island, Thailand. Besides, the Pareto highest quality answer is carried out with each E-MMGA and NSGA-II to reduce the difficulties of oil spill footprint boundary detection due to the fact of the existence of a look-alike in SAR data. The find out about indicates that the implementation of a Pareto most reliable solution and weight sum in E-MMGA and NSGA-II generated a correct sample of the oil slick. Furthermore, the thick oil spill has the best possible rate of 2.3 NSGA-II than tiny and medium spills. The NSGA-II has the absolute best overall performance as in contrast to E-MMGA, which is capable to preserve the morphology of oil spill footprint boundaries, i.e. thick, medium, and mild the In conclusion, NSGA-II is viewed as an exquisite algorithm to discriminate oil spill from look-alike and additionally to perceive thick oil spill from the tiny one inside the shortest computing period time.

References

Barni, M., Betti, M., and Mecocci, A.(1995). A fuzzy approach to oil spill detection an SAR images, Geoscience and Remote Sensing Symposium, 1995. IGARSS'95.'Quantitative Remote Sensing for Science and Applications', International, 1995, 157-159.

Calabresi, G., Del Frate, F., Lichtenegger, J., Petrocchi, A., and Trivero, P.(1999). Neural networks for the oil spill detection using ERS-SAR data, Geoscience and Remote Sensing Symposium, 1999. IGARSS'99 Proceedings. IEEE 1999 International, 1999, 215-217.

Deb, K.; Agrawal, S.; Pratap, A.; Meyarivan, T. (2000). A Fast Elitist Non-Dominated Sorting Genetic Algorithm for Multi-Objective Optimization: NSGA-II; In Parallel Problem Solving from Nature-PPSN VI, Proceeding of 6th International Conference, Paris, France, 18–20 September 2000; Schoenauer, M., Deb, K., Rudolph, G., Yao, X., Lutton, E., Merelo, J.J., Schwefel, H.P., Eds.; Springer: Berlin, Germany, 2000; Volume 1917, pp. 849–858.

Deb,K. (2001). Multi-Objective Optimization Using Evolutionary Algorithms, Wiley.

Garcia-Pineda, O., MacDonald, I. R., Li, X., Jackson, C. R., and Pichel, W. G.(2013). Oil spill mapping and measurement in the Gulf of Mexico with Textural Classifier Neural Network Algorithm (TCNNA), Selected Topics in Applied Earth Observations and Remote Sensing, IEEE Journal of, 6, 2517-2525.

Marghany, M. (2014a) Utilization of a genetic algorithm for the automatic detection of oil spill from RADARSAT-2 SAR satellite data, Marine pollution bulletin, 89, 20-29.

Marghany, M. (2014b). Multi-Objective Evolutionary Algorithm for Oil Spill Detection from COSMO-SkeyMed Satellite, in: Computational Science and Its Applications–ICCSA 2014, Springer, 355-371.

Marghany, M., (2014c). Utilization of a genetic algorithm for the automatic detection of oil spill from RADARSAT-2 SAR satellite data. *Marine pollution bulletin*, *89*(1), pp.20-29.

Marghany, M., and van Genderen, J.: (2014d). Entropy algorithm for automatic detection of oil spill from radarsat-2 SAR data, IOP Conference Series: Earth and Environmental Science, 2014, 012051.

Marghany, M. (2016). Automatic Mexico Gulf oil spill detection from Radarsat-2 SAR satellite data using genetic algorithm. Acta Geophysica. 64, (5): 1916–1941.

Marghany, M., (2017). Automatic Detection of Oil Spill Disasters Along Gulf of Mexico Using RADARSAT-2 SAR Data. *Journal of the Indian Society of Remote Sensing*, *45*(3), pp.503-511.

Mohanta, R. K., and Sethi, B. (2012). A Review of Genetic Algorithm application for Image Segmentation, International Journal of Computer Technology & Applications, 3.

Skrunes, S., Brekke, C., and Eltoft, T. (2012). An experimental study on oil spill characterization by multi-polarization SAR, Synthetic Aperture Radar, 2012. EUSAR. 9th European Conference on, 2012, 139-142.

Topouzelis, K., Stathakis, D., and Karathanassi, V. (2009). Investigation of genetic algorithms contribution to feature selection for oil spill detection, International Journal of Remote Sensing, 30, 611-625.

Trivero, P., Biamino, W., and Nirchio, F. (2007). High-resolution COSMO-SkyMed SAR images for oil spills automatic detection, Geoscience and Remote Sensing Symposium, 2007. IGARSS 2007. IEEE International, 2007, 2-5.

AUTOMATIC DETECTION OF 2004 TSUNAMI GENERATING INTERNAL WAVE ALONG ANDAMAN SEA USING ENVISAT SATELLITE DATA

[1,2] Maged Marghany
[1]School of Humanities, Geography Section,
Universiti Sains Malaysia,
11800 USM Penang, Malaysia
[2]Faculty Geospatial and Real Estate,
Geomatika University College,
Kuala Lumpur

Email :magedupm@hotmail.com

KEYWORDS: Internal wave, automatic detection, the ENVISAT SAR radar image, Particle Swarm Optimization algorithm.

ABSTRACT: In remote-sensing images, internal waves are among the foremost simply recognized of the oceanographic phenomena. The distinctive signatures of alternating bands of sunshine and dark, the quasilinear strips are perceived in images of the ocean surface, in multispectral radiometer data, and in real and synthetic aperture radar data. The novelty of this work is to implement the Particle Swarm Optimization algorithm for automatic detection of the internal wave from ENVISAT data during the 2004 tsunami event. The results show the normalized radar cross section is ranged between -24 to -4 dB. The lowest normalized radar cross section of -28dB is described the low window zone shelter along the Andaman and Nicobar Islands. However, the highest backscatter of -4 dB describes the occurrence of the whirlpool in the east of the Andaman Sea. This whirlpool is located between the latitude of 14° N to 15° N and longitude of 94° E and 96°E. The whirlpool has a radius of 1.9 km and located above of water depth gradient of 1000 m. In conclusion, the Particle Swarm Optimization has automatically detected internal wave. In conclusion, 2004 tsunami generated internal wave along the Andaman Sea.

1. INTRODUCTION

Internal waves exist as a result of the deep waters of the ocean are denser than the surface waters (Alpers 1985). If a parcel of deep (heavy) water was to be pulled up towards the surface, gravity would force it back downward. It is the identical concern that may occur if a parcel of ocean water is raised into the air. The buoyancy of surface waters makes them come back to the surface if they are momentarily pushed downward (Apel et al., 1975 and Bowden, 1983). The tidally created internal waves are normally extremely nonlinear and occur regularly in wave packets. The gap between the waves in an exceedingly wave packet and conjointly the amplitude decrease from the front to the rear. The amplitude of enormous internal waves can exceed 50 m in some cases. Hypothetically, these extremely nonlinear waves are usually delineated in terms of internal solitons. Accordingly, a wave packet consists of many solitons. Solitary wave theories applied to the outline of the generation and propagation of internal solitary waves predict that, if the depth of the higher water layer is far smaller than the depth of the lower layer, then the inner soliton should be a "wave of depression" (Hsu et al, 2000).

Since SAR data became broadly accessible, SAR sensors suited the foremost vital remote sensors for IW detection. Nonetheless, there exist conjointly alternative microwave radar signatures of internal waves: generally, they consist merely of bright lines or exclusively of dark bands. As soon as the wind speed is below the threshold for general wave generation, exclusively bright bands are encountered and once surface slicks are existent, solely dark lines are clearly seen (Da Silva et al., 1998). Conversely, microwave radar detection imaging theories capable of explaining these, exceptional radar signatures of internal waves quantitatively still do not exist. Consistent with Da Silva et al., (1998),Satellite Synthetic Aperture Radar (SAR) observations that provide the best evidence for the presence of the shorter period internal solitary waves (ISWs) in the ocean. This is due to a mechanism whereby horizontally-propagating internal waves, centred on the thermocline typically some tens of meters below the surface, can generate a signature in the surface roughness field because of the modulating effect of convergence and divergence in the near-surface currents associated with the internal waves. This modulation is more effective for short period (30 minutes or shorter) ISWs because the straining of short (Bragg) surface waves (or ripples) is strongest in these periods. It may also be possible to detect tidal period internal waves (with periods of 12.4 hours) in the presence of surface films and/or when the surface currents associated with the ITs induce alternating wind conditions relative to

the surface with wind against tide exhibiting larger radar backscatter than wind with the tide. Since the tidal wave can be used to describe the tsunami, so how can tsunami generate internal wave? In fact, there is a doubt that the tsunami can reform the ocean water properties. As said by Marghany (2014a), the salinity was extremely increased due to tsunami effects.

Though, there are different sorts of microwave radar signatures of short-period, internal wave trains that may be terribly disruptive to interpret. They convey specific data about the characteristics of the interior waveforms that, properly understood, provide distinctive measurements, not solely concerning the IWs however conjointly the inside ocean and the ocean surface microlayer (Da Silva et al., 1998). Owing to the fluid mechanics interaction of the variable surface current with the surface waves, the amplitude of the Bragg waves is enlarged in convergent flow regions and is diminished in divergent flow regions. As a consequence, the microwave radar signatures of oceanic internal waves incorporate alternating bright and dark bands on an identical background (Alpers 1985).

The uniqueness of this investigation is to implement the Particle Swarm Optimization algorithm for automatic detection of the internal wave (IW) from ENVISAT data during the 2004 tsunami event. This study conjectures that IW can also be inevitably detected by the use of the Particle Swarm Optimization (PSO) algorithm in ENVISAT satellite data. In this perspective, PSO has taken into deliberation to optimize the primary IW detection utilising a 2-D wavelet transform.

2. ALGORITHM
2.1 WAVELET TRANSFORM

Wavelet transform tool is commonly used for analysing time-varying signals. This technique generates spectral decomposition through the scale model. In remote sensing images investigation, the two-dimensional wavelet transform (2-DWT) serves up as an incredibly effective band-pass filter. With this regard, 2-DWT operated to discrete approaches with altered scales. Beyond, the brilliant proficiency of wavelet transforms in time localization for one-dimensional presentation. Under this circumstance, it can supply particular evidence on the characteristic description in remote sensing data (Marghany 1999). These functions nominate the wavelet transform a valuable module for extorting aspects, physical properties exactly in remote sensing data. Two-dimensional wavelet characteristic having oscillation in x-direction only can be written as follows (Marghany 2002):

$$\Psi_{s,\tau}(t) = \frac{1}{\sqrt{s}} \Psi\left(\frac{t-\tau}{s}\right) \qquad (1.0)$$

where, $\Psi(t)$ is the transforming function, and it is called the mother wavelet. The two new variables, s and τ are the scale and translation of the daughter wavelet. The term $\sqrt{s}$ normalizes the energy for different scales, whereas the other terms define the width and the translation of the wavelet.

2.2 PARTICLE SWARM OPTIMIZATION (PSO)

Succeeding Kennedy and Eberhart (1995) and Marghany (2015), Particle Swarm Optimization (PSO) is a population-based randomly searching process. It is assumed that there are N "particles" i.e. physical properties of internal wave and its surrounding environments: bright and dark backscatter variations, linearity, depressions, and direction of propagation in ASAR data. These internal wave features invasive contacts randomly seem in a "solution space" (Xie et al., 2003). Thus the optimization problem can be solved for data clustering, there is always a criteria (for example, the squared error function) for every single particle at their position in the solution space (Kennedy et al., 1997). The N particles will keep moving and calculating the criteria in every position the remain which is named as fitness in PSO pending the criteria reaches satisfied threshold. Therefore, each internal wave features (particles) maintains its coordinates in the solution space of ASAR which are combined with the finest fitness that has extremely accomplished by requested physical features i.e. particles. In fact, the pixel of each feature i.e. particle (m,n,l) denotes a probable solution to the optimization problem. Following Kennedy and Eberhart (1995), each agent moves the particle with a direction and velocity $v_{m,n,l}$,

$$p_{m,n,l} = p_{m,n,l} + v_{m,n,l}, \qquad (2.0)$$

where $p_{m,n,l}$ represent particle and $v_{m,n,l}$ is the velocity of the 4-D particle in the i,j,k agents, respectively.

$$v_{m,n,l} = v_{m,n,l} + c_1 r_1 (lbest_{m,n,l} - p_{m,n,l}) + c_2 r_2 (gbest_{m,n,l} - p_{m,n,l}) \tag{3.0}$$

where $lbest_{m,n,l}$ is the local best particle, $gbest_{m,n,l}$ is the global best particle, r_1 and r_2 are random variables and c_1 c_2 are the swarm system variables. After each iteration, the global best g_{best} particle and the agent local best l_{best} particle are evaluated based on the maximum fitness functions of all particles in the solution space. Then equation 1 can be expressed as follows (Marghany 2014b; Marghany 2018a; Marghany 2018b)

$$\begin{aligned} v_{m,n,l} = w \cdot v_{m,n,l}(t-1) + c_1 \cdot r_1 (p_{m,n,l}(t-1) \\ - \psi_{m,n,l}(t-1)) + c_2 \cdot r_2 (p_{m,n,l}(t-1) \\ - \psi_{m,n,l}(t-1)) \end{aligned} \tag{4.0}$$

$$\psi_{m,n,l} = \psi_{m,n,l}(t-1) + v_{m,n,l}(t) \tag{5.0}$$

where $\psi_{m,n,l}$ is the position of the particle for wavelet transforming, $v_{m,n,l}$ is the current velocity of the particles in $m \times n \times l$. The velocity is regulated by a set of rules that influence the dynamics of the swarm. Further, there are several parameters must be considered such as the initial population, representation of position and velocity strategies, fitness function identification and the limitation (Dorigo et al., 2008). These parameters are for PSO performances. Following Ibrahim et al., (2010) the initial swarm particles proposed PSO is initialized to contain 3000 points of particles for $\psi_{m,n,l}$ and velocity $v_{m,n,l}$. The points had been randomly selected in the azimuth and range directions wavelet transform of ASAR data.

3. RESULTS AND DISCUSSION

The Andaman and Nicobar Islands on the western side of the Andaman Sea are volcanic in origin, where the Sunda trench is running into the Andaman Basin(Figure 1) (Marghany 2018b). The sills between the islands, as well as a number of underwater volcanic seamounts, are all potential sources of internal waves. The result is an area rich in internal wave excitations and complex soliton - soliton interaction (Figure 1). Figure 2 shows the bathymetry variations of the Andaman and Nicobar Islands. The water depth along Andaman and Nicobar Islands is ranged between 200 m to 3000 m.

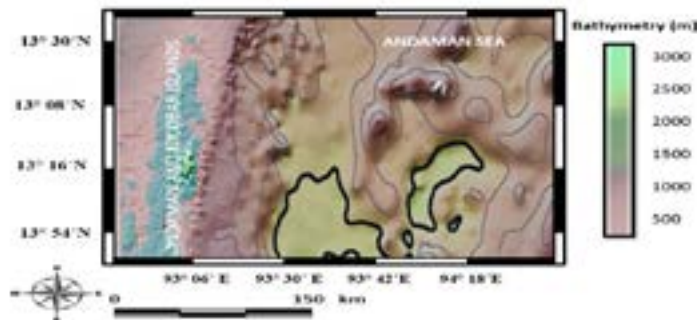**Figure 1. Sunda trench running into the Andaman Sea.**

**Figure 1. Bathymetry along Andaman and Nicobar Islands.**

Figure 3 shows the ENVISAT SAR radar image (Orbit 148) was acquired on 28 December 2004, two days after the tsunami hit Asia. It shows the Indian Andaman Islands and the Ritches Archipelago. The normalized radar cross section is ranged between -24 to -4 dB. The lowest normalized radar cross section of -28dB is described the low window zone shelter along the Andaman and Nicobar Islands. However, the highest backscatter of -4 dB has described the occurrence of the whirlpool in the east of the Andaman Sea. This whirlpool is located between the latitude of 14° N to 15° N and longitude of 94° E and 96°E. The whirlpool has a radius of 1.9 km and located above of water depth gradient of 1000 m. It was rotated in an anticlockwise direction (Figure 3) (Marghany 2018b).
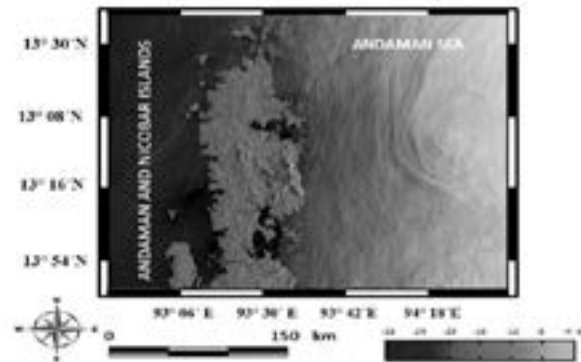
Figure 3. ENVISAT of Andaman and Nicobar Islands.

The execution of PSO with 2-D wavelet radically change section assisted to determine foremost grows regions across the persevering with and discontinuing internal wave edges. In fact, in the PSO system, particles are unbiased of every other and their moves are ruled by the useful resource of a set of rules. With this concern, PSO synchronized sequences aspects of the interior wave side (Figure 4). Figure 4 indicates the ensuing optimization of wavelet transforms the usage of the PSO algorithm. It is obvious the clear look of the part of the inside wave. In fact, the PSO circumvents a reducing decision by using making a weighted combination of strolling average with the neighbours surrounding pixels of the two wavelet transform.

This decreased the noise in the function s' aspect areas except dropping edge sharpness. Clearly, PSO inside about 1 hour within a thousand iterations is capable to reconstruct 2-D of the inner wave with RMSE of 0.43. The PSO algorithm commences by means of growing random locations for the particles, inside an initialization pixel of the inside waves in ASAR image. Particles in PSO algorithm can additionally be modified to zero or to minor random values to keep away from particles from withdrawal the search area of internal wave pixels all through the first iterations (figure 3a). Throughout the core loop of the algorithm, the velocities and locations of the particles are iteratively rationalized until a ending condition is encountered.
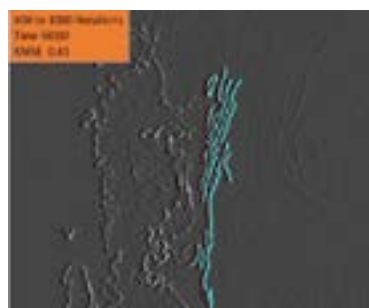
Figure 4. Particle Swarm Optimization for internal wave automatic detection.

Moreover, PSO algorithms constructed the discontinuity in first-rate order. This is appropriate in the high-intensity line or curve of constant size and locally low curvature boundary is known to exist between area elements and high noise levels in ASAR data. This agrees with the work is delivered by means of Kennedy et al., 1997; Marghany 2014; and Marghany 2015). It ought to be stated that sturdy 2004 earthquakes have an ample to the reserve of strength for the vital transformation of the ocean stratification shape. Tenths of a share of the strength of an earthquake are sufficient for formation on the ocean floor of a temperature anomaly with a function horizontal size, measured through way of loads of kilometres and with a temperature deviation of the order of 1 ∘C. Note, that a similar extent of power (less than 1% of the earthquake power) is spent at the formation of tsunami waves.

6. CONCLUSIONS

This investigation presents a new approach for automatic detection of an internal wave due to tsunami impact. In doing so, such optimization algorithm of particle swarm is implemented with involving of ENVISAT satellite data. The Particle Swarm Optimization algorithm is designed for automatic detection of the internal wave from ENVISAT data. The study shows that Particle automatically detects the shows the ENVISAT SAR radar image (Orbit 148) was acquired on 28 December 2004, two days after the tsunami hit Asia. It shows the Indian Andaman Islands and the Ritches Archipelago. The normalized radar cross section is ranged between -4 to -24 dB. The lowest normalized radar cross section of -28dB is described the low window zone shelter along the Andaman and Nicobar Islands. However, the highest backscatter of -4 dB has described the occurrence of the whirlpool in the east of the Andaman Sea. This whirlpool is located between the latitude of 14° N to 15° N and longitude of 94° E and 96°E. The whirlpool has a radius of 1.9 km and located above of water depth gradient of 1000 m. In conclusion, the Particle Swarm Optimization has automatically detected internal wave. It can be said that the 2004 tsunami generated internal wave along the Andaman Sea.

References

Alpers, W.,1985. Theory of radar imaging of internal waves, Nature, 314, 245-247.

Apel, J.R., Byrne, H.M., Proni, J.R. & Charnell, R.L., 1975. Observation of oceanic internal and surface waves from the Earth Resources Technology Satellite, J. Geophys. Res., 80, 865-881.

Da Silva, J.C.B., Ermakov, S.A., Robinson, I.S., Jeans, D.R.G. & Kijashko, S.V., 1998.Role of surface films in ERS SAR signatures of internal waves on the shelf, 1. Short-period internal waves, J. Geophys. Res., 8009-8031.

Bowden, K. F., 1983, "Physical oceanography of coastal waters.

Dorigo, M., de Oca, M.A.M. and Engelbrecht, A., 2008. Particle swarm optimization. *Scholarpedia*, *3*(11), p.1486.

Kennedy, James, and Russell C. Eberhart, 1997. "A discrete binary version of the particle swarm algorithm." *Systems, Man, and Cybernetics, 1997. Computational Cybernetics and Simulation., 1997 IEEE International Conference on*. Vol. 5. IEEE, 1997.

Kennedy, J. and Eberhart, R. 1995. Particle Swarm Optimization. (14): 1942--1948.

Ibrahim, S., Abdul Khalid, N.E., Manaf, M. 2010. Computer aided system for brain abnormalities segmentation. Malaysian Journal of Computing (MJOC) 1(1)*: 22-39.*

Hsu, M.-K., Liu, A.K. and Liu, Ch, 2000. A study of internal waves in the China Seas and Yellow Sea using SAR, Continental Shelf Research, 20, 389-410.

Marghany, M., 1999. Internal wave detection and wavelength estimation. In *Geoscience and Remote Sensing Symposium, 1999. IGARSS'99 Proceedings. IEEE 1999 International* (Vol. 1, pp. 163-165). IEEE.

Marghany, M., 2002. Polarised TOPSAR operational model of internal wave generation mechanism. In *Geoscience and Remote Sensing Symposium, 2002. IGARSS'02. 2002 IEEE International* (Vol. 5, pp. 2847-2849). IEEE.

Marghany,M 2014a, "Simulation of Tsunami Impact on Sea Surface Salinity along Banda Aceh Coastal Waters, Indonesia. Advanced Geoscience Remote Sensing". In M. Marghany (ed.), Intech publisher, Croatia, pp.229-251.

Marghany 2014b. Particle Swarm Optimization for Geological Feature Detection from PALSAR Data. 35th Asian Conference of remote sensing, at Nay Pyi Taw, Myanmar, 27-31 October 2014. a-a-r-s.org/acrs/administrator/components/com.../OS-140%20.pdf. [Access August 29 2017].

Marghany 2015. Copper mine automatic detection from TerraSAR-X using particle swarm optimization. CD of 36th Asian Conference on Remote Sensing (ACRS 2015), Manila, Philippines, 24-28 October 2015,a-a-r-s.org/acrs/administrator/components/com.../files/.../TH3-2-1.pdf.

Marghany, M., 2018a. Automatic detection of internal wave using particle swarm optimization algorithm. In *IOP Conference Series: Earth and Environmental Science* (Vol. 169, No. 1, p. 012049). IOP Publishing.

Marghany, M., 2018b. Advanced Remote Sensing Technology for Tsunami Modelling and Forecasting.CRC Press, Taylor &Francis Group, New York.

Xie, X., Zhang, W. and Yang, L., 2003. Particle swarm optimization. *Control and Decision*, *18*, pp.129-134.

Kenta Miyao (1), Kazuhiro Naoki (1) and Kohei Cho (1)

[1]Tokai University Research & Information Center (TRIC),
2-28-4, Tomigaya, Shibuya-k, Tokyo 151-0063, Japan,
Email: kohei.cho@tokai-u.jp

KEY WORDS: Sea ice, Passive microwave radiometer, GCOM-W, global warming

ABSTRACT: The heat flux of ice in thin ice areas is strongly affected by the ice thickness difference. Therefore, ice thickness is important parameter of sea ice. In the previous studies, the authors have developed a thin ice area extraction algorithm using passive microwave radiometer AMSR2 for the Sea of Okhotsk. The basic idea of the algorithm is to use the brightness temperature scatter plots of AMSR2 19GHz polarization difference (V-H) vs 19GHz V polarization. However, when the authors have applied the algorithm to the Bering Sea, two problems have become clear. One was that some thin ice areas were not well extracted, and the other was some of the big ice floe were extracted as thin ice areas. In this study, the authors have improved the thin ice area extraction algorithm to solve these problems. By adjusting the parameters of the algorithm applied to the brightness temperature scatter plots of AMSR2 19GHz polarization difference (V-H) vs 19GHz V polarization, most of the thin ice areas were also well extracted in the Bering Sea. The authors also introduced an equation using the brightness temperatures difference of 89GHz vertical and horizontal polarization to reject the thin ice area mis-extracted over big ice floe.

1. INTRODUCTION

The sea ice observation with passive microwave radiometer started in 1978 by SMMR on board Nimbus-7. Since then, a series of passive microwave radiometers, including AMSR2 onboard GCOM-W satellite, have been continuously observing the earth for 40 years. The long-term sea ice extent derived from the passive microwave observation showed clear decline trend of the Arctic sea ice cover (Comiso, 2012) which is used as an evidence of global warming in the Fifth Assessment Report of IPCC (2014). The importance of sea ice monitoring from space is increasing. Usually, ice concentrations calculated from brightness temperatures measured by passive microwave radiometers are used for estimating the global sea ice extent. There are number of sea ice concentration algorithms including NASA Team Algorithm (Cavarieli et al., 1984) and Bootstrap Algorithm (Comiso, 1995). Ice thickness is another important parameter of sea ice. Studies on estimating ice thickness from the brightness temperature data acquired from passive microwave radiometers onboard satellites have been done in the past including those of Tateyama et al. (2002), Martin et al. (2005), and Tamura et al. (2007). However, the detailed validation of the accuracy of the estimated sea ice thickness is still on the way. Estimating ice thickness from passive microwave radiometer is still a challenge. The authors have been developed a method to detect thin ice area using brightness temperature scatter plots of AMSR2 19GHz polarization difference (V-H) vs 19GHz V polarization (Cho et. Al, 2012, Tokutsu et. Al, 2014). The thin ice area extraction results were compared with simultaneously collected MODIS images for the Sea of Okhotsk for verification. It worked quite well in the Sea of Okhotsk. The algorithm was also applicable to the Bering Sea and the Gulf of St. Lawrence (Miyao et. Al., 2017). However, when the authors have applied the algorithm to the Bering Sea, two problems have become clear. One was that some thin ice areas were not well extracted, and the other was some of the big ice floe (consolidated ice) were extracted as thin ice areas. In this study, the authors have improved the thin ice area extraction algorithm to solve these problems.

2. TEST SITE

In this study, one of the seasonal sea ice zone in the Northern Hemisphere namely the Bering Sea was selected as the test site for the evaluation of thin ice area extraction. Figure 1 show the maps of the test sites. The Bering Sea is located at the northernmost part of the Pacific Ocean connected to Arctic Ocean by the Bering Strait. The sea is surrounded by the Siberia, the Kamchatka Peninsula, the Alaska Peninsula and the Aleutian Islands.
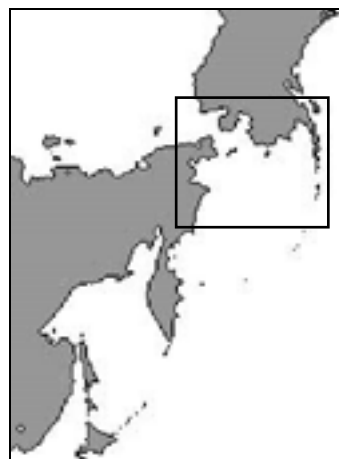
Figure 1. Test Site: Bering Sea

The brightness temperature data acquired from passive microwave radiometer AMSR2 onboard GCOM-W satellite were used in this study. GCOM-W was launched by JAXA in 2012 and AMSR2 has been observing the earth for over 6 years. The diameter of the main reflector of AMSR2 is 2.0m, which is one of the largest reflectors used for passive microwave radiometer is space. Table 1 shows the specifications of AMSR2. The ice concentration data derived from AMSR2 data using Bootstrap Algorithm (Comiso, 2009) is also used in this study. In order to identify thin ice areas, data collected by optical sensor MODIS onboard Aqua satellite were used as reference. Table 3 show the specifications of MODIS. As for MODIS, only the Band 1 and 2 which have the 250m resolution were used in this study. Under the cloud free condition, detailed distribution of sea ice can be observed from MODIS images. Since Aqua and GCOM-W are in the same orbital "track" under the frame work of the NASA's A-Train, the constellation of satellites, MODIS onboard Aqua observed the same area four minutes after the observation of AMSR2 onboard GCOM-W. Therefore, MODIS data is one of the most effective validation data for AMSR2 data.

Table 1.   Specifications of AMSR2

Frequency (polarization)	IFOV	Swath	Incident angle
6.925GHz（V,H）	35×62 km		
10.65GHz（V,H）	24×42 km		
18.7GHz（V,H）	14×22 km	1450 km	55 deg
23.8GHz（V,H）	15×26 km		
36.5GHz（V,H）	7×12 km		
89.0GHz（V,H）	3×5 km		

Table 2.   Specifications of MODIS

Band	Wavelength	IFOV	Swath
1	0.620-0.670 μm	250 m	2330 km
2	0.841-0.876 μm		

4. RESEARCH METHOD

4. 1. Sample area selection

Since the spatial resolution of satellite passive microwave radiometers are rather low as shown on Table 1, it is difficult to identify ice types from the images. Under the cloud free condition, detailed conditions of sea ice can be identified from the images taken by the higher resolution optical sensors, such as MODIS. Figure 2 show the comparison of simultaneously collected AMSR2 ice concentration image and MODIS image of the Bering Sea taken on March 19, 2016. The AMSR2 ice concentrations were derive from the AMSR2 data using AMSR Bootstrap Algorithm. From (Figure 2(a)), The clear distribution of sea ice in the Bering Sea can be identified from the AMSR2 ice concentration image. However, it is difficult to identify ice thickness differences or thin ice areas from the image. On the other hand, in the MODIS image of Figure 2(b), more detailed sea ice distributions can be observed. Through the comparison of the sea ice thickness measurements with data collected by optical sensor on board satellites, the authors have verified that under the less snow cover and cloud free condition, thin sea ice areas, where the ice thicknesses are less than around 30cm, can be identified in MODIS images (Cho et. al., 2012). In this study, the color composite images of MODIS (Band 1 to blue and red, Band 2 to green) were used for selecting sample areas of thin sea ice, big ice floe, open water and mixed sea ice. In thick ice area, since the albedo of both Band 1 and 2 are high, the area appears in white in the color composite image of MODIS. On the other hand, in thin ice area, the albedo of both band are low, the area becomes dark. Especially, since the surface and around of thin ice are rather wet, the albedo of Band 2(near infrared) become much lower compared with that of Band 1(visible). As a result, most of the thin ice areas appear in dark purple in the color composite image of MODIS as sown on Figure 2(b). In this study, the authors defined these dark purple sea ice areas in the MODIS images as thin ice areas.
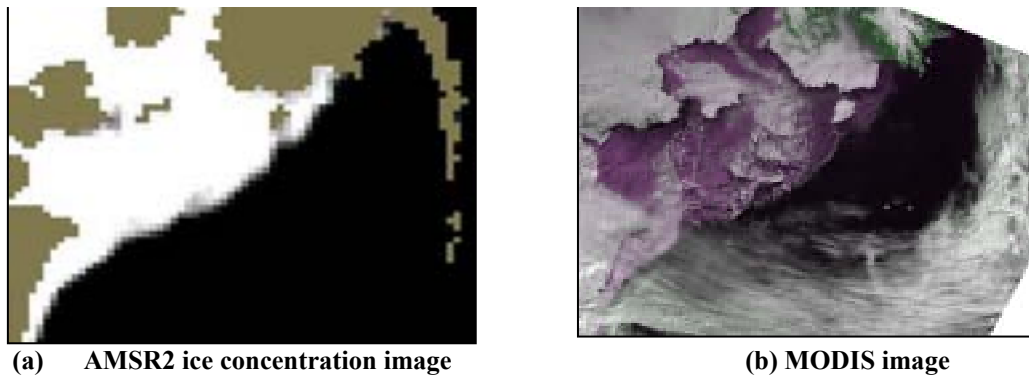
(a)   AMSR2 ice concentration image   **(b) MODIS image**
Figure 2. Comparison of AMSR2 and MODIS images.
(Bering Sea, March 19, 2016)

In order to examine the microwave brightness temperature characteristics of big ice floe, thin ice, mixed ice, and open water, the sample area of each item was selected in the MODIS image of the Bering Sea observed on March 19, 2016 as shown on Figure 3(b). Then, the sample areas were overlaid on the AMSR2 image and the AMSR2 brightness temperature data of the sample areas were extracted as shown on Figure 3(a). Figure 3 shows the enlarged MODIS image of each sample area.
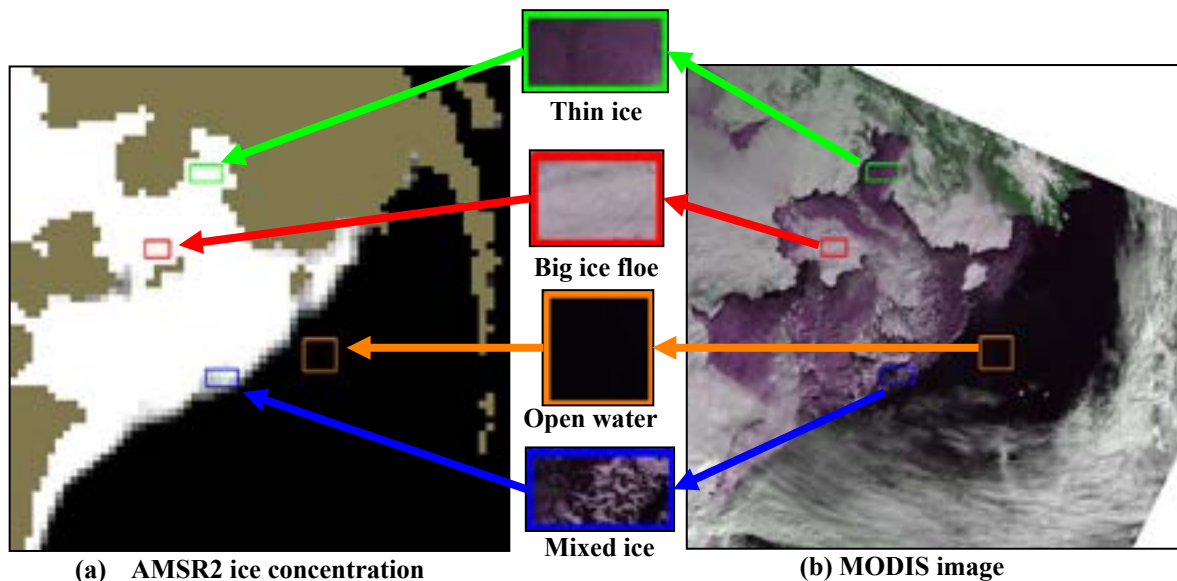
(a)   AMSR2 ice concentration   **(b) MODIS image**
Figure 3. Selection of sample areas using MODIS and AMSR2 images. (Bering Sea, March 19, 2016)

4.2. Thin ice area extraction algorithm

Figure 4 shows the scatter plot of AMSR2 19GHz V versus 19GHz (V-H) of the Bering Sea observed on March 19, 2016. The brightness temperature of the sample areas extracted in Section 4.1 are plotted in different colors. ● represents open water, ▲ represents mixed ice, ◆ represents thin ice,   and ■ represents big ice floe. In AMSR2 19GHz V polarization, the brightness temperature increases as the ice concentration increases. Since in low ice concentration sea ice area, sea ice and open water are mixed within one footprint size of a passive microwave radiometer, it is impossible to identify the ice thickness of the area. So, in this study, the thin ice areas are only extracted within high ice concentration areas. To do this, firstly we used the following equation to extract sea ice area with 80% or higher sea ice concentration.

$$(Tb19GHzV)>245K \quad\quad\quad (1)$$
where Tb19GHzV: Brightness temperature of AMSR2 19GHz V polarization

The microwave brightness temperature of water is much lower in H polarization than in that of V polarization. As explained in Section 4.1, thin ice areas are rather wet. Therefore, in thin ice areas, the microwave brightness temperature of thin ice areas become much lower in H polarization than in that of V polarization. While the microwave brightness temperature of consolidated ice does not show big difference between V and H polarization.

$$(Tb19GHzV - Tb19GHzH) > -Tb19GHzV + 300K \qquad (2)$$

where Tb19GHzH: Brightness temperature of AMSR2 19GHz H polarization

Since the brightness temperature difference between V and H polarization is much bigger for thin ice than for big ice floe, extraction of thin ice area can be expected using the equation (2). The parameters of the both equations were specified for the Sea of Okhotsk in our previous studies(Cho et. Al, 2012, Tokutsu et. Al, 2014).
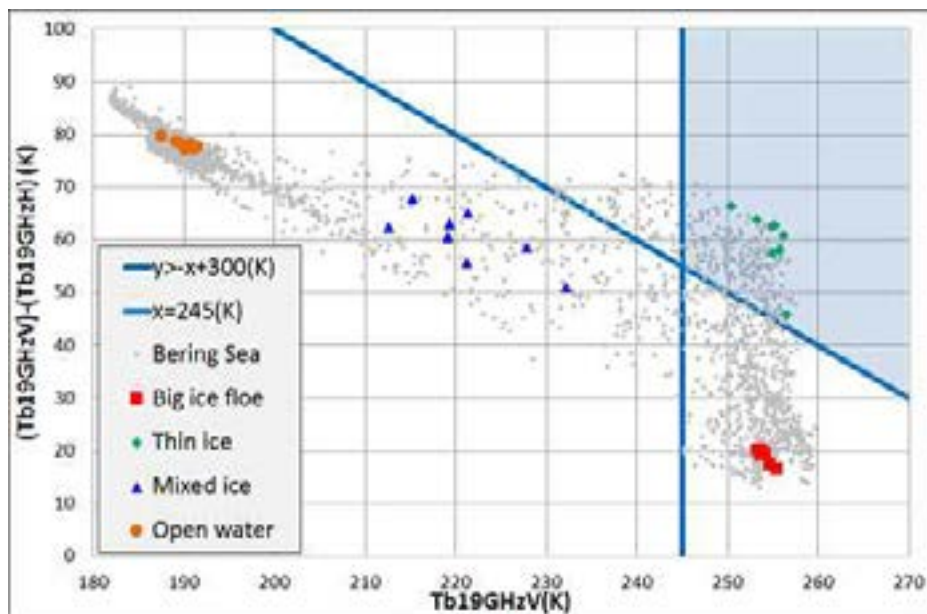

Figure 4. Scatter plots of (19GHzV – 19GHzH) Vs 19GHzV polarization
(Bering Sea, March 19, 2016)

4.3. Evaluation of the previous method

The authors have applied the thin ice area extraction algorithm to several scenes of AMSR2 data for the Bering Sea. Though most of the thin ice areas were well extracted, two problems have become clear. Figure 5(a) show the extracted thin ice areas overlaid on the AMSR2 sea ice concentration image of the Bering Sea observed on March 19,
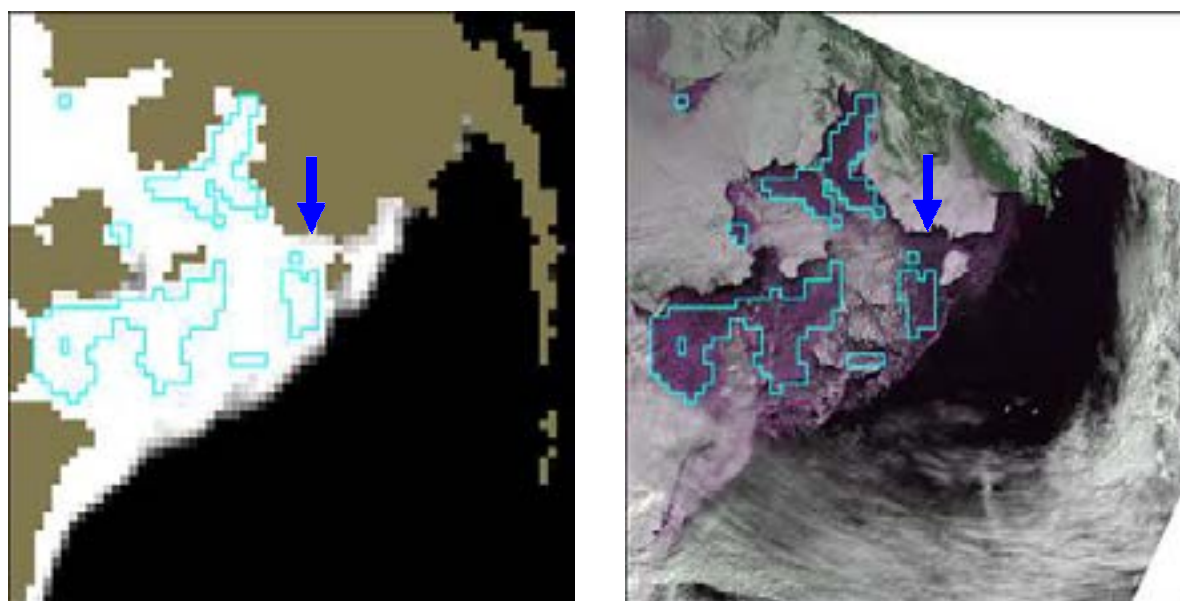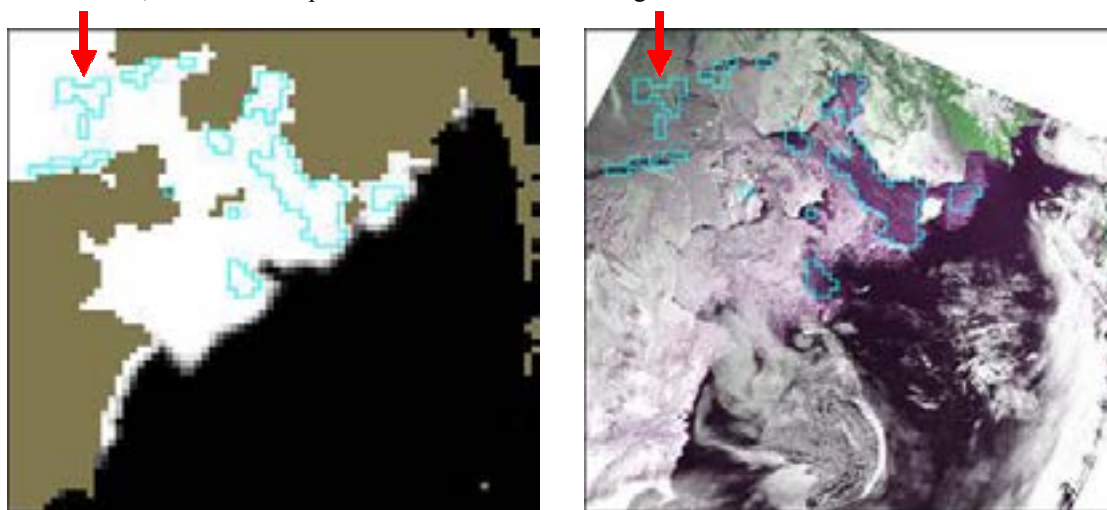

(a)AMSR2 image   **(b) MODIS image**
Figure 5. Thin ice area extraction result (Cyan: extracted area)
(Bering Sea, March 19, 2016)

extracted with the proposed method, some of the thin ice areas were not extracted (see the area specified by the blue arrow in both images of Figure 5). Figure 6(a) show the extracted thin ice areas overlaid on the AMSR2 sea ice concentration image of the Bering Sea observed on February 10, 2014. Figure 6(b) show the extracted thin ice areas overlaid on the MODIS image of the Bering Sea observed on the same day. In this case, some bib ice flow areas were mis-extracted as thin ice areas (see the area specified by the red arrow in both images of Figure 6). Therefore, based on these two cases, the authors improve the thin ice extraction algorithm.

(a)AMSR2 image　　　　　　　　　　　　　**(b) MODIS image**

Figure 6. Thin ice area extraction result (Cyan: extracted area)
(Bering Sea, February 10, 2014)

4.4. Algorithm improvement

(a) Parameter tuning for thin ice area extraction

In order to improve the thin ice area extraction algorithm, the microwave brightness temperature characteristics of un-extracted thin ice areas were examined. Figure 7 shows the sample area of the un-extracted thin ice areas. The other sample areas of big ice floe, thin ice, mixed ice and open water are same with Figure 3.
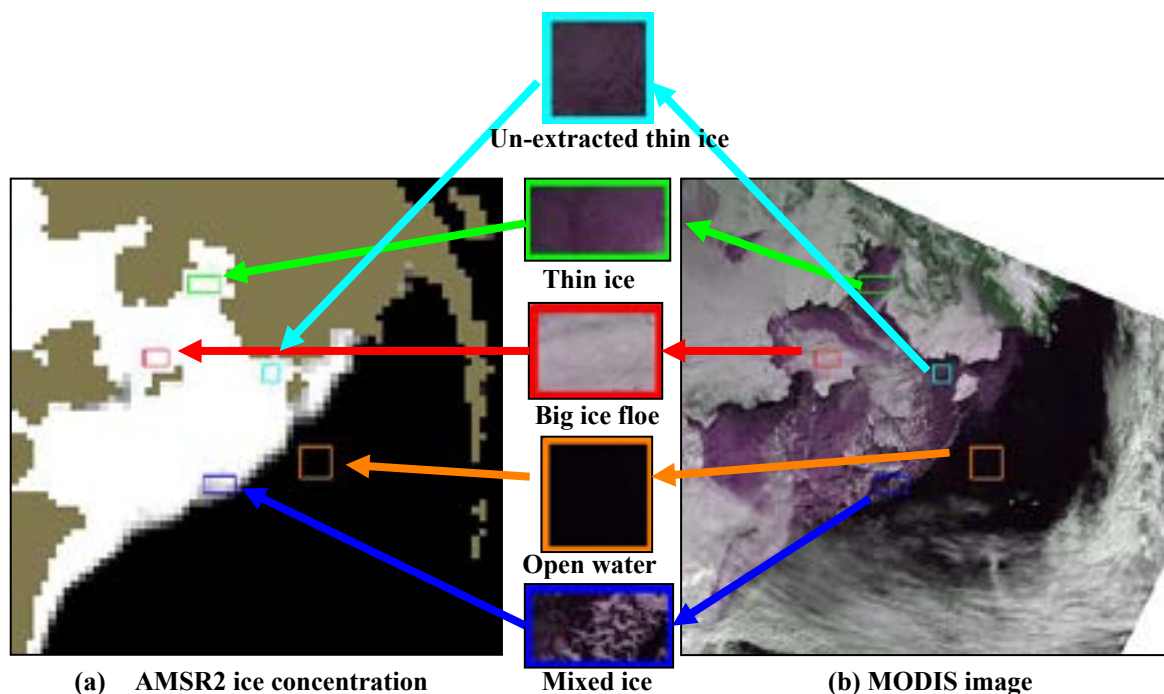
(a) AMSR2 ice concentration　　　　　　**(b) MODIS image**

Figure 7. Selection of sample areas using MODIS and AMSR2 images. (Bering Sea, March 19, 2016)

the un-extracted sea ice areas(■) are distributed outside of the blue meshed area. Therefore, we have moved the threshold of equation (1) from 245K to235K.

$$(Tb19GHzV) > 235K \qquad\qquad\qquad\qquad (1)'$$

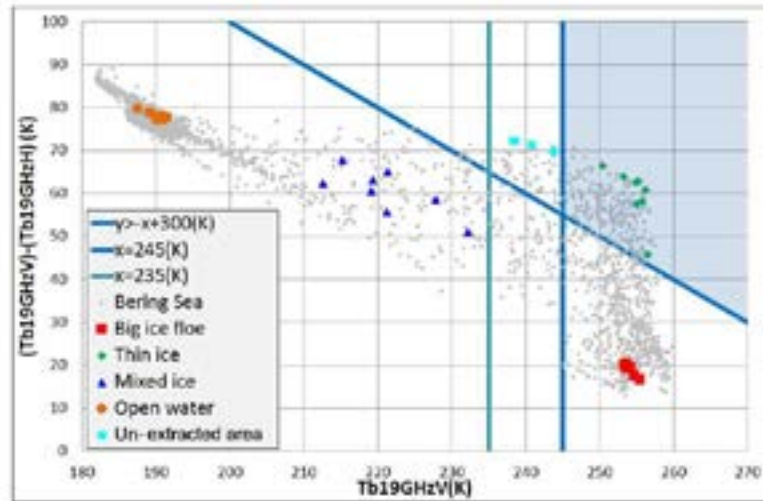where Tb19GHzV: Brightness temperature of AMSR2 19GHz V polarization

Figure 8. Scatter plots of (19GHzV – 19GHzH) Vs 19GHzV polarization (Bering Sea, March 19, 2016)

(b) Rejection of the big ice floe areas extracted as thin ice areas

In order to reject the big ice flow areas extracted as thin ice areas (here after described as "mis-extracted area", the microwave brightness temperature characteristics of the sea ice areas were examined. The sample areas of big ice floe, thin ice, mixed ice and open water, and big ice floe areas extracted ice thin ice areas extracted from MODIS image and overlaid on the AMSR2 image of February 10, 2014 as sown on Figure 9.

Figure 10 shows the scatter plot of AMSR2 19GHz V versus 19GHz (V-H) of the Bering Sea observed on February 10, 2014. The blue meshed area represents the thin ice area extracted with equation (1)' and (2). It is clear that the mis-extracted areas are distributed in the blue meshed area. In order to solve the problem, the authors have re-examined the brightness temperature characteristics of mis-extracted thin ice, big ice floe, thin ice, mixed ice and
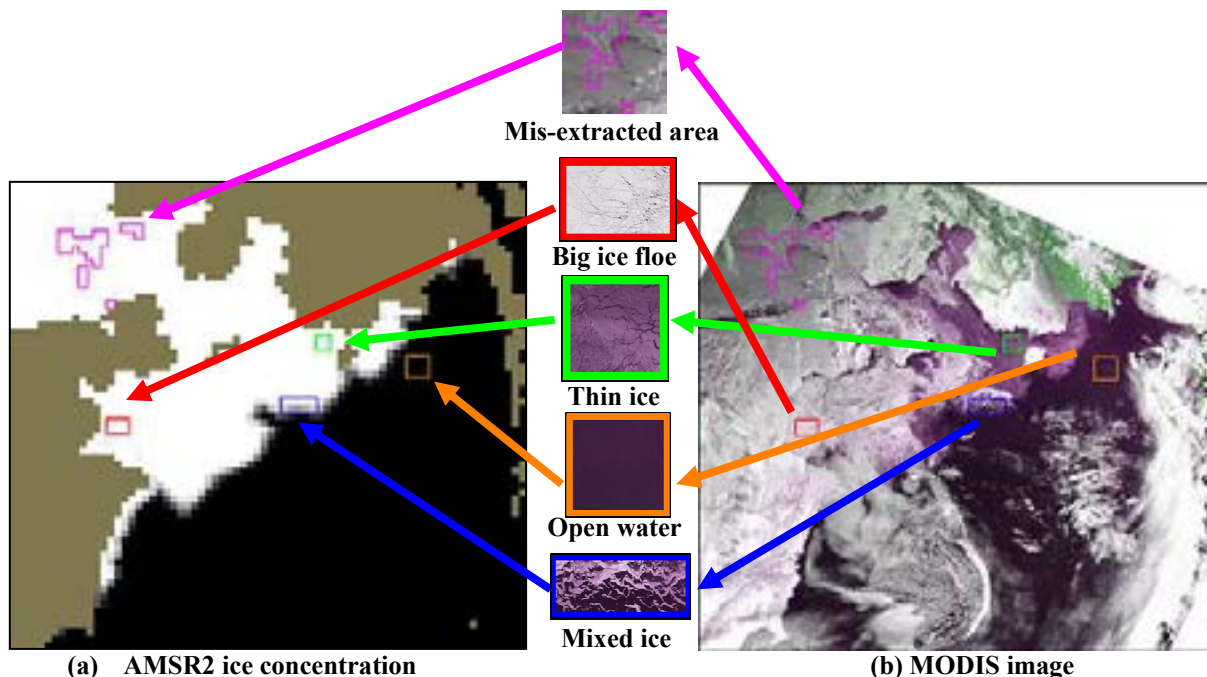

(a) AMSR2 ice concentration　　　　　　**(b) MODIS image**
Figure 9. Selection of sample areas using MODIS and AMSR2 images. (Bering Sea, February 10, 2014)

area. However, The mis-extracted areas also show the brightness temperature similarly to the actual thin ice in both vertical and horizontal polarization. The water existence on and/or around the big ice floe may causing this phenomenon. So, the authors have decided to use 89 GHz for rejecting the mis-extracted areas. The brightness temperature difference between Vertical and Horizontal polarization in 89GHz is rather large in the thin ice area and small in the mis-extracted area. Figure 12 shows the scatter plot of AMSR2 19GHz V versus 89GHz (V-H) of the Bering Sea observed on February 10, 2014. Considering this feature space, the authors have derived the equation (3) to reject the mis-extraction areas.

$$(Tb89GHzV - Tb89GHzH) > 20K \qquad\qquad (3)$$

where Tb89GHzV: Brightness temperature of AMSR2 89GHz V polarization
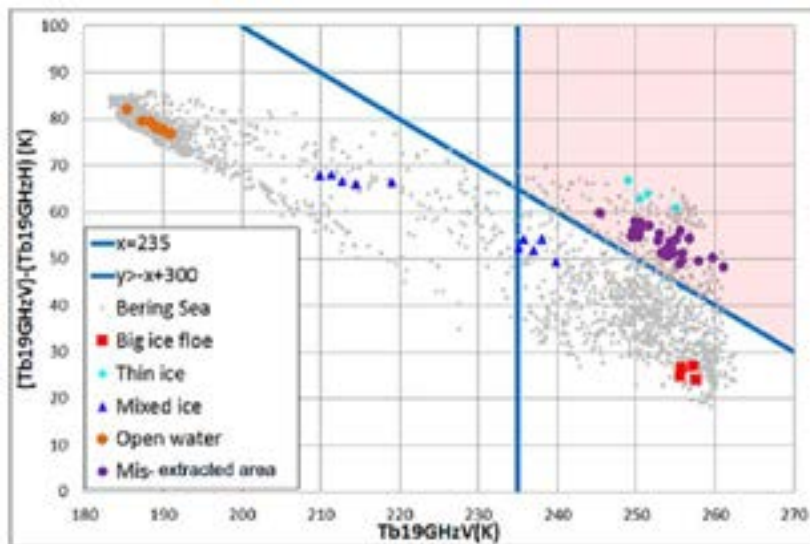Tb89GHzH: Brightness temperature of AMSR2 89GHz H polarization

Figure 10. Scatter plots of (19GHzV – 19GHzH) Vs 19GHzV polarization
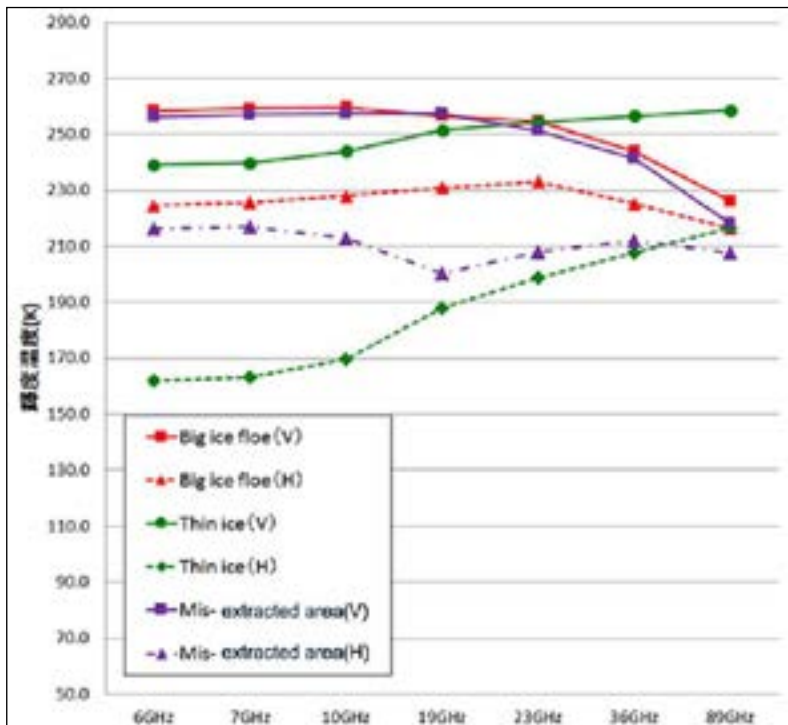**(Bering Sea, February 10, 2014)**

Figure 11. Brightness temperature characteristics graph of test area
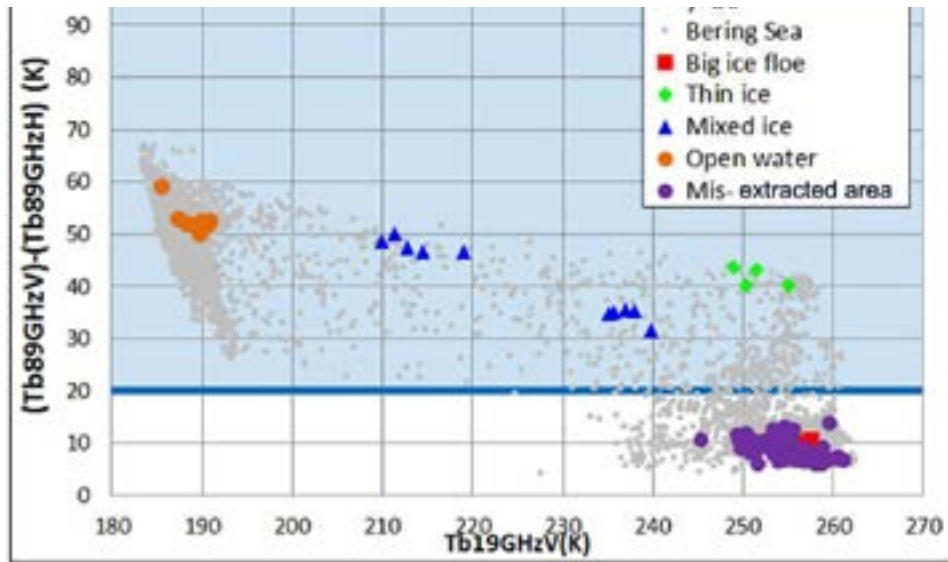**(Bering Sea, February 10, 2014)**

3169

Figure 12. Scatter plots of (89GHzV – 89GHzH) Vs 19GHzV polarization
**(Bering Sea, February 10, 2014)**

5. RESULT

The authors have applied equation (1)', (2) and (3) to the previous AMSR2 data of the Bering Sea to verify the algorithm improvement.

5.1 Parameter tuning for thin ice area extraction

Figure 13 show the result of thin ice area extraction after threshold change of equation (1) to equation (1)'. Figure 13(b) show that most of the thin ice areas including the un-extracted thin ice areas indicated by the arrow in Figure 6 are well extracted as thin ice areas.
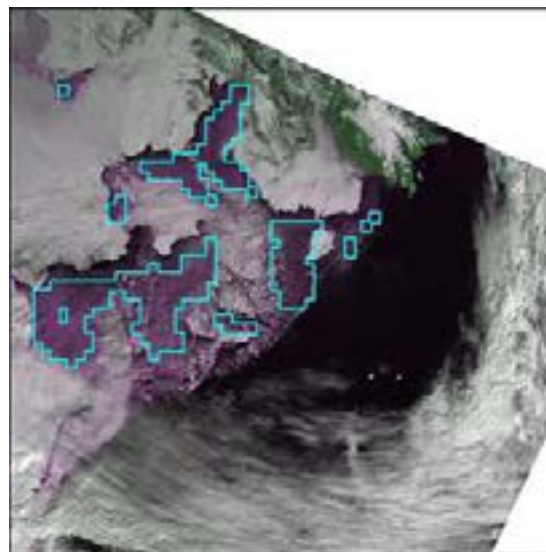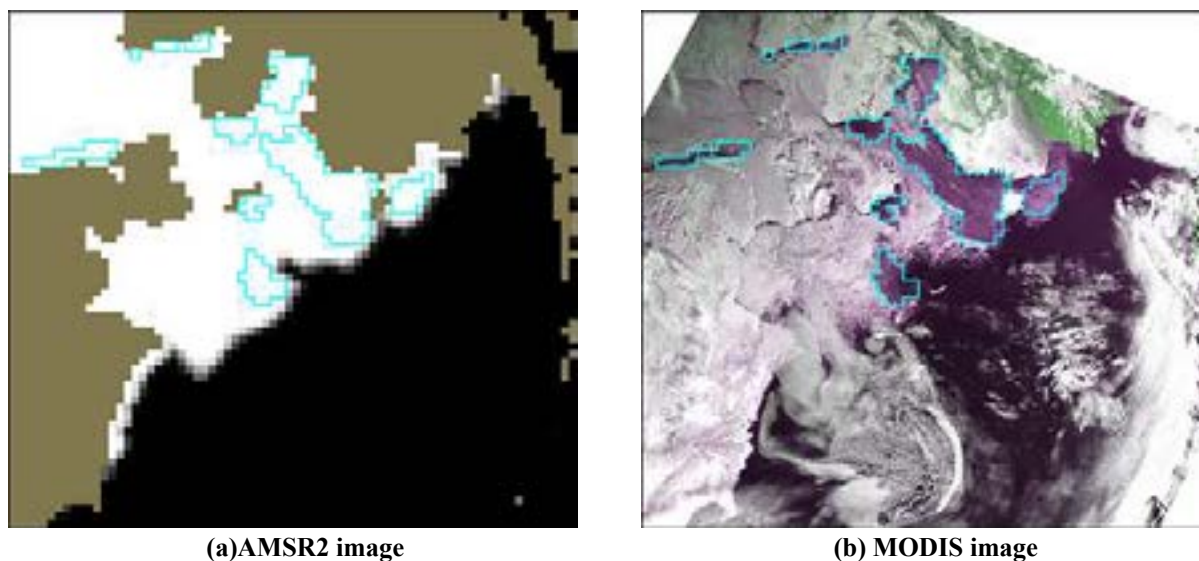

(a)AMSR2 image   (b) MODIS image
Figure 13. Thin ice area extraction result (Cyan: extracted area)
(Bering Sea, March 19, 2016)

Figure 14 shows the result of rejection of mis-extracted thin ice areas by introduction equation (3). Figure 14(b) show that most of the mis-extracted thin ice areas over big ice floe as indicated by the red arrow in Figure 7 are well rejected.

| (a)AMSR2 image | (b) MODIS image |

Figure 14. Thin ice area extraction result (Cyan: extracted area)
((Bering Sea, February 10, 2014)

6. CONCLUSIONS

In this study, authors have applied the AMSR2 thin ice area extraction algorithm (Cho et. Al, 2012) which was developed for the Sea of Okhotsk to the Bering Sea. The extracted thin sea ice areas were validated by comparing with simultaneously collected MODIS images. After analyzing several scenes of the Bering Sea, two problems became clear. One was some of the thin ice areas were not extracted, and the other was some of the big ice floe were mis-extracted as thin ice areas. To solve these problems, the authors have improved the thin ice area extraction algorithm by tuning the threshold of previous equation and introducing an new equation using polarization difference between vertical and horizontal polarization of 89GHz. The result suggested that the improved algorithm could extract most of the thin ice areas which could be identified in MODIS images by image interpretation.

ACKNOWLEDGEMENT

REFERENCES

Comiso, J., 2012, Large Decadal Decline of the Arctic Multiyear Ice Cover, Journal of Climate, Vol. 25, pp.1176-1193.
IPCC. 2014. "Summary for Policymakers." *In Climate Change 2013: The Physical Basis*. Contribution of Working Group I to the Fifth Assessment Report of the Intergovernmental Panel on Climate Change, edited by T.F. Stocker, D. Qin, G.K. Plattner, *et al*., Cambridge: Cambridge University Press.
Cavalieri, D. J. and P. Gloersen, 1984, Determination of sea ice parameters with the NIMBUS 7 SMMR, J. Geophys. Res., Vol.89, pp.5355-5369.
Comiso, J. C., 1995 ,SSM/I Sea Ice Concentrations Using the Bootstrap Algorithm", NASA Reference Publication 1380, Maryland, NASA Center for AeroSpace Information.
Tateyama K., H. Enomoto,, T. Toyota. and S. Uto, 2002, Sea ice thickness estimated from passive microwave radiometers, Polar Meteorol. Glaciol., National Institute of Polar Research, Vol. 16, pp.15-31.
Martin S. and R. Drucker, 2005, Improvements in the estimates of ice thickness and production in the Chukchi Sea

Thickness and Detection of Fast Ice from SSM/I Data in the Antarctic Ocean, Journal of Atmospheric and Oceanic Technology, Vol. 24, pp.1757-1772.

Cho, K., Y. Mochizuki, Y. Yoshida, 2012, Thin ice area extraction using AMSR-E data in the Sea of Okhotsk, Proceedings of the 33rd Asian Conference on Remote Sensing, TS-E6-3, pp.1-6.

Tokutsu Y., K. Cho, 2014, Thin Ice Area Extraction Algorithm Using AMSR2 Data for the Sea of Okhotsk, Proceedings of the 35th Asian Conference on Remote Sensing, OS-101, pp.1-6.

Miyao, K., T. Kasuda, K. Naoki, K. Cho, Thin Ice Area Extraction in the Bering Sea & the Gulf of St. Lawrence Using AMSR2 Data, Proceedings of the 38th Asian Conference on Remote Sensing, PS-04-ID-843, pp.1-4. October 2017

Comiso, J. C., 2009, Enhanced Sea Ice Concentrations and Ice Extent from AMSR-E Data, Journal of the Remote Sensing Society of Japan, Vol.29, No.1, pp.199-215.

Cho K., Y. Mochizuki, Y. Yoshida, H. Shimoda and C. F. CHEN, 2012, A study on extracting thin sea ice area from space, International Archives of the Photogrammetry, Remote Sensing and Spatial Information Sciences, Vol. XXXIX-B8, pp.561-566.

The Plan of Integrated Long Endurance UAV with Lidar

Ming-Yuan Yeh (1), Huan-Jung Lin (2), Jer Ling (1)

[1] National Space Organization, NARL, 8F, 9 Prosperity 1st Road, Science-based
Industrial Park Hsin-Chu City, Taiwan
[2] Aeronautical Engineering Department, NFU, 64, Wunhua Rd., Huwei Township, Yunlin County, Taiwan
Email: marco@nspo.narl.org.tw; nfu.edu.tw ; jl@ nspo.narl.org.tw

KEY WORDS: Lidar, GPS, INS, UAV

ABSTRACT: Light detection and ranging (Lidar) mapping is an accepted method of generating precise and directly georeferenced spatial information about the shape and surface characteristics of the Earth. This paper describes the project plans to carry out the airborne Lidar function test verification and ground operation concept with the long endurance solar-powered UAV.

The plan is to use a long-endurance solar drone to cruise in the air 1~5km above with cruise speed about 30~35km/hr. The UAV will integrate Lidar with GPS and inertial navigation system (INS) to establish a higher resolution 3D terrain collection data without the need for personnel to conduct field surveys. Since the long-endurance drone can stay in the air for a long time and collect the flight data with stable attitude, it can be carried out away from the drone ground station for 3D mapping measurement tasks, and return to the ground station for fast transmission of measurement data every half-day or one-day cycle. Then, fly back to the mission to continue the mapping measurement task to achieve the function of a satellite like Pseudo Satellite.

This paper describes the integration of long-endurance UAV and Lidar; its study will be used as a pathfinder of the space borne Lidar planned for the future space program in Taiwan.

1. INTRODUCTION

Taiwan's hillsides cover a large area, and are affected by several typhoons and earthquakes every year. After several typhoons and earthquakes are affected each year, there are often collapses and earth-rock flows. It is important to monitor the terrain regularly or quickly after the event. Traditional measurement or aerial photography stereo pairs generate elevation information, and compare the trend of terrain changes before and after the disaster. It often takes more time and manpower to measure or obtain complete aerial photography information in the field. Lidar data can construct accurate, high-resolution DEMs to identify morphologic features indicative of landslides, such as head scarps, hummocky topography, convex and concave areas, and mid slope terraces (Schulz 2004). As a result, hydrologists and geologists can objectively delineate landslide features, generate mechanical inferences about landslide behavior, and evaluate recent slide events. In addition, they can identify the sources for major sediment influx in a watershed, which helps prioritize rehabilitation efforts.

Lidar measures distances. It measures distances by sending thousands of laser light pulses every second which strike and reflect from the surfaces on the earth. The Lidar system then measures the time of the pulse returns. The measures times are converted to distance-from-sensor data using the formula

$$D = r * t / 2$$

A Lidar system consists of several advanced technologies that allow conversion of the distance-from-sensor data into accurately georeferenced data in the near real time. This greatly facilitates getting the Lidar data into our GIS applications.

Since Lidar is an active sensor, Lidar data can be acquired day or night as long as the atmosphere is clear. Lidar generates very large datasets; it is not uncommon for the system to collect 300-500 thousand positions (or more) per second. Despite their large size, the data can be post-processed

and densities and more (depending somewhat on how the data is collected).

There are several variations of Lidar including terrestrial and atmospheric Lidar. Within terrestrial Lidar there are variant of surface and bathymetric Lidar. Even further divisions exist within surface Lidar including discrete and waveform Lidar. A Lidar system consists of several advanced technologies. The four major components of Lidar include: 1) flight platform (aircraft or UAV), 2) GPS, 3) INS and 4) the laser scanner system, these components must be very tightly integrated as figure 1.
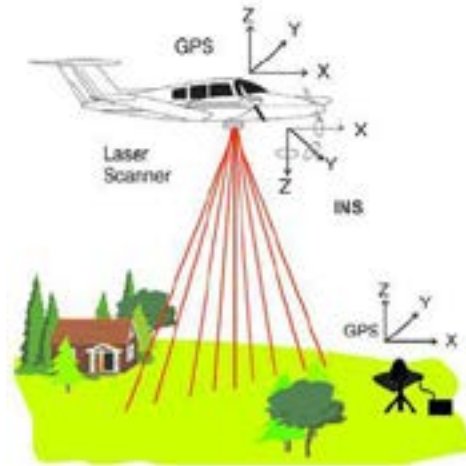

Fig 1 the components of an operating Lidar system (Renslow 2001)

The laser scanner system is the heart of the Lidar system that includes laser source, the laser detector, the scanning mechanism, and the electronic for timing the pulses and returns, and records the data in real time.

2. PROPOSED LIDAR SYSTEM DESCRITIONS

The RIEGL VUX-1LR is a very lightweight and compact laser scanner, meeting the challenges of airborne laser scanning by UAV both in measurement performance as well as in system integration. It provides high speed data acquisition using a narrow infrared laser beam and a fast line scanning mechanism. The scanning mechanism is based on an extremely fast rotating mirror, which provides fully linear unidirectional and parallel scan lines, resulting in excellent regular point. The sensor provides a maximum measurement range of 1,350 m, an effective measurement rate of up to 750,000 measurements/sec, and an operating flight altitude of up to 1,740 ft AGL.

In conjunction with an appropriate IMU/GPS unit with antenna, a control unit, and a digital camera the sensor is integrated into the Long-endurance UAV. The detailed specifications of the proposed components are shown in the table 1.

Device	Product	Spec.
IMU/AHRS	Ellipse2-A or ADIS16488, 3-Space™ Sensor Embedded	• Roll / Pitch 0.1 °, Heading <0.5 °, 200~1k Hz • -40 to 85 °C
GPS	CAM-M8 or SAM-M8Q	• Horizontal position accuracy 2.5 m • update rate 10 Hz • Velocity accuracy 0.05m/s Heading accuracy 0.3 degrees • Operating temperature Topr –40~85 °C • Average supply current 29mA@3V

2D LiDAR	Riegl VUX-1LR designed for airborne	• 15mm accuracy • 200 scans/sec • Scan range up to 1000m • FOV up to 330° • Size(227x180x125 mm)weight (3.5 kg) • scan data storage on internal 240 GBytes SSD Memory • TCP/IP Interface

Table 1 The proposed components of the project

The RIEGL VUX-1LR allows ranging beyond the maximum unambiguous measurement range using a sophisticated modulation scheme applied to the train of emitted laser pulses. It is designed to be mounted in any orientation and even under limited weight and space conditions. Modest in power consumption, the instrument requires only a single power supply. The entire data set of an acquisition campaign is stored onto an internal 240 GByte SSD and/or provided as real-time line scan data via the integrated LAN-TCP/IP interface.

3. UAV SYSTEM DESCRIPTIONS

Unmanned aerial vehicles (UAVs) provide a low-cost, rapid deployment method of obtaining high-resolution aerial photography over areas of varying size. Long-endurance fixed-wing UAV provides a viable alternative to traditional surveying techniques which can deployed in a range of situations and locations. Although strict restrictions apply with regards to their use and deployment in many locations, their application in a wide range of geomorphological environments (glacial, fluvial, hillslope, coastal) means UAVs are becoming more and more popular in geomorphological research.

3.1 Proposed UAV Descriptions

NSPO has been built a long-endurance UAV with NFC and successfully performed flight testing. The key parameters of UAV are shown in Table 2, its flight testing scenarios and collection testing data are showing in Figure 2.

Item	Specification	Item	Specification
Payload	0.3kg	Wingspan	10m
Structure	9.1kg	Aspect Ratio	20
Total Weight	20.5kg	Wing Area	5m^2
Cruise Speed	9.75m/s	Level Flight Power	63.5W
Battery	12S16P (18650 type Li-Ion)	Battery Weight	7.8kg
Solar cell	21% C60 cell(198 cells/3 modules)	Solar panel Weight	1.9kg (including packing)

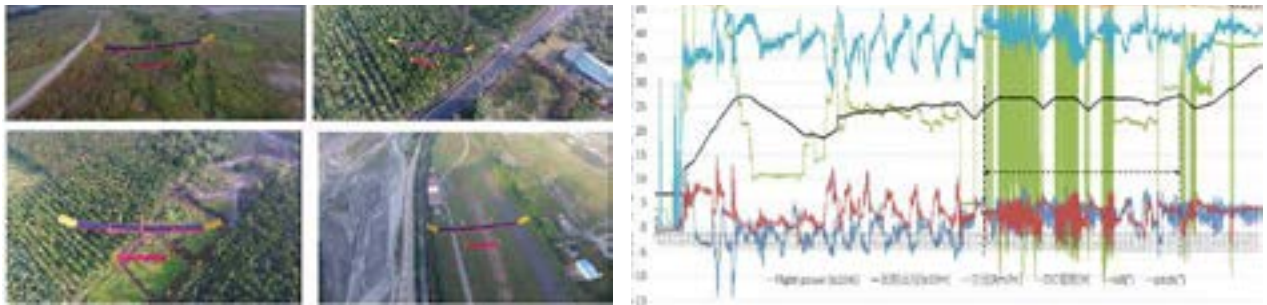Table 2 the key parameters of long-endurance UAV

Fig 2 UAV flight testing scenarios and collection testing data

Using a long-endurance solar UAV to cruise a high altitude of 1~5km above the land (30~35km/hr), integrate Lidar with GPS and inertial navigation system (INS) to establish a precise 3D landform with high plane resolution.

UAV have seen an increase in their flight endurance enabling greater areas to be covered with more ease. They are often controlled in-flight by built-in autopilots, with flight plans pre-programmed before deployment. This means they require less user interaction in flight, and are stable. However, this has implications for topographic data sets derived from photos obtained from fixed-wing platforms, as the increased stability of the platform and pre-programmed, often parallel flight lines may introduce errors into the topographic dataset (James and Robson, 2014).

Because the long-endurance solar drone can fly day and night by daytime solar panel power generation and battery storage for long-term cruise. Among them, the battery is about 10kg, which accounts for half of the total weight of the aircraft. If the weight of the space-based Lidar is more than 3kg, it will reduce the battery from 12S16P to 12S12P or less, without affecting the execution of 3D mapping tasks, and at least maintain the ability to vacate for 8 hours. The following are the methods and steps used in this project.

In general, Lidar has two axial scan ranges. For example, the Velodyne VLP-32C Lidar has a Horizontal FOV of 360° and the vertical FOV is 40° (-25° to +15°), so Lidar solves the observed points in the air. The coordinates are as shown in the Fig. 3. The horizontal scanning angle α and the vertical scanning angle ω, and the scanning distance from the observed point are R, and the coordinates of the origin and the reflection point centered on LiDAR can be calculated.
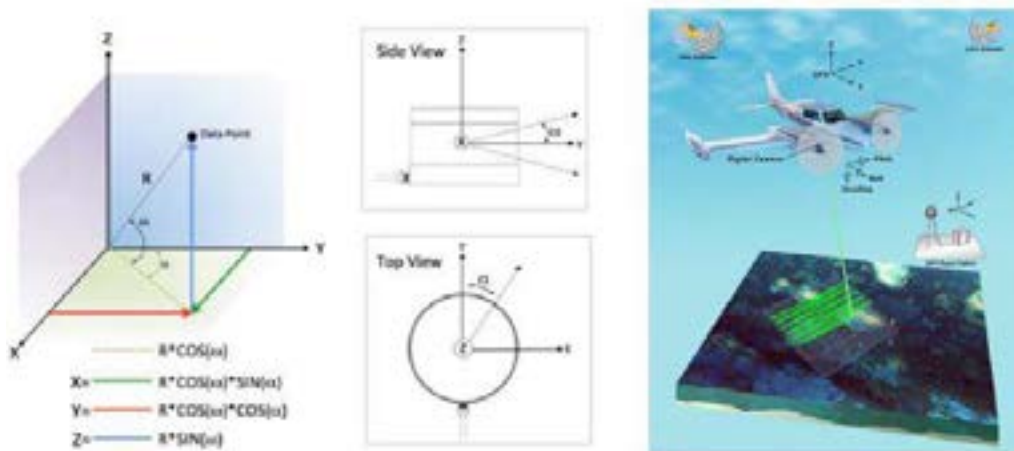

Fig 3 the coordinate calculation relation between UAV and Lidar observation point

However, the UAV's attitude angle also affects the on-board scanning angle of the onboard LiDAR, so two coordinate conversions are required. The airborne Lidar scanning system uses the method of ranging and angle measurement to obtain the 3-D coordinates of the object to be measured as follows:

$$X_G = X_{UAV} + R_{Pitch,Roll,Yaw} \cdot P_G + R_{Pitch,Roll,Yaw} \cdot R_{\omega,\alpha} \cdot \begin{bmatrix} 0 \\ 0 \\ -R \end{bmatrix}$$

Where, X_G is the coordinate of the scanned point in the ground coordinate system; X_{UAV} is the

coordinates of the UAV vehicle's GPS instantaneous position; $R_{yaw,\ pitch,\ roll}$ is the corresponding UAV transient attitude angle obtained by the IMU system Rotation matrix; P_G is the arm offset vector in the Lidar system placement parameters; and $R_{\omega,\ \alpha}$ is the two scan angles ω and α of the instantaneous Lidar and the corresponding rotation matrix (this project is expected to use only vertical axial scanning Lidar, that is, $\alpha=0$); R is the scanning ranging value of the observed point. In this way, the absolute coordinates of the Lidar points cloud can be estimated to achieve the direct georeferencing results required for mobile mapping.

3.2 Flight Planning

A proper flight planning pattern is essential for LiDAR acquisition. The recommended flight pattern is a grid image with parallel flight lines that have the right amount of overlap at a constant height over the terrain.

Systematic misalignment between an IMU and a LiDAR sensor or camera can be solved reliably through the execution of a calibration flight. A proper calibration flight plan should consider the importance of flight location and data coverage in order to facilitate the determination of roll, pitch, and heading observations. The calibration site should contain primarily hard surfaces and be free of vegetation. A well- defined ground surface per each discrete flight line will allow for improvements of sensor alignment. An area should be chosen that has flat ground as well as some sloped terrain. Flat ground is useful for roll observations, while slopes help to solve for pitch and heading.

The UAV mission can be divided into two types of Lidar imaging tasks for the specified area and along the path. The flight paths of the two tasks are as Fig. 4:

Fig 4 the flight path planning of UAV mission

Since the long-endurance solar-powered UAV can stay in the air for a long time and the flight is relatively stable, it can be carried out away from the unmanned aerial station for 3D geomorphological measurement tasks, and return to the ground point near the ground station every half-day or day cycle. The data is then returned to the mission to continue the geomorphological measurement work to achieve the function of a satellite like Pseudo Satellite. In order to achieve this effect, there must be a communication system that quickly transmits data. The table-3 shows the expected communication equipment.

Solution 1	Digital Data Link UAV	pDDL2400	• Up to 25Mbps • Serial interface • 2.4GHz • Up to 1W • -40 to 85 °C • 10 grams
	Digital Data Link GCS		• Up to 25Mbps • Ethernet or USB • 2.4GHz • Up to 1W • -40 to 85 °C • 175 grams
Solution 2 (WiFi through TCP/IP)	WiFi	TP-Link TL-WR941HP 高功率無線 N 路由器	• IEEE 802.11b/g/n 2.4GHz • Up to 1W • 3 x 9dBi 高增益外接天線 • Up to 300m
Solution 3	4G module	4G / LTE modem	• Download speed up to 100Mbps and an Upload speed of 50Mbps • high speed LTE, HSPA+, WCDMA cellular networks • Class 4 (2 W, 33 dBm)@GSM 900 • Protocols: TCP/UDP, HTTP, FTP

Table 3 Data downlink device solution

4. Post Data Processing and Its Applications

Fusion is a powerful Lidar viewing and analysis software suite developed by the Silviculture and Forest Models Team of the Pacific Northwest Research Station. Fusion is readily installed and will run on corporate hardware without the need to obtain administrator privileges and it's provides free. It allows the user to quickly view the Lidar data and create products such as ground surface models and canopy surface models.
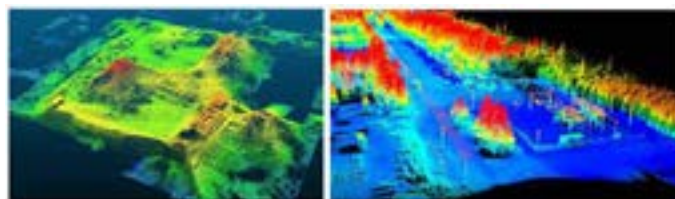
Fig 5 Point-cloud data from UAV with Lidar
http://flight-evolved.com/new-lidar-transmission-line-case-study/
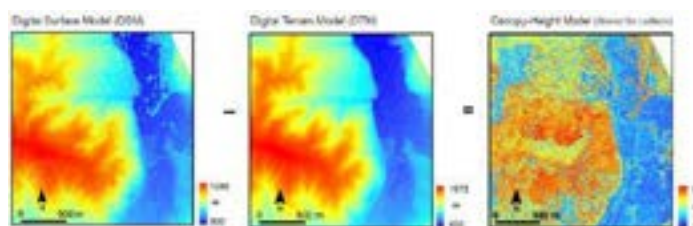
Figure 6   A canopy-height model (right) is created by subtracting the DTM (center) from the DSM (left).

4.1 Lidar Data Formats

Processed Lidar data can be delivered in several formats as shown in table 5. The most basic format is an ASCII XYZ file. This is a text file listing the three-dimensional location of every point, often referred to as a *point cloud*. For example, the data may be processed to separate the point cloud into different returns representing the ground and higher surfaces such as canopies or buildings. Separate XYZ files may be created for each return.

	points							
ASCII XYZ	∨							Relatively large
Data-base	∨	∨	∨	∨	∨	∨		Relatively small
Binary LAS	∨	∨	∨	∨	∨	∨	∨	Relatively small

Table 5 A simplified comparisons of Lidar data formats

The standard XYZ format does not contain ancillary data such as the number of the return associated with the point, the intensity of the return, the scan angle of the outgoing signal, or the scan direction. These attributes can be saved in a database format such as a DBF or MDB file.

4.2 Applications

As Lidar systems and the associated technologies improve and become more user-friendly, the applications of Lidar will undoubtedly increase.
There are two general mapping applications for Lidar data:
● Vegetation mapping: vertical structure or the three-dimensional characteristics of vegetation communities.
● Topographic mapping: surface mapping such as digital elevation models (DEMs) and digital terrain models (DTMs).
Topographic Lidar data are typically gathered from UAV and have benefited from recent advancements in GPS and IMU technology. The technique can provide a dense suite of highly accurate elevation measurements over a large area. While Lidar cannot penetrate through trees, the point coverage is dense enough to allow for ample ground measurement through small holes in the canopy in most forested environments. Many of the traditional elevation applications benefit from this increased accuracy and coverage, and new applications are being made possible because of the rich data density and high quality. There are three kinds of pulse density specification list in the Table 6.
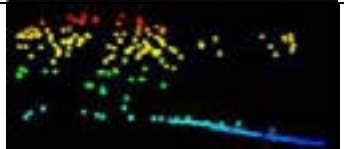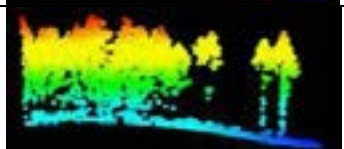
	Low Pulse density ($\leq$ 1 Pulse/m^2) - Product: Moderate Resolution Topographic Products ($\geq$ 2 m grid)
	Moderate Pulse density (1 ~ 3 Pulse/m^2) - Products: Stand Level Vegetation Metrics and High Resolution Topographic Products
	High Pulse density ($\geq$ 3 Pulse/m^2) - Product: Forest Structure • Modeling and Field Data Collection Required

Table 6 Pulse density specification for Lidar Application

5. CONCLUSIONS

Long-endurance UAV provides a low-cost, rapid deployment method of obtaining high-resolution aerial photography over areas of varying size. It also provides a viable alternative to traditional surveying techniques which can deployed in a range of situations and locations. Although strict restrictions apply with regards to their use and deployment in many locations, their application in a wide range of geomorphological environments (glacial, fluvial, hillslope, coastal) means UAVs

3-D data about the Earth's surface. The two main types of information generated from Lidar data are the vertical structure of surface features and detailed measurements of topography. Developing accurate information on vegetation characteristics is valuable to assess numerous forest conditions and useful for a variety of natural-resource projects.

Existing and potential uses for Lidar include forest inventories, fuel modeling, wildlife habitat assessment, corridor mapping, flood/hydrological analysis, determination of geomorphologic hazards, vegetation mapping, and visualization.

This project integrates the long-endurance UAV with Lidar, after perform system verification and validation; it will be used as a pathfinder of the space borne Lidar planned for the future space program in Taiwan.

6. REFERENCES

1. Lelin Li and San Jiang, "A quasi-rigorous model based on improved ICP algorithm in the application of auto-calibration of airborne LiDAR system", Ninth International Symposium on Multispectral Image Processing and Pattern Recognition (MIPPR2015)
2. Anderson K, Gaston KJ. 2013 Lightweight unmanned aerial vehicles will revolutionize spatial ecology, *Frontiers in Ecology and the Environment* **11**: 138-146. DOI: 10.1890/120150.
3. Bennett MR. 2001 The morphology, structural evolution and significance of push moraines. *Earth-Science Reviews* **53**(3-4): 197-236. DOI: 10.1016/S0012-8252(00)00039-8.
4. d'Oleire-Oltmanns S, Marzolff I, Peter KD, Ries JB. 2012. Unmanned aerial vehicles (UAVs) for monitoring soil erosion in Morocco. *Remote Sensing* **4**: 3390-3416. DOI: 10.3390/rs4113390.
5. Dunford R, Michel K, Gagnage M, Piegay H, Tremelo ML. 2009. Potential and constraints of unmanned aerial vehicle technology for characterization of Mediterranean riparian forest. *International Journal of Remote Sensing* **30**(19): 4915-4935.
6. James M, Robson S. 2014 Mitigating systematic error in topographic models derived from UAV and ground-based image networks. *Earth Surface Processes and Landforms* **39**(10): 1413-1420. DOI: 10.1002/esp.3609.
7. Lejot J, Delacourt C, Piegay H, Fourier T, Tremelo ML, Allemand P. 2007. Very high spatial resolution imagery for channel bathymetry and topography from an unmanned mapping controlled platform. *Earth Surface Processes and Landforms* **32**: 1705-1725. DOI: 10.1002/esp.1595.
8. Lin Y, Hyyppa J, Jaakkola A. 2011. Mini-UAV-Borne LIDAR for fine-scale mapping. *IEEE Geoscience and Remote Sensing Letters* **8**(3): 426-430.
9. Mancini F, Dubbini M, Gattelli M, Stecchi F, Fabbri S, Gabbianelli G. 2013. Using unmanned aerial vehicles (UAV) for high-resolution reconstructions of topography: the structure from motion approach on coastal environments. *Remote Sensing* **5**(12): 6880-6898. DOI: 10.3390/rs5126880.

Joint Model of Point Clouds Registration and Its Solution

Zhou Tengfei (1), Cheng Xiaojun (1), Xu Wenbing (2)

(1) College of Surveying and Geo-Informatics, Tongji University, Shanghai 200092, China
(2) School of Environment & Resource, Zhejiang A&F University, Hangzhou, Zhejiang 311300, China
Email: tfzhou5713@163.com; cxj@tongji.edu.cn; xuwb97@163.com

KEY WORDS: Terrestrial laser scanning; Point clouds registration; Non-linear model; Gauss-Newton approach

ABSTRACT: The point clouds registration based on feature points is usually divided into two steps. Firstly, using some feature points to calculate the parameters of rigid body transformation via the least square principle, and then transforming the non-public part in original point cloud (point cloud *I*) according to these parameters into target point cloud (point cloud *II*). The point cloud coordinates are treated as equal precision during the registration process, and the coordinate errors of the non-common part in point cloud *I* are generally ignored. In view of such procedure, a joint model of point cloud registration is proposed that takes the transform parameters calculating and non-public part transforming into account simultaneously. The coordinate errors of all points in both two sets and corresponding variance-covariance information are taken into consideration. Finally, the registration parameters and predicted values of the non-common parts in point cloud *II* are derived by the Gauss-Newton iterative algorithm in detail. Simulation experiments are conducted, and the results validate the superiority of the proposed method compared with the previous algorithm.

1. INTRODUCTION

Compared with traditional methods, terrestrial laser scanning (TLS) has the ability to acquire massive 3D point cloud data on the surface of objects fleetly, providing a new technical means for constructing 3D solid models (Cheng, 2014). In order to obtain the complete 3D point cloud data, it is often necessary to perform multi-angle scanning on the object, and then register the multi-view cloud into a unified coordinate system (LISKA and SABLATNING, 2000). Suppose there are two sets of point cloud data, namely, point cloud *I* and point cloud *II*. The purpose of registration is to predict the coordinates of non-public points in *I* to *II*. The registration based on features usually needs six parameters (three transformation parameters and three rotation parameters, while registration among different platform still needs one scale parameter), that is, first obtain the rigid body transformation parameters, and then use them to convert non-common points.

Points are widely used in the feature-based point clouds registration (Weinmann, 2016; Liang et al., 2018). Therefore, how to obtain corresponding feature points from massive point clouds and improve the efficiency with robustness need to be focused. Barnea and Filin (2007) proposed a scale invariant feature transform (SIFT) algorithm to extract feature points, which keeps invariant to rotation, scale scaling, brightness change, and stability to the change of view angle, affine transformation and noise. Rusu et al. (2009) generated a fast point feature histogram (FPFH) solution to realize registration via the angles of the normal vector of every point and its neighbors. Aiger et al. (2008) proposed the 4-points congruent sets (4PCS) method to achieve global registration. Yang et al. (2016) used the intersections of the vertical feature lines and the ground as semantic feature points, and then generated matching point pairs through geometric constraints and semantic information.

On the other hand, how to derive more accurate registration parameters according to these feature points is also worth studying. Seeber (2003) and Wang (2017) indicated that if the rotation angles are small enough, the registration formulation can be simplified as Bursa model and one can use the extracted feature points to predict the registration parameters based on the least square (LS) principle. To simplify the calculation, Yan et al. (2013) and Tao and Da (2013) derived rotation matrix and translation matrix by dual quaternion method. Furthermore, they still could be obtained according to covariance analysis (Meng et al., 2010). Zou (2017) presented the Delaunay-TLS algorithm for multi-view cloud registration based on the principle of total least square, which overcomes the shortcoming of rigid body transformation only for small rotation angle and gets higher registration accuracy than traditional LS algorithm. Zai (2017) proposed a pairwise registration algorithm based on covariance descriptors and non-cooperative game construction.

During the registration process, the calculation of the parameters is usually performed independently with the non-common point conversion in point cloud *I*, and the non-common point errors are usually ignored. In addition, due to the influence of distance, incident angle, reflectivity et al., the scan data is not the equal precision observations (Cang et al., 2014). In this paper, we propose a joint model of point clouds registration, which

combines the solution of registration parameters with the transformation of non-common points together and takes into account the variance-covariance information synthetically. The model established in this paper is a non-linear model. The linearization model is derived based on the Gauss-Newton method (Shen et al., 2011). Finally, the feasibility of the algorithm is verified by simulation examples.

2. JOINT MODEL AND ITS SOLUTION

2.1 Joint model of point clouds

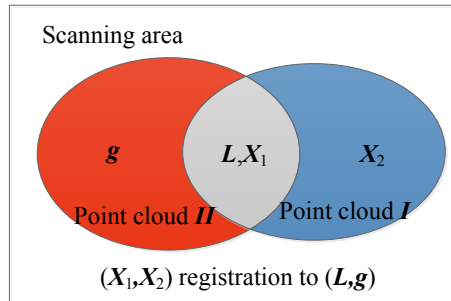The sketch of the point cloud registration can be illustrated as below,

Fig. 1. Point clouds registration sketch. X_1 and L are the feature point pairs (common part point cloud) in point cloud I and point cloud II, respectively; X_2 is the point set to be registered in point cloud I (non-public part point cloud); g is the predicted part.

Assuming a registration from I to II, and the corresponding function model (Cheng, 2014; Zhang et al., 2007) can be expressed as:

$$\begin{bmatrix} X_i \\ Y_i \\ Z_i \end{bmatrix}_{II} = R \begin{bmatrix} x_i \\ y_i \\ z_i \end{bmatrix}_{I} + \begin{bmatrix} \Delta x \\ \Delta y \\ \Delta z \end{bmatrix} \tag{1}$$

Where $\begin{bmatrix} x_i & y_i & z_i \end{bmatrix}_{I}^{T}$ and $\begin{bmatrix} X_i & Y_i & Z_i \end{bmatrix}_{II}^{T}$ represent the point coordinates of the ith pair of feature points in point clouds I and II, respectively; R is a rotation matrix, and defined as below,

$$R = R_3 \cdot R_2 \cdot R_1 \tag{2}$$

$$R_1 = \begin{bmatrix} 1 & 0 & 0 \\ 0 & \cos\alpha & \sin\alpha \\ 0 & -\sin\alpha & \cos\alpha \end{bmatrix}, \quad R_2 = \begin{bmatrix} \cos\beta & 0 & -\sin\beta \\ 0 & 1 & 0 \\ \sin\beta & 0 & \cos\beta \end{bmatrix}, \quad R_3 = \begin{bmatrix} \cos\gamma & \sin\gamma & 0 \\ -\sin\gamma & \cos\gamma & 0 \\ 0 & 0 & 1 \end{bmatrix} \tag{3}$$

We define x as registration parameters vector,

$$x = \begin{bmatrix} \Delta x & \Delta y & \Delta z & \alpha & \beta & \gamma \end{bmatrix}^{T} \tag{4}$$

Which contains three translation parameters ($\Delta x, \Delta y, \Delta z$) and three rotation parameters (α, β, γ). Thus the non-common points in set I can be converted to II via estimated transformation parameters.

In the procedure of solving the registration parameters, the point coordinates are inevitably affected by the observation error. Substituting the error vector and Eq. (1) can be presented as,

$$\begin{bmatrix} X_i - e_{X_i} \\ Y_i - e_{Y_i} \\ Z_i - e_{Z_i} \end{bmatrix}_{II} = R \begin{bmatrix} x_i - e_{x_i} \\ y_i - e_{y_i} \\ z_i - e_{z_i} \end{bmatrix}_I + \begin{bmatrix} \Delta x \\ \Delta y \\ \Delta z \end{bmatrix} \tag{5}$$

Where $\begin{bmatrix} e_{x_i} & e_{y_i} & e_{z_i} \end{bmatrix}_I^T$ and $\begin{bmatrix} e_{X_i} & e_{Y_i} & e_{Z_i} \end{bmatrix}_{II}^T$ are the corresponding residual error vectors of X_1 and L, respectively.

For non-common points in point cloud I, it's predicted values in point cloud II can be expressed as following,

$$\begin{bmatrix} \bar{X} \\ \bar{Y} \\ \bar{Z} \end{bmatrix}_{II} = R \begin{bmatrix} x_r - e_{x_r} \\ y_r - e_{y_r} \\ z_r - e_{z_r} \end{bmatrix}_I + \begin{bmatrix} \Delta x \\ \Delta y \\ \Delta z \end{bmatrix} \tag{6}$$

We define that $L = \begin{bmatrix} X_i & Y_i & Z_i \end{bmatrix}_{II}^T$, $e_L = \begin{bmatrix} e_{X_i} & e_{Y_i} & e_{Z_i} \end{bmatrix}_{II}^T$, $X_1 = \begin{bmatrix} x_i & y_i & z_i \end{bmatrix}_I^T$, $e_1 = \begin{bmatrix} e_{x_i} & e_{y_i} & e_{z_i} \end{bmatrix}_I^T$, $\Delta X = \begin{bmatrix} \Delta x & \Delta y & \Delta z \end{bmatrix}^T$, $g = \begin{bmatrix} \bar{X} & \bar{Y} & \bar{Z} \end{bmatrix}_{II}^T$, $X_2 = \begin{bmatrix} x_r & y_r & z_r \end{bmatrix}_I^T$, $e_2 = \begin{bmatrix} e_{x_r} & e_{y_r} & e_{z_r} \end{bmatrix}_I^T$.

According to Eqs. (5) and (6), the joint model of point clouds registration is,

$$\begin{cases} L - e_L = R(X_1 - e_1) + \Delta X \\ g = R(X_2 - e_2) + \Delta X \end{cases} \tag{7}$$

Where X_1 and L represent the coordinates of the common points in point clouds I and II, respectively; e_1 and e_L are their corresponding random error vectors; X_2 and g represent the coordinates of the non-common point in the point cloud I and the predicted values in the point cloud II, respectively; ΔX represents the translation parameter vector, and R represents the rotation parameter matrix.

The corresponding stochastic model is,

$$e \sim N\left(0, \ \sigma_o^2 Q_e\right) \tag{8}$$

Where

$$e = \begin{bmatrix} e_L \\ e_1 \\ e_2 \end{bmatrix}, \quad Q_e = \begin{bmatrix} Q_{LL} & Q_{Lx_1} & Q_{Lx_2} \\ Q_{x_1 L} & Q_{x_1 x_1} & Q_{x_1 x_2} \\ Q_{x_2 L} & Q_{x_2 x_1} & Q_{x_2 x_2} \end{bmatrix} \tag{9}$$

The estimation criterion for the model is presented as below,

$$e^T P e = \min \tag{10}$$

Where P represents the weight matrix, and $P = Q_e^{-1}$.

2.2 Solution to joint model

The point cloud registration joint model, Eq. (7), is absolutely a non-linear model. We linearize it based on the Gauss-Newton approach (Shen et al., 2011). Let the approximate values of the parameter vector and residual vectors be $\lambda^i = \begin{bmatrix} \Delta x^i & \Delta y^i & \Delta z^i & \alpha^i & \beta^i & \gamma^i \end{bmatrix}^T$, e_1^i and e_2^i, respectively (superscript i represents the iteration index). The right-hand of equation (7) is expanded at $\left(\lambda^i, \ e_1^i, \ e_2^i\right)$ according to Taylor series,

$$\begin{cases} \boldsymbol{L} - \boldsymbol{e_L} = \boldsymbol{R}^i \left(\boldsymbol{X}_1 - \boldsymbol{e}_1^i \right) + \boldsymbol{\Delta X}^i + \left(\dfrac{\partial \boldsymbol{R}}{\partial \alpha} d\alpha \quad \dfrac{\partial \boldsymbol{R}}{\partial \beta} d\beta \quad \dfrac{\partial \boldsymbol{R}}{\partial \gamma} d\gamma \right) \left(\boldsymbol{X}_1 - \boldsymbol{e}_1^i \right) + \begin{bmatrix} d\Delta x \\ d\Delta y \\ d\Delta z \end{bmatrix} - \boldsymbol{R}^i d\boldsymbol{e}_1 \\[4mm] \boldsymbol{g} = \boldsymbol{R}^i \left(\boldsymbol{X}_2 - \boldsymbol{e}_2^i \right) + \boldsymbol{\Delta X}^i + \left(\dfrac{\partial \boldsymbol{R}}{\partial \alpha} d\alpha \quad \dfrac{\partial \boldsymbol{R}}{\partial \beta} d\beta \quad \dfrac{\partial \boldsymbol{R}}{\partial \gamma} d\gamma \right) \left(\boldsymbol{X}_2 - \boldsymbol{e}_2^i \right) + \begin{bmatrix} d\Delta x \\ d\Delta y \\ d\Delta z \end{bmatrix} - \boldsymbol{R}^i d\boldsymbol{e}_2 \end{cases}$$

(11)

Simplify the above equation,

$$\begin{cases} \boldsymbol{L} - \boldsymbol{e_L} = \boldsymbol{R}^i \boldsymbol{X}_1 - \boldsymbol{R}^i \boldsymbol{e}_1 + \boldsymbol{\Delta X}^i + \boldsymbol{A}^i d\boldsymbol{x} \\ \boldsymbol{g} = \boldsymbol{R}^i \boldsymbol{X}_2 - \boldsymbol{R}^i \boldsymbol{e}_2 + \boldsymbol{\Delta X}^i + \boldsymbol{B}^i d\boldsymbol{x} \end{cases}$$

(12)

Where

$$\boldsymbol{A}^i = \left[\boldsymbol{I}_{3\times3} \quad \left(\dfrac{\partial \boldsymbol{R}}{\partial \alpha} \quad \dfrac{\partial \boldsymbol{R}}{\partial \beta} \quad \dfrac{\partial \boldsymbol{R}}{\partial \gamma} \right) \left(\boldsymbol{X}_1 - \boldsymbol{e}_1^i \right) \right], \quad \boldsymbol{B}^i = \left[\boldsymbol{I}_{3\times3} \quad \left(\dfrac{\partial \boldsymbol{R}}{\partial \alpha} \quad \dfrac{\partial \boldsymbol{R}}{\partial \beta} \quad \dfrac{\partial \boldsymbol{R}}{\partial \gamma} \right) \left(\boldsymbol{X}_2 - \boldsymbol{e}_2^i \right) \right],$$

$$d\boldsymbol{x} = \begin{bmatrix} d\Delta x & d\Delta y & d\Delta z & d\alpha & d\beta & d\gamma \end{bmatrix}^T, \quad \boldsymbol{\Delta X}^i = \begin{bmatrix} \Delta x^i & \Delta y^i & \Delta z^i \end{bmatrix}^T$$

The Lagrange objective function of the joint model can be constructed as below,

$$\begin{aligned} \Phi &= \boldsymbol{e}^T \boldsymbol{pe} + 2\boldsymbol{K}^T \left(\boldsymbol{L} - \boldsymbol{e_L} - \boldsymbol{R}^i \boldsymbol{X}_1 + \boldsymbol{R}^i \boldsymbol{e}_1 - \boldsymbol{\Delta X}^i - \boldsymbol{A}^i d\boldsymbol{x} \right) \\ &\quad + 2\boldsymbol{\xi}^T \left(\boldsymbol{g} - \boldsymbol{R}^i \boldsymbol{X}_2 + \boldsymbol{R}^i \boldsymbol{e}_2 - \boldsymbol{\Delta X}^i - \boldsymbol{B}^i d\boldsymbol{x} \right) \end{aligned}$$

(13)

Where $\boldsymbol{K}$ and $\boldsymbol{\xi}$ denote the vectors of "Lagrange multipliers". According to the necessary conditions of Euler-Lagrange, the solution of the joint model can be readily derived as following,

$$d\hat{\boldsymbol{x}}^i = \left(\left(\boldsymbol{A}^i \right)^T \left(\boldsymbol{Q}_c^i \right)^{-1} \boldsymbol{A}^i \right)^{-1} \left(\boldsymbol{A}^i \right)^T \left(\boldsymbol{Q}_c^i \right)^{-1} \left(\boldsymbol{L} - \boldsymbol{R}^i \boldsymbol{X}_1 - \boldsymbol{\Delta X}^i \right)$$

(14)

$d\hat{\boldsymbol{x}}$ indicates the incremental estimation of the parameters vector to be sought.

$$\bar{\boldsymbol{e}}^{i+1} = \begin{bmatrix} \bar{\boldsymbol{e}}_L^{i+1} \\ \bar{\boldsymbol{e}}_1^{i+1} \\ \bar{\boldsymbol{e}}_2^{i+1} \end{bmatrix} = \begin{bmatrix} \left(\boldsymbol{Q}_{LL} - \boldsymbol{Q}_{Lx_1} \left(\boldsymbol{R}^i \right)^T \right) \left(\boldsymbol{Q}_c^i \right)^{-1} \left(\boldsymbol{L} - \boldsymbol{R}^i \boldsymbol{X}_1 - \boldsymbol{\Delta X}^i - \boldsymbol{A}^i d\hat{\boldsymbol{x}} \right) \\ \left(\boldsymbol{Q}_{x_1 L} - \boldsymbol{Q}_{x_1 x_1} \left(\boldsymbol{R}^i \right)^T \right) \left(\boldsymbol{Q}_c^i \right)^{-1} \left(\boldsymbol{L} - \boldsymbol{R}^i \boldsymbol{X}_1 - \boldsymbol{\Delta X}^i - \boldsymbol{A}^i d\hat{\boldsymbol{x}} \right) \\ \left(\boldsymbol{Q}_{x_2 L} - \boldsymbol{Q}_{x_2 x_1} \left(\boldsymbol{R}^i \right)^T \right) \left(\boldsymbol{Q}_c^i \right)^{-1} \left(\boldsymbol{L} - \boldsymbol{R}^i \boldsymbol{X}_1 - \boldsymbol{\Delta X}^i - \boldsymbol{A}^i d\hat{\boldsymbol{x}} \right) \end{bmatrix}$$

(15)

Where

$$\boldsymbol{Q}_c^i = \boldsymbol{Q}_{LL} - \boldsymbol{Q}_{Lx_1} \left(\boldsymbol{R}^i \right)^T - \boldsymbol{R}^i \boldsymbol{Q}_{x_1 L} + \boldsymbol{R}^i \boldsymbol{Q}_{x_1 x_1} \left(\boldsymbol{R}^i \right)^T$$

(16)

And the predicted value is expressed as,

$$\bar{\boldsymbol{g}}^i = \boldsymbol{R}^i \boldsymbol{X}_2 - \boldsymbol{R}^i \boldsymbol{e}_2^i + \boldsymbol{\Delta X}^i + \boldsymbol{B}^i d\hat{\boldsymbol{x}}$$

(17)

$\bar{\boldsymbol{e}}^{i+1}$, $\bar{\boldsymbol{g}}^i$ represent the residual vector and the predicted value, respectively.

Updated parameter estimates,

$$\hat{\boldsymbol{x}}^{i+1} = \hat{\boldsymbol{x}}^i + d\hat{\boldsymbol{x}}^i$$

(18)

The sum of residual weighted squared may be presented as,

$$\tilde{e}^T P \dot{e} = \begin{bmatrix} \hat{K}^T & -\hat{K}^T R^i & 0 \end{bmatrix} Q_e P Q_e \begin{bmatrix} \hat{K} & -(R^i)^T \hat{K} & 0 \end{bmatrix}^T = \hat{K}^T Q_c \hat{K} \tag{19}$$

Thus, the above derivation process can get the error in unit weight,

$$\sigma_0^2 = \frac{\dot{e}^T P \dot{e}}{r} \tag{20}$$

Where r represents the degree of freedom. Eqs. (14) to (18) are the iterative procedure, and will be terminated at $\|d\hat{x}\| < \varepsilon_0$, where ε_0 is a positive threshold close to 0. Eq. (12) can be implemented after iteration. However, it should be denoted that the solution together with its precision assessment is biased, which related to the precision of observations and non-linear derivation.

3. EXPERIMENT ANALYSIS

Suppose that there are 200 points distributed randomly in the space, and the coordinates of all the points are all true values, in which 6 points are corresponding feature point pairs(common point cloud), and the rest 194 points are check point cloud data. The spatial distribution of points is shown in Figure 2.
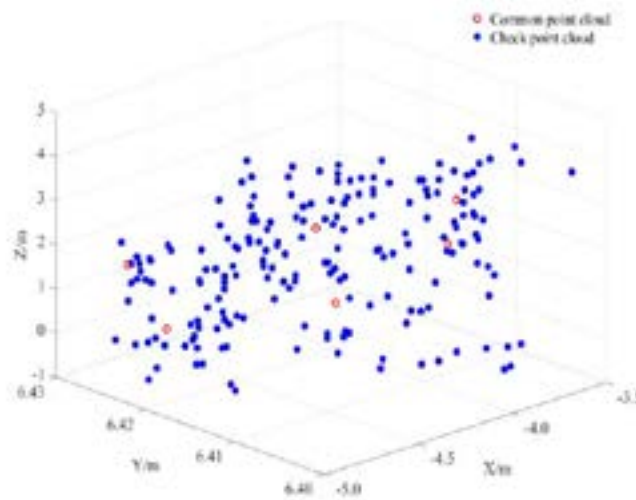

Fig. 2 Points distribution. The blue points indicate the check points and the red circles indicate the feature point pairs.

The registration parameters are designated as following: $\Delta x = 20$, $\Delta y = 30$, $\Delta z = 1$, $\alpha = 1.0 rad$, $\beta = 1.5 rad$, $\gamma = 0.1 rad$. We calculate the true value of 200 points in set $\boldsymbol{II}$ according to Eq. (1) and use the Monte Carlo method (Wen et al., 2012; Lin et al. 2017) to simulate the variance-covariance information for two sets. Random errors with unequal precision are obtained via the variance-covariance matrix and added to the common points in both point clouds and the non-common point in point cloud $\boldsymbol{I}$, repeating 1000 times.

The Monte Carlo simulation steps are as follows: specify the mean square error of each coordinate component in point cloud $\boldsymbol{I}$ and generate the corresponding variance-covariance diagonal matrix $\boldsymbol{D}_1$; generate a standard normal distribution matrix $\boldsymbol{s}$, and perform QR decomposition, $\boldsymbol{s} = \boldsymbol{Q}_1 \boldsymbol{R}_1$; designate mean square error as 1.0, then $\boldsymbol{Q}_I = \boldsymbol{Q}_1 \boldsymbol{D}_1 \boldsymbol{Q}_1^T$; generate random error matrix via conducting the Cholesky decomposition to $\boldsymbol{Q}_I$. The generation of $\boldsymbol{Q}_{II}$ is the same as $\boldsymbol{Q}_I$. In practical applications, the point cloud $\boldsymbol{I}$ and the point cloud $\boldsymbol{II}$ are usually not related, namely, $\boldsymbol{Q}_{Lx_1} = \boldsymbol{Q}_{Lx_2} = \boldsymbol{0}$.

The experiment is designed as: Scheme ①, non-linear transformation model (Zou, 2017); Scheme ②, the joint

model.
Calculate registration parameters and predict point values of non-public parts in point cloud I according to two schemes, respectively. Then compare the above result with the designated true value to evaluate the precision of parameters and coordinate components via root mean square error (RMSE) in Eq. (21).

$$RMSE(\cdot) = \sqrt{\frac{\sum_{i=1}^{194}(X_{obs,i} - X_{model,i})^2}{194}} \tag{21}$$
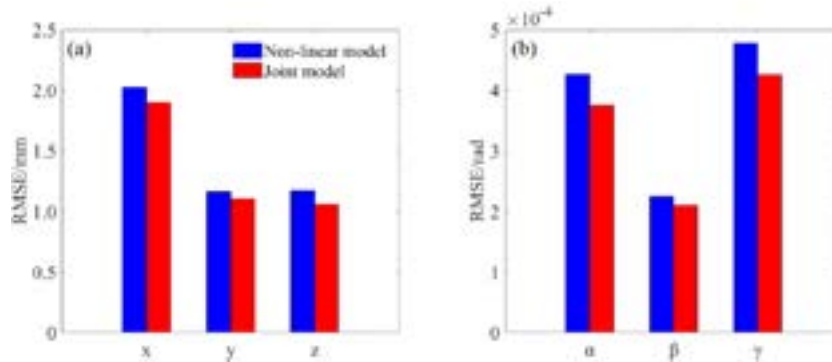

Fig. 3. Registration parameters estimation accuracy. (a) Translation parameters; (b) rotation parameters. The Blue bars represent the non-linear model and the red bars represent the joint model.

The results of 1000 simulations are statistically analyzed. The average and maximum values of the RMSE for each coordinate component and point accuracy are shown in Table 1. In addition, Fig. 4 and Fig. 5 are the RMSE sequences for coordinate components of feature point pairs and check points , respectively.

Tab. 1. Statistic result of check points for two scheme.

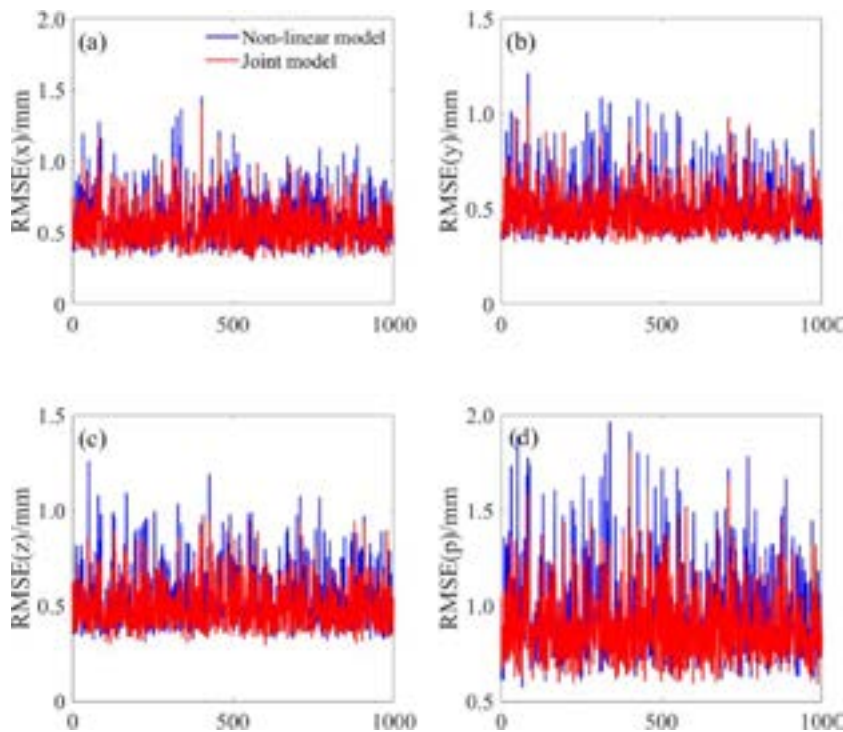| Scheme	Mean(x)	Mean(y)	Mean(z)	Mean(p)	Max(x)	Max(y)	Max(z)	Max(p)
1	0.6	0.5	0.5	0.9	1.5	1.3	1.3	2.0
2	0.5	0.4	0.4	0.8	1.4	1.0	0.9	1.8

Fig. 4. RMSE sequences for 6 common points. (a) x component; (b) y component; (c) z component; (d) point. The blue lines represent the non-linear model and the red lines represent the joint model.
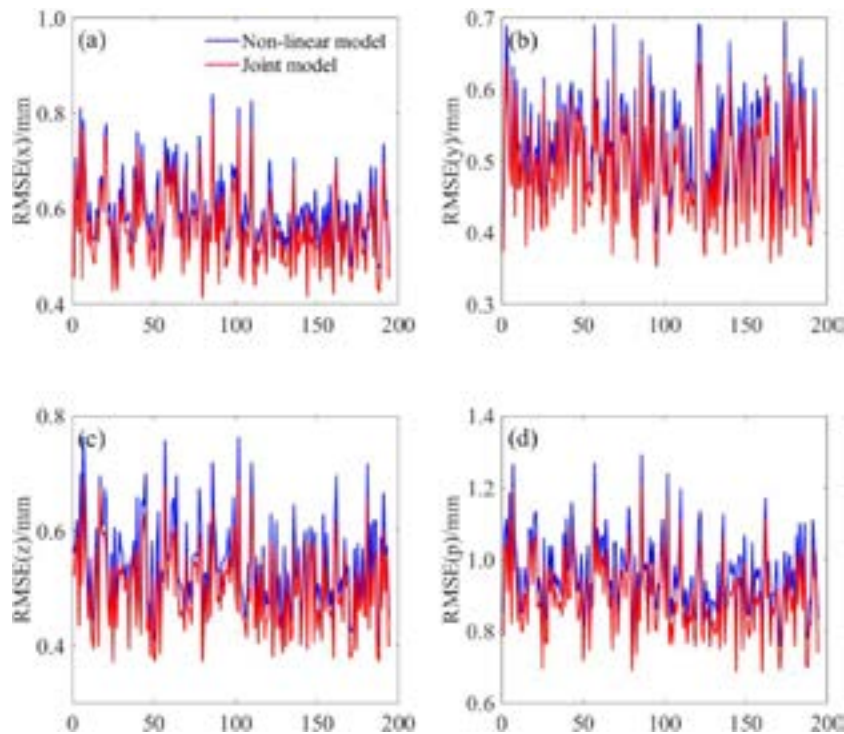
Fig. 5. RMSE sequences for 194 check points. (a) x component; (b) y component; (c) z component; (d) point. The blue lines represent the non-linear model and the red lines represent the joint model.

It can be found in Fig. 3 that the RMSE for translation parameters and rotation parameters of Scheme 2 are smaller than Scheme 1, which indicates joint model performs better than the non-linear algorithm. Tab. 1 and Fig. 4-5 show that the joint model can get more accurate registration parameters and predicted coordinates than those transformed by estimated parameters to some extent. Therefore, the joint model has more superiorities than the non-linear model. However, from Fig. 4, there are also some points along with its coordinate component that the precision of the joint model is not as good as traditional ones, even lower. The reason account for this phenomenon may be that the solution to the joint model is biased and original observations are more accurate than the estimated. The essential reason for which is worth further study.

4. CONCLUSION

Aiming at the registration of point clouds, we proposed a joint model, a non-linear model, which takes parameters solving and non-common point cloud registration into account simultaneously. The linear model is derived based on the Gauss-Newton method and the numerical characteristics of registration parameters. Through experiments and analysis, the following conclusions can be drawn,

(1) The point cloud registration joint model comprehensively considers the coordinate errors of all points in the point cloud data, and uses the variance-covariance information to correct the non-common part errors in the non-public part conversion. Therefore joint model is more reasonable in theory than the non-linear ones.

(2) The experimental results show that the accuracy of the registration parameters calculated by the new model and non-common part conversion is higher than that of the non-linear transformation model. The new model can effectively improve the registration accuracy of the point clouds to some extent.

(3) Joint model is derived based on the condition that both of the two point clouds have the same variance-covariance matrix. However, in practical applications, there are many factors affecting the point coordinates, how to determine the variance-covariance matrix of points reasonably needs further research.

5. REFERENCES

Cheng Xiaojun., 2014. Theory and technology of massive point cloud data processing. Shanghai: Tongji University Press, pp. 1-2.

Liska, C., & Sablatnig, R., 2000. Adaptive 3D acquisition using laser light, pp. 111-116

Weinmann, M., 2016. Reconstruction and analysis of 3D scenes: from irregularly distributed 3d points to object classes. Reconstruction and Analysis of 3D Scenes. Springer International Publishing, pp. 55-110

Cheng, L. et al., 2018. Registration of laser scanning point clouds: a review. Sensors, 18(5), 1641.

Barnea, S., Filin, S., & Wg, C. V., 2008. Registration of terrestrial laser scans via image based features. International Archives of Photogrammetry, Remote Sensing and Spatial Information Sciences, pp. 32-37.

Rusu, R. B., Blodow, N., & Beetz, M., 2009. Fast point feature histograms (FPFH) for 3D registration. pp.3212-3217.

Aiger, D., Mitra, N. J., & Cohen-Or, D., 2008. 4-points congruent sets for robust pairwise surface registration. Acm Transactions on Graphics, 27(3), pp. 1-10.

Yang B, Dong Z, Liang F, et al., 2016. Automatic registration of large-scale urban scene point clouds based on semantic feature points. Isprs Journal of Photogrammetry & Remote Sensing, 113, pp.43-58.

Seeber, G., 2003. Satellite geodesy: foundations, methods, and applications. Monte Carlo Methods & Applications, 13(13), pp. 405-453.

Wang, B., Li, J., Liu, C., & Yu, J., 2017. Generalized total least squares prediction algorithm for universal 3d similarity transformation. Advances in Space Research, 59(3), pp. 815-823

Yan Jianfeng, Deng Kazhong., 2013. Point cloud registration algorithm based on extracting and matching feature points. Bulletin of Surveying and Mapping, 2013(9), pp. 62-65.

Tao Haiji, Da Feipeng., 2013. Automatic registration algorithm for the point clouds based on the normal vector. Chinese Journal of Lasers, 2013(8), 0809001.

Meng, F., Lushen, W. U., & Luo, L., 2010. Study on point cloud registration of raster projection in reverse engineering. Machine Tool & Hydraulics. 38(15).

Zou Min., 2017. The study of multi-view point cloud registration method based on total least squares. Huai Nan: Anhui University of Science and Technology.

Zai, D., Li, J., Guo, Y., et al., 2017. Pairwise registration of TLS point clouds using covariance descriptors and a non-cooperative game. Isprs Journal of Photogrammetry & Remote Sensing, 134.

Cang Guihua, Li Mingfeng, Yue Jianping.,2014. Study on point clouds plane fitting with weighter total least squares on incidence angle weighting. Journal of Geodesy and Geodynamics, 34(3), pp. 95-98.

Shen Y, Li B, Chen Y.,2011. An iterative solution of weighted total least-squares adjustment. Journal of Geodesy, 85(4), pp. 229-238.

Zhang Jianqing, Zhai Ruifang, Zheng Shunyi., 2007. Automatic seamless registration of 3D multiple range views. Geometrics and Information Science of Wuhan University, 32(2), pp. 100-103.

Wen Dezhi, Zhuo Renhong, Ding Dajie., 2012. Generation of correlated pseudorandom variables in Monte Carlo simulation. Acta Physica Sinica, 61(22), pp. 20-27.

Lin P, Chang G, Gao J, et al., 2017. Helmert transformation with mixed geodetic and Cartesian coordinates. Adv. Space Res.

MOTOR BIKES USING UAV

Kento Kojima (1), Kazuhiro Naoki (1) and Kohei Cho (1)

[1]Tokai University
4-1-1 Kitakaname Hiratsuka, Kanagawa 259-1292, Japan,
Email: kohei.cho@tokai-u.jp

KEY WORDS: Disaster, Police, Camera, Drone

ABSTRACT: Due to the rapid advancement of the unmanned aerial vehicle (**UAV**) technologies, the ways of using UAVs, or drones, are expanding in the field of remote sensing. The authors have been using UAVs for connecting satellite images with in situ measurements. One of the interests for police to use UAV is to identify the number plates of cars and motor bikes. Under the cooperation with the Tokyo Metropolitan Police Office, the authors are investigating the suitable flight height of UAVs and the suitable view angle of the cameras onboard the UAV for the purpose. In this study, the authors have used Zenmuse X3 camera attached on an Inspire-1 UAV of DJI for the investigation. In case of the above system, the flight height had to be lower than 20m for identifying the number of the motor bikes. However, the color difference reflecting the motor bike class could be identified up to 40m height.

1. INTRODUCTION

In the history of remote sensing, satellites and aircrafts have been used as the main platforms for observing the earth. However, in recent years, compact and inexpensive UAVs (Unmanned Arial Vehicle), popularly known as drones, are also widely used for various observations in remote sensing (Watts et al., 2012, Themistocleousa, 2014, Matese et al., 2015). By attaching compact camera or other sensors on a UAV, one can easily perform a local area observation with high spatial resolution. Especially, UAV is a strong tool to connect satellite remote sensing with ground observation (Cho et al., 2014). Figure 1 shows an example of comparing a satellite image, a UAV image and an on-site photo of a same area. The UAV image makes it easy to identify the ground features in the satellite image. The purpose of this study is to investigate on-site survey method using images taken from UAV. In this presentation, as experimental results conducted to grasp performance and characteristics of UAV to be used and examples of use Present the interpretation result of the motorcycle license plate number.

(a)FORMOSAT-2 image (2014/9/29) **(b)UAV image (2015/3/6)** **(c) On-site photo (2015/3/6)**
Red allow in figure1(a) shows the location and attitude of the camera of Figure 1(b) and 1(c).
Figure 1. An example of comparing a satellite image, a UAV image and an on-site photo of Omagari Area, Miyagi Prefecture, Japan.

2. OBSERVATION SYSTEM

In this study, DJI 's Inspire1 UAV and ZenmuseX camera were used for the experiment. The Figure 1 show the outlook of the UAV and the Camera. Table 1 and 2 show the specification of them.

(a) Inspire-1 **(b) ZenmuseX**
Figure 2. Outlook of the UAV system (DJI, 2018)

Weight	2845g (including propeller and battery)
GPS hovering system	vertical :0.5m, horizontal: 2.5m
Maximum rotation speed pitch	pitch: 300deg./s Yaw: 150 deg./s
Maximum inclination angle	35 deg.
Maximum ascent speed	5 m/s
Maximum descent speed	4 m/s
Maximum speed	22m/s (ATTI mode, no wind)
Max service ceiling above sea level	4,500 m
Maximum wind speed resistance	10 m/s
Maximum flight time	18 min.
Operating Temperature	-10 to 40 deg.
Physical dimensions	581 mm
Maximum takeoff weight	3,500 g

Table 2. Specifications of Zenmuse X3 camera

Maximum size	4000 × 3000 pixel
ISO Range	100- 1600 (Photo)
Electronic shutter speed	8 to 1/8000 seconds
Viewing angle	94 deg.
Sensor	CMOS 1/2.33"
lens	20 mm (equivalent to 35 mm format) , f / 2.8 Focus at ∞
Operating environment Temperature(℃)	0 to 40℃

3. TEST SITE

The parking area of Tokai University Shonan Campus located in Kanagawa Prefecture, Japan was selected for the test site.   Figure 3 shows the location of the Shonan Campus and Figure 4 shows the UAV image of the parking area.

Figure 3. Location of the Shonan Campus

（Google map）

Figure 4. UAV image of the parking area

4.1 Spatial Resolution Measurement

In order to identify the spatial resolution of the images taken by the Zenmuse X3 camera on board Inspire1, a laboratory experiment was performed. Figure 5 shows the diagram of the experiment. The camera is placed on the floor and the photo of the wall was taken from 2m distance. Then, the pixel number of the wall width was calculated. Once the pixel size from 2m distance is calculated, one can easily calculated the spatial resolution R of UAV images taken at certain altitude H using the Zenmuse X3 camera.

$$R = H \times W / 2N \qquad (1)$$

R: Resolution of the image taken from altitude H using the Zenmuse X3 camera (mm/pix)
H: Altitude of Inspire1 (m)
W: Wall width(mm)
N: Number of pixels corresponds to the wall width

Figure 5, Laboratory experiment for identifying the spatial resolution of the Camera.

In case of 1m altitude, the resolution R1 will be expressed in the following equation

$$R1 = W / 2N \qquad (1)'$$

By using equation (1) and (2), the relationship between the altitude of Inspire1 H and the resolution R of the image can be defined by the following equation.

$$R = H \times R1 \qquad (2)$$

4.2 Altitude Estimation Accuracy Evaluation

The altitude of Inspire1 is estimated by the onboard GPS and displayed on a screen of the smart phone attached to the remote controller. The height estimation accuracy of Inspire1 was evaluated by performing the following procedure. The authors have prepared a 5m ruler and set on the ground to be captured in the images taken from the inspire1. The images were taken at the altitudes starting from 10m to 150m with 10m interval. By counting the number of pixels L corresponds to the 5m ruler captured in the Inspire1 image, one can calculate the spatial resolution of altitude of the Inspore1 which took the image as follows.

$$R = 5 / L \qquad (3)$$

By using equation (2) and (3), the altitude H can be calculated by the following equation.

$$H = 5 / (L \times R1) \qquad (4)$$

4.3 Target Identification Experiment

In this study we have examined the limitation of the Inspire1 altitude for identifying two targets captured in the images taken by Zenmuse X3 camera onboard Inspire1. The two targets were human body and number plate of motor bike.

(a) Human Body Posture Identification

A student operating remote controller were captured by the camera the UAV in different altitude, and the possibility of identifying the human body posture was examined.

(b) Number Plate Identification

In order to examine the possibility of identifying the number of the number plate of the motor bikes, the bikes in the parking place were captured by the camera the UAV in different altitude.
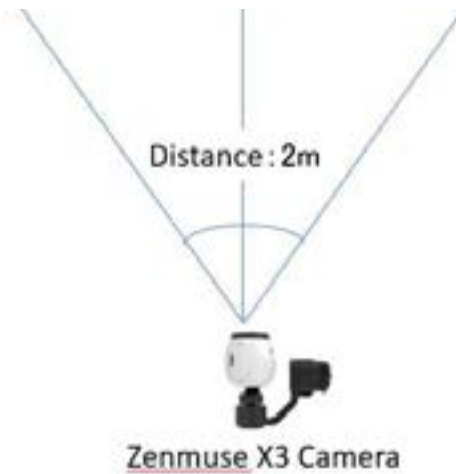
5.1 Spatial Resolution Measurement

Figure 6 shows the image of the wall taken by the Zenmuse X3 camera which was placed on the floor 2m distance from the wall. The wall width was 3.621m. Since the number of the pixels of the wall width in the image was 4000 pixels, the spatial resolution of the image taken by the Zenmuse X3 camera from 1 m distance was calculated as the following using equation (1)'

$$R1 = W / 2N = 3621 / (2 \times 4000) = 0.455 (mm/pixel) \qquad (5)$$

5.2 Altitude Estimation Accuracy Measurement

Figure 7 shows an image of the parking place including the 5m ruler. The images from the altitude starting from 10m to 150m with 10m interval were taken. Since the 5m ruler is captured in each image, by using the equation (4), the exact altitude of shooting each image was calculated. Figure 8 shows the relationship between the altitude estimated by the onboard GSP and altitude calculated from each image. The correlation coefficient of them was 0.9997, which proved the reliability of the altitude estimated by the GPS. However, it should be noted that there was 0.95m bias in altitude estimated by GPS.
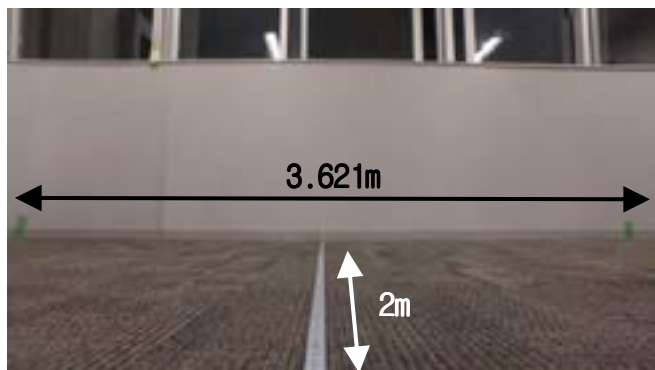

Fig.6 The image of the Wall taken by the Zenmuse X3 for evaluating the spatial resolution of the camera.
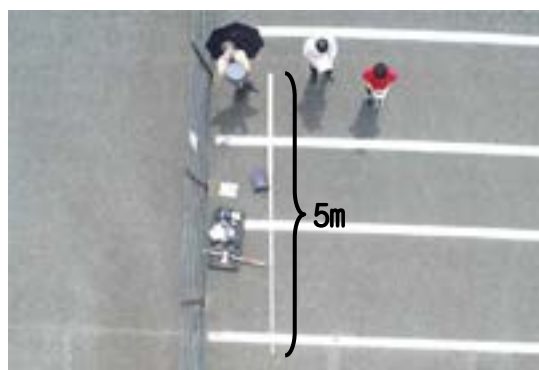

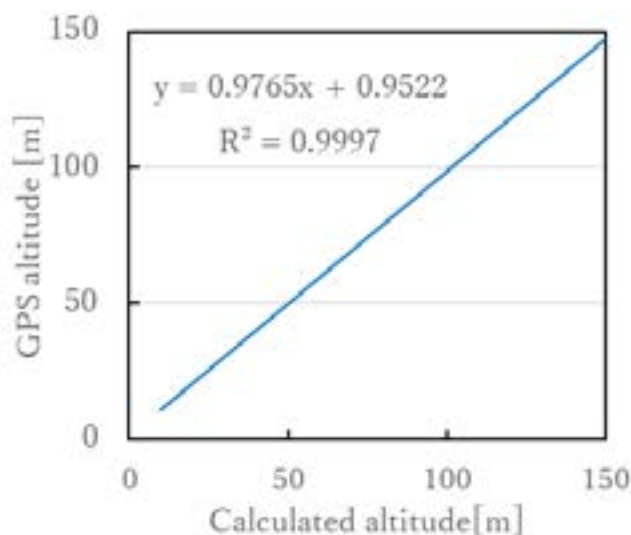**Fig.7 An image of the parking area of Tokai Univ. Including the 5m ruler taken from Inspire1.**

Figure 8. The relationship between the altitude estimated by GPS and the altitude calculated From each image taken by Zenmuse X3 onboard Inspire1.

(a) Human Body Posture Identification
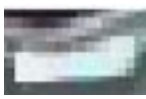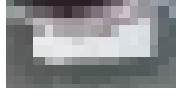
Figure 7 shows the images of a student operating remote controller. The images were taken from the altitude of 10m to 70m with 10m interval. If the altitude of Inspire1 was less than 50m, which spatial resolution was 29mm/pixel in this experiment, one could recognize the posture of the student. However, if the altitude was higher than 60m, which spatial resolution was 34mm/pixel in this experiment, it was difficult to recognize the posture of the student.

Image						
Altitude	10m	30m	40m	50m	60m	70m
Resolution	6mm/pixel	17mm/pixel	23mm/pixel	29mm/pixel	34mm/pixel	40mm/pixel

Figure 9. Evaluating the human body identification from the UAV images taken from various altitude

(b) Number Plate Identification

Figure 7 shows the images of a motor bike in the parking place. The images were taken from the altitude of 20m to 50m with 10m interval. We have evaluated the possibility of identifying the number printed on the number plate of the motor bike. In this case, if the altitude of Inspire1 was less than 20m, which spatial resolution was 8,4mm/pixel in this experiment, one could recognize the number. However, if the altitude was higher than 30m, which spatial resolution was 12.4mm/pixel in this experiment, it was difficult to identify the number. It should also be noted that the angle of number plates and the look angle of the camera also affect the number identification.

Image				
Enlarged image				
Altitude	20m	30m	40m	50m
Resolution	8.4mm/pixel	12.4mm/pixel	16.3mm/pixel	20mm/pixel

Figure 10. Evaluating the number plate identification from the UAV images taken from various altitude

6. CONCLUSION

In this study, the authors have investigated how the identification of the target object such as Human Body and number plate of a motor bike capture in UAV images are affected by the altitude difference of the UAV. In our experiment, in order to identify the human body posture, the Zenmuse X3 camera onboard Inspire1 should fly lower than 50m with spatial resolution higher than 29mm/pixel. As for identifying the number plate of a motor bike, the

be noted that the altitude condition discussed could change due to the specification of the camera onboard the UAV.

ACNOWLEDGEMENT

REFERENCES

Watts, A.C., V. G. Ambrosia, E. A. Hinkley, 2012, Unmanned Aircraft Systems in Remote Sensing and Scientific Research: Classification and Considerations of Use, Remote Sens., Vol.4, pp.1671-1692.

Themistocleousa, K., 2014, The Use of UAV Platforms for Remote Sensing Applications:Case Studies In Cyprus, Proceedings of SPIE, The International Society for Optical Engineering, DOI: 10.1117/12.2069514.

Matese, A., P. Toscano, S. F. D. Gennaro, L. Genesio, F. P. Vaccari, J. Primicerio, C. Belli, A. Zaldei, R. Bianconi and B. Gioli, 2015, Intercomparison of UAV, Aircraft and Satellite Remote Sensing Platforms for Precision Viticulture, Remote Sens. Vol.7, pp.2971-2990.

Cho K., E. Baltsavias, F. Remondino, U. Soergel, H. Wakabayashi, 2014, RAPIDMAP Project for Disaster Monitoring, Proceedings of the 35th Asian Conference on Remote Sensing, OS-145, pp.1-6.

DJI https://www.dji.com/jp, 2018.

DEVELOPING WEB GIS-BASED DASHBOARD PLATFORM FOR MONITORING DISASTER MANAGEMENT IN MALAYSIA

Siti Nor Afzan Abdul Habib, Az-Azira Abd Aziz, Siti Nordiana Mohd Rabai

Malaysian Remote Sensing Agency, Ministry of Energy, Science, Technology, Environment and Climate Change (MESTECC), No. 13, Jalan Tun Ismail, 50480 Kuala Lumpur, Malaysia Email: afzan@remotesensing.gov.my; azazira@remotesensing.gov.my; diana@remotesensing.gov.my;

KEY WORDS: Dashboard, WebGIS, Disaster Management

ABSTRACT: This research describes the development of dashboard in geospatial information web application for disaster management. The main aspects of the development including data collection, data integration, geospatial database design, data presentation and dashboard design are discussed in this paper. Malaysia has experienced various of disasters like floods, forest fires, landslides and haze. It is important for agencies at regional level to monitor and manage for preparedness, response, recovery and mitigation. However, overloaded disaster information in many types of formats and applications from different sources made decision makers facing difficulties to gather and select the most significant data that should be used in disaster situation. Web GIS-based dashboards are designed to display multiple visualizations that work together on a single screen to help the decision makers understand and analyze the information easier, therefore process of decision making more effective and efficient.

1. INTRODUCTION

Disasters have proven that loss of life and property is unavoidable despite past experience and good disaster management. Disaster management involves various events and activities, for which IT plays a significant role (Davenport and Prusak, 1998). IT can support the creation, sharing, and dissemination of information as well as the creation of a useful organizational memory system to enhance emergency planning and response (Alavi and Liedner, 2001; Turoff et al., 2004).

A geographic information system (GIS) is a system designed to capture, store, manipulate, analyze, manage, and present spatial or geographic data. GIS applications are tools that allow users to create interactive queries (user-created searches), analyze spatial information, edit data in maps, and present the results of all these operations. On the other hand, web GIS provides many more opportunities to provide broader access to authoritative GIS data, enabling users to access information timely with visual interaction using web browsers.

The usage of dashboards in organizations has become increasingly popular due to their usefulness in enhancing the user's decision-making ability. A dashboard is defined as "a visual display of the most important information needed to achieve one or more objectives; consolidated and organized on a single screen so the information can be monitored at a glance (Few, 2006)." Shadan Malik (2005) used the terminology "enterprise dashboard", which is defined as an interface computer that presents information in the form of tables, reports, visual indicators, and alert mechanism dynamically and with relevance.

This paper will explain the development process of a web GIS-based dashboard that can support disaster's information and analysis while at the same time generate report as an input in decision making for search and rescue, mitigation, rehabilitation and damage assessment in Malaysia. The process starts with data collection in many different sources, types and formats from related agencies. Then, data integration process will take part to combine all data into a centralized database. In order to make sure this centralized database work efficiently, a database design must be done well so that all data are structured and manageable because most of the data are dynamic and based on real time event. Finally, all data will be visualized in a dashboard according to user requirements and suitability. Since most data are dynamically change, web GIS dashboard is the best way to visualize these data to make sure users especially decision makers get access to the updated information when disasters occurred. The last few chapters will give the results and conclusion of the research.

2.   RESEARCH METHODOLOGY

2.1 Data Collection

In this phase, a feasibility study will be done where researchers gather data to determine a workable solution for disaster management. The needs of data to design the system is outlined in this feasibility study. Before collecting data, researchers have to identify issues and indicate the right methods to achieve the research goals. The main issue in collecting data is identifying the most significant information or data related to disaster occurred in Malaysia.

There are numbers of alternative methods available for collecting data such as observation, work measurement, sampling and questionnaires. In this research, work measurement is used as the main method to collect real data on actual events. Researchers must analyze the flow of pre, during and post disasters. All data found will be classified according to disaster types which contains floods, landslides, haze, storm and tsunami. Based on other researches, these classified disasters are likely occurred in Malaysia between 1992 and 2011 (Raman et al, 2014).

Other than that, various data from different agencies are indispensable in handling disaster. Authorize agencies are required to distribute the information as below.

- a. **Main Data**
  - i.   Haze - Air Pollutions Index (API)
  - ii. Flood - real time hydrological information
  - iii. Storm and tsunami - weather forecasting and tsunami early warning system
  - iv. Landslide - slope management and road diversion information

- b. **Secondary data**
  - i.   Administrative information - boundaries, localities, road networks, river networks, etc.
  - ii. Infrastructure and public facilities information - railways, bridges, school, hospitals and other health centres, airports, terminals, hotels, railways stations, police stations, fire stations, buildings and landmarks, etc.
  - iii. Population and land use information - population density, land use
  - iv. Satellite imagery

2.2 Data Integration

Data Integration involves a combination of data which is accumulated to a centralized system from different data sources, formats and types (such as documents, text, services, table, spatial data). All data in different sources are extracted using various technologies in order to present them in desired end-user information (Gauraw, 2015). This data could be structured, semi structured and unstructured. That's why data integration is important in cases to 1) reduce the complexity and 2) increase the value of data.

Researchers have identified the information and data needed in this web GIS dashboard are coming from different sources, formats and types. This will lead to several potential interfaces of applications. Thus, end-users or decision makers are difficult to monitor disaster event because they must refer to many of applications and documents separately. To reduce the complexity, researchers have implemented a single database platform to perform data integration. Python script (Extract, Transform and Load, ETL technology) is used to extract, transform and load the data into database. For example, researchers write a program to read different web services (sources) for air pollution index (API) and weather forecasting information from authorize agencies and process it into value added information. Then, the data are merged before loaded into the database.

Figure 1 Data Integration Concept

Single database platform
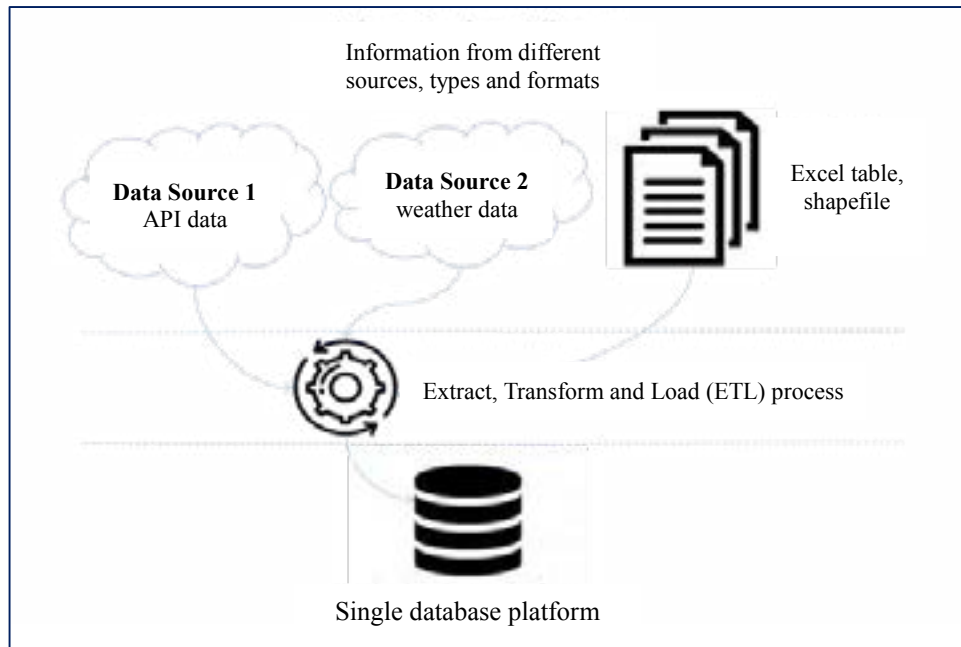
2.3 Database Design

Database is collection of information that is organized into rows, columns and tables. Database design is the database model of the system involves classifying data, identifying relationship and maintaining data management. Database is important in developing web GIS dashboard for disaster to store data in centralized, secured database.

The researchers have design a database for disaster management as below:

a. Multidimensional database contains two (2) main parts of data which are disaster information as main data and basic information as a secondary data.

b. Disaster data have six (6) tables.
    i. Air Pollution Index - Table IDMS_JAS_API is a spatial table that has seven (7) attributes station code, station longitude, station latitude, station location name, API value, time and date. This table also have value added information which is severity risk category Good (0-500), Moderate (51-100), Unhealthy (201-300) and hazardous (>300).
    ii. Weather Forecasting - Table IDMS_MET_WEA is a spatial table join with data table to store data weather forecast by state, district, and town; and tourist destination. Weather forecast information has attribute location code, location name, location longitude, location latitude and weather reading (FGM, FGN, FGA, and FSIGW) for seven (7) days from date request.
    iii. Road Diversion - Table IDMS_JKR_RDDIVRT is a spatial table join with data table to store data of road networks including expressway, federal, state, municipal and private. Road diversion has attribute road code, road type, road name, point of barrier and type of disaster.
    iv. Slope management - Table IDMS_JKR_SLOPE stored data on slope. Table has attribute cross code, plan code, geo code, wall code, slope length, slope height, slope angle, wall location, wall height, wall length and type of slope.
    v. Tsunami Early Warning System - Table IDMS_MET_TSUNAMI is a spatial table that stored the tsunami information. Table has attribute longitude, latitude, location and depth, distance, date and time.
    vi. Hydrological information - Table IDMS_JPS_HYDRO stored water tide data. Table has attribute, station code, station name, longitude, latitude, height date and time.

c. Secondary data is supporting data in disaster management.
    i. State - Table IDMS_ALL_STATE is a spatial table that stored data boundary state in Malaysia. Table has attribute state code, state name.
    ii. District - Table IDMS_ALL_DISTRICT is a spatial table that stored data boundary district in Malaysia. Table has attribute district code, district name and state code.

iii. Localities - Table IDMS_ALL_LOCALITIES is a spatial table that stored point of localities. Table has attribute localities code, localities name and district code.
iv. Road networks - Table IDMS_ALL_ROAD is a spatial table that stored available road including expressway, federal, state, municipal and private. Table has attribute road code, road type and road name.
v. River networks -Table IDMS_ALL _RIVER is a spatial table that stored rivers network in Malaysia. Table has attribute road code, road type and road name
vi. Infrastructure and public facilities - Table IDMS_ALL_INFRAFAC is a table to store data school, hospital, health centre, police station, fire station, airport, terminals and railway station. This table has attribute infra/facilities code, infra/facilities name, type of infra/facilities.
vii. Population - Table IDMS_ALL_POPULATION is a spatial table that stored density population in Malaysia by district. Table has attribute state code, district code, district name, total population, number of citizen, number of non-citizen, number of male, number of female and number of population by age.
viii. Land use - Table IDMS_ALL_LANDUSE is a spatial table that stored land use information. Table has attribute ALU code, ALU legend and ALU type.

2.4 Data Visualization

Data visualization has become standard modern visual communications to help people comprehend the significance of data. Today's data visualization are more sophisticated than before. It can display data as info graphic, spark lines, dials and gauges, geographic map, heat maps, detailed bar, pie and fever charts. Dashboard is one of the data visualization tool whereas a visual the information of the most important information to achieve the organization objectives.

The researchers have applied this technology on monitoring disaster in Malaysia. Spatial information (GIS) are used to create the web GIS based dashboard. Thus, users or decision makers can get access to the updated data in areas or location besides other complimentary information during disaster.

Figure 2: Haze Disaster Information Dashboard Design Interface
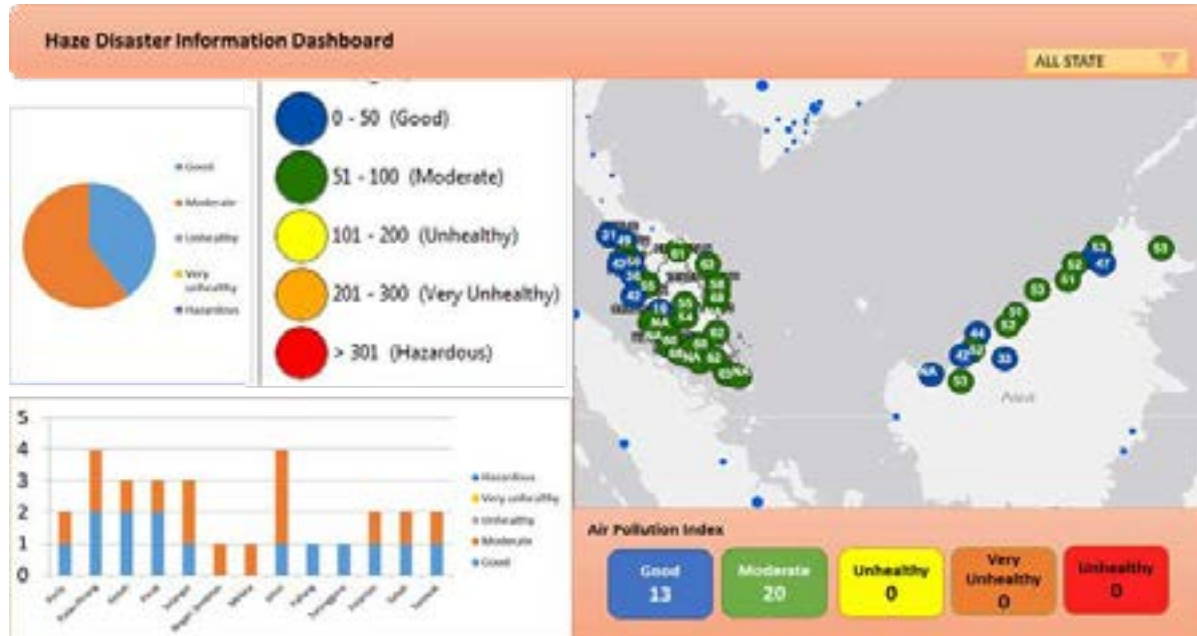
3. RESULTS AND CONCLUSION

As of this writing, the first phase of the research has been developed and being used by the stakeholders. In the meantime, researchers will improve the performance and efficiency of the dashboard while continue with the second phase. From the research, it can be concluded that three (3) objectives have been achieved which are: the right methods to use for data collection, data integration, database design and finally generating the dashboard; a centralized database for all data and finally an output which is a dashboard that meet user requirements.

4. ACKNOWLEDMENT

5. REFERENCE

Alavi, M. and Leidner, D.E., 2001. Review: Knowledge Management and Knowledge Management Systems: Conceptual Foundations and Research Issues. MIS Quarterly, 25(1), 107-136.

Davenport, T.H. and Prusak, L. (1998). Working Knowledge. Harvard Business School Press.

Few, Stephen, 2006. Information dashboard design. O'Reilly.

Gauraw, K., 2015. Data Integration Techniques and Their Challenges, Retrieved February 27, 2015 from http://www.dataintegration.ninja/data-integration-techniques-and-its-challenges/

Malik, Shadan, 2005. Enterprise Dashboards: Design and Best Practices for IT. Hoboken, John Wiley & Sons, Inc.

Raman, M., Dorasamy, M., Muthaiyah, S., Kaliannan, M., 2014. Web-based Community Disaster Management and Awareness System (CEMAS) in Malaysia, pp. 386-391.

Turoff, M., Chumer, M., Walle, B.V.D, and Yao, X., 2004. The design of a dynamic emergency response management information system (DERMIS), Journal of Information Technology Theory and Application, 5,4, 1-5.

Spatial and Temporal Changes on Land Surface Temperature

by Land use/ Land cover of Paung Township, Mon State, Myanmar

Dr. Khin Mar Yee, Dr. Mu Mu Than, Dr. Kyi Lint, Dr. May Myat Thu,

Dr. Mar Lar Han, Candidates of PGDGIS

Rapid changes in the land use and land cover of a region have become a major environmental concern in recent time. The main goal of this paper is to quantify the changes in the land cover and consequent changes in surface temperature. For this research, Landsat satellite images of 1997, 2007 and 2017 of Paung township area were used. Geospatial technologies such as remote sensing and GIS are very effectiveness in measuring, monitoring and predicating the land use/land cover changes. The findings of this paper revealed a notable land use and land cover change and surface temperature for the future sustainable mining related areas; Paung Township. This study demonstrates that rapid human actives and mining areas significantly decreases the dense forest areas, hence increased the surface temperature and modified around the Pound Township microclimate. This has led to unsustainable development with the reduction of green spaces and also changes in local climate a formation of region heat.

Key words: land cover change and surface temperature, Geospatial technologies, human actives

Introduction

Mining is a site-specific activity and is done at the sites where minerals exist. Also, mining is considered as an environmentally hostile activity. Global attention has been drawn towards the environmental impacts of mining and associated activities in mining complexes, and the action that are required to be taken for minimization prevention and mitigation of these impact (Manisha Garg, et al, 2009). Myanmar as a developing country has still a long way to go when it comes to developing its infrastructure. The country needs granite and gravel then ever for its infrastructure development. On the other hand, granite quarry/mining and production activities have negative impacts on the environment. There are 88 mining companies producing gravel for road paving permitted by the Union Government to operate in Mon State. Most of the mining companies are operating in Kalama Mountain including 22 companies in Paung Township.

Rapid changes in land use and land cover (LULC) of a region have become a major environmental concern in recent time. This has leads to unsustainable development with the reduction of green spaces and also changes in local climate and formation of region heat (Ramachandra T. V et.al, 2012). Therefore, it is essential to analyze these impacts in terms of spatial and temporal domain and with time, the significance of mapping and monitoring the changes in LULC has been widely recognized by the scientific of mapping and monitoring the changes in LULC has been widely recognized by the scientific community. Remote sensing and geographic information systems (GIS) are important tools for assessing and monitoring environmental impacts due to synoptic coverage and repetitive coverage of space borne imagery to detect the changes at various resolutions and thereby generating information on LULC change dynamics for sound planning and a cost-effective decision making (Areendran G et.al, 2012). This study is to focus on the serious changes of the land cover and land surface temperature (LST) of Paung township.

Objectives

The objectives of this paper is

- ❑ to examine the changes of land cover with change detection

- ❑ to measure the changes of the surface temperature with thermal bands

- ❑ to analysis on the relationship between the land cover changes and surface temperature changes and the environmental conservation for the sustainable development of Paung township area

Study Area

The study area is Paung, a township of Thaton District in the Mon state of Myanmar. The study area is located between North Latitudes 16° 29' 13.54'' to16° 48' 59.78'' N and East longitudes 97° 13' 14.50'' to 97° 38' 55.00'' E, and the total area is 1052.81 sq ki (Figure 1).

Figure 1. Study Area

Research Design
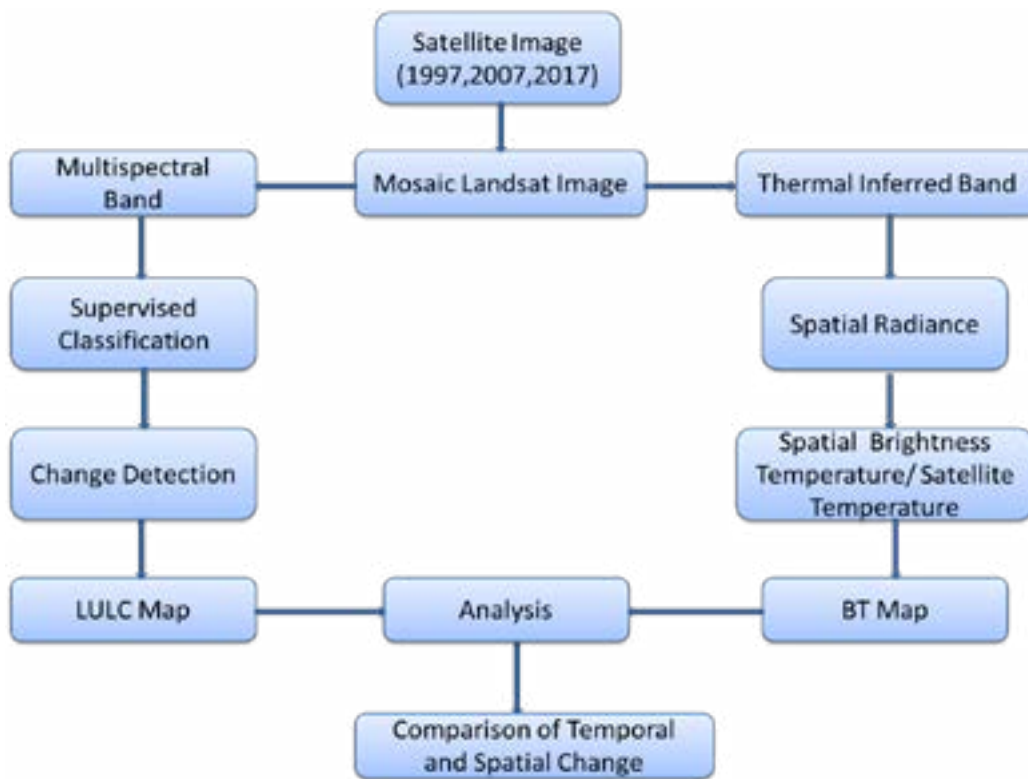
Figure 2. Resign Design of research work

Data and Methodology

Landsat 5 multispectral image and Landsat 8 multispectral image series were used as remote sensing data source for the study. Landsat satellite images (1997, 2007 and 2017) were downloaded from the official website of United States Geological Survey (USGS) and used in order to reach the research objectives. The data used in the study includes Landsat 5 data for 1996 and 2007, and Landsat 8 (OLI) 2017 which cloudless area. Spatial resolution is 30x30 m. UTM zone is 47 and Datum is WGS 84. The procedures of this paper consist of three phases. The first phase is land cover classification with training sample and calculation of change area by change detection of three periods. The second phase is retrieval of the surface temperature of 1997, 2007 and 2017. The third phase is the data analysis on the land use/land cover and land surface temperature changes.

Table 1. Details of Satellite Image Used

Respective Year	Path	Row	Date acquired	Cloud Cover(%)	Scene Center Time	Spatial resolutio	Sensor	Origin
1997	131	48	1997/02/01	0.00%	03:13:46.7940750	30x30 m	Landsat4-5 Thematic Mapper	Image courtesy of the U.S. Geological Survey
	131	49	1997/02/01	0.00%	03:14:10.7010750			
	132	48	1997/02/24	1.00%	03:20:56.2960250			
2007	131	48	2007/02/13	3.00%	03:44:19.0660130		Landsat 4-5 Thematic Mapper	
	131	49	2007/02/13	3.00%	03:44:43.0390250			
	132	48	2007/02/20	0.00%	03:50:30.1740810			
2017	131	48	2017/02/24	0.00%	03:49:13.4469620		Landsat 8 OLI/ IRS	
	131	49	2017/02/24	0.08%	03:49:37.3464710			
	132	48	2017/02/15	1.08%	03:55:27.1524450			

Derivation of LU/LC

The using satellite images were classified into seven classes of land use and land cover classes, as shown in Table 2. The chosen color composite for Landsat 5 (band 4, 3 and 2) and Landsat (band 5, 4 and 3) were used with training sample sites for land cover classification. The training sites developed for this research were based on the reference data and ancillary information collected from various sources. For the making map of land cover classification, the land use and land cover pattern was mapped by supervised classification with the support vector machine classification algorithm of ArcMap 10.2.

Table 2. Description of LU/LC Type

Land cover Type	Description
Water	Water body of river, lake, ponds, low lying areas and stream area
Agricultural Land	Crops fields and agricultural land
Dense Forest	Reserved forest and forest area
Open forest	Scatter Vegetation and mixed vegetation which has a scattered distribution,
Barren land	rock land, swamp and sand dunes in the river and stream
Bare land	Mining area, unused land, clear forest area
Built up area	All infrastructure - residential, commercial, mixed use and industrial areas, villages, settlements, road network, pavements, and man-made structures

Table 2 and Figure 2 illustrated the area and percentage of LULC classes for three periods. According to data, the agricultural land, water body, dense forest was decreased from 1997 to 2017 and open forest and built up area were increased nearly two times within 20 years.

Table 2. The Area of LULC types in Paung Township (1997, 2007 and 2017)

LULC	1997 Area (sq-km)	%	2007 Area (sq-km)	%	2017 Area (sq-km)	%
Water	71.99	6.84	47.53	4.51	32.15	3.05
Agricultural Land	563.96	53.57	521.75	49.56	398.05	37.81
Dense forest	90.42	8.59	82.7	7.86	74.7	7.1
Open forest	216.22	20.54	282.41	26.83	405.19	38.49
Barren land	93.28	8.86	90.27	8.57	108.42	10.3
Bare land	1.4	0.13	9.19	0.87	7.24	0.69
Built up area	15.54	1.47	18.96	1.8	27.06	2.56
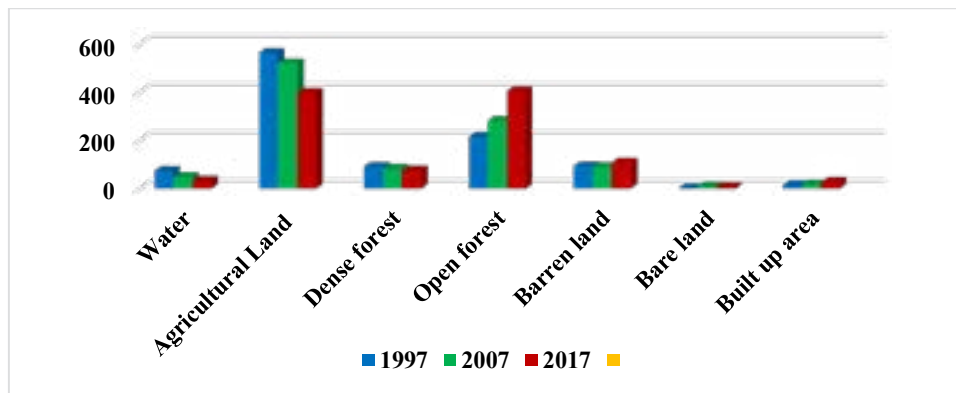
Figure 2. The Area of LULC types in Paung Township (1997, 2007 and 2017)

Derivation of Brightness Temperature (TB)

The thermal infrared band (Band 6) records the radiation with spectral range between 10.4 and 12.5 μm from the surface of the earth (Liu & Zhang, 2011), Land surface temperature plays an important role in many environmental processes. It can provide primary information on the surface physical properties and climate (Weng, 2001). The LST of 1997, 2007 and 2017 are obtained by applying the following equations. In the first step, the DNs of thermal bands were converted to radiance based on the following formula where, information can be obtained from the header file of the images. In the second step, the effective at-satellite temperature of the viewed Earth-atmosphere system, under the assumption of a uniform emissivity, could be obtained by the following equation.

$$L_\lambda = \text{gain x DN + offset}$$

Where L_λ is the radiance of the thermal band pixels in W/(m^2 ster mm μ), gain is the slope of the radiance?DN conversion function, and offset is the intercept of the radiance/DN conversion.

$$T_B = K_2 / \text{In} (1+k_1 / L_\lambda)$$

Where T_B is the effective at-satellite temperature in K, and both k_1 and K_2 are pre-lunch calibration constants (K_2 ¼ 1282.71 K, k_1 ¼ 666.9 m W cm_2_sr_1 mm_1). The different levels of LST located in the certain regions corresponding to the location of the land cover classes. The high LST located in the built up area, agricultural land, bare land and barren land. Low LST scattered in the dense forest, open forest and the water.

Table 3. LST of Paung Township (1997, 2007 and 2017)

TB	Max	Mean	Min
1997	32° C	24° C	17° C
2007	34° C	28° C	21° C
2017	42° C	32° C	24° C
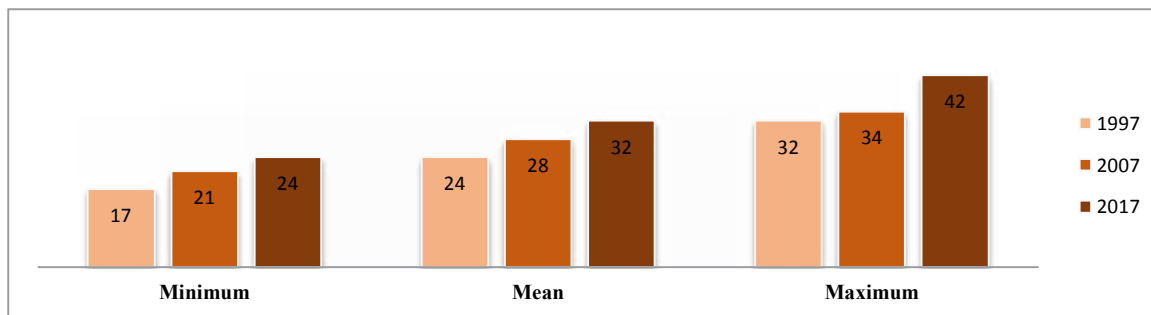
Figure 3. LST of Paung Township (1997, 2007 and 2017)

Results and Discussion

Changes of LULC

The due to human activities results of land use and land cover classification of three periods, the results of land use and land cover classes describe in Figure 3 and the results of change is the change area of land use and land cover classes of study area of 1997, 2007 and 2017.

Table 6. LULC Change area

LULC	1997		2007		2017	
	Area (sq-km)	%	Area (sq-km)	%	Area (sq-km)	%
Water	-24.46	-2.32	-15.37	-1.46	-39.83	-3.78
Agricultural Land	-42.21	-4.01	-123.7	-11.75	-169.91	-15.76
Dense forest	-7.72	-0.73	-7.99	-0.76	-15.71	-1.49
Open forest	66.2	6.29	122.78	11.66	188.97	17.95
Barren land	-3.01	-0.29	18.15	1.72	15.14	1.44
Bare land	7.79	0.74	-1.96	-0.19	5.84	0.55
Built up area	3.4	0.32	8.1	0.77	11.49	1.09
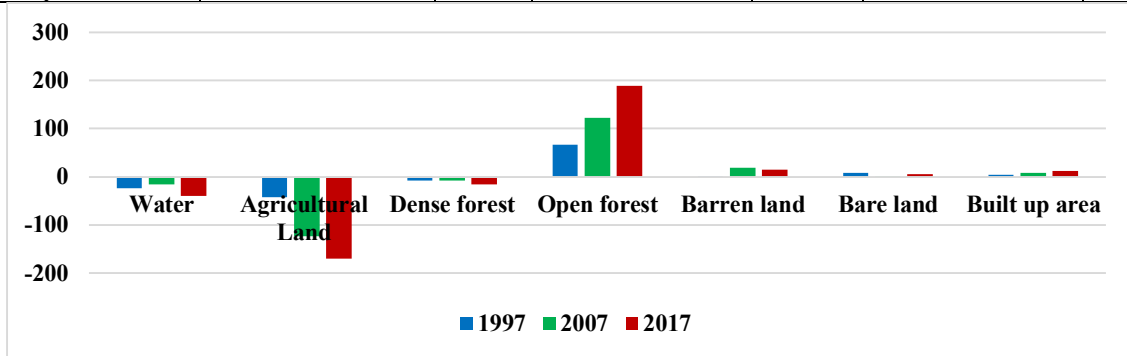
Figure 4. LULC Change area

Figure: 5 Spatial Distribution of LULC (1997, 2007 and 2017)

According to the change detection algorithm, dense forest is decreased. Dense forest area was decreased clearly very much 90.42 sq km to 82.70 sq km from 1997 to 2007 and decreased again to 74.70 sq km in 2017. Water body were nearly the same are within three periods. Bare land was increased from 1.4 to 9.19 sq km from 1997 to 2007. These area was nearly the same between 2007 and 2017 but bare land area was increased a little area in Lalama Taung area. Built up area was nearly the same between 1997 and 2007. In 2017, built up area raised to 27.06 sq km respectively. Open forest was increased clearly very much from 216.22 to 282.41 sq km from 1997 to 2007 and increased again to 405.19 sq km in 2017.

Changes in Land Surface Temperature

Figure 6 showed the distribution and changes of LST within three periods in Paung Township. The results of the image processing pointed out that LST ranged from 17° C, 21° C and 24° C to 32° C, 34° C and 42° C for three periods.
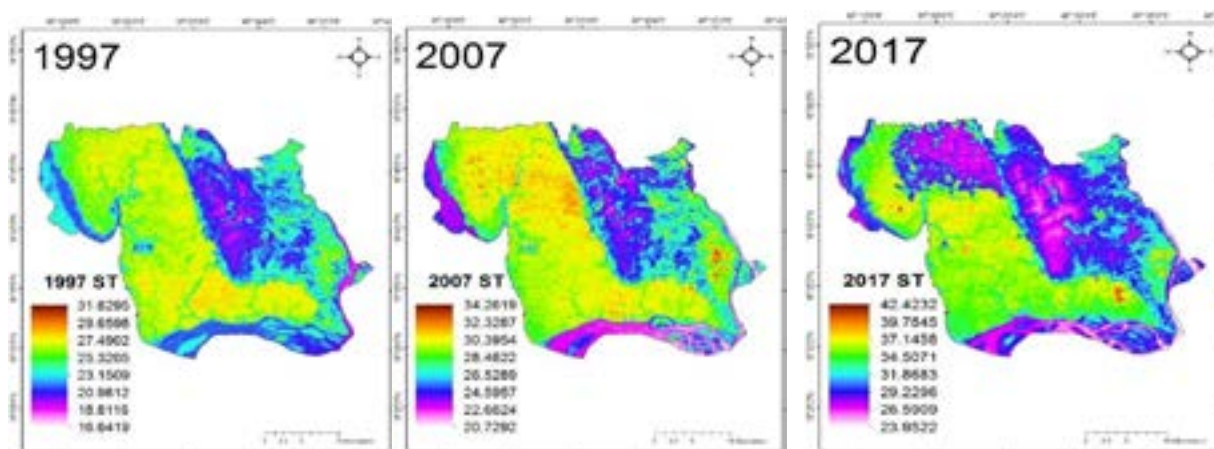
Figure: 6 Spatial Distribution of Land Surface Temperature (1997, 2007, 2017)

The Relationship between LULC and LST

The LST was wider to the built up area, agricultural land, open forest area and bare land. The different levels of LST found in the certain regions corresponding to the location of the LULC classes. The high LST occurred at the built up area, agricultural land and bare land. Low LST covered in dense forest and water area. The extension of bare land to the northern side and eastern site of the study area. Dense forest area is gradually decreased and replaced open forest area and bare land. According to decreasing dense forest area, the temperature was wider and hotter to barren land, bare land, agricultural land and built up area.

Conclusion

Landsat 5 TM and Landsat 8 TM are used to monitor the land cover changes, and to analyze the spatial distribution of brightness temperature. Due to urban growth, shifting cultivation and mining area of the Paung Township, there have been significant changes in the land use/land cover of the study area. There have been significant decreased in the forest. The results indicated that Paung township mining areas expanded dramatically while agricultural and forest land declined. The result also showed that Brightness temperature and thermal signal of built-up areas and bare land

has increase the radiant temperature This research work observed the changes of LULC were largely attributed to mining project on the area, a rapidly growing built-up area.

References

Areendran G, Parkash R, Krishna R, Sraboni M & Kanchan P (2012), Land use/ land cover change dynamics analysis in mining areas of Singrali district in Madhya Pradesh, India. Tropical Ecology, 54(2): 239-250.

Li, J., Song, C., Cao, L., Zhu, F., Meng, X. and Wu, J (2011), Impacts of landscape structure on surface urban heat islands: a case study of Shanghai, China. Remote Sensing of Environment, Vol. 115, No.12, pp. 3249-3263.

Manisha G, Arun J, Sandhya C (2013), Land Use Land Cover Classification in Jamuna- Kotma Coal Field Region, Anuppur District MP. IOSR Journal of Agriculture and Veterinary Science (IOSR-JAVS) e-ISSN: 2319-2380, p-ISSN: 2319-2372. Volume 6, Issue 2 (Nov. - Dec. 2013), PP 38-43.

Ramachandra T. V, Bharath H. Aithal, Durgappa Sanna D (2012), Land Surface Temperature Analysis in an Urbanising Landscape through MultiResolution Data. Research & Reviews: Journal of Space Science & Technology.Volume 1, Issue 1, Pages 1-10.

Weng, Q, (2001), A remote sensing? GIS evaluation of urban expansion and its impact on surface temperature in the Zhujiang Delta, China. International Journal of Remote Sensing, Vol. 22, No. 10, pp. 1999-2014.

AUTOMATIC PADDY GROWTH STAGE IDENTIFICATION BASED ON CONVOLUTIONAL NEURAL NETWORK

Agustan (1), Swasetyo Yulianto (1), Robby Arifandri (1), Heri Sadmono (1), Yudi Anantasena (1)

[1] Center for Regional Resources Development (PTPSW), Agency for the Assessment and Application of Technology (BPPT), Jalan M.H. Thamrin No. 8, Jakarta, Indonesia
Email: agustan@bppt.go.id

KEY WORDS: paddy, convolutional neural network, area frame sampling, image classification

ABSTRACT: Recently, two methods have been developed for paddy growth stage monitoring which are satellite-based remote sensing and statistic-based terrestrial observation. Satellite-based remote sensing method has the advantage on area coverage and repeat observations (temporal resolution), whereas statistic-based terrestrial observation method has the advantage on informing actual paddy condition. One of the statistic-based terrestrial observations used is the Area Frame Sampling method. Area frame sampling method recently is assessed as paddy reporting mechanism in Indonesia that is conducted on monthly basis. With this method, the observers report paddy growth stage manually by a developed mobile phone application in the last week of each month and attach photos of paddy as evidence. Photo recording techniques are carried out with standard operating procedures. Paddy conditions are reported into five classes, namely land preparation, early vegetative (V1), late vegetative (V2), generative, and harvesting. However, the photos are very diverse due to the observation time factor i.e. taken in the morning or afternoon or even in the evening, and also due to the specifications of camera-phone that are not the same. To mitigate the observer's subjective assessment of the paddy growth stage, a pattern recognition method will be introduced and implanted in a mobile device. Thus the application will automatically classify the recorded photos and become a reference for observers in determining the paddy growth stage. This paper discusses the process of photo classification using Convolutional Neural Network (CNN). Recently, CNN are getting used more commonly and getting better to do image classification. In this research, we utilize TensorFlow with retraining method, which gets ImageNet model that has been already trained and then create new classification layer on the final layer. With this method we can get new classifier based on 3.000 photos with accuracy around 70% with 3-5 hours training time using consumer-grade computing machine.

1. INTRODUCTION

Information regarding rice stock is important to ensure food resilience in one country, especially in Indonesia. For that reason, Indonesian government put more efforts to establish crop-monitoring system, especially for rice. At the beginning, information related to paddy field condition including its growth stages should be gathered and then analyzed to make an approximation of potential harvest for certain time range in advance. For analysis

purposes, paddy field condition is observed based on paddy growth stages, which are classified into five classes, namely land preparation (LP), early vegetative (V1), late vegetative (V2), generative (G) and harvesting (H).

Recently, at least there are two methods developed for paddy growth stages observation: satellite-based remote sensing method i.e. Salmon et al. (2015), Dong et al. (2015), Huang et al. (2018); and terrestrial-based spatial statistic method i.e. You et al. (2014) and Sun et al. (2018). Since late 2010s, Agency for the Assessment and Application of Technology (BPPT) - an Indonesian government research institution - developed a terrestrial-based spatial statistic method called Area Frame Sampling (Agustan et al., 2018). This method is continuously improved by enhancing the observation or data collection tool that is embedded in smartphones called SwasApp.

One feature that is embedded to this system is an automatic image classification for paddy photos that are collected. Since an enormous growth of digital image analysis, automated paddy growth stages classification based on paddy photos are possible through machine learning method. The theory of machine learning for supervised image classification had been reviewed by Kotsiantis et al. (2007) and Zhang et al. (2012). Recently, the utilization of Convolutional Neural Network (CNN) as a part of machine learning had been broadly used for image classification. Therefore, this paper discusses the possibility to identify the paddy growth stages from photos collected from paddy field based on TensorFlow (Abadi et al., 2016) with retraining method, which gets ImageNet model (Krizhevsky et al., 2012) that has been already trained and then create new classification layer on the final layer.

2. DATA AND METHOD

Approximately 3000 paddy photos from different location across the country that are collected on every last week of January 2018 to June 2018 by using SwasApp are analyzed in consumer grade computing machine. This data collection system is installed in various smartphone with minimum requirements of having positioning tools i.e. GPS, data packet transmission and camera. Since this experiment wants to recognize paddy growth stage, therefore land preparation class is excluded in training and classification.
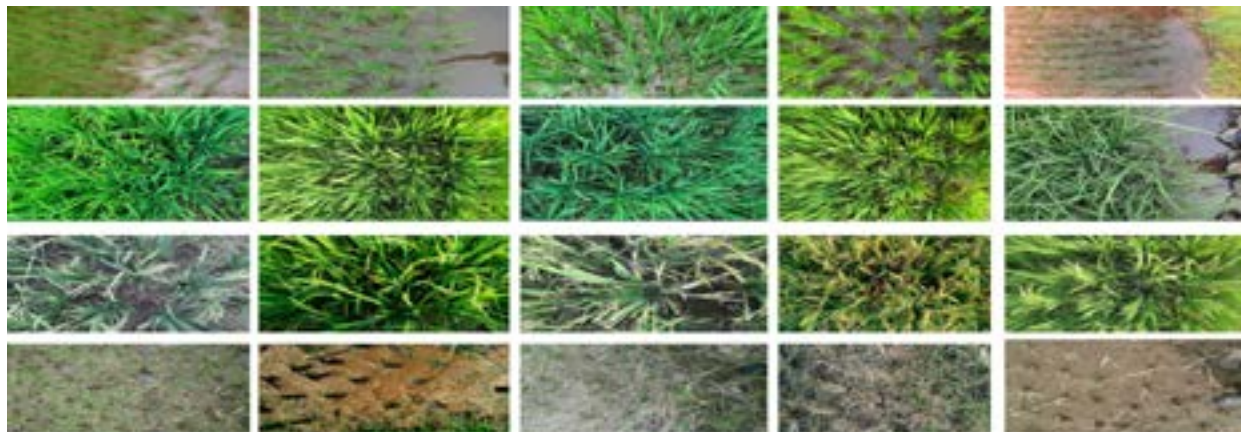
Figure 1. Examples of paddy photos collected by SwasApp, line 1 represents early vegetative stage, line 2 represents late vegetative stage, line 3 represents generative stage, whereas line 4 represents harvesting stage.

Generally, the processing chains in this experiment are: preparing working folder for each class, exploring the effect of data set number, and accuracy check. The research utilizes retraining method where first training step uses a model from ImageNet, and then last layer is replaced with the new layer classifier. This strategy allows training process consumes shorter time for up to 4000 steps training that is used in this research.
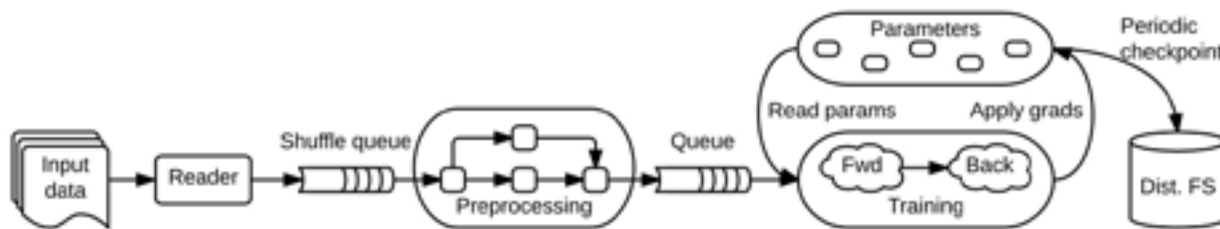
Figure 2. Illustration of TensorFlow data processing (Abadi et al., 2016).

In addition, to get an accurate and valid training results, this research conducts data training by dividing the data into three sets: training set (80%), validation set (10%), and final test set (10%). Training data set will be used for training, then validation will be used for routine validation at each step of the training, and the final test set functions for final validation. By separating data that is used, it is expected that accuracy can describe the real conditions for classification. The effect of number data sets is explored by designing the samples to 100, 500, 1000 and 2000 photos.

3. RESULT AND DISCUSSION

By running the script and tuning the parameter based on TensorFlow scheme as illustrated in Figure 2, it is found that the overall accuracy is around 70%. Figure 3 illustrates the result of training data sets that shows 71.9% accuracy for 100 samples, 77.1% for 500 samples, 72.6% for 1000 samples and 73.5% for 2000 samples.
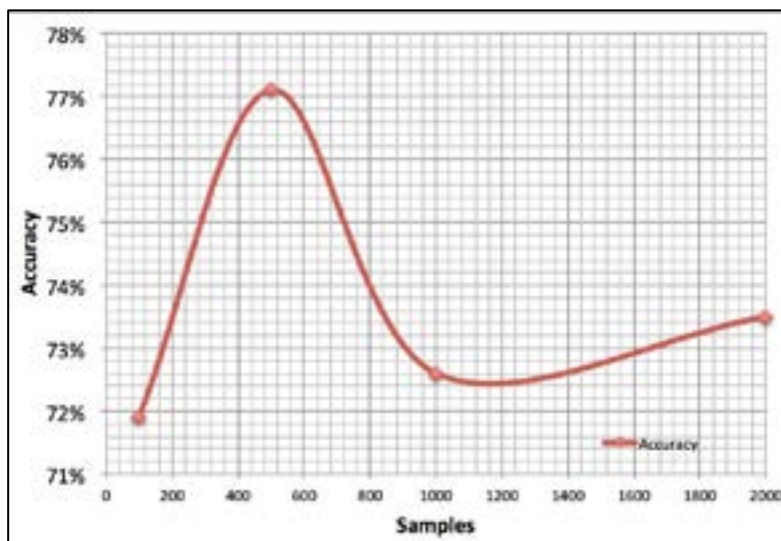
Figure 3. Accuracy of training results

It is shown that by increasing number of photos, the accuracy will slightly improve with the highest accuracy of 77% from 500 samples. This is interesting because by increasing data sets to 1000 and 2000, the accuracy is lower compare to 500 samples. This is perhaps due to the better quality photos within the 500 samples data set that are randomly selected.
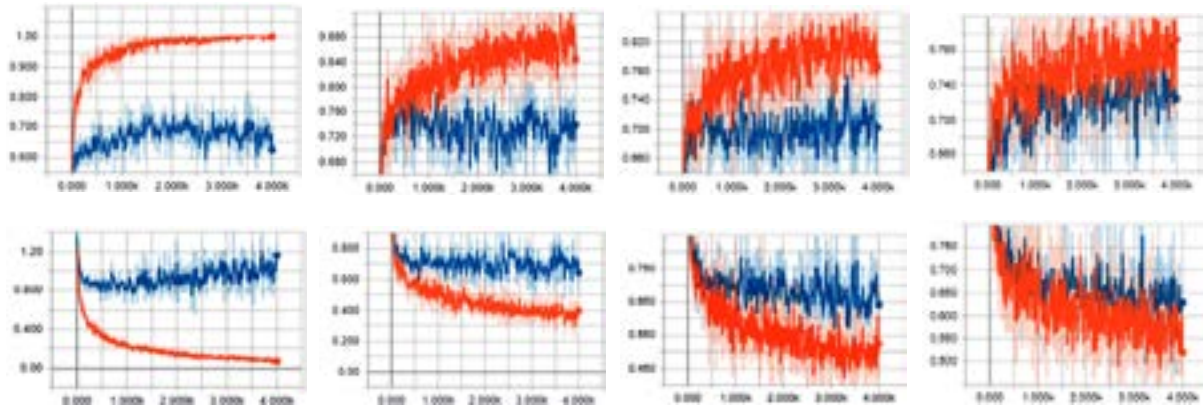
Figure 4. Accuracy (upper graphs) and cross-entropy (lower graphs) for train results (orange line) and validation results (blue line) for 100, 500, 1000 and 2000 samples respectively.

Figure 4 illustrates the performance of training data sets and their validation for automatic image classification. It is shown that the accuracy of training process (orange line at upper graphs) for all experiments tends to stable after 500th step, and the accuracy for validation data sets (blue line at upper graphs) are more stable. Therefore the experiments indicate that bigger data sets need more training steps to achieve a convergence results.
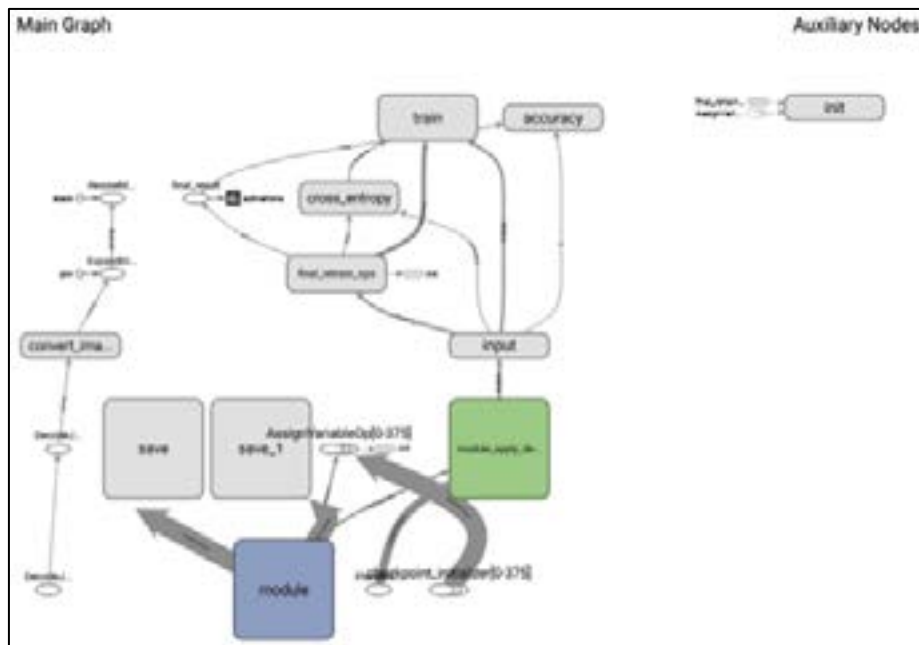
Figure 5. Illustration of data processing chain in TensorFlow.

During data processing, there are some photos that cannot be classified for each experiment. By assessing these unclassified photos, it is found that these photos do not contain specific features that can be recognized. This can happen since there are no specific rules in taking picture in the field such as standard for angle, height, and illumination.

4. CONCLUSION

This research shows the possibility to utilize a CNN method that is implemented in TensorFlow to classify paddy growth stage based on paddy photos automatically. There are two key factors that should be taken into account: standard operating procedures for taking picture include time and technique; and smartphone or device specification. Various device specification gives different photos quality that is affected by size, color deep, pixel resolution and exposure. These factors will affect the photos quality and their classification process.

It is shown that there is a possibility to increase the accuracy by adding number or samples. However, time of data processing also becomes longer for consumer grade computing machine. In the future, once the algorithm can provide more than 85% accuracy, this utility will be embedded to SwasApp to improve data interpretation.

5. REFERENCES

Abadi, M., Barham, P., Chen, J., Chen, Z., Davis, A., Dean, J., Devin, M., Ghemawat, S., Irving, G., Isard, M. and Kudlur, M., 2016. Tensorflow: a system for large-scale machine learning. In the Proceedings of the 12th USENIX Symposium on Operating Systems Design and Implementation (OSDI), Vol. 16, pp. 265-283, ISBN 978-1-931971-33-1.

Agustan, Yulianto, S., Sumargana, L., Sadmono, H. and Alhasanah, F., 2018. Innovation on Geolocation and Pattern Recognition for Paddy Growth Stages Reporting in Indonesia, IOP Conf. Ser.: Earth Environ. Sci. Vol. 165, 012001 doi:10.1088/1755-1315/165/1/012001

Dong, J., Xiao, X., Kou, W., Qin, Y., Zhang, G., Li L., Jin, C., Zhou, Y., Wang, J., Biradar, C., Liu, J. and Moore, B., 2015. Tracking the dynamics of paddy rice planting area in 1986–2010 through time series Landsat images and phenology-based algorithms, Remote Sensing of Environment, Vol. 160, pp. 99-113, ISSN 0034-4257, https://doi.org/10.1016/j.rse.2015.01.004.

Huang, Y., Ryu, Y., Jiang, C., Kimm, H., Kim, S., Kang, M. and Shim, K., 2018. BESS-Rice: A remote sensing derived and biophysical process-based rice productivity simulation model, Agricultural and Forest Meteorology, Vol. 256–257, pp. 253-269, ISSN 0168-1923, https://doi.org/10.1016/j.agrformet.2018.03.014.

Kotsiantis, S.B., Zaharakis, I. and Pintelas, P., 2007. Supervised machine learning: A review of classification techniques. Emerging artificial intelligence applications in computer engineering, 160, pp. 3-24.

Krizhevsky, A., Sutskever, I. and Hinton, G.E., 2012. Imagenet classification with deep convolutional neural networks. In Advances in neural information processing systems, pp. 1097-1105.

Salmon, J.M., Friedl, M. A., Wisser, D., Frolking, S. and Douglas, E. M., 2015. Global rain-fed, irrigated, and paddy croplands: A new high resolution map derived from remote sensing, crop inventories and climate data, International Journal of Applied Earth Observation and Geoinformation, Vol. 38, pp. 321-334.

Sun P., Zhang, J., Congalton, R .G., Pan, Y. and Zhu, X., 2018. A quantitative performance comparison of paddy rice acreage estimation using stratified sampling strategies with different stratification indicators, International Journal of Digital Earth, 11:10, 1001-1019, DOI: 10.1080/17538947.2017.1371256.

You, L., Wood, S., Wood-Sichra, U. and Wu, W., 2014. Generating global crop distribution maps: From census to grid, Agricultural Systems, Vol. 127, pp. 53-60, ISSN 0308-521X, https://doi.org/10.1016/j.agsy.2014.01.002.

Zhang, D., Islam, Md. M. and Lu, G., 2012. A review on automatic image annotation techniques, Pattern Recognition, Vol. 45 (1), pp. 346-362, ISSN 0031-3203, https://doi.org/10.1016/j.patcog.2011.05.013.

---o0o---

Feasibility Study of Normal Height System in Taiwan

Chun-Jia Huang (1), Jen-Wei Hsu (1), Jen-Yu Han (1)

1 Department of Civil Engineering, National Taiwan University, No. 1,

Sec. 4, Roosevelt Rd., Taipei 10617, Taiwan (R.O.C.)
Email: d05521008@ntu.edu.tw; r06521805@ntu.edu.tw; jyhan@ntu.edu.tw

KEY WORDS: Normal Heights, Height datum, Global Navigation Satellite System (GNSS), Earth Gravity Model

ABSTRACT: The normal height system is based on the quasi-geoid, which represents the vertical distance from the quasi-geoid to terrain surface. To make possible an accurate normal height system, the normal gravity should be first determined. This study aims to build the quasi-geoid by using local gravity observations and a global spherical harmonic model in Taiwan. The quasi-geoid undulation was first computed by using the global Earth Gravity Model 2008 (EGM08) with a spherical harmonic model. In addition, the influence of terrain was also considered in the residual terrain model. The hybrid method was then used to construct a high-accurate quasi-geoid component model in conjunction with the remove-compute-restore method, which includes surface curve fitting method. Finally, the normal heights were transformed by calculating the difference between the GNSS-derived geometric heights and the results of quasi-geoid undulation model. To evaluate its practical feasibility, the estimated normal heights were compared to the orthometric heights as adopted in Taiwan's national datum. Based on the numerical results, the mean relative difference to the orthometric heights is about 1.5cm per kilometer. It reaches the accuracy level that fulfils the needs of most engineering applications, but with less cost than that of the traditional approach for maintaining the orthometric height system.

1.INTRODUCTION

The normal heights system is based on the quasi-geoid, which represents the vertical distance from the quasi-geoid to terrain surface. The more comprehensively quasi-geoid model is constructed, the more accurately normal height could be estimated. There are three ways to construct normal heights system, one of which is the mathematical method (Pick,1970). It defines the earth as a rotational ellipsoid, and calculates the ideal geoid by gravity. It is a convenient way, but lack of physical and geometric meanings. Another approach is Global Gravitational Model method, proposed by Heiskanen and Moritz (1967). The method tries to calculate global gravitational potential, and constructs the normal height system by geopotential. The last one is gravity observation method (Torge,1991). It calculates the Geopotentials by gravities and leveling, and obtains the normal height by average gravities.

This study aims to construct normal height system using the Global Gravitational Model method, with an emphasis to build the quasi-geoid by using local gravity observations and a global spherical harmonic model in Taiwan. The hybrid method constructs a high-accurate quasi-geoid component model in conjunction with the remove-compute-restore method, which includes surface curve fitting method. The normal height could be transformed by calculating the difference between the GNSS-derived ellipsoid height and the result of quasi-geoid undulation model.

2.METHODOLOGY

2.1 Spherical harmonic model calculation

The global gravity field model is a spherical harmonic function which represents the true gravitational field of the earth. It is used toestimate global gravity field function values, such as geoidal undulation, gravity anomalies. The conversion formula is as shown in Equation (1). The Cartesian coordinates (x, y, z) of the observation points are converted into spherical coordinates, where (r, θ, λ) are expressed as the geocentric radial, the geocentric latitude, and the geocentric longitude, respectively. The geopotential of point P on the ground surface which can be calculated by EGM08 as following (Heiskanen and Moritz, 1967 ; NGA, 2013).

$$\begin{vmatrix} r \\ \theta \\ \lambda \end{vmatrix} = \begin{vmatrix} \sqrt{x^2 + y^2 + z^2} \\ tan^{-1}\left(\frac{z}{\sqrt{x^2+y^2}}\right) \\ tan^{-1}\left(\frac{y}{x}\right) \end{vmatrix} \qquad (1)$$

$$V(r, \theta, \lambda) = \frac{GM}{r}\left[1 + \sum_{n=2}^{N}\left(\frac{a}{r}\right)^n \sum_{m=0}^{n}(\bar{C}_{nm}cosm\lambda + \bar{S}_{nm}sinm\lambda) \cdot \bar{P}_{nm}(cos\theta)\right] \tag{2}$$

In Equation (2), GM is the gravitational constant of $3986004.418 \times 10^{-8}$, where a is the long radius of 6378136.3m, $\bar{C}_{nm}$ and $\bar{S}_{nm}$ are the gravitational spherical harmonic coefficients. $\bar{P}_{nm}$ is a normalized association of the Legendre function. In this Equation, the geopotential W of point P on the surface space which can be calculated by using Earth Gravity Model . The geopotential W(P) is the sum of the gravitational potential and the centrifugal force potential Q(P) (Mortiz,1993):

$$W = V + Q = V + \frac{1}{2}\omega^2(x^2 + y^2) = V + \frac{1}{2}\omega^2 r^2 sin^2\theta \tag{3}$$

where ω is angle of rotation for the earth, The disturbing potential at point P is defined by the difference between the geopotential W and the normal gravity potential U:

$$T = W - U \; ; \; U = \frac{GM}{\varepsilon}tan^{-1}\frac{\varepsilon}{b} + \frac{1}{3}\omega^2 a^2 \tag{4}$$

In a normal height system, the calculation method of normal gravity can be written as Equation(5) through (9), where γ_a is equatorial gravity, γ_b is bipolar gravity, β is gravity flatness, and β_1 is square coefficient of the compression of the earth. The disturbing potential energy T is calculated by Equation (4) and the normal gravity value γ_Q is calculated by Equation (5). The quasi-geoid value of any coordinate Q on the surface can be calculated according to the Bruns formula, as shown in Equation (10) (Heiskanen and Moritz, 1967). Finally, the normal heights were transformed by calculating the difference between the GNSS-derived geometric heights. The following are examples of Equation (11).

$$\gamma_Q = \gamma_0 + \frac{\partial\gamma}{\partial h} \cdot H_P + \left(\frac{1}{2!}\right) \cdot \left(\frac{\partial^2\gamma}{\partial h^2}\right) \cdot H_\infty{}^2 \tag{5}$$

$$\gamma_0 = \frac{a\gamma_a cos^2\varphi + b\gamma_b sin^2\varphi}{\sqrt{a^2 cos^2\varphi + b^2 sin^2\varphi}} \tag{6}$$

$$\gamma_0 = \gamma_a(1 + \beta sin^2\varphi + \beta_1 sin^2 2\varphi) \tag{7}$$

$$\beta = \frac{\gamma_b - \gamma_a}{\gamma_a} \tag{8}$$

$$\beta_1 = \frac{1}{8}f^2 + \frac{1}{4}f\beta \tag{9}$$

$$N = \frac{T}{\gamma_Q} \tag{10}$$

$$H_{normal\ heights} = h_{GNSS} - N_{quasi-geoid} \tag{11}$$

2.2 Residual Terrain Model

While using the Erath gravity model to calculate the quasi-geoid undulation model, it is impossible to accurately describe the quasi-geoid undulation complete signal. Especially in mountainous areas, height differences makes much significant inaccuracy, which could reach the error level of more than 10 cm. Therefore, it is also necessary to consider the detailed differences caused by the terrain and make corrections. The residual terrain model is constructed on the effect of the terrain, and the error caused by the short-wavelength component can be improved (Forsberg, 1984). As shown in Figure 1, the diagonal line is the residual terrain and considers the high-frequency terrain mass effect between the ground surface and the average terrain reference plane. The method for calculating the residual terrain model is the Fast Fourier transform Method (Schwarz et al.,1990). The short-wavelength component N^{RTM} generated for the residual topographic effect can be obtained using Equation (12):

$$N^{RTM}(x_P, y_P) = \frac{G}{\gamma}\int\frac{\rho(x,y)\left|h(x,y) - h_{ref}(x,y)\right|}{\sqrt{(x-x_a)^2 + (y-y_a)^2}}dxdy = \frac{G}{\gamma}\left[\rho(h - h_{ref})\right] * \frac{1}{r} \tag{12}$$

Figure 1. Residual Terrain Model (Forsberg, 1984)

where x_a, y_a are the points to be solved; h is the point elevation value of each integral element; h_{ref} is the reference height value of each integral element; ρ is the geological density of each integral element; γ is the normal gravity value of the points. In general, the density of the formation will be based on the mass of 2670 kg/m^3. Taiwan has a variety of geological features with a geological density of 1800 kg/m^3 to 3000 kg/m^3. This study used a 1/250,000 geological map and constructed a digital geological density map with reference to geological property data. Finally, the 5-m high-resolution digital terrain model is used and the residual terrain estimation is constructed.

2.3 Remove-Restore Method

The long-wavelength component can be calculated from the global spherical harmonic, and the short-wavelength component is obtained from the residual terrain model. However, in the mid-wavelength component, the required observation data needs to be obtained through the measured gravity observation data, which could incur relatively high cost. Therefore, in this study, the known GNSS observations on the first-order level and the normal height calculated from the height difference data on the levelling course are used to obtain the mid-wavelength component (Zhu et al., 2011). The mathematical form is expressed as Equation (13), where N^{GPS} is the difference between the ellipsoid height and the normal height, which is used as the true value in this study.

$$N^{res} = N^{GPS} - N^{ref} - N^{RTM} \tag{13}$$

According to the calculation and obtaining N^{res} and using the surface fitting method to build a model of N^{res} in Taiwan. This study applied quadric surface fitting Equation (14) and cubic surface fitting Equation (15) to fit the surface as a mid-wavelength model. The calculation flow chart is shown in Figure 2.

$$N^{res}(x,y) = a_0 + a_1 x_i + a_2 y_i + a_3 x_i^2 + a_4 y_i^2 + a_5 x_i y_i \tag{14}$$

$$N^{res}(x,y) = a_0 + a_1 x_i + a_2 y_i + a_3 x_i y_i + a_4 x_i^2 + a_5 y_i^2 + a_6 x_i^3 + a_7 y_i^3 + a_8 x_i^2 y_i + a_9 x_i y_i^2 \tag{15}$$

Figure 2. Remove-Restore Method Calculation Process

3. RESULTS ANALYSIS

3.1 Experimental Setup

After obtaining the orthometric heights and ellipsoid heights of first order benchmarks, the quasi-geoid model according to the 1′×1′ grid of global Earth Gravity Model 2008(EGM08) was first constructed. Then ellipsoid heights were transformed into normal heights using the approach described in this study. The result of the normal heights as test group, and the orthometric heights as comparison group. Each of group calculates the height differences separately, and estimates the average value and standard deviation. Table 1 lists the evaluation methods of this study. The result is compared to the orthometric heights of first order benchmarks, and divides into (a)absolute height differences and (b)normalized relative height differences to analyze the results.

Table1. Evaluation Methods

Height Datum: Orthometric Heights		Methods		
		EGM08	EGM08+RTM	EGM08+RTM+Fitting
Absolute Height Differences	(a)	$\Delta_{H,HN} = HN - H$		
Normalized Relative Height Differences	(b)	$\bar{\delta}_{H,HN} = \dfrac{\Delta HN - \Delta H}{\sqrt{s}}$		

3.2 Quasi-Geoid Model

This study uses 1784 first-order benchmarks in Taiwan as the height datum, with a total of 1441 leveling course. The quasi-geoid undulation can be estimated by the global spherical harmonic model. The calculation of the quasi-geoid undulation is shown in Figure 3(a). In order to incorporate the calculation of the residual terrain model, this study uses 5m × 5m resolution grid interpolation. The residual terrain model calculated using fast Fourier transform is represented as shown in the figure 3(b). The mid-wavelength fitting model is shown in Figure 4.

(a)   (b)

Figure 3. (a) Taiwan Quasi-Geoid Model (EGM08) (b) Taiwan RTM Model

Figure 4. Taiwan N^{res} Model (surface fitting)

3.3 Normal Heights and Orthometric Heights Analysis

In the absolute height difference, the difference between the normal heights of 1784 points (global spherical harmonic + residual terrain model+ surface fitting) and the orthometric heights are obtained, and then interpolated map as shown in Figure 5. The difference value range is about 0.5~1.5 m, indicating that the heights difference is greater than 0; However, the color of each bench marks in the figure indicates the interval corresponding to the orthometric heights. It can be seen that there is no significant correlation between the absolute of between the normal heights (global spherical harmonic + residual terrain model+ surface fitting) and the absolute difference of orthometric heights. This relationship can also be verified by Figure 6(a). (representing the difference and orthometric heights relationship). In addition, the statistical indicators of the elevation difference are shown in Figure 6(b) and Table 2. The RMES value of the elevation difference is 0.730 m, the average value is 0.723 m, and the elevation difference is mostly around 0.6~0.8 m (plain and hilly area).

Figure 5. Height difference between HN and HO (Interpolation Map)

| (a) | (b) |

Figure 6. Height difference between HN and HO (Scatter map & Histogram)

Table2. Normal heights(absolute heights difference statistics)

Topography	Heights (m)		Normal Heights(HN)−Orthometric Height(HO)(m)		
	Interval		Mean	Standard Deviation	RMSE
Plain	0	100	-0.002	0.038	0.038
Hills	100	1000	0.009	0.048	0.049
Mountain	1000	2000	-0.035	0.042	0.055
Mountain	2000	3500	-0.002	0.105	0.105
All	**0**	**3500**	**0.007**	**0.046**	**0.0461**

For the relative height difference per unit distance, the height difference between the normal heights of the 1441 levelling course (global spherical harmonic + residual terrain model+ surface fitting) and the orthometric heights difference is calculated. In addition to the corresponding leveling course (unit: km), interpolated as shown in Figure 7, and calculate the difference between the two height differences, and divide the difference by the distance of the leveling course (unit: km). The range of the difference value range is about $-0.5\sim0.5 \mathrm{m}/\sqrt{km}$, which means that the relative height difference (normalization) is positive and negative, and the average is distributed in the figure 8(a). In the figure, the color of bench marks in the map indicates its orthometric height corresponding interval. It can be seen that there is no significant correlation between the normal heights (global spherical harmonic + residual terrain model+ surface fitting) and the orthometric height (after normalization) and the orthometric height of the point. It can be verified by Figure (representing the normalized relative difference and orthometric heights relationship). In addition, the statistical indicators of the relative height difference (normalization) are shown in Figure 8(b)and Table 3. The RMES value of the relative height difference (normalization) is 0.015 m/$\sqrt{km}$, and the average value is 0.0001 m/$\sqrt{km}$,. The relative height difference (normalization) mostly around near $-0.01\sim0.01$m/km (plain and hilly area).

Figure 7. Height difference between HN and HO (Interpolation Map)

| (a) | (b) |

Figure 8. Height difference between HN and HO (Scatter map & Histogram)

Table3. Normal heights(relative heights difference statistics)

Topography	Heights (m)		Normal Heights(HN)−Orthometric Height(HO)(m)		
	Interval		Mean	Standard Deviation	RMSE
Plain	0	100	0.001	0.011	0.017
Hills	100	1000	0.001	0.012	0.018
Mountain	1000	2000	-0.001	0.013	0.019
Mountain	2000	3500	0.002	0.020	0.021
All	**0**	**3500**	**0.0001**	**0.015**	**0.018**

4. CONCLUSION

According to the result of the proposed methods, in the normal height system The mean relative difference to the orthometric heights is about 0.018 meters per kilometer. The results of this study are compared to specification of survey, and the accuracy of the engineering is $20\text{mm}\sqrt{km}$ in the specification of leveling surveying, obviously, the study shows results better than engineering accuracy in the relative height differences. Therefore, the methods can reach the accuracy level that fulfils the needs of most engineering applications.

In most engineering applications, such as Hydraulic engineering or Geotechnical engineering. The transformation between different height systems is often used. The hybrid method and the gravity observation method could meet the need of engineering accuracy. In the future, the study would try to use artificial intelligence method to improve the accuracy of the model, and optimize the model with different methods.

5. REFERENCE

Filmer, M. S., Featherstone, W. E., and Kuhn, M, 2010. The effect of EGM08-based normal, normal-orthometric and Helmert orthometric height systems on the Australian levelling network, Journal of Geodesy,84(8),pp.501-513.

Forsberg, R., 1984. A Study of Terrain Reductions, Dendity Anomalies and Geophysical Inversion Methods in Gravity Field Modellingm. Ph.D. Dissertation, The Ohio State University, Columbus.

Heiskanen, W. A., and Moritz, H,1967. Physical Geodesy, W. H. Freeman Publishers, San Francisco, 364p.
Hirt, C., Featherstone, W.E., and Marti, U, 2010 Combining EGM08 and SRTM/DTM2006.0 residual terrain model data to improve quasigeoid computations in mountainous areas devoid of gravity data, Journal of Geodesy,84,557-597.

Moritz, H, 1993.The Figure of the Earth : Geodesy and the Earth's Interior, Wichmann Publishers,292p.

NGA, 2013, EGM08 - WGS 84 Version, URL: http://earth-info.nga.mil/GandG/wgs84/gravitymod/EGM08/egm08_wgs84.html (last date accessed: 14 Oct 2016).

Patroba, A. O., Yoichi F., and Yuki, K, 2012. A high-resolution gravimetric geoid model for Japan from EGM08 and local gravity data, Earth Planets Space, 64, 361-368.

Pavlis, N. K., Simon, A. H., Steve C. K., and John, K. F, 2012. The development and evaluation of the Earth Gravitational Model 2008 (EGM08). Journal of Geophysical Research, 117(4).

Ramazan, A., Bihter, E., and Aydin, U, 2012. Comparison of the kth and remove–cmpute– rstore tchniques to geoid modelling in a mountainous area, Computers & Geosciences, 48, 34-40.

Schwarz, K. P., Sideris, M. G., and Forsberg, R, 1990. The Use of FFT Techniques in Physical Geodesy, Geophys. J. Int,100, 485-514.

Zhu, Y., Gao, X., Liu, Y., et al, 2011. Study on the elevation determination based on EGM08 model. journal of university of jinan, 25(4), 410-413.

ACKNOWLEDGEMENT

SYSTEM USING GEONODE AS OPENSOURCE PLATFORM

Arif Wijayanto (1, 2), Sahid Hudjimartsu (1), Lilik Prasetyo (1), Yudi Setiawan (1, 2), Desi Suyamto (1)

[1]Forests 2020, Environmental Analysis and Spatial Modelling Laboratory, Department of Forest Resources Conservation and Ecotourism, Faculty of Forestry, Bogor Agricultural University, Darmaga Campus, Bogor District, West Java Province, Indonesia 16680
[2]Environmental Research Center, Bogor Agricultural University, Darmaga Campus, Bogor District, West Java Province, Indonesia 16680
Email: akwijayanto@apps.ipb.ac.id; s.hudjimartsu@apps.ipb.ac.id; lbprastdp@apps.ipb.ac.id; setiawan.yudi@apps.ipb.ac.id; d.suyamto@apps.ipb.ac.id

KEY WORDS: monitoring, national forest, GeoNode, opensource

ABSTRACT: Monitoring of national forest resources is needed to provide information on the condition of national forests as a whole. The Indonesian Ministry of Environmental and Forestry (MoEF) conducts the national forests monitoring by involving several parties spread throughout Indonesia. To publish the data, the institution serves the data as online services using proprietary platform. The objective of this study is to provide alternative solution for Indonesia's national forest monitoring using opensource platform. GeoNode as an opensource platform for managing geospatial data, can be alternative to the proprietary platform by concerning cost, reliability, and performance. GeoNode is a geoportal opensource system with a combination of Django as framework and Python as programming language that can display the visualization of spatial dynamic information with interactive way. The application was designed to be used as support tool for decision makers related to national forests policy. The objective of this study is to provide alternative solution for Indonesia's national forest monitoring using GeoNode as opensource platform

1. INTRODUCTION

Monitoring of national forest resources is needed to provide information on the condition of national forests as a whole. The Indonesian Ministry of Environmental and Forestry (MoEF) conducts the national forests monitoring by involving several parties spread throughout Indonesia. To publish the data, the institution serves the data as online services using proprietary platform. From a licensing perspective, the main problem of proprietary platform is related to the cost and the conditions of using the platform. The utilization of opensource platform can significantly reduce costs, since it gives freedom to the users to run the platform for any purposes and on any number of machines.

GeoNode as an opensource platform for managing geospatial data, can be alternative to the proprietary platform by concerning cost, reliability, and performance. GeoNode is an open source online platform for geospatial data sharing (Balbo, 2014). GeoNode is a combination of Django as framework and Python as programming language that can display the visualization of spatial dynamic information with interactive way. This platform brings mature and stable opensource software projects under a consistent and easy-to-use interface that allows non-specialized users to share data and create interactive maps. At its core, GeoNode is built on a stack based on GeoServer, pycsw, Django, and GeoExt that provides a platform for sophisticated web browser spatial visualization and analysis as shown by Figure 1.

Many institutions around the world have utilized GeoNode to build their geospatial data sharing infrastructure. The World Agroforestry Center (ICRAF) developed a system namely The Landscape Portal (http://landscapeportal.org/), an interactive online spatial data storage and visualization platform to visualize their spatial data (Reisdorf, 2016). The International Hydrological Programme

GeoNode makes data distribution through nodes possible to promote the collaborative use of spatial data (Boccardo, 2012).
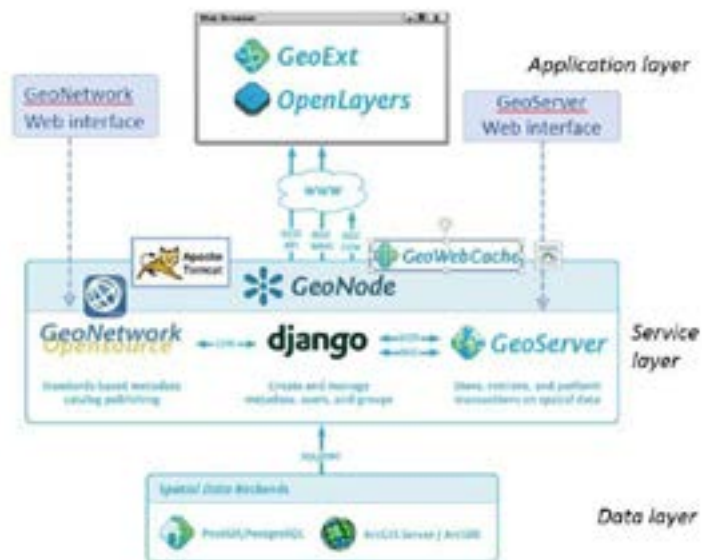
Figure 1. GeoNode stack block diagram (World Bank, 2013)

The objective of this study is to provide alternative solution for Indonesia's national forest monitoring using GeoNode as opensource platform. As the first stage of the study, it is aimed that the system could be utilized as spatial data sharing tools of national forests monitoring spatial data.

2. IMPLEMENTATION
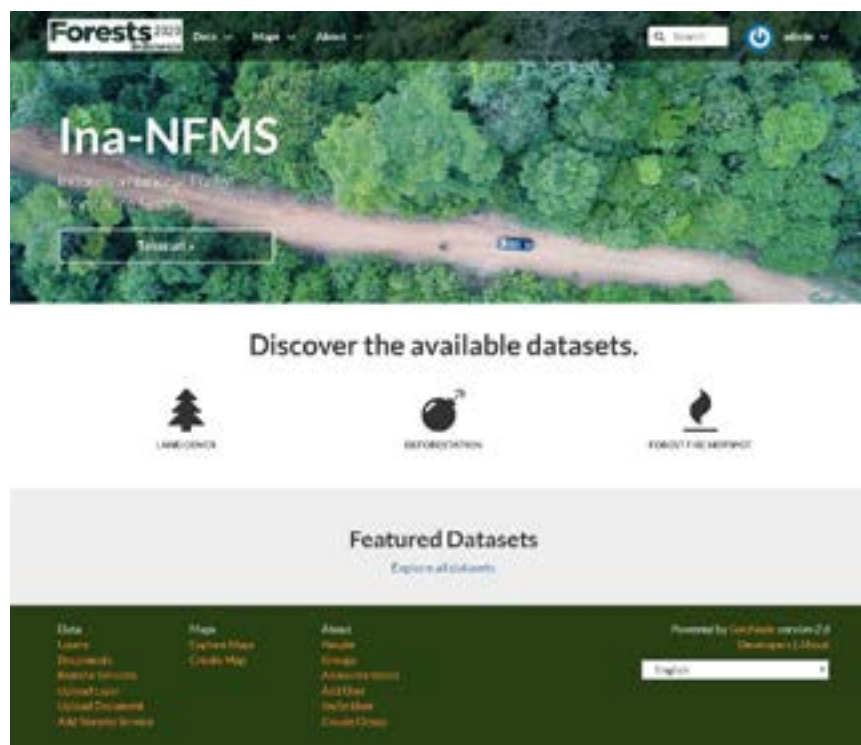
Figure 2. Homepage of the system. The system temporarily named as Ina-NFMS: Indonesia National Forest Monitoring System

The national area of Indonesia was chosen as study case of this study. Sample data are Indonesia

National Institute of Aeronautics and Space (LAPAN), the Geospatial Information Agency (BIG) and the Technical Implementation Unit of the Directorate General of Planology and Environmental Management, namely the Center for Forest Area Stabilization (BPKH) spread throughout Indonesia. The data has 23 classes of landcover, consist of 7 classes of forest cover, and 16 classes of non-forest cover. To date, available land cover data are 1990, 1996, 2000, 2003, 2006, 2009, 2011, 2012, 2013, 2014, 2015, 2016, and 2017. Dataset used as case study is landcover map of 2016.

The platform was installed in development stage on virtual machine (VM) running Windows Server 2012 R2 as host machine and Ubuntu 16.04 LTS as guest machine. All of the GeoNode stack software are installed on the same host. Currently, the system can be accessed online through intranet.

2.1. User Acceptance Testing (UAT)

The developed system should be able to be a spatial data sharing platform. It is because the national forest monitoring system in Indonesia is done by dividing the task into several sub-level of institution. The User Acceptance Testing (UAT) was done to make sure that the system which is built from GeoNode as its core, could facilitate the users to share their data among the institutions. Yet still considering the data sharing security.

Since the system is still in development stage, the UAT is only done to test a small amount of UAT test. The UAT test done to answer questions such as:
1. Does the system crash?
2. Can the application display the data correctly?
3. Does the application give the users options for data sharing privileges or restriction?
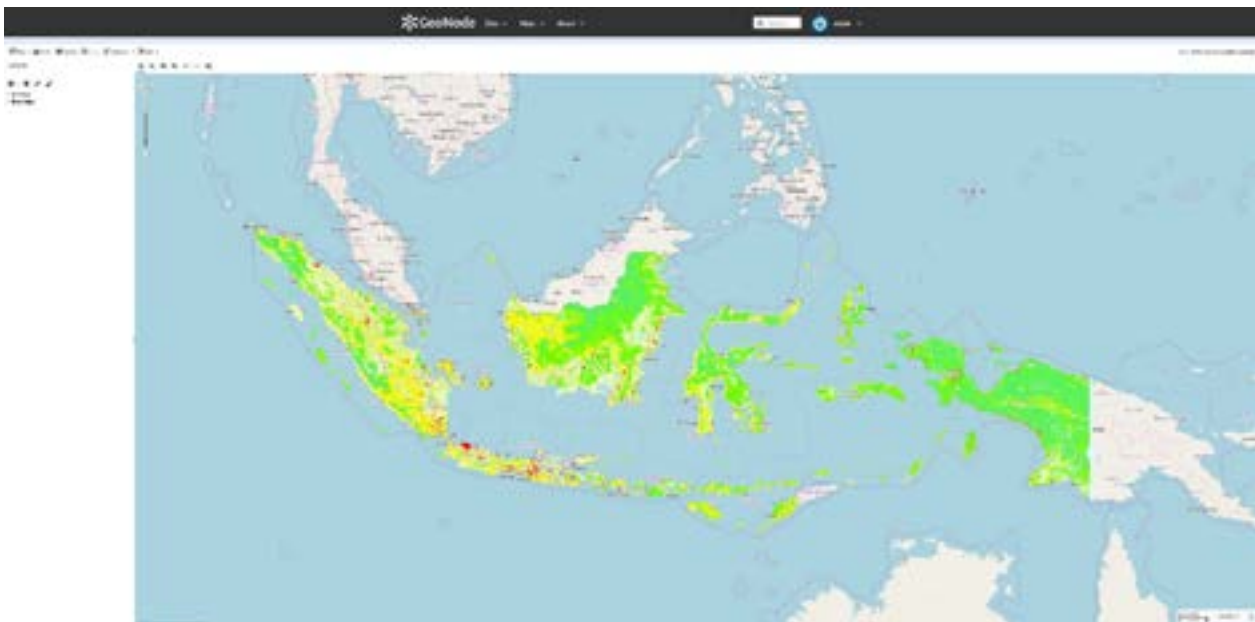
Figure 3. Display Layer in GeoNode

The result of UAT for displaying data can be seen in Figure 3, the figure shown that the application can display correctly the data (raster data) for all classes of landcover in Indonesia.

Figure 4. Layer permission settings in GeoNode

By default, GeoNode has feature to set permissions of uploaded layers (Figure 3). The permission consists of who can view the layer, who can download it, who can change the metadata, who can edit the data, who can edit the style, and who can manage it. This is addressing the third question regarding data sharing privilege and restriction.

In generally, the application runs well to provide spatial data sharing for Indonesia national forest monitoring despite of using large data.

3. NEXT STAGE DEVELOPMENT

In this stage, the developed system has been able to provide spatial data sharing for Indonesia national forest monitoring. Hopefully, this system can be developed further with more advance spatial analysis and assessment tools. Advanced function such as spatial analysis based on user input shape, raster-based analysis, time-series analysis, etc., hopefully will be added in further development.

4. CONCLUSIONS

Based on the initial development, it is concluded that GeoNode can be an alternative for national forest monitoring system. The characteristic of Indonesia as a huge country with large area of forest that makes the ministry to manage the national forest monitoring system done by many sub-levels of institution, is fit to GeoNode as spatial data sharing platform.

5. ACKNOWLEDGMENT

6. REFERENCES

Data Sharing for Disaster Management. In: International Archives of Photogrammetry and Remote Sensing, Padua, Vol.XL, Part W3, pp.189-195

Boccardo, P., and Pasquali, P., 2012. Web Mapping Services in a Crowdsource Environment for Disaster Management: State-Of-The-Art and Further Development. In: International Archives of Photogrammetry and Remote Sensing, Melbourne, Vol.XXXIX, Part B4, pp.543-548

Reisdorf, K., 2016. ICRAF's Landscape Portal: Data Geeks Build Global Public Good, Retrieved September 13, 2018, from http://foreststreesagroforestry.org/icrafs-landscape-portal-data-geeks-building-a-global-public-good

Skoulikaris, C., Filali-Meknassi, Y., Aureli, A., Amani, A., and Jiménez-Cisneros, B. E. 2018. Information-Communication Technologies as an Integrated Water Resources Management (IWRM) Tool for Sustainable Development. In Achievements and Challenges of Integrated River Basin Management. IntechOpen.

World Bank. 2013. Advanced Training on Spatial Data Management: Training Manual for GIS Data Manager

DETECTION OF FOREST FIRES IN TROPICAL FORESTS

USING SENTINEL-3 SLSTR DATA

Noel Iván Ulloa[1], Shou-Hao Chiang[1]
[1]Center for Space and Remote Sensing Research Center (CSRSR)
No.300, Jhongda Rd., Jhongli City, Taoyuan, Taiwan 32001, Republic of China
Email: ulloa_noel@hotmail.com

KEY WORDS: Sentinel 3, SLSTR, wildfire, protected areas.

ABSTRACT

Forest fires are considered a major hazard and environmental issue worldwide. The substantial ecological damage of wildfires is caused by the considerable amounts of greenhouse gases emitted during the biomass burning process, as well as by the changes in the soil properties, thus accelerating the erosion rate. The objective of this study is to detect wildfire events in tropical areas using satellite data acquired by Sentinel-3 Sea and Land Surface Temperature Radiometer (SLSTR), the latest Earth Observation Satellite from the European Space Agency. The SLSTR sensor includes bands dedicated to detect active fire, and thanks to its fast revisit period and high spectral resolution it is suitable for rapid detection of forest fires, in addition to monitoring the recovery of burned forests.

For this study, a single forest fire event that took place in the Indio Maiz Biological Reserve, Nicaragua, during April 3-13th of 2018, was selected as the study case. A total of six S3-SLSTR images were downloaded and preprocessed. The images were visualized with different combinations of bands, including those specific for active fire detection. Additionally, optical images from MODIS and Sentinel-2 were also acquired and compared to the S3-SLSTR, in terms of fire detection capabilities.

The results indicate that S3-SLSTR imagery is capable of detecting active fire events in remote areas. Despite its coarse resolution of 500 m, S3 is a valuable addition to emergency response and disaster management team's toolkit, who will definitely benefit from the fire-monitoring optimized images. Moreover, a twin Sentinel-3 satellite was launched on April 25, 2018, meaning that the twin S3 satellites could be employed the monitor wildfires on daily basis, even in remote areas of the tropical region.

1. INTRODUCTION

Forest gains and losses, a type of land cover change, cause impacts on global environment through the absorption or emission of greenhouse gases and by modifying the physical properties of land surface (Foley et al., 2005). Some of most noteworthy effects are changes in surface fluxes of radiation, heat, and moisture that can further affect the climate at different scales (Bonan, 2008). The global forest assessment conducted by the Food and Agriculture Organization (FAO) in 2015 exposed that the extent of the world's forest continues to decline as human populations continue to grow and demand for food and land increases. It also showed that South America and Africa presented the highest net annual loss of forest in 2010-2015, with 2.8 and 2 million hectares respectively. In the aforementioned region, forest fires are considered as one of the main causes of deforestation and forest degradation (Julio-Alvear, 2008).

The Central American region is a clear example of forest degradation as a consequence of ineffective management of protected areas. Forest protection is essential to reduce the deforestation rates worldwide. This can be achieved through legislation that includes, but not limited to, the assessing and monitoring of forest resources.

On April 3, 2018 a wildfire was originated inside the Indio Maiz Biological Reserve, which is part of the Rio San Juan Biosphere Reserve, in the southeast of Nicaragua (Torrez, 2018). Thanks to the continued and arduous effort from the local authorities, the fire was extinguished on the afternoon of April 13 (Associated Press, 2018).

The inaccessibility of this region represented an obstacle to estimations of the magnitude and extension of the fire based on in situ data, especially during its initial stages. Earth Obsertation Satellites allows users to overcome these limitations imposed by distance to the site, since they are more than capable of delivering crucial information (e.g. burned area, ignition point and displacement of rim of fire) to the emergency response teams.

The Sea and Land Surface Temperature Radiometer (SLSTR) sensor on board of the Sentinel 3A and 3B satellites is newest member of orbiting spaceborne optical sensors. They were launched by the ESA (European Space

Agency) in February of 2016, and April 8, 2018, respectively (European Space Agency, 2018). The twin satellites provide images with spatial resolution of 500 and 1000 m over a swath of 1420 Km in the visible, infrared and thermal bands, with a temporal resolution of 1 day at the equator (ESA, 2018). The SLSTR sensor possesses bands specifically designed for fire detection. Thanks to its technical design, high temporal and spectral resolution, the data provided by these satellites is suitable for quick detection and tracking of forest fires, in addition to the monitoring of the recovery process of burned areas.

2. STUDY AREA

The Indio Maiz Biological Reserve (IMBR), located in the Republic of Nicaragua, Central America. It covers an area of 263980 Ha (Ministerio del Ambiente y Recursos Naturales, 2005), and it is one of the seven protected areas inside the Rio San Juan Biosphere Reserve (1392900 Ha) (Munera, 2014). IMBR is considered as one of the largest and most pristine protected areas in the Central American region, mainly due to its secluded location, challenging accessibility and small population. This reserve is also part of the Mesoamerican Biological Corridor (MBC), an area of high biodiversity created in the late 1990s with the aim of preserving the biological connectivity and protect threatened and endangered wildlife (Finley-Brook, 2007).
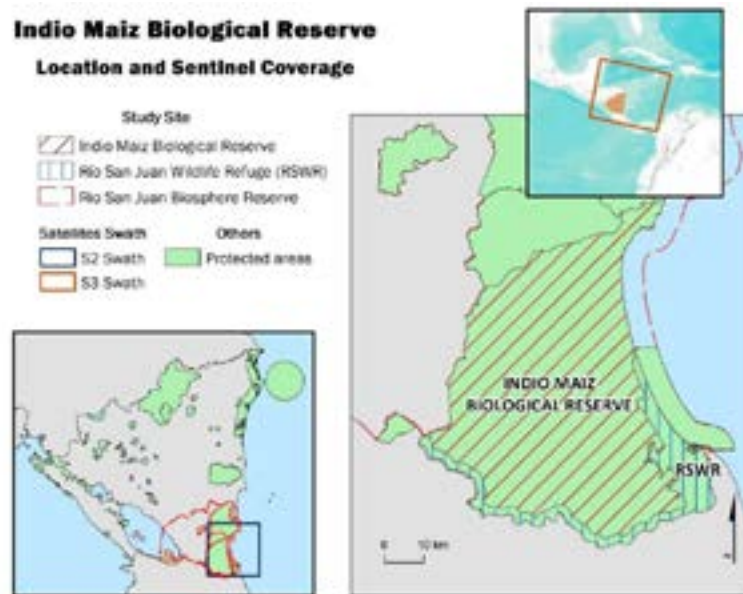
Figure 1. Location map of the Bosawas Biosphere Reserve

3. METHODS

3.1 Data acquisition

Sentinel 3A SLSTR data was downloaded as Level-1 Radiance and Brightness Temperature (SL_1_RBT) from the Copernicus Online Data Access (CODE; https://coda.eumetsat.int/#/home), corresponding to the period April 4-23, 2018. The data was preprocessed using the SNAP Sentinel 3 toolbox (https://coda.eumetsat.int/#/home): the images were projected to UTM WGS 84, and radiance was converted to Top-Of-Atmosphere reflectance. A composite of the 500 meters spatial resolution bands was created and exported as GeoTIFF. Sentinel 2 MSI images were also acquired for the dates of April 6th and April 11th.

3.2 Burned area detection

Normalized Difference Vegetation Index (NDVI) (Rouse et al., 1973), Normalized Difference Water Index (NDWI) (Liu et al., 2014), and Normalized Burn Ratio (NBR) (Miller and Yool, 2002) were derived for each scene. These normalized indices were combined with the red, NIR and SWIR bands of their respective scene. Next, each

composite image was segmented using eCognition Developer (http://www.ecognition.com/). The segmentation parameters are presented in Table 1.

Table 1. Parameter values used during segmentation

Dataset	Scale	Shape	Compactness
MSI	5	0.1	0.5
SLSTR	20	0.1	0.5

The image objects located in the proximity of the reported fire site were merged into larger objects and labeled as burned area. Subsequently, they were exported as shapefile, and the area of each polygon was then calculated in ArcGIS. Finally, the burned areas derived from S2 and S3 datasets were compared to one another, and to the official burn area reported by local authorities to assess the feasibility of Sentinel 3 SLSTR data for burn area estimation.

4. RESULTS

4.1 Wildfire detection

By combining the NIR, SWIR and SWIR 2 bands into a false color composite it is possible to penetrate atmospheric particles, smoke and haze. Moreover, the shortwave infrared bands are capable of detecting zones with high heat output, such as active fire. Figure 2 shows the atmospheric penetration composite for MSI and SLSRT while the wildfire was still active.
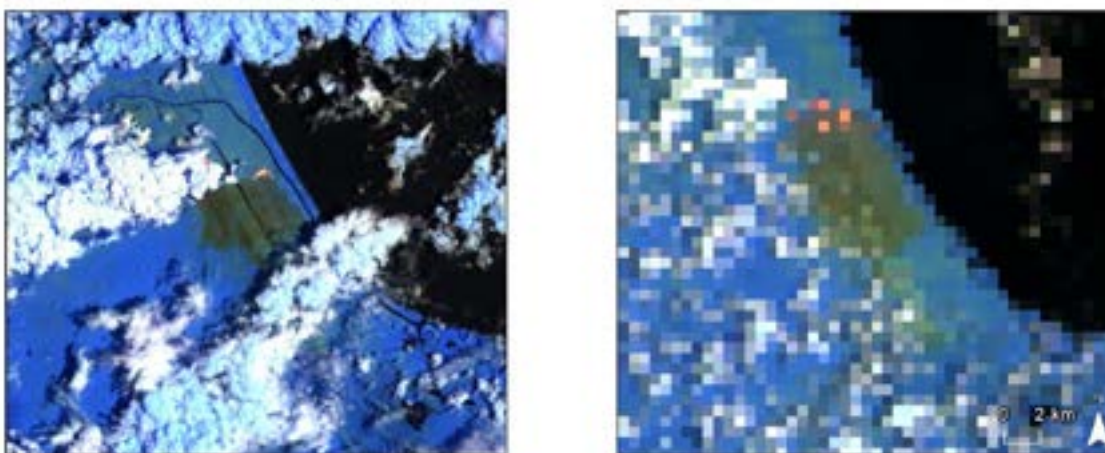
Figure 2. Atmospheric penetration composite for Sentinel-2 (a) and Sentinel-3 SLSTR9 (b)

Sentinel 3 SLSTR also has the ability to detect the burn scars by combining bands 6,3,2 (SWIR, NIR and Red), as shown in Figure 3. In this images, the recent burned areas appear in a brown hue. This estimation is possible because of the lasting spectral signal emitted by the charcoal residue.
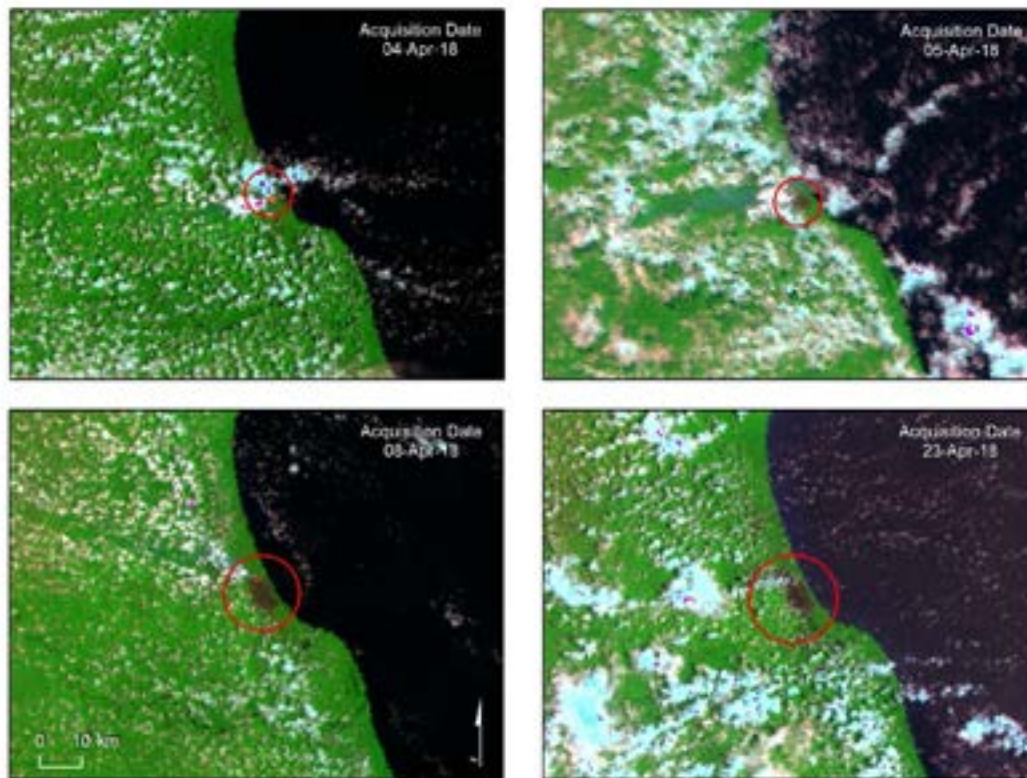
Figure 3. Tracking the burn scar, Sentinel-3 SLSTR for April 4- 23, 2018

Although the coarse resolution of Sentinel 3 SLSTR can be considered a limitation when analyzing fire events with small extension, its fast revisit period makes it suitable to track and keeping record of areas affected by wildfires. In order to make a substantial improvement in fire-fighting decision making, a high frequency of observation is needed (Pilar, 1999)

4.2 Burned area estimations

Figure 4 exhibits the burned area derived from the Sentinel satellites datasets, as well as the spatial coherence with the MODIS and VIIRS active fire products. The estimated total burned area is 5187.29 Ha (S2) and 5870.66 (S3). The differences in the total burnt area values among the three datasets area mainly due to the cloud cover issue and different spatial resolution.

Nicaraguan authorities reported estimated that 5945 Ha were affected by the wildfire, which stretched across the IMBR and the Rio San Juan Wildlife Refuge (El Nuevo Diario, 2018). The reported area in higher than the estimations based on S2 and S3 images. Nevertheless, the results indicate that it is possible to use S3 data to obtain close estimations of forest areas affected by fire with high temporal resolution, even in situations where the burning area is limited to a small zone.
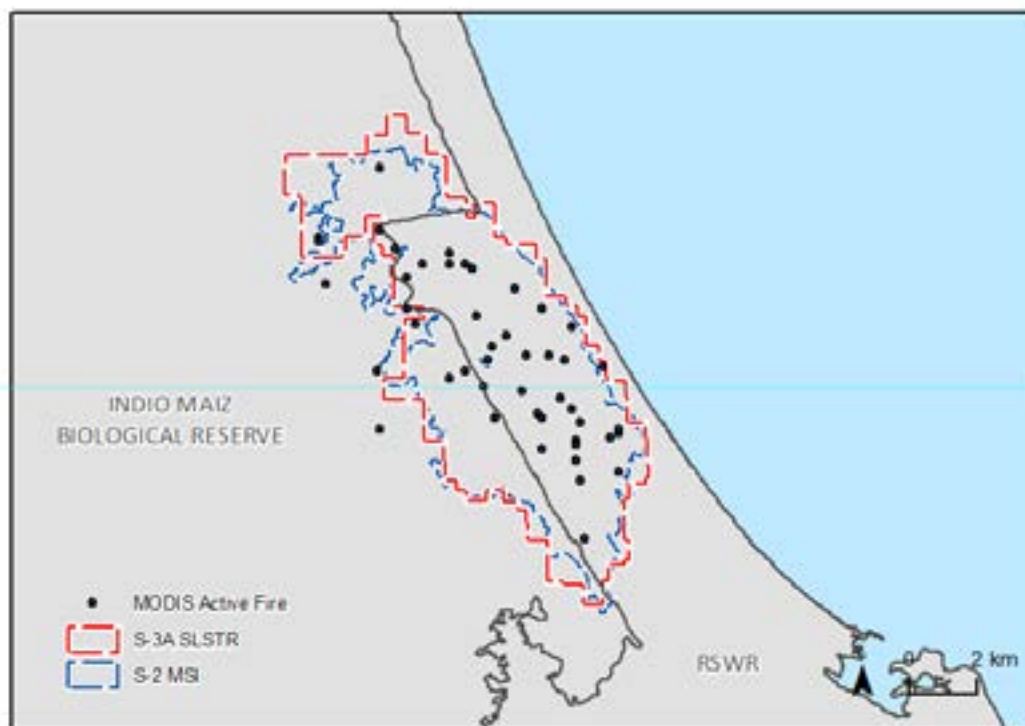
Figure 3. Land cover of the nucleus zone of the Bosawas Biosphere Reserve for 2015

CONCLUSIONS

This study verifies the applicability of Sentinel 3A SLSTR data to identify and monitor the occurrence of wildfires in tropical forests, as well as to generate burned area estimations with a high temporal resolution. Analysis of SLSTR data shows that 5870.66 Ha of forest were affected during the wildfire event that took place in the Indio Maiz Biological Reserve, in April 2018. This value is close to the 5945 Ha reported by the local authorities.

The underestimation of burned area for each sensor can be attributed to the effect of cloud contamination, changes at subpixel level, and to human error during the visual identification of burned areas. Further improvements in the methodology are required to generate more accurate burned area estimation.

REFERENCES

Bonan, G.B., 2008. Forests and climate change: forcings, feedbacks, and the climate benefits of forests. Science, 320 (5882), pp. 1444-1449.

C. Munera, "Biocultural design as a framework to identify sustainability issues in Rio San Juan Biosphere Reserve and Fortress of the Immaculate Conception, Nicaragua," UNESCO, 2014.

European Space Agency, "Sentinel 3 - Data Access and Products," March 2015. [Online]. Available: https://sentinels.copernicus.eu/documents/247904/1848151/Sentinel-3_SLSTR_Data_Access_and_Products.pdf. [Accessed 3 May 2018].

Food and Agriculture Organization of the United Nations. Global Forest Resources Assessment 2015, April 2015.. [Online]. Available: http://www.fao.org/3/ai4793e.pdf

Foley, J. A., DeFries, R., et al., 2005. Global Consequences of Land Use. Science, 309 (5734), pp. 570-574.

"Incendio en Indio Maíz afectó 2 de las 8 áreas protegidas de la Reserva de Biosfera Río San Juan," El Nuevo Diario, 18 April 2018. [Online]. Available: https://www.elnuevodiario.com.ni. [Accessed 20 April 2018].

J. Miller and S. Yool, "Mapping forest post-fire canopy consumption in several overstory types using multi-temporal Landsat TM and ETM data," Remote Sensing of Environment, vol. 82, pp. 481-496, 2002.

J. Rouse, R. Haas, J. Schell and D. Deering, "Monitoring Vegetation Systems in the Great Plains with ERTS," in Third Earth Resources Technology Satellite-1 Symposium, Washington DC, 1973.

Julio-Alvear, G., "Managing efforts to prevent forest fires in South America," in Proceedings of the second international symposium on fire economics, planning, and policy: a global view, Albany, CA, 2008.

M. Finley-Brook, "Green Neoliberal Space: The Mesoamerican Biological Corridor," Journal of Latin American Geography, vol. 6, no. 1, pp. 101-124, 2007.

Ministerio del Ambiente Y Recursos Naturales, "Plan de Manejo Reserva Biologica Indio Maiz 2005-2010," Managua, 2005.

"Nicaragua puts out forest fire in southern nature reserve," Associated Press, 13 April 2018. [Online]. Available: https://apnews.com/. [Accessed 5 May 2018].

M. Pilar, P. Ceccato, S. Flasse and I. Downey, "Fire detection and fire growth monitoring using satellite data," in Remote Sensing of Large Wildfires, Berlin, Springer, 1999, pp. 101-122.

Torrez, C., "Ambientalistas sospechan de mano criminal en incendio en la Reserva Indio Maíz," 5 April 2018. [Online]. Available: https://www.laprensa.com.ni/. [Accessed 5 April 2018]

Y. Liu, Q. Dai, J. Liu, S. Liu and J. Yang, "Study of Burn Scar Extraction Automatically Based on Level Set Method using Remote Sensing Data," PLOS ONE, 2014.

Ho-Lin Tsay, Shenq-Tsong Chang, Yi-Hao Lin and Ming-Fu Chen

Smart Inspection and Remote Sensing Division,Instrument Technology research Center, National Applied Research Laboratories, 20 R&D Road VI, HsinChu Science Park, 30076 HsinChu City, Taiwan, Republic of China.
Email: hltsay@narlabs.org.tw; stc@narlabs.org.tw ; 1609809@ narlabs.org.tw ; mfchen@narlabs.org.tw

KEY WORDS: Collimation, Quantitative measurement, Theodolite

ABSTRACT: Optical collimator is a test equipment for the simulation of infinite-finite objects in the laboratory. It is used to focus and measure the remote sensing telescope. This paper proposes a quantitative measurement method for collimation of collimator. In this method, we use a moving theodolite to measure relative angle at different aperture positions of the collimator, which lead to collimator's quantitative collimation and its corresponding object distance.

1. INTRODUCTION

An optical collimator can be used to calibrate other optical devices to check that all elements are aligned on the optical axis, set the components in the proper focus position, or align two or more devices, such as binoculars or barrels and pistols. Measuring cameras can be collimated by setting its trusted mark to define the principal point for photogrammetry.

Optical collimators can be divided into two types, one is a refractive collimator, which is mainly used for visible light applications. The other is a reflective collimator, which can be used for visible and infrared applications. Reflective collimator can be divided into two types: obscuration in cenral aperture and no obscuration in the central aperture. Reflective collimator with an obscuration is a kind of a reflective telescope. Reflective collimator with no obscuration projects collimating light with an off-axis parabolic mirror.
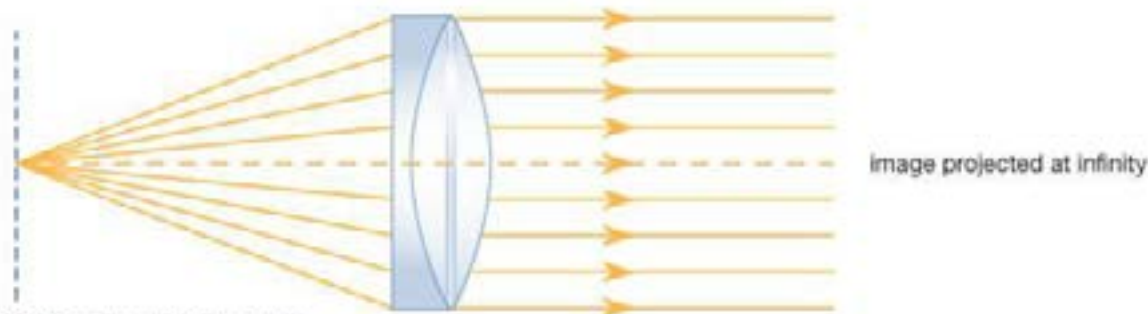
Figure 1. Schematic diagram of a refractive collimator.
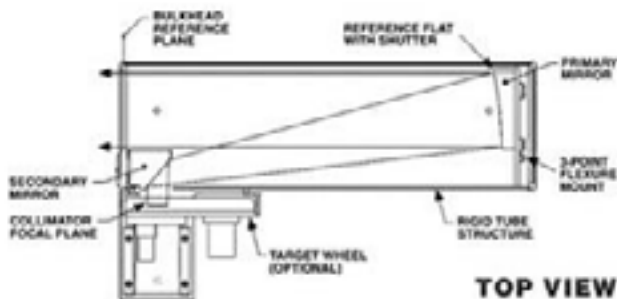
Figure 2. Schematic diagram of an off-axis reflective collimator.

Self-collimation check is an optical qualitative inspection method. In this method, a collimated beam (parallel light) from a collimator was reflected back to the same system by a flat mirror. By adjusting

original pattern of the collimator. Comparing the pattern size on the same plane can qualitatively check the collimation of this collimator. This method can also be used to measure the small tilt angle of the mirror.

Another qualitative inspection method is to calibrate the collimator with another collimator. To perform this method, align the two collimators, and to project the collimated light with the calibrated collimator to adjust the focus to the collimator to be calibrated. Prerequisite is that the standard collimator should cover all of effective aperture for the piece to be calibrated.

There is a quantitative method for the calibration of the collimation of the large-aperture collimator. This method calibrates the collimation of the collimator by measuring the relative angle with a theodolite. There are two ways of setting up the measurement [1], this paper introduce its measurement setup, measurement process and data analysis.

2. MEASUREMENT SETUP

Figure 3. Schematic diagram of the collimation measurement in vertical direction.
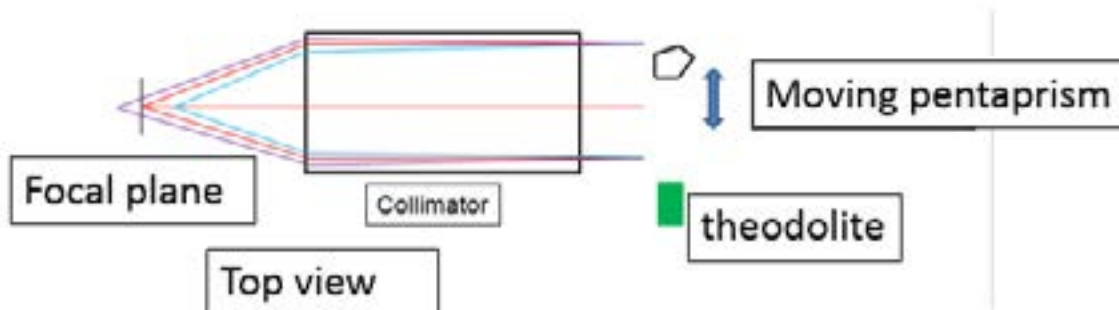
Figure 4. Schematic diagram of the collimation measurement in horizontal direction.

Measuring method is schematic shown in Fig. 3 and Fig. 4. In Fig. 3, theodolite was moved up and down to observe the same position on the focal plane through optical system of collimator, measuring vertical angle at every vertical position, and relative angle deviation of the relative position within the aperture of the collimator was derived. In Fig. 4, a pentaprism was horizontally moved to the relative position within the aperture of collimator, and horizontal angle deviation was measured by theodolite. As depicted in measuring diagram of Fig. 3, in case that collimator projection pattern is not on the predetermined focal plane, light projected through the collimator is not parallel, and the vertical angle measured by theodolite deviates due to the position in aperture of the collimator. Through the relative angle measurement, collimator focal plane position deviation and its equivalent object distance can be derived. In the measurement diagram of Fig. 4, light was deflected by pentaprism by 90 degrees, and the position of the pentaprism was moved horizontally. Through the horizontal angle change measurement, the collimator focal plane position deviation and its equivalent object distance can be calculated. Fig. 5 shows the focal plane image of the collimator observed by theodolite.
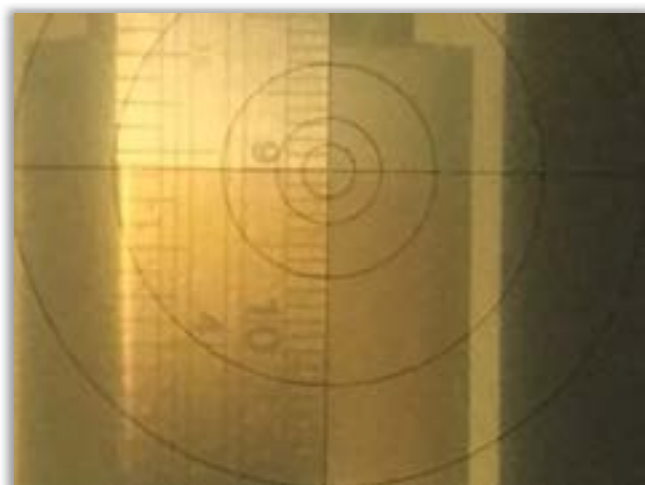
Figure 5. Focal plane image of the collimator observed by theodolite through collimator's optical system. A ruler was place at the focal plane of collimator.

3 MEASUREMENT RESULT ANALYSIS

Fig. 6 and Fig. 7 show the vertical measurement results with theodolite. The horizontal axis is the relative position of the theodolite, unit is mm. Vertical axis is the relative deviation of measuring angle, unit is one millionth of a radians. In the relationship between the relative angle of the measurement and the relative position of the theodolite, the inverse of the slope is the projection object distance. Using the optical relationship of the collimator, the object distance multiplied by the effective focal length square, the image distance can be solved. The physical meaning of the image distance is the distance between the position of the existing pattern and the nominal focal plane of the collimator. Fig. 6 and Fig. 7 are different in sign to each other. This means positions of the two measured patterns are on the opposite side of nominal focal plane of the collimator. When the collimator focal plane adjustment is performed in this way, the collimator pattern position is adjusted until the measurement slope approaches zero.
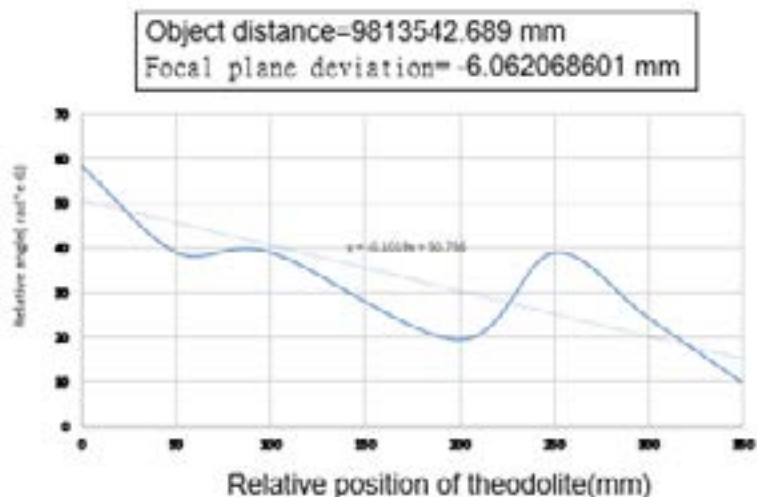
Figure 6: Collimation vertical measurement results (1).
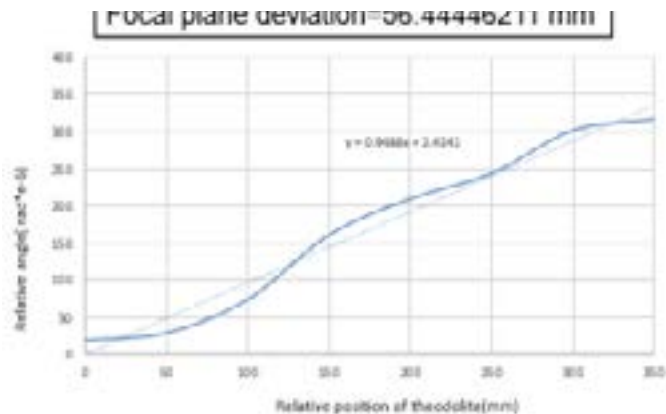
Figure 7: Collimation vertical measurement results (2).

4 INTERFEROMETER METHOD

Collimation measurement can also be performed using an interferometer and a standard flat plane [2], which is shown schematically in Fig. 8. After removing light source of collimator, the interferometer is placed on a moving platform, interferometric beam was focused on the collimator's focal plane. Shifting position of interferometer to zero focus term. Then align direction of AC flat to make beam back to focal point of measuring beam. Focus term in interferometric analysis is a quantitative indication of collimator's focus offset.
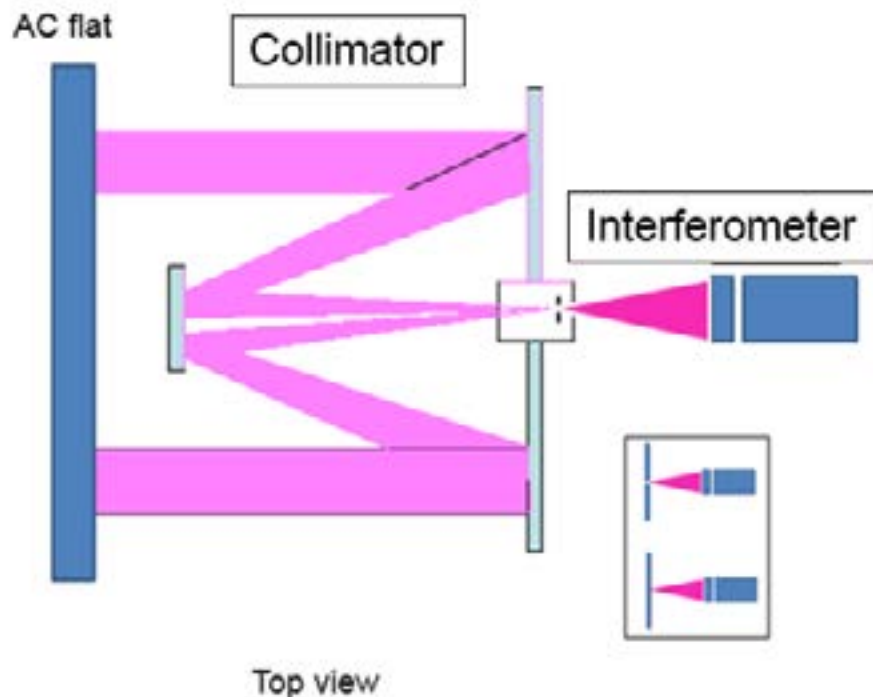
Figure 8: Schematic diagram of measuring collimation of the collimator with an interferometer.

5 CONCLUSION

This paper proposes a method for measuring the collimation of the collimator with theodolite. The output ray angle of relative position of the collimator can be quantitatively measured. Focus offset and the equivalent projection distance can be derived.

REFERENCES

1. ISO 11421:1997,Optics and optical instruments -- Accuracy of optical transfer function (OTF) measurement.
2. H. L. Tsay, Y. C. Lin , S. T. Chang and T. M. Huang, "Collimator focus check with interferometer" roc. SPIE 10373, Applied Optical Metrology II, 103730V (23 August 2017); doi:10.1117/12.2272105.

AN EXAMINATION OF METHODS FOR EVALUATING DIFFERENCES AMONG HIGHLY ACCURATE LAND COVER CLASSIFIERS

Hidetake Hirayama (1), Mizuki Tomita (2), Keitarou Hara (2)

[1] Graduate School of Tokyo University of Information Sciences, 4-1 Onaridai, Wakaba-ku, Chiba 265-8501, Japan
[2] Department of Informatics, Tokyo University of Information Sciences, 4-1 Onaridai, Wakaba-ku, Chiba 265-8501, Japan

Email: h17002hh@edu.tuis.ac.jp; tomita@rsch.tuis.ac.jp; hara@rsch.tuis.ac.jp

KEY WORDS: Land cover classification, Highly accurate classifiers, Accuracy assessment, McNemar's test, RapidEye

ABSTRACT: Many researches have focused on creating land cover maps from satellite images. Recently, advanced machine learning techniques have made it possible to create classifiers that are far more accurate than the earlier methods. The Kappa coefficient has been widely used for evaluation of classification accuracy, but with the new highly accurate classifiers there is often little difference among the Kappa coefficients. As a result, the Kappa coefficient alone is no longer sufficient for comparing classification results. The purpose of this research was to examine alternative methods that can appropriately evaluate the differences among highly accurate classifiers. RapidEye satellite images were analyzed using six machine learning techniques (Random Forests, Bagging, XGBoost, Support vector machine, Neural network and K-nearest neighbor). The overall results for these classifiers were then compared using Kappa coefficient-based Z-test and McNemar's test implemented on paired nominal data. For the McNemar's test, the classification results among the six classifiers were also compared pixel by pixel for each of six land cover class to generate p-values. The results showed that the classifiers with the highest Kappa values were XGBoost (0.966), Random Forests (0.961) and Bagging (0.943). The Z-test analysis of these results showed that the scores ranged from 0.57 to 2.45, and that although Bagging exhibited a significant difference between the other classifiers, there was no significant difference between XGBoost and Random Forests. In the McNemar's test, the p-value ranged from 0.00029 to 0.31, and there was not significant overall difference between XGBoost and Random Forests. When the McNemar's test was implemented for each land cover class, however, a significant difference was confirmed between Random Forests and XGBoost. For example, in the cropland cover class, although the user accuracies were almost the same for Random Forests (0.961) and XGBoost (0.966), the McNemar's test ($p < 0.016$) showed a significant difference between the two classifiers. These results show that differences among highly accurate classifiers can be statistically confirmed by performing McNemar's test for each land cover class, even when there is almost no difference in overall or class accuracy between classifiers.

1. INTRODUCTION

Many researches have focused on creating land cover maps from satellite images. Recently, advanced machine learning techniques have made it possible to create classifiers that are far more accurate than the earlier methods. The Kappa coefficient and Kappa coefficient-based Z-test have been widely used to select a better classification result (Congalton and Green, 2008; Robertson and King, 2011; Raczko and Zagajewski, 2017). However, with the highly accurate classifiers there is often little difference among the Kappa coefficients. As a result, the Kappa coefficient and Z-test might not be sufficient for comparing highly accurate classification results. Regardless of the high classification accuracy obtained from the machine learning classifiers, the resulting map might not be promising because of the reason that the classification accuracy is sensitive to test data used for the calculation. Therefore, an efficient method for the selection of better classification result from different machine learning classifiers is immensely important.

2. PURPOSE OF THE STUDY

The purpose of this research was to examine alternative methods that can appropriately evaluate highly accurate classification results obtained from different machine learning classifiers.

3. METHODOLOGY

RapidEye satellite images were classified using six machine learning techniques (Random Forests, Bagging, XGBoost, Support vector machine, Neural network and K-nearest neighbor). The overall results for these classifiers were then compared using Kappa coefficient-based Z-test and McNemar's test implemented on paired nominal data (Figure 1).

```
┌──────────────────────┐   ┌──────────────────────┐
│   Satellite images   │   │   Ground truth data  │
└──────────────────────┘   └──────────────────────┘

        ┌──────────────────────────────────────┐
        │     Six machine learning techniques  │
        └──────────────────────────────────────┘

┌──────────────────────┐   ┌──────────────────────┐
│    Unpaired test     │   │     Paired test      │
│                      │   │                      │
│  ┌────────────────┐  │   │                      │
│  │ Confusion matrix│ │   │  ┌────────────────┐  │
│  └────────────────┘  │   │  │   Cross table  │  │
│                      │   │  └────────────────┘  │
│  ┌────────────────┐  │   │                      │
│  │Kappa coefficient│ │   │                      │
│  └────────────────┘  │   │  ┌────────────────┐  │
│                      │   │  │ McNemar's test │  │
│  ┌────────────────┐  │   │  └────────────────┘  │
│  │     Z-test     │  │   │                      │
│  └────────────────┘  │   │                      │
└──────────────────────┘   └──────────────────────┘

        ┌──────────────────────────────────────┐
        │         Compare test results         │
        └──────────────────────────────────────┘
```
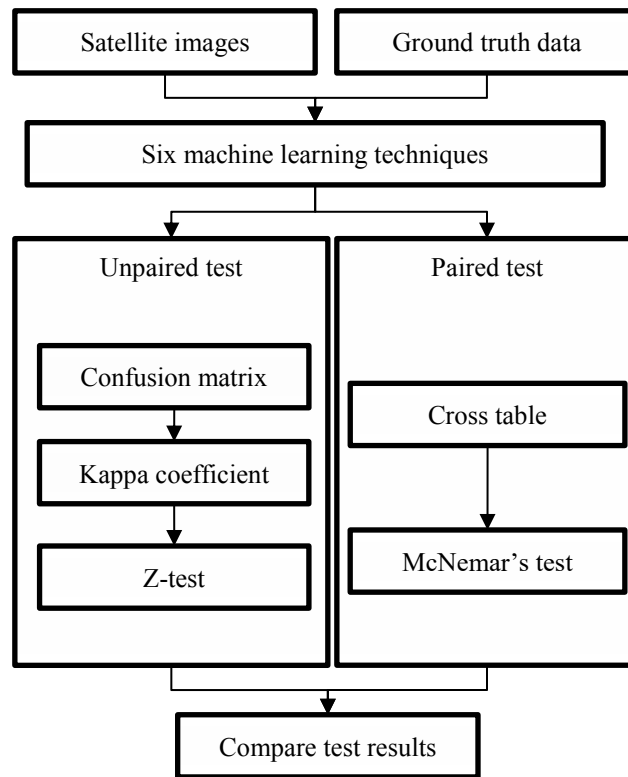
Figure 1. Flowchart of the research methodology

3.1 Satellite data

We used RapidEye satellite data with spatial resolution of 6.5m. It was Level 1B data, recorded on April 4, 2010, which consists of top of atmosphere reflectance in five channels (Blue, Green, Red, Red edge, and Near infrared). Five spectral indices, NDVI, ReNDVI, NDVIre, EVI and NDWI, were calculated pixel by pixel. In addition, we used 5m spatial resolution Digital Elevation Model (DEM) data, available from the Ministry of Land, Infrastructure, Transport and Tourism of Japan, and land surface slope (in degrees) data.

3.2 Ground truth data

Ground truth data were prepared based on field survey information and visual interpretation of the Google Earth images. Six land cover classes (forest, shrub/grassland, cropland, urban area, water body, bare ground) were defined and established in the research. We prepared 2076 ground truth points as training data, and 1495 points as test data.

3.3 Machine learning classifiers

Six machine learning classifiers, as shown in Table 1, were used. The parameters for each classifier were selected by the highest Kappa coefficient value, through trial and error method.

Table 1. Machine learning classifiers used in the research

Name	References
Random forests (RF)	Breiman, 2001
Bagging (BAG)	Breiman, 1996
eXtreme Gradient Boosting (XGB)	Chen and Guestrin, 2016
Support vector machine (SVM)	Mountrakis et al., 2011
Feed-forward neural networks (NNET)	Lek and Guégan, 1999
K-nearest neighbor (KNN)	Beckmann et al., 2015

3.4 Comparison of classifiers

Each classifier was then compared using Kappa coefficient-based Z-test and McNemar's test implemented on paired

nominal data.

3.4.1 Kappa coefficient and Z-test

The Kappa coefficient was calculated using the test data (Cohen, 1960). Kappa coefficient-based Z-test was used to test whether two classifiers produced similar accuracy or not (Congalton and Green, 2008). The value obtained by Z-test was converted to p-value after taking absolute value. The significance level was set to 0.003 (0.05/15) based on Bonferroni method, in consideration of the number of 15 tests (Tomoyuki and Naoko, 2005).

3.4.2 McNemar's test

McNemar's test is a statistical test used on paired nominal data. It is applied to 2×2 contingency tables with a dichotomous trait, with matched pairs of subjects, to determine whether the row and column marginal frequencies are equal (McNemar, 1947). In this study, cross table were created by the results of matched/unmatched of test data with each classifier (Table 2, Table 3).

Table 2. Matched/unmatched data for cross table

Test data	Classification results	
	Classifier A	Classifier B
Forest	Forest (matched)	Crop (unmatched)
Forest	Forest (matched)	Bare (unmatched)
	…	
Urban	Bare (unmatched)	Urban (match)

Table 3. Example of cross table

Classifier A	Classifier B	
	Matched	Unmatched
Matched	650 (a)	34 (b)
Unmatched	9 (c)	23 (d)

The test is based on a chi-square statistic, computed as follows:

$$x^2 = \frac{(b - c)^2}{b + c} \qquad (1)$$

In the McNemar's test, the p-value was obtained from the chi-square value. The significance level used for the McNemar's test was 0.003, which was similar to the significance level of the Z-test. While applying the McNemar's test for comparing the class wise results, the significance level 0.05 divided by the number of classifiers was used.

4. RESULTS

4.1 Kappa coefficient and Z-test

Kappa coefficients obtained from six individual classifiers have been presented in Table 4. As can be seen, XGB provided the highest Kappa coefficient (0.966) among all individual classifiers, followed by RF (Kappa coefficient = 0.961) and BAG (Kappa coefficient = 0.943). The difference between the Kappa coefficients obtained from XGB and BAG was 0.023 only, which is a very close value. NNET yielded the lowest Kappa coefficient (0.737). A large difference (0.124) between the Kappa coefficients was observed among three classifiers (SVM, KNN, and NNET).

Table 4. Kappa coefficient for six individual classifiers

	RF	BAG	XGB	SVM	NNET	KNN
Kappa	0.961	0.943	0.966	0.861	0.737	0.794

Z-test was performed on all paired combinations of six classifiers; and the result has been presented in Table 5. SVM, NNET, KNN showed significant difference between themselves and with other classifiers (p < 0.003). However, combination of RF and BAG, and RF and XGB did not show significant differences (p > 0.003).

Table 5. Z-test for all paired combinations of six classifiers

	RF	BAG	XGB	SVM	NNET	KNN
RF	-	0.03	0.28	1.6×10^{-16}	9.8×10^{-52}	1.0×10^{-33}
BAG		-	0.01	7.1×10^{-11}	1.6×10^{-41}	1.6×10^{-25}
XGB			-	8.6×10^{-18}	8.6×10^{-55}	3.0×10^{-36}
SVM				-	4.8×10^{-13}	2.8×10^{-5}
NNET					-	9.6×10^{-4}
KNN						-

4.2 McNemar's test

McNemar's test was performed on all paired combinations of six classifiers; and the result has been presented in Table 6. SVM, NNET, KNN showed significant difference between themselves and with other classifiers, similar to the results of the Z-test ($p < 0.003$). Also, there was a significant difference between BAG and RF ($p < 0.003$), and BAG and XGB ($p < 0.003$). Nevertheless, RF and XGB did not show significant difference ($p = 0.31 > 0.003$).

Table 6. McNemar's test for all paired combinations of six classifiers

	RF	BAG	XGB	SVM	NNET	KNN
RF	-	2.5×10^{-4}	3.1×10^{-1}	2.7×10^{-21}	7.0×10^{-53}	1.1×10^{-39}
BAG		-	2.9×10^{-4}	9.8×10^{-14}	5.0×10^{-43}	1.6×10^{-31}
XGB			-	2.5×10^{-23}	3.6×10^{-53}	2.2×10^{-40}
SVM				-	3.4×10^{-20}	1.2×10^{-8}
NNET					-	3.0×10^{-4}
KNN						-

Furthermore, McNemar's test was performed class wise for top three classifiers (XGB, BAG, and RF); and the result has been presented in Table 6. The Kappa coefficient values were very close for these classifiers (XGB, BAG, and RF). A significant difference was obtained only for the cropland class ($p < 0.016$).

Table 7. Class wise McNemar's test for the top three classifiers

	RF-BAG	RF-XGB	BAG-XGB
Forest	-	-	-
Shrub/Grassland	0.3173	-	0.3173
Cropland	0.0106	0.0411	0.0001
Urban area	-	-	-
Water body	-	-	-
Bare ground	-	-	-

5. DISCUSSION

5.1 Limitations of the Z-test

The Kappa coefficients obtained from XGB, RF and BAG classifiers were very close to each other; the maximum difference was only 0.023. And, significant difference was not found by the Z-test among XGB, RF and BAG. On the other hand, Kappa coefficients obtained from SVM, NNET, and KNN showed a maximum difference of 0.124; and significant differences were obtained among these classifiers. These results indicate that comparison with the Z-test is effective when there is a large difference among the Kappa coefficients. However, with the advancement of machine learning methods in recent years, it has become possible to obtain classifications with very high accuracy. Therefore, comparison with the Z-test seems inefficient.

5.2 Potentiality of the McNemar's test

Significant differences were found between BAG and RF, and BAG and XGB classifications. Z-test did not show significant differences between both of them. Therefore, McNemar's test was found to be efficient for comparing the classification results associated with high Kappa coefficients. Both the Z-test and McNemar's test used the same test data in the research; and both tests were applied for all paired combinations of six classifiers used in the research. McNemar's test was found to be efficient for comparing the classification results using the paired nominal data as in this research. However, McNemar's test also did not show a significant difference between RF and XGB. The

difference between the Kappa coefficients obtained from RF and XGB was even smaller than the difference between the Kappa coefficients obtained from BAG and XGB. However, while performing the McNemar's test class wise, significant difference was found with a class. More recently, a method to obtain better classification results by aggregating results from different machine learning classifiers has been established (Yang *et al.*, 2014; Hirayama *et al.*, 2018). Since the comparison of the resulted classification accuracies have not been used often in the previous research, the methods presented in this research are expected to be very useful.

6. CONCLUSION

In this research, we evaluated the performance of two statistical tests, Z-test and McNemar's test for comparing the classification results obtained from a number of machine learning classifiers. Our analysis showed that McNemar's test is more effective for comparing the classification results than the Z-test.

References

Beckmann, M., Ebecken, N. F. F., Lima, B. S. L., Lima, P. De, 2015. A KNN Undersampling Approach for Data Balancing. Journal of Intelligent Learning Systems and Applications, 7(November), 104-116.

Breiman, L., 1996. Bagging Predictors. Machine Learning, 24(2), 123-140.

Breiman, L., 2001. Random forests. Machine learning, 45, 5-32.

Chen, T., Guestrin, C., 2016. XGBoost: A Scalable Tree Boosting System. Kdd, 1-10.

Cohen, J., 1960. A coefficient of agreement for nominal scales. Educational and psychological measurement, 20(1), 37-46.

Congalton, R., Green, K., 2008. Assessing the Accuracy of Remotely Sensed Data. Mapping Science, 105-120.

Hirayama, H., Sharma, R. C., Tomita, M., Hara, K., 2018. Evaluating multiple classifier system for the reduction of salt-and-pepper noise in classification of very-high-resolution satellite images. International Journal of Remote Sensing. (Accepted)

Lek, S., Guégan, J.-F., 1999. Artificial neural networks as a tool in ecological modelling, an introduction. Ecological modelling, 120(2), 65-73.

McNemar, Q., 1947. Note on the sampling error of the difference between correlated proportions or percentages. Psychometrika, 12(2), 153-157.

Mountrakis, G., Im, J., Ogole, C., 2011. Support vector machines in remote sensing: A review. ISPRS Journal of Photogrammetry and Remote Sensing, 66(3), 247-259.

Raczko, E., Zagajewski, B., 2017. Comparison of support vector machine, random forest and neural network classifiers for tree species classification on airborne hyperspectral APEX images. European Journal of Remote Sensing, 50(1), 144-154.

Robertson, L. D., King, D. J., 2011. Comparison of pixel-and object-based classification in land cover change mapping. International Journal of Remote Sensing, 32(6), 1505-1529.

Tomoyuki, H., Naoko, N., 2005. Tightening arrangement of multiple comparison tests. Bulletin of the Graduate School of Education, Hiroshima University, 54, 189.

Yang, B., Cao, C., Xing, Y., Li, X., 2014. Automatic Classification of Remote Sensing Images Using Multiple Classifier Systems. Mathematical Problems in Engineering, 2015.

THE ACCURACY OF EIGHT CHANGE DETECTION PROCEDURES FOR ISOLATING EXTREME VALUES RELATED TO CLOUDS: CASES OF MOUNTAINOUS AND COASTAL TROPICS

Dyah R Panuju[1,2], David J. Paull[1], Amy L. Griffin[3]

[1] School of Physical, Environmental and Mathematical Sciences, UNSW Canberra, Northcott Drive, Campbell, ACT 2600, Australia
[2] Department of Soil Science and Land Resource, Bogor Agricultural University, Jalan Meranti Kampus IPB Darmaga, Bogor 16680, Indonesia
[3] Geospatial Science Discipline, Royal Melbourne Institute of Technology (RMIT) University, Australia
Email: panuju@apps.ipb.ac.id

KEYWORDS: change detection, cloud isolation, tropics, IRMAD chi-square, PCA differencing

ABSTRACT. Detecting the alteration of features captured in two or more digital images is an essential step for understanding ecological process. Numerous techniques of bi-temporal analysis have been developed to detect change processes employing clear optical images. Each technique has advantages, nonetheless landscape complexity and noise affect the results. Cloud has been an important challenge for change detection employing optical images in tropical regions. Selecting appropriate methods to detect change while overcoming cloud problems is the main target of this research. A third class was added to the binary change map to isolate extreme values related to clouds. Two sites located in tropical regions representing predominantly mountainous and coastal zones were selected to evaluate the performance of eight change detection procedures. The results show that combining Iteratively Reweighted Multivariate Alteration Detection (IRMAD) with kernel clustering produced the best accuracy (92.7%) for the mountainous region of Halimun Salak National Park while a combination of PCA of index differencing with kernel clustering generated the highest accuracy (95.2%) for the coastal area in the North Coastal Region of West Java. The additional class used to isolate change was responded differently across procedures and sites, resulting in either increasing or decreasing accuracies. A few procedures increased while others decreased in missed detections and false alarms when including an additional class for isolating extreme pixels related to cloud.

1   INTRODUCTION

Rapid alteration of land surfaces have occurred in many tropical countries as a consequence of efforts to improve economic growth through increasing the intensity and modes of production of goods and services. Forest and agricultural management practices have adapted by changing activities from non-productive into more productive ones, which are reflected in alterations of land cover and land use. Various types of changed uses can be found in forest and agricultural uses, such as selective logging, replanting, or even a complete alteration into non-forest uses such as crop production, mining, or industrial activities. Similarly, agricultural management has intensified through activities such as cultivating crops with shorter growth cycles or converting agricultural land into industrial/services uses. Land surface monitoring should adapt to the heterogeneity of these dynamics.

Remote sensing plays an important role in monitoring the change of the environment. Advances in satellite and computing technologies support the possibility through the rise of freely accessible images that benefit from the acceleration of innovations in science and environmental monitoring (Wulder and Nicholas, 2014). Freely available Landsat images provided by the United States of Geological Survey in 2008 followed by MODIS products provided by the National Aeronautics and Space Administration (NASA) and MERIS from European Space Agency (ESA) allow continual monitoring, the scrutiny of change detection techniques, as well as their global application (Wulder and Nicholas, 2014). Available pre-processed images have accelerated the development of freely accessible tools such as SNAP (ESA) and R statistical software, which allows the comparison and selection of a range of available techniques suitable for specific locations. Meanwhile, the availability of very-high-resolution images such as IKONOS and Quickbird Google Earth assist in developing ground-truthing datasets for examining the accuracy of evaluated procedures.

Change detection techniques are generally grouped into bi-temporal or trajectory analysis (Singh, 1989). The differences between bi-temporal change detection and temporal trajectory analysis lie in the frequency of observations and information resulting from the analytical process (Gong et al., 2008). Bi-temporal analysis utilises two image acquisitions while trajectory analysis employs more frequent images from periodical observations. Bi-temporal analysis generally produces the location of change pixels, composition of change, or the direction of change,

while trajectory analysis mainly generates the temporal pattern of change (Mama, 1980, Mena, 2008). This research focuses on bi-temporal change detection.

Research comparing the robustness of bi-temporal change detection has demonstrated that no single technique consistently outperforms other techniques. For example, Macleod and Congalton (1998) demonstrated that differencing outperformed PCA and post-classification for detecting change in submerged aquatic vegetation while Ridd and Liu (1998) concluded that differencing and regression-based change detection methods resulted in comparable accuracies. By contrast, other research showed that post-classification outperformed differencing and principal components analysis (Mas, 1999). These variations in performance indicate the importance of assessing the performance of procedures when applying procedures for an area.

1.1   Bitemporal Change Detection

Bi-temporal change detection is a standard technique that is often used to identify land cover change processes using two image acquisitions. Reviews of bi-temporal change detection techniques showed the importance of pre-processing in ensuring that detected differences are due to change, not to other factors such as atmospheric disturbances or geometric factors (Lu et al., 2004; Singh, 1989). Pre-processing includes geometric, atmospheric and radiometric corrections, as well as transformation of images into new forms to represent physical properties, such as tasselled cap and indices.

A range of techniques have been developed to accurately generate change or probability of change maps. In their review, Lu et al. (2004) classified change detection techniques into several groups including map algebra operations, transforming images before implementing analysis, comparing post-classified images, advanced models, integrating GIS and remote sensing, visual analysis, and other techniques. An example of simple map algebra is differencing, which is the simplest concept for change analysis, subtracting reflectance observed at two time points to reveal change when noise can be suppressed.

Another simple map algebra technique is ratioing, which is recommended to deal with the effect of multiple values of reflectance from the same object observed at different times due to differences in gain and illumination. Ratioing has been applied to SAR and optical data (Chi et al., 2009; Holben and Justice, 1981). Applying ratioing to Landsat TM appeared to reduce topographical effects on radiance (Holben and Justice, 1981). Meanwhile, the use of ratioing in SAR images demonstrated its superior performance compared to differencing (Rignot and Van Zyl, 1993).

PCA is a transformation procedure that converts original spectral images into linear combinations by reducing redundancy of information in the original data (Richards, 1984). This transformation generates new datasets that contain decreasing proportions of variance and uncorrelated spectral information called components (Deng et al., 2008). According to Richards (1984), there are three main steps to performing PCA, i.e. deriving the covariance or correlation matrix, computing the eigenvectors, and transforming the datasets based on linear principles. In this research, image data inputs into the PCA are differenced or ratioed images from two image acquisitions. With descending variance across the components, it is expected that general pattern of change represented in the first components and the variance would gradually reduce by subsequent components.

A more recently developed technique for change detection is Iteratively Reweighted Multivariate Alteration Detection (IRMAD) (Nielsen, 2007). IRMAD is the modification of MAD, itself a well-established method for bi-temporal change detection (Marpu et al., 2011), that shows improvements in handling registration, spectral normalization, and spatial autocorrelation combined in one technique (Nielsen et al., 1998). The method is based on Hotteling's (1936) canonical correlation in which two sets of vector images taken at the same place, acquired at two time points, A=(A$_1$, ..., A$_k$) and B=(B$_1$, ..., B$_k$), are transformed into new images X= a^T A and Y= b^T B. From p spectral bands in two original images, a new image can be generated composed of p MAD-variates. The MAD-variates are orthogonal to each other and are ordered by descending variance or correlation if image vectors are standardised. The first variate contains the largest scale of change. To deal with different scales due to different gain factors and atmospheric conditions, standardising values by computing their correlation instead of their covariance was suggested. IRMAD's iterative processing is performed to improve separation among classes by adding more weight to no-change probabilities during the process (Nielsen, 2007). MAD has been applied to various ecological conditions, for instance in a coastal ecosystem (Bernardo et al., 2016) and forested areas (Schroeder et al., 2006). The procedure was tested on original and transformed Landsat images (Panuju et al., 2017).

A comparison of techniques showed the accuracy of change detection varied over various applications and sometimes was contrasting. Comparing differencing with PCA and post-classification detection, Macleod and Congalton (1998) showed that differencing outperformed PCA and post-classification detection. In contrast, Mas (1999) demonstrated

that post-classification detection was superior compared to differencing. An accurate technique for one specific application appears inaccurate in other applications. Therefore, comparing techniques applied to a site or data pair is essential to selecting the best technique for the case.

1.2 The Accuracy of Bi-temporal Techniques for the Detection of Land Cover Change

Common measures of the accuracy of bi-temporal change detection are similar to those applied to classification techniques, i.e. overall accuracy or the Kappa statistic (Fung and LeDrew, 1988). This measure generally calculates the proportion of observations that match with the reference (Lunetta et al., 1991). Accurate measures result in higher proportions of observations that match with the reference. Another measure that is used to assess accuracy is the error of the detection, for instance root mean square error (RMSE). Typically in change detection cases, error detection is employed to evaluate accuracy by assessing missed detections and false alarms (Bruzzone and Prieto, 2000; Zhuang et al., 2017). The overall error (OE) can be expressed as (Gong et al., 2017):

$$OE = FA + MD$$

where FA refers to false alarms denoting the number of pixels that are identified as changed by the change detection procedure that do not change in the reference image or called as error type I (Griffin and Bell, 2009). MD signifies missed detections, referring to the number of pixels, which are identified as unchanged by the applied change detection procedures but that did change in the reference image.

2 METHODOLOGY

2.1 Sites

This research was conducted in two locations in West Java. The first location is a predominantly mountainous area in the southern part of Jakarta, Indonesia's capital city. The first site extends from flat to undulating slopes with altitudes spanning between 0 and 2900 meters above sea level. Two national parks are found within this extent, i.e. Taman Nasional Gunung Halimun Salak and Taman Nasional Gede Pangrango, therefore we refer to it as National Parks (NP). The second site is located in the eastern part of Jakarta and is mainly a coastal area that was previously a major rice production area. We refer to it as the North Coastal Region of West Java (NCR). Its irrigation networks were built to support paddy and crop production in this region. The two sites are expected to provide a comparison of techniques applied to different microclimates.
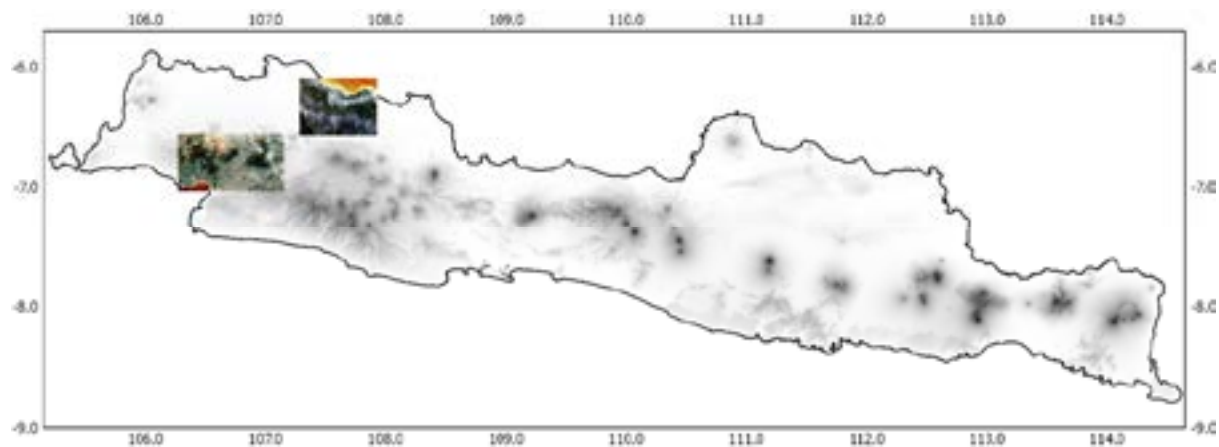

Figure 1. The site of change analyses representing predominantly mountainous (bottom) and coastal areas (top), located on Java. The images are RGB 1,2,3 from Landsat TM5 (bottom) and Landsat 8 (top).

2.2 Datasets

We employed Landsat TM5 and Landsat 8 to compare the performance of eight bi-temporal change detection procedures. The four images we studied were composed of an image from Landsat TM5 path 122, row 65 and a scene from Landsat 8 from the same path row, a scene of Landsat TM5 path 122, row 64, and an image from Landsat 8 from the same path/row. The characteristics of the data are presented in Table 1.

Table 1. Pairs of Landsat images (path 122, row 65) used for IRMAD processing

Properties	Pair-1	Pair-2
Path/row	122/065	122/064
Date-1 (t0)	24/7/2007	22/7/2007
Date-2 (t1)	17/6/2017	17/7/2017
Scene cloud cover (%) t0 & t1	9 & 27.79	6 & 3.75
Sun elevation of t0 and t1	48.9 & 48.8	48.81 & 50.00
Sun azimuth of t0 and t1	47.91 & 41.24	43.72 & 42.16
Sites name	National parks (NP)	North coastal region (NCR)

The images were in the form of surface reflectance, which is an atmospherically corrected product, systematically generated by the United States Geological Survey's (USGS) Landsat Ecosystem Disturbance Adaptive Processing System (LEDAPS). The products are freely available by order, and are specifically designed to support land use and land cover change studies and are sufficiently accurate for land monitoring services (Vuolo et al., 2015). Each pair consist of images acquired in July 2007 and July 2017. The images have relatively small amounts of cloud cover.

2.3 Methods

2.3.1 Pre-processing and the analysis

First, the images were reprojected, sub-setted, and concatenated from the multispectral images of surface reflectance provided by the USGS. Reprojected images were used to derive a set of indices comprising the Brightness Index (BI), Normalised Difference Vegetation Index (NDVI), and Normalised Difference Water Index (NDWI). Another transformation that we applied was tasselled cap, referring to Kauth and Thomas's procedure to derive Brightness, Greenness, and Wetness Indexes (Kauth and Thomas, 1976). The parameters for calculating tasselled cap for Landsat TM5 were based on Crist (1985), while for Landsat 8 we used the coefficients from Baig et al. (2014). Original surface reflectance and indices were then used as inputs for differencing and ratioing. The results of differencing and ratioing were analysed using principal components analysis (PCA). Meanwhile, for each pair, six bands of the original surface reflectance were processed with Iteratively Multivariate Alteration Detection (IRMAD), resulting six MAD-variates and a chi-square image.

Further processing included performing kernel k-means on each bundle of the chi square images from IRMAD, six MAD-variates, selected PCs that had at least 85% variance of kernel PCA, differencing and ratioing of TC, and differencing and ratioing of the set of indices. Kernel k-means is used to produce two and three classes by assuming that there may be an amplification of values due to cloud presence even if the atmospheric correction has been suppressed during surface reflectance transformation. These classes included unchanged, changed (in the case of two classes), and an additional class that is expected to represent cloud cover or shadow (in the case of three classes).

For the PCA, the graph of consecutive principal components eigenvalues was used to determine the number of components to be included. The number of components is determined by the point where the slope is approaching zero, meaning that any additional contribution of the remaining components is trivial to the variances of the dataset. Four components were identified from the analysis, thus the clustering employed four PCA components from the differencing or ratioing of the image pairs. The proportional variances of the components derived from PC differencing and ratioing of first dataset (The National Parks - NP) were 92.0% and 89.1%, respectively, while for the second dataset (North Coastal Region of West Java – NCR) were 90.6% and 91.8%, respectively. The proportions were considered sufficient to represent the information of the images.

2.3.2 Accuracy assessment

The accuracy of these eights techniques was assessed by taking training samples whose selection was guided by the original images, Google Earth, and field surveys. The total number of samples for the first site (NP) was 260 and included three classes, changed, unchanged, and extreme values due to clouds. The second site (NCR) was tested with 310 samples. Training samples were chosen using stratified random sampling to include proportional representation from each of the classes. Samples were then examined and matched with historical images available in Google Earth. When nearby dates for employed image pair were not available then images from dates immediately before and after these dates were recorded. At least two dates were observed as the reference for examining change processes. Most locations were recorded at more than three high resolution images such as IKONOS, Quickbird, or Geo Eye available in Google Earth. Change detection accuracy was assessed using overall accuracy and two

components of error detection, i.e. missed detections and false alarms. The use of missed detection and false alarms was found in change detection of images applied by researchers such as Bruzzone and Prieto (2000).

3   RESULT AND DISCUSSION

3.1   The accuracy of eight techniques for change, unchanged and extreme classes

Table 2 presents the accuracy comparison for the eight change detection procedures. A trade-off between error and accuracy was shown, as commonly found in accuracy assessment. For the two-class NP case, IRMAD variates followed by differencing indices generated the highest accuracies at 91.2% and 90.8%, respectively. Different techniques produce the highest accuracy at NCR, i.e. PCA ratioing followed by PCA differencing at 90.6% and 75.8%, respectively.

The accuracy of several techniques increased by adding a class for isolating extreme values, but more procedures resulted in lower accuracies. The highest three-class accuracy found in NP occurred with IRMAD chi-square followed by ratioing of tasselled cap. Those procedures resulted in accuracies of 92.7% and 82.3%, respectively. On the other hand, the lowest accuracy was generated by differencing the tasselled cap indexes at 39.6%. Superior techniques for NCR appeared to be different from NP. The three procedures generating the highest accuracies were PCA differencing (95.2%), followed by differencing indices (85.8%), and IRMAD variates (76.5%).

Table 2. Comparing the accuracy of two and three classes of change at two sites, NP and NCR. Bold letters indicate accuracy greater than 75%. Red and blue letters indicate decreasing and increasing accuracy of at least 10% accuracy by adding an additional class for extreme values isolation.

Sites	Methods	Accuracy of (%)		Δ accuracy
		2 classes	3 classes	
National parks (NP)	Differencing indices	**90.8**	62.7	-28.1
	Differencing TC	51.9	39.6	-12.3
	PCA differencing	63.5	62.3	-1.2
	Ratioing indices	45.8	66.9	21.1
	Ratioing TC	**76.2**	**82.3**	6.1
	PCA ratioing	55.8	68.8	13.0
	IRMAD variates	**91.2**	73.8	-17.4
	IRMAD chi-square	73.8	**92.7**	18.9
North coastal region (NCR)	Differencing indices	49.4	31.3	-18.1
	Differencing TC	70.3	42.3	-28.0
	PCA differencing	**75.8**	**95.2**	19.4
	Ratioing indices	56.8	37.4	-19.4
	Ratioing TC	60.3	38.4	-21.9
	PCA ratioing	**90.6**	**85.8**	-4.8
	IRMAD variates	67.7	**76.5**	8.8
	IRMAD chi-square	66.5	60.0	-6.5

There was a variable response in terms of change detection accuracy levels when adding a third class. For national parks (NP), three procedures increased in accuracy by more than 10% using three classes, including ratioing indices, chi-square IRMAD, and PCA ratioing, respectively. Three procedures that decreased in accuracy by 10% with class addition were differencing indices, MAD-variates and differencing TC, respectively. For the NCR site, differencing indices and differencing TC consistently decreased by more than 10% with an additional class to isolate extreme values. The opposite response when compared with NP of increasing accuracy by adding a class was observed for NCR for ratioing indices and ratioing TC. These two techniques decreased in accuracy by -19.4% and -21.9, respectively, with the additional class to isolate extreme values.

Various factors may dictate the performance of change detection procedures, including the quality of images represented by the distribution of clouds and other noise over the images, the differing conditions between the pairs,

and the sensitivity of procedures to deal with those factors. The cloud difference between pairs (18% for NP and 5% for NCR) and their distribution may have affected accuracies. A slightly bigger proportion of cloud cover in NP compared to NCR may have contributed to generated accuracies.

3.2 Error detection for eight change detection procedures and extreme value isolation

The error detection including missed detections and false alarms were used to group the responses of tested procedures in isolating extreme values. The results show that none of techniques consistently generated typical patterns of error rates across sites or classes (changed, unchanged, and extreme). Figure 2 shows missed detections and false alarms generated by procedures across sites and classes. The reduction of missed detections by adding a class for National Parks was identified in five procedures including chi-square IRMAD, ratioing TC, ratioing indices, PCA ratioing, and PCA differencing, respectively. Three other procedures increased the missed detections when adding an additional class, i.e. differencing indices, MAD-variates, and differencing TC, respectively. Using the same strategy for the NP site, one technique generated fewer missed detections after adding an additional class in NCR, i.e. ratioing indices. Other techniques produced more missed detection by a class.

Different patterns of decreased numbers of false alarms were found across the change detection procedures by additional class for extreme value isolation. Two procedures, i.e. ratioing indices and PCA ratioing produced fewer false alarms when the third class was added, while false alarms increased for other techniques at the NP site. Two different procedures had increased numbers of false alarms for the NCR site, i.e. ratioing TC and differencing TC.

Generally, missed detections indicate the insensitivity of a technique to detect changes or extreme values, while false alarms suggest oversensitivity of a technique to differing spectral values. Experts have demonstrated the importance of geometric correction to reduce error detection. Nonetheless, since the analysis was performed on the same post-geometrically-corrected images, this factor should not be varying. It is likely that other non-geometric factors are affecting the error detection, such as the heterogeneity within the spatial extent and between pairs.
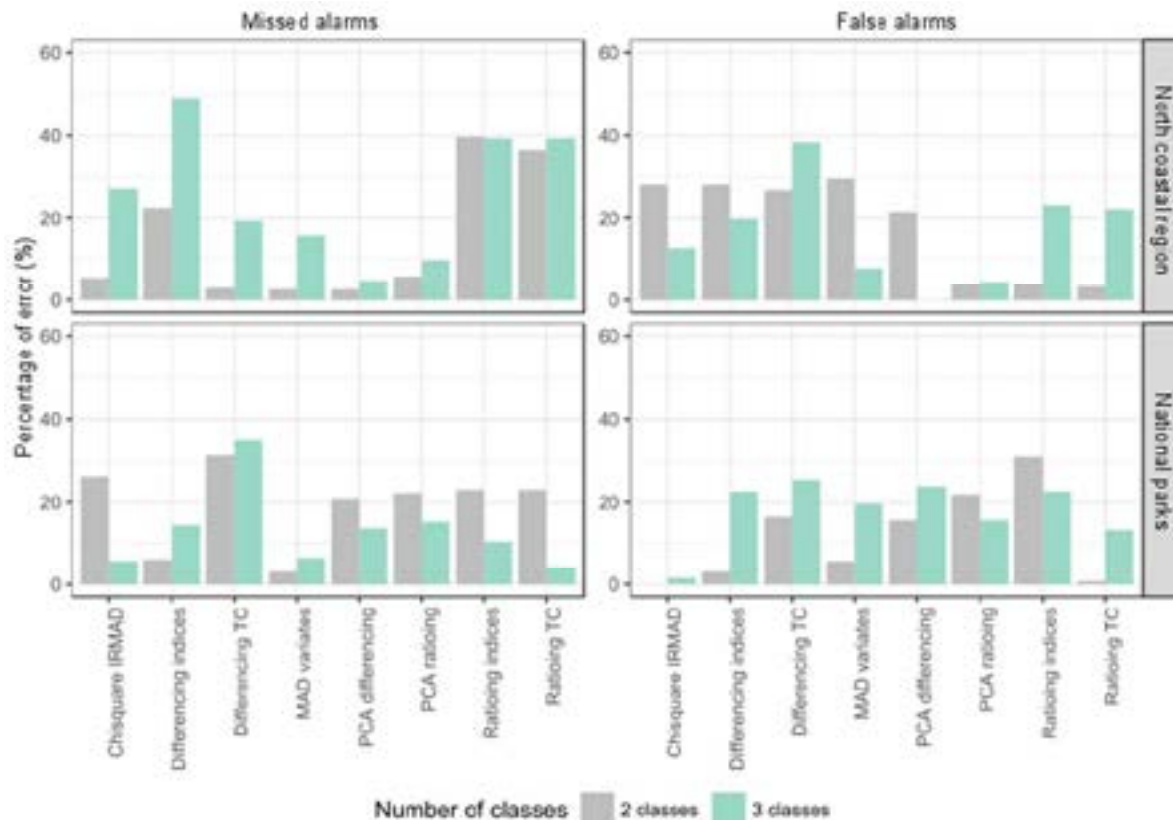

Figure 2. Missed detections and false alarms resulted from eight change detection procedures at two sites, i.e. NP and NCR

With a higher proportion of cloud cover in NP than NCR, change can be detected more accurately in NP using IRMAD or ratioing TC. These two procedures appear to be suitable for dealing with mountainous areas predominantly covered by vegetation. As suggested by Yuan and Elvidge (1998), a PCA of either differencing or

rationing may not be suitable for heterogeneously vegetated areas. Our results confirm the suggestion that PCA is not particularly suitable for vegetated areas. Meanwhile, the higher proportion of cloud cover in the NP site appears to be efficiently tackled using IRMAD and ratioing TC and results in comparable accuracy that achieved for NCR, which has a lower proportion of cloud cover.

NCR is a coastal region that is mainly covered by paddy fields, ponds, and beaches. A lower percentage of cloud appears to result in somewhat greater change detection accuracy. PCA of either differencing or ratioing appears superior when dealing with more waterbodies with less cloud at NCR. Other techniques were less efficient in detecting change, resulting in more false alarms or missed detections. Research conducted in swamp forests concluded that false alarms were often associated with waterlogging (Whittle et al., 2012).

4 CONCLUSION

Research comparing the robustness of bi-temporal change detection procedures demonstrated that no single procedure consistently outperformed other techniques. Many researches concluded variably on the accuracy performance of techniques resulted from optical sensors. Eight bi-temporal techniques were investigated to compare the robustness of the techniques across two different micro-climates, mountainous and coastal areas. The procedures included differencing indices, differencing tasselled cap, ratioing indices, ratioing tasselled cap, PCA differencing, PCA ratioing, IRMAD variates, and IRMAD chi-square.

The highest accuracy found in NP, a site characterised by mountainous areas, resulted when IRMAD chi-square was applied, followed by ratioing of tasselled cap, while superior procedures for the coastal area (NCR) were PCA differencing followed by PCA ratioing. Change occurrences from images affected by higher proportion of cloud cover predominated with vegetation in the NP can be better detected with IRMAD or ratioing TC. The change and extreme pixels at NCR predominated with waterlogged areas appearing to be better detected when using PCA differencing and PCA ratioing. Additional classes for extreme values isolation appear to either reduce or increase error detection. It is likely that non-geometric factors are affecting the error detection, such as the heterogeneity within the spatial extent and between pairs.

5 ACKNOWLEDGEMENT

REFERENCES

Baig, M.H.A., Zhang, L., Shuai, T. and Tong, Q., 2014. Derivation of a tasselled cap transformation based on Landsat 8 at-satellite reflectance. Remote Sensing Letters, 5 (5), pp. 423-431.

Bernardo, N., Watanabe, F., Rodrigues, T. and Alcântara, E., 2016. An investigation into the effectiveness of relative and absolute atmospheric correction for retrieval the TSM concentration in inland waters. Modeling Earth Systems and Environment, 2 (3), pp. 114.

Bruzzone, L. and Prieto, D.F., 2000. Automatic analysis of the difference image for unsupervised change detection. IEEE Transactions on Geoscience and Remote Sensing, 38 (3), pp. 1171-1182.

Chi, H., Sun, G. and Ling, F., 2009. Urban dynamic change detection in southeastern China based on interferometric SAR, 2009 IEEE International Geoscience and Remote Sensing Symposium, pp. III-432-III-435.

Crist, E.P., 1985. A TM tasseled cap equivalent transformation for reflectance factor data. Remote Sensing of Environment, 17 (3), pp. 301-306.

Deng, J.S., Wang, K., Deng, Y.H. and Qi, G.J., 2008. PCA-based land-use change detection and analysis using multitemporal and multisensor satellite data. International Journal of Remote Sensing, 29 (16), pp. 4823-4838.

Fung, T. and LeDrew, E., 1988. The determination of optimal threshold levels for change detection using various accuracy indices. Photogrammetric Engineering and Remote Sensing, 54 (10), pp. 1449-1454.

Gong, J., Sui, H., Ma, G. and Zhou, Q., 2008. A review of multi-temporal remote sensing data change detection algorithms. The International Archives of the Photogrammetry, Remote Sensing and Spatial Information Sciences, 37 (B7), pp. 757-762.

Gong, M., Zhan, T., Zhang, P. and Miao, Q., 2017. Superpixel-based difference representation learning for change detection in multispectral remote sensing images. IEEE Transactions on Geoscience and Remote Sensing, 55 (5), pp. 2658-2673.

Griffin, A.L. and Bell, S., 2009. Applications of Signal Detection Theory to Geographic Information Science. Cartographica: The International Journal for Geographic Information and Geovisualization, 44 (3), pp. 145-158.

Holben, B. and Justice, C., 1981. An examination of spectral band ratioing to reduce the topographic effect on remotely sensed data. International journal of remote sensing, 2 (2), pp. 115-133.

Kauth, R. and Thomas, G., 1976. The tasselled cap--a graphic description of the spectral-temporal development of agricultural crops as seen by Landsat, LARS Symposia, pp. 159.

Lu, D., Mausel, P., Brondízio, E. and Moran, E., 2004. Change detection techniques. International Journal of Remote Sensing, 25 (12), pp. 2365-2401.

Lunetta, R.S., Congalton, R.G., Fenstermaker, L.K., Jensen, J.R., McGwire, K.C. and Tinney, L.R., 1991. Remote sensing and geographic information system data integration: error sources and research issues. Photogrammetric Engineering & Remote Sensing, 57 (5), pp. 677-687.

Macleod, R.D. and Congalton, R.G., 1998. A quantitative comparison of change-detection algorithms for monitoring eelgrass from remotely sensed data. Photogrammetric Engineering and Remote Sensing, 64 (3), pp. 207-216.

Malila, W.A., 1980. Change vector analysis: an approach for detecting forest changes with Landsat, LARS symposia, pp. 385.

Marpu, P.R., Gamba, P. and Canty, M.J., 2011. Improving change detection results of IRMAD by eliminating strong changes. IEEE Geoscience and Remote Sensing Letters, 8 (4), pp. 799-803.

Mas, J.F., 1999. Monitoring land-cover changes: a comparison of change detection techniques. International Journal of Remote Sensing, 20 (1), pp. 139-152.

Mena, C.F., 2008. Trajectories of land-use and land-cover in the northern Ecuadorian Amazon: Temporal composition, spatial configuration, and probability of change. Photogrammetric Engineering and Remote Sensing, 74 (6), pp. 737-751.

Nielsen, A.A., 2007. The regularized iteratively reweighted MAD method for change detection in multi- and hyperspectral data. IEEE Transactions on Image Processing, 16 (2), pp. 463-478.

Nielsen, A.A., Conradsen, K. and Simpson, J.J., 1998. Multivariate alteration detection (MAD) and MAF postprocessing in multispectral, bitemporal image data: New approaches to change detection studies. Remote Sensing of Environment, 64 (1), pp. 1-19.

Panuju, D.R., Paull, D.J., Griffin, A.L. and Trisasongko, B.H., 2017. The performance of iteratively reweighted multivariate alteration detection (IRMAD) applied on untransformed and transformed Landsat surface reflectance, 38th Asian Conference on Remote Sensing - Space Applications: Touching Human Lives. Asian Association on Remote Sensing, New Delhi, India, pp. 317-325.

Richards, J.A., 1984. Thematic mapping from multitemporal image data using the principal components transformation. Remote Sensing of Environment, 16 (1), pp. 35-46.

Ridd, M.K. and Liu, J.J., 1998. A comparison of four algorithms for change detection in an urban environment. Remote Sensing of Environment, 63 (2), pp. 95-100.

Rignot, E.J. and Van Zyl, J.J., 1993. Change detection techniques for ERS-1 SAR data. IEEE Transactions on Geoscience and Remote sensing, 31 (4), pp. 896-906.

Schroeder, T.A., Cohen, W.B., Song, C., Canty, M.J. and Yang, Z., 2006. Radiometric correction of multi-temporal Landsat data for characterization of early successional forest patterns in western Oregon. Remote Sensing of Environment, 103 (1), pp. 16-26.

Singh, A.N., 1989. Review Article Digital change detection techniques using remotely-sensed data. International Journal of Remote Sensing, 10 (6), pp. 989-1003.

Vuolo, F., Mattiuzzi, M. and Atzberger, C., 2015. Comparison of the Landsat Surface Reflectance Climate Data Record (CDR) and manually atmospherically corrected data in a semi-arid European study area. International Journal of Applied Earth Observation and Geoinformation, 42, pp. 1-10.

Whittle, M., Quegan, S., Uryu, Y., Stuewe, M. and Yulianto, K., 2012. Detection of tropical deforestation using ALOS-PALSAR: A Sumatran case study. Remote Sensing of Environment, 124, pp. 83-98.

Wulder, M.A. and Nicholas, C.C., 2014. Make Earth observations open access: freely available satellite imagery will improve science and environmental-monitoring products. Nature, 513 (7516), pp. 30.

Yuan, D. and Elvidge, C., 1998. NALC land cover change detection pilot study: Washington DC area experiments. Remote sensing of environment, 66 (2), pp. 166-178.

Zhuang, H.F., Deng, K.Z. and Fan, H.D., 2017. Filtering Approach Based on Voter Model and Spatial-Contextual Information to the Binary Change Map in SAR Images. Journal of the Indian Society of Remote Sensing, 45 (5), pp. 733-741.

OIL SPILL SIGNATURE VARIANTS FOR OPTIMUM DETECTION AND TRACKING WITHIN VISIBLE SHORTWAVE TO THERMAL INFRARED BANDS

Jamal Jasim Abdulla Althawadi (1)(2), Mazlan Hashim(1)(2)(*)

[1]Geoscience & Digital Earth Centre (INSTEG), Research Institute for Sustainable Environment (RISE), Universiti Teknologi Malaysia, Johor Bahru, Malaysia
[2]Faculty of Built Environment & Surveying, Universiti Teknologi Malaysia, Johor Bahru, Malaysia

*corresponding author: E-Mail mazlanhashim@utm.my

ABSTRACT: This paper reports on the variations analyses of oil spill signatures with visible-shortwave bands of Landsat ETM+, Landsat OLI and Sentinel-2 MSI sensors over Arabian Gulf area. Factors to spill signature variants are emphasized within the inherent scalar element of the data acquisition of the sensors systems. Feature-based detection employing both point and region-based techniques were adopted to suit the multi-sensor data spatial-resolutions in detecting the spills, later employed for extraction of spill-pixels for the signature's analyses. Variants between spill signatures were characterized by calibration analysis approach. Results indicated that pre-processed and atmospherically corrected spill signatures is reasonably consistence with standard spills records with high correlation ($R^2 > 0.85$, $p < 0.001$). Calibration matrices for calibrating spill pixels for ETM+, OLI and MSI have been formulated, crucial input for spill monitoring system against local uncertainties of look-alikes.

KEYWORDS: oil spills, spectral signatures, variants, Landsat-7 ETM+, Landsat 8 OLI, Sentinel-2 MSI index

1. INTRODUCTION

Remarkable advances have been made on satellite-based oil spills detection and tracking. The most significant spectral regions actively engaged in these studies ranging from the visible, shortwave to thermal infrared (optical), and the microwave radar bands. The key elements in detecting the spill in both optical and radar bands are the ability to characterize the uniqueness of emanating interactions of incident energy on spills against the background, respectively. Given the background settings determined by the sea/ocean surfaces conditions and corresponding local weather systems, such as producing large variations in resultant signatures of spills. Large variants within spill signatures caused high uncertainties in delineating between spills and look-alikes. As in the past 2 decades researchers have invested efforts on studies that emphasizes on detection and mapping spills against the background (Garcia-Pineda *et al.*, 2017; Mullin, 2017; Topouzelis, 2008). These are rather relative analysis of spills signatures against the lookalikes and backgrounds. The previous studies rarely addressed the uniqueness of oil spills at absolute level, neither reporting the vectors of spills against background targets.

Oil spills originates at time of spills (fresh occurrence) with the characteristics of its viscosity and floating on above water surface, which depends on the volume and the surrounding environmental factors such as wind velocity. The models used for spills with environmental dynamics have been addressed in numerous past studies (Cheng *et al.*, 2011; Guo, 2017; Spaulding, 2017), however the characteristics of the spill signatures interactions within the environment is also not being addressed. Nonetheless, development in remote sensing (RS) applications of characterization particularly in extracting oil spill signatures, have been a progressive process and an evergreen study, from 2000 to the recent years (Bhangale *et al.*, 2017; Fiscella *et al.*, 2000). Satellite-based RS for oil spill monitoring based on medium-resolution data of MODIS, infrared, hyperspectral, multi-source, multi-temporal and multispectral, as well as radar data have adequately been explored. This article aimed at reporting on the spectral signatures of oil spills using various optical-based medium-resolution satellites data, namely Landsat TM, Landsat OLI, and Sentinel2-MSI. Specifically, the objective is to identify the variants within signatures of the oil spills around Arabian Gulf, from multi-satellite sensors after being treated for pre-processing and producing the complete signatures matrix, which is very essential for calibration of all the satellite-based oil spill-leaving reflectance. Furthermore, the known spectral library of the spill was used as standard in the calibration, while the spectral of NASA oil films (Clark *et al.*, 2010) is used in the calibration.

2.   MATERIALS AND METHOD

2.1   Study Area

The study area is the Arabian Gulf (see Figure 1). Geographically located between Arabian Peninsula and southwestern Iran, covering a sea area of about 241,000 km^2 with 990 km total length and width range from 55km to 340km (Powers *et al.*, 1966). It is part of Indian Ocean shallow region that surrounded by Kuwait, Saudi Arabia, Bahrain, Qatar, United Arab Emirates, Iraq, Oman and Iran. In this study, recent spill occurrences from January 2016 to January 2018 have been compiled for the signature studies, together with the corresponding spill records filed from Marine Emergency Mutual Aid Centre (MEMAC). Within this period, 7 main spill locations, designated as A to G in Figure 1. For each of the location, the 3 subsets of satellite image namely Landsat-7 ETM+, Landsat-8 OLI and Sentinel-2 MSI were extracted to show the spills area. Spill areas were noted ranging from area of 800-contiguous pixels to nearly 50,000 pixels, of various shapes, influenced by local wind and current conditions.
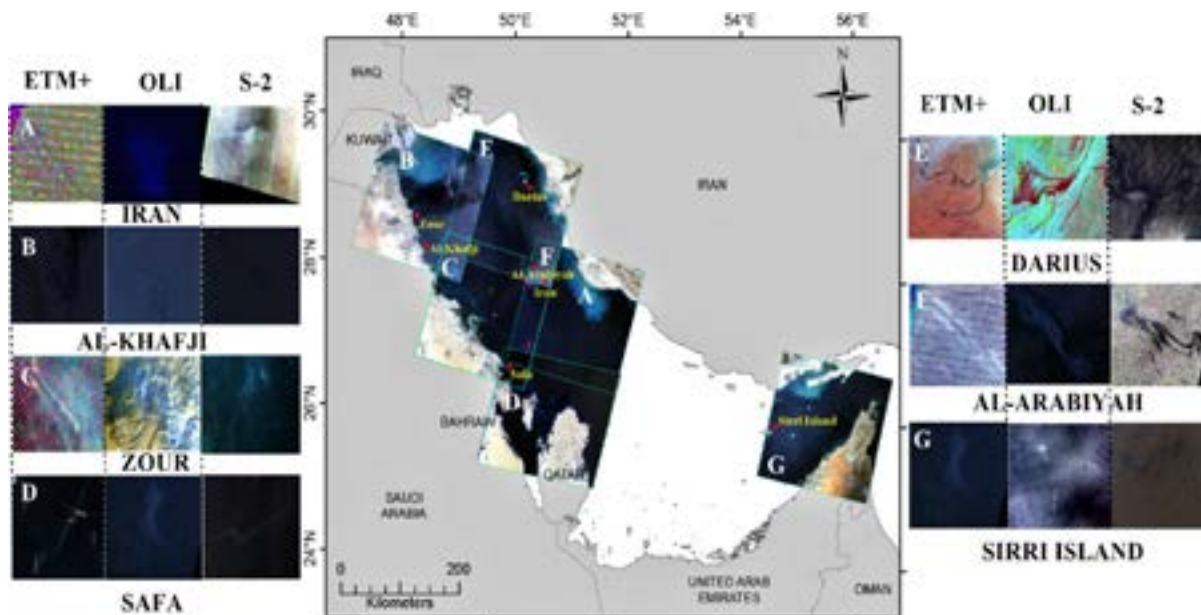

Figure 1. Study area – oil spills occurrences 2016-2017. Scene boundary line between all satellite images selected and used in this study.

Table 1. Date of satellite imagery used for oil detection in Arabian Gulf

Location	Date of oil spill	Landsat 7 ETM+	Landsat 8 OLI	Sentinel-2 MSI
Al-Khafji	9/5/2016	18/5	10/5	17/7
Iran	9/10/2016	11/10	19/10	12/10
Zour	10/8/2017	18/8	17/8	11/8
Darius	8/8/2017	18/8	10/8	11/8
Al-Arabiyah	26/9/2017	28/9	27/9	30/9
Safa Oilfield	25/8/2017	27/8	26/8	28/8
Sirri Island	7/9/2017	7/9	15/9	14/9

2.2   Satellite Data

The three sets of satellite data used in this study are Landsat-7 ETM+, Landsat-8 OLI and Sentinel-2 MSI. These data were acquired during spill occurrences. Detailed of the data sets are tabulated in Table 1. The sea-truths for oil spill occurrences records and look-likes were obtained from the records of maritime notices and costal authorities of the region.

2.3 Satellite Data Processing

The entire satellite images used were pre-processed for radiometric, atmospheric and geometric corrections. Feature-extractions for spill pixels were also carried out in the data processing stage, followed by the related signature analyses. In pre-processing stage, image subset and image masking were performed in order to minimize all geometric distortions inherent in the image. The image was geo-referenced to the UTM coordinate system, datum WGS-84 area 48N using a set of ground control points (GCP) identifiable both in the satellite. Digital map of the study area from reliable source is used as reference to correct geometric distortion of both the images. A sentinel threshold value of ± 0.5 pixel or less was enforced in the geometric correction, hence ensuring all images used were accurately registered to corresponding map of the area. The resampling schemes of nearest neighbor were finally selected to transform all pixel brightness recorded in digital number (DN) from raw images so as to ensure minimal radiometric alterations.

The atmospheric corrections of these image set were performed in order to minimize the atmospheric effects at the time of data acquisition. This includes the minimization of scattering effects on adjacent pixels. The atmospheric correction for all the spectral bands of all images used (Fast Line-of-sight Atmospheric Analysis of Hypercubes) FLAASH program of the ENVI V5 software. The algorithm is presented in equation 1.

$$L_i = \left(\frac{A_\rho}{1 - \rho_e S} \right) + \left(\frac{B\rho_e}{1 - \rho_e S} \right) + L_a \tag{1}$$

where:

L_i = the spectral radiance at sensor pixel;
ρ = the pixel surface reflectance;
ρ_e = an average surface reflectance for the pixel and a surrounding region;
S = the spherical albedo of the atmosphere;
L_a = the radiance back scattered by the atmosphere; and
A and B = coefficients that depend on atmospheric and geometric conditions but not on the surface.

Next, radiometric correction involves conversion of digital value in all pixels into reflectance of radiance unit. Landsat ETM+, Landsat OLI and Sentinel-2 has different mathematic model to convert the pixel. In opposite to Landsat ETM+, Landsat OLI image can directly convert its DN to reflectance value (L_λ). The rescaling gains and biases for Landsat 8 OLI satellite data were obtained following:

$$\rho_\lambda' = M\rho Qcal + A_{p\;AL} \tag{2}$$

where:

ρ_λ' = TOA spectral radiance (Watts/ (m^2 * srad * μm));
$M\rho$ = Band-specific multiplicative rescaling factor from the metadata;
$A\rho$ = Band-specific additive rescaling factor from the metadata; and
Q_{cal} = Quantized and calibrated standard product pixel values (DN).

Lastly, the spill signatures within the spectral band were performed, extracting all spill pixels using both spatial and feature based entities. Within the spatial-based context, the location of each pixels is noted, while the features are DN values within all the spectral bands. The DN of pixel of Landsat ETM we extracted using established calibration tool for Landsat ETM+ in ENVI software where all input parameters at the time of satellite data acquired including the illumination geometry such as sun elevation angle (Roy et al., 2008) are essential, and these were obtained from the respective image file header. For the Sentinel-2 MSI data, this DN conversion was performed by dividing each spectral band (visible bands) with absolute 10 to obtain reflectance unit of each pixel (refs on sentinel visible conversion) (Toming *et al.*, 2016). The region-based segmentation technique in ENVI system was used to extract all pixels, initiating seed points to identified locations of spill as reported in the ancillary information of the

respective 7 locations. The generated spill segments are shown in insets of Figure 1 (A – G), whereas, summary of the spills locations are tabulated in Table 2.

Table 2. Summary of spills identified based on regions grown from satellite images by initial seed points located at location of reported spill occurrences.

Location	Landsat-7 ETM+		Landsat-8 OLI		Sentinel-2 MSI	
	Total pixel	Area (km²)	Total pixel	km²	Total pixel	km²
Iran	1,033	0.92	8,106	7.3	167,317	16.73
Al-Arabiyah	5,271	4.74	51,492	46.34	559, 343	55.93
Zour	222	0.2	3,470	3.12	73,753	7.38
Darius	9,519	8.57	6,508	5.86	101,877	10.19
Alkhafji	98	0.09	853	0.77	64,594	6.46
Safa	810	0.73	55,887	50.3	33,285	3.33
Sirri	17,786	16.01	2,091	1.88	72,450	7.25

3. RESULTS & DISCUSSION

The spill signatures from all the visible bands of the satellite image sets were categorized into 3 main spectral visible regions namely red (R), green (G) and blue (B). All the spill signatures extracted for each location were averaged out for each spill events, recorded in the 3 spectral regions according to the sensor systems. Hence, the study utilized 3 sets of RGB signatures for ETM+, OLI and MSI, respectively.

To analyses, the variants of these signatures RGB spectral bands were plotted against the corresponding spectral responses recorded of oil slick film over seawater (Clark*, et al.*, 2010). See Figure 2 for illustrations of variations, where comparator spectra are marked as in-situ reflectance. Each column (left to right) represents signatures of Landsat-7 ETM+, Landsat-8 OLI and Sentinel-2 MSI. The row (top to bottom) represents the blue, green and red spectral regions. Linear regression analyses were carried out of these plotted signatures sets, reporting at 0.001 significant level, the R^2 were reported consistence ranges of 0.79 – 0.99, 0.72- 0.86, and 0.82 – 0.98 for ETM+, OLI and MSI, respectively. The MSI higher range is expected as the finer spatial resolution where depicting finer detailed spills superbly noted. Likewise, analyses on the spectral regions, clear indication of consistencies in the processed satellite-derived signatures. The blue signatures are observed more variants compared to green and red, and these can be explained due to more intricateness of interaction of incoming solar radiation to the surface targets (spills, and water surface background). Scattering effects also noted higher theoretically within blue spectral region compared to green and red. The least variation is in red, observed with R^2 of more than 0.86. Within this Figure 2, one of the most important results is the contribution on the reporting on absolute oil spill signatures within visible bands for the region (Arabian Gulf). This is partial outputs of the on-going works for the entire spectral region including near Infra-red and Thermal infrared regions. Without these absolute signatures indicators of spill, a monitoring spill system would be based on relative analysis, risky on reporting the look-alikes. A full spectral library of spills of the area can now be anticipated for high certainty future spill monitoring system.

The other important inference that could be derived these signature variations reported is the opportunity of using this information create a calibration matrix for spill calibrations obtained from images, e.g. in this case acquired from ETM+, OLI and MSI, such that:

$$\begin{bmatrix} R_{ETM} \\ G_{ETM} \\ B_{ETM} \end{bmatrix} = \begin{bmatrix} R_i & G_i & B_i \end{bmatrix}. \begin{bmatrix} 0.3662 \\ 1.0642 \\ 5.0216 \end{bmatrix} + \begin{bmatrix} -0.0603 \\ -0.0137 \\ 0.0012 \end{bmatrix} \qquad (3)$$

$$\begin{bmatrix} R_{OLI} \\ G_{OLI} \\ B_{OLI} \end{bmatrix} = [R_i \quad G_i \quad B_i] . \begin{bmatrix} 7.5500 \\ 1.6630 \\ 2.2480 \end{bmatrix} + \begin{bmatrix} -0.1479 \\ -0.0044 \\ -0.1222 \end{bmatrix} \qquad (4)$$

$$\begin{bmatrix} R_{MSI} \\ G_{MSI} \\ B_{MSI} \end{bmatrix} = [R_i \quad G_i \quad B_i] . \begin{bmatrix} 0.7504 \\ 2.0856 \\ 0.7504 \end{bmatrix} + \begin{bmatrix} 0.0072 \\ -0.0361 \\ 0.0072 \end{bmatrix} \qquad (5)$$

where:

R_{ETM}, G_{ETM}, B_{ETM} are calibrated ETM bands in red, green and blue spectral region,
R_{OLI}, G_{OLI}, B_{OLI} are calibrated OLI bands in red, green and blue spectral region,
R_{MSI}, G_{MSI}, B_{MSI} are calibrated MSI bands in red, green and blue spectral region,
R_i, G_i and B_i are spill pixels within red, green and blue spectral region,
The coefficients for R_i, G_i and B_i are gains for red, green and blue spectral region, and
The constants in last matrix term are the offsets for red, green and blue spectral region.
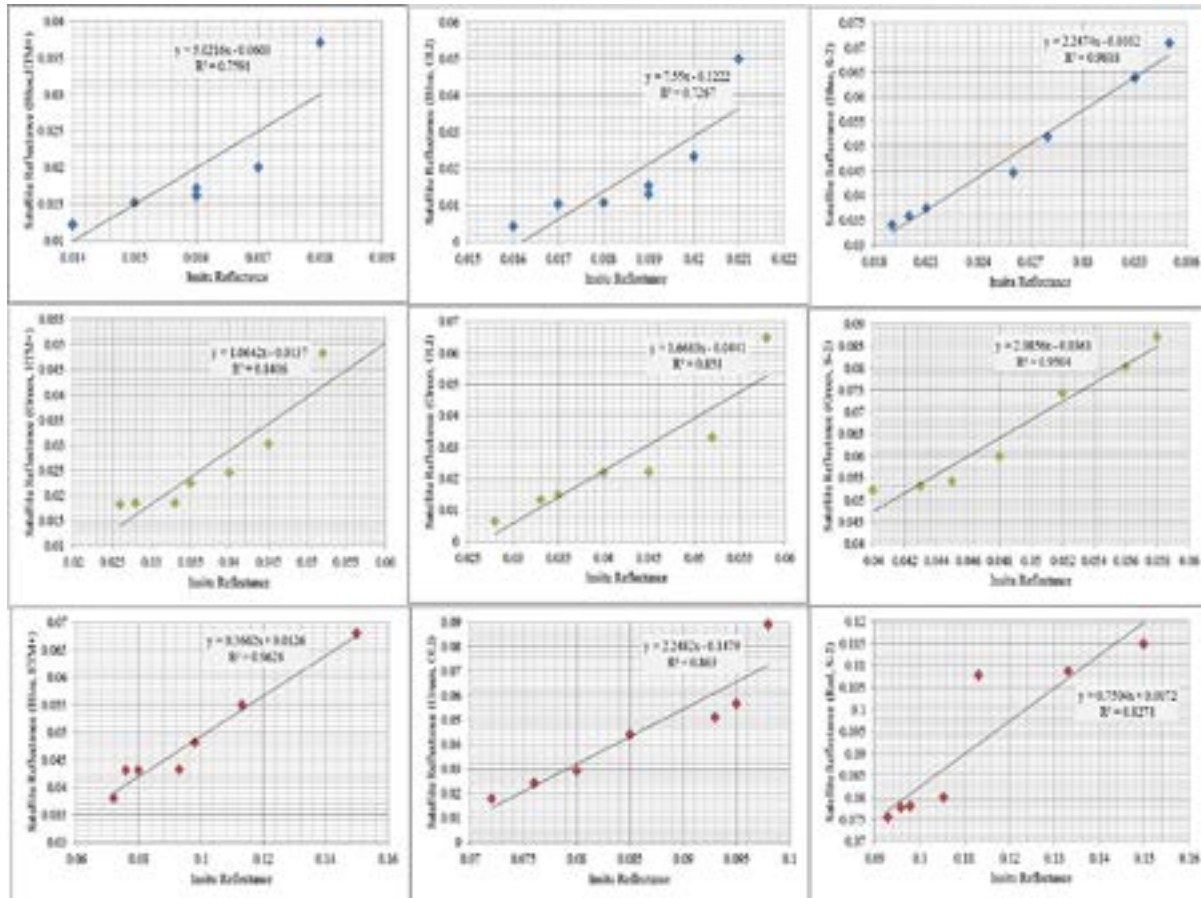
Figure 2. Variations of means-of-spill signatures from 7 occurrences against spill signatures of NASA (Clark, *et al.*, 2010). Each column (left to right) represents signatures of Landsat-7 ETM+, Landsat-8 OLI and Sentinel-2 MSI. The row (top to bottom) represents the blue, green and red spectral regions.

The signature calibration matrix and the related concept would be of crucial inputs in automated spill-monitoring system in two folds: extraction absolute spills signatures within the known spectral regions irrespective of satellite system used. Secondly, the matrices provide ready-ingest for rigorous computational aspects in the digital image processing of the system.

Final assessment of the calibrated signatures spill pixels in Al-khafji (Site B in Fig. 1) for significant tests for:

(i) T-test for Ho : the means of calibrated spill pixels treated using matrices of (3), (4), (5) for ETM+, OLI and MSI is similar to standard in-situ oil film signatures in Red, Blue and Green bands; and
(ii) F-test for Ho: the variation of treated spill pixels is similar to the variation of standard in-situ oil film signatures in Red, Blue and Green bands. Results of the test are tabulated in Table 3, where all test results indicated acceptances of similar mean and variations. This confirms the usability of these matrices for spill signatures calibration at absolute spectral values.

Table 3. Summary of significant tests for mean and variance of spill signatures treated with calibrated matrices.

	t-Test	F-test	p	inference
Landsat ETM+	0.000935	0.000320	0.005	Accept Ho
Landsat OLI	0.073551	0.150965	0.005	Accept Ho
Sentinel-2 MSI	1.20E-14	0.011874	0.005	Accept Ho

4. CONCLUSION AND FUTURE DIRECTION

In summary, variations within oil spill signatures for Arabian Gulf occurred within 2016-2017, within this period, 7 reported main spill locations, have been highlighted. Emphasis on these variations against standard signature of oil film over water within visible spectral bands was reported. This study has evidently shown the requirements of the appropriate digital image processing and treatment to enable absolute signatures derived without any uncertainties. These signature variations were then used to formulate the calibration matrices for spills identified from satellite images, hence contributing a value-adding processing for spill monitoring system.

Reference

Bhangale, U., Durbha, S. S., King, R. L., Younan, N. H. and Vatsavai, R., 2017. High performance GPU computing based approaches for oil spill detection from multi-temporal remote sensing data. Remote Sensing of Environment, PP. 202, 28-44.

Cheng, Y., Li, X., Xu, Q., Garcia-Pineda, O., Andersen, O. B. and Pichel, W. G., 2011. SAR observation and model tracking of an oil spill event in coastal waters. Marine pollution bulletin. 62(2), pp. 350-363.

Clark, R. N., Swayze, G. A., Leifer, I., Livo, K. E., Kokaly, R., Hoefen, T., Lundeen, S., Eastwood, M., Green, R. O. and Pearson, N., 2010. A method for quantitative mapping of thick oil spills using imaging spectroscopy. US Geological Survey Open-File Report. 1167(2010), pp. 1-51.

Fiscella, B., Giancaspro, A., Nirchio, F., Pavese, P. and Trivero, P., 2000. Oil spill detection using marine SAR images. International Journal of Remote Sensing. 21(18), pp. 3561-3566.

Garcia-Pineda, O., Holmes, J., Rissing, M., Jones, R., Wobus, C., Svejkovsky, J. and Hess, M. (2017). Detection of Oil near Shorelines during the Deepwater Horizon Oil Spill Using Synthetic Aperture Radar (SAR). Remote Sensing. 9(6), pp. 567.

Guo, W., 2017. Development of a statistical oil spill model for risk assessment. Environmental Pollution, pp. 230, 945-953.

Mullin, J. V., 2017. Advances from Arctic Oil Spill Response Research. Proceedings of the 2017 International Oil Spill Conference Proceedings: International Oil Spill Conference. 1487-1506.

Powers, R., Ramirez, L., Redmond, C. and Elberg, E., 1966. Geology of the Arabian Peninsula. Geological survey professional paper, PP. 560, 1-147.

Roy, D. P., Ju, J., Lewis, P., Schaaf, C., Gao, F., Hansen, M. and Lindquist, E., 2008. Multi-temporal MODIS–Landsat data fusion for relative radiometric normalization, gap filling, and prediction of Landsat data. Remote Sensing of Environment. 112(6), pp 3112-3130.

Spaulding, M. L., 2017. State of the art review and future directions in oil spill modeling. Marine pollution bulletin. 115(1-2),pp. 7-19.

Toming, K., Kutser, T., Laas, A., Sepp, M., Paavel, B. and Nõges, T., 2016. First experiences in mapping lake water
	quality parameters with Sentinel-2 MSI imagery. Remote Sensing. 8(8),pp. 640.
Topouzelis, K. N.,2008. Oil spill detection by SAR images: dark formation detection, feature extraction and
classification algorithms. Sensors. 8(10),pp. 6642-6659.

APPLICATION OF LANDSAT DATA FOR COASTLINE CHANGES DETECTION IN SOUTH MINAHASA REGENCY

Munawaroh Munawaroh (1), Ibnu Sofian (1), Aninda W. Rudiastuti (1)

[1] Indonesia Geospatial Information Agency,
Jl. Raya Bogor Km. 46, Cibinong – Jawa Barat, 16911, Indonesia
Email: munawaroh@big.go.id; ibnu.sofian@big.go.id; aninda.wisaksanti@big.go.id

ABSTRACT: Coastline mapping becomes the fundamental of environmental monitoring and management of coastal areas. Utilizing satellite data and ocean models, coastline change analysis was carried on. The purpose is to analyze the coastline changes at South Minahasa bay, North Sulawesi Province. Simulated wave height nearshore were performed using SWAN. The wave height data is used to perceive the effect on the erosion and accretion patterns of the shoreline changes. Coastline mapping and its change detection was performed using Landsat data interpretation results from 1972 to 2017. Simulation results showed that significant wave heights in Amurang Bay ranged from 0.4m to 1.2m in extreme conditions, while the extreme significant wave height at Tanjung Kapitu and Waeontulap reaches 2m. Thus, the Amurang Bay area is relatively safe from erosion and abrasion due to high waves, which is inversely proportional to the conditions in Tanjung Kapitu and Waeontulap which are susceptible to erosion and abrasion due to high waves. The results of the wave height simulation are also consistent with the results of the shoreline change analysis that conducted using multi-temporal Landsat series (Sensor TM and OLI TRS) with Modified Normalized Difference Water Index (MNDWI). The result of analysis from Landsat data shows that the length of the coastline of South Minahasa Regency in 1972, 1990, 1995, 2000, 2015, and 2017 respectively are 93,156.4 meters; 95,424.83 m, 94,985.60 m; 96,360.69 m, 95,257.98 m, and 95,386.20 m. Coastline changes mostly occur in the cape region of South Minahasa Regency, while in Amurang Bay is relatively stable. Thus, coastal protection by mangrove reforestation becomes the best solution in maintaining coastal, to prevent erosion and abrasion in the cape and Amurang Bay.

1.   INTRODUCTION

The coastline is susceptible to change, due to natural processes such as erosion and changes in sea level and also related to human activities. The process of coastline change is a process that occurs continuously, which includes the erosion process (erosion) as well as the addition (accretion) caused by sedimentation, longshore current, ocean waves, and land use (Vreugdenhil, 1999). These factors can indicate the tendency of shoreline changes to erode (increase to land) or increase (jutting into the sea) (Arief et al., 2011).

Coastline mapping is fundamental in environmental monitoring and coastal area management (Moore, 2000; Aedla et al., 2015; Lira et al., 2016; Liu, 2017). The use of remote sensing data such as Landsat TM imagery for mapping and coastal area management has been carried out (El-Askary et al., 2014; Pu & Bell, 2017; Sulong & Ismail, 2002). Open water information extraction using ratio of 2 multispectral channels, namely visible and near-infrared (NIR) waves, which were first introduced by McFeeters (1996), from now on referred as Normalized Difference Water Index (NDWI). In its development, the flaw of the NDWI method found since noise produced in the extraction of the territorial waters. Jensen (2004) then modified the method by replacing the NIR channel to MIR (Middle Infrared) Modification of the NDWI method resulted in feature extraction of open water areas more accurate One application of the NDWI Modification method is shoreline extraction previously using this method included Dong (2014) and Liu (2017). Dong (2014) used the Modified NDWI method to automate the coastline mapping, China and measure the changes using the Landsat imagery series. Liu (2017) uses the MNDWI method for shoreline extraction using Landsat 8 OLS TRS in the coastal area of Zhejiang, China.
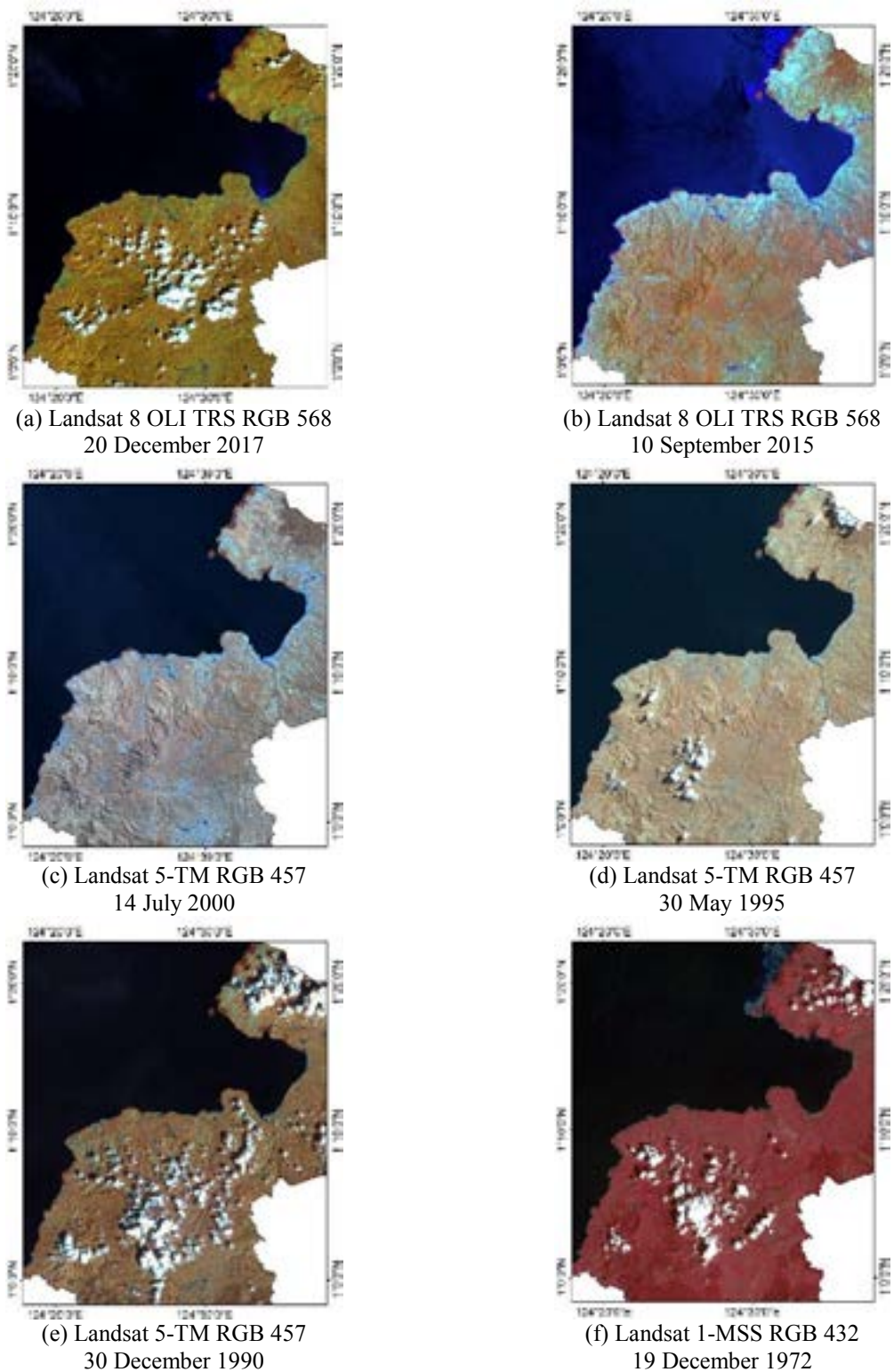
Beach in South Minahasa Regency is one of the dynamic coastal areas. The beach is affected by seasonal winds. Global climate change causes changes in seasonal patterns by strengthening and weakening seasonal winds. Thus, it may have an impact on the changing ecosystems of coastal areas and coastlines in South Minahasa Regency. Coastline changes analysis was carried out using multi-temporal satellite data from 1972 to 2017; further, it will be used to generate input into coastal conservation in South Minahasa.

2.   METHODS

2.1   Image Interpretation

The data used in this study are Landsat 5 and Landsat 8 satellite images which are downloaded from the USGS page. **Table 1** presented the detail of data used in this research. The overlaid result of Landsat images which have been

corrected radiometrically and geometrically, and integrated with the administrative boundaries of South Minahasa Regency are presented in **Figure 1**.

(a) Landsat 8 OLI TRS RGB 568
20 December 2017

(b) Landsat 8 OLI TRS RGB 568
10 September 2015

(c) Landsat 5-TM RGB 457
14 July 2000

(d) Landsat 5-TM RGB 457
30 May 1995

(e) Landsat 5-TM RGB 457
30 December 1990

(f) Landsat 1-MSS RGB 432
19 December 1972

Figure 1. RGB imageries from Landsat (MSS, TM, ETM+ and OLI) and each acquisition date.

The Landsat imagery has a relatively good geometric correction. Moreover, the radiometric correction needs to be done in order to correct pixel values that do not match the object's reflection value. The equation used for radiometric correction is as follows (Danoedoro, 2012):

$$L'_\lambda = \frac{c \quad x}{c \quad d}$$

(1)

Lλ   = spectral radiation before correction,
X   = sensor's point of view and
θ   = zenith angle of the sun

Table 1. Data Specification

No	Data	Acquisition Time	Source
1	Landsat 1 MSS Path 112 Row 059	19 December 1972	USGS
2	Landsat 5 TM Path 112 Row 059	10 December 1990 / 30 May 1995 / 14 July 2000	
3	Landsat 8 OLI Path 112 Row 059	10 September 2015 / 20 December 2017	
4	Indonesia Topographic Map	2016	Badan Informasi
5	High-Resolution Imagery	2015	Geospasial (BIG)

2.2   Coastline extraction

The coastline extraction method use Modified NDWI by Jensen (2004). In this study, the coastline extraction was based on the edge of the water. Thus, it was ignoring the tidal factors and others. The Modified NDWI equations are:

$$M = \frac{G - M}{G + M} \qquad (2)$$

Where:
MIR   = Middle Infrared (band 5 on Landsat 5-TM and band 6 on Landsat 8 OLI TRS)

These calculations resulted in (1) The object of water will have a positive value because water absorbs MIR waves; (2) The object of the built area will have a negative value, and (3) Land and vegetation objects remain negative because they reflect MIR waves. The extraction results then are used for shoreline extraction by converting the polygon to the line **(Figure 2)**

2.3   Wave Height Simulation

Wave data is needed to determine wave height in the bay area in South Minahasa, and its effect on erosion patterns and accretion to shoreline changes. For the local scale, we use SWAN or Simulating Waves Nearshore (Booij et al., 1999; Rogers et al., 2003). The model will estimate wave parameters in coastal, lake and estuary areas from known wind conditions, bathymetry and currents. The swan model is nesting on the Wavewatch model on a regional scale, using Wavewatch output outcome data at a regional scale. Calculations in the SWAN model use the equilibrium wave action density formed in spherical coordinate as follows:

$$\frac{\partial N}{\partial t} + (cos\emptyset)^{-1}\frac{\partial}{\partial\emptyset}(C_\emptyset cos\emptyset N) + \frac{\partial}{\partial\lambda}(C_\lambda N) + \frac{\partial}{\partial\sigma}(C_\sigma N) + \frac{\partial}{\partial\theta}(C_\theta N) = \frac{S_{tot}}{\sigma} \qquad (3)$$

Where :
$$C_\theta = \frac{C_g cos\theta + U}{R} \qquad (4)$$
$$C_\lambda = \frac{C_g sin\theta + U}{Rcos\emptyset} \qquad (5)$$
$$C_\sigma = \frac{\partial}{\partial t}(\sqrt{gk}\tanh(kd) - k.U \qquad (6)$$

$$C_\theta = \frac{C_g sin\theta tan\emptyset}{R} + \frac{1}{kR}\left(sin\theta\frac{\partial}{\partial\emptyset} - \frac{cos\theta}{cos\emptyset}\frac{\partial}{\partial\lambda}\right)(\sqrt{gk}\tanh(kd) - k.U) \qquad (7)$$

Wave height estimates from altimetry data are used to validate the SWAN model results. The accuracy test

implemented using altimeter data at the openf sea near to the mouth of the South Minahasa bay, located at 124.5°E and 1.5°N. Overall, the research method divided into three stages; image processing, coastline extraction, and analysis of coastline changes (**Figure 3**).

| (a) | (b) | (c) |
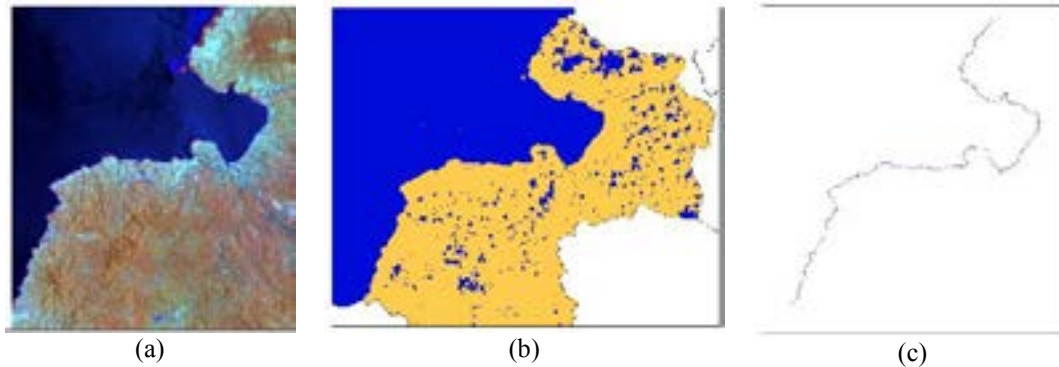
Figure 2. Coastline extraction process: (a) Radiometric correction; (b) Calculation of NDWI Modification Method; and (c) Extraction of coastlines with polygon to line conversion.
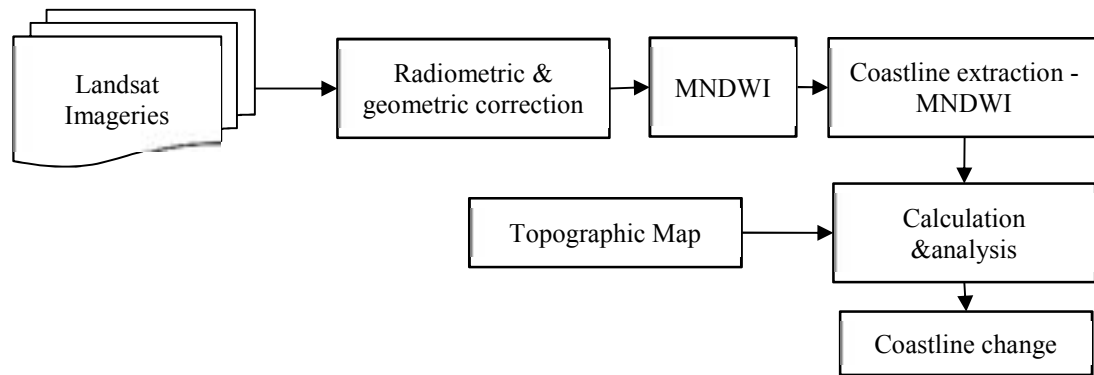
Figure 3. Flowchart

3.   RESULTS AND DISCUSSIONS

3.1   Coastline changes

Based on Landsat imageries acquired in 1972, 1990, 1995, 2000, 2015, and 2017, the coastlines in South Minahasa Regency produced using Modified NDWI. From overlay analysis of those yearly images, the coastlines changes at South Minahasa clustered in a map as shown on **Figure 4**.

By the Landsat imageries interpretation result for coastline in Minahasa Selatan Regency, in 1972 it was 93,156.41 meters for length, in 1990, 1995, 000, 2015 and 2017 respectively change to 95.424.83 meters, 94.985.60 meters, 96.360.69 meters, 95,257.98 meters, and 95,386.20 meters. Thus, the rate of change in the coastline of South Minahasa Regency from 1972 to 1990 was 126.02 meters per year; 1990 to 1995 was -87.85 meters per year; from 1995 to 2000 it was 275.02 meters per year; 2000 to 2015 was -61.21 meters per year; and 2015 to 2017 is 327.92 meters per year. Furthermore, the average rate of change in the coastline of South Minahasa Regency from 1972 to 2017 is 65.38 meters per year. The changes in the length of the coastline in Minahasa Regency are presented in **Table 2**.
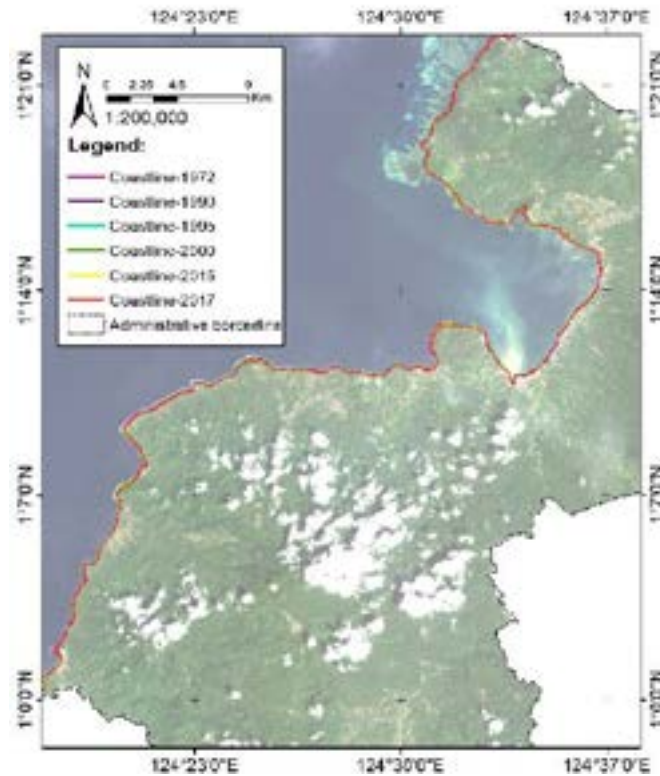
Figure 4. The coastline changes at South Minahasa Regency in 1972, 1990, 1995, 2000, 2015, dan 2017.

Table 2. Coastline changes at South Minahasa Regency from 1990 - 2017

No	Year	Coastline (m)	Coastline changes (m)	Rate of changes (m/year)
1	1972	93,156.41		65.38
2	1990	95,424.83	2,268.43	
3	1995	94,985.60	-439.23	
4	2000	96,360.69	1,375.09	
5	2015	95,442.57	-918.12	
6	2017	96,098.42	655.85	

Source: Analysis result, 2018

As seen in **Figure 4,** the coastline of South Minahasa Regency is relatively stable, although in some locations process of accretion and erosion occurred. **Figures 5** showed that there had been coastal erosion in Tanjung Kapitu and Tanjung Waeontulap where is indicated by the retreat of the coastline towards land from 1972 to 2017.

(a)

(b)
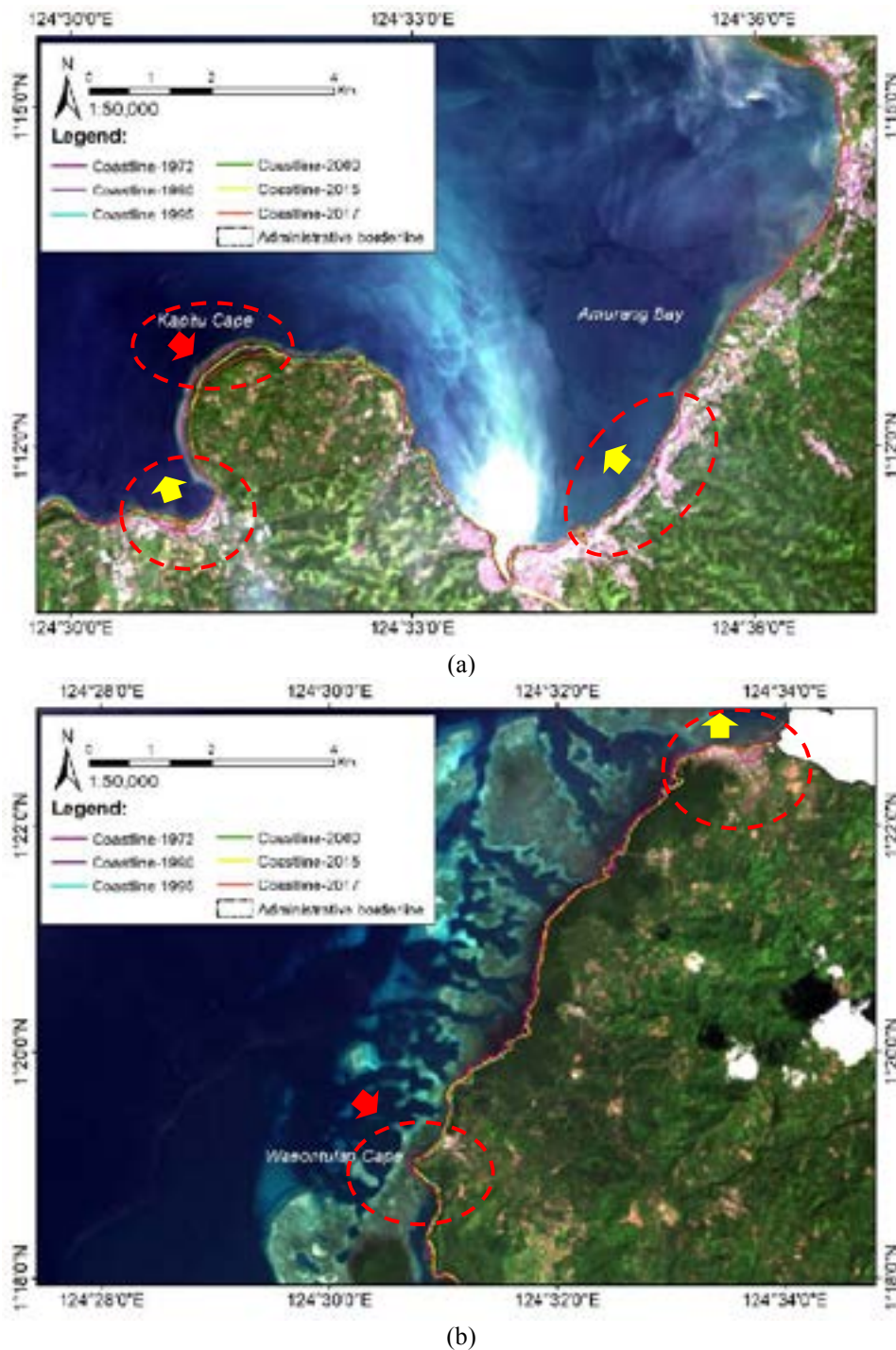
Figure 5. The coastline changes at (a) Amurang Bay and (b) Waeontulap Cape in 1972, 1990, 1995, 2000, 2015, dan 2017.

3.2 Significant Wave Height

For supporting the analysis of coastline changes in South Minahasa Bay, we use the result of Significant Wave Height model between 2008 – 2017. In general, significant wave height in the Amurang Bay is high in November to February and low in June to October. In January, wave propagation moved from the north with varying heights, where waves were significant, high in the open seas and low in the bay.

Figure 6 shows the wave height and direction taken from the daily average in January for ten years, from 2008 to 2017. Wave height in the Sulawesi Sea (**Figure 6(a)**) ranged from 1m to 2m and weakened when it reached the coast. Significant wave heights reaching 2m or more occur in the Makassar Strait and weaken after entering the Sulawesi Sea after being reduced by the distribution of the small outermost islands such as Sangihe Island, Talaut and others.
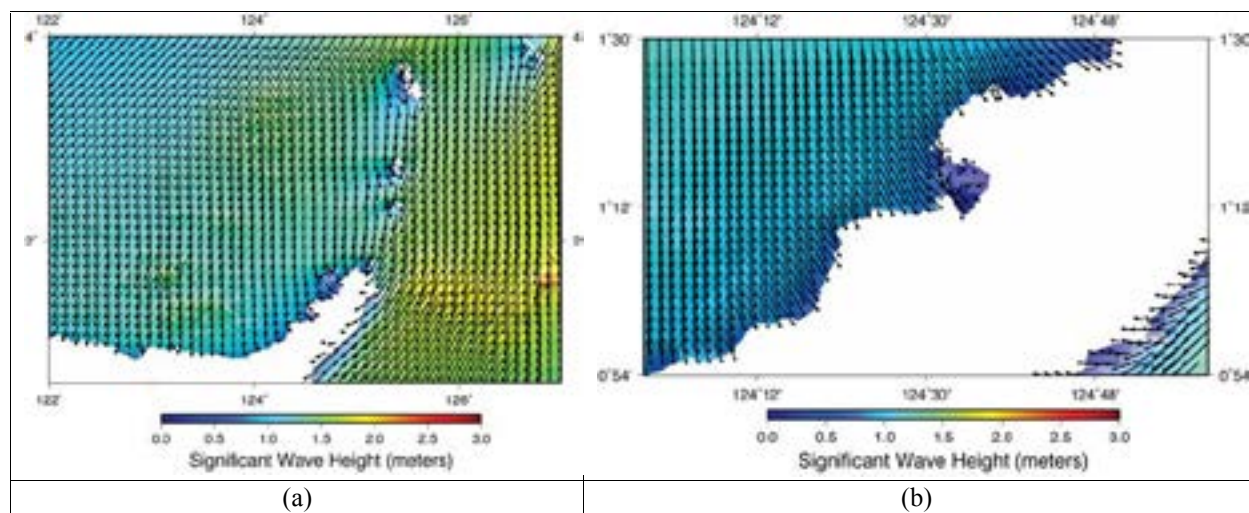
Figure 6. Spatial distribution of significant wave heights in (a) Sulawesi Sea around Manado and Gorontalo Provinces and (b) Amurang Bay and Surroundings, in January

Furthermore, in general, the distribution of significant wave height around the Amurang Bay in January attached in **Figure 6 (b).** The wave height in the Amurang Bay is lower than the surrounding area, due to a reduction in the change in depth and obstruction from Tanjung Waeontulap. The Tanjung Kapitu and Waeontulap regions are more exposed to the influence of wave height.
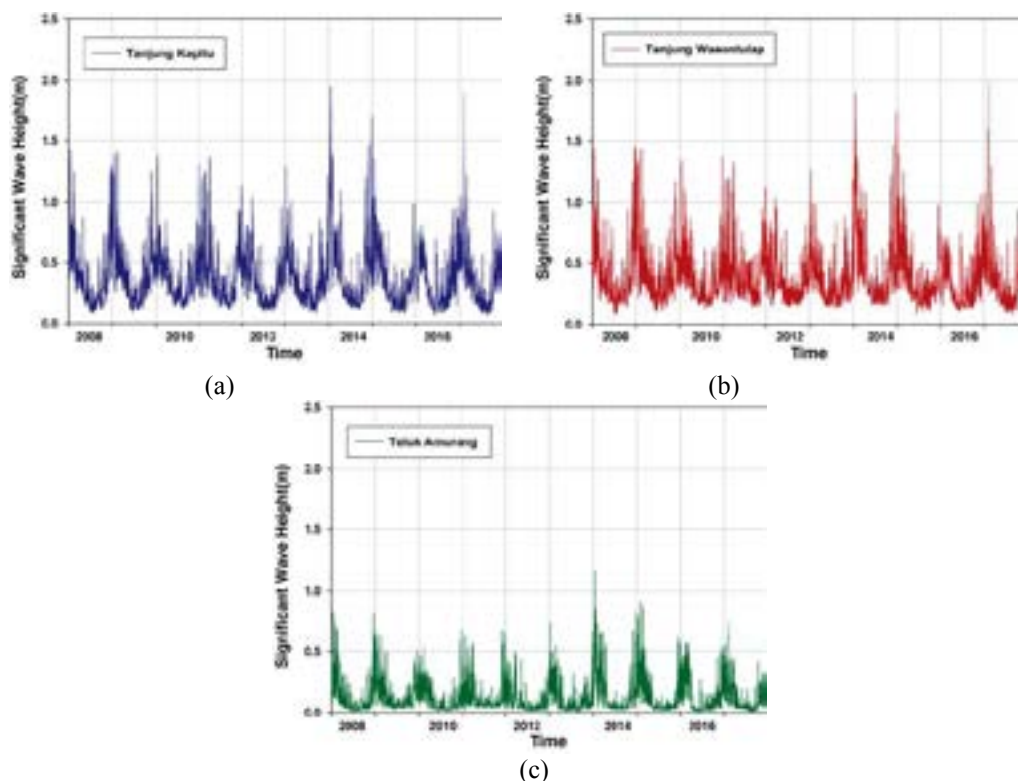
Figure 7. Time-series of significant wave height in (a) Kapitu Cape, (b) Waeontulap Cape, and (c) Amurang Bay from January 1, 2008, to December 31, 2017

Figure 7 shows significant time-series wave height in 3 locations, namely Kapitu Cape, Amurang Bay, and Waeontulap Cape. From the ten years of simulation results, it can be concluded that the significant wave height in the Bay of Amurang is relatively low with the height at extreme conditions of around 1.2m, while in Tanjung Kapitu and Waeontulat, significant wave height reaches 2m. Furthermore, by using conversions commonly used to obtain the maximum wave height from significant measurable waves, the maximum wave height in Teluk Amurang is 1.8m, Tanjung Kapitu and Waeontulap reach 2.9m.

Spatial distribution of extreme wave height in the waters around Manado and Gorontalo Provinces that occurred on January 17, 2014, is shown in Figure 12. From **Figure 8 a** and **b**, it can be seen that the extreme wave height in the

open sea north of Manado, extreme significant wave height reaches more than 3m. While around the coast, extreme wave height only ranges from 2 - 2.5m. Furthermore, in Figure 12b, it can be seen that extreme significant wave heights are high in the Tanjung Kapitu and Waeontulap regions, and low in the Amurang Bay, which only reaches 1.2m. The extreme significant wave height distribution pattern means that the Kapitu Cape and Waeontulap areas are more exposed to wave height compared to the coastal areas in the Amurang Bay. The results of the distribution analysis and the significant wave height pattern on the potential for erosion and abrasion are also getting along with the results of the analysis of shoreline changes using satellite data.

| (a) | (b) |
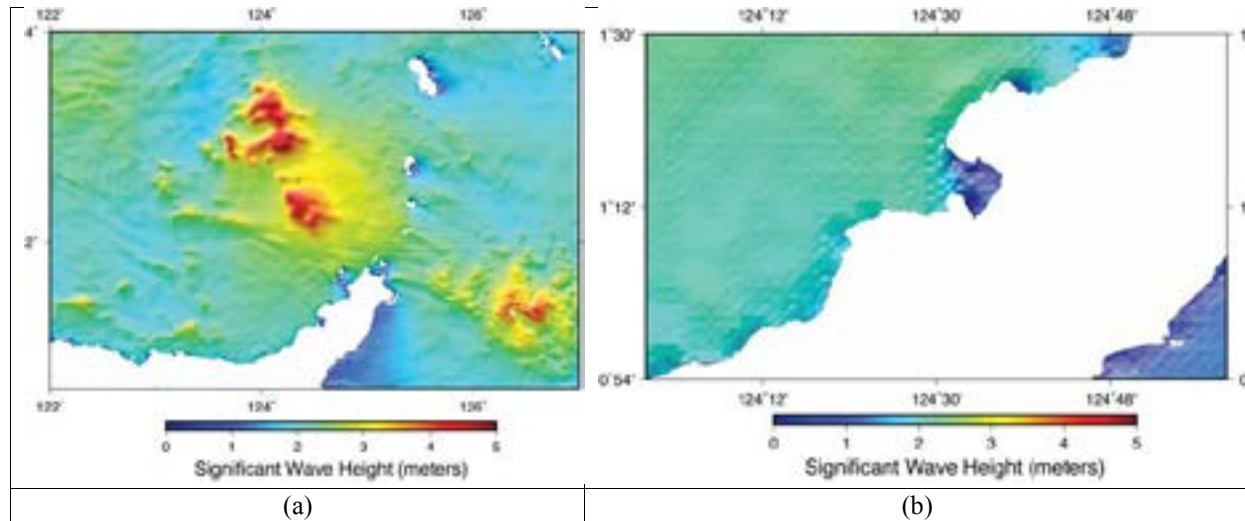
Figure 8. Spatial distribution of extreme wave height on January 17, 2014, in (a) Sulawesi Sea and (b) Amurang Bay, in January

3.3. Coastal Condition of South Minahasa

In the Tanjung Batutinoung and Tanjung Kayuwale region, the sedimentation process lasts in the estuary of the Pamurapa River and several other large river estuaries. Thus, these locations tend to experience accretion or additional land. As shown in **Figure 9**, in general, the area built by the retaining wall showed significant shoreline changes between 1972 to 2017. Meanwhile, the image also shows that some areas that experience accretion are locations that are overgrown by mangroves. Mangroves are the essential ecosystem that lives in intertidal areas. Mangrove vegetation is complex, consisting of a collection of mangroves themselves and shrubs, which serves to reduce the hazards that exist in coastal areas such as tidal floods and exposure to waves. Mangroves are also a buffer zone between land and sea. Furthermore, mangroves also often contribute to wave attenuation in areas that do not have strong wave restraint structures (Quartel et al., 2007), and for coastal stabilization (Alongi, 2008).

Due to the bio-physics functions, besides being able to retain waves, Mangrove forests also act as catchers of sedimentary material (Horstman et al., 2014). So that the planting and conservation of mangrove forests (mangroves) is one of the disaster mitigation efforts undertaken to prevent coastal erosion. Mangrove forests can reduce height and wind and wave energy that passes through it, which in turn reduces the ability of sediment erosion and destruction of building structures such as sea walls and dikes. During high tide, when seawater with waves enters mangroves, high waves lose energy as they pass through steep roots and branches above the ground and their height rapidly decreases, between 13 and 66% more when passing 100m of mangrove forests. When this happens, ocean waves will lose the ability to explore the seabed and transport sediment. Mangroves also reduce wind speed at sea level to prevent the propagation or formation of ocean waves (Wetland International and Nature Conservacy, 2014).

The level of mangrove forest density has a significant effect on its ability to reduce wave and wind energy. The denser the mangrove forest with many roots that stick in the air (aerial roots) will inhibit the rate and propagation of waves. When the water gets more profound, and the number of aerial roots decreases due to water submergence, the branch function and the dense canopy switch function into a wave inhibitor. Thus, mixed mangrove forests concerning age and different sizes and densities of aerial roots will be very useful in reducing wind and ocean energy and wave height (Wetland International and Nature Conservacy, 2014). Based on the existence of several mangrove locations in the Amurang Bay means the condition of Amurang Bay coastal fitted for mangrove forest conservation. Pictures of the existing mangrove that remain around the bay shown in **Figure 10**.

Coastal protection from extreme waves, tidal wave, and other threats could be run by two approaches. Firstly, by hard protections such as build wall, jetty, breakwater, and so on. Secondly, by coastal conservation, that means use mangroves presence or thirdly combine those two methods. In term of doing coastal protection, accomplished planning based on scientific research accompanied by environmental impact analysis and the socio-economic impact

is mandatory. Otherwise, failure will resulted as the outcomes such as under-design, over-design due to the inappropriate method that implements. The example of coastal protection which carried on without good planning shown in **Figure 11**. Suggestion on mangrove rehabilitation are preferred for coastal protection especially in Amurang Bay.
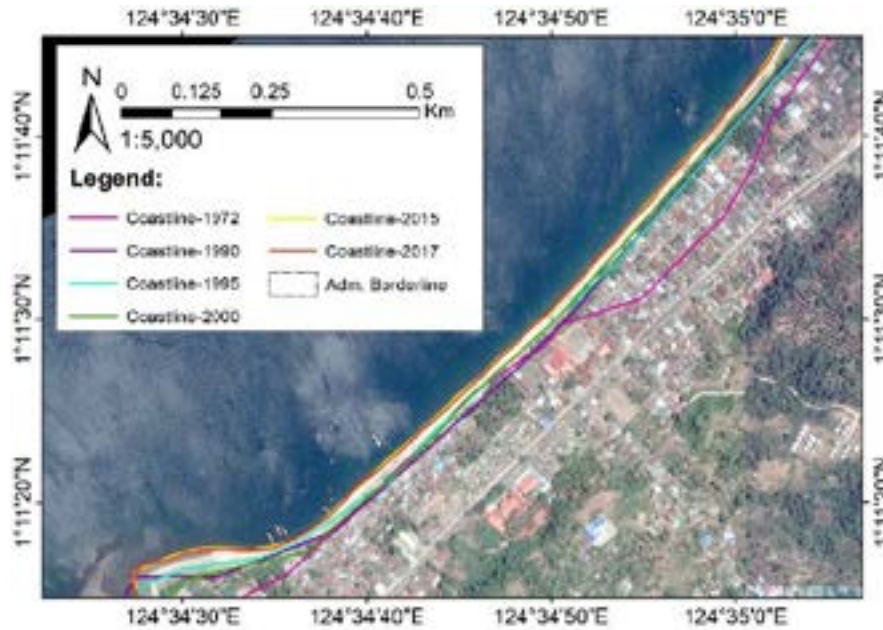
Figure 9. The coastline changes at part of Amurang Bay (zoom) in 1990, 1995, 2000, 2015, dan 2017.

Figure 10. Mangrove at Teluk Amurang

Figure 11. Inappropriate wall built for coastal protection. (Source: Latief, 2015)

4.　　CONCLUSION

Significant wave height in Amurang Bay ranges from 0.4m to 1.2m in extreme conditions. Meanwhile, the extreme significant wave height in Tanjung Kapitu and Waeontulap reaches 2m. Thus, the Amurang Bay area is relatively safe from erosion and abrasion due to high waves, which is inversely proportional to the conditions in Tanjung Kapitu and Waeontulap which are vulnerable and experience erosion and abrasion due to wave height.

Coastline changes in South Minahasa Regency mostly occur in the Tanjung area, while in the Amurang Bay region it is relatively stable and there is an increase in the coastline in several locations. Furthermore, coastal protection by replanting mangrove forests predicts as the best solution to safeguarding coastal ecosystems and preventing erosion and abrasion in Tanjung and Amurang Bay areas. Mangrove forests function as a reduction in energy and wave height, as well as ocean tides and binder of sedimentary material from river-flow. Based on the results of the analysis and the condition of the coastal ecosystem, mangrove forest conservation is the recommended protection option in Amurang Bay.

5.　　REFERENCES

El-Askary, H., Abd El-Mawla, S. H., Li, J., El-Hattab, M. M., & El-Raey, M. 2014. Change detection of coral reef habitat using Landsat-5 TM, Landsat 7 ETM+ and Landsat 8 OLI data in the Red Sea (Hurghada, Egypt). International Journal of Remote Sensing, 35(6), 2327–2346. https://doi.org/10.1080/01431161.2014.894656

Pu, R., & Bell, S. 2017. Mapping seagrass coverage and spatial patterns with high spatial resolution IKONOS imagery. International Journal of Applied Earth Observation and Geoinformation, 54, 145–158. https://doi.org/10.1016/j.jag.2016.09.011

Sulong, I., & Ismail, A. 2002. Mangrove Mapping Using Landsat Imagery and Aerial Photographs : Kemaman District ,. East, 135–152. https://doi.org/10.1023/A:1020844620215

Aedla, R.; Dwarakish, G.S.; Reddy, D.V. 2015. Automatic shoreline detection and change detection analysis of Netravati-Gurpur River mouth using histogram equalization and adaptive thresholding techniques. Aquat. Procedia 2015, 4, 563–570.

Alongi, D.M., 2008. Mangrove forests: resilience, protection from tsunamis, and responses to global climate change. Estuar. Coast. Shelf Sci. 76, 1–13.

Arief, M., Winarso, G., Prayogo, T. 2011. Kajian Perubahan Garis Pantai Menggunakan Data Satelit Landsat di Kabupaten Kendal. Jurnal Penginderaan Jauh Vol. 8 2011:71-80.

Danoedoro, Projo. 2012. Pengantar Penginderaan Jauh Dijital. Yogyakarta, Andi Offset

Davidson-Arnott, Robin. 2010. An Introduction to Coastal Processes and Geomorphology. United States of America by Cambridge University Press, New York

Hasselmann, D. E., M. Dunckel, and J. A. Ewing, 1980, Directional wave spectra observed during JONSWAP 1973, J. Phys. Oceanography, 10, 529-549.

Horstman, E.M, C.M. Dohmen-Janssen, P.M.F. Narra, N.J.F. vanden Berg, M. Siemerink, S.J.M.H. Hulscher, 2014, Wave Attenuation in Mangroves: A quantitative approach to field observations, Coastal Eng. 94, 47-62.

Jensen, J.R., 2004, Introductory digital image processing: A remote sensing perspective, 3rd edition. NJ: Prentice Hall Logicon Geodynamics, Inc.

McFeeters, S.K., 1996, The Use Of Normalized Difference Water Index (NDWI) In The Delineation Of Open Water Features. International Journal Of Remote Sensing, 17, Pp.1425–1432.

Moore, L.J. 2000. Shoreline mapping techniques. J. Coast. Res. 2000, 16, 111–124.

Lira, C.P.; Silva, A.N.; Taborda, R.; de Andrade, C.F. 2016. Coastline evolution of Portuguese low-lying sandy coast in the last 50 years: An integrated approach. Earth Syst. Sci. Data 2016, 8, 265–278.

Quartel, S., Kroon, A., Augustinus, P.G.E.F., Van Santen, P., Tri, N.H., 2007. Wave attenuation in coastal mangroves in the red river delta, Vietnam. J. Asian Earth Sci. 29, 576–584.

Rundquist, D., Lawson, M., Queen, L. And Cerveny, R., 1987, The Relationship between the Timing of Summer-Season Rainfall Events and Lake-Surface Area. Water Resources Bulletin, 23, pp. 493–508.

Tolman, H. L. And D. V. Chalikov, 1996, Source terms in a third-generation wind wave model, J. Phys. Oceanography, 26, 2497-2518.

Tolman, H. L., 2009, User manual and system documentation of WAVEWATCH-III version 3.14, NOAA/NWS/NCEP, 110 pp.

Vreugdenhil, C. B., 1999. Transport Problems in Shallow Water, Battle-neeks and Appropriate Modelling. Twente University, Department of Civil Engineering and Management. Seminar on Sediment Transport.

Wetland International and Nature Conservacy, 2014, Mangroves for Coastal Defense: Guidelines for Coastal Managers and Policy Makers, 38pp.

ACRS 2018
THE 39TH ASIAN CONFERENCE ON REMOTE SENSING
KUALA LUMPUR
"REMOTE SENSING ENABLING PROSPERITY"

COMMERCIAL SESSION
SESSION 01, 02, 03 & 04

SESSION	COMMERCIAL SESSION (CS01)

NO.	SPEAKER
1.	Spectris Pte. Ltd.
2.	GPS Lands (M) Sdn. Bhd.
3.	Surrey Satellite Technology Limited
4.	Beijing Space View Technology Co. Ltd.
5.	Sky-Shine Corporation (M) Sdn. Bhd.
6.	Twenty First Century Aerospace Technology (Asia) Pte. Ltd.

SESSION	COMMERCIAL SESSION (CS02)

NO.	SPEAKER
1.	Ground Data Solutions R&D Sdn. Bhd.
2.	KQ GEO Technologies Co. Ltd
3.	Infinity Success Solutions Sdn. Bhd.
4.	Remote Sensing Technology Center of Japan (RESTEC)
5.	National Space Organization
6.	RedPlanet Solutions Sdn. Bhd.

SESSION	COMMERCIAL SESSION (CS03)

NO.	SPEAKER
1.	Beijing PIESAT Information Technology Co. Ltd.
2.	ST Electronics (Satcom & Sensor Systems) Pte Ltd
3.	LARS Department of Geoinformatics, University of Seoul

SESSION	COMMERCIAL SESSION (CS04)

NO.	SPEAKER
1.	PCI Geomatics
2.	SI Imaging Services
3.	Japan Aerospace Exploration Agency (JAXA)
4.	Daejeon International Marketing Enterprise

GLOCAL MONITORING SESSION
SESSION 01

SESSION	GLOCAL MONITORING SESSION (GMS01)
CHAIRMAN	PROF. DR. KOHEI CHO

NO.	SPEAKER
1.	**Prof. Dr. Kohei Cho** General Secretary Asian Association on Remote Sensing
2.	**Prof. Osamu Uchida** Department of Human and Information Science, School of Information Science and Technology, Tokai University, Japan Title: Integration of Twitter-Based Disaster-Information Sharing System and Satellite Imagery
3.	**Dr. Husi Letu** Institute of Remote Sensing and Digital Earth, Chinese Academy of Sciences (CAS), Beijing, China
4.	**Dr. Enrico C. Paringit** University of the Philippines Diliman, Philippines
5.	**Mrs. Norizan Abdul Patah** Malaysian Remote Sensing Agency

ACRS 2018
THE 39TH ASIAN CONFERENCE ON REMOTE SENSING
KUALA LUMPUR
"REMOTE SENSING ENABLING PROSPERITY"

ASIAN SATELLITE PROGRAMME SESSION
SESSION 01

SESSION	ASIAN SATELLITE PROGRAMME SESSION (ASPS01)
CHAIRMAN	DR. LAL SAMARAKOON

NO.	AGENDA	SPEAKER
1.	China	**Prof. Dr. GU Xingfa** Director Institute of Remote Sensing and Digital Earth (RADI), Chinese Academy of Siences Title : Earth Observation in China
2.	China-Taipei	**Dr. Kuo-Hsien Hsu** Associate Researcher Satellite image division, National Space Organization, National Applied Research Laboratories (NSPO)
3.	India	**Dr. Sameer Saran** Secretary Indian Society of Remote Sensing (ISR)
4.	Indonesia	**Mr. Wahyudi Hasb** Head of Dissemination Division Satellite Technology Center, National Institute of Aeronautics and Space (LAPAN)
5.	Japan	**Dr. Shiro Ochi** Visiting Scientist Japan Aerospace Exploration Agency (JAXA)
6.	Malaysia	**Prof. Ir. Dr. Md. Azlin Md Said** Universiti Sains Malaysia
7.	Thailand	**Dr. Warinthorn Kiadtikornthaweeyot** Researcher Geo-Informatics and Space Technology Development Agency (GISTDA)
8.	Korea	

ACRS 2018
THE 39TH ASIAN CONFERENCE ON REMOTE SENSING
KUALA LUMPUR
"REMOTE SENSING ENABLING PROSPERITY"

ERRATUM

This paper entitled **"Supervised Classification for Flood Extent Mapping Using Sentinel-1 Radar Data"** was presented at TS43- Disaster Management (2), 17th October 2018, ACRS2018.

Supervised classification for flood extent identification using sentinel-1 radar data

Gomathi.M
CIIRC-Jyothy Institute of Technology
Bengaluru,India
goms.mano1992@gmail.com

*Dr.Geetha Priya.M
Department of ECE
CIIRC-Jyothy Institute of Technology
Bengaluru,India
geetha.sri82@gmail.com

Krishnaveni. D
Department of ECE
CIIRC-Jyothy Institute of Technology
Bengaluru,India
mailkveni@gmail.com

The flood inundated studies are important now days due to the uncontrolled human settlements and development in flood plains especially in countries like India. To regularize the development in flood plains it is needed to identify the flood prone zones by mapping the recurrently inundating areas. The objective of the paper is to map the flood inundation areas in parts of Godavari river basin using Sentinel-1A data during monsoon time. The Godavari basin is chosen as study area as it has witnessed severe flood impacts on its flood plains in recent years. Supervised classification techniques including random forest, KNN, KD-tree KNN, maximum likelihood and minimum distance to mean are used as classifiers in this study for extraction of water pixels and to quantify the amount of area flooded. On an average it has been estimated that an area of 27.4412 Km^2 is flooded excluding existing water bodies before monsoon for the given subset of Sentinel-1A image covering a part of Godavari delta region using different classifiers. It has been observed that random forest classifier has performed in flood area extraction with nearly less than 1% variation with respect to the average value of extracted flood area obtained in comparison with other classifiers for a given set of data and training samples.

Key words: Sentinel-1A, supervised classification, Flood extent, Godavari, classifiers

I. INTRODUCTION

Dynamic climate provokes most weather related disasters which are supplementary to other natural disasters. In most of the cases, weather related disasters are unpredictable even though the preparedness is essential. Flood is one of the disasters which can develop slowly or suddenly like flash flood. Due to its widespread and frequent nature, it is one of the devastating natural hazards. The immediate impacts of flood are damage to properties, environment and also includes loss of human life. Human civilization had grown on the river banks where human habitation is high even today. So to minimize their exposure to hazards, the warning system is essential. Fore casting of any natural disaster needs (a) examination of history of disaster (b) re-occurrence intervals of disaster events (c) extrapolation of the collected data for future probabilities [1].

A. River basins and causes of flood

The causes for flood events based on the examinations of historical events are indicated below

- Inadequate drainage system, capacity of streams, catchments and rivers to carry away the rainwater.
- Obstruction in the paths of rivers caused by landslides, siltation, erosion process.
- Unplanned / uncontrolled development of urban areas in flood plains.
- Failure of manmade hydrological structures like dams, reservoirs.
- Heavy rain falls in coastal areas due to cyclone formation

Over the past years, many parts of India have witnessed almost smaller to larger flooding events. Uncontrolled developments in flood plain areas due to the increased population have led to the worst situations during flooding. The major flood prone zones in India include a) Ganga Basin b) Brahmaputra and Barak basins c) Deccan river basins. The flood prone zones in India are shown in Fig. 1 Deccan plateau consist of 6 major rivers namely Narmada, Tapti, Mahanadi, Krishna, Godavari and Kaveri.The source of the Deccan river flow is based on its monsoon rainfall. In dry seasons the flow will be relatively less or even dry. Deccan plateau has emerged as one of the most flooding areas in recent years, especially in human habitat areas due to insufficient drainage and silting action [2].

Fig. 1: (a) Deccan rives (b) flood prone zones in India

A Deccan River is further classified as eastern flow or western flow river depending on its direction of flow. Western Flow Rivers are Narmada, Tapti, and eastern flow rivers are Mahanadi, Krishna, Godavari and Kaveri. The eastern flow rivers irrigate fertile land and are thus called "the rice bowl of India". Krishna and Godavari flow along the eastern coastal zones, so the tropical cyclones are the recurrent event in these areas.

Disaster prone areas need to be monitored using remote sensing techniques, to prevent massive destruction and damage. In this paper an attempt has been made to study various classification techniques of flood inundation mapping using SAR data for Godavari delta region during September 2016.

B. Remote sensing applications in flood studies

Recording of extreme flood events at river gauging stations for future predictions are difficult to perform with currently available instruments. Remote sensing is a boon to disaster

management studies due to availability of wide range of data with its unrivalled properties.

It rectifies the scarcity of data due to the hampers in climatic conditions with its wide spread EM spectrum range as shown in Fig. 2.The temporal resolution of remotely sensed data is useful in analysis of damage assessment on post events and also helpful in change detection analysis with its multi temporal data.
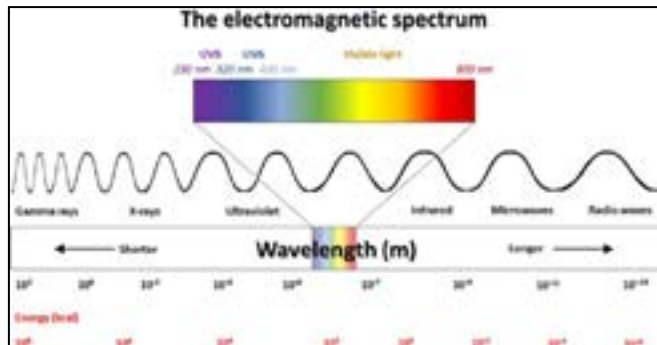

Fig. 2*:* Electromagnetic spectrum

C. *Microwave remote sensing in flood studies*

The flood events occur mainly during monsoon seasons making optical data unsuitable for flood related studies due to cloud coverage. Microwave data are reliable in providing the data during weather related disasters to overcome the limitations in optical remote sensing. The longer wavelength range (1cm-1m) tends to penetrate into dust, haze and clouds. It is less affected by atmospheric scattering which is accumulated in optical wavelengths. Due to the unique characteristics of SAR, delineation of water surface studies can be performed effectively. The specular reflection of reflected radar signal is used to identify the water surface which is associated with its low back scatter values. In specular reflection, the incidence angle is equal to the reflected angle and the backscatter will be away from the sensor (Fig. 3).
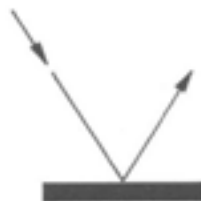
Fig. 3: Specular Reflection

The backscatter coefficient varies with the type of surface and properties of the target. In flood inundation analysis, the existing water bodies can be delineated with pre-event data images using the low back scatter values (dB). During the flood event with mixed reflection and diffused reflection (low dB values) it is possible to identify the affected areas [3].

II. STUDY AREA

A.*Godavari river*

Godavari river (Fig. 4) basin is located in Deccan plateau of southern India covering some parts of Telangana and Andra Pradesh state. It is the second largest river in India and longest river in south India. River basin covers an area of 3,105 Km^2.It flows across the Deccan Plateau in the

eastward direction, turning southeast, dividing the Godavari district into east and west. Later it splits into two distributaries that debouch into a large river delta flowing into the Bay of Bengal. The total length of Godavari from its origin to outfall into the Bay of Bengal is 1,465 km. It is also well known for its mangrove formation. The multipurpose project named Sriram Sagar is located in parts of Godavari river. Table 1 gives the glimpse of Godavari river. An attempt is made in this paper, to study flood affected areas in the Godavari delta region as it is an area under development and recurrently affected by north east monsoon which brings one third of rainfall in Andhra Pradesh.

Fig. 4 Godavari River basin

TABLE I - DESCRIPTION ABOUT THE STUDY AREA

Description	Details
River length	1,465 Km.
Basin area	3,13,812 Sq.
Population	142 million.
States covered in basin	Maharashtra,Orissa,Karnataka,Telangana, Andhra Pradesh
Mean annual water discharge	2,830 m^3/s
Climate of study area	Semi-arid to monsoonal
Min & max temperature of river basin	Min 8º to 9º(winter(Dec-Jan)) Max 45º- 46º(summer(Apr-May))

B. *Flood scenario in Godavari*

In India, Godavari is one of the frequently flooding river as the flood producing monsoons are periodic. Monsoon seasons in Godavari river basins bring heavy to very heavy rain falls [4]. Intensity and duration of rainfall plays a vital role in major floods. Some of the Major flood events in the Godavari river are listed below:

- **September9, 2014** – West and East Godavari districts were affected by flood. Water reached a level of 14.30 feet. As a relief remedy 13.54 Lakh cusecs of flood water discharged into Bay of Bengal. It left 15 families homeless and 20 people trapped in the flood.

- **Sep 18, 2015-** Heavy rain in its origin district, Nasik brought heavy flood in Godavari river.10 people were stacked in Sangameshwar temple

- **August 3, 2016-** Heavy rain in Nasik district triggered the Godavari river basin flood. Water was logged in Ramwadi, Boorpatti, Bhandi bazar, Safar bazar and some of slum pockets. Temples located on the banks of the river submerged due to flood.

- **September 26,2016**- The heavy rain in parts of Telangana made over 1000 people from six villages homeless, and 17people died due to rain related incidents. The images of flood affected region are shown in Fig.5.

Fig. 5: Flood affected areas

It has been analyzed from previous flood events that the major inducing factor for flood in Godavari is heavy rain fall. This area is studied during the days it is flooded with heavy rainfall. The days on which flood was induced by intense rainfall and inflow into the river are 14th Aug 2006, 03rdNov2006, and 04thOct2009, 26th September as collected from the IMD website (5).

For the present study, September, 2016flood event is being considered. The main reason for the flood is heavy rainfall followed by huge inflow into the Godavari river. The rainfall data from IMD website is shown in Fig.6.which infers heavy rain fall in the month of September, 2016(retrieved from IMD website).The highly affected areas in the flood were Adilabad, Nizamabad, Karimnagar, Warangal and Khammam of Andhra Pradesh Fig.7.
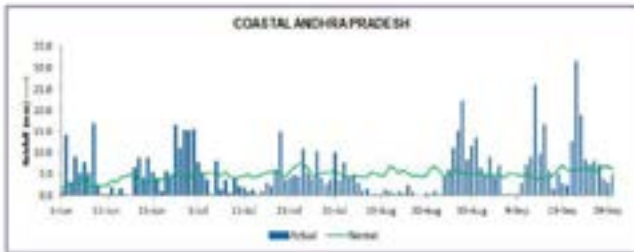
Fig.6.Rainfall data from IMD report [5]

(a)   (b)

Fig. 7: Flood image of (a) Khammam district (b) Singoor reservoir Medak district of Telangana during September 2016

III. SATELLITE DATA

ESA Sentinel satellites are a part of Copernicus program aiming autonomous observations of earth. Each mission of the sentinel series focuses on six branches viz. land, emergency response, atmosphere, ocean, security and

climate change. The timely and easy accessibility of the data from Sentinel satellites allows us to use it for the disaster management studies effectively [6]. The sentinel mission information is shown in the table II.

TABLE II- SENTINEL 1MISSION

Description	Details
Satellite	Sentinel 1A & B (European Space Agency-ESA)
Sensor	SAR
Frequency	5.4 GHz
Wavelength	7.5 – 3.75 cm
Year of launch	2014
Repeat cycle	175 orbits in 12 days
Modes of image acquisition(spatial resolution)	Strip map mode(5x5 m), Interferometry wide swath (5x20 m),Extra wide swath(25x100 m),Wave mode(5 x20 m)
Levels of data	Level-0(raw data),Level 1(GRD and SLC), Level 2

Sensitivity of backscatter signal to water surface makes the sentinel data useful effectively for flood related studies. The images have been downloaded from Alaska Satellite facility website (ASF). The Earth Observation (EO) data exploitation is performed in the open source software SNAP (Sentinel Application Platform) which contains ESA tool Box. A pair of Sentinel-1 SAR images are used (Fig.8) to perform the inundation analysis as per the dataset given in table III.
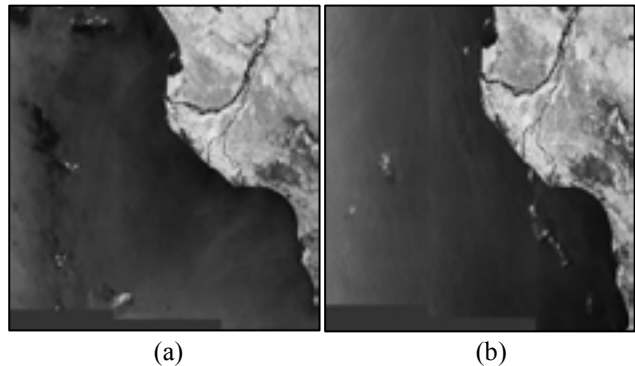

(a)   (b)

Fig.8: (a) Sentinel-1 data pre- event data on 26th September 2016.
(b) post- event data on 14th September 2016.

TABLE III-SENTINEL 1 DATASET

DESCRIPTION	PRE EVENT	POST EVENT
Acquisition date	29-06-2016	14-09-2016
Beam mode	IW	IW
Path / frame	19/538	19/534
Ascending/descending	Descending	Descending
Polarization	VV	VV
Absolute orbit	13216	13041
Data product type	Level 1 GRD	Level 1 GRD

IV.METHODOLOGY

The preprocessing of a SAR image is necessary to obtain the high accuracy details in the application of mapping. The preprocessing steps may vary with the recent demands on the levels of data [7]. When analysis is carried out for change detection and image processing it is necessary to

ensure the compatibility between spectral, spatial, and temporal properties of satellite imagery. The preprocessing steps involved in sentinel 1A level 1 data are shown in the Fig.9.
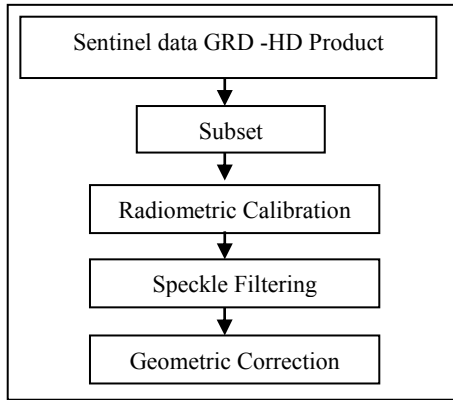

Fig.9: Preprocessing of sentinel 1 data

A. subset

The process of extracting the area of interest is called subsetting. By performing the subset the file size will reduce and it tends to improve the processing time of the image. The reduction of data is also known as subsetting process which reduces computational times and the memory utilization of algorithms. The subset image of study area is shown in Fig.10.
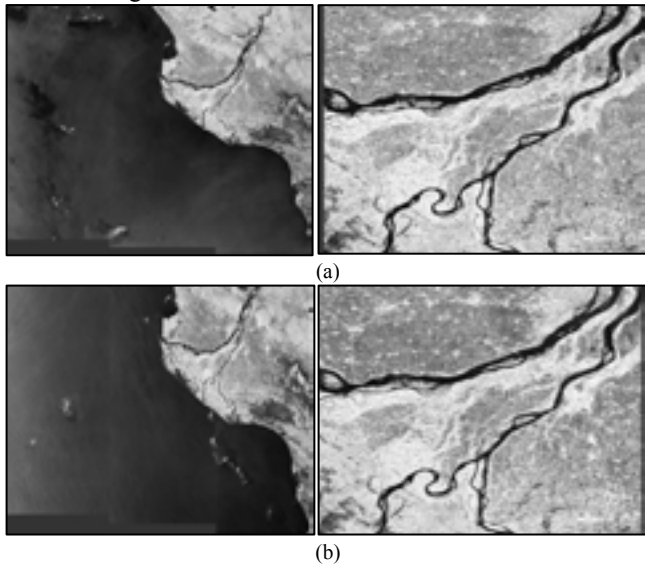
Fig.10: subset image (a) pre -event (b) post- event

B. Radiometric calibration:

The radiometric calibration rectifies the errors that occur due to sun's azimuth, elevation and atmospheric conditions. The difference in energy levels of target feature can be easily identified using its radiometric properties. It describes the actual content and spatial structure of image by arrangement of pixels. Radiometric correction is the process of converting DN (Digital Number) into radar backscattering coefficient (σ_0 in dB). It is also known as energy ratio of the total energy to energy reflections in diffused angles reflected away from radar sensor. The pixels representing water bodies will have lower backscattering coefficient σ_0 (Sigma naught) compared to other features. Fig.11.shows the radiometrically calibrated images.
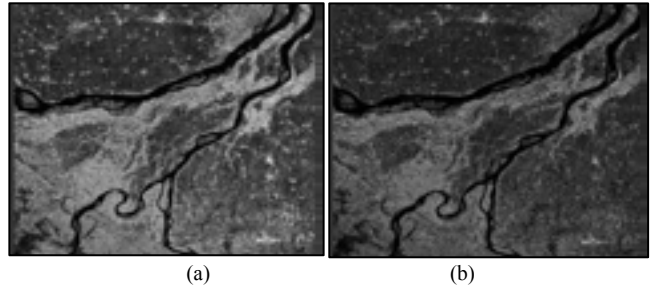
Fig.11: Sigma naught image of (a) pre event (b) post event.

C. speckle filtering

Speckle noise degrades the quality of the image and makes interpretation of features more difficult. Filtering uses the standard deviation of the pixels within a local box surrounding 3 pixels each to calculate a new pixel value. Lee-sigma is widely used and its performance is better than any other filters. For present study Lee-sigma filter with 3x3 window sizes has been used. The speckle filtered image is shown in Fig.12. The window size of speckle filter is indirectly proportional to the quality of image. The multilooking criterion is used prior to choosing the window size.Multilooking is performed while collecting the data. It is also called as the subdivision of radar beam which is used for averaging the pixels values.
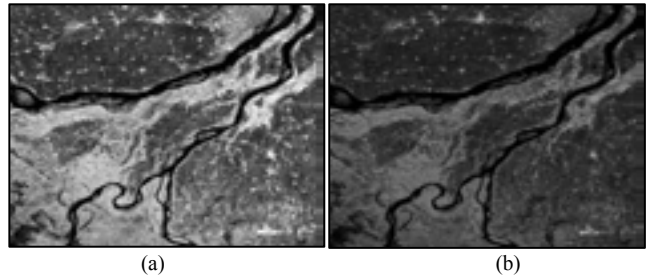

Fig.12: Speckle filtered image (a) pre- event (b) post event.

D.Geometric Correction:

Geometric correction need to be performed to remove the effects of side looking geometry of SAR images. To perform the overlay analysis with different sensor based products it is very essential to correct it geometrically. The process consists of conversion of 2D image from sensor coordinates to map coordinates. The SRTM 3 Sec DEM (Digital Elevation Model) along with Bilinear interpolation is used for geometric correction. The geometrically corrected image is shown in Fig.13.
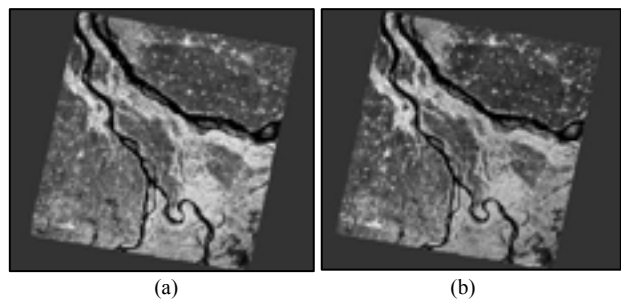

Fig.13: Geometrically corrected image of (a) pre- event (b) Post event

In this study to extract the water pixels, supervised classification methods are used. The classifiers used are Random forest classifier, KD tree KNN classifier, KNN

classifier, Minimum distance and Maximum likelihood classifier. The overall SAR data processing is shown in Fig.14.
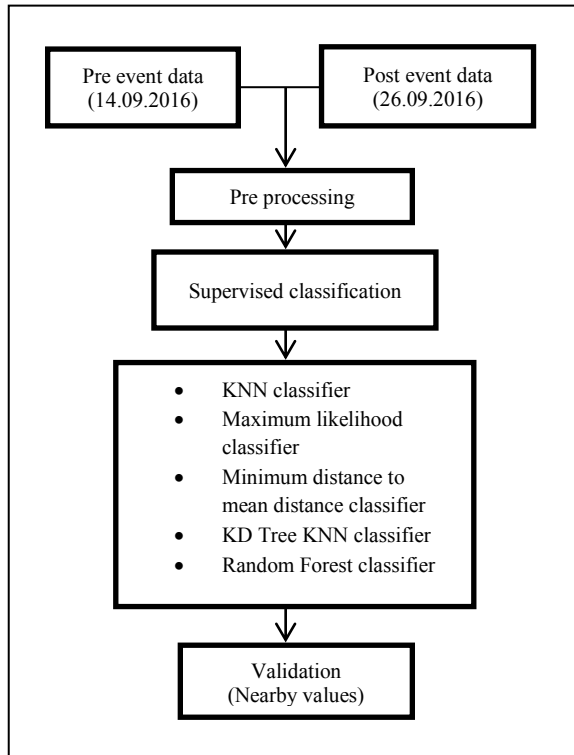

Fig.14. SAR data processing for flood extent mapping

E. Supervised Classification

In supervised classification, information from a preprocessed SAR image is extracted based on the feature of pixels in two stages (training and classification of pixels).User defined training samples (contains training vector) such as vegetation, settlements, water bodies were used to train the classifier. Based on its highest probability, each pixel is classified under a particular feature in the given classification stage. It is the process done by an analyst to identify homogenous group of pixels by assigning the training data sets. It will classify the pixels by collecting the signatures that creates feature classes. This is performed by algorithms and regression analysis with the signature of training data. While creating the training data set, it should be compared with the features present in reference imagery or ground truth verification for improving the reliability [8]. Due to layover and foreshortening misclassification could lead to erroneous results sometimes.

F. Random forest classifier

Random forest classifier method classifies the pixels randomly. Training of datasets consists of creating decision trees. Based on the training dataset same values of pixels is matched randomly (by averaging).The performance will be based on the number of generated decision trees. Random forest classified images were shown in Fig.15.It gives nearby results even though it has minimum decision trees. Standard deviation (σ) of the predictions from individual regression tress on x' is given by (1)

$$\sigma = \sqrt{\frac{\sum_{b=1}^{B}(f_b(x')-f)^2}{B-1}} \qquad (1)$$

Where, B= Number of samples, f_b = regression tree on X_b&Y_b.
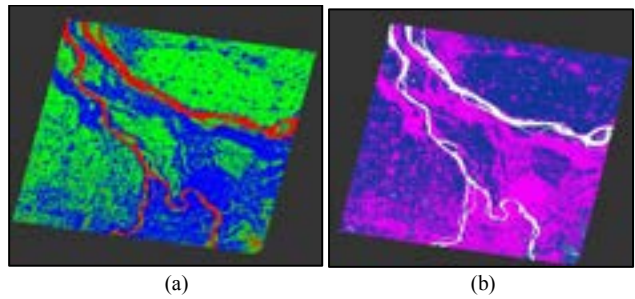

Fig.15: Random forest classified image (a) pre event (b) post event

G.KNN classifier

The KNN classification is based on the distance between training pixels and k values (Information retrieval). This is a reliable method used for image classification. It purely depends on k values which is closer to the query. KNN classified images are shown in Fig.16.The classification performance may interrupt more number of mixture pixels other than the assigned training data sets. It follows the Euclidean distance function given by (2).

$$\text{Euclidean distance} = \sqrt{\sum_{i=1}^{k}(x_i-y_i)^2} \qquad (2)$$

Where the difference between two variables (x_i-y_i) value is taken, squared and summed for k number of pixels.
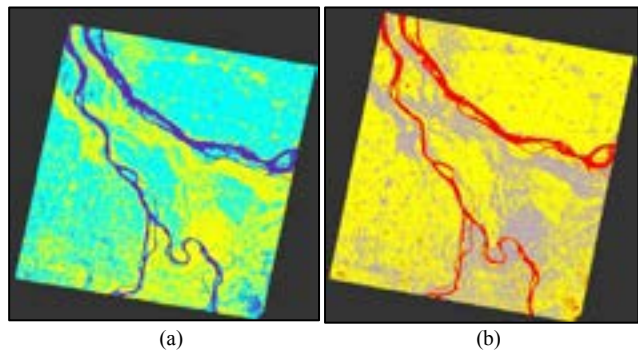

Fig.16- KNN classified image (a) pre event (b) post event

H.KD-Tree KNN classifier

KD-tree KNN (K dimensional tree) classifier help in organizing and partitioning the data points based on specific conditions. The implementation of this algorithm is similar to distance metrics "Hamming distance". The KD-Tree KNN classified images are shown in Fig.17.
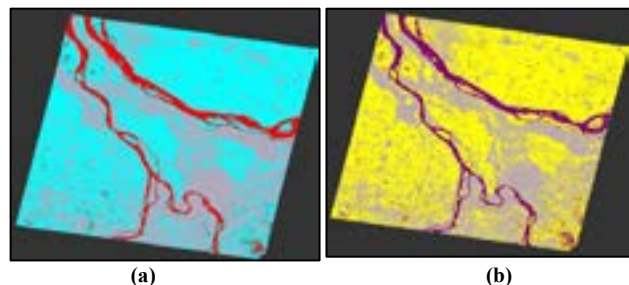

Fig.17- KD -Tree KNN classified image of (a) pre event (b) post event

I. Maximum Likelihood classifier

In maximum likelihood classification, threshold value for each class is obtained from the training data sets (signature). Depending on the threshold value the classifier calculates the likelihood probability of a given pixel that belongs to a specific class. All pixels are classified to a particular class

3281

based on the highest probability of the assigned class [9].Maximum likelihood classified images are shown in Fig.18. In this classification the water pixels are identified based on:

- Bayes theorem of decision making
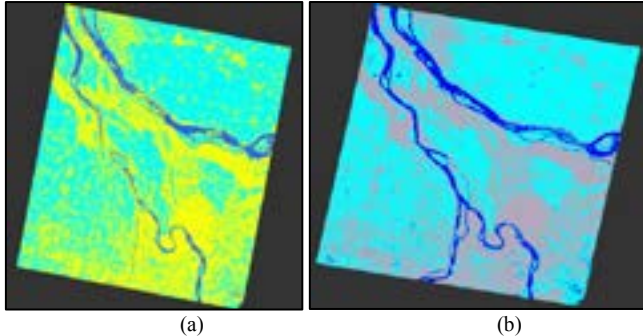- Statistical analysis algorithm estimating the mean variances of given training data sets.

(a)   (b)

Fig 18- Maximum likelihood classified image (a) pre event (b) post *event*

J.Minimum distance to mean classifier

In minimum distance to mean classification, the vector created on the basis of known features is represented by its mean vector [10]. The training sets used in the previous classifications are applied in this classification. The algorithm will cluster the same group of pixels of nearby values. Minimum distance to mean classified images are shown in Fig.19.The classification algorithm ignores the pixels with distance greater than threshold.

The spectral response of training pixels intensifies the degree of variance and covariance. The pixels are allotted to a particular class based on the closest mean using decision function given in (3).

$$D_i(X) = X^T \mu_i - \frac{1}{2}\mu_i^T \mu_i \qquad (3)$$

Where X= pixels; $D_i(X)$ class with closest distance; μ_i= mean of the class i

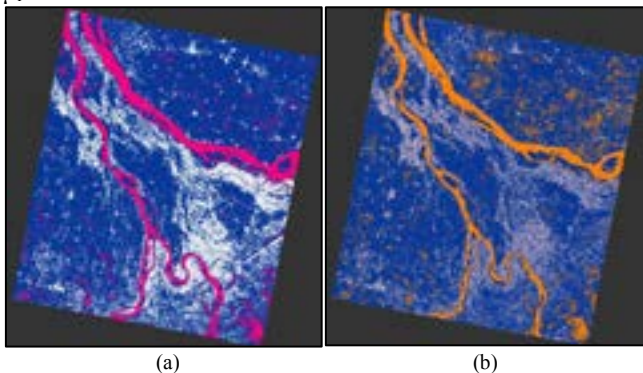(a)   (b)

Fig.19- Minimum distance to mean classified image (a) prevent (b) post event

V.RESULTS

In this paper, Sentinel-1 data has been used to identify the flood inundated areas using supervised classification techniques. The overall process involved in the classifiers is to cluster the pixels and classify the water pixel which has lower backscattered values [11]. The supervised classification techniques such as Random forest classifier, KNN classifier, KD-Tree KNN classifier, maximum likelihood classifier and minimum distance to mean

classifier are used for extraction of water pixels and flood extent area as shown in Fig 20 - 24 respectively.

The extracted water pixels and corresponding area calculated in each classifier for pre and post events are shown in table 4 and Fig 25.The result obtained from different classification techniques with identical dataset with similar training samples has some variations due to differences in the algorithms followed in individual techniques [12]. The classifiers are ranked on the basis of variation of their respective results from average calculated flooded area (27.4412 Km^2) as shown in table 5.
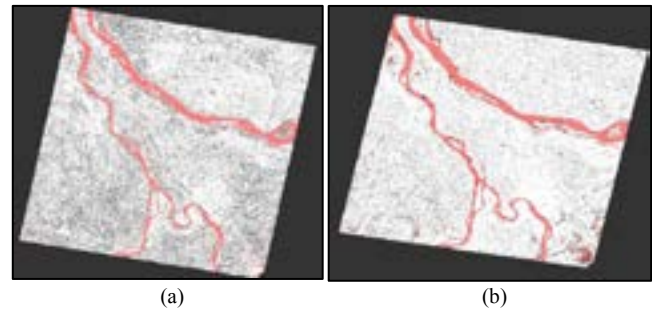

(a)   (b)

Fig 20: Water pixel extracted from Random forest classifier (a) pre event (b) post event
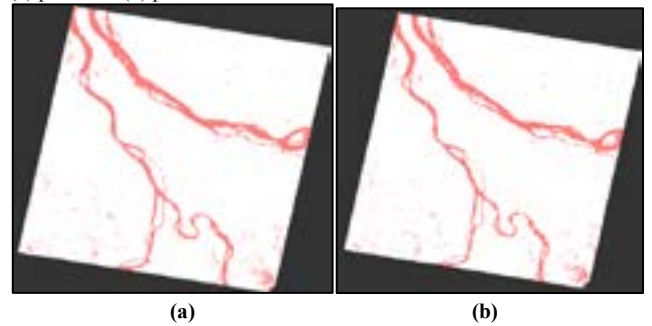

(a)   **(b)**

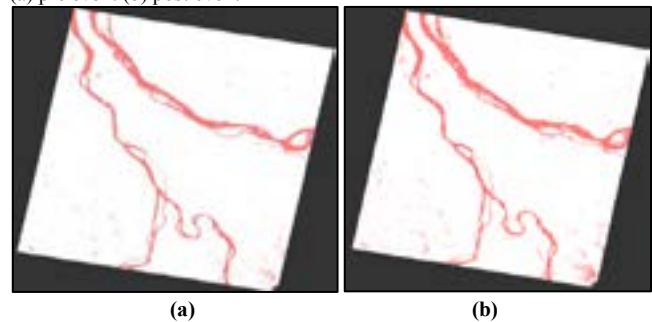Fig 21: Water pixel extracted from KNN classifier (a) pre event (b) post event

(a)   **(b)**

Fig 22: Water pixel extracted from KD –Tree KNN classifier (a) pre event (b) Post event
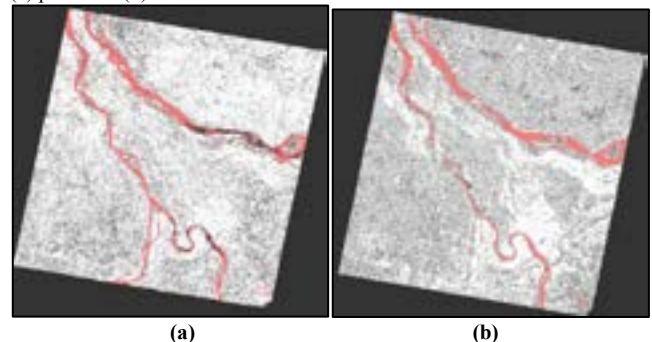

(a)   **(b)**

Fig 23: Water pixel extracted from Maximum likelihood classifier (a) pre event (b) post event
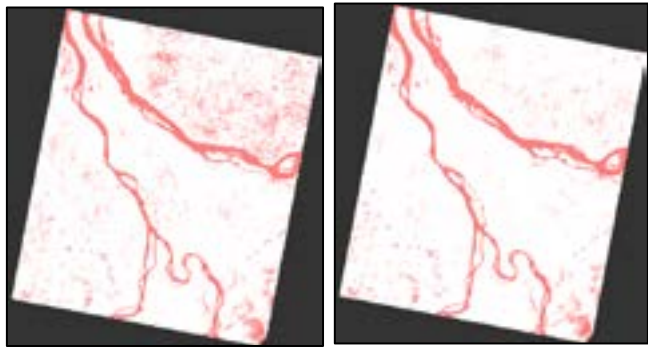
(a)   **(b)**

Fig 24: Water pixel extracted from Minimum distance to mean classifier (a) pre event (b) Post event

TABLE IV- RESULTS OF CLASSIFIERS

| Sl. NO	Classifier	Data	Water pixels	Area (Km^2)
1.	Random forest	pre event	14,03,112.	134.391
		Post event	16,88,715.	161.749
2.	KNN classifier	pre event	9,11,095.	87.255
		Post event	11,59,854.	111.089
3.	KD-Tree classifier	pre event	17,46,999.	167.333
		Post event	17,84,691.	170.946
4.	Maximum likelihood classifier	pre event	14,42,542.	138.169
		Post event	17,23,075.	165.041
5.	Minimum distance to mean classifier	pre event	21,97,955.	210.532
		Post event	27,77,921.	266.061
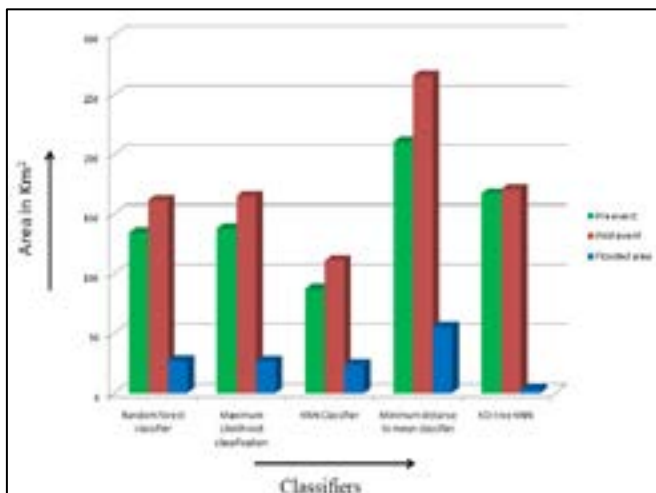
Fig 25   Water area extracted from different classifiers

TABLE V - RANKING OF THE CLASSIFIER

Rank	Classifier	Flooded area in sq.km.
1.	Random forest classifier	27.358
2.	Maximum Likelihood classification	26.872
3.	KNN Classifier	23.834
4.	Minimum distance to mean classifier	55.529
5.	KD-tree KNN	3.613

It has been observed that for KD tree and minimum distance to mean classifier, the variation is more in terms of extracted flood area in comparison with other classifiers results. This might have resulted as, the nearest neighbor water pixel within the constraints is identified by induction on the size

of the KD-tree [13].   In minimum distance to mean classifier, the pixels in nearby range are also classified as water pixels so that the flooded area can be easily identifiable resulting in variations from calculated average flood extent value [10].   KD tree KNN classifier and Minimum distance to mean classifier need more number of training datasets to obtain results effectively, however in this work, the training set provided may not be large enough for certain classifiers.   In random forest classifier the specified number of classification tress(k) and number of prediction variables(m) for the given training set has increased the correlation and strength of the algorithm resulting in better results (Fig 26) in comparison with other classifiers in terms of calculated average flood area [14].
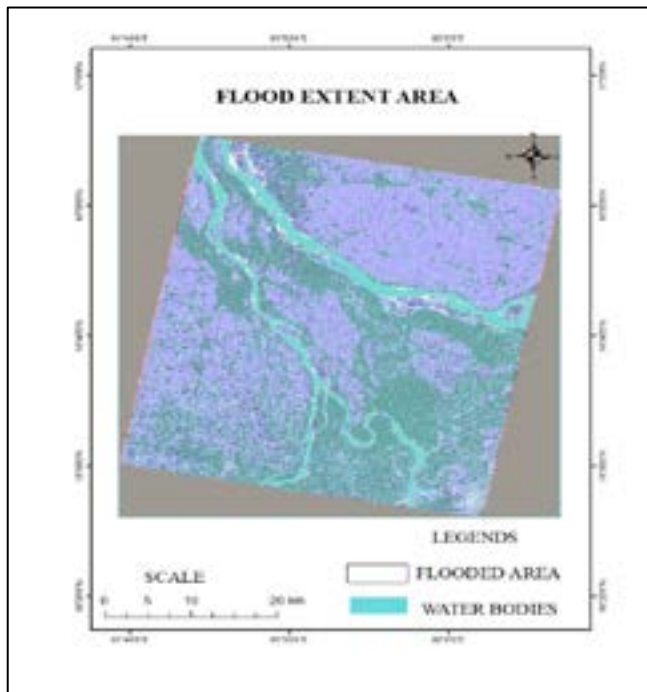

Fig 26   Flood extent map using Random forest classifier

VI.CONCLUSION

Sentinel-1A GRD data for Godavari delta (subset image) has been processed for the flood event during September 2016 using supervised classification techniques. The random forest classifier in supervised classification has been observed to provide better results for the given dataset with a nominal training set in estimating the amount of flood area followed maximum likelihood and KNN classifiers. Misclassification of water pixels with non-water pixels in supervised classification may sometime lead to over or under estimation of extracted flood covered area. This can be avoided in supervised classification by assigning the training data sets with the knowledge of ground truth verification.

ACKNOWLEDGMENT

Karnataka and Sri Sringeri Sharada Peetham, Sringeri, Karnataka, India.

REFERENCE

[1] M.A. Clement, C.G. Kilsby and P. Moore "Multi-Temporal SAR Flood Mapping using Change Detection"

[2] Emmanouil Psomiadis-"flash flood area mapping utilizing sentinel-1 radar data"-Earth Resources and Environmental Remote Sensing/GIS Applications Vol. 10005, 100051G.

[3] Filsa Bioresita , Anne Puissant, André Stumpf and Jean-Philippe MaletA "Method for Automatic and Rapid Mapping of Water Surfaces from Sentinel-1 Imagery"-Remote Sens. 2018, 10, 217;

[4] G NageswaraRao-"Monsoon rainfall and its variability in Godavari river basin" -Proc. Indian Acad. Sci. (Earth Planet. Sci.), 108, No. 4, December 1999, pp. 327-332.

[5] M. K. Purohit and SurinderKaur, "Rainfall Statistics of India – 2016", India meteorological department (ministry of earth sciences) report no. esso/imd/hs/r. f. report/01(2017)/23.

[6] Md.SurabuddinMondal, Nayan Sharma, P K Garg, Bettina Böhm, Wolfgang-Albert Flügel , R D Garg, R P Singh-"Water Area Extraction Using Geocoded High Resolution Imagery of TerraSAR-X RadarSatellite in Cloud Prone Brahmaputra River Valley"Journal of Geomatics -Vol 3 No.1 April 2009.

[7] FilsaBioresita , Anne Puissant , André Stumpfand Jean-Philippe Malet-journal/remote sensing2018, 10, 217 -"A Method for Automatic and Rapid Mapping of Water Surfaces from Sentinel-1 Imagery"

[8] Suresh Babu AV, Shanker M and Venkateshwar Rao V Water Resource Group, National Remote Sensing CentreISRO, Department of Space, Hyderabad - 500 037,"Inventory, mapping and monitoring of surface water bodies".

[9] Kuldeepa, P. K. Garga-"The Role Of Satellite Derived Data For Flood Inundation Mapping Using GIS"-The International Archives of the Photogrammetry, Remote Sensing and Spatial Information Sciences, Volume XL-3/W3, 2015.

[10] A.G.Wacker,D.A.Landgrebe-"Minimum Distance Classification in Remote Sensing"- The Laboratory for Applications of Remote Sensing Purdue University Lafayette, Indiana

[11] Joy Sanyal ,"X.X." Lu- "Application of Remote Sensing in Flood Management with Special Reference to Monsoon Asia: A Review"-Article in Natural Hazards · October 2004DOI: 10.1023/B:NHAZ.0000037035.65105.95.

[12] Assefa M. Melesse, Vijay Nangia, XixiWang-"Hydrology and Water Balance of Devils Lake Basin: Part 1 Hydro meteorological Analysis and Lake Surface Area Mapping"- Journal of Spatial HydrologyVol.6, No.1 Spring 2006 Andrew W. Moore" An introductory tutorial on KD-trees-Extract from Andrew Moore's PhD Thesis: E

JOINTLY ORGANISED

Malaysian Remote Sensing Agency (MRSA),
Ministry of Energy, Science, Technology,
Environment & Climate Change (MESTECC), Malaysia
and
Asian Association on Remote Sensing (AARS)

Strategic Partners

AIRBUS MDA
A MAXAR COMPANY